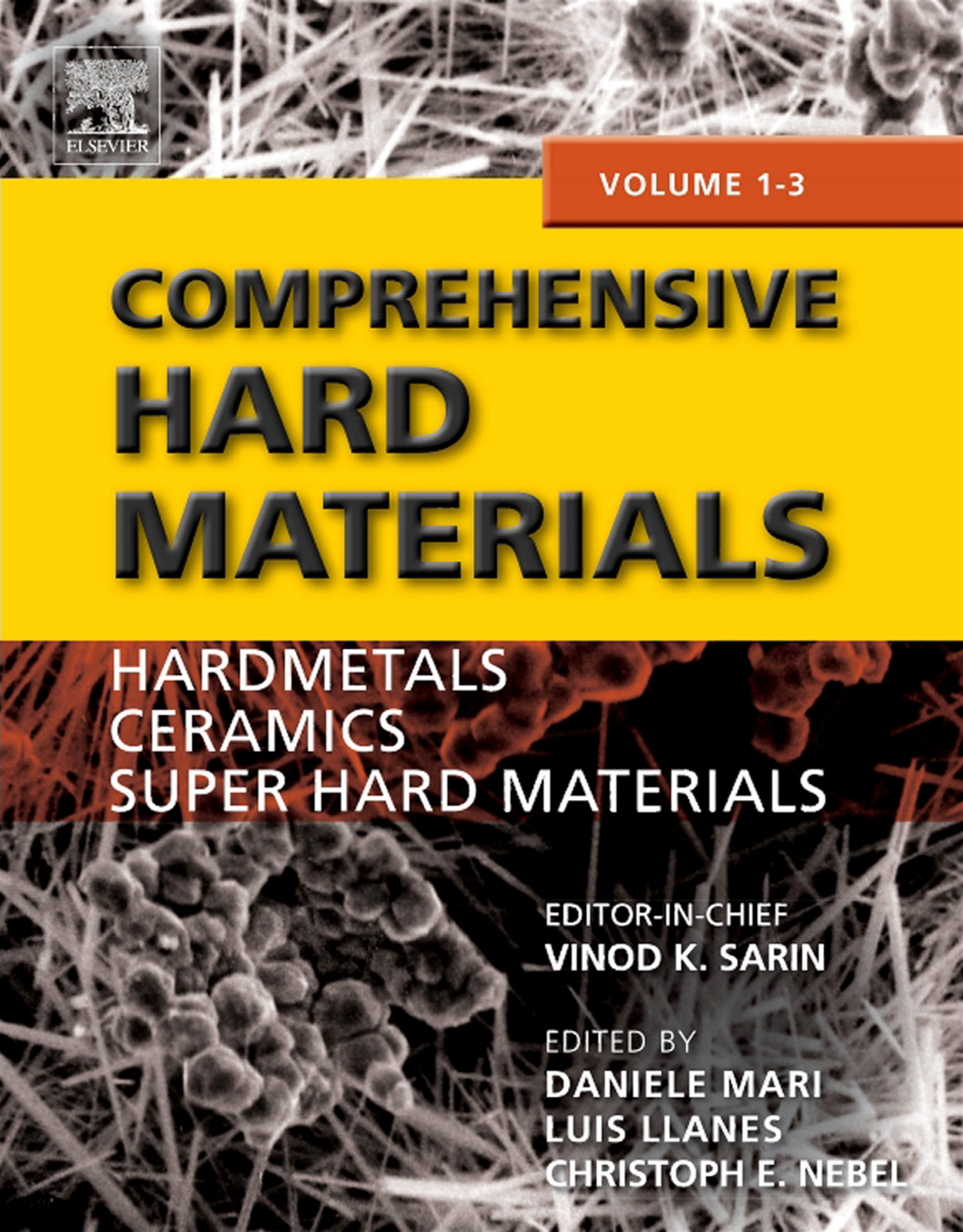

ELSEVIER

VOLUME 1-3

COMPREHENSIVE HARD MATERIALS

HARDMETALS
CERAMICS
SUPER HARD MATERIALS

EDITOR-IN-CHIEF
VINOD K. SARIN

EDITED BY
DANIELE MARI
LUIS LLANES
CHRISTOPH E. NEBEL

COMPREHENSIVE HARD MATERIALS

VOLUME 3

SUPER HARD MATERIALS

This page intentionally left blank

COMPREHENSIVE HARD MATERIALS

VOLUME 3

SUPER HARD MATERIALS

EDITOR-IN-CHIEF
VINOD K. SARIN
College of Engineering, Boston University
Boston, MA, USA

EDITED BY
CHRISTOPH E. NEBEL
Department Micro - and Nanosensors
Fraunhofer-Institute for Applied Solid State Physics (IAF)
Tullastrasse 72, Freiburg, Germany

ELSEVIER
AMSTERDAM • WALTHAM • HEIDELBERG • LONDON • NEW YORK • OXFORD
PARIS • SAN DIEGO • SAN FRANCISCO • SINGAPORE • SYDNEY • TOKYO

Elsevier
The Boulevard, Langford Lane, Kidlington, Oxford OX5 1GB, UK
225 Wyman Street, Waltham, MA 02451, USA

© 2014 Elsevier Ltd. All rights reserved.

No part of this publication may be reproduced, stored in a retrieval system or transmitted in any form or by any means electronic, mechanical, photocopying, recording or otherwise without the prior written permission of the publisher.

Permissions may be sought directly from Elsevier's Science & Technology Rights Department in Oxford, UK: phone (+44) (0) 1865 843830; fax (+44) (0) 1865 853333; email: permissions@elsevier.com. Alternatively you can submit your request online by visiting the Elsevier web site at http://elsevier.com/ locate/permissions, and selecting Obtaining permission to use Elsevier material.

Notice
No responsibility is assumed by the publisher for any injury and/or damage to persons or property as a matter of products liability, negligence or otherwise, or from any use or operation of any methods, products, instructions or ideas contained in the material herein. Because of rapid advances in the medical sciences, in particular, independent verification of diagnoses and drug dosages should be made.

British Library Cataloguing in Publication Data
A catalogue record for this book is available from the British Library

Library of Congress Cataloging in Publication Data
A catalog record for this book is available from the Library of Congress

Volume 1 ISBN: 978-0-444-63385-9
Volume 2 ISBN: 978-0-444-63384-2
Volume 3 ISBN: 978-0-444-63383-5
SET ISBN: 978-0-08-096527-7

For information on all Elsevier publications
visit our website at www.store.elsevier.com

Printed and bound in UK
14 15 16 17 10 9 8 7 6 5 4 3 2 1

ELSEVIER
Book Aid
International
Working together
to grow libraries in
developing countries

www.elsevier.com • www.bookaid.org

CONTENTS

Volume 1 — Hardmetals

Section I Introduction to Hardmetals

Section II Classes of Materials

Section III Synthesis and Processing

Section IV Mechanical Properties

Section V Applications

Volume 2 - Ceramics

Section I Introduction

Section II Synthesis and Processing

Section III Microstructure and Properties

Section IV Coatings and Applications

Volume 3 - Super Hard Materials

Section I Theory

Section II Materials: Growth, Properties and Applications: Carbon-Based DLC

Section III Nano— and Poly—Diamond

Section IV Single Crystalline Diamond

Section V Selected Properties of Diamond and Applications

Section VI Other Carbon Phases

Section VII III-V Based and Novel Materials

PREFACE

Comprehensive Hard Materials, first reference work of its types, is intended to merge together the myriad facets of this class of materials in a three volume series that reflect the abundance of established and novel uses across industry, from tribology to electronics and from transportation to energy. The range, growth, and innovations of the hard/superhard materials field has become commonplace within materials science as is evident from the vibrant growth of research across and within hardmetals (cemented carbides), ceramics, and superhard materials. Furthermore, the global nature of material science is also reflected by this work and contributors have been drawn from a panorama of global research hubs, with many chapters addressing the specific resource and application challenges within basic research, development, and emergent industrial markets. It is in the true spirit of collaboration across the range of these otherwise hermetically sealed areas of research that this work has been conceived and built. The reader will find original articles covering many relatively unexamined but converging research spaces and the content fully examines the various relationships that focus on fundamentals, properties, characterization, and applications of such materials. It was the objective of the editorial team to assemble a work that would provide strategic insights into hard/superhard materials.

The first volume is devoted to hardmetals, generally known as cemented carbides in the US. This class of materials is composed of unique combinations of carbides and nitrides of transition metals ranging from the fourth to the sixth group of the periodic table and ferrous metals such as Co, Ni, Fe. Since the discovery of WC–Co by Schröter in 1922, they have epitomized a century of industrial applications mainly as cutting tools and wear resistant parts. Probably, without them many challenging enterprises in the field of rock drilling, mechanics or just wire manufacture would not have been possible. Starting from a historical viewpoint the volume contains detailed aspects of manufacturing, composition/structure/properties, and applications. The aim was to define the state of the art in hardmetal manufacturing together with a thorough illustration of the most recent progress obtained by scientific research.

Volume 2 is devoted to hard ceramics—a unique group of materials with a long-standing technical success history but subjected to permanent scientific and technological evolution. Representative ceramics within this subgroup of hard materials are alumina, silicon nitride, silicon carbide, their composites, in the form of bulk material and coatings. Also included are transition metal nitrides, carbides, borides, oxides, and mullite-based environmental barrier coatings. The intention was not only to project the substantial progress achieved in this field, but also to illustrate how scientific research findings are continuously transferred into industrial and technological advances. The overall aim of this volume was to present a critical review of established knowledge and recent advances of hard ceramics covering both their materials science and engineering aspects.

Volume 3 is devoted to superhard materials—materials resistant to a change of shape under applied force, and with a Vickers hardness value exceeding 40 GPa. The strongest of these are composed out of boron, carbon, nitrogen, and oxygen, and can be classified into two categories: intrinsic compounds and extrinsic compounds. The intrinsic group includes diamond as hardest material, cubic boron nitride (c-BN), carbon nitrides and ternary compounds such as B–N–C. Extrinsic materials are those that show super hardness determined by microstructure rather than composition, such as nanocrystalline diamond. These materials are of great interest in many industrial applications such as abrasives, polishing and cutting tools, wear-resistant, and protective coatings. Furthermore, diamond is emerging as an attractive material for new device applications in the field of power electronics, room temperature quantum computing, biosensing, biointerfaces, microelectromechanical systems, color centers and high energy radiation, and particle detectors to name a few. The aim of volume 3 was to present all the critical areas related to superhard materials with an emphasis on recently achieved progress in research, development, and applications.

The Elsevier publication team, especially Paul Prasad Chandramohan, has worked tirelessly to make this publication possible and available in two formats:

- An online version via the Science Direct platform that will guarantee easy worldwide distribution.
- A hard copy version that will be made available based on orders received.

This dual concept readily lends itself to maintaining this reference work current via additions and modifications. Elsevier (Donna de Weerd-Wilson) has discussed this concept with the editors and is in the process of moving on it in the near future.

The idea for this multivolume major reference work originated through discussions at the International Conferences on the Science of Hard Materials. From the outset, David Sleeman and Graham Nisbet (Elsevier) identified not only an overwhelming qualitative demand for extensive, international, innovative, methodologically sound coverage of the subject matter, but also keen interest in a quantitative form as well. Given this encouragement the volume editors Daniele Mari, Luis Miguel Llanes, Christoph E. Nebel, numerous expert contributors and reviewers are responsible for the creation of this definitive publication to encompass the full breadth and considerable depth of the hard/superhard materials field. The editors, contributors, and publishers invested 5 years of time and effort culminating in this, *Comprehensive Hard Materials*, and we are proud to present it to our colleagues and the community it is intended to serve.

Vinod K. Sarin
Boston University
Boston, MA 02215
USA

EDITOR-IN-CHIEF

Prof. Sarin graduated from MIT (Boston, MA) with an Sc.D in material science. He then joined Sandvik's Coromant Research Center, Stockholm, Sweden. Four years later he came back to the US, joined Adamas Carbide and then GTE, where he started an R&D group on hardmetals and ceramics, and was promoted to senior research scientist (Fellow) at GTE. After nearly 20 years of industrial experience he joined academia (Boston University) as professor in the College of Engineering. He has been the recipient of several technical, achievement, and industrial awards, invited distinguished scientist at the Max Planck Institute (Germany), University of Linkoping (Sweden), Visiting Professor, University of Lund (Sweden), Visiting Scholar/Professor Universitat Politècnica de Catalunya (Spain), and a global industrial R&D consultant. He singly or jointly holds over 80 patents, has edited several books, has authored or coauthored several chapters, and over a hundred technical publications. He is a member of the editorial board of several journals, and has chaired several technical sessions and organized several conferences on hard materials.

VOLUME EDITORS

Daniele Mari graduated in physics in 1986, and in 1991 obtained his PhD at the Federal Institute of Technology (EPFL) in Lausanne, Switzerland, with a study on high temperature properties of hardmetals. From 1992 to 1993, he continues his research at the Massachusetts Institute of Technology working in the field of shape memory alloys. In 1993, he joins the company Amysa Yverdon SA (Switzerland) as director of R&D and creates Advanced Composite & Microwave Engineering with activities in the fields of the electromagnetic heating and materials. In 2004, he returns to academia at EPFL with a research group specialized in mechanical spectroscopy. He is the co-author of more than 70 scientific papers and is presently deputy director of the physics section at EPFL. He is a member of the Editorial Board of the International Journal of Refractory Metals and Hard Materials. He has been co-chairman of the last two International Conferences on the Science of Hard Materials (ICSHM).

Luis Llanes is a full professor and current chairman in the Department of Materials Science and Metallurgical Engineering, as well as board member of the Research Center of Nanoengineering in the Technical University of Catalonia (UPC). He graduated in materials engineering from Simon Bolivar University and received his PhD degree in 1992 from the University of Pennsylvania. He carries out his research activities within the Structural Integrity, Micromechanics and Reliability of Engineering Materials (CIEFMA) group at UPC. His research interests include mechanical integrity and damage assessment of structural materials, particularly hardmetals, advanced ceramics, stainless steels, and hard coatings. He is the co-author of more than 70 papers published in top journals in these fields. In addition, he has a track record of technology transfer and consultancy with hard materials industries. He is member of the Editorial Board of the International Journal of Refractory Metals and Hard Materials as well as of the Steering Committee of the European Hard Materials Group within the European Powder Metallurgy Association. He has been co-chairman of the last three ICSHM.

Chrsitoph E. Nebel graduated in electrical engineering at the University of Stuttgart where he also got his PhD in 1989. He became a postdoc at the Xerox Research Center, Palo Alto, USA between 1990 and 1992 funded by the Alexander v. Humboldt Foundation, Germany. He joined the team of Martin Stutzmann at the Walter Schottky Institute of the Technical University Munich in 1993 where he habilitated in 1998. In 2004, he joined the Diamond Research Center of the National Institute of Advanced Industrial Science and Technology, Japan, where he was leading the "Bio-Functionalized Device Team". In 2008, he went back to Germany to become head of the Micro- and Nano-Sensor Department of the Fraunhofer-Institute for Applied Solid State Physics in Freiburg.

LIST OF CONTRIBUTORS

Jocelyn Achard
Laboratoire des Sciences des Procédés et des Matériaux (LSPM), UPR3407 CNRS, Université Paris 13, France; Laboratoire d'Excellence Sciences and Engineering for Advanced Materials and devices (SEAM), Villetaneuse, France

Igor Aharonovich
School of Physics and Advanced Materials, University of Technology Sydney, Ultimo, New South Wales, Australia

Marc Anglada
Departament de Ciència dels Materials i Enginyeria Metal·lúrgica, Universitat Politècnica de Catalunya · Barcelona Tech, Barcelona, Spain

Thomas Babinec
Departments of Electrical Engineering and Applied Physics, Stanford University, CA, USA

Soumendra N. Basu
Division of Materials Science and Engineering, Department of Mechanical Engineering, Boston University, Boston, MA, USA

Bikramjit Basu
Materials Research Center, Indian Institute of Science, Bangalore, India

Carmen Baudín
Instituto de Cerámica y Vidrio, CSIC, Madrid, Spain

I. Bello
Center of Super-Diamond and Advanced Films (COSDAF), and Department of Physics and Materials Sciences, City University of Hong Kong, Tat Chee Avenue, Hong Kong SAR, P.R. China

Eleni Berdermann
GSI Helmholtzzentrum für Schwerionenforschung GmbH, Darmstadt, Germany

Raul Bermejo
Institut für Struktur- und Funktionskeramik, Montanuniversität Leoben, Leoben, Austria

Vladimir Blank
Technological Institute for Superhard and Novel Carbon Materials, Moscow, Russia

Vadim Brazkin
Institute for High Pressure Physics, Russian Academy of Sciences, Troitsk, Moscow, Russia

Ovidiu Brinza
Laboratoire des Sciences des Procédés et des Matériaux (LSPM), UPR3407 CNRS, Université Paris 13, France; Laboratoire d'Excellence Sciences and Engineering for Advanced Materials and devices (SEAM), Villetaneuse, France

Y.M. Chong
Center of Super-Diamond and Advanced Films (COSDAF), and Department of Physics and Materials Sciences, City University of Hong Kong, Tat Chee Avenue, Hong Kong SAR, P.R. China

Marvin L. Cohen
Department of Physics, University of California at Berkeley, Berkeley, CA, USA; Materials Sciences Division, Lawrence Berkeley National Laboratory, Berkeley, CA, USA

Christoph Czettl
CERATIZIT Austria GmbH, Reutte, Austria

Robert Danzer
Institut für Struktur- und Funktionskeramik, Montanuniversität Leoben, Leoben, Austria

Goffredo de Portu
National Research Council of Italy (CNR), Chemical Science & Materials Technology Department, Institute of Science and Technology for Ceramics (ISTEC), Faenza, Italy

Nadira Derkaoui
Laboratoire des Sciences des Procédés et des Matériaux (LSPM), UPR3407 CNRS, Université Paris 13, France; Laboratoire d'Excellence Sciences and Engineering for Advanced Materials and devices (SEAM), Villetaneuse, France

Eric F. Drake
Rice University, Houston, Texas, USA

Yasuaki Einaga
Department of Chemistry, Keio University, Yokohama, Japan

Peter Ettmayer
Vienna University of Technology, Institue of Chemical Technologies and Analytics, Vienna, Austria

Z. Zak Fang
Department of Metallurgical Engineering, University of Utah, Salt Lake City, UT, USA

Gilbert Fantozzi
INSA de Lyon, MATEIS (UMR CNRS 5510), Villeurbanne, France

S.A. Firstov
Department of Physics of Strength and Plasticity of Materials, Frantsevich Institute for Problems of Materials Science, Kiev, Ukraine

Rainer Gadow
University of Stuttgart, Institute for Manufacturing Technology of Ceramic Components and Composites, Stuttgart, Germany

A.J. Gant
National Physical Laboratory, Teddington, Middlesex, TW, UK

Mark G. Gee
National Physical Laboratory, Teddington, Middlesex, TW, UK

Randall M. German
Department of Mechanical Engineering, College of Engineering, San Diego State University, San Diego, CA, USA

Alix Gicquel
Laboratoire des Sciences des Procédés et des Matériaux (LSPM), UPR3407 CNRS, Université Paris 13, France; Laboratoire d'Excellence Sciences and Engineering for Advanced Materials and devices (SEAM), Villetaneuse, France

Brahma Raju Golla
Engineering Ceramics Research Group, Korea Institute of Materials Science, Changwon, Gyeongnam, Korea

Stefano Guicciardi
National Research Council of Italy (CNR), Chemical Science & Materials Technology Department, Institute of Science and Technology for Ceramics (ISTEC), Faenza, Italy

Stuart Hampshire
Materials and Surface Science Institute, University of Limerick, Limerick, Ireland

Khaled Hassouni
Laboratoire des Sciences des Procédés et des Matériaux (LSPM), UPR3407 CNRS, Université Paris 13, France; Laboratoire d'Excellence Sciences and Engineering for Advanced Materials and devices (SEAM), Villetaneuse, France

Bin He
Center of Super-Diamond and Advanced Films (COSDAF), and Department of Physics and Materials Sciences, City University of Hong Kong, Tat Chee Avenue, Hong Kong SAR, P.R. China

Mathias Herrmann
Fraunhofer-Institut für Keramische Technologien und Systeme IKTS, (www.ikts.fraunhofer.de) Dresden, Germany

Jonathan Hird
Schlumberger Gould Research, Cambridge, United Kingdom

Tetsuo Irifune
Geodynamics Research Center, Ehime University, Matsuyama, Japan; Earth-Life Scinece Institute, Tokyo Institute of Technology, Tokyo, Japan

Thomas J. Jewett
Global Tungsten and Powders Corporation, Towanda, Pennsylvania, USA

Emilio Jiménez-Piqué
Departament de Ciència dels Materials i Enginyeria Metal·lúrgica, Universitat Politècnica de Catalunya · Barcelona Tech, Barcelona, Spain

Shinhoo Kang
Department of Materials Science and Engineering, Seoul National University, Gwanak-ku, Seoul, Korea

Hiromitsu Kato
Energy Technology Research Institute, AIST, Japan

Frank Kern
University of Stuttgart, Institute for Manufacturing Technology of Ceramic Components and Composites, Stuttgart, Germany

Hagen Klemm
Fraunhofer-Institut für Keramische Technologien und Systeme IKTS, (www.ikts.fraunhofer.de) Dresden, Germany

Hans Kolaska
Fachverband für Pulvermetallurgie e.V., Hagen, Germany

Igor Konyashin
Element Six Hard Materials, Element Six GmbH, Städeweg, Burghaun, Germany

Mark C. Koopman
Department of Metallurgical Engineering, University of Utah, Salt Lake City, UT, USA

Aaron D. Krawitz
University of Missouri, Columbia, Missouri, USA

Jochen Kriegesmann
Department of Materials Technology, Glass and Ceramics, University of Applied Sciences Koblenz, Höhr-Grenzhausen, Germany

Anke Krueger
Institute for Organic Chemistry, Julius-Maximiliaus University würzburg, Am Hubland, 97074 Würzburg, Germany

Boris Kulnitskiy
Technological Institute for Superhard and Novel Carbon Materials, Moscow, Russia

Sabine Lay
Grenoble Institute of Technology, Saint-Martin d'Hères, France

Shuit-Tong Lee
Center of Super-Diamond and Advanced Films (COSDAF), and Department of Physics and Materials Sciences, City University of Hong Kong, Tat Chee Avenue, Hong Kong SAR, P.R. China

Luis Llanes
Departament de Ciència dels Materials i Enginyeria Metal·lúrgica, Universitat Politècnica de Catalunya · Barcelona Tech, Barcelona, Spain

Kian Ping Loh
Department of Chemistry, National University of Singapore, Singapore

Guillaume Lombardi
Laboratoire des Sciences des Procédés et des Matériaux (LSPM), UPR3407 CNRS, Université Paris 13, France; Laboratoire d'Excellence Sciences and Engineering for Advanced Materials and devices (SEAM), Villetaneuse, France

John E. Lowther
School of Physics and DST/NRF Centre of Excellence in Strong Materials, University of the Witwatersrand, Johannesburg, South Africa

Andriy O. Lyakhov
Department of Geosciences, Stony Brook University, Stony Brook, NY, USA

Alexander Lyapin
Institute for High Pressure Physics, Russian Academy of Sciences, Troitsk, Moscow, Russia

Daniele Mari
Laboratoire de Physique de la Matière Complexe, Ecole Polytechnique Fédérale Lausanne, Lausanne, Switzerland

Julián Martínez-Fernández
Dpto. Física de la Materia Condensada—ICMS, Universidad de Sevilla—CSIC, Sevilla, Spain

Pankaj K. Mehrotra
Kennametal Inc., Latrobe, PA, USA

Jan Meijer
Nuclear Solid State Physics, University Leipzig, Leipzig, Saxony, Germany

Lutz-Michael Berger
Fraunhofer Institute IWS, Dresden, Germany

Armelle Michau
Laboratoire des Sciences des Procédés et des Matériaux (LSPM), UPR3407 CNRS, Université Paris 13, France; Laboratoire d'Excellence Sciences and Engineering for Advanced Materials and devices (SEAM), Villetaneuse, France

Claude Michotte
CERATIZIT Luxembourg S. à. r. l., Route de Holzem, Mamer, Luxembourg

K.P. Mingard
National Physical Laboratory, Teddington, Middlesex, TW, UK

Rosa M. Miranda
UNIDEMI, Departamento de Engenharia Mecânica e Industrial, Faculdade de Ciências e Tecnologia, Universidade Nova de Lisboa, Caparica, Portugal

Pilar Miranzo
Institute of Ceramics and Glass, CSIC. Kelsen, 5, Madrid, Spain

Jean-Michel Missiaen
Grenoble Institute of Technology, Saint-Martin d'Hères, France

Christian Mitterer
Department of Physical Metallurgy and Materials Testing, Montanuniversität Leoben, Leoben, Austria

Michael Moseler
Fraunhofer Institute for Mechanics of Materials IWM, Freiburg, Germany

Christoph E. Nebel
Fraunhofer-Institute for Applied Solid State Physics, Freiburg, Germany

Steffen Nowotny
Fraunhofer Institut IWS, Dresden, Germany

Artem R. Oganov
Department of Geosciences, Center for Materials by Design, Institute for Advanced Computational Science, Stony Brook University, Stony Brook, NY, USA; Moscow Institute of Physics and Technology, Dolgoprudny city, Moscow Region, Russian Federation; Northwestern Polytechnical University, Xi'an, China

Hugo M. Ortner
Darmstadt University of Technology, Department of Material Sciences: Materials Characterization, Darmstadt, Germany

Maria Isabel Osendi
Institute of Ceramics and Glass, CSIC. Kelsen, 5, Madrid, Spain

Lars Pastewka
Fraunhofer Institute for Mechanics of Materials IWM, Freiburg, Germany

Arvid Eric Pasto
Retired from Sparks, NV, USA

Sébastien Pezzagna
Nuclear Solid State Physics, University Leipzig, Leipzig, Saxony, Germany

S.S. Ponomarev
Department of Physics of Strength and Plasticity of Materials, Frantsevich Institute for Problems of Materials Science, Kiev, Ukraine

Michail Popov
Technological Institute for Superhard and Novel Carbon Materials, Moscow, Russia

Leo Prakash
Kyocera Unimerco Tooling A/S, Sunds, Denmark

Joaquin Ramírez-Rico
Dpto. Física de la Materia Condensada—ICMS, Universidad de Sevilla—CSIC, Sevilla, Spain

Pascal Reynaud
INSA de Lyon, MATEIS (UMR CNRS 5510), Villeurbanne, France

John Robertson
Department of Engineering, Cambridge University, Cambridge, UK

B. Roebuck
National Physical Laboratory, TW, UK

Gregory S. Rohrer
Department of Materials Science and Engineering, Carnegie Mellon University, Pittsburgh, PA, USA

Catherine Rond
Laboratoire des Sciences des Procédés et des Matériaux (LSPM), UPR3407 CNRS, Université Paris 13, France; Laboratoire d'Excellence Sciences and Engineering for Advanced Materials and devices (SEAM), Villetaneuse, France

Malika Saâdaoui
LERSIM Ecole Mohammadia d'Ingénieurs, Université Mohamed V Agdal, Rabat, Morocco

Vinod K. Sarin
Division of Materials Science and Engineering, Department of Mechanical Engineering, Boston University, Boston, MA, USA

Uwe Schleinkofer
CERATIZIT Austria GmbH, Reutte, Austria

Matthias Schreck
Universität Augsburg, Institut für Physik, Augsburg, Germany

Alex V. Shatov
8 Parkside Drive, Jamesburg, NJ, USA

Olga A. Shenderova
International Technology Center, Raleigh, NC, USA; Adámas Nanotechnologies, NC, USA

François Silva
Laboratoire des Sciences des Procédés et des Matériaux (LSPM), UPR3407 CNRS, Université Paris 13, France; Laboratoire d'Excellence Sciences and Engineering for Advanced Materials and devices (SEAM), Villetaneuse, France

Raj P. Singh Gaur
Global Tungsten and Powders Corporation, Towanda, Pennsylvania, USA

Vladimir L. Solozhenko
LSPM–CNRS, Université Paris 13, Villetaneuse, France

Jörg Spatzier
Fraunhofer Institut IWS, Dresden, Germany

Hitoshi Sumiya
Electronics Materials R&D Laboratories, Sumitomo Electric Industries Ltd, Itami, Japan

Alexandre Tallaire
Laboratoire des Sciences des Procédés et des Matériaux (LSPM), UPR3407 CNRS, Université Paris 13, France; Laboratoire d'Excellence Sciences and Engineering for Advanced Materials and devices (SEAM), Villetaneuse, France

Takashi Taniguchi
Advanced Key Technology Division, National Institute for Materials Science, Tsukuba, Ibaraki, Japan

Shi Wun Tong
Department of Chemistry, National University of Singapore, Singapore

Yadir Torres
Universidad de Sevilla, Department of Mechanical and Materials Engineering—ETSI, Sevilla, Spain

Vladimir Turkevich
Synthesis and Sintering of Superhard Materials at High Pressures and High Temperatures, Institute for Superhard Materials of the Ukrainian National Academy of Sciences, Kiev, Ukraine

Hongtao Wang
Kennametal Inc., Rogers, AR, USA

Maxime Wartel
Laboratoire des Sciences des Procédés et des Matériaux (LSPM), UPR3407 CNRS, Université Paris 13, France; Laboratoire d'Excellence Sciences and Engineering for Advanced Materials and devices (SEAM), Villetaneuse, France

Dow Whitney
Retired from Department of Materials Science and Engineering at the University of Florida, Gainesville, Florida, USA

Christoph Wild
Diamond Materials GmbH, Freiburg, Germany

Thomas A. Wolfe
Global Tungsten and Powders Corporation, Towanda, Pennsylvania, USA

Eckhard Wörner
Diamond Materials GmbH, Freiburg, Germany

Wenjun J. Zhang
Center of Super-Diamond and Advanced Films (COSDAF), and Department of Physics and Materials Sciences, City University of Hong Kong, Tat Chee Avenue, Hong Kong SAR, P.R. China

Qiang Zhu
Department of Geosciences, Stony Brook University, Stony Brook, NY, USA

SECTION I

THEORY

3.01 The Physics of Strong Bonds

Marvin L. Cohen, Department of Physics, University of California at Berkeley, Berkeley, CA, USA;
Materials Sciences Division, Lawrence Berkeley National Laboratory, Berkeley, CA, USA

3.01.1 Introduction and Background

Although the relationship between the bulk modulus *B* of a pure material and its hardness is complex, usually a large *B* implies a high degree of hardness. This relationship is further complicated by the fact that impurities, direction of the hardness probe, and surface treatment among other conditions can change how *B* and hardness depend on microscopic properties such as atomic composition and crystal structure. Even the scales for hardness vary, and this makes comparisons between experiments, between materials, and between theoretical and experimental results difficult. In fact, despite the existence of good modern hardness scales such as the Vickers scale (Kittel, 2005; Smith & Sandland, 1922). Because of its simplicity, the empirical scratch test and its related scale developed by Friedrich Mohs in 1822 are sometimes still used to illustrate the concept of hardness. Despite these caveats, this review will concentrate on the question of whether it is possible to use microscopic theory to explain and predict the nature of the variation of *B* in materials.

Microscopically, *B* depends on the strength of the bonding between atoms, and since covalent bonds can be very strong, this type of bonding will be the main focus here. Roughly, covalent and ionic crystals have cohesive energies of the order of 10 eV/atom, which is large compared to van der Waals bonded molecular crystals with 0.05 eV/molecule and metals with 1 to 5 eV/atom. It can be argued that the larger cohesive energy solids should have a larger *B* and be better candidates for hard materials.

For many solid systems, quantum mechanical calculations of the total energies of solids can be done with only microscopic information about the constituent atoms and the crystal structures as inputs (Cohen, 1982). These studies give reliable estimates of the lattice constants and *B* and sometimes predict high-pressure structural phases of materials (Yin & Cohen, 1980). In some cases, ab initio calculations lead to semiempirical theories and expressions to predict *B* (Cohen, 1985). Another approach to obtain empirical formulae for *B* is to explore the theories of bonding. The Pauling (Pauling, 1960) and Phillips (Phillips & Lucovsky, 2009) scales for ionicity are helpful in describing bonds. The latter scale is derived from spectroscopic data, and it will be shown that the conceptual basis of this approach can lead to a useful simple relationship between *B*, the bond length d, and the ionicity I for a class of semiconductors and insulators (Cohen, 1985,1988).

In the next section, we discuss some of the characteristics of the ab initio and semiempirical theories along with applications.

3.01.2 Ab Initio and Semiempirical Methods

The quantum theories of Bohr, Dirac, Schrodinger, and Heisenberg in the 1920s focused first on atomic properties. This led to an understanding of atomic structure and contributed to the development of quantum theory. Calculating the properties of solids using quantum theory and starting from a knowledge of their constituent atoms started in the 1920s and 1930s with the work of Born, Sommerfeld, Bethe, and others (Sommerfeld & Bethe, 1933, Chap. 3), but the actual applications to explaining and predicting the properties of real solid materials took many years. As in the study of atoms, a critical part in developing an atomic and ultimately a quantum theory was the use of optical spectral studies. However, because solid-state spectra are

http://dx.doi.org/10.1016/B978-0-08-096527-7.00038-6

broad and relatively featureless compared to atomic spectra, unraveling their message was difficult. In the 1960s and 1970s, the optical properties of semiconductors originating from interband electronic transitions were essentially explained by an international experimental–theoretical collaboration (Cohen & Chelikowsky, 1989). On the experimental side, new techniques provided reliable data to build semiempirical theories. The most popular of these was the Empirical Pseudopotential Method (EPM) wherein the crystalline potential was determined by comparing the calculated optical properties with the experimental data (Chelikowsky & Cohen, 1976; Cohen & Bergstresser, 1966; Cohen & Chelikowsky, 1989). This approach was based on a theoretical model in which each ion of the crystal had an appropriate potential to simulate valence electron–ion interactions. In addition, the EPM sets the stage for the development of ab initio theories (Cohen, 1982; Ihm, Zunger, & Cohen, 1979) and methods that were capable of calculating structural and mechanical properties.

At this point, we have an ab initio theory appropriate for many systems and applicable for studies of electronic structure, crystal structures and structural transitions, structural and mechanical properties, lattice vibrational properties, electron–lattice interactions, superconductivity, optical properties, photoemission spectra, etc. Not only have these approaches helped in explaining properties, they have been predictive.

In the 1930s, Fermi (Fermi, 1934), Hellmann (Hellmann, 1935) and others explored the construction of a pseudopotential to give the electron–ion interaction. Over the years, many forms have been introduced and used with success. If one adopts a model of a crystal as a periodic array of pseudoatoms or cores surrounded by a gas of valence electrons as shown in **Figure 1**, then in the case of the EPM mentioned above, all that is needed is an average potential to reproduce the optical data. For electronic band structure calculations, we only need the values of $V(q = \mathbf{G})$, where $\mathbf{G}$ is a reciprocal lattice vector. This is shown in **Figure 2**. For systems like diamond, Si, and Ge in the diamond structure, only the first three $\mathbf{G}$ values for $V(\mathbf{G})$ need to be considered. Hence, by fitting just three Fourier coefficients or form factors, it is possible to get a band structure $E(k)$, which is in agreement with the experimental data to within a few tenths of an electronvolt over a range of a Rydberg. Not only were the energy levels accurate, the electronic density obtained by squaring the pseudowave function gave a successful prediction of the X-ray results measuring the valence electron or "charge density". **Figure 3** illustrates a comparison of the calculated (Cohen & Chelikowsky, 1989) and measured (Yang & Coppens, 1974) Si charge density. So the EPM approach shown in **Figure 4** was highly successful in interpreting many properties of semiconductors and explained the optical properties, and the electronic charge densities calculated from the wave functions allowed the interpretation of bonding properties and ionicity in semiconductors and insulators.

Despite the successes of the EPM, what was needed for calculating structural properties was a method to create the potentials from first principles using only the atomic number as input. This is achieved in several ways. The usual approach is to construct a potential that gives the same results for a calculated wave function as

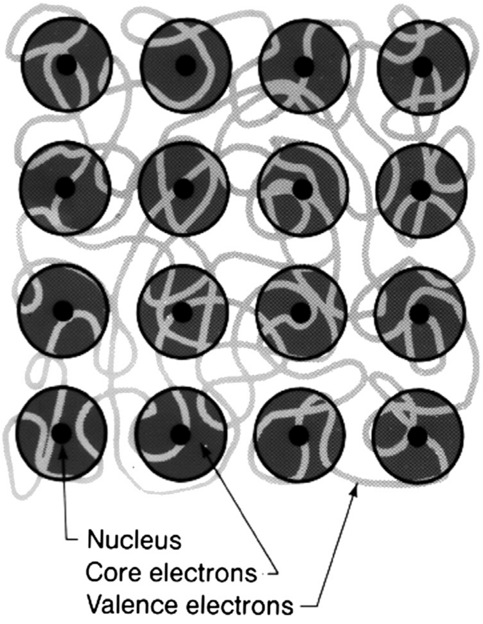

Figure 1 Pseudopotential model with cores in a sea of valence electrons.

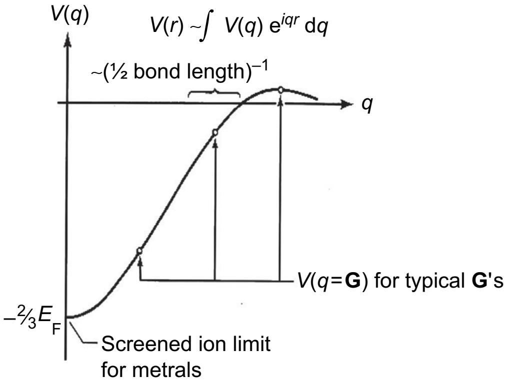

Figure 2 Schematic drawing of a pseudopotential in reciprocal space.

that obtained for an all-electron atomic calculation in **Figure 5**, but with a smooth nodeless tail in the core region (Hamann, Schluter, & Chiang, 1979; Vanderbilt, 1985; Troullier & Martins, 1991). With this potential to express the electron–core interaction, the Coulomb core–core interaction, the Hartree mean field electron–electron interaction, and the electronic kinetic energy and exchange-correlation contribution calculated using the density functional theory (Kohn & Sham, 1965) within the local density approximation (LDA), it was possible to calculate the total energy of a solid for a specific crystal structure:

$$E(\text{tot}) = E(\text{c}-\text{c}) + E(\text{kinetic}) + E(\text{el}-\text{core}) + (\text{Hartree}) + E(\text{xch}) + E(\text{corr}). \tag{1}$$

This method was first applied to study structural parameters and high-pressure phases of Si and Ge (Yin & Cohen, 1980; Yin & Cohen, 1982). The energy versus volume $E(V)$ for Si calculated using this method is given in **Figure 6**. The lattice constants, bulk moduli, and transition volumes and pressures are obtained in these studies (**Table 1**). Several of the high-pressure phases of Si and Ge were predicted using this approach. By inputting the atomic masses, this total energy approach could be used to calculate phonon spectra and electron–phonon interaction parameters. Hence, many properties of solids could be calculated with only the crystal structure and the atomic numbers and masses as input (Cohen, 1982).

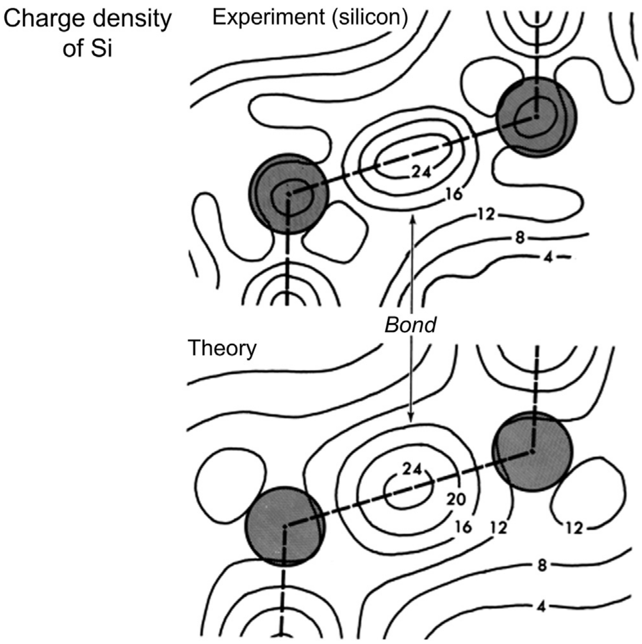

Figure 3 Valence-electron charge density comparison between theory and experiment for silicon.

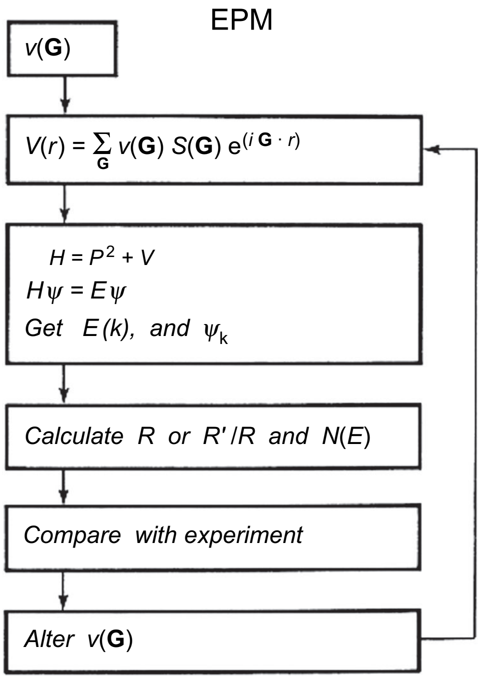

Figure 4 Block diagram illustrating the EPM approach.

It is interesting to note that once the inner working of the ab initio and EPM is understood, then semi-empirical theories can be developed for calculating specific properties. An example is that it can be shown that the bulk modulus for group IV, III–V, II–VI diamond and zincblende semiconductors is proportional to the bond length to the -3.5 power (Cohen, 1985). Using this relationship and a single ionicity parameter for the III–V semiconductors and double that parameter for all the II–VI semiconductors, it is possible to obtain an agreement with measured values to $<2\%$ for these materials (Cohen, 1988). The values for B using the empirical approach can be compared with the ab initio results of **Table 1** for the group IV materials. Using the experimental bond lengths, the calculated values $B = 98$, 76, and 435 GPa for Si, Ge, and diamond are in excellent

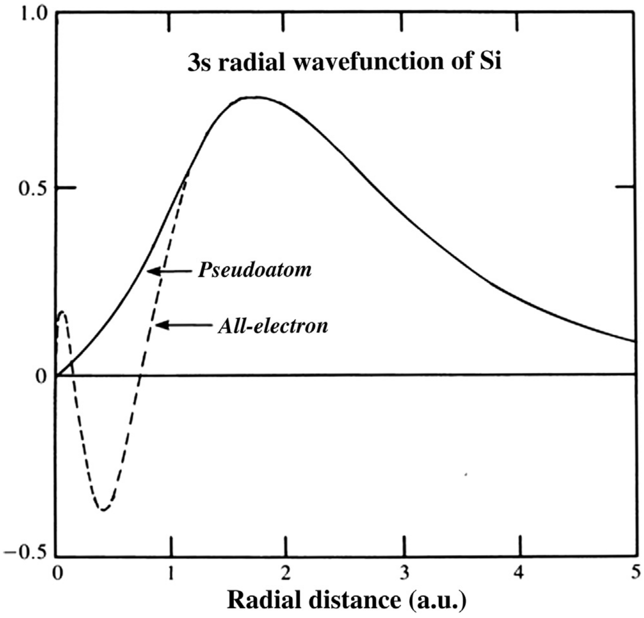

Figure 5 The construction of an ab initio pseudopotential.

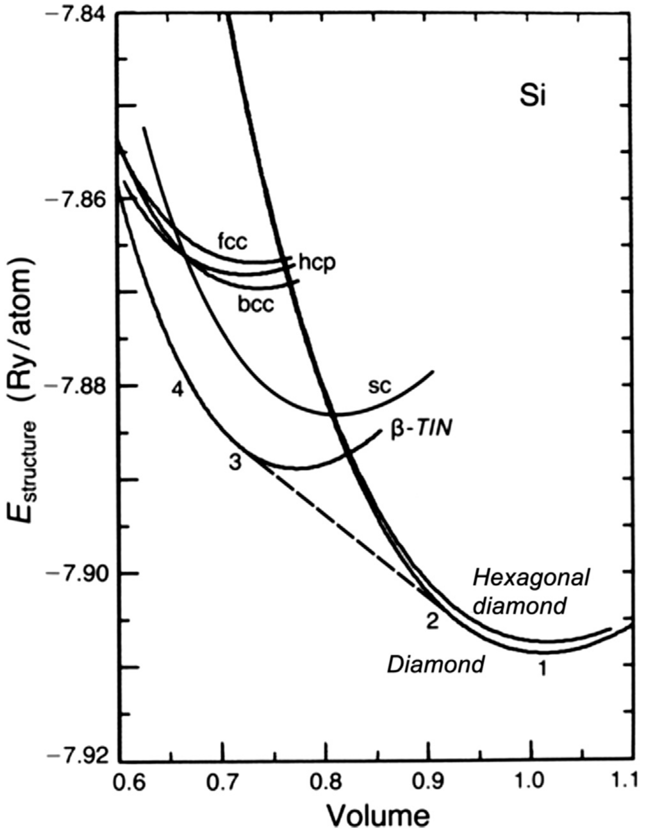

Figure 6 Calculated total energies as a function of volume for several structures of silicon.

agreement with the values given in Table 1. A similar agreement is found for the zincblende compounds as shown in Table 2.

This approach starts with a view of a free electron system where the textbook calculation (Kittel, 2005) gives

$$B = (2/3)nE_F, \tag{2}$$

where E_F is the Fermi energy. We note that dimensional analysis suggests that B scales like the Fermi energy divided by the volume per electron. So carrying this idea forward, we note that for covalent materials the charge

Table 1 Static structural properties for silicon, germanium, and diamond using ab initio theory

Static structural properties	*Lattice constant (Å)*	*Bulk modulus (GPa)*
Si		
Calc.	5.45	98
Expt.	5.43	99
% Diff.	0.4%	−1%
Ge		
Calc.	5.66	73
Expt.	5.65	77
% Diff.	0.1%	−5%
C		
Calc.	3.60	441
Expt.	3.57	443
% Diff.	0.8%	−1%

Table 2 Comparison of calculated group III–V and II–VI bulk moduli using Eqn [5] and the measured bond lengths

Material	d *(nm)*	*Experimental* B_0 *(GPa)*	*Calculated* B_0 *(GPa)*
III–V			
AlP	0.236	86.0	86.7
AlAs	0.243	77.0	78.3
AlSb	0.266	58.2	57.0
GaP	0.236	88.7	86.7
GaAs	0.245	74.8	76.1
GaSb	0.265	57.0	57.8
InP	0.254	71.0	67.0
InAs	0.261	60.0	61.0
InSb	0.281	47.4	47.1
II–VI			
ZnS	0.234	77.1	78.1
ZnSe	0.245	62.4	66.5
ZnTe	0.264	51.0	51.2
CdS	0.252	62.0	60.3
CdSe	0.262	53.0	52.6
CdTe	0.281	42.4	41.2
HgSe	0.263	50.0	51.9
HgTe	0.278	42.3	42.7

is not evenly dispersed but concentrated in bonds; hence, it is reasonable to argue that B should scale like the covalent bond energy divided by the bond volume. It is possible to get a measure of the covalent bond energy by examining the optical properties of semiconductors and insulators to determine the average covalent gap E_h for a particular system (Phillips & Lucovsky, 2009; Cohen & Chelikowsky, 1989). This gap can be related to the bond length d if the bond volume is approximated by a cylinder. The result is (Cohen, 1982)

$$B = 45.6E_\mathrm{h}/d, \tag{3}$$

where B is in gigapascals, E_h is in electronvolts, and the bond length d is in Angstroms. Using the scaling of E_h with d, the expression for B becomes

$$B = 1761d^{-3.5}. \tag{4}$$

To include the effects of ionicity, one introduces a parameter I where for tetrahedral 4-folded materials, $I = 0$ for group IV materials, $I = 1$ for III–VI compounds, and $I = 2$ for group II–VI compounds. The resulting expression

$$B = (1971 - 220I)d^{-3.5} \tag{5}$$

gives remarkably accurate values for B as shown in **Table 2**. Some extensions of the formula in Eqn [5] to nontetrahedral systems have been made (Cohen, 1996).

So armed with the ab initio approach and the semiempirical approach, it is reasonable to ask about how these approaches apply to systems with strong bonds and potentially large B.

3.01.3 Materials, Bonding, and Mechanical Properties

We begin by considering materials where s and p electrons dominate the bonding. Carbon is the prototype element here. Diamond with its sp^3 bonds is at or near the top of all known materials when considering B or hardness. Graphene and graphite with sp^2 planar bonding is another prototypical example for the concepts discussed above. The strong and relatively confined bond charge in these materials along with their short bond length suggests (Eqn [5]) that these nonpolar materials will have large values of B. Inputting the experimental bond length for diamond yields a value of $B = 435$ GPa, which is close to the measured value of $B = 442$ GPa, as discussed above. It is interesting to note that the shorter bond length in graphene or in the graphite plane would yield a larger value; however, despite attempts to construct nonplanar three-dimensional sp^2 structures, these have been found to be unstable up to this time. It is expected that if one were to pull graphene in its plane, it would be extremely strong. The effect of this property is seen in carbon nanotube studies (Saito & Zettl, 2008) where Young's modulus is very large.

Ab initio calculations for diamond, carbon nanotubes, and carbon in other forms are consistent with measurements where available. Hence, we have an ab initio theory capable of describing the structural properties accurately and a semiempirical approach that yields accurate values for B, so it is possible to explore other structures in this group to search for a larger B. A study (Ribeiro, Tangney, Louie, & Cohen, 2006) of hypothetical hard structures of carbon with cubic symmetry is a typical example where an ab initio pseudopotential/density functional calculation study was done for the structure and electronic properties of two hypothetical carbon structures with cubic symmetry: C_6 bcc, which is a body centered cubic structure with 12 atoms per cubic unit cell, and C_{20} sc, which is a simple cubic structure with 20 atoms per unit cell. It was found that the former is semiconducting with an indirect gap of 2.5 eV, within the LDA to the exchange and correlation energy functional, while the latter is metallic. Both have similar zero-pressure densities of about one atom per 6.9 $Å^3$, which is intermediate between graphite and diamond, and similar bulk moduli of about 350 GPa at ambient conditions. Both are metastable with respect to graphite and diamond, and no phase transition is expected in the range of the pressures studied. Similar results are obtained for BN crystals. The extension to BP and BAs has also been examined, and interesting information about bonding in these systems was obtained; however, to a first approximation, the ionic character introduced for these materials weakens the bond. Hence, these systems although interesting do not have ultrahigh values for B.

An interesting compound was suggested as a member of this group C_3N_4. The first suggestions (Cohen, 1985; Liu & Cohen, 1989) were based on the idea that short bonds in these materials should lead to a larger B as shown in Eqn [5]. To estimate the bond length, the ionic radii of C and N were taken from other studies such as the Pauling radii. These led to a possible bond length of about 1.47–1.49 Å, and these would suggest very high B values in the range of those found for diamond. Another consideration is the coordination of the atoms in this hypothetical material. A reasonable guess for the structure is the known structures of Si_3N_4. If the expression for B of Eqn [5] is scaled by the coordination number N, then a factor $N/4$ should multiply this expression. For the cases considered before $N = 4$. An estimate for the coordination in C_3N_4 yields $N = 3.43$. With this value and $0 < \text{ionicity} < 1$, the estimates for B are still in the upper range of what has been observed for high B materials.

An ab initio calculation (Liu & Cohen, 1989; Liu & Cohen, 1990) yields similar results. Here, both Si_3N_4 and C_3N_4 were considered using a first-principles pseudopotential study of the structural and electronic properties of a specific structure type, that is, β-Si_3N_4. The hypothetical compound β-C_3N_4, which is C_3N_4 in the β-Si_3N_4 structure (**Figure 7**) with C substituted for Si for the case of C_3N_4, was used as a prototype for investigating the properties of possible covalent C–N solids. The calculated lattice constant, bulk modulus, and electronic band structure of β-Si_3N_4 were found to be in good agreement with experimental results. This calculation was done as a test to give support for the predicted properties of β-C_3N_4. The bulk modulus of β-C_3N_4 was found to be

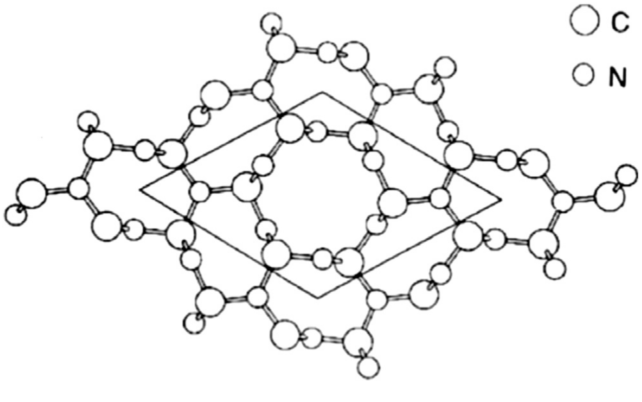

Figure 7 Structure of Si3N4 and C3N4. The c axis is normal to the page. Half of the atoms illustrated are located in the z = −c/4 plane and the other half are in the z = c/4 plane. The structure consists of these buckled plane stacked in AAA…sequence. The parallelogram indicates the unit cell.

comparable to diamond, and its moderately large cohesive energy suggests that the prototype structure may be metastable. Although the crystal structure and the valences of the constituent atoms are similar in β-Si_3N_4 and β-C_3N_4, the electronic bonding properties in these two solids are found to differ. The large core size and repulsive *p* pseudopotential of the second-row element, Si, results in a more ionic Si–N bond compared with a covalent C–N bond. This calculation supports the proposal that the empirical approach is sufficiently precise to be used for predicting and explaining structural properties. Similar results for B–C–N compounds have been found.

Another study (Han, Ihm, Louie, & Cohen, 1998) showing the importance of the bond length in determining the strength of materials for the sp^3 systems involves the possibility of enhancing the hardness of surfaces. A specific system, boron on the (111) surface of diamond, was considered as a prototype for studying this effect involving short bonds. The motivation was to look for the possible enhancement of the surface hardness. Again, the ab initio or first-principles pseudopotential approach was used. The calculations involved studies of the diamond (111) surface with nitrogen or boron replacing the surface carbon atoms (**Figure 8**). Surface boron atoms form planar sp^2 bonds with carbon atoms and the compressive stress from the underlying bulk diamond lattice squeezes the B–C bonds significantly. Bulk and shear moduli in the surface region increased substantially, surpassing those of bulk diamond. In contrast, for the nitrogen-covered surface, N–C bonds are elongated because of the tensile stress from bulk diamond and the elastic stiffness decreases. This study illustrates the power of the ab initio approach. The semiempirical scheme can rapidly survey many possible systems, but findings such as the fact that the constraining force from the underlying diamond lattice for the case considered of *B* on diamond (111) is beyond the scope of the empirical approach. This constraining force plays a major role because it compresses the sp^2 bonds between B and C atoms. If we assume that the elastic moduli and

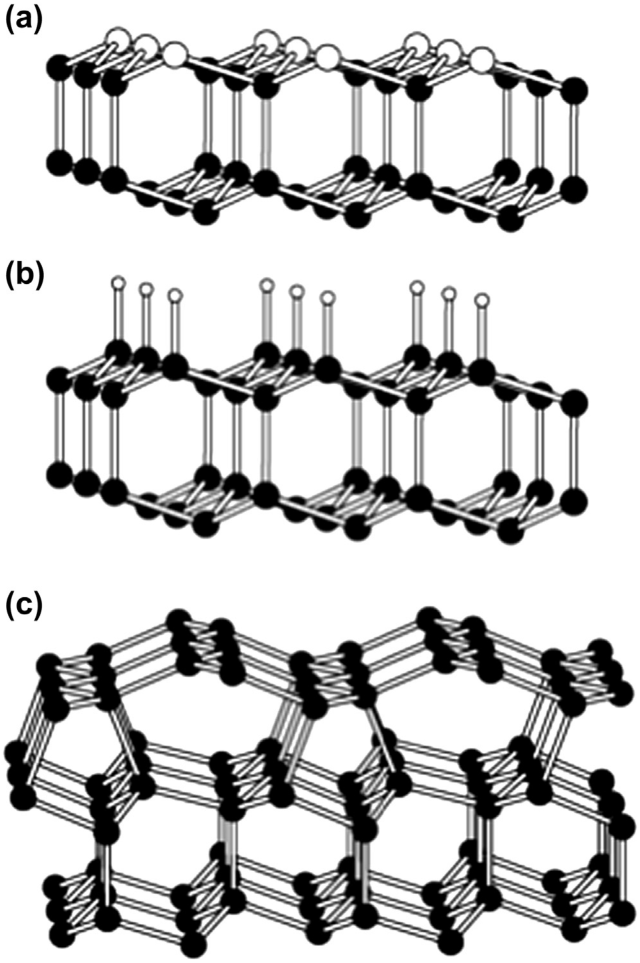

Figure 8 Geometry of top layers of (a) nitrogen coated or boron coated, (b) hydrogenated (131), and (c) (231) reconstructed C(111) surfaces. Black circles are carbon atoms. White circles are nitrogen or boron atoms in (a) and hydrogen atoms in (b), respectively.

mechanical hardness in covalent materials are related, this effect can have important consequences when considering surface coating to increase hardness.

When considering d-electrons involved in bonding, there are many ultrahard materials and many studies have been done. Unfortunately, to our knowledge, a formula comparable to Eqn [5] for sp^3 materials is not available. The prototypical materials in this class are the transition-metal carbonitrides. For the sp^3 materials, we considered electronic bonding properties and their relationship to hardness. For the d-electron case, it is instructive to examine an electronic mechanism of hardness enhancement in transition-metal carbonitrides (Jhi, Ihm, Louie, & Cohen, 1999). These materials are hard materials that are widely used for cutting tools and wear-resistant coatings. Their hardness is not yet understood at a fundamental level. A clue may lie in the puzzling fact that transition-metal carbonitrides that have the rock-salt structure (such as TiC_xN_{1-x}) have the greatest hardness for a valence-electron concentration of about 8.4 per cell (Figure 9), which suggests that the hardness may be determined more by the nature of the bonding than by the conventional microstructural features that determine the hardness of structural metals and alloys. To investigate this possibility, the shear modulus of various transition-metal carbides and nitrides were examined using the ab initio pseudopotential

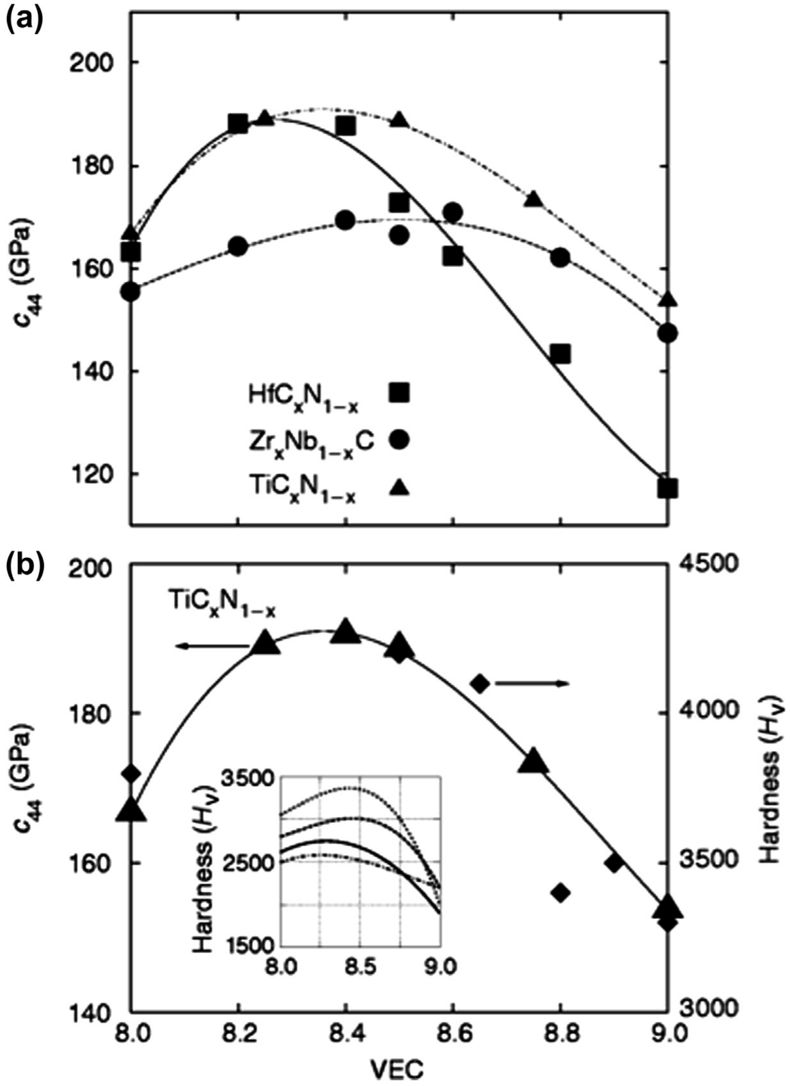

Figure 9 (a) Calculated shear modulus c_{44} in gigapascals for TiC_xN_{1-x} (filled triangles), HfC_xN_{1-x} (filled boxes), and $Zr_xNb_{1-x}C$ (filled circles) as a function of the valence-electron concentration (VEC). The curves are polynomial fits to the calculated c_{44}. (b) Measured microhardness of TiC_xN_{1-x} cermets from (Richter et al., 1996) in Hv units (filled diamonds). For comparison, the calculated c_{44} (filled triangles) in gigapascals is plotted in the same figure. The thin solid line is a guide to the eye. Inset, microhardness of bulk alloys and substoichiometric compounds (Ti(CN), dotted line; (ZrNb)C, dashed line; Hf(CN), solid line; and NbC_{1-x}, dash-dotted line).

approach. The results show that the behavior of these materials can be understood at a fundamental level in terms of their electronic band structure. The unusual hardness originates from a particular band of σ-bonding states, between the nonmetal p orbitals and the metal d orbitals, which strongly resists shearing strain or shape change. Filling of these states is completed at a valence-electron concentration of about 8.4, and any additional electrons would go into a higher band that produces an electronic configuration that is unstable against shear deformations. Hence, for more complex bonding situations with multiple orbital character, it is possible to determine which combinations offer the most stability.

The effects of vacancies on the mechanical properties of the transition-metal carbides and nitrides can be studied (Jhi, Louie, Cohen, & Ihm, 2001) using the pseudopotential approach. The calculated shear elastic stiffness and electronic structures show that a vacancy produces entirely different effects on the mechanical strength of groups IVb nitrides and Vb carbides. It is found that the occupation of shear-unstable metallic d–d bonding states changes essentially in an opposite way for the carbides and nitrides in the presence of vacancies (**Figure 10**), resulting in different responses to shear stress. This study provides an atomistic understanding of the anomaly in hardness for these substoichiometric materials. Hence, this is another path to study hardness using theoretical approaches.

3.01.4 Conclusions

The picture of going from a free electron-type metal with an isotropic electron distribution to a ball and stick-type model of a covalently bonded system like diamond is instructive since it appears that we can make simple models for both cases. Although ab initio approaches work for both and in between, deciphering the physics of "what is going on physically" is not always clear. The change in bonding with the orbital angular momentum changes of the electrons adds another complication. This is why alloys are of interest since by changing the alloy concentration it is possible to change the contributions of different orbitals to the bonding. For example, the amount of d-electron character of a bond will determine its strength and bonding directions. Finally, the effects of vacancies can be large. All these cases have been discussed here with the objective of describing their role in bonding and in their effect on the bulk modulus and perhaps hardness.

An interesting illustration of the physics that can lead to the strong bonds and high *B* of diamond is shown in **Figure 11** where the electron density (Yin & Cohen, 1981) is plotted for Si and C (in the diamond structure). Unlike Si, a C atom has no p electrons in its core, which has only 2 s electrons; therefore, the valence p electrons do not experience a repulsive pseudopotential (Cohen & Chelikowsky, 1989) and are not pushed out for the core as in the case of Si. Hence, the density for the valence p electrons peaks near their atomic positions and not closer to the center of the covalent bond as in the Si case. The result for C is a double humped bond density

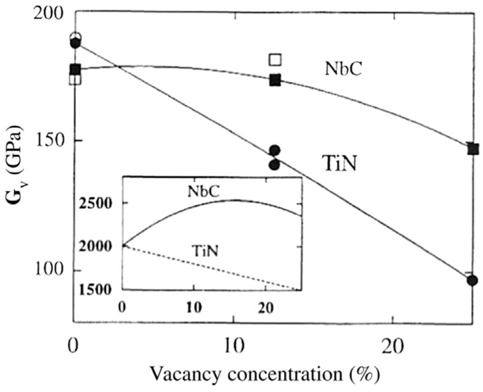

Figure 10 Calculated Voigt elastic stiffness at variable vacancy concentrations. Filled circles and boxes representing the calculated vacancy concentration of 12.5% that come from different supercell values for TiC and NbC, respectively. Different data points at the structures (for NbC, however, the calculated values at different supercells are almost the same and are hardly distinguishable). Experimental data at some vacancy concentrations are also plotted for comparison (open circles for TiN and open boxes for NbC, respectively). Solid lines are guides for the eye. The inset shows the measured hardness of NbC (solid line) and TiN (dashed line), respectively, in units of Vickers hardness (H_V).

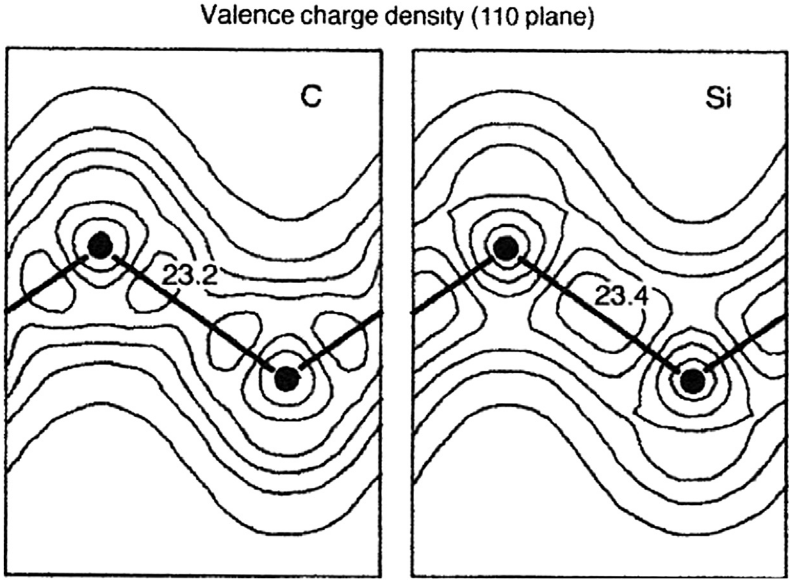

Figure 11 Total valence-charge density plots in the (110) plane for diamond and Si. The charge density is in units of electrons per primitive cell. The contour step is 4. The axes are scaled to facilitate comparison; hence, the length scale is different in these two plots. The black dots denote the atomic positions. Straight lines are drawn to illustrate the atomic chains.

structure compared to Si, which essentially has one hump near the center of the bond; this results in a short dense bond for diamond. Similar cases for other orbital filling effects are probably observable.

The rough message is that it is advantageous to have a high electron density concentrated in short bonds.

Acknowledgments

This work was supported by the National Science Foundation Grant No DMR10-1006184 and Director, Office of Science, Basic Energy Sciences, Materials Sciences and Engineering Division of the US Department of Energy under Contract No. DE-AC02-05CH11231.

References

Chelikowsky, J. R., & Cohen, M. L. (1976). Nonlocal pseudopotential calculations for the electronic structure of eleven diamond and zincblende semiconductors. *Physical Review B, 14*, 556 (Erratum: Physical Review B 30, 4828 (1984)).

Cohen, M. L. (1982). Pseudopotentials and total energy calculations. *Physica Scripta, T1*, 5.

Cohen, M. L. (1985). Calculation of bulk moduli of diamond and zincblende solids. *Physical Review B, 32*, 7988.

Cohen, M. L. (1988). Theory of bulk moduli of hard solids. *Materials Science and Engineering A, 105/106*, 11 (Also, in Proceedings of the 3rd Conference on Science of Hard Materials (Elsevier, Oxford, 1988), p. 11).

Cohen, M. L. (1996). Structural, electronic and optical properties of carbon nitride. *Materials Science and Engineering A, 209*, 1 (Also in Proceedings 5th Conference on Science of Hard Materials, p. 1. Oxford: Elsevier.)

Cohen, M. L., & Bergstresser, T. K. (1966). Band structures and pseudopotential form factors for fourteen semiconductors of the diamond and zincblende structures. *Physical Review, 141*, 789.

Cohen, M. L., & Chelikowsky, J. R. (1989). *Electronic structure and optical properties of semiconductors* (2nd ed.). Berlin: Springer.

Fermi, E. (1934). Sullo spostamento per pressione dei termini elevati delle serie spettrali (on the pressure displacement of higher terms in spectral series). *Nuovo Cimento, 11*, 157.

Hamann, D. R., Schluter, M., & Chiang, C. (1979). Norm-conserving pseudopotentials. *Physical Review Letters, 43*, 1494.

Han, S., Ihm, J., Louie, S. G., & Cohen, M. L. (1998). Enhancement of surface hardness: boron on diamond (111). *Physical Review Letters, 80*, 995.

Hellmann, H. (1935). A new approximation method in the problem of many electrons. *Journal of Chemical Physics, 3*, 61.

Ihm, J., Zunger, A., & Cohen, M. L. (1979). Momentum-space formalism for the total energy of solids. *Journal of Physics C, 12*, 4409 (Erratum: Journal of Physics C 13, 3095(1980)).

Jhi, S.-H., Ihm, J., Louie, S. G., & Cohen, M. L. (1999). Electronic mechanism of hardness enhancement in transition-metal carbonitrides. *Nature, 399*, 132.

Jhi, S.-H., Louie, S. G., Cohen, M. L., & Ihm, J. (2001). Vacancy hardening and softening in transition metal carbides and nitrides. *Physical Review Letters, 86*, 3348.

Kittel, C. (2005). *Introduction to solid state physics* (8th ed.). New Jersey: John Wiley & Sons Inc.

Kohn, W., & Sham, L. J. (1965). Self-consistent equations including exchange and correlation effects. *Physical Review, 140*, A1133.

Liu, A. Y., & Cohen, M. L. (1989). Prediction of new low compressibility solids. *Science, 245*, 841.

Liu, A. Y., & Cohen, M. L. (1990). Structural properties and electronic structure of low-compressibility materials: ß -Si_3N_4 and hypothetical ß-C_3N_4. *Physical Review B, 41*, 10727.

Pauling, L. (1960). *The nature of the chemical bond* (3rd ed.). Ithaca, NY: Cornell University Press.

Phillips, J. C., & Lucovsky, G. (2009). *Bonds and bands in semiconductors*. New York: Momentum Press.

Ribeiro, F. J., Tangney, P., Louie, S. G., & Cohen, M. L. (2006). Hypothetical hard structures of carbon with cubic symmetry. *Physical Review B, 74*, 172101.

Richter, V., Beger, A., Drobniewski, J., Endler, I., & Wolf, E. (1996). Characterisation and wear behaviour of TiN- and TiC_xN_{1-x}-coated cermets. *Materials Science and Engineering A, 209*, 353–357.

Saito, S., & Zettl, A. (2008). *Carbon nanotubes: quantum cylinders of graphene*. Amsterdam: Elsevier.

Smith, R. L., & Sandland, G. E. (1922). An accurate method of determining the hardness of metals, with particular reference to those of a high degree of hardness. *Proceedings of the Institution of Mechanical Engineers, 1*, 623–641.

Sommerfeld, A., & Bethe, H. (1933). *Electronentheorie der metalle*. In *Handbuch der physik* (Vol. 24, Pt. 2, Ch. 3). Berlin: Springer.

Troullier, N., & Martins, J. (1991). Efficient pseudopotentials for planewave calculations. *Physical Review B, 43*, 1993.

Vanderbilt, D. (1985). Optimally smooth norm-conserving pseudopotentials. *Physical Review B, 32*, 8412.

Yang, Y. W., & Coppens, P. (1974). On the experimental electron distribution in silicon. *Solid State Communications, 15*, 1555.

Yin, M. T., & Cohen, M. L. (1980). Microscopic theory of the phase transformation and lattice dynamics of Si. *Physical Review Letters, 45*, 1004.

Yin, M. T., & Cohen, M. L. (1981). Ground-state properties of diamond. *Physical Review B, 24*, 6121.

Yin, M. T., & Cohen, M. L. (1982). Theory of static structural properties, crystal stability, and phase transformations: application to Si and Ge. *Physical Review B, 26*, 5668.

3.02 From Diamond to Superhard Borides and Oxides

John E. Lowther, School of Physics and DST/NRF Centre of Excellence in Strong Materials, University of the Witwatersrand, Johannesburg, South Africa

3.02.1 Introduction

Hardness is a feature of materials as we all know, yet its origin is difficult to describe at the fundamental or even applied level (Brazhkin et al., 2004). It can be considered as being *the resistance of a material to a change of shape under an applied force*, but the changes taking place as well as the resistance to these changes need to be quantified. Diamond is the hardest known material—it has the largest bulk, shear, and Young elastic moduli and it is these elastic properties that are often used to quantify hardness. At the applied level, there are several ways to measure hardness—and in the end these ultimately involve measuring the effect of a single indentation on the material. Thus, really hardness is the relative property of two materials—indenter and material— and for this reason diamond is often used as the major probe.

What happens under an applied force perhaps can be placed into two categories. The first relates to the *static* properties of the material being examined. These would ultimately relate to the nature and the strength of the chemical bond between the atoms in the material. Using modern computational techniques—and especially elaborate quantum mechanical formalisms—notably density functional theory, it is possible to study the properties of the chemical bond. The other relates to the *dynamic* properties and these relate to the movement of defects like dislocations, etc. Often the rate of movement of dislocations also relates to the elastic constants, so dislocations are also associated with the chemical bond.

One measurement of hardness is the Vickers hardness, which is obtained via an indentation technique. In the case of diamond the value is in excess of 70 GPa. There are not many other materials that can approach this value of hardness even though such materials may have a compressibility similar to diamond's but have vastly different properties under shear. Superhard materials in some ways can formally be considered as those having a Vickers hardness of more than about half that of diamond, that is, 30 GPa on the Vickers scale. However, this is a speculative way to quantify superhard properties as the Vickers hardness is essentially an overall isotropic estimate of the behavior of the materials and many materials exhibit a strong anisotropy. A trivial example of this is graphite where there is significant strength in the graphene planes but negligible strength between planes. In fact, it has been suggested that graphene sheets are harder than diamond.

Superhard materials are widely used as tools for industrial applications such as cutting, grinding, chopping, drilling, and milling, as well as sawing and wear parts. Materials of this nature come in different forms such as ceramics, hard metals, and strong alloys and have superior properties to many materials. Often, they resist corrosion, and have high stiffness, high mechanical strength, and most are radiation resistant (Cullen; Qin et al., 2008; Sung & Sung, 1996; Zerr & Riedel, 2000). Diamond is the hardest naturally occurring material known to mankind with a Vickers hardness ranging between 70 and 100 GPa, followed by cubic boron nitride (c-BN). But c-BN is not found naturally and requires harsh and expensive conditions for it to be synthesized. The single crystal hardness of c-BN is between 45 and 50 GPa. Synthetic materials such as polycrystalline diamond (pcD) and polycrystalline cubic boron nitride (pc-BN) are also produced at an economical cost with varying properties for the engineering and manufacturing industries such as drill and cutting inserts (Cullen).

New superhard materials with comparable or even superior properties to diamond are continuously being investigated (Bogdanov, Shulzhenko, Zakora, Isonkin, & Gargin, 2007; Haines Leger, & Bocquillon, 2001; Veprek, 1999) and potentially new superhard materials are presently being designed and examined fundamentally not only for scientific interest but also for commercial usage. Different techniques, both theoretical and experimental, are employed in an attempt to replace expensive diamond for applications where abrasive wear resistance is of great importance. Understanding the fundamental properties of existing superhard materials or what makes them special is of utmost importance in rediscovering and synthesizing the new ones.

It was often thought that hardness was related to compressibility. Diamond has a bulk modulus of 440 GPa whereas c-BN has a bulk modulus of 360 GPa (Brazhkin, Lyapin, & Hemley, 2002). Indeed a number of researchers (Zhang, Li, Li, Zhou, & Cao, 2007) have focused upon the bulk modulus in their search for new superhard materials because hardness correlates well with the bulk modulus for groups IV (Sung & Sung, 1996), III–V (Cohen, 1985), and II–VI (Cohen, 1993) materials.

The strongest materials always contain boron, carbon, nitrogen, and oxygen (Kelly, 1973), and frequently only these light-weight elements are found in superhard structures or compounds (Wu, Sung, Lee, & Tai, 2002). These are the first elements in the second period of the periodic table. In their atomic structure, there are no inner p-electrons in the core to push the valence electrons outward from these elements; then the absence of p-orbitals in the electron core and small atomic volumes result in a high bonding strength. For example, diamond is the hardest because of localized electrons in covalent bonding. Boron carbide (B_4C) and boron suboxides (B_6O) are also hard materials after diamond and cBN and presently there are intense investigations in hard materials involving the B–C–N–O system. Incorporation of transition metal ions into borides and carbides (Mmethi & Lowther, 2009; Okeke & Lowther, 2008) is also a wealthy field of investigation for new superhard materials.

The alloying of diamond with c-BN to identify superhard materials with a B–C–N structure (Mattesini & Matar, 2001; Weihrich, Matar, & Betranhandy, 2003) is producing fascinating new materials. One structure in particular a diamond-like B-C structure has now been synthesized (Solozhenko, Kurakevych, Andrault, Le Godec, & Mezouar, 2009) and is undoubtedly the *lightest hard material ever known*. Properties of this material had been predicted earlier (Lowther, 2005) and so far the predictions are consistent with experiments. It is hoped that the synthesis of dense ternary B–C–N compounds could also exhibit novel properties between diamond and c-BN, and the dense phases may be considered as potential superhard materials. Dense B–C–N phases are expected to be harder than c-BN, but still retain thermal and chemical stabilities of c-BN and this would be an excellent material for the high speed cutting and polishing of ferrous alloys where diamond fails (Chen & Gong, 2007).

Boron-based materials have offered many potential applications (Cook et al., 2004). Many boron-based structures contain a boron icosahedron (Aselage & Tallant, 1998; He, Wu, Wang, Liu, & Tian, 2005; Shirai, 1997; Vast et al., 1997) formed from 12 B atoms and have the potential to contribute as an important hard material. Light-weight C, N, and O atoms are found in such materials with C, N, or O connecting the B icosahedra (Lundstom & Andreev, 1996). Recently, other elements like Mg and Al have also been used and found to be very important (Adasch, Hess, Ludwing, Vojteer, & Hillebrecht, 2007; Cook, Harringa, Lewis, & Russell, 2000; Hubert et al., 1998; Tian et al., 2003). Some of these materials have advantages over diamond and c-BN in that they are easier to synthesize (McColm, 1990) and therefore offer great excitement in new applications of superhard materials.

The search for new superhard materials has been greatly aided by considerable theoretical and computational efforts (Zerr et al., 2006). Theoretical predictions have now demonstrated the potential to contribute toward the development of many new materials (Cohen, 1993), and notably ab initio pseudopotential approaches and molecular dynamic simulation have played an important role. Computer simulation gives information at a microscopic atomic level from which experimental properties are derived or predicted. Ab initio approaches can now quite accurately predict many properties but have computational limitations with numbers of atoms. There still remains the computational challenge of dealing with a very large number of atoms and notably the high-temperature/pressure situations needed for superhard material synthesis that really are metastable states of matter.

This chapter examines the recent developments in superhard materials and how such materials compare with diamond. Although primarily restricted to borides and oxides this chapter is far from exclusive with other recent work covering the developments on advanced superhard nitrides (Zerr et al., 2006).

3.02.2 Hardness and Elastic Constants

Teter argued that there is a good correlation of hardness with the shear constant (Teter, 1998) but for new superhard materials there remains caution and really low compressibility together with high shear are important leading factors. The trend of hardness with bulk and shear modulus is shown in **Figure 1**.

However, this apparent trend has to be regarded with some caution especially for structures with a very low symmetry where the elastic constants can be asymmetric. A simple example of such a material is graphite—in the a–b graphite plane the elastic constants are very large but between planes the weak bonding results in very low elastic constants.

The calculation of elastic constants at an ab initio level has been the subject of several discussions (Mehl, Klein, & Papaconstantantopoulos, 1993; Ravindran et al., 1998). By placing a specific strain on the crystal

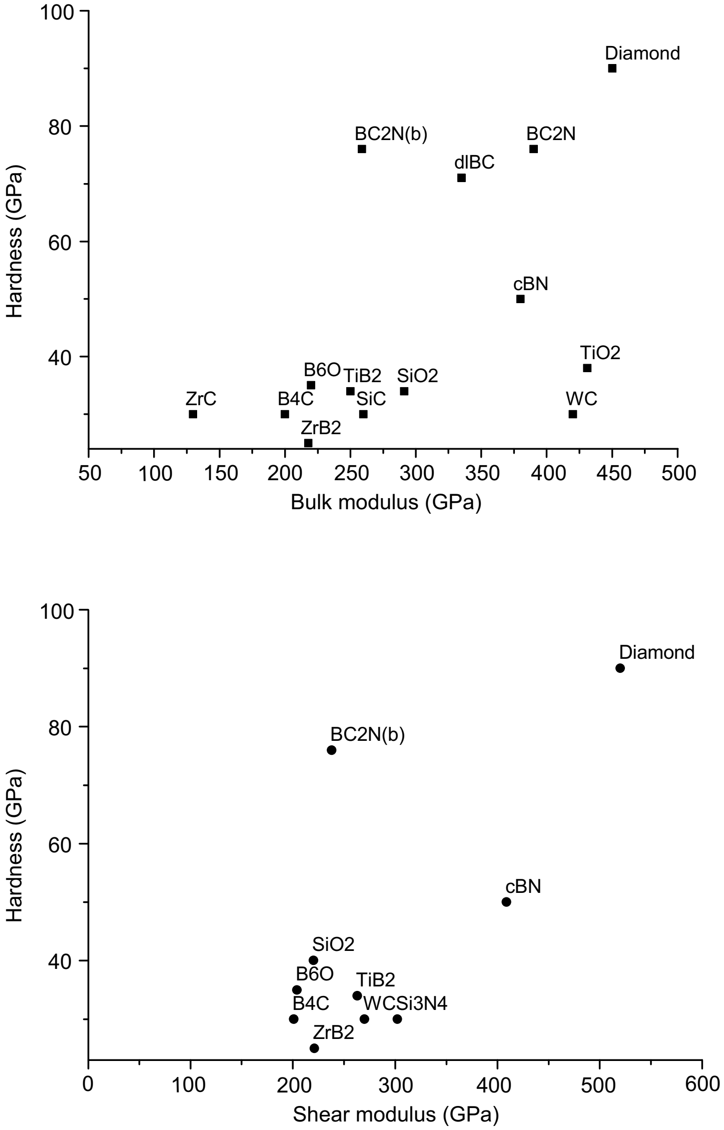

Figure 1 Hardness compared with bulk and shear modulus (taken from Haines et al., 2001). (b) Denotes the values taken from Tkachev, Solozhenko, Zinin, Manghnani, and Ming (2003), the other value for c-$BC_{2.5}N$ taken from Komatsu, Samedima, Awano, Fujiwara, & Kakadate (1999).

structure and then measuring the change in energy as a function of the deformation as specified by a dimensionless parameter x, the elastic moduli can be deduced for a specific system. In general, this strain can be described by the matrix:

$$e = \begin{pmatrix} e_1 & e_6/2 & e_5/2 \\ e_6/2 & e_2 & e_4/2 \\ e_5/2 & e_4/2 & e_3 \end{pmatrix}$$

The elastic stress tensor σ_{ij} may be generally expressed in terms of the elastic strain tensor $\varepsilon_{\mathrm{ij}}$ according to

$$\sigma_{\mathrm{ij}} = c_{\mathrm{ijkl}} e_{\mathrm{ij}}$$

where the c_{ijkl} are the elastic stiffness constants of the crystal. Then the calculated change in energy variation with deformation is obtained approximately as

$$\frac{\Delta E}{V} = f(x)x^2$$

where $f(x)$ is the specific stress appropriate strain.

The elastic constant matrix can also be directly calculated through the second derivative of the energy as formally defined in the elastic constant matrix

$$c_{\mathrm{ijkl}} = \frac{\partial^2 E}{\partial e_{\mathrm{ij}} \partial e_{\mathrm{kl}}}$$

although this approach involves energy derivatives and can be quite sensitive.

The calculation of the energies is obtained from a variety of available electronic ab initio electronic structure (and other) codes that have now proved to be quite reliable in the predictive modeling of materials. Once the elastic moduli are obtained an effective isotropic bulk (B), shear (G), Young modulus (E), or Poisson ratio (ν) can be obtained using the following expressions:

$$B_V = \frac{1}{9}[c_{11} + c_{22} + c_{33} + 2(c_{12} + c_{13} + c_{23})]$$

$$G_V = \frac{1}{15}[c_{11} + c_{22} + c_{33} + 3(c_{44} + c_{55} + c_{66}) - c_{12} - c_{13} - c_{23}]$$

in the case of Voigt moduli and

$$\frac{1}{B_{\mathrm{R}}} = \frac{1}{15}[s_{11} + s_{22} + s_{33} - 2(s_{12} + s_{13} + s_{23})]$$

$$\frac{1}{G_{\mathrm{R}}} = \frac{4}{15}\left[s_{11} + s_{22} + s_{33} - \frac{4}{15}(s_{44} + s_{55} + s_{66}) + \frac{3}{15}(s_{12} + s_{13} + s_{23})\right]$$

in the case of the Reuss moduli where

$$s = \frac{1}{c}$$

are the elastic compliance constants. Often a Hill's modulus is used that is the arithmetic average of the Voigt and Reuss values.

Finally, the Young Modulus and Poisson ratio are given as

$$E = \frac{9BG}{3B + G} \quad \nu = \frac{3B - 2G}{2(3B + G)}$$

Whereas these isotropic values offer considerable guidance in the properties of the material, anisotropic concerns should not be overlooked and it is only the elastic constants that can provide an insight into the overall material strength. Isotropic bulk or shear elastic constants offer only a guide to the overall use of a material for the purposes of hardness.

3.02.3 Diamond and Related Cubic Superhard Structures

Two chemical defects boron and nitrogen are readily absorbed into diamond and nitrogen absorbed into diamond with nitrogen. Nitrogen leads to Type I and Type IIA diamond and boron to Type IIB diamond. Nitrogen is responsible for yellow-colored diamond, and boron for slightly blue—or more particularly quite clear diamond. Type IIB diamonds are the most valuable. Synthetic diamond is mostly used for abrasive purposes and is now relatively inexpensive to produce. The hardening of diamond surfaces has also been discussed (Han, Ihm, Louie, & Cohen, 1998) with nitrogen or boron replacing the surface carbon atoms although surface charge transfer effects may be uncertain (Larsson & Ristein, 2005). It is quite unlikely that there will be a harder natural material than diamond but with its cost and physical limitations alternatives are needed.

The exact maximum concentration of nitrogen and boron defects that can be included into diamond has not yet been established, although under extreme conditions this content could be of great significance. As a single substitutional point defect, boron gives rise to an electronic defect level lying at 0.37 eV above the valence band edge and is responsible for making the material p-type (Chrenko, 1973; Custers, 1955). Infrared optical spectroscopy has now revealed that the ground state of the bound hole of the B acceptor is associated with and pinned to the valence band (Collins & Lightowlers, 1968; Crowther, Dean, & Sherman, 1967). More recent work has also shown the existence of Lyman excited hole states of this shallow defect (Nebel, Rohrer, & Stutzmann, 2001) again showing the shallow nature of the B acceptor.

At very high concentrations of boron yet another but far more elaborate mechanism of conductivity appears to emerge. This has been deduced from an apparent metal–insulator transition in single crystal diamond that has been *very* heavily doped with boron using low-temperature ion implantation methods followed by subtle high-temperature annealing (Sshepe, Prins, & Hoch, 1999). Electrical transport measurements made on this system, at low temperatures also showed the presence of hopping conduction as observed by Mamin et al. (Mamin & Inushima, 2001), but with even heavier doping in these samples a change in the metallic conduction was found. These centers give rise to a complicated electrical conductivity (Wilson, 1962) and, if diamond is subject to extreme conditions such as pressure, possibly even to superconductivity (Ekimov et al., 2004). In fact, conditions that have been reported to lead to superconductivity are $P = 8\text{–}9$ GPa and $T = 2500\text{–}2800$ K (Ekimov et al., 2004).

Although diamond is the hardest known material, postdiamond phases have been observed (Ferroir et al., 2010). The postdiamond phase was found in natural occurrences of a meteorite and is a superhard rhombohedral carbon polymorph with a structure quite close to diamond but only with a partial occupancy of some of the carbon sites. The observation is of significance as the structure has a strong similarity to postdiamond phases that had been previously predicted (Scandolo, Bernasconi, Chiariot, Focher, & Tosatti, 1995; Scandolo, Chiarotti, & Tosatti, 1996) using ab initio calculations. The realization of such postdiamond structures is anticipated to require very extreme conditions (in excess of 500 GPa) and as such would not be viable with present technology. The calculations however do suggest interesting speculation as to the history of the meteorites where the postdiamond phase was observed and notably implications for understanding the interiors of planets such as Uranus and Neptune (Nellis, Mitchell, & McMahan, 2001).

One synthetic alternative to diamond is cubic boron nitride (c-BN). This material has the same face centered structure as diamond—as shown in **Figure 2**—and is a material with important potential as cutting tools.

Presently, there are at least five BN crystalline forms that have attracted interest; hexagonal BN (h-BN), cubic zinc-blende (c-BN), the wurtzite structure (w-BN), the rhombohedral structure (r-BN), and the rock salt structure. Cubic (zinc-blende) BN represents one of the simplest III–V compounds. This structure is diamond-like, but the space group symmetry is changed from the centrosymmetric F3dm of diamond to the non-centrosymmetric F_{43m} group for c-BN. As with numerous boron compounds, c-BN has a high melting

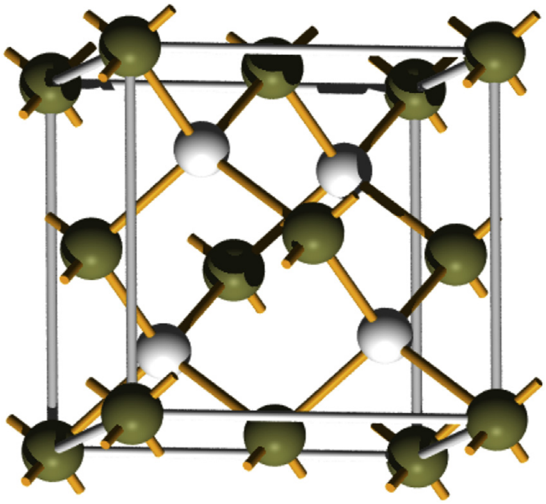

Figure 2 Face centered structure of c-BN.

temperature and a very high hardness, and is also characterized by a high thermal conductivity. Both diamond and c-BN are made of atoms belonging to the first row of the periodic table and can be considered as model systems of the elemental IV and III–V group semiconductors. This material is not generally found in nature (Chen & Gong, 2007; Kaner, Gilman, & Tolbert, 2005; Mattesini & Matar, 2001) and has to be prepared synthetically (Tersoff, 1989).

3.02.3.1 Precursor Phases

The usual precursor phase of diamond is graphite and for c-BN a similar graphitic structure. Both are hexagonal structures but differ in the way that the layers are stacked. There is a very low energy difference between the stacking and the use of catalysts has played an important role in controlling the phase transition from the graphitic structures to the superhard phases.

The hexagonal structure of BN has four atoms in the unit cell. It may exhibit a simple AaAa.. stacking sequence such that the B atoms in the layer are placed directly below the N atoms. This is different from the hexagonal form of graphite where only half of the C atoms are directly above or below the C atoms in the adjacent layers. Other hexagonal AaAa.. stacked structures of BN may also be possible with a stacking sequence arranged in such a way that the B atoms in adjacent layers lie at different locations relative to the N atoms. The measured lattice parameters are very close to those of graphite although h-BN differs from graphite in that it is white and an insulating material whereas graphite is black and an electrical conductor. Both materials are strongly bonded within an atomic layer, but bonding between layers is weak. The anisotropic character of these layer structures has inspired many studies of the lattice heat capacity. In both hexagonal BN and graphite, the lattice heat capacity varies as T^2 in some temperature region. This has been interpreted as being a consequence of anisotropic lattice forces. At sufficiently low temperatures, the lattice heat capacity is expected to have a T^3 dependence. This has been observed in graphite, but in the case of hexagonal BN no low-temperature data have so far been reported.

Boron nitride is commonly crystallized in a graphite-like form, and this fact led to the speculation many years ago that BN might also be synthesized into a diamond-like (zinc-blende). It was subsequently found that conditions of high pressure and temperature similar to those found for diamond synthesis were suitable for the preparation of c-BN. In both syntheses, the cubic product may be produced at pressures and temperatures appropriate for its thermodynamic stability by means of catalyst action upon the hexagonal starting material. The catalysts effective for the formation of cubic boron nitride however are different from those required for diamond synthesis (Solozhenko et al., 2002), and consist of alkali and alkali-earth metals, their nitrides, and antimony, tin, and lead. The transformation may possibly be described in the same way as the transformations between layered and tetrahedral phases of carbon (C) in terms of a progressive buckling of the hexagonal layers. Cubic BN may be synthesized under pressure and elevated temperature from rhombohedral BN, and wurtzite

BN, at somewhat lower temperatures from hexagonal BN. At higher temperatures, a catalyst is needed for the hexagonal BN and wurtzite BN transformation to the cubic BN phase. This implies that the hexagonal and wurtzite BN structure is a metastable phase.

The h-BN to c-BN transformation, unlike that of graphite to diamond, is very much dependent upon kinetic factors. Albe (Albe & Moller, 1998) has recently presented quite a novel argument to account for this. Essentially, the model presented is that the vibrational energy of the hexagonal sheet has a two-dimensional behavior whereas the c-BN vibrational energy behaves as a three-dimension system in the harmonic approximation. The relative energies of these effective two- and three-dimensional systems behave differently with temperature and this reduces the overall Free energy of h-BN and c-BN and is responsible for the h-BN to c-BN phase transition. Thus, whereas the precursor phases of diamond and c-BN have quite similar structures, there are important differences in that the relative energy of diamond lies above that of graphite whereas the h-BN is above that of c-BN.

3.02.3.2 Diamond-like Materials

As graphite leads to diamond and hexagonal BN(h-BN) leads to cubic BN(c-BN), hexagonal structures are the usual precursor phases to superhard diamond-like (cubic) structures. A range of graphitic structures of boron–carbon phases are also known to exist. Graphitic BC_3 has been deduced from experimental and computational study with suggestions of superconductivity in the material. The formation of a hexagonal boron carbon nitride thin film has been attained by the irradiation of B_4C by nitrogen molecules (Gagoa, Jiménez, Agulló-Rueda, Albella, & Hultman, 2002). As the irradiation dosage is increased, a film structure evolves from an amorphous boron carbide network and leads to a hexagonal ternary compound h-BC_2N. Brillouin scattering was used to identify the elastic properties of the phase (Kurdyumov et al., 2000; Tkachev et al., 2003), which suggested the existence of several possible phases of the material with a similar stoichiometry. Based upon the large values of the elastic constants and subsequent measurements, it was suggested that the BC_2N material could be the second hardest material after diamond.

Various theoretical models have been proposed to describe the most probable structure of this cubic phase (Sun et al., 2003) of BC_2N within an eight-atom zinc-blende structure forming the basis for the investigation. Typically, in these models, B, C, and N atoms have an orderly distribution on the diamond lattice sites with a certain space group symmetry and are constructed by avoiding the low energy bonds, B–B and N–N and separating the BN layer from the carbon layer in the unit cell. Similarly, a theoretical model was proposed for various B–C diamond-like structures (Lowther, 2005). All structures were metastable relative to, for example, diamond and c-BN. As with BC_2N, the predicted B–C material was subsequently synthesized (Solozhenko et al., 2009; Zinin et al., 2005) and this diamond-like B-C material must be considered as being the *lightest weight* strong material. The prediction together with synthesis is a typical example of the usefulness of prediction and related synthesis of new materials.

More recently, other materials like B–C and B–C–N have also been examined as these too have elastic properties approaching those of diamond (Letsoalo & Lowther, 2008; Masago, Shirai, & Katayama-Yoshida, 2006). The material synthesized by the Solozhenko group (Solozhenko et al., 2009) appeared to have a stoichiometry of BC_5 and is a randomly dispersed distribution of boron in diamond. As discussed within the 8-atom unit cell model of the simple diamond lattice model with B, C, or N atoms placed at the various lattice points according to the lattice stoichiometry (Sun, Jhi, Roundy, Cohen, & Louie, 2003) the relative energetics between the hexagonal and diamond-like phases can be deduced. In the case of a simple binary B–C structure both ab initio and bond-order potentials have been used to examine the elastic properties of a typical crystalline or random B–C structure (Nkambule & Lowther, 2010). The results are shown in **Figure 3** where it is implied that there is a steady decrease in the hardness of the material with B concentration as expected. In fact, this also relates to the number of C–C bonds present in the structure.

3.02.3.2.1 Diamond-like B–C–N Phases

The hardness of BC_2N has also been discussed at length (Guo et al., 2007) and several possible structural forms of BC_2N have now been proposed. These include cubic c-BC_2N (Sun et al., 2003), chalcopyrite (Guo et al., 2007), body-centered (Xiaoguang et al., 2007), tetragonal (Luo et al., 2007), rhombohedral (Li et al.), low-density BC_2N (Kim, Pang, Utsumi, Solozhenko, & Zhao, 2008), a superlattice structure (Chen, Gong, & Wei, 2007), and orthorhombic-BC_2N (Cheng, Wu, Li, & Chu, 2008). Cubic c-BC_2N has been considered to be a more likely phase due to its simulated X-ray diffraction (XRD) spectrum which agreed well with the experimental data

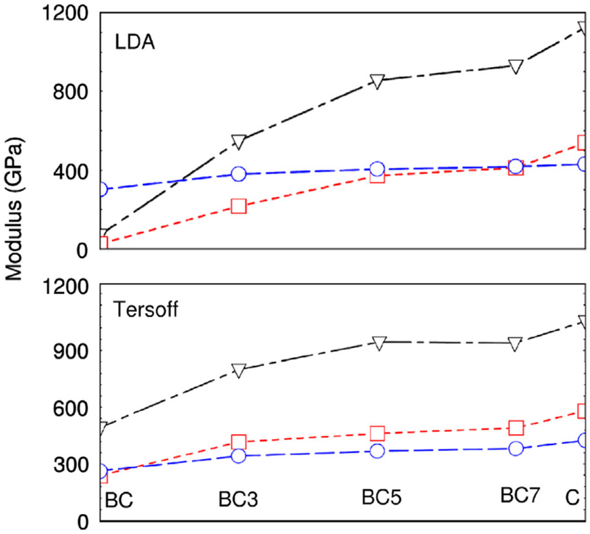

Figure 3 Bulk (○), shear (□), and Young moduli (▿) of crystal structures.

(Zhou et al., 2007), although the exact atomic configuration is still unknown. In 2001, Solozhenko et al. (Solozhenko, Andrault, Fiquet, Mezouar, & Rubie, 2001) synthesized c-BC_2N using graphite-like BC_2 N as a starting material above P = 18 GPa and more than T = 2200 K, which had a Vickers hardness of 76 GPa, higher than that of cubic boron nitride. Zhou et al. (2008) also reported that the BC_2N synthesized with a zinc-blende structure has a nominal hardness of 62 Pa. Various theoretical models have been proposed to describe the most probable structure of this cubic phase. Sun et al. (Sun et al., 2003) have identified seven topologically possible configurations of c-BC2N within an eight-atom zinc-blende structure. Typically, in these models, B, C, and N atoms have an orderly distribution in the diamond lattice sites with a certain space group symmetry and are constructed by avoiding low energetic bonds, B–B and N–N and separating the BN layer from the carbon layer in the unit cell. Random distributions of B, C, and N atoms over the lattice sites have also been strongly suggested by XRD data (Knittle, Kaner, Jeanloz, & Cohen, 1995; Solozhenko et al., 2001; Zhou et al.) and Raman analysis (Hubble et al., 2004). Hubble and his group (Hubble et al., 2004) observed a wide peak at 1325.7 cm^{-1} in the Raman spectrum of c-BC2N, and they speculated that the C atoms were substituted randomly by B and N atoms on the host diamond crystal lattice. Such random distributions seem plausible and will likely reveal that the hardness of a typical B–C–N structure again relates to the distribution of C–C bonds in the material.

3.02.3.3 Cubic Spinels

The unit cell of a typical spinel material contains 56 atoms and belongs to the space group F_{d3m}. Some halides, nitrides, and sulfides also crystallize in a spinel structure and the most notable of these are Si_3N_3 and Ge_3N_4. Si_3N_3 in particular is an important new synthetic superhard material recently found with the spinel structure (Ching, Mo, Tanaka, & Yoshiya, 2001; Mo, Ouyang, Ching, Tanaka, & Riedel, 1999; Tanaka et al., 2002; Zerr et al., 1999). In the case of spinel ternary or quaternary oxides, the cation-to-anion ratio distribution of such spinels is 3:4 irrespective of the many different phases such as binary (Fe_3O_4), ternary ($MgAl_2O_4$), and quaternary phases ($Si_{6-z}Al_zO_zN_{8-z}$) that could have applications as a hard material. A typical spinel structure is shown in Figure 4.

There are two types of limiting configurations of cations in the spinel-structured compounds called normal (or direct) spinel and inverse (or indirect) spinel. The normal spinel refers to a compound that is composed of divalent and trivalent cations, where the less abundant divalent cations occupy tetrahedral A-sites and the more abundant trivalent cations occupy octahedral B-sites. However, the work done by Barth and Posenjak (Barth & Posnjak, 1932), who based their conclusions upon a detailed discussion of the intensities of XRD pictures, pointed out a second possibility called the inverse spinel, $B(AB)O_4$, which is composed of tetravalent and divalent cations, where half the divalent cations occupy tetrahedral A-sites and all the tetravalent cations and together with the other half the divalent cations occupying the octahedral B-sites. Besides these two

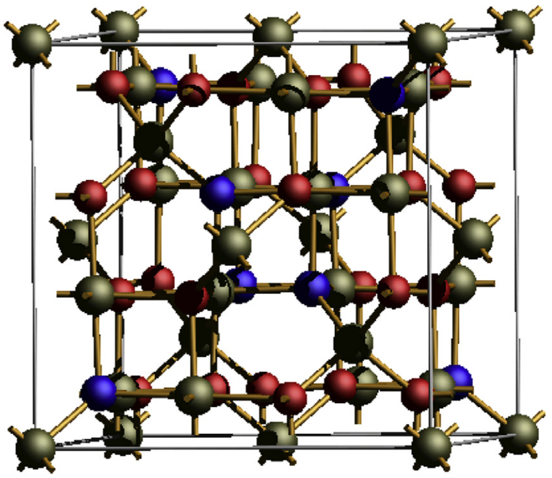

Figure 4 The cubic spinel structure.

arrangements there are possibilities for some intermediate arrangements of the form $(A_{1-2x}B_{2x})(A_{2x}B_{2-2x})O_4$ with an average distribution of all ions about the spinel cation positions. Spinels with these configurations are known as intermediate or random spinels. They are located somewhere between the normal and the inverse arrangements. The variable x is the so-called inversion parameter, which specifies the fraction of A-sites occupied by the majority of ions. It ranges from 0 for the normal spinel to 0.5 for the inverse spinel. In addition, there are ternary spinels of the type $A_x\ B_2\ S_4$ where A = Al, Ga, and B = Mo, V, Cr (Brasen et al., 1975) or quaternary spinels with Si, Al, O, or N (Lowther, Schwarz, Kroke, & Riedel, 2003; Schwarz et al, 2001). Thus, we see that the structure that is called a spinel is highly variable chemically, stoichiometrically, as well as topologically. An essential structure of the spinels is that they are composed of either a 12-fold or a fourfold degenerate symmetry site depending upon the occupancy of the octahedral or tetrahedral interstices.

In **Figure 5** we show some recently calculated values of the Bulk Modulus of various single spinel nitrides as obtained from Ching, Mo, and Chen (2002) and Okeke and Lowther (2008). As can be seen, there is some dependence of the Bulk modulus on the lattice constant.

Recent studies have also shown that spinel materials containing oxygen and nitrogen are advanced materials with various potential superhard material applications (Fang et al., 2000; Kroll, Dronskowski, & Martin, 2005; Lowther, Amkreutz, Frauenheim, Kroke, & Riedel, 2003; Lowther, Wagner, Isabel, & Riedel, 2004; Okeke & Lowther, 2009; Soignard et al., 2005), and one of these systems is the oxynitride of aluminum (Al–O–N)

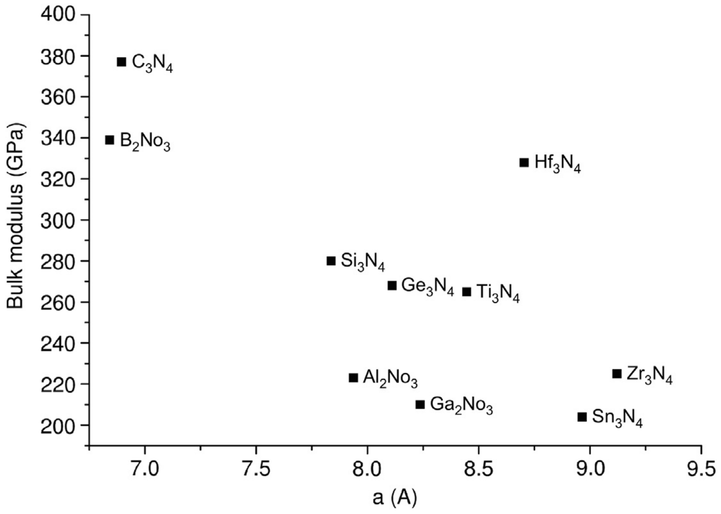

Figure 5 Bulk moduli of some cubic spinel structures: nitrides (Ching et al., 2002) and oxynitrides (Okeke & Lowther, 2008).

(Hartnett, Bernstein, Maguire, & Tustison, 1998; Miller & Kaplan, 2008; Tabary & Servant, 1999; Willems, Hendrix, Metselaar, & de With, 1992). The ideal Al_3NO_3 in the stable state is an incompressible structure and could possibly be a novel superhard material with a possible application as industrial abrasive device. $Al_{23}N_5O_{27}$ (Corbin, 1989; Graham, Munly, McCauley, & Corbin, 1988; McCauley et al., 2009) is an advanced polycrystalline ceramic material for refractory industries and for protective windows in optical systems (Fukuyama, Nakao, Susa, & Nagata, 1999). Where optical transparency is needed, $Al_{23}N_5O_{27}$ is a better candidate than $\alpha - Al_2O_3$ because of its chemical stability with the addition of nitrogen into an isotropic alumina-based material. It is one of the leading candidates for manufacturing transparent armors (Patel, Gilde, Dehmer, & McCauley, 2000). $Al_{22}N_2O$ (Corbin, 1989) on the other hand has not been much investigated but is seemingly one of the stable phases of the Al–O–N compounds. More recent studies (Fukuyama et al., 1999; Zientara, Buckó, & Lis, 2007) on Al–O–N phases have focused on the synthesis and fabrication as well as the phase relation of this system both at the experimental and theoretical levels; however, relatively little work has been directed toward the elastic properties of these structures. The calculated elastic constants and their effective isotropic elastic moduli show that with a decrease in the nitrogen content, the $c_{1.1}$ and $c_{1,2}$ are relatively the same but $c_{4,4}$ decreases steadily when N occupies different locations in the spinel lattice. There are no experimental values of $c_{1.2}$ for the defective structures, although McCauley et al. (2009) have recently reported $c_{1.2}$ for $Al_{23}N_5O_{27}$ using the formula, $c_{1,2} = c_{1.1} - 2c_{4,4}$, which is in excellent agreement with theoretical values (Okeke & Lowther, 2010).

3.02.3.3.1 Precursor Phases of Superhard Spinel Si–C–N

Silicon nitride in the form of Si_3N_4 is expected to take either the α or β hexagonal forms although recently yet another higher density structure has been identified (Zerr et al., 1999) with a cubic spinel structure. The possible incorporation of C into the Si_3N_4 material is expected to considerably enhance its potential as a superhard material (Badzian, 2002). Some phases have been suggested as a possible precursor (Riedel et al., 1997) to the superhard phases. It has been shown (Lowther, Amkreutz, Frauenheim, Kroke, & Riedel, 2003) that it is the strength of the C–N bond that connects the layers in this material that may be the major hindrance for its use as a possible precursor phase although the extreme compression of the CN bond will significantly deform. The conditions under which this bond effectively collapses is also consistent with the predicted synthesis pressure on the Aba2 phase that leads to either the β or spinel structures.

The C–N bond is far more covalent than Si–N bonds and as such more significant for a superhard material. The importance of C in affecting the bonding in these structures is also consistent with recent results (Ching et al., 2001) on a series of spinel-related structures where the inclusion of C is associated with a larger bulk moduli.

3.02.4 Superhard Borides

Boron-based hard materials of the binary or ternary systems, B–C, B–N, B–O, or Mg–Al–B (e.g. B_4 C, B_4 N, or $MgAlB_{14}$) all have good technological applications and are commercially available hard materials due to their combined hardness and good oxidation resistance at elevated temperatures. Boron carbide (B_4 C) is one of the hardest materials. As with many borides, B_4 C is composed of simple B icosahedra, the most stable building block in the boride. Technical application of boron-rich materials is presently largely limited to boron carbide, and B_4 C is the carbon-rich limit of the homogeneity range. Industrially, boron carbide powder is used as an abrasive in polishing and lapping applications, and also as a loose abrasive in cutting applications such as water jet cutting. It can also be used for dressing diamond tools.

3.02.4.1 Icosahedral Boron-Based Borides

Crystalline boron-rich nitrides (B_x N) of the compositions B_{25} N up to B_{53} N as well as amorphous phases of the composition B_3 N and B_5 N have also been synthesized by chemical vapor deposition methods (Ploog, Rauh, Stoeger, & Schmidt, 1972). A B_4N phase with an analogous structure to B_4C has been examined (Ploog et al., 1972) with a crystal structure also consisting of boron icosahedra as in B_4 C. It is expected that this phase can be expected to exhibit interesting hardness properties (Ploog, Schmidt, Amberger, Will, & Kossobutzki, 1972; Saitoh, Yoshida, & Yarbrough, 1993). B–O materials are highly refractory and also suitable for use on surfaces subject to abrasion, for example, grinding wheels, drill bits, and machine tools and in structures employed in extreme conditions. Aluminium infiltrated B_6O drill bits have been successfully made and their stability tested at temperatures higher than 1800 °C which exceeds that of polycrystalline diamond (Kayhan & Inal, 1999).

$MgAlB_{14}$ films also serve as an excellent protective coating for microdevices because of extreme hardness, exceptionally low coefficient of friction, and strong adhesion to a wide range of substrate materials. Boron aluminum magnesium materials are cheaper to manufacture compared to diamond and c-BN, and they have been successfully used as coating materials on WC/Co cutting tool inserts. It is well accepted that the development of boride-based materials has been driven by the fact that they have a better oxidation resistance than diamond-based materials. Therefore, boride materials are expected to have a great potential for new superhard materials with industrial applications in the future.

Table 1 shows some measured values of the hardness of these materials with the crystal structure shown in **Figure 6**.

Table 1 Vickers hardness (GPa) of some B-related structures

Material	*Hardness*
$NaAlB_{14}$	23–28
$MgAlB_{14}$	20–46
B_4C	27–30
B_6O	45
c-BN	60
Diamond	75

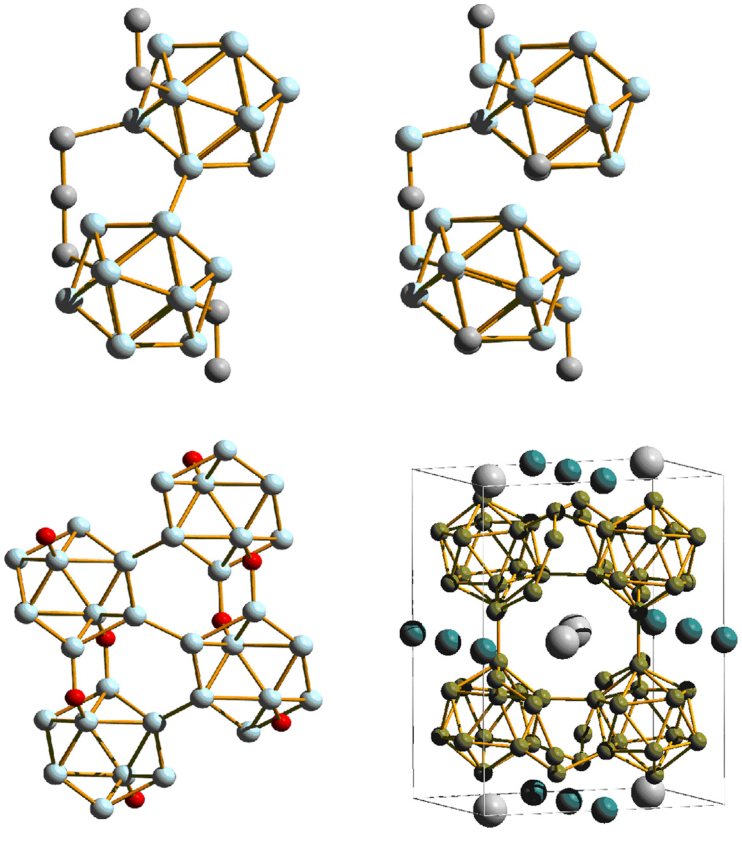

Figure 6 Various boride phases top: B_4C (polar and chain configurations), lower left: B_6O, lower right: $MgAlB_{14}$.

There have been several considerations as to why this material is so hard (Chen & Gong, 2007; Emin, 1987; Gao, Hou, & He, 2004; Kaner et al., 2005; Letsoalo & Lowther, 2008; Lowther, 2002; Mattesini & Matar, 2001) but it is now agreed that the hardness essentially results from electronic structure changes taking place mainly within the boron icosahedron. Probably one main shortcoming of the boride-based materials is that they have some brittle characteristics but this may be overcome by the inclusion of additional chemical structures into a sintering process (Johnson et al., 2010). Further work is needed here that could lead to new materials.

3.02.5 Superhard Oxides

Unlike carbides and borides or even nitrides, oxides offer a unique chemical character for potential refractory applications mainly because of low reactivity with the atmosphere. Moreover, some of the oxide ceramic materials are moldable materials with beneficial mechanical properties such as considerable hardness, good chemical resistance, high tensile strength, and a good fracture toughness. Silica (SiO_2) with its many polytypes is often thought as being a basis for the simplest of the oxides. Under compression, the relative volume per molecular unit of SiO_2 decreases indicative of reduced compressibility and enhanced hardness. Two of the higher density structures of SiO_2 have Si in a sixfold coordination and a related high hardness—one of these is stishovite. Normally, Si does not care for such a high coordination and thus the stability of the high compression phase may be difficult. On the contrary with metal oxides, the flexibility of the metal d-bonding character enhances metal coordination possibilities and very high oxygen coordinations are now observed under compression. Zirconia is one well-known ceramic and of the various polytypes of ZrO_2, Zr is observed to have an O coordination number of nine.

Stabilization of the oxide structures is presently the main challenging task facing the rapidly oxide ceramics. To date, SiO_2 in the high-temperature and high-pressure form of stishovite has not been stabilized and with modest temperatures rapidly reverts to quartz. ZrO_2 on the other hand has two high-temperature phases (tetragonal and cubic) that can be stabilized with the addition of modest amounts of other chemical impurities that are thought to affect the oxygen sublattice. Aside from SiO_2 and ZrO_2, many other oxides have been considered for potential use as refractory materials—HfO_2 and RuO_2 are two oxides and there has been much recent emphasis on TiO_2 (Dubrovinsky et al., 2001) such that cotunnite TiO_2 is claimed to be the hardest known oxide material (Dubrovinsky et al., 2001). However synthesis pressures in excess of 50 GPa seem to be required to achieve this structure.

3.02.5.1 Silica

Many of the phases of SiO_2 are of the reconstructive type possibly as a result of ordering and displacive mechanisms from a parent disordered body-centered cubic structure possessing different fractional occupancies of SiO_2 molecules (Dmitriev, Tolédano, & Salje, 1998). Various types of calculational modeling procedures have indicated that under pressure rotations of the SiO_4 tetrahedra in quartz produce edge-sharing SiO_6 octahedra that are observed in the stishovite structure (Tjabane & Lowther, 1999; Tse, Klug, & Bernasconi, 1997; Wentzcovitch, Da Silva, & Chelikowsky, 1998) (though possibly not exactly the exact stishovite structure (Tjabane & Lowther, 1999)) consistent with observations on the quartz–stishovite transition (Hemley, Prewitt, & Klima, 1994).

Alpha quartz when compressed above 300 K is found to undergo pressure-induced amorphization (Hemley, Jepheoat, Mao, Ming, & Manghani, 1988) starting at about 15 GPa, but at 21 GPa another phase of quartz appears (Hemley et al., 1994) that could be associated with a crystalline–crystalline transition rather than a crystalline–amorphous transition. With further pressure, amorphization of the quartz structure is observed and a new phase eventually appears with Si in sixfold coordination with O. Constant volume molecular dynamical simulations (Hemley et al., 1994) have pointed to the importance of stress-induced amorphization with highly metastable crystalline phases and Binggeli and Chelikowsky (Binggeli & Chelikowsy, 1992) related the transformation of quartz to critical changes in the atomic structure arguing that the amorphization of quartz is triggered by a lattice shear instability associated with closely spaced O atoms. Ab initio plane wave pseudopotential calculations have now suggested the possibility of an extensive polymorphism in silica at a high pressure, with an essentially infinite number of metastable structures following a small compression of quartz (Teter, Hemley, Kresse, & Hafner, 1998). However, these calculations do not stress the importance of closely spaced O atoms in affecting the phase transformations but rather that the disordered locations of Si are important in the metastable amorphous structure.

Despite very many extensive studies in understanding the complex behavior of the relation between the SiO_2 polytypes, the essential focus, namely, stabilization of the high-pressure superhard phases of SiO_2 appears to be a formidable challenge.

3.02.5.2 TiO_2

Rutile is the most abundant TiO_2 polymorph found in nature, having a very similar crystallographic structure as stishovite and has been one of the most studied phases of TiO_2 (Haines, Léger, & Blanzat, 1994). The structure of rutile is shown in **Figure 7**.

TiO_2 also exists naturally as anatase and brookite. With the application of high pressure, other phases of TiO_2 are important (Haines & Leger, 1993; Dubrovinsky et al., 2001)—some properties are given in **Table 2** where an increase in the Bulk modulus with coordination is evident. Pressure studies indicate that rutile is preserved up to 8–12 GPa (the higher value being for a nanophase), where it transforms to a baddeleyite-type structure (Sato et al., 1991; Wang, Saxena, Pischedda, Liermann, & Zha, 2001) and under decompression, the latter phase transforms to the α-PbO_2 phase at 7 GPa (Haines & Leger, 1993). The latter phase has tentatively been suggested as a potential candidate, along with fluorite-type structures, for the structure of a high-pressure phase of TiO_2 (Haines, Leger, & Schulte, 1996). Starting from another natural phase of TiO_2, anatase, it has been observed that the α-PbO_2 is obtained at pressures of 4.5–7 GPa (Arlt et al., 2000; Lagarec & Desgreniers, 1995) and then the baddeleyite phase is reached at pressures between 13 and 17 GPa. Thus, in the case of TiO_2, there is more than one specific high-pressure route that can find the baddeleyite structure starting from either the rutile or anatase ambient structures. In fact, the relative stability of rutile compared to other polytypes is now well studied (Arlt et al., 2000; Calatayud et al., 2001; Dewhurst & Lowther, 1997; Glassford & Chelikowsky, 1992; Keskar & Chelikowsky, 1992) using ab initio computational modeling. Quite recently, the cotunnite structure of TiO_2 has

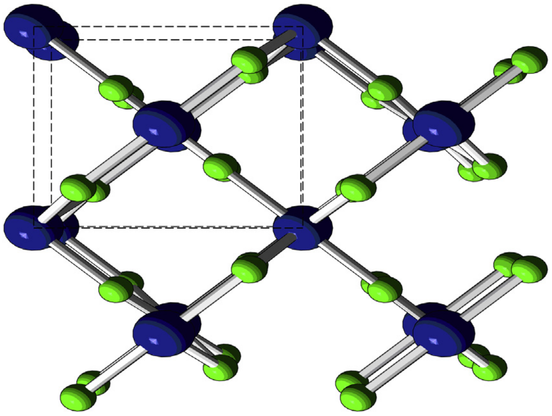

Figure 7 Rutile TiO_2, the larger atoms are Ti. This structure is observed in several metal oxide ceramics.

Table 2 Crystal phases and bulk moduli of TiO_2

Phase	*Coordination*	*B(GPa) (calculated)*	*B (GPa) (experimental.)*
Anatase	6	194 (Dewhurst & Lowther, 1997), 189 (Arlt et al., 2000)	179 (Arlt et al., 2000)
Rutile (*P*42/*nmc*)	6	243 (Dewhurst & Lowther, 1997)	211 (Arlt et al., 2000)
Baddeleyite ($P2_1/c$)[a]	7	249 (Dewhurst & Lowther, 1997)	235 (Arlt et al., 2000)
Cotunnite (*Pnma*)[a]	9	310 (Dewhurst & Lowther, 2001), 380 (Dubrovinsky et al., 2001)	431 (Dubrovinsky et al., 2001)

[a] *High-pressure phases.*

also been synthesized (Dubrovinsky et al., 2001) and the structure determined. It has been established that this structure is the hardest phase identified for binary oxides.

Nanophase TiO_2 and other materials are also considered important in the high P–T processing of advanced engineering materials, since they may have enhanced mechanical properties compared to their bulk counterparts. For example, there is improved sinterability at low temperatures and pressures to obtain densified compacts that potentially have enhanced toughness and low-temperature superplastic deformation (Stir et al., 2003), and may therefore be useful for relatively cheap long-lifetime cutting and grinding tools. Several studies indicate that a reduction of particle size results in a significant enhancement of Young's modulus or Poisson's ratio that can lead to an increase in the room temperature bulk modulus, but below a critical size, both these properties exhibit a remarkable softening (Villain, Godeau, Renault, & Badawi, 2002; SchiÃtz, Tolla, & Jacobsen 1998). The analysis of the high-pressure Raman data of anatase TiO_2 has led to suggestions that compared with bulk anatase, there is a decrease or similar compressibility for the 7- to 11- and 12-nm nanophase material (Hearne et al., 2004; Wang & Saxena, 2001). This enhancement has been interpreted as being due to the formation of a dense surface region on the nanoparticle with the core of the particle retaining some degree of crystallinity and dilute defective structure (Pischedda et al.).

3.02.5.3 ZrO_2 and HfO_2

It is well known that ZrO_2 assumes a monoclinic (McCullough & Trueblood, 1959) (baddeleyite) unit cell containing four ZrO_2 molecules ($Z=4$) at ambient conditions. It transforms into a tetragonal (Aldebert & Traverse, 1985) form at about 1440 K and a cubic (fluorite) form (Smith & Cline, 1962) around 2640 K and then finally a melt at about 2950 K. Qualitatively, HfO_2 follows quite similar properties to those of ZrO_2 but there are significant differences in the elastic behavior and synthesis transition pressures. The properties of the main phases are given in **Table 3**. The occurrence of phase transitions to the orthorhombic or monoclinic modification of amorphous ZrO_2 on laser parameters dependency has also been established (Starbova et al., 2001) for the surface modification of vapor-grown amorphous ZrO_2 thin films and also for HfO_2 (Aarik et al., 2001).

There is less consensus on the structure of the high-pressure phases, the main reason for this being the difficulty associated with in situ high-pressure experiments. Confusion also arises from the differing sets of

Table 3 Crystal phases and bulk moduli of ZrO_2 and HfO_2

		ZrO_2		*HfO_2*	
Phase	*Coordination*	*B (calculated)*	*B (experimental)*	*B (calculated)*	*B (experimental)*
Baddeleyite (*P*2_1/*c*)	7	157 (Dewhurst & Lowther, 1998)	212 (Desgreniers & Lagarec, 1999)	251 (Lowther et al., 1999)	284 (Desgreniers & Lagarec, 1999)
Tetragonal (*P*42/*nmc*)	6	200 (Dewhurst & Lowther, 1998)	205 (Ohtaka et al., 2001a)		
Fluorite (*Fm*3*m*)	8	267 (Dewhurst & Lowther, 1998)	215 (Ingel & Lewis, 1988)	280 (Lowther et al., 1999)	
*Pbc*21[a]	7	264 (Dewhurst and Lowther, 1998)		272 (Lowther et al., 1999)	
Cubic (*Pa*3)	8	257 (Dewhurst and Lowther, 1998)		262 (Lowther et al., 1999)	
Ortho-I (*Pbca*)[a]	8	272 (Dewhurst & Lowther, 1998)	243 (Desgreniers & Lagarec, 1999)	256 (Lowther et al., 1999)	281 (Desgreniers & Lagarec, 1999), 220 (Ohtaka et al., 2001b)
Ortho-II cotunnite (*Pnma*)[a]	9	314 (Cohen et al., 1988), 305 (Dewhurst & Lowther, 2001)	425–444 (Desgreniers & Lagarec, 1999) 265–332 (Ohtaka et al., 2001a)	306 (Dewhurst & Lowther, 2001)	340–400 (Desgreniers & Lagarec, 1999) 312 (Ohtaka et al., 2001b)

[a] *High-pressure phases.*

conditions and histories of the various samples, but it is generally accepted that ZrO_2 assumes an orthorhombic symmetry at two regions in its phase diagram. Magnesia-stabilized tetragonal ZrO_2 cooled to around 30 K has been found to transform to an orthorhombic phase (Kisi et al., 1989) with space group $Pbc2_1$. A closely related structure, with space group *Pbca*, has been found by quenching powdered ZrO_2 from 900 K to 6 GPa (Ohtaka et al., 1990), from in situ experiments (Leger & Blanzat, 1993) at room temperature, and as small grains in a ZrO_2–$MgAl_2$ O_4 composite (Guinebretière et al., 1996). This phase is isostructural with (TiO_2, $Z=8$) and consists of alternate domains of $Pbc2_1$ oxygen nets resulting in the doubling of the lattice parameter.

Yet another related orthorhombic phase with space group *Pbcm* has been observed twice (Heuer et al., 1989; Kudoh et al., 1986). This phase is unusual in that it is disordered with an oxygen sublattice consisting of the average of differing $Pbc2_1$ domains that occur with an equal probability. This type of disorder is rare at low temperatures and a consequence of this is that there is a large increase in entropy across the phase transition. *Pbca* (one domain) and $Pbc2_1$ are both maximal subgroups of *Pbcm* (Howard, Kisi, & Ohtaka, 1991) and virtually indistinguishable by XRD techniques due to the low oxygen scattering factors. They are however easily distinguishable by neutron diffraction. The first high-pressure orthorhombic phase of baddeleyite encountered at low temperature is labeled OrthoI (Desgreniers & Lagarec, 1999; Leger & Blanzat, 1993).

Another orthorhombic phase has been reported by several authors (Block, da Jornada, & Piermarini, 1985; Haines, Leger, & Atouf, 1995; Liu, 1979; Liu, 1980; Ming & Manghnani, 1985) and determined to be isostructural to the ninefold coordinated cotunnite ($PbCl_2$) structure (**Figure 8**). This phase is readily obtained after quenching from about 1000 °C to 18 GPa. An X-ray study at an ambient temperature by Block et al. (1985) reportedly produced the cotunnite phase at pressures >16.6 GPa. However, Leger et al. (Leger & Blanzat, 1993) also using in situ XRD at room temperature found a phase transition from OrthoI to another orthorhombic phase at around 22 GPa, but guarded against it having a cotunnite-type structure. Similarly Arashi, Yagi, Akimoto, and Kudoh (1990) observed a phase transition at 13 and 15 GPa using in situ XRD and micro-Raman spectroscopy, respectively, but were not able to confirm a cotunnite structure. The cotunnite phase is promising as a new superhard material as it appears to have a high bulk modulus of about 320 GPa (Block et al., 1985; Dewhurst & Lowther, 2001; Haines et al., 1995), which approaches that of diamond (440 GPa). This phase appears to be quenchable (Haines et al., 1995; Liu, 1979) and a cotunnite structure has also been proposed for Ca- and Y-stabilized ZrO_2 (Dev, Ming, & Manghnani, 1987; Ohtaka, Kume, & Ito, 1988). The cotunnite phase is often labeled as OrthoII and is now a well-identified high-pressure phase of ZrO_2 (Haines et al., 2001).

The nature of the postcotunnite phase is not known, but a quenchable tetragonal phase distinct from the high-temperature tetragonal structure was reported by Arashi et al. (1990) at 35 GPa and was retained up to 60 GPa. The low number of Raman bands indicated that this phase had a possible inversion symmetry and that the most likely space groups were $P4/m$, $P4_2/n$, $P4/mmm$, or $P4/mbm$.

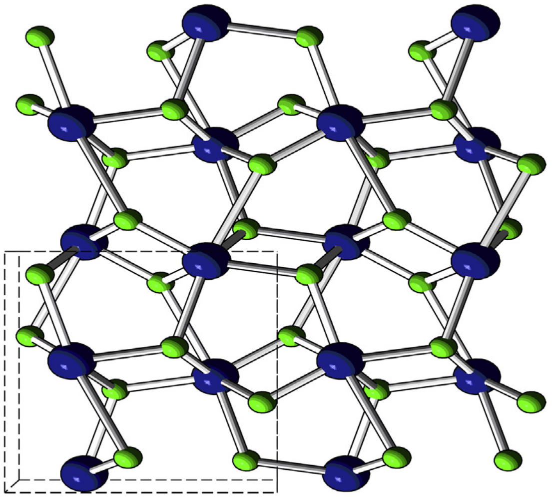

Figure 8 The high-pressure cotunnite phase displayed by ZrO_2 and HfO_2 and several other oxides when subject to pressure. The metal atoms have a very high oxygen coordination in this phase.

Minute amounts of Yttria strongly affect the structural stability of ZrO_2 thereby enhancing the industrial applicability of the material. When trivalent cations such as Y are substituted for Zr ions, vacancies are created in the O sublattice for charge neutrality. In the case of the tetragonal or cubic phases, rapid stabilization toward lower temperatures with increasing Y content is found. However, the physical mechanism for this stabilization of the high-temperature ZrO_2 polymorphs has been the subject of controversy (Stapper, Bernasconi, Nicoloso, & Parrinello, 2000; Stefanovich, Shluger, & Catlow, 1994), but a speculative explanation is that Zr ions assume the sevenfold anion coordination of the lowest-energy monoclinic phase when the dopant is present. Defect ordering in relation to how the vacancies are distributed within the doped ZrO_2 could be important (Bogicevic, Wolverton, Crosbie, & Stechel, 2001) and this point merits further investigation.

3.02.6 Conclusion

Currently, there is enormous potential to obtain new materials that can compete with diamond. To achieve this sophisticated synthesis methods are needed. In this respect, ab initio theory plays an important role in guiding the effort. In spite of the fact that no structure harder than diamond has been realized, it is necessary to remember that diamond has many shortcomings. Although borides, oxides, and even admixtures with nitrogen have the potential to be alternatives, problems to stabilize many of these hard phases, and in some cases to commercially synthesize them is a problem. Undoubtedly, synthesizing conditions will be the main thrust of research in the next few years as the expectations of this exciting family of new superhard materials is realized. Yet in many respects such problems are similar to those encountered during the early laboratory synthesis of synthetic diamond and cubic boron nitride and, as with these materials, it is likely that such problems will be overcome. A fascinating feature of the way that this new family of borides and oxides has been characterized has been the impact that predictive computer modeling has made in guiding the properties of the potentially new series of superhard materials.

Acknowledgments

The DST/NRF Centre of Excellence in Strong Materials, South Africa, and Element Six are thanked for their support. Drs T. Letsoalo and O. Okeke are also acknowledged for useful discussions.

References

Aarik, B., Aidla, A., Mandar, H., Uustare, T., Kukli, K., & Schuisky, M. (2001). *Applied Surface Science, 173*, 15.
Adasch, V., Hess, K. U., Ludwing, T., Vojteer, N., & Hillebrecht, H. (2007). *Chemistry European Journal, 13*, 3450.
Albe, K., & Moller, W. (1998). *Computational Materials Science, 10*(1–4), 111–115.
Aldebert, P., & Traverse, J. P. (1985). *Journal of the American Ceramic Society, 68*, 34.
Arashi, H., Yagi, T., Akimoto, S., & Kudoh, Y. (1990). *Physical Review B, 41*, 4309.
Arlt, T., Bermejo, M., Blanco, M. A., Gerward, L., Jiang, J. Z., Staun Olsen, J., et al. (2000). *Physical Review B, 61*, 14414.
Aselage, T. L., & Tallant, D. R. (1998). *Physical Review B, 57*, 2675.
Badzian, A. (2002). *Journal of the American Ceramic Society, 85*, 16.
Barth, T. F. W., & Posnjak, E. (1932). *Zeitschrift fur Kristallographie, 82*, 325.
Binggeli, N., & Chelikowsky, J. R. (1992). *Physical Review Letters, 69*, 2220.
Block, S., da Jornada, J. A. H., & Piermarini, G. J. (1985). *Journal of the American Ceramic Society, 68*, 497.
Bogdanov, R. K., Shulzhenko, A. A., Zakora, A. P., Isonkin, A. M., & Gargin, V. G. (2007). *Journal of Superhard Materials, 29*, 56.
Bogicevic, A., Wolverton, C., Crosbie, G. M., & Stechel, E. B. (2001). *Physical Review B, 64*, 104106.
Brasen, D., Vandenberg, J., Robbins, M., Willens, R., Reed, W., Sherwood, R., et al. (1975). *Journal of Solid State Chemistry, 13*, 298.
Brazhkin, V. V., Lyapin, A., & Hemley, R. (2002). *Philosophical Magazine A, 82*, 231.
Brazhkin, V., Dubrovinskaia, N., Nicol, A., Novikov, N., Riedel, R., Solozhenko, R., et al. (2004). *Nature Materials, 3*, 576.
Calatayud, M., Mori-Sanchez, P., Beltran, A., Pendas, A. M., Francisco, E., Andres, J., et al. (2001). *Physical Review B, 6418*, 4113.
Chen, S., & Gong, X. G. (2007). *Physical Review Letters, 98*, 015502.
Chen, S. Y., Gong, X. G., & Wei, S. H. (2007). *Physical Review B, 98*, 011502.
Cheng, Y. C., Wu, X. L., Li, S. H., & Chu, P. K. (2008). *Solid State Communications, 146*, 69.
Ching, W. Y., Mo, S.-D., Tanaka, I., & Yoshiya, M. (2001). *Physical Review B, 63*, 064102.
Ching, W., Mo, S.-D., & Chen, Y. (2002). *Journal of the American Ceramic Society, 85*(1), 11.
Chrenko, R. M. (1973). *Physical Review B, 7*, 4560.
Cohen, R. E., Mehl, M. J., & Boyer, L. L. (1988). *Physica B, 150*, 1.

Cohen, M. L. (1985). *Physical Review B, 32*, 7988.
Cohen, M. L. (1993). *Science, 261*, 307.
Collins, A. T., & Lightowlers, E. C. (1968). *Physical Review, 171*, 843.
Cook, B. A., Snyder, J. E., Constant, A. P., & Tian, Y. (2004). US Patent US 7 375 343 B1.
Cook, B. A., Harringa, J. L., Lewis, T. L., & Russell, A. M. (2000). *Scripta Materialia, 42*, 597.
Corbin, N. D. (1989). *Journal of the European Ceramic Society, 5*, 143.
Crowther, P. A., Dean, P. J., & Sherman, W. F. (1967). *Physical Review, 154*, 772.
Cullen, B. J. US Patent US 6 605 798 B1.
Custers, J. F. (1955). *Nature, 176*, 173.
Desgreniers, S., & Lagarec, K. (1999). *Physical Review B, 59*, 8467.
Dev, S. R. U., Ming, L. C., & Manghnani, M. H. (1987). *Journal of the American Ceramic Society, 70*, C218.
Dewhurst, J. K., & Lowther, J. E. (1997). *Physical Review B, 54*, R1234.
Dewhurst, J. K., & Lowther, J. E. (1998). *Physical Review B, 57*, 741.
Dewhurst, J. K., & Lowther, J. E. (2001). *Physical Review B, 64*, 14104.
Dmitriev, V. P., Tolédano, P., & Salje, E. K. H. (1998). *Physical Review B, 58*, 11911.
Dubrovinsky, L. S., Dubrovinskaia, N. A., Swamy, V., Muscat, J., Harrison, N. M., Ahuja, R., et al. (2001). *Nature, 410*, 653.
Ekimov, E. A., Sidorov, V. A., Bauer, E. D., Mel'nik, N. N., Curro, N. J., Thompson, J. D., et al. (2004). *Nature, 428*, 542.
Emin, D. (1987). *Physics Today, 20*, 55.
Fang, C. M., de Wijs, G. A., de Groot, R. A., Metselaar, R., Hintzen, H. T., & de With, G. (2000). *Chemistry of Materials, 12*, 1071.
Ferroir, T., Dubrovinsky, L., El Goresy, A., Simionovici, A., Nakamura, T., & Gillet, P. (2010). *Earth and Planetary Science Letters, 290*, 150.
Fukuyama, H., Nakao, W., Susa, M., & Nagata, K. (1999). *Journal of the American Ceramic Society, 82*, 1381.
Gagoa, R., Jiménez, I., Aguiló-Rueda, F., Albella, J. M., & Hultman, L. (2002). *Journal of Applied Physics, 92*, 5177.
Gao, F., Hou, L., & He, Y. (2004). *Journal of Physical Chemistry B, 108*, 13069.
Glassford, K. M., & Chelikowsky, J. R. (1992). *Physical Review B, 46*, 1284.
Graham, E. K., Munly, W. C., McCauley, J. W., & Corbin, N. D. (1988). *Journal of the American Ceramic Society, 71*, 807.
Guinebretière, R., Oudjedi, Z., & Dauger, A. (1996). *Scripta Metallurgica et Materialia, 34*, 1039.
Guo, X. J., Liu, Z. Y., Luo, X. G., Yu, D. L., He, J. L., Tian, Y. J., et al. (2007). *Diamond and Related Materials, 16*, 526.
Haines, J., & Leger, J. M. (1993). *Physica, 192*, 233.
Haines, J., Léger, J. M., & Blanzat, B. (1994). *Journal of Materials Science Letters, 44*, 1688.
Haines, J., Leger, J. M., & Atouf, A. (1995). *Journal of the American Ceramic Society, 78*, 445.
Haines, J., Leger, J. M., & Schulte, O. (1996). *Journal of Physics C: Condensed Matter Physics, 8*, 1631.
Haines, J., Leger, J. M., & Bocquillon, G. (2001). *Annual Review of Materials Science, 31*, 1.
Han, S., Ihm, J., Louie, S. G., & Cohen, M. L. (1998). *Physical Review Letters, 80*, 995.
Hartnett, T. M., Bernstein, S. D., Maguire, E. A., & Tustison, R. W. (1998). *Infrared Physics and Technology, 39*, 203.
He, J. L., Wu, E. D., Wang, H. T., Liu, R., & Tian, Y. (2005). *Physical Review Letters, 94*, 015504.
Hearne, G. R., Zhao, J., Dawe, A. M., Pischedda, V., Maaza, M., Nieuwoudt, M. K., et al. (2004). *Physical Review B, 70*, 134102.
Hemley, R. J., Jepheoat, A. P., Mao, H. K., Ming, L. C., & Manghani, M. H. (1988). *Nature, 334*, 52.
Hemley, R. J., Prewitt, C. T., & Klima, K. J. (1994). *Physical behavior, geochemistry and material applications.* Washington, D.C: Mineralogical Society of America.
Heuer, A. H., Lanteri, V., Farmer, S. C., Chaim, R., Lee, R. R., Kibbel, B. W., et al. (1989). *Journal of Materials Science, 24*, 124.
Howard, C. J., Kisi, E. H., & Ohtaka, O. (1991). *Journal of the American Ceramic Society, 74*, 2321.
Hubble, H. W., Kudryashov, I., Solozhenko, V. L., Zinin, P. V., Sharma, S. K., & Ming, L. C. (2004). *Journal of Raman Spectroscopy, 35*, 822.
Hubert, H., Devouard, B., Garvie, L. A. G., O'Keeffe, M., Buseck, P. R., Petuskey, W. T., et al. (1998). *Nature, 391*, 376.
Ingel, R. P., & Lewis, D. (1988). *Journal of the American Ceramic Society, 71*, 265.
Johnson, O. T., Sigalas, I., Ogunmuyiwa, E. N., Kleebe, H. J., Muller, M. M., & Herrmann, M. (2010). *Ceramics International, 36*, 1762.
Kaner, R. B., Gilman, J. J., & Tolbert, S. H. (2005). *Science, 308*, 1268.
Kayhan, I. O., & Inal, O. T. (1999). *Journal of Materials Science, 34*, 4105.
Kelly, A. (1973). *Strong solids.* Oxford University Press.
Keskar, N. R., & Chelikowsky, J. R. (1992). *Physical Review B, 46*, 1.
Kim, E., Pang, T., Utsumi, W., Solozhenko, V. L., & Zhao, Y. S. (2008). *Physical Review B, 75*, 18.
Kisi, E. H., Howard, C. J., & Hill, R. J. (1989). *Journal of the American Ceramic Society, 72*, 1757.
Knittle, E., Kaner, R. B., Jeanloz, R., & Cohen, M. L. (1995). *Physical Review B, 51*, 12149.
Komatsu, T., Samedima, M., Awano, T., Fujiwara, S., & Kakadate, Y. (1999). *Journal of Materials Processing Technology, 85*, 69.
Kroll, P., Dronskowski, R., & Martin, M. (2005). *Journal of Materials Chemistry, 15*, 3296.
Kudoh, Y., Takeda, H., & Arashi, H. (1986). *Physics and Chemistry of Minerals, 13*, 233.
Kurdyumov, A. V., Solozhenko, V. L., Gubachek, M., Borimchuk, N. I., Zelyavskii, V. B., Ostrovskaya, N. F., et al. (2000). *Powder Metallurgy and Metal Ceramics, 39*, 467.
Lagarec, K., & Desgreniers, S. (1995). *Solid State Communications, 94*, 519.
Larsson, K., & Ristein, J. (2005). *Journal of Physical Chemistry B, 109*(20), 10304.
Leger, J. M., & Blanzat, R. (1993). *Journal of Materials Science, 44*, 1688.
Letsoalo, T. E., & Lowther, J. E. (2008). *Physica B, 403*, 2760.
Li, Q., Wang, M., Oganov, A. R., Cui, T., Ma, Y. M., & Zou, G. *Journal of Applied Physics, 5*(200), 105.
Liu, L. G. (1979). *Earth and Planetary Science Letters, 44*, 390.
Liu, L.-G. (1980). *Journal of Physics and Chemistry, 41*, 331.
Lowther, J. E., Dewhurst, J. K., Léger, J. M., & Haines, J. (1999). *Physical Review B, 60*, 14485.

Lowther, J. E., Schwarz, M., Kroke, E., & Riedel, R. (2003). *Journal of Solid State Chemistry, 176*, 549.

Lowther, J. E., Amkreutz, M., Frauenheim, T., Kroke, E., & Riedel, R. (2003). *Physical Review B: Condensed Matter and Materials Physics, 68*, 33201.

Lowther, J. E., Wagner, M., Isabel, K., & Riedel, R. (2004). *Journal of Alloys and Compounds, 374*, 1.

Lowther, J. E. (2002). *Physica B, 322*, 173.

Lowther, J. E. (2005). *Journal of Physics: Condensed Matter, 17*(21), 3221.

Lundstom, T., & Andreev, Y. G. (1996). *Materials Science and Engineering A, 209*, 16.

Luo, X. G., Guo, X. J., Liu, Z. Y., He, J. L., Yu, D. L., Xu, B., et al. (2007). *Physical Review B, 76*, 4.

Mamin, R. F., & Inushima, T. (2001). *Physical Review B, 63*, 033201.

Masago, A., Shirai, K., & Katayama-Yoshida, H. (2006). *Physical Review B, 73*, 104102.

Mattesini, M., & Matar, S. F. (2001). *International Journal of Inorganic Materials, 3*, 943.

McCauley, J. W., Patel, P., Chen, M., Gilde, G., Strassburger, E., Paliwal, B., et al. (2009). *Journal of the European Ceramic Society, 29*, 223.

McColm, I. J. (1990). *Ceramic hardness.* Plenum Press.

McCullough, J. D., & Trueblood, K. N. (1959). *Acta Crystallographica, 12*, 507.

Mehl, M. J., Klein, B. M., & Papaconstantantopoulos, D. M. (1993). *First principles calculations of elastic properties of metals.* In *Intermetallic compounds: principles and practice* (Vol. 1). London: John Wiley and Sons.

Miller, L., & Kaplan, W. D. (2008). *International Journal of Applied Ceramic Technology, 5*, 641.

Ming, L. C., & Manghnani, M. H. (1985). In S. Minomura (Ed.), *Solid state physics under pressure* (pp. 135). Tokyo: KTK Science.

Mmethi, F. M., & Lowther, J. E. (2009). *High Pressure Research, 29*, 212.

Mo, S.-D., Ouyang, L., Ching, W. Y., Tanaka, I., & Riedel, R. (1999). *Physical Review Letters, 83*, 5046.

Nebel, C. E., Rohrer, E., & Stutzmann, M. (2001). *Journal of Applied Physics, 89*, 2237.

Nellis, W. J., Mitchell, A. C., & McMahan, A. K. (2001). *Journal of Applied Physics, 90*, 696.

Nkambule, S. M., & Lowther, J. E. (2010). *Solid State Communications, 150*(1–2), 133.

Ohtaka, O., Kume, S., & Ito, E. (1988). *Journal of the American Ceramic Society, 71*, C448.

Ohtaka, O., Yamanaka, T., Kume, S., Hara, N., Asano, H., & Izumi, F. (1990). *Proceedings of the Japan Academy, Series B, 66*, 193.

Ohtaka, O., Fukui, H., Kunisada, T., Fujisawa, T., Funakoski, K., Utsumi, W., et al. (2001). *Physical Review B, 63*, 4108.

Ohtaka, O., Fukui, H., Kunisada, T., Fujisawa, T., Funakoshi, K., Irifune, T., et al. (2001). *Journal of the American Ceramic Society, 84*, 1369.

Okeke, O. U., & Lowther, J. E. (2008). *Physical Review B, 77*, 094129.

Okeke, O. U., & Lowther, J. E. (2009). *Physica B, 404*, 3577.

Okeke, O. U., & Lowther, J. E. (2010). *Chemical Physics Letters, 494*, 323.

Patel, P. J., Gilde, G. A., Dehmer, P. G., & McCauley, J. W. (2000). *The Amptiac Newsletter, 4*, 4.

Pischedda, V., Hearne, G., Dawe, A., & Lowther, J. (2006). *Physical Review Letters, 96*(3), 035509.

Ploog, K., Rauh, P., Stoeger, W., & Schmidt, H. (1972). *Journal of Crystal Growth, 13*, 350.

Ploog, K., Schmidt, H., Amberger, E., Will, G., & Kossobutzki, K. H. (1972). *Journal of the Less Common Metals, 29*, 161.

Qin, J., He, D., Wang, J., Fang, L., Lei, L., Li, Y., et al. (2008). *Advanced Materials, 20*, 4780.

Ravindran, P., Lars, F., Korzhavyi, P. A., Johansson, B., Wills, J., & Eriksson, O. (1998). *Journal of Applied Physics, 84*, 4891.

Riedel, R., Greiner, A., Miche, G., Dressler, W., Fuess, H., Bill, J., et al. (1997). *Angewandte Chemie International Edition in English, 36*, 603.

Saitoh, H., Yoshida, K., & Yarbrough, W. A. (1993). *Journal of Materials Research, 8*, 8.

Sato, H., Endo, S., Sugiyama, M., Kikegawa, T., Shimomura, O., & Kusaba, K. (1991). *Science, 251*, 786.

Scandolo, S., Bernasconi, M., Chiariot, G. L., Focher, P., & Tosatti, E. (1995). *Physical Review Letters, 74*, 4015.

Scandolo, S., Chiarotti, G. L., & Tosatti, E. (1996). *Physical Review B, 43*, 5051.

SchiÃtz, J., Tolla, F. D. D., & Jacobsen, K. W. (1998). *Nature, 391*, 561.

Schwarz, M., Miehe, G., Zerr, A., Kroke, E., Heck, M., Thybusch, B., et al. (2001). *Angewandte Chemie International Edition, 41*, 789.

Shirai, K. (1997). *Physical Review B, 55*, 12235.

Smith, D. K., & Cline, C. F. (1962). *Journal of the American Ceramic Society, 45*, 249.

Soignard, E., Machon, D., McMillan, D. M., Dong, B., Xu, J., & Leinenweber, K. (2005). *Chemistry of Materials, 17*, 5465.

Solozhenko, V. L., Andrault, D., Fiquet, G., Mezouar, M., & Rubie, D. C. (2001). *Applied Physics Letters, 78*, 1385.

Solozhenko, V. L., Le Godec, Y., Klotz, S., Mezouar, M., Turkevich, V. Z., & Besson, J. M. (2002). *Physical Chemistry Chemical Physics, 4*(21), 5386.

Solozhenko, V. L., Kurakevych, O. O., Andrault, D., Le Godec, Y., & Mezouar, M. (2009). *Physical Review Letters, 102*, 015506.

Sshepe, T., Prins, J. F., & Hoch, M. J. (1999). *Diamond and Related Materials, 8*, 1508.

Stapper, G., Bernasconi, M., Nicoloso, N., & Parrinello, M. (2000). *Physical Review B, 59*, 797.

Starbova, B., Mankov, V., Starbov, N., Popov, D., Nihtianova, D., Kolev, K., et al. (2001). *Applied Surface Science, 173*, 177.

Stefanovich, E. V., Shluger, A. L., & Catlow, C. R. A. (1994). *Physical Review B, 49*, 11560.

Stir, M., Traykova, T., Nicula, R., Burkel, E., Baehtz, C., Knapp, M., et al. (2003). *Nuclear Instruments and Methods in Physics Research B, 199*, 59.

Sung, C., & Sung, M. (1996). *Materials Chemistry and Physics, 43*, 1.

Sun, H., Jhi, S. H., Roundy, D., Cohen, M. L., & Louie, S. G. (2003). *Physical Review B, 64*, 094108.

Tabary, P., & Servant, C. (1999). *Journal of Applied Crystallography, 32*, 241.

Tanaka, I., Oba, F., Sekine, T., Ito, E., Kubo, A., Tatsumi, K., et al. (2002). *Journal of Materials Research, 17*, 731.

Tersoff, J. (1989). *Physical Review B, 39*, 5566.

Teter, D. M., Hemley, R. J., Kresse, G., & Hafner, J. (1998). *Physical Review Letters, 80*, 2145.

Teter, D. M. (1998). *M.R.S. Bulletin, 23*, 22.

Tian, Y., Bastawros, A. F., Lo, C. C. H., Constant, A. P., Russell, A. M., & Cook, B. A. (2003). *Applied Physics Letters, 83*, 2781.

Tjabane, M., & Lowther, J. E. (1999). *Physica B, 270*, 164.

Tkachev, S. N., Solozhenko, V. L., Zinin, P. V., Manghnani, M. H., & Ming, L. C. (2003). *Physical Review B, 68*, 052104.

Tse, J. S., Klug, D. D., & Bernasconi, M. (1997). *Physical Review B, 56*, 10878.

Vast, N., Baroni, S., Zerah, G., Besson, J. M., Polian, A., Grimsditch, M., et al. (1997). *Physical Review Letters, 78*, 693.

Veprek, S. (1999). *Journal of Vacuum Science and Technology A, 17*, 2401.
Villain, P., Godeau, P., Renault, P. O., & Badawi, K. F. (2002). *Applied Physics Letters, 81*, 4365.
Wang, Z., & Saxena, S. K. (2001). *Solid State Communications, 118*, 75.
Wang, Z., Saxena, S. K., Pischedda, V., Liermann, H. P., & Zha, C. S. (2001). *Journal of Physics C: Condensed Matter Physics, 13*, 8317.
Weihrich, R., Matar, S. F., & Betranhandy, E. (2003). *Jounal of Physics and Chemistry of Solids, 64*, 1539.
Wentzcovitch, R. M., Da Silva, C., & Chelikowsky, J. R. (1998). *Physical Review Letters, 80*, 2149.
Willems, H. X., Hendrix, M. M. R., Metselaar, R., & de With, G. (1992). *Journal of the European Ceramic Society, 10*, 327.
Wilson, W. B. (1962). *Physical Review, 127*, 1549.
Wu, B. R., Sung, C. M., Lee, S. L., & Tai, M. F. (2002). *Chinesse Journal of Physics, 40*, 187.
Xiaoguang, L., Xiaoju, G., Bo, X., Qinghua, W., Qianku, H., Zhongyuan, L., et al. (2007). *Physical Review B: Condensed Matter and Materials Physics*, 101103.
Zerr, A., & Riedel, R. (2000). Novel ultrahard materials. In *Handbook of ceramic hard materials* (Vol. 1). Wiley-VCH Verlag.
Zerr, A., Miehe, G., Serghiou, G., Schwarz, M., Kroke, E., Riedel, R., et al. (1999). *Nature, 400*, 340.
Zerr, A., Riedel, R., Selike, T., Lowther, J., Ching, W., & Tanaka, I. (2006). *Advanced Materials, 18*, 2933.
Zhang, S., Li, H., Li, H., Zhou, S., & Cao, X. (2007). *Journal of Physical Chemistry B, 111*, 1304.
Zhou, S. J., Zhou, X. Y., & Zhao, Y. S. (2008). *Journal of Applied Physics, 10*, 053508.
Zhou, X. F., Sun, J., Fan, Y. X., Chen, J., Wang, H. T., Guo, X. J., et al. (2007). *Physical Review B, 76*, 4.
Zientara, D., Buckó, M. M., & Lis, J. (2007). *Journal of the European Ceramic Society, 27*, 775.
Zinin, P. V., Kudryashov, I., Konishi, N., Ming, L. C., Solozhenko, V. L., & Sharma, S. K. (2005). *Spectrochimica Acta Part A, 61*, 2386.

3.03 High-Pressure Phase Diagrams of the Systems Containing Carbon and BN

Vladimir Turkevich, Synthesis and Sintering of Superhard Materials at High Pressures and High Temperatures, Institute for Superhard Materials of the Ukrainian National Academy of Sciences, Kiev, Ukraine

Nomenclature

MPa, GPa Megapascal, Gigapascal	**hBN** Hexagonal boron nitride
K Kelvin degree	**cBN** Cubic boron nitride
L Liquid phase	γ fcc phase
G Graphite	δ bcc phase
D Diamond	

3.03.1 Introduction

The hardest known substances, diamond and cubic boron nitride (cBN), have isoelectronic structure and are polymorphous modifications of carbon and boron nitride, respectively, with the same crystalline structure of the sphalerite type. Due to low values of the molar volume, these substances are characterized by a wide region

http://dx.doi.org/10.1016/B978-0-08-096527-7.00040-4

of thermodynamic stability at high pressures. They are produced by (1) a direct phase transformation of corresponding low-density polymorphous modifications and (2) by the crystallization from melt solutions of carbon or boron nitride-containing multicomponent systems at high pressures and temperatures. In addition, diamond and cBN films are prepared by epitaxial growth on substrates at low pressures in the diamond and cBN thermodynamic instability regions.

The pressure of the direct phase transformation far exceeds the equilibrium pressure (especially at low temperatures) because of the necessity of overcoming a high activation barrier. The emergence of a liquid phase in the system abruptly decreases the activation barrier and lowers the parameters of diamond and cBN synthesis. Graphite (hexagonal boron nitride (hBN)) dissolves in the melt of the system, saturates it with respect to the hexagonal, and supersaturates with respect to the cubic phase and as a result, diamond (cBN) crystallizes from the supersaturated melt solution. An obligatory condition for the crystallization is a stable equilibrium of the cubic modification with the melt. The crystallization, as such, becomes possible at temperatures exceeding those of eutectic and peritectic reactions with carbon (boron nitride) participation. Phase diagrams of carbon- or boron nitride-containing systems show the existence of the above-mentioned reactions and indicate the lowest parameters of diamond and cBN syntheses in particular systems. In this chapter, spontaneous crystallizations of diamond and cBN at high pressure have been analyzed in terms of phase diagrams and rate of nucleation and crystal growth.

3.03.2 One-Component Systems

The *p*,*T* diagram of carbon is a typical phase diagram of a one-component system. Boron nitride is a two-component chemical compound and it is also can be considered as a one-component system since the equation of the reaction of the BN formation decreases the number of the degrees of freedom by one.

Over the past few decades, phase diagrams of carbon and boron nitride have been under constant revision. The latest versions of the diagrams are given in **Figure 1** (Bundy, 1989) and **Figure 2** (Solozhenko, Turkevich, & Holzapfel, 1999a), respectively. Our attention has been engaged by the fact that the positions of the equilibrium

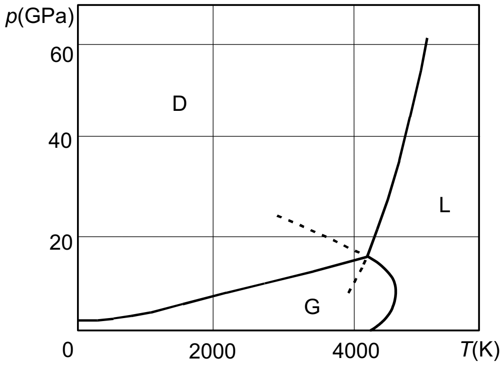

Figure 1 Phase diagram of carbon.

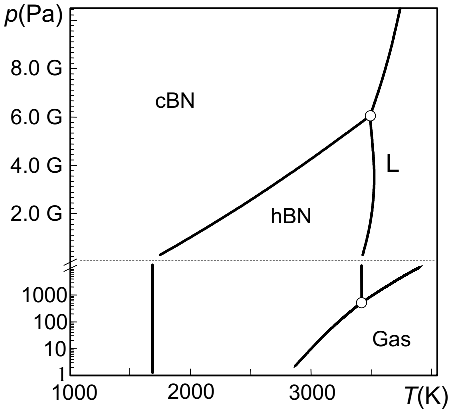

Figure 2 Phase diagram of boron nitride.

lines of cubic and graphite-like hexagonal modifications in the diagrams of carbon and boron nitride differ greatly. This difference suggests that cBN is stable under standard conditions, while diamond is a metastable phase at atmospheric pressure over the whole temperature range.

3.03.3 Binary and Ternary Systems

The information of the majority of phase diagrams of metal–carbon binary systems at atmospheric pressure can be found in Massalski, Subramanian, Okamoto, and Kacprzak (1990). The pressure application, as a rule, induces an increase in the melting temperatures of the components and chemical compounds (by about 30–60 K/GPa) and in the temperatures of eutectic and peritectic reactions (by about 10–20 K/GPa). The carbon and boron solubilities in the melt increase with the pressure as well. In addition to the above-mentioned quantitative variations, qualitative changes in the diagram topology are also possible because of the stabilization of high-pressure phases. An example of such a situation is the region of thermodynamic stability of diamond (cBN) in the diagram. Stabilization of carbides and boron nitrides in systems with carbon and boron nitride, respectively, is not uncommon under pressure. The pressure can also cause destabilization and, hence, removal of the thermodynamic stability region of a relatively low-density phase, e.g. body-centered cubic (bcc) solid solution in the Fe–C system, from the phase diagram. Because the experimental study of the phase equilibria at high pressure presents great difficulties, information on the p,T,c phase diagrams is limited.

3.03.3.1 High-Pressure Phase Diagrams of Systems Containing Carbon

3.03.3.1.1 The Ni–C System

The Ni–C system is best understood at high pressures. At atmospheric pressure, the system is characterized by a simple eutectic-type phase diagram (Figure 3(a)). With increasing pressure, the eutectic temperature and carbon

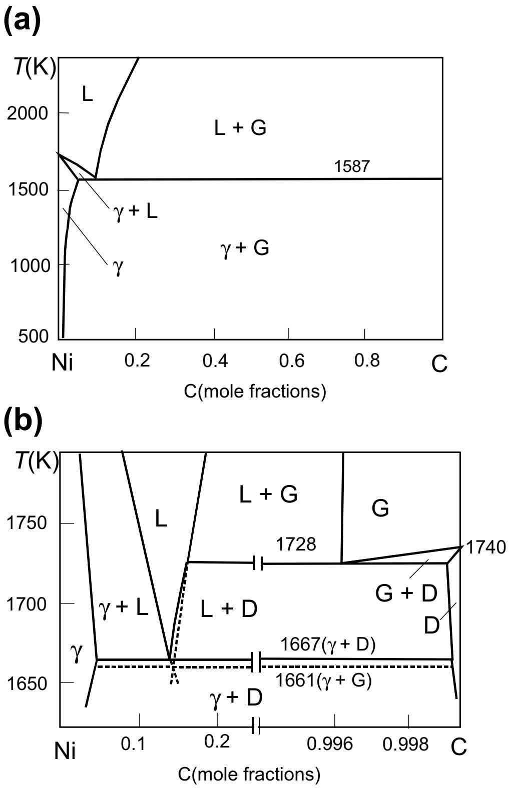

Figure 3 Isobaric sections of the phase diagram of the Ni–C system at 0.1 MPa (a) and 5.4 GPa (b).

content of eutectics increase (Ershova, Kamenetskaya, & Il'ina, 1981; Muncke, 1979; Strong & Hanneman, 1967), and the temperature of the equilibrium between graphite and diamond increases at a high rate (about 400 K GPa^{-1}). At a pressure of 5.25 GPa, the temperatures of eutectics and of the graphite–diamond equilibrium are the same; high pressures result in stable equilibrium between diamond and a liquid phase, i.e. recrystallization of graphite to diamond through the melt becomes a possibility (**Figure 3(b)**). The lowest temperature of diamond crystallization in the system is 1667 K. The minor solubility of nickel in graphite (up to 0.4%) ensures the existence of the $G \rightleftarrows L + D$ metatectic equilibrium with a temperature (1728 K at 5.4 GPa) that differs from that of G–D equilibrium (1740 K) only slightly.

3.03.3.1.2 The Co–C System

At atmospheric pressure, the phase diagram of the Co–C system is similar to that of the Ni–C system and includes the $L \rightleftarrows \gamma + G$ eutectic with 0.11 mol part of carbon and a temperature of 1582 K (**Figure 4(a)**). Pressures exceeding 6 GPa (Muncke, 1974; Turkevich & Kulik, 1993) stabilize Co_3C and the $L + D \rightleftarrows Co_3C$ peritectic equilibrium. Above the temperature of this equilibrium, equilibrium between diamond and the liquid phase is observed. The $L \rightleftarrows \gamma + Co_3C$ eutectic equilibrium at a temperature somewhat below that of the peritectics is also retained. **Figure 4(b)** (Ershova, Kamenetskaya, & Il'ina, 1982) shows the isobaric section of the phase diagram of the Co–C system at 8 GPa. The lowest parameters (pressure and temperature) for diamond crystallization from the melt of the Co–C system are slightly higher than those in the Ni–C system.

3.03.3.1.3 The Fe–C System

At atmospheric pressure, the Fe_3C cementite is a metastable phase; therefore, the phase diagram of the Fe–C system is characterized by the $L \rightleftarrows \gamma + G$ eutectic equilibrium (1426 K, 0.171 mol parts of carbon) and in parallel with the above, by the $L + \delta \rightleftarrows \gamma$ peritectic equilibrium with no carbon participation.

An increase in pressure destabilizes the δ solid solution with the bcc structure but stabilizes the Fe_3C cementite at 0.1 GPa (Korsunskaya, Kamenetskaya, & Ershova, 1973) and Fe_7C_3 carbide at 5.9 GPa

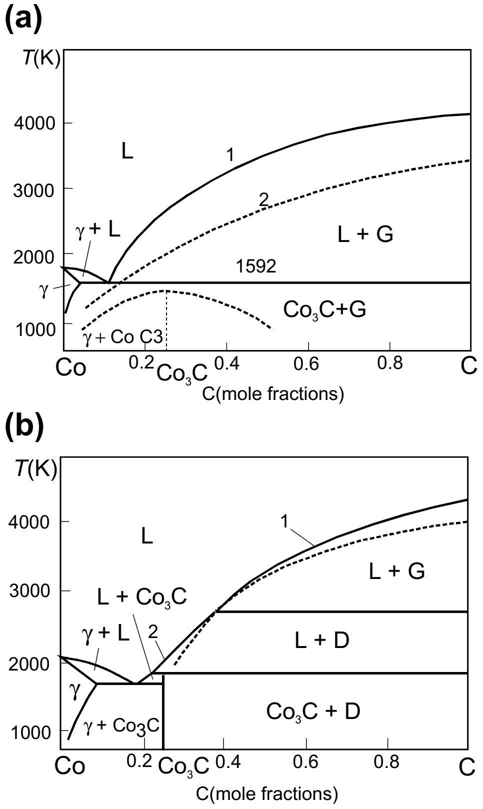

Figure 4 Isobaric sections of the phase diagram of the Co–C system at 0.1 MPa (a) and 8 GPa (b); 1, the liquidus of graphite and 2, the liquidus of diamond.

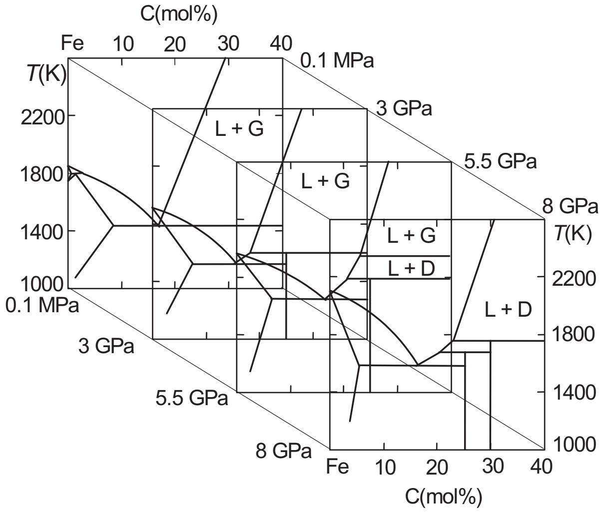

Figure 5 Variations in topology of the phase diagram of the Fe–C system with pressure.

(Kocherzhinsky, Kulik, Turkevich, et al., 1992). As a result, the L + δ ⇄ γ equilibrium disappears, the L ⇄ γ + G eutectics is replaced by the L ⇄ γ + Fe_3C eutectic equilibrium and the L + Fe_7C_3 ⇄ Fe_3C peritectic equilibrium appears. The behavior of the phase diagram of the Fe–C system with the pressure application is shown in **Figure 5** (Kocherzhinsky et al., 1992). To ensure diamond crystallization, temperature somewhat exceeding the incongruent melting temperatures of the carbides (Fe_3C or Fe_7C_3 depending on pressure), i.e. 1600 K at 5.3 GPa (Strong & Chrenko, 1971) or 1650 K at 5.9 GPa (Kocherzhinsky et al., 1992), is needed.

3.03.3.1.4 The Mn–C System

The phase diagram of the Mn–C system is much more complicated than those of the Ni–C and Co–C systems. The system is characterized by six carbides, of which the ε-carbide and Mn_7C_3 carbide are in equilibrium with the liquid phase (Massalski et.al., 1990).

The phase diagram of the Mn–C system at atmospheric pressure is given in **Figure 6(a)**. The congruently melting carbide is in equilibrium with carbon. According to the experimental data (Butylenko & Ignat'eva, 1977), Mn–C system does not change qualitatively in the range from 0.1 MPa to 6 GPa. Calculations (Turkevich & Kulik, 1995) have shown that pressure widens the Mn_7C_3 primary crystallization region and increases the temperature of the L ⇄ Mn_7C_3 + D eutectics up to 1780 K at 6 GPa (**Figure 6(b)**). The stable diamond liquidus appears in the Mn–C system at 5.7 GPa and 1825 K (Ershova & Kamenetskaya, 1982).

3.03.3.1.5 The Ta–C System

Two carbides (Ta_2C and TaC) form in the Ta–C system. The phase diagram of this system at atmospheric pressure is given in **Figure 7(a)** (Massalski et al., 1990). The TaC carbide is one of the most high-melting compounds, its melting temperature is above 4000 K. The temperature of the L ⇄ TaC + G eutectics is also very high (3600 K). Pressure further increases the eutectics temperature: at 6 GPa it is 3680 K (**Figure 7(b)**) (Kamenetskaya & Shterenberg, 1982), while the temperature of the equilibrium between graphite and diamond at this pressure is only 2000 K. The stable diamond liquidus appears in the Ta–C system at pressures above 10 GPa. Nevertheless, in this system, diamond has been experimentally produced by heating graphite in contact with tantalum at 6.5 GPa and 2000 K (Kamenetskaya & Shterenberg, 1980). The most likely causes of the phenomenon are contact melting at the tantalum–graphite interface and recrystallization of graphite into diamond through the metastable liquid (**Figure 7(b)**).

3.03.3.1.6 The Nb–C System

The phase diagram of the Nb–C system at high pressures is similar to that of the Ta–C system. The liquid phase forms eutectic equilibrium with the NbC carbide and graphite at 3550 K (8 GPa) (Kamenetskaya & Shterenberg, 1989). The temperature of the equilibrium between NbC and graphite and diamond at this pressure is 2800 K (**Figure 8**). The equilibria between diamond and the melt are stable only at pressures exceeding 10 GPa. However, diamond has been experimentally produced in the Nb–graphite contact zone at 8 GPa and 2100 K.

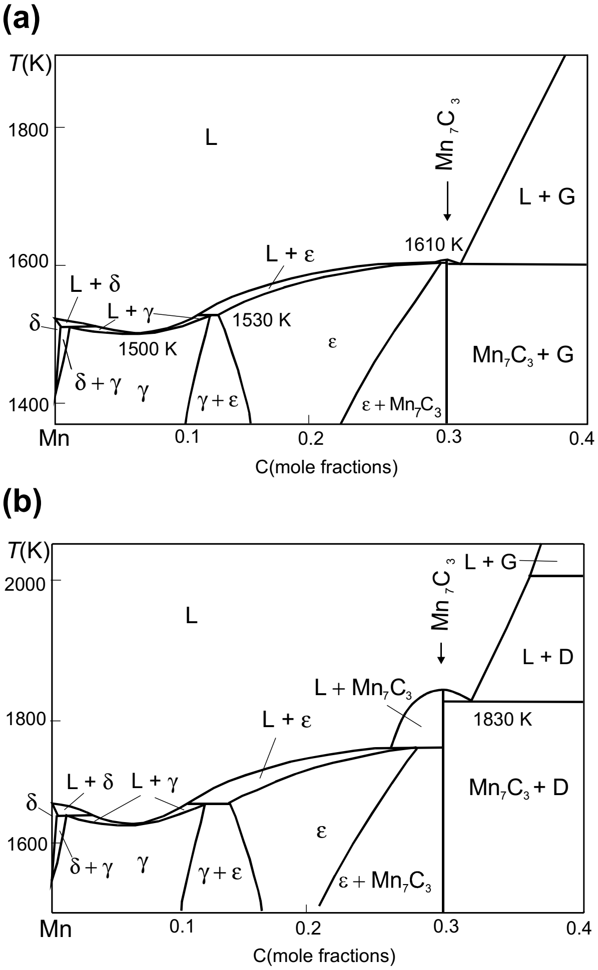

Figure 6 Isobaric sections of the phase diagram of the Mn–C system at 0.1 MPa (a) and 6 GPa (b).

3.03.3.1.7 The V–C System

In the V–C system, the pressure increase from 0.1 MPa to 9 GPa causes the temperature of the $L \rightleftarrows VC + C$ eutectics to increase from 2850 to 2950 K (Kamenetskaya, Shterenberg, & Ponizovsky, 1991). An isobaric section of the phase diagram of the VC–C system at 9 GPa is given in **Figure 9**. Unlike the Ta–C and Nb–C systems, in the VC–C system, even this level of pressure is sufficient for the stable equilibrium between diamond and the melt to appear.

3.03.3.1.8 The Mg–C System

In the Mg–C system, at atmospheric pressure MgC carbide, at 7.7 GPa MgC and MgC_2 carbides, and at 10 GPa MgC_2 carbide form (Shulzhhenko & Ignat'eva, 1989). Thus, high pressures stabilize and expand the region of existence of the densest phase, i.e. MgC_2 carbide, whose liquidus at 10 GPa is above the liquidus of MgC with the result that the latter destabilizes. The stable equilibria between diamond and the melt appear at temperatures above 2100 and 1800 K and pressures of 7.7 and 10 GPa, respectively (**Figure 10**). Diamonds that have been crystallized in the Mg–C system melts show semiconducting properties.

3.03.3.1.9 The Ca–C System

The phase diagram of the Ca–C system at atmospheric pressure has not yet been constructed. Only the fact of the formation of CaC_2 carbide with the melting temperature of 2430 K has been reported in the literature (Massalski et al., 1990). At 7.7 GPa, this carbide melts congruently (2570 K) and participates in the $L \rightleftarrows CaC_2 + G$ eutectic equilibrium at 2420 K (**Figure 11**) (Shulzhhenko & Ignat'eva, 1989). The stable equilibria between diamond and the melt are possible at pressures above 8 GPa and temperatures exceeding 2450 K.

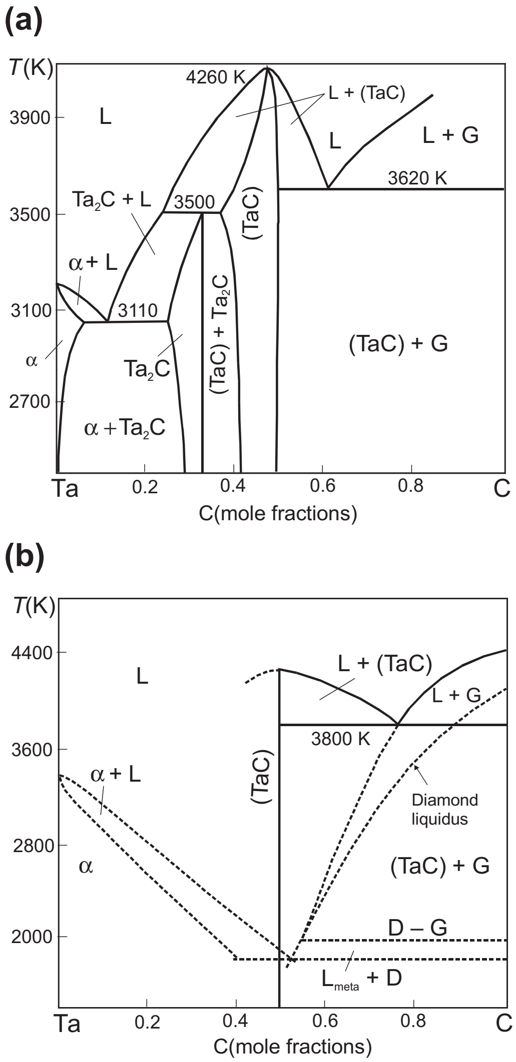

Figure 7 Isobaric sections of the phase diagram of the Ta–C system at 0.1 MPa (a) and 6 GPa (b).

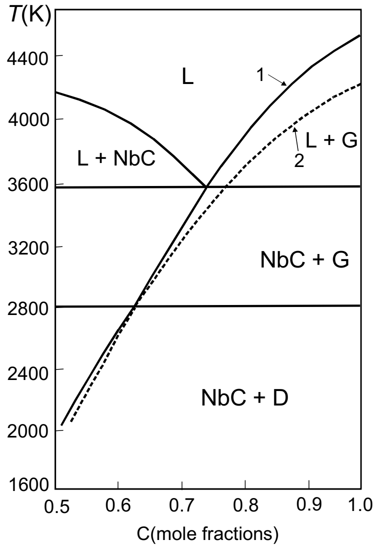

Figure 8 Phase diagram of the Nb–C system at 8 GPa. 1, the liquidus of graphite; 2, the liquidus of diamond.

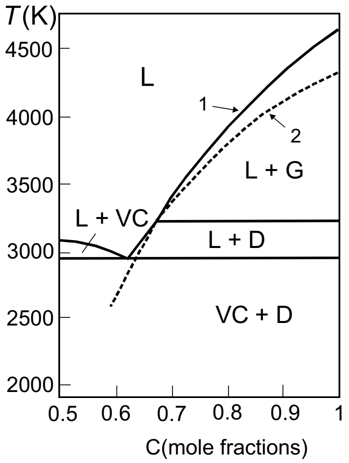

Figure 9 Phase diagram of the V–C system at 9 GPa. 1, the liquidus of graphite; 2, the liquidus of diamond.

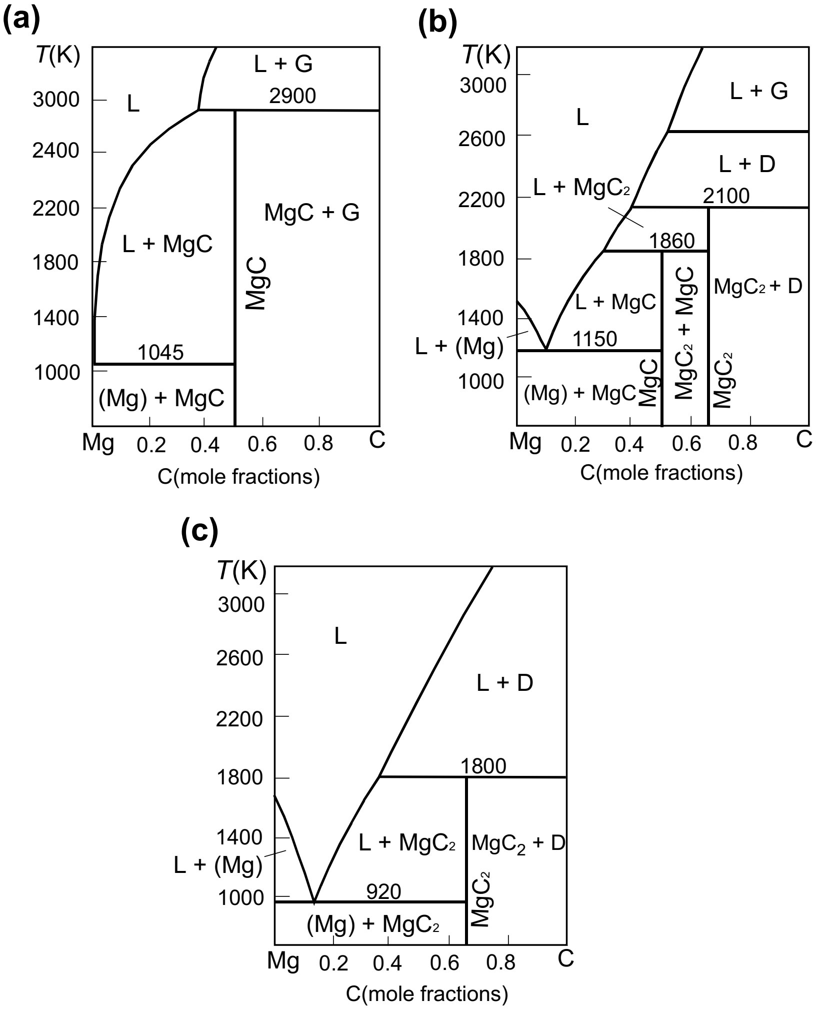

Figure 10 Phase diagram of the Mg–C system at 0.1 MPa (a), 7.7 GPa (b), and 10 GPa (c).

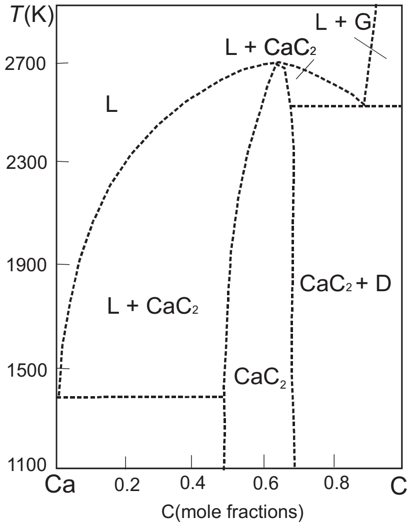

Figure 11 Phase diagram of the Ca–C system at 7.7 GPa.

3.03.3.1.10 The Zn–C System

The phase diagram of the Zn–C system at atmospheric pressure has not been experimentally constructed because of experimental problems due to high partial pressure of zinc vapors. The experimental results reported (Shulzhenko, Ignatieva, Osipov, et al., 2000) have allowed thermodynamic calculation of the phase diagrams of the Zn–C system at 0.1 MPa, 4 GPa, and 8 GPa (**Figure 12**) (Turkevich, 2000).

The phase diagram of the Zn–C system at 8 GPa is characterized by two invariant equilibria, the $L \rightleftarrows Zn + ZnC_2$ eutectic at 980 K and the $L + D \rightleftarrows ZnC_2$ peritectic at 2100 K. Above the latter temperature, stable equilibrium between the liquid and diamond is observed, which at 2800 K is replaced by the equilibrium between the liquid and graphite.

A decrease in pressure to 4 GPa reduces the carbon solubility in the melt with the result that eutectic point abruptly approaches zinc in composition. The diamond thermodynamic stability region disappears in the diagram. Above 1600 K (the temperature of the $L + G \rightleftarrows ZnC_2$ nonvariant peritectic reaction), the liquid is in equilibrium with graphite.

The calculated phase diagram of the Zn–C system at 0.1 MPa exhibits only one degenerate eutectic equilibrium ($L \rightleftarrows Zn + G$) at 650 K.

3.03.3.1.11 The Al–C System

The Al–C system has been experimentally studied (Turkevich, Garan, Kulik, & Petrusha, 2005). Thermodynamically calculated phase diagram of the Al–C system at 0.1 MPa (Turkevich, Kulik, Garan, et al., 2004) and 8 GPa is given in **Figure 13**. Dotted lines indicate metastable continuations of the stable equilibria. At 8 GPa, the diagram is characterized by the $L \rightleftarrows Al + Al_4C_3$ (1430 K) eutectic equilibrium, $L + D \rightleftarrows Al_4C_3$ (2470 K) peritectic equilibrium, and the equilibrium between diamond and graphite ($D \rightleftarrows G$ at 2800 K). The diagram topology of the Al–C system does not change up to 8 GPa; the incongruent type of melting of the Al_4C_3 carbide holds. Qualitative variations of the phase diagram are observed, the limiting solubility of carbon in the melt increases drastically, and the temperature of the $L \rightleftarrows Al + Al_4C_3$ eutectic equilibrium at 8 GPa increases by 460 K.

3.03.3.1.12 The Fe–Ni–C System

At atmospheric pressure in the Fe-Ni-C system, the $L \rightleftarrows \gamma + G$ univariant eutectics, the melting temperature increases from that of the binary eutectics in the Fe–C system to the melting temperature of the binary eutectics in the Ni–C system (**Figure 14(a)**) (Kocherzhinsky, Kulik, & Turkevich, 1993). Experimental construction of the isothermal section of the Fe–Ni–C system (1670 K) at 5.7 GPa has been reported in (Strong & Chrenko, 1971) (**Figure 14(b)**). Pressure-induced stabilization of the $(Fe, Ni)_3C$ carbide initiates the $L \rightleftarrows \gamma + (Fe, Ni)_3C$ invariant four-phase eutectics, whose melting temperature (1500 K) is just the lowest temperature of diamond crystallization in the Fe–Ni–C system at a pressure of 5.7 GPa. Further increase in pressure (>6 GPa) initiates stabilization of one more carbide (Fe_7C_3) and gives rise to the $L + Fe_7C_3 \rightleftarrows (Fe, Ni)_3C + D$ four-phase transition-type equilibrium (Kocherzhinsky et al., 1993).

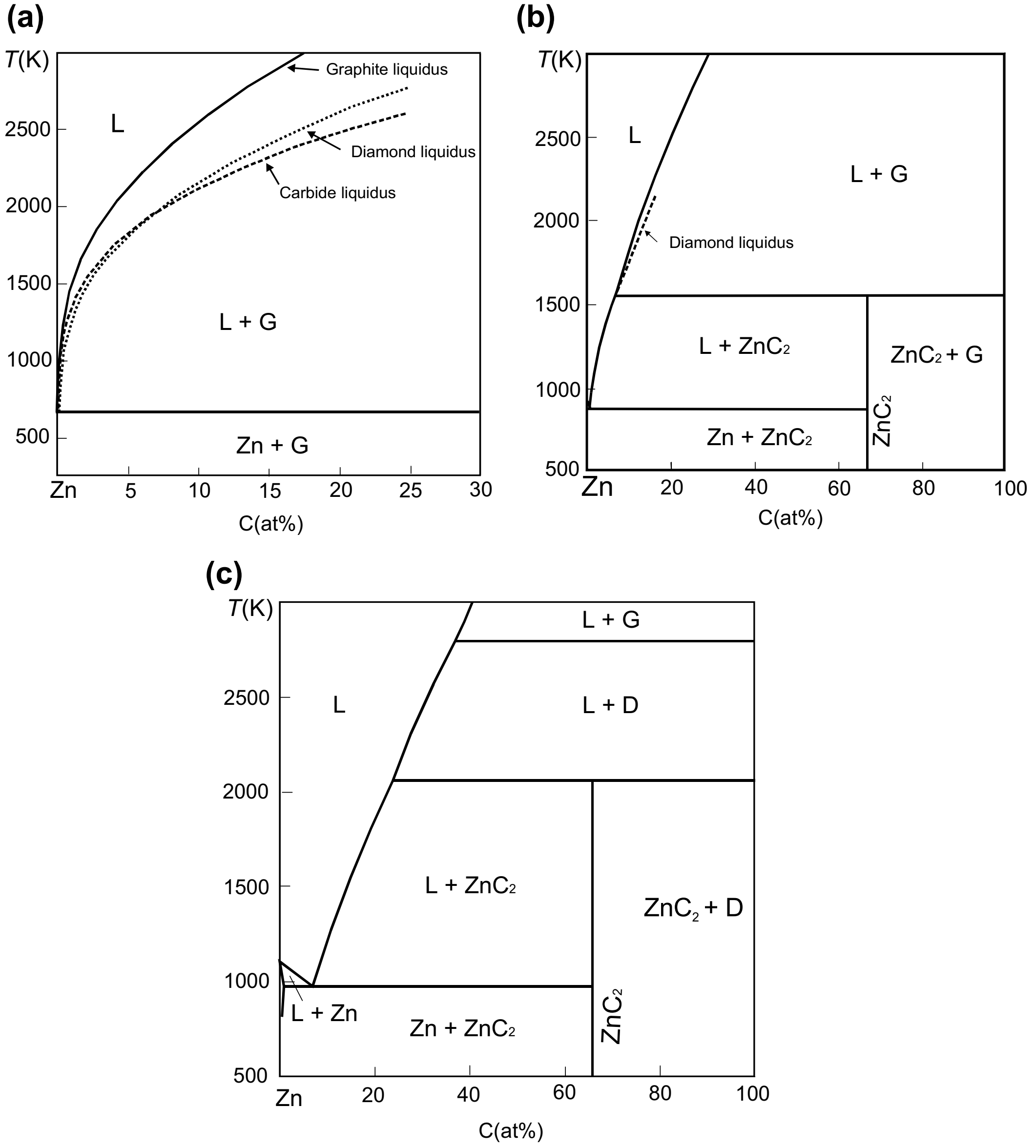

Figure 12 Phase diagram of the Zn–C system at 0.1 MPa (a), 4 GPa (b), and 8 GPa (c).

3.03.3.1.13 The Fe–Co–C System

As in the Fe–Ni–C system, at atmospheric pressure in the Fe–Co–C system, only the $L \rightleftarrows \gamma + G$ univariant eutectics is stable. With increasing pressure, the phase diagram of the Fe–Co–C changes greatly. Stabilization of cementite (already at 0.1 GPa) gives rise to the $L \rightleftarrows \gamma + (Fe, Co)_3C + G$ ternary eutectics (**Figure 15(a)**); at 6 GPa, the region of primary crystallization of the Fe_7C_3 carbide and the $L + Fe_7C_3 \rightleftarrows (Fe, Co)_3C + D$ nonvariant transition-type equilibrium appear (**Figure 15(b)**) (Kocherzhinsky, Kulik, Turkevich, et al., 1994). The existence of the ternary eutectics offers the possibility of diamond crystallization from the melt of the Fe–Co–C system at a pressure and temperature lower than those in the Fe–C and Co–C binary systems, namely, at 4.7 GPa and 1500 K. **Figure 15(a)** shows that the region of diamond primary crystallization does not reach binary systems. The topology of melting diagrams of the Fe–Ni–C and Fe–Co–C system is similar not only in quality but also in quantity. The differences in temperature and concentration of nonvariant points do not exceed the error of their determination (±30 K in temperature and ±0.05 mol parts in composition).

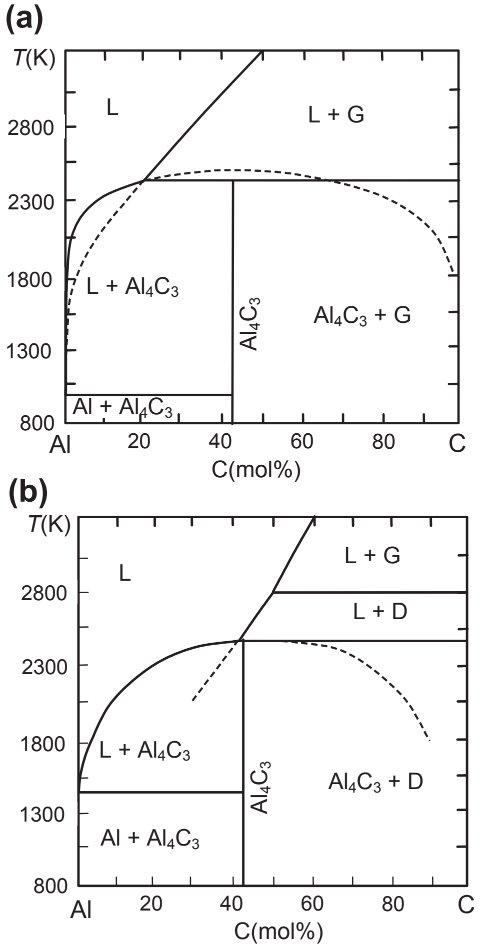

Figure 13 Phase diagram of the Al–C system at 0.1 MPa (a) and 8 GPa (b).

3.03.3.1.14 The Mn–Ni–C System

Both at atmospheric pressure and at 6 GPa, the Mn–Ni–C system is characterized by two four-phase nonvariant equilibria: the $L + \varepsilon \rightleftarrows Mn_7C_3 + \gamma$ transition type and $L \rightleftarrows Mn_7C_3 + \gamma + C$ eutectic ones (Ignat'eva & Butylenko, 1977). An increase in pressure causes the position of the point of the ternary eutectics to shift to higher concentrations of nickel and carbon. The phase diagram of the Mn–Ni–C system at 4.7 GPa constructed based on the thermodynamic calculation (Turkevich, 1994) is shown in **Figure 16**. Even at this pressure, inside the concentration triangle, there is the diamond primary crystallization region. From the polythermal section through the C vertex of the concentration triangle and a point (0.6 mol part Mn, 0.4 mol part Ni) in the Mn–Ni axis (**Figure 17**) it is evident that the stable diamond liquidus is retained between 1420 and 1510 K, while the melting temperature of the ternary eutectics is 1390 K.

3.03.3.1.15 The Fe–Al–C System

It has been reported (Strong & Chrenko, 1971) that at 5.7 GPa, the liquid phase appears in the Fe–Al–C system at a temperature below 1600 K. The thermodynamic calculation of equilibria between austenite, cementite and carbon and the melt of the Fe–Al–C system in alloys containing more than 80% iron is made (Kamenetskaya, Korsunskaya, & Litvin, 1978) (**Figure 18**). For alloys containing 4 wt% aluminum, the equilibrium between the melt and diamond is established at 5.7 GPa and 1870 K. The experimental results (Putyatin, Davidov, & Nesterenko, 1992) have shown that at 6 GPa the arrangements of the fields of the primary crystallization of phases fit to those calculated in Kamenetskaya et al. (1978).

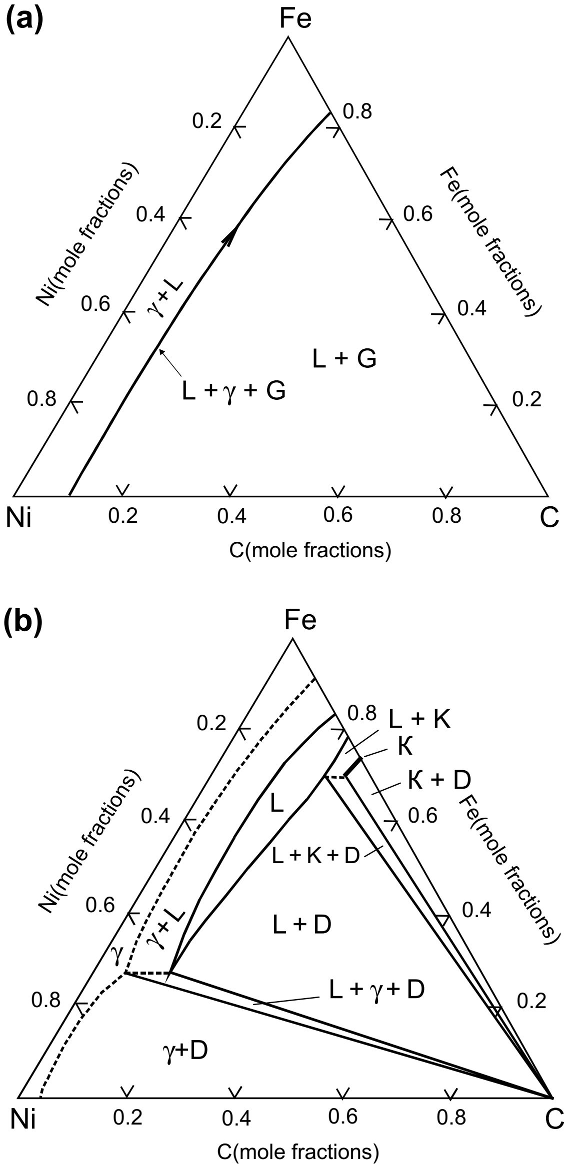

Figure 14 Phase diagram of the Fe–Ni–C system: projection of the liquidus surface at 0.1 MPa (a), isothermal–isobaric section at 1670 K and 5.7 GPa (b).

3.03.3.1.16 The Fe–Si–C System

The isobaric section of the phase diagram of the Fe–Si–C system at 8 GPa calculated in Kamenetskaya et al. (1978) is shown in Figure 19. The system is characterized by the presence of the $L \rightleftarrows \gamma + K + D$ (K is the Fe_3C iron carbide) ternary eutectics. The liquid phase contains 4 wt% C and 8 wt% Si.

3.03.3.1.17 The Mg–Zn–C System

By reacting in the Mg–Zn–C system with magnesium, carbon and zinc, $MgZn_2$ promotes the existence of two nonvariant four-phase equilibria of the eutectic type (Figure 20), i.e. $L \rightleftarrows Mg + MgZn_2 + D(E_2)$ and $L \rightleftarrows Zn + MgZn_2 + D(E_1)$. The composition of the ternary eutectics is Zn 70, Mg 15, and Zn 15 at%. This equilibrium is established at a relatively low temperature (1030 K at 7.7 GPa) (Shulzhenko, Ignat'eva, & Osipov, 2000). At higher temperatures, diamond is in equilibrium with the liquid phase, and therefore, diamond crystallization from the melt under thermodynamic stability conditions is a possibility. The lowest temperature of experimental diamond making with the use of a metal alloy with a composition located in a section through carbon and point E_1 (Zn 83, Mg 17 at%) has been 1630 K at 7.7 GPa. Diamond nucleation and crystal growth

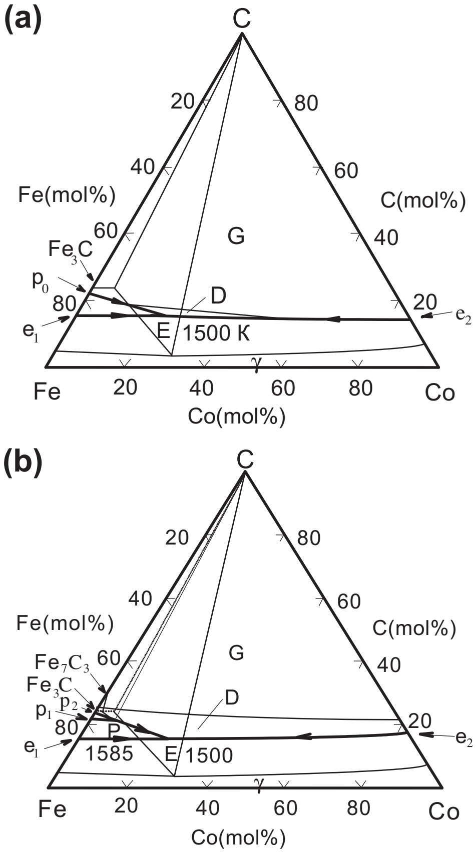

Figure 15 Phase diagram of the Fe–Co–C system at 4.7 GPa (a) and 6 GPa (b).

are temperature-activated diffusion processes. Kinetic difficulties do not allow the temperature of diamond synthesis in the Mg–Zn–C system to decrease below 1630 K, despite the fact that the reduction is permissible in terms of thermodynamics.

3.03.3.1.18 The Al–Ni–C System

Phase equilibria in the Al–Ni–C system have been experimentally studied at pressures from 5.5 to 8.0 GPa on samples prepared by the quenching method (Turkevich & Garan, 2006). Thermodynamic calculation has been performed and the melting diagram of the Al–Ni–C system has been constructed at 0.1 MPa and 6 GPa

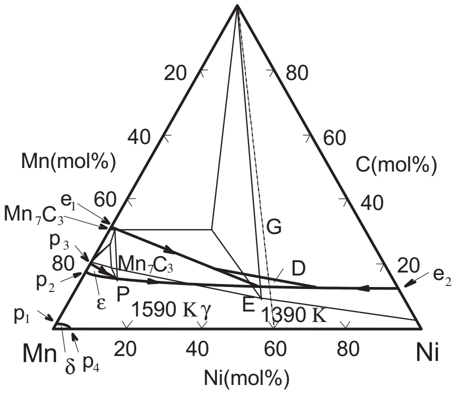

Figure 16 Phase diagram of the Mn–Ni–C system at 4.7 GPa.

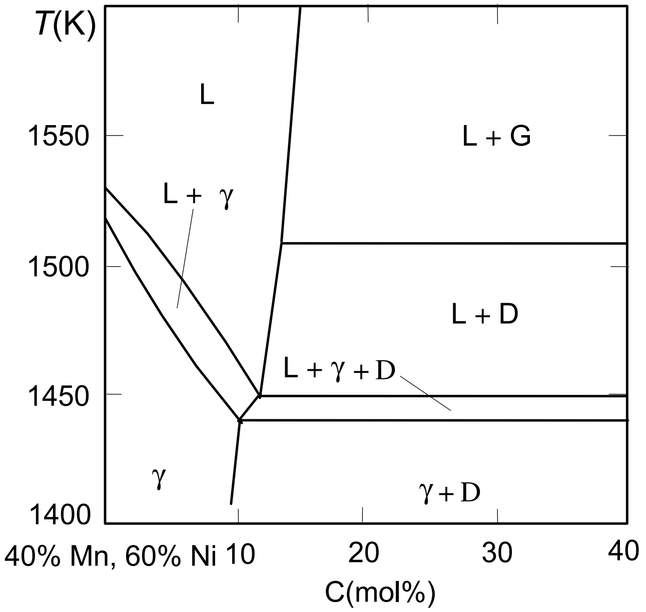

Figure 17 Polythermal section (C—60 mol% Mn, 40 mol% Ni) of the Mn–Ni–C system at 4.7 GPa.

(Figure 21). The concentration range of stable liquid–diamond equilibrium has been specified. At 6 GPa, it extends from the Ni–C binary system to the $Ni_{30}Al_{70}$–C vertical section. The minimum diamond crystallization temperature has been defined to be at 1620 K at 6 GPa. It exists in $Ni_{90}Al_{10}$–C vertical section, which comprises the eutectic $L \rightleftarrows \gamma + \gamma' + C(E_1,\ 1430\ K)$.

3.03.3.2 High-Pressure Phase Diagrams of the Systems Containing Boron Nitride

3.03.3.2.1 The NH_3–BN System

Supercritical ammonia dissolves boron nitride and in the presence of lithium (magnesium or aluminum) nitride promotes cBN crystallization at 2 GPa (Solozhenko, Mukhanov, & Novikov, 1989). The phase diagram of the NH_3–BN system that reflects equilibrium between condensed phases is the curves of the hBN and cBN limiting solubility in supercritical ammonia. Figure 22 demonstrates the results of experimental determination and thermodynamic calculation of the limiting solubility of BN polymorphous modifications in a fluid of the

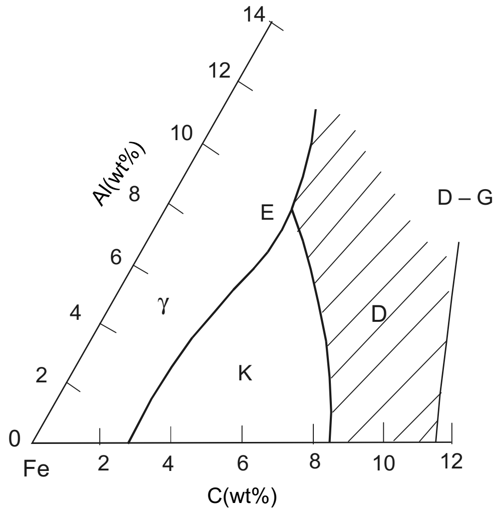

Figure 18 Projection of the liquidus surface of the phase diagram of the Fe–Al–C system at 8 GPa.

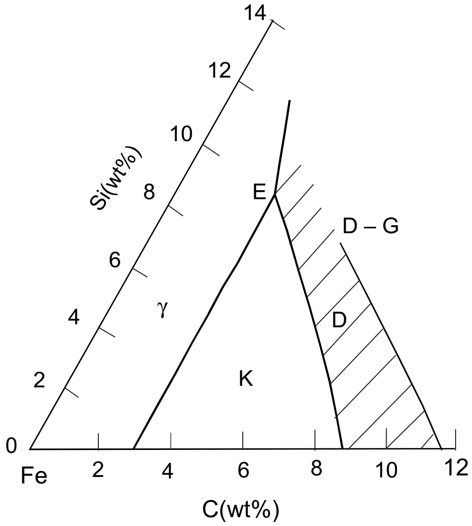

Figure 19 Projection of the liquidus surface of the phase diagram of the Fe–Si–C system at 8 GPa.

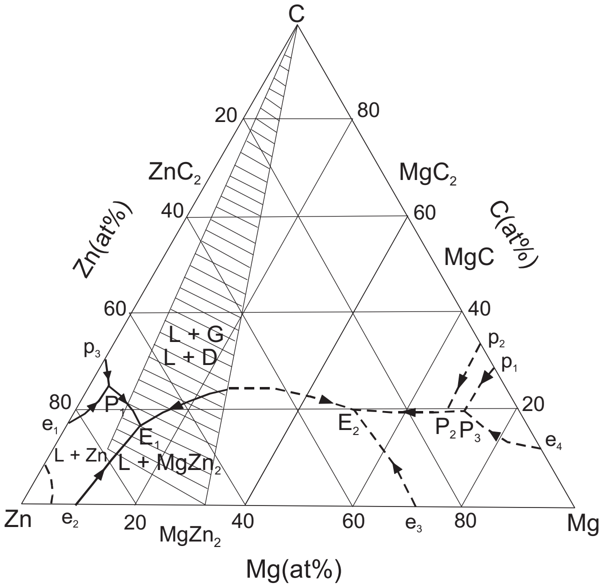

Figure 20 Melting diagram of the Mg–Zn–C ternary system at 7.7 GPa.

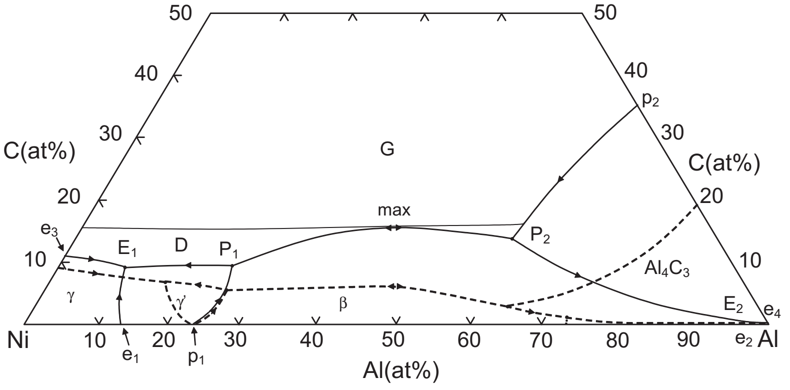

Figure 21 Projection of the liquidus surface of the phase diagram of the Al–Ni–C system at 0.1 MPa (dotted lines) and 6 GPa (solid lines).

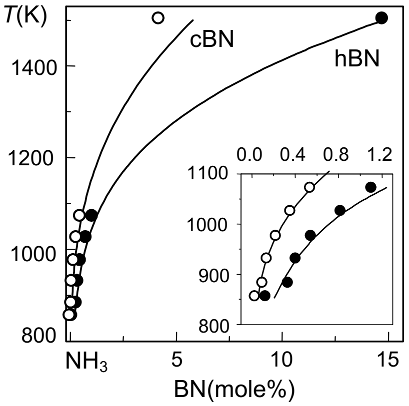

Figure 22 Experimental (circles) and calculated (lines) values of hBN and cBN solubility in supercritical ammonia between 0.065 and 4.2 GPa.

NH_3–BN system (Solozhenko, Turkevich, & Will, 1996). The difference in limiting solubility between graphite-like hexagonal BN and cBN modifications is well described based on the value of the enthalpy of the transformation $\Delta H_{\mathrm{hBN-cBN}} \rightleftarrows -17$ kJ/mol.

3.03.3.2.2 The B–BN System

The chemical interaction and phase relations in the B–BN system have been studied in situ at 5 GPa and temperatures up to 2800 K using powder X-ray diffraction with synchrotron radiation (Solozhenko, Kurakevych, Turkevich, & Turkevich, 2010). It has been reported that $B_{13}N_2$ is the only thermodynamically stable boron subnitride that melts incongruently at 5 GPa, while $B_{50}N_2$ is metastable. The equilibrium phase diagram (**Figure 23**) is characterized by the $L + cBN \rightleftarrows B_{13}N_2$ (2600 K, 12 at% N in the liquid phase) peritectic and $L \rightleftarrows \beta - B + B_{13}N_2$ (2300 K, 4 at% N) eutectic equilibria.

3.03.3.2.3 The Mg–B–N System

To synthesize cBN in the Mg–B–N system, mixtures of hBN with Mg_3N_2 magnesium nitride, pure magnesium, and MgB_2 magnesium boride are used. The lowest synthesis parameters (4.7 GPa and 1670 K) have been achieved with Mg_3N_2 as a solvent (DeVries & Fleischer, 1972). With Mg present, the pressure and temperature of the cBN crystallization is somewhat higher, i.e. 5 GPa and 1770 K (Bocquillon, Loriers-Susse, & Loriers, 1993; Endo, Fukunaga, & Iwata, 1979b).

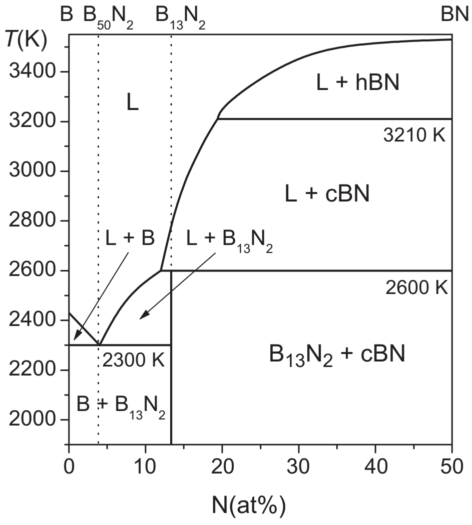

Figure 23 Phase diagram of the B–BN system at 5 GPa.

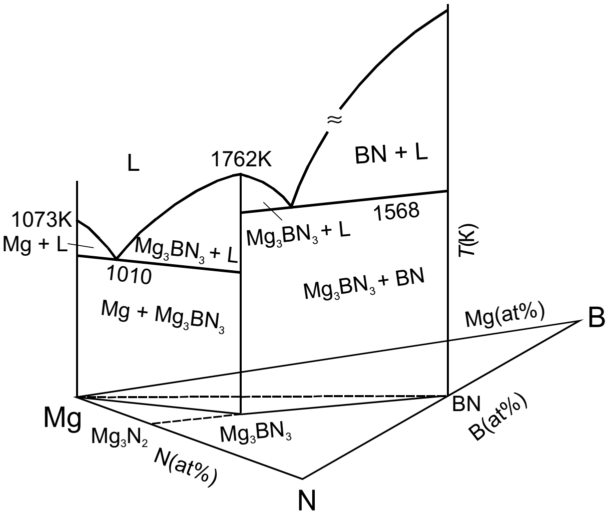

Figure 24 Mg–Mg_3BN_3 and Mg_3BN_3–BN quasi-binary sections of the Mg–B–N ternary system at 2.5 GPa.

Data on the equilibria between the phases and boron nitride in this system at atmospheric pressure cannot be found in the literature. Two quasi-binary sections (Mg–Mg_3BN_3 and Mg_3N_2–BN) at high pressures have been constructed (**Figures 24** and **25**). Mg_3BN_3 has two polymorphous modifications (low- and high-pressure phases). The equilibrium line between them can be described as $p(GPa) = 7.2 - 0.0025 \times (T - 273)(K)$ (Nakano, Ikawa, & Fukunaga, 1993). The existence of $Mg_3B_2N_4$ magnesium boron nitride has not been taken into account in the earlier paper (Endo, Fukunaga, & Iwata, 1979a). The incongruent character of the $Mg_3B_2N_4$ melting by the $L + BN \rightleftarrows Mg_3B_2N_4$ reaction has been reported in (Lorenz, Peun, & Orgzall, 1997). As opposed to the authors Lorenz et al. (1997), the authors Gladkaya, Kremkova, Bendeliani, et al. (1994) reason that $Mg_3B_2N_4$ melts congruently and the $L \rightleftarrows Mg_3B_2N_4 + BN$ eutectic equilibrium takes place.

The MgB_2–BN section of the Mg–B–N ternary system is not quasi-binary. On the high-pressure–high-temperature treatment of the hBN–MgB_2 initial mixtures, the phase composition of samples has been found to change to $cBN + MgB_6 + Mg_3BN_3$ (Solozhenko, Turkevich, & Holzapfel, 1999b). Thermodynamically calculated melting diagram of the Mg–B–N system at 4.5 GPa is presented in **Figure 26** (Turkevich, Solozhenko, Kulik, et al., 2003).

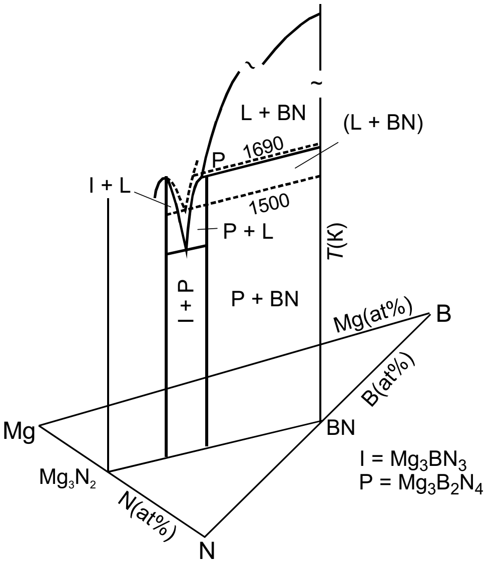

Figure 25 Mg_3N_2–BN quasi-binary section of the Mg–B–N ternary system at 5.5 GPa.

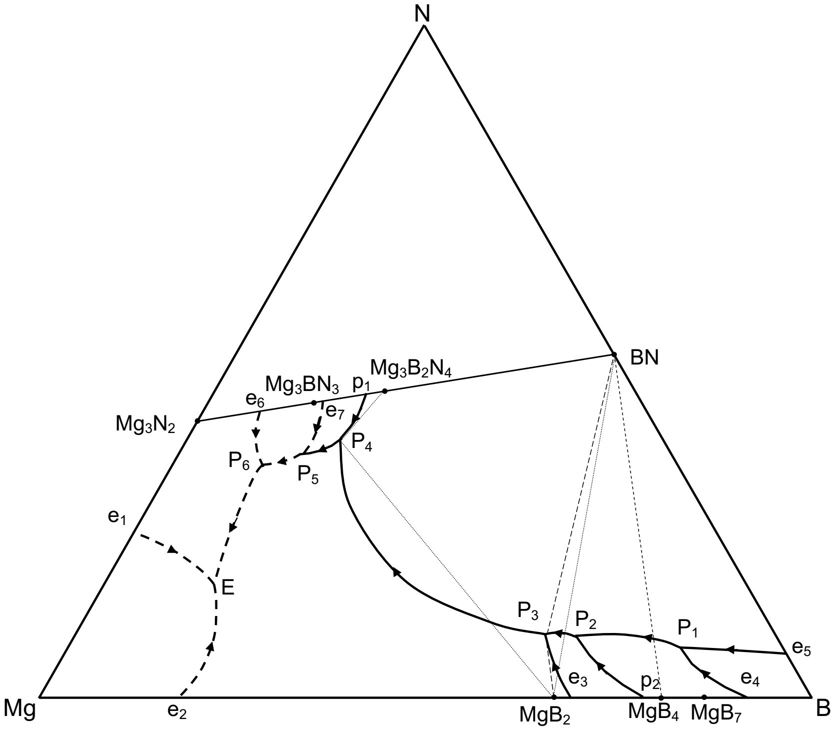

Figure 26 Projection of the liquidus and solidus surfaces of the phase diagram of the Mg–B–N system at 4.5 GPa.

3.03.3.2.4 The Ca–B–N System

Figure 27 shows two quasi-binary sections ($Ca_3B_2N_4$ and $Ca_3B_2N_4$–BN) of the Ca–B–N ternary system at 2.5 GPa (Endo, Fukunaga, & Iwata, 1981). The sections are of a simple eutectic type: $L \rightleftarrows Ca_3B_2N_4 + hBN(1590\ K)$ and $L \rightleftarrows Ca + Ca_3B_2N_4(1305\ K)$. At 2.5 GPa, $Ca_3B_2N_4$ melts at 1685 K.

At pressures below 6.5 GPa, the temperature of cBN synthesis in the Ca–BN and $Ca_3B_2N_4$–BN systems has been found to be almost the same (1670 K) (Endo et al., 1981; Sato, Endo, Kashima, et al., 1983). The $Ca_3B_2N_4$–BN quasi-binary section according to the data reported in Sato et al. (1983) is given in **Figure 28**.

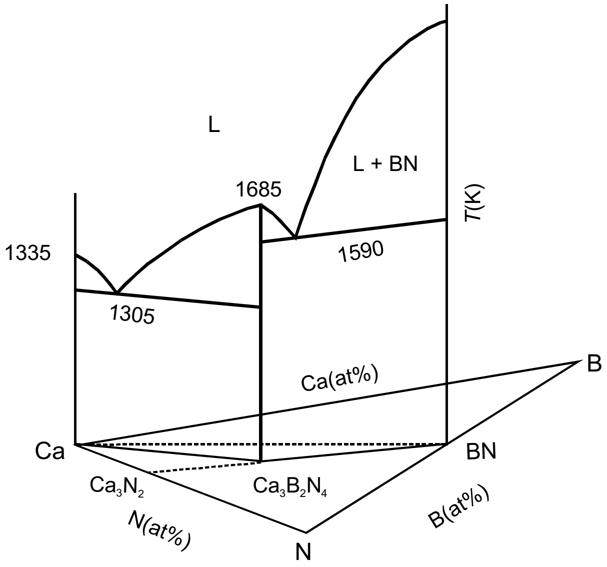

Figure 27 Ca–$Ca_3B_2N_4$ and $Ca_3B_2N_4$–BN quasi-binary sections of the Ca–B–N ternary system at 2.5 GPa.

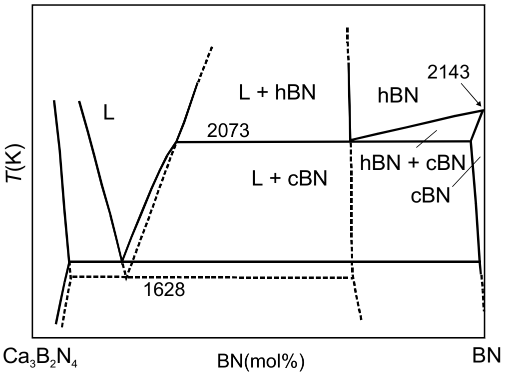

Figure 28 $Ca_3B_2N_4$–BN quasi-binary section of the Ca–B–N ternary system at 5.4 GPa.

3.03.3.2.5 The Li–B–N System

The only ternary compound (Li_3BN_2 lithium boron nitride) forms in the Li–B–N system. Li_3BN_2 has three polymorphous modifications, two of which are high-pressure modifications (DeVries & Fleischer, 1972). The Li_3BN_2 section is quasi-binary and characterized by the $L \rightleftarrows Li_3BN_2 + cBN$ eutectic equilibrium at 1883 K in the case of 6 at% BN (**Figure 29**).

According to DeVries and Fleischer (1972), the lowest temperature of the cBN crystallization in the Li–B–N system at 6 GPa is 1823 K. It is lower than that of the $L \rightleftarrows Li_3BN_2 + cBN$ eutectics and is appropriate to cBN synthesis in the presence of lithium (Rogl & Schuster, 1992). In refinement of the data reported in DeVries and Fleischer (1972), the authors Solozhenko and Turkevich (1997), Solozhenko and Turkevich (1998) have found that Li_3BN_2 melts incongruently and the temperature of the $L + BN \rightleftarrows Li_3BN_2$ peritectic equilibrium (1620 K) is the lowest temperature of cBN synthesis in the Li–B–N system at 5.3 GPa (**Figure 30**).

3.03.3.2.6 The B–N–O System

Data on synthesis of cBN in the presence of the H_3BO_3, boric acid, which is the product of the reaction between the B_2O_3 boron oxide and H_2O, are given by Golubev, Kurdyumov, and Pilyankevich (1987). A very low value of the minimal cBN synthesis temperature (1100–1300 K at 6 GPa) is observed. Using dehydrated B_2O_3, the researchers (Turkevich, Voronin, & Lutsenko, 1999) have concluded that the difference in pressure and temperature between the hBN-to-cBN transformations with and without boron oxide is insignificant. The B_2O_3–BN quasi-binary section of the B–N–O ternary system is constructed based on the findings of Turkevich et al. (1999) (**Figure 31**).

B_2O_3, boron oxide, that has a high negative value of the free energy of formation reacts with boron nitride relatively slightly, while the formation of oxygen solid solutions in BN considerably decreases the temperature of the cBN-to-hBN phase transformation causing the transformation to proceed in a certain temperature range (Turkevich, 1999). By dissolving in BN, oxygen substitutes for nitrogen atoms, and therefore, all compositions of BN(O) solid solutions are in the BN–BO section (**Figure 32**).

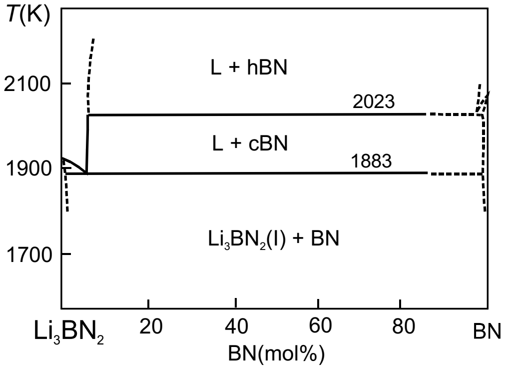

Figure 29 Li_3BN_2–BN quasi-binary section of the Li–B–N ternary system at 5 GPa.

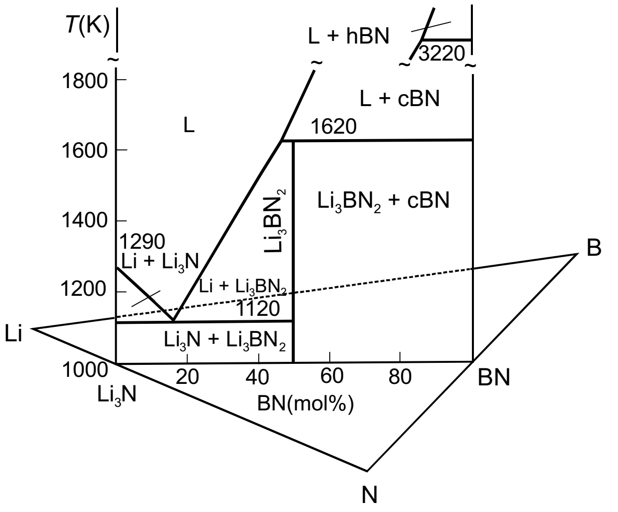

Figure 30 Li_3N–BN quasi-binary section of the Li–B–N ternary system at 5.3 GPa.

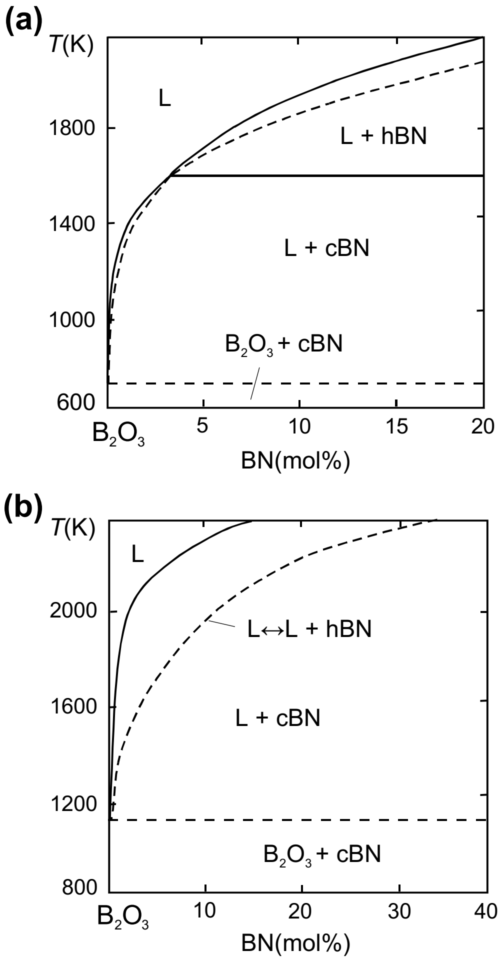

Figure 31 B_2O_3–BN quasi-binary section of the B–N–O ternary system at 0.1 MPa (a) and 7.5 GPa (b).

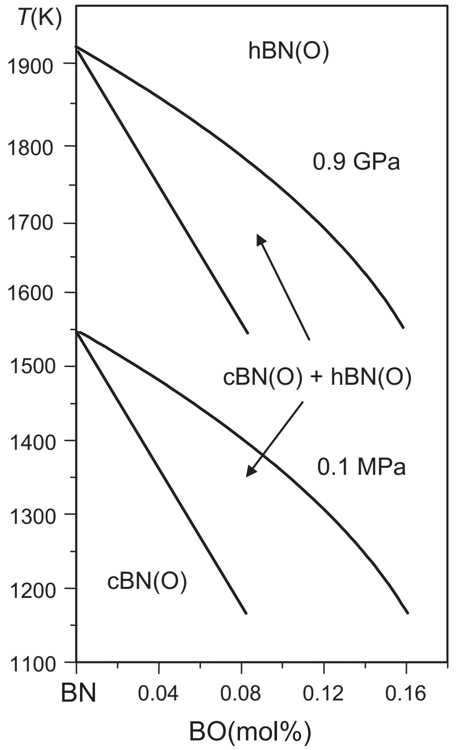

Figure 32 Fragment of the BN–BO quasi-binary section of the B–N–O ternary system.

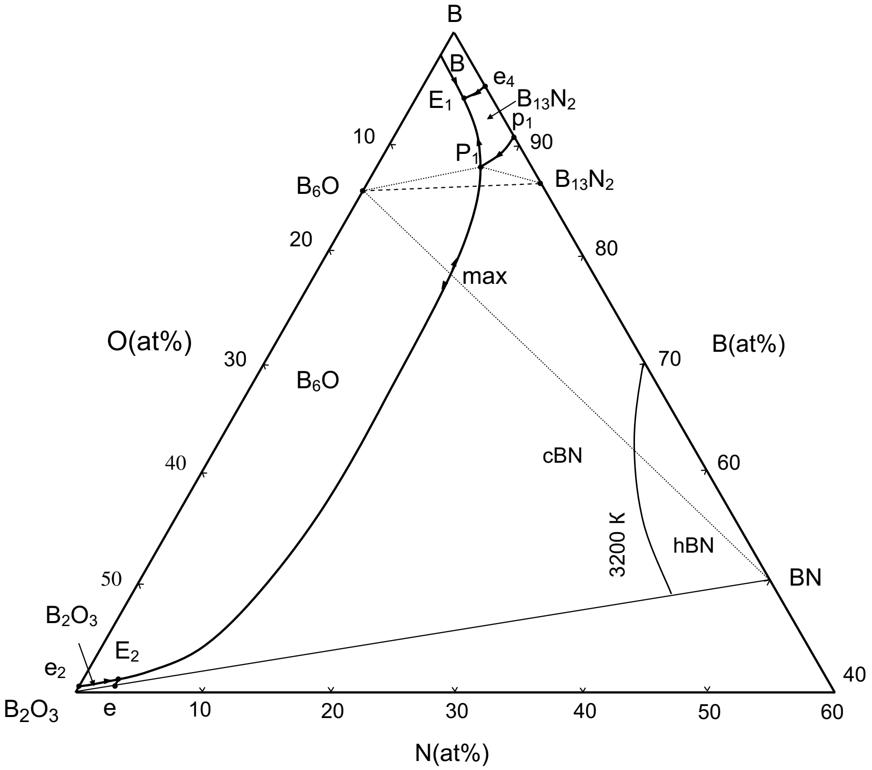

Figure 33 Projection of the liquidus and solidus surfaces of the phase diagram of the B–N–O system at 5 GPa.

The melting diagram of the $B–B_2O_3–BN$ ternary system at 5 GPa has been calculated in the framework of phenomenological thermodynamics models (Turkevich, Solozhenko, Prikhna, & Turkevich, 2009). The diagram (**Figure 33**) is characterized by the existence of two eutectic: $L \rightleftarrows B + B_6O + B_{13}N_2(E_1,\ 2320\ K)$, $L \rightleftarrows B_6O + B_2O_3 + cBN(E_2,\ 1300\ K)$; one transition type: $L + cBN \rightleftarrows B_6O + B_{13}N_2(U_1,\ 2480\ K)$; and the maximum in univariant eutectic line invariant equilibria: $L \rightleftarrows B_2O_3 + cBN(2550\ K)$

3.03.4 Conclusions

All the considered phase diagrams of binary and ternary systems that include either carbon or boron nitride have a common property. They indicate the pressure, temperature and composition, at which compounds that form in these systems melt and the stable liquidus of the cubic phase appears, i.e. the crystallization of diamond and cBN from melt solutions becomes possible. The above condition does not, however, guarantee the formation of cubic phases under the experimental conditions. Frequently, to overcome the kinetic difficulties that are inherent in diffusion transformations, pressures and temperatures, which considerably exceed the equilibrium values, are necessary.

References

Bocquillon, G., Loriers-Susse, C., & Loriers, J. (1993). Synthesis of cubic boron nitride using Mg and pure or M′-doped Li_3N, Ca_3N_2 and Mg_3N_2 with M′ = Al, B, Si, Ti. *Journal of Materials Science, 28*, 3547–3556.

Bundy, F. P. (1989). Pressure–temperature phase diagram of elemental carbon. *Physica A, 156*, 169–178.

Butylenko, A. K., & Ignat'eva, I. Yu (1977). Effect of a pressure up to 60 kbar on the melting diagram of the Mn–Ni–C system. *Doklady Akademii Nauk Ukrainskoi SSR, Seriya A, 2*, 161–164.

DeVries, R. C., & Fleischer, J. F. (1972). Phase equilibria pertinent to the growth of cubic boron nitride. *Journal of Crystal Growth, 13/14*, 88–92.

Endo, T., Fukunaga, O., & Iwata, M. (1979a). Precipitation mechanism of BN in the ternary system of B–Mg–N. *Journal of Materials Science, 14*, 1676–1680.

Endo, T., Fukunaga, O., & Iwata, M. (1979b). Growth pressure-temperature region of cubic BN in the system BN–Mg. *Journal of Materials Science, 14*, 1375–1380.

Endo, T., Fukunaga, O., & Iwata, M. (1981). The synthesis of cBN using $Ca_3B_2N_4$. *Journal of Materials Science, 16*, 2227–2232.

Ershova, T. P., & Kamenetskaya, D. S. (1982). Pressure effect on the equilibrium of diamond with graphite, diamond and Mn_7C_3 carbide in the Mn–C system. *Izvestiya Akademii Nauk SSSR, Metally, 3*, 180–184.

Ershova, T. P., Kamenetskaya, D. S., & Il'ina, L. P. (1981). Calculation of the *T–P–N* phase diagram of the Ni–C system up to 100 kbar. *Izvestiya Akademii Nauk SSSR, Metally, 4*, 201–210.

Ershova, T. P., Kamenetskaya, D. S., & Il'ina, L. P. (1982). Construction of the *T–P–N* phase diagram of the Co–C system up to 100 kbar. *Izvestiya Akademii Nauk SSSR, Metally, 1*, 153–160.

Gladkaya, I. S., Kremkova, G. N., Bendeliani, N. A., Lorenz, H., & Kuehne, U. (1994). The binary system of BN–Mg_3N_2 under high pressures and temperatures. *Journal of Materials Science, 29*, 6616–6619.

Golubev, A. S., Kurdyumov, A. V., & Pilyankevich, A. N. (1987). *Boron nitride. Structure, properties, application*. Kiev: Naukova Dumka.

Ignat'eva, I. Yu., & Butylenko, A. K. (1977). The melting diagram of the Mn–Ni–C system at 60 kbar. *High Temperatures–High Pressures, 9*, 677–679.

Kamenetskaya, D. S., Korsunskaya, I. A., & Litvin, Yu. A. (1978). The effect of graphitizing elements on the equilibria with the melt in the iron–carbon system at high pressures. *Fizika Metallov i Metallovedenie, 45*, 569–579.

Kamenetskaya, D. S., & Shterenberg, L. E. (1980). The *T–P–N* phase diagram of the tantalum–carbon system. In V. V. Skorokhod (Ed.), *Phase diagrams of refractory systems* (pp. 32–38). Kiev: Institute of Materials Science Problems of the UkrSSR Academy of Sciences.

Kamenetskaya, D. S., & Shterenberg, L. E. (1982). Thermodynamic calculation of phase equilibria in the Ta–C system at pressures up to 10 GPa. *Sverkhtverdye Materialy, 3*, 7–11.

Kamenetskaya, D. S., & Shterenberg, L. E. (1989). Phase diagram of the Nb–C system at high pressure. *Sverkhtverdye Materialy, 5*, 6–11.

Kamenetskaya, D. S., Shterenberg, L. E., & Ponizovsky, L. Z. (1991). Thermodynamic calculation of the phase diagram of the VC–C system at high pressure. *Sverkhtverdye Materialy, 2*, 7–11.

Kocherzhinsky, Yu. A., Kulik, O. G., & Turkevich, V. Z. (1993). Phase equilibria in the Fe–Ni–C and Fe–Co–C systems under high temperatures and high pressures. *High Temperatures–High Pressures, 25*, 113–116.

Kocherzhinsky, Yu. A., Kulik, O. G., Turkevich, V. Z., Ivakhnenko, S. A., Chipenko, G. V., Cherepenina, E. S., et al. (1992). Phase equilibria in the Fe–C system at high pressures. *Sverkhtverdye Materialy, 6*, 3–9.

Kocherzhinsky, Yu. A., Kulik, O. G., Turkevich, V. Z., & Vasilenko, V. I. (1994). An experimental investigation of the phase equilibria in the Co–Fe–C system at high pressures. *Sverkhtverdye Materialy, 3*, 6–11.

Korsunskaya, I. A., Kamenetskaya, D. S., & Ershova, T. P. (1973). Calculation of the *T–P–N* phase diagram of the Fe–C system in the region of the equilibrium with the melt up to 100 kbar. *Doklady Akademii Nauk SSSR, 210*, 577–580.

Lorenz, H., Peun, T., & Orgzall, I. (1997). Kinetic and thermodynamic investigation of cBN formation in the system BN–Mg_3N_2. *Journal of Applied Physics A, 65*, 487–495.

Massalski, T. B., Subramanian, P. R., Okamoto, H., & Kacprzak, L. (Eds.). (1990). *Binary alloy phase diagrams* (2nd ed.). Metals Park, Ohio: ASM International.

Muncke, G. (1974). Phase diagram calculation for diamond synthesis. *Diamond Research, 5*, 7–9.

Muncke, G. (1979). Physics of diamond growth. In J. F. Field (Ed.), *The properties of diamond* (pp. 473–497). London: Academic Press.

Nakano, S., Ikawa, H., & Fukunaga, O. (1993). High pressure reactions and formation mechanism of cubic boron nitride in the system BN–Mg_3N_2. *Diamond and Related Materials, 2*, 1168–1174.

Putyatin, F. F., Davidov, V. E., & Nesterenko, S. N. (1992). High temperature interactions in the Fe–Al–C system at 6 GPa pressure. *Journal of Alloys and Compounds, 179*, 165–175.

Rogl, P., & Schuster, J. C. (1992). *Phase diagrams of ternary boron nitride and silicon nitride systems*. Ohio: ASM International.

Sato, T., Endo, T., Kashima, S., Fukunaga, O., & Iwata, M. (1983). Formation mechanism of cBN crystals under isothermal conditions in the system BN–$Ca_3B_2N_4$. *Journal of Materials Science, 18*, 3054–3062.

Shulzhhenko, A. A., & Ignat'eva, I. Yu (1989). An investigation of the *P–T–C* phase diagrams of carbon-containing systems with magnesium and calcium. In N. V. Novikov (Ed.), *Development of superhard materials synthesis* (pp. 5–13). Kiev: Institute for Superhard Materials of the UkrSSR Academy of Sciences.

Shulzhenko, A. A., Ignat'eva, I. Yu., & Osipov, A. S. (2000). Peculiarities of diamond synthesis in the zinc- and magnesium-containing systems. In N. V. Novikov (Ed.), *Synthesis, sintering and properties of superhard Materials* (pp. 12–19). Kiev: Institute for Superhard Materials.

Shulzhenko, A. A., Ignatieva, I. Yu., Osipov, A. S., Smirnova, T. I., Dub, S. N., Belyavina, N. N., et al. (2000). Phase diagram of the Zn–C system at 7.7 GPa. *Sverkhtverdye Materialy, 4*, 10–13.

Solozhenko, V. L., Kurakevych, O. O., Turkevich, V. Z., & Turkevich, D. V. (2010). Phase diagram of the B–BN system at 5 GPa. *Journal of Physical Chemistry B, 114*, 5819–5822.

Solozhenko, V. L., Mukhanov, V. A., & Novikov, N. V. (1989). On the *p*, *T*-region of sphaleritic boron nitride formation. *Doklady Akademii Nauk SSSR, 308*, 131–133.

Solozhenko, V. L., & Turkevich, V. Z. (1997). High pressure phase equilibria in the Li_3N–BN system: in situ studies. *Materials Letters, 32*, 179–184.

Solozhenko, V. L., & Turkevich, V. Z. (1998). Kinetics of cBN crystallization in the Li_3N–BN system at 6.6 GPa. *Diamond and Related Materials, 7*, 43–46.

Solozhenko, V. L., Turkevich, V. Z., & Holzapfel, W. B. (1999a). Refined phase diagram of boron nitride. *Journal of Physical Chemistry B, 103*, 2903–2905.

Solozhenko, V. L., Turkevich, V. Z., & Holzapfel, W. B. (1999b). On nucleation of cubic boron nitride in the BN–MgB_2 system. *Journal of Physical Chemistry B, 103*, 8137–8140.

Solozhenko, V. L., Turkevich, V. Z., & Will, G. (1996). Thermodynamic analysis of the BN–NH_3 system at high pressures. *High Pressure Research, 10*, 135–141.

Strong, H. M., & Chrenko, R. M. (1971). Further studies on diamond growth rates and physical properties of laboratory-made diamond. *Journal of Physical Chemistry, 75*, 1838–1843.

Strong, H. M., & Hanneman, R. E. (1967). Crystallization of diamond and graphite. *Journal of Chemical Physics, 46*, 3668–3676.

Turkevich, V. Z. (1994). Thermodynamic calculation of the melting diagram of the Mn–Ni–C system at atmospheric and high pressures. *Fizika i Tekhnika Vysokikh Davlenii, 4*, 11–18.

Turkevich, V. Z. (1999). The parameters of equilibrium between oxygen solid solutions in cubic and graphite-like hexagonal boron nitrides. *Diamond and Related Materials, 8*, 2032–2035.

Turkevich, V. Z. (2000). Thermodynamic calculation of the phase diagram of the Zn–C system to 8 GPa. *Sverkhtverdye Materialy, 4*, 14–18.

Turkevich, V., Garan, A., Kulik, O., & Petrusha, I. (2005). Phase diagram and diamond synthesis in the aluminum–carbon system at a pressure of 8 GPa. In J. Lee, & N. V. Novikov (Eds.), *Innovative superhard materials and sustainable coatings for advanced manufacturing* (pp. 335–343). Dordrecht: Springer.

Turkevich, V. Z., & Garan, A. G. (2006). Thermodynamic calculation of phase diagram of the Al–Ni–C system at pressure of 6 GPa. *Fizika i Tekhnika Vysokikh Davlenii, 16*, 64–70.

Turkevich, V. Z., & Kulik, O. G. (1993). Calculation of phase diagrams of the Fe–Co–C and Fe–Ni–C systems at 6 GPa in the region of equilibria with the melt. *Dopovidi Akademii Nauk Ukrainy, 7*, 75–80.

Turkevich, V. Z., & Kulik, O. G. (1995). High pressure influence on the phase diagram construction of 3-d transition metals with carbon systems. *High Pressure Research, 14*, 175–180.

Turkevich, V. Z., Kulik, O. G., Garan, A. G., Petrusha, I. A., Lutsenko, A. N., & Vashchenko, A. N. (2004). Phase diagram of the Al–C system at a pressure of 8 GPa. *Sverkhtverdye Materialy, 4*, 29–34.

Turkevich, V. Z., Solozhenko, V. L., Kulik, O. G., Itsenko, P. P., Sokolov, A. N., Lutsenko, A. N., et al. (2003). Phase diagram of the Mg–B–N system at high pressures. *Sverkhtverdye Materially, 6*, 18–25.

Turkevich, V. Z., Solozhenko, V. L., Prikhna, T. A., & Turkevich, D. V. (2009). Melting diagram of the B–BN–B_2O_3 system at 5 GPa. *Dopovidi Natsional'noi Akademii Nauk Ukraini, 9*, 156–159.

Turkevich, V. Z., Voronin, G. A., & Lutsenko, A. N. (1999). Interaction of phases in the BN–B_2O_3 system. *Sverkhtverdye Materially, 2*, 49–53.

3.04 Theory of Superhard Materials

Artem R. Oganov, Department of Geosciences, Center for Materials by Design, Institute for Advanced Computational Science, Stony Brook University, Stony Brook, NY, USA; Moscow Institute of Physics and Technology, Dolgoprudny city, Moscow Region, Russian Federation; Northwestern Polytechnical University, Xi'an, China
Andriy O. Lyakhov and Qiang Zhu, Department of Geosciences, Stony Brook University, Stony Brook, NY, USA

3.04.1 Hardness: A Brief Introduction

Superhard materials find a variety of uses, especially in cutting, drilling, and abrasive tools. Apart from hardness, they frequently turn out to have other unique properties coming from the remarkable strength of interatomic bonds in their structure. Yet, although the hardness of a material is a property that seems so obvious, it is remarkably difficult to quantify, analyze, and predict hardness. The topic of this review is the prediction of hardness and new superhard materials.

There are many definitions of the hardness. First of all, hardness can be measured in two nonequivalent ways—by scratching or by indentation. Mohs' relative scale of hardness appeared in the nineteenth century and is still widely used by mineralogists; on this scale, talc has a hardness of 1, and diamond has a hardness of 10. Mohs' scratch hardness is semiquantitative; all modern quantitative definitions are based on indentation tests. The most popular of the latter are the Knoop and Vickers tests, which involve differently shaped indenters. The Knoop or Vickers microhardnesses, which for most materials are identical within a (considerable) experimental uncertainty, are measured as the ratio between the load and the imprint area of the indenter and depend on the duration of indentation, on the load, grain size, and concentration of dislocations in the crystal. Of course, hardness is an anisotropic property and can have remarkably different values in different crystallographic directions. To have well-defined numbers, one usually considers microhardness values of polycrystals at high loads.

Measured as the ratio between the load and the imprint area, the indentation microhardness (Knoop or Vickers) has the units of gigapascals, the same units as pressure or elastic moduli (bulk modulus, shear modulus). This hints that hardness may be correlated with the elastic properties—indeed, there is such a correlation, especially with the shear modulus (Brazhkin, Lyapin, & Hemley, 2002). However, hardness is obviously a much more complex property than elasticity, as it also involves plastic deformation and brittle failure. For these reasons, a complete picture of hardness cannot be given only by the ideal crystal structure and its properties, but must also include defects (in particular, dislocations) and grain size. The latter is related to hardness through a particularly important phenomenon, known as the Hall–Petch effect—hardness increases as the particle size D decreases. The actual dependence of hardness on the particle size is thought to be of the form

$$H = H_0 + \frac{a}{D^{1/2}} + \frac{b}{D}, \qquad (1)$$

where H_0 is the hardness of the bulk crystal, D is the diameter of the particle, and a and b are coefficients. The $D^{-1/2}$ term in Eqn (1) describes the Hall–Petch effect, and the next term (proportional to $1/D$) is thought to represent quantum confinement effects related to the increase of the band gap with decreasing particle size. The latter term can be given a more transparent interpretation—since coordination numbers of the atoms at surfaces are much lower than in the bulk; the bonds at the surface are stronger and shorter. Since the proportion of surface atoms is proportional to $1/D$, so will the average bond strength in the nanoparticle. Since bond strengths can be correlated with the hardness, as we discuss below, the third term in Eqn (1) gets a simple and intuitive explanation. According to Eqn (1), it is possible to significantly boost a material's hardness by creating nanoparticle aggregates and nanocomposites: while the hardness of diamond single crystals varies between 60 and 120 GPa depending on the direction (Brookes & Brookes, 1991), nanodiamond turns out to be much harder, with the isotropic hardness of up to 120–140 GPa (Irifune, Kurio, Sakamoto, Inoue, & Sumiya, 2003). Cubic BN has a Vickers hardness of 40–60 GPa in bulk crystals, but its nanocomposites are almost as hard as diamond, with a Vickers hardness of 85 GPa (Solozhenko, 2009). In this chapter, we will concentrate on the hardness of bulk crystals, H_0 in Eqn (1), which from now on we denote simply as H.

3.04.2 Brief Overview of the Models of Hardness. Li's Model. Accounting for Structural Topology and Distortions

Can one invent a practical recipe for predicting the hardness of a material on the basis of its crystal structure? This might be realistic for nanohardness (which can also be measured today), but for the conventional Vickers or Knoop microhardness this means ignoring dislocations and grain boundaries and is fundamentally incorrect. Yet, a number of practical recipes, invented recently, turned out to provide very reasonable results, certain predictive power, and great fundamental value. Some of these models are based on correlations of the hardness with the elastic properties (Chen, Niu, Li, & Li, 2011), another approach uses the ideal strength of the macroscopic crystal as a measure of hardness (indeed, the ideal strength often attains values in surprisingly good agreement with experimental microhardnesses), while other models (Gao et al., 2003; Li et al., 2008; Lyakhov & Oganov, 2011; Simunek, 2009) analytically represent the hardness as a function of the bond strength.

The first, pioneering attempts to correlate hardness with the crystal structure and thermodynamic properties were made in the 1960s by Povarennykh (1963), continued by Urusov (1975), and put on a modern foundation by Mukhanov et al. (2008). Shifting the accent from the microscopic thermodynamic properties to the strength of individual bonds, another breakthrough was achieved by Gao et al. (2003), Simunek and Vackar (2006), and Li et al. (2008). This new wave of research into the microscopic factors determining the hardness is still continuing. The emerging theory of hardness holds potential for revolutionizing the field of superhard materials. We address the interested reader to the original publications referred above and to the very recent Special Issue "Theory of Superhard Materials" of the *Journal of Superhard Materials* (Oganov & Lyakhov, 2010, and subsequent articles). Below, instead of giving a comprehensive overview of all the existing models, we focus our attention on some of the fundamental principles, new ideas, and some applications.

Perhaps the simplest approach to grasp is based on the elastic moduli. It is known that the correlation of the hardness with the bulk modulus is rather poor, but is better (still very imperfect) with the shear modulus (Brazhkin et al., 2002). Pugh (1954) formulated an extremely useful criterion of brittleness versus ductility, based solely on the bulk (K) and shear (μ) moduli:

$$\begin{gathered}\text{if } n = K/\mu > 1.75, \text{ the material is ductile,}\\ \text{if } n = K/\mu < 1.75, \text{ it is brittle.}\end{gathered} \tag{2}$$

Pugh's paper was a classical "sleeping beauty" paper, which was nearly forgotten for a long time and whose citation now, over 50 years after publication, increases explosively with time. Involving Pugh's brittleness criterion, Chen at al. (2011) have proposed an improved formula for hardness:

$$H = 2\left(\frac{\mu}{n^2}\right)^{0.585} - 3 \ \text{(GPa)} \tag{3}$$

It follows from this formula that hard materials tend to be brittle.

Concerning the most popular models of hardness, which are based on different estimates of bond strength, one can notice that, differing in mathematical and also somewhat in physical details, various analytical models have much in common; hardness is high when

1. the average bond strength is high
2. the number of bonds per unit volume is high
3. the average number of valence electrons per atom is high
4. bonds are strongly directional (i.e., have a large covalent component)—ionicity and metallicity decrease hardness.

The requirement of high bond strength indicates that compounds of light elements, which form extremely strong and short bonds, are particularly promising; some transition metals (e.g., W, Ta, Mo, and Re) can also form very strong (although not quite as directional) bonds and have a large number of valence electrons, thus their compounds may also be promising.

Diamond, a dense phase with strong and fully covalent bonds, satisfies all conditions (1)–(4). Cubic BN, with partially ionic bonds, has a somewhat lower hardness. Graphite, though containing stronger bonds than in diamond, has a much lower number of atoms and bonds per unit volume, and must therefore be softer[1]. Cold compression of graphite (Mao et al., 2003) resulted in a peculiar superhard phase, the structure of which has been understood only recently (Li et al., 2009) and has a much greater density and lower anisotropy than graphite.

The requirement of a high bond density means that often superhard materials will have to be synthesized at high pressure—this is the case of diamond (Bovenkirk, Bundy, Hall, Strong, & Wentorf, 1959; Bundy, Hall, Strong, & Wentorf, 1955), cubic BN (Wentorf, 1957), cubic BC_2N (Solozhenko, Andrault, Fiquet, Mezouar, & Rubie, 2001), and BCN (Solozhenko, 2002), boron-enriched diamond with the approximate composition BC_5 (Solozhenko, Kurakevych, Andrault, Le Godec, & Mezouar, 2009), and the novel partially ionic phase of elemental boron, γ-B_{28} (Oganov, Chen, Gatti, et al., 2009; Solozhenko, Kurakevych, & Oganov, 2008). All the listed materials can be decompressed to ambient conditions as metastable phases, but this is hardly a limitation to their performance. Much more critical is the fact that to be practically useful, the material should be synthesizable at pressures not higher than approximately 10 GPa, because at higher pressures synthesis can be done only in tiny volumes (except in shock-wave synthesis, which may be a viable route for useful materials at ultrahigh pressures). High-pressure studies of materials are often tricky, and the field of high-pressure research is full of both exciting discoveries and misdiscoveries. For instance, it has been claimed by Dubrovinsky et al. (2001) that TiO_2–cotunnite, quenched from high pressure, is the hardest known oxide with a Vickers hardness of 38 GPa. While it is hard to experimentally appraise such results obtained on tiny samples, theoretical models can help one to distinguish facts from artifacts: as we show below, the "experimental" result of Dubrovinsky et al. (2001) is clearly an artifact. Such theoretical models can also greatly speed up the discovery of new superhard materials.

To illustrate the concepts involved, let us consider in more detail the most recent model due to Li et al. (2008). This model computes the hardness from the electronegativities and covalent radii of the atoms. The central formula for the Knoop hardness is

$$H = \frac{423.8}{V} n \left[\prod_{k=1}^{n} N_k X_k e^{-2.7 f_k} \right]^{1/n} - 3.4 \ \ (\text{in GPa}). \tag{4}$$

Here V is the volume of the unit cell and N_k is the number of bonds of type k in the unit cell, n is the number of different bond types in the unit cell, X_k and f_k are the bond strength (referred to by Li et al. as the electron holding energy) and degree of ionicity, respectively, which are obtained as

$$X_k = \sqrt{\frac{\chi_i^k \chi_j^k}{\mathrm{CN}_i^k \mathrm{CN}_j^k}} \qquad f_k = \frac{\left|\chi_i^k - \chi_j^k\right|}{4\sqrt{\chi_i^k \chi_j^k}}, \tag{5}$$

---

[1] For graphite, it is also important to take into account its anisotropy and the fact that the structure deforms by breaking not the strong intralayer bonds, but the weak van der Waals bonds between the layers. The discussions here are concerned only with the orientationally averaged hardness (for an anisotropic model see Simunek (2009)).

using atomic electronegativities χ_i and coordination numbers CN_i. In this model, electronegativities are defined as $\chi_i = 0.481 n_i/R_i$, where n_i and R_i are the number of valence electrons and univalent covalent radius of this atom, respectively.

Coefficients 423.8, 2.7 and −3.4 were obtained in Li et al. (2008) by fitting to experimental data for hard materials. Small negative hardnesses (not lower than −3.4 GPa) can be obtained with Eqn (3) and serve as an indication of a very soft structure, a potential lubricant. For very hard materials, remarkably accurate results can be obtained. Note also the very similar structure of Eqn (2), which can also lead to negative values. Instead of assigning any special physical meaning to the constant term of −3 or −3.4 GPa, we are more inclined to treat it as the minimum meaningful resolution of Eqns (2) and (4), that is, discussing the predicted values with greater precision makes little sense.

Like most of the existing models of hardness, this model involves analytical formulas that give good results for simple high-symmetry isotropic structures, but its results for low-symmetry and/or anisotropic structures are much less satisfactory. This does not only limit the applicability of the method to simple and symmetric structures but also brings a general problem whenever one wants to perform any kind of global optimization (searching, e.g., for the hardest possible structure in a given compound), as the majority of structures produced during global optimization will be rather complex and low-symmetry, and an incorrect estimation of their hardness will thwart global search even when the global optimum is a simple and symmetric structure. For complex and low-symmetry structures, the concept of well-defined integer coordination number (used in the method of Li et al. (2008)) is often not adequate. Moreover, while taking into account the strength of bonds in the unit cell, this model does not consider structural topology, which is essential for hardness. There is a whole class of structures where the formulas from Li et al. (2008) that take into account only strong covalent bonds will give incorrect results: for instance, layered structures or molecular crystals. For instance, according to these formulas, graphite should be a superhard material. We have generalized the approach of Li et al. (2008) to overcome the difficulties described above (Lyakhov & Oganov, 2011). Our extended method recovers results of the original model (Li et al., 2008) for "good" structures and resolves pathological cases related to the distorted coordination and low-dimensional bond topologies. For graphite, the model of Li et al. (2008) gives a hardness $H = 57$ GPa, whereas our extended model gives $H = 0.17$ GPa, in agreement with our everyday experience that graphite is an ultrasoft solid and a lubricant. What are these improvements?

First, the choice of bonds to be included in Eqn (4) is essential. From Eqn (4) one can see that the hardness (as a geometric average) is strongly affected by the weakest included bonds. The case of graphite is very instructive. Using the standard coordination number (three) implicitly includes only the strong covalent bonds in Eqn (4) and gives an unrealistically high $H = 57$ GPa. Yet, the real hardness is determined by the weak van der Waal bonds between the layers of the structure. It is the breaking of these bonds that occurs during deformation and leads to the breakdown of the crystal. Therefore, by *hardness-defining* (or structure-forming) bonds we mean the strongest chemical bonds, augmented by a set of bonds necessary to maintain the three-dimensionality of the crystal structure. These are the bonds that need to be included in Eqn (4), and we discovered an automatic way to find them. Let us describe the crystal as a graph where atoms are vertices and *hardness-defining* bonds are edges. One of the main challenges for the algorithm is to determine edges knowing only the geometrical arrangement of atoms and their chemical identities. We do this by gradually adding to the graph those weak bond groups that decrease the number of its connected components. This allows one to include the shortest bonds between layers in a layered structure or between molecules in molecular crystals and at the same time neglect "fake" bonds between the atoms within the same layer or molecule. The complete connectivity of the graph is a sufficient but not necessary condition for determining whether all *hardness-defining* bonds are taken into account. There is one important general case where a disconnected graph will still represent a 3D-bonded structure. A simple illustration of this phenomenon is a 3D chess board, in which all white and black cubes build their own connected subgraphs, and those subgraphs are not connected with each other—a hypothetical structure of this kind is shown in **Figure 1**. Another representative of such exotic structures is the well-known structure of mineral cuprite (Cu_2O). Such nonconnected but intersecting graphs can be detected using multicolor graph theory.

Second, we replace coordination numbers in Eqn (5) by better-behaved quantities—being discreet and in many cases ill-defined, coordination number brings certain problems both for the calculation of hardness and for its global optimization. Furthermore, in cases of irregular coordination, where different bonds within the same coordination polyhedron have dramatically different strengths, the use of a single coordination number is undesirable.

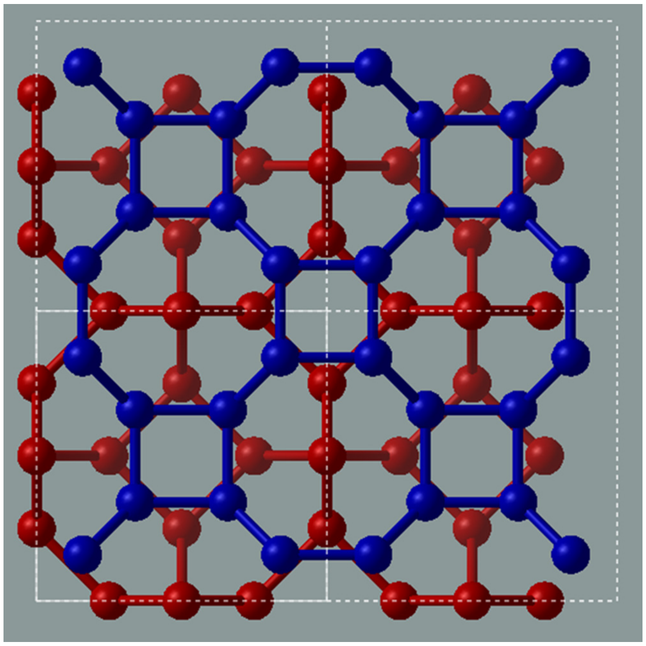

Figure 1 Example of a structure, consisting of two nonintersecting but interpenetrating 3D graphs (one graph is shown in blue, the other in red).

In our definition, it is a continuous function of structure and can take noninteger values (unlike classical coordination numbers), which is very useful for global optimization. Now we can substitute these generalized formulas into the original formulas (Li et al., 2008) for hardness. The "effective coordination number" describing the atomic valence involved in each bond is defined as $\mathrm{CN}_i^k = v_i/s_i^k$, where v_i is the valence of atom i (in general not equal to the number of valence electrons) and s_i^k is a bond valence that can be calculated using the model of Brown (1992):

$$s_i^k = \frac{v_i \exp(-\Delta_k/0.37)}{\sum\limits_{k'} \exp(-\Delta_{k'}/0.37)},$$

here the sum goes over all bonds k' where atom i participates. This definition satisfies the sum rule (Brown, 1992) $\sum\limits_{k'} s_i^{k'} = v_i$. To take into account the dependence of the electronegativity on the environment and deviations of actual bond lengths R_k from the sum of covalent radii, we correct the electronegativities of atoms i and j participating in bond k

$$\chi_i^k = 0.481\frac{n_i}{R_i + \Delta_k/2} \qquad \chi_j^k = 0.481\frac{n_j}{R_j + \Delta_k/2} \tag{6}$$

by equally distributing $\Delta_k = R_k - R_i - R_j$ between the bonded atoms. This introduces explicit dependence of the electronegativities and hardness on bond lengths.

With these extensions, the model of Li et al. (2008) shows an excellent performance without the need for changing the final formulas or refitting the coefficients, as illustrated in **Table 1**. We note that similar extensions can be easily done for other models of hardness.

It is believed that such models are valid only for ionic–covalent crystals with two-center bonding, which is the most important case. Most researchers state that such models cannot be applied to metals and boron-rich solids. Both limitations are essentially linked to delocalized bonding—election gas in the case of metals and multicenter bonding in the case of boron-rich solids. Multicenter bonding is, in principle, much more general and upon further thinking, one should be surprised that such hardness models work well for other compounds with some contribution of multicenter bonding, but are believed not to be applicable to boron-rich solids, where

Table 1 Hardness of different materials (in gigapascals)

Material	*Model* (*Li et al., 2008*)	*Model* (*Lyakhov & Oganov, 2011*)	*Experiment*
Diamond	91.2	89.7	90 (Brookes & Brookes, 1991)
Graphite	57.4	0.17	0.14 (Patterson, Cartledge, Vohra, Akella, & Weir, 2000)
Rutile, TiO_2	12.9	14.0	8–11 (Li & Bradt, 1990)
TiO_2 cotunnite	16.6	15.3	38 (controversial) (Dubrovinsky et al., 2001)
β-Si_3N_4	23.4	26.8	21 (Sung & Sung, 1996)
Stishovite, SiO_2	31.8	33.8	33 (Leger et al., 1996)

From Lyakhov and Oganov (2011).

multicenter bonding is essential. We have conducted tests of this model of hardness on three boron allotropes, α-B_{12}, β-B_{106}, and γ-B_{28}. The hardnesses we obtained are 39.9, 37.9, and 42.5 GPa, respectively—while the experimental values, characterized by large uncertainties, are 42, 45, and 50 GPa, respectively. Given the large experimental uncertainties (of order of approximately 10 GPa), one can accept such estimates as very reasonable. We note that Gao, Hou, and He (2004) have devised a special approach for compounds with three-center bonding, but it relies on specifications of which interactions are two-center, and which are three-center in nature, and having a unified approach applicable both to two-center and three-center bonding situations would be more satisfactory.

The limitation for metals is easy to understand: the election gas has a zero shear modulus and therefore a zero hardness. When computing the hardness of the crystal, the number of delocalized electrons of the electron gas has to be subtracted from the total number of valence electrons (as suggested by Gou, Hou, Zhang, and Gao (2008)). While this suggests that the same equations are still valid, here we have a clear limitation on the predictive power of the method, because it is not a priori clear as to how many electrons should be counted as electron gas. It is possible that determining the effective number of electrons in the free-election gas across many metals, by fitting to their observed hardnesses, could show interesting chemical regularities.

3.04.3 Global Optimization and its Application for the Discovery of Superhard Materials

Being able to compute the hardness (at least for insulators and semiconductors) just from the crystal structure opens up the possibility of global optimization of hardness, aimed at the computational discovery of new superhard materials. For the first time, such a possibility was demonstrated by Oganov and Lyakhov (2010). Here, we elaborate on this possibility in greater detail. Note that the successful global optimization of the hardness is a proof of principle for the global optimization of many other physical properties, and as such opens a new chapter in computational materials design.

The global optimization method that we are using is the evolutionary crystal structure prediction methodology USPEX (Glass, Oganov, & Hansen, 2006; Lyakhov, Oganov, & Valle, 2010; Oganov & Glass, 2006). For a review of this methodology, see Oganov, Ma, Lyakhov, Valle, and Gatti (2010), Oganov, Lyakhov, Valle (2011). In the standard implementation, one is looking for the global minimum of the free energy, that is, the thermodynamically stable structure at given pressure–temperature conditions. This method has been successfully tested on systems containing up to several hundred atoms in the unit cell—**Figure 2** shows how within just a few generations of the evolutionary search one finds the correct ground state for the Lennard-Jones system with 256 atoms in the unit cell. In the most recent version of this method (Lyakhov et al., 2010), we introduced local measures of the quality of structure, such as the local order parameter—**Figure 3** shows how with the local order parameter one can easily locate defective regions in the crystal. Such (automated) knowledge turns out to greatly speed up the search for the global minimum. Other tricks that we have found to be powerful include fingerprint niching, soft-mode mutation, symmetry- and pseudosymmetry-enabled generation of structures (Lyakhov et al., 2010).

Figure 4 shows another successful challenging test—prediction of the structure of $MgSiO_3$ post-perovskite with 80 atoms per cell. This prediction was already achieved with the old version of the method (Glass et al., 2006; Oganov & Glass, 2006) that did not include the above-mentioned powerful developments.

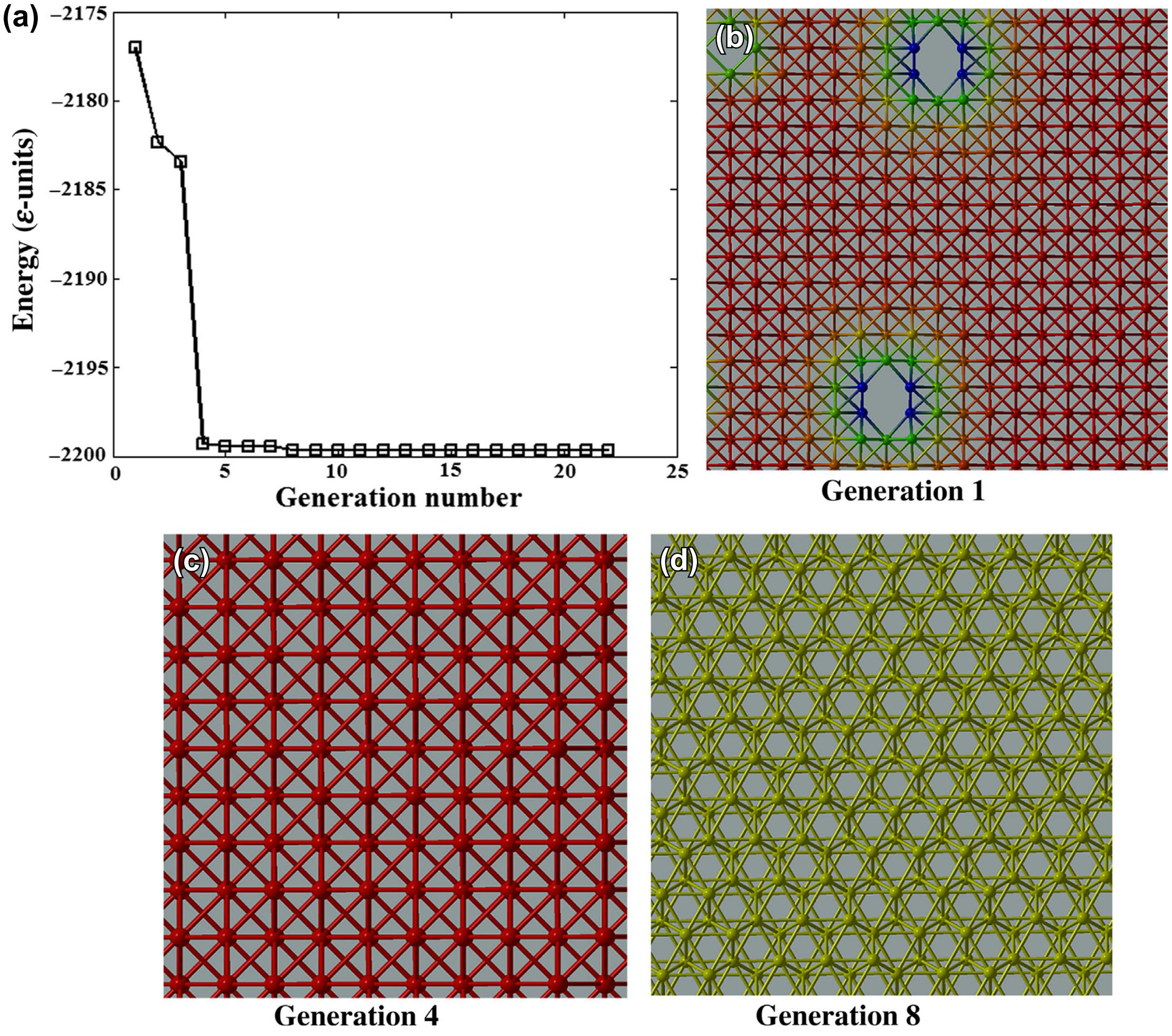

Figure 2 Example of global energy minimization: 256-atom Lennard-Jones system. (a) Evolution of the lowest energy as a function of generation (each generation consists of 30–38 structure relaxations), (b–d) lowest-energy structures found in (a) first generation (defective face centered cubic (fcc) structure), (b) fourth generation (ideal fcc structure), (c) eighth generation (ideal hexagonal close packed (hcp) structure—the ground state of this system). In (b–d) the atoms are colored according to their local order parameter (Lyakhov et al., 2010). The potential is of the Lennard-Jones form for each atomic ij pair: $U = \varepsilon\left[\left(\frac{R_{\min}}{R}\right)^{12} - 2\left(\frac{R_{\min}}{R}\right)^{6}\right]$, where $R_{\min}$ is the distance at which the potential reaches a minimum, and ε is the depth of the minimum.

The USPEX method has been extended to the case of variable chemical composition—where one does not start with a known chemical composition and fixed number of atoms in the unit cell, but searches for all stable compositions (and the corresponding crystal structures) in the system defined by a range of chemical compositions and system sizes. Such an extension involves very little programming and was trivially achieved (Oganov et al., 2010; Wang & Oganov, 2008) on the basis of our original USPEX implementation. Figure 4 shows an example of such simulations, where a number of stable states have been mapped. Note that the system used for this illustration, the binary Lennard-Jones mixture, possesses extremely complex ground states, and a successful finding of these ground states is indeed a very impressive success of the method.

One can ask whether, instead of the (free) energy, one could use a physical property, such as the hardness, as the objective function for global optimization. The answer is indeed positive, as we will show in the two tests below and in the applications in the next section.

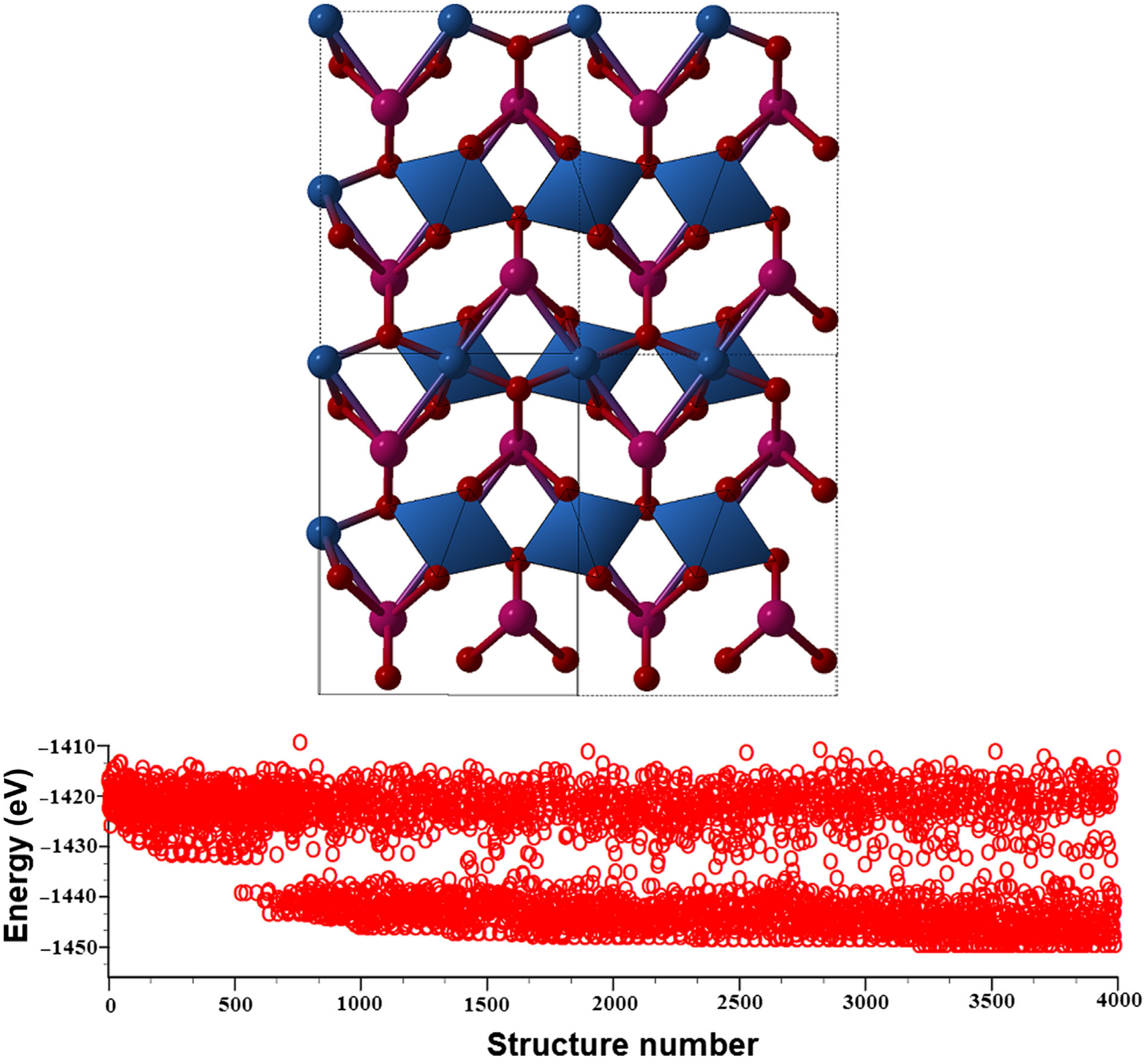

Figure 3 Example of global energy minimization: 80-atom cell of $MgSiO_3$. The correct post-perovskite structure, successfully found in this run, and evolution of structural energies along the run are shown. From Oganov and Glass (2008).

As the first test, let us consider the search for the hardest phase of SiO_2 (Oganov & Lyakhov, 2010). This test was done with a simple Buckingham-type pairwise interatomic potential—such calculations are not only extremely fast (a couple of hours on a single-core personal computer), but turn out to yield remarkably meaningful and accurate results; the hardest structures were then re-relaxed using *ab initio* calculations. **Figure 5** shows the evolutionary optimization of the hardness of SiO_2 and how harder and harder structures are found as the run progresses. Four hardest structures, with almost identical hardnesses, have been found (**Figure 6**)—(1–2) two well-known phases stishovite (rutile-type structure, $H = 28.9$ GPa) and seifertite (α-PbO_2-type structure, $H = 29.6$ GPa), (3) a 3 × 3 kinked-chain structure, intermediate between stishovite and seifertite ($H = 29.3$ GPa), and (4) a cuprite-type phase with $H = 29.5$ GPa (cuprite-type SiO_2 is not experimentally unknown, but cuprite-type ice X is the densest known phase of ice (Hemley et al., 1987)—and ice phases have strong structural similarities with tetrahedral silica polymorphs). If, instead of the ab initio structure of stishovite, one uses the experimental one, the hardness of 33.8 GPa will result, in excellent agreement with the experimental value of 33 GPa (Leger et al., 1996).

One of the holy grails in the field of superhard materials has been to find a material harder than diamond, and one of the main proposed candidates was C_3N_4, some hypothetical structures of which have

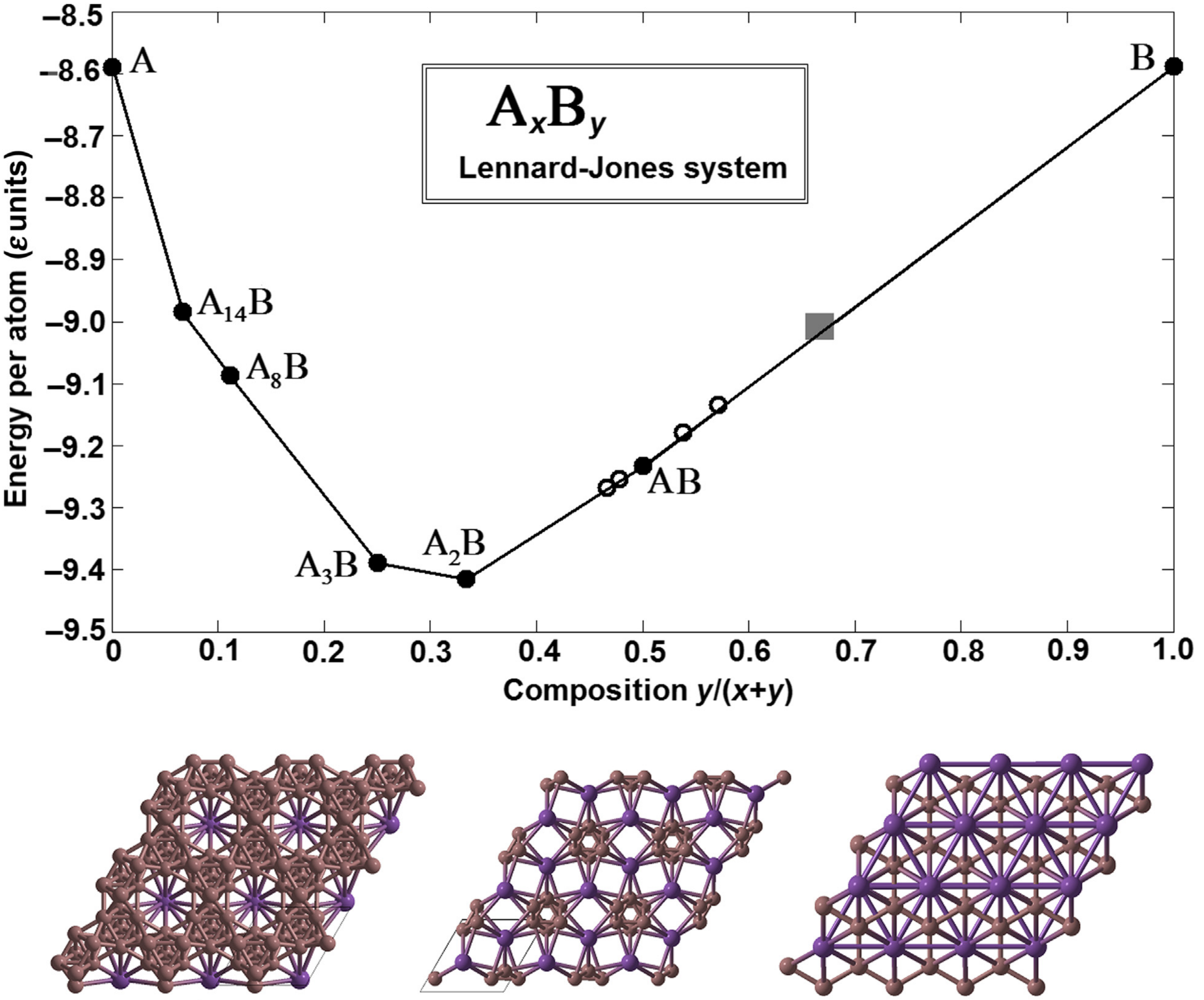

$A_{14}B$ $P\bar{3}m1$

A_3B $P\frac{6_3}{m}mc$

A_2B (AlB_2-type) $P\frac{6}{m}mm$

Figure 4 Variable-composition USPEX simulation of the A_xB_y binary Lennard-Jones system. In the upper panel: filled circles—stable compositions, open circles—marginally unstable compositions (A_8B_7, $A_{12}B_{11}$, A_6B_7, and A_3B_4). While the ground state of the one-component Lennard-Jones crystal has a hexagonal close packed (hcp) structure, ground states of the binary Lennard-Jones system are rather complex (e.g., $A_{14}B$) and the A_2B structure is of the well-known AlB_2 type. The potential for each atomic *ij* pair is $U_{ij} = \varepsilon_{ij}\left[\left(\frac{R_{\min,ij}}{R}\right)^{12} - 2\left(\frac{R_{\min,ij}}{R}\right)^{6}\right]$, where $R_{\min,ij}$ is the distance at which the potential reaches a minimum, and ε is the depth of the minimum. In these simulations, we use additive atomic dimensions: $R_{\min,BB} = 1.5R_{\min,AB} = 2R_{\min,AA}$ and nonadditive energies (to favor compound formation): $\varepsilon_{AB} = 1.25\varepsilon_{AA} = 1.25\varepsilon_{BB}$. From Oganov et al. (2010).

been shown to be somewhat less compressible than diamond (Liu & Cohen, 1989; Teter & Hemley, 1996). We have performed a search for the hardest phase in the binary C–N system (**Figure 7**). Diamond came out as the hardest phase, but it is also quite clear that it is much easier to create a superhard phase in pure carbon than in any carbon–nitrogen compound. One can see from **Figure 7** how the hardness increases and compositions zoom in on to the carbon-rich side as the grant proceeds. If we look at the hardest C–N compounds, even there we find blocks of the diamond structure, and hardness much inferior (78.1 GPa) to pure diamond (89.7 GPa). These results suggest that the addition of nitrogen to carbon is unlikely to produce a phase harder than diamond.

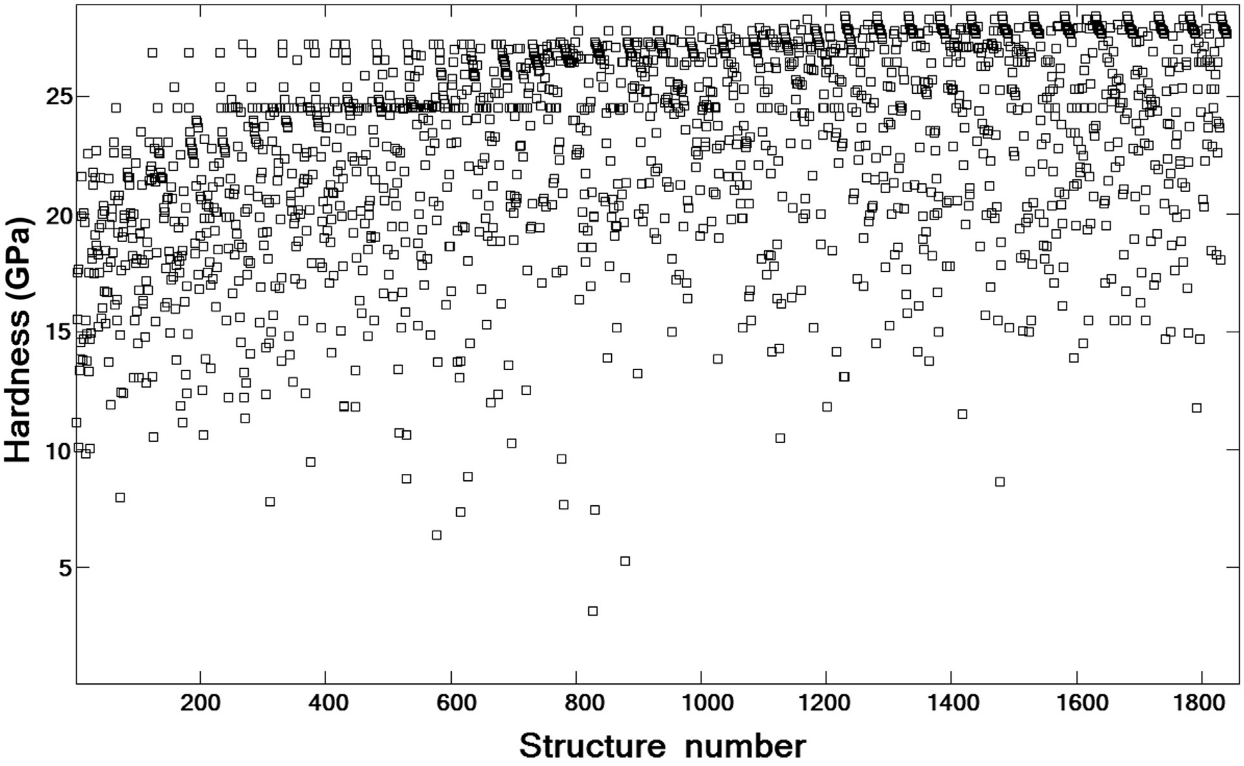

Figure 5 Evolution of the theoretical hardness in an evolutionary global optimization run for SiO_2 with 24 atoms in the unit cell. From Oganov and Lyakhov (2010).

3.04.4 Some Applications

3.04.4.1 Carbon Allotropes with Special Properties

Diamond is not only the hardest known material but it also has the highest number density of all known materials (Brazhkin, 2009). Although diamond is the densest known carbon allotrope at a wide range of pressures, theoretical studies proposed bc8 or *R*8 to be denser and perhaps the densest possible phases of carbon (Clark, Ackland, & Crain, 1995; Fahy & Louie, 1987; Kasper & Richards, 1964). Whether there are even denser allotropes is unknown. Performing global optimization using the USPEX method with respect to density of all possible carbon allotropes, we found (Zhu, Oganov, Salvado, Pertierra, & Lyakhov, 2011) three novel allotropes of carbon, which are denser than diamond or any previously proposed structures and possess remarkable physical properties.

To search for the densest structures, evolutionary structure prediction was performed using the USPEX code (Glass et al., 2006; Lyakhov et al., 2010; Oganov & Glass, 2006) in conjunction with ab initio structure relaxations using density functional theory (DFT) within the Perdew–Burke–Ernzerhof generalized gradient approximation (GGA) (Perdew, Burke, & Ernzerhof, 1996), as implemented in the VASP code (Kresse & Furthmüller, 1996). This level of theory provides an excellent description of the density of the tetrahedral phases of carbon—the computed densities are 3.504 g cm^{-3} for diamond (3.50–3.53 g cm^{-3} from experiment).

Our global optimizations produced the already known structures of diamond, hexagonal diamond (lonsdaleite), and the bc8 structure, but the highest density was indicated for the two hitherto unknown structures, which are *t*I12 (with the *I*-42d symmetry and 12 atoms in the unit cell), and *h*P3 (with the $P6_222$ symmetry and 3 atoms in the unit cell). The two structures have nearly the same density, which is 3.2% denser than diamond at 1 atm and 2.2% denser than bc8. We have found yet another superdense structure, isotypic with the newly discovered allotrope of germanium (*t*P12) (Schwarz et al., 2008; Wosylus, Prots, Schnelle, Hanfland, & Schwarz, 2008). All these three allotropes have carbon atoms in the tetrahedral coordination (sp^3 hybridization). Interestingly, the structure motif of the *h*P3 phase has a binary counterpart in the β-quartz

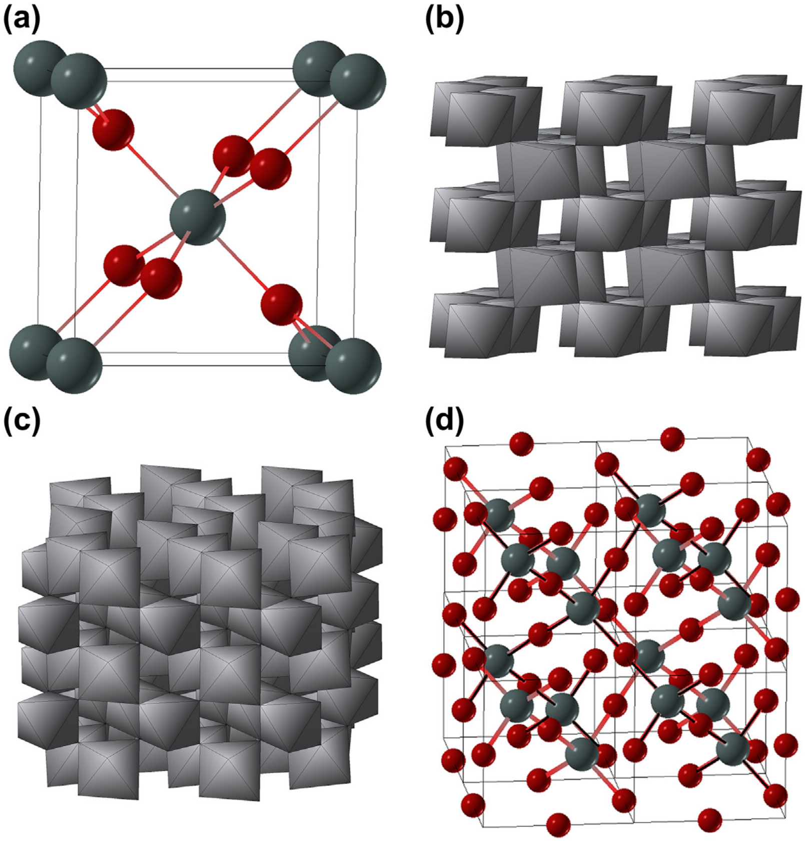

Figure 6 Structures of (a) stishovite, (b) seifertite, (c) 3 × 3 phase, and (d) cuprite-type modifications of SiO_2. The cuprite structure has two interpenetrating cristobalite-type (or diamond-like) structures (it is a "3D-catenane", as P.M. Zorkii christened it by analogy with interlocked catenane molecules)—not surprisingly, this structure is almost twice (1.88 times) as dense as high cristobalite (it is also 1.45 times denser than quartz, and 1.14 times less dense than stishovite). Our computed bulk modulus of SiO_2 cuprite is 276 GPa, its pressure derivative $K_0' = 6.4$. This phase is 0.38 eV per atom less stable than quartz, and 0.2 eV per atom less stable than stishovite. From Oganov and Lyakhov (2010).

modification with silicon atoms occupying the carbon positions. *t*I12, another superdense polymorph, is related to high-pressure SiS_2 polymorph with both Si and S atomic positions occupied by C. The crystal structure of *t*P12 is also related to the silicon sublattice in the SiO_2 modification keatite. Note that while *t*I12 structure has a *I*-42d symmetry, *h*P3 ($P6_222$ symmetry) and *t*P12 (space group $P4_32_12$) allotropes are chiral, that is, will rotate the plane of polarization of light. All these three structures are higher (by 0.9–1.1 eV per atom) in energy than diamond, which can be viewed as a penalty against ultradense packing and bond strain induced by it. However, they are all dynamically stable (i.e., there are no imaginary phonon frequencies) and thus may exist at ambient conditions as metastable phases. Furthermore, some experimentally well-known allotropes have comparable energies (e.g., amorphous carbon is 0.70–0.99 eV per atom higher in energy than diamond). Interestingly, *h*P3-carbon is slightly less compressible than diamond. We have also investigated the intrinsic hardness of these three materials using the model of Gao et al. (2003). The predicted hardness for *h*P3 is 87.6 GPa, which is quite comparable to (but slightly lower than) that of diamond. Similarly, the theoretical hardnesses of *t*I12 and *t*P12 are 87.2 and 88.3 GPa respectively. The reason why the hardness of *h*P3, *t*I12, or *t*P12 is slightly lower than that of diamond is in the difference of bond strength. While both *h*P3 and *t*P12 have a greater bond density than diamond, these bonds are longer and weaker than in diamond, for example, the average C–C bond length in *h*P3 is 1.60 Å, significantly longer than 1.54 Å in diamond.

A systematic search (Lyakhov & Oganov, 2011) for the hardest possible carbon allotrope has found that diamond is the hardest one; however, a number of other allotropes have comparable hardnesses. The physical properties of some of the most interesting allotropes that we have found in our runs are summarized in Table 2.

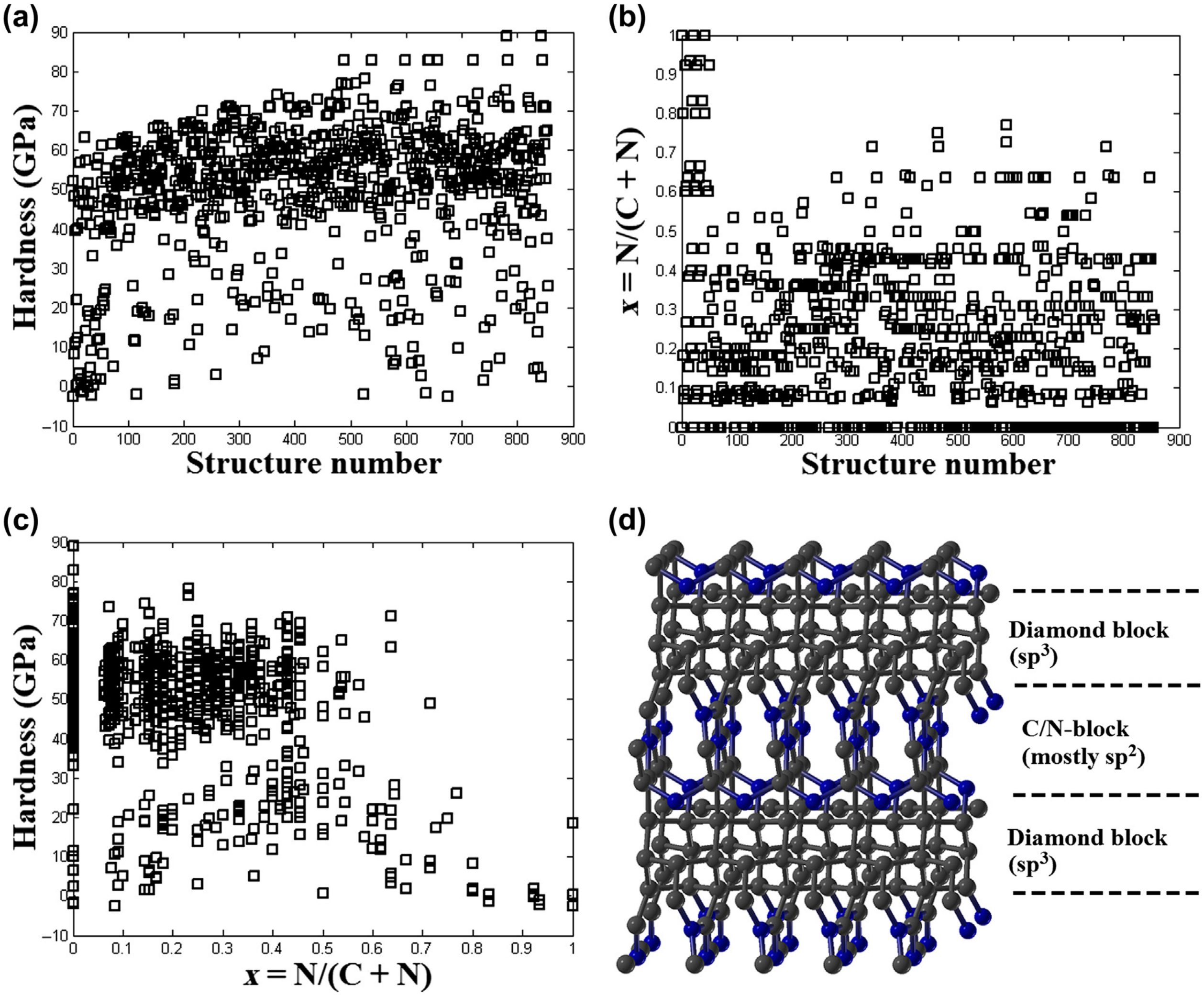

Figure 7 Variable-composition USPEX run for hardness optimization in the C–N system. One can see (a) how increasingly harder structures are discovered during the simulation, and (b,c) that pure carbon produces the hardest structures. The hardest material found in this simulation is diamond. Here we illustrate that (d) the hardest found hypothetical C–N compound $C_{10}N_3$ (theoretical hardness 78.1 GPa) is also made of diamond blocks alternating with C–N blocks.

Table 2 Properties of dense and hard carbon allotropes. Listed are the energy relative to diamond (ΔE), volume (V), bulk modulus (K_0), its pressure derivative K_0', hardness (H) computed using Gao's and Lyakhov-Li model, and band gap computed with the GGA/B3LYP/GW methods for the investigated structures. Experimental data are in parentheses.

Allotrope	*ΔE, eV per atom*	V, *Å³ per atom*	K_0, *GPa*	K_0'	H_{Gao}, *GPa (*Vickers*)*	H_{LL}, *GPa (*Knoop*)*	*Band gap, eV*
Diamond	0	5.70	431.1	3.74	94.3	89.7	4.2/5.6/5.4
	(0)	(5.68)	(446)		(96)	(90)	(5.5)
Lonsdaleite	0.024	5.71	437.3	3.63	93.2	89.1	3.6/4.8/5.0
M-carbon	0.159	5.97	392.7	3.88	89.8	84.3	3.6/4.8/5.0
bct4	0.196	6.01	411.4	3.50	91.1	84.0	2.7/3.9/3.8
$P6_522$	0.112	6.22	389.0	3.72	86.5	81.3	4.1/5.4/5.5
bc8	0.697	5.60	389.6	4.03	88.8	–	2.7/3.8/3.5
Cmcm-16	0.282	6.036	–	–	–	83.5	–
Cmcm-12	0.224	6.157	–	–	–	82.0	–
*h*P3	1.113	5.49	432.7	3.71	87.6	–	2.0/3.4/3.0
*tI*12	1.140	5.48	425.0	3.83	87.2	–	4.1/5.4/5.5
*t*P12	0.883	5.64	396.0	3.79	88.3	–	5.4/6.4/7.3

From Lyakhov and Oganov (2011) and Zhu et al. (2011).

Table 3 Crystal structures of dense and hard carbon allotropes

M-carbon. Space group *C2/m*. $a = 9.191$ Å, $b = 2.524$ Å, $c = 4.148$ Å, $\beta = 97.03^\circ$

	x	*y*	*z*
C1(4i)	0.9427	0.0000	0.6205
C2(4i)	0.4418	0.0000	0.8464
C3(4i)	0.7857	0.0000	0.4408
C4(4i)	0.2713	0.0000	0.9147

bct4-carbon. Space group *I4/mmm*. $a = b = 4.371$ Å, $c = 2.509$ Å

	x	*y*	*z*
C(16n)	0.9427	0.0000	0.6205

***Cmcm*-16 structure. Space group *Cmcm*. $a = 4.327$ Å, $b = 8.753$ Å, $c = 2.550$ Å**

	x	*y*	*z*
C1(8g)	0.8179	0.9509	0.2500
C2(8g)	0.8162	0.7089	0.7500

***Cmcm*-12 structure. Space group *Cmcm*. $a = 3.781$ Å, $b = 7.772$ Å, $c = 2.514$ Å**

	x	*y*	*z*
C1(8g)	0.7045	0.8050	0.2500
C2(4c)	0.0000	0.9445	0.2500

$P6_522$ structure. Space group $P6_522$. $a = b = 3.571$ Å, $c = 3.370$ Å

	x	*y*	*z*
C(6b)	0.7676	0.2324	0.0833

***h*P3 structure. Space group $P6_222$. $a = b = 2.605$ Å, $c = 2.801$ Å**

	x	*y*	*z*
C(3c)	0.500	0.000	0.000

***t*I12 structure. Space group *I*-42d. $a = b = 2.705$ Å, $c = 8.989$ Å**

	x	*y*	*z*
C1(4a)	0.000	0.000	0.000
C2(8d)	0.833	0.250	0.625

***t*P12 structure. Space group $P4_32_12$. $a = b = 3.790$ Å, $c = 4.6611$ Å**

	x	*y*	*z*
C1(4a)	0.0756	0.0756	0.0000
C2(8b)	0.1668	0.3793	0.2171

From Lyakhov and Oganov (2011) and Zhu et al. (2011).

One can see that two models of hardness that we have used, the model of Gao et al. (2003) and modified Li's model (Lyakhov & Oganov, 2011) give highly consistent results. It is also clear from Table 2 that different allotropes, even within the class of superhard phases with sp^3 hybridization, have widely different electronic properties. Table 2 gives band gaps computed (1) using DFT (at the GGA level), which are known to be significantly below the actual values of the band gap, and more accurate band gaps computed using the (2) B3LYP (Becke, 1993) hybrid functional and (3) the GW approximation. One can see that the latter two approaches give overall consistent results that match available experimental data (e.g., the experimental band gap of 5.5 eV for diamond). The possibility to engineer the band gap for novel superhard carbon allotropes is indeed very exciting—the computed GW band gaps of the allotropes presented in Table 2 range from 3.0 to 7.3 eV! Crystal structures of the reported allotropes are presented in Table 3 (some of these are shown in Figure 8). To summarize our findings, there are hypothetical carbon allotropes that are substantially denser than diamond, but no carbon allotrope (even hypothetically) can be harder than diamond.

3.04.4.2 Discovery of γ-B_{28}: A New Superhard Allotrope of Boron

Boron is an element with very complex chemical bonding, involving icosahedral B_{12} clusters with metallic-like 3-center bonds within the icosahedra and covalent 2-center and 3-center bonds between the icosahedra. Such bonding produces a delicate insulating state, susceptible to impurities and the changes of pressure and temperature. At least 16 crystalline allotropes have been reported (Douglas & Ho, 2006), among which

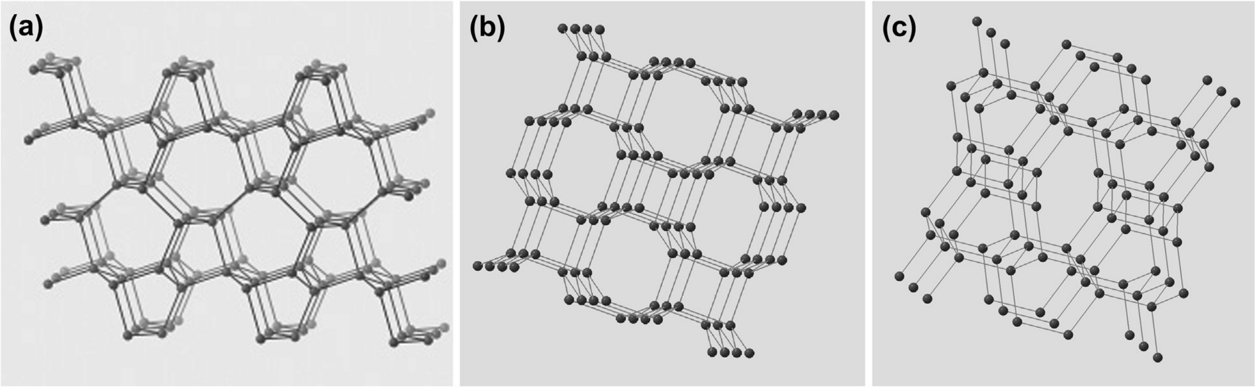

Figure 8 Predicted superhard carbon allotropes. (a) M-carbon, (b) bct4-carbon, and (c) *Cmcm*-16 structure. From Lyakhov and Oganov (2011).

probably only three correspond to the pure element (Amberger & Ploog, 1971; Douglas & Ho, 2006): rhombohedral α-B_{12} and β-B_{106} phases (with 12 and 106 atoms in the unit cell, respectively) and tetragonal T-192 (with 190–192 atoms per cell). Their crystal structures, together with the structure of the newly discovered fourth pure phase, γ-B_{28} (Oganov, Chen, et al., 2009), are shown in **Figure 9**. Until 2007, it was the only light element, for which the ground state was not known even at ambient conditions. None of the polymorphs reported before 1957 actually correspond to pure boron. Largely due to its complicated chemistry, experimental studies of boron proved to be highly nontrivial, often leading to erroneous results even with modern methods (see the comment of Oganov, Solozhenko, et al., 2009), and the history of studies of boron has many examples of this (Oganov & Solozhenko, 2009). **Figure 10** shows the first phase diagram obtained in 2007 (Oganov, Chen, et al., 2009).

This phase diagram shows that the stability field of the newly discovered γ-B_{28} is greater than the fields of the three previously known phases (α-, β-, and T-192) combined; the predicted high-pressure superconducting α-Ga-type phase still needs to be experimentally confirmed. **Table 4** gives the predicted (at the DFT–GGA level of theory) structural parameters of γ-B_{28} and two other stable boron phases with relatively simple structures. An excellent agreement with available experimental data can be seen.

Figure 11 shows the results of ab initio calculations of relative stability of different phases of boron. As expected, the impurity-stabilized T-50 phase is energetically unfavorable, while the α-B_{12}, β-B_{106}, T-192, and γ-B_{28} phases are competitive and energetically nearly degenerate at low pressures (this explains why it has been so difficult to experimentally determine which phase is the most stable one at 1 atm). According to these calculations, γ-B_{28} is energetically more favorable than any known or hypothetical phase of boron at pressures between 19 and 89 GPa.

The γ-B_{28} structure is quite unique: centers of the B_{12} icosahedra (formed by sites B2–B5—**Table 4**) form a slightly distorted cubic close packing (as in α-B_{12}), in which all octahedral voids are occupied by B_2 pairs (formed by site B1). It can be represented as an NaCl-type structure, the roles of "anion" and "cation" being played by the B_{12} icosahedra and B_2 pairs, respectively (**Figure 9(d)**). γ-B_{28} is structurally similar to α-B_{12}, but is denser due to the presence of interstitial B_2 pairs. The average intraicosahedral bond length is 1.80 Å and the B–B bond length within the B_2 pairs is 1.73 Å.

γ-B_{28} is the densest, and the hardest, of all known boron phases (all of which are superhard). The best estimates of the hardness of β-B_{106} and α-B_{12} are 45 GPa (Gabunia et al., 2004) and 42 GPa (Amberger & Stumpf, 1981), respectively. For γ-B_{28}, the measured Vickers hardness is 50 GPa (Solozhenko et al., 2008), which puts it among half a dozen hardest materials known to date. This value of hardness is consistent with that of theoretical models (49.0 GPa from Eqn (3) using theoretical values of $K = 224$ GPa and $G = 236$ GPa (Jiang, Lin, Zhang, & Zhao, 2009), or 48.8 GPa from the thermodynamic model of hardness (Mukhanov et al., 2008), but much less consistent with the likely incorrect value (58 GPa) obtained by Zarechnaya et al. (2009).

Detailed investigations showed that the B_{12} and B_2 clusters have very different electronic properties and there is charge transfer of approximately 0.5e from B_2 to B_{12} (Oganov, Chen, et al., 2009), and this is correlated with

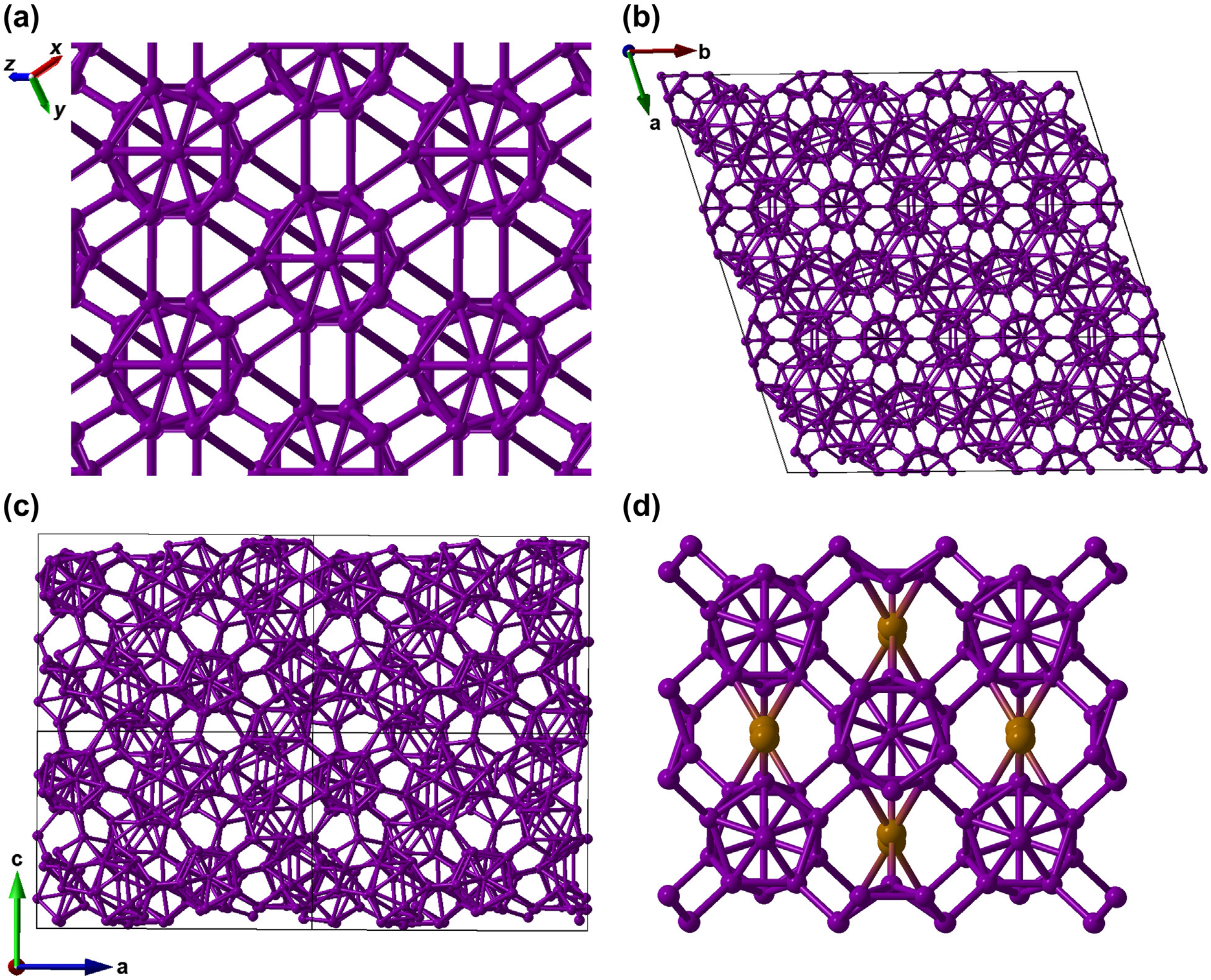

Figure 9 Crystal structures of boron allotropes. (a) α-B_{12}, (b) β-B_{106}, (c) T-192, and (d) γ-B_{28}. From Oganov, Chen, et al. (2009), Oganov and Solozhenko (2009).

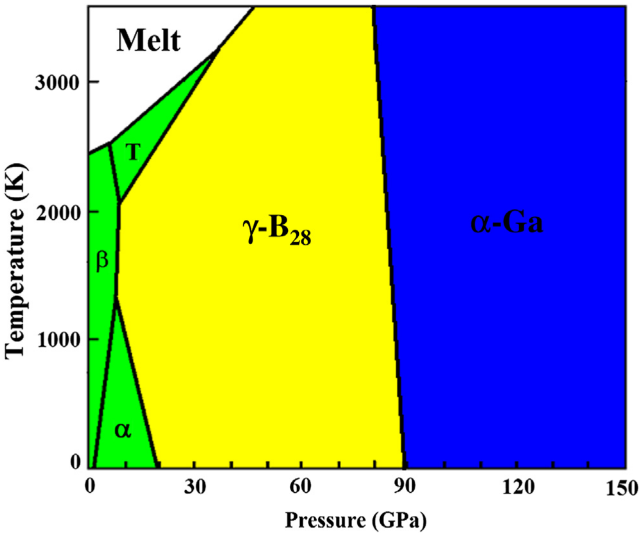

Figure 10 Phase diagram of boron. Reproduced from Oganov, Chen, et al. (2009).

Table 4 Structures of stable boron phases (optimized at 1 atm), with Bader charges (*Q*)

Wyckoff position	x	y	z	*Q*, |*e*|
γ-B_{28}. Space group *Pnnm*.$a = 5.043\ (5.054)$ Å, $b = 5.612\ (5.620)$ Å, $c = 6.921\ (6.987)$ Å.				
B1 (4g)	0.1702	0.5206	0	+0.2418
B2 (8h)	0.1606	0.2810	0.3743	−0.1680
B3 (8h)	0.3472	0.0924	0.2093	+0.0029
B4 (4g)	0.3520	0.2711	0	+0.0636
B5 (4g)	0.1644	0.0080	0	+0.0255
α-B_{12}. Space group $R\bar{3}m$.$a = b = c = 5.051\ (5.064)$ Å, $\alpha = \beta = \gamma = 58.04\ (58.10)^\circ$.				
B1 (18h)	0.0103 (0.0102)	0.0103 (0.0102)	0.6540 (0.6536)	+0.0565
B2 (18h)	0.2211 (0.2212)	0.2211 (0.2212)	0.6305 (0.6306)	−0.0565
α-Ga structure. Space group *Cmca*.$a = 2.939$ Å, $b = 5.330$ Å, $c = 3.260$ Å.				
B1 (8f)	0	0.1558	0.0899	0

From Oganov, Chen, et al. (2009).

the strong infrared absorption and high dynamical charges on atoms. γ-B_{28} is structurally related to several well-known compounds—for instance, $B_{12}P_2$ or $B_{13}C_2$, where the two sublattices are occupied by different chemical species (instead of interstitial B_2 pairs there are P atoms or C–B–C groups, respectively). This fact again highlights the chemical difference between the two constituent clusters. This also gives one the right to call γ-B_{28} a "boron boride" $(B_2)^{\delta+}(B_{12})^{\delta-}$ with partial charge transfer δ.

Additional insight is provided by detailed analysis of the electronic density of states (**Figure 12**). Again, it is clear that the lowest-energy valence electrons are concentrated around the B_{12} icosahedra, while highest occupied molecular orbital and lowest unoccupied molecular orbital levels are B_2 dominated.

After the structure of γ-B_{28} was discovered, Le Godec, Kurakevych, Munsch, Garbarino, and Solozhenko (2009) determined the equation of state of this phase and found it to be in excellent agreement with theoretical calculations (Oganov, Chen, et al., 2009). The crystal structure was subsequently experimentally verified by Zarechnaya et al. (2008, 2009). Concerning the latter papers, their main achievement was the synthesis of micron-sized single crystals and single-crystal confirmation of the structure, but unfortunately conditions of synthesis were suboptimal (e.g., the capsules reacted with boron sample), and their papers contained many errors (Oganov, Solozhenko, et al., 2009). For instance, their estimated density differences between boron

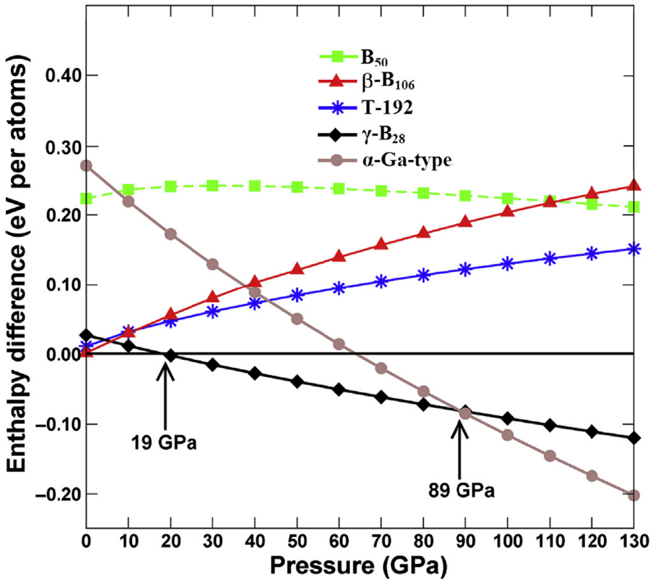

Figure 11 Stability of boron phases at 0 K. Enthalpies are shown relative to α-B_{12}. Phase transformations occur at 19 GPa (α-B_{12} to γ-B_{28}) and 89 GPa (γ-B_{28} to α-Ga-type). From Oganov, Chen, et al. (2009).

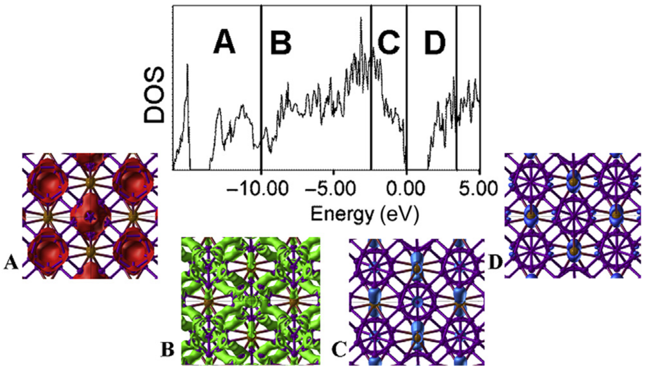

Figure 12 Electronic structure of γ-B_{28}. The total density of states is shown, together with the electron density corresponding to four different energy regions denoted by letters A, B, C, and D. Note that the lowest-energy electrons are preferentially localized around the B_{12} icosahedra, whereas the highest-energy electrons (including the bottom of the conduction band—"holes") are concentrated near the B_2 pairs. The fact that the lowest-energy electrons belong to the B_{12} clusters, and the highest-energy—to B_2 units, is consistent with the direction of charge transfer: $B_2 \rightarrow B_{12}$. From Oganov and Solozhenko (2009).

polymorphs were wrong by an order of magnitude (they claimed that γ-B_{28} is 1% denser than all other forms of boron, while it is actually 8.3% denser than β-B_{106}), which is possibly a result of incorrectly performed ab initio calculations in their papers. Their equation of state, measured to 30 GPa (Zarechnaya et al., 2009), shows large discrepancies with theory (Oganov, Chen, et al., 2009) and earlier more careful experiment (Le Godec et al., 2009; see **Figure 13**). We should also mention the work of Jiang et al. (2009), who computed the elastic constants (from which the bulk and shear moduli are 224 GPa and 236 GPa, respectively - while the experimental bulk modulus (Le Godec et al., 2009) is 238 GPa), the equation of state, and reported remarkably high ideal tensile strengths (65, 51, and 52 GPa along the three crystallographic axes).

We draw the attention of the reader to a recent detailed discussion (Oganov et al., 2011) of the results on the mechanical properties and chemical bonding of γ-B_{28} by Dubrovinsky, Mikhaylushkin, and their coauthors (Haussermann & Mikhaylushkin, 2010; Mondal et al., 2011; Zarechnaya et al., 2009). For instance,

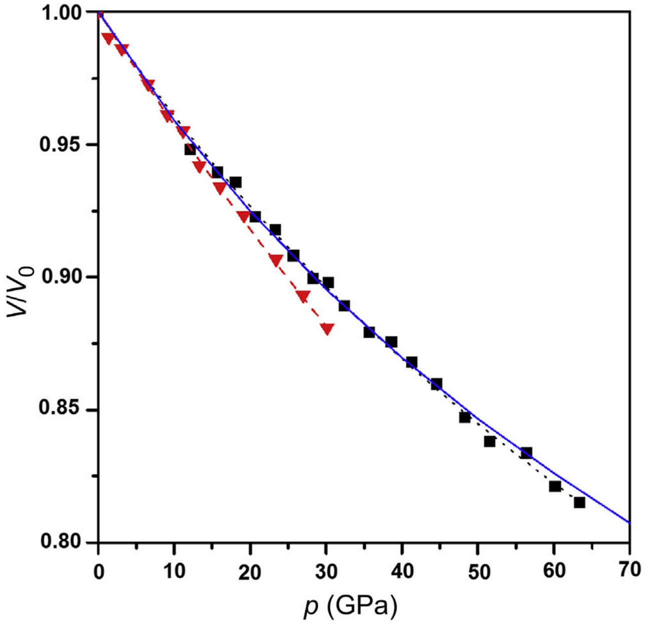

Figure 13 Equation of state of γ-B_{28}. *Red triangles* (and dashed line)—experiment (Zarechnaya et al., 2009), *black squares* (and dotted line)—more controlled experiment (Le Godec et al., 2009), *solid line*—ab initio results (Oganov, Chen, et al., 2009). Figure courtesy V.L. Solozhenko and O.O. Kurakevych, from Oganov, Solozhenko, et al. (2009).

Table 5 Interatomic distances in γ-B_{28}. Lengths of 2c–2e bonds, differing significantly between Haussermann and Milhaylushkin (2010), Oganov, Chen, et al. (2009), and Zarechnaya et al. (2009) are shown in bold font

	Haussermann and Milhaylushkin (2010)			*Zarechnaya et al. (2009)*			*Oganov, Chen, et al. (2009)*		
	Skeletal	*2c–2e*	*3c–2e*	*Skeletal*	*2c–2e*	*3c–2e*	*Skeletal*	*2c–2e*	*3c–2e*
B1		B4 × 1 **1.606**	B2 × 2 1.983		B4 × 1 **1.668**	B2 × 2 1.927		B4 × 1 **1.674**	B2 × 2 1.903
		B1 × 1 **1.659**	B3 × 2 2.101		B1 × 1 **1.721**	B3 × 2 2.089		B1 × 1 **1.732**	B3 × 2 2.054
B2	B2 × 1 1.765		B3 × 1 1.826	B2 × 1 1.765		B3 × 1 1.826	B2 × 1 1.740		B3 × 1 1.819
	B5 × 1 1.814		B1 × 1 1.983	B5 × 1 1.786		B1 × 1 1.927	B5 × 1 1.777		B1 × 1 1.903
	B4 × 1 1.821			B4 × 1 1.814			B4 × 1 1.807		
	B3 × 1 1.831			B3 × 1 1.831			B3 × 1 1.827		
	B3 × 1 1.849			B3 × 1 1.849			B3 × 1 1.841		
B3	B5 × 1 1.758		B2 × 1 1.826	B5 × 1 1.786		B2 × 1 1.826	B5 × 1 1.781		B2 × 1.819
	B4 × 1 1.784		B1 × 1 2.101	B4 × 1 1.762		B1 × 1 2.098	B4 × 1 1.762		B1 × 1 2.054
	B2 × 1 1.831			B2 × 1 1.831			B2 × 1 1.827		
	B2 × 1 1.849			B2 × 1 1.849			B2 × 1 1.841		
	B3 × 1 1.881			B3 × 1 1.881			B3 × 1 1.858		
B4	B5 × 1 1.737	B1 × 1 **1.61**		B5 × 1 1.767	B1 × 1 **1.668**		B5 × 1 1.754	B1 × 1 **1.674**	
	B3 × 2 1.784			B3 × 2 1.762			B3 × 2 1.762		
	B2 × 2 1.821			B2 × 2 1.814			B2 × 2 1.807		
B5	B4 × 1 1.737	B5 × 1 **1.72**		B4 × 1 1.767	B5 × 1 **1.659**		B4 × 1 1.754	B5 × 1 **1.661**	
	B3 × 2 1.758			B3 × 2 1.786			B3 × 2 1.781		
	B2 × 2 1.814			B2 × 2 1.786			B2 × 2 1.777		

the use of incorrect geometries in (Haussermann & Milhaylushkin, 2010) (**Table 5**) was partly responsible for errors in the interpretation of chemical bonding, and Mikhaylushkin soon afterward published a study (Mondal et al., 2011) essentially retracting many of their older views, yet still falling short of presenting correct analysis (Macchi, 2011). For more details, see recent review (Oganov, Solozhenko, Gatti, Kurakevych, & Le Godec, 2011).

3.04.4.3 Why TiO_2 is Not the Hardest Known Oxide?

Dubrovinsky et al. (2001) have claimed that TiO_2 with the cotunnite structure is the hardest known oxide. The search for the hardest oxide is another important problem: while diamond burns in an oxygen atmosphere at high temperatures, oxides can be inert to oxygen. The main proposals are stishovite (Leger et al., 1996), TiO_2-cotunnite (Dubrovinsky et al., 2001), and B_6O (He et al., 2002). While boron suboxide B_6O has the highest reported hardness among these three materials ($H = 45$ GPa), its thermal stability in an oxygen atmosphere is rather poor. Other ultrahard oxides are stishovite with $H = 33$ GPa (Leger et al., 1996), seifertite (high-pressure polymorph of SiO_2, predicted (Oganov & Lyakhov, 2010) to be slightly harder than stishovite), and TiO_2-cotunnite with the reported hardness $H = 38$ GPa (Dubrovinsky et al., 2001).

However, our simulations of TiO_2 indicated that the reported hardness of 38 GPa (Dubrovinsky et al., 2001) is extremely unlikely to be correct. The highest possible hardness for any real or hypothetical TiO_2 polymorph is 16.5 GPa (from ab initio calculations) or 15 GPa (classical force field). The "ultrahard" TiO_2-cotunnite with $H = 38$ GPa is therefore an artifact. For this phase, our model gives $H = 15.3$ GPa (**Table 1**). In this structure, each Ti atom has nine bonds with O atoms (cotunnite structure type is characterized by 9-coordinate cations), their lengths ranging from 2.03 to 2.56 Å; the relatively low hardness of TiO_2-cotunnite is caused by the high coordination number and a relatively high ionicity. Also, theoretical calculations (Kim, de Almeida, Koci, & Ahuja, 2007) suggest that this structure is dynamically unstable at 1 atm (which means not only that it cannot be very hard, but also that it cannot exist even as a metastable phase at this pressure) and careful measurements of the equation of state (Al-Khatatbeh, Lee, & Kiefer, 2009; Nishio-Hamane et al., 2010) showed that the measurements of Dubrovinsky et al. (2001) overestimated the bulk modulus by the unprecedented 40%. Therefore, the experimental data of Dubrovinsky et al. (2001) need to be reconsidered. Our theoretical results imply that this material is about as soft as common quartz (whose Vickers hardness is 12 GPa) and softer than common corundum, Al_2O_3 (21 GPa), or stishovite, SiO_2 (33 GPa), or B_6O (45 GPa). None of the polymorphs of TiO_2 can possess hardness above $\sim$17 GPa (Lyakhov & Oganov, 2011; Oganov & Lyakhov, 2010).

3.04.5 Conclusions

Hardness, a technologically very important property, until recently remained virtually inaccessible to theory and computation. Now, the situation is rapidly changing and models based on chemical bonding, elasticity, or thermodynamics show great promise. We have discussed a model of Li et al. (2008) and its extension undertaken by us (Lyakhov & Oganov, 2011; Oganov & Lyakhov, 2010). We have shown that such a model can describe many cases that were out of reach for previous models. This was achieved by explicitly taking into account the topology of crystal structures and detailed information about individual bond lengths with the help of the bond valence model. Coupling hardness models with the global optimization evolutionary algorithm USPEX (Lyakhov et al., 2010; Oganov & Glass, 2006) has yielded a powerful tool for the computational design of novel superhard materials. We have found a number of new allotropes of carbon that possess interesting mechanical (high density, high hardness) and electronic (a wide range of band gaps) properties. We have shown that C–N compounds are unlikely to exceed the hardness of diamond. The discovery of a novel superhard phase, γ-B_{28}, exemplifies the power of global optimization methods and the exciting crystal structure and chemical bonding discovered for this phase as well as challenges associated with the study of boron. Finally, we have demonstrated that, contrary to the published claims, TiO_2-cotunnite cannot be the hardest oxide; furthermore, its hardness is inferior to that of the common oxide, corundum (Al_2O_3). These examples show that modern theoretical methods can be used to guide the search for novel superhard materials, to gain insights into the mechanical properties of materials and assess controversial experimental data, thus accelerating the development of these exciting fields. The topic of this chapter is related to several other chapters in this volume, most closely to Cohen (2012) and Solozhenko (2012).

Acknowledgments

I thank the National Science Foundation (EAR-1114313, DMR-1231586), DARPA (Grants No. W31P4Q1310005 and No. W31P4Q1210008), CRDF Global (UKE2-7034-KV-11), the Government (No. 14.A12.31.0003) and the Ministry of Education and Science of Russian Federation (Project No. 8512) for financial support, and Foreign Talents Introduction and Academic Exchange Program (No. B08040). Calculations were performed on XSEDE facilities and on the cluster of the Center for Functional Nanomaterials, Brookhaven National Laboratory, which is supported by the DOE-BES under contract no. DE-AC02-98CH10086. I especially thank A.O. Lyakhov, Q. Zhu and X.F. Zhou for discussions.

References

Al-Khatatbeh, Y., Lee, K. K. M., & Kiefer, B. (2009). High-pressure behavior of TiO_2 as determined by experiment and theory. *Physical Review B, 79*, 134114.

Amberger, E., & Ploog, K. (1971). Bildung der Gitter des Reinen Bors. *Journal of the Less-Common Metals, 23*, 21–31.

Amberger, E., & Stumpf, W. (1981). *Gmelin handbook of inorganic chemistry*. Berlin: Springer-Verlag, 1960, pp. 112–238.

Becke, A. D. (1993). Density-functional thermochemistry. 3. The role of exact exchange. *Journal of Chemical Physics, 98*, 5648–5652.

Bovenkerk, H. P., Bundy, F. P., Hall, H. T., Strong, H. M., & Wentorf, R. H. (1959). Preparation of diamond. *Nature, 184*, 1094–1098.

Brazhkin, V. V. (2009). Interparticle interaction in condensed media: some elements are 'more equal than others'. *Physics Uspekhi, 52*, 369–376.

Brazhkin, V. V., Lyapin, A. G., & Hemley, R. J. (2002). Harder than diamond: dreams and reality. *Philisophical Magazine A, 82*, 231–253.

Brookes, C. A., & Brookes, E. J. (1991). Diamond in perspective—a review of mechanical properties of natural diamond. *Diamond and Related Materials, 1*, 13–17.

Brown, I. D. (1992). Chemical and steric constraints in inorganic solids. *Acta Crystallographica Section B, 48*, 553–572.

Bundy, F. P., Hall, H. T., Strong, H. M., & Wentorf, R. H. (1955). Man-made diamonds. *Nature, 176*, 51–55.

Chen, X.-Q., Niu, H., Li, D., & Li, Y. (2011). Modeling hardness of polycrystalline materials and bulk metallic glasses. *Intermetallics, 19*, 1275–1281.

Clark, S. J., Ackland, G. J., & Crain, J. (1995). Theoretical stability limit of diamond at ultrahigh pressure. *Physical Review B, 52*, 15035–15038.

Cohen, M. L. (2012). *Introduction to superhard materials, this volume*.

Douglas, B. E., & Ho, S.-M. (2006). *Structure and chemistry of crystalline solids*. N.Y.: Springer.

Dubrovinsky, L. S., Dubrovinskaia, N. A., Swamy, V., Muscat, J., Harrison, N. M., Ahuja, R., et al. (2001). Materials science—the hardest known oxide. *Nature, 410*, 653–654.

Fahy, S., & Louie, S. G. (1987). High-pressure structural and electronic properties of carbon. *Physical Review B, 36*, 3373–3385.

Gabunia, D., Tsagareishvili, O., Darsavelidze, G., Lezhava, G., Antadze, M., & Gabunia, L. (2004). Preparation, structure and some properties of boron crystals with different content of ^{10}B and ^{11}B isotopes. *Journal of Solid State Chemistry, 177*, 600–604.

Gao, F. M., He, J. L., Wu, E. D., Liu, S. M., Yu, D. L., Li, D. C., et al. (2003). Hardness of covalent crystals. *Physical Review Letters, 91*. art. 0155021.

Gao, F. M., Hou, L., & He, Y. H. (2004). Origin of superhardness of icosahedral B_{12} materials. *Journal of Physical Chemistry B, 108*, 13069–13073.

Glass, C. W., Oganov, A. R., & Hansen, N. (2006). USPEX—evolutionary crystal structure prediction. *Computer Physics Communications, 175*, 713–720.

Gou, H. Y., Hou, L., Zhang, J. W., & Gao, F. M. (2008). Pressure-induced incompressibility of ReC and effect of metallic bonding on its hardness. *Applied Physics Letters, 92*, 241901.

Haussermann, U., & Mikhaylushkin, A. S. (2010). Structure and bonding of γ-B_{28}: is the high pressure form of elemental boron ionic? *Inorganic Chemistry, 49*, 11270–11275.

He, D. W., Zhao, Y. S., Daemen, L., Qian, J., Shen, T. D., & Zerda, T. W. (2002). Boron suboxide: as hard as cubic boron nitride. *Applied Physics Letters, 81*, 643–645.

Hemley, R. J., Jephcoat, A. P., Mao, H. K., Zha, C. S., Finger, L. W., & Cox, D. E. (1987). Static compression of H_2O–ice to 128 GPa (1.28 Mbar). *Nature, 330*, 737–740.

Irifune, T., Kurio, A., Sakamoto, S., Inoue, T., & Sumiya, H. (2003). Ultrahard polycrystalline diamond from graphite. *Nature, 421*, 599–600.

Jiang, C., Lin, Z., Zhang, Z., & Zhao, Y. (2009). First-principles prediction of mechanical properties of γ-boron. *Applied Physics Letters, 94*, 191906.

Kasper, J. S., & Richards, S. M. (1964). The crystal structures of new forms of silicon and germanium. *Acta Crystallographica, 17*, 752–755.

Kim, D. Y., de Almeida, J. S., Koci, L., & Ahuja, R. (2007). Dynamical stability of the hardest known oxide and the cubic solar material: TiO_2. *Applied Physics Letters, 90*, 171903.

Kresse, G., & Furthmüller, J. (1996). Efficient iterative schemes for *ab initio* total-energy calculations using a plane wave basis set. *Physical Review B, 54*, 11169–11186.

Le Godec, Y., Kurakevych, O. O., Munsch, P., Garbarino, G., & Solozhenko, V. L. (2009). Equation of state of orthorhombic boron, γ-B_{28}. *Solid State Communications, 149*, 1356–1358.

Leger, J. M., Haines, J., Schmidt, M., Petitet, J. P., Pereira, A. S., & da Jornada, J. A. H. (1996). Discovery of hardest known oxide. *Nature, 383*, 401.

Li, H., & Bradt, R. C. (1990). Knoop microhardness anisotropy of single-crystal rutile. *Journal of the American Ceramic Society, 73*, 1360–1364.

Li, Q., Ma, Y., Oganov, A. R., Wang, H. B., Wang, H., Xu, Y., et al. (2009). Superhard monoclinic polymorph of carbon. *Physical Review Letters, 102*, 175506.

Li, K. Y., Wang, X. T., Zhang, F. F., & Xue, D. F. (2008). Electronegativity identification of novel superhard materials. *Physical Review Letters, 100*. art. 235504.

Liu, A. Y., & Cohen, M. L. (1989). Prediction of new low compressibility solids. *Science, 245*, 841–842.

Lyakhov, A. O., & Oganov, A. R. (2011). Evolutionary search for superhard materials applied to forms of carbon and TiO_2. *Physical Review B, 84*, 092103.

Lyakhov, A. O., Oganov, A. R., & Valle, M. (2010). How to predict very large and complex crystal structures. *Computer Physics Communications, 181*, 1623–1632.

Macchi, P. (2011). On the nature of chemical bonding in gamma-boron. *Journal of Superhard Materials, 33*, 380–387.

Mao, W. L., Mao, H. K., Eng, P. J., Trainor, T. P., Newville, M., Kao, C. C., et al. (2003). Bonding changes in compressed superhard graphite. *Science, 302*, 425–427.

Mondal, S., van Smaalen, S., Schonleber, A., Filinchuk, Y., Chernyshov, D., Simak, S. I., et al. (2011). Electron-deficient and polycenter bonds in the high-pressure γ-B_{28} phase of boron. *Physical Review Letters, 106*, 215502.

Mukhanov, V. A., Kurakevych, O. O., & Solozhenko, V. L. (2008). The interrelation between hardness and compressibility of substances and their structure and thermodynamic properties. *Journal of Superhard Materials, 30*, 368–378.

Nishio-Hamane, D., Shimizu, A., Nakahira, R., Niwa, K., Sano-Furukawa, A., Okada, T., et al. (2010). The stability and equation of state for the cotunnite phase of TiO_2 up to 70 GPa. *Physics and Chemistry of Minerals, 37*, 129–136.

Occelli, F., Loubeyre, P., & LeToullec, R. (2003). Properties of diamond under hydrostatic pressures up to 140 GPa. *Nature Materials, 2*, 151–154.

Oganov, A. R. (2011). Discovery of g-B_{28}, a Novel Boron Allotrope with Partially Ionic Bonding. In: Boron and boron compounds – from fundamentals to applications. *Materials Research Society,* ISBN 978-1-61839-514-6, Chapter 1, pp. 1–15.

Oganov, A. R., Chen, J., Gatti, C., Ma, Y.-M., Yu, T., Liu, Z., et al. (2009). Ionic high-pressure form of elemental boron. *Nature, 457*, 863–867.

Oganov, A. R., & Glass, C. W. (2006). Crystal structure prediction using *ab initio* evolutionary techniques: principles and applications. *Journal of Chemical Physics, 124*. art. 244704.

Oganov, A. R., & Glass, C. W. (2008). Evolutionary crystal structure prediction as a tool in materials design. *Journal of Physics: Condensed Matter, 20*. art. 064210.

Oganov, A. R., & Lyakhov, A. O. (2010). Towards the theory of hardness of materials. *Journal of Superhard Materials, 32*, 143–147 [Special issue "Theory of Superhard Materials"].

Oganov, A. R., Lyakhov, A. O., & Valle, M. (2011). How evolutionary crystal structure prediction works—and why. *Accounts of Chemical Research, 44*, 227–237.

Oganov, A. R., Ma, Y., Lyakhov, A. O., Valle, M., & Gatti, C. (2010). Evolutionary crystal structure prediction as a method for the discovery of minerals and materials. *Reviews in Mineralogy and Geochemistry, 71*, 271–298.

Oganov, A. R., & Solozhenko, V. L. (2009). Boron: a hunt for superhard polymorphs. *Journal of Superhard Materials, 31*, 285–291.

Oganov, A. R., Solozhenko, V. L., Gatti, C., Kurakevych, O. O., & Le Godec, Y. (2011). The high-pressure phase of boron, γ-B_{28}: disputes and conclusions of 5 years after discovery. *Journal of Superhard Materials, 33*, 363–379.

Oganov, A. R., Solozhenko, V. L., Kurakevych, O. O., Gatti, C., Ma, Y., Chen, J., et al. (2009). *Comment on "Superhard Semiconducting Optically Transparent High Pressure Phase of Boron"*. http://arxiv.org/abs/0908.2126.

Patterson, J. R., Cartledge, S. A., Vohra, Y. K., Akella, J., & Weir, S. T. (2000). Electrical and mechanical properties of C_{70} fullerene and graphite under high pressures studied using designer diamond anvil cells. *Physical Review Letters, 85*, 5364–5367.

Perdew, J. P., Burke, K., & Ernzerhof, M. (1996). Generalized gradient approximation made simple. *Physical Review Letters, 77*, 3865–3868.

Povarennykh, A. S. (1963). *Hardness of minerals.* Kiev: Press of the Academy of Sciences of the USSR.

Pugh, S. F. (1954). Relations between the elastic moduli and the plastic properties of polycrystalline pure metals. *Philosophical Magazine, 45*, 823–843.

Schwarz, U., Wosylus, A., Bohne, B., Baitinger, M., Hanfland, M., & Grin, Y. (2008). A 3D network of four-bonded germanium: a link between open and dense. *Angewandte Chemie (International Edition in English), 47*, 6790–6793.

Simunek, A. (2009). Anisotropy of hardness from first principles: the cases of ReB_2 and OsB_2. *Physical Review B, 80*. art. 060103.

Simunek, A., & Vackar, J. (2006). Hardness of covalent and ionic crystals: first-principle calculations. *Physical Review Letters, 96*. art. 0855011.

Solozenko, V. L. (2012). *High-pressure synthesis of novel superhard materials, this volume*.

Solozhenko, V. L. (2002). Synthesis of novel superhard phases in the B–C–N system. *High Pressure Research, 22*, 519–524.

Solozhenko, V. L. (2009). High-pressure synthesis of novel superhard phases in the B–C–N system: recent achievements. *High Pressure Research, 29*, 612–617.

Solozhenko, V. L., Andrault, D., Fiquet, G., Mezouar, M., & Rubie, D. C. (2001). Synthesis of superhard cubic BC_2N. *Applied Physics Letters, 78*, 1385–1387.

Solozhenko, V. L., Kurakevych, O. O., Andrault, D., Le Godec, Y., & Mezouar, M. (2009). Ultimate metastable solubility of boron in diamond: synthesis of superhard diamondlike BC_5. *Physical Review Letters, 102*. art. 015506.

Solozhenko, V. L., Kurakevych, O. O., & Oganov, A. R. (2008). On the hardness of a new boron phase, orthorhombic γ-B_{28}. *Journal of Superhard Materials, 30*, 428–429.

Sung, C. M., & Sung, M. (1996). Carbon nitride and other speculative superhard materials. *Materials Chemistry and Physics, 43*, 1–18.

Teter, D. M., & Hemley, R. J. (1996). Low-compressibility carbon nitrides. *Science, 271*, 53–55.

Urusov, V. S. (1975). *Energetic crystal chemistry.* Moscow: Nauka (in Russian).

Wang, Y., & Oganov, A. R. (2008). *Research on the evolutionary prediction of very complex crystal structures.* IEEE Report.

Wentorf, R. H. (1957). Cubic form of boron nitride. *Journal of Chemical Physics, 26*, 956.

Wosylus, A., Prots, Y., Schnelle, W., Hanfland, M., & Schwarz, U. (2008). Crystal structure refinements of Ge(*t*P12), physical properties and pressure-induced phase transformation Ge(*t*P12) ↔ Ge(*t*I4). *Zeitschrift für Naturforschung B, 63*, 608–614.

Zarechnaya, E. Y., Dubrovinsky, L., Dubrovinskaia, N., Filinchuk, Y., Chernyshov, D., Dmitriev, V., et al. (2009). Superhard semiconducting optically transparent high pressure phase of boron. *Physical Review Letters, 102*, 185501.

Zarechnaya, E. Y., Dubrovinsky, L., Dubrovinskaia, N., Miyajima, N., Filinchuk, Y., Chernyshov, D., et al. (2008). Synthesis of an orthorhombic high pressure boron phase. *Science and Technology of Advanced Materials, 9*, 044209.

Zhu, Q., Oganov, A. R., Salvado, M., Pertierra, P., & Lyakhov, A. O. (2011). Denser than diamond: ab initio search for superdense carbon allotropes. *Physical Review B, 83*, 193410.

3.05 Taming the Untamable—The Art and Science of Diamond Polishing

Michael Moseler and Lars Pastewka, Fraunhofer Institute for Mechanics of Materials IWM, Freiburg, Germany
Jonathan Hird, Schlumberger Gould Research, Cambridge, United Kingdom

3.05.1 Introduction

The word "diamond" derives from the Greek term "adamas," which means untamable and refers to its main physical feature: its extreme hardness. Although the exact place and date of origin of diamond polishing is unknown (Lenzen, 1966), the fact that the first guild of diamond cutters and polishers (diamantaire) was formed in 1375 in Nuremberg, Germany (Tolansky, 1961) suggests that mankind learned to tame the untamable more than 600 years ago. For almost a century, the art of traditional diamond polishing has been studied scientifically with the aim of answering one key question: how is material removed from the diamond when it is worn or polished? Diamond is the hardest known material, has a high degree of resistance to chemical wear and has a high thermal conductivity; enacting wear on such a substance to form smooth facets would initially appear impossible to achieve. The subject is not just scientific curiosity, however. Optimizing a lapping process that has remained largely unchanged for centuries has become somewhat urgent with the current surge of interest in the use of diamond in many high-technology applications. Such applications demand high-quality planar surfaces, which must be free from surface damage. Eventually, a technique must be found that will provide the necessary scaling required for high-throughput low-cost manufacturing.

Scientific investigations on diamond polishing have, until recently, been mainly experimental and forensic in scope and have examined various aspects of the large number of parameters hypothesized to be involved with the wear of diamond. For instance, there have been studies of the scaife preparation technique, the chemical identity of the wear debris, the diamond surface and the scaife surface and these will be described in detail during later sections of this chapter. More recently, with the advent of high-performance computing, predictive models are beginning to emerge, heralding a new era of polishing technology and insights into the scientific mechanisms which produce wear on diamond. These models will be reviewed in the second part of this contribution.

3.05.2 Experiment

3.05.2.1 Tribological Anisotropy and Associated Phenomena

The scientific story of diamond polishing begins with the work of Tolkowsky (1920) who encapsulated the observations of centuries of lapidaries in the language of crystallography. During the traditional diamond

http://dx.doi.org/10.1016/B978-0-08-096527-7.00042-8

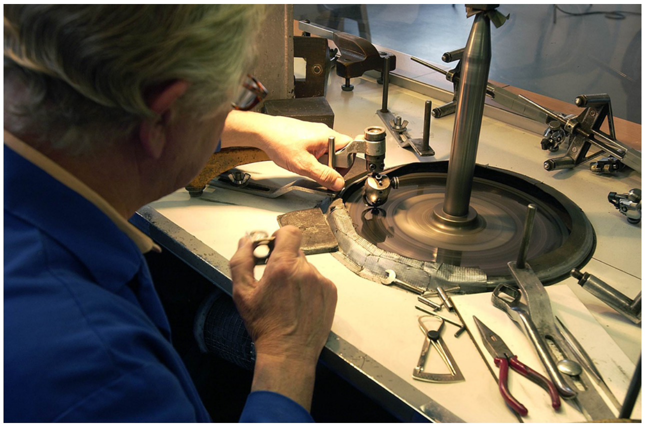

Figure 1 A diamantaire at a typical diamond polishing bench showing the scaife plate, the dop, and the tang. Image: Wikimedia commons.

polishing process, a very marked dependence on orientation of the diamond under polish with respect to the rotation of the polishing wheel, or *scaife* in the parlance of the industry, is observed. The scaife, shown in **Figure 1**, is a circular disc of cast iron about 0.3 m in diameter which rotates at roughly 3000 rpm (tangential linear velocity of 30 m s^{-1}). In this respect it is not dissimilar from other lapping operations other than the scaife is loaded with diamond grit; viz. the same material that it is to polish. The grit typically has a size <40 μm, the size distribution being chosen to reflect the operation, and must be worked into the polishing wheel prior to its use (see later), and periodically through the life of the scaife plate. The diamond to be polished is usually held in a *dop* (a small cup or collet) that in turn is held in a hand tool called a *tang*. Using this apparatus, the diamond is gently placed onto the scaife, and it is at this point that the anisotropy in wear will be noticed. Practical aspects of diamond lapidary techniques can be found by the standard practical text by Watermeyer (1982).

The polishing directions $\langle d \rangle$ on any diamond surface $\{s\}$ in which a diamond can be worn with relative ease are known as "soft" directions of polish. If the diamond is rotated azimuthally from these directions, the wear rate will decrease to a minimum. These are known as "hard" directions. For the basal planes of diamond, this anisotropy can be stated as follows: for the cube plane ($\{s\}=\{100\}$), the directions of polish $\langle 100 \rangle$ are known to be "soft," while $\langle 110 \rangle$ are "hard"; that is to say there is fourfold symmetry. The dodecahedral plane ($\{s\}=\{110\}$) has two polishing directions, $\langle 100 \rangle$, on which polishing proceeds fastest, relative to all other crystallographic planes, while $\langle 110 \rangle$ are hard. The octahedral plane ($\{s\}=\{111\}$), also the predominant cleavage plane in diamond (Field, 2012), is almost uniformly difficult to polish, but it may be polished in $\langle 112 \rangle$ directions, of which there are three. These relationships were first mapped out by Tolkowsky (1920), whose data is replotted in **Figure 2**, and have since been reproduced numerous times using a variety of techniques (Bergheimer, 1938; Denning, 1953; Grillo, Field, & van Bouwelen, 2000; Grodzinski & Stern, 1949; Grodzinski, 1949, 1953; Hukao, 1955; Knight & White, 1989; Kraus & Slawson, 1939; Slawson & Kohn, 1950; Whittaker & Slawson, 1946; Wilks & Wilks, 1954, 1959, 1972; Wilks, 1952; Winchell, 1946). Grillo, Field & van Bouwelen have correlated this wear anisotropy to a frictional anisotropy; "soft" directions of polish are associated with high friction and "hard" directions with low friction.

A consequence of the high friction in soft directions is the frictional heating of the diamond that will occur when the correct polishing direction is found. However, the diamond should never be allowed to become candescent, as this will damage the lap of the scaife and increase the probability of thermal fracture of the diamond. Another consequence of the anisotropy in friction is the vibration and audible noise emitted from the diamond under polish which can be used as a guide to orientation.

A well-polished diamond will come off the scaife with a facet having the appearance of a mirror; wear and polishing have occurred simultaneously and this is considered favorable. This is, however, not the only method of producing wear on diamond. Examples of abrasive wear can be observed on natural alluvial diamonds that may have rounded facets. Bruting, a precursor to forming diamond into many gemstone cuts, is also an abrasive wear process which involves the diamond being turned on a lathe using another diamond, appropriately orientated, as the "tool" to produce a cylindrical form.

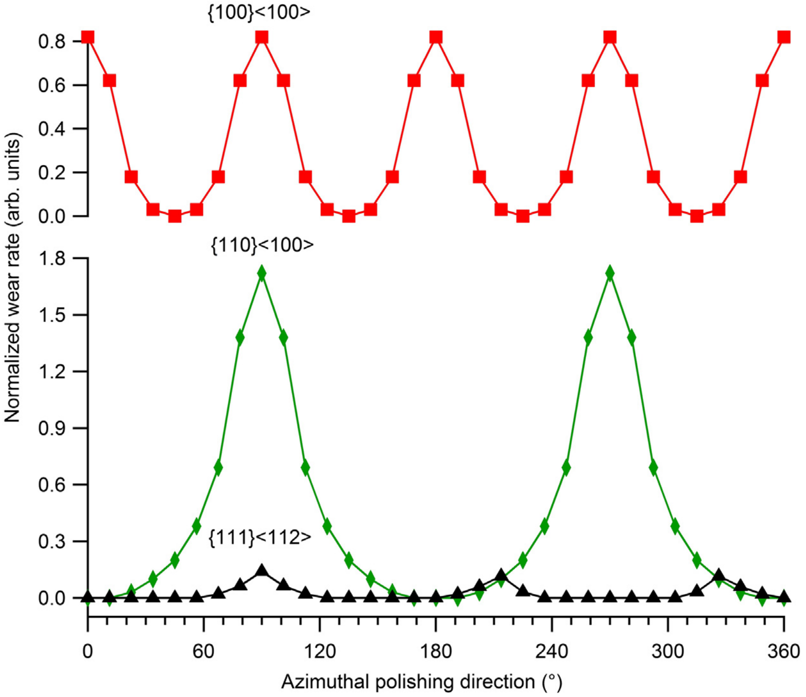

Figure 2 Wear anisotropy exhibited by the three basal planes of diamond as a function of azimuthal angle relative to the direction of rotation of the scaife. The plots are reproduced from the results of Tolkowsky (1920) and show minima at zero. It is likely that wear in these directions does occur but was below the sensitivity of his apparatus.

The anisotropy in wear noted during polishing on diamond is not unique to high-speed sliding where considerable heating can occur, but is also observed during low-speed, small-contact area friction experiments. Kenyon (Bowden, 1954) was the first to observe this and it was later investigated by Seal (1958). These experiments were conducted with reciprocating friction measuring apparatus whereby a polished planar surface of diamond is displaced at a speed <2 mm s^{-1} to and fro under a diamond stylus, or octahedral tip of diamond, having a hemispherical radius of a few tens of micrometers. The diamond stylus is typically orientated in a hard direction relative to the direction of sliding. The friction coefficients found during diamond–diamond sliding are generally very low and range from between 0.05 and 0.15 depending on the direction of sliding and crystallographic planes. Experiments have demonstrated that hard directions of polish coincide with low friction and "soft" directions of polish with high friction. On octahedral surfaces, the friction coefficient is very low with a value of ~0.05. A variety of factors, both mechanical and chemical, have been found which change the coefficient of friction. For instance, the anisotropy is noted to become more marked when the cone angle of the stylus is increased (Bowden & Brookes, 1966; Bowden, Brookes, & Hanwell, 1964). The extent of loading and apparent area of contact is also important (Enomoto & Tabor, 1981; Samuels & Wilks, 1988) and may produce tracks ranging from heavy damage suggestive of plastic deformation or alternatively Hertzian failure (Seal, 1958). Another mechanical factor which can influence friction is whether the polishing lines are oriented parallel or perpendicular to the direction of sliding (Samuels & Wilks, 1988).

The chemistry of the experimental environment is found to have a dominant effect on the friction coefficient (Bowden & Hanwell, 1964; Bowden & Young, 1951). Experiments in ultrahigh vacuum (UHV) (Feng, Tzeng, & Field, 1992) have shown that the friction coefficient becomes very high >1.2 after the stylus has completed a few traversals and experiments under partial pressure of a variety of gases find that presence of oxygen reduces friction, while nitrogen does not. When oxygen and nitrogen are ionized, however, strong reductions in friction can be achieved. Chemical changes affecting low-speed friction can also occur when heating in air, water and paraffin (Feng & Field, 1991, 1992; Feng, Tzeng & Field, 1992; Grillo & Field, 2000a, 2000b).

The presence of water lubricates the contact to the extent that an initial friction coefficient of ~0.11 may be decreased to ~0.025 after 1000 traversals on the same track (Feng & Field, 1992). The pH of the water is also found to cause small variations in the friction coefficient and shows a minimum centered on between pH 6 and 7 (Grillo & Field, 2000b).

The friction of diamond sliding against other materials, such as metals, is not well documented, however. Enomoto and Tabor (1981) have shown that the anisotropy shown by a diamond stylus on a diamond {100} surface is not present when the diamond stylus is switched to one manufactured from tungsten carbide. In vacuum, metals sliding against diamond tend to produce high friction and a correlation has been noted between the relative chemical activity of the transition metal and friction (Miyoshi & Buckley, 1980).

The friction of diamond surfaces over a variety of length scales remains an active research area with a large number of parameters responsible for the energy dissipation mechanism. These include fracture, adhesion, plastic deformation, topology, chemical nature of the surface, environment, and phononic vibrations (Cannara, Brukman, Cimatu, et al., 2007) all playing a role.

The apparent deconstruction of the diamond polishing problem using a stylus to represent singular diamond grit on a scaife is an experimental advantage in a research field where the consumables are expensive. However, caution must be exercised with the orders of difference magnitude in sliding speeds and the differences between the polishing environment and that of the experimental friction rig.

Despite these differences, there are a number of similarities including the anisotropy and atmosphere dependence. The only open-literature research reporting these findings, however, are experiments conducted with bonded scaifes used to polish diamond in a hard direction $\{110\}\langle 011\rangle$ (Hitchiner, Wilks, & Wilks, 1984). Nevertheless, the experiment showed that when diamond was polished in a low vacuum (0.1 Torr), the wear rate was found to decrease. The wear rate was found to recover on readmitting air to the chamber. In an inert gas (Ar), a similar trend was found. Viewed under a microscope, the diamond surfaces polished in air and vacuum were found to be different. In another experiment, a bonded scaife fitted with a lip to contain liquids was used to investigate the presence of liquids at the diamond $\{011\}\langle 100\rangle$ scaife interface. Isopropanol and water were both found to increase the wear rate (Wilks & Wilks, 1991). Yarnitsky et al. (unpublished) have reported that nitrogen, carbon dioxide, and oxygen were found to increase the rate of wear of diamond.

The emission of light at the scaife–diamond interface has often been noted. This is a form of triboluminescence (Walton, 1977) and has been investigated by Hird, Chakravarty, and Walton (2007) using a traditional cast-iron scaife and by Chapman (unpublished) who used a bonded scaife. In both experiments, the intensity of the light emission was found to reflect the anisotropy in wear. Hird, Chakravarty & Walton (2007) found that "hard" direction polishing had a more intense light emission than "soft" direction polishing on a traditional scaife. Using a bonded scaife, Chapman observed the contrary and found that the emitted light bore resemblance to the UV-stimulated fluorescence of the diamond under polish. Hird et al. measured a spectrum consistent with the electroluminescence of diamond (Prior & Champion, 1962) and showed that small changes in orientation of the stone under polish could change the spectral envelope as would be expected if frictional differences introduced a change of temperature. Light may also be emitted from the polishing track on the scaife. This, however, is very low in intensity and requires dark adaption to be visible to the unassisted eye, but spectral analysis has shown that it to be broadband in nature and has a decay time of seconds. Both these characteristics are indicative of a chemisorptive luminescence (McCarroll, 1969) and are probably associated with iron oxide. If nothing else, it indicates the level of complexity of tribochemistry occurring on a scaife.

3.05.2.2 Dependence on Scaife Speed

While it is relatively easy to arrive at the general result that diamond exhibits anisotropy in wear, quantification of wear as a function of contact area, scaife speed, load and other basic parameters quickly becomes problematic owing to small sample sizes, minute wear rates ($<50\ \mu\text{m min}^{-1}$ are typical), compensating for thermal expansion and the tendency for misalignment during experimental runs owing to the extreme wear anisotropy. Such measurements are necessary in order to gain insights into wear mechanism(s) (Ashby & Lim, 1990).

A number of experimental approaches have been taken in the quest for reproducible results. These have variously been to observe the wear in situ through the use of a depth gauge (Hird, 2002; Hird & Field, 2004, 2005; Tolkowsky, 1920), or by examining the stone after polishing using an optical technique (Hukao, 1955; Wilks, 1952; Wilks & Wilks, 1954, 1959, 1972). The Grodzinski–Stern investigation (Grodzinski & Stern, 1949) and Hird (Hird, 2002) used mass loss of the diamond, removed from the experiment at regular intervals of time, the mass of which was determined on a chemical balance to measure wear. To circumvent the use of a scaife in an attempt to obtain greater control of variables, Grodzinski (Grodzinski, 1949, 1953; Grodzinski & Stern, 1949) and Wilks and Wilks (Wilks & Wilks, 1954, 1959, 1972) have been to use a miniature grinding wheel manufactured from cast iron and embedded with diamond grit or from diamond grit embedded in a matrix.

This approach has not been successful in reproducing some of the results observed on a traditional scaife. These discrepancies probably arise from the higher rotation speeds, smaller circumference (i.e. less grit particles per revolution) and a dissimilar geometry.

Hird and Field (Hird, 2002; Hird & Field, 2004, 2005) have succeeded in measuring wear of diamond via three different experiments and arrive at the same result. A bench-mounted tang, or static tang, equipped with a dop with jaws facilitating removal of the diamond was employed in each case. X-ray diffraction (XRD) using the Laue geometry was used to orient the diamonds into the preferential polishing directions. The diamonds used were high-pressure, high-temperature (HPHT) synthetic monocrystals which had been laser cut to provide a constant cross-section. The first set of experiments used mass loss as a measurement of wear (Hird, 2002). The diamond was removed from the dop at intervals, sonicated in acetone, dried and weighed on a chemical balance. The second set of experiments used a depth gauge which measured the height of the diamond relative to a datum (Hird & Field, 2004). The experiment was stopped at intervals and the apparatus was allowed to cool. At 300 K, the measurement device was placed over the diamond where it rested on a kinetic mount to ensure an accurate location. In the third set of experiment, this depth gauge was replaced with linear variable displacement transducer and data logger that could monitor and record the wear in real time (Hird & Field, 2005). In each of the experiments, lead masses could be placed on top of the tang to increase the contact force on the diamond.

The results clearly show that wear rate is a nonlinear function of the tangential velocity of the scaife. The data show three regimes. Between 0 and 20 m s^{-1}, there is either very low wear or the diamond does not wear at all. After 20 m s^{-1}, the wear increases fairly uniformly until 50 m s^{-1}. At this point, a tail-off in the wear occurs. This is thought to be due to a change in surface conditions on the scaife (Hird, 2002).

3.05.2.3 Postwear Analyses

Another approach employed to decipher the mechanism of diamond polishing is to carry out forensic examinations of the polishing debris and to examine the contacting surfaces: both the scaife and workpiece. Both these techniques have yielded fascinating insights into the degradation of diamond.

Diamond wear debris have been studied with a plethora of techniques including Raman (Couto, van Enckevort, & Seal, 1994a; Hird, Bloomfield, & Hayward, 2007), IR spectroscopy, XRD (Feng & Field, 1992) and, perhaps most powerfully, by electron-energy loss spectroscopy (Grillo & Field, 1997; van Bouwelen, Bleloch, Field, & Brown, 1996; van Bouwelen, Field, & Brown, 2003). All the results from these experiments indicate that a phase transformation occurs during polishing which transforms the diamond to a lower density, lower order carbon which is sp^2-bonded and/or amorphous. A surprising result, perhaps, is low abundance of iron compounds, whose presence one might have expected as it is this material from which the scaife is manufactured. Similar studies of the wear debris from low-speed frictional sliding experiments have yielded similar carbonaceous debris, which Seal (1958) described as straw colored and waxy in appearance. The material ejected during diamond polishing is, however, dark in color.

It might be expected that a layer of such debris might be observed on a diamond surface soon after it is removed from the scaife. However, as noted earlier, a diamond fresh from being polished on a scaife will often appear very clean with a mirror-like facet when observed above the critical angle. A study using Raman spectroscopy on an as-polished surface did not detect any layer of nondiamond carbon debris (Hird, Bloomfield & Hayward, 2007). However, recently, atomically thin adlayers of amorphous carbon were detected in a near-edge X-ray absorption structure study of wear tracks on nanocrystalline diamond films (Konicek, Grierson, Gilbert, Sawyer, Sumant & Carpick, 2008).

The topology of the diamond surface has been well studied over the years using various forms of electron microscopes (Bailey & Seal, 1956; Postek & Evans, 1989; Seal, 1958; Seal & Menter, 1953; Thornton & Wilks, 1976; Wang, Feng, & Field, 1991). Surface structures including microcracks, nanometer-sized grooving, and subsurface damage have all been reported. A major difficulty in examining diamond surfaces in an electron microscope can be the interpretation of electrical charge deposited by the electron beam on the (usually) insulating surface, the growth of structures under the electron beam (Ennos, 1953), and the possibility of obtaining inaccurate replicas when metallic films are deposited onto the surface of diamond (Thornton & Wilks, 1976; Postek & Evans, 1989). The advent of atomic force microscopes has cleared this ambiguity. Couto et al. (Couto, van Enekevort, Wichman, & Seal, 1992; Couto, van Enckevort, & Seal, 1994a, 1994b, 1997) made numerous studies of polished HPHT diamond and diamond surfaces produced by chemical vapor deposition (CVD) using various scanning probe microscopies. These studies undeniably demonstrate that diamonds polished in different crystallographic directions have different topologies. Those polished in "soft" directions exhibit smooth parallel grooves (**Figure 3**), with walls having no preferred crystallographic orientation (measurements indicated a Gaussian distribution of wall angles) and measuring tens of nanometers in dimension; orders of magnitude smaller than the "running lines" that can be seen on diamond surfaces using an optical microscope using differential interference contrast.

This result immediately put to rest the theory that diamonds are polished via microfracture; a theory that was first proposed by Tolkowsky (1920) and extended by Wilks and Wilks (Wilks & Wilks, 1972, 1991). Diamonds polished in "hard" directions, however, showed topologies consistent with having been formed via some fracture-based mechanism. Interestingly, low-speed sliding experiments using very sharp indenters had also hinted at grooving several orders of magnitude smaller than the apparent contact area several decades before Couto's work (Seal, 1958).

3.05.2.4 The Scaife; Its Preparation and Function

Although the role of the scaife is central to the diamond polishing operation, until relatively recently it was considered to consist of a matrix of randomly oriented diamond particles and, as such, all but neglected. It was believed that only those grit particles oriented in a hard direction with respect to the oncoming diamond could wear and polish it. Several complementary studies of the scaife have been made (Couto, van Enckevort & Seal, 1994a; Hird, Bloomfield & Hayward, 2007; Hird & Field, 2004) which have challenged that view and will be described in detail in due course. First, given the importance of the scaife in the process, it is worth considering how a scaife is prepared prior to its use and also how the lap is kept in good condition.

To prepare a scaife for use, a few drops of olive oil are evenly smeared on to the surface of the scaife. To this is added a small amount of diamond grit (0.2–0.4 g = 1–2 carats is sufficient) and rubbed in with the finger tips to yield an evenly distributed layer which will appear a light matt gray in color. This is worked in using a diamond of inferior quality, traditionally boart or carbonado. A more recent development is the use of a sintered polycrystalline diamond material which may be used in place of boart. The diamond is pressed on to the newly dressed scaife and moved across the radius until the color of the scaife changes from its initial matt gray to one that is glossy and dark. The appearance of this color is considered desirous for good polishing to occur and is sometimes referred to as the *black layer*. When the scaife is stationary, this layer will feel waxy and

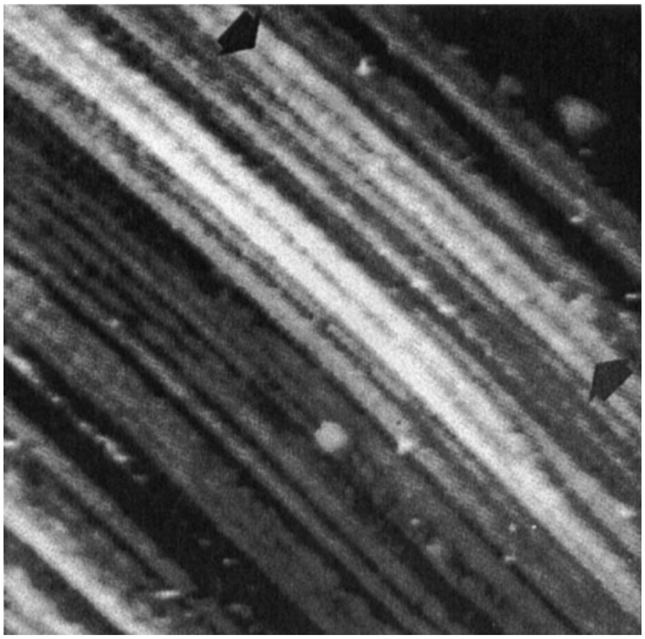

Figure 3 Typical STM image of a {110} diamond surface polished in the ⟨001⟩ direction. Diamond surfaces polished in "soft" directions exhibit smooth grooving with dimensions of tens of nanometer width. From Couto, van Enckevort & Seal (1994a).

smooth to the touch. There should be no trace of oil left on the surface. At this point, the scaife is considered ready to polish a diamond.

Couto et al. have made a comprehensive study using a variety of techniques that showed that the debris on the scaife (the black layer) is composed of amorphous carbon, oxides, and carbides of iron in addition to Na, Cl, Si, and Ca. The latter elements were postulated to have been present through contamination. Importantly, Couto, van Enckevort & Seal (1994a) also examined the scaife under an optical microscope and found it had been plastically grooved by the motion of grit particles and also observed that some of the grit particles had been polished (**Figure 3**). This line of enquiry was continued by Hird and Field (2004) who used both optical and electron microscopes to study the surface of the scaife. Their approach was to use a gas torch to remove the black layer, which had initially obscured the true surface of the scaife. They observed flat-topped grit particles at the end of comet-like grooves in the cast iron (**Figure 4**) showing that the grits had rotated through the frictional interaction with the diamond workpiece. The grit particles also showed sharp leading edges, reminiscent of chisels. A major result was finding that grooves having nanometer dimensions were observed on the top of these flat-topped grit particles.

These observations demonstrated that grits and diamond workpiece were all oriented in “soft” directions and that reciprocal polishing had occurred. Hird and Field postulated that smaller grit particles could be formed during comminution during the preparation process and these might be responsible for the nanogrooves present on both diamond workpiece and diamond grit. These particles were envisaged as entities entrapped in the black layer present on the surface of the scaife. Estimates of dimensions at which the brittle–ductile transition (Hagan, 1981) occurs for diamond are in agreement with the width of the nanogrooves. Calculation puts them at between 32 and 230 nm. The brittle–ductile transition represents the point at which a grit particle is no longer any use as a sliding indenter. Importantly, this also imposes a fundamental limit on the level of roughness that can be achieved with a traditional scaife.

The process of preparing a scaife has been investigated by Hird, Bloomfield, et al (2007). They studied the evolution of debris as two scaife plates were prepared with two different oils; one was prepared using silicone oil, the other with olive oil. In the first few minutes of preparation, traces of oil were found in addition to diamond particles. After further preparation, the Raman signature of both oils disappeared. In the case of the silicone oil-prepared scaife, small diamond particles were ejected in addition to amorphous carbon. The scaife surface was covered in a fine, unconstrained powder of dull color and of a different dimension to the original grit particles. Raman spectra taken of some grit particles showed unusual spectra sometimes associated with hexagonal diamond or lonsdaleite with peaks at 1326 cm^{-1} (Knight & White, 1989). The olive oil-prepared scaife was sticky to the touch, exhibited no unconfined powder and was of a glossy black luster. The ejected debris comprised large amounts of amorphous carbon and few diamond particles. Analysis of burnt olive oil has the same chemical signature as the ejected debris and exhibits D and G bands of amorphous carbon.

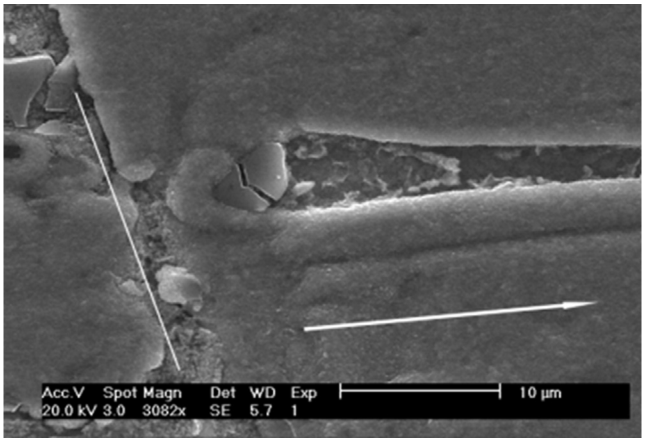

Figure 4 Flat-topped grit particle on a scaife surface. The white arrow denotes the direction of rotation of the scaife. The grit particle has become aligned and polished through preparation and use of the scaife. From Hird and Field (2004).

3.05.3 Wear Models and Wear Modeling

3.05.3.1 Empirical Wear Models

The anisotropy in wear rates on the different diamond surfaces (as detailed in Section 3.05.2.1) has spurred interest in developing models and a microscopic understanding for the wear phenomena with particular focus on the pronounced anisotropy. Diamond is a brittle material, but it has a hardness and thermal conductivity exceeding that of any other material (Field, 1992, 2012). Because of these properties, a wear mechanism involving fracture initially seemed attractive. Tolkowsky (1920), realizing that diamonds could be found in both tetrahedral and octahedral forms, proposed an abrasive wear mechanism of diamond proceeding by the removal of small diamond particles. The anisotropy in wear was explained by the ease of removing small octahedral and tetrahedral fragments from the bulk diamond. In more recent years, an updated version of this model has been used by Wilks and Wilks (1972). It has been pointed out in Section 3.05.2.3 that the failing of a fracture-based wear mechanism for diamond stems from three experimental facts. First, the model is unable to explain the anisotropy observed in the coefficient of sliding friction for diamond on diamond. Second, it cannot account for the nondiamond carbon produced as polishing debris. Third, examinations of polished diamond surfaces reveal smooth grooved surfaces for some directions of polish, which are inconsistent with any model of wear produced by abrasion.

van Bouwelen (van Bouwelen & van Enckevort, 1999) argued that under large shear forces present at the scaife–diamond interface, it becomes energetically more favorable for the diamond bonding to rehybridize to an sp^2 configuration if the crystal structure is deformed sufficiently through shear. A softer material forms that can be removed by the pass of another grit particle and the process repeats itself. This microscopic work tried to establish a correlation between elastic constants of diamond and the anisotropy in wear (van Bouwelen, 2000), or the microscopic structure of diamond and the anisotropy of wear (van Bouwelen & van Enckevort, 1999). Both models, however, did not go beyond a simple phenomenological treatment.

3.05.3.2 Atomistic Simulations of Diamond Friction and Wear

The nature of tribological processes such as diamond polishing involves a "buried interface" that allows only limited online measurements of the mechanics and chemistry of surfaces in contact (Sawyer & Wahl, 2008). Most analysis is therefore carried out *postmortem*, with a necessary indirect inference of the underlying mechanisms. Therefore, the basic microscopic wear mechanisms are hard to elucidate by experiments alone, despite the enormous experimental progress achieved during one century of scientific research on diamond polishing that was described in the preceding sections. The grit particles that are embedded in the scaife are micron-sized and thus the crucial elementary wear processes act on the nanoscale. The maximum linear velocity of the scaife exceeds 30 m s^{-1}. At these speeds, an atomistic system displaces $\sim$100 atomic distances within 1 ns. Both scales are accessible in molecular dynamics (MD) calculations. Atomic scale simulations can hence complement experiments and provide valuable insights into the contact during sliding to answer the remaining questions. Some of these are the following: How is carbon removed from the diamond lattice? What explains the wear anisotropy? Why is most of the debris nondiamond carbon? Under which circumstance can crystalline debris form? Why is the wear rate in UHV reduced?

In MD simulations, the atoms are modeled as classical point particles whose trajectories are governed by Newton's equations of motion. Forces are derived from an interatomic potential energy function that reflects the atomic bonding behavior induced by the quantum mechanics of the valence electrons (Pettifor, 1995). MD is ideally suited to study a basic wear event during diamond polishing (**Figure 5**). During polishing, micron-sized asperities of the diamond workpiece collide with the diamond grits of the scaife. Collision times are of the order of 100 ns and accessible by MD. On the other hand, the length scale of 1 μm is still challenging for classical MD. Currently, there are two strategies to circumvent such a length-scale limitation: (a) studying smaller (nanoscale) asperities or (b) focusing on a region in the middle of the mesa-shaped diamond asperities and represent this region by a small MD system subject to lateral periodic boundary conditions (inset in **Figure 5**).

3.05.3.3 Sliding of Hydrogenated Diamond; the Mild Wear Regime

Some of the earliest MD work of friction and wear of diamond was carried out by Harrison & Brenner (1994). They used a novel interatomic potential (Brenner, 1990) that for the first time allowed the chemically accurate

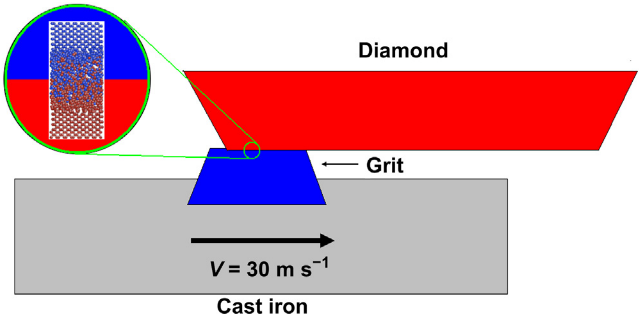

Figure 5 Schematic drawing of a basic wear event during diamond polishing. A micron-sized diamond particle (blue body embedded into the cast-iron wheel depicted in gray) collides with an asperity of the diamond workpiece (red). On the nanoscale, this collision can be represented by two flat diamond surfaces in relative motion (inset).

propagation of hydrocarbon systems consisting of a couple of hundreds of atoms over picoseconds simulation time. Their sliding system consistent of two hydrogen-terminated surfaces exposing the octahedral plane (thus using strategy (b) of the previous section). The primary wear event identified by Harrison and Brenner was the abstraction of surface hydrogen, or functional groups attached to the surface (**Figure 6(a)**). They found that the rate of abstraction and the nature of that reaction markedly depended on the sliding direction. This and a previous study (Harrison, White, Colton, & Brenner, 1992) also established a direction dependence of the friction coefficient. Absorbed hydrocarbons act as lubricant and lower the coefficient of friction (Harrison, White, Colton, & Brenner, 1993; Perry & Harrison, 1996).

The specific interaction between two atomic scale asperities that exposed the dodecahedral plane and consisted of a few tens of atoms was studied by Jarvis, Pérez, van Bouwelen, and Payne (1998) using chemically accurate quantum calculations. They found that the force to peel such an asperity off the surface is highest in the hard direction. Their final model proposed that wear in the soft direction on the dodecahedral plane progresses by peeling off individual carbon atoms (**Figure 6(b)**).

3.05.3.4 Collision of Nanoscale Diamond Asperities; the Severe Wear Regime

In most tribological simulations involving diamond (Harrison & Brenner, 1994), interatomic forces are computed using Brenner's reactive empirical bond-order (REBO) potential (Brenner, 1990; Brenner, Shenderova, Harrison, Stuart, Ni & Sinnott, 2002). While appropriate for equilibrium properties of matter, it has been pointed out that modification is necessary to properly describe severely stressed bonds under harsh contact

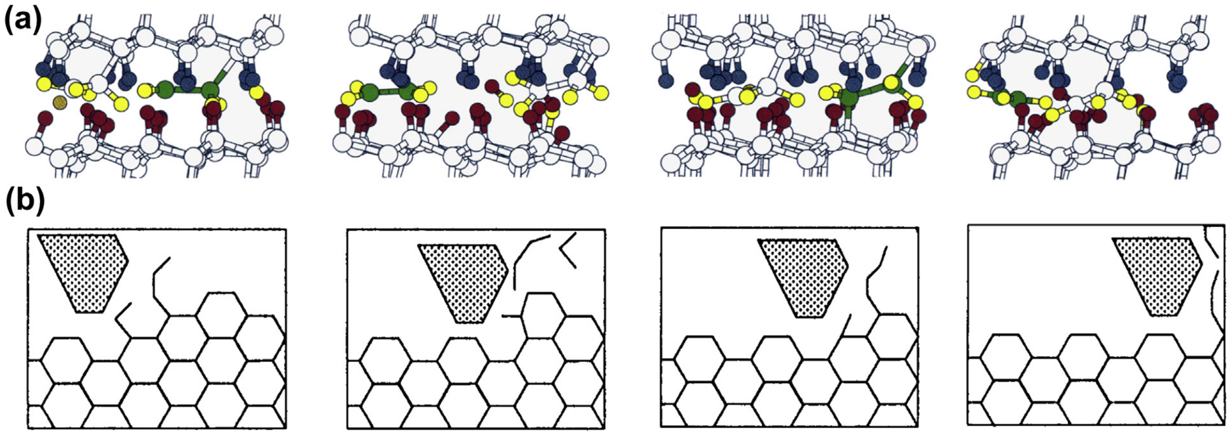

Figure 6 (a) Hydrogen abstraction events observed by Harrison and Brenner. In the temporal progression from left to right, the green hydrocarbon molecule forms an adhesive bridge between the two surfaces. Subsequent tribochemical stress leads to the breaking of both bonds that results in a free ethylene molecule. (b) Abrasion model proposed by Jarvis et al. A diamond asperity peels off individual layers of the {110} surface. Adapted from Harrison and Brenner (1994) and Jarvis, Pérez, van Bouwelen and Payne (1998) with permission.

conditions. Pastewka, Pou, Pérez, Gumbsch and Moseler (2008) proposed to dynamically adjust the interaction range of the potential to describe tribology of diamond and amorphous carbon. This allows bonds to be broken smoothly, hence avoiding the well-known overestimation of yield forces in interatomic potentials for covalent materials (Pastewka, Mrovec, Moseler, & Gumbsch, 2012). Studies on cracks and amorphous hydrocarbon using this modified REBO potential have shown good agreement with experiments and density functional theory (Pastewka, Pou, Pérez, Gumbsch & Moseler, 2008; Pastewka, Moser, Moseler, Blug, Meier, Hollstein, et. al. 2008; Pastewka, Moser, & Moseler, 2010). This preliminary work enabled accurate calculation of large asperity collision processes involving processes such as fracture and amorphization.

Scaling down the microscale asperity collision of diamond polishing to the nanoscale (strategy (a) of Section 3.05.3.1) makes basic wear processes accessible in MD simulations and provides crucial insights into the nature of diamond wear (Von Lautz, Pastewka, & Moseler, in preparation). **Figure 7** shows the typical outcome of such an MD simulation carried out with the modified REBO. Initially ($t = 0$ ps) the lower asperity is located in the center of the simulation cell while half of the upper asperity can be seen on the left border (note that due to the lateral periodic boundary conditions, the other half is shifted to the right side of the panel). In the first stage of the collision, the onset of plastic deformation and the abstraction of passivating groups (in the simulation, the asperities are covered with hydrogen atoms depicted as white spheres) can be observed ($t = 15$ ps). Later on, an amorphous zone develops between the two asperities ($t = 25$ ps) followed by a fracture event that results in the formation of a nanocrystalline diamond particle ($t = 33$ ps). After separation of the asperities, the diamond is covered by a thin layer of sp^2-hybridized amorphous carbon (a-C).

Generalizing this result to microscale asperity collisions, one can conclude that wear in diamond polishing involves at least three processes: (1) abstraction of surface passivation, (2) cold welding of asperities accompanied by plastic deformation and the formation of an a-C layer, and (3) abrasion of crystalline wear particles from the edge of the asperities. Different researchers studied each of these processes individually. Abstraction of surface passivation was described in detail earlier in this text and investigated by Harrison and Brenner (1994). Cold welding and formation of a-C was discussed in detail by Pastewka et al. (Pastewka, Moser, Gumbsch, & Moseler, 2011) and will be described in the following. The third process, abrasion of crystalline wear particles, has so far attracted the least attention from atomistic simulations, probably because the system sizes necessary to capture fracture of asperities are larger than what was accessible in state-of-the-art computer simulations until recently (Von Lautz, Pastewka, & Moseler, in preparation). Note, that the process chain (1)–(3) is still incomplete since it lacks the description of the final removal of the amorphous phase. In Section 3.05.4 "Removal scenarios for the amorphous phase; etching versus plowing" two additional processes will be described that finally provide a consistent atomistic wear model.

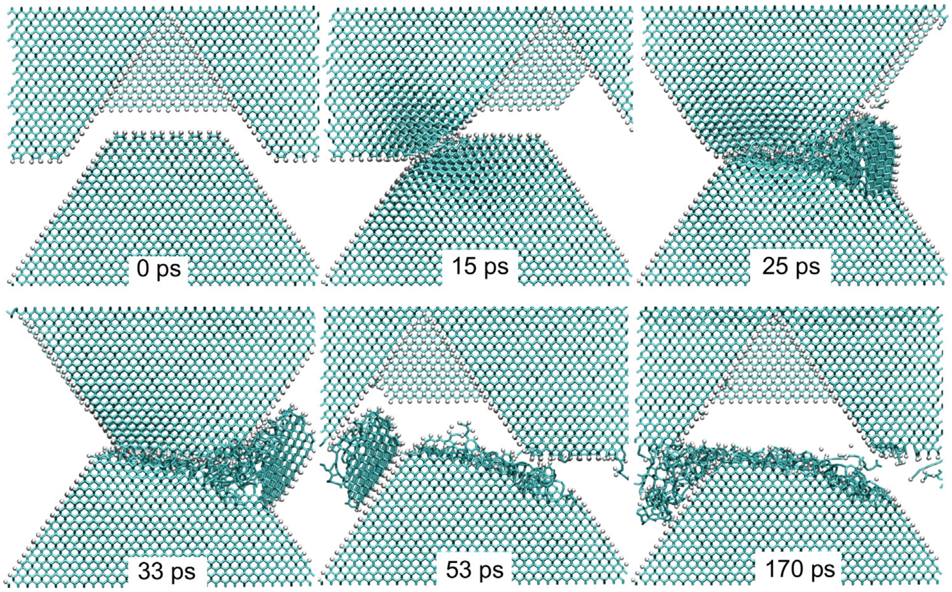

Figure 7 Collision of two nanoscale diamond asperities sliding with 10 m s^{-1}. The panels show snapshots at six different times. The horizontals facets of both asperities are cubic diamond planes, while the tilted side facets are octahedral surfaces. From Von Lautz, Pastewka, & Moseler. (In preparation).

In the following section, a more detailed description of Pastewka, Moser, Gumbsch, and Moseler's (2011) simulations and resulting conclusions for the mechanisms underlying the polishing of diamond will be given. It is very likely that similar processes occur in other tribological systems and lead to the well-known intermediate layer that develops at the sliding interface, sometimes termed Beilby layer (Beilby, 1903) in the case of machining (cutting or polishing) or "third-body" (Singer, 1998) in the case of bearing applications. Insights into the formation of this layer (for diamond polishing an amorphous carbon layer) within the simple single-element system diamond can thus aid the understanding of much more complicated multielement tribological systems, and allows insights into the mechanisms of nonabrasive wear. In this sense, diamond polishing in addition to its technical importance is also of central interest for fundamental tribologists (Fineberg, 2011).

3.05.3.5 Sliding of Two Flat Diamond Surfaces; the Cold-Welded Regime

The faces of diamond asperities in experimental polishing are typically more than two orders of magnitude wider than the ones displayed in **Figure 7**. Therefore, more time is available for the amorphous layer to grow in experiments than in the simulations described in Section 3.05.3.4. Nevertheless, the MD results shown in **Figure 7** capture the embryonic phase of a-C formation and show the basic mechanisms. In order to investigate the long-time evolution of the amorphous carbon layer, the simulation of two flat diamond surfaces in sliding motion (inset of **Figure 5**) can be used. Sliding of two unsaturated diamond surfaces with the experimental velocity of $v = 30\ \mathrm{m\ s^{-1}}$ and 10 GPa load leads to the gradual destruction of the diamond surfaces (Pastewka, Moser, Gumbsch, & Moseler, 2011; Moras, Pastewka, Gumbsch, & Moseler, 2011). The resulting amorphous interface layer grows steadily during sliding as shown exemplarily for a symmetric pairing of the $\{001\}$ surface rubbed in the $\langle 100 \rangle$ direction in **Figure 8**. This amorphization can be characterized as an sp^3–sp^2 order–disorder transition because the amorphous phase consists of roughly 60% sp^2 and 20% sp^1 carbon. Interestingly, upon separation of the two flat surfaces, the newly formed interfaces are covered by linear carbon chains—or (in more chemical terms) by carbynes. These are depicted in brown in the last panel of **Figure 8**. The presence of carbynes has important implications for the final material removal and will be discussed in detail in Section 3.05.4.

It is instructive to look at the speed of the order–disorder transition on different surface orientations (Pastewka, Moser, Gumbsch, & Moseler, 2011). As mentioned in Section 3.05.2.4, grit particles rotate in the cast-iron matrix during polishing experiments until a soft orientation faces the gemstone. Therefore, pairings of many $\{s\}\langle d \rangle$ orientations with either of the two soft orientations were considered by Pastewka, Moser, Gumbsch, & Moseler (2011). **Figure 9** shows how the thicknesses of the amorphous interface layer evolves on the $\{110\}\langle 100 \rangle$ surface and the thickness after 20 ns sliding for all scaife and gemstone orientations. A clear hierarchy emerges with $\{110\}\langle 100 \rangle$ exhibiting the highest and $\{111\}\langle 110 \rangle$ the lowest amorphization rate resembling the ordering of the experimental wear rates for different surface orientations (**Figure 9**). This suggests that the sp^3–sp^2 order–disorder transition is the crucial rate-limiting step in diamond polishing.

Interestingly, the anisotropy of the amorphization cannot be detected from the shear stress, which remains at roughly 15 GPa independent of crystallographic orientation and the sliding direction. This suggests that shear yielding occurs mainly in the amorphous phase. **Figure 10** shows the density, velocity, and temperature for a symmetric pairing of the $\{100\}\langle 100 \rangle$ surface after 20 ns sliding. The a-C is homogeneous in density and shows small-density oscillations close to the a-C/diamond interface reminiscent of fluid layering close to boundaries (Thompson & Robbins, 1990). In the middle of the a-C layer, the velocity profile is linear and

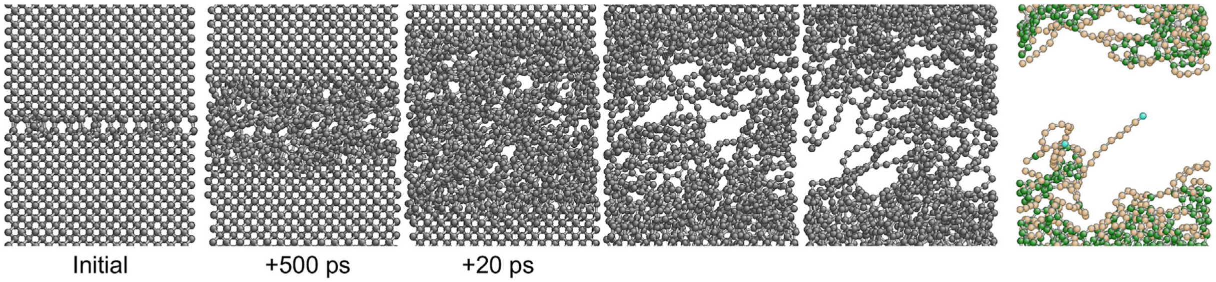

Figure 8 Snapshots from classical MD simulations of sliding and detachment of two diamond surfaces. An a-C zone with mainly sp^2 hybridized atoms (green spheres in the last panel) is formed and grows continuously during sliding. Upon detachment of the two surfaces, carbon chains (carbynes) form (sp^1 hybridized atoms depicted in brown). From Moras, Pastewka, Gumbsch, & Moseler (2011).

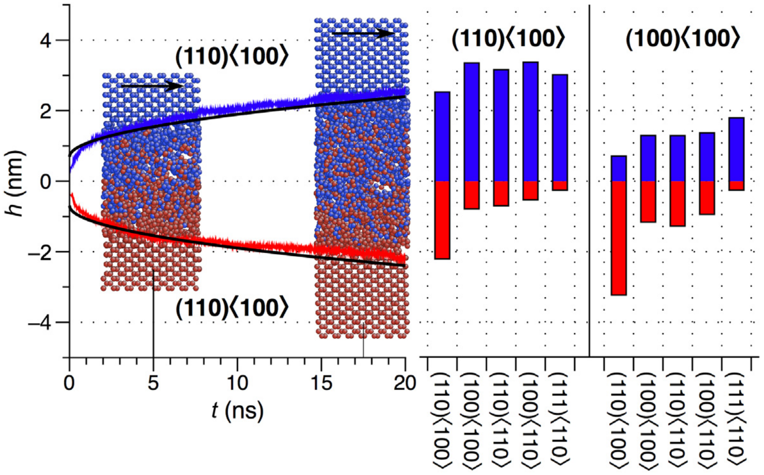

Figure 9 (a) Time evolution of the thickness of the amorphous layer for a symmetric pairing of the $\{110\}\langle 100\rangle$ surface. The insets show snapshots after 5 and 17.5 ns. The colors mark whether an atom stems from the top or bottom slab of diamond. Black solid lines: continuum model results. (b) Final thickness of the amorphous layer after 20 ns for various surface pairings. From Pastewka, Moser, Gumbsch, & Moseler (2011).

hence Couette-like. At the interface, the a-C phase sticks to the crystal, which is similar to fluid flow at large fluid–boundary interaction energies. While the Couette profile indicates fluidity, the temperature remains as low as 400 K (**Figure 10**). This is well below the melting point of diamond at 3500–5000 K (Bundy, Bassett, Weathers, Hemley, Mao, & Goncharov, 1996) that is accurately captured by the interatomic potential used in this study (Pastewka, Klemenz, Gumbsch, & Moseler, 2013). The latter observation rules out equilibrium melting as an explanation for the amorphization. Other arguments for equilibrium transitions can be ruled out on similar grounds (Pastewka, Moser, Gumbsch, & Moseler, 2011). Yet, the cohesive energy (or equivalent the heat of formation) of the amorphous phase is about 0.5–1.0 eV lower than for the diamond crystal. Hence, there must be some nonequilibrium mechanism that drives this phase transformation.

The observed sp^3–sp^2 order–disorder transition can be explained within a mechanochemical picture (Pastewka, Moser, Gumbsch, & Moseler, 2011). The mechanochemistry of force-driven surface reactions requires formalism beyond Arrhenius activation (Beyer & Clausen-Schaumann, 2005), which is at the heart of all equilibrium thermodynamical processes. Inspection of individual trajectories revealed that the amorphization happens an atom at a time (see supplementary movies in Pastewka, Moser, Gumbsch, & Moseler, 2011), suggesting a simple microscopic picture involving "pilot" atoms in the first amorphous adlayer that move slowly over the crystalline surface (**Figure 11**) and exert time-dependent forces on the terminating surface atoms. Depending on the chemical environment, these atoms are able to form a bond that is strong enough to remove the surface atom from its crystalline position, leading to an amorphization event. Assuming that the a-C

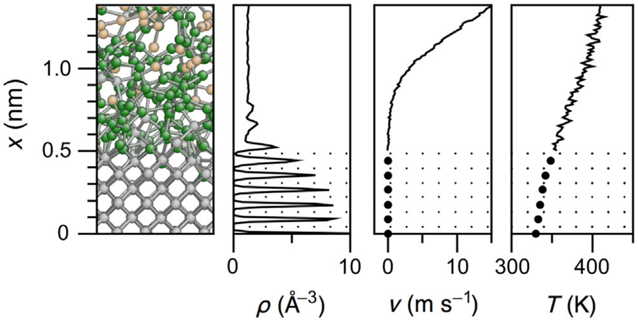

Figure 10 Snapshot of the $\{100\}\langle 100\rangle$ surface after 20 ns of sliding. The density, velocity, and temperature profile is a 1 ns average at 20 ns. The colors indicate atomic coordination. From Pastewka, Moser, Gumbsch, & Moseler (2011).

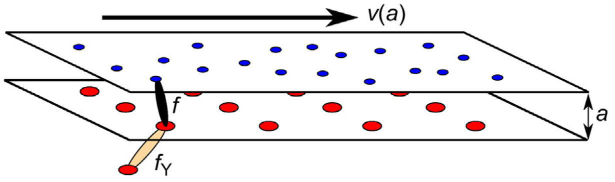

Figure 11 Pilot atom picture. A layer of amorphous carbon atoms (blue circles) creep over a terminal layer of diamond atoms (red) and act as pilots for the diamond atoms. The terminal diamond atoms are anchored with bonds (light brown) of strength detailed experimental analysis as well as modeling approaches to these planarization processes. The final picture will be of much higher complexity than the simplicity of the classical mechanical process described here.

pilot atoms slide over the diamond surface at a fixed height $a = 0.1$ nm (**Figure 10**) with a velocity $v(a)$, the time evolution of the thickness h of the a-C can be solved (Pastewka, Moser, Gumbsch, & Moseler, 2011) to give a dependence of the form $h(t) \propto \sqrt{t}$. This square-root behavior (the black curve in **Figure 9**) agrees with the evolution of the thickness of the amorphous zone from the MD (the red and blue curves in **Figure 9**) and with experimental observations on the time evolution of wear during polishing of diamond (Wilks & Wilks, 1972).

In this pilot-atom picture, it is straightforward to link the anisotropy in amorphization rate to the crystal structure. The important microscopic quantity is the force that a pilot needs to exert on a crystal atom to move it from the crystalline interfacial position to the amorphous phase. This force is easily computed from atomistic calculations. The top row in **Figure 12**a shows a top and side view of the octahedral {111}, dodecahedral {110} and cubic {100} planes. The topmost atoms have been saturated by hydrogen to mimic bonding to the amorphous phase. Breaking a colored bond in **Figure12**a leads to the propagation of the bonded atom to the first adlayer. This is an amorphization event. By stepwise elongating the length of an orange bond while equilibrating the rest of the system it is possible to determine the yield force f_Y. The respective force distance curves are given in 12b. These curves have a maximum that gives the value of f_Y.

These simulations also reveal that the most complex amorphization process happens on the softest {110} surface in the softest <100> direction. The details of this process are shown in **Figure 13**. There are two steps, the first of which is the flipping of a π-bonded zig-zag chain into an upright position. The second step involves the incorporation of that flipped zig-zag into the amorphous phase. It turns out, that the force required to flip the zig-zag is lower than any process on the {111} and {100} surfaces (see green bond in **Figure 12**). The process resembles the wear model proposed by Jarvis *et al.* (Jarvis, Pérez, Van Bouwelen & Payne, 1998) for the {110} surface (see **Figure 6**b).

3.05.4 Removal Scenarios for the Amorphous Phase; Etching vs. Plowing

Any correlation between amorphous interface thickness and experimental wear rate is based on the conjecture that the amorphous film is somehow removed after the two sliding surfaces are separated. Two mechanisms for the removal of the amorphous layer can be proposed on the basis of atomistic simulations. First, after separation of the two sliding partners the surface consists mainly of carbon chains (Figure 8). These are known to be unstable towards the formation of CO and CO_2 under atmospheric conditions (Casari, Li Bassi, Ravagnan, *et al.*, 2004a, 2004b). Additional quantum chemical calculations (Moras, Pastewka, Walter, *et al.*, 2011; Moras, Pastewka, Gumbsch & Moseler, 2011) show that very low barrier pathways for the oxidation of these chains exist. Carbon chains can be "scissored" by an O_2 molecule. This mechanism eventually leads to the formation of CO_2 as shown in **Figure 14**. The ambient air does thus act as a natural etchant. This conjecture is supported by the fact, that decreasing the air pressure leads to a decrease in wear rate (Hitchiner, Wilks & Wilks, 1984). The second removal mechanism is dust formation. A crystalline diamond edge sliding over the amorphous layer can lead to the formation of small amorphous carbon clusters (see **Figure 14**b). Such clusters are experimentally found besides wear tracks (van Bouwelen, Bleloch, Field & Brown, 1996) and could also detach as dust.

These removal scenarios allow for a comparison with *post-mortem* experiments and can explain some of the observed properties. However, other details still remain elusive. All simulations to date were carried out on samples smaller than the nanogrooves that are observed after polishing (Couto, Van Enckevort & Seal, 1994a). To understand the underlying self-organizing mechanisms much larger simulation volumes will be necessary

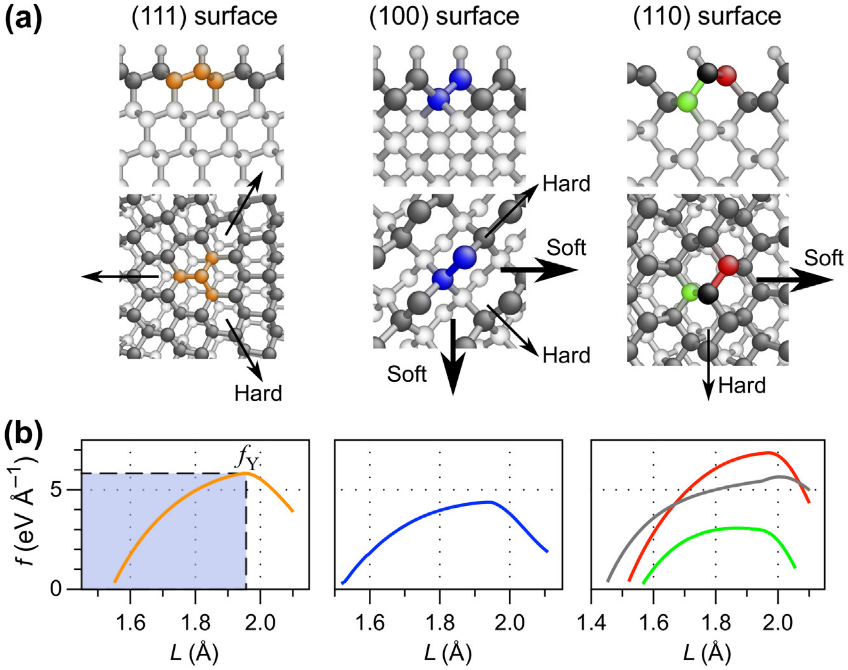

Figure 12 Microscopic origin of the amorphization. **(a)** Sketches of the low-index diamond {111}, {100} and {110} surfaces. The hard and soft polishing directions are marked by thin and thick arrows, respectively. Bonds that break during an amorphization event are in orange, blue, red and green. The large spheres represent carbon and the small spheres terminating hydrogen atoms. Whereas on the {111} and {100} surfaces all topmost atoms are connected to the amorphous phase, on the {110} surface only every second atom forms a bond to a-C. Therefore, the hydrogen termination on the {110} surface is chosen to give chemical environments similar to the molecular dynamics simulations. **(b)** Constraint force as a function of bond length for the bonds that are color-coded in (a). The red curve shows the yield function for the red {110} bond after flipping in an upright position. From (Pastewka, 2009).

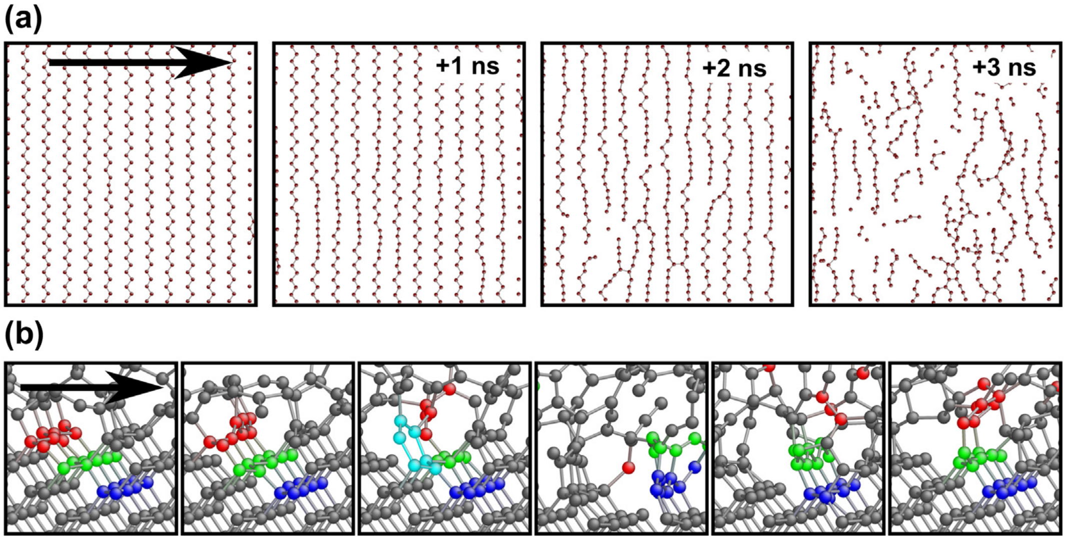

Figure 13 Elementary amorphization process on the {110} surface sliding in <100> direction. The arrows indicate the sliding direction. **(a)** View on a single atomic layer of a {110} surface exposing the π-bonded chains. These "zig-zag" chains are flipped into an upright position which leads to a straightening of the zig-zags when viewed from the top. Once flipped, atoms are pulled into the amorphous phase. **(b)** Close-up view of this process, where the different colors mark the relevant atoms in the respective zig-zag layers that are viewed from top in panel (a). The zig-zag is first flipped upright. This straightens a hexagon on the {110} plane (marked cyan in the third panel). By pulling the top of this hexagon, the next "zig-zag" layer (green) will be flipped into an upright position. This way, the original hexagon is flattened leading to a graphite-like structure. Subsequently, this hexagon is amorphized. From (Pastewka, 2009).

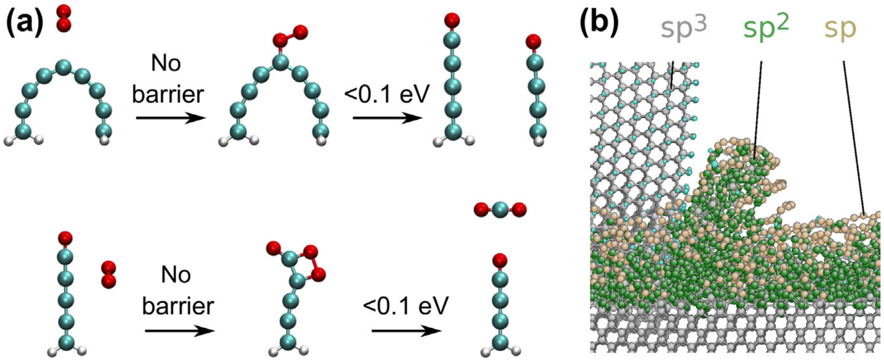

Figure 14 Removal of the amorphous carbon from the diamond surface. **(a)** Spin polarized density-functional calculations (Moras, Pastewka, Walter, et al., 2011; Moras, Pastewka, Gumbsch & Moseler, 2011) of the oxidation of carbyne chains reveal low barrier pathways towards the formation of CO_2. The carbon chains are initially saturated with two hydrogens that mimic an sp^2 substrate. **(b)** A diamond blade sliding over a diamond surface leads to the formation of an amorphous carbon cluster which could detach as dust. The blade is fully hydrogen terminated. From (Pastewka, Moser, Gumbsch & Moseler, 2011).

that require either advances in simulation methodology or faster computers. Correlation of the spectra obtained from diamond's triboluminescense (Hird, Chakravarty & Walton, 2007) with the underlying surface chemistry could also lead to more *in-situ* insights into the tribochemistry of diamond. A proper treatment of triboluminescence in computer models requires the treatment of excited electronic states during sliding. While such computer models exist, the simulation of two surfaces in contact during sliding motion is still at least a decade away.

3.05.5 Conclusions and Future Challenges

Over the last century, the science of diamond polishing has caught up to the art of polishing which has been passed down through many generations from at least the 14th century (Tolansky, 1961; Lenzen, 1966). The polishing process described in this chapter is this very classical process that is still used for gemstones. Coincidentally, this process delivers the highest surface quality and is therefore also highly relevant for modern technology (May, 2000). Recently chemical mechanical polishing (Krishnan, Nalaskowski & Cook, 2010) and other techniques (Schuelke & Grotjohn, 2013) have advanced to a point where they have become useful in technical applications. Complex slurry chemistry complicates detailed experimental analysis as well as modeling approaches to these planarization processes. The final picture will be of much higher complexity than the simplicity of the classical mechanical process described here.

Yet, insights into mechanical polishing yield valuable information for slurry processes or more generally wear of brittle materials. Tribological loading here activates surfaces to the point where they become perceptive to chemistry. This is indicated by many experimental works that show the formation of amorphous grit particles (van Bouwelen, Bleloch, Field, & Brown, 1996) over a dependence of the wear rate on air pressure (Hitchiner, Wilks, & Wilks, 1984) to atomistic insights gained from the computer simulations described above. It is likely that such mechanical activation occurs in most tribological processes, in particular when designed for wear and not for frictional applications.

What do we learn for practical applications from this analysis of diamond polishing? Even without slurry, the key to optimizing polishing is the influence of ambient chemistry. Tailoring the atmosphere during polishing by, for example, increasing the oxygen partial pressure could lead to higher wear rates without sacrificing surface quality. However, a simple postcontact oxidation mechanism (Moras, Pastewka, Gumbsch, & Moseler, 2011) ignores the fact that some of the oxygen is likely to stay at the surface and probably worked into the amorphous layer, thus changing its properties. Much is yet to be learned about the influence of other elements such as nitrogen and carbon dioxide that appear to also influence the wear rate on diamond. Recent advances in combined online friction measurements and spectroscopy (Sawyer & Wahl, 2008; Wahl & Sawyer, 2008) appear to be suitable for the study of wear in diamond—in particular since diamond is transparent for far-infrared radiation. Potential techniques here include in-situ FTIR, thermography, Raman spectroscopy, or triboluminescence. Another quickly advancing technique is nanotribology where single atomic force microscopy tips are used as asperity models (Bennewitz & Dickinson, 2011). In-situ nanotribological investigations have been carried out to understand the wear of metals (Merkle & Marks, 2008). Such in-situ analysis has recently been applied for the wear of silicon tips on a diamond substrate (Jacobs & Carpick, 2013). It seems straightforward to extend these studies to diamond sliding on diamond (Konicek, Grierson, Gilbert, Sawyer, Sumant, & Carpick, 2008), although contact pressure and sliding velocities will be different than those found in a typical scaife process.

Most of the polishing experiments discussed in this chapter have been carried out on single crystal diamonds. However, the expense of single crystals makes them unsuitable for industrial applications. Polycrystalline and ultrananocrystalline (UNCD) CVD diamond (Butler & Sumant, 2008) is cheaper, but also harder to polish because the polishing anisotropy can lead to a roughening of the surfaces (El-Dasher, Gray, Tringe, Biener, Hamza, Wild, et al. 2006). Yet, polishing of polycrystals to an extraordinary surface finish is possible (Biener, Ho, Wild, Woerner, et al. 2009), although most of the advanced polishing processes are neither patented nor disclosed in another medium. Excellent surface finish is important for most potential applications such as, for example, diamond electronics. For UNCD, it is conceivable that wear progresses by the removal of individual grains from the surface. The latter materials have grain sizes that are accessible in computer simulations (Mo, Stone, & Szlufarska, 2012) such that progress here appears within reach.

Despite all these complications, diamond's surface mechanics and chemistry is simpler than that of most materials. Indeed, surface geometry suggests a very simple explanation of the wear anisotropy (Fineberg, 2011). Each surface has a particular structure of atomic scale surface bumps that appear to determine the wear rate. The softest dodecahedral plane, for example, looks like parallel furrows, and sliding perpendicular to these trenches increases wear. It is these simple models that are most useful for experimentalist and theoreticians alike. Even without applications in mind, diamond is therefore an excellent material for understanding the fundamentals of friction and wear. Surely, diamond tribology has yet to reveal many insights into these important processes that impact our everyday life.

References

Ashby, M. F., & Lim, S. C. (1990). Wear-mechanism maps. *Scripta Metallurgica et Materialia, 24*, 805–810.

Bailey, A. I., & Seal, M. (1956). The surface topography of a polished diamond. *Industrial Diamond Review, 16*, 145–148.

Beilby, G. T. (1903). Surface flow in crystalline solids under mechanical disturbance. *Proceedings of the Royal Society of London, 72*, 218–225.

Bennewitz, R., & Dickinson, J. T. (2011). Fundamental studies of nanometer-scale wear mechanisms. *MRS Bulletin, 33*, 1174–1180.

Bergheimer, H. N. (1938). Die Schleifhärte des Diamanten und seine Struktur. *Neues Jahrbuch fuer Mineralogie, Geologie und Palaeontologie Beilagen Bd., 74*, 318–332.

Beyer, M. K., & Clausen-Schaumann, H. (2005). Mechanochemistry: the mechanical activation of covalent bonds. *Chemical Reviews, 105*, 2921–2948.

Biener, J., Ho, D. D., Wild, C., Woerner, E., Biener, M. M., El-Dasher, B. S., et al. (2009). Diamond spheres for inertial confinement fusion. *Nuclear Fusion, 49*, 112001.

Bowden, F. P. (1954). Redwood lecture: the friction of non-metallic solids. *Journal of the Institute of Petroleum, 40*, 89–103.

Bowden, F. P., & Brookes, C. A. (1966). Frictional anisotropy in nonmetallic crystals. *Proceedings of the Royal Society of London, Series A, 295*, 244–258.

Bowden, F. P., Brookes, C. A., & Hanwell, A. E. (1964). Anisotropy of friction in crystals. *Nature, 203*, 27–30.

Bowden, F. P., & Hanwell, A. E. (1964). Friction and wear of diamond in high vacuum. *Nature, 201*, 1279–1281.

Bowden, F. P., & Young, J. E. (1951). Friction of diamond, graphite, and carbon and the influence of surface films. *Proceedings of the Royal Society of London, Series A, 208*, 444–455.

Brenner, D. W. (1990). Empirical potential for hydrocarbons for use in simulating chemical vapor deposition of diamond films. *Physical Review B, 42*, 9458–9471.

Brenner, D. W., Shenderova, O. A., Harrison, J. A., Stuart, S. J., Ni, B., & Sinnott, S. B. (2002). A second-generation reactive empirical bond order (REBO) potential energy expression for hydrocarbons. *Journal of Physics: Condensed Matter, 14*, 783–802.

Bundy, F. P., Bassett, W. A., Weathers, M. S., Hemley, R. J., Mao, H. K., & Goncharov, A. F. (1996). The pressure-temperature phase and transformation diagram for carbon; updated through 1994. *Carbon, 34*, 141–153.

Butler, J. E., & Sumant, A. V. (2008). The CVD of nanodiamond materials. *Chemical Vapor Deposition, 14*, 145–160.

Cannara, R. J., Brukman, M. J., Cimatu, K., Sumant, A. V., Baldelli, S., Carpick, R. W., et al. (2007). Nanoscale friction varied by isotopic shifting of surface vibrational frequencies. *Science, 318*, 780–783.

Casari, C. S., Li Bassi, A., Ravagnan, L., et al. (2004a). Chemical and thermal stability of carbyne-like structures in cluster-assembled carbon films. *Physical Review B, 69*, 75422.

Casari, C. S., Li Bassi, A., Ravagnan, L., et al. (2004b). Gas exposure and thermal stability of linear carbon chains in nanostructured carbon films investigated by in situ Raman spectroscopy. *Carbon, 42*, 1103–1106.

Couto, M. S., van Enckevort, W. J. P., & Seal, M. (1994a). Diamond polishing mechanisms: an investigation by scanning tunnelling microscopy. *Philosophical Magazine Part B, 69*, 621–641.

Couto, M. S., van Enckevort, W. J. P., & Seal, M. (1994b). On the mechanism of diamond polishing in the soft directions. *Journal of Hard Materials, 5*, 31–47.

Couto, M. S., van Enckevort, W. J. P., & Seal, M. (1997). Friction tracks on diamond surfaces imaged by atomic force microscopy. *Diamond and Related Materials, 6*, 975–982.

Couto, M., van Enekevort, W. J. P., Wichman, B., & Seal, M. (1992). Scanning tunneling microscopy of polished diamond surfaces. *Applied Surface Science, 62*, 263–268.

Denning, R. M. (1953). Directional grinding hardness in diamond. *American Mineralogist, 38*, 108–117.

El-Dasher, B. S., Gray, J., Tringe, J., Biener, J., Hamza, A. V, Wild, C., et al. (2006). Crystallographic anisotropy of wear on a polycrystalline diamond surface. *Applied Physics Letters, 88*, 241915.

Ennos, A. E. (1953). The origin of specimen contamination in the electron microscope. *British Journal of Applied Physics, 4*, 101–106.

Enomoto, Y., & Tabor, D. (1981). The frictional anisotropy of diamond. *Proceedings of the Royal Society of London, Series A, 373*, 405–417.

Feng, Z., & Field, J. E. (1991). Friction of diamond on diamond and chemical vapour deposition diamond coatings. *Surface and Coatings Technology, 47*, 631–645.

Feng, Z., & Field, J. E. (1992). The friction and wear of diamond sliding on diamond. *Journal of Physics D: Applied Physics, 25*, A33–A37.

Feng, Z., Tzeng, Y., & Field, J. E. (1992). Friction of diamond on diamond in ultra-high vacuum and low-pressure environments. *Journal of Physics D: Applied Physics, 25*, 1418–1424.

Field, J. E. (1992). *The properties of natural and synthetic diamond.* London: Academic Press.

Field, J. E. (2012). The mechanical and strength properties of diamond. *Reports on Progress in Physics, 75*, 126505.

Fineberg, J. (2011). Tribology: diamonds are forever – or are they? *Nature Materials, 10*, 3–4.

Grillo, S. E., & Field, J. E. (1997). The polishing of diamond. *Journal of Physics D: Applied Physics, 30*, 202–209.

Grillo, S. E., & Field, J. E. (2000a). High reduction of diamond friction by oxygen containing liquids. *Diamond and Related Materials, 9*, 185–190.

Grillo, S. E., & Field, J. E. (2000b). Very low friction for natural diamond in water of different pH values. *European Physical Journal B, 13*, 405–408.

Grillo, S. E., Field, J. E., & van Bouwelen, F. M. (2000). Diamond polishing: the dependency of friction and wear on load and crystal orientation. *Journal of Physics D: Applied Physics, 33*, 985–990.

Grodzinski, P. (1949). Diamond and gemstone industrial production methods. *Industrial Diamond Review, 9*, 152–156.

Grodzinski, P. (1953). *Diamond technology: Production methods for diamond and gem stones.* London: N.A.G. Press.

Grodzinski, P., & Stern, W. (1949). Abrasion tests on diamonds. *Nature, 164*, 193–194.

Hagan, J. T. (1981). Impossibility of fragmenting small particles: brittle-ductile transition. *Journal of Material Science, 16*, 2909–2911.

Harrison, J. A., & Brenner, D. W. (1994). Simulated tribochemistry: an atomic-scale view of the wear of diamond. *Journal of the American Chemical Society, 116*, 10399–10402.

Harrison, J. A., White, C. T., Colton, R., & Brenner, D. W. (1992). Molecular-dynamics simulations of atomic-scale friction of diamond surfaces. *Physical Review B, 46*, 9700–9708.

Harrison, J. A., White, C. T., Colton, R. J., & Brenner, D. W. (1993). Effects of chemically bound, flexible hydrocarbon species on the frictional properties of diamond surfaces. *Journal of Physical Chemistry, 97*, 6573–6576.

Hird, J. R. (2002). *The polishing of diamond* (Ph.D. thesis). University of Cambridge.

Hird, J. R., Bloomfield, M., & Hayward, I. P. (2007). Investigating the mechanisms of diamond polishing using Raman spectroscopy. *Philosophical Magazine, 87*, 267–280.

Hird, J. R., Chakravarty, A., & Walton, A. J. (2007). Triboluminescence from diamond. *Journal of Physics D: Applied Physics, 40*, 1464–1472.

Hird, J. R., & Field, J. E. (2004). Diamond polishing. *Proceedings of the Royal Society of London, Series A, 460*, 3547–3568.

Hird, J. R., & Field, J. E. (2005). A wear mechanism map for the diamond polishing process. *Wear, 258*, 18–25.

Hitchiner, M. P., Wilks, E. M., & Wilks, J. (1984). The polishing of diamond and diamond composite materials. *Wear, 94*, 103–120.

Hukao, Y. (1955). Abrading tests of diamond. *Industrial Diamond Review, 15*, 107–109.

Jacobs, T. D. B., & Carpick, R. W. (2013). Nanoscale wear as a stress-assisted chemical reaction. *Nature Nanotechnology, 8*, 108–112.

Jarvis, M. R., Pérez, R., van Bouwelen, F. M., & Payne, M. C. (1998). Microscopic mechanism for mechanical polishing of diamond (110) surfaces. *Physical Review Letters, 80*, 3428–3431.

Knight, D. S., & White, W. B. (1989). Characterization of diamond films by Raman spectroscopy. *Journal of Materials Research, 4*, 385–393.

Konicek, A. R., Grierson, D. S., Gilbert, P. U. P. A., Sawyer, W. G., Sumant, A. V., Carpick, R. W., et al. (2008). Origin of ultralow friction and wear in ultrananocrystalline diamond. *Physical Review Letters, 100*, 235502.

Kraus, E. H., & Slawson, C. B. (1939). Variation of hardness in the diamond. *American Mineralogist, 24*, 661–676.

Krishnan, M., Nalaskowski, J., & Cook, L. (2010). Chemical mechanical planarization: slurry chemistry, materials, and mechanisms. *Chemical Reviews, 110*, 178–204.

Lenzen, G. (1966). *Produktions- und Handelsgeschichte des Diamanten.* Berlin: Duncker & Humblot.

May, P. W. (2000). Diamond thin films: a 21st-century material. *Philosophical Transactions of the Royal Society of London, Series A, 358*, 473–495.

McCarroll, B. (1969). Chemisorptive luminescence. *Journal of Chemical Physics, 50*, 4758–4765.

Merkle, A. P., & Marks, L. D. (2008). Liquid-like tribology of gold studied by in situ TEM. *Wear, 265*, 1864–1869.

Miyoshi, K., & Buckley, D. H. (1980). Adhesion and friction of single-crystal diamond in contact with transition metals. *Applications of Surface Science, 6*, 161–172.

Moras, G., Pastewka, L., Gumbsch, P., & Moseler, M. (2011). Formation and oxidation of linear carbon chains and their role in the wear of carbon materials. *Tribology Letters, 44*, 355–365.

Moras, G., Pastewka, L., Walter, M., et al. (2011). Progressive shortening of sp-hybridized carbon chains through oxygen-induced cleavage. *Journal of Physical Chemistry C, 115*, 24653–24661.

Mo, Y., Stone, D., & Szlufarska, I. (2012). Strength of ultrananocrystalline diamond controlled by friction of buried interfaces. *Journal of Physics D: Applied Physics, 45*, 069501.

Pastewka, L. (2009). *Multi-scale simulations of carbon nanomaterials for supercapacitors, actuators, and low-friction coatings* (Ph.D. thesis). Albert-Ludwig University of Freiburg.

Pastewka, L., Klemenz, A., Gumbsch, P., & Moseler, M. (2013). Screened empirical bond-order potentials for Si-C. *Physical Review B 87*, 205410.

Pastewka, L., Moser, S., Gumbsch, P., & Moseler, M. (2011). Anisotropic mechanical amorphization drives wear in diamond. *Nature Materials, 10*, 34–38.

Pastewka, L., Moser, S., & Moseler, M. (2010). Atomistic insights into the running-in, lubrication, and failure of hydrogenated diamond-like carbon coatings. *Tribology Letters, 39*, 49–61.

Pastewka, L., Moser, S., Moseler, M., Blug, B., Meier, S., Hollstein, T., et al. (2008). The running-in of amorphous hydrocarbon tribocoatings: a comparison between experiment and molecular dynamics simulations. *International Journal of Materials Research, 99*, 1136–1143.

Pastewka, L., Mrovec, M., Moseler, M., & Gumbsch, P. (2012). Bond order potentials for fracture, wear, and plasticity. *MRS Bulletin, 37*, 493–503.

Pastewka, L., Pou, P., Pérez, R., Gumbsch, P., Moseler, M., et al. (2008). Describing bond-breaking processes by reactive potentials: importance of an environment-dependent interaction range. *Physical Review B, 78*, 161402(R).

Perry, M. D., & Harrison, J. A. (1996). Molecular dynamics investigations of the effects of debris molecules on the friction and wear of diamond. *Thin Solid Films, 290–291*, 211–215.

Pettifor, D. G. (1995). *Bonding and structure of molecules and solids*. Oxford University Press.

Postek, M. T., & Evans, C. J. (1989). Inspection of single-point diamond turning tools at low accelerating voltage in a scanning electron-microscope. *Scanning Microscopy, 3*, 435–442.

Prior, J. R., & Champion, F. C. (1962). Electroluminescence in diamond. *Proceedings of the Physical Society, 80*, 849–859.

Samuels, B., & Wilks, J. (1988). The friction of diamond sliding on diamond. *Journal of Material Science, 23*, 2846–2864.

Sawyer, W. G., & Wahl, K. J. (2008). Accessing inaccessible interfaces: in situ approaches to materials tribology. *MRS Bulletin, 33*, 1145–1150.

Schuelke, T., & Grotjohn, T. A. (2013). Diamond polishing. *Diamond and Related Materials, 32*, 17–26.

Seal, M. (1958). The abrasion of diamond. *Proceedings of the Royal Society of London, Series A, 248*, 379–393.

Seal, M., & Menter, J. W. (1953). Crystallographic slip in diamond. *Philosophical Magazine, 44*, 1408–1410.

Singer, I. L. (1998). How third-body processes affect friction and wear. *MRS Bulletin, 23*, 37–40.

Slawson, C. B., & Kohn, J. A. (1950). Maximum hardness vectors in the diamond. *Industrial Diamond Review, 10*, 168–172.

Thompson, P. A., & Robbins, M. O. (1990). Shear flow near solids: epitaxial order and flow boundary conditions. *Physical Review A, 41*, 6830–6837.

Thornton, A. G., & Wilks, J. (1976). An examination of polished diamond surfaces in the electron microscope. *Journal of Physics D: Applied Physics, 9*, 27–35.

Tolansky, S. (1961). Some folklore and history of diamond. *Journal of the Royal Society of Arts, 109*, 743–763.

Tolkowsky, W. (1920). *Research on the abrading, grinding or polishing of diamond*. University of London.

van Bouwelen, F. M. (2000). Diamond polishing from different angles. *Diamond and Related Materials, 9*, 925–928.

van Bouwelen, F. M., Bleloch, A. L., Field, J. E., & Brown, L. M. (1996). Wear by friction between diamonds studied by electron microscopical techniques. *Diamond and Related Materials, 5*, 654–657.

van Bouwelen, F. M., Field, J. E., & Brown, L. M. (2003). Electron microscopy analysis of debris produced during diamond polishing. *Philosophical Magazine, 83*, 839–855.

van Bouwelen, F. M., & van Enckevort, W. J. P. (1999). A simple model to describe the anisotropy of diamond polishing. *Diamond and Related Materials, 8*, 840–844.

Von Lautz, J., Pastewka, L., & Moseler, M. (in preparation).

Wahl, K. J., & Sawyer, W. G. (2008). Observing interfacial sliding processes in solid–solid contacts. *MRS Bulletin, 33*, 1159–1167.

Walton, A. J. (1977). Triboluminescence. *Advances in Physics, 26*, 887–948.

Wang, Z. L., Feng, Z., & Field, J. E. (1991). Imaging friction tracks on diamond surfaces using reflection electron microscopy (REM). *Philosophical Magazine Part A, 63*, 1275–1289.

Watermeyer, B. (1982). *Diamond cutting: a complete guide to diamond processing*. Johannesburg: Centaur.

Whittaker, H., & Slawson, C. B. (1946). Vector hardness in diamond tools. *American Mineralogist, 31*, 143–149.

Wilks, E. M. (1952). An interferometric investigation of the abrasion hardness properties of diamond. *Philosophical Magazine, 43*, 1140–1145.

Wilks, E. M., & Wilks, J. (1954). The hardness properties of cube faces of diamond. *Philosophical Magazine, 45*, 844–850.

Wilks, E. M., & Wilks, J. (1959). The resistance of diamond to abrasion. *Philosophical Magazine, 4*, 158–170.

Wilks, E. M., & Wilks, J. (1972). The resistance of diamond to abrasion. *Journal of Physics D: Applied Physics, 4*, 1902–1919.

Wilks, E., & Wilks, J. (1991). *Properties and applications of diamond*. Butterworth-Heinemann.

Winchell, H. (1946). Observation on orientation hardness variations. *American Mineralogist, 31*, 149–152.

SECTION II

MATERIALS: GROWTH, PROPERTIES AND APPLICATIONS: CARBON-BASED DLC

3.06 Diamond-Like Carbon Films, Properties and Applications

John Robertson, Department of Engineering, Cambridge University, Cambridge, UK

3.06.1 Introduction

Diamond is the metastable, higher density phase of solid carbon (Figure 1). Diamond has a unique set of properties, such as a high Young's modulus, a high hardness, a wide band gap, a high thermal conductivity, good biocompatibility, and a high carrier mobility as a semiconductor. However, the cost of producing single crystals of diamond or polycrystalline diamond films is still too high. For other applications such as micromechanical devices and biosensors, nanocrystalline diamond films are useful because of their greater smoothness at lower cost.

On the other hand, there are many applications such as in protective coatings where diamond-like carbon (DLC) is the most suitable, due to its low cost, room-temperature deposition, good mechanical properties, absence of grain boundaries, extreme smoothness and biocompatibility. This chapter will describe the production, characterization, mechanical properties, and mechanical applications of DLC, with only a short discussion of its electronic properties.

3.06.2 Definition of Diamond-Like Carbon

Physically, DLC is an amorphous network solid, containing a high fraction of carbon sp^3 sites, but it can also contain sp^2 sites and often hydrogen (Robertson, 1986) (Figure 2). Its overall atomic composition can be

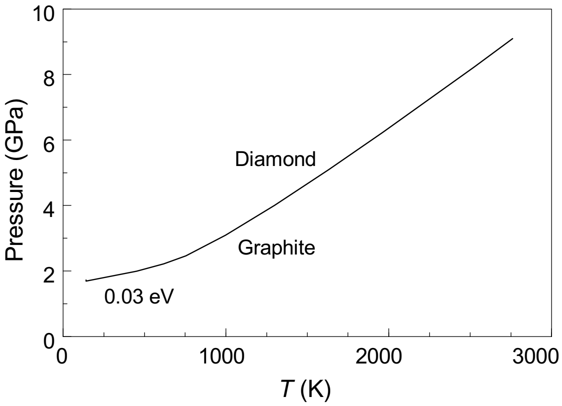

Figure 1 Berman–Simon phase diagram for carbon.

http://dx.doi.org/10.1016/B978-0-08-096527-7.00043-X

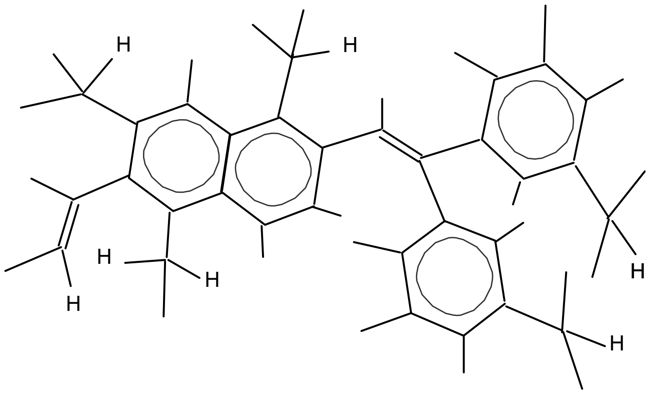

Figure 2 Ternary phase diagram of C, H system showing a-C:H and ta-C (Robertson, 2002a).

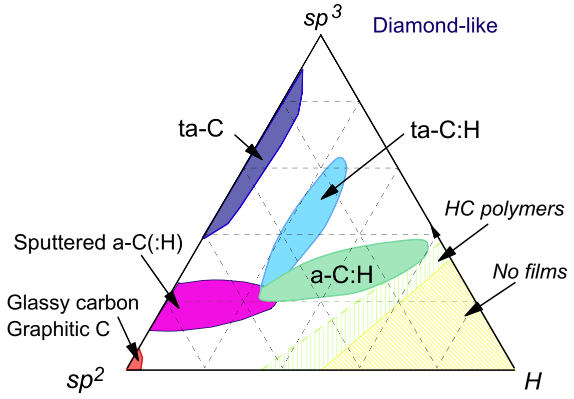

Figure 3 Schematic diagram of the bond network of a-C:H (Robertson, 2002a).

represented by the ternary phase diagram (Robertson, 1994b) (**Figure 3**). **Figure 3** emphasizes the names of different types of amorphous carbon, depending on the composition. sp^2 sites are always present to some degree in DLC, so the films are never truly "amorphous diamond". The maximum sp^3 content obtained so far occurs in tetrahedral amorphous carbon (ta-C) and is about 90% (Fallon et al., 1993; McKenzie, Muller, & Pailthorpe, 1991; Lifshitz, 1996; Polo, Andujar, Hart, Robertson, & Milne, 2000; Robertson, 2002a; Xu et al., 1996). The degree of diamond-like properties depends on the fraction of $C(sp^3)$–H bonding, in that $C–C(sp^2)$ and C–H bonds do not confer any mechanical strength, as will be explained later.

The material is always a thin film, not a bulk, because its sp^3 sites must be created by an ion beam process, whose range limit is only 10 nm, so that each layer must be created individually as sp^3.

3.06.3 Growth Methods

DLC is prepared by vacuum deposition methods as a thin film. There are also numerous reports of preparation of solid hydrocarbon films by electrolytic methods which are sometimes called "diamond like". However, these films are more accurately called hydrogenated pyrolitic carbon films rather than DLC, in that their sp^3-C sites arise only from hydrogenation.

DLC occurs by deposition from energetic ion beams, either of carbon ions, or of hydrocarbon ions (Angus & Hayman, 1988; Bubenzer, Dischler, Brandt, & Koidl, 1983; Dischler, Bubenzer, & Koidl, 1983; Lifshitz, Kasi, & Rabalais, 1989; Robertson, 2002a) (**Figure 4**). The carbon ion beams are created by the sputtering of graphite or by the formation of an arc from a graphite target. Hydrocarbon ions are created by a discharge or plasma formed in a hydrocarbon gas or by sputtering graphite in hydrogen-containing atmosphere. The

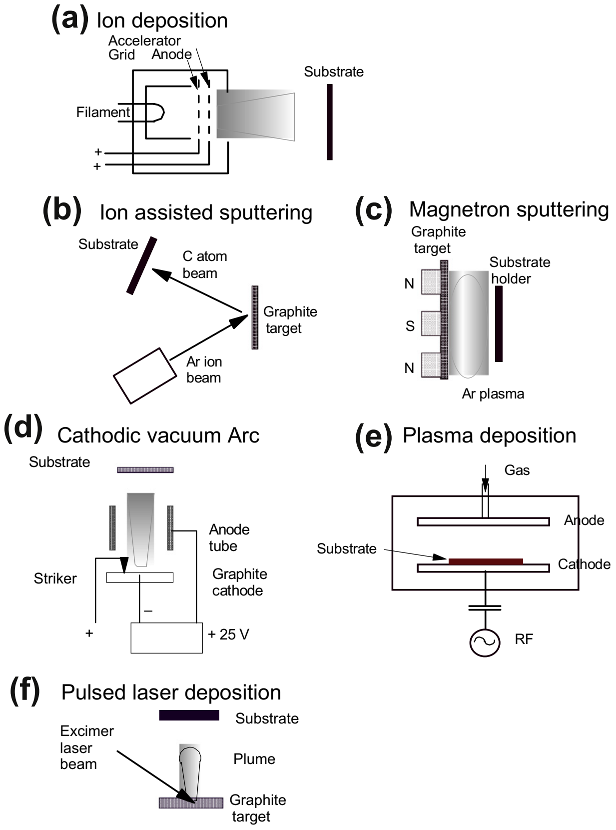

Figure 4 Schematics of various deposition systems for DLC (Robertson, 2002a).

optimum ion energy to deposit highly sp^3-bonded DLC is medium ion energy of about 100 eV per C atom, as explained in Section 3.06.4.

The simplest system to understand is ta-C. ta-C is deposited from an energetic carbon ion beam. The first experiments used the so-called mass selected ion beam (MSIB) system (Lifshitz et al., 1989), in which a specific carbon ion C^+ is selected from a plasma, and then accelerated and decelerated in a high vacuum to arrive at the substrate with a certain controlled ion energy. The substrate is typically at room temperature. It was found that its sp^3 fraction and thus the mass density depends only on the incident ion energy. However, MSIB systems are not widely available (Anders et al., 1994,1995).

A form convenient lab-scale system for ta-C deposition is the filtered cathodic vacuum arc (FCVA) (**Figure 5**). In this system, also at high vacuum (10^{-6} mbar), an arc is struck on a graphite target, and the intense carbon

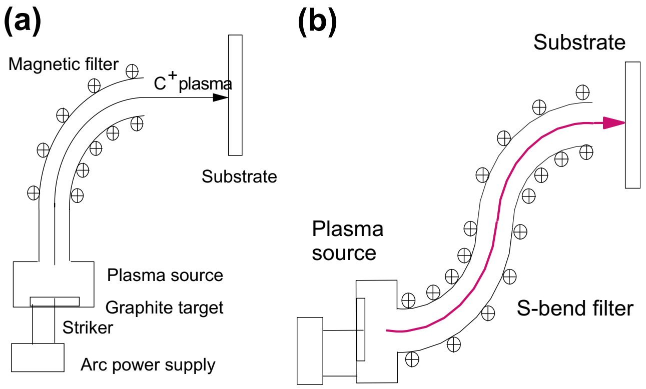

Figure 5 Schematic of filtered cathodic vacuum arc (FCVA) systems: (a) single-bend and (b) double-bend filters (Robertson, 2002a).

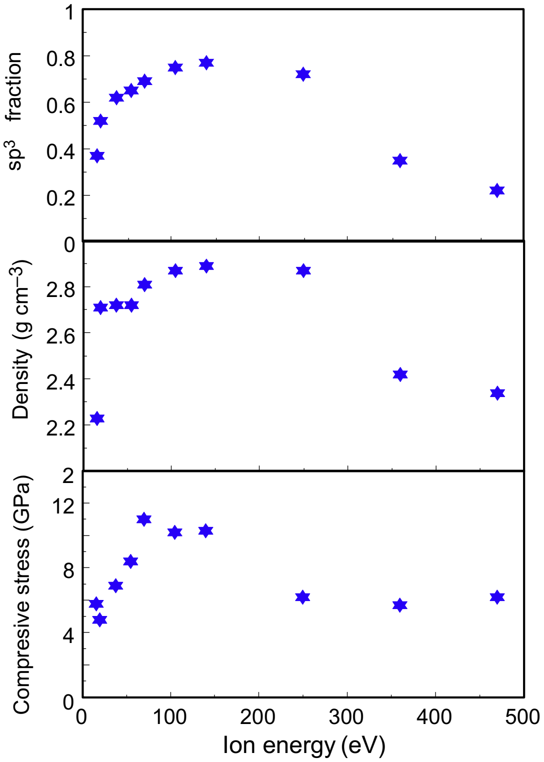

Figure 6 Measured sp^3 fraction vs ion energy for ta-C deposited by FCVA, compared to prediction from the subplantation model (Eqn [1]) (Robertson, 2002a).

plasma is then led through a filter system and deposited on a substrate held at room temperature. The cathodic arc has a very high ionization fraction, but it also contains numerous graphitic particles, which must be filtered out. This is done by passing the beam through a curved toroidal filter (**Figure 5(a)**). Unlike the MSIB, the carbon beam is a neutral plasma beam, not an ion beam. The toroidal filter causes the electrons to spiral around its axial magnetic field, guiding these to the substrate (Anders, Anders, & Brown, 1994, 1995). The more massive ions are forced to follow the electron stream to conserve charge neutrality. The depositing ion energy is controlled by biasing the substrate with a positive voltage, adding to the existing 20–40 eV intrinsic ion energy of the carbon plasma. Again, it is found that the sp^3 fraction and mass density of the resulting films depend only on the ion energy of the ion beam. This is very useful. FCVA machines have either of these two types of designs—direct current (DC) or pulsed.

Figure 6 shows the variation of sp^3 fraction, mass density, compressive stress and optical band gap on the ion energy, for room-temperature deposition by FCVA (Fallon et al., 1993). **Figure 7** shows that the variation of sp^3 fraction with ion energy is in fact slightly different for ta-C films grown by MSIB or FCVAs. The minimum ion energy for a reasonable sp^3 fraction is about 25 eV (Polo et al., 2000), which is the initial ion energy of the typical arc. The optimum ion energy is of order 100 eV. For MSIB, the optimum ion energy range extends over a fair range, from 25 to 600 eV. The compressive stress is an undesirable by-product of the deposition mechanism, but it is essential for the process of forming sp^3 bonding. The maximum sp^3 content can exceed 80% by FCVA or MSIB methods; the highest sp^3 content is about 88% (Polo et al., 2000; Lifshitz, 1996; Xu et al., 1996). The growth rates achievable by FCVA can be high, nanometers per second, as long as the filters are efficient.

It is also possible to form hydrogen-free a-C films with considerable sp^3 content by magnetron sputtering (**Figure 4**). The sputtering methods are widely used industrially, and more versatile than cathodic arcs, but they tend not to reach the very high sp^3 values achievable by FCVA-grown ta-C. The magnetron is set up to be unbalanced. This leads to a cobombardment of the growing film with energetic Ar ions as well as the incident C^+ ions. A second variant has a separate beam for C^+ and Ar^+ ions. The sp^3 content does not reach the high values in sputter deposition because the system is usually run at moderate pressures, so that the incident beams contain unenergetic species as well as energetic ions.

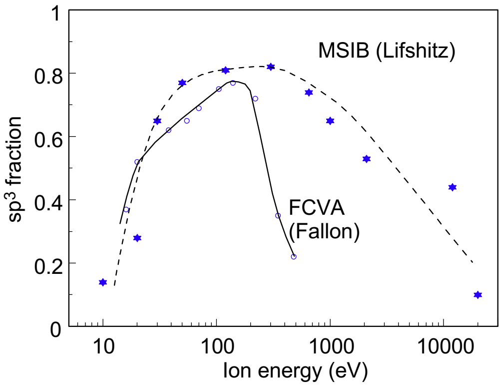

Figure 7 Comparison of sp^3 fraction of ta-C deposited by FCVA and by MSIB (Robertson, 2002a).

The more common type of DLC is hydrogenated amorphous carbon (a-C:H) which can be formed by plasma-enhanced chemical vapor deposition (PECVD) (Bubenzer et al., 1983; Dischler et al., 1983; Koidl, Wagner, Dischler, Wagner, & Ramsteiner, 1990), or by reactive sputtering with hydrocarbon precursors (**Figure 4**). The standard 13.6 MHz parallel plate PECVD reactor runs at moderate pressures of about 0.01 mbar for best results. The radiofrequency (RF) power creates a plasma of typical density 10^9 ions cm^{-3}. Due to the larger mobility of electrons than ions, there is a net negative current to the electrodes and side walls, so that plasma body biases itself positively to remain on average neutral (**Figure 8**). This creates an ionized depletion zone called the sheath over which this voltage is dropped. The DC bias voltage equals roughly the peak of the applied AC voltage (Bubenzer et al., 1983). This DC voltage accelerates the ions to the substrate. However, because the gas pressure is higher than in FCVA, the ions undergo collisions and loose perhaps 70% of the peak ion energy, so the average ion energy at the substrate is only ~30% of the applied voltage, and is not constant through the AC cycle. **Figure 9(a)** shows a typical ion energy distribution for PECVD. The other problem is that energetic ions contribute only about 10% of the total film-forming flux in these conditions. The remaining 90% comes from unenergetic neutral species. The parallel plate RF PECVD reactor is low cost, versatile and efficient. But it does not produce DLC with the highest sp^3 fraction. The maximum fraction of C (sp^3)–H is typically 25%.

Improved DLCs can be deposited by so-called high-density plasmas, such as those produced by electron cyclotron resonance (ECR) sources, plasma beam sources (PBS) or electron cyclotron wave resonance (ECWR)

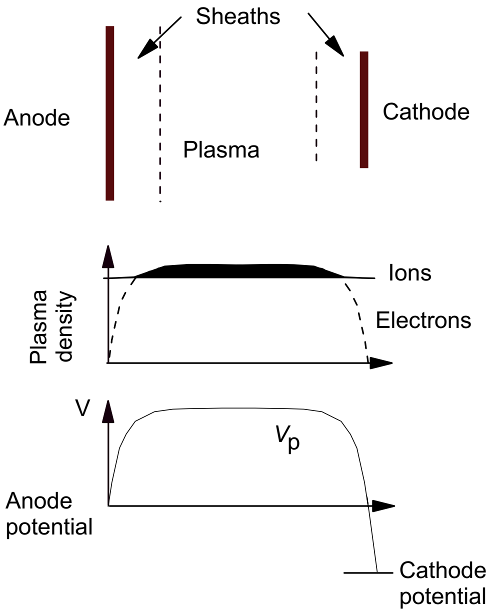

Figure 8 Electron and ion distributions which create sheaths between the neutral plasma and the walls in PECVD.

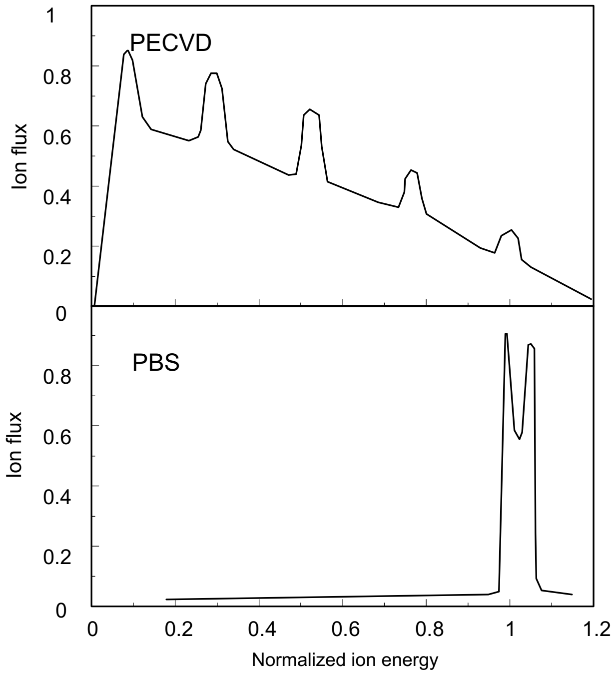

Figure 9 Ion energy distributions in conventional plasma deposition at 0.01 mbar pressure and in the plasma beam source (Robertson, 2002a).

reactors (Morrison et al., 1999; Sattel, Robertson, & Ehrhardt, 1997; Weiler et al., 1994, 1996; Weiler, Lang, Li, & Robertson, 1998; Yoon, Yang, & Rusli, 1998) (**Figure 10**). High-density plasmas run at lower pressures (10^{-3} Torr or less) to increase the ionization fraction. To do this, a magnetic field must be applied, to increase the electron path length and to create the plasma at these low pressures. Plasma densities from 10^{11} and 10^{12} cm^{-3} are possible with the best of these methods. The lower operating pressure means that the ions undergo fewer collisions with gas molecules and loose less of their energy. The ion energy distribution becomes much sharper and centered on the applied bias voltage (**Figure 9(b)**). The ideal plasma source is the one in which there is independent control of both the plasma power (ion flux/growth rate) and the ion energy. This is possible with ECR and ECWR plasmas, and by a mechanical method in the PBS. The film-forming flux in these systems approaches 100% (Weiler et al., 1998), as in the FCVA and MSIB systems. This means that the sp^3

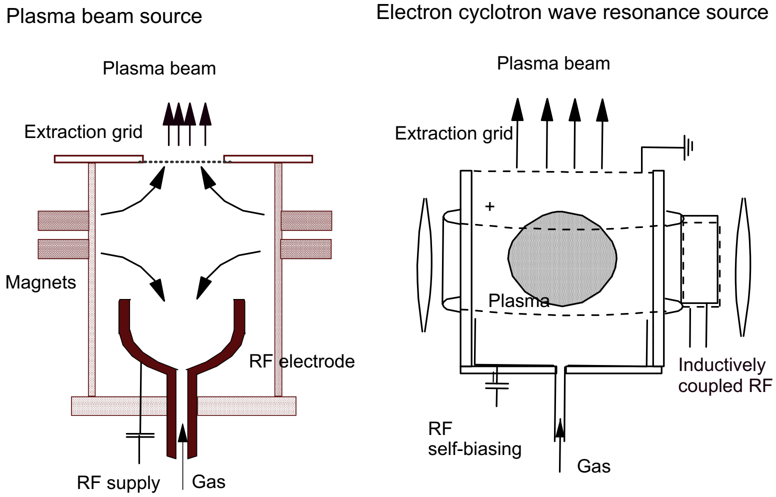

Figure 10 Schematic diagrams of the plasma beam source and the ECWR source (Robertson, 2002a).

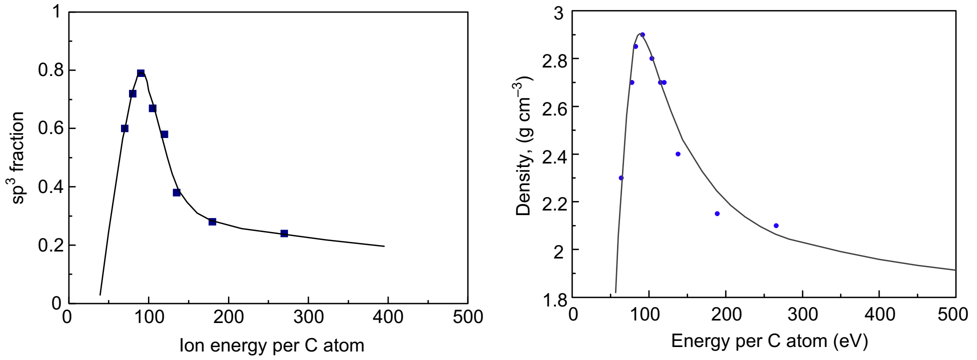

Figure 11 (a) sp3 fraction and density vs ion energy per C atom, for PBS deposited ta-C:H. (b) Density vs bias voltage per C atom for PBS-deposited ta-C:H.

fraction can approach the highest levels. This is shown in **Figure 11**, where the high-density plasma systems produce so-called ta-C:H (**Figure 3**).

A further factor of importance is the film growth rate. It is useful to choose the precursor gas to maximize the growth rate. The observed growth rate depends mainly on the ionization potential of the precursor gas (**Figure 12**), so that acetylene (C_2H_2) is advantageous (Weiler et al., 1996). C_2H_2 is also useful in having a low H/C fraction. However, it does suffer from impurity gases used to stabilize it.

A number of high-deposition-rate plasma sources are now available, such as the cascade arc, and high-rate microwave sources (Boutroy et al., 2006; Lusk et al., 2008; Sullivan, Saied, & Zaharai, 2011; Zaharia et al., 2007). An important recent development is the attempt to deposit DLC by atmospheric pressure plasmas, particularly for roll to roll operations (Kodama, Shirakura, Hotta, & Suzuki, 2006; Ladwig, Koch, Wenski, & Hicks, 2009; Sasaki, Kodama, Hayashi, Shimo, & Suzuki, 2010; Suzuki & Kodama, 2009).

It is very useful to summarize the practical advantages of DLC as a coating material by comparing its growth rate with that of various types of diamond (Robertson, 2008). Thin-film diamond is grown by chemical vapor deposition (CVD), typically in a microwave-assisted CVD reactor from hydrogen-diluted methane plasma. The growth species is the methyl radical, CH_3. The growth mechanism involves the thermally activated abstraction of hydrogen from surface C–H bonds in an Eley–Rideal mechanism (Butler & Woodin, 1993; Goodwin, 1993), and this leads to a strong temperature dependence of the growth rate with an activation energy of 1.2 eV (Kondoh, Ohta, Mitomo, & Ohtsuka, 1991) (**Figure 13**). This limits the growth rate. The use of high-power, high-methane content plasmas has considerably increased the growth rates, within the same mechanistic framework (Silva et al., 2009). It is also possible to grow ultrananocrystalline diamond with smaller temperature dependence (McCauley, Gruen, & Krauss, 1998; Williams, 2011), so that temperatures down to ~400 °C are possible (**Figure 1**). Again the growth species is mainly CH_3. Recently, Tsugawa, Kawaki, et al. (2011) used a high-power plasma to grow nanocrystalline diamond down to very low temperatures of order 100 °C, with an implied activation energy

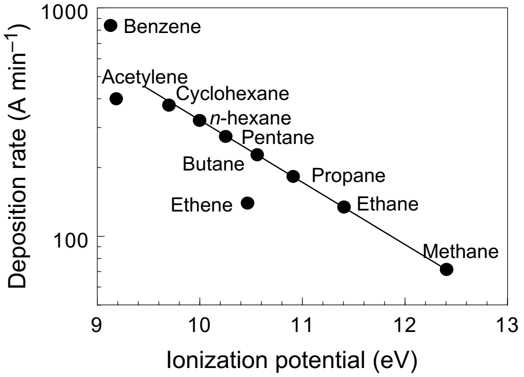

Figure 12 Deposition rates of a-C:H by PECVD for various precursor gases vs gaseous ionization potentials, after Koidl et al. (Koidl et al., 1990; Robertson, 2002a).

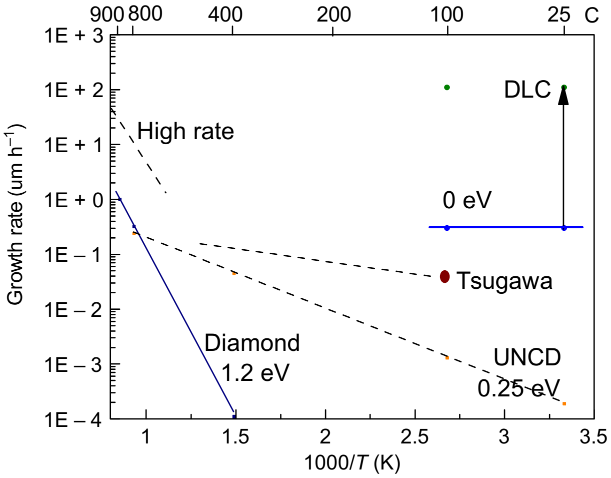

Figure 13 Typical growth rates and temperature dependences of diamond, ultrananocrystalline diamond and diamond-like carbon.

of 0.1 eV. However, this plasma type is costly, and not scalable. Overall, we see that the growth rate of DLC at room temperature would be 12 orders of magnitude higher than that of standard diamond, and about 3–4 orders of magnitude higher than that of the Hasegawa method (Robertson, 2008). Note that CVD creates sp^3-bonded diamond, because the hydrogen termination maintains the sp^3 bonds of the surface layer.

3.06.4 Deposition Mechanism of DLC

DLC has a fundamentally different growth mechanism to that of diamonds—it is physical vapor deposition (PVD). For DLC, a large fraction of the film-forming flux must be energetic species (ions). This energy causes the ions to be "subplanted" (subimplanted) below the film surface to form a densified phase (Angus & Hayman, 1988), where they adopt the denser, metastable sp^3 configuration instead of the sp^2 configuration (Robertson, 1993; Robertson, 1994a). As the growth mechanism is PVD, it is not thermally activated. This means that DLC can be grown at high rates at room temperature, a tremendous practical advantage. Typical growth rates are 0.1–1 nm s^{-1} (or 0.3–3 μm h^{-1}), with values up to 20 nm s^{-1} being possible (**Figure 13**) (Robertson, 2002a; Dischler et al., 1983).

The deposition mechanism giving rise to the sp^3 bonding is called *subplantation* (Lifshitz, 1996). Only energetic ions participate. Other depositing species of low energy (<10 eV) will simply stick to the outer film surface, forming sp^2 sites, or bounce off, according to the sticking probability of that species. If the ion energy exceeds a penetration threshold energy of about 30 eV, the ion will penetrate the outer atomic layer of the film and enter a subsurface site (**Figure 14(a)**) (Robertson, 1993; Robertson, 1994a). The penetration densifies the network locally, and this densification converts sp^2 sites into sp^3 sites. The ion energy is higher than any possible nucleation barrier to form a new phase, so this process is not thermally activated.

Subplantation increases in efficiency with ion energy, and reaches almost 100% at 100 eV. However, at higher ion energies, the ions have excess energy, which is converted into vibrations and atomic displacements which allow the densified material to relax. The excess energy is lost by various stopping processes, such as phonon emission or atomic displacements in the host lattice. A simple model of this process is the thermal spike (Davis 1993). This model says that the ion energy converts mostly into heat within a small volume, and this volume expands and cools down under conservation of energy, spreading the energy by equipartition across all atoms within that volume. This describes the temperature evolution. The local heating allows thermally activated relaxation of excess density by diffusion of atoms to the surface. This leads to a competition between densification and relaxation. The fractional increase in density by subplantation is (Robertson, 1994a)

$$\frac{\Delta\rho}{\rho} = \frac{f\phi}{1 - f\phi + 0.016\left(\frac{E_{\mathrm{i}}}{E_0}\right)^{5/3}} \qquad (1)$$

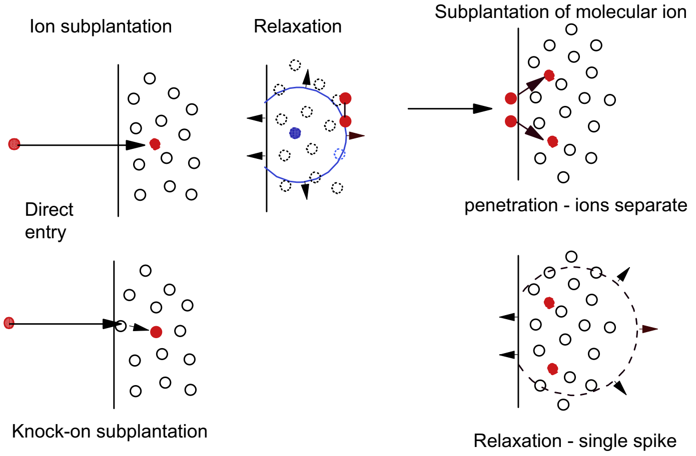

Figure 14 Subplantation and relaxation mechanisms occurring during energetic ion beam deposition of a-C, and for ta-C:H.

where E_i is the ion energy, E_0 is the carbon diffusion activation energy ($\sim$3 eV), ϕ is the fraction of energetic ions in the deposition flux, and f is the penetration fraction given by

$$f = 1 - \exp\left(-\frac{E_i - E_p}{E_s}\right) \tag{2}$$

where E_p is the penetration threshold ($\sim$30 eV) and E_s is the spread parameter. **Figure 6** shows the predicted variation of density with ion energy, it reaches a maximum at roughly 100 eV. Other variants of this model have been proposed.

Experimentally, in ta-C, the ion energy for maximum sp^3 content is found to be about 100 eV, consistent with this model (Figures 6, 7), but it varies somewhat with deposition method, whether it is FCVA or ion beam, etc (Fallon et al., 1993; McKenzie et al., 1991; Polo et al., 2000; Xu et al., 1996). Ion energies as low as 30 eV can give adequate sp^3 contents in some deposition systems.

Turning to PECVD, there are two basic processes during the plasma deposition of a-C:H, the subplantation of carbon ions, and the preferential sputtering of hydrogen (Boutard, Moller, & Scherzer, 1988; Jacob, 1998; von Keudell, Schwarz-Sellinger, & Jacob, 2001; Robertson, 1994a; Robertson, 2002a) (**Figure 15**). Incoming energetic molecular ions disintegrate on the film surface, sharing their kinetic energy between the component atoms according to momentum conservation, so energy mainly goes to the carbon atoms (Weiler et al., 1994, 1996). The carbon ions then penetrate the film as in the a-C case above. Low-energy ions just stick to the other surface, as above. The second process is that energetic C atoms cause a preferential displacement of hydrogen from C–H bonds, and the released hydrogen recombine into H_2 molecules and exit the film (**Figure 14(b)**).

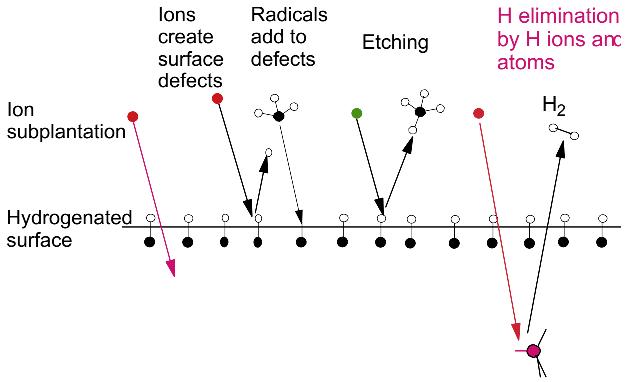

Figure 15 Ion bombardment and preferential displacement processes during deposition of a-C:H (Robertson, 2002a).

This leads to two dependences on ion energy. If the ion film-forming fraction (ϕ) is high, as in high-density plasmas, this produces ta-C:H with a hydrogen content under 30% over most of the ion energy range, and the sp^3 and density both showing a clear maximum at around 100 eV per C atom (Weiler et al., 1996), as in ta-C. Note that the energy per C atom in the molecule is half the bias voltage, for C_2H_2. A typical example of the energy dependence of the density of ta-C:H for deposition from the PBS is shown in **Figure 11**.

On the other hand, if the ion fraction ϕ is low, as in conventional PECVD, then the dominant trend is a decline in hydrogen content with increasing ion energy (Robertson, 2002a; Koidl et al., 1990; Robertson, 1991). The C–C sp^3 fraction does show a maximum at $\sim$100 eV, but this effect is outweighed by the variation of the C–H content. At low ion energy, the dominant species is C–H bonds, not C sp^2 sites, the film is called polymeric a-C:H. It is a low-density, low-hardness film with high sp^3 fraction. But the sp^3 fraction comes from chemical saturation of the C=C bonds by hydrogen (CVD) as C–H bonds, not the PVD process of subplantation. At $\sim$100 eV, the hydrogen content has declined to $\sim$35% atomic fraction. The fraction of C–C sp^3 bonds and the mass density now reaches a maximum (**Figure 16**). At ion energies over 300 eV, the H content has decreased further, subplantation is now in the relaxation regime, and the dominant species is C sp^2 sites. The density again declines. Thus, there is a clear contrast between the behavior of a-C:H and the ta-C:H at low ion energy, it is polymeric in a-C:H and more graphitic in ta-C:H. Note, the bias voltage necessary to achieve the ion energy will be higher in higher pressure plasmas due to ion collisions.

There are two aspects of the deposition mechanism that are not fully settled. One is the temperature dependence of deposition in ta-C (Chhowalla, Robertson, Chen, Silva, & Amaratunga, 1997; Sattel et al., 1997), and the second is the stress. If ta-C is deposited in a continuous (nonpulsed) process, as in DC FCVA, then there is a transition temperature T_1 of order 150 °C above which the film is no longer fully sp^3, but is mainly sp^2 and rougher (Chhowalla et al., 1997; Sattel et al., 1997). This T_1 decreases with increasing ion energy. Presumably, the substrate temperature adds to the effect of the thermal spike effect in promoting atomic relaxation. However, in any simple analysis, this requires the thermal energy kT_1 (0.1 eV) to be of similar magnitude to the relaxation activation energy E_0 in Eqn [1] ($\sim$3 eV) (Chhowalla et al., 1997), which is clearly not the case. The problem was solved empirically by defining a more complex configuration diagram for the implanted ions (Robertson, 2005). Implantation creates interstitials, which are mobile and need only a small activation energy to convert from sp^2 to sp^3, but an ion already within the lattice needs the larger energy E_0 to excite into the interstitial state, before it can relax from sp^3 to sp^2. This rationalizes use of small and large activation energies simultaneously.

The process is more completely described by molecular dynamics (MD) by Marks (Marks, Cover, & Kocer, 2006). He pointed out that MD must correctly handle infrequent events to describe the relaxation processes correctly. Simulated annealing is used to do this.

The second controversial topic is the role of stress in the sp^2 to sp^3 transition. McKenzie et al. (1991) have emphasized that the sp^2 to sp^3 transition can be viewed as a thermodynamic transition, defined by a critical

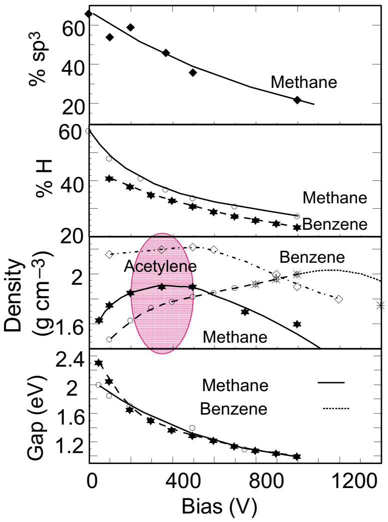

Figure 16 Variation of sp^3 fraction, density, hydrogen content and optical band gap of plasma-deposited a-C:H as a function of bias voltage (ion energy equals about 0.4 of bias voltage) (Robertson, 2002a).

pressure or compressive stress for transition to the denser sp^3 phase. However, a wide collection of experimental data suggests that while a high stress favors sp^3 bonding, the boundary is broad, and there is no one-to-one correspondence (Ferrari, Rodil, Robertson, & Milne, 2002). Recently, Lau et al. (2008, 2009) revisited this proposal and showed data apparently giving a sharp transition at a certain pressure. However, the ion energy values were not quoted. The difficulty in this viewpoint is that such a transition should be universal over deposition methods; however, there are numerous cases such as Schwan et al. (1996) where films with huge compressive stresses were not very sp^3-rich. It is difficult to understand why not in this model.

3.06.5 Basic Properties

3.06.5.1 Atomic Structure

Crystalline diamond consists of only sp^3 sites, and so an ideal crystalline diamond has a band gap of 5.5 eV with no gap states. The sp^3 bonds of crystalline diamond are very strong and are the source of diamond's large Young's modulus, high Debye temperature, and high carrier mobility. Grain boundaries in polycrystalline diamond introduce some sp^2 sites and their π states create gap states and cause subgap optical absorption.

DLC always contains both sp^3 and sp^2 sites, and this makes its electronic structure fundamentally different to that of ideal diamond. The sp^2 sites tend to form clusters to lower their free energy. ta-C is an atomic disordered alloy of sp^3 and sp^2 sites, where the sp^2 sites are not strongly clustered. This means that the density depends linearly on the sp^3 content (Ferrari et al., 2000; Ferrari, Robertson et al., 1999; Robertson, 1986; Waidmann, Knupfer, Fink, Kleinsorge, & Robertson, 2001), as seen experimentally (**Figure 17**) and also in theoretical calculations (Drabold, Fedders, & Grumbach, 1996; Galli, Martin, Car, & Parrinello, 1990; Jungnickel, Frauenheim, Proezag, Blaudeck, & Stephan, 1994; Kelires, 1993; Marks, McKenzie, Pailthorpe, Bernasconi, & Parrinello, 1996; McCulloch, McKenzie, & Goringe, 2000; Wang, Ho, & Chan, 1993) (**Figure 18**). The line for ta-C:H lies at a lower density value in **Figure 17** (Ferrari et al., 2000; Yoon et al., 1998).

The Young's modulus depends on the fraction of C–C sp^3 sites, as only the sp^3 sites contribute significantly to the modulus (Robertson, 1992). The C–H bonds add no rigidity to the network, so that the Young's modulus depends on only the C–C coordination and thus on the sp^3 fraction (Robertson, 1992; Robertson, 1994a; Tamor, Vassell, & Cardunder, 1991), as shown later in **Figure 39**. This can also be related to the density. The dependence is at a power of 2/3 on the coordination number in excess of 2.4, according to percolation theory (Robertson, 1992). Thus, when the C–C sp^3 fraction is large, as in ta-C, the Young's modulus and hardness approach that of crystalline diamond itself. The hardness is roughly 10% of the Young's modulus. The refractive index squared also varies linearly with density (**Figure 19**).

The properties of a-C:H depend in a more complex manner on their sp^3 fraction and hydrogen content, as summarized for one type of a-C:H (Koidl et al., 1990; Robertson, 2002a) in **Figure 17**. At low sp^3 content, as the hydrogen content increases, the density first increases as the hydrogen first converts sp^2 sites to sp^3 sites, but then further increase in hydrogen content increases the H coordination around each C sp^3 site to form $=CH_2$ sites with much lower density. The density changes can also be understood from **Figure 3**.

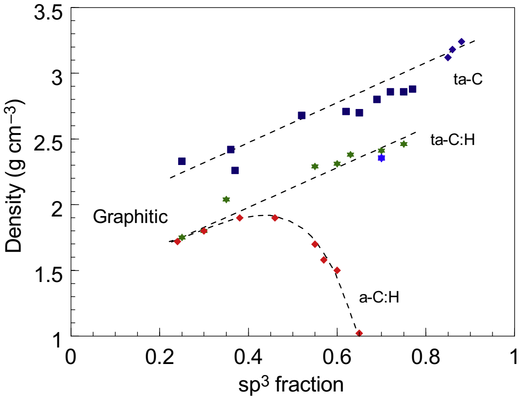

Figure 17 Density vs sp^3 fraction for the various types of amorphous carbon, showing the linear correlation for ta-C and the peak in density for a-C:H, with lower density for most sp^2-rich films and for polymeric highly sp^3-rich a-C:H (Robertson, 2002a).

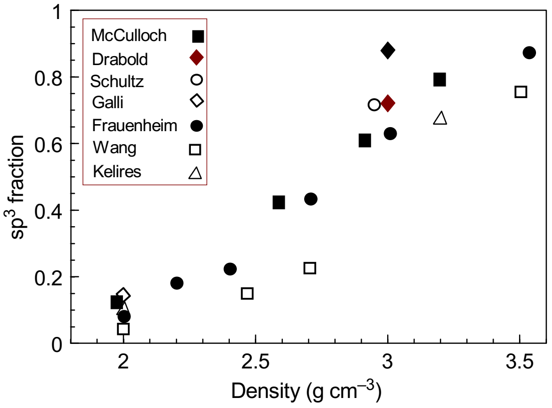

Figure 18 Density vs sp^3 fraction for amorphous carbon from theory (Jungnickel et al., 1994; Drabold et al., 1996; Galli et al., 1990; Marks et al., 1996; McCulloch et al., 2000; Wang et al., 1993; Kelires, 1993).

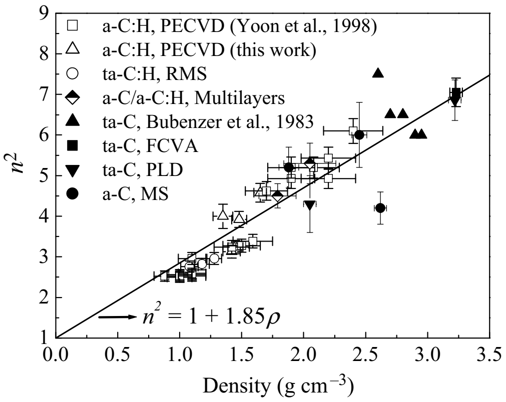

Figure 19 Refractive index vs density for different forms of carbon (Casiraghi et al., 2005).

3.06.5.2 Electronic Structure

DLC always contains both sp^3 and sp^2 sites, and this makes its electronic structure fundamentally different to that of diamond. The sp^3 sites each form four two-centered σ bonds, while the sp^2 sites form three σ bonds plus a π bond with their single π electron. The σ bonds form states deep in the valence band and conduction band, while the weaker π bonds form states at the band edges of both valence and conduction bands, **Figure 20(a)**. **Figure 20(b)** shows a more detailed plot of the density of states for various random network models containing different fractions of sp^3 bonding. An important difference to a-Si:H is that the π states are localized.

The sp^2 sites tend to form clusters to lower their free energy, and their π states form the band edge states (Chen & Robertson, 1998; Robertson, 1986; Robertson, 2002a). Thus, the electronic structure depends on the configuration of the sp^2 sites. In simple models, the band gap of the clusters varies inversely with the diameter of the cluster (Robertson, 1986). This is related to the electronic structure of carbon nanotubes (CNT) or graphene nanoribbons, where the band gap depends on the CNT diameter or ribbon width. In as-deposited DLC films, there is a strong experimental correlation between the average configuration of sp^2 sites and the sp^2 concentration, so that the band gap of ta-C and a-C:H depends on the average sp^2 fraction as shown in **Figure 21** (Yoon et al., 1998).

In summary, the mechanical properties depend on the fraction of sp^3 sites, sp^2 sites and hydrogen, with only sp^3–sp^3 bonds contributing to elastic modulus and hardness, while the electronic properties depend on the fraction and configuration of the sp^2 sites (Robertson, 1986).

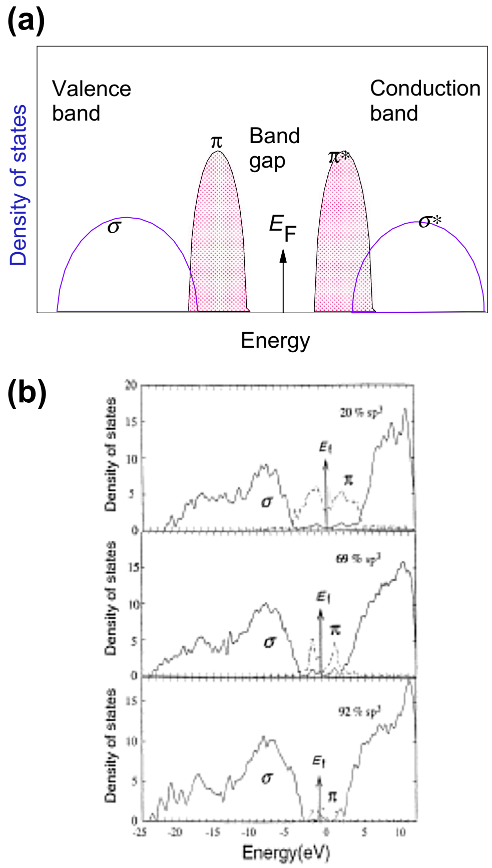

Figure 20 Schematic of the density of states of amorphous carbons. Calculated density of states for random network models of a-C, for different sp^3 fractions (Chen & Robertson, 1998).

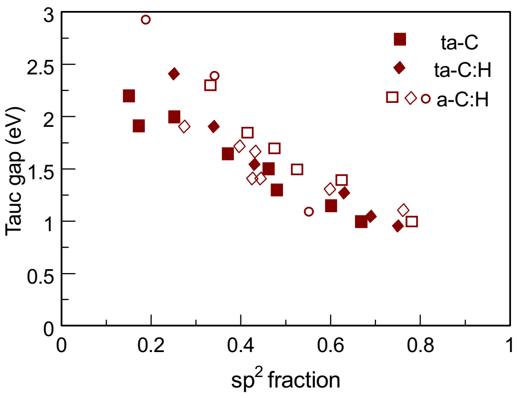

Figure 21 Variation of optical band gap with sp^3 fraction for different types of DLC (Robertson, 2002a).

3.06.6 Characterisation

As the mechanical and electronic properties of DLCs are so closely related to the atomic structure, it is very important to have ways to characterize this. There are four important parameters to measure: the mass density, the fraction of sp^3 sites, the fraction of hydrogen, and the configuration of the sp^2 sites.

The mass density can be measured by weight gain during deposition, by X-ray reflectivity (XRR) or indirectly by electron energy loss spectroscopy (EELS). Weight gain was the first method and is still useful (McKenzie et al., 1991).

The XRR method is widely available in semiconductor and thin-film research labs. XRR uses the total internal reflection of X-rays from the surface and interfaces of the films, due to the refractive index of material to X-rays being slightly below 1. For DLC on Si, the density can be extracted from the size of the critical angle of reflection at the top of the reflectivity spectrum (Ferrari et al., 2000) (**Figure 22**). The reflectivity then decays as a series of oscillations, and the period of the oscillations gives the film thickness. The advantage of XRR is that it has no adjustable parameters, but it does usually require a curve fitting of the reflectivity spectrum.

The mass density can be derived using EELS through the measurement of the low-energy EELS spectrum. This allows the valence electron density to be calculated, which gives the mass density (Fallon et al., 1993; Ferrari et al., 2000; Waidmann et al., 2001). **Figure 23(a)** shows typical energy EELS spectra of different forms of carbon. The valence plasmon energy E_p depends on the valence electron density N as

$$E_p = \hbar\left(\frac{Ne^2}{\varepsilon_0 m^*}\right)^{1/2}$$

where ε_0 is the permittivity of free space. The actual conversion of valence density to mass density requires a value for the effective electron mass, m^*. This is often taken as 1, but in fact this must be set by fitting the plasmon energy of crystalline diamond 34 eV to the density of diamond 3.515 g cm^{-3}, which gives $m^* = 0.87$ times the free mass. If this is not done, the mass density of the DLC is overestimated (Ferrari et al., 2000). A related spectrum is the optical dielectric loss function ε2 which can be derived from the energy loss spectrum by Kramers-Kronig analysis, and is shown in **Figure 23(b)**.

The hydrogen content of DLC can be measured by nuclear methods such as elastic recoil detection analysis (ERDA) or nuclear reaction analysis (NRA), by combustion analysis, by hydrogen evolution (Jacob & Unger, 1996; Jiang, Beyer, & Riechelt, 1990; Ristein, Stief, Ley, & Beyer, 1998; Wild & Koidl, 1987), and indirectly by infrared (IR) spectroscopy or photoluminescence (PL). ERDA and NRA give reliable values. The IR vibration modes seen in a-C:H have been assigned (Ristein et al., 1998; Robertson, 2002a; Robertson, 1991). The intensity of the various C–H modes could be used to derive a hydrogen content. This follows the practice in a-Si:H where the oscillator strength of the various Si–H modes are reasonably constant. But this is not true for the C–H modes, and this method can give poor estimates of hydrogen content in critical cases (Grill & Patel, 1992; Jacob & Moller, 1993; Jacob & Unger, 1996; Ristein et al., 1998).

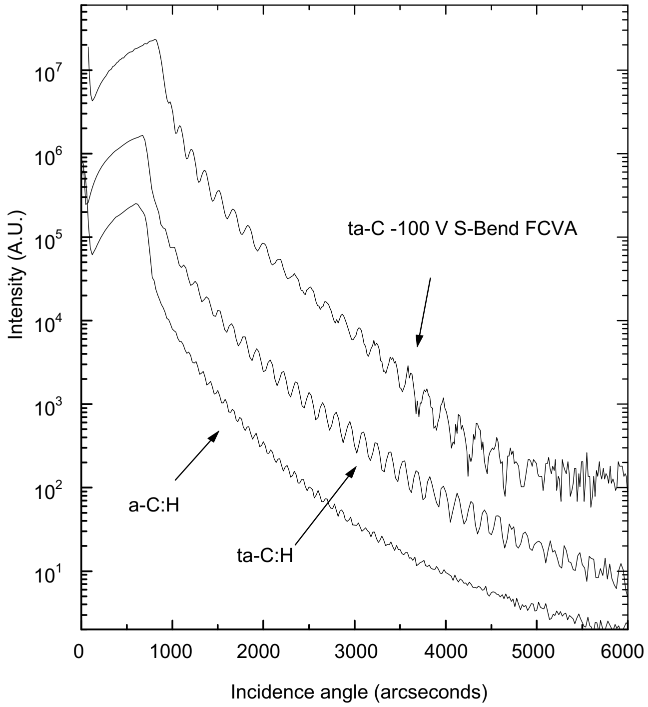

Figure 22 X-ray reflectivity spectrum for different types of DLC.

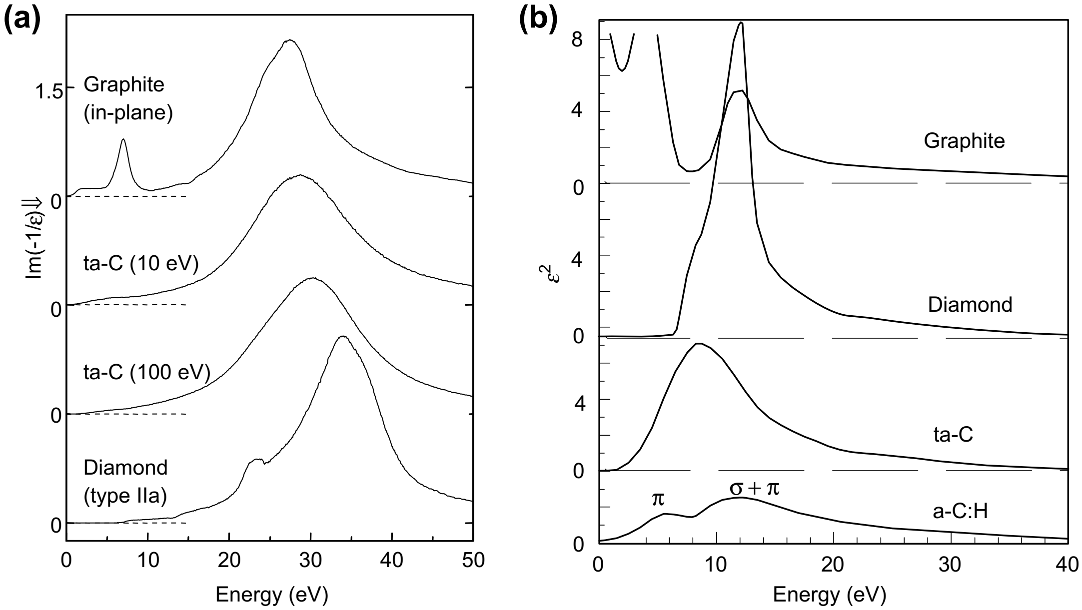

Figure 23 (a) Low energy electron loss spectra (EELS) of different forms of carbon, showing the valence Plasmon peak at 20–34 eV, (b) dielectric loss spectrum e2 for different forms of carbon.

A useful, indirect way to derive the hydrogen content is from the size of the background PL intensity on the Raman spectrum (Casiraghi, Ferrari, & Robertson, 2005; Marchon, 1990). The logarithm of the slope of the background is found to be proportional to the hydrogen content (**Figure 24**). This arises roughly because, in practice, the band gap in a-C:H is related to the hydrogen content, and the PL efficiency follows the band gap (Robertson, 2002a). The fundamental reasons behind this method have not been fully tested.

The sp^3:sp^2 fraction is perhaps the most important value for DLC. There are numerous ways to extract it, but not all are reliable. Magic angle spinning nuclear magnetic resonance with C^{13}-enriched samples is the most accurate, but is rarely used due to cost. The sp^3:sp^2 fraction can be derived from the shift of the 1s core level signal. The shift has been validated by modeling (Haerle, Riedo, Pasquarello, & Baldereschi, 2001). However, the shift is rather small, as it is not due to charge transfer. Other methods such as IR spectra (Jacob & Moller, 1993) and spectroscopic ellipsometry have been used, but are more complex.

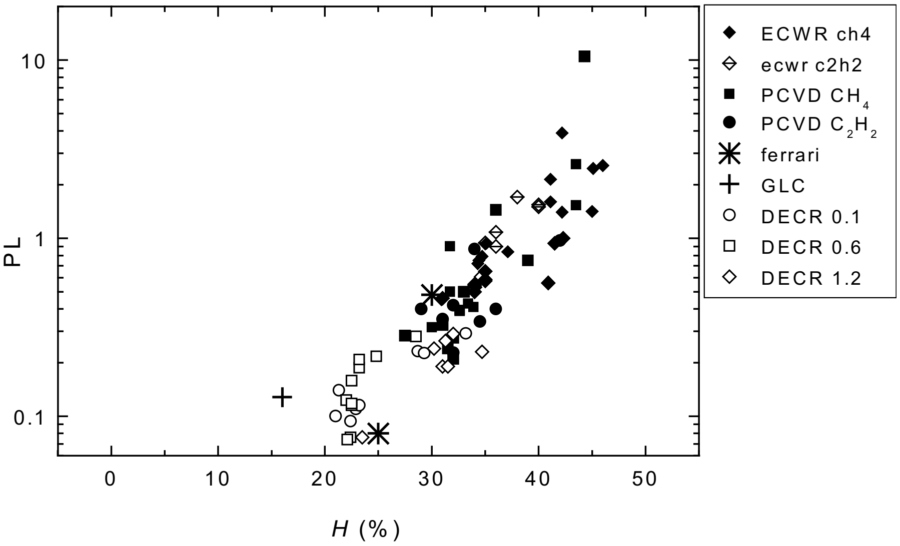

Figure 24 Variation of slope of photoluminescence background in a-C:H with its hydrogen content (Casiraghi et al., 2005).

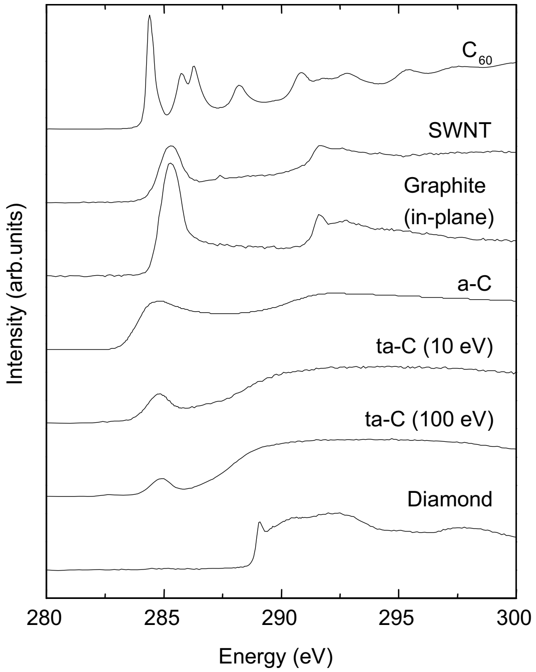

Figure 25 Carbon 1s EELS spectra for various forms of carbon.

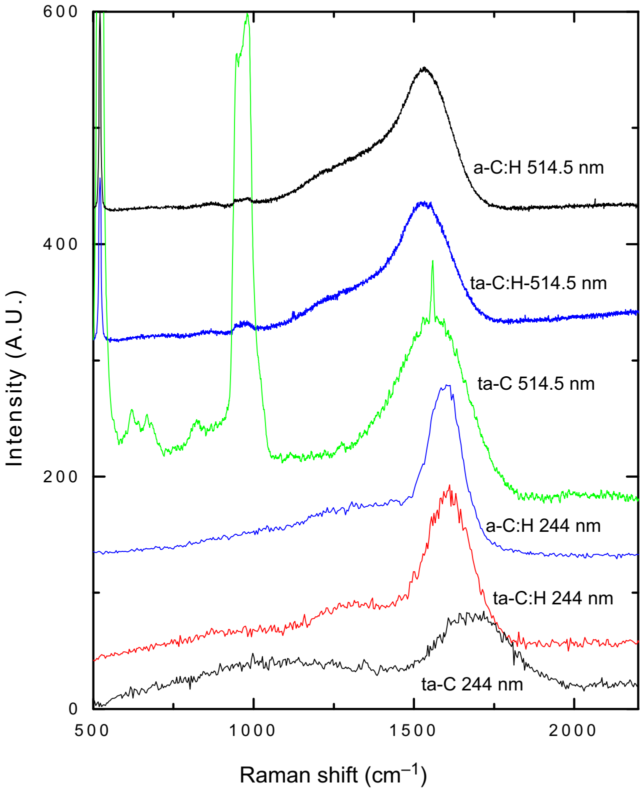

Figure 26 Raman spectra of ta-C, ta-C:H and a-C:H samples, for 514 and 244 nm excitations.

The most reliable method to give the sp^3 content for ta-C is the EELS C 1s core level excitation spectrum (Fallon & Brown, 1993; Fallon et al., 1993; Ferrari et al., 2000; Fink, 1989; Fink et al., 1983; McKenzie et al., 1991; Waidmann et al., 2001). Typical spectra are shown in **Figure 25** for various forms of carbon (Robertson, 2002a). Excitations to the empty π^* states of sp^2 sites give rise to a peak at 285 eV before the main edge at 290 eV due to the σ^* states of sp^2 and sp^3 sites. The 285 eV peak intensity is proportional to the concentration of sp^2 sites, if it is normalized to the peak height in graphite, and allowance is made for its angular variation in graphite.

The most widely used characterization method now is Raman spectroscopy, it gives a lot of information but it is indirect (Ferrari & Robertson, 2000; Ferrari & Robertson, 2001; Tamor & Vassell, 1994). The Raman spectrum of different types of DLC consists of four main features, shown in **Figure 26**; the main "G" peak at around 1550 cm^{-1} due to the stretching modes of pairs of sp^2 sites, the "D" (defect) peak at around 1350 cm^{-1} due to breathing mode of clusters of sp^2 sites, a density of states feature around 1050 cm^{-1} due to sp^3 modes seem only in UV excitation, and a "2D" mode at 2660 cm^{-1}. Examples of spectra are given in **Figures 26–28**.

The Raman spectrum of carbons is a resonant process (Ferrari & Robertson, 2001; Thomsen & Reich, 2000), so that the spectral intensity of any peak depends critically on the laser excitation energy (**Figure 27**). The normal visible excitation only probes π states of sp^2 sites, so that only the G, D and 2D peaks are seen (**Figure 26**). UV excitation at 514 nm is required to probe excitations of σ states, and thus sp^3 sites. The simplest derivation of sp^3 fraction is from the intensity of the *T* peak at around 1050 cm^{-1} (Gilkes et al., 2000; Gilkes, Sands, Batchelder, Robertson, & Milne, 1997) (**Figure 30**). This peak moves downward slightly in ta-C:H, but is barely seen in a-C:H (Ferrari & Robertson, 2001) (**Figure 28**).

The easiest way to extract the sp^3 content by visible Raman for hydrogen-free DLC is to follow the case of ta-C. There, the shift of the G peak is proportional to the sp^3 fraction (Ferrari & Robertson, 2000). This shift is due to the fact that the degree of clustering of sp^2 sites varies inversely with sp^2 content, with sp^2 sites being highly clustered in sputtered sp^2 a-C, but being mainly as C=C pairs in ta-C. The C–C bond length is shorter in ethylene than in benzene, so the vibration mode is higher in ethylene or ta-C. In ta-C, the G mode exceeds is wave number in graphite, being over 1600 cm^{-1} for this reason. The G peak shows dispersion with excitation energy for this reason.

The complex dependence of G-peak frequency shift and the D- to G-peak intensity ratio, $I(D)/I(G)$, on the clustering of sp^2 sites has been explained by the three-stage model (Ferrari & Robertson, 2000), shown in

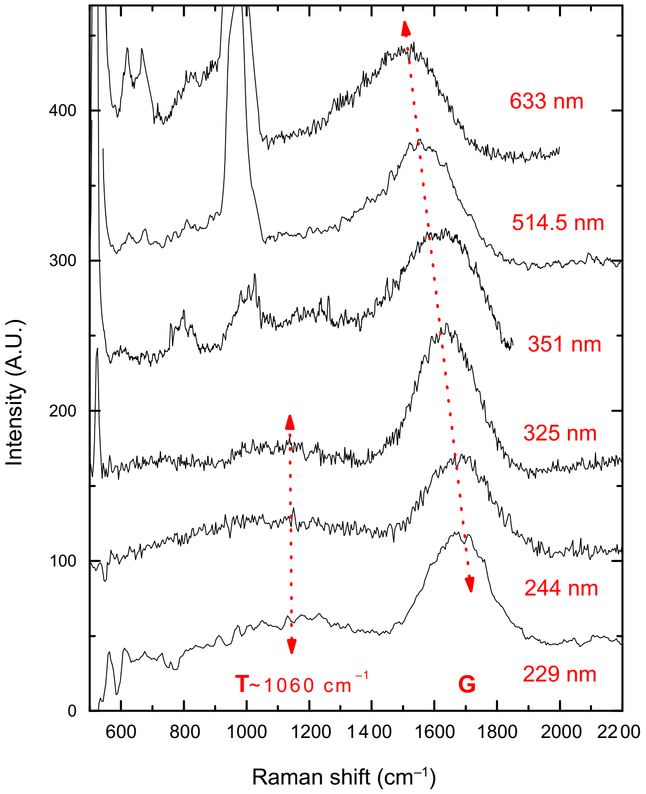

Figure 27 Raman spectra of ta-C, for different excitation energies.

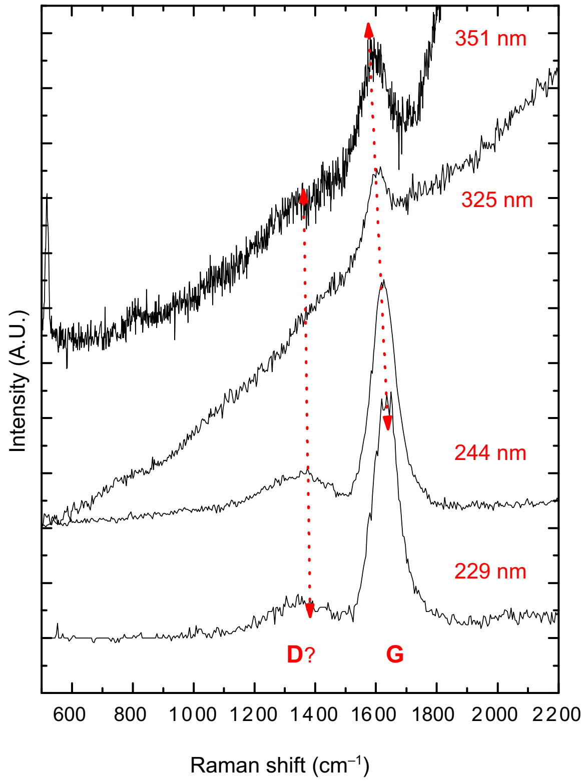

Figure 28 Raman spectra of a-C:H for different excitation energies.

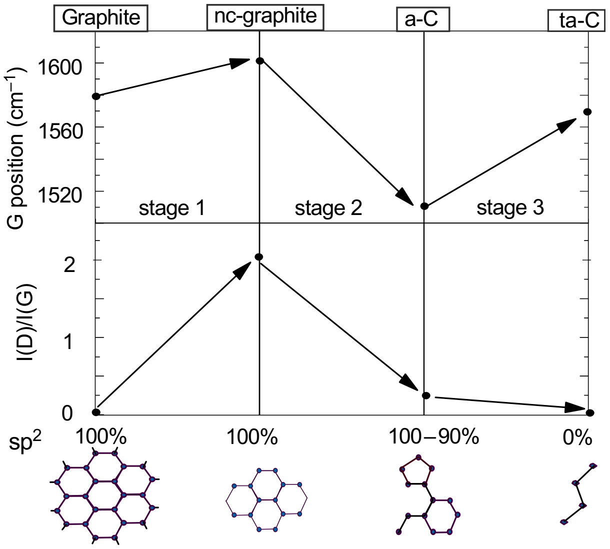

Figure 29 The three-stage model of how disorder affects the Raman spectra of disordered carbons.

Figure 29. The D-peak is the breathing mode of clusters of sp^2 sites. It only exists due to a resonant, two-phonon process, so that its frequency shifts linearly with the excitation energy (Ferrari & Robertson, 2001). The D-peak intensity varies inversely with the cluster size until the cluster is 2 nm across (the Tuinstra–Koenig relationship), and then declines for smaller clusters (Ferrari & Robertson, 2000; Robertson, 1991) (**Figure 31**). The D-peak line width varies inversely with cluster size over the whole range of cluster size (**Figure 32**), which can be used to check which regime applies.

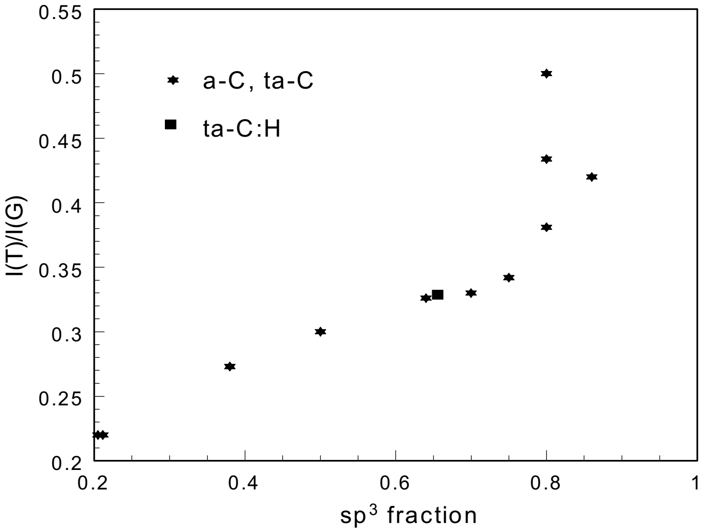

Figure 30 Variation of the T-peak intensity with sp^3 fraction, for UV Raman.

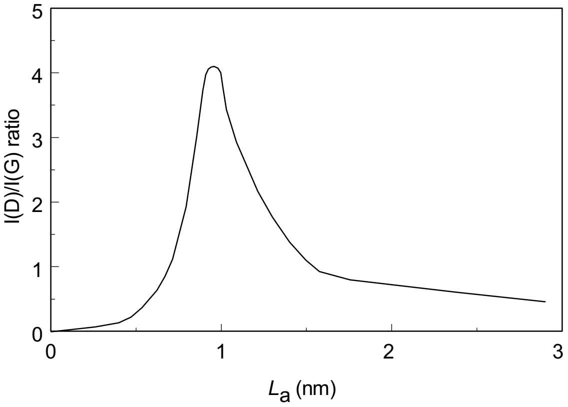

Figure 31 D to G Raman intensity ratio I(D)/I(G) vs sp^2 cluster size or interdefect separation L_a (Robertson, 1991).

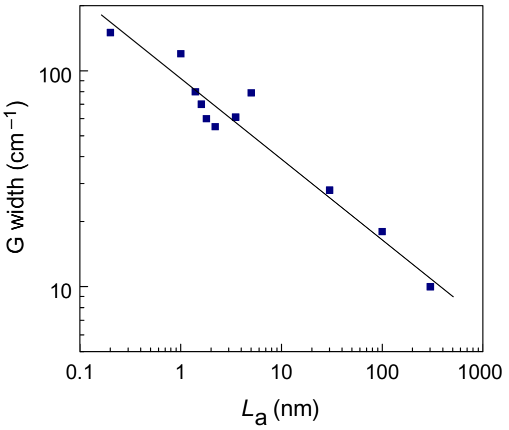

Figure 32 Variation of G line width with cluster size, L_a (Robertson, 1991).

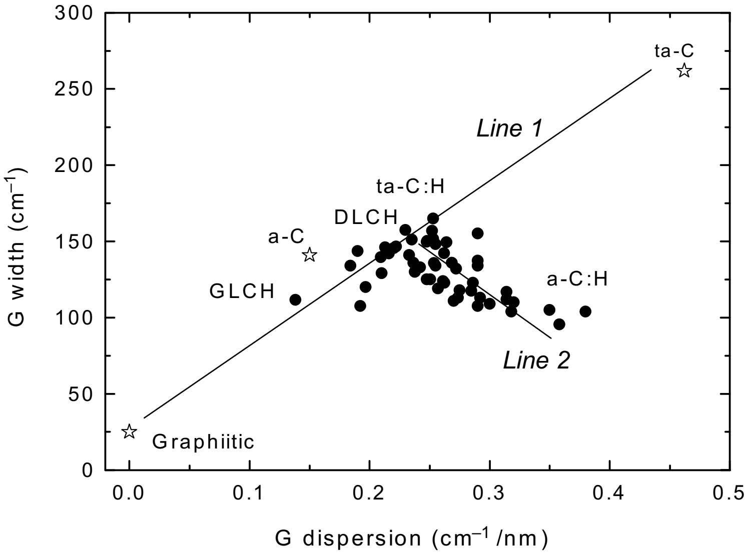

Figure 33 G line width vs G peak dispersion with excitation energy for all types of carbons, showing how this classifies carbons.

The resonant process means that it generally requires Raman spectra measured at two frequencies to derive correctly the sp^2 fraction and sp^2 configuration. It is found that the variation of G-peak width with G-peak dispersion (**Figure 33**) resembles that of density vs sp^3 fraction (**Figure 17**). This arises because the G-peak width describes density/stress and the G dispersion describes sp^3 fraction. In fact, a simplified method based on single wavelength excitation and analysis of the G-peak shift and $I(\mathrm{D})/I(\mathrm{G})$ intensity ratio does in fact define the type of DLC under study, based on a large database of spectra (Casiraghi et al., 2005).

3.06.7 Film Adhesion

The major use of DLC films is in wear-protective layers. This requires thick films that adhere to the substrate. However, the compressive stress limits the maximum thickness of adherent films (Robertson, 2002a). The ion deposition process creates compressive stresses, which result in the sp^3 bonding (McKenzie et al., 1991; Robertson, 1993). It is *intrinsic* to the subplantation growth mechanism (Section 3.06.4). Davis (Gilkes et al., 2000) derived an equation similar to Eqn [1] describing the variation of stress with ion energy.

The compressive stress limits the maximum thickness, h, of adherent films. For a stress σ, surface fracture energy γ, and Young's modulus of E, the maximum thickness of an adherent film is given by (Robertson, 2002a)

$$h = \frac{2\gamma E}{\sigma^2} \tag{3}$$

For DLC, σ and E both tend to correlate linearly with the sp^3 fraction, $\sigma = k_1(\mathrm{sp}^3)$, $E = k_2(\mathrm{sp}^3)$. While we can reduce stress by lowering the sp^3 fraction, this will also lower E and thus the hardness H, as $H = 0.1\ E$. As γ is roughly constant, Eqn [3] says that harder films have a lower maximum adherent thickness, $h = k_3/H$. Hence, paradoxically, it is not advantageous to have a harder film.

There are various strategies to reduce the compressive stress in DLC films and improve their adhesion to the substrate. For ta-C, the first process is to anneal the film to 500–600 °C (**Figure 34**) (Ferrari, Kleinsorge et al., 1999; Friedmann, Sullivan, & Knapp, 1997; Sullivan, Friedmann, & Baca, 1997). This is found to remove the stress in ta-C, while only slightly lowering the sp^3 content. Practical implementation requires a cyclic deposition and an annealing process to build up thicker films. This method is not useful for a-C:H because the hydrogen is lost first, so the film is no longer diamond-like.

This annealing process has been analyzed in some detail. Annealing converts a small fraction of sp^3 sites to sp^2 sites, the stress is removed, but the sp^3 content and hardness are almost unchanged (Ferrari, Kleinsorge et al., 1999; Sullivan et al., 1997) (sp^3 films are stable to over 1200 °C in a vacuum). It is believed that the annealing causes a small fraction of sp^3 sites to convert to sp^2 sites, oriented in the substrate plane, and the smaller bond

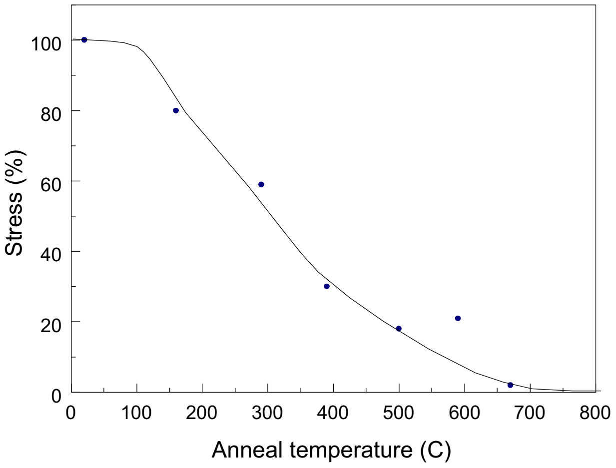

Figure 34 Compressive stress vs annealing temperature for ta-C.

length relaxes the compressive strain (**Figure 35**). The film volume actually increases because sp^2 sites have larger volume than sp^3 sites, but this does not matter if the volume expansion is perpendicular to the substrate (Sullivan et al., 1997).

A second method to reduce stress is to alloy DLC with Si or various metals (Anttila, Lappalainen, Tiainen, & Hakovirta, 1997; Oguri & Arai, 1991; Voevodin, Capano, & Laube, 1997; Voevodin, Prasad, & Zabinski, 1997; Zehnder & Patscheider, 2000). Si is recommended if an optical gap must be retained. The mechanism is unclear. Metals relieve stress by introducing a ductile component and generally by creating a nanocomposite whose phase boundaries are used to stop crack propagation. In some cases, carbide-forming metals such as Cr or Ti are used; in others, softer metals such as Al have been used. Another method to reduce stress are forming multilayers (**Figure 37(a)**) and graded layers, particularly of a-C:H and carbides in the latter case (Anttila et al., 1997).

Some of the adhesion methods are related to using nanocomposites to increase the film toughness. This links to the more general field of nanocomposite hard films (Patscheider, Zehnder, & Diserens, 2001; Veprek & Reiprich, 1995). The carbides form nanoinclusions in the a-C:H host (**Figure 37(b)**). The carbides act as crack-blunting centers, and thereby they increase toughness. They also add ductility to the film, as do the simpler metals like Al if used instead.

Finally, metallic and graded adhesion layers are used between the DLC and substrate (Anttila et al., 1997; Voevodin, Capano et al., 1997; Voevodin, Prasad et al., 1997). The adhesion layer approach is the main method

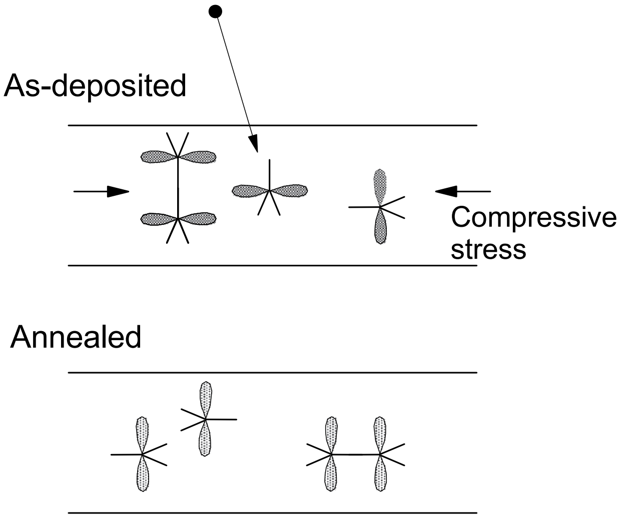

Figure 35 Schematic of the stress annealing mechanism for ta-C.

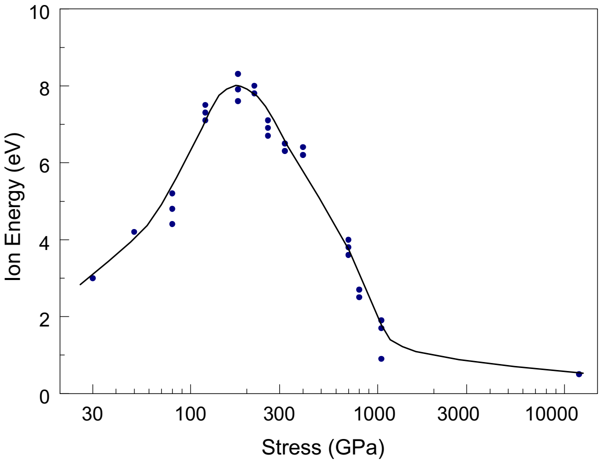

Figure 36 Variation of compressive stress with pulse voltage for pulsed FCVA deposition.

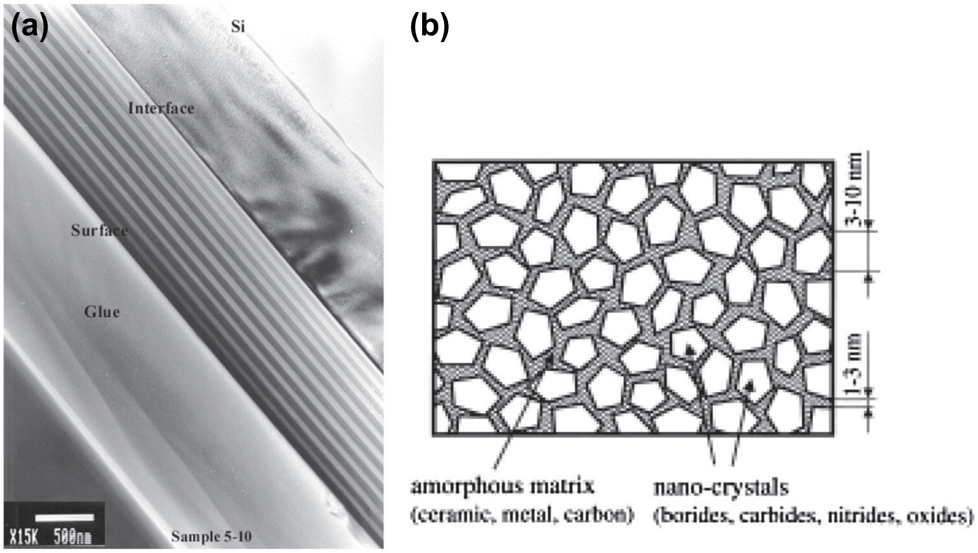

Figure 37 (a) Transverse section TEM of a layered ta-C film (Anttila et al., 1997). (b) Schematic of nanocomposite film, carbon matrix, carbide inclusions.

employed industrially. The idea is a gradual interface between the metallic substrate and the ceramic film, via a tougher interfacial layer.

Compressive stress is considered to be an intrinsic property of DLC, and thus unavoidable. Recently, Bilek and McKenzie (2006) noted that such stress could be reduced if deposition was accompanied by high-voltage pulses, with pulsed ion energies of order 1000 eV (**Figure 36**). This process is related to the plasma ion immersion implantation method. Interestingly, this process does not cause much loss of sp^3 bonding or hardness of the DLC.

This method was first implemented on FCVA for C$^+$ ions (Bilek & McKenzie, 2006). It is now being applied to a-C:H and also to provide better adhesion between film and substrate (Lusk et al., 2008; Oka, Yatsuzuka, Nishijima, & Hiraga, 2008; Walter, Natasi, & Munson, 1997). Oka et al. (2008) achieved a remarkable 0.4-mm-thick DLC on aluminum alloy.

Recently, Lusk et al. (2008) implemented this method on a 50 kHz pulsed high-voltage asymmetric bipolar DC hollow cathode source with pulse voltages of 1 kV. This method can produce adherent a-C:H layers of over 50 μm thickness with a 1 μm min^{-} growth rate and retaining a hardness of 15–20 GPa (**Figure 38**). The stress in these films was derived from the curvature measured by profilometry and Stoney's equation. The stress is found

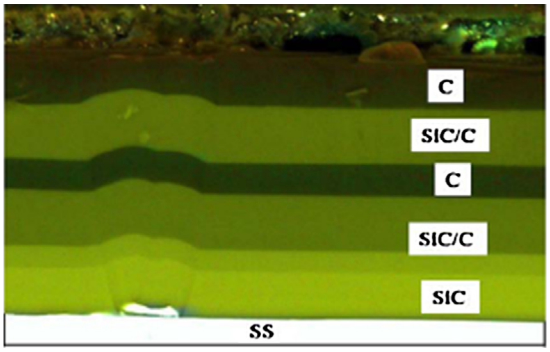

Figure 38 Cross-section of low-stress DLC-based films formed by pulsed PECVD process (Lusk et al., 2008).

to be at least 10 times lower than for conventional PECVD films of the same hardness, as seen in **Figure 39**. Si was added to the film from trimethylsilane as a stress reduction and grading adhesion layer, but the main effect is ion energy pulsing. This allows an increase in sp^3 content and hardness without sacrificing thickness. This method is of considerable importance for wear resistance coatings in general.

The possible stress reduction mechanism is this. The average ion energy during a-C:H PECVD is close to the optimum 100 eV per C atom. The high-voltage pulse is typically 1000 eV. The resulting film retains much sp^3 character according to Raman, and a high hardness. About 0.02 Å of a-C:H is deposited during each low-voltage part of the cycle. In the high-voltage pulse, the high-energy ions penetrate about 100 nm, and create a thermal spike in this zone. This converts a fraction of its sp^3 sites into sp^2 sites, giving strain relief, as in the thermal annealing process discussed above. The high-voltage pulsing provides a thermal annealing of each just-deposited layer. The pulsing is equivalent to repeated deposition and anneal cycles.

3.06.8 Mechanical Properties

The mechanical properties of DLCs are of great importance because of the use of DLC as a protective coating (Dasch et al., 2006; Donnet & Erdimir, 2008; Erdemir & Donnet, 2006; Fukui, Okida, Omori, Moriguchi, & Tsuda, 2004). ta-C films are also studied for use in micro-electro mechanical system (MEMs) instead of polysilicon. This is because ta-C is the hardest material known after diamond itself. A great advantage of DLC compared to diamond is that it is amorphous with no grain boundaries. This means the films are extremely smooth. DLC is also deposited at room temperature, which is an advantage for temperature-sensitive substrates such as plastic. DLC films also have extremely good coverage, so they act as good corrosion barriers. This is particularly useful in a major application, which is to coat hard disks and recording heads in the magnetic storage technology.

The mechanical properties of DLC thin films are often measured by nanoindenter (Friedmann et al., 1997; Jiang, Reichelt, & Stritzker, 1990a; Jiang, Zou, Reichelt, & Grunberg, 1989; Koidl et al., 1990; Martinez et al.,

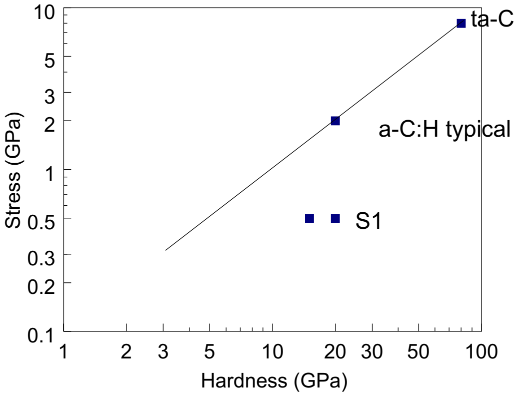

Figure 39 Compressive stress of a-C:H films deposited by the Lusk et al. (Dischler et al., 1983) process.

2001; Pharr et al., 1996; Sattel et al., 1997; Shi et al., 1997). In this experiment, a small diamond tip is progressively forced into the film, and the force–displacement curve is measured. The hardness is defined as the pressure under the tip, given by the ratio of force to the projected area of plastic deformation. For accuracy, the indentation depth must be limited to a fraction of order 10% of the total film thickness (Pharr et al., 1996).

A rapid nondestructive method to measure the elastic moduli is by surface acoustic waves. An example is laser-induced surface acoustic waves (Schultrich, Scheibe, Dreschler, & Ziegele, 1998). Surface acoustic waves actually measure the shear modulus, *S*. The Young's modulus *E* can only be derived from this if a value for the Poisson's ratio ν is assumed (typically 0.1). A related method to measure elastic moduli is surface Brillouin scattering (Ferrari, Robertson et al., 1999).

Table 1 compares the elastic constants of some types of DLC (Jiang, 1991; Jiang, Reichelt, & Sritzker, 1990; Ferrari, Robertson et al., 1999; Schultrich et al., 1998) with those of diamond (Field, 1993). The Young's modulus of ta-C with 88% sp^3 bonding is found to be 757 GPa (Ferrari, Robertson et al., 1999), compared to 1144 GPa for diamond itself. The bulk modulus of ta-C is found to be 344 GPa compared to the diamond value of 444 GPa. The Poisson's ratio of ta-C is found to be ~0.12, nearly as low as that of diamond itself, 0.07. On the other hand, ta-C:H is found to have a Youngs modulus of 300 GPa, much less than that of diamond (Field, 1993). This shows the strong effect of how hydrogen has lowered the network coordination of ta-C:H. Its Poisson's ratio is about 0.3, much larger than diamond's and closer to the larger values found by Brillouin scattering for PECVD a-C:H (Jiang, 1991).

Table 1 Comparison of major properties of amorphous carbons with those of reference materials diamond, graphite, C_{60} and polyethylene.

	% sp^3	*% H*	*Density (g cm^{-3})*	*Gap (eV)*	*Hardness (GPa)*
Diamond	100	0	3.515	5.5	100
Graphite	0	0	2.267	0	
C_{60}	0	0		1.6	
Glassy C	0	0	1.3–1.55	0.01	3
Evaporated C	0	0	1.9	0.4–0.7	3
Sputtered C	5	0	2.2	0.5	
ta-C	80–88	0	3.1	2.5	80
a-C:H hard	40	30–40	1.6–2.2	1.1–1.7	10–20
a-C:H soft	60	40–50	1.2–1.6	1.7–4	<10
ta-C:H	70	30	2.4	2.0–2.5	50
Polyethylene	100	67	0.92	6	0.01

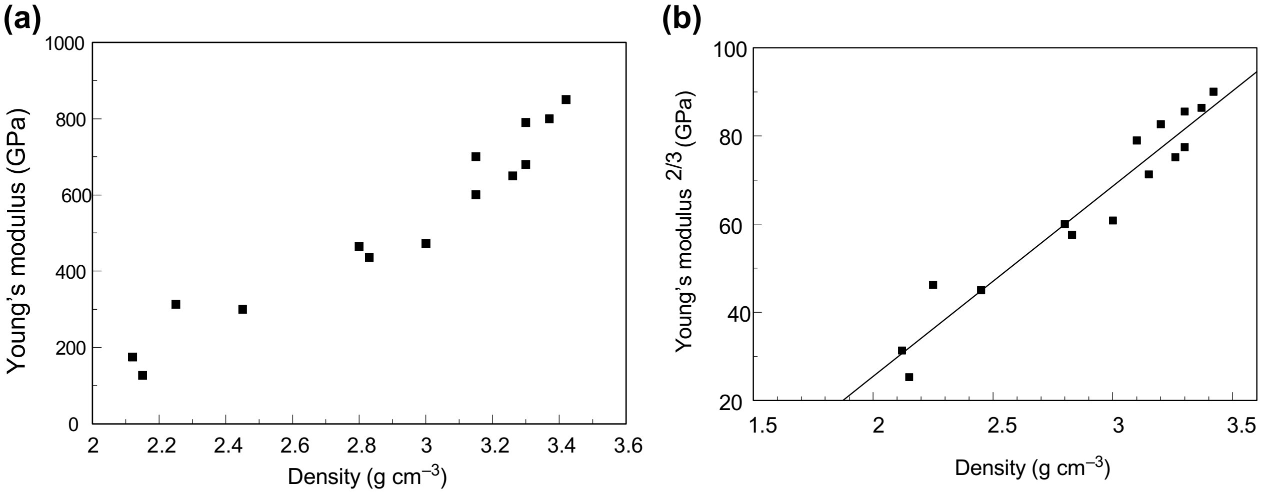

Figure 40 (a) Young's modulus of a-C versus density, from scattering measurements (Weiler et al., 1994). (b) Plot of power law of Youngs modulus vs density for ta-C.

Figure 40 shows the corresponding variation of Young's modulus of ta-C deposited by laser arc (Ferrari, Robertson et al., 1999) as a function of the ta-C density. A steady increase in elastic modulus occurs due to the change from sp^2 to sp^3 bonding with increasing density. For hydrogen-free a-C, the elastic modulus is expected to vary with the bond-density N as $N^{2/3}$, as is found in **Figure 39(b)** (Robertson, 1992).

The hardness is a measure of the yield stress of a material. Hardness is related to the yield stress Y and Young's modulus E, and empirically we find $H/E \sim 0.16$ for DLCs. The nanohardness of ta-C with 85–90% sp^3 bonding has been measured to be at least 60 GPa by Pharr (Pharr et al., 1996), 54 GPa by Shi (Shi et al., 1997), 45–50 GPa by Martinez et al. (Martinez et al., 2001) and 80–88 GPa by Friedmann (Friedmann et al., 1997).

Figure 41 shows the hardness of a-C:H deposited by PECVD from methane and benzene precursors (Jiang et al., 1989; Koidl et al., 1990). The hardness is relatively low at low bias voltages, for the polymeric a-C:H films. The hardness then rises to a maximum where the films have their maximum diamond-like character and highest mass density, and then it decreases as the films become more graphitic. The hardness reaches a maximum at low bias voltages for methane a-C:H, just like the variation of density and Young's modulus.

Friction occurs by contact between the two surfaces at a few high points or asperities. The real area of contact is much less than the apparent area of contact, so that the real contact pressure is much greater than the average load pressure. The friction force arises from adhesion, deformation or abrasion at the contact. Adhesive contact dominates for elastic materials with high H/E ratios, including ceramic materials like DLC. The friction then depends on the transfer layer, which is believed to be graphitic carbon.

DLCs are notable for their low friction coefficients (Enke, 1981; Enke, Dimigen, & Hubsch, 1980; Gangopadhyay et al., 2011; Gangopadhyay, 1998; Voevodin, Phelps, Zabinski, & Donley, 1996). The friction properties of DLC have been reviewed by Donnet (Erdemir & Donnet, 2006) and Gangopadhyay (Gangopadhyay et al., 2011; Gangopadhyay, Willermet, Vassell, & Tamor, 1997). The unlubricated friction coefficient of DLC on steel is similar to the lubricated friction coefficient of steel on steel (Gangopadhyay et al., 1997).

For a-C:H, the friction coefficient μ depends strongly on the relative humidity (**Figure 42**). Values of μ below 0.05 are found in a vacuum and at low humidity and μ increases strongly at high humidity (Enke et al., 1980). ta-C and ta-C:H behave differently. Voevodin et al. (1996) finds that ta-C has a larger μ than a-C:H in the vacuum of about 0.1–0.15. The μ then decreases weakly as the relative humidity increases (**Figure 42**). ta-C:H deposited from acetylene appears to behave in the same way to the ta-C itself (Robertson, 2002a).

Erdemir et al. (Erdemir & Donnet, 2006) found that the friction coefficient of a-C:H in the low-humidity regime depends strongly on the precursor used to make the a-C:H. It varies with the ratio of H/C in the precursor, with a-C:H from CH_4 having the lowest μ and a-C:H from C_2H_2 having the largest μ. a-C:H prepared from hydrogen-diluted methane has the lowest friction coefficient of all (Erdemir & Donnet, 2006; Colaco, Serro, & Erdemir, 2009; Eryilmaz & Erdemir, 2008). The μ increases to 0.1–0.15 when the humidity rises to normal atmospheric values of 30% and above. In situ studies have shown that the higher μ arise from the water, not oxygen in the atmosphere (Eryilmaz & Erdemir, 2008).

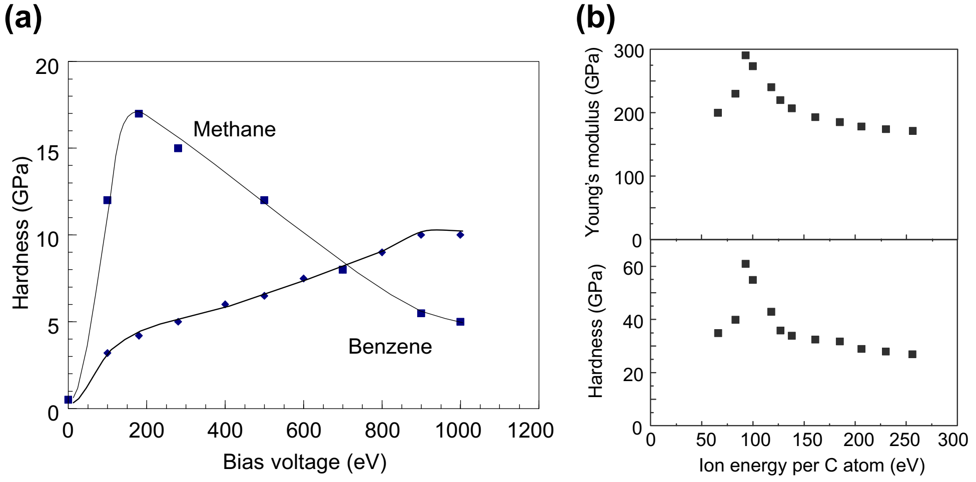

Figure 41 (a) Variation of hardness with bias voltage for a-C:H deposited from methane and from benzene; (b) and hardness of ta-C:H.

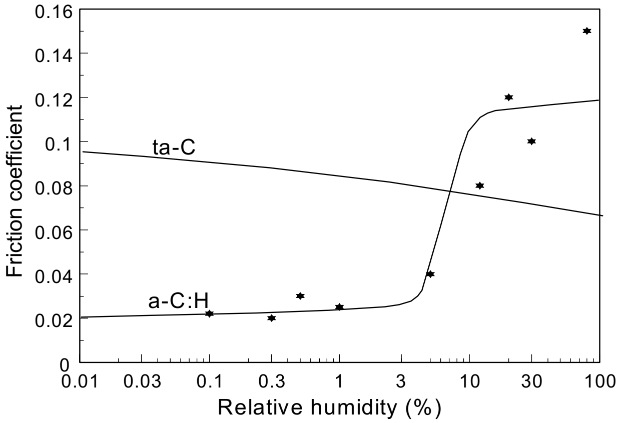

Figure 42 Variation of friction coefficient of a-C:H and ta-C with humidity.

Erdemir et al. (Erdemir & Donnet, 2006) finds that a-C:H in a vacuum can have a friction coefficient μ as low as 0.01. These ultralow friction coefficients arise because the transfer layer no longer occurs, and the contact surfaces are separated by a hydrogenated layer. This has led to the development of even lower friction coefficient layer using glycerol on DLC (Kano et al., 2005; Matta, Joly-Pottuz, Bouchet, & Martin, 2008).

Wear is the removal of material during the contact process (Field, 1993). Wear occurs by adhesion, abrasion or by corrosive/oxidative wear. The wear is the volume of a material removed from a surface by contact. The volume of wear per unit track length, Q, is proportional to the real contact area, which in turn is given by the ratio of load W to the hardness H of the softer surface. This gives the Archard equation,

$$Q = K \cdot \frac{W}{H} \tag{4}$$

where K is the dimensionless wear coefficient. A dimensional wear coefficient k is often used, defined by

$$Q = \frac{K}{H} W = \mathrm{k} \cdot \mathrm{W} \tag{5}$$

where k is typically given in units of $\mathrm{mm}^3\ (\mathrm{N\ m})^{-1}$. The Archard equation shows that the wear coefficient is inversely proportional to the hardness of the surface so that harder surfaces wear less.

Voevodin (Voevodin et al., 1996) and Gangopadhyay (Gangopadhyay et al., 2011) compared wear rates for the various types of DLC. It is found that ta-C has an extremely low wear rate of order $10^{-9}\ \mathrm{mm}^3/\mathrm{N\ m}$, this is about a 100 times lower than that of a-C:H at 10^{-6}–$10^{-7}\ \mathrm{mm}^{-3}/\mathrm{N\ m}$. The value for ta-C is impressively low. Note that the wear rate of ta-C is much less than expected by the Archard equation. It is the low wear rate of ta-C which fundamentally makes ta-C so suitable for MEMs devices. Martinez (Martinez et al., 2001) found that the wear rate of ta-C had a minimum at the maximum of hardness.

The wear mechanism of ta-C and a-C:H is like the friction mechanism, adhesive wear via transfer layers. ta-C undergoes a stress-induced transformation to a graphitic overlayer, which then acts as a lubricant and transfer layer, whereas a-C:H forms a C:H transfer later on the counter surface (Voevodin et al., 1996). The more sp^2-bonded a-C was found to wear by oxidation to CO_2 in an air ambient.

3.06.9 Some Applications of DLC

The main applications of DLC are as a wear-resistant coating material (Dasch et al., 2006; Donnet & Erdimir, 2008; Erdemir & Donnet, 2006; Fukui et al., 2004). A major sector is now a wear-resistant coatings of components in the automotive sector where low-friction, wear-resistant surfaces are needed (Dasch et al., 2006; Fukui et al., 2004). DLC provides a hard, smooth, low-friction surface. The coating maintains these properties if its temperature does not exceed ~400 °C. a-C:H is suitable to coat components such as cam-shaft bearings, tappets, plungers and diesel injectors (**Figure 43**). a-C:H is less suitable for components such as piston rings

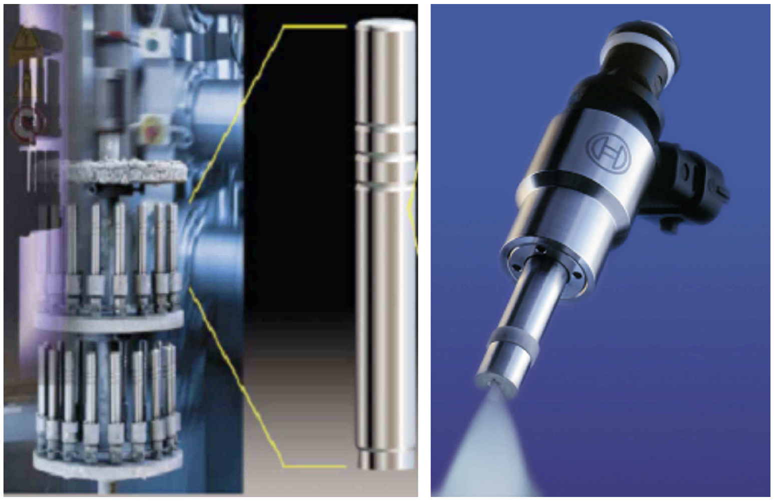

Figure 43 Images of DLC-coated car components.

exposed to high-temperature oxidative conditions, for which ta-C should be used. A key criterion in the automotive sector is very low cost.

A second use is for coating cutting tool bits for the dry machining of aluminum. The bits might be cemented carbides (Fukui et al., 2004). The role of the DLC is to stop the adhesion of Al to the tool during the cutting process. For this role, ta-C deposited by cathodic arc is valuable due to its high hardness.

ta-C films are also studied for use in MEMs such as accelerometers instead of polysilicon (Cho, Chasiotis, Friedmann, & Sullivan, 2005; Sullivan & Friedmann, 2001; Luo et al., 2007). This is because ta-C is the hardest material known after diamond itself. It is also highly smooth and has no grain boundaries. It is hydrophobic, and so it does not suffer from water-related stiction forces, and the devices do not need to be "released" after manufacture. Nanocrystalline diamond has also been developed for MEMs (Auciello et al., 2004; Hutchinson et al., 2004; Philips, Hess, Feygelson, & Butler, 2003; Sekaric, Parpia, & Butler, 2002; Williams, 2011). ta-C and nanodiamond share many of the same properties. The advantage of ta-C is cost. The disadvantage of ta-C compared to nanodiamond is that the stress of ta-C really must be reduced to zero, as otherwise it leads to unwanted curvature of the device. **Figure 44** shows the microgripper made from a ta-C/Ni bimorph (Luo et al., 2007).

The third use of DLC is for coatings on razor blades. Major manufacturers have used this coating. **Figure 45** shows the cross-sectional transmission electron microscopy image through a slice of a razor blade edge. The DLC lies on the steel blade. There is also an outer polymer layer and an adhesion under layer. The role of the DLC is to keep the blade sharp. There is a minimum radius of curvature for ductile materials like metals. Usage blunts the blade edge. Carbon is harder than steel, which stops blade blunting. The carbon coating is not highly sp^3 as seen from its EELS spectrum (**Figure 46**).

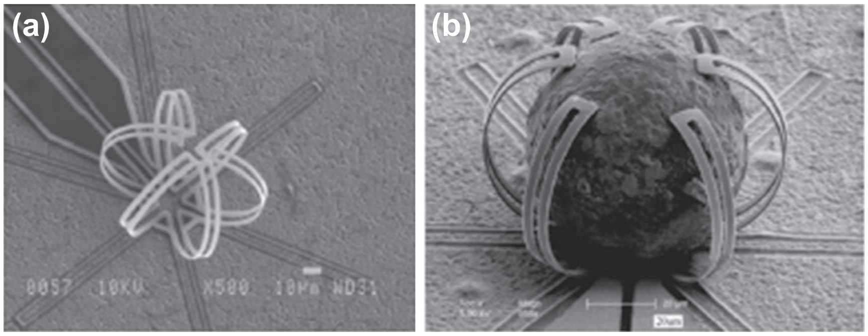

Figure 44 ta-C-based microgripper MEMs from Luo et al.

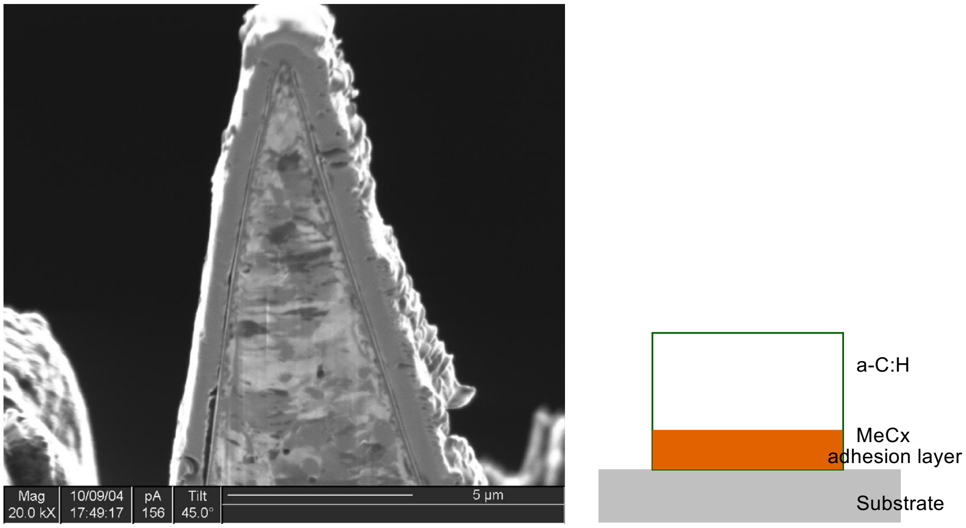

Figure 45 Electron microscopy image of cross-section of a diamond-like carbon-coated razor blade.

The most studied use of DLC in the literature is as a protective coating for magnetic storage disks and their read/write heads (Bhatia,; Bhushan, 1999; Goglia, Berkowitz, Hoehn, Xidis, & Stover, 2001; Gui, 2003; Marchon & Olson, 2009; Mate, Toney, & Leach, 2001; Robertson, 2002b; Robertson, 2003). The DLC acts mainly as a pin-hole-free corrosion barrier to water. Magnetic disks store data as horizontally magnetized domains on a Co-based layer on a disk (**Figure 47**). The information is read by a read-head using giant magneto-resistive or spin-valve sensors. Both disk and head are coated by a DLC layer for protection. On top of this lies a perfluoro-poly-ether layer acting as a lubricant. The storage densities have increased rapidly with year, by scaling down the size of the stored bit (**Figure 48**). This requires a simultaneous downscaling of all dimensions of the disk and head device, such as the head–disk separation, (**Figure 49**), to keep the read sensitivity. Presently, this magnetic spacing is below 10 nm and reaching 5 nm, its natural limit (Gui, 2003; Mate et al., 2001). For this spacing, the DLC layer is only 1.5 nm thick at most. The natural limit is ~1 nm if

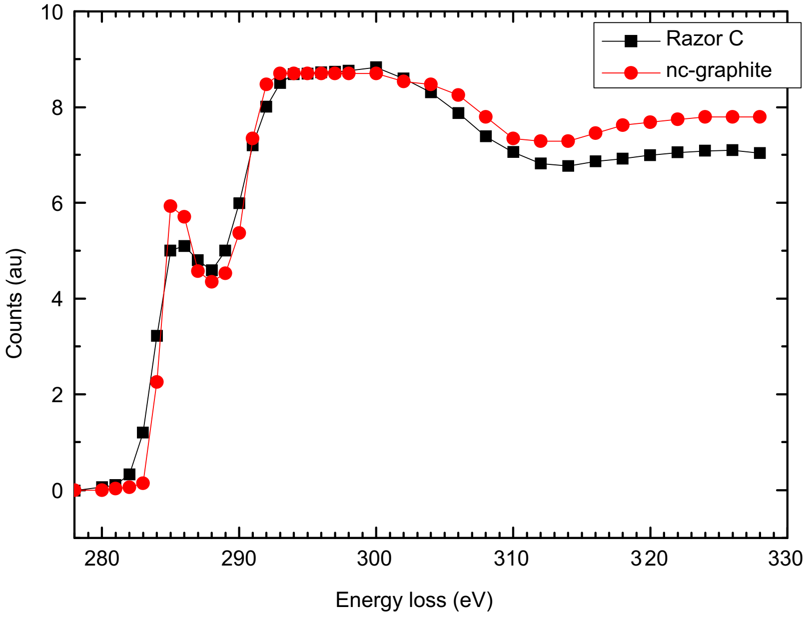

Figure 46 EELS spectra of carbon film on the razor blade.

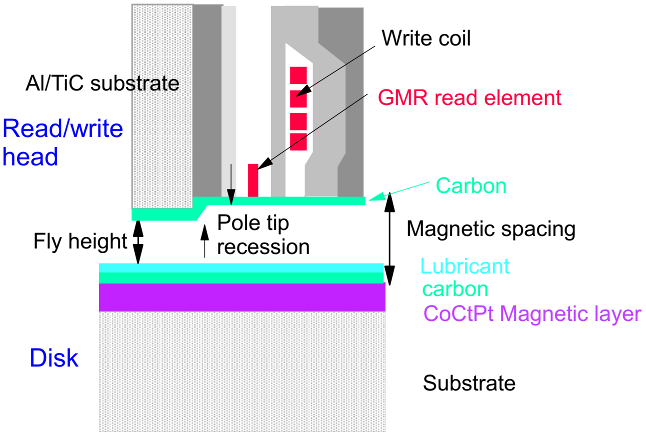

Figure 47 Schematic of a head–disk interface of a hard disk drive.

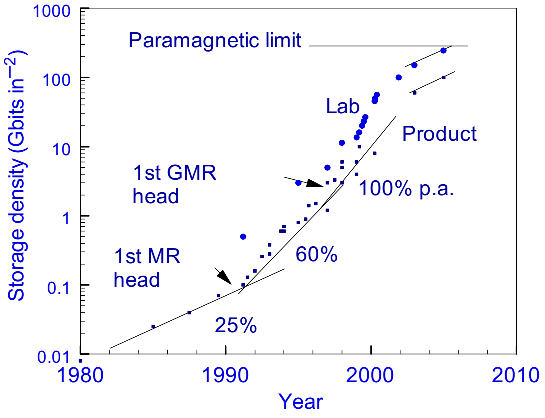

Figure 48 Variation of areal storage densities with date for magnetic hard disk drives.

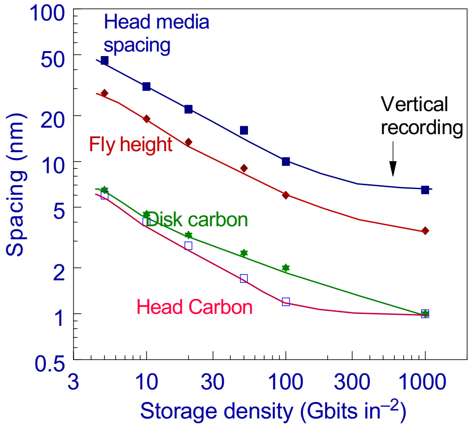

Figure 49 Scaling of vertical fly height, magnetic separation, and diamond-like carbon thickness versus storage density for hard disk drives.

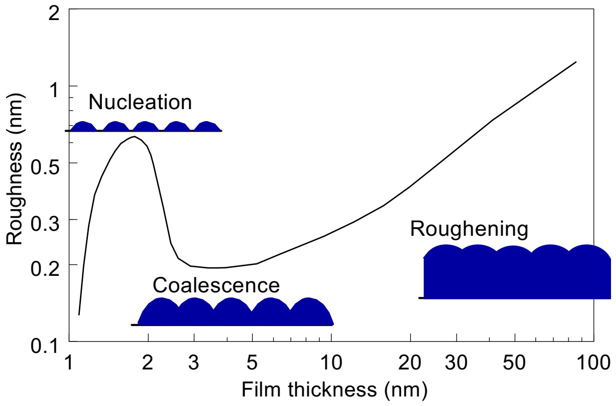

Figure 50 Schematic of nucleation processes for thin films, showing evolution of roughness for moderate nucleation density.

this is manufacturable. Continued density scaling is possible because the technology is switching from horizontal to perpendicular recording (Marchon & Olson, 2009), in which each bit occupies less lateral space.

The key condition for hard disk drive (HDD) coating is that the film be pinhole free over a certain area. For many years, the a-C:H films were produced by reactive sputtering (Robertson, 2003; Robertson, 2002b). This method was replaced by sputtered a-CN_x as this allowed thinner continuous films. Now the industry uses FCVA ta-C in a batch process for coating heads and uses high-density plasma PECVD ta-C:H in a continuous process for coating disks.

It is interesting why DLC is so good for this application (Robertson, 2002b). Originally, the DLC layer acted as a wear-resistant coating. For today's disks, wear protection is not longer an issue for such thin films. The films must be pinhole free, to act as an efficient corrosion barrier against aqueous corrosion of the read head and disk metals (Fe and Co). For this, the films must be amorphous—no grain boundaries—and as smooth as possible. This is equivalent to having the maximum nucleation density. DLC is able to achieve this because it nucleates wherever C ions impact the surface (**Figure 50**). Nevertheless, the density of the film and its elastic modulus does decrease for ultrathin films (**Figure 51**).

The film smoothness has been measured by atomic force microscopy, as a function of DLC type, for a range of deposition ion energies (Lifshitz, 1996; Peng, Barber, & Clyne, 2001; Shi et al., 1997), and also versus film thickness (Casiraghi et al., 2003; Patsalas, Logothetidis, & Kelires, 2005; Pisana, Casiraghi, Ferrari, & Robertson, 2006) (**Figures 52–54**). It is found that most DLCs, both a-C:H and ta-C, are highly smooth, with an RMS roughness of order 0.1 nm. They achieve this provided that the deposition ion energy lies in the range 20–200 eV (**Figure 52(a)**).

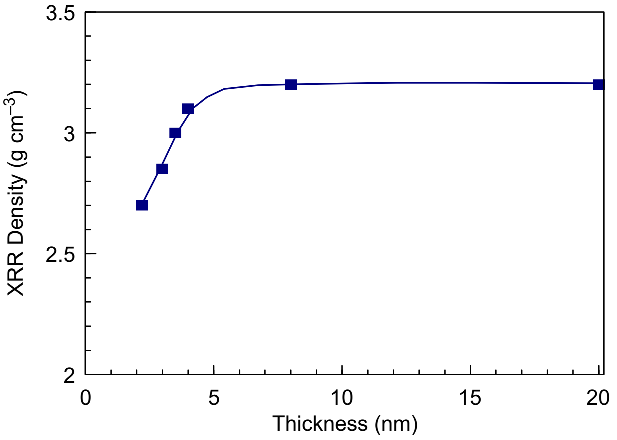

Figure 51 XRR density of ta-C films versus film thickness.

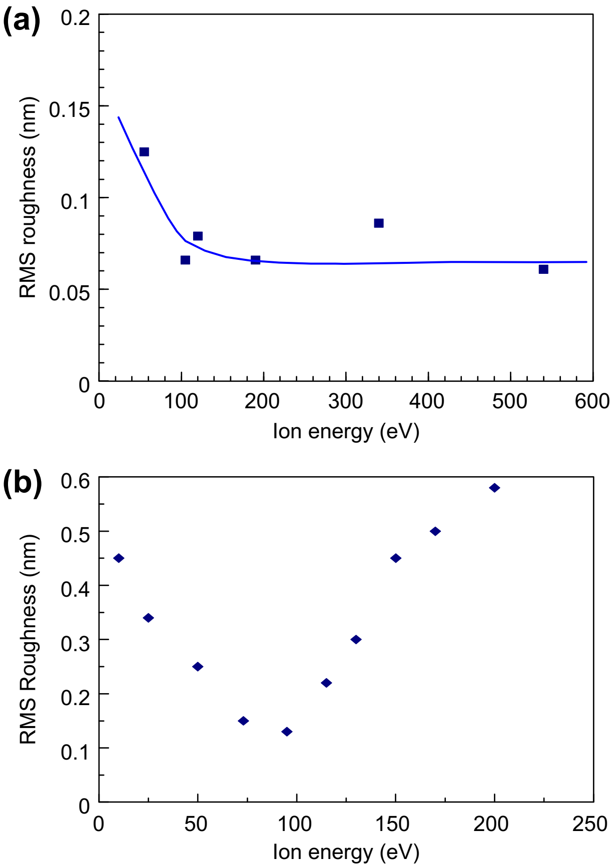

Figure 52 (a) Variation of RMS roughness versus deposition ion energy for a-C:H films (Peng et al., 2001). (b) Variation of RMS roughness versus film thickness for ta-C films from Shi et al. (1997). The variation in (a) is found by more groups.

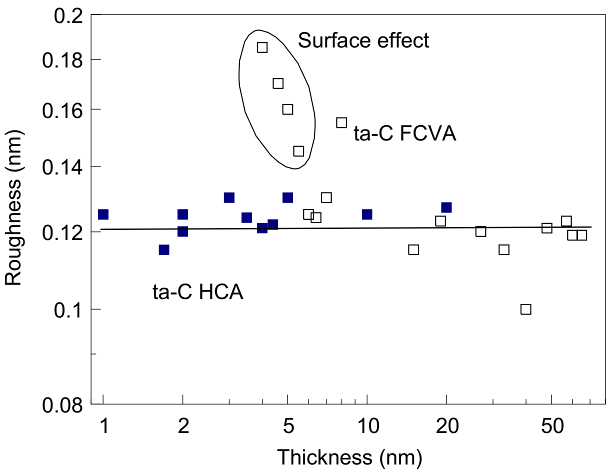

Figure 53 Variation of RMS roughness of ta-C vs film thickness (Casiraghi et al., 2003).

A very interesting fact is that the evolution of film roughness with film thickness shows no increase of roughness with increasing thickness (Casiraghi et al., 2003; Patsalas et al., 2005; Pisana et al., 2006) (**Figures 53** and 54). Thus, expressing RMS roughness, r, as a function of average film thickness, h, we find

$$r = r_0 h^{\beta}$$

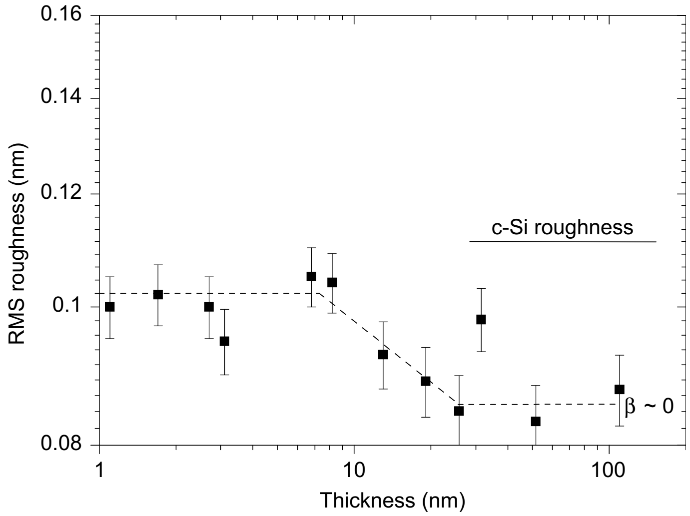

Figure 54 Variation of RMS roughness of ta-C:H vs film thickness (Pisana et al., 2006).

with $\beta \sim 0$. For most material systems, first, there is a nucleation barrier, giving an initial hump in roughness, and then for larger h, we usually get $\beta \sim 0.5$, due to random growth. $\beta \sim 0$ has been identified as due to downhill deposition (due to energetic ions) (Moseler, Gumbsch, Casiraghi, Ferrari, & Robertson, 2005).

Another interesting coating application of DLC is the gas membrane barrier on polyethylene terephthalate (PET) bottles used for drink and foodstuffs (Boutroy et al., 2006; Silva et al., 2007), **Figure 55**. PET is a transparent plastic used in the drinks industry. However, it has a slight permeability to gases and oxygen can oxidize the contents, while CO_2 can escape, leading to a loss of fizz. Diamond is well known to have the highest atomic density of any solid (Jansen & Angus, 1988). DLC also has a high atomic density, so it acts as a gas diffusion barrier. The critical thing is to make it transparent and economically.

The optical band gap of a typical hard DLC is only 1.5 eV, and it also has a broad optical absorption edge (Robertson, 2002a). This film would be dark brown, and an unsuitable coating. We must increase the band gap to over 2.5 eV to make it transparent. The requires film is a more polymeric a-C:H, with a higher CH_x content and low density to open up the band gap (Boutroy et al., 2006). However, the C-atom density decreases as the CH_x content increases. **Figure 56** shows the variation of optical band gap with density, and **Figure 57** shows an optical absorption edge for a typical a-C:H film. Thus, the gas impermeability varies inversely with transparency.

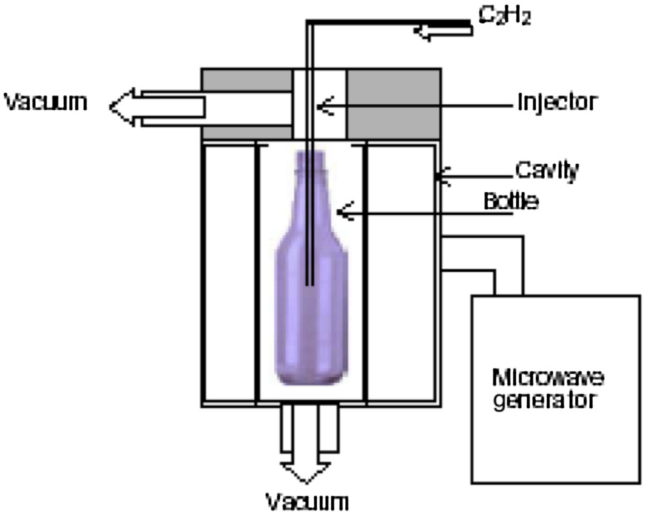

Figure 55 Schematic of the microwave plasma deposition system to grow a-C:H gas barrier films inside PET bottles (Boutroy et al., 2006).

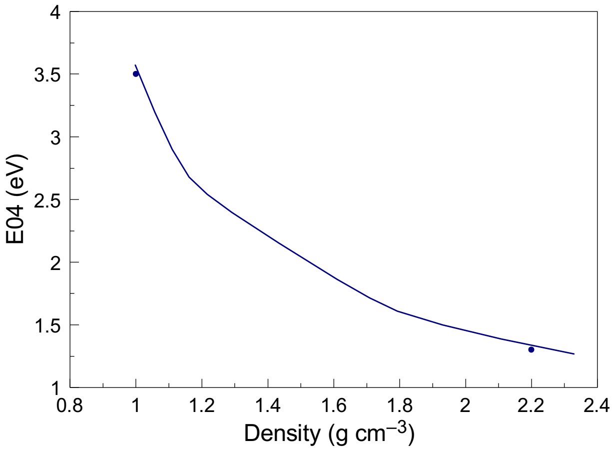

Figure 56 Variation of optical gap vs density for a-C:H in the low-density region (Boutroy et al., 2006).

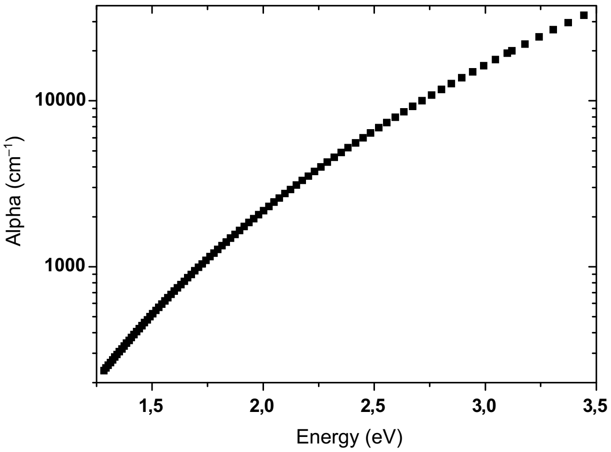

Figure 57 Optical absorption edge of a-C:H film on PET (Boutroy et al., 2006).

We must optimize the bonding of the a-C:H film, in terms of precursor gas and growth conditions, to maximize the C-atom density and also the band gap. Many factors will narrow the band gap or widen the Urbach tail, and thus loose transparency (Piazza et al., 2005). The optimization for the case of PET bottles was carried out, the resulting films were characterized in terms of C–H IR spectra (Figure 59(a)), Raman (Figure 59(b)) and ERDA to determine the hydrogen content (Figure 59(c)) (Boutroy et al., 2006). The latter shows that the a-C:H adheres to the PET due to a degree of ion mixing. Figure 58 shows the reduction of oxygen transmission coefficient with a-C:H thickness on the PET.

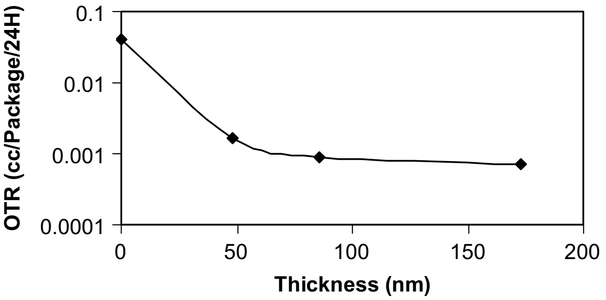

Figure 58 Oxygen transmission coefficient of a-C:H-coated PET, showing dramatic reduction in oxygen ingress by a-C:H coating.

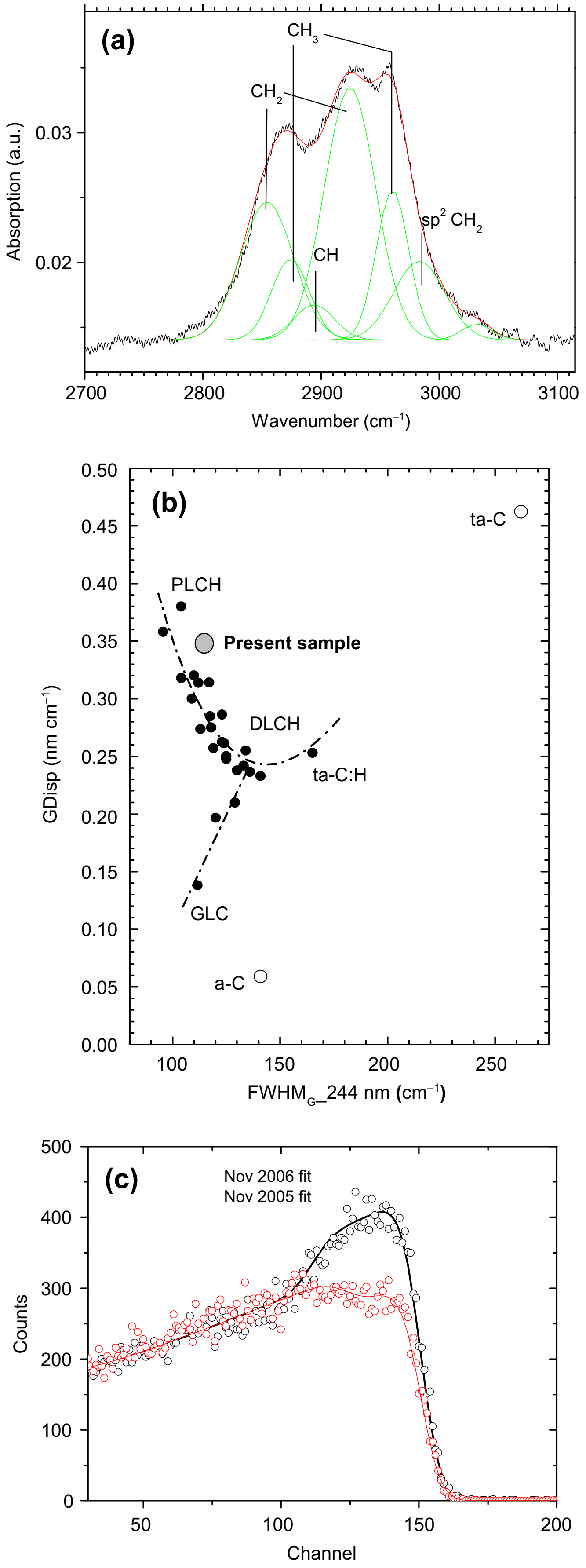

Figure 59 (a) Infrared spectra of the C–H modes in the a-C:H film. (b) Raman assessment of the a-C:H on global diagram. (c) ERDA plot of hydrogen content (Boutroy et al., 2006).

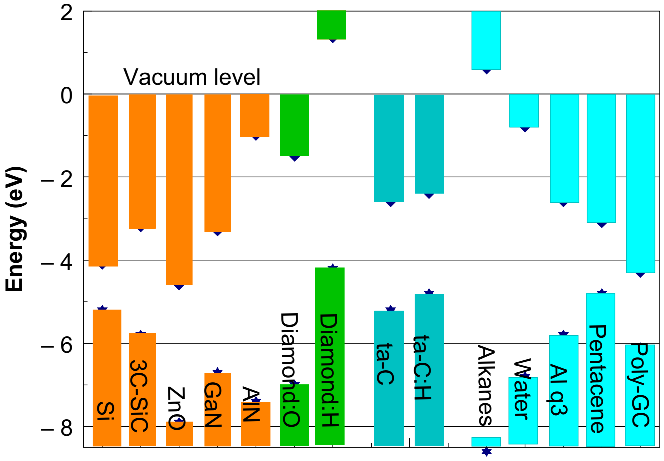

Figure 60 Band alignment diagram of a-C:H and ta-C vs other semiconductors.

The other key requirement is an economic deposition rate. In a low-cost industry like packaging, a DLC coating is only useful if it can be applied economically, to add little cost. A 50 nm thickness is needed for sufficient barrier. Economics allows a cycle time of ~4 s. Allowing 2 s for pumping to vacuum, this allows only 2 s for deposition. The industrial process of Sidel (Boutroy et al., 2006) uses a microwave plasma and C_2H_2 as the source gas (**Figure 55**).

A recent advance in this field is the development of atmospheric plasmas for a-C:H deposition (Kodama et al., 2006; Sasaki et al., 2010; Suzuki & Kodama, 2009; Ladwig et al., 2009), for coating plastics in a roll to roll process. This uses low-frequency RF plasmas constructed as line plasma sources, and will be of importance in the future. This removes one of the cost obstacles.

A final interesting use of DLC could be as a biosensor layer (Yu, Li, & Robertson, 2011). In this, it would compete with diamond and now graphene-type layers (Hamers et al., 2005; Hartl et al., 2004; Stutzmann, Garrido, Eickoff, & Brandt, 2006; Yang et al., 2002). Diamond is of value because it is biocompatible (Hauert,

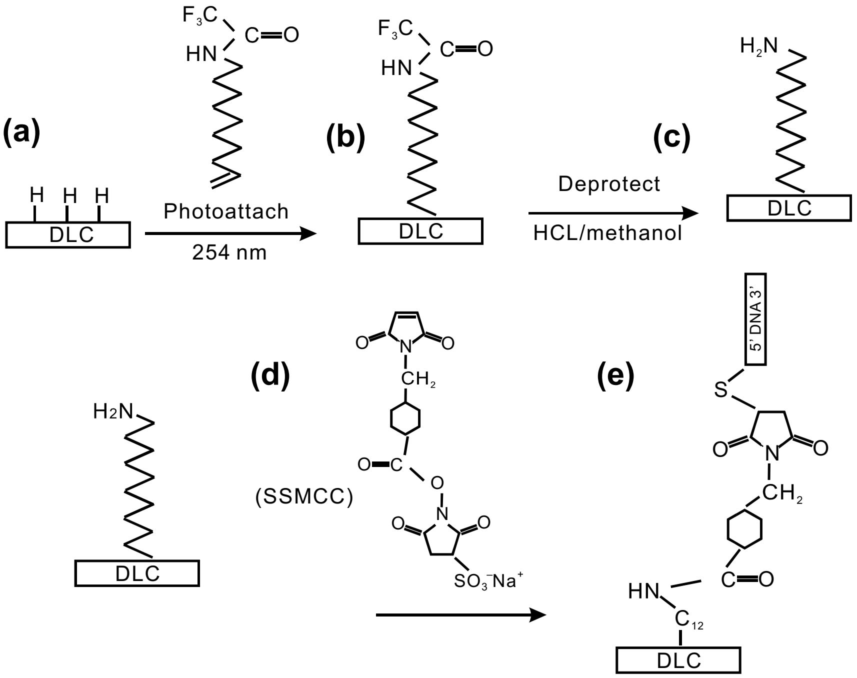

Figure 61 Functionalization pathway on ta-C (Yu et al., 2011).

2003). Diamond and ta-C are useful as a biosensor because it can be functionalized and fundamentally because its band line-up is compatible with biomolecules, as shown in **Figure 60**. The diamond surface is inert, but it can be functionalized by treatment with an additive molecule (**Figure 61**). The same treatment is found to be effective for ta-C (Yu et al., 2011). The ta-C surface is first given a hydrogen plasma treatment. Nitrogen-doped ta-C is used, as this increases its electrical conductivity, without loosing its sp^3 bonding and wide band gap. The process flow diagram is shown in **Figure 61**. The resulting surface is found to act as a sensor for DNA-based molecules, detected by electrochemical impedance analysis. It was proposed that the functionalization mechanism required the diamond to have a negative electron affinity (Colavita, Sun, Tse, & Hamers, 2007), but ta-C does not have a negative electron affinity, so this is not the case.

3.06.10 Conclusions

DLC is the coating material with the advantage of a high deposition rate at low temperatures. Its applications are discussed. It has a number of present day applications as a protective coating material, in magnetic disk technology, car components, food containers, and razor blades.

References

Anders, A., Anders, A., & Brown, I. G. (1994). Effect of vacuum arc deposition parameters on properties of amorphous carbon films. *Surface and Coatings Technology, 68*, 388.

Anders, A., Anders, S., & Brown, I. G. (1995). Transport of vacuum arc plasmas through magnetic macroparticle filters. *Plasma Sources Science & Technology, 4*, 1.

Angus, J. C., & Hayman, C. C. (1988). Low pressure metastable growth of diamond and diamondlike phases. *Science, 241*, 913.

Anttila, A., Lappalainen, R., Tiainen, V. M., & Hakovirta, M. (1997). Superior attachment of high-quality hydrogen-free amorphous diamond films to solid materials. *Advanced Materials, 9*, 1161.

Auciello, O., Birrell, J., Carlisle, J. A., Gerbi, J. E., Peng, B., & Espinosa, H. D. (2004). *Journal of Physics: Condensed Matter, 16*, R552.

Bhatia, C. S., Fong, W., Chen, C. Y., Wei, J., Bogy, D. B., Anders, S., Strammler, T., & Stohr, J. (1999). *IEEE Transactions on Magnetics, 35*, 910.

Bhushan, B. (1999). Chemical, mechanical, and tribological characterization of ultra-thin and hard amorphous carbon coatings 3.5 nm. *Diamond and Related Materials, 8*, 1985.

Bilek, M. M. M., & McKenzie, D. R. (2006). Comprehensive model of stress generation and relief processes in thin films deposited with energetic ions. *Surface and Coatings Technology, 200*, 4345.

Boutard, D., Moller, W., & Scherzer, J. (1988). *Physical Review B, 38*, 2988.

Boutroy, N., Pernel, Y., Rius, J. M., Auger, F., von Bardeleben, H. J., Cantin, J. L., et al. (2006). Hydrogenated amorphous carbon film coating of PET bottles for gas diffusion barriers. *Diamond and Related Materials, 15*, 921.

Bubenzer, A., Dischler, B., Brandt, G., & Koidl, P. (1983). RF plasma deposited amorphous hydrogenated hard carbon films – preparation properties and applications. *Journal of Applied Physics, 54*, 4590.

Butler, J. E., & Woodin, R. L. (1993). Thin film diamond growth mechanisms. *Philosophical Transactions of the Royal Society, A: Mathematical, Physical & Engineering Sciences, 342*, 209.

Casiraghi, C., Ferrari, A. C., & Robertson, J. (2005). Raman spectroscopy of hydrogenated amorphous carbon. *Physical Review B, 72*, 085401.

Casiraghi, C., Ferrari, A. C., Ohr, R., Flewitt, A. J., Chu, D. P., & Robertson, J. (2003). Dynamic roughening of tetrahedral amorphous carbon. *Physical Review Letters, 91*, 226104.

Chen, C. W., & Robertson, J. (1998). *Journal of Non-Crystalline Solids, 227*, 602.

Chhowalla, M., Robertson, J., Chen, C. W., Silva, S., & Amaratunga, G. (1997). Influence of ion energy and substrate temperature on the optical and electronic properties of tetrahedral amorphous carbon films. *Journal of Applied Physics, 81*, 139.

Cho, S., Chasiotis, I., Friedmann, T. A., & Sullivan, J. P. (2005). *Journal of Micromechanics and Microengineering, 15*, 728.

Colaco, R., Serro, A. P., & Erdemir, A. (2009). Micro to nano triboactivity of hydrogenated DLC films. *Journal of Physics D, 42*, 085307.

Colavita, P. E., Sun, B., Tse, K. Y., & Hamers, R. J. (2007). *Journal of the American Chemical Society, 129*, 13554.

Dasch, J. M., Ang, C. C., Wong, C. A., Chang, Y. T., Weiner, A. M., Ley, L. C., et al. (2006). A comparison of five categories of carbon based tool coatings for dry drilling of aluminum. *Surface and Coatings Technology, 200*, 2970.

Davis, C. A. (1993). Simple model for formation of compressive stress in thin films by ion bombardment. *Thin Solid Films, 226*, 30.

Dischler, B., Bubenzer, A., & Koidl, P. (1983). Hard carbon coatings with low optical absorption. *Applied Physics Letters, 42*, 636.

Donnet, C., & Erdimir, A. (2008). *Tribology of diamond-like carbon films.* Springer.

Drabold, D. A., Fedders, P. A., & Grumbach, M. P. (1996). *Physical Review B, 54*, 5480.

Enke, K. (1981). *Thin Solid Films, 80*, 227.

Enke, K., Dimigen, H., & Hubsch, H. (1980). *Applied Physics Letters, 36*, 291.

Erdemir, A., & Donnet, C. (2006). Tribology of diamond like carbon films, recent progress. *Journal of Physics D, 39*, R311.

Eryilmaz, O. L., & Erdemir, A. (2008). On the hydrogen lubrication mechanism of DLC films, a imaging TOF-SIMS study. *Surface and Coatings Technology, 203*, 750.

Fallon, P. J., & Brown, L. M. (1993). *Diamond and Related Materials, 2*, 1004.

Fallon, P. J., Veerasamy, V. S., Davis, C. A., Robertson, J., Amaratunga, G., Milne, W. I., et al. (1993). Properties of filtered ion beam deposited diamond like carbon as a function of ion energy. *Physical Review B, 48*, 4777.

Ferrari, A. C., Kleinsorge, B., Morrison, N. A., Hart, A., Stolojan, V., & Robertson, J. (1999). Stress reduction and bond stability during thermal annealing of tetrahedral amorphous carbon. *Journal of Applied Physics, 85*, 7191.

Ferrari, A. C., LiBassi, A., Tanner, B. K., Stolojan, V., Yuan, J., Brown, L. M., et al. (2000). Density, sp^3 fraction, and cross-sectional structure of amorphous carbon films determined by X-ray reflectivity and electron energy loss spectroscopy. *Physical Review B, 62*, 11089.

Ferrari, A. C., & Robertson, J. (2000). Interpretation of Raman spectra of disordered and amorphous carbon. *Physical Review B, 61*, 14095.

Ferrari, A. C., & Robertson, J. (2001). *PRB*.

Ferrari, A. C., Robertson, J., Beghi, M. G., Bottani, C. E., Ferulano, R., & Pastorelli, R. (1999). Elastic constants of tetrahedral amorphous carbon films by surface Brillouin scattering. *Applied Physics Letters, 75*, 1893.

Ferrari, A. C., Rodil, S. E., Robertson, J., & Milne, W. I. (2002). *Diamond and Related Materials, 11*, 994.

Field, J. E. (1993). *Properties of diamond*. London: Academic Press.

Fink, J. (1989). *Advances in Electronics and Electron Physics, 75*, 121.

Fink, J., Müller-Heinzerling, T., Pflüger, J., Bubenzer, A., Koidl, P., & Crecelius, G. (1983). *Solid State Communications, 47*, 687.

Friedmann, T. A., Sullivan, J. P., & Knapp, J. A. (1997). Thick stress-free amorphous tetrahedral amorphous carbon films with hardness near that of diamond. *Applied Physics Letters, 71*, 3820.

Fukui, H., Okida, J., Omori, N., Moriguchi, H., & Tsuda, H. (2004). Cutting performance of DLC coated tools in dry machining of aluminum alloys. *Surface and Coatings Technology, 187*, 70.

Galli, G., Martin, R. A., Car, R., & Parrinello, M. (1990). *Physical Review B, 42*, 7470.

Gangopadhyay, A. (1998). Mechanical and tribological properties of amorphous carbon films. *Tribology Letters, 5*, 25.

Gangopadhyay, A. K., Willermet, P. A., Vassell, W. C., & Tamor, M. A. (1997). *Tribology International, 30*, 9.

Gangopadhyay, A., et al. (2011). Friction, wear and surface film formation characteristics of diamond like carbon. *Tribology Transactions, 54*, 104.

Gilkes, K. W. R., Prawer, S., Nugent, K. W., Robertson, J., Sands, H. S., Lifshitz, Y., et al. (2000). *Journal of Applied Physics, 87*, 7283.

Gilkes, K. W. R., Sands, H. S., Batchelder, D. N., Robertson, J., & Milne, W. I. (1997). *Applied Physics Letters, 70*, 1980.

Goglia, P., Berkowitz, J., Hoehn, J., Xidis, A., & Stover, L. (2001). Diamond like carbon applications in high density hard disc recording heads. *Diamond and Related Materials, 10*, 271.

Goodwin, D. G. (1993). Scaling laws for diamond chemical vapor deposition, 1 diamond surface chemistry. *Journal of Applied Physics, 74*, 6888.

Grill, A., & Patel, V. (1992). *Applied Physics Letters, 60*, 2089.

Gui, J. (2003). Tribology challenges for head disk interface toward 1 Tb/in2. *IEEE Transactions on Magnetics, 39*, 716.

Haerle, R., Riedo, E., Pasquarello, A., & Baldereschi, A. (2001). *Physical Review B, 65*, 045101.

Hamers, R. J., Butler, J. E., Lassiter, T., Nichols, B. M., Russell, J. N., Tse, K. Y., et al. (2005). *DRM, 14*, 661.

Hartl, A., Chmich, E. S., Garrido, J. A., Hernando, J., Cathrino, S., Walter, S., et al. (2004). *Nature Materials, 3*, 730.

Hauert, R. (2003). *Diamond and Related Materials, 12*, 583.

Hutchinson, A. B., et al. (2004). *Applied Physics Letters, 84*, 972.

Jacob, W. (1998). *Thin Solid Films, 326*, 1.

Jacob, W., & Moller, W. (1993). *Applied Physics Letters, 63*, 1771.

Jacob, W., & Unger, M. (1996). *Applied Physics Letters, 68*, 475.

Jansen, F., & Angus, J. C. (1988). Dense diamondlike hydrocarbons as random covalent networks. *Journal of Vacuum Science & Technology, A, 6*, 1778.

Jiang, X. (1991). *Physical Review B, 43*, 2372.

Jiang, X., Beyer, W., & Reichelt, K. (1990). *Journal of Applied Physics, 68*, 1378.

Jiang, X., Reichelt, K., & Stritzker, B. (1990a). *Journal of Applied Physics, 66*, 5805.

Jiang, X., Reichelt, K., & Stritzker, B. (1990b). *Journal of Applied Physics, 68*, 1018.

Jiang, X., Zou, J. W., Reichelt, K., & Grunberg, P. (1989). *Journal of Applied Physics, 66*, 4729.

Jungnickel, G., Frauenheim, T., Proezag, D., Blaudeck, P., & Stephan, U. (1994). *Physical Review B, 50*, 6709.

Kano, M., Yasuda, Y., Okamoto, Y., Mabuchi, Y., Hamada, T., Ueno, T., et al. (2005). Ultra-low friction of DLC in presence of glycerol mono-oleate. *Tribology Letters, 18*, 245.

Kelires, P. C. (1993). *Physical Review B, 47*, 1829.

von Keudell, A., Schwarz-Sellinger, T., & Jacob, W. (2001). *Journal of Applied Physics, 89*, 2719.

Kodama, H., Shirakura, A., Hotta, A., & Suzuki, T. (2006). *Surface and Coatings Technology, 201*, 913.

Koidl, P., Wagner, C., Dischler, B., Wagner, J., & Ramsteiner, M. (1990). *Materials Science Forum, 52*, 41.

Kondoh, E., Ohta, T., Mitomo, T., & Ohtsuka, K. (1991). Determination of activation energies for diamond growth by hot filament chemical vapor deposition. *Applied Physics Letters, 59*, 488.

Ladwig, A. M., Koch, R. D., Wenski, E. G., & Hicks, R. F. (2009). Atmospheric plasma deposition of diamond like carbon coatings. *Diamond and Related Materials, 18*, 1129.

Lau, D. W. M., McCulloch, D. G., Taylor, M. B., Partridge, J. G., McKenzie, D. R., Marks, N. A., et al. (2008). Abrupt stress induced transformation in amorphous carbon with highly conductive transition region. *Physical Review Letters, 100*, 176101.

Lau, D. W. M., Partidge, J. G., Taylor, M. B., McCulloch, D. G., Wasyluk, J., Perova, T. S., et al. (2009). Microstructural investigation supporting abrupt stress induced transformation in amorphous carbon films. *Journal of Applied Physics, 105*, 084302.

Lifshitz, Y. (1996). *Diamond and Related Materials, 6*, 388.

Lifshitz, Y., Kasi, S. R., & Rabalais, J. W. (1989). Subplantation model for growth from hyper-thermal species:diamond. *Physical Review Letters, 68*, 1290.

Luo, J. K., et al. (2007). *Journal of Micromechanics and Microengineering, 17*, S147.

Lusk, D., Gore, M., Boardman, W., Casserly, Y., Boinapally, K., Oppus, M., et al. (2008). Thick DLC films deposited by PECVD on the internal surface of cylindrical substrates. *Diamond and Related Materials, 17*, 1613.

Marchon, B. (1990). *IEEE Transactions on Magnetics, 26*, 168.

Marchon, B., & Olson, T. (2009). Magnetic spacing trends, from LMR to PME and beyond. *IEEE Transactions on Magnetics, 45*, 3608.

Marks, N. A., Cover, M. F., & Kocer, C. (2006). Simulating temperature effects in growth of tetrahedral amorphous carbon. *Applied Physics Letters, 89*, 131924.

Marks, N. A., McKenzie, D. R., Pailthorpe, B. A., Bernasconi, M., & Parrinello, M. A. (1996). *Physical Review Letters, 76*, 768.

Martinez, E., Andujar, J. L., Polo, M. C., Esteve, J., Robertson, J., & Milne, W. I. (2001). *Diamond and Related Materials, 10*, 145.

Mate, C. M., Toney, M. F., & Leach, K. A. (2001). Roughness of thin perfluoro-polyether lubricant films, influence on disk drive technology. *IEEE Transactions on Magnetics, 37*, 1821.

Matta, C., Joly-Pottuz, L., Bouchet, M. I. D., & Martin, J. M. (2008). Super-lubricity and tribo-chemistry of polyhydric alcohols. *Physical Review B, 78*, 085436.

McCauley, T. G., Gruen, D. M., & Krauss, A. R. (1998). Temperature dependence of growth rate for nanocrystalline diamond deposited from an Ar/CH_4 plasma. *Applied Physics Letters, 73*, 1646.

McCulloch, D. G., McKenzie, D. R., & Goringe, C. M. (2000). *Physical Review B, 61*, 2349.

McKenzie, D. R., Muller, D., & Pailthorpe, B. A. (1991). Compressive stress induced formation of thin film tetrahedral amorphous carbon. *Physical Review Letters, 67*, 773.

Morrison, N. A., Muhl, S., Rodil, S. E., Ferrari, A. C., Nesladek, M., & Milne, W. I. (1999). Preparation characterization and tribological properties of ta-C:H deposited by electron cyclotron wave resonance plasma source. *Physica Status Solidi A, 172*, 79.

Moseler, M., Gumbsch, P., Casiraghi, C., Ferrari, A. C., & Robertson, J. (2005). The ultra-smoothness of diamond like carbon surfaces. *Science, 309*, 1545.

Oguri, K., & Arai, T. (1991). Tribological properties and characterization of diamond like carbon coatings with silicon prepared by PECVD. *Surface and Coatings Technology, 47*, 710.

Oka, Y., Yatsuzuka, M., Nishijima, M., & Hiraga, K. (2008). A 400 μm thickness diamond like carbon preparation. *Diamond and Related Materials, 17*, 405.

Patsalas, P., Logothetidis, S., & Kelires, P. C. (2005). Surface and interface morphology of amorphous carbon thin and multiplayer films. *Diamond and Related Materials, 14*, 1241.

Patscheider, J., Zehnder, T., & Diserens, M. (2001). Structure performance relations in nano-composite coatings. *Surface and Coatings Technology, 146*, 201.

Peng, L., Barber, Z. H., & Clyne, T. W. (2001). Surface roughness of diamond like carbon films prepared by various techniques. *Surface and Coatings Technology, 138*, 23.

Pharr, G. M., Callahan, D. L., McAdams, S. D., Tsui, T. Y., Anders, S., Anders, A., et al. (1996). Hardness, elastic modulus, structure of very hard carbon films produced by cathodic arc deposition with substrate pulse biasing. *Applied Physics Letters, 68*, 779.

Philips, J., Hess, P., Feygelson, T., & Butler, J. E. (2003). *Journal of Applied Physics, 93*, 2164.

Piazza, F., Grambole, D., Schneider, D., Casiraghi, S., Ferrari, A. C., & Robertson, J. (2005). Protective carbon films for future optical storage disks. *Diamond and Related Materials, 14*, 994.

Pisana, S., Casiraghi, C., Ferrari, A. C., & Robertson, J. (2006). Roughness evolution during growth of hydrogenated tetrahedral amorphous carbon. *Diamond and Related Materials, 15*, 898.

Polo, M. C., Andujar, J. L., Hart, A., Robertson, J., & Milne, W. I. (2000). Preparation of tetrahedral amorphous carbon films by filtered cathodic vacuum arc. *Diamond and Related Materials, 9*, 663.

Ristein, J., Stief, R. T., Ley, L., & Beyer, W. (1998). *Journal of Applied Physics, 84*, 3836.

Robertson, J. (1986). Amorphous carbon. *Advanced Physics, 35*, 317.

Robertson, J. (1991). *Progress in Solid State Chemistry, 21*, 199.

Robertson, J. (1992). Mechanical properties of amorphous carbon. *Physical Review Letters, 68*, 220.

Robertson, J. (1993). Deposition mechanisms for promoting sp^3 bonding in diamond-like carbon. *Diamond and Related Materials, 2*, 984.

Robertson, J. (1994a). Deposition mechanism of diamond-like carbon. *Diamond and Related Materials, 3*, 361.

Robertson, J. (1994b). Diamond like carbon. *Pure and Applied Chemistry, 66*, 1789.

Robertson, J. (2002a). Diamond like amorphous Carbon. *Materials Science & Engineering, R: Reports, 37*, 129.

Robertson, J. (2002b). *Thin Solid Films*.

Robertson, J. (2003). *Tribology International, 36*, 405.

Robertson, J. (2005). *Diamond and Related Materials, 14*, 942.

Robertson, J. (2008). Comparison of diamond-like carbon and diamond for applications. *Physica Status Solidi A, 205*, 2233.

Sasaki, T., Kodama, H., Hayashi, H., Shimo, T., & Suzuki, T. (2010). Effects of substrate temperature on physical properties of amorphous carbon film synthesized under atmospheric pressure. *Surface and Coatings Technology, 205*, S414.

Sattel, S., Robertson, J., & Ehrhardt, H. (1997). Effects of deposition temperature on the properties of hydrogenated tetrahedral amorphous carbon. *Journal of Applied Physics, 82*, 4566.

Schultrich, B., Scheibe, H. J., Dreschler, D., & Ziegele, H. (1998). Deposition of superhard amorphous carbon films by pulsed vacuum arc deposition. *Surface and Coatings Technology, 98*, 1097.

Schwan, J., Ulrich, S., Roth, H., Ehrhardt, H., Silva, S. R. P., Robertson, J., et al. (1996). Tetrahedral amorphous carbon films prepare by magnetron sputtering and ion plating. *Journal of Applied Physics, 79*, 1416.

Sekaric, L., Parpia, J. M., & Butler, J. E. (2002). *Applied Physics Letters, 81*, 4455.

Shi, X., Flynn, D., Tay, B. K., Prawer, S., Nugent, K. W., Silva, S. R. P., et al. (1997). *Philosophical Magazine B, 76*, 351.

Silva, F., Achard, J., Brinza, O., Bonnin, X., Hassouni, K., Anthonis, A., et al. (2009). High quality large area homo-epitaxial MPCVD diamond. *Diamond and Related Materials, 18*, 683.

Silva, F., Michau, A., Bonnin, X., Gicquel, A., Boutroy, N., Chomel, N., et al. (2007). Electromagnetic modelling of a microwave cavity used for deposition of carbon films on inner wall of PET bottles. *Diamond and Related Materials, 16*, 1278.

Stutzmann, M., Garrido, J. A., Eickoff, M., & Brandt, M. S. (2006). *Physica Status Solidi A, 203*, 3424.

Sullivan, J. P., & Friedmann, T. A. (2001). *MRS Bulletin, 26*, 309.

Sullivan, J. P., Friedmann, T. A., & Baca, A. G. (1997). Stress relaxation and thermal evolution of film properties in amorphous carbon. *Journal of Electronic Materials, 26*, 1021.

Sullivan, J. L., Saied, S. O., & Zaharai, T. (2011). *Acta Physica Polonica, 120*, 156.

Suzuki, T., & Kodama, H. (2009). Diamond like carbon films synthesized under atmospheric pressure on PET substrates. *Diamond and Related Materials, 18*, 990.

Tamor, M. A., & Vassell, W. C. (1994). Raman finger-printing of amorphous carbon films. *Journal of Applied Physics, 76*, 3823.

Tamor, M. A., Vassell, W. C., & Cardunder, K. R. (1991). Atomic constraint model in hydrogen diamond like carbon. *Applied Physics Letters, 58*, 592.

Thomsen, C., & Reich, S. (2000). *Physical Review Letters, 85*, 5214.

Tsugawa, K., Kawaki, S., Ishihara, M., Koga, Y., Sakakita, H., & Hasegawa, M. (2011). Nanocrystalline diamond growth in a surface wave plasma. *Diamond and Related Materials, 20*, 833.

Veprek, S., & Reiprich, S. (1995). Concept for design of novel superhard coatings. *Thin Solid Films, 268*, 64.

Voevodin, A. A., Capano, M. A., & Laube, S. J. P. (1997). Design of a Ti/TiC/DLC functionally gradient coating based on structural transitions in Ti-C films. *Thin Solid Films, 298*, 107.

Voevodin, A. A., Phelps, A. W., Zabinski, J. S., & Donley, M. S. (1996). *Diamond and Related Materials, 5*, 1264.

Voevodin, A. A., Prasad, S. V., & Zabinski, J. S. (1997). Nanocrystalline carbide amorphous carbon composites. *Journal of Applied Physics, 82*, 855.

Waidmann, S., Knupfer, M., Fink, J., Kleinsorge, B., & Robertson, J. (2001). Electronic structure studies of undoped and nitrogen doped tetrahedral amorphous carbon using high resolution electron energy loss spectroscopy. *Journal of Applied Physics, 89*, 3783.

Walter, K. C., Natasi, M., & Munson, C. (1997). Adherent diamond like carbon coatings on metals via plasma source ion implantation. *Surface and Coatings Technology, 93*, 287.

Wang, C. Z., Ho, K. H., & Chan, C. T. (1993). *Physical Review Letters, 70*, 611.

Weiler, M., Lang, K., Li, E., & Robertson, J. (1998). Deposition of tetrahedral hydrogenated amorphous carbon using an electron cyclotron wave resonance reactor. *Applied Physics Letters, 72*, 1314.

Weiler, M., Sattel, S., Giessen, T., Jung, K., Ehrhardt, H., Veerasamy, V. S., et al. (1996). Preparation and properties of highly tetrahedral hydrogenated amorphous carbon. *Physical Review B, 53*, 1594.

Weiler, M., Sattel, S., Jung, K., Ehrhardt, H., Veerasamy, V. S., & Robertson, J. (1994). Highly tetrahedral diamond-like carbon from a novel plasma beam source. *Applied Physics Letters, 64*, 2797.

Wild, C., & Koidl, P. (1987). *Applied Physics Letters, 51*, 1506.

Williams, O. A. (2011). Nanocrystalline diamond. *Diamond and Related Materials, 20*, 621.

Xu, S., Tay, B. K., Tan, H. S., Zhong, L., Tu, Y. Q., Silva, S. R. P., et al. (1996). Properties of carbon ion deposited tetrahedral amorphous carbon films as a function of ion energy. *Journal of Applied Physics, 79*, 7234.

Yang, W., Auciello, O., Butler, J. E., Cai, W., Carlisle, J. A., Gerbi, J., et al. (2002). *Nature Materials, 1*, 253.

Yoon, S. F., Yang, H., & Rusli. (1998). DC bias effects in deposition of a-C:H films in electron cyclotron resonance plasma. *Diamond and Related Materials, 7*, 70.

Yu, H., Li, P., & Robertson, J. (2011). Fabrication and functionalization of tetrahedral amorphous carbon thin films for biosensor applications. *Diamond and Related Materials, 20*, 1015.

Zaharia, T., et al. (2007). *Diamond and Related Materials, 16*, 623.

Zehnder, T., & Patscheider, J. (2000). Nano-composite TiC/a-C:H hard coatings deposited by reactive PVD. *Surface and Coatings Technology, 133*, 138.

SECTION III

NANO– AND POLY–DIAMOND

3.07 Production of Nanodiamond Particles

Olga A. Shenderova, International Technology Center, Raleigh, NC, USA; Adámas Nanotechnologies, NC, USA

3.07.1 Introduction

Nanodiamond (ND) particles have become an object of keen scientific interest all over the world within the last 4–5 years. The reason for this is fourfold. First, colloidal suspensions of individual ND particles of only 4–5 nm in size (so-called single-digit ND) became available recently (Osawa, 2007). Second, production of ND particles containing specific impurity defects seems poised to revolutionize biological imaging and quantum optics applications (Balasubramanian et al., 2008; Jelezko et al., 2004). Third, the chemical reactivity of the ND surface which allows it to participate in a wide range of chemical reactions and its facile surface functionalization (Krueger, 2008) permit it to be utilized readily in many applications. Fourth, ND is reported to have the lowest toxicity among all known carbon nanoparticles (Schrand et al., 2007).

The availability of single-digit ND particles produced by detonation of explosives in kilograms quantity opened broad perspectives for the application of ND in composites, nanolubricants and as drug delivery vehicles. Indeed, the specific surface area of ND particles with 4 nm and 30 nm in diameter are 428 m^2/g and 57 m^2/g, correspondingly, making a noticeable 7× difference in the adsorbing and loading capacity of the nanoparticles. Moreover, the extremely high density of surface sites (18.5 carbon atom nm^{-2} within the (111) crystallographic plane) available for bond formation may facilitates a high degree of cross-linking with molecules of the matrix material. The interparticle distance between 5 nm particles uniformly dispersed at 1 vol% in a polymer matrix would be around 20 nm, on the order of radii of gyration for polymer chains, while100 nm particles at the same loading will be separated by a distance of 370 nm, resulting in much less configurational confinement of the polymer chains and, therefore, resulting in less effect on the composite mechanical properties. The availability of single-digit ND particles is also important for biomedical applications for delivery of biologically active molecules, for example, through the blood–brain barrier (Chang et al., 2009).

A central focus of many research groups remains the controlled production of nitrogen-vacancy (NV) centers in nanoscale diamond. Due to the strong optical transition, single defects can be detected using a fluorescence microscope. The spin state of the negatively charged NV centers can be polarized by optical pumping and can be manipulated using electron paramagnetic resonance (EPR), permitting the implementation of efficient single photon emitters for quantum information processing (Jelezko et al., 2004) or a magnetic sensor with nanoscale resolution (Balasubramanian et al., 2008). Single-color centers show outstandingly high photostability, even at room temperature (Chang et al., 2008). Thus, on-demand production of NV centers in ND is important for several emerging applications like quantum information, nanoscale sensing and photoluminescent markers for microscopy. Bright photoluminescent NDs were produced using high-pressure high-temperature (HPHT) diamond, containing 10–300 ppm of native substitutional nitrogen defects (N_s), ground to nanosized particles (Boudou, Curmi, Jelezko, et al., 2009; Chang et al., 2008). To produce the NV centers, either the initial diamond material or nanoscale diamond particles obtained by grinding are irradiated with energetic particles (e.g. electrons, protons, etc.) to create vacancies. Subsequent annealing in vacuum at 600–800 °C causes vacancy diffusion and formation of the NV centers. While 7 nm HPHT ND particles were obtained on a laboratory scale (Boudou et al., 2009), 20 nm particles are the only commercially available fraction of HPHT ND (for example, from Van Mopes, Co). Cost is also an important factor in ND particle applications. Cost of HPHT ND ground to nanometer sizes is an order of magnitude higher than that of deagglomerated detonation nanodiamond (DND).

The two major breakthroughs, the production of ND particles 4–5 nm in size and the ND particles containing impurity defects exhibiting stable luminescence and unique spin properties, are related to ND particles synthesized by different techniques, detonation of explosives and grinding of HPHT diamond, correspondingly. Thus, these two important characteristics are not available through a single synthesis route. Synthesis of ND few nanometers in size with specific color centers remain elusive.

For a newcomer to the field, there is a baffling array of types of ND particles available for research. Besides the detonation of explosives technique, diamond with characteristic sizes encompassing several nanometers has been also synthesized by other methods, particularly by chlorination of carbides (Gogotsi, Welz, Ersoy, & McNallan, 2001), ion irradiation of graphite (Daulton, Kirk, Lewis, & Rehn, 2001), electron irradiation of carbon onions (Banhart & Ajayan, 1996), laser ablation of carbon precursors (Yang, Wang, & Liu, 1998) and in the vapor phase, in a substrate-free low-pressure microwave-plasma chemical vapor deposition (CVD) reactor (Frenklach, Howard, et al., 1991). Moreover, astronomical observations suggest that as much as 10–20% of the interstellar carbon is in the form of NDs (Tielens, Seab, Hollenbach, et al., 1987). The questions of when and how does ND originate in the Cosmos remain open.

A central goal of this chapter is to present a brief survey of the different classes of ND particles and provide a comparison of their purity, structure and physical properties. Another purpose of this chapter is a review of applications where properties of ND particles as superhard additives provide significant benefits, such as superfinish polishing, nanocomposites and nanolubricants.

3.07.2 Stability of Diamond at the Nanoscale

It is well known that the most stable carbon phase on the macroscale is graphite and that diamond is metastable. The energy difference between the two phases is only 0.02 eV per atom. However, because of the high activation barrier for a phase transition ($\sim$0.4 eV per atom), very high temperatures and pressures and/or the use of a catalyst are required to realize the phase transformation. At the nanoscale, however, the carbon phase diagram has to be reconsidered by introducing in addition to pressure and temperature a third parameter—cluster size (Viecelli, Bastea, Glosli, & Ree, 2001; Viecelli & Ree, 2000). In the expressions for the Gibbs free energy of a carbon cluster in a given phase, the surface energy contribution has to be added to the bulk free energy. Estimates of the displacement of the phase equilibrium lines for small carbon particles containing from several hundreds to several tens of thousands of atoms had been recently made (Viecelli & Ree, 2000; Viecelli et al., 2001) (**Figure 1**). The authors report better agreement with calculations for experimental shock pressure–volume and temperature data using "nanocarbon phase diagram" than those obtained with a bulk carbon equation of state. The results also suggest that carbon particles, of the order of 10^3–10^4 atoms, can exist in the liquid state at lower temperatures than bulk carbon (**Figure 1**). Danilenko (2005) obtained, in general, similar results on the transformation of the phase diagram for the nanocarbon phases and applied them to a detailed elaboration of the mechanism of DND formation, which will be described in Section 3.07.3.1.3. Chevrot et al.

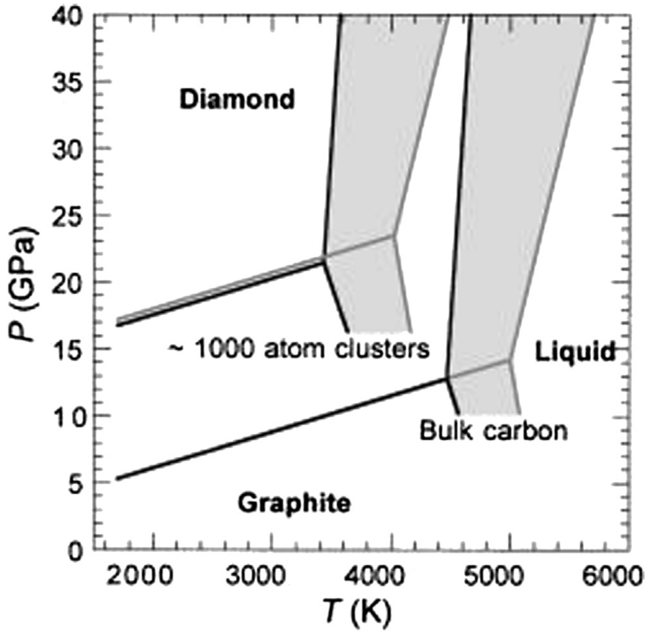

Figure 1 Approximate phase diagram for 1000 atoms carbon cluster. Shadowed region corresponds to estimated uncertainties in location of equilibrium lines derived from available experimental data. From Viecelli and Ree (2000). With permission.

(Chevrot, Bourasseau, Pineau, & Maillet, 2009) performed a molecular dynamics study of carbon nanoparticles of different sizes in sp^2 and sp^3 starting configurations under high temperature (1000–7000 K) and high pressure (2–45 GPa) conditions. For finite size clusters, the transition line between the graphite and the diamond structure was shifted to higher pressures as the size of the cluster decreases, supporting the findings by Viecelli et al. and Danilenko.

Relative phase stability of carbon nanoparticles was a focus of numerous theoretical and computational studies. First, Badziag, Verwoerd, Ellis, and Greiner (1990) using simple atomistic models predicted that between 3 and 6 nm, diamond clusters become more stable than their graphitic counterparts. Later, it was discovered that the morphology plays a very important role in cluster stability in terms of surface reconstructions and appearance of sp^2 carbon fragments (Barnard, Russo, & Snook, 2003a,b,c; Winter & Ree, 1998). While the bare (non-functionalized) surfaces of the cubic crystals exhibit structures similar to bulk diamond, the surfaces of the octahedral, cuboctahedral and spherical clusters showed a transition from sp^3 to sp^2 bonding. The preferential exfoliation of the (111) surfaces begins for clusters in the subnanometer size range and promotes the cluster transition to endofullerene for small clusters ($\sim$tens of atoms) and onion-like shells with diamond cores (bucky diamond) for larger clusters (Barnard et al., 2003a). Barnard et al. analyzing carbon structures identified two important size regimes, where sp^2 to sp^3 or sp^3 to sp^2 phase transitions may be readily expected (Barnard, Russo, & Snook, 2003d). As the system size for the carbon particles is increased, the most stable carbon form at the nanoscale changes from fullerene—to onions—to bucky diamond—to ND—to graphite. For smaller particles, the crossover between ND and fullerenic particles may be expected at 1.5–2 nm and for larger particles, the crossover in stability between ND and nanographite may be expected at around 5–10 nm in diameter.

Raty and Galli (Raty & Galli, 2003) used first principles calculations to examine the relative stability of ND as a function of hydrogen coverage at different particle sizes. Their results indicated that when the size of diamond is about 3 nm and larger, bucky diamonds are energetically preferred even over hydrogenated NDs. The difference in formation energy between particles with hydrogenated surfaces (most stable in the simulated size regime $\sim$1–2 nm) and those with bare reconstructed surfaces was found to decrease as the size of the nanoparticle increases and an extrapolation of this difference to larger sizes provided a crossover point in stability around 3 nm. While Raty and Galli observed graphitization of (111) facets ("buckyfication") on NDs with diameters of 1–2 nm (**Figure 2(a)**), at large sizes, however, other reconstructions, such as the Pandey π-bonded chains should become energetically favorable (Pandey, 1982). The size of a diamond particle at which this transition from full graphitization to π chains occurs needs to be determined.

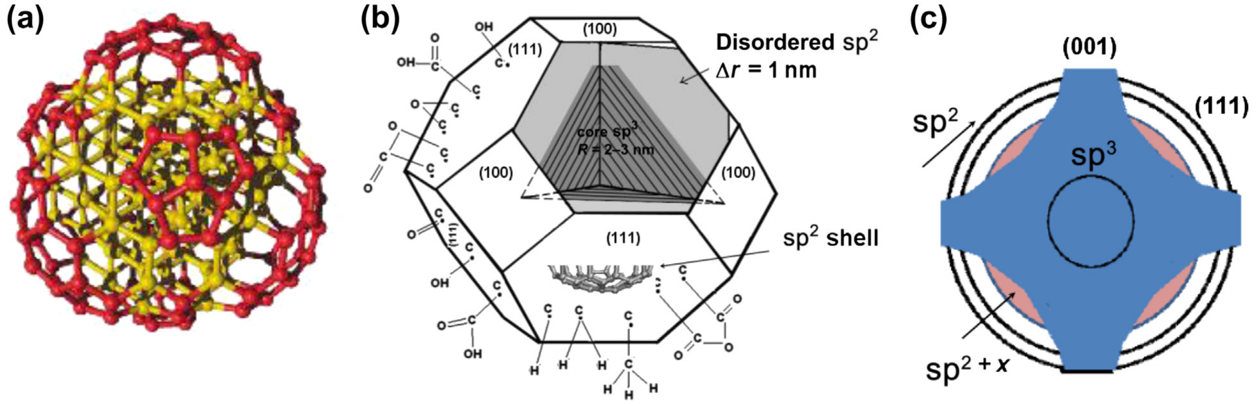

Figure 2 Structural models of nanodiamond clusters. (a) Bare surface of nonhydrogenated diamond clusters experiences surface reconstruction resulting in a cluster with a diamond core and a fullerene-like shell: bucky diamond. Red-colored atoms are sp^2 carbon atoms. (b) Schematic model of DND structure in the form of a truncated octahedron. The DND is covered by the surface groups. The (100) facets are reconstructed and the (111) facets can be either reconstructed and feature a fullerene-like shell or be terminated by the surface groups. (c) A model of the triple-decked core–shell structure of DND. **Figure 2(a)** is courtesy of Guilia Galli, Lawrence Livermore National Laboratory. **Figure 2(b)** is adapted from Alexenskiy (2010), courtesy of Alexander Vul', Ioffe Institute, S-Petersburg. **Figure 2(c)** is adapted from Osawa, 2010.

Barnard et al. (Barnard & Sternberg, 2007) examined the crystallinity of diamond nanoparticles of various shapes between ~1–3.3 nm in diameter, particularly the evolution of the core–shell structure for bare (not-functionalized) octahedral, truncated octahedral (~76% of (111) surfaces), cuboctahedral (~36% of (111) surfaces) and cuboid shapes over this size range. (111) ND surfaces are prone to graphitization, involving also graphitization of the subsurface layers depending on the particles size and shape. The octahedral and truncated octahedral particles contain relatively large fractions of sp^2 and sp^{2+x} ($x < 1$) atoms in the relaxed structures. It was concluded that if there is <76% surface graphitization, particles are likely to be stable in the diamond structure with a thin (either single or double layer) shell. These results were obtained for particles containing larger than approximately 600 atoms (smaller particles did not contain pronounced diamond structure). Importantly, the simulations implicated a strong correlation between structure, shape and the sign of electrostatic potential, with the (100) surfaces exhibiting a positive electrostatic potential, and significant regions of (111) surface graphitization exhibiting a negative electrostatic potential. These findings imply that bare ND particles with reconstructed surfaces will be prone to aggregation due to electrostatic interactions between particles.

Currently, different structural models of ND particles have been suggested for DND (Figure 2). In one of the earliest models, Alexenskii et al. considered the diamond nanocluster as a crystalline diamond core coated by an onion-like carbon (OLC) shell (core–shell model). The model was derived based on experimental data obtained from XRD and small-angle X-ray scattering (SAXS) of DND of different level of purification. In the core–shell model by Mykhaylyk et al., also based on X-ray studies, the DND particle is composed of an ordered diamond core (~3 nm in diameter) covered by a disordered amorphous outer shell formed by mixed sp^2/sp^3 bonding of carbon atoms (Mykhaylyk, Solonin, Batchelder, & Brydson, 2005). Later models suggested the presence of an intermediate layer between the perfect ND core and the sp^2 shell, resulting in a three-layer model of the DND particles (Aleksenskii et al., 1999; Baidakova & Vul, 2007; Hawelek et al., 2008; Kulakova, 2004; Palosz, et al., 2006). But these models do not take into account surface functional groups present on DND due to different oxidation treatments of detonation soot (Baidakova & Vul, 2007; Kuznetsov & Butenko, 2006).

Fang et al. (2009) proposed a nonaromatic core–shell structural model of DND particles based on nuclear magnetic resonance (NMR) studies. It was concluded that sp^2-hybridized carbon makes up <1% of the material, ruling out fullerenic or graphitic surface layers in the studied samples. The surface layer of the DND particles consisted mostly of sp^3-hybridized C that was protonated or bonded to OH groups. The unpaired electrons were mostly located in the disordered shell, at distances between 0.4 and 1 nm from the surface. Most nitrogen was located in the particles interior.

Another NMR study provided information resulting in a DND model assuming that the central part of the diamond core consists (Panich et al., 2006) of sp^3 hybridized carbon and the core is partially covered by a fullerene-like shell of sp^2 carbon. The carbon atoms located at the uncoated spots of the outer surface are bound to hydrogen and oxygen atoms, thus giving rise to a variety of functional groups that saturate the dangling bonds.

The DND models which originated from the experimental observations listed above assumed a spherical shape of DND particles, based on the earliest TEM low-resolution observations of aggregates of DND (Chen, Ding, Chen, Huang, & Yun, 2000). Graphitization of the DND surface that might be initiated by the high-energy electron beam during TEM observations (Iakoubovskii, Mitsuishi, & Furuya, 2008) also contributes to the impression of the ND particles having spherical shapes. However, using a nondestructive high-vacuum aberration-corrected electron microscope, Iakoubovskii et al. demonstrated that DND grains could have crystalline structure with negligible fractions of nondiamond carbon (Iakoubovskii et al., 2008). These findings are consistent with earlier reports by Tyler et al. (see also Shenderova, Zhirnov, & Brenner, 2002), on clear diamond facets of individual polyhedral DND particles obtained by electrodeposition of ozone-purified DND on Mo tips (Petrov et al., 2007; Tyler, Zhirnov, Kvit, Kang, & Hren, 2003) (**Figure 3(a), (b)**). Recently Turner confirmed the absence of sp^2 carbon phase on small fractions of ozone-purified DND (see Section 3.07.4.2 of this chapter).

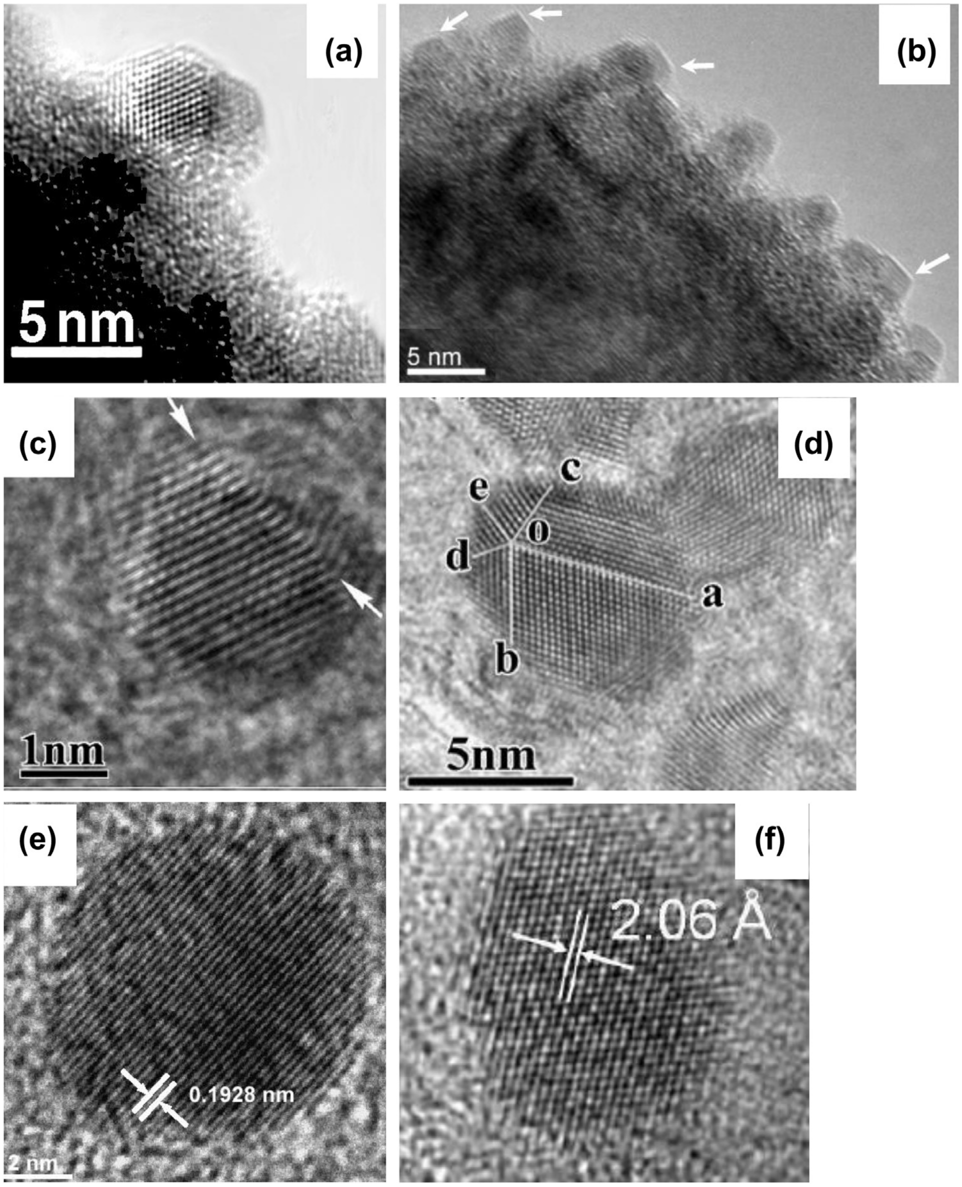

Figure 3 (a,b) HRTEM images of polyhedral particles of detonation UNCD; (c) a single crystal structure and (d) multiply twinning structure of nanodiamonds synthesized by pulsed-laser irradiation; (e) a spherical diamond in a carbide matrix synthesized by carbide chlorination process and (f) a spherical HPHT ND particle obtained by high-energy ball milling. Figures are from Tyler et al. (2003); (a) a courtesy of Talmage Tyler, ITC; (b) Hu (2008); (c,d) Welz et al. (2003); (e) Boudou et al. (2009); (f). With permission.

The above findings and models of DND were combined by Aleksenskiy et al. as follows (Aleksenskiy, Baidakova, Osipov, & Vul', 2010). DND particles are polyhedra consisting of a diamond core built up of sp^3 carbon, joined by a region of disordered sp^3 carbon, which, in turn, is partially coated by a fullerene-like shell of sp^2 carbons (**Figure 2(b)**). Carbon atoms containing dangling bonds on the outer surface are bonded to functional groups. Additional characteristic features of the DND not included in the model are the presence of twins and grain boundaries in the crystallites as well as nitrogen impurities (up to 2–3 wt%), which can form complexes in the core of DND particles (Turner, Lebedev, Shenderova, et al., 2009; Vlasov, Shenderova, Turner, et al., 2010). The existence of these features was not taking into account in the interpretation of the X-ray experimental data and their contribution into X-ray spectra could, potentially, be a reason for the introduction of a region of disordered sp^3 carbon to explain experimental data.

In an attempt to describe the properties of single-digit ND obtained by a bead milling (high graphitization of the particles and high tendency to agglomeration), Osawa (2010) suggested a so-called triple-decked core–shell structure (**Figure 2(c)**), which is a modified Barnard–Sternberg model (Barnard & Sternberg, 2007). Namely, the diamond core is surrounded by a few layers of strained structures in between diamond and graphitic shell, and one or two layers of graphitic shell covers the core (**Figure 2(c)**). A partial surface exposure of diamond internal structure is taking place along (001) facets which, in turn, underwent surface reconstructions. This model denies the existence of functional groups on the DND surface, except adsorbed water, based on the FTIR and titration experiments (Osawa, 2010). These features might be a special attributes of the bead mill-processed DND.

The survey of the existing DND models indicates that currently there is still no full agreement on the DND structure. Since the authors have studied differently synthesized and processed DND particles, it is quite possible that a single model cannot describe all kinds of NDs and probably different models should be developed depending on manufacturing and purification methods.

ND particles produced by other methods also have specific features. For example, Hu et al. (Hu, 2008) reports that for NDs synthesized by pulsed-laser irradiation, a preferred structure for smaller particles is a single crystal structure (**Figure 3(c)**), while for larger particles, a multiply twinning structure was observed (**Figure 3(d)**). The authors conclude, based on thermodynamic calculation, that the multiply twinning structure is more stable than single crystal structure in a certain size range. Welz et al. reported spherical shapes of ND particles in a carbide matrix synthesized by carbide chlorination process (Welz, Gogotsi, & McNallan, 2003) (**Figure 3(e)**). **Figure 3(f)** demonstrates a spherical, free of sp^2 carbon particle of HPHT ND ground by high-energy ball milling to sub-10 nm size range (Boudou et al., 2009). Thus, ND shape and composition, to a large extent, depend on the method of synthesis and postsynthesis processing.

3.07.3 Types of Nanodiamond Particles

Diamond structures at the nanoscale (the length scale of approximately 1–100 nm) include pure-phase diamond films, diamond particles, recently fabricated 1-D diamond nanorods and 2-D diamond nanoplatelets. Nanoscale diamond structures of different dimensions were reviewed in several publications (Shenderova et al., 2002; Shenderova & Gruen, 2006). A focus of this chapter is zero-dimensional ND, e.g. nanoparticles.

ND particles can be conveniently categorized into three groups according to the size of their primary particles (**Figure 4**): nanocrystalline particles, ultrananocrystalline particles and diamondoids. Characteristic sizes of nanocrystalline particles encompass the size range of tens of nanometers, while sizes of primary particles of ultrananocrystalline diamond are within several nanometers (Shenderova & Gruen, 2006). Diamondoids are well-defined hydrogen-terminated molecular forms consisting of several tens of carbon atoms with characteristic sizes ~1–2 nm (Dahl, Liu, & Carlson, 2003). While a choice of 10 nm as the margin between two classes of NDs seems arbitrary, however, it reflects a difference in properties of the resulting products using diamond nanoparticles of different sizes, as it was demonstrated in the Introduction. The term "single-digit ND"coined by Osawa (2007) seems to be gaining broader acceptance in the community for sub-10 nm ND particles, rather than "ultrananocrystalline" ND particle.

The class of nanocrystalline diamond particles includes subgroups of monocrystalline and polycrystalline particles (**Figure 4**). Monocrystalline nanoparticles include ND particles processed from HPHT synthetic diamond as well as from natural diamond powders, commercially available with smallest average particle size around 20 nm (produced, for example, by *Microdiamant AG*). Polycrystalline ND powder is processed from micron-sized polycrystalline diamond particles obtained by shock compression of graphite mixed with metals (Decarli & Jamieson, 1961) (DuPont de Nemours's method) or by detonation of a mixture of graphite and

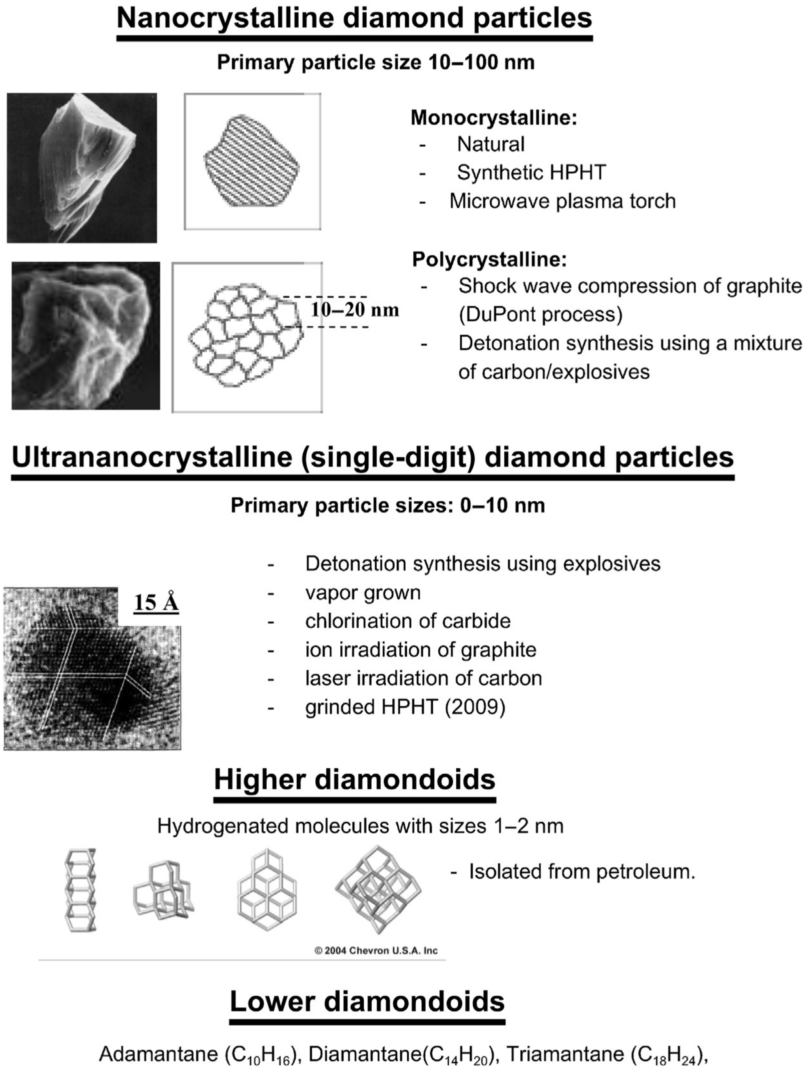

Figure 4 Summary of the types of nanoscale diamond particles and molecular forms (low diamondoids) according to the primary particle size. (Pictures on nanocrystalline diamond are courtesy of Microdiamant AG, Switzerland. Pictures on UNCD single particles are Courtesy of T. L. Daulton, Naval Research Laboratory.) Examples of higher diamondoids from petroleum, 1–2 nm hydrogen-terminated diamond molecules (left to right): rod-shaped [1212] pentamantane $C_{26}H_{32}$, pyramid-shaped [1(2,3)4] pentamantane $C_{26}H_{32}$, irregular disc-shaped [121321] heptamantane $C_{30}H_{34}$, octahedral [1231241(2)3] decamantane $C_{35}H_{36}$. Graphics courtesy of ChevronTexaco MolecularDiamond Technologies.

explosives (Tacii). Polycrystalline particles consist of nanometer-sized diamond grains (~10–20 nm). The finest diamond fraction produced by micronizing followed by grading has an average size of an individual particle of ~25 nm (available at *Microdiamant AG*).

Out of several types of ultrananocrystalline diamond particles (Figure 4), only DND, obtained by the detonation of solid explosives in an inert atmosphere, has been commercialized on a large scale. The average size of primary DND particles produced by most vendors lies in the range of 3.5–6 nm. Recently, single-digit ND produced by laser ablation of carbon precursors has become commercially available (Ray Technologies). Details on the methods of synthesis of other single-digit ND particles are provided in the next section.

Higher diamondoids (Figure 4) are highly rigid, well-defined hydrogen-terminated diamond species (Dahl et al., 2003; Schwertfeger, Fokin, & Schreiner, 2008). With more than three crystal diamond cages, higher diamondoids are intermediate in size to the adamantane molecule, the smallest species of H-terminated cubic diamond containing only 10 carbon atoms, and ultrananocrystalline diamond particles with sizes more than 3 nm as described above. Higher diamondoids are extracted from petroleum as diamond molecules in the form

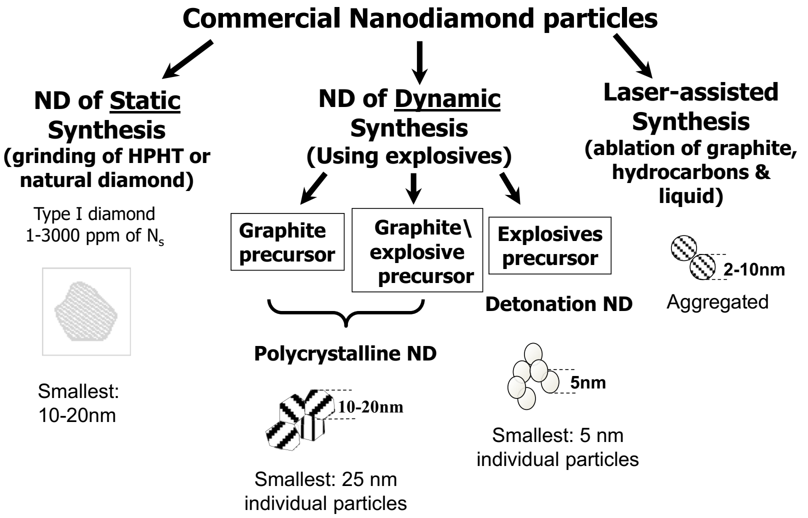

Figure 5 Summary of types of commercial nanodiamonds.

of nanometer-sized rods, helices, discs, pyramids, etc. (Carlson, Dahl, & Liu, 2005; Dahl et al., 2003) So far, it has not been possible to synthesize higher diamondoids except antitetramantane, a tetramantane isomer (Schwertfeger et al., 2008). By comparison, lower diamondoids (adamantane, diadamantane and triadamantane), extracted from crude oil much earlier than larger members of the diamondoid series, are currently available in kilograms quantities (Schwertfeger et al., 2008) and can be synthesized.

Figure 5 summarizes commercially available ND particles based on their method of synthesis. Major classes of commercial ND are ND of *static* and *dynamic* synthesis. While ND of static synthesis is by 1–2 orders of magnitude more expensive than ND of dynamic synthesis, this material is a primary material for production of photoluminescent ND particles. ND of static synthesis can be HPHT ND type Ib, with substitutional nitrogen (Ns) concentration of 1–300 ppm. ND produced from natural diamond type Ia (Ns concentration up to 3000 ppm) is also available. Irradiation by high-energy particles of type Ib ND causes formation of NV centers with red emission, while ND from diamond Ia demonstrates green luminescence originating from formation of N–V–N centers after irradiation and annealing. A large subgroup of ND is produced via *dynamic synthesis*, harnessing the energy of explosives and different carbon-containing precursor materials. Three classes of dynamically synthesized NDs are manufactured on an industrial scale (see also Figure 6):

1. NDs produced by direct phase transformation of graphite induced by an external shock wave (the DuPont method) (Decarli & Jamieson, 1961);

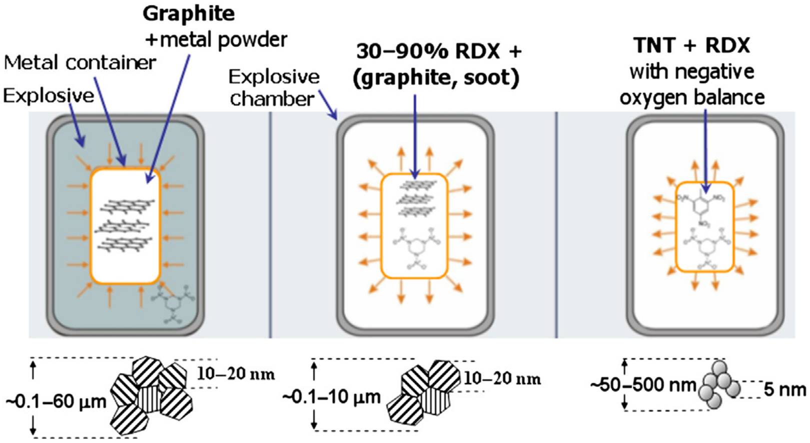

Figure 6 Classes of dynamically synthesized NDs manufactured on an industrial scale.

2. NDs produced from a mixture of a carbon precursor and explosives (Tatcii, 2009);
3. NDs produced from the carbon contained in high-energy explosives (so-called DND), or ultradispersed diamond (Danilenko, 2003; Dolmatov, 2003). Such explosive compounds simultaneously serve as sources of energy and carbon.

Depending on the precursor material in a dynamic synthesis, NDs with monocrystal sizes between 4 and 25 nm can be synthesized (Osawa, 2007). Slurries of 4 nm individual DND particles or NDs synthesized from graphite and graphite\hexogen precursors with average aggregate size of 20–30 nm are commercially available.

While the first publications on laser irradiation of graphite precursors in liquids appeared a decade ago (Yang et al., 1998), ND produced using a laser only became commercially available very recently (Ray Technologies). Primary particle size, as reported by the vendor, ranges between 2 and 10 nm. Aggregate size in water suspensions is about 100 nm. At the moment, this type of ND is two orders of magnitude more expensive than DND.

Section 3.07.3.1 provides more details on manufacturing of ND of dynamic synthesis, currently a major approach for synthesis of inexpensive ND particles in bulk quantities, followed by a brief survey of methods of synthesis of ND particles produced at a laboratory scale.

3.07.3.1 Nanodiamond of Dynamic Synthesis

Below, we briefly survey methods of synthesis and characteristics (crystal size, morphology) of the three classes of dynamically synthesized NDs manufactured on an industrial scale (**Figure 6**).

3.07.3.1.1 Nanodiamond Produced by Shock Conversion of Graphite

Synthesis of polycrystalline diamond particles produced by direct phase transformation of graphite induced by an *external* plain shock wave was first reported by Decarli and Jamieson (1961) and patented by DeCarli (1966). A patent by Cowan, Woodbury, Dunnington, et al. (1968) (assigned to du Pont de Nemours and Co) provided a means for significant increase of diamond yield during shock wave transformation of graphite by mixing graphite with cooling media. In 1976, this technology was commercialized by DuPont producing microcrystalline diamond powder under a trade name “Mypolex” (Danilenko, 2006). In parallel, studies of the formation of diamond in shock-loaded graphite were taking place in the former USSR, VNIITF institute (Snezinsk) (Danilenko, 2006). Diamond production by the shock synthesis technique in spherical and cylindrical encloses was first demonstrated in 1962 (2% diamond yield), followed by experiments with mixtures of graphite or soot with metals, resulting in 20% yield of diamond product (1963) (Danilenko, 2004, 2006).

More specifically, under suitable conditions, explosively produced shock waves can create high pressure (~20–200 GPa) high temperature (>2000 K) conditions in confined volumes (**Figure 6**) for a sufficient duration to achieve partial conversion of graphite into nanometer-sized diamond grains (~20 nm) which compact into micron-sized, polycrystalline particles. Copper is mixed with graphite utilized in shock wave synthesis to provide fast heat dissipation at the high temperatures that are reached during the explosion in order to avoid transformation of the diamond back to graphite (Cowan et al., 1968). The diamond powder with characteristic sizes of particles in the submicron range can be processed from micron-sized polycrystalline diamond particles obtained by shock synthesis. Polycrystalline diamond particles are more friable than monocrystalline diamond microparticles (natural or produced by HPHT) and are widely used in fine polishing applications. It is important to note that agglomerate-free suspensions of nanocrystalline diamond particles (for both monocrystalline and polycrystalline forms) in water and oil are commercially available (Microdiamant AG, Lengwil, Switzerland).

3.07.3.1.2 Nanodiamond Produced from Carbon Precursor\Explosive Mixture

NDs produced by another dynamic method, detonation of a mixture of a carbon precursor (graphite or carbon black) and explosives, is much less known in the community. This approach was invented in the Institute of Problems of Chemical Physics, Russian Academy of Sciences, Chernogolovka (Adadurov, Baluev, Breusov, et al, 1977) and registered under the trademark DALAN (Russian acronym for detonation diamonds of the Academy of Sciences). Tatcii (2009) summarized data on the production of DALAN ND from three types of the precursor: mixture of RDX and carbon black (charge density 1.34–1.39 g cm^{-3}), RDX and graphite (charge density 1.61–1.67 g cm^{-3}), and gunpowder/carbon/RDX (charge density 1.67–1.75 g cm^{-3}). The concentration of carbon precursor materials can be varied between 5 and 35%. The detonation pressure measured by dynamic methods (in the Chapman–Jouguet plane) was about 27.5–14.5 GPa. It was concluded that the diamond powders synthesized from graphite consists of 1–3 μm particles of lamellar shape with different phase composition (diamond, lonsdaleite, graphite) and different grains size. The particles of diamond powder synthesized from carbon black are aggregates consisting of 20–80 nm grains of cubic phase diamond exhibiting round or polyhedral shape. The particles of diamond extracted from the solid detonation products (DPs) of the gunpowder/carbon black/RDX mixture are single-phase particles having a homogeneous grain structure with a grain size of mainly 1–3 nm. These smaller grains form spherule-shaped aggregates. These findings demonstrate the key role of the carbon precursor material in the phase composition and primary particle size of the resulting products. Currently polycrystalline diamond produced from graphite\RDX mixture is a valuable commercial product for polishing applications. While micron-sized particles (1–10 μm) with narrow size distribution are of most demand, the fractions of polycrystalline diamond with sub-100 nm particle sizes are also utilized.

3.07.3.1.3 Nanodiamond Produced from High-Energy Explosives

A method of production of ND from the carbon contained in high-energy explosives (DND) was developed in the former USSR in the 1960s (Danilenko, 2004). The conversion of the carbon-containing explosive compounds into diamond occurs by firing the explosives in a detonation chamber (Danilenko, 2003). The resultant product is a mixture of diamond particles with a primary particle size of 4–5 nm, other carbon compounds and metallic impurities. A wide variety of explosive materials may be used. A typical explosive mixture is TNT (2-methyl-1,3,5-trinitrobenzene) and hexogen (in the proportion 60:40) composed of C, N, O, and H with a negative oxygen balance, so that free nonoxidized carbon is present in the system. The explosion takes place in an inert medium of either gas (N_2, CO_2, Ar, or other medium that can be under pressure) or water (ice), called "dry" or "wet" synthesis, respectively. The medium acts as a coolant.

The product of detonation synthesis, called detonation soot or diamond blend, contains 40–80 wt% diamond phase depending on the detonation conditions (Dolmatov, 2003, 2007). The carbon yield is 4–10% of the weight of the explosive charge, depending on a cooling media.

Taking into account that the carbon phase diagram at the nanoscale is different from that for bulk carbon materials (Section 3.07.2), formation of DNDs was elaborated in great detail by Danilenko (2005, 2006, 2010) as follows. The initial shock from a detonator compresses the high-explosive material, heating it and causing chemical decomposition, thereby releasing enormous amounts of energy in a fraction of a microsecond. The detonation wave includes (**Figure 7(a)**) a shock wave, a zone of detonation-induced decomposition of explosive molecules (a zone of chemical reaction) and a zone of expanding DPs. The zones of chemical reaction and expanding DPs are shown for the so-called composition B explosive at the corresponding phase diagram (**Figure 7(b)**) as A–B and B–C lines, correspondingly (Danilenko, 2006). Decomposition of explosive molecules with the formation of free carbon (for an explosive with a negative oxygen balance) proceeds according to the formula:

$$\mathrm{CNOH} \rightarrow \mathrm{N_2} + \mathrm{H_2O} + \mathrm{CO} + \mathrm{CO_2} + \mathrm{C}$$

Point B in **Figure 7(b)** is the termination of the decomposition (the Jouguet point). It can be seen in **Figure 7(b)** that *P–T* values in the Jouguet point do not reach a region of liquid carbon for a bulk carbon phase diagram, while conditions for the existence of liquid carbon can be achieved on the phase diagram for nanoscale carbon. Importantly, the Jouguet point of several powerful explosives is located in the region of liquid carbon in the nanocarbon phase diagrams, as confirmed by calculations of two different groups (Danilenko, 2005; Viecelli & Ree, 2000, 2001). Line 1–2 in **Figure 1(b)** denotes positions of the triple points for phase diagrams of ND particles of different sizes, starting from the bulk phase (point 1) down to a particle of 2 nm in size (point 2) (Danilenko, 2005). Thus, it can be seen that the region of liquid carbon is expanded to lower temperatures for nanocarbon. At the same time, the region of stability of ND is shifted to higher pressures. Thus, it is speculated that formation of DND is taking place according to the theory of homogeneous nucleation of the ultradispersed phase in the volume of the supersaturated carbon vapor via vapor\liquid\crystal transition. First, after decomposition of the explosive molecules (during ~1 ns), primary carbon embryos (<2 nm in size) are formed in the zone of a chemical reaction (during ~10 ns), followed by their coagulation into carbon droplets >2 nm in size along the isentrope of expanding DP above 16.5 GPa (this stage lasts $\sim 10^2$–10^3 ns) (**Figure 7(a)**). Finally, ND particles are formed by crystallization of the liquid carbon droplets along the isentrope of expanding DP in the region 9–16.5 GPa (duration of this stage $>10^3$ ns).

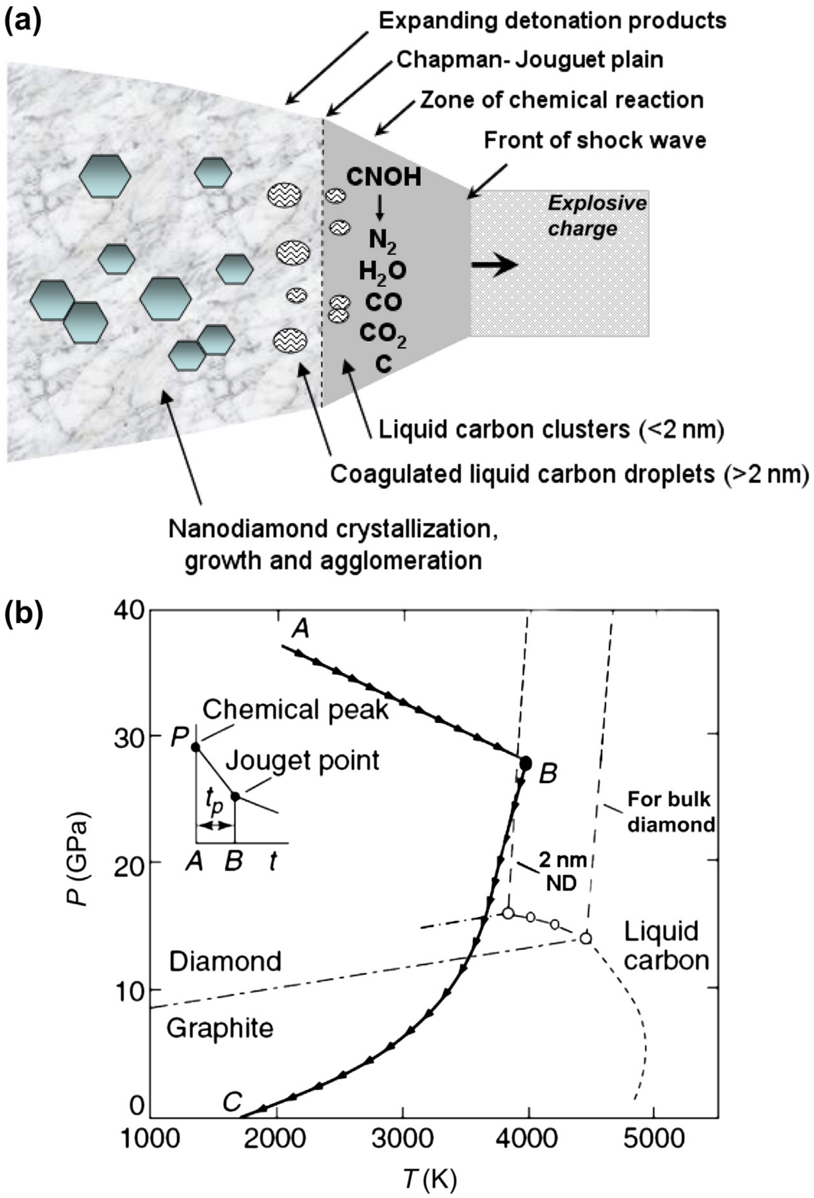

Figure 7 (a) Schematic structure of a detonation wave. (b) Approximate phase diagram for bulk carbon and 2 nm carbon cluster and a pressure–temperature trajectory (A-B-C) in a detonation wave (for the composition RDX/TNT 64/36%). The inset illustrates the pressure profile in a detonation wave: *A* corresponds to the shock compression of the explosives (chemical peak), *AB* corresponds to decomposition of explosive molecules; *B* is termination of decomposition (the Jouguet point), and t_p is the duration of decomposition. Figure (a) is adapted from Novikov, Danilenko, Bogatyreva, and Padalko (2010). Figure (b) is adapted from Danilenko (2006).

Mechanism of DND formation through crystallization of liquid carbon droplets formed from free carbon was also described in the work by Viecelli et al. (Viecelli & Ree, 2000), who demonstrated that the Chapman–Jouguet states of all of the explosives fall in the liquid phase region for carbon clusters with less than approximately 1000 atoms.

3.07.3.1.4 Structure of Different Types of Dynamically Synthesized Nanodiamonds

Recently, Shenderova et al. carried out a thorough comparative analysis of the structure and composition of the ND of the dynamic synthesis produced by the three major methods described above. Polycrystalline diamond from Microdiamant (produced by shock wave conversion of graphite) and from Real-Dzerzinsk (obtained from a graphite\RDX mixture), as well as DND synthesized from different explosives were studied. Aggregates with sizes below 100 nm were chosen for the investigation. The phase composition and size distribution of the ND crystallites in the ND powders were analyzed by XRD and SAXS. For all samples, the diamond phase in the XRD patterns dominated. However, the presence of various amounts of graphitic carbon was also observed (peak at ~26.9°), most pronounced in ND from Microdiamant. The diamond 111 diffraction peak was nonsymmetric due to overlap of the diamond 111 and graphite 101 peaks. The dimensions of the diamond crystallites were estimated from the Debye–Scherrer formula and were approximately 13.6 nm for the 111 reflection and 9.6 nm for the 110 peak for the ND produced from graphite\RDX; 8 nm for the ND obtained from graphite and 4 nm for DNDs produced from explosives. A very rough estimation of the possible lonsdaleite grain size in the Microdiamant's ND gives ~2.4 nm.

For all samples, the crystal size of the dominant fraction determined by SAXS was larger than the size determined from the broadening of the Bragg peaks. This difference originates in the different principles used for size determination in both techniques. The width of the Bragg peaks in an XRD pattern reflects the size of so-called "coherently scattering domains", which is usually smaller (rarely equal) than the entire particle size. SAXS is based on the electron density contrast between the scatterer and the surrounding medium, thus providing information about the overall size of an ND particle. The discrepancy in the crystal size determined by both techniques reflects the fact that diamond particles consist of several crystallites within a single grain.

The SAXS data for the ND from graphite sample showed a bimodal size distribution of the particles with peaks (diameters) at ~6 nm (possibly graphite or lonsdaleite) and at ~23 nm. The size distribution for the ND from graphite\RDX mixture possessed a relatively broad size distribution centered at ~34 nm. Finally, the size distribution of the NDs produced from explosives (TNT\RDX and TNT\HNS) was typical for DNDs: the main peak shows diameters around 6 nm and a broad tail stretching out to larger sizes.

Figure 8 shows high-resolution TEM (HRTEM) images of the different ND samples. ND produced from graphite contained only abundant large, rounded or elongated diamond particles without a clear morphology (Figure 8(a)). These structures often consist of agglomerates of smaller particles and show the presence of large amounts of defects in the diamond lattice. These particles can also be found in ND produced from a graphite\RDX mixture, but in combination with rounded or well-faceted polyhedral and truncated octahedral

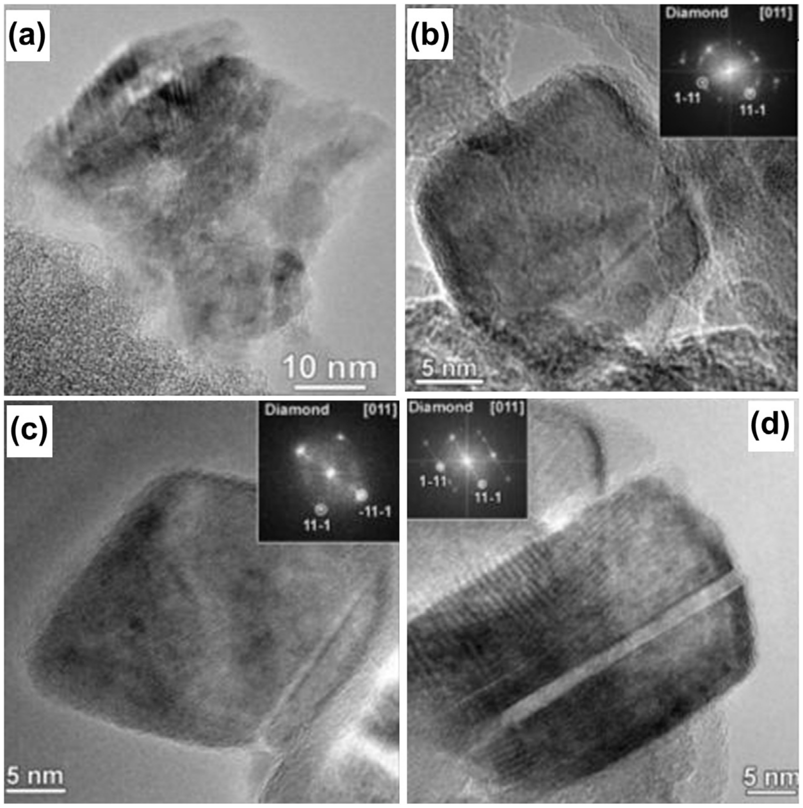

Figure 8 HRTEM images of ND synthesized (a) by shock compression of graphite and (b) by detonation of graphite\RDX mixture (b–d).

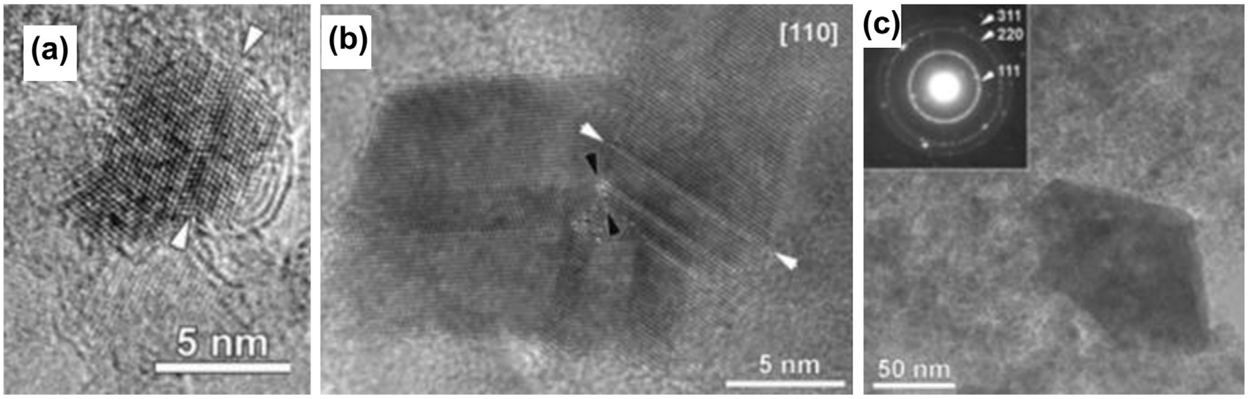

Figure 9 HRTEM images of ND synthesized by detonation of TNT\RDX explosives. (a) The main fraction of DND particles has a particle size close to 6 nm. Twinning is frequently observed in these small particles, with all visible twinning occurring along a (111) twin plane (examples of twin planes are indicated by white arrows in (a) and (b)). (b) Larger, multiple-twinned ND particle. An incoherent region is indicated by black arrows. (c) A rarely observed 100 nm octahedral particle. The inset electron diffraction ring pattern is typical for all DND samples and clearly evidences the cubic diamond crystal structure of all of the nanoparticles. The figures are reproduced from (a) Turner et al. (2009) and (b,c) Vlasov et al. (2010), with permission.

particles with low-index facets (**Figure 8(b), (c)**). The smaller DND particles below 6 nm in diameter show mainly {111} and {100} facets typical for small DND particles (**Figure 9(a)**), while larger particles also show higher index facets (**Figure 9(b)**). These particles show the presence of coherent $\Sigma = 3$ {111} twinning, common for DND. Large, multiply twinned particles with diameters up to 100 nm can be found occasionally in DND sample (**Figure 9(c)**).

Raman spectra of the samples were acquired in a range of 1200–1700 cm^{-1} (**Figure 10**). Typically, the first-order Raman spectrum of highly purified DND consists of two peaks. The first one is located in the vicinity of 1332.5 cm^{-1} and corresponds to the vibrational mode of a diamond lattice from the center of its Brillouin zone. The origin of the second one observed at 1630 cm^{-1} is still a subject of debate. When an abundance of sp^2-bonded carbon clusters is present in ND, another two peaks characteristic for sp^2 carbon appear between 1350

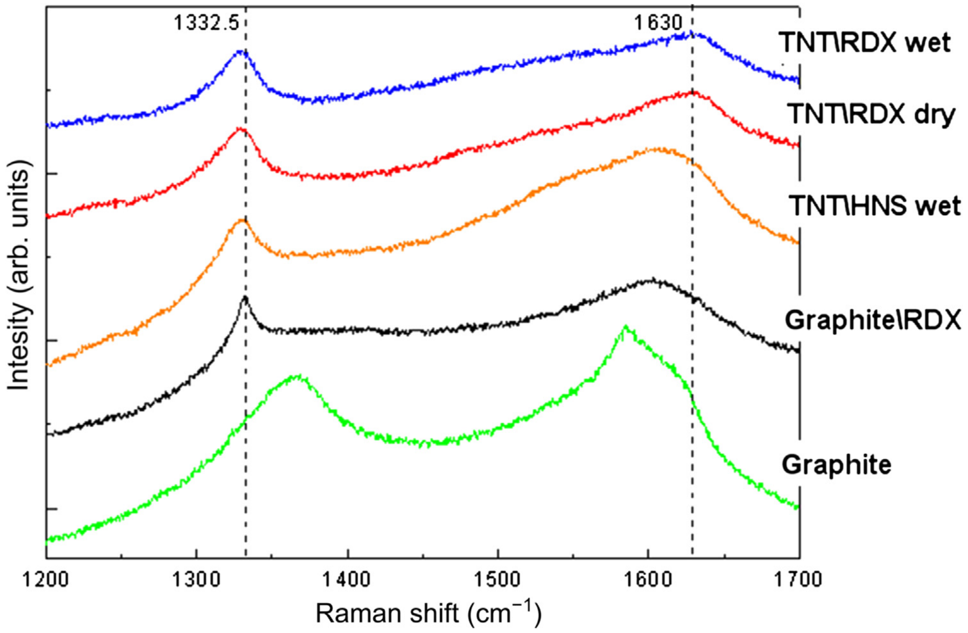

Figure 10 Raman spectra of the dynamically synthesized ND samples. Figure courtesy of I. Vlasov, General Institute of Physics, Moscow.

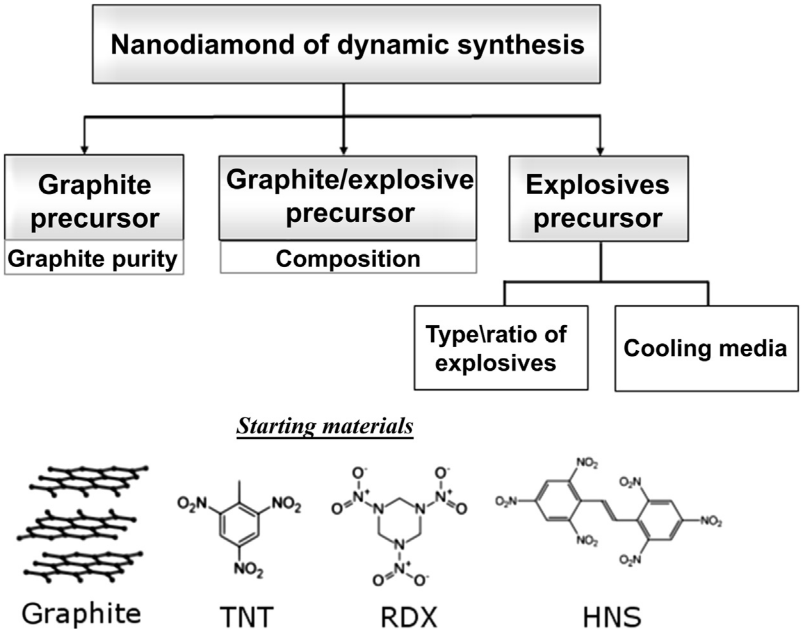

Figure 11 A scheme of the carbon-containing precursors for the three major methods of dynamic synthesis of nanodiamonds and factors influencing the nitrogen content in the produced nanodiamond material.

and 1380 cm^{-1} (the D-band) and 1580–1610 cm^{-1} (the G-band). The G-band and D-band, obscuring the diamond peak in the ND produced from graphite, indicate a high content of sp^2-bonded carbon in this sample. Large primary particles of the ND produced from graphite\RDX are not influenced by the phonon confinement effect and the diamond line position is actually not shifted from the 1332.5 cm^{-1} position characteristic for the bulk material. All samples of detonation-type synthesis demonstrate a shift in the diamond Raman line down to 1328.5 cm^{-1}, which is explained by the phonon confinement effect observed for small nanocrystals (Ager, Veirs, & Rosenblatt, 1991).

Besides the morphological characteristics, of particular interest is investigation of the effect of the type of synthesis on N content, N location in the ND core and its ability to form optically active centers through the creation of complexes with vacancies. A scheme of the carbon-containing precursors for the three major methods of dynamic synthesis of NDs and factors influencing the nitrogen content in the produced ND material is presented in Figure 11. In ND synthesis using explosives, N is an integral part of the high-energy explosive compounds. It can also be present as an impurity or an on-purpose dopant in graphite (or other carbon-containing materials) (Shenderova et al., 2011) in the methods of the dynamic synthesis involving bulk carbon precursors for NDs production. The nitrogen content in the ND samples measured using combustion analysis indicated that N concentration in the ND produced from a mixture of TNT\RDX explosives is higher than 2–2.5 wt%, from TNT-HNS lower than 1% and in ND from graphite and graphite\RDX mixture, lower than 0.5%. Thus, variations in the type of explosives can provide variation in the N content in the final ND product. It is possible that the N–N units of RDX (Figure 11) contribute to enhanced N aggregation in the ND core if they are not completely destroyed during detonation and are incorporated into the ND core as neighboring nitrogen atoms. Substituting RDX with HNS significantly reduces the N content. These issues require further study. Thus, variations in the types of explosives can be used together with the addition of other carbon precursor materials (for example, combination of graphite and HNS) to achieve the desired N content.

3.07.3.2 Survey of Laboratory-Scale Methods of Nanodiamond Synthesis

There are numerous reports on experimental observations of nanosized diamond, summarized in Shenderova et al. (2002) and Shenderova and McGuire (2006). In this section, we will provide a brief overview of ND particles synthesized at the laboratory scale.

3.07.3.2.1 Milling of HPHT Microdiamond

The shape of diamond nanoparticles obtained by ball milling of micron-sized HPHT or natural diamond particles typically have sharp edges and look in HRTEM like shattered glass particles (Boudou et al., 2009). Remarkably, ND particles with rounded shapes and particle sizes below 10 nm were recently obtained by a group of researches starting with HPHT diamond (Boudou et al., 2009). The reported method is an important breakthrough in the production of single-digit ND containing NV centers, as it was demonstrated by the authors through processing of Ib type diamond. The initial raw material was a highly crystalline synthetic micron diamond powder (from Element Six) containing 80–100 mesh (150–190 μm) blocky, very uniformly shaped cuboctahedral diamond crystals. The first step included nitrogen jet milling micronization resulting in a powder with 97% of particles having sizes below 2 μm. Then, an aliquot was ball milled under argon using a planetary ball mill (Vario-Planetary Mill, Pulverisette 4, Fritsch, Germany), with 10 mm balls made of WC–Co cemented carbide for 24 h of effective grinding time. NDs appear as deformed polygons with a quasispherical shape and an aspect ratio varying from 1.13 to 1.75. The overall yield of this method is about 15 wt% of the microdiamond mass converted into sub-10 nm diamond nanoparticles. The authors attribute the success of the production of the quasispherical particles to complex loading regimes of the Vario-Planetary Mill as compared to regular planetary mills (Gaffet, Bernard, Niepce, et al., 1999).

3.07.3.2.2 HPHT Synthesis

While a particular class of NDs is obtained as a commercial byproduct of HPHT synthesis, there are laboratory studies of HPHT conversion of exotic carbon forms to ND. The HPHT process requires approximately 6 GPa pressure and 1500 °C to convert graphite powder into diamond in the presence of a catalyst. Use of exotic precursor materials such as fullerenes (Núñez-Regueiro, Monceau, & Hodeau, 1992) as well as carbon nanotubes (Cao, Gao, Sun, et al., 2001) allows much lower temperatures and externally applied pressures as compared to the use of graphite in order to synthesize diamond. For example, the transformation of buckyballs to diamond at high static pressure can be done at room temperature and does not require a catalyst at all (Núñez-Regueiro et al., 1992). Another group of authors reported conversion of fullerenes to diamond under "moderate" conditions of 5.0–5.5 GPa and 1400 °C (Ma, Zou, Yang, & Meng, 1994). Carbon nanotubes have been converted to diamond at 4.5 GPa and 1300 °C using NiMnCo catalyst (Cao et al., 2001). Based upon HRTEM observations, the authors suggest that under HPHT conditions, the tubular structures collapse and broken graphitic shells curl up and close into spheroidal networks to eliminate the dangling bonds at the edges.

Multiwalled carbon nanotubes (MCWNTs) were heated by a laser in a diamond anvil cell to above 17 GPa and 2500 K (Yusa, 2002). The recovered product consisted of nanosized octahedral crystals (diamond) of $<$50 nm. The tubular structure completely changed to granular and the grain sizes corresponded to the diameter of the nanotubes. The grain size of the diamond suggests that the transformation took place by direct conversion of nanotubes that might provide a means to control diamond size by the choice of the MWNT size.

An interesting implementation of HPHT treatment was reported by Soltamova, Ilyin, and Shakhov (2010). Sintering experiments were carried out on DND with average particle sizes 4.5 nm at temperatures 1500–1700 °C and pressure 6–7 GPa. According to the results of the XRD, the average size of the primary particles became 8.5 nm after sintering. When the sintering temperature is above 800 °C, vacancies start to diffuse. The presence of a significant amount of NV centers was detected in 10 μm aggregates using pulsed EPR (Soltamova et al., 2010). Formation of the NV centers can be possibly attributed to the combination of elimination of surface paramagnetic centers and to vacancy diffusion at the high temperature of the process.

3.07.3.2.3 ND Particles Synthesis Based upon the CVD Technique

Frenklach, Kematick, Huang, et al. (1989) studied nucleation and growth of ND powder directly from the vapor phase in a substrate-free low-pressure microwave-plasma CVD reactor. The particles were collected downstream of the reaction zone on a filter within the tubular flow reactor and subjected to wet oxidation to remove nondiamond carbon. The homogeneous diamond nucleation took place when the dichloromethane- and trichloroethylene-oxygen mixture was used as source material. The particles formed had crystalline shapes with an average particle size around 50 nm. A mixture of diamond polytypes were observed in the powder.

Frenklach et al. (1991) also studied the effects of heteroatom addition on the nucleation of solid carbon in a low-pressure plasma reactor. The addition of diborane (B_2H_6) resulted in substantial production of diamond particles, 5–450 nm in diameter, under the same conditions that show no diamond formation without the presence of diborane. The observed yield of the oxidation-resistant powder produced in boron-containing mixtures reached 1.3 mg h^{-1}. It was found that NDs in the CVD residue have an abundance of linear twins and star-twin microstructures consistent with radial (isotropic) gas phase growth conditions. Studies of diamond nucleation directly from an activated gas phase have important implications in revealing mechanisms of interstellar dust formation.

Another example of homogeneous diamond nucleation in the gas phase is laser-induced decomposition of C_2H_4 at low pressures and temperatures (Buerki & Leutwyler, 1991) that results in diamond powder formation with grain diameters of 6 nm–18 μm. According to the authors, the high purity homogeneously nucleated diamond nanoparticles had spherical and faceted morphology.

Ting, Young, and Jwo (2007) developed a method of ND particle synthesis with 25–50 nm diameters using microwave plasma torch system operating at near atmospheric pressure. Gas mixtures of CH_4 with Ar or N_2 were used for ND particles synthesis, with Ar or N_2 serving as catalysts. The larger flow rate of Ar and N_2 or the greater pressure in the reaction chamber produced larger nanoparticles.

The CVD technique was recently used for the production of electrically conductive ND in particulate form by CVD growth of boron-doped ND films around a dielectric core of diamond nanoparticles (Ay, Swope, & Swain, 2008). Production of electroconductive boron-doped ND particles can be very beneficial and can find broad applications in high surface area carbon electrode materials in electroanalysis, electrochemical double-layer capacitors, storage materials for batteries, as a possible electrocatalyst support material for fuel cells, stationary support for liquid chromatography and other applications (Ay et al., 2008).

3.07.3.2.4 Methods Using Radiation and High-Energetic Particles

Another group of methods of ND formation include direct transformation of carbon solids to ND. Recent experiments have shown that heavy ion or electron irradiation induces the nucleation of diamond crystallites inside concentric nested carbon fullerenes (Banhart & Ajayan, 1996; Wesolowski, Lyutovich, Banhart, et al., 1997). High-energy electron irradiation (1.2 MeV, $>10^{24}$ e cm^{-2}; $\sim$100 dpa) was successfully used to convert the cores of concentric-shell graphitic onions into nanometer-size diamonds at irradiation temperatures above 900 K (Banhart & Ajayan, 1996). These experiments were performed in-situ in an electron microscope, which allowed continuous observation of the formation process. A strong compression in the interior of the onion was inferred by the observed reduction in the spacing between adjacent concentric shells during irradiation. Ion beam irradiation of carbon solids also resulted in formation of ND (Wesolowski et al., 1997). Irradiation with Ne^+ (3 MeV, 4×10^{19} cm^{-2}; $\sim$600 dpa) at temperatures between 700 °C and 1100 °C converted graphitic carbon soot into nanometer-size diamonds (Wesolowski et al., 1997). Again, the diamonds were found to nucleate in the cores of graphitic onions that developed under irradiation. The increased diamond yield as compared to e-beam irradiation is explained by the higher displacement cross-section, the higher energy transfer, and the higher total beam current on the specimen.

Other carbon materials can also be transformed to ND by using MeV electron or ion beams. ND nucleation occurs inside graphite under ion irradiation at ambient temperature when implanted with Kr^+ ions (350 MeV, 6×10^{12} cm^{-2}) (Daulton et al., 2001). The residue of the ion-irradiated graphite was found to contain NDs with an average diameter of 7.5 nm. Another example of ND formation includes irradiation of highly oriented pyrolytic graphite surfaces using a highly charged ion (Meguro, Hida, Suzuki, et al., 2001).

3.07.3.2.5 Laser-Assisted Synthesis of Nanodiamond Particles

Generation of nanoparticles by laser ablation in liquids is a relatively new approach that has been actively explored between 2001 and 2010 (Yang, 2007). It has a number of important advantages over conventional multistep chemical synthesis methods that introduce contamination from the intermediate reactants and/or produce agglomerated structures with degraded functionality. The direct laser ablation eliminates the need for chemical precursors and enables generation of "clean" nanoparticles. Due to the highly nonequilibrium nature of laser ablation process, the structure and composition of nanoparticles produced in laser ablation can be very far from the equilibrium ones, opening an exciting range of opportunities for generation of novel nanostructures with unique properties.

Nanocrystalline diamond has also been produced by pulsed laser ablation using a graphite target along with water or acetone as the liquid medium (Yang, 2007). The authors suggested that OH groups formed from the oxygen-containing liquids were etching nondiamond carbon species from the surface, thereby allowing diamond to form preferentially. Diamond nanocrystals have been produced by pulsed laser ablation of graphite at room temperature and pressure in two liquids (water and cyclohexane) by Pearce, Henley, Claeyssens, et al. (2004). The ND formation was attributed to the extreme temperature/pressure conditions created by collapse of bubbles. The sequence of processes in laser ablation of liquids is likely to include an explosive decomposition of the overheated surface region of the absorbing target, ejection of clusters and vapor into the surrounding liquid, mixing of the ejected ablation plume with the liquid and bringing the liquid to boiling or supercritical states, growth and solidification of the nanoparticles under conditions of fast quenching. The final size, structure, and composition of the produced nanoparticles are defined by the heat and mass transfer occurring under highly nonequilibrium and quickly evolving conditions that are poorly understood at this time.

ND particles have also been synthesized from fine particles of carbon black exposed to intense laser irradiation (Fedoseev, Bukhovets, Varshavskaya, et.al., 1983; Pearce et al., 2004). Similarly, the transformation from carbon nanotubes to carbon onions and then to ND as a result of laser irradiation had been reported in Wei, Zhang, Liang, and Wu (1998).

3.07.3.2.6 Diamond Synthesis Using Ultrasound Cavitation

Temperatures and pressures required for synthesis of diamond material can be achieved by different means, including ultrasound cavitation as a result of the rapid collapse of cavitation bubbles generated in a suitable liquid medium (Flynn, 1986). Depending upon the cavitation conditions, the pressure and temperature inside the cavity at the moment of collapse may reach extremely high instantaneous values $\sim 10^5$–10^6 bar and 1000 K, correspondingly (Brennen, 1995).

Two research groups reported formation of nanostructured (Galimov, Kudin, Skorobogatski, et al., 2004) and monocrystalline (Khachatryan, Aloyan, May, et al., 2008) micron-sized diamond particles. Cavitation destruction of benzene resulted in production of particles consisting of aggregate of nanocrystallites of 10–30 nm in size (Galimov et al., 2004). Micron-sized diamond crystals (5–10 μm) were produced by the cavitation synthesis method from a suspension of powdered graphite (100–200 μm) in organic liquid (Khachatryan et al., 2008). The major factor influencing the diamond yield in the cavitation process was the composition of the cavitation medium. The diamond yield was about 10% of the initial graphite weight. As cavitation fluids, a series of aromatic C–H–O oligomers with low saturated vapor pressure and high boiling temperatures was used.

3.07.3.2.7 Carbide-Derived Diamond

Selective etching of carbides is an attractive technique for the synthesis of various carbon structures including nanocrystalline diamond (Gogotsi et al., 2001; Nikitin & Gogotsi, 2004; Welz et al., 2003). Carbon produced by extraction of metals from carbides is called carbide-derived carbon (Nikitin & Gogotsi, 2004). As it is summarized in Nikitin and Gogotsi (2004), leaching in supercritical water, high-temperature treatment in halogens, vacuum decomposition, and other methods can be used to remove metals from carbides to produce carbon coatings or bulk and powdered carbon. In principle, chlorination of carbides for the production of carbon-based materials and, particularly, nanoporous carbon, is a relatively mature technology that has been commercialized (see, for example, http://www.skeleton-technologies.com). However, the synthesis of nanocrystalline diamond by this technique (Gogotsi et al., 2001) is a recent achievement.

Particularly, during extraction of silicon from silicon carbide or metal carbide using chlorine-containing gases at ambient pressure and temperatures not exceeding 1000 °C (Welz et al., 2003), nanocrystalline diamond with an average crystallite size of 5 nm was formed. Nanocrystalline diamond is usually surrounded by amorphous carbon.

3.07.4 Recent Achievements in Production of Detonation Nanodiamond

The three major steps in the conversion of carbon-containing explosives to DND products include synthesis, postsynthesis processing and modification, which are discussed in detail in the following sections. Postsynthesis processing includes purification of detonation soot from metallic impurities and nondiamond carbon and is typically performed in conjunction with detonation soot synthesis by the same vendor. The result of the processing is DND of a certain purity (presently at a level of incombustible impurity content 0.5–5 wt% depending on the vendor) that is available on a large scale (thousands of kilograms). DND treatments, tentatively called *modification*, can include additional deep purification, surface functionalization toward specific applications, and deagglomeration or size fractionation. In the past 3–4 years, the development of approaches for DND modifications has been the major focus of research activity. Although, initially, DND modifications were performed on a small scale, currently these steps are being implemented on a large scale on site at DND production centers (Larionova et al., 2006). Of primary importance is the method of disintegration of ND aggregates by stirred-media milling with micron-sized ceramic beads suggested by Osawa and coworkers (Krueger, Kataoka, et al., 2005), resulting in diamond slurries containing primary 4–5 nm DND particles. The single-digit DND immediately attracted the attention of a relatively large number of researchers working in the area of nanoscale materials, which was demonstrated by recent publications in high profile journals (Huang, Pierstorff, Osawa, & Ho, 2007, 2008).

3.07.4.1 Synthesis of Detonation Nanodiamond

Details on the synthesis and processing of DND were briefly discussed in Section 3.07.3.1 and can be found in books (Danilenko, 2010; Dolmatov, 2003; Shenderova & Gruen, 2006; Vereschagin, 2005) and reviews (Dolmatov, 2001; Holt, 2007; Krueger, 2008; Schrand, Hens & Shenderova, 2009; Shenderova et al., 2002). In the current section, we emphasize recent new advances in the methods of synthesis of DND.

The major focuses of novel approaches for DND synthesis are as follows:

1. further reduction of the primary particle size,
2. control of the level of aggregation of DND at a stage of synthesis,
3. increased sp^3 carbon content in detonation soot (in terms of reduction of noncarbon elements and sp^2 carbon on DND particle surfaces) and
4. doping of DND during synthesis, including control of the amount of substitutional nitrogen in the diamond core.

Reducing DND primary particle size down to the range of 1–3 nm may further increase their capability for penetrating cells and organelle membranes including nuclear pores. ND particles with sizes ~2 nm and smaller show quantum confinement effects (Raty, Galli, Bostedt, Van Buuren, & Terminello, 2003). Thus, synthesis of small particles would open perspectives for the development of diamond quantum dots. An increase of the ND specific surface area to a level, compared to that for carbon nanotubes, would bring ND to the stage of perspective materials for hydrogen storage, catalyst support, fuel cells and other applications.

In principle, the XRD data on the size distribution of primary DND particles within detonation soot, which were reported in a limited number of publications (Danilenko, 2003; Yur'ev & Dolmatov, 2010), include 2 nm peaks. It was reported by Dolmatov (Yur'ev & Dolmatov, 2010) that his novel method of using reducing agents (for example, urea, ammonia) in water cooling media allows the preservation of the DND fraction with a primary particle size <3 nm along with a "typical" fraction of 5 nm primary particles. In general, production of several classes of DND with average primary particle sizes from the 2 nm–10 nm size range (for example, classes with 2–3 nm, 4–5 nm and 10 nm average sizes) would be beneficial for various applications.

Also, a method reported by Dolmatov (Yur'ev & Dolmatov, 2010) of using reducing agents provides the benefits of increased DND yield from soot (by 2–5 wt%) as well as overall yield of soot itself (by 100%) (Yur'ev & Dolmatov, 2010) as well as an increased carbon content (up to 96 mass%) within DND particle composition, where the total content of C, H, N and O corresponds to 100 mass%. A possible mechanism of action of the reducing agents in the cooling media is suggested to be as follows (Yur'ev & Dolmatov, 2010). In the presence of reducing agents, the oxidants (the DPs CO_2, H_2O, O_2, NO_2, N_2O_3) interact primarily with the reducing agents, instead of oxidizing the carbon and particularly DND. This increases the yield of detonation soot and DND and quantitatively changes their elemental composition, including carbon. Besides, the presence of readily oxidizable reducing agents among the DPs helps to reduce graphitization of DND. Besides, the smallest amount of incombustible impurities (0.1–0.3 wt%) was found in the DND synthesized in the presence of urotropine. This is due to the fact that urotropine is a strong complexing agent and captures impurities (metals Fe, Ni, Cr, Cu, Ti, etc.) to form soluble complexes which are easy to remove by subsequent chemical purification, i.e. treatment with nitric acid.

Another question is related to the possibility of optimizing the detonation process to produce mostly isolated primary particles and only small size aggregates in the detonation soot. This would significantly reduce the cost of the final DND product. In fact, it has been recognized that the dry DND synthesis results in smaller primary DND particle sizes and smaller average aggregate sizes as compared to wet synthesis. Another factor that influences the aggregation of DNDs during synthesis is the mass of the charge and a ratio between masses of the charge and wet cooling media used (Danilenko, 2010).

Tailoring of DND electronic and optical properties for specific applications can be possibly done at the stage of synthesis by development of different combinations of explosive materials with possible solid dopants, as well as using the nontraditional cooling media (both gaseous and liquid) with possible additives to alter the

DND composition (both bulk defects/doping content and surface groups). The possibility to control N content by a proper choice of the precursor material was demonstrated in Section 3.07.3.1.4.

3.07.4.2 DND Postsynthesis Processing

The development of DND products of ultrahigh purity remains an important goal for many applications. In addition to the diamond phase, the detonation soot contains both graphite-like structures (25–55 wt.%) and incombustible impurities (metals and their oxides—1–8 wt.%) (30). The metal impurities originate from the detonator and from the walls of the detonation chamber. After typical purification steps, powders of DND can be considered a composite consisting of different forms of carbon (~80–89%), nitrogen (~2–3%), hydrogen (~0.5–1.5%), oxygen (up to ~10%) and an incombustible residue (~0.5–8%) (Dolmatov, 2001). The carbon phase consists of a mixture of diamond (90–99%) and nondiamond carbon (1–10%).

Both nondiamond carbon and metallic, incombustible impurities can be located externally or internally relatively to the tight DND aggregates. In order to remove the internal metal impurities and internal nondiamond carbon, tight DND agglomerates should be disintegrated. Currently detonation soot can be industrially purified to a level of remaining incombustible impurities about 0.5–0.6 wt%. In general, methods of DND purification as well as DND purity vary from vendor to vendor (Dolmatov, 2001). "Classical" purification methods, based upon the use of liquid oxidizers for the removal of metallic impurities, include sulfuric acid, a mixture of sulfuric and nitric acids, hydrochloric acid, potassium dichromate in sulfuric acid as well as other schemes. A brief review on the numerous methods of detonation soot purification developed in the former USSR is provided in Petrov and Shenderova (2006). For the oxidation of sp^2 carbons, the purification schemes include KOH/KNO_3, Na_2O_2, CrO_3/H_2SO_4, HNO_3/H_2O_2 under pressure, mixtures of concentrated sulfuric and perchloric acids and other approaches (Dolmatov, 2001). To remove noncarbon impurities, the chemically purified product is subjected, in some cases, to an additional purification process using ion-exchange and membrane technologies. Currently, the majority of DND vendors use strong liquid oxidizers at elevated temperatures and pressures. However, liquid-phase purification is both hazardous and costly, contributing up to 40% of the product cost. Alternatively, DND can be very effectively purified from nondiamond carbon in a more environmentally friendly manner by a gas phase treatment using ozone at elevated temperatures (Petrov et al., 2007) to eliminate the need for the use of corrosive liquid oxidizers. Ozone is generated using corona discharge at the input of the reactor and is destroyed at the output of the gas flow. Ozone oxidation is more efficient for sp^2 carbon oxidation than oxygen. The ozone-modified nanodiamonds (NDO) were found to have a number of distinctive characteristics. The size of polydispersed NDO in water suspensions is about 160–180 nm as measured by dynamic light scattering (Malvern Zetasizer). This number is the smallest average size reported for commercially available polydispersed unfractionated DNDs. In addition, the content of the primary, polyhedrally shaped, faceted particles with a size of 3–5 nm in the polydispersed NDO is substantially higher than that of the acid-purified DNDs. The NDO hydrosols were found to possess a very low pH (1.6–2 for 10% hydrosol), low negative zeta potential (−50 mV for polydispersed sample) and down to −100 mV for 20–30 nm fraction and feature a constant zeta potential (~−40/−50 mV) over a wide pH range of 2–12, apparently due to the enrichment of the surface with oxygen-containing strong-acid groups. **Figure 12** demonstrates HRTEM image of NDO particle with low sp^2 content, as well as EELS, demonstrating lower content of sp^2 carbon in NDO as compared to ND purified using etching in hydrogen, as well as to other types of DND.

There were several efforts underway to purify DND by oxidation of detonation soot with air at elevated temperatures. The method allowed for a significant decrease in the nondiamond carbon content. Larionova et al. purified DND using soot treatment with air at 380–440 °C for several hours (Larionova, Molostov, et al., 1999). Soot purification through a combination of liquid oxidizers and air treatment at temperatures up to 600 °C was reported by Mitev, Dimitrova, Spassova, Minchev, and Stavrev (2007). Osswald, Yushin, Mochalin, et al. (2006) demonstrated that for the soot, the optimal temperature for the heat treatment in air within several hours is 400–430 °C.

3.07.4.3 Advances in Detonation Nanodiamond Deagglomeration and Fractionation

DND obtained from commercial vendors often requires additional processing and modification since the content of incombustible impurities and nondiamond carbon can be too high, with an average aggregate size that is too large and with surface chemistry that is not suitable for a specific application. The poor colloidal stability of commercially available DND powders after liquid dispersion is a common problem. Besides, there is

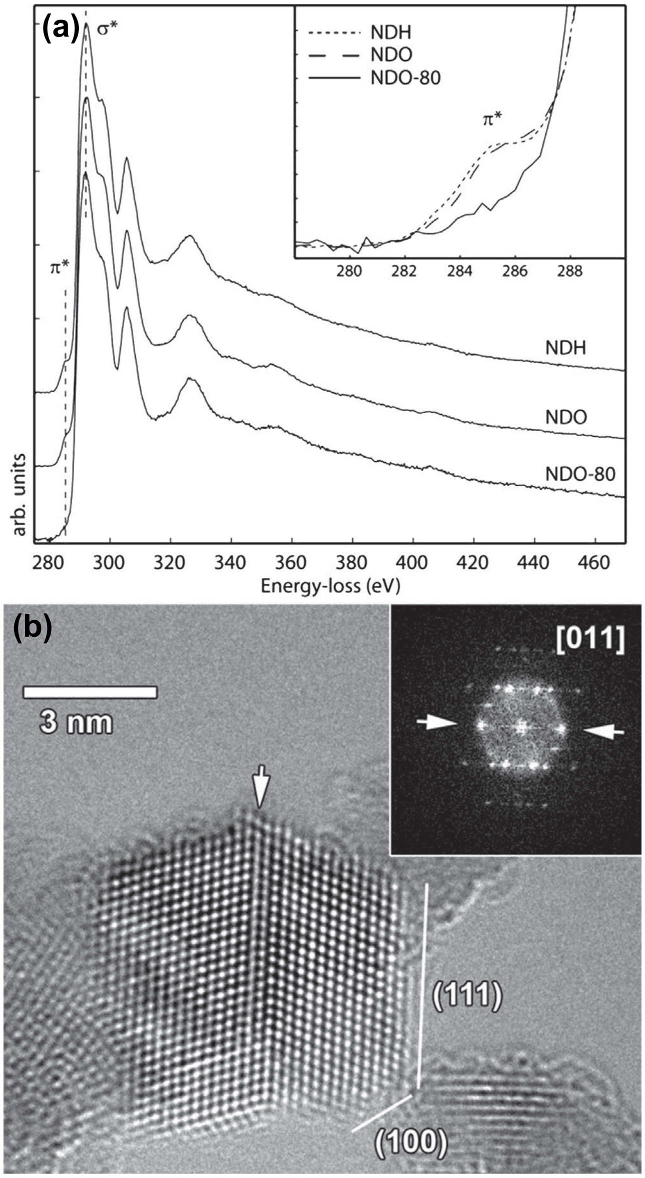

Figure 12 (a) Background subtracted, normalized core-loss carbon K-edge EELS spectra of ozone-purified DND. The fine structures mainly show a diamond σ^* (sp^3) contribution at 292 eV and a small π^* (sp^2, sp) contribution at 285 eV. Nitrogen is detected in all samples through the K-edge with maximum at 406 eV. Inset: Carbon K-edge onset showing the π^* contribution for each sample at 285 eV. (b) Typical ozone-purified DND particle showing the presence of a (111) twin plane indicated by an arrow. The FFT of the nanoparticle evidences the [011] zone axis orientation, as well as the twinning over a (111) twin plane through a mirroring of the FFT (mirror plane indicated by two arrows perpendicular to the twin plane in real space). The main surface facets of the DND particles are (111) and (100)-like and show only a minimal presence of non-sp^3 carbon. From (Shenderova et al., 2011b), submitted.

no universal material called "detonation nanodiamond" since materials properties are specific to the synthesis and postsynthesis purification methods adapted by the vendor. As a means to improve the quality of the DND product, methods of fractionation and deaggregation are discussed below. ND surface functionalization is discussed in depth in Chapter 3.16 of this book by Krueger.

While the primary DND particle size is 4–5 nm, the primary particles form tightly and loosely bound aggregates. The typical commercial polydispersed ND suspensions that are subjected to powerful ultrasound treatments routinely exhibit 200–400 nm average aggregate sizes, which are unbreakable by the ultrasonic treatment. An approach to effectively separate the particles and achieve narrow size distribution is centrifugal fractionation (Chukhaeva, Detkov, Tkachenko, & Toropov, 1998; Larionova et al., 2006; Shenderova, Petrov, Walsh, et al., 2006). Importantly, DND suspensions must possess high colloidal stability for centrifugal fractionation. It is difficult, if not impossible, to fractionate an unstable suspension.

DND fractionation has several attractive aspects. First, it is a contamination-free approach as compared, for example, with bead milling, which introduces impurities from ceramic beads which require further purification (Osawa, 2007). It is also convenient to be able to fractionate DND into different, narrow distributions of sizes for different niche applications. For example, only DND with aggregate sizes of more than 100 nm can form photonic structures that diffract light in the visible region (Grichko, 2008). Finally, after deep purification or treatment with ozone/air, the content of DND with small-sized aggregates can be significantly increased and the production of suspensions with small fractions of pure DND without added contaminants becomes economically feasible. In fact, suspensions of 5 wt% of 25 nm size DND fraction in water have been produced using the fractionation method (Larionova et al., 2006; Xu et al., 2005a,b,c). Importantly, it is possible to extract only primary DND particles by centrifugal fractionation, including ultracentrifugation (Morita, Takimoto, Yamanaka, et al., 2008).

Deagglomeration of ND aggregates into individual primary particles is an important goal for a variety of applications. Methods of mechanical deagglomeration of DND dispersion in suspensions by stirred media milling (Osawa, 2007) or bead-assisted sonic disintegration (Ozawa et al., 2007) were developed and suspensions of individual 4–5 nm DND particles have been produced.

Undesirable side effects upon bead milling are contamination with bead material and generation of graphitic layers on the particle surface (Osawa, 2007). Attempts to purify bead-milled DND with liquid oxidizers lead to aggregation of the primary particles (Osawa, 2007). Fortunately, by optimizing the bead milling process, it is possible to minimize the contamination by bead milling media below 0.2%. Purification from the bead-milled material using NaOH solution in water was considered (Huang et al., 2008) as well as molten NaOH. In addition, amorphous carbon and metal contaminants confined within DND aggregates and released during bead milling also need to be removed from the resulting suspension of primary particles. Nevertheless, the production in kilograms quantity of the so-called “Nanoamando” ND had been started. Nanoamando has become very popular ND material for biomedical research and has permitted the successful development of applications thereof.

A novel method of ND deaggregation by salt- or sugar-assisted dry milling was recently explored and yielded 5–20 nm ND particles with much fewer impurities than in the bead milling method (Pentecost, Gour, Mochalin, Knoke, & Gogotsi, 2010; Xu et al., 2004).

Several other methods have been proposed for DND deagglomeration. Xu et al. developed a two-step deagglomeration procedure that included graphitization of by-products of detonation in N_2 atmosphere at 1000 °C for 1 h followed by their oxidation with air at 450 °C for several hours (Xu, Yu, Zhu, & Wang, 2004). The final powdered product contained at least 50% DND with the particle size of <50 nm. Krueger reported using DND reduced in borane (accompanied by ultrasonic treatment) resulting in significantly smaller sized aggregates (Krueger, Stegk, Liang, Lu, & Jarre, 2008). Treatment of DND powder in an atmospheric pressure plasma also reduced the average DND aggregate size by $\sim 20\%$ (Gibson, Shenderova, Luo, et al., 2009).

A concern that requires thorough study is the possible reagglomeration of single-digit DND or small-sized fractions subjected to further surface functionalization or drying for storage. Typically, during drying of ND from water and other solvents, ND aggregation is further increased due to capillary forces pulling together individual particles. Attractive Van der Waals forces also play a major role in particle agglomeration. Agglomeration during drying makes ND functionalization more difficult since it often requires dry starting ND material. Puzyr et al. has developed a modification based upon sonication-assisted treatment of NDs in an NaCl solution (Bondar & Puzyr, 2004), which results in the purification of the NDs and, possibly, the incorporation of Na^+ ions into the ND surface. The attractive feature of the NaCl treatment method of ND modification (Bondar & Puzyr, 2004) is the possibility of drying NDs from a hydrosol to a powder form with subsequent resuspension without agglomeration. DND powder with average aggregate size ~ 40 nm after dispersion in water was obtained through this method.

3.07.5 Brief Survey of Applications of Nanodiamond Particles as Superhard Additives

The market for ND particles has been expanding rapidly worldwide following the release of previously tightly held information by the former Russian Soviet Union related to DNDs. Consumption of DND is still largely centered around many of the core applications identified in the former USSR: additives to galvanic coatings, polishing and lubricant additives (Dolmatov, 2001; Shenderova et al., 2002). Marketing has made industries around the world aware of the applications where DND provides benefit through enhancement of material properties in a wide range of applications. Research in both university and industrial laboratories is revealing new applications as a rapidly expanding number of scientists explore this new (to them) nanomaterial, which arguably may become the most widely used (in terms of number of applications) in the largest volume of any of the new nanomaterials. Below we survey selected applications which benefit from the property of ND as a superhard additive. This survey is far from being comprehensive and is intended to provide a flavor of the rapidly growing field.

Polycrystalline diamond particles produced by shock conversion of graphite or detonation of a graphite\RDX mixture are steadily consumed for several decades as micron-sized particles for lapping and polishing. In this capacity, micron-sized diamond is indispensable despite its high cost (more than $\$6\ g^{-1}$) providing high removal rate during polishing of hard carbide and nitrate substrates for microelectronic devices. For the fine finish polishing, requiring abrasives of the sub-100 nm size, much less expensive colloidal silica is widely used. It was recently reported, however, that a combination of colloidal silica and nanosized diamond particles can provide the most beneficial effect through an increase in polishing rates leading to a reduction in production time and surface finish better than 4 Å (Nanodiamond Product, Ltd, Ireland; An, Lee, Lee, et al., 2008). Since the amount of added ND is low (~10%), the cost of the synergistic composition is increased insignificantly. For example, An et al (2008) investigated the effect of addition of nanosized diamond slurry (grain size 25 nm) into conventional KOH-based colloidal silica slurry in the chemical mechanical planarization of SiC materials. Addition of ND slurry resulted in the surface roughness Ra ~2.2 Å (after 1 h of polishing) as compared to 5.9 Å when colloidal silica alone was used. Moreover, addition of a strong oxidizer NaOCl into the ND–silica composition resulted in a material removal rate (MRR) 0.3 mg h^{-1} (versus 0.06 mg h^{-1} in the slurry without NaOCl) and an Ra ~1.08 Å. Improvement in the Ra and MRR after addition of ND particles can be explained as follows. Colloidal silica acts as a wet-chemical surface oxidizer that generates an SiO_2 layer on the SiC surface and etches the surface to reveal the damaged layer from mechanical polishing. The ND particles remove (abrade) the silica layer increasing the MRR and polish the damaged layer revealed by KOH-based colloidal silica slurry, decreasing Ra. Addition of NaOCl further enhances the chemical reaction on SiC surface with KOH-based colloidal silica, producing much thicker SiO_2 layer which can be efficiently removed by ND particles. Nanodiamond Products, Ltd report that ND additive to colloidal silica enhances production of EPI ready electronic substrate materials such as sapphire, silicon carbide—4H/6H poly types, silicon nitride and gallium nitride, lithium niobate, gallium arsenide, calcium fluoride windows, fiber optical bundle ends for greater data transmission, LCD, LED/OLED displays. The addition of an ND slurry to existing colloidal solutions is also used for metallographic polishing.

A broad area of application of NDs utilizing their high chemical inertness and superhardness is incorporation of DND into different matrixes and production of composites (**Figure 13**). Numerous applications of DND-based nanocomposites are under development including wear-resistant additives to metal coatings; antifriction additives to lubricants and oils; polymer nanocomposites and coatings with enhanced strength, impact resistance, and scratch resistance; nanocomposites with improved thermal stability and thermal conductivity. Below we list several examples of nontraditional applications under development in our laboratory. It was demonstrated that ND particles in a polydimethilsiloxane matrix attain very pronounced photoluminescence when irradiated with a flux of MeV protons (Borjanovic, Lawrence, Hens, et al., 2008). This suggests application of the ND-polymer coatings as fluorescence-induced indicators of acquired proton dose, for example, by spacecraft. Other examples include fabrication of novel composites of carbon nanotubes incorporated into an ND matrix (Hens, Cunningham, McGuire, & Shenderova, 2011; Shenderova, Jones, Borjanovic, et al., 2008), photonic structures made of DND (Grichko, Tyler, Grishko, & Shenderova, 2008) and DND-based UV-protection coatings and sunscreens (Shenderova, 2007a). Also, DNDs serve as a source material for the production of OLC by high-temperature annealing of DND in an inert atmosphere. Recently, it was demonstrated that OLCs are strong absorbers of electromagnetic (EM) radiation from the gigahertz, to terahertz, to visible spectral ranges, providing efficient EMI shielding (Macutkevic, Seliuta Valusis, et al., 2009; Shenderova, Grishko, Cunningham, et al., 2008).

The addition of DND to polymers provides an increase in their mechanical strength, wear resistance and heat-aging resistance (Dolmatov, 2001, 2006). Highly effective coatings based on the incorporation of DND in fluoroelastomers and polysiloxanes were developed, and the elastic strengths of rubbers based on polyisoprene, butadiene-styrene, butadiene-nitrile and natural rubbers were considerably improved. For example, fluoroelastomers filled with DND particles showed an increase in the tensile modulus at 100% elongation (from

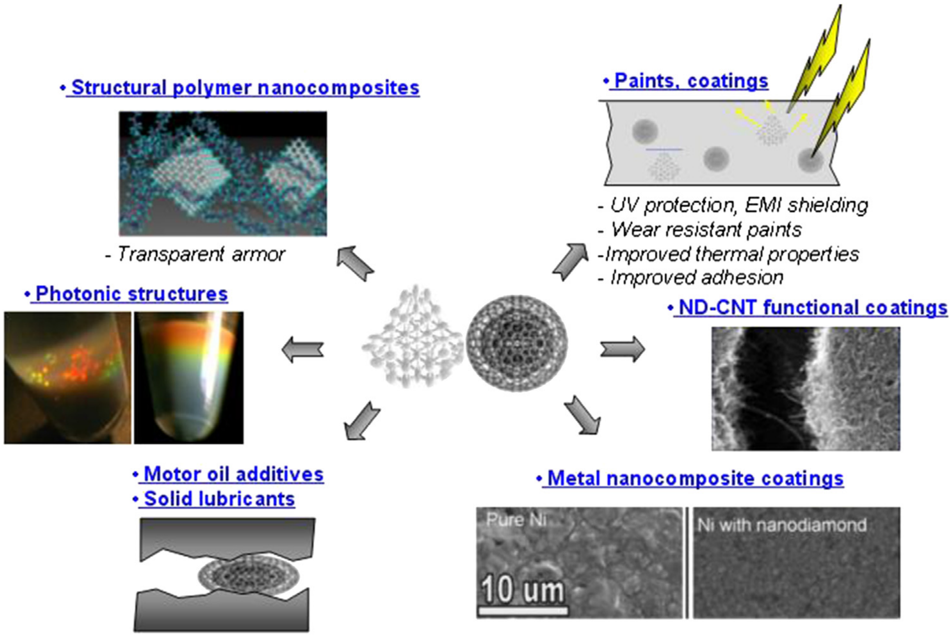

Figure 13 Schematics of applications of DND and onion-like carbon in nanocomposites.

280% to 480%) and in the conditional rupture strength (from 8.5 MPa to 92 MPa and from 15.7 MPa to 173 MPa, respectively). According to Dolmatov (2001), the addition of DND into the rubbers decreases attrition wear by an average of three to five times and increases rupture strength by 30%. Based upon experiments conducted on several polymer materials (poly(methyl methacrylate), benzocyclobutene, polyimide) with 1–2% by mass of ND particles incorporated, the thermal stability of the materials increased by at least 30 °C (Shenderova et al., 2007b).

In most recent publications, incorporation of octadecylamine-functionalized ND into biodegradable polymer, poly(L-lactic acid), intended for bone scaffold material application, resulted in a significant increase in hardness and Young's modulus of the composites (Zhang, Mochalin, Neitzel, et al., 2011). Addition of 10% wt of ND-ODA resulted in more than 200% increase in Young's modulus and 800% increase in hardness, bringing the nanocomposite properties close to that of the human cortical bone. ND/poly (lactic acid) (PLA) nanocomposites with potential for biological and biomedical applications also demonstrated improved mechanical properties and thermal stability of PLA matrix (Zhao, Lau, Kim, et al., 2010). The storage modulus of 3 wt% ND/PLA nanocomposites was increased by 75% and decomposition temperature was increased by 10° for 1 wt % ND/PLA nanocomposites as compared with the pure PLA. Maitra, Prasad, Ramamurty, and Rao (2009) produced poly(vinyl alcohol)-matrix reinforced with DND particles (content up to 0.6 wt%) and demonstrated significant enhancement in the hardness and elastic modulus of PVA. Using an electrospinning technique, polyamide 11-ND composite fibers and coatings were produced with a 400% increase in Young's modulus and a 200% increase in hardness in the case of 20 wt% ND in polyamide (Behler et al., 2009). Neitzel et al. studied mechanical and thermal properties of ND-epoxy composites at high content of ND (Neitzel, Mochalin, Knoke, Palmese, & Gogotsi, 2011). The composites with 25 vol% ND showed an increase in Young's modulus (up to 470%) and hardness (up to 300%) as compared to neat epoxy. A significant increase in scratch resistance and thermal conductivity of the composites were observed as well. The improved thermal conductivity of the composites with high contents of ND is explained by direct contacts between single ND particles forming an interconnected network held together by a polymer binder.

Several nanoadditives can be incorporated into a matrix simultaneously. Prasad et al. fabricated polyvinyl alcohol-based composites with the simultaneous addition of carbon nanotubes (CNT) and ND and observed a synergistic effect with a 400% increase in stiffness and hardness of the resulting composites, as compared to those obtained with single nanocarbon reinforcements (Prasad, Das, Maitra, et al., 2009). Another aspect of combined use of ND particles and CNT was recently reported by Shenderova et al. (2008) and Hens et al. (2011). Formation of ND/CNT composites produced by codeposition of CNT and ND from a suspension was reported (Hens et al., 2011; Shenderova et al., 2008). At certain ND/CNT weight ratios, it was possible to form large-area ND/CNT films that adhered strongly to a substrate with uniformly distributed MCWNTs within an ND matrix. ND particles were also used to disperse carbon nanotubes, allowing the formation of their stable colloidal suspensions. Both MCWNTs and single-walled carbon nanotubes (SWCNTs) could be suspended in deionized water and organosols using NDs. It was demonstrated that NDs stabilize CNTs in organic solutions that are commonly used for polymer films, coating, and composites. Thus, the development of nanocomposites may be facilitated with the addition of NDs that serve as both a dispersive and filler material. It was demonstrated that a urethane film with added NDs showed greater dispersivity of CNTs as compared to the CNT containing film without NDs (Hens et al., 2011). Therefore, NDs promote the dispersivity of CNTs in prepolymer solutions and retain this function throughout the curing process.

Borjanovich et al. studied irradiation with 2 MeV proton beams of pure poly(dimethylsiloxane) (PDMS) polymer and PDMS–DND composite with 1 wt% of DND (Borjanovic, Bistricic, Vlasov, et al., 2009). Based on spectroscopic analysis of vibrational dynamics, it was concluded that structural degradation of PDMS–DND composites takes place at an order of magnitude higher fluency than for pure PDMS, indicating the potential of using DND-based polymer composites for application in high radiation environments. The appearance of strong photoluminescence following irradiation was more pronounced for PDMS–DND composites as compared to pure PDMS. Gupta et al. reported a decrease of damage of SWCNT by gamma irradiation when they were mixed with ND particles, providing a healing effect to SWCNT (possibly by charge transfer and dangling bond formation and passivation) (Gupta, Scuttler, & Farmer, 2010).

An explanation of the enhanced mechanical and thermal properties of the composites with incorporated DNDs can be as follows. Within the current nanocomposite concept (Banerjee, Souri, Kapur, & Saraswat, 2001; Viai, 2001), there are three major characteristics defining the polymer nanocomposite performance: a nanoscopically confined polymer matrix, nanoscale inorganic reinforcing elements and the nanoscale arrangement of these elements. The effect of the nanoelements on the surrounding matrix is related to a fundamental length scale of the adjacent matrix, which is on the order of their radii of gyration for polymers (5–10 nm). The distances between the reinforcing elements in composites with a few volume percentage of nanoelements are of the same order of magnitude as the radius of gyration. Therefore, it appears that a majority of the polymer molecules reside near nanoelements. Because an interface limits the number of conformations of a polymer molecule, the entire matrix may be considered to be nanoscopically confined. These restrictions on chain conformations alter molecular mobility, relaxation behavior, free volume and thermal transitions (Banerjee et al., 2001; Viai, 2001). Configurational confinement provided by nanoelements results in increased mechanical strength and thermal stability of the polymer composite. Thus, mechanically and thermally stable nanoelements well dispersed in the matrix provide beneficial effects. Formation of chemical bonds between polymer molecules and ND particles will also reduce the mobility of the chain molecules and improve the overall rigidity of the matrix resulting in enhanced thermal and mechanical properties. More importantly, ND-based nanoelements are expected to exert significant influence on polymer properties because the surface of ND elements contains a significant number of carbon sites for bonding with the matrix. ND-based nanoelements are readily functionalized and it is possible to design DND surface functionalization that will result in cross-linking with polymer chains during nanocomposite curing.

However, addition of nanofillers into a matrix does not necessarily produce a positive effect. Comet, Pichot, Siegert, et al. (2010) reported an attempt to enclose diamond nanoparticles produced by detonation into a Kevlar matrix (40 wt% diamond). The hydrogen interactions between carboxylic groups on the ND surface and the amide groups of Kevlar destroyed the "rod-like" structure and the classical three-dimensional organization of this polymer, reducing the macroscopic hardness of Kevlar doped by NDs by approximately a factor of two as compared to pure Kevlar.

Electrochemical deposition of DND together with metals using standard galvanic equipment has been demonstrated to be beneficial in a variety of applications for coatings of components of transportation units, tools for electronics, electrical engineering, medicine, watch and jewelry industry (Dolmatov, 2001, 2006). The advantages of adding DND to galvanic coatings include increase in wear resistance (2–13 times depending on the metal); microhardness (may be up to two times depending on the metal); an increase in corrosion resistance (2–6 times depending on the metals); decrease in porosity (pores can be completely eliminated depending on metal); significant decrease of friction coefficient; considerable improvement of adhesion and cohesion; high throwing power of electrolyte. According to Dolmatov (2001, 2006), the service life of products is increased 2–10 times even when the coating thickness is decreased by a factor of 2–3. The strengthening effect is observed for coatings of many metals, including silver, gold, and platinum. Particularly, DND is most widely used in strengthening chromium coatings deposited using an electrolytic process. In this process, DND-containing additives are added to the chrome plating electrolyte without any modification of the standard production line. Such coatings increase by a few times the operating life of moulds, high-precision bearing surfaces and other similar components Dolmatov (2001, 2006). Interestingly, recently, it was demonstrated that the best result in terms of the coating microhardness for the coatings prepared by the hard chromium plating method has been achieved using "Nanoamando", ND particles deagglomerated to individual primary particles (Burkat, Dolmatov, Osawa, & Orlova, 2010).

A different approach for production of DND–metal matrix composites was reported by Nunes et al., who suggested a novel material design for nuclear fusion reactors based on Cu-Diamond and W-Diamond nanocomposites (Nunes, Livramento, Correia, et al., 2009). The proposed design involves the production of W/W-Diamond/Cu-Diamond/Cu functionally graded material. W,W-Diamond, Cu-Diamond and Cu nanostructured composite powders were produced independently by mechanical alloying and subsequently consolidated/welded through spark plasma sintering.

A wide variety of nanomaterials in powder and colloidal forms have emerged as potential antifriction and antiwear additives to different classes of base lubricants (Martin & Ohmae, 2008). DNDs with 4–5 nm primary particle size and spherical shape seem to be among the most promising candidates as additives to such lubricants. Until recently, detonation soot, which is a mixture of graphite and ND particles, has been the predominant material of the class used as an additive to lubricants (Dolmatov, 2010). It was assumed that the combination of ND and the graphite phase is beneficial since graphite on its own has lubricating properties, while DND contributes by polishing of asperities on friction surfaces and thus reducing friction. Concerns on using DND alone without a protective sp^2 shell were related to the abrasive nature of diamond powder. To a large extent, the absence of positive results on using purified DND in lubricate applications was related to the fact that until recently, DND was available only as a polydispersed material. However, studies by Ivanov et al. (Ivanov et al., 2004, Ivanov, Pavlyshko, Ivanov, Petrov, & Shenderova, 2010, 2010b) demonstrated successful application of purified DND for enhanced tribological performance of greases and oils when used as synergistic compositions with other additives. Specifically, Ivanov et al. demonstrated that a combination of DND with ultradispersed PTFE particles provides excellent lubrication properties in mineral oils of Class I and greases, well exceeding those for soot and when using only PTFE additives alone (Ivanov et al., 2004). Beside 90% improvement in friction coefficient, 100% descrease in a wear spot, extreme pressure to failure was increased up to seven times for polyalphaolephine oil-based compositions (Ivanov et al., 2010,b).

In summary, there is striking evidence that niche applications for ND, and, particularly, ND of detonation origin that is a commercial product, are expanding significantly.

3.07.6 Future Directions of Production and Applications

Compared to many other nanomaterials, DND produced by detonation of explosives (also called DND) is relatively expensive since it has not experienced scale-up to large volume production. As in any market, price is a factor which inhibits expansion of the materials use. Even at the current purity and particle size, the demand for DND will increase dramatically with even a factor of two reduction of price. Advances in the methods of separation and fractionation of DND have lead to the availability of 50 nm, 20 nm and 5 nm particle sizes (average agglomerate size) versus typical 200–300 nm agglomerates, which were not readily available even 5 years ago. Production volumes of these smaller size fractions opens up new markets and expands existing ones as the material meets the demand for specific uses. Examples include the use of DND in polymers, sunscreens and lubricants. New technologies are providing the means to increase the production of small size fractions in larger volumes. However, the method of production of the initial soot has largely remained the same for the past 30 years. Modern methods of increased production of DND by using larger detonation charges were recently outlined by Danilenko (2009). Other methods of ND synthesis, such as laser-assisted synthesis (Yang, 2007), are intended to be brought up to a large-scale production (Ray Technologies, Inc).

The availability of single-digit ND particles produced by detonation of explosives in kilograms quantities (Osawa, 2007) has opened broad perspectives for the application of ND in composites and nanolubricants. Breaking of HPHT diamond to sub-10 nm particles is an important breakthrough for quantum optics and luminescent markers applications. Both approaches (DND deagglomeration and HPHT ND milling) require further development of inexpensive methods of processing to be affordable for large-scale production and applications.

Production of electroconductive (for example, boron-doped) ND particles during their synthesis can be very beneficial and can find broad applications in high-surface area carbon electrode materials in electroanalysis and energy storage applications. If inexpensive methods of HPHT ND milling will be developed, grinding of electrically conductive HPHT diamond will be advantageous also.

It is the large and reactive surface area of NDs that allows a broad range of modifications without compromising the superior properties of the chemically inert diamond core. Recent achievements in functionalization of ND led to a whole new range of applications, and this topic remains of an object of intense research.

It can be concluded that the "golden age" for ND particles has started and will result in the near-term in wide spread application of NDs in commodity products as well as in the most sophisticated future materials.

Acknowledgments

Gary McGuire, International Technology Center and Vyacheslav Danilenko, Russia are acknowledged for their valuable comments.

References

Adadurov, G. A., Baluev, A. V., Breusov, O. N., et al. (1977). Some properties of diamonds produced by an explosive method. *Izvestiya Akademii Nauk SSSR, Series Neorganicheskie Materialy, 13*(4), 649–653.

Ager, J. W., Veirs, D. K., & Rosenblatt, G. M. (1991). Spatially resolved Raman studies of diamond films grown by chemical vapor deposition. *Physical Review B, 43*, 6491.

Aleksenskii, A. E., Baidakova, M. V., Vul', A. Ya., & Siklitskii, V. I. (1999). The structure of diamond nanoclusters. *Physics of the Solid State, 41*, 668–671.

Aleksenskiy, A., Baidakova, M., Osipov, V., & Vul', A. (2010). The fundamental properties and characteristics of nanodiamonds. In D. Ho (Ed.), *Nanodiamond. Applications in biology and nanoscale medicine* (pp. 55–79). Springer.

An, J. H., Lee, G. S., Lee, W. J., et al. (2008). Effect of process parameters on material removal rate in chemical mechanical polishing of 6H-SiC(0001). *Materials Science Forum, 600–603*, 831–837.

Ay, A., Swope, V. M., & Swain, G. M. (2008). The physicochemical and electrochemical properties of 100 and 500 nm Diameter diamond powders coated with boron-doped nanocrystalline diamond. *Journal of The Electrochemical Society, 155*(10), B1013–B1022.

Badziag, P., Verwoerd, W. S., Ellis, W. P., & Greiner, N. R. (1990). Nanometre-sized diamonds are more stable than graphite. *Nature, 343*, 244–245.

Baidakova, M., & Vul, A. (2007). New prospects and frontiers of nanodiamond clusters. *Journal of Physics D: Applied Physics, 40*(20), 6300–6311.

Balasubramanian, G., Chan, I. Y., Kolesov, R., et al. (2008). Nanoscale imaging magnetometry with diamond spins under ambient conditions. *Nature, 455*, 648–651.

Banerjee, K., Souri, S. J., Kapur, P., & Saraswat, K. C. (2001). 3D ICs: a novel chip design for improving deepsubmicrometer interconnect performance and systems-on-chip integration. *Proceedings of the IEEE, 89*, 602–609.

Banhart, F., & Ajayan, P. M. (1996). Carbon onion as nanoscopic pressure cell for diamond formation. *Nature, 382*, 433–437.

Barnard, A. S., Russo, S. P., & Snook, I. K. (2003a). Structural relaxation and relative stability of nanodiamond morphologies. *Diamond and Related Materials, 12*, 1867–1873.

Barnard, A. S., Russo, S. P., & Snook, I. K. (2003b). Size dependent phase stability of carbon nanoparticles: nanodiamond versus fullerenes. *Journal of Chemical Physics, 118*, 5094–5098.

Barnard, A. S., Russo, S. P., & Snook, I. K. (2003c). Ab initio modelling of stability of nanodiamond morphologies. *Philosophical Magazine Letters, 83*, 39–42.

Barnard, A. S., Russo, S. P., & Snook, I. K. (2003d). Coexistence of bucky diamond with nanodiamond and fullerene carbon phases. *Physical Review B, 68*, 73406–73410.

Barnard, A. S., & Sternberg, M. (2007). Crystallinity and surface electrostatics of diamond nanocrystals. *Journal of Materials Chemistry, 17*, 4811–4819.

Behler, K. D., Stravato, A., Mochalin, V., Korneva, G., Yushin, G., & Gogotsi, Y. (2009). Nanodiamond-polymer composite fibers and coatings. *ACS Nano, 3*(2), 363–369.

Bondar, V. S., & Puzyr, A. P. (2004). Nanodiamonds for biological investigations. *Physics of the Solid State, 46*(4), 716–719.

Borjanovic, V., Bistricic, L., Vlasov, I., et al. (2009). Influence of proton irradiation on the structure and stability of poly(dimethylsiloxane) and poly(dimethylsiloxane)-nanodiamond composite. *Journal of Vacuum Science and Technology B, 27*, 2396–2404.

Borjanovic, V., Lawrence, W. G., Hens, S., et al. (2008). Effect of proton irradiation on photoluminescent properties of PDMS nanodiamond composites. *Nanotechnology, 19*(50), 509901–509909.

Boudou, J.-P., Curmi, P. A., Jelezko, F., et al. (2009). High yield fabrication of fluorescent nanodiamonds. *Nanotechnology, 20*, 235602.

Brennen, C. E. (1995). *Cavitation and bubble dynamics.* Oxford: Oxford University Press.

Buerki, P. R., & Leutwyler, S. (1991). Homogeneous nucleation of diamond powder by CO_2 laser-driven reactions. *Journal of Applied Physics, 69*, 3739–3745.

Burkat, G. K., Dolmatov, V. Y., Osawa, E., & Orlova, E. K. (2010). A study of properties of chromium-diamond coatings using nanodiamonds from various producers. *Journal of Superhard Materials, 32*(2), 98–111.

Cao, L. M., Gao, C. X., Sun, H. P., et al. (2001). Synthesis of diamond from carbon nanotubes under high pressure and high temperature. *Carbon, 39*, 311–317.

Carlson, R. M. K., Dahl, J. E. P., & Liu, S. G. (2005). Diamond molecules found in petroleum. In D. M. Gruen, A. Vul, & O. A. Shenderova (Eds.), *Synthesis, properties, and applications of ultrananocrystallline diamond*. Dordrecht, The Netherlands: Springer.

Chang, J. A., Jallouli, Y., Barras, A., et al. (2009). Drug delivery to the brain using colloidal carriers. *Progress in Brain Research, 180*, 3–17.

Chang, Y.-R., Lee, H.-Y., Chen, K., Chang, C.-C., et al. (2008). Mass production and dynamic imaging of fluorescent nanodiamonds. *Nature Nanotechnology, 3*, 284–288.

Chen, P. W., Ding, Y. S., Chen, Q., Huang, F. L., & Yun, S. R. (2000). Spherical nanometer-sized diamond obtain from detonation. *Diamond and Related Materials, 9*, 1722–1729.

Chevrot, G., Bourasseau, E., Pineau, N., & Maillet, J.-B. (2009). *Carbon, 4*(7), 3392–3402.

Chukhaeva, S. I., Detkov, P., Tkachenko, A., & Toropov, A. (1998). Physicochemical properties of fractions isolated from ultradispersed diamonds. *Superhard Materials, 4*, 29–36.

Comet, M., Pichot, V., Siegert, B., et al. (2010). Detonation nanodiamonds for doping Kevlar. *Journal for Nanoscience and Nanotechnology, 10*(7), 4286–4292.

Cowan, G. R., Woodbury, N. J., & Dunnington B. W., et al. (1968). Process for synthesizing diamond. US patent 3,401,019.

Dahl, J. E., Liu, S. G., & Carlson, R. M. K. (2003). Isolation and structure of higher diamondoids, nanometer-sized diamond molecules. *Science, 299*, 96–102.

Danilenko, V. V. (2003). *Synthesis and sintering of diamond by explosion*. Moscow: Energoatomizdat.

Danilenko, V. V. (2004). On the history of the discovery of nanodiamond synthesis. *Physics of the Solid State, 46*(4), 595–599.

Danilenko, V. V. (2005). In D. M. Gruen, O. A. Shenderova, A. Y. Vul, & St. Petersburg (Eds.), *Proceedings of the NATO advanced research workshop on synthesis, properties and applications of ultrananocrystalline diamond* (pp. 181–198). Netherlands: Springer. Russia, June 7–10, 2004.

Danilenko, V. V. (2006). On the discovery of detonation nanodiamond. In O. A. Shenderova, & D. M. Gruen (Eds.), *Ultrananocrystalline diamond* (pp. 335–344). Norwich, New York, USA: William Andrew Publishing.

Danilenko, V. V. (2009). Nanodiamonds: problems and prospects. *Journal of Superhard Materials, 32*(5), 301–310.

Danilenko, V. V. (2010). *Explosion. Physics. Technique. Technology*. Moscow: Energoatomizdat.

Daulton, T. L., Kirk, M. A., Lewis, R. S., & Rehn, L. E. (2001). Production of nanodiamonds by high-energy ion irradiation of graphite at room temperature. *Nuclear Instruments and Methods in Physics Research Section B, 175*, 12–18.

Decarli, P. S., & Jamieson, J. C. (1961). Formation of diamond by explosive shock. *Science, 133*(346), 1821.

DeCarli, (1966). Method of making diamond. US patent 3,238,019.

Dolmatov, V. Y. (2001). Detonation synthesis ultradispersed diamonds: properties and applications. *Russian Chemical Review, 70*, 607–626.

Dolmatov, V. Y. (2003). *Detonation synthesis ultradispersed diamonds (Russian edition)*. Saint-Petersburg: Publ.house of Saint-Petersburg State Polytechnic University.

Dolmatov, V. Y. (2006). Application of detonation nanodiamond. In O. A. Shenderova, & D. M. Gruen (Eds.), *Ultrananocrystalline diamond* (pp. 513–527). Norwich, New York, USA: William Andrew Publishing.

Dolmatov, V. Y. (2007). Detonation nanodiamonds: synthesis, structure, properties and applications. *Uspekhi Khimii, 76*(4), 375–397.

Dolmatov, V. Y. (2010). Detonation nanodiamonds in oils and lubricants. *Journal of Superhard Materials, 32*(1), 14–20.

Fang, X. W., Mao, J. D., Levin, E. M., et al. (2009). Nonaromatic Core-Shell Structure of Nanodiamond from Solid-State NMR Spectroscopy. *Journal of American Chemical Society, 131*(4), 1426–1435.

Fedoseev, V. D., Bukhovets, V. L., Varshavskaya, et al.. (1983). Transition of graphite into diamond in a solid state under the atmospheric pressure. *Carbon, 21*, 237–243.

Flynn H. G. Method and means for converting graphite to diamond. US Patent 4,563,341, January 7, 1986.

Frenklach, M., Kematick, R., Huang, D., et al. (1989). Homogeneous nucleation of diamond powder in the gas phase. *Journal of Applied Physics, 66*, 395–399.

Frenklach, M., Howard, W., et al. (1991). Induced nucleation of diamond powder. *Applied Physics Letters, 59*(5), 546–548.

Gaffet, E., Bernard, F., Niepce, J.-C., et al. (1999). Some recent developments in mechanical activation and mechanosynthesis. *Journal of Materials Chemistry, 9*, 305–314.

Galimov, E. M., Kudin, S., Skorobogatski, V. N., et al. (2004). Experimental corroboration of the synthesis of diamond in the cavitation process. *Doklady Physics, 49*, 150–156.

Gibson, N., Shenderova, O., Luo, T. J. M., et al. (2009). Colloidal stability of modified nanodiamond particles. *Diamond and Related Materials, 18*(4), 620–626.

Gogotsi, Y., Welz, S., Ersoy, D. A., & McNallan, M. J. (2001). Conversion of silicon carbide to crystalline diamond-structured carbon at ambient pressure. *Nature, 411*, 283–287.

Grichko, V., Tyler, T., Grishko, V., & Shenderova, O. (2008). Nanodiamond particles forming photonic structures. *Nanotechnology, 19*(22), 225201–225207.

Gupta, S., Scuttler, A. M., & Farmer, J. (2010). Novel nanocarbon hybrids of single-walled carbon nanotubes and dispersed nanodiamond: structure and hierarchical defects evolution irradiated with gamma rays. *Journal of Applied Physics, 107*(10), 104308–104318.

Hawelek, L., Brodka, A., Dore, J. C., Honkimaki, V., Tomita, S., & Burian, A. (2008). Structural studies of nanodiamond by high-energy X-ray diffraction. *Diamond and Related Materials, 17*, 1186–1193.

Hens, S., Cunningham, G., McGuire, G., & Shenderova, O. (2011). Nanodiamond-assisted dispersion of carbon nanotubes and hybrid nanocarbon-based composites. *Nanoscience and Nanotechnology Letters, 3*(1), 75–82.

Holt, K. B. (2007). Diamond at the nanoscale: applications of diamond nanoparticles from cellular biomarkers to quantum computing. *Philosophical Transactions. Series A, Mathematical, Physical, and Engineering Sciences, 365*, 2845–2861.

Hu, S., Sun, J., Du, X., Tian, F., & Jiang, L. (2008). The formation of multiply twinning structure and photoluminescence of well-dispersed nanodiamonds produced by pulsed-laser irradiation. *Diamond and Related Materials, 17*, 142–146.

Huang, H., Pierstorff, E., Osawa, E., & Ho, D. (2007). Active nanodiamond hydrogels for chemotherapeutic delivery. *Nano Letters, 7*, 3305–3314.

Huang, H. J., Pierstorff, E., Osawa, E., & Ho, D. (2008). Protein-mediated assembly of nanodiamond hydrogels into a biocompatible and biofunctional multilayer nanofilm. *ACS Nano, 2*, 203–212.

Huang, H. J., Dai, L. M., Wang, D. H., Tan, L. S., & Osawa, E. (2008b). Large-scale self-assembly of dispersed nanodiamonds. *Journal of Materials Chemistry, 18*, 1347–1355.

Iakoubovskii, K., Mitsuishi, K., & Furuya, K. (2008). High-resolution electron microscopy of detonation nanodiamond. *Nanotechnology, 19*, 155705–155710.

Ivanov, M. G., Kharlamov, V. V., Buznik, V. M., Ivanov, D. M., Pavlushko, S. G., & Tsvetnikov, A. K. (2004). Tribological properties of the grease containing polytetrafluorethylene and ultrafine diamond. *Friction and Wear, 25*(1), 99–105.

Ivanov, M. G., Pavlyshko, S. V., Ivanov, D. M., Petrov, I., & Shenderova, O. (2010a). Synergistic compositions of colloidal nanodiamond as lubricant-additive. *Journal of Vacuum Science and Technology B, 28*, 869–878.

Ivanov, M. G., Pavlyshko, S. V., Ivanov, D. M., Petrov, I., McGuire, G., & Shenderova, O. (2010b). Nanodiamonds particles as additives in lubricants. *Materials Research Society Symposium Proceedings, 1203*, 1203-J17-16.

Jelezko, F., Gaebel, T., Popa, I., Gruber, A., & Wrachtrup, J. (2004). Observation of coherent oscillations in a single electron spin. *Physical Review Letters, 92*(7), 076401–076405.

Khachatryan, A. Kh., Aloyan, S., May, P. W., et al. (2008). Graphite-to-diamond transformation induced by ultrasonic cavitation. *Diamond and Related Materials, 17*, 931–937.

Krueger, A., Kataoka, F., et al. (2005). Unusually tight aggregation in detonation nanodiamond: identification and disintegration. *Carbon, 43*(8), 1722–1730.

Krueger, A., Stegk, J., Liang, Y., Lu, L., & Jarre, G. (2008). Biotinylated nanodiamond: simple and efficient functionalization of detonation diamond. *Langmuir, 24*, 4200–4204.

Krueger, A. (2008). Diamond nanoparticles: jewels for chemistry and physics. *Advanced Materials, 20*(12), 2445–2449.

Kulakova, I. I. (2004). Chemistry of nanodiamond surface. *Solid State Physics, 46*(4), 621–629.

Kuznetsov, V. L., & Butenko, Yu V. (2006). Diamond phase transitions. In O. Shenderova, & D. Gruen (Eds.), *Ultra-nanocrystalline diamond: Syntheses, properties and applications* (pp. 405–463). New York: Andrew.

Larionova, I. S., Molostov, I. N., et al. (1999). Method of purification of synthetic ultradispersed diamonds. Patent RU 2168462.

Larionova, I., Kuznetsov, V., Frolov, A., Shenderova, O., Moseenkov, S., & Mazov, I. (2006). Properties of individual fractions of detonation nanodiamond. *Diamond and Related Materials, 15*, 1804–1808.

Ma, Y. Z., Zou, G. T., Yang, H. B., & Meng, J. F. (1994). Conversion of fullerenes to diamond under high pressure and high temperature. *Applied Physics Letters, 65*, 822–826.

Macutkevic, J., Seliuta, D., Valusis, G., et al. (2009). High dielectric permittivity of percolative composites based on onion-like carbon. *Applied Physics Letters, 95*(11), 112901–112905.

Maitra, U., Prasad, K. E., Ramamurty, U., & Rao, C. N. R. (2009). Mechanical properties of nanodiamond-reinforced polymer-matrix composites. *Solid State Communications, 149*(39–40), 1693–1697.

Martin, J. M., & Ohmae, N. (Eds.). (2008). *Nanolubricants.* Wiley.

Meguro, T., Hida, M., Suzuki, M., et al. (2001). Creation of nanodiamonds by single impacts of highly charged ions upon graphite. *Applied Physics Letters, 79*, 3866–3870.

Mitev, D., Dimitrova, R., Spassova, M., Minchev, C., & Stavrev, S. (2007). Surface peculiarities of detonation nanodiamonds in dependence of fabrication and purification methods. *Diamond and Related Materials, 16*, 776.

Morita, Y., Takimoto, T., Yamanaka, H., et al. (2008). A facile and scalable process for size-controllable separation of nanodiamond particles as small as 4 nm. *Small, 4*, 2154–2160.

Mykhaylyk, O. O., Solonin, Y. M., Batchelder, D. N., & Brydson, R. J. (2005). Transformation of nanodiamond into carbon onions: a comparative study by high-resolution transmission electron microscopy, electron energy-loss spectroscopy, X-ray diffraction, small-angle X-ray scattering, and ultraviolet Raman spectroscopy. *Journal of Applied Physics, 97*(7), 074302.

Neitzel, I., Mochalin, V., Knoke, I., Palmese, G. R., & Gogotsi, Y. (2011). Mechanical properties of epoxy composites with high contents of nanodiamond. *Composites Science and Technology*. http://dx.doi.org/10.1016/j.compscitech.2011.01.016.

Nikitin, A., & Gogotsi, Y. (2004). Nanostructured carbide-derived carbon. *Encyclopedia of Nanoscience and Nanotechnology, 7*, 553–574.

Novikov, N. B., Danilenko, V. V., Bogatyreva, G. P., & Padalko, V. I. (2010). Nanodiamonds: synthesis, properties, applications. *Contenant*4–22. June issue.

Nunes, D., Livramento, V., Correia, J. B., et al. (2009). W-diamond/Cu-diamond nanostructured composites for fusion devices. *Materials for Future Fusion and Fission Technologies, MRS Symposium Proceedings, 1125*, 59–64.

Núñez-Regueiro, M., Monceau, P., & Hodeau, J.-L. (1992). Crushing C60 to diamond at room temperature. *Nature, 355*, 237–239.

Osawa, E. (2007). Recent progress and perspectives in single-digit nanodiamond. *Diamond and Related Materials, 16*(12), 2018–2022.

Osawa, E. (2010). Single-nano buckydiamond particles. In D. Ho (Ed.), *Nanodiamond. Applications in biology and nanoscale medicine* (pp. 55–79). Springer.

Osswald, S., Yushin, G., Mochalin, V., et al. (2006). Control of sp2/sp3 carbon ratio and surface chemistry of nanodiamond powders by selective oxidation in air. *Journal of the American Chemical Society, 128*(35), 11635–11642.

Ozawa, M., Inaguma, M., Takahashi, M., Kataoka, F., Kruger, A., & Osawa, E. (2007). Preparation and behavior of brownish, clear nanodiamond colloids. *Advanced Materials, 19*, 1201.

Palosz, B., Pantea, C., Grzanka, E., et al. (2006). Investigation of relaxation of nanodiamond surface in real and reciprocal space. *Diamond and Related Materials, 15*(11–12), 1813–1817.

Pandey, K. C. (1982). New dimerized-chain model for the reconstruction of the diamond (111)-(2x1) surface. *Physical Review B, 25*(6), 4338–4341.

Panich, A. M., Shames, A. I., Vieth, H.-M., Osawa, E., Takahashi, M., & Vul', A. Y. (2006). Nuclear magnetic resonance study of ultrananocrystalline diamond. *The European Physical Journal B, 52*, 397–402.

Pearce, S. R. J., Henley, S. J., Claeyssens, F., et al. (2004). Production of nanocrystalline diamond by laser ablation at the solid/liquid interface. *Diamond and Related Materials, 13*, 661–665.

Pentecost, A., Gour, S., Mochalin, V., Knoke, I., & Gogotsi, Y. (2010). De-aggregation of nanodiamond powders using salt- and sugar-assisted milling. *ACS Applied Materials & Interfaces, 2*(11), 3289–3294.

Petrov, I., & Shenderova, O. (2006). History of Russian patents on detonation nanodiamonds. In O. A. Shenderova, & D. M. Gruen (Eds.), *Ultrananocrystalline diamond* (pp. 559–589). Norwich, New York, USA: William Andrew Publishing.

Petrov, I., Shenderova, O., Grishko, V., Grichko, V., Tyler, T., Cunningham, G., et al. (2007). Detonation nanodiamonds simultaneously purified and modified by gas treatment. *Diamond and Related Materials, 16*, 2098–2103.

Prasad, K. E., Das, B., Maitra, U., et al. (2009). Extraordinary synergy in the mechanical properties of polymer matrix composites reinforced with two nanocarbons. *PNAS, 106*(32), 13186–13189.

Raty, J. Y., & Galli, G. (2003). Ultradispersity of diamond at the nanoscale. *Nature Materials, 2*(12), 792–795.

Raty, J. Y., Galli, G., Bostedt, C., Van Buuren, T. W., & Terminello, L. J. (2003). Quantum confinement and fullerenelike surface reconstructions in nanodiamonds. *Physical Review Letters, 90*, 037401.

Schrand, A. M., Huang, H. J., Carlson, C., et al. (2007). Are diamond nanoparticles cytotoxic? *Journal of Physical Chemistry B, 111*(1), 2–7.

Schrand, A. M., Hens, S. A., & Shenderova, O. A. (2009). Nanodiamond particles: properties and perspectives for bioapplications. *Critical Reviews in Solid State and Materials Sciences, 34*(1), 18–74.

Schwertfeger, H., Fokin, A. A., & Schreiner, P. R. (2008). Diamonds are a chemist's best friend: diamondoid chemistry beyond adamantane. *Angewandte Chemie International Edition in English, 47*, 1022–1036.

Shenderova, O., & Gruen, D. (Eds.). (2006). *Ultrananocrystalline diamond*. Norwich, New York, USA: William Andrew Publishing.

Shenderova, O., & McGuire, G. (2006b). Types of nanocrystalline diamond. In O. Shenderova, & D. Gruen (Eds.), *Ultrananocrystalline diamond* (pp. 79–109). William-Andrew.

Shenderova, O. A., Zhirnov, V. V., & Brenner, D. W. (2002). Carbon nanostructures. *Critical Reviews in Solid State, 27*, 227–356.

Shenderova, O., Petrov, I., Walsh, J., et al. (2006). Modification of detonation nanodiamonds by heat treatment in air. *Diamond and Related Materials, 15*(11–12), 1799–1803.

Shenderova, O., Grichko, V., Hens, S., et al. (2007). Detonation nanodiamonds as UV radiation filter. *Diamond and Related Materials, 16*(12), 2003–2008.

Shenderova, O., Tyler, T., Cunningham, G., et al. (2007). Nanodiamond and onion-like carbon polymer nanocomposites. *Diamond and Related Materials, 16*(4–7), 1213–1217.

Shenderova, O., Jones, C., Borjanovic, V., et al. (2008). Detonation nanodiamond and onion-like carbon: applications in composites. *Physica Status Solidi A, 205*(9), 2245–2251.

Shenderova, O., Grishko, V., Cunningham, G., et al. (2008). Onion-like carbon for terahertz electromagnetic shielding. *Diamond and Related Materials, 17*(4–5), 462–466.

Soltamova, A. A., Ilyin, I. V., & Shakhov, F. M. (2010). Electron paramagnetic resonance detection of the giant concentration of nitrogen vacancy defects in sintered detonation nanodiamonds. *JETP Letters, 92*(2), 106–110.

Shenderova, O. (2011a). Nitrogen control in nanodiamond produced by detonation shock-wave-assisted synthesis. *Journal of Physical Chemistry, 115*, 14014–14024.

Shenderova, O. (2011b). Surface chemistry and properties of ozone-purified detonation nanodiamonds. *Journal of Physical Chemistry, 115*, 9827–9837.

Tatcii, V. F., Bochko, A. V., & Oleinik, G. S. (2009). Structure and properties of dalan detonation diamonds. *Combustion, Explosion, and Shock Waves, 45*(1), 95–103.

Tielens, A., Seab, C., Hollenbach, D., et al. (1987). Shock processing of interstellar dust – diamonds in the sky. *Astrophysical Journal, 319*, L109–L113.

Ting, C. C., Young, T., & Jwo, C. S. (2007). Fabrication of diamond nanopowder using microwave plasma torch technique. *International Journal of Advanced Manufacturing Technology, 34*, 316–322.

Turner, S., Lebedev, O. I., Shenderova, O., et al. (2009). Determination of size, morphology, and nitrogen impurity location in treated detonation nanodiamond by transmission electron microscopy. *Advanced Functional Materials, 19*(13), 2116–2124.

Tyler, T., Zhirnov, V. V., Kvit, A. V., Kang, D., & Hren, J. J. (2003). Electron emission from diamond nanoparticles on metal tips. *Applied Physics Letters, 82*(17), 2904–2906.

Vaia, R. A., & Giannelis, E. P. (2001). Polymer nanocomposites: status and opportunities. *MRS Bulletin, 26*, 394.

Vereschagin, A. L. (2005). *Properties of detonation nanodiamonds*. Altay Region: Barnaul State Technical University.

Viecelli, J. A., & Ree, F. H. (2000). Carbon particle phase transformation kinetics in detonation waves. *Journal of Applied Physics, 88*, 683–690.

Viecelli, J. A., Bastea, S., Glosli, J. N., & Ree, F. H. (2001). Phase transformations of nanometer size carbon particles in shocked hydrocarbons and explosives. *Journal of Chemical Physics, 115*, 2730–2735.

Vlasov, , II, Shenderova, O., Turner, S., et al. (2010). Nitrogen and luminescent nitrogen-vacancy defects in detonation nanodiamond. *Small, 6*(5), 687–694.

Wei, B., Zhang, J., Liang, J., & Wu, D. (1998). The mechanism of phase transformation from carbon nanotube to diamond. *Carbon, 36*, 997–1002.

Welz, S., Gogotsi, Y., & McNallan, M. J. (2003). Nucleation, growth, and graphitization of diamond nanocrystals during chlorination of carbides. *Journal of Applied Physics, 93*, 4207.

Wesolowski, P., Lyutovich, Y., Banhart, F., et al. (1997). Formation of diamond in carbon onions under MeV ion irradiation. *Applied Physics Letters, 71*, 1948–1951.

Winter, N. W., & Ree, F. H. (1998). Carbon particle phase stability as a function of size. *Journal of Computer-Aided Materials Design, 5*, 279–294.

Xu, K., & Xue, Q. J. (2004). A new method for deaggregation of nanodiamond from explosive detonation: graphitization-oxidation method. *Physics of the Solid State, 46*, 649–650.

Xu, X. Y., Yu, Z. M., Zhu, Y. M., & Wang, B. C. (2004). Dispersion and stability of nanodiamond in clean oil. *Advances in Materials Manufacturing Science and Technology Materials Science Forum, 471*, 779–783.

Xu, X. Y., Yu, Z. M., Zhu, Y. M., & Wang, B. C. (2005a). Effect of sodium oleate adsorption on the colloidal stability and zeta potential of detonation synthesized diamond particles in aqueous solutions. *Diamond and Related Materials, 14*, 206–212.

Xu, X. Y., Yu, Z. M., Zhu, Y. W., & Wang, B. C. (2005b). Influence of surface modification adopting thermal treatments on dispersion of detonation nanodiamond. *Journal of Solid State Chemistry, 178*, 688–693.

Xu, X. Y., Zhu, Y. W., Wang, B. C., Yu, Z. M., & Xie, S. Z. (2005c). Mechanochemical dispersion of nanodiamond aggregates in aqueous media. *Journal of Materials Science and Technology, 21*, 109–112.

Yang, G. W., Wang, J. B., & Liu, Q. X. (1998). Preparation of nano-crystalline diamonds using pulsed laser induced reactive quenching. *Journal of Physics: Condensed Matter, 10*, 7923–7928.

Yang, G. W. (2007). Laser ablation in liquids: applications in the synthesis of nanocrystals. *Progress in Materials Science, 52*, 648–698.

Yur'ev, G. S., & Dolmatov, V. Y. (2010). X-ray diffraction study of detonation nanodiamonds. *Journal of Superhard Materials, 32*(5), 29–50.

Yusa, H. (2002). Nanocrystalline diamond directly transformed from carbon nanotubes under high pressure. *Diamond and Related Materials, 11*, 87–91.

Zhang, Q. W., Mochalin, V. N., Neitzel, I., et al. (2011). Fluorescent PLLA-nanodiamond composites for bone tissue engineering. *Biomaterials, 32*(1), 87–94.

Zhao, Y. Q., Lau, K. T., Kim, J. K., et al. (2010). Nanodiamond/poly (lactic acid) nanocomposites: effect of nanodiamond on structure and properties of poly (lactic acid). *Composites Part B, 41*(8), 646–653.

3.08 Nanopolycrystalline Diamond without Binder and its Application to Various High-Pressure Apparatus

Tetsuo Irifune, Geodynamics Research Center, Ehime University, Matsuyama, Japan; Earth-Life Scinece Institute, Tokyo Institute of Technology, Tokyo, Japan
Hitoshi Sumiya, Electronics Materials R&D Laboratories, Sumitomo Electric Industries Ltd, Itami, Japan

Glossary

Belt-type apparatus A high-pressure apparatus used for materials synthesis up to 10 GPa, where a pair of pistons made of tungsten carbide is inserted in a tapered cylinder.

Diamond anvil cell (DAC) A high-pressure apparatus which can produce static pressures up to 400 GPa. A pair of single-crystal diamonds is generally used to pressurize a tiny sample of 10–100 μm in dimension.

Extended X-ray absorption fine structure (ESAFS) spectroscopy A powerful technique to study local structures around elements in any aggregated states, generally using synchrotron radiation as the X-ray source.

Hexagonal diamond A metastable high-pressure polymorph of carbon with a hexagonal crystallographic structure (named as lonsdaleite), which is found in some meteorites subjected shock compression upon impact on some planetary bodies.

Multianvil apparatus (MA) One of the most popular high-pressure apparatus used in high-pressure Earth and materials sciences. Several blocks made of hard materials, which are called as anvils, are used for high-pressure generation, operated in a hydraulic press. Cubic-press and Kawai-type multianvil apparatus (KMA) are in this category of static high-pressure apparatus.

Polycrystalline diamond A body of aggregated small grains of diamond, which is not suitable for gem but is useful for industrial tools because it is generally tougher than single-crystal diamond.

Pulsed laser Lasers operated in pulsed mode, where the optical power appears in pulses of short durations at some repetition rate.

3.08.1 Introduction

Most natural diamonds originated deep in the Earth's mantle, which were brought to the surface of the Earth in association with the eruption of kimberlitic magma during the Precambrian age (older than some 540 million years ago). Such diamonds are typically single crystals, whose very high hardness, thermal conductivity and refractive indices make this mineral highly useful for industrial applications, as well as

http://dx.doi.org/10.1016/B978-0-08-096527-7.00045-3

for jewels and ornaments. Since the first successful laboratory synthesis of single-crystal diamonds (e.g. Bundy, Hall, Strong, & Wentorf, 1955) in the 1950s, they have been produced on a commercial basis at pressures of 5–6 GPa and temperatures of 1800–2000 K with some catalysts/solvents, using large-volume presses (LVPs) such as the Belt-type apparatus or Cubic press (**Figure 1**). Even colorless single-crystal diamonds, with dimensions as large as 1 cm and of very high purity, can now be synthesized using some special techniques in the LVP (Sumiya, Toda, & Satoh, 2000; Chapter 3.09). Recent development of the high-speed chemical vapor deposition (CVD) technique also allows the synthesis of single crystals of a similar size, some of which are reported to become ultrahard (Yan et al., 2004) and highly transparent to a wide wavelength range of light (Meng, Yan, Lai, Kransnicki, Shu, et al., 2008) after annealing at high pressure.

On the other hand, polycrystalline diamonds with various microstructures, such as carbonado and ballas, have been reported. Although these polycrystalline diamonds are not gem quality since they contain various impurities along the grain boundaries, these diamonds are valuable for industrial applications because they tend to be tougher than single crystals. The origin of these natural polycrystalline diamonds has been a matter of debate: studies on inclusions and isotopic signatures of such diamonds suggest their carbon source originated from Earth's crustal material (e.g. Kirkley, Gurney, Otter, Hill, & Daniers, 1991), but various mechanisms of formation of the diamond, including deep subduction of the crust material (e.g. Kagi, Takahashi, Hidaka, & Masuda, 1994), meteorite impact (e.g. Smith & Dawson, 1985), and radiogenic fission (e.g. Daulton & Ozima, 1996; Ozima, Zashu, Tomura, & Matsushita, 1991), have been proposed. However, the puzzle as to which of these mechanisms is correct has not yet been solved. Furthermore, it has also been suggested that some carbonados are of deep-mantle origin, and crystallized directly from komatiite volatiles (Cartigny, 2010).

Synthesis of polycrystalline diamond at static high pressure has been attempted by both a flash heating method (e.g. Bundy, 1963; Wakatsuki, Ichinose, & Aoki, 1972) and directly passing electric current through a graphite rod (e.g. Higashi & Onodera, 1986; Naka, Horii, Takeda, & Hanawa, 1976) using LVPs. The laser-heated diamond anvil cell (LHDAC) was also used (Yusa, 2002; Yusa et al., 1998) for the direct conversion of graphite at high pressure and temperature. These studies demonstrated that cubic and/or hexagonal diamond was formed directly from graphite, but failed to produce sintered polycrystalline bodies made of pure cubic diamond grains. This failure was primarily due to the short heating durations in these high-pressure and high-temperature techniques. In fact, in these experiments, the maximum temperature under pressure was maintained only for a period of up to a few seconds. This is because graphite itself was used for the heating element, either as a heater or a laser absorber, and heating was terminated when the graphite partially transformed to diamond, as diamond is an electrical insulator and also does not absorb the laser efficiently.

On the other hand, synthesis of polycrystalline diamond by sintering diamond powders has also been tried at pressures below ~8 GPa, but has not been very successful because the extremely hard nature of diamond hinders sintering of diamond powders mainly due to the localized lower pressure regions that cause partial transformation of diamond to graphite (e.g. Bochechka, Romanko, Garvilova, Konoval, & Nazarchuk, 2007; Osipov, Nauyoks, Zerda, & Zaporozhets, 2009). Thus, various binders/catalysts, such as Co, Ni, $MgCO_3$, SiC, and so on, that fill intergrain pores in the compressed diamond powders and help binding between diamond grains have been introduced to synthesize sintered polycrystalline diamond (SD) (e.g. Akaishi, Yamaoka,

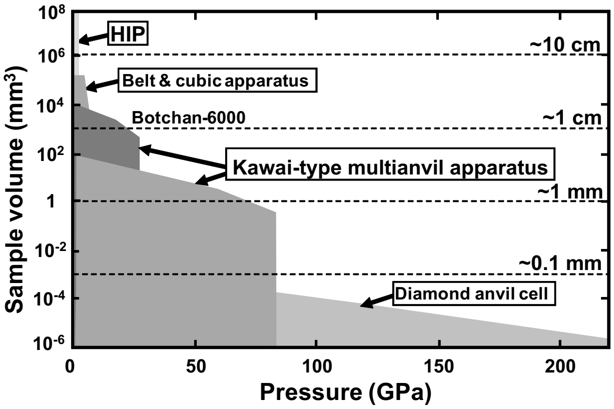

Figure 1 Pressures and volumes available in typical static high-pressure apparatus used for material synthesis. Typical dimensions of the sample are also shown for guidance. HIP, hot isostatic press.

Ueda, & Ohashi, 1996; Ohtaka, Shimono, Ohnishi, Fukui, Takebe, et al., 2004; Wentorf, DeVries, & Bundy, 1980), some of which are commercially available for industrial use. Furthermore, nanopolycrystalline diamond (NPD) was synthesized from a diamond powder of ~100 nm using $CaCO_3$ and other sintering agents (Akaishi, 2003). Nevertheless, a sintered body of pure polycrystalline diamond has not been made, and the hardness of those with various binders has been limited to up to about 70 GPa (Akaishi, 2003).

The successful synthesis of pure polycrystalline diamond at high pressure and temperature by direct conversion of graphite without any additional materials was first achieved using a Kawai-type multianvil apparatus (Irifune et al., 2004; Irifune, Kurio, Sakamoto, Inoue, & Sumiya, 2003; Irifune & Sumiya, 2004; Sumiya & Irifune, 2004). This polycrystalline diamond was made up of peculiar nanotextures and exhibited ultrahigh hardness, even harder than most gem-quality single-crystal diamonds. The progress in synthesis of the NPD, some physical properties of NPD, and its applications to various high-pressure apparatus are reviewed in this chapter. Future perspectives in synthesis of NPD with larger dimensions and higher quality, as well as their applications to high-pressure experimental studies, are also discussed. Although there have been a number of reports on new materials which claim to be harder than diamond, none of these materials have actually been used for industrial and scientific applications and the synthesis of some of these ultrahard materials is not reproducible. They are therefore not referred in this chapter except when they have some relevance to the NPD. Furthermore, it is not within the scope of this chapter to review the nature of polycrystalline diamonds produced by CVD methods as these diamonds generally contain hydrogen impurities or growth defects and also are not as hard as the NPD synthesized at high pressure and high temperature.

3.08.2 Synthesis of NPD Using Large-Volume KMA

KMA uses eight cubic tungsten carbide anvils with each edge being truncated to form a regular triangle shape on the corner (Kawai & Endo, 1970). An octahedral pressure medium, such as made of Co-doped semisintered magnesia, is placed in the middle of the assembled anvils. A furnace assembly—made of heater, electrode, thermal insulator, and capsule—is inserted into the pressure medium. Schematic illustrations of the KMA and an example of the furnace assembly are shown in Figure 2. Temperature is measured with a thermocouple, but in most synthesis runs a preestablished relationship between the temperature and input electric power is used

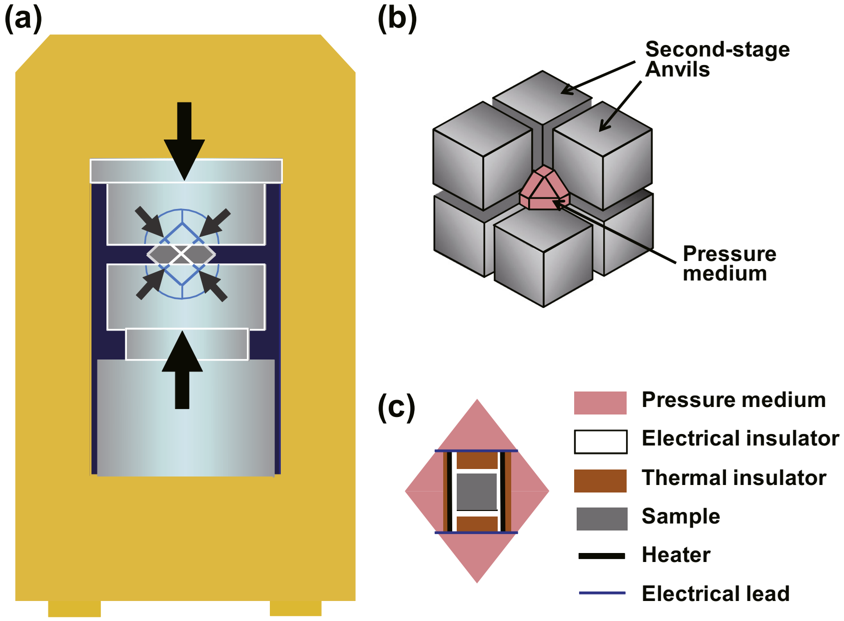

Figure 2 Schematic illustrations of KMA. (a) A large-volume press, in which the second-stage anvils are compressed with a uniaxial hydraulic ram. (b) Second-stage anvil cubes and the octahedral pressure medium. (c) A cross-section of a typical furnace assemblage used for synthesis of NPD.

for the temperature evaluation in order to fully utilize the available sample volume and to avoid complexities in the cell assemblage and in handling the cell parts.

Figure 3 shows the *P*–*T* conditions where the NPD with high optical transparency, made of almost pure cubic diamond, was formed within a run duration of ~10–20 min (Irifune et al., 2004). The lowest pressure so far confirmed for synthesis of NPD is ~12 GPa, although temperatures as high as 3000 K are required at these pressures (Isobe et al., 2010; Yusa, 2002). Since the stable generation of such high temperatures is quite difficult in KMA, NPD is normally synthesized at pressures near 15 GPa, where the temperature needed for the synthesis is substantially lower (~2600 K) than those at lower pressures. Although thus synthesized NPD is identified as cubic diamond based on X-ray diffraction, detailed transmission electron microscopy (TEM) observations demonstrates the presence of a small amount of hexagonal diamond in some samples, particularly in the regions made of lamellar fine structures, as shown later (Sumiya, Irifune, Kurio, Sakamoto, & Inoue, 2004). On the other hand, the coexistence of hexagonal diamond (and also compressed graphite in some cases) is observed by X-ray diffraction at lower temperatures (**Figure 3**).

Various forms of carbon, including fullerene, carbon nanotubes, glassy carbon, and amorphous carbon, have been used in addition to graphite as the starting material for synthesis of NPD (Guillou, Brunet, Irifune, Ohfuji, & Rouzaud, 2007; Sumiya, Yusa, Inoue, Ohfuji, & Irifune, 2006). It has been observed that all these non-graphitic carbons substantially reduce the temperature needed for synthesis of NPD and the NPDs obtained are made only of granular cubic nanodiamond without any lamellar textures. Hardness of the NPD made from the nongraphitic carbons is significantly lower (Hk = ~100 GPa; Sumiya & Irifune, 2007) than those synthesized from graphite (Hk = 130–145 GPa). Thus, polycrystalline graphite is used as the starting material to synthesize ultrahard NPD. In contrast, it is claimed that polycrystalline diamond of 5–20 nm with rod shapes (aggregated diamond nanorod (ADNR)) is formed from fullerene under the *P*–*T* conditions (20 GPa, 2500 K) similar to those for NPD synthesis, which was reported to be 0.2–0.4% denser than single-crystal diamond (Dubrovinskaia, Dubrovinsky, Langenhorst, Jacobsen, & Liebske, 2005). However, the ADNR has been shown to be substantially less hard (Hk = 105 GPa; Dubrovinskaia, Dub, & Dubrovinsky, 2006) compared to NPD.

The NPD samples reported in earlier studies were those with dimensions of about 1 mm in diameter and 0.5 mm in length, and exhibited a number of major cracks (e.g. Irifune et al., 2003). Efforts have since been made to synthesize larger samples with higher quality, using a conventional KMA operated in a press with a capacity of applying 1000–2000 tons, which resulted in a routine basis for synthesis of target value to yield 15 GPa, and the sample was heated to the target value (2600 K). The high-pressure and -temperature conditions were kept for about 20 min for the conversion from graphite to diamond. Then, the pressure was gradually released, keeping the appropriate temperatures depending on the pressure range so that the deviatoric stress acting on the sample was minimized during this process.

Recently, a new KMA was introduced with a 6000 ton RAM capacity (BOTCHAN-6000) at the Geodynamics Research Center, Ehime University (Irifune, 2010; Figures 1 and 4(a)), which is currently the largest KMA in the world. The cell assembly has been optimized for synthesis of larger NPD samples, using large second-stage tungsten carbide anvils with up to 75 mm edge lengths (c.f. 25–30 mm in conventional KMA). The maximum anvil truncation size so far tested is 22 mm (TEL = 22 mm), where an octahedral pressure medium

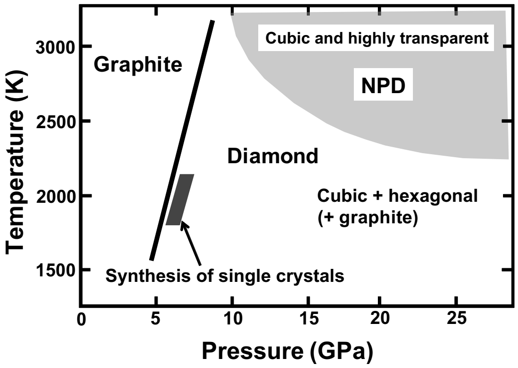

Figure 3 *P*–*T* phase boundary between graphite and diamond, and the region where NPD is synthesized by the direct conversion from graphite (after Irifune et al., 2004; Yusa, 2002; Isobe et al., 2010). Synthesis conditions of commercially available single crystals with catalysts/solvents are also shown by the shaded region.

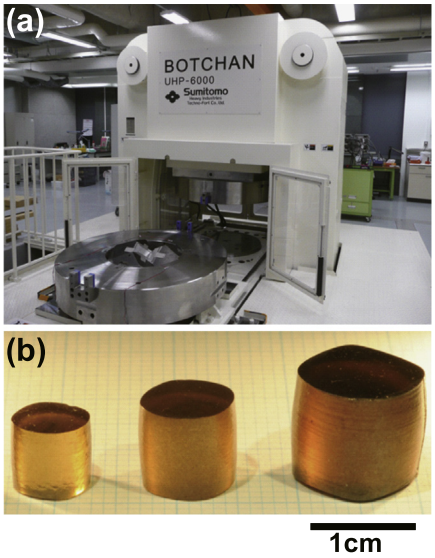

Figure 4 A 6000 ton KMA (BOTCHAN-6000) for synthesis of NPD at GRC, Ehime University (a), and some examples of the NPD rods (b) with dimensions up to about 1 cm produced with BOTCHAN.

with an edge length of 38 mm (OEL = 38 mm) was accommodated. Using the optimized furnace assembly for these large TEL and OEL, NPD rods of about 1 cm both in diameter and length (Figure 4(b)) at a press load of 4700 tons (Irifune, Isobe, & Shimei, 2013) have been synthesized.

3.08.3 Nature of NPD

3.08.3.1 Fine Textures

Figure 5 shows the TEM images of NPD synthesized by using a polycrystalline graphite rod of very high purity (99.9995%), where the coexistence of granular and lamellar textures is seen (Irifune et al., 2003; Sumiya et al., 2004). The granular grains are of cubic diamond, which are believed to be formed by a nucleation and growth mechanism without formation of hexagonal diamond. In contrast, the existence of a small amount of hexagonal diamond was sometimes noted in the latter portions with lamellar textures.

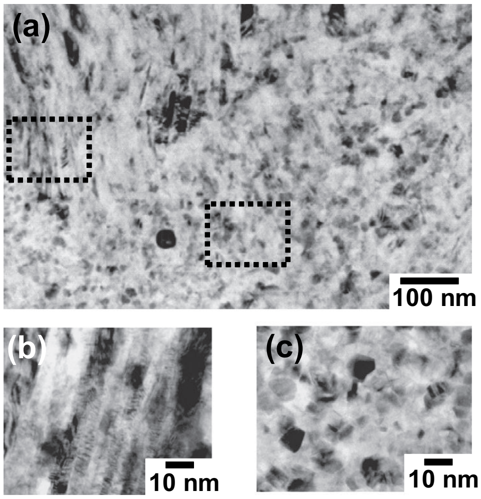

Figure 5 TEM images of the NPD sample synthesized at 18 GPa, 2800 K (after Irifune et al., 2003; Irifune et al., 2004). The lamellar (b) and granular (c) textures coexist in some areas of the sample (a), as indicated by the dotted squares.

Electron diffraction measurements show that the lamellar cubic diamond grains are topotaxially formed from hexagonal diamond, suggesting that the cubic diamond is formed via a two-step martensitic transition from graphite in such regions: first from graphite to hexagonal diamond with a directional relationship of (100) of hexagonal diamond being parallel to (001) graphite, followed by the transition keeping the mutual orientation of (100) of hexagonal and (111) of cubic diamonds parallel (Sumiya et al., 2004). Other modes of the martensitic transition from hexagonal to cubic diamonds have also been suggested (Ohfuji, Okimoto, Kunimoto, et al., 2012).

The grain size of NPD is independent on the reaction time since for the heating durations from 10 to 10^4 s at 2600 K, at 18 GPa, no notable grain growth of diamond (Sumiya et al., 2004) was observed. As NPD is formed at pressures far higher than the equilibrium boundary between graphite and diamond (~5 GPa), the rapid formation of an enormous amount of diamond crystallites may mutually suppress their crystal growth. Slight grain growth was also observed with increasing temperature up to ~2900 K at this pressure, where growth of diamond up to 200 nm was observed in 10 min (Sumiya et al., 2004).

On the other hand, the grain size of NPD largely depends on the nature of the graphite starting material, particularly on the size and homogeneity of the graphite crystals (Ohfuiji et al., in press). Thus, grain growth of diamond up to a few hundred nanometers is observed even near the lower temperature boundary (e.g. 2600 K, 15 GPa; **Figure 3**) for the formation of NPD when some other graphite rods supplied by different manufacturers are used as a starting material.

3.08.3.2 Hardness and Toughness

Although diamond is known to be the hardest material, the hardness of single-crystal diamond varies significantly depending on the crystallographic planes and directions (e.g. Brookes & Brookes, 1991). Hardness of diamond is generally evaluated by measuring the size of the indentation made with a Knoop indenter, but careful measurements are required, taking into account issues such as the condition of the indenter, dependency of the applied load, and the existence of microcracks. Depending on the planes and directions (**Figure 6**), some of the NPDs had Knoop hardness of 130–145 GPa (Irifune et al., 2003; Sumiya & Irifune, 2004) which are harder than normal gem-quality diamonds with hardness of 60–130 GPa (Brookes & Brookes, 1991; Sumiya, Toda, & Satoh, 1997).

It has been reported that (001)⟨110⟩ of synthetic IIa-type single-crystal diamond possesses a Knoop hardness of >140 GPa, but the hardness of some other planes/directions of this diamond is lower than 100 GPa (Sumiya et al., 1997). In contrast, the hardness of NPD has no such orientation/plane dependency as it is a homogeneous polycrystalline material without any notable preferred orientation of the constituent diamond grains. Thus, NPD may be referred to as the hardest diamond and accordingly the hardest bulk material ever synthesized.

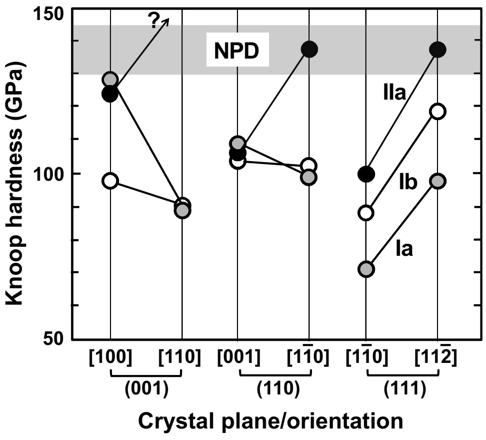

Figure 6 Knoop hardness of some single-crystal diamonds (Ia, natural Ia-type; Ib, synthetic Ib-type; IIa, synthetic high-purity IIa-type) on different crystallographic planes and directions, compared to the hardness of NPD (shadow region). Ia, natural Ia; Ib, synthetic Ib; IIa synthetic high purity IIa (after Sumiya & Irifune, 2004).

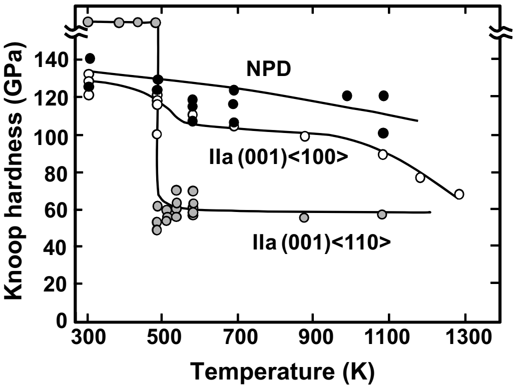

Figure 7 Knoop hardness changes in NPD (solid line), and (001)⟨100⟩ (dotted line) and (001)⟨110⟩ of synthetic pure IIa single-crystal diamond (after Sumiya et al., 2010) as a function of temperature.

Furthermore, it has been demonstrated that the hardness of NPD is maintained even at high temperatures (Sumiya, Harano, Sato, & Kukino, 2010), as illustrated in **Figure 7**. Although the (001)⟨110⟩ of the synthetic IIa single crystal exhibits very high Knoop hardness of over 140 GPa, the hardness suddenly drops to about 60 GPa at temperatures around 500 K, while the hardness of NPD remains stable above 100 GPa even at temperatures as high as ~1100 K. This is due to activation of some slip systems in the single-crystal diamond at high temperature (Sumiya, 2006), while such deformation within the grain is effectively blocked in the polycrystals.

The reason for the exceptionally high hardness of NPD has been a matter of discussion. It has been shown that some metals with grains in the submicron regime tend to be harder with decreasing grain size and reach maximum hardness up to 10 nm, as the propagation of dislocations/microfractures is effectively blocked by the grain boundaries (the Hall–Petch effect; Hall, 1951; Petch, 1953). The hardness is supposed to decrease with further decreasing grain size from such a critical size, as the grain boundary sliding would become a more effective mechanism for plastic deformation (the revered Hall–Petch effect; Chokshi, Rosen, Karch, & Gleiter, 1989; Schlotz, Di Tolla, & Jcobsen, 1998). Thus, the ultrahard nature of NPD may be explained by the grain-size effect as typical PND possesses diamond grains ~10–20 nm in length.

Alternatively, the peculiar textural features of NPD may be related to its hardness. The existence of lamellar regions in fine matrices has been shown to enhance the mechanical strength of some hard ceramics due to the effective blocking of crack propagation. In fact, blocking of cracks by the lamellar diamond crystals is clearly shown by a TEM observation of the NPD sample used for the indentation test (Sumiya & Irifune, 2007).

On the other hand, a recent theoretical study based on ab initio calculations suggested that hexagonal diamond is harder than cubic diamond (Pan, Sun, Zhang, & Chen, 2009). This prediction was made to account for experimental results that suggest wurtzite-type BN, which is analogous to hexagonal diamond, is harder than cubic BN possessing the same crystal structure as cubic diamond (Dubrovinskaia et al., 2007). Nevertheless, further study is necessary to prove this hypothesis of the ultrahard nature of hexagonal diamond, which is difficult to retrieve at ambient pressure as a single phase and the measurement of its hardness has never been made.

The transverse rupture strength (TRS) of NPD is around 3 GPa (Sumiya, & Harano, 2012), which is even higher than that of SD (generally ~2 GPa) with Co and other binders, and is similar to those of tungsten carbides of the hardest grade (**Table 1**). This is quite different from the general trend of hard materials that show a negative correlation between their hardness and TRS. The relatively high toughness of NPD, in addition to its ultrahard nature, may be at least partly due to the presence of its peculiar lamellar texture, as discussed above. Thus, NPD should be an ideal material for anvils for high-pressure apparatus, particularly those for higher pressure generation.

3.08.3.3 Elastic Properties

In general, harder materials have higher elastic stiffness. As single-crystal diamond has a cubic crystallographic symmetry, three independent elastic constants, i.e. C_{11}, C_{12}, and C_{44}, have been determined by measuring

Table 1 A comparison of some key physical properties of diamond-related materials and tungsten carbides

Material	*Knoop hardness (GPa)*	*Transverse rupture strength (GPa)*	*Young's modulus (GPa)*	*Thermal conductivity (W/mK)*
NPD	135	3	1170	300
SCD[a]	60–130	1–2	1140	800–2000
SD[b]	50–70	1–3	850–950	200–400
WC[b]	15–25	2–5	450–650	25–100

[a] *Knoop hardnesses of some of the planes/directions are higher than this limit in synthetic pure IIa single-crystal diamond. The value for Young's modulus is based on McSkimin and Bond (1957). The variations in thermal conductivity are due to different types of single crystals with different impurities.*

[b] *The variations of the values for SD and WC are due to those from different products/companies (e.g.: http://www.fujidie.co.jp/e/seihin/taimamou/material/ultra_hard.htm; http://www.ancodiamond.com/tripie.htm#phy).*

The uncertainty of each value is up to about 10%, depending on the methods and quality of the measurements. Other data source: Brookes and Brookes (1991); Irifune et al. (2003); Sumiya and Irifune (2004); Sumiya et al. (1997); McSkimin and Bond (1957); Kono, Nakamoto, Irifune (2010).

sound velocities of diamond using ultrasonic pulse-echo or Brillouin scattering techniques (e.g. McSkimin & Bond, 1957; Zouboulis, Grimsditch, Ramdas, & Rodriguez, 1998). By adopting some averaging schemes, such as Voigt and Reuss averages (e.g. Hill, 1952), and using density of diamond, one can derive a set of two independent elastic moduli (e.g. bulk modulus, K, and shear modulus, G) of homogeneous polycrystalline materials. Young's modulus (E) is calculated from these moduli, which is defined as the ratio of the uniaxial stress over the uniaxial strain in the elastic deformation regime, and often used as a measure of the stiffness of bulk materials. The E values of diamonds so far obtained based on sound-velocity measurements are rather scattered, but are in the range of 1100–1200 GPa.

Sound velocities of NPD measured by ultrasonic pulse-echo methods with independent techniques yielded the mutually consistent values of Young's modulus $E = 1163$ GPa (Kono et al., 2010) and 1140 GPa (Chang, Jacabsen, Kimura, Irifune, & Ohna, 2013), which are close to those predicted based on the elastic moduli of single-crystal diamond. In contrast, the averaged Young's modulus for ADNR is reported to be $E = 1070$ GPa, with a large scattering of values from 600 to 1270 GPa (Dubrovinskaia et al., 2006; Richter, Smith, Dubrovinskaia, & McGee, 2006), while Young's moduli of polycrystalline nanodiamonds obtained by sintering nanosize diamond powders and direct conversion of graphite with a quite short (~30 s) reaction time are reported to be $E = 457$–528 GPa (Osipov et al., 2009) and $E = 707$ GPa (Couvy, Lahiri, Chen, Agarwal, & Sen, 2011), respectively. Thus, NPD certainly has the highest Young's modulus among those observed for the polycrystalline nanodiamond materials.

Figure 8 shows a comparison of Young's moduli of NPD and SDs with Co binders as a function of Co content (Kono et al., 2010). Although SDs are the hardest commercially available materials so far, their Young's moduli, generally ranging from ~850 to ~950 GPa (**Table 1**; **Figure 8**), are substantially lower than that of NPD. It has been reported that pressures approaching the Mbar regime have been realized using SDs as second-stage anvils for KMA (e.g. Ito, 2007; Tange, Irifune, & Funakoshi, 2008). As these pressures are achieved under the elastic deformation regimes of SD anvils, NPD should have the potential to produce far higher pressures in this apparatus because of its exceptionally high elastic stiffness.

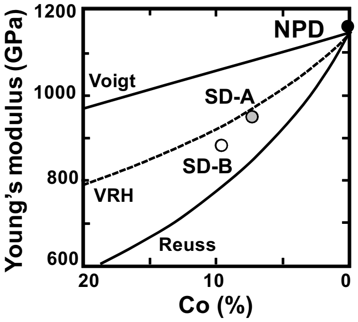

Figure 8 Young's moduli of NPD and SDs with different Co contents (SD-A and SD-B; after Kono et al., 2010). Voigt and Reuss are the results of the calculated averaged values using the elasticity data on diamond and cobalt based on the standard averaging schemes. VRH is the Hill average of the values based on the Voigt and Reuss scheme.

Temperature dependencies of the bulk and shear moduli of NPD are quite small, being $dK/dT = -0.0030$ GPa K^{-1} and $dG/dT = -0.0048$ GPa K^{-1}, respectively (Chang, Jacobsen, Kimura, Irifune, Ohno, 2013), which is consistent with the small temperature dependency of the elastic moduli of single-crystal diamond measured with a Brillouin scattering technique (Zouboulis et al., 1998). The absolute values of these temperature derivatives are almost one order of magnitude lower than those of major high-pressure minerals, which are generally in the ranges of $-0.02 \sim -0.03$ and $-001 \sim -0.03$ GPa K^{-1}, respectively. The very small temperature dependency of the elastic moduli of NPD is also consistent with the observation that the Knoop hardness of NPD does not drop significantly with increasing temperature (**Figure 7**), and is feasible in the application of this material to high-pressure anvils and industrial machining tools.

3.08.3.4 Optical and Other Spectroscopic Signatures

NPD is highly transparent to optical lights, showing yellowish brown in color (**Figure 4(b)**). **Figure 9(a)** shows the transmittance of lights in an ultraviolet–far-red region for various diamonds with a thickness of 1 mm (Sumiya et al., 2009). One of the characteristics of the optical transmittance in NPD is the presence of a continuous absorption in the visible light region, similar to that of natural IIa diamond. The continuous absorption in the latter single crystal is believed to be due to the presence of a number of defects/dislocations (e.g. Hounsome et al., 2006), while that in NPD may be related to the numerous grain boundaries with larger dimensions present in this polycrystalline material, being rather dark in color.

On the other hand, the sharp decrease in the transmittance of NPD below about 500 nm is caused by the absorption due to the electron transition from A color center to the conduction band, as is the case for natural Ia-type diamond. The characteristic absorption due to the presence of an isolated form of nitrogen around 500 nm is not confirmed in NPD, in contrast to Ib-type synthetic diamond, although secondary ion mass spectrometry analyses revealed that NPD contains 50–100 ppm nitrogen atoms. This suggests that the nitrogen in NPD is distributed in aggregated forms. In fact, photoluminescence measurements demonstrate the presence of N_3 and H_3 color centers, indicative of the aggregated forms of nitrogen in NPD (Sumiya et al., 2009).

Figure 9(b) shows the corresponding IR spectra for the diamonds shown in **Figure 9(a)**. NPD has absorption bands in a range around 1750–2750 cm^{-1} due to multiphonon absorption similar to those of single-crystal diamonds. The absorption band near 1220 cm^{-1} may be attributed to that of a small amount of 6H-type hexagonal diamond (Wu, 2007), which is diminished in the NPD sample where the conversion to cubic diamond is completed at higher temperatures. The fact that the absence of the absorption band near 1130 cm^{-1}, which is characteristic of the isolated form of nitrogen seen in natural Ia-type diamond, also confirms that the nitrogen in NPD is in aggregated forms (Sumiya et al., 2009). As the starting graphite contains virtually no nitrogen, the small amount of nitrogen found in NPD might originate from the air present in the pores/grain boundaries of the graphite polycrystals.

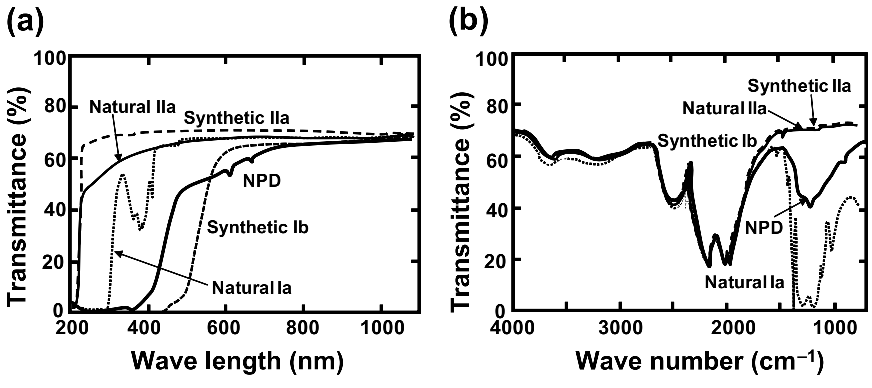

Figure 9 Optical and IR spectra of NPD (after Sumiya et al., 2009). (a) Transmittance of the light around the ultraviolet–visible regions for some synthetic and natural single crystals and for NPD. (b) The corresponding transmittance of the various diamonds in the infrared regions.

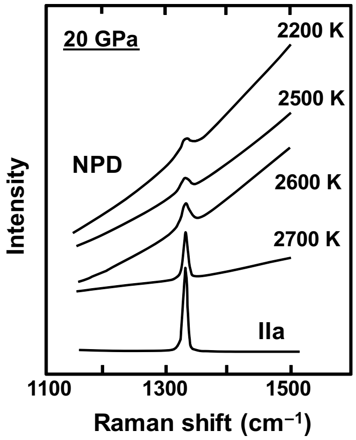

Figure 10 Examples of the T_{2g} mode of Raman spectra for NPDs synthesized at various temperatures at 20 GPa and for IIa-type single-crystal diamond.

Figure 10 shows the typical Raman peak (T_{2g} mode) of NPD compared to that of single-crystal diamond. The position of the peak is at 1332 cm^{-1}, which is virtually the same as that of single-crystal diamond. However, as the peak is generally quite broad and the background is very high, the S/N ratio of NPD is small and the peak is sometimes difficult to identify. The intensity and the full width at half maximum of the Raman peak of NPD depend largely on the grain size of NPD, consistent with some earlier studies on diamond powders (Namba, Heidarpour, & Nakayama, 1992; Yoshikawa et al., 1993). Actually, those of the NPD samples synthesized at the highest temperature of ~2700 K are relatively sharp (**Figure 10**), where the grain grew to 100–200 nm. In contrast with these earlier studies, no systematic change in the Raman peak position has been observed in NPD within the uncertainty of the measurement (~±0.5 cm^{-1}).

3.08.3.5 Other Features and Machining Efficiency

Diamond is known to have the highest thermal conductivity. NPD, however, is found to have a thermal conductivity lower than those of single-crystal diamond by a factor of five orders of magnitude (**Table 1**; Odake et al., 2009). This is presumably caused by strong grain-boundary phonon scattering, as is shown for polycrystalline materials with grain sizes smaller than 100 nm (Morelli, Beetz, & Perry, 1988). Thus, NPD may be inadequate as a device for a heat sink, but is suitable for anvil materials for high-pressure and -temperature experiments, because the lower thermal conductivity should contribute to keep the temperature of the sample higher than those using single-crystal anvils with higher thermal conductivities.

As NPD is extremely hard, it is quite difficult to process it with the conventional polishing method using diamond powders. In fact, it takes about one order of magnitude longer duration to polish NPD as compared to those for single crystals, which is not practical to fabricate industrial tools and anvils for high-pressure apparatus. This hinders application of NPD to these purposes, in spite of its outstanding nature as an ultrahard material.

Introduction of nano- to femtosecond pulsed lasers is found to yield satisfactory machining results of NPD (**Figure 11(a) and (b)** Odake et al., 2009; Okuchi et al., 2009). It is demonstrated that NPD can be processed even more efficiently compared to single-crystal diamond. This is primarily due to the relatively low thermal conductivity of NPD as the heat generated by the laser beam is concentrated at the cutting front, which effectively accelerates the graphitization, melting, and evaporation processes. As a result, the grooves formed in NPD by laser cutting are both sharper and deeper than those formed in single crystals (**Figure 11(c)**). It was also observed that the resultant surface of the groove by the pulsed laser, covered by a graphite layer a few hundred nanometers thick, is very smooth and intact (**Figure 11(d)**). Thus, the use of the pulsed laser for machining of NPD, combined with an adequate computer-controlled stage, has made it possible to fabricate NPD anvils and other tools with arbitrary shapes (**Figure 11**). Further detailed discussion on the mechanism of the laser cutting of NPD is given in Ohfuji, Okuchi, et al. (2010).

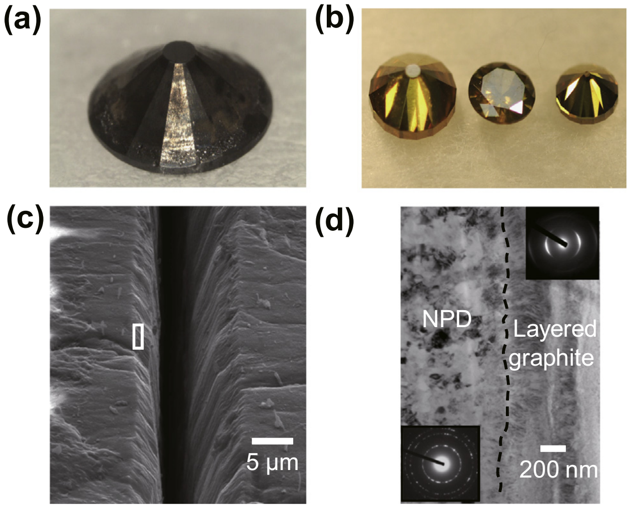

Figure 11 Examples of pulsed laser-processed NPD (a, b), an SEM image near the groove cut with the laser (c), and a TEM image of the NPD near the groove (square area of (c)). The latter SEM and TEM images are from Odake et al. (2009).

3.08.4 Application to High-Pressure Studies

3.08.4.1 High-Pressure Generation in DAC

Figure 12 shows a relationship between the Knoop hardness of typical anvil materials and the attainable pressures (Ito, 2007). It is predicted that the NPD anvils may have potential to reach pressures in the terapascal regime, if its hardness is fully utilized and the relation shown in Figure 12 is applicable to these regions. Thus, attempts have been made to generate higher pressures using the DAC, replacing a pair of single-crystal diamond anvils by those made of NPD.

Figure 13 depicts the results of high-pressure generation using the NPD anvils, which are compared with those using ultrahard synthetic IIa diamond according to Nakamoto et al. (2007). A beveled anvil top with a diameter of 30 μm is adopted, and the deformation of the anvil top is monitored using an in situ X-ray imaging technique (Figure 13(a)). Figure 13(b) shows the efficiency of pressure generation as a function of applied load monitored by the piston stroke to pressurize the sample. The pressure generation efficiency with NPD anvils is slightly better than or similar to that using IIa anvils with an anvil top of the hardest (111) plane. The deformation of the anvil top of NPD is also slightly smaller than or similar to that of the IIa anvil as seen in Figure 13(a).

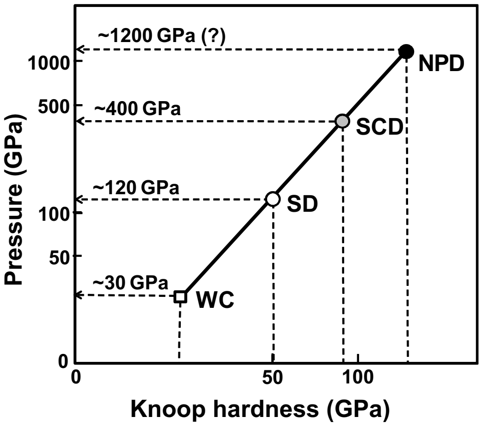

Figure 12 A prediction of the pressure limits in static high-pressure apparatus using various anvil materials based on an empirical pressure–hardness relationship (after Ito, 2007).

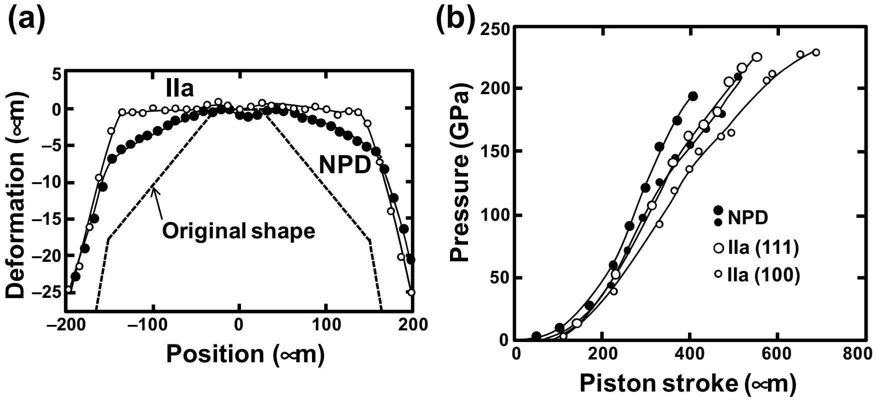

Figure 13 (a) Deformation of NPD ($P = 193$ GPa) and hard single-crystal IIa ($P = 233$ GPa) anvils around 200 GPa (after Nakamoto et al., 2007). Original shape of the anvil is shown by the dashed line. (b) Pressure generation in the DAC with NPD (solid circles) and IIa (open circles) anvils. The culet surfaces of the latter anvils are (111) (large open circles) and (100) (small open circles) planes of the single-crystal diamond.

The pressures achieved by using NPD anvils (200–210 GPa) are, however, significantly lower than those produced with IIa single-crystal anvils (~230 GPa). The highest pressure reported in the DAC using NPD anvils has also been limited to about 250 GPa to date (Nakamoto, Sakata, Sumiya, et al., 2011), in spite of the prediction based on the relation shown in **Figure 12**, mainly because of the occurrence of anvil failure under these pressures. This may be partly because the NPD used for these DAC experiments possess a relatively large grain size of 100–200 nm, due to the use of different starting material with higher purity for its synthesis. The larger grain size might have yielded a lower hardness in such NPD anvils relative to those with smaller sizes reported earlier (Irifune et al., 2003; Sumiya et al., 2004). Furthermore, possible stress concentrations and the resultant minor defects at the grain boundaries after laser machining and the subsequent polishing should also have initiated the development of minor cracks in the NPD anvils, which may also be related to the strength of the intergranular cohesion of diamond grains upon the high-pressure and high-temperature synthesis. On the other hand, it is noted that even if the occurrence of cracks hinders further compression in the NPD–DAC, the pressure drop due to such an anvil failure is significantly lower than the case for using single-crystal anvils, which normally break into pieces, yielding substantial pressure drop. This should be due to the superior toughness of NPD relative to single-crystal diamond.

In contrast, the ultrahard and tough nature of NPD has been found to produce significantly higher pressure when using the DAC with relatively a large anvil culet when compared to single-crystal diamond anvils (Nakamoto, Sakata, Sumiya, et al., 2011). For instance, by using NPD anvils with a culet of 300 μm in diameter, pressures as high as 140 GPa were achieved while the pressures reached using single-crystal diamond anvils are generally limited to about 90 GPa (**Figure 14**). Similarly, pressures up to 120 GPa are produced with NPD anvils of either a 400- or 500-μm culet, while pressures achieved using the single-crystal anvils with the same dimensions are generally lower than 60 GPa. Thus, the DAC with NPD anvils yields pressures nearly twice as high as those available with single-crystal anvils demonstrating great potential for NPD anvils at higher pressures and larger sample volumes in the DAC.

3.08.4.2 Laser Heating and Other Studies Using the DAC

Although a wide range of wavelengths, particularly those in the ultraviolet and part of the visible light spectrum, are substantially absorbed by NPD, the transmittance of light near 1 μm in wavelength is similar to those of other single-crystal diamonds. This has lead to successful heating of the sample in the DAC using a yttrium aluminum garnet (YAG) laser, which typically emits light with a wavelength of 1064 nm in the infrared region. The lower thermal conductivity of NPD relative to those of single crystals may contribute to efficient heating of the sample at very high pressure, as the loss of heat becomes more significant at higher pressures where the sample becomes thinner and comes into close contact with a pair of diamond anvils.

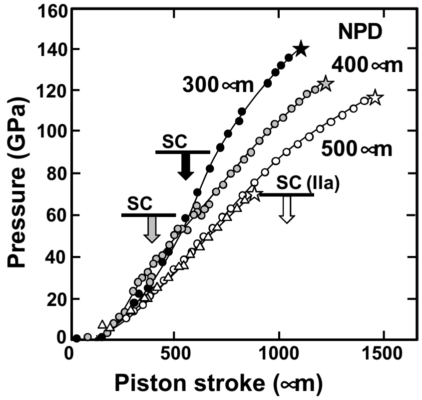

Figure 14 Comparison of pressure generation in the DAC using NPD and single-crystal diamond anvils with various culet sizes (after Nakamoto, Sakata, Sumiya, et al., 2011). The single crystals used for the culet size of 500 μm are made of very hard synthetic IIa-type diamond, while those for 300 and 400 μm are taken from literature. The star symbols show the pressures where the anvil failure occurred.

LHDAC experiments were made at pressures up to 170 GPa using double-sided heating with a YAG laser (Ohfuji, Okada, Yagi, Sumiya, & Irifune, 2010), which demonstrated that heating up to about 5000 K is possible using NPD anvils with a culet of 300 μm. Moreover, higher efficiency in heating using NPD anvils relative to the heating efficiency with single-crystal anvils was confirmed, presumably because of the lower thermal conductivity of NPD. Temperature can be determined by the conventional method using thermal radiation emitted from the sample, but the pressure determinations using the ruby fluorescence method and/or Raman shifts of diamond are quite difficult because of the low transmittance of visible light and the high fluorescence of NPD.

In situ X-ray observations at high pressure and temperature have been made using a combination of synchrotron radiation and LHDAC with NPD anvils (Ohfuji, Okada, et al., 2010). As the NPD anvil yields strong powder diffractions, it is difficult to resolve the diffraction peaks when those from the sample overlap. Nevertheless, as the number of the diffraction peaks is very limited for the diamond structure with cubic symmetry, and such overlapping of the diffraction peaks generally would not cause serious problems in identifying the phases. Moreover, such diffraction peaks of diamond can be easily subtracted using available software.

The disadvantage of NPD anvils in X-ray diffraction measurements relative to single-crystal anvils turns out to be rather advantage in some high-pressure extended X-ray absorption fine structure (EXAFS) measurements (Baldini et al., 2011; Kawamura, Ishimatsu, & Maruyama, 2010; Matsumoto, Maruyama, Ishimatsu, et al., 2011). Single-crystal diamond in a DAC causes discontinuous X-ray absorption when the Bragg's reflection rule is met, causing an artificial jump (glitch) in the absorption spectra (**Figure 15**). Therefore, it is difficult to perform an accurate and sophisticate analyses of the EXAFS profiles. As the polycrystalline nature of NPD causes no such jump in the X-ray absorption spectra, glitch-free spectra have been obtained, which makes subsequent

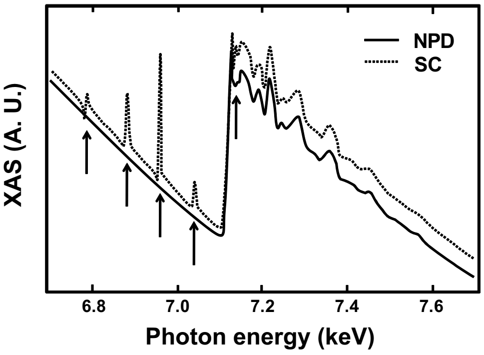

Figure 15 An example of a glitch-free X-ray absorption spectrum (XAS) as a function of photon energy obtained for the sample in DAC with NPD anvils (solid curve) after Kawamura et al. (2010). The corresponding spectrum with single-crystal (SC) diamond anvils is also shown for comparison (dotted curve).

analytical procedures much easier and more reliable. Thus, the use of NPD for high-pressure EXAFS studies is expected to open new windows to the studies of magnetic properties (Kawamura et al., 2010; Matsumoto, Maruyama, Ishimatsu, et al., 2011) and structures of amorphous compounds (Baldini et al., 2011) under pressure.

3.08.4.3 Multianvil Devices

The first application of NPD to the multianvil apparatus was made in the 6–8–2 multianvil system (Endo & Ito, 1982), using NPD as the third-stage anvils (Kunimoto & Irifune, 2010). A pair of third-stage NPD anvils is placed in an octahedral pressure medium of a Kawai-type apparatus (or 6–8 multianvil apparatus), by which the sample was compressed and subjected to high pressures. The sample was heated with a tube heater and temperature was measured using a thermocouple, while pressure was evaluated by the unit-cell volume of some pressure reference materials, such as gold and NaCl, using in situ X-ray diffraction and adequate equations of state of these materials.

In order to compare the performance of various diamond anvils, a pressure generation test was carried out using the third-stage anvils made of SD with Co binder, Ib-type single-crystal diamond, and NPD. **Figure 16** shows the results of such a performance test. No significant difference in pressure generation efficiency was observed with these three types of anvils at pressures up to ~80 GPa at 300 K (**Figure 16(a)**). In this pressure range, a slight difference in the sizes of anvils and of the various parts constituting the cell assemblage may have larger influences on the efficiency than the difference in hardness of the anvils.

In contrast, a significant difference was observed upon increasing temperature at a fixed press load: pressures in the sample using both SD and single-crystal anvils substantially dropped at about 800 K, while pressure was maintained at higher temperatures above 1200 K using NPD anvils (**Figure 16(b)**). The pressure drop in the 6–8–2 system using single-crystal anvils is rather sharp compared to other results. This may be due to the activation of the slip system (111)⟨110⟩ of single-crystal diamond (Brookes, Howes, & Parry, 1988), which is responsible for the significant plastic deformation of the anvil top surface. On the other hand, the commencement of the pressure drop in the sample using SD anvils should be related to the softening of the Co binder, but the pressure decreases rather gradually with increasing temperature compared to those in single-crystal anvils. When the temperature was decreased from the maximum temperature of ~1400 K, where the pressures were around 30 GPa, by terminating the electric power supply, the pressures slightly decreased to about 25 GPa at room temperature in both cases with SD and single-crystal anvils.

For the 6–8–2 system using NPD anvils, the pressure remained virtually constant or even slightly increased with increasing temperature above the critical temperature of ~800 K. This slight increase of pressure may be due to the enhancement of the forward movement of the third-stage NPD anvils during heating under a constant press load, in addition to the ultrahard nature of NPD. Then, commencement of the pressure drop was noted at a temperature around 1200 K, followed by a gradual decrease of pressure similar to that observed in the runs with SD anvils. Pressures as high as ~60 GPa were maintained even near the highest temperature of ~1400 K, which did not change significantly upon quenching (**Figure 16(b)**).

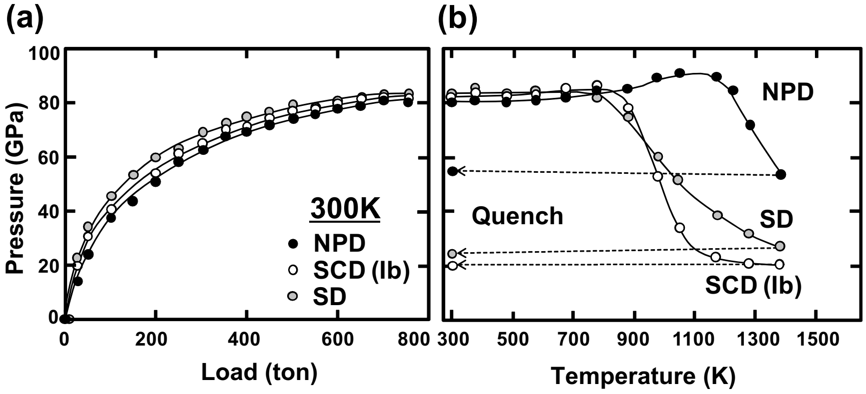

Figure 16 Performance of various diamond anvils used for the third-stage anvils of the 6–8–2 multianvil system. (a) Generated pressures at room temperature as a function of press load. (b) The variations of pressure with increasing temperature with a fixed press load (800 ton). The pressure values immediately after quenching are shown with arrows.

Scanning electron microscope (SEM) and microscope observations demonstrated that the top surfaces of both SD and single-crystal anvils deformed to form a crater-like shape with depressions of the central regions by about 30–40 μm, while such a depression of <15 μm was noted in the NPD anvils. SEM observations on the single crystal showed that the deformation was caused by square stepwise depressions, indicating operation of the slip system (111)⟨110⟩, which should have caused a rather sudden drop of pressure upon increasing temperature. The small plastic deformation in NPD anvil is consistent with the observation that the Knoop hardness of NPD does not largely decrease with increasing temperature. Thus, the NPD may be used for anvils in various types of high-pressure apparatus, including the DAC with external heating.

3.08.5 Future Perspectives

Apart from industrial applications, the use of NPD as anvils for high-pressure apparatus is an important subject for this novel material. In spite of its apparent ultrahard nature, the pressures available in the DAC have been limited to ~250 GPa. This may be partly due to the relatively large grain size and the lower proportion of lamellar textures of currently produced NPD anvils relative to those of the earlier studies. The microstructure of the graphite starting material yields NPD with a different grain size and microstructures (Ohfuji, Okimoto, Kunimoto, 2012), and the use of adequate starting material may result in harder NPD suitable for anvils toward higher pressure generation. In any case, controlling the grain size and the texture may be an important issue in full application of NPD to the DAC for higher pressure generation.

The other issue to be solved in application of NPD to DAC experiments is to reduce its absorption of visible light for optical measurements through the anvil. One possible reason for such absorption is the presence of a small amount (~100 ppm) of nitrogen in NPD. As the starting graphite contains only a very limited amount of nitrogen (<5 ppm), most of the nitrogen in NPD may originate from the air that resides in the pores and grain boundaries of the relatively loose aggregate of polycrystalline graphite. Thus, removal of the air in the starting graphite may result in the reduction of the characteristic yellowish color of NPD, although the continuous absorption of visible light due to the presence of numerous grain boundaries may be unavoidable.

As for the applications to multianvil apparatus, the 6–8–2 system using NPD anvils yielded the highest pressure of 115 GPa at temperatures up to 1300 K (Kunimoto & Irifune, 2010). However, the sample dimensions available for this apparatus are quite small (typically ~0.3 mm in diameter and ~0.1 mm in length upon compression) compared to those in conventional multianvil apparatus, and the achievable temperature has been limited to ~1500–1600 K. Although the sample volume is still larger than those available in the DAC and stable temperatures can be maintained for a certain period of time (>1 h), some of the advantages in multianvil apparatus over the DAC, such as the reproducibility of temperature/pressure generation against the applied load, homogeneities of temperature and pressure distribution within the sample, and usability of adequate capsule materials, are sacrificed in the 6–8–2 MA. Thus, this system should be regarded as a modified version of the DAC rather than a kind of MA. It should also be noted that the use of synchrotron in situ X-ray measurement is needed to evaluate the produced pressures in this system.

One of the promising applications of NPD to the multianvil apparatus is to use it as the second-stage anvils for the MA6–6 system, which was recently invented and used for experiments up to 25 GPa using the D-DIA-type cubic press and tungsten carbide second-stage anvils (Kawazoe, Nishiyama, Nishihara, & Irifune, 2010; Nishiyama, Wang, Sanehira, Irifune, & Rivers, 2008). The MA6–6 system uses second-stage six anvils that were assembled in a guide cage and compressed in the cubic press. This system has great advantages in operating small second-stage anvils, keeping excellent alignment of these anvils, which is ideal in the application of NPD anvils with limited dimensions to multianvil apparatus. Pressure generation with the MA6–6 system using NPD anvils is currently being tested (**Figure 17**). Optical measurements of the sample temperature and pressure may be achieved via the highly transparent NPD anvils by using optical radiation spectra and ruby fluorescence spectra, respectively, which are used to cross-check the temperature and pressure determined by conventional methods using thermocouples and in situ X-ray observations in the multianvil apparatus.

NPD may also be used as the second-stage anvils for the Kawai-type MA6–8 system although the maximum size of the NPD cube has been limited to 6–7 mm in edge length. When the first-stage anvil is made of tungsten carbide, the press load applicable to the second-stage anvils with such dimensions should

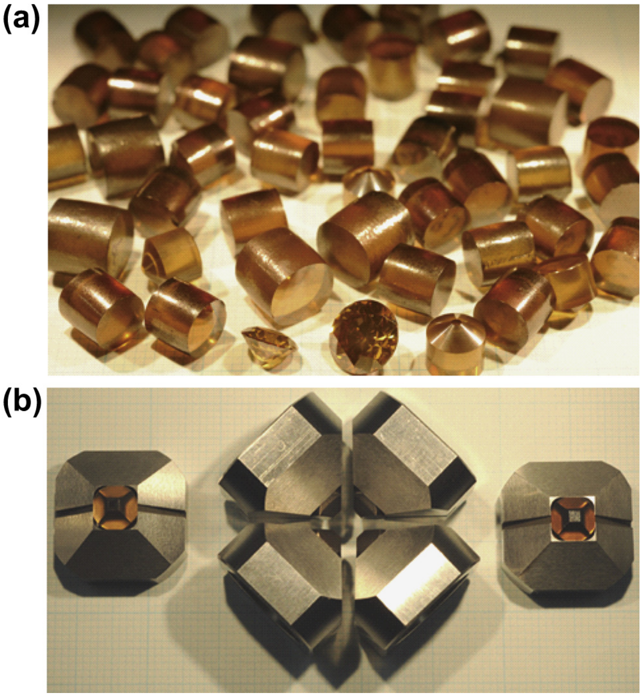

Figure 17 Some NPD samples produced with BOTCHAN-6000 (a) and those used for anvils for the 6–6 compression system (b).

be limited to 200–300 tons, considering the compressional strength of the first-stage tungsten carbide anvils. Pressures as high as 50–60 GPa can be produced by using SD second-stage anvils at these press loads, those exceeding 100 GPa are expected to be attainable with harder NPD anvils at these press loads. Nevertheless, it is better to use larger NPD cubes for higher pressure generation, and synthesis of further larger NPD samples is required.

The maximum size of NPD is limited by the size of the cell assemblage for generation of the pressure and temperature required for the synthesis; in general terms, the lower the pressure and temperature, the larger the sample volume in the LVP. NPD rods have been synthesized at 15 GPa and at 2600 K, but recent studies demonstrated that they can also be produced at significantly lower pressures of 12 GPa, although somewhat higher temperatures of ∼2800–2900 K are needed at this pressure (Isobe et al., 2010). The larger cell volume can be used for synthesis at lower pressures, yielding NPDs with larger dimensions. On the other hand, when the potential of BOTCHAN-6000 is fully used, press loads near 6000 tons can be applied (c.f. the synthesis is currently made at about 4700 tons) and larger cell volumes are available for the same pressure. Furthermore, the reduction of dimensions of the graphite rod is about 20% after the conversion to NPD, which may be suppressed if the starting graphite sample is precompressed or partially transformed to diamond at lower pressures and temperatures. Such high-density graphite can be used as the starting material of the synthesis of NPD, which should result in a lesser degree of volume reduction. Thus, we expect that NPD rods of ∼1.5 cm in both diameter and length will be synthesized without any significant difficulty in the near future.

The technique for NPD synthesis by direct conversion of graphite at high pressure and temperature can also be applied to the synthesis of bulk samples of high-pressure phases with peculiar hardness and other interesting physical properties. One example of such a material is nanopolycrystalline stishovite (NPS) recently synthesized using virtually the same technique (Nishiyama, Seike, Hamaguchi, et al., 2012). Stishovite is known as the hardest oxide and NPS is found to have a nanotexture similar to that of NPD. Moreover, it has been demonstrated that NPS has exceptionally high fracture toughness (∼13 MPa $M^{1/2}$) presumably due to the peculiar texture of NPS with a tabular fine structure made of nanocrystals. Thus, the direct conversion method at pressures significantly higher than those at the equilibrium phase boundary, as developed for the synthesis of NPD, may result in novel nanopolycrystalline hard and tough materials for industrial and scientific applications.

Acknowledgments

This chapter is largely based on the recent studies conducted at the Geodynamics Research Center, Ehime University, and relevant laboratories. The authors thank the following people for collaborations, discussions, and providing some unpublished results: T. Shinmei, F. Isobe, N. Nishiyama, H. Ohfuji, Y. Tange, T. Inoue, M. Kimura, Y. Kono, A. Kurio, H. Hirai, H. Kagi, S. Odake, T. Yagi, T. Okuchi, Y. Nakamoto, K. Shimizu, N. Kawamura, N. Ishimatsu, H. Yusa.

References

Akaishi, M. (2003). Nanocrystalline diamond ceramics by a static high pressure method. *Review of High Pressure Science and Technology, 13*, 36–42.

Akaishi, M., Yamaoka, S., Ueda, F., & Ohashi, T. (1996). Synthesis of polycrystalline diamond compact with magnesium carbonate and its physical properties. *Diamond and Related Materials, 5*, 2–7.

Baldini, M., Yang, W., Aquilanti, G., Zhang, L., Ding, Y., Pascarelli, S., et al. (2011). High pressure EXAFS measurements on Ge using nano-crystalline anvils. *Journal of Applied Physics*, http://dx.doi.org/10.1103/PhysRevB.84.014111.

Bochechka, A. A., Romanko, L. A., Garvilova, V. S., Konoval, S. M., & Nazarchuk, S. N. (2007). Special features of sintering diamond powders of various dispersions at high pressure. *Journal of Superhard Materials, 29*, 17–23.

Brookes, C. A., & Brookes, E. J. (1991). Diamond I perspective: a review of mechanical properties of natural diamond. *Diamond and Related Materials, 1*, 13–17.

Brookes, C. A., Howes, V. R., & Parry, A. R. (1988). Multiple slip in diamond due to a nominal contact pressure of 10 GPa at 1000 °C. *Nature, 332*, 139–141.

Bundy, F. P. (1963). Direct conversion of graphite to diamond in static pressure apparatus. *Journal of Chemistry and Physics, 38*, 631–643.

Bundy, F. P., Hall, H. T., Strong, H. M., & Wentorf, R. H., Jr. (1955). Man-made diamonds. *Nature, 176*, 51–55.

Cartigny, P. (2010). Mantle-related carbonados? Geochemical insights from diamonds from the Dachine komatiite (French Guiana). *Earth and Planetary Science Letters, 296*, 329–339.

Chang, Y.-Y., Jacobsen, S. D., Kimura, M., Irifune, T., & Ohno, I. (2013). Elastic properties of transparent nano-polycrystalline diamond measured by GHz-ultrasonic interferometry and resonant sphere methods. *Physics of the Earth and Planetary Interiors*. Available at: http://dx.doi.org/10.1016/j.pepi.2013.09.009.

Chokshi, A. H., Rosen, A., Karch, J., & Gleiter, H. (1989). On the validity of the Hall-Petch relationship in nanocrystalline materials. *Scripta Metallurgica, 23*, 1679–1684.

Couvy, H., Lahiri, D., Chen, J., Agarwal, A., & Sen, G. (2011). Nanohardness and Young's modulus of nanopolycrystalline diamond. *Scripta Materialia, 64*, 1019–1022.

Daulton, T. L., & Ozima, M. (1996). Radiation-induced diamond formation in uranium-rich carbonaceous materials. *Nature, 271*, 1260–1263.

Dubrovinskaia, N., Dub, S., & Dubrovinsky, L. (2006). Superior wear resistance of aggregated diamond nanorods. *Nano Letters, 6*, 824–826.

Dubrovinskaia, N., Dubrovinsky, L., Langenhorst, F., Jacobsen, S., & Liebske, C. (2005). Nanocrystalline diamond synthesized from C60. *Diamond and Related Materials, 14*, 16–22.

Dubrovinskaia, N., Solozhenko, V. L., Miyajima, N., Dmitriev, V., Kurakevych, O. O., & Dubrovinsky, L. (2007). Superhard nanocomposite of dense polymorphs of boron nitride: noncarbon material has reached diamond hardness. *Applied Physics Letters, 90*. Art. No. 101912.

Endo, S., & Ito, K. (1982). Triple-stage high pressure apparatus using sintered diamond anvils. In S. Akimoto, & M. H. Manghnani (Eds.), *High pressure research in geophysics* (pp. 3–12). Tokyo/Dordrecht: Center for Academic Publications Japan/D. Reidel Publishing Company.

Guillou, C. L., Brunet, F., Irifune, T., Ohfuji, H., & Rouzaud, J.-N. (2007). Nanodiamond nucleation below 2273 K at 15 GPa from carbons with different structural organizations. *Carbon, 45*, 636–648.

Hall, E. O. (1951). The deformation and ageing of mild steel: III discussion of results. *Proceedings of Physical Society of London B, 64*, 747–753.

Higashi, K., & Onodera, A. (1986). Non-catalytic synthesis of diamond from amorphous carbon at high static pressure. *Physica B+C, 139/140*, 813–815.

Hill, R. (1952). The elastic behavior of a crystalline aggregate. *Proceedings of Physical Society of London A, 65*, 349–354.

Hounsome, L. S., Jones, R., Martineau, P. M., Fisher, D., Shaw, M. J., Briddon, P. R., et al. (2006). Origin of brown coloration in diamond. *Physical Review B, 73*. Art. No. 125203.

Irifune, T. (2010). Frontiers in deep earth mineralogy using new large-volume D-DIA and KMA apparatus. *Review of High Pressure Science and Technology, 20*, 158–165.

Irifune, T., Kurio, A., Sakamoto, S., Inoue, T., & Sumiya, H. (2003). Ultrahard polycrystalline diamond from graphite. *Nature, 421*, 599–600.

Irifune, T., Kurio, A., Sakamoto, S., Inoue, T., Sumiya, H., & Funakoshi, K. (2004). Formation of pure polycrystalline diamond by direct conversion of graphite at high pressure and high temperature. *Physics of the Earth and Planetary Interiors, 133/144*, 593–600.

Irifune, T., & Sumiya, H. (2004). Nature of polycrystalline diamond synthesized by direct conversion of graphite using Kawai-type multianvil apparatus. *New Diamond and Frontier Carbon Technology, 14*, 313–327.

Irifune, T., Isobe, F., & Shimei, T. (2013). A novel large-volume Kawai-type apparatus and its application to the synthesis of sintered bodies of nano-polycrystalline diamond. *Physics of the Earth and Planetary Interiors*. Available at: http://dx.doi.org/10.1016/j.pepi.2013.09.007.

Isobe, F., Irifune, T., Shinmei, T., Suga, S., Nishiyama, N., & Sumiya, H. (2010). Lowering P, T boundary for synthesis of pure nano-polycrystalline diamond. *Journal of Physics: Conference Series, 215*. Art. No. 012136.

Ito, E. (2007). Multianvil cells and high-pressure experimental methods. In G. D. Price (Ed.), *Treatise on geophysics* (Vol. 2; pp. 197–230). Amsterdam: Elsevier B. V.

Kagi, H., Takahashi, K., Hidaka, H., & Masuda, A. (1994). Chemical properties of Central African carbonado and its genetic implication. *Geochemica Cosmochimica et Acta, 58*, 2629–2638.

Kawai, N., & Endo, S. (1970). The generation of ultrahigh pressure by a split sphere apparatus. *Review of Scientific Instruments, 41*, 1178–1181.

Kawamura, N., Ishimatsu, N., & Maruyama, H. (2010). Study of magnetism at high pressure using X-ray magnetic circular dichroism in hard X-ray region. Development of XMCD measurement under high pressure, high magnetic field and low temperature. *Journal of Japanese Society for Synchrotron Radiation Research, 23*, 340–357.

Kawazoe, T., Nishiyama, N., Nishihara, Y., & Irifune, T. (2010). Pressure generation to 25 GPa using a cubic anvil apparatus with a multi-anvil 6-6 assembly. *High Pressure Research, 30*, 167–174.

Kirkley, M. B., Gurney, J. J., Otter, M. L., Hill, S. J., & Daniers, L. R. (1991). The application of C isotope measurements to the identification of the sources of C in diamonds: a review. *Applied Geochemistry, 6*, 477–494.

Kono, Y., Nakamoto, M., & Irifune, T. (2010). Elastic properties of sintered diamonds with and without Co binder. *Journal of Physics: Conference Series, 215* (012134).

Kunimoto, T., & Irifune, T. (2010). Pressure generation to 125 GPa using a 6-8-2 type multianvil apparatus with nano-polycrystalline diamond anvils. *Journal of Physics: Conference Series, 215.* Art No. 012190.

Matsumoto, K., Maruyama, H., Ishimatsu, N., Kawamura, N., Mizumaki, M., Irifune, T., & Sumiya, H. (2011). Noncollinear spin structure in Fe-Ni invar alloy probed by magnetic EXAFS at high pressure. *Journal of the Physical Society of Japan, 80*, 023709.

McSkimin, H. J., & Bond, W. L. (1957). Elastic moduli of diamond. *Physical Review, 105*, 116–121.

Meng, Y.-F., Yan, C.-S., Lai, J., Kransnicki, S., Shu, H., et al. (2008). Enhanced optical properties of chemical vapor deposited single crystal diamond by low-pressure/high-temperature annealing. *Proceedings of National Academy of Science, 105*, 17620–17625.

Morelli, D. T., Beetz, C. P., & Perry, T. A. (1988). Thermal conductivity of synthetic diamond films. *Journal of Applied Physics, 64*, 3063–3066.

Naka, S., Horii, K., Takeda, Y., & Hanawa, T. (1976). Direct conversion of graphite to diamond under static pressure. *Nature, 259*, 38–39.

Nakamoto, Y., Sakata, M., Sumiya, H., Shimizu, K., Irifune, T., Matsuoka, T., et al. (2011). Diamond anvil using nano-polycrystalline diamonds for high-pressure generation with large culet size. *Rev. Sci. Instrunm., 82*(6), 066104.

Nakamoto, Y., Sumiya, H., Matsuoka, T., Shimizu, K., Irifune, T., & Ohishi, Y. (2007). Generation of multi-megabar pressure using nano-polycrystalline diamond anvils. *Japanese Journal of Applied Physics, 46*, 066104.

Namba, Y., Heidarpour, E., & Nakayama, M. (1992). Size effects appearing in the Raman spectra of polycrystalline diamonds. *Journal of Applied Physics, 72*, 1748–1751.

Nishiyama, N., Wang, Y., Sanehira, T., Irifune, T., & Rivers, M. L. (2008). Development of the multi-anvil assembly 6-6 for DIA and D-DIA type high-pressure apparatus. *High Pressure Research, 28*, 307–314.

Nishiyama, N., Seike, S., Hamaguchi, S., Irifune, T., Matsushita, M., Tahahashi, M., et al. (2012). Synthesis of nanocrystalline bulk SiO2 stishovite with very high toughness. *Scripta Materialia*. Available at: http://dx.doi.org/10.1016/j.scriptamat.2012.08.028.

Odake, S., Ohfuji, H., Okuchi, T., Kagi, H., Sumiya, H., & Irifune, T. (2009). Pulsed laser processing of nano-polycrystalline diamond: a comparative study with single crystal diamond. *Diamond and Related Materials, 18*, 877–880.

Ohfuji, H., Okada, T., Yagi, T., Sumiya, H., & Irifune, T. (2010). Application of nano-polycrystalline diamond to laser-heated diamond anvil cell experiments. *High Pressure Research, 30*, 142–150.

Ohfuji, H., Okimoto, S., Kunimoto, T., Isobe, F., Sumiya, H., Komatsu, K., & Irifune, T. (2012). Influence of graphite crystallinity on the microtexture of nano-polycrystalline diamond obtained by direct conversion. *Phys. Chem. Miner., 39*(7), 543–552.

Ohfuji, H., Okuchi, T., Odake, S., Kagi, H., Sumiya, H., & Irifune, T. (2010). Micro-/nanostructual investigation of laser-cut surfaces of single- and polycrystalline diamonds. *Diamond and Related Materials, 19*, 1040–1051.

Ohtaka, O., Shimono, M., Ohnishi, N., Fukui, H., Takebe, H., et al. (2004). *Physics of the Earth and Planetary Interiors, 143*, 587–591.

Okuchi, T., Ohfuji, H., Odake, S., Kagi, H., Nagatomo, S., Sugata, M., et al. (2009). Micromachining and surface processing of the super-hard nano-polycrystalline diamond by three types of pulsed lasers. *Applied Physics A, 96*, 388–842.

Osipov, A. S., Nauyoks, S., Zerda, T. W., & Zaporozhets, O. I. (2009). *Diamond and Related Materials, 18*, 1061–1064.

Ozima, M., Zashu, S., Tomura, K., & Matsushita, Y. (1991). Constraints from noble-gas contents on the origin of carbonado diamonds. *Nature, 351*, 472–474.

Pan, Z., Sun, H., Zhang, Y., & Chen, C. (2009). Harder than diamond: superior indentation strength of wurtzite BN and lonsdaleite. *Physical Review Letters, 102*. Art. No. 05503.

Petch, N. J. (1953). The cleavage of polycrystals. *Journal of the Iron and Steel Institute, 174*, 25–28.

Richter, A., Smith, R., Dubrovinskaia, N., & McGee, E. (2006). Mechanical properties of superhard materials synthesized at various pressure-temperature conditions investigated by nanoindentation. *High Pressure Research, 26*, 99–109.

Schlotz, J., Di Tolla, F. D., & Jcobsen, K. W. (1998). Softening of nanocrystalline metals at very small sizes. *Nature, 391*, 561–563.

Smith, J. V., & Dawson, J. B. (1985). Diamond aggregates from early impacts of crustal rocks? *Geology, 13*, 342–343.

Sumiya, H. (2006). Thermally activated deformation under Knoop indentations in super-hard directions of high-quality type-IIa diamond crystals. *Diamond and Related Materials, 15*, 1576–1579.

Sumiya, H., Harano, K., Arimoto, K., Kagi, H., Odake, S., & Irifune, T. (2009). Optical characteristics of nano-polycrystalline diamond synthesized directly from graphite under high pressure and high temperature. *Japanese Journal of Applied Physics, 48*. Art. No. 120206.

Sumiya, H., Harano, K., Sato, T., & Kukino, S. (2010). Mechanical properties and cutting performance of nano-polycrystalline diamond. In *Proceedings of CIRP international conference on high performance cutting* (Vol. 12; pp. 347–350).

Sumiya, H., & Irifune, T. (2004). Indentation hardness of nano-polycrystalline diamond prepared from graphite by direct conversion. *Diamond and Related Materials, 13*, 1771–1776.

Sumiya, H., & Irifune, T. (2007). Hardness and deformation microstructure of nano-polycrystalline diamonds synthesized from various carbons under high pressure and high temperature. *Journal of Materials Research, 22*, 2345–2351.

Sumiya, H., & Harano, K. (2012). Distinctive mechanical properties of nano-polycrystalline diamond synthesized by direct conversion sintering under HPHT. *Diamond and Related Materials, 24*, 44–48.

Sumiya, H., Irifune, T., Kurio, A., Sakamoto, S., & Inoue, T. (2004). Microstructure features of polycrystalline diamond synthesized directly from graphite under static high pressure. *Journal of Materials Science, 39*, 445–450.

Sumiya, H., Toda, N., & Satoh, S. (1997). Mechanical properties of synthetic type IIa diamond crystal. *Diamond and Related Materials, 6*, 1841–1846.

Sumiya, H., Toda, N., & Satoh, S. (2000). High-quality large diamond crystals. *New Diamond and Frontier Carbon Technology, 10*, 233–251.

Sumiya, H., Yusa, H., Inoue, T., Ohfuji, H., & Irifune, T. (2006). Conditions and mechanism of formation of nano-polycrystalline diamonds on direct transformation from graphite and non-graphitic carbon at high pressure and temperature. *High Pressure Research, 26*, 63–69.

Tange, Y., Irifune, T., & Funakoshi, K. (2008). Pressure generation to 80 GPa using multianvil apparatus with sintered diamond anvils. *High Pressure Research, 28*, 245–254.

Wakatsuki, M., Ichinose, K., & Aoki, T. (1972). Notes on compressible gasket and Bridgman-anvil-type high pressure apparatus. *Japanese Journal of Applied Physics, 11*, 578–590.

Wentorf, R. H., DeVries, R. C., & Bundy, F. P. (1980). Sintered superhard materials. *Science, 208*, 873–880.

Wu, B. R. (2007). Structural and vibrational properties of the 6H diamond: first-principles study. *Diamond and Related Materials, 16*, 21–28.

Yan, C. S., Mao, H.-K., Li, W., Qian, J., Zhao, Y., & Hemley, R. J. Y. (2004). Ultrahard diamond single crystals from chemical vapor deposition. *Physica Status Solidi (A) Applied Research, 201*, R25–R27.

Yoshikawa, M., Mori, Y., Maegawa, M., Katagiri, G., Ishida, H., & Ishitani, A. (1993). Raman scattering from diamond particles. *Applied Physics Letters, 62*, 3114–3116.

Yusa, H. (2002). Nanocrystalline diamond directly transformed from carbon nanotubes under high pressure. *Diamond and Related Materials, 11*, 87–91.

Yusa, H., Takemura, K., Matsui, Y., Morishima, H., Watanabe, K., Yamaguchi, H., et al. (1998). Direct transformation of graphite to cubic diamond observed in a laser-heated diamond anvil cell. *Applied Physics Letters, 72*, 1843–1845.

Zouboulis, E. S., Grimsditch, M., Ramdas, A. K., & Rodriguez, S. (1998). Temperature dependence of the elastic moduli of diamond: a Brillouin-scattering study. *Physical Review B, 57*, 2889–2896.

SECTION IV

SINGLE CRYSTALLINE DIAMOND

3.09 HPHT Synthesis of Large, High-Quality, Single Crystal Diamonds

Hitoshi Sumiya, Electronics Materials R&D Laboratories, Sumitomo Electric Industries Ltd, Itami, Japan

Glossary

Diamond grit A diamond powder or grain used to grind, smoothen, cut, or polish another substance, also known as diamond abrasive.

Dislocation A defect occurring along certain lines in the crystal structure and present as a closed ring or a line anchored at its ends to other dislocations, grain boundaries, the surface, or other structural feature, also known as line defect.

Monochromator An optical device that transmits a mechanically selectable narrow band of wavelengths of light or other radiations chosen from a wider range of wavelengths available at the input.

Plastic deformation A permanent change in the shape or size of an object without breaking it or putting it under excessive stress.

Stacking fault Planar defects, a one- or two-layer interruption in the stacking sequence.

Synchrotron radiation Electromagnetic radiation generated by the acceleration of charged relativistic particles, usually electrons, in a magnetic field.

X-ray topography X-ray diffraction methods for studying various structural defects in near-perfect crystals.

Nomenclature

Carat (ct) A unit for measuring the weight of diamonds and other precious stones, equal to 200 mg.

FWHM Full width at half maximum. An expression of the extent of a function, given by the

http://dx.doi.org/10.1016/B978-0-08-096527-7.00046-5

difference between the two extreme values of the independent variable at which the dependent variable is equal to half of its maximum value.

Knoop hardness test A diamond pyramid indenter, which has a rhombic base with included angles of 172°30′ and 130°, is pressed onto the specimen under a test force F. The hardness number (HK) is obtained by dividing the test force F by the projected area of the indentation. The area is calculated from the longer diagonal length of the indentation when the indenter is removed.

3.09.1 Introduction

Diamond has the highest hardness among all materials and has superior thermal conductivity, as well as excellent chemical stability and transparency. Owing to these outstanding properties, diamond has been employed in a wide range of applications. Diamond powders or grits with sizes up to 1 mm have been used globally in large quantities as abrasives for polishing, grinding, and cutting processes. Large diamond crystals several millimeters in size are used for high-precision cutting tools, wire drawing dies, heat sinks, optical windows, surgical blades, etc. In many fields of scientific research such as space, high pressure, and radiation, large diamond crystals are the essential components of research equipment. They are also subjected to investigating crystal habits, morphology, and spectroscopy. It is projected that large diamond crystals will become much more essential for a wider variety of commercial and scientific applications and become an important material to support technological advancement in both industry and science.

As natural diamonds have grown under various conditions and in different ways, the amount of impurities and the degree of lattice defects in the crystals are greatly varied. Thus, they exhibit various physical and mechanical properties. The main impurity in diamond is generally nitrogen (Kaiser and Bond, 1959). Depending on the content of nitrogen impurity and the form in which it is present, diamonds are classified into three different types, that is, Ia, Ib, and IIa (Bibby, 1982). Diamonds that contain boron impurity are grouped into the fourth category, namely, type IIb. Most natural diamonds ($\sim$98%) are type Ia and contain large amounts of nitrogen ($\sim$0.1%) in aggregated forms. Their thermal conductivity, hardness, and other physical properties are affected by these aggregated nitrogen impurities, and optically they absorb light in the ultraviolet (UV) and infrared regions. Diamonds containing nitrogen of approximately 100 ppm in the form of isolated substitutional (dispersed) impurities are classified as type Ib. High-purity diamonds that contain impurities of less than about 1 ppm are called type IIa. Type IIa diamonds exhibit only multiphonon absorption, which is intrinsic to diamond, and are optically transparent down to an absorption edge at 225 nm. However, type IIa diamond crystals that are several millimeters in size account for a mere 1–2% of mined diamonds and large-size (>5 mm, 1 ct) crystals are very rare. Besides, such high-purity natural diamonds always have many dislocations and much residual strain. It is therefore very difficult to consistently obtain high-quality, large-size, natural diamond crystals with small amounts of impurities and dislocations. In addition, very high prices restrict the accessibility to such diamond crystals. The low quality, diversity, and high price of large natural diamond crystals present serious problems when industrial applications are planned. On that account, demands for high-quality large diamond crystals from synthetic processes have been growing recently.

Among various methods of diamond synthesis, the most effective one to grow large diamond single crystals is the temperature-gradient method under static high-pressure and high-temperature (HPHT; Strong and Chrenko, 1971; Wentorf, 1971). In the 1980s, Sumitomo Electric Industries (SEI) developed a creative mass-production process of diamond crystals based on the temperature-gradient method. This enabled the commercialization of type Ib diamonds (containing dispersed nitrogen impurities of several tens of parts per million) of 1–2 ct (or 5–6 mm in diameter). The synthetic type Ib diamonds were applied in heat sinks, wire drawing dies, cutting tools for high-precision machining, and other products (Hara, 1985). In the 1990s, SEI also succeeded in producing synthetic type IIa diamonds that had previously been impossible (Sumiya & Satoh, 1996; Sumiya, Satoh, Nishibayashi, & Goda, 1995). The synthetic type IIa diamonds were applied to the optical parts for Fourier transform infrared (FT-IR) spectroscopy. Synthetic type IIa diamonds are transparent over a wide range of wavelengths from UV to far infrared regions, showing no absorptions due to impurities. They also have a high crystalline quality with fewer crystal defects, less internal strain, and less variations in defects among crystals than those of natural diamonds or conventional synthetic type Ib diamonds (Sumiya, Toda, Nishibayashi, & Satoh, 1997). The outstanding characteristics of synthetic type IIa diamonds permit their applications to new industrial and scientific uses such as monochromators, semiconductor substrates, high-pressure anvils, and radiation detectors. Recently, it has been possible to grow much larger high-quality type IIa diamond crystals of 8–10 ct (10–12 mm across) with prolonged high-precision temperature control and adequate selection of solvent metal and additives (Sumiya, 2010, p. 96; Sumiya, Toda, & Satoh, 2005). In this chapter, we review the HPHT synthetic method to produce high-quality large synthetic type IIa diamonds, and discuss their distinctive properties and applications.

3.09.2 HPHT Synthesis of High-Purity Large Single Crystal Diamond

3.09.2.1 Temperature-Gradient Method under High Pressure

As is well known, there are various methods for diamond synthesis such as the temperature-gradient (difference) method or the solubility difference method under static high-pressure, dynamic high-pressure (shock wave) method, and chemical vapor deposition (CVD) method (**Figure 1**).

Among these methods, the temperature-gradient method under static high pressure is thought to be the most effective to grow large good-quality diamond crystals of a dimension of several millimeters. In this method, the carbon source is placed at the hotter part above the solvent (made from ferrous metals, such as Fe, Ni, and Co) and the seed crystal is positioned at the cooler part under the solvent in the high-pressure reaction cell. The driving force for the crystallization arises from the difference in the solubility of diamond in the solvent that is caused by the temperature gradient in the reaction cell.

In 1971, the General Electric Research Center reported that it succeeded in growing diamond crystals up to 1 ct using this method (Strong and Chrenko, 1971; Wentorf, 1971). The process, however, was considered too costly to translate into the commercial production at that time, because the growth rate must be restricted to be very slow in order to grow good-quality diamond. When attempts were made to grow them more rapidly than a certain limit of growth rate (hereinafter referred to as "limited growth rate"), a lot of solvent metals would be included in the grown crystals (metal inclusions) otherwise polycrystallization or skeletonization would occur. At that time, it was reported that the limited growth rate of a type Ib diamond containing nitrogen impurities of 10–100 ppm is about 2.5 mg h^{-1}, and that of a type IIa diamond is $<$1.5 mg h^{-1} (Strong and Chrenko, 1971).

In 1985, the commercialization of type Ib diamond crystals of 1–2 ct (5–6 mm across) was enabled, due to the increase of the limited growth rate up to 4 mg h^{-1} by an optimization of the solvent metal and growth conditions in addition to the development of a mass-production process of the temperature-gradient method (Hara, 1985). Further, in 1990, larger type Ib diamond crystals of about 10 ct (rectangular shaped, 12 mm on a side) were grown at a growth rate as high as 15 mg h^{-1} by using the large seed method (Sumiya, Satoh, Tsuji, & Yazu, 1990, pp. 48-49; Sumiya, Toda, & Satoh, 2002). Thus, large yellow type Ib diamond crystals could be grown at a high growth rate, and be produced commercially. It had been impossible, however, to produce high-purity type IIa diamond crystals commercially because of the difficulty in increasing the limited growth rate. The

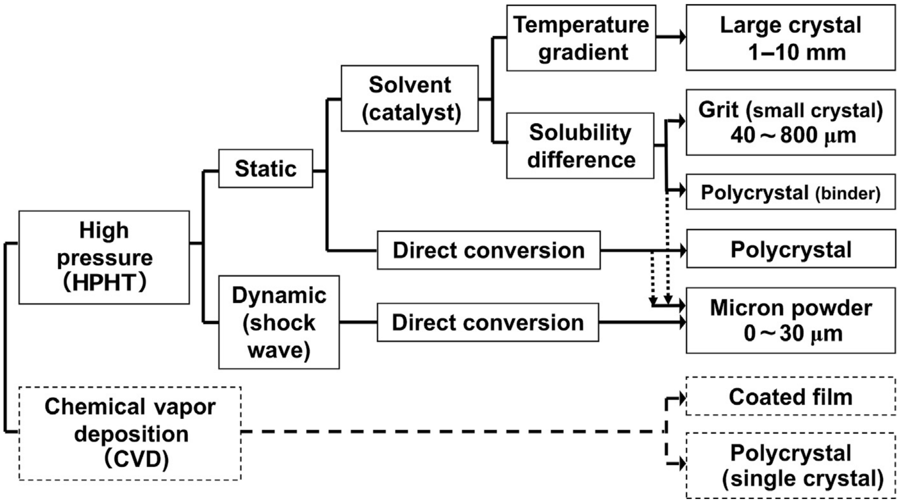

Figure 1 Synthetic methods for diamonds.

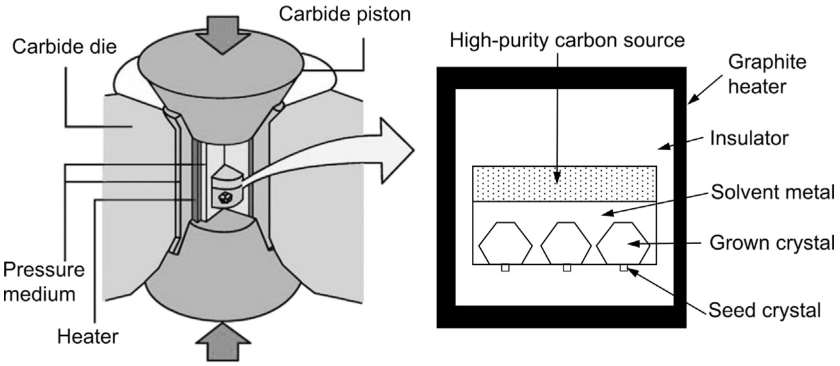

Figure 2 Growth method of large diamond crystals (temperature-gradient method).

entrapment of inclusions in the crystal tends to be facilitated when a nitrogen getter is added to the solvent metal for synthesizing type IIa diamond. To avoid the occurrence of inclusions, growth rates had to be kept very low such as at 1 mg h^{-1}.

3.09.2.2 Synthesis of High-Purity Diamond Crystals

In the 1990s, high-purity (type IIa) diamond crystals containing impurities <0.1 ppm were successfully synthesized even at a high growth rate of 3–4 mg h^{-1} (Sumiya & Satoh, 1996; Sumiya et al., 1995). This finally enabled the commercial production of type IIa diamond crystals. The following is an outline of the technique.

Figure 2 shows the method developed for growing high-purity IIa diamond crystals. It is well known that nitrogen (N), boron (B), and nickel (Ni) are easily incorporated into synthetic diamond as chemical impurities. Therefore, this method has been designed to eliminate these impurities. High-purity carbon material containing less than 1 ppm of boron is used as the carbon source. High-purity Fe–Co alloy is used as the solvent metal, and Ti is added to the solvent as the nitrogen getter. Here, when Ti is added, a large amount of TiC is formed in the solvent. The formation of TiC inhibits the transport and diffusion of carbon, thus reducing the amount of carbon supplied to the crystal growth surface and delaying the growth along the crystal surface. This leads to the trapping of metal inclusions. The TiC particles themselves are also trapped into the grown crystal as fine inclusions. On the other hand, it is known that TiC is decomposed in molten group Ib metals such as Cu, Ag, and Au (Wakatsuki, 1966). Based on this fact, besides adding Ti as the nitrogen getter, a molten group Ib metal was also added to the solvent to suppress the formation of TiC.

Figure 3 shows the UV–visible absorption spectra of diamond crystals synthesized by adding different amounts of Ti. For the diamond grown by the addition of 1.5 wt% Ti, the absorption at 270 nm due to the

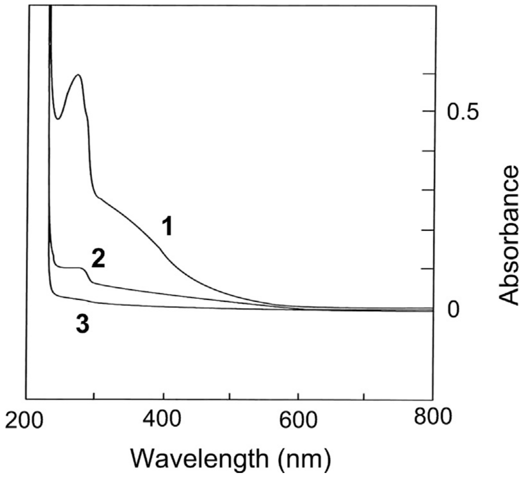

Figure 3 UV and visible absorption spectra of synthetic diamonds by adding Ti of (1) 0.5 wt%, (2) 1.0 wt%, and (3) 1.5 wt%. The nitrogen concentrations are, respectively, estimated to be (1) 2.8 ppm, (2) 0.3 ppm, and (3) <0.1 ppm (Sumiya et al., 1995).

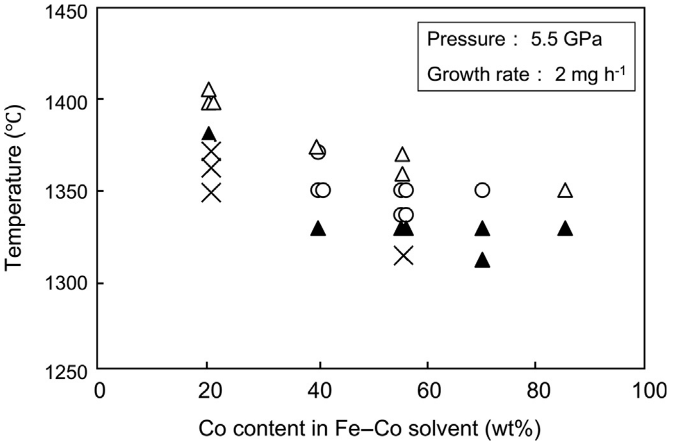

Figure 4 Conditions of type IIa diamond formation against the Co content of Fe–Co solvent by adding Ti: (○) good crystal, (△) crystal containing many inclusions, (▲) skeleton crystal, (×) no diamond formation (Sumiya et al., 2005).

nitrogen impurities is not observed, and the amount of the nitrogen estimated from electron spin resonance is <0.1 ppm (undetectable level). Nitrogen impurities can be eliminated almost completely when the added amount of Ti is >1.5 wt%.

The conditions of type IIa diamond formation against the Co content of the Fe–Co solvent by adding Ti as the nitrogen getter are shown in Figure 4. Good crystals (without containing inclusions) are obtained in a considerably limited condition. When the Co content is too low or too high, good crystals cannot be obtained because of the formation of inclusions or skeleton crystals. In addition, the valid growth temperature region is very narrow even with a suitable Fe–Co composition of the solvent. The width of the synthesis temperature region for good type IIa diamond crystals is <10 °C.

Figure 5 shows the pressure and temperature regions for growing good diamond crystals without containing inclusions. Good type Ib diamond crystals can be obtained in region A. Region B for growing good type IIa crystals is much narrower than region A. The width of the allowable temperature of A and B at 5.5 GPa is about 40 and 10 °C, respectively. If the temperature condition is higher than that of these valid regions, many inclusions are contained in the grown crystals. At a lower temperature than that of the valid regions, well-formed

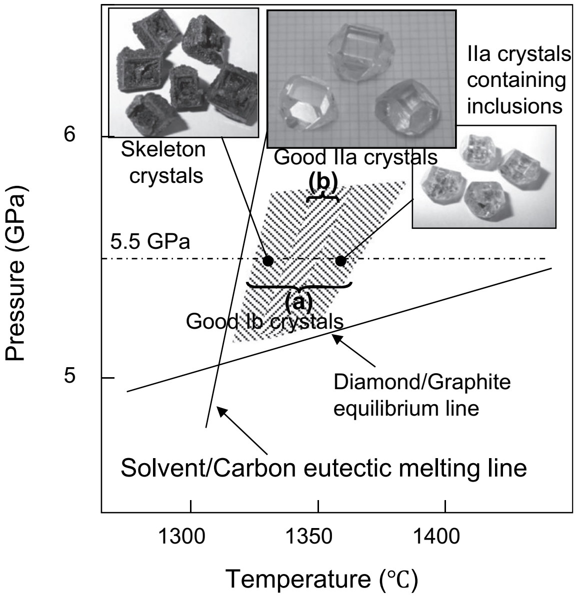

Figure 5 Growth regions of good diamond crystals: (a) type Ib diamond, (b) type IIa diamond.

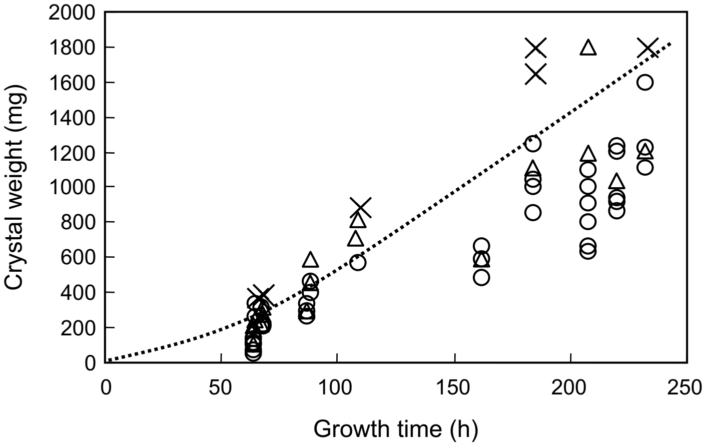

Figure 6 Experimental results of the growth tests for large-size type IIa diamonds. The dotted line shows the limited growth rate to grow good crystals: (○) good crystals, (△) crystal containing inclusions, (×) crystal containing many inclusions (Sumiya et al., 2005).

diamond crystals cannot be obtained because of the formation of skeleton crystals. The lower limit of the growth temperature becomes 20–30 °C higher by adding the nitrogen getter such as Ti to the solvent. Thus, the allowable temperature region for growing good type IIa diamond crystals is considerably narrow. Therefore, a high-precision temperature control technique is required for growing good type IIa diamond crystals containing no inclusions.

3.09.2.3 Growth of Large High-Purity Diamond Crystals

Based on the technical knowledge mentioned in Section 3.09.2.2, further growth tests on much larger-size type IIa diamond crystals have been carried out conducting precision temperature control at 1340–1350 °C for 150–250 h. The volume of the solvent was made larger and the temperature gradient was adjusted by changing the heater shape to grow the larger-size crystals. The experimental results of these long growth tests are shown in Figure 6. In this figure, the dotted line shows the limited growth rate to grow good crystals. In the early stage (growth time <60–70 h, crystal size <2 ct or 400 mg), the limited growth rate is 3–4 mg h^{-1}. However, when the growth time is over about 100 h, good diamond crystals can be obtained even at a high growth rate of 6–8 mg h^{-1}. Thus, it is apparent that the limit growth rate increases as the crystals grow. This tendency can also be seen when growing type Ib diamonds. This is attributed to the enlargement of the surface area of the grown crystal.

Thus, large type IIa diamond crystals of 8–10 ct (10–12 mm across) can be grown at a high growth rate of 6–8 mg h^{-1} through the high-precision temperature control over prolonged time with an adequate selection of solvent metal and additives. The growth rate is much higher than those (1.5–1.8 mg h^{-1}) reported previously (Burns et al., 1999; Strong and Chrenko, 1971). Figure 7 (right photograph) shows a large diamond

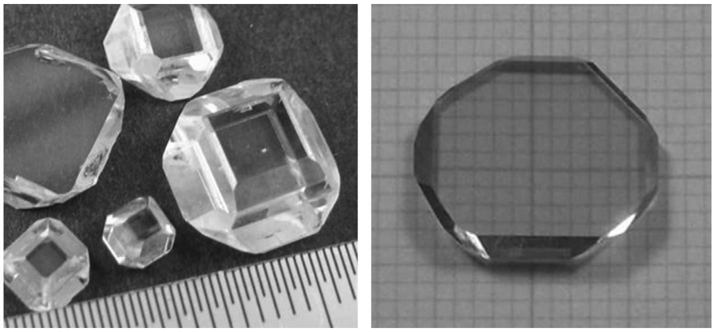

Figure 7 Large-size synthetic type IIa diamond crystals.

plate ($12 \times 12 \times 1$ mm) prepared from the 10 ct type IIa diamond crystal obtained by the method described above. The diamond plates are applied to monochromators of synchrotron X-ray radiation beams.

3.09.3 Crystalline Quality

Natural diamond crystals have been grown under various conditions and in different ways, consequently exhibiting a variety of properties and crystal imperfections. Most natural diamonds contain many nitrogen impurities (type I), and almost all natural diamonds have a number of defects and much strain in the crystals because of the complicated and various growth processes occurring in the earth's interior (Harrison and Tolansky, 1964; Moor, 1988; Tolansky, 1966). This is also seen even in high-purity natural type II diamonds (Lang, 1967). It is then very difficult to find high-quality crystals containing few impurities and also few crystal defects from natural diamonds.

High-purity type IIa diamond crystals with impurities <0.1 ppm have been synthesized by the temperature-gradient method under HPHT (Section 3.09.2). In the absence of any crystal defects caused by impurities, and while growing under a controlled condition of HPHT in a thermodynamically stable region, high-purity synthetic type IIa diamonds are expected to have a much higher and invariable crystalline quality in comparison with natural diamonds or conventional synthetic type Ib diamonds.

In this section, we describe the crystalline quality of the synthetic type IIa diamonds mentioned in Section 3.09.2, evaluated by double-crystal X-ray rocking-curve measurement, polarizing microscopy, X-ray topography, and Raman spectroscopy. The crystalline quality of the synthetic type IIa diamond is compared with the conventional synthetic diamond (type Ib) and two common kinds of natural diamond (types Ia and IIa). In addition, a method to improve the crystalline quality of the synthetic type IIa diamonds much more is presented.

3.09.3.1 Comparison of the Crystalline Quality

Figure 8 shows the rocking curves of various types of diamonds (Sumiya, Toda, Nishibayashi, et al., 1997). The synthetic type IIa diamond has a considerably sharper rocking curve than conventional synthetic type Ib diamond as well as natural type Ia and type IIa diamonds. The full width at half maximum (FWHM) of the rocking curve of the synthetic type IIa diamond is very close to the theoretical value (4.2 as for CuKα_1 derived from a dynamical theory of diffraction). This indicates that the high-purity type IIa diamond has little internal strain

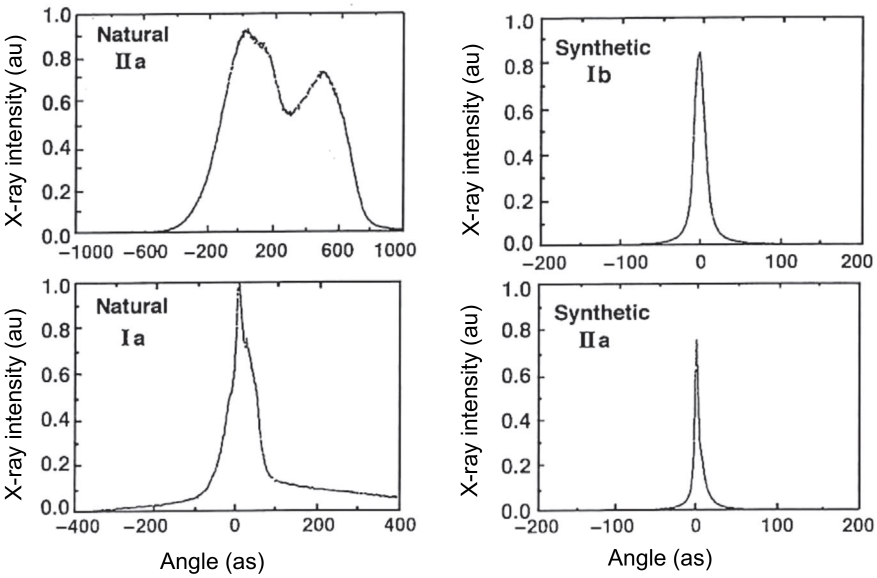

Figure 8 Double-crystal rocking curves of various diamonds for the (004) reflection under CuKα_1 radiation (Sumiya, Toda, Nishibayashi, et al., 1997).

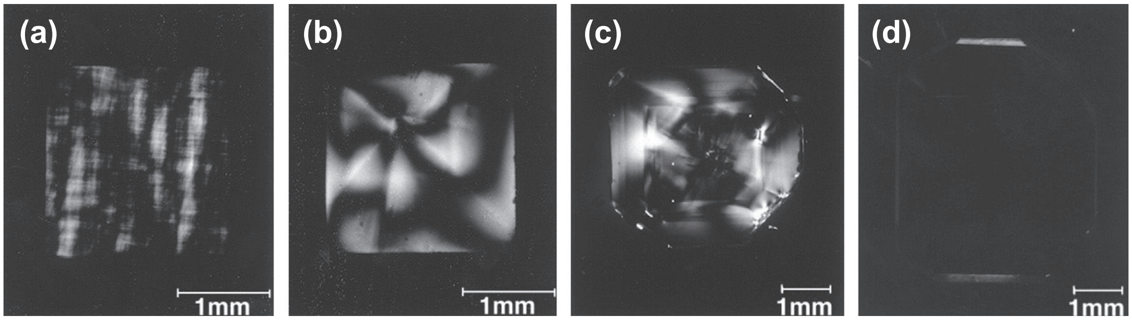

Figure 9 Polarized light images of various diamonds (polished plates): (a) natural type IIa; (b) natural type Ia; (c) synthetic type Ib; and (d) synthetic type IIa (Sumiya, Toda, Nishibayashi, et al., 1997).

and few crystal defects. Natural diamonds show broad and complicated rocking curves, indicating that natural diamonds have considerable internal strain and many defects in their crystals. Natural type Ia diamond is less strained than natural type IIa diamond, in agreement with earlier works (Black, Burdette, & Banholzer, 1993; Lang, Moor, Makepeace, Wierzchowski, & Welbourn, 1991). The slightly broad rocking curve observed in conventional synthetic type Ib diamond is attributed to the degraded crystal perfection caused by dispersed nitrogen (Burns et al., 2009).

The polarized light images of various diamonds (polished plates) are shown in **Figure 9** (Sumiya,Toda, Nishibayashi, et al., 1997). Natural type IIa diamond has fine sharp strain images because of deformations of tatami-like structure, and natural type Ia diamond shows radial patterns due to line defects of dislocation bundles (Lang, 1967). The polarized light image of synthetic Ib diamond shows stripe-like growth layer patterns parallel to growth surfaces in addition to radial patterns. Similar patterns in synthetic type Ib diamond crystals have been reported in earlier studies (Frank and Lang, 1990; Lang, Moor, et al., 1991; Wierzchowski, Moore, & Makepeace, 1991). The concentration of the dispersed nitrogen impurity in synthetic type Ib diamonds differs between the growth sectors and also there are some shadings of the nitrogen concentration (growth layers patterns) in a growth sector (Burns et al., 1990; Satoh, Sumiya, Tsuji, & Yazu, 1990, pp. 351-355). This inhomogeneous distribution of nitrogen impurities may cause a change in lattice parameter to some extent (Burns et al., 2009; Lang, Moor, et al., 1991; Macrander, Krasnicki, Zhong, Maj, & Chu, 2005; Wierzchowski et al., 1991), which is considered to induce the strain images as described above. In synthetic type IIa diamonds such strain images as observed in synthetic type Ib and natural diamonds are not perceivable.

Figure 10 shows the X-ray projection topographs of these diamonds (polished plates). In natural type IIa diamond, many dislocations of tatami-like pattern are observed. In natural type Ia diamond, linear dislocations radiating from the center can be seen. These dislocation images of natural diamonds correspond to the strain images observed by polarized light microscopy. Such dislocations of natural diamonds have been investigated in detail by Lang et al. (Lang, 1967; Lang, 1979, p. 425; Lang, Moore, & Walmsley, 1992, p. 215). Synthetic type Ib diamond has many linear dislocations that radiate outward from the seed crystal in addition to the stripe-like defect images corresponding to the inhomogeneous distributions of the nitrogen impurity as also observed in polarized light images. In synthetic type IIa diamond, any such stripe-like defects are not detected, but some line

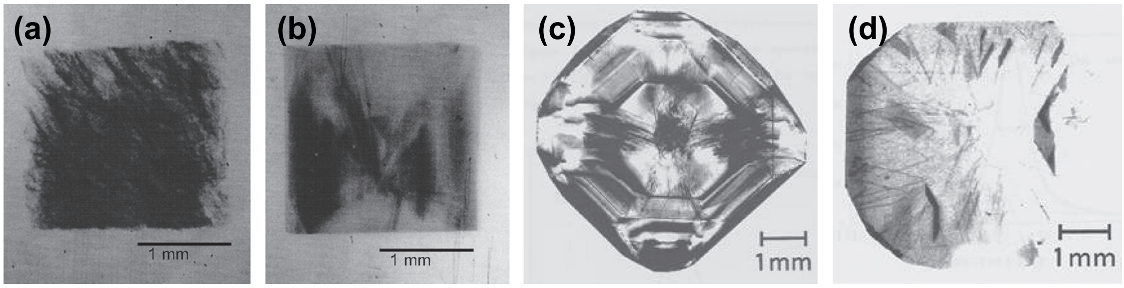

Figure 10 X-ray projection topograph images of various diamonds (polished plates) for (220) reflection under MoKα_1 radiation: (a) natural type IIa, (b) natural type Ia, (c) synthetic type Ib, and (d) synthetic type IIa.

Table 1 Crystalline perfections of various diamonds

	Natural IIa	*Natural Ia*	*Synthetic Ib*	*Synthetic IIb*
Natural abundance (%)	1–2	~98	–	–
Nitrogen content (ppm)	<1	~1000 (aggregated)	~100 (dispersed)	<0.1
Internal strain by polarizing microscopy	Much (tatami)	Much (radical, stripe)	Much (radical, stripe)	None to little
Defects by X-ray topography	Very many (tatami)	Many (line, stripe)	Many (line, stripe)	Some (line, plane)
FWHM of rocking curves (CuKα_1, as)	200–2500	7–60	6–20	4–6
FWHM of Raman spectra (cm^{-1})	2.0–2.5	3.2–3.8	1.8–2.6	1.6–1.8

defects and plane-shaped defects are observed. We will discuss the defects in synthetic type IIa diamond in detail in the next section.

The line width of the Raman spectrum peak of the diamonds can be a measure of evaluating the microstrain in diamonds. When the microstain contributes to phonon scattering, it will demonstrate a broadening of the Raman spectrum peak. The results of measuring the FWHM of Raman spectrum peaks at 1332 cm^{-1} (Sumiya, Toda, Nishibayashi, et al., 1997) show the synthetic IIa diamond has a considerably smaller FWHM (1.6–1.8 cm^{-1}) than synthetic type Ib diamond (1.8–2.6 cm^{-1}) or natural diamonds (2.0–3.8 cm^{-1}). This suggests that the synthetic IIa diamond also has little microstrain that can arise from isolated dispersed impurities (nitrogen, nickel), point defects, etc.

Table 1 summarizes the evaluation results of crystalline perfection of the diamonds (Sumiya, Toda, Nishibayashi, et al., 1997). It is obvious that the synthetic IIa diamond has a much higher crystalline quality with considerably fewer crystal defects and less residual strain than those of natural diamonds or conventional synthetic Ib diamond.

3.09.3.2 Crystal Defects in Synthetic Diamond Crystals

As shown in the previous section, the FWHM of the rocking curves of the synthetic type IIa diamond measured by using CuKα_1 radiation is very close to the theoretical value (4.2 as); therefore, the clear differences between synthetic type IIa diamond crystals are not detectable. However, when we used MoKα_1 as the X-ray radiation, some differences in crystalline quality among the synthetic type IIa diamond crystals can be observed as exemplified by the fact that the FWHM of rocking curves ranges from 1.5 to 6 as. The theoretical value of a perfect diamond crystal is about 1.0 as for MoKα_1 radiation. The variation in the FWHM of the rocking curves of synthetic type IIa diamond crystals is ascribed mainly to the line defects (dislocation bundles), which are seen in **Figure 10(d)**.

Figure 11(a) shows the X-ray projection topograph of an as-grown synthetic type IIa diamond crystal. The dislocation bundles are spreading outward from the seed crystal positioned approximately at the center of the

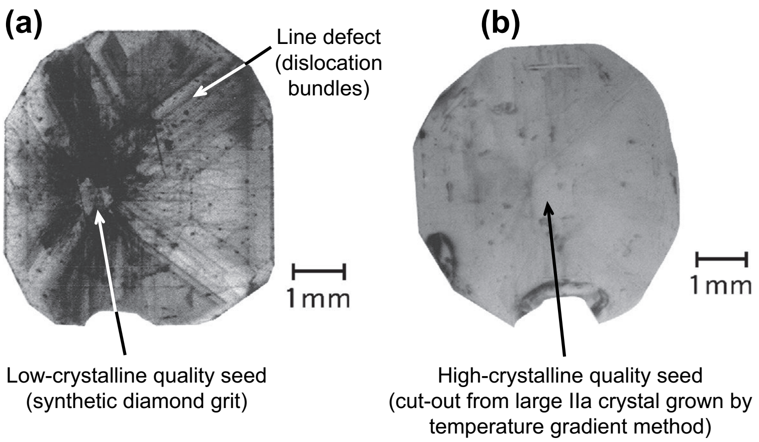

Figure 11 X-ray projection topograph of an as-grown synthetic IIa diamonds for the (220) reflection under MoKα_1 radiation. (a) Grown on diamond grit seeds, (b) grown on high-quality diamond seeds.

figure. The dislocation bundles are located parallel to the ⟨001⟩ and ⟨±1 ± 12⟩ directions. Such dislocation bundles developing from seed crystals are also normally present in conventional synthetic Ib diamonds (Wierzchowski et al., 1991; Woods and Lang, 1975).

Some plane defects (stacking faults) are also observed in synthetic IIa diamond (**Figure 10(d)**). All the plane defects are lined on the (±1 ± 11) planes. Most of the plane defects develop from the bottom of the crystal near the seed, but some of them generate from metal inclusions as well.

3.09.3.3 Improvement of Crystalline Quality

The synthetic type IIa diamond has a higher crystalline quality than natural diamonds or synthetic type Ib diamond; however, the synthetic type IIa diamond has some line defects as shown in Section 3.09.3.2. The origin of the line defects observed in synthetic IIa diamond crystals is attributed to the crystal imperfections present in the seed crystals. The synthetic diamond crystals described above were grown on diamond grits synthesized by the film-growth method (phase-difference mechanism). It is known that the synthetic diamond grits have many crystal defects, and the degree of the inclusion and strain in the diamond grits is also much larger than that of synthetic diamond crystals grown by the temperature-gradient method. It has been reported that the FWHMs of the rocking curves of the diamond grits (25–85 as under $\text{MoK}\alpha_1$ radiation) is much wider than those of synthetic type IIa diamond crystals grown by the temperature-gradient method (2–6 as) (Sumiya, Toda, Nishibayashi, et al., 1997). Then, it was attempted to synthesize type IIa diamond crystals with much fewer defects by using high-quality diamond seed cut from large synthetic IIa crystals grown by the temperature-gradient method (Sumiya, Toda, Nishibayashi, et al., 1997). **Figure 11(b)** shows the X-ray topographic image of the synthetic IIa diamond crystal grown on the high-quality seed. It is found that there are very few line defects in the crystals.

Figure 12 shows the FWHMs of the rocking curves of synthetic IIa diamonds (nitrogen concentration <0.1 ppm) grown on the high-quality seeds and on synthetic diamond grit seeds (Toda, Sumiya, Satoh, & Ishikawa, 1997). For comparison, the FWHMs of the rocking curves of synthetic Ib diamonds containing dispersed nitrogen impurities of 60–170 ppm are also plotted in the figure. The FWHMs of type IIa diamonds grown on the high-quality seeds (1–2 as under $\text{MoK}\alpha_1$ radiation) are significantly smaller than those of the type IIa diamonds grown on the diamond grit seeds. The results in **Figure 12** also show that the amount of nitrogen impurity has an influence on the FWHM. The substitutional (P1) nitrogen impurities dilate the diamond lattice, leading to the degradation of crystalline quality (Burns et al., 2009).

These results indicate that the line defects in the grown crystals can be reduced and the crystalline quality can be improved significantly by using high-quality diamond as the seed crystal. Highly resolved rocking-curve measurements using a synchrotron beam have supported these findings. **Figure 13** shows an X-ray projection

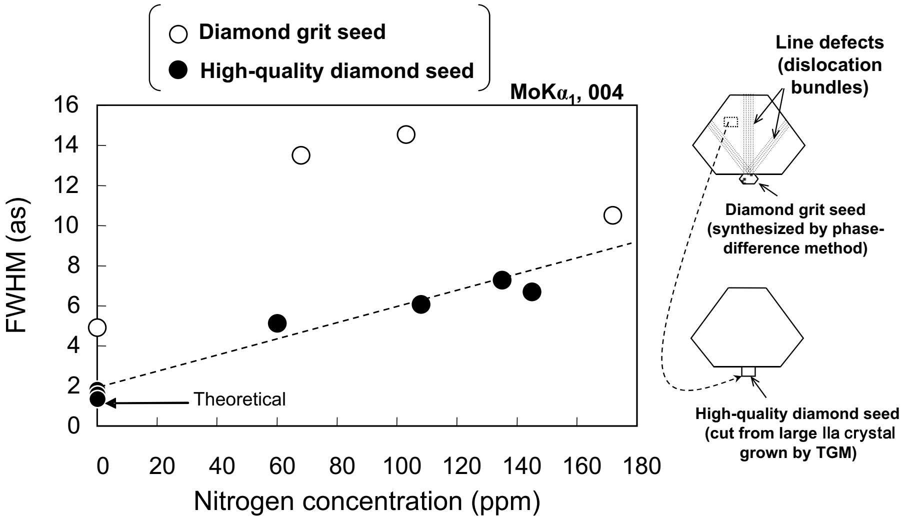

Figure 12 FWHM of X-ray rocking curves of synthetic IIa and Ib diamonds grown on the high-quality seeds and on synthetic diamond grit seeds for the (004) reflection under $\text{MoK}\alpha_1$ radiation.

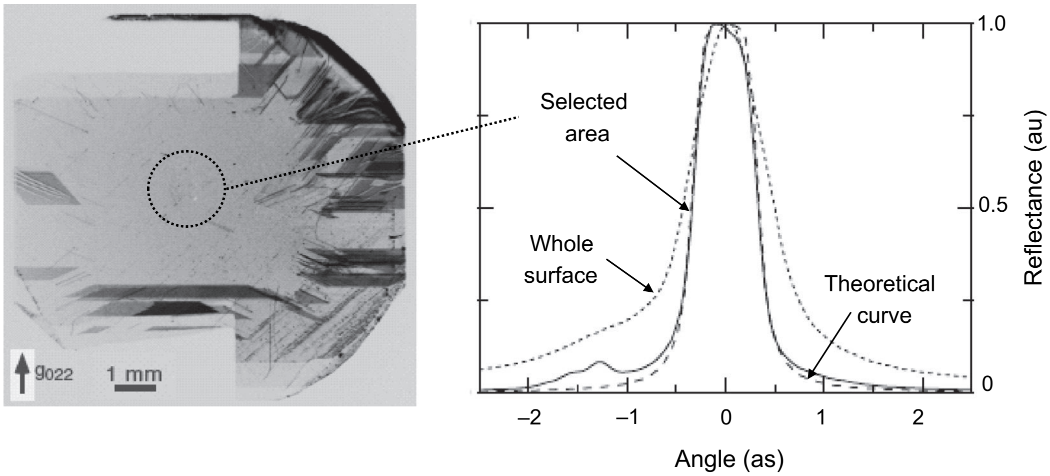

Figure 13 X-ray topograph (left) and highly resolved rocking curves (right) of high-quality large diamond crystals measured at SPring-8 (Tamasaku et al., 2005).

topograph and the double-crystal X-ray rocking curve of the high-quality type IIa diamond plate prepared from a large type IIa diamond crystal (10 mm across) grown on the high-quality seed, measured by using a synchrotron beam (Tamasaku, Ueda, Miwa, & Ishikawa, 2005). The crystal has a large defect-free region at the center ((100) growth sectors), where no dislocation bundles exist. The defects observed in the peripheral region of (111) growth sectors are stacking faults. The rocking curve corresponded with the theoretical one when we chose the defect-free area at the center for the smaller beam size. This indicates that the crystalline quality of this area is almost perfect.

3.09.4 Physical Properties

3.09.4.1 Optical Properties

Figure 14 shows the UV–visible and infrared transmission spectra of the synthetic type IIa diamond with spectra of natural diamonds and synthetic type Ib diamond (Sumiya, Toda, Nishibayashi, et al., 1997). In both spectra, the synthetic type IIa diamond has no absorption bands due to impurities in any wavelength region. The absorption bands seen near 2000 cm^{-1} in the infrared region of synthetic type IIa diamond are due to multiphonon absorption, which is intrinsic to diamond. Natural type Ia and synthetic type Ib diamonds have absorption bands due to nitrogen impurities in aggregated forms and dispersed forms, respectively. Natural type

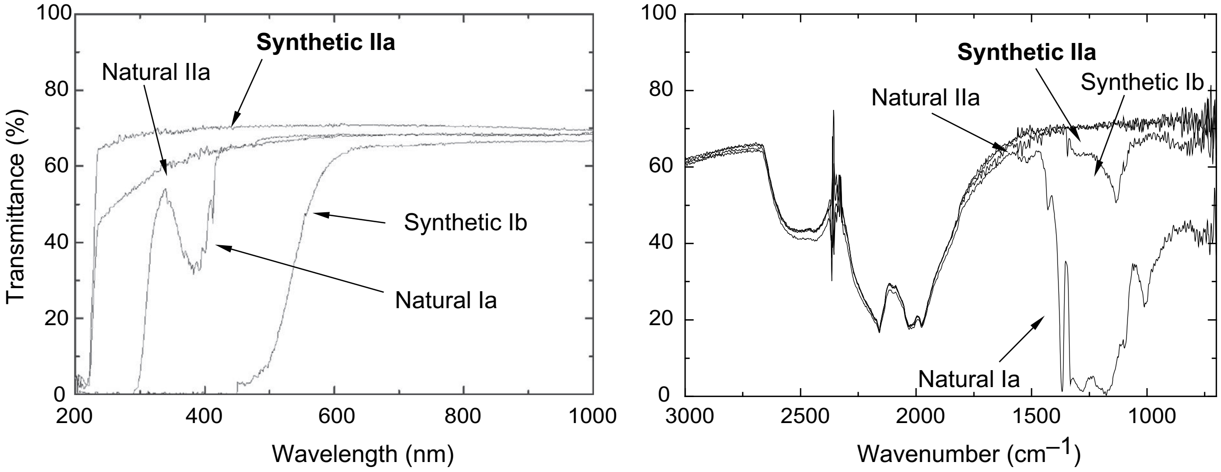

Figure 14 UV–visible (left) and IR (right) transmission spectra of various diamond crystals (thickness; 1.0 mm).

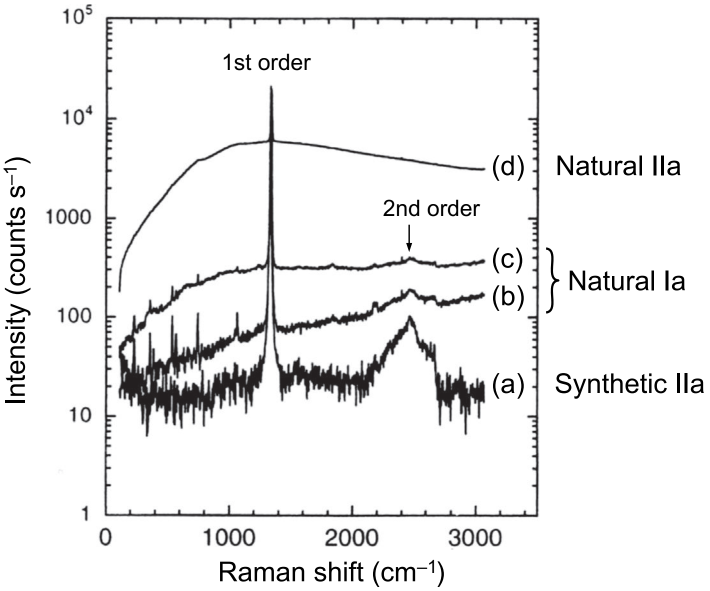

Figure 15 Raman spectra of various diamond crystals: (a) high-quality synthetic IIa, (b, c) natural Ia, and (d) natural IIa (Aoki, 1999).

IIa diamond has a tail or shoulder at the absorption edge of 225 nm. The tail is attributed to strains or defects in the crystal. The synthetic type IIa diamond does not have such a tail at the absorption edge. This indicates that the synthetic type IIa diamond has a high crystalline quality.

In addition, the laser-excited luminescence level of the synthetic type IIa diamond is considerably low. All natural diamonds have various crystal defects and impurities differing from each other, emitting luminescence in varying degrees (Walker, 1979). Conventional synthetic type Ib diamonds also emit luminescence caused by impurities. The high-quality synthetic type IIa diamond without such crystal defects and impurities has almost no luminescence in response to the excitation of visible light lasers such as argon ion lasers for Raman scattering spectroscopy as shown in **Figure 15** (Aoki, 1999).

3.09.4.2 Thermal Properties

Figure 16 shows the thermal conductivities of synthetic diamonds as a function of the concentration of nitrogen impurity (Sumiya, Toda, & Satoh, 1996; Yamamoto et al., 1997). The thermal conductivities of synthetic type IIa diamonds are 22–23 W/cm·K, which is higher than that of type Ib diamond and higher than that of natural

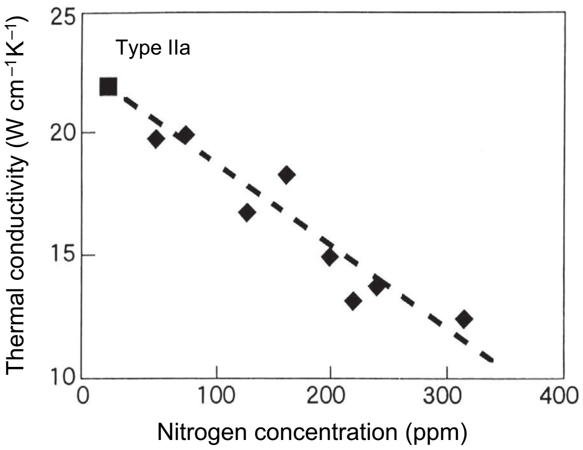

Figure 16 Thermal conductivity of synthetic diamonds as a function of the concentration of nitrogen impurities.

type IIa diamond (20 W/cm·K) as well. Because the synthetic type IIa diamond has very few impurities and few crystal defects that cause phonon scattering, the thermal conductivity is improved compared with that of natural or synthetic type Ib diamond.

3.09.5 Mechanical Properties

Various types of crystal defects, such as impurities, inclusions, or dislocations, are introduced into diamond crystals during growth. Such defects have a significant influence on the mechanical properties of crystals. Although there have been various investigations on the mechanical properties of natural diamond or conventional synthetic type Ib diamond, the essential nature is thought to be not fully understood owing to the existence of the impurities and crystal defects.

The high-quality synthetic type IIa diamond crystals mentioned above have a high crystalline quality with very few crystal defects and little internal strain (Section 3.09.3), being considerably near to the perfect (ideal) crystal. Therefore, information on the mechanical properties of the high-quality synthetic type IIa diamond can allow us to understand the essential mechanical properties of diamonds and also to further clarify the effect of the impurities and defects on the properties of the diamond.

3.09.5.1 Indentation Hardness

The most prominent mechanical property of diamond is its extreme hardness. Then, we will be concerned with the hardness of the high-quality synthetic type IIa diamond. It is known that indentation techniques are the main methods for assessing the hardness of brittle materials. Among the various indentation techniques, the Knoop hardness test is believed to be appropriate for hard and brittle single crystals such as diamonds (Brookes, 1970; Knoop, Peters, & Emerson, 1939).

3.09.5.1.1 Influence of Nitrogen Impurity

Figure 17 shows the Knoop hardness at room temperature (load: 4.9 N) of a high-quality synthetic type IIa diamond in (001)⟨100⟩ (the ⟨100⟩ direction on the (001) plane: henceforth, similar expressions will be employed) plotted against the concentration of nitrogen impurity (Sumiya, Toda, & Satoh, 1997). As can be seen from the figure, the hardness increases with decreasing nitrogen concentrations. Therefore, the synthetic type IIa diamond containing no nitrogen impurity exhibits the highest hardness value among synthetic diamonds. Diamond behaves as a brittle material; however, plastic deformation in diamond can occur even at room temperature under the specific conditions of Knoop indentation (Brookes, 1970; Sumiya, Yamaguchi, & Ogata, 2006). The behavior of such local plastic deformation is affected by the amount and state of impurities. The isolated substitutional nitrogen impurity in synthetic diamond gives rise to local internal stress in the crystal. Such local stress can trigger the inhomogeneous onset of dislocation movements near the Knoop indentation. In this way, the hardness of synthetic diamond decreases with increasing nitrogen concentration. In the synthetic type IIa diamond containing very few impurities, the plastic deformation responsible for the dislocation movement seems to be difficult to occur.

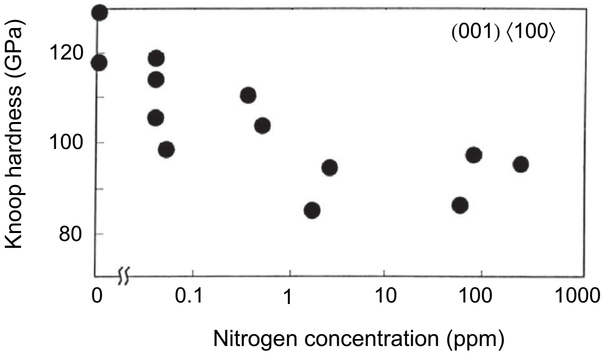

Figure 17 Knoop hardness of synthetic diamond crystals in the ⟨100⟩ directions on the (001) surfaces plotted against the concentrations of nitrogen impurities.

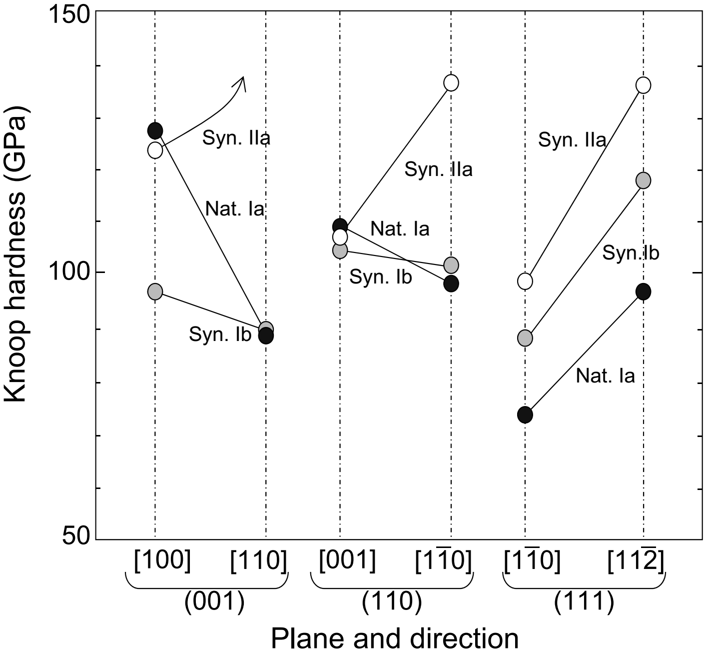

Figure 18 Knoop hardness in each plane/direction of synthetic type IIa, synthetic type Ib, and natural type Ia diamond crystals (load: 4.9 N).

3.09.5.1.2 Anisotropy in Hardness

It is known that the hardness of single crystal diamond has a significant anisotropic feature (Brookes, 1970; Brookes and Brookes, 1991). **Figure 18** shows the Knoop hardness measured on each plane/direction of synthetic type IIa, synthetic type Ib, and natural type Ia diamond crystals (Sumiya, Toda, & Satoh, 1997, 2004). The experimental results indicate that the synthetic type IIa diamond has the highest hardness among existing diamond types.

It is notable that the Knoop hardness in (001)⟨110⟩ of synthetic diamond containing few nitrogen impurities is extremely hard (>140 GPa) such that any normal indentations cannot be formed (Sumiya, Toda, & Satoh, 1997). Namely, the Knoop hardness in (001)⟨110⟩ of the diamond is much higher than that in (001)⟨100⟩. On the contrary, normal cuneiform indentations were formed in (001)⟨110⟩ of synthetic type Ib diamonds containing isolated substitutional nitrogen impurity and of natural type Ia diamonds (Doi, Sato, Sumiya, & Yazu, 1986, p. 233; Sumiya, Toda, & Satoh, 1997).

The anisotropy of the Knoop hardness on (001) plane of the synthetic type IIa diamond shows a conflict with that of natural diamonds and synthetic type Ib diamonds. According to Brookes (1970), the Knoop hardness of natural diamonds in the ⟨100⟩ directions is higher than that in the ⟨110⟩ direction on (001) surfaces. It has been reported that synthetic type Ib diamond also has the same anisotropy in hardness, although the degree of variation is smaller than that in natural diamonds (Doi et al., 1986, p. 233; Sumiya, Toda, & Satoh, 1997). The same tendency can be seen in **Figure 18**. Brookes explained the anisotropy in terms of a resolved shear stress model for the {111}⟨1$\bar{1}$0⟩ slip deformation (Brookes, 1970; Brookes, O'Neill, & Redfern, 1971). Solely the model cannot explain the anisotropy in the Knoop hardness of the synthetic type IIa diamond. The heterogeneous formation of dislocations seems to be almost impossible in the synthetic type IIa diamond containing few impurities or crystal defects, which act as origins of slip deformation. When the Knoop indenter is applied to (001)⟨110⟩, the two indenter facets adjacent to each other share the same {111} slip plane, but their slip directions of ⟨1$\bar{1}$0⟩ are independent. In such a case, the critical value for slip deformations would be extremely high if the diamond has a few impurities or crystal defects that can be origins of the slip deformation.

3.09.5.1.3 Superhard Diamond Indenter

As mentioned above, the resistance to the deformation in synthetic type IIa diamond is considered to be extremely high in (001)⟨110⟩. Hence, a Knoop indenter prepared from the synthetic type IIa diamond by taking the tip orientation to the hard crystal orientation of the diamonds is expected to be extremely rigid and show

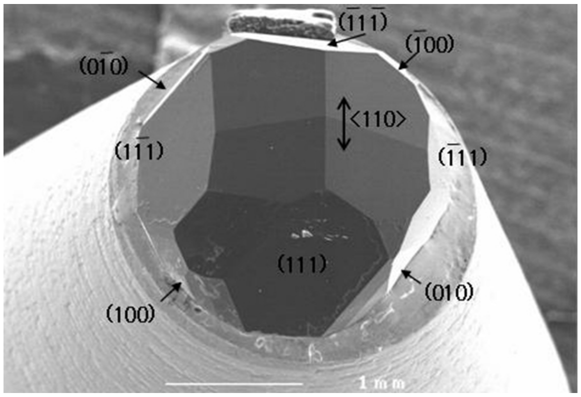

Figure 19 Knoop indenter prepared from synthetic type IIa diamond crystal.

high-performance for indentation hardness tests of superhard materials. Thereupon such Knoop indenters were prepared from the synthetic type IIa diamond crystals (Sumiya, 2005). High-quality type IIa diamond crystals were brazed on diamond holders by adjusting the ⟨001⟩ of the diamonds to the load direction (z-axis). The tips of the diamonds were polished into Knoop indenter shapes (Knoop et al., 1939) by taking the longitudinal direction of the indenter tip in the ⟨110⟩ direction of the diamond crystal. **Figure 19** shows a Knoop indenter prepared in this manner.

To evaluate the durability of the synthetic type IIa diamond (001)⟨110⟩ Knoop indenters (hereinafter referred to as SD (001)⟨110⟩ indenter), indentation tests in various directions on synthetic diamond crystals were carried out using the indenters (Sumiya, 2005). For comparing commercially available natural diamond (type Ia) Knoop indenters (hereinafter referred to as ND indenter) were also used for the evaluation. The longitudinal direction of the ND indenters were nearly parallel to (001)⟨100⟩ of the crystal. The Numerous indentation tests have revealed that SD (001)⟨110⟩ Knoop indenters are unbroken despite performing >200 indentations while ND indenters are easily broken at 1–23 indentations. The large variation in the life duration between ND indenters is due to the diversity of the contents of the impurities or crystal defects, which may be the origin of the destruction. These results indicate that the SD (001)⟨110⟩ indenter is considerably stronger and more stable than the ND indenter. Therefore, the SD (001)⟨110⟩ indenter would be very useful for the hardness measurement of ultrahard materials such as nanopolycrystalline diamonds synthesized by direct conversion under HPHT (Sumiya & Irifune, 2008; Sumiya and Irifune, 2007).

3.09.5.2 Deformation Behavior

3.09.5.2.1 Plastic Deformation at Room Temperature

In some of the previous articles, it has been reported that plastic deformation (generation and multiplication of dislocations) in diamonds can be induced even at room temperature under ultrahigh compressive pressure conditions (>100 GPa) using Knoop indenters (Brookes, 1970; Humble and Hannink, 1978) and high-pressure anvils (Mao and Bell, 1978). In these investigations, natural diamonds were used as specimens. As mentioned in Section 3.09.3, natural diamonds contain considerable internal strain and numerous dislocation defects. Such crystal defects may trigger the onset of dislocation movements. The possibility that the dislocation defects observed by Humble & Hannink, (1978) may have preexisted in the natural diamond crystal before indentation has been pointed out (Wilkes et al., 1991). Wilkes et al. examined a Knoop indentation in detail and observed zigzag-shaped cracks of (111) cleavage, which therefore raised questions concerning plastic deformation at room temperature (Wilkes et al., 1991). Thus, whether plastic deformation in diamond can occur at room temperature or not has been an issue of dispute for a long time. The crystal defects that originally exist in diamonds prevent definitive conclusions regarding this issue.

The synthetic type IIa diamond crystals not only have high purity but they also contain extremely few dislocation defects and little internal strain (Section 3.09.3). Therefore, the possibility of plastic deformation of diamonds at room temperature was examined using synthetic type IIa diamond crystals as samples (Sumiya et al., 2006). Indentations were formed in the ⟨100⟩ direction on the (001) plane of synthetic type IIa diamond crystals using a Knoop indenter with a load of 4.9 N for 15 s at room temperature, and the deformation

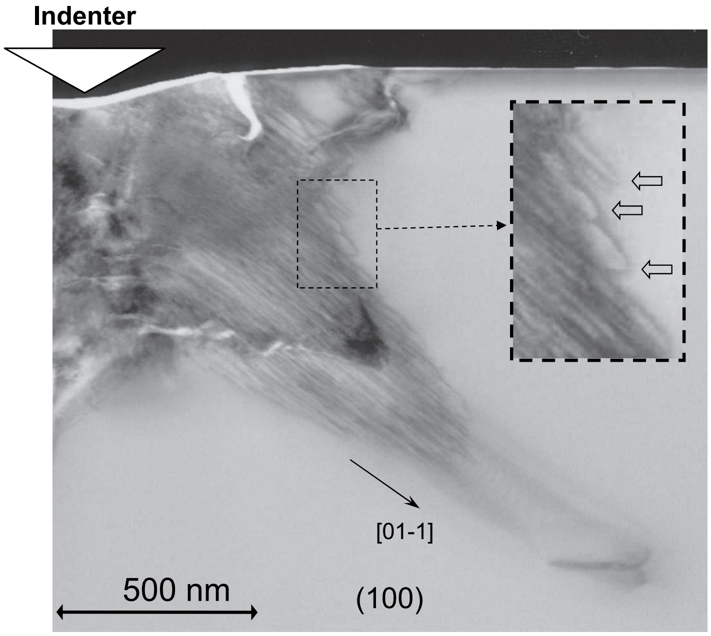

Figure 20 TEM image (bright field) of the microstructure under Knoop indentation formed on (001)⟨100⟩ of synthetic high-purity type IIa diamond crystals at room temperature.

microstructure around the indentations was investigated using a transmission electron microscope (TEM). A thin sample for TEM observation was carved out from the vicinity of the edge area of the indentation using a focused ion beam fabrication. **Figure 20** shows a TEM image (bright field) of the cross-section of the Knoop indentation, observed along the [100] direction. In the area close to the indentation, some fractures and microcracks can be seen. From a point around 500 nm from the indentation, however, many line defects developing 45° downward in the figure are observed clearly. These line defects extend to a depth of about 1 μm. No other defects are seen around these defects. This indicates that this synthetic type IIa diamond crystal originally contained very few defects. Therefore, all these defects around the indentation are apparently newly generated due to deformation during indentation. At the tip of each line defect, loop-like dislocation lines can be seen as indicated by the arrow. The loop-like dislocation lines develop in the $[01\bar{1}]$ direction and lie on the (111) or $(\bar{1}11)$ plane. This observation suggests that plastic deformation ascribed to the (111)⟨110⟩ slip system occurs under Knoop indentation.

Contrast experiments using different diffraction vectors indicated that the dislocation lines have Burgers vectors in the $[01\bar{1}]$ direction (Sumiya et al., 2006). These results indicate that plastic deformation ascribed to the {111}⟨110⟩ slip system occurs under Knoop indentation. Thus, it was clearly confirmed that plastic deformation in diamond is possible even at room temperature, through the observation of microstructures around the Knoop indentation formed on the synthetic type IIa diamond crystal, which has very few dislocations originally.

3.09.5.2.2 Thermally Activated Deformation

As mentioned in Section 3.09.5.1.2, the deformation resistance against a Knoop indentation in (001)⟨110⟩ of a high-quality synthetic type IIa diamond is extremely high at room temperature, and the anisotropy in the Knoop hardness of the synthetic type IIa diamond conflicts with those of natural diamonds and conventional synthetic type Ib diamonds (Sumiya, Toda, & Satoh, 1997). The high-quality synthetic type IIa diamond has very few impurities and defects that act as origins of the heterogeneous formation of dislocations, which leads to the extremely high deformation resistance against Knoop indentation along (001)⟨110⟩. The high deformation resistance is expected to be reduced by applying thermal energy that would induce dislocation generation and mobility, leading to the formation of impressions.

Then, the behavior of deformation in the hard direction activated thermally by heating was investigated, using superhard Knoop indenters prepared from high-quality type IIa diamond crystals by taking the tip orientation to (001)⟨110⟩ described in Section 3.09.5.1.3 (Sumiya, 2005, 2006). Indentation tests in

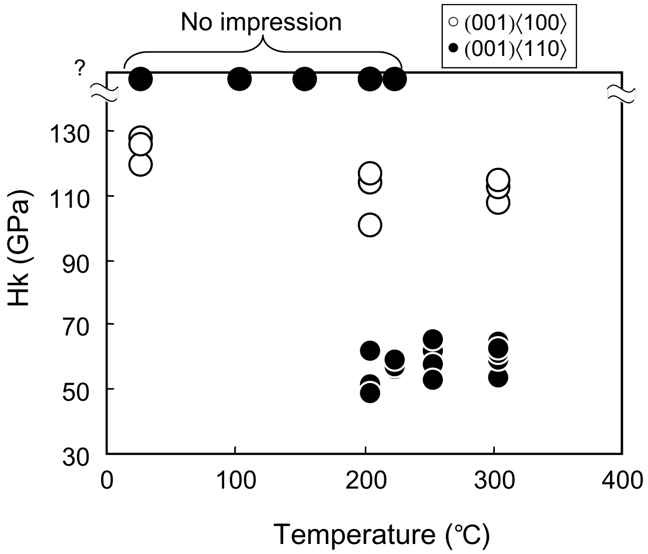

Figure 21 Knoop hardness in (001)⟨100⟩ and (001)⟨100⟩ of synthetic type IIa diamonds at temperatures of RT-300 °C (load: 4.9 N).

(001)⟨110⟩ with a load of 4.9 N revealed that the formation of normal Knoop impressions arises suddenly at a threshold temperature of 200–240 °C, whereas no impressions are observed up to 200 °C. Figure 21 shows the variations of the Knoop hardness in the (001)⟨100⟩ and (001)⟨110⟩ of high-quality type IIa diamond crystals at temperatures ranging from RT to 300 °C. The Knoop hardness in (001)⟨110⟩ decreases rapidly to about 60 GPa from an extremely hard condition (>140 GPa, unable to be measured) at the threshold temperature, whereas the hardness in (001)⟨100⟩ decreases gradually as the temperature rises. The Knoop hardness in the (001)⟨110⟩ of a synthetic diamond crystal at a temperature above the threshold temperature is obviously lower than that in (001)⟨100⟩ at the same temperature.

Figure 22 shows the anisotropy in the Knoop hardness on the (001) plane of the synthetic type IIa diamond at 300 °C with that at RT. The data for a synthetic type Ib diamond are also plotted in the figure for comparison. The anisotropy of synthetic type IIa diamond at 300 °C differs completely from that at RT, showing that the hardness in ⟨110⟩ is lower than that in ⟨100⟩, which corresponds with those of natural diamond and synthetic type Ib diamond at RT (Brookes, 1970; Sumiya, Toda, & Satoh, 1997). The curve of the anisotropy lines up with

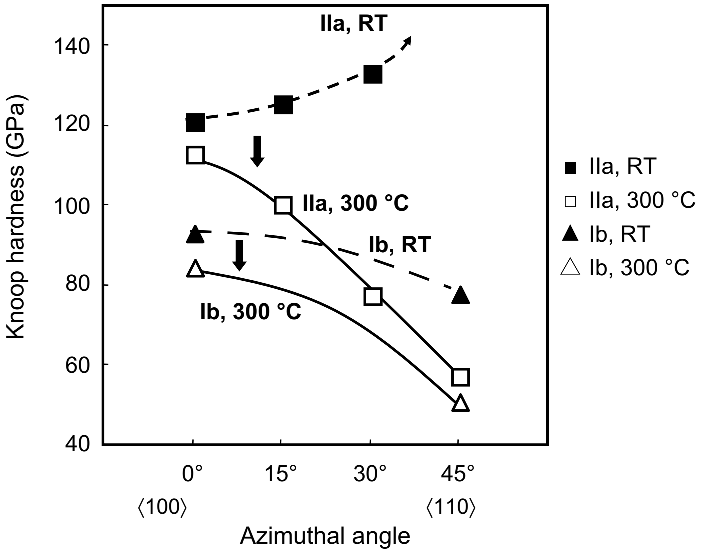

Figure 22 Anisotropy in the Knoop hardness on (001) of synthetic type-IIa diamond at RT and 300 °C (load: 4.9 N).

that calculated on the basis of an effective resolved shear stress of a diamond cubic crystal with {111}⟨110⟩ slip systems (Brookes, 1970; Brookes et al., 1971).

These results suggest that at high temperatures above the threshold temperature the plastic deformation based on the {111}⟨110⟩ slip system occurs even under the Knoop indentation in the (001)⟨110⟩ of the high-quality synthetic type IIa diamond, for which the deformation resistance is extremely high at room temperature. The thermal fluctuations promoted at high temperatures >200–240 °C seem to activate the homogeneous nucleation of dislocations, which trigger the sudden slip deformations against the Knoop indentation along the (001)⟨110⟩ direction. The threshold temperature is influenced by the concentration of nitrogen impurities (Sumiya, 2006). The mean effective resolved shear stress, calculated for the (001) diamond plane beneath the Knoop indenter assuming {111}⟨110⟩ slip systems, is maximum when the indenter is aligned along the (001)⟨110⟩ direction (Brookes et al., 1971). Therefore, once the slip deformations are activated, the deformation by the Knoop indentation along these directions progress rapidly.

3.09.5.2.3 Optical Behavior Due to Plastic Deformation

It was identified that plastic deformation formed around Knoop indentations on the surface of a high-quality synthetic type diamond crystal with few crystal defects, verifying that plastic deformation can occur even at room temperature as mentioned in Section 3.09.5.2.1. Plastic deformation of diamond at room temperature is known to occur also when super-high pressure of about 200 GPa is applied to diamond crystals positioned as anvils (Eremets et al., 2005; Mao and Bell, 1978; Sumiya, Nakamoto, Matsuoka, Shimizu, & Ohishi, 2008).

The optical behavior around the plastically deformed area (culet center) of the diamond anvil made of high-quality synthetic type IIa diamond crystals has been investigated by cathodoluminescence spectroscopy (Sumiya, Nakamoto, Shimizu, & Kanda, 2008). The experimental results revealed that the free exciton peaks weaken while the A-band and 2BD bands appear at the culet center where plastic deformation occurred. The A-band and 2BD bands are known centers observed in type IIa diamond having dislocation defects (Hanley, Kiflawi, & Lang, 1997; Kanda, Ahmadjan, & Kitawaki, 2005; Kanda and Watanabe, 2004). It was also found that the free exciton peaks near the edge of the culet shift to the long wavelength side as shown in Figure 23. This indicates that the band structure of the peripheral areas of the culet changes because of residual strain caused by the plastic deformation in the culet center. Naka et al. reported that the degeneration in the conduction band of

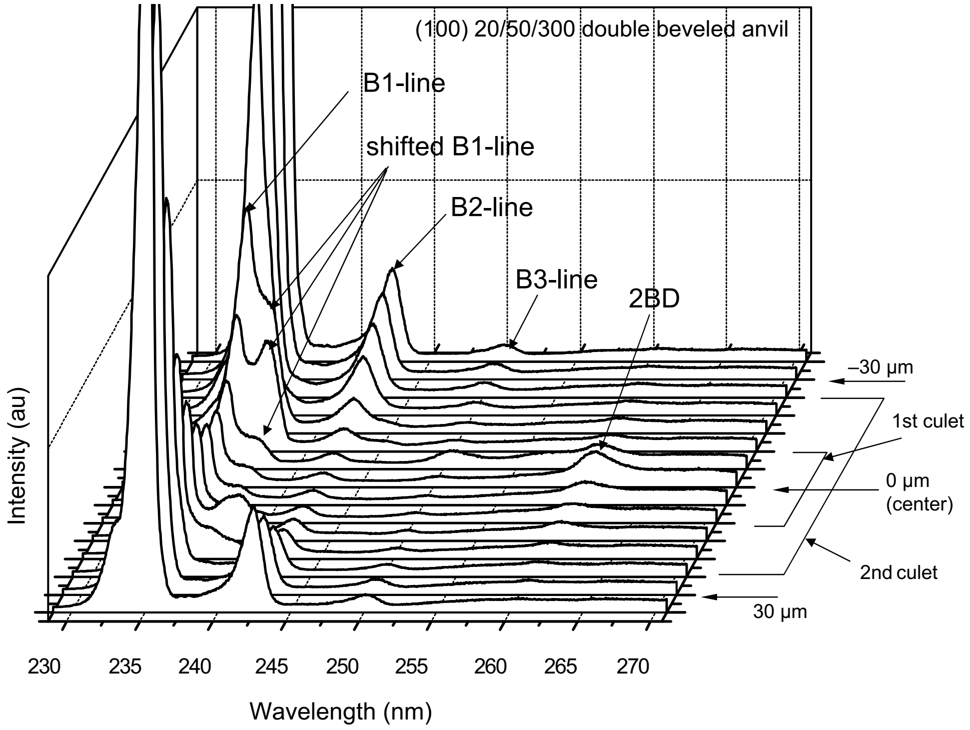

Figure 23 Cathodoluminescence spectra of the culet surface of the synthetic type IIa diamond anvil after the high-pressure generation up to 210 GPa (5-μm intervals).

diamond unfolded and lowered the exciton level by about 10 meV when a stress of 1.1 GPa was applied to high-quality synthetic diamond in the [011] direction (Naka, Omachi, & Kuwata-Gonokami, 2007). Based on their results, it is reasonable to assume that there was a residual stress of 5–10 GPa around the culet of the diamond anvil in the study. These findings were able to be achieved by using high-quality synthetic type IIa diamond crystals with minimal crystal defects.

3.09.6 Applications

The high-quality synthetic type IIa diamond has a high crystalline quality (Section 3.09.3) and excellent properties (Sections 3.09.4 and 3.09.5). These salient characteristics of the high-quality diamond permit the application to a wide range of industrial and scientific uses (Sumiya, Satoh, & Yazu, 1998; Sumiya et al., 2005). In this section, we present some examples of the particularly useful and notable applications of the high-quality diamond originating from its distinctive features.

3.09.6.1 Monochromators

The most distinctive application of the high-quality large diamond is as a monochromator crystal for a synchrotron X-ray radiation beam. The high-quality synthetic type IIa diamond in which impurities and defects have been controlled has a consistently very high crystalline quality (Section 3.09.3). The measured X-ray rocking-curve width is close to the theoretical one. This indicates that the synthetic IIa diamonds are very useful as X-ray monochromators for high power synchrotron radiation beams (Burns et al., 2009; Tamasaku et al., 2005). A large diamond plate shown in **Figure 7** (right) is an example for monochromators prepared from large high-quality diamonds. Some high-quality synthetic diamond monochromators have been installed at SPring-8 and other synchrotron facilities.

3.09.6.2 High-Pressure Anvils

Diamond crystals have been used as anvils for the generation of ultrahigh pressure. Diamond anvils are utilized for studying material science, condensed matter physics, geophysics, and so on. Natural diamond crystals have been employed for anvils but there are limitations pertinent to stability, attainable pressure, lifetime, and luminescence because of crystal defects or diversity of quality. High-quality synthetic type IIa diamond crystals show no absorption in wide-ranging wavelengths and have few crystal defects and nominal internal strain, which may be the origin of destruction or deformation. Actually, the synthetic type IIa diamond has a higher resistance to plastic deformation as mentioned in Section 3.09.5.1. In addition, synthetic diamond has very low luminescence in response to the excitation of ultraviolet or visible light lasers (Section 3.09.4.1). The low luminescence of diamond anvils permits us to measure Raman scattering spectra precisely under high pressure. Consequently, high-quality synthetic type IIa diamond crystals are very useful as high-pressure diamond anvils.

3.09.6.3 Optical Parts

Synthetic type IIa diamond is transparent over a wide range of wavelengths from ultraviolet to far infrared regions (Section 3.09.4.1). Because of its excellent optical transmission properties, coupled with diamond properties of high strength and excellent chemical stability, synthetic type IIa diamond is a very useful material in optical applications for infrared rays or laser lights. Some optical parts for FT-IR spectroscopy using synthetic type IIa diamond, such as sample plates, compression cells and attenuated total reflection prisms, have been produced. The synthetic type IIa diamond is also useful for optical windows exposed to special harsh or hostile environments, for example, a window for high-pressure vessels for chemical investigations, or for planetary probes.

3.09.6.4 Others

Since high-quality synthetic type IIa diamonds have very few impurities and few crystal defects that cause the inhomogeneous formation of internal stress and phonon scattering, the mechanical and physical properties are greatly improved compared with those of natural diamonds or conventional synthetic type Ib diamonds

(Sections 3.09.4 and 3.09.5). Therefore, the use of synthetic type IIa diamond may lead to an improvement in the performance characteristics and the reliability of conventional diamond products such as high-precision cutting tools, wear-resisting tools, and heat sinks.

Besides, high-quality synthetic diamonds are very useful for various scientific purposes, such as specimens for the determination of essential diamond properties, raw materials for the studies of crystallography, and reference materials for various kinds of analysis (Naka et al., 2009; Sumiya et al., 2006). They are also used as substrata for CVD diamond epitaxial growth, specimens for positron annihilation experiments (Tang et al., 1998), detectors for neutron radiation (Tanaka et al., 2001), and so on.

References

Aoki, K. (1999). *The Review of High Pressure Science and Technology, 9*, 270.

Bibby, D. M. (1982). Impurities in natural diamond. *Chemistry and Physics of Carbon, 18*, 1.

Black, D. R., Burdette, H. E., & Banholzer, W. (1993). X-ray diffraction imaging of man-made and natural diamond. *Diamond and Related Materials, 2*, 121–125.

Brookes, C. A. (1970). Plastic deformation and anisotropy in the hardness of diamond. *Nature, 228*, 660.

Brookes, C. A., & Brookes, E. J. (1991). Diamond in perspective: a review of mechanical properties of natural diamond. *Diamond and Related Materials, 1*, 13–17.

Brookes, C. A., O'Neill, J. B., & Redfern, B. A. W. (1971). Anisotropy in the hardness of single crystals. *Proceedings of the Royal Society of London, Series A, 322*, 73.

Burns, R. C., Chumakov, A. I., Connell, S. H., Dube, D., Godfried, H. P., Hansen, J. O., et al. (2009). HPHT growth and x-ray characterization of high-quality type IIa diamond. *Journal of Physics Condensed Matter, 21*, 364224.

Burns, R. C., Cvetkovic, V., Dodge, N., Evans, D. J. F., Rooney, M. L., Spear, P. M., et al. (1990). Growth-sector dependence of optical features in large synthetic diamonds. *Journal of Crystal Growth, 104*, 257.

Burns, R. C., Hansen, J. O., Spits, R. A., Sibanda, M., Welbourn, C. M., & Welch, D. L. (1999). Growth of high purity large synthetic diamond crystals. *Diamond and Related Materials, 8*, 1433–1437.

Doi, Y., Sato, S., Sumiya, H., & Yazu, S. (1986). Hardness of synthesized diamond crystals. *Inst. phys. conf. ser. no.75: C3, paper presented at 2nd int. conf. science hard mater., Rhodes,* 233.

Eremets, M. I., Trojan, I. A., Gwaze, P., Huth, J., Boehler, R., & Blank, V. D. (2005). The strength of diamond. *Applied Physics Letter, 87*, 141902.

Frank, F. C., & Lang, A. R. (1990). Orientation-dependent nitrogen incorporation on vicinals on synthetic diamond cube growth surfaces. *Journal of Crystal Growth, 100*, 354–376.

Hanley, P. L., Kiflawi, I., & Lang, A. R. (1977). On topographically identifiable sources of cathodoluminescence in natural diamond. *Philosophical Transactions of the Royal Society London, Series A, 284*, 329–368.

Hara, A. (1985). *Seimitsu Kikai, 51*, 1497 (in Japanese).

Harrison, E. R., & Tolansky, S. (1964). Growth history of a natural octahedral diamond. *Proceedings of the Royal Society, Series A, 279*, 490–496.

Humble, P., & Hannink, R. H. J. (1978). Plastic deformation of diamond at room temperature. *Nature, 273*, 37.

Kaiser, W., & Bond, W. L. (1959). Nitrogen, a major impurity in common type I diamond. *Physical Review, 115*, 857.

Kanda, H., Ahmadjan, A., & Kitawaki, H. (2005). Change in cathodoluminescence spectra and images of type II high-pressure synthetic diamond produced with high pressure and temperature treatment. *Diamond and Related Materials, 14*, 1928–1931.

Kanda, H., & Watanabe, K. (2004). Change of cathodoluminescence spectra of natural diamond with HPHT treatment. *Diamond and Related Materials, 13*, 904–908.

Knoop, F., Peters, C. G., & Emerson, W. B. (1939). A sensitive pyramidal-diamond tool for indentation measurements. *Journal of Research of the Natural Bureau of Standards, 23*, 39–61.

Lang, A. R. (1967). Causes of birefringence in diamond. *Nature, 213*, 248–251.

Lang, A. R. (1979). In J. E. Field (Ed.), *The properties of diamond.* London: Academic Press.

Lang, A. R., Kowalski, G., & Makepeace, A. P. W. (1991). On long-range lattice perfection in natural type Ia diamond. *Philosophical Magazine A, 64*, 543–560.

Lang, A. R., Moor, M., Makepeace, A. P. W., Wierzchowski, W., & Welbourn, C. M. (1991). On the dilation of synthetic type 1b diamond by substitutional nitrogen impurity. *Philosophical Transactions of the Royal Society London A, 337*, 497–520.

Lang, A. R., Moore, M., & Walmsley, J. C. (1992). In J. E. Field (Ed.), *The properties of natural and synthetic diamond.* London: Academic Press.

Macrander, A. T., Krasnicki, S., Zhong, Y., Maj, J., & Chu, Y. S. (2005). Strain mapping with parts-per-million resolution in synthetic type Ib diamond plates. *Applied Physics Letter, 87*, 194113.

Mao, H. K., & Bell, P. M. (1978). High-pressure physics: sustained static generation of 1.36 to 1.72 megabars. *Science, 200*, 1145–1147.

Moore, M. (1988). X-ray studies of the growth of natural diamond. *Industrial Diamond Review, 48*, 59.

Naka, N., Omachi, J. T., & Kuwata-Gonokami, M. (2007). Suppressed formation of electron–hole droplets in diamond under a strain field. *Physical Review B, 76*, 193202.

Naka, N., Omachi, J., Sumiya, H., Tamasaku, K., Ishikawa, T., & Kuwata-Gonokami, M. (2009). Density-dependent exciton kinetics in synthetic diamond crystals. *Physical Review B, 80*, 035201.

Satoh, S., Sumiya, H., Tsuji, K., & Yazu, S. (1990). In S. Saito, O. Fukunaga, & M. Yoshikawa (Eds.), *Difference in nitrogen concentration and aggregation among (111) and (100) growth sectors of large synthetic diamonds, science and technology of new diamond.* Tokyo, Japan: KTK.

Strong, H. M., & Chrenko, R. M. (1971). Further studies on diamond growth rates and physical properties of laboratory-made diamond. *Journal of Physical Chemistry, 75*, 1838–1843.

Sumiya, H. (2005). Super-hard diamond indenter prepared from high-purity synthetic diamond crystal. *Review of Scientific Instruments, 76*, 026112.

Sumiya, H. (2006). Thermally activated deformation under Knoop indentations in super-hard directions of high-quality synthetic type IIa diamond crystals. *Diamond and Related Materials, 15*, 1576–1579.

Sumiya, H. (2010). High-pressure synthesis and properties of high-quality large diamond crystal. *The 4th international conference on New Diamond and Nano Carbons (NDNC 2010),* P.96.

Sumiya, H., & Irifune, T. (2004). Indentation hardness of nano-polycrystalline diamond prepared from graphite by direct conversion. *Diamond and Related Materials, 13*, 1771–1776.

Sumiya, H., & Irifune, T. (2007). Hardness and deformation microstructures of nano-polycrystalline diamonds synthesized from various carbons under high pressure and high temperature. *Journal of Materials Research, 22*, 2345–2351.

Sumiya, H., & Irifune, T. (2008). Microstructure and mechanical properties of high hardness polycrystalline diamonds. *SEI Technical Review, 66*, 85–92.

Sumiya, H., Nakamoto, Y., Matsuoka, T., Shimizu, K., & Ohishi, Y. (2008). High-pressure generation using high-purity synthetic type IIa diamond anvils. *High Pressure Research, 28*, 217–223.

Sumiya, H., Nakamoto, Y., Shimizu, K., & Kanda, H. (2008). Plastic deformation and optical behavior of high-purity synthetic diamond crystal subjected to high stress load at room temperature. *Applied Physics Letters, 93*, 101915.

Sumiya, H., & Satoh, S. (1996). High pressure synthesis of high purity diamond crystal. *Diamond and Related Materials, 5*, 1359–1365.

Sumiya, H., Satoh, S., Nishibayashi, Y., & Goda, Y. (1995). Development of high-purity synthetic diamonds. *Sumitomo Electric Technical Review, 39*, 69–73.

Sumiya, H., Satoh, S., Tsuji, K., & Yazu, S. (1990). *31st high pressure conf. Japan, programme and abstracts* (pp. 48–49, in Japanese).

Sumiya, H., Satoh, H., & Yazu, S. (1998). High-quality synthetic diamond crystal. *Review of High Pressure Science and Technology, 7*, 960–965.

Sumiya, H., Toda, N., Nishibayashi, Y., & Satoh, S. (1997). Crystalline perfection of high purity synthetic diamond crystal. *Journal of Crystal Growth, 178*, 485–494.

Sumiya, H., Toda, N., & Satoh, S. (1996). *Special Issue of The Review of High Pressure Science and Technology, 5*, 233 (in Japanese).

Sumiya, H., Toda, N., & Satoh, S. (1997). Mechanical properties of synthetic type IIa diamond crystal. *Diamond and Related Materials, 6*, 1841–1846.

Sumiya, H., Toda, N., & Satoh, S. (2002). Growth rate of high-quality large diamond crystals. *Journal of Crystal Growth, 237-239*, 1281–1285.

Sumiya, H., Toda, N., & Satoh, S. (2005). Development of high-quality large synthetic diamond crystals. *SEI Technical Review, 60*, 10–16.

Sumiya, H., Yamaguchi, K., & Ogata, S. (2006). Deformation microstructure of high-quality synthetic diamond crystal subjected to Knoop indentation. *Applied Physics Letters, 88*, 161904.

Tamasaku, K., Ueda, T., Miwa, D., & Ishikawa, T. (2005). Goniometric and topographic characterization of synthetic IIa diamonds. *Journal of Physics D: Applied Physics, 38*, A61–A66.

Tanaka, T., Kaneko, J., Takeuchi, D., Sumiya, H., Katagiri, M., Nishitani, T., et al. (2001). Diamond radiation detector made of an ultrahigh-purity type IIa diamond crystal grown by high-pressure and high-temperature synthesis. *Review of Scientific Instruments, 72*, 1406–1410.

Tang, Z., Hasegawa, M., Chiba, T., Saito, M., Sumiya, H., Kawazoe, Y., et al. (1998). Electron momentum distributions in elemental semiconductors probed by positrons. *Physical Review B, 57*, 12219–12228.

Toda, N., Sumiya, H., Satoh, S., & Ishikawa, T. (1997). High-quality synthetic diamond for the monochromator of synchrotron radiation beams. *Proceedings of SPIE, 3151*, 329–336.

Tolansky, S. (1966). Birefringence of diamond. *Nature, 211*, 158.

Wakatsuki, M. (1966). New catalyst for synthesis of diamond. *Japanese Journal of Applied Physics, 5*, 337.

Walker, J. (1979). Optical absorption and luminescence in diamond. *Reports on Progress in Physics, 42*, 1605–1659.

Wentorf, R. H., Jr (1971). Some studies of diamond growth rates. *Journal of Physical Chemistry, 75*, 1833–1837.

Wierzchowski, W., Moore, M., & Makepeace, A. P. W. (1991). X-ray topograhic studies and measurement of lattice parameter difference with in synthetic diamonds grown by reconstitution technique. *Journal of Crystal Growth, 114*, 209–227.

Wilks, J., & Wilks, E. (1991). *Properties and applications of diamond*. Oxford: Butterworth-Heinemann Ltd.

Woods, G. S., & Lang, A. R. (1975). Cathodoluminescence, optical absorption and x-ray topographic studies of synthetic diamond. *Journal of Crystal Growth, 28*, 215–226.

Yamamoto, Y., Imai, T., Tanabe, K., Tsuno, T., Kumazawa, T., & Fujimori, N. (1997). The measurement of thermal properties of diamond. *Diamond and Related Materials, 6*, 1057–1061.

3.10 Ultrafast Deposition of Diamond by Plasma-Enhanced CVD

Alix Gicquel, François Silva, Catherine Rond, Nadira Derkaoui, Ovidiu Brinza, Jocelyn Achard, Guillaume Lombardi, Alexandre Tallaire, Armelle Michau, Maxime Wartel, and Khaled Hassouni, Laboratoire des Sciences des Procédés et des Matériaux (LSPM), UPR3407 CNRS, Université Paris 13, France; Laboratoire d'Excellence Sciences and Engineering for Advanced Materials and devices (SEAM), Villetaneuse, France

Glossary

Actinometry Actinometry is a technique to access relative species density provided the emission intensity ratio of an excited state of the species of interest and an actinometer. The actinometer must present an electron excitation cross-section proportional to that of the species of interested and an excitation threshold similar to that of the species.

Nomenclature

D Diffusion coefficient ($m^2\ s^{-1}$)
$[H]_s$ Mole concentration at surface (mol cm^{-3})
I Intensity (Arb. Units)
k Boltzmann constant ($m^2\ kg\ s^{-2}\ K^{-1}$)
$k_{a,exc}$ Excitation rate constant of a radiative state a
k_s Kinetic rate constant at surface ($cm^3\ mol^{-1}\ s^{-1}$/$cm^6\ mol^{-2}\ s^{-1}$)
m_s Mass of species (kg)
n Density (cm^{-3} or m^{-3})
N Concentration (mol cm^{-3})
Q Rate constant for collisional quenching
R_H H volume loss rate (s^{-1})
R_{SH} Total H-atom surface consumption (s^{-1})
r_{s-wall} Rate of production due to surface processes ($m^{-2}\ s^{-1}$)
t Time (s)
T_e Electron temperature (K)
T_{gmax} Maximum plasma temperature (K)

http://dx.doi.org/10.1016/B978-0-08-096527-7.00047-7

T_∞ Maximum plasma temperature (K)
T_s Substrate surface temperature (K)
T_w Wall surface temperature (K)
u Gas velocity (m s^{-1})
v_s^* Thermal velocity (m s^{-1})
V_b Bohm velocity (m s^{-1})
W_s Mass production rate (kg m^{-3} s^{-1})
x Mole fraction
Y_S Mass fraction
Z Position (M)
δ_T Thermal boundary layer thickness (M)
δ_H Chemical boundary layer thickness (M)
ρ Density (kg m^{-3})
ν Frequency of the radiative de-excitation (s^{-1})
γ Recombination/de-excitation coefficient
T Characteristic time (s)
τ_{diff} Diffusion characteristic time (s)
τ_{volRec} Volume consumption characteristic time (s)

3.10.1 Introduction

The answer to the question "how can we deposit diamond of very high purity/high quality at ultrahigh growth rate by chemical vapor deposition (CVD)" can be expressed in very simple words: just produce as much as possible hydrogen atoms in a very clean system, and prevent their loss until they get to the growing surface!

Growing diamond at high growth rate is linked to the ability in producing a large amount of hydrogen atoms into the gas phase, and in transporting them up to the diamond surface. It is also related to the ability in managing thermal transfers and hydrocarbon (HC) introduction, and in keeping high the deposition environment cleanness. Microwave (MW) cavity-based reactors of 2.45 GHz, with their capability in coupling up to 6 kW power in a plasma volume varying from 10 to 100 cm^3, are today, most of the time, the favorite reactors to grow 2 in in diameter high-purity polycrystalline thick diamond films or thick single-crystal films. Typical growth rates of 2–5 μm h^{-1} are currently reported although up to 70 μm h^{-1} has been obtained in Laboratoire des Sciences des Procédés et des Matériaux (LSPM) for a single crystal containing <0.2 ppb of nitrogen in this kind of reactors.

To evaluate a reactor's efficiency, other criteria such as the area onto which diamond is deposited or the uniformity of the films must be taken into account. Since diamond deposition is mainly H-atom diffusion limited, the area onto which diamond is deposited as well as the thickness uniformity are directly related to the ability in producing a uniform hydrogen-atom density at the growing diamond surface. Thus, thin polycrystalline films are commonly grown over very large areas in hot filament reactors (HF reactors) (Matsumoto, Kobayashi & Hino, 1987) since adapted filament networks can be designed and mastered to ensure a good uniformity (Lin et al.). However, typical growth rates are not far from 1 μm h^{-1}, and the purity of the films cannot equal that obtained in plasma reactors.

In MW cavity-based reactors, the area onto which diamond can be deposited is defined by the MW wavelength (Sevillano et al., 1998; Tachibana et al., 2000). Decreasing the frequency down to 915 MHz (or even less) provides an alternative to increase up to 6 in (or even more) the maximum deposition diameter (Grotjohn, Liske, Hassouni, & Asmussen, 2005; Ralchenko et al., 1997; Schelz et al., 1998).

Others reactors (Gicquel, 1996) that are able to grow diamond at high growth rate have been developed such as combustion flame (Hirose & Kondo, 1988), high-velocity MW torch (Mitsuda, Tanaka, & Yoshida, 1990;), atmospheric radiofrequency (RF) plasma torch (Girshick, 1988; Gordon, Owano, Kruger, & Cappelli, 1989; Yu & Girshick, 1994a) as well as arc jet (Loh & Cappelli, 1992; Lu, Heberlien, & Pfender, 1992b). Thus, arc plasma torch were seen to provide growth rate up to 100 μm h^{-1} even over a 30 mm in diameter substrate. In addition, reduced pressure RF or MW plasmas operating at high flow were also interesting although a strong nonuniformity in thickness has been reported. Let us also mention that the magnetized high-power arc plasma torch developed by the NORTON company in collaboration with Technion company in the 1990s are able to produce at an industrial level large diamond wafers for mechanical applications (Gray & Windischmann, 1999; Woodin et al., 1991). Except for the arc jet, these systems were unable to reach the high-purity level required for single crystals. As far as the 60 to 600 hPa arc-jet is concerned, although very attractive for the diamond quality/purity associated to very high growth rates (200 to 2 μm h^{-1} for areas varying from 0.02 to 11 cm^2) (Ohtake, Tokura, Kuriyama, Mashino, & Yoshikawa, 1989), the too small deposition area and/or the difficulty in controlling the system have limited its use. To the contrary, MW cavity-based reactors are easy to control (cleanness, gas purity, deposition area, substrate temperature…) and can operate at relatively low flow rate which make them attractive for growing high-purity/high-quality diamond single crystals (Achard et al., 2007; Bachmann & van Enckevort, 1992), as well as polycrystalline films.

Although most of the answers to the question of how growing diamond at ultrahigh rate have been already discussed by Goodwin (1993a, 1993b), our goal here is to provide experimental and theoretical quantitative evidences on the mechanisms that drive the operation of MW plasma reactor and to show how MW plasma reactors can be improved. We will analyze the possibility to push forward the limits of conventional 2.45 GHz excited MW plasma reactors, largely used in the diamond community. To be able to draw conclusions, a restricted frame of conditions will be taken into account. Thus, we will consider that growth occurs on a defined (100) diamond crystal. The effects of simultaneous increase in power coupled to the plasma and pressure (i.e. the power density (in W cm^{-3})), methane addition, duty cycle when using pulsed plasma and argon addition on the driving parameters such as gas temperature and key species densities, and their spatial distributions, the chemical processes, and the mass and thermal diffusivities, will be discussed. The effects of the local parameters on the growth rates will be shown. The results obtained at LSPM (formerly LIMHP (Laboratoire d'Ingénierie des Matériaux et des Hautes Pressions)) will be compared in particular with those obtained at the University of Bristol (theoretical and experimental values) and by David Goodwin through simulation in the 1990s.

In this chapter, nothing will be said about the question of crystalline quality, in particular on dislocations, although it is the main bottlenecks to be solved today to develop high-power electronic devices.

This chapter is divided into five sections. After an introduction (Section 3.10.1), Section 3.10.2 is dedicated to positioning the problem in order to grow ultrafast diamond. The purpose of Section 3.10.3 is to describe the two main tools on which our work is based: the plasma model and the spectroscopic diagnostics. Furthermore, a review of the main diagnostics used to study the diamond deposition reactors is provided. In Section 3.10.4, experimental measurements and theoretical results are given allowing us to analyze the plasma behavior and to determine the main local parameters and processes responsible for the production and loss of the active species, i.e. the H atoms and the CH_3 radicals. Finally, before concluding, Section 3.10.5 reports the main actions that one can use to increase growth rates. A word will be said on the possibility to increase the deposition area.

3.10.2 Growth Rate and Active Species

Under moderate pressures typically used in MW and HF reactors, it is now largely accepted by the community that H atoms and CH_3 radicals constitute the main governing species for growing polycrystalline and single-crystal diamond layers (Frenklach & Spear, 1988; Harris, 1990; Harris & Weiner, 1993). On (100) diamond faces, the simplified growth model proposed by Harris and Goodwin in the 1990s has been seen to relatively well describe reality:

$$C_dH + H \rightarrow C_d^{\bullet} + H_2 \tag{1}$$

$$C_d^{\bullet} + H \rightarrow C_dH \tag{2}$$

$$C_d^{\bullet} + CH_3 \rightarrow C_dCH_3 \tag{3}$$

$$C_dCH_3 \rightarrow C_d^{\bullet} + CH_3 \tag{4}$$

$$C_dCH_3 + H \rightarrow C_dCH_2 + H_2 \tag{5}$$

$$C_dCH_2 + C_d + H \rightarrow C_dH + C_d + H_2 \tag{6}$$

A rather simple growth law, valid for CH_3 radical and H-atom densities in the range of $[3 \times 10^{-10}, 10^{-5}]$ mol cm^3 and $[10^{-11}, 10^{-6}]$ mol cm^3, respectively, has been deduced from this model (Goodwin, 1993a).

$$\text{Growth rate } = k(T_s)([CH_3]_s\,[H]_s/(5 \times 10^{-9} + [H]_s)) \tag{7}$$

where $k(T_s) = 1.8 \times 10^{11}$ assuming a methyl radical coverage of 0.2 (Goodwin, 1993a) at $T_s = 1200$ K (and 1.35×10^{11} at 1100 K), and $[H]_s$ and $[CH_3]_s$ are the surface concentrations of H-atom and CH_3-radical (in mol cm^{-3}), respectively.

From Eqn (7), it comes that to increase growth rate, one can act on either increasing the surface H-atom density or increasing the surface CH_3-radical density, either on increasing both simultaneously.

To estimate the best way to improve growth rates, one must identify not only how and where H atoms and CH_3 radicals are produced into the gas phase but once they are produced, how they can be lost in the gas phase and how they are transported to the diamond surface. Thus, one must be concerned by the species production, which is related to the precursors used and the kinetics dynamics, i.e. the plasma conditions, and by the transport of the species to the surface. One must identify the processes, if any, able to consume the key species before their arrival to the surface. The governing parameters of these processes must be identified in order to reduce their effects.

The capability in increasing the H-atom and CH_3-radical densities (or fluxes) at the surface proceeds from the understanding of the chemical processes occurring into the plasma and at the plasma/surface interface which constitutes the engine of production of the key species. Transportation of the species to the surface must also be well mastered.

The next section is dedicated to the means necessary to study the H-atom and CH_3-radical production and loss into the plasma, and their transport toward the surface.

3.10.3 Means for Studying the Plasma: Modeling and Optical Diagnostics

3.10.3.1 How does a Plasma Work under Typical Diamond Deposition Conditions?

HC-containing plasmas used for diamond deposition and studied here work under moderate-pressure conditions in a MW cavity coupling-based reactor (**Figure 1**) (Gicquel, 1996; Glass, Williams, & Davis, 1988; Hassouni et al., 2010). The gas activation is provided via an electrical discharge that results from stationary waves formed between an antenna and a cavity, or between an applicator and a cavity.

In these systems, some seed electrons present in the reduced gas pressure in the MW cavity are heated by the high-frequency (HiF) electric field of the excitation wave. Collisions with the feed gas species result in the transfer of the energy they gain from the electromagnetic (EM) field to the heavy species (hs) of the gas. With high-enough electron energy, reactive processes can occur, especially ionization and dissociation. As a result, electron multiplication takes place and other species such as atoms, ions and radicals are produced. Therefore, the plasma is an ionized reactive multicomponent medium with active species that interact with the diamond surface and the reactor walls. The ionization degree in the discharges used for diamond deposition is typically below 10^{-4} (Moisan & Pelletier, 1992). As a result, the frequency of electron–electron collisions is not high enough to ensure Maxwellian electron energy distribution function (eedf) (Capitelli et al., 1996; Capitelli, Colonna, Hassouni & Gicquel, 1994). Furthermore, the large difference between hs and electron masses results in an incomplete thermalization of the electron energy mode (Capitelli et al., 1996; Koemtzopoulos, Economou, & Pollard, 1993). The electron kinetic mode shows a significant thermal nonequilibrium with a non-Maxwellian eedf and a much greater average energy than that of the translational neutral energy mode. The primary electron-heavy species (e-hs) collisions, especially some intermediate and high-energy threshold key reactions such as ionization or dissociation, may be very sensitive to this thermal nonequilibrium (Cacciatore, Capitelli, & Celiberto, 1992; Hassouni, Scott, Farhat, Gicquel, & Capitelli, 1997). The large pressure values used for the generation of these discharges, i.e. between few hPa and several hundreds of hPa, result in a fairly high

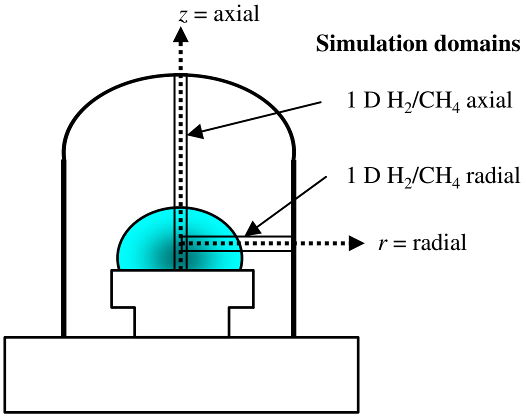

Figure 1 MW cavity-based bell-jar reactor schematics and domains of simulation of the 1D code.

e-hs collision frequency. As a result, an enhanced energy transfer between the electron and the internal and kinetic modes of hs takes place. Basically, the electrons transfer a significant amount of their energy to the internal modes, and more specifically to the molecular vibrational modes (Capitelli, Gorse, Berlemont, Skinner, & Bacal, 1991; Loureiro & Ferreira, 1989). Under these moderate-pressure conditions, collisions between hs (hs–hs collisions) take place and lead to a quite fast redistribution of the energy among the different excitation modes (Hassouni, Duten, Rousseau, & Gicquel, 2001). Significant values of the gas temperature (1500–4000 K), i.e. the temperature of the hs translational mode, characterize moderate-pressure plasmas used for diamond deposition (Erickson et al., 1996; Gicquel, Hassouni, Breton, Chenevier, & Cubertafon, 1996). An important thermal chemistry between hs takes place in these moderate-pressure/high-temperature conditions. The characteristic times of the different processes extend over several orders of magnitude (Hassouni et al., 2001). Some processes, such as some HC radical conversions, are very fast and others, such as volume atom and ion recombination, are very slow except at high pressure. Some of the chemical processes show characteristic times that are similar to those of the transport phenomena, i.e. diffusion (Girshick, Li, Yu & Han, 1993; Goodwin, 1993b; Hassouni et al., 2001). This leads to a significant nonequilibrium chemistry, especially at the plasma–substrate boundary layers where high gradients of gas temperature and species densities are present due to surface reactions and energy transfer to the surface. This nonequilibrium chemistry is further enhanced by the thermal nonequilibrium condition of the discharge (Hassouni, Scott, et al., 1997; Koemtzopoulos et al., 1993). It appears therefore that the discharge composition in the vicinity of the growing substrate surface depends on the whole series of phenomena that take place into the plasma phase. These include the electron heating under the HF electric field, the energy transfer between the different excitation modes, the nonequilibrium chemistry, and the transport phenomena. The understanding of the growth process and the determination of the plasma composition at the growing substrate surface requires therefore a thorough investigation of the whole energy transfer, chemistry, and transport phenomena.

Due to the fairly high pressure in the investigated plasma, the electron heating is essentially collisional and ohmic in nature (Lieberman & Lichtenberg, 1994). The power density absorbed by the plasma depends in particular on the electric field and the electron density (Ferreira, 1992; Moisan & Pelletier, 1992). The latter is governed by the balance between the rates of ionization and charged species losses (Moisan & Pelletier, 1992). The ionization rate depends on the reduced electric field, i.e. the ratio of electric field to gas density, in the discharge. On the other hand, the space distribution of the electric field strongly depends on the electrical permittivity of the plasma that may be considered as a dielectric medium. The plasma permittivity is linked to the electron density and the e-hs momentum transfer collision frequency and therefore depends on the gas density and the electron temperature (Lieberman & Lichtenberg, 1994; Moisan & Pelletier, 1992). It appears therefore that there is a strong coupling between the plasma characteristics and the EM field distribution. Taking into account, this coupling calls for the development of self-consistent EM and plasma models (Tan & Grotjohn, 1994; Tan & Grotjohn, 1995). The pictures of the coupled phenomena that have to be taken into account in such models are depicted in **Figure 2**.

Understanding diamond-deposition process requires the development of satisfactory (validated by experiment) H_2/CH_4 plasma models that provide the estimation of the spatial distributions of species densities into the deposition reactor. Due to the strong coupling between the EM, thermal, chemistry and transport phenomena that take place in the plasma, such models require taking into account the following effects:

1. Excitation wave propagation in the reactor and its interaction with the plasma.
2. Electrons kinetics and its impact on the energy distribution function (eedf) and the thermal nonequilibrium in the plasma.
3. Chemical kinetic, including e-hs and hs–hs collisions in the discharge.
4. Energy transfer between the different energy modes of the plasma.
5. Transport of energy and chemical species in the plasma.
6. Interactions between the plasma species and the diamond surface and the reactor walls.

It appears that a complete modeling of the deposition reactor is in fact very complex (Girshick et al., 1993; Harris, 1989; Schwärzler, Schnabl, Laimer, & Störi, 1996), and a step-by-step approach has been chosen at LSPM. According to the specific phenomena we wanted to analyze, specific models have been constructed. In addition, the experimental validation has been performed progressively although there is still a lot to be done. Thus, progressively, according to the conditions of power and pressure, the main processes have been identified. This approach has allowed us to reduce the complexity before including additional phenomena into the model. Finally, a reliable 1D model able to run in H_2/CH_4 and $Ar/CH_4/H_2$ mixtures with a reasonable computational

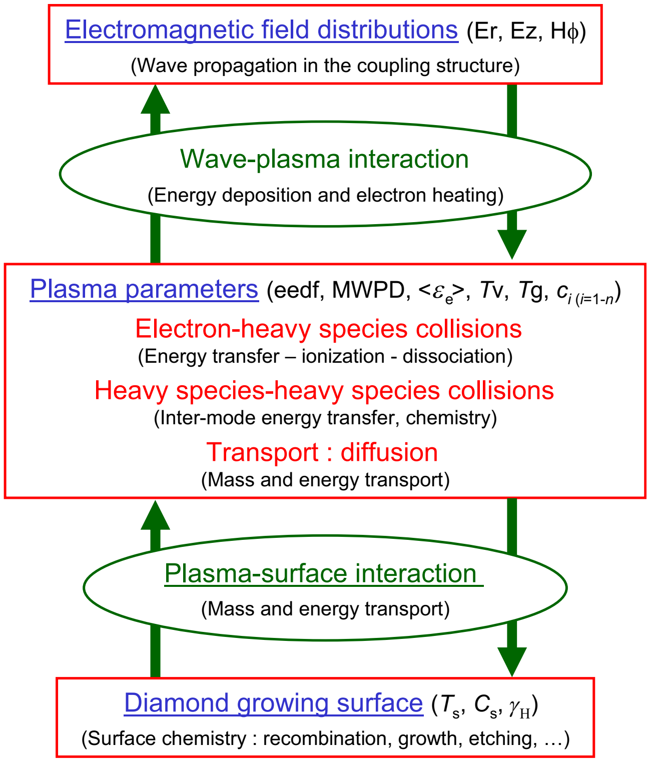

Figure 2 Picture of the coupled phenomena taken into account for modelling (Hassouni et al., 2010).

time is currently used at LSPM. This model, recently improved, is still under progress for studying very high pressure and power conditions (>200 hPa, >3000 W) and is being enriched to take into account for the presence of impurities in gas phase. This model allows us to understand, as a function of the conditions, the respective roles of chemical and transport processes that affect diamond deposition (Gicquel, Hassouni, Silva, & Achard, 2001; Gicquel, Silva, & Hassouni, 2000).

It is worth noting that most of the 2.45 GHz cavity-based reactors operate usually at low flow rate (a few hundreds of sccm), and they are characterized by a velocity of around $u = 1\ \mathrm{cm\ s^{-1}}$, giving a mass Peclet's number ($\mathrm{Pe_M} = ul/D$, where l is the characteristic length such as the reactor diameter and D is the mass diffusivity) of typically 0.1. Generally, the diamond substrate is positioned at a stagnation point, and typical boundary layers thicknesses of some tenths to some millimeters are observed. In the MW cavity-based plasmas, the gas-temperature distributions are very different than those in HF reactors. Thanks to the very high temperature values, the H-atom densities are much higher, in particular at the near-surface vicinity that allows a higher production of CH_3 radicals in this region. In addition, high thermal fluxes are observed, resulting in high energy transfer, the surface power densities typically ranging from 20 to 200 W $\mathrm{cm^{-2}}$.

With these systems, based on a single-mode cavity, 2 in polycrystalline deposits are rarely uniform due to the nonuniformity of the plasma phase. The definition of cavities providing much uniform plasma is obviously of major interest for developing more efficient reactors (Grotjohn et al., 2005; King et al., 2008; Silva, Hassouni, Bonnin, & Gicquel, 2009).

3.10.3.2 On the Construction of a Reliable 1D Model

3.10.3.2.1 H_2 Plasma Model

A first homogeneous (0D) collisional radiative model has allowed us to solve the Boltzmann equation for the electrons and demonstrating that it is non-Maxwellian (Hassouni, Farhat, Scott, & Gicquel, 1996). Two sets of electrons (hot and cold electrons) were observed, each presenting a Boltzmann distribution characterized by an electron temperature, the cold electron having a temperature higher than the hot electrons. From the analysis of the electron distribution and the adequacy with the main processes occurring in the plasma, it has been deduced that the average energy $<\varepsilon_e>$ was a relevant parameter to use. With this reduction of complexity, a 2D diffusive self-consistent model was developed in collaboration with Tim Grotjohn from Michigan State University (Hassouni, Grotjohn, & Gicquel, 1999). This latter model, which has been validated by coherent anti-stokes Raman spectroscopy (CARS) and two-photon absorption laser-induced fluorescence (TALIF) measurements (Gicquel et al., 1994; Gicquel, Chenevier, et al., 1996) for low- to moderate-pressure and power conditions, was found to be very relevant to understand how hydrogen cavity-based MW plasmas are working under moderate power density (<200 hPa, <3000 W). It has been shown that for more than 1000 W coupled to the plasma operating under a pressure of 50 hPa ($MWPD_{av} > 15\ W\ cm^{-3}$), molecular hydrogen and methane dissociations are only driven by thermal processes, while at lower power and pressure, electron dissociation is prevailing (**Figure 3**).

Thus, at moderate to high power density, the gas temperature and its distribution are governing the operation of the MW plasma diamond-deposition reactors: the higher the temperature, the higher the H-atom density into the plasma phase. In **Figure 4** are shown the results of the 2D self-consistent model concerning electron density, H-atom density and gas-temperature distributions obtained for two discharge conditions of power and pressure. It appears that similar plasma configurations, i.e. shape, position and volume, can be obtained for different power and pressure provided that the injected power over the total density (P/N_{tot}, where P denotes the injected power and N_{tot}, the total gas density) remains rather constant. Despite the similarity in the discharge configuration (plasma shape and position), strong differences in local plasma characteristics, i.e. gas temperature, H-atom density and electron density, appear as a function of the conditions.

Increasing the driving parameters keeping constant the deposition area requires simultaneous variation of the pressure and the input power so as to keep the plasma volume constant, which is defined, by convention, as the one obtained in the absence of the substrate holder, i.e. when the plasma shape is close to a sphere. The discharge can be therefore characterized by the average power density that represents the ratio of the input power to the constant plasma volume.

It is worth noting that this procedure was reasonable when working at low to moderate power density as shown by Gordon, Duten, Hassouni, and Gicquel (2001) who have established that more than 90% of the power was effectively coupled to the plasma. However, increasing power leads to important leaks by Joule effect into different components of the system (wave guide, reactor walls…) that lowers the effective power coupled to the plasma. Then, when working at high power density, we have decided to present the results associated with their respective power and pressure even if we keep the same approach that tries to maintain constant the plasma volume when increasing power (see Section 3.10.4 concerning the study at high power density).

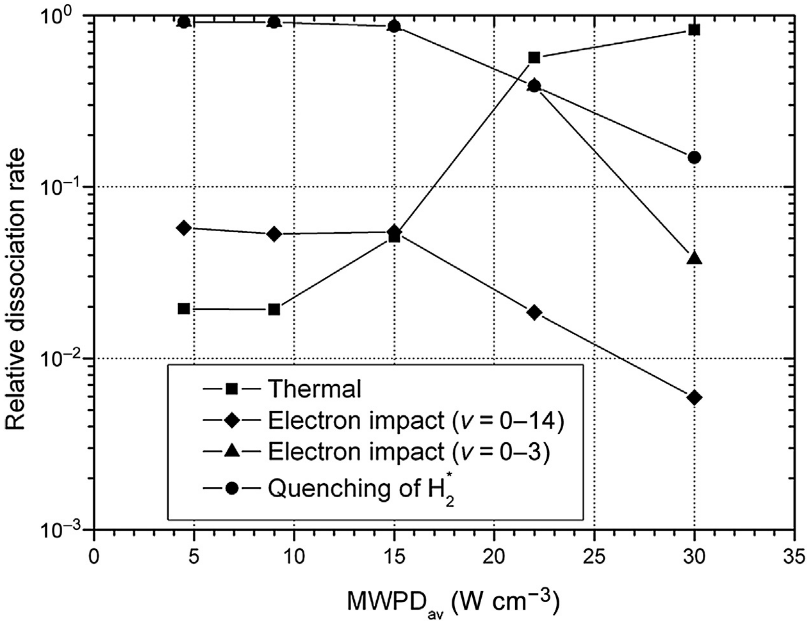

Figure 3 Relative predominance of the different H_2 dissociation channels as a function of the discharge conditions. The rates are calculated for average MW power density values of 4.5, 9, 15, 22 and 30 W/cm^3. One may distinguish two power density domains. At low average power density, i.e., typically below 15 W/cm^3, the dissociation of hydrogen proceeds through electron impact excitation of the dissociative $b^3\Sigma_u^+$ triplet state and the quenching of the other electronically excited state. The significant contribution of the quenching processes is quite specific to this discharge as compared to low pressure plasmas, i.e., p<100 Pa. Hassouni et al., 2010. Simulation made in the "bell jar" reactor configuration.

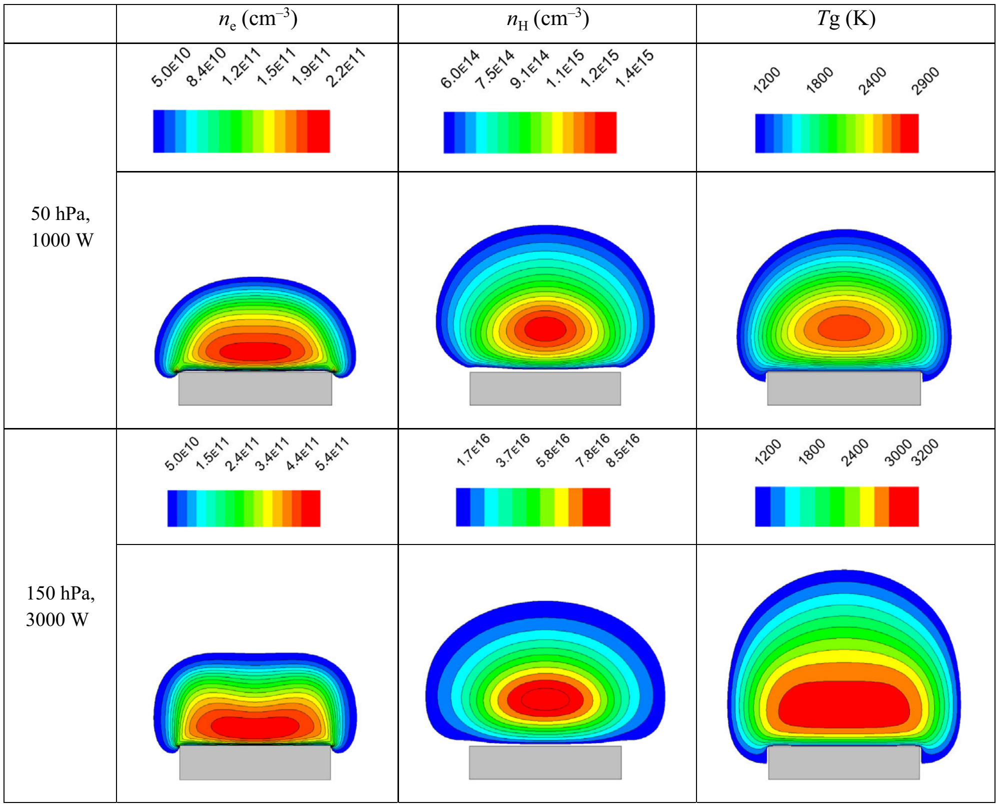

Figure 4 Change in plasma distributions as function of input microwave power and pressure. Pressure and power are varied in such a way to keep optimal plasma volume and avoid plasma instability (Silva, Hassouni, et al., 2009). Simulation made in a "bell jar" configuration.

The evolution shown here (**Figures 3** and **4**) indicates that when increasing the pressure and power simultaneously, the plasma behavior goes from a cold nonequilibrium discharge to an almost "thermal plasma". The increase of the gas temperature strongly enhances the thermal chemistry, and the increase in the hydrogen density is mainly due to a strong enhancement of the thermal dissociation processes that become dominant over the electron impact dissociation processes when the gas temperature exceeds 2600 K.

3.10.3.2.2 H_2–CH_4 Plasma Model

The introduction of <10% of methane in a pure hydrogen discharge induces three kinds of effects. First, a very rich chemistry of neutral species appears that taking into account the temperature and feed gas composition is rather similar to that resulting from HC cracking processes (Girshick et al., 1993; Harris, 1989; Janev & Reiter, 2004; Mechold et al., 2001; Mankelevich, Rakhimov, & Suetin, 1995; Schwärzler et al., 1996; Yu & Girshick, 1994b). This chemistry may lead to the formation of a large variety of neutral species that can interact with the electrons of the plasma. This secondary effect is related to the energy transfer from the electron to the different modes of HC molecular species. Despite their small amount with respect to hydrogen, the HC species show a large number of excitation modes that can significantly absorb the electron energy. This can in turn affect the electron kinetics and the characteristics of the thermal nonequilibrium in the plasma. The third effect is linked to the probable change in the ionization kinetics. As mentioned previously, the electron impact ionization of HCs takes place with an energy threshold that is smaller than that of molecular hydrogen. HC ionization should therefore be favored in the quite moderate electron average energy discharges used for diamond deposition. Further, ion conversion and ion recombination processes affect the ionization kinetics and the population distributions of the ions (Mankelevich et al., 1995; Tachibana et al., 1984). The change in the ionization kinetics would in principle result in a change in the plasma density and therefore in the plasma EM properties.

In some papers (Hassouni et al., 2010; Mankelevich, Ashfold, & Ma, 2008; Mankelevich, Ashfold, & Orr-Ewing, 2007), the effect of adding a small amount of methane to a pure hydrogen plasma was shown to lead to a change in the ionization kinetics, and then to an evolution of the densities of the major ions into the plasma. Although the primary ionization processes mainly involve hydrogen, i.e. through reactions (R1) and

Table 1 Simplified kinetic model for moderate pressure H_2 plasmas (species considered are H_2, H, H(n=2), H(n=3), H^+, H_2^+, H_3^+ and e^-).

No.	Reactions	*Cross Sections σ or Arrhenius Law A in $m^3\ s^{-1}\ mol^{-1}$ or $m^6\ s^{-1}\ mol^{-2}$*, n *Dimensionless*, T_a *(K)*	*References*
1	$e^- + H_2 \rightarrow e^- + 2H$	σ	Tawara, Nishimura, Tanaka, and Nakamura (1990)
2	$e^- + H_2 \rightarrow 2e^- + H_2^+$	σ	Tawara, Nishimura, Tanaka, et al. (1990)
3	$e^- + H \rightarrow 2e^- + H^+$	σ	Janev and William (1987)
4	$e^- + H_3^+ \rightarrow 3H$	σ	Janev and William (1987)
5	$e^- + H_3^+ \rightarrow H_{(n=2)} + H_2$	σ	Janev and William (1987)
6	$e^- + H^+ \rightarrow H + h\nu$	σ	Massey (1969)
7	$2H + H_2 \rightarrow 2H_2$	$10^5 \times T^{-0.6}$	Cohen and Westberg (1983)
8	$3H \rightarrow H_2 + H$	3.2×10^3	Cohen and Westberg (1983)
9	$H_2 + H_2^+ \rightarrow H_3^+ + H$	1.27×10^9	Karpasb, Anicich and Huntress (1979)
10	$2H_2 \rightarrow 2H + H_2$	$8.61 \times 10^{11} \times T^{-0.7} \cdot \exp(-52530/T)$	Cohen and Westberg (1983)
11	$H_2 + H \rightarrow 3H$	$2.7 \times 10^{10} \times T^{-0.1} \cdot \exp(-52530/T)$	Cohen and Westberg (1983)
12	$e^- + H_2 \rightarrow e^- + H_{(n=2)} + H$	σ	Janev and William (1987)
13	$e^- + H_2 \rightarrow e^- + H_{(n=3)} + H$	σ	Janev and William (1987)
14	$e^- + H \rightarrow e^- + H_{(n=2)}$	σ	Janev and William (1987)
15	$e^- + H \rightarrow e^- + H_{(n=3)}$	σ	Janev and William (1987)
16	$H_{(n=2)} + H_2 \rightarrow H_3^+ + e^-$	$1.68 \times 10^7 \times T^{0.5}$	Bittner, Kohse-höinghaus, Meier, and Just (1988), Preppernau, Pearce, Tserepi, Wurzberg, and Miller (1995)
17	$H_{(n=3)} + H_2 \rightarrow H_3^+ + e^-$	$1.68 \times 10^7 \times T^{0.5}$	Estimated from reaction 16
18	$H_{(n=3)} \rightarrow H_{(n=2)} + h\nu$	Einstein coefficient $4.36 \times 10^7\ s^{-1}$	Preppernau et al. (1995)
19	$e^- + H_{(n=2)} \rightarrow H + e^-$	σ	Janev and William (1987)
20	$e^- + H_{(n=3)} \rightarrow H + e^-$	σ	Janev and William (1987)
103	$e^- + H^+ \rightarrow H_{(n=2)} + h\nu$	σ	Janev and William (1987)
104	$e^- + H^+ \rightarrow H_{(n=3)} + h\nu$	σ	Janev and William (1987)

Table issued from **Tables 3** and **Table 4**, Hassouni, K., Silva, F., Gicquel, A., (April 21, 2010). Modelling of diamond deposition microwave cavity generated plasmas. *Journal of Physics D-Applied Physics*, 43(15)153001 DOI:10.1088/0022-3727/43/15/153001.

(R2) (**Table 1**), and result in the formation of H_3^+, the fast ion conversion processes between H_3^+ and HCs results in the formation of HC ions that become the major charged species even at methane percentage as low as 0.1% (Butler et al., 2009; Gicquel et al., 2001; Hassouni et al., 2010). This scenario is however more specifically observed for the low-pressure/low-power discharge conditions. At high pressure/high power, the dissociation degree in the discharge is more important and the ionization of hydrogen mainly leads to H^+ formation. The direct ionization of HC becomes efficient and exceeds the H_3^+ conversion as a source of HC ions.

The experimental investigations performed on diamond-deposition plasmas have shown however that the coupling configuration, i.e. plasma shape, plasma position, optimal power deposited, etc. is not significantly affected when introducing a small amount of methane, although a slight increase in the gas temperature has been reported (Gicquel, Hassouni, et al., 1996; Gicquel, Chenevier, Hassouni, Tserepi, & Dubus, 1998). This has been confirmed by emission spectroscopy measurements that have showed that the introduction of methane does not lead to a significant change in the plasma excitation, as inferred from the emission lines of argon probe species introduced as an impurity in the discharge (1–3%) (**Figure 5**) (Gicquel, Chenevier, et al., 1996; Gicquel, Chenevier, Hassouni, et al., 1998; Gicquel, Hassouni, et al., 1996).

Therefore, since the absorbed power density distribution is not drastically affected by the introduction of methane, we decided, instead of modeling the H_2/CH_4 mixture discharges with a rather complex 2D self-consistent model, to develop a 1D diffusive (convective) model for modeling the H_2/CH_4 mixture discharges. This approach needs however to have access to the spatial distribution of the absorbed MW power density in the plasma.

Two methods have been explored. The first consists in measuring the emission intensity of the argon line emitting at 750 nm (**Figure 5**) and in solving the electron energy balance equation as reported in Hassouni, Leroy, Farhat, and Gicquel (1998). Such an approach provides an electron temperature axial profile that can be

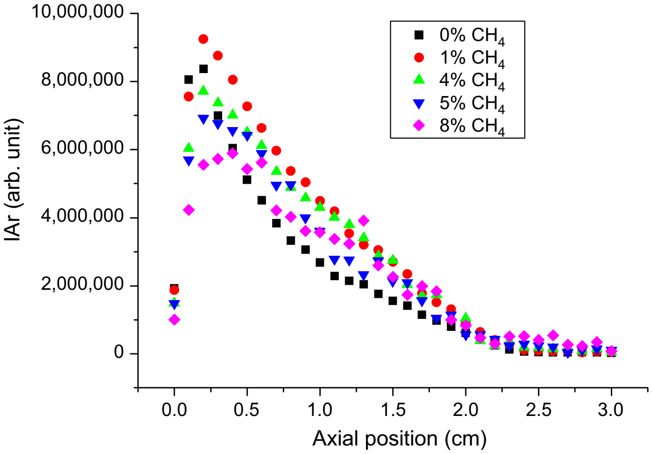

Figure 5 Variation of the 750 nm emission argon line intensity as a function of the methane percentage introduced in the feed gas (power 3000W, pressure 200 hPa) (Gicquel et al., 2012). Measurements made in the stainless steel reactor configuration.

compared with the electron temperature deduced from experiments (see later and **Figure 6(a) and (b)**). The second consists in directly extracting from the 2D consistent model, the averaged power distribution into the discharge. For high-power density studies, we made use of the first technique.

To derive balance equations that govern H_2/CH_4 plasmas, one has to define collisional and energy transfer models. The chemical kinetics schemes have been largely based on HC cracking processes proposed in the literature, and take into account the main reactions occurring at the high gas temperatures characterizing the plasmas studied here. The discussion on all these aspects can be found in Hassouni et al. (2010). Finally, the chemical kinetics model considered here is given in **Tables 1** and **2**.

3.10.3.2.3 Species Transport

As mentioned previously, the H_2/CH_4 plasma represents a quite complex media. Actually more than the number of species and reactions, the very high stiffness of the chemistry makes the modeling of this system difficult. This stiffness is further enhanced under conditions of very high-gas-temperature gradient that induces a huge change in the chemistry over 1 mm in distance in the near diamond surface vicinity (Hassouni et al., 1999). To the best of our knowledge, most of the modeling studies on the coupled phenomena of species chemistry and energy transport in H_2/CH_4 discharges were performed for one-dimensional geometry, except for the work performed by Mankelevich et al. who have considered two-dimensional axisymmetric geometry (Mankelevich & May, 2008; Wang & Frenklach, 1997). However, the models developed by these authors were mainly focused on the neutral chemistry and did not treat in detail the discharge phenomena like the ionization kinetics, the thermal nonequilibrium, and the charged species transport. Our choice was to use a 1D model that enabled us to make use of a detailed description of the plasma physics and chemistry and that has been validated by experiments (see later on).

In the 1D model, the plasma is described on the whole stagnation line involving the bulk of the plasma and the reacting plasma/substrate boundary layer. A radial term taking into account for diffusion to the reactor walls (due to surface recombination and energy transfer at the reactor walls) is included, using characteristic diffusion lengths. As far as thermal nonequilibrium is concerned, one can use a two-temperature model similar to the one developed for hydrogen. Transport equations, similar to those used in the case of pure hydrogen discharges, that express the energy conservation can be derived for the electron and total energy. In addition, for each species, except H_2 and electrons that can be estimated from the equations of state and charge conservation assuming a constant pressure and locally neutral plasma, a continuity equation can be derived. The nonstationary species continuity equations can be expressed in terms of mass fraction as:

$$\frac{\mathrm{d}Y_\mathrm{s}}{\mathrm{d}t} = \frac{W_\mathrm{s}}{\rho} - \frac{1}{\rho}\cdot\frac{\mathrm{d}}{\mathrm{d}z}\left(-\frac{\rho}{\rho_\mathrm{s}}D_\mathrm{s}\frac{\mathrm{d}Y_\mathrm{s}}{\mathrm{d}z}\right) \tag{8}$$

where Y_s and W_s are the mass fraction and mass production rate of species s, respectively. W_s is estimated on the basis of the chemical model described in **Tables 1** and **2**.

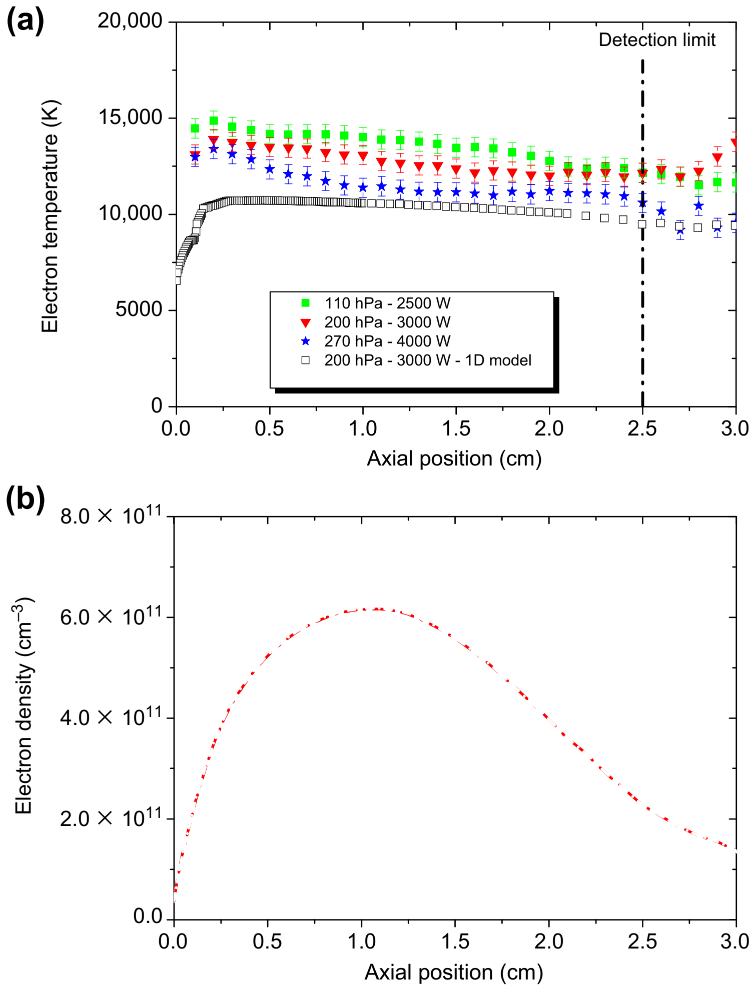

Figure 6 (a) Experimental electron temperature axial profiles for the conditions: H_2/CH_4 at 200 hPa, 3000 W, 4 % of CH_4,500 sccm; 110 hPa, 2500 W, 4 % of CH_4, 500 sccm; and H_2/CH_4 at 270 hPa, 4000 W, 4 % of CH_4, 500 sccm. (b) Calculated electron density axial profile for the condition at 200 hPa, 3000 W (Derkaoui, 2012; Derkaoui, work in progress; Gicquel et al., 2012).

The source terms and transport coefficients are determined in a similar way as in the case of pure hydrogen. Since H_2 and H are the major chemical species in the plasma, diffusion is assumed to take place in the H_2/H mixture. Lennard-Jones potential is used to estimate the binary diffusion coefficients of HC species in H_2 and H and the mixing rule described in Rebrion-Rowe, Lehfaoui, Rowe, and Mitchell (1998) and Yos (1963) is used to estimate the diffusion coefficients in the H_2/H mixture from the binary diffusion coefficients. Another specificity of H_2/CH_4 plasmas is the possible coexistence of several ionic species. This makes the estimation of the ambipolar diffusion fluxes much less straightforward than in the case of a single ion discharge. The treatment of ambipolar diffusion in the case of multicomponent and electronegative discharge plasmas received a lot of attention and many approximate solutions were proposed to estimate the charged species fluxes in this situation (Bird, Stewart, & Lightfoot, 1960). A discussion on this aspect for diamond-deposition reactors can be found in Hassouni et al. (2010).

The time variations of the axial distributions on the stagnation line for gas and electron temperature, species densities can be predicted by solving the transport equations. The solution of these equations requires specifying boundary conditions for temperature and species on the limit of the computational domain. The gas temperature is set to 300 K at the inlet of the computational domain and to 1100 K at the substrate surface. A zero gradient is assumed for the electron temperature at the two boundaries. The gas composition at the inlet of the computation domain is chosen in agreement with the feed gas. At the substrate surface, catalytic boundary

Table 2a Reactions involving neutral hydrocarbons (Girshick et al., 1993; Hassouni et al., 1997; Hassouni et al., 1998; Yu and Bauer, 1998)

No	Reactions ($k = A \cdot T^n \cdot \exp(-E_a/k_BT)$)	A in $m^3\ s^{-1}\ mol^{-1}$ or $m^6\ s^{-1}\ mol^{-2}$	n	E_a in J
47	$CH + H \leftrightarrow C + H_2$	4.00×10^8	0	11,776
48	$C + CH \leftrightarrow C_2 + H$	2.00×10^8	0	0
49	$C + CH_2 \leftrightarrow C_2H + H$	5.00×10^7	0	0
50	$C + CH_3 \leftrightarrow C_2H_2 + H$	5.00×10^7	0	0
51	$C + CH_4 \leftrightarrow CH_3 + CH$	5.00×10^7	0	12077.9
52	$CH + M \leftrightarrow C + H + M$	1.90×10^8	0	33717.6
53	$2CH \leftrightarrow C_2H + H$	1.50×10^8	0	0
54	$CH + CH_2 \leftrightarrow C_2H_2 + H$	4.0×10^7	0	0
55	$CH + CH_3 \leftrightarrow C_2H_3 + H$	3.0×10^7	0	0
56	$CH + CH_4 \leftrightarrow C_2H_4 + H$	6.0×10^7	0	0
57	$CH + C_2H \leftrightarrow C_2H_2 + C$	10^8	0	0
58	$CH + C_2H_3 \leftrightarrow C_2H_2 + CH_2$	5×10^7	0	0
59	$CH_2 + M \leftrightarrow CH + H + M$	4.0×10^9	0	41769.5
60	$CH_2 + M \leftrightarrow C + H_2 + M$	1.3×10^8	0	29641.0
61	$CH + H_2 \leftrightarrow CH_2 + H$	1.08×10^8	0	1555
62	$CH_2 + CH_2 \leftrightarrow C_2H_2 + H_2$	1.6×10^9	0	5957
63	$CH_2 + CH_2 \leftrightarrow C_2H_2 + 2H$	2.0×10^8	0	5594.5
64	$CH_3 + CH_2 \leftrightarrow C_2H_4 + H$	4.0×10^7	0	0
65	$CH_4 + CH_2 \leftrightarrow 2CH_3$	2.46×10^0	2.0	4135.0
66	$CH_2 + C_2H_3 \leftrightarrow C_2H_2 + CH_3$	3×10^7	0	0
67	$^1CH_2 + M \leftrightarrow CH_2 + M$	1.8×10^7	0	301.4
68	$^1CH_2 + H \leftrightarrow CH_2 + H$	2×10^8	0	0
69	$^1CH_2 + H \leftrightarrow CH + H_2$	3×10^7	0	0
70	$^1CH_2 + H_2 \leftrightarrow CH_3 + H$	7×10^7	0	0
71	$CH_2 + CH_3 \leftrightarrow C_2H_4 + H$	1.2×10^7	0	285.0
72	$^1CH_2 + CH_4 \leftrightarrow 2CH_3$	1.6×10^7	0	285
73	$^1CH_2 + C_2H_6 \leftrightarrow CH_3 + C_2H_5$	4.0×10^7	0	275.0
74	$CH_2 + H + M \leftrightarrow CH_3 + M$	$k_0 = 1.04 \times 10^{14}$	−2.76	800
		$k_{low} = 6.0 \times 10^8$	0	0
		Troe: $a = 0$, $b = 0.562$, $c = 91$, $d = 5836$, $e = 8552$		
75	$CH + H_2 + M \leftrightarrow CH_3 + M$	$k_0 = 4.83 \times 10^{13}$	−2.8	295
		$k_{low} = 1.98 \times 10^6$	0.43	185
		Troe: $a = 0$, $b = 0.578$, $c = 122$, $d = 2535$, $e = 9365$		
76	$CH_2 + H_2 \leftrightarrow CH_3 + H$	5.0×10^{-1}	2.0	3615.0
77	$CH_3 + H + M \leftrightarrow CH_4 + M$	$k_0 = 2.62 \times 10^{21}$	−4.76	1220
		$k_{low} = 1.393 \times 10^{10}$	−0.63	268.0
		Troe: $a = 0.0$, $b = 0.783$, $c = 74$, $d = 2941$, $e = 6964$		
78	$CH_3 + CH_3 \leftrightarrow C_2H_4 + H_2$	1.0×10^{10}	0	15999.2
79	$2CH_3 + M \leftrightarrow C_2H_6 + M$	$k_0 = 3.4 \times 10^{29}$	−7.03	1381.5
		$k_{low} = 6.77 \times 10^{10}$	−1.18	327.0
		Troe: $a = 0.0$, $b = 0.619$, $c = 73.2$, $d = 1180$, $e = 9999$		
80	$CH_3 + CH_4 \leftrightarrow C_2H_5 + H_2$	1.0×10^7	0	11574.7
81	$C_2H_3 + CH_3 \leftrightarrow C_2H_2 + CH_4$	7.90×10^5	0	0
82	$C_2H_4 + CH_3 \leftrightarrow CH_4 + C_2H_3$	2.27×10^{-1}	2.0	4600
83	$C_2H_5 + CH_3 \leftrightarrow C_2H_4 + CH_4$	7.2×10^5	0	0
84	$C_2H_6 + CH_3 \leftrightarrow C_2H_5 + CH_4$	6.14	1.74	5253.91
85	$CH_4 + H \leftrightarrow CH_3 + H_2$	6.6×10^2	1.62	5420
86	$C_2 + M \leftrightarrow 2C + M$	3.72×10^5	0	72276.5
87	$C_2 + H_2 + M \leftrightarrow C_2H_2 + M$	1.81×10^{-2}	0	0

Table 2a Reactions involving neutral hydrocarbons (Girshick et al, 1993; Hassouni et al., 1997; Hassouni et al., 1998; Yu and Bauer, 1998)—cont'd

No	*Reactions* ($k = A\cdot T^n\cdot exp(-E_a/k_BT)$)	*A in* $m^3\ s^{-1}\ mol^{-1}$ *or* $m^6\ s^{-1}\ mol^{-2}$	*n*	E_a *in J*
88	$C_2H + M \leftrightarrow C_2 + H + M$	3.61×10^9	0	72412.3
89	$C_2H + H \leftrightarrow C_2 + H_2$	6.03×10^7	0	14647.5
90	$C_2H + H_2 \leftrightarrow C_2H_2 + H$	5.68×10^4	0.9	997.5
91	$C_2H + C_2H_3 \leftrightarrow 2C_2H_2$	3×10^7	0	0
92	$C_2H + H + M \leftrightarrow C_2H_2 + M$	$k_0 = 3.75 \times 10^{21}$	−4.8	950.0
		$k_{low} = 10^{11}$	0	0
		Troe: $a = 0$, $b = 0.646$, $c = 132$, $d = 1315$, $e = 5566$		
93	$C_2H_2 + H + M \leftrightarrow C_2H_3 + M$	$k_0 = 3.8 \times 10^{28}$	−7.27	3610.0
		$k_{low} = 5.6 \times 10^6$	0	1200.0
		Troe: $a = 0$, $b = 0.751$, $c = 98.5$, $d = 1302$, $e = 4167$		
94	$C_2H_3 + H \leftrightarrow C_2H_2 + H_2$	3.0×10^7	0	0
95	$C_2H_4 + M \leftrightarrow C_2H_2 + H_2 + M$	$k_0 = 1.58 \times 10^{39}$	−9.3	48,900
		$k_{low} = 8 \times 10^6$	0.44	44,385
		Troe: $a = 0.0$, $b = 0.735$, $c = 180$, $d = 1035$, e = 5417		
96	$C_2H_3 + H + M \leftrightarrow C_2H_4 + M$	$k_0 = 1.4 \times 10^{18}$	−3.86	1660.0
		$k_{low} = 6.08 \times 10^6$	0.27	140.0
		Troe: $a = 0$, $b = 0.782$, $c = 207.5$, $d = 2663$, $e = 6095$.		
97	$C_2H_4 + H \leftrightarrow C_2H_3 + H_2$	1.32	2.53	6120
98	$C_2H_4 + H + M \leftrightarrow C_2H_5 + M$	$k_0 = 5.40 \times 10^5$	0.45	910.0
		$k_{low} = 6.0 \times 10^{29}$	−7.62	3485.0
		Troe: $a = 0$, $b = 0.975$, $c = 210.0$, $d = 984.0$, $e = 4374.0$		
99	$2CH_3 \leftrightarrow C_2H_5 + H$	6.84×10^6	0.1	5300.0
100	$C_2H_6 + H \leftrightarrow C_2H_5 + H_2$	1.15×10^2	1.9	3765.0
101	$C_2H_5 + H + M \leftrightarrow C_2H_6 + M$	1.99×10^{29}	−7.08	3342.5
		5.21×10^{11}	−0.99	−790
102	$H + C_2H_5 \leftrightarrow H_2 + C_2H_4$	2.0×10^6	0	0

Table issued from **Table 5**, Hassouni, K., Silva, F.,Gicquel, A., (April 21, 2010). Modelling of diamond deposition microwave cavity generated plasmas. *Journal of Physics D-Applied Physics*, 43(15)153001 DOI:10.1088/0022-3727/43/15/153,001.

conditions similar to those described in Hassouni et al. (2001), Scott, Farhat, Gicquel, Hassouni, and Lefebvre (1996), Hassouni, Farhat, and Scott (1997) are used. Basically, for each species, the boundary conditions are derived from the balance between the diffusion flux and the net production rate by surface chemistry. This may be expressed as

$$D_s \vec{\nabla}\, n_s \cdot \vec{n}\big|_{wall} = r_{s-wall} \tag{9}$$

where n_s, D_s and r_s represent the density, diffusion coefficient, and rate of production due to surface processes for species s. $\vec{n}$ represents the normal to the surface.

For example, for atoms and ions that mainly undergo catalytic recombination at the substrate surface, surface reaction rate is essentially determined by the recombination probability and the collision frequency of the species with the surface. In this case, the boundary conditions can be expressed as

$$D_s \vec{\nabla}\, n_s \cdot \vec{n}\big|_{wall} = \gamma_s \frac{v_s{}^*}{4} n_{s-w} \quad \text{for neutral species} \tag{10}$$

Table 2b Reactions involving hydrocarbon ions

N°	*Reactions*	*References*
21	$e^- + CH_4 \rightarrow e^- + CH_3 + H$	Tawara, Nishimura, and Yoshino (1990)
22	$e^- + CH_4 \rightarrow e^- + CH_2 + H_2$	Tawara, Nishimura, and Yoshino (1990)
23	$e^- + CH_4 \rightarrow 2e^- + CH_4^+$	Tawara, Nishimura, and Yoshino (1990)
24	$e^- + C_2H_2 \rightarrow e^- + C_2H + H$	Tawara, Nishimura, and Yoshino (1990)
25	$e^- + C_2H_2 \rightarrow 2e^- + C_2H_2^+$	Tawara, Nishimura, and Yoshino (1990)
26	$e^- + C_2H_4 \rightarrow 2e^- + C_2H_4^+$	Tawara, Nishimura, and Yoshino (1990)
27	$e^- + C_2H_6 \rightarrow e^- + C_2H_4 + H_2$	Tawara, Nishimura, and Yoshino (1990)
28	$e^- + C_2H_6 \rightarrow 2e^- + C_2H_6^+$	Tawara, Nishimura, and Yoshino (1990)
29	$e^- + C_2H_6 \rightarrow 2e^- + C_2H_5^+ + H$	Tawara, Nishimura, and Yoshino (1990)
30	$e^- + C_2H_6 \rightarrow 2e^- + C_2H_4^+ + H_2$	Tawara, Nishimura, and Yoshino (1990)
31	$e^- + C_2H_4 \rightarrow e^- + C_2H_2 + H_2$	Tawara, Nishimura, and Yoshino (1990)
32	$e^- + CH_5^+ \rightarrow CH_4 + H$	Lehfaoui, Rebrion-Rowe, Laubé, Mitchell, and Rowe (1997)
33	$e^- + CH_4^+ \rightarrow CH_3 + H$	Assumption: same constant as R32:
34	$e^- + C_2H_6^+ \rightarrow C_2H_5 + H$	Assumption: same constant as R35
35	$e^- + C_2H_5^+ \rightarrow C_2H_4 + H$	Lehfaoui et al. (1997)
36	$e^- + C_2H_4^+ \rightarrow C_2H_3 + H$	Assumption: same constant as R35
37	$e^- + C_2H_3^+ \rightarrow C_2H_2 + H$	Assumption: same constant as R35
38	$e^- + C_2H_2^+ \rightarrow C_2H + H$	Assumption: same constant as R35
39	$CH_4^+ + CH_4 \rightarrow CH_5^+ + CH_3$	Tahara, Murai, Yasi, and Yoshikawa (1995)
40	$H_3^+ + CH_4 \rightarrow CH_5^+ + H_2$	Tahara et al. (1995)
41	$H_3^+ + C_2H_2 \rightarrow C_2H_3^+ + H_2$	Tahara et al. (1995)
42	$H_3^+ + C_2H_4 \rightarrow C_2H_5^+ + H_2$	Tahara et al. (1995)
43	$CH_5^+ + C_2H_6 \rightarrow C_2H_5^+ + H_2 + CH_4$	Tahara et al. (1995)
44	$CH_4^+ + H_2 \rightarrow CH_5^+ + H$	Tahara et al. (1995)
45	$C_2H_3^+ + C_2H_4 \rightarrow C_2H_5^+ + C_2H_2$	Tahara et al. (1995)
46	$C_2H_2^+ + CH_4 \rightarrow C_2H_3^+ + CH_3$	Tahara et al. (1995)

Table issued from **Table 5,** Hassouni, K., Silva, F.,Gicquel, A., (April 21, 2010). Modelling of diamond deposition microwave cavity generated plasmas. *Journal of Physics D-Applied Physics*, 43(15)153001 DOI:10.1088/0022-3727/43/15/153,001.

and

$$D_s \vec{\nabla} n_s \cdot \vec{n}\Big|_{\text{wall}} = \gamma_s v_b n_{s-w} \quad \text{for charged species} \tag{11}$$

where γ_s is the recombination/de-excitation probability (coefficient). v_s^* given by $(8kT_w/\pi m_s)^{1/2}$ is the thermal velocity of species s. v_b is the Böhm velocity for ions that is given by $(kT_{e-w}/\pi m_e)^{1/2}$ for a single ion plasma. n_{s-w} is the density of species s at the wall.

Since the ions totally recombine on the reactor's walls, their recombination coefficients were taken equal to 1. The recombination coefficient of H atom on the quartz surface was taken from reference (Green, Jennings, Linnett, & Schoffield, 1959; Oskam, 1958) ($\gamma_H = 10^{-4}$). Very little is known on the recombination coefficients of unstable HC radicals on quartz surfaces. We therefore assume a value of 10^{-3} similar to that found for CH_3 recombination on diamond (Krasnoperov, Kalinovski, Chu, & Gutman, 1993) for the recombination probabilities of the entire HC radicals. This assumption should not have an important consequence on the model results since, as shown in Hassouni et al. (1998), surface reactions have almost no effect on the density distributions of HC species under moderate-pressure discharge conditions. As a matter of fact, the populations of these species are mainly governed by gas phase chemistry.

Deposition experiments can be performed under continuous wave discharges. In this case, the deposition process is essentially stationary and its investigation requires determining the stationary solution of the transport equations. Deposition can also be performed using discharges that are generated under a pulsed mode. In this case, the deposition process is nonstationary in nature and a time-accurate integration is required to access the peculiarities of the deposition process. This regime provides more flexibility in controlling the plasma thermochemistry (Brinza et al., 2007; Chatei et al., 1997; Duten, Rousseau, Gicquel, Hassouni, & Leprince, 2002). The chemical composition and gas heating can indeed be monitored through an appropriate choice of the pulse waveform. We will analyze in Section 3.10.5.6 how working under pulsed mode can help in optimizing the deposition process.

3.10.3.3 Spectroscopic Analysis of the Plasma

Plasma modeling needs an important step of validation. As a matter of fact, the complexity due to many coupled phenomena leads us to reduce the phenomena taken into account. Although this has been done on the basis of a careful analysis, comparison between calculated results to experimental ones provides an additional degree of confidence.

3.10.3.3.1 H-Atom Density and Gas-Temperature Measurements

H-atom density and temperature measurements have been the object of many investigations in HF reactors (Chenevier, Cubertafon, Campargue, & Booth, 1994; Hsu, 1992; Schafer, Klages, Meier, & Kohse-Hoinghaus, 1991; St-Onge et Moisan, 1994; Vetterhöffer, Campargue, Chenevier, & Stoeckel, 1993; Whitfield et al., 2000), and MW plasma reactors, in particular in our laboratory and the Bristol Lab. Thus, H-atom densities have been measured by resonance-enhanced multiphoton ionization (REMPI) (in HF reactors) (Celii & Butler, 1989), third harmonic generation (Celii, Thorsheim, Butler, Plano, & Pinneo, 1990), CARS (Chen, Chuang, Penney, & Banholzer, 1992; Gicquel et al., 1994; Hay, Roman, & Colket, 1990), TALIF (Bittner, Kohse-höinghaus, Meier, & Just, 1988; Chenevier et al., 1994; Gicquel, Chenevier, et al., 1996; Gicquel, Chenevier, & Lefebvre, 1998; Preppernau, Pearce, Tserepi, Wurzberg, & Miller, 1995) and optical emission spectroscopy (OES) (Gicquel et al., 1994; Gicquel, Chenevier, et al., 1996; Gicquel, Chenevier, & Lefebvre, 1998; Gicquel, Hassouni, et al., 1996; Ma, Ashfold, & Mankelevich, 2009). Also has been carried out spatially resolved measurements of H ($n=2$) density using cavity ring-down spectroscopy (CRDS) (Ma, Richley, Ashfold, & Mankelevich, 2008; Rennick et al., 2007).

Concerning the gas temperature, it has been obtained from measurements of rotational ground-state molecular hydrogen temperatures by CARS (Kaminski & Ewart, 1996), ground-state H-atom temperature by TALIF (Gicquel, Chenevier, et al., 1996), and from measurements of the $n=3$ excited state H-atom temperature by OES (Gicquel, Hassouni, et al., 1996). In addition, carbon-containing species or boron-containing species have been seen to be relevant for assessing gas temperature. Degenerate four-wave mixing (DFWM) (Connell et al., 1995; Green et al., 1993) allows probing CH, absorption to probe C_2 (Lombardi, Benedic, Mohasseb, Hassouni, & Gicquel, 2004), and OES probing for instance C_2, BH (Lavrov et al., 2003; Rayar et al., 2006), and measuring their respective rotational temperatures.

All these measurements have allowed validating the models that describe the H_2, H_2–CH_4, and even H_2–CH_4–B_2H_6 plasmas, however under conditions of relatively low power density. The multiplicity of measurements also allowed validating the different techniques, in particular OES.

OES is a very simple and powerful technique that can be used routinely while laser-based techniques cannot. However, OES can only be used under some restrictive conditions. As a matter of fact, OES probes excited state species of which densities are around 10^{-4} of the ground electronic state species density. The only case where information on ground state species may be obtained from these measurements is when the electronic species are excited from their ground state through a direct collision with an electron. In this case, the electronic state and its internal energy distribution represent an image of its ground electronic state. Although the electronic excitation dynamics must be analyzed carefully, the de-excitation processes must also be analyzed, in particular because quenching and energy transfer processes may occur. The cases where the electronic state is excited through different steps involving metastable states for instance, or where self-absorption exists, are out of the scope for using OES technique to assess electronic ground state species behavior. Gicquel, Hassouni, et al. (1996), Gicquel, Chenevier, et al. (1996), Gicquel, Chenevier, and Lefebvre (1998), and Gicquel, Chenevier, Hassouni, et al. (1998) will provide the reader an extended discussion on actinometry validity and temperature measurements from either molecular hydrogen or H atoms.

Spatially resolved spectroscopic analysis of the plasma provides measurements of local characteristics in the plasma and at the plasma/surface interface (temperatures and densities). Their knowledge allows validating the models and increasing our understanding of the phenomena. The spectroscopic analysis also provides a mean for monitoring reactors.

3.10.3.3.1.1 Optical Emission Spectroscopy Measurements

Under conditions where self-absorption is negligible, the intensity of a given emission line provided by radiation of an electronic excited species that has been excited through a direct electron collision from its ground state is linked to the electron density and the electron temperature through (Gicquel, Chenevier, Hassouni, et al., 1998):

$$I_{a,i} \propto \left(\frac{k_{a,exc}(T_e) n_e n_a}{1 + \frac{Q_a n + \sum_{k \neq i} \nu_{a,k}}{\nu_{a-i}}} \right) \tag{12}$$

where $I_{a,i}$ is the intensity of the ith emission line of the excited species a, $k_{a,exc}$, the excitation rate constant of the radiative state, Q_a, the rate constant for the collisional quenching of the emissive state with the main species, $Q_a n = \sum_{k \neq i} Q_{i,k} n_k$, where $Q_{i,k}$ represents the quenching term between the emissive i and k states and n_a, the a-species density. ν_{a-i} is the frequency of the radiative de-excitation that corresponds to the ith emission line.

Equation (13) may be used to describe the ratio of emission line intensity of two lines as a function of the position (z, r) from

$$\frac{I_{a,i}(z,r)}{I_{b,j}(z,r)} \propto \left(\frac{k_{a,exc}(T_e) n_e n_a}{k_{b,exc}(T_e) n_e n_b} \right) \times \left(\frac{1 + \frac{Q_b n + \sum_{k \neq j} \nu_{b,k}}{\nu_{b-j}}}{1 + \frac{Q_a n + \sum_{k \neq i} \nu_{a,k}}{\nu_{a-i}}} \right) \tag{13}$$

Equation (13) can be used to plot the variations of two lines of the same species, H atom ($I_{Hn=4}/I_{Hn=3}$) for instance, or that of lines of H atom and argon (I_H/I_{Ar}) as a function of the position (z, r) and for different experimental conditions. These measurements are relevant to provide information on the spatial variations of the electron temperature and of the species relative density as a function of the variables such as the power and pressure, the methane percentage introduced in the gas phase, the introduction of rare gases… However, in order to obtain absolute numbers, calibration is necessary.

In LSPM, up to 2012, calibration for electron temperature was taken from simulations carried out at 25 hPa and 600 W (9 W cm^{-3}), where the electron temperature (T_e) for cold electrons shows a maximum of around 16,000 K in the near-surface vicinity (Gicquel et al., 2001; Gicquel et al., 2012). Concerning H-atom mole fraction, calibration was based on the calculations carried out for the condition of 15 W cm^{-3} (50 hPa/1000 W) that is corresponding to the lower limit where thermal dissociation is mainly responsible for H-atom production. An H-atom mole fraction of 1.6% was obtained for this condition. Since 2012, TALIF measurements were performed to measure H-atom density in the same reactor as this is used for actinometry measurements. Calibration was made using krypton density TALIF measurements. A perfect agreement between TALIF and actinometry measurements, as well as with calculations, has been obtained (see later in the text), confirming the validity of the approach we were using previously. Concerning electron density, MW interferometry has been carried out, confirming the order of magnitude obtained through simulation (see later and Derkaoui et al., work in progress).

In LSPM and other groups, up to 2011 most of the measurements have been performed under conditions of low to medium power density with pressure in the range of 10 to 200 hPa, and power in the range of 600–3000 W. Such conditions correspond to approximately power density varying typically in the range of 6 W cm^{-3} to <50 W cm^{-3}. In the next section, spatially resolved measurements obtained in more energetic conditions, i.e. with a pressure–power up to 270 hPa–4 kW or 400 hPa–3000 W are presented (very high power density) (Derkaoui, 2012; Derkaoui et al., work in progress; Gicquel et al., 2012).

3.10.3.3.2 Carbon-Containing Species Analysis

Owing to the relatively low electron density in moderate- to high-pressure (10 hPa to 1 atm) H_2/CH_4 plasma systems, the dissociation of methane introduced in low amount (<10%) is mainly controlled by the gas temperature and by the H-atom density (see later). Its destruction/production is due mostly to gas phase reactions (effect of pressure and temperature) and in a lower importance to surface reactions (Gicquel et al., 2001; Hassouni et al., 2010; Ma, Cheesman, et al., 2009; Mankelevich et al., 2008).

Transient molecular species, in particular radicals, influence the properties of nearly all molecular plasmas, both in the laboratory and in nature. They are of great importance for several areas of reaction kinetics and chemistry. The study of the radical behavior together with their associated stable products provides a very effective approach to understanding phenomena in molecular plasmas and then to validate models. Radicals containing carbon are of special interest for basic studies, in particular, the methyl radical for diamond-deposition reactors. Thus, CH_3 radical density measurements together with those of other carbon-containing species density, as a function of some plasma variables, have been carried out to validate the chemical kinetics model in $CH_4 + H_2$ plasma reactors.

Owing to the diversity of the carbon-containing species, it is almost impossible to detect and to measure all of them. Laser diagnostics such as laser-induced fluorescence (Kaminski & Ewart, 1995), UV absorption spectroscopy, IR absorption using tunable diode lasers and/or quantum cascade lasers (Butler et al., 1989; Celii, Pehrsson, Wang, & Butler, 1988; Fan et al., 1999; Himke et al., 2007; Lombardi et al., 2005a; Ma, Cheesman, et al., 2009; Röckpe et al., 1999), DFWM (Owano et al., 1991; Owano, Kruger, Green, Williams, & Zare, 1993), CRDS (Lommatzsch, Wahl, Owano, Kruger, & Zare, 2000; Ma et al., 2008; Rennick et al., 2004), mass spectrometry (Hsu, 1992), and REMPI (Cappelli et Loh, 1994; Celii & Butler, 1992; Smith, Cameron, Ashfold, Mankelevich, & Suetin, 2001) have been used for measuring some major species such as CH_3, CH, CH_4, C_2, C_2H_2, and C_2H_6 (Cappelli, Owano, Gicquel, & Duten, 2000; Girshick et al., 1993; Wahl et al., 1996). OES (Butler, 1990; Lombardi, Benedic, et al., 2004; Osiac et al., 2002; Reeve & Weimer, 1995; Sugai et al., 1990) can also provide some key information, although the detailed analysis of the different channels for populating electronic excited states is more difficult than for H atoms, C_2 radical being an exception.

In collaboration with Jurgen Röpcke and his group, LSPM has focused on measuring the methyl radical density, together with that of three stable carbon-containing species (CH_4, C_2H_2 and C_2H_6) using infrared tuneable diode laser absorption spectroscopy (IR TDLAS) in MW ($f = 2.45$ GHz) bell-jar reactor (Lombardi et al., 2005b; Lombardi, Stancu, Hempel, Gicquel, & Roepcke, 2004). In the Bristol group that is also strongly involved in understanding diamond-deposition MW plasma reactors, they have most specifically focused their measurements on $H(n = 2)$, CH(X), C_2(a) and C_2(X) using CRDS and more recently on CH_4 and C_2H_2 density measurements using quantum cascade lasers (Ma, Cheesman, et al., 2009).

It is worth noting that these MW plasma reactors are inherently difficult to analyze due to the strong spatial variation of gas temperature, not only in the plasma region but also outside the plasma. The consequence is a strong variation of the transient and stable species over a line-of-sight beam. Deducing absolute variations of carbon-containing species inside the plasma from line-of-sight measurements provided by absorption requires developing a method that links very closely measurements and modeling (Butler et al., 2009; Gicquel et al., 2001; Gicquel et al., 2000; Goodwin, 1993a, 1993b; Hassouni & et al., 2010).

3.10.3.3.2.1 CH_3 Detection

For in situ detection of the methyl radical, only two approaches are suitable: optical methods and mass spectroscopy. In the latter case, threshold ionization mass spectrometry (TIMS) and photoionization mass spectrometry (PIMS) are suitable for detection of radicals. TIMS uses the direct ionization threshold of 9.8 eV for the neutral methyl radical. Measurements of the methyl radical using TIMS have been reported by several authors (Sugai & Toyoda, 1992; Zarrabian et al., 1998). In PIMS, a UV radiation beam is used for selective ionization of the methyl radical. Measurements using PIMS were published by Celii & Butler (1992) and Ando, Shinohara, and Takayama (1998). These studies represent a combination of mass spectroscopy and radiative interaction.

Noninvasive optical methods for detecting the methyl radical are based on absorption spectroscopy either with ultraviolet radiation at about 216 nm or in the mid-infrared near 3100 or 606 cm^{-1} (Amano et al., 1982; Davis & Martineau, 1992a; Davis & Martineau, 1992b; Fan et al., 1999). In order to reach absolute ground state density of the methyl radical, the frequencies, absorption cross-sections and the pressure-broadening coefficients of its lines have to be accurately known. The number of quantitative studies focused on the absorption cross-section and pressure-broadening coefficients of lines of the methyl radical is relatively small and the validity of the reported values is limited, depending on the pressure and temperature ranges over which they were verified. In 1986, Arthur critically discussed all the studies of the methyl absorption cross-section at 216.4 nm, mainly derived from photolysis techniques using several precursors. Based on molecular modulation spectrometry, which is similar to repetitive flash photolysis, the author proposed a peak absorption cross-section for methyl of $\sigma = 3.9 \times 10^{-17}$ cm^2, measured at room temperature (Arthur, 1986). In 1993, Davidson and coworkers, who used shock tube experiments, compiled the results of other groups in this field and derived the absorption coefficient of the methyl absorption in the UV spectral range at 216 nm from their own measurements at pressures near 1 atm and at temperatures between 1300 and 2500 K. The reported accuracy was about 20% (Davidson, Chang, Di Rosa, & Hanson, 1993). In 1995, the group revised their data to about one-half of the former expression (Davidson, Di Rosa, Chang, & Hanson, 1995).

In the first broadband UV absorption measurements for quantitative detection of methyl radicals in a HF reactor containing HCs, Childs et al. (1992) used the absorption cross-section reported by Arthur (1986) and neglected the influence of temperature on the cross-section. In succeeding papers, the same group extended its studies to DC glow discharges and calculated concentrations of the methyl radical using the temperature-dependent cross-sections of Davidson et al. (1993), $\sigma = 7.665 \times 10^{-17} \times \exp(-T/1087\ \mathrm{K})\ \mathrm{cm}^2$ (Menningen et al., 1993), and the derived data of Glänzer, Quack, and Troe (1977), $\sigma = 3.88 \times 10^{-17} \times \exp(-T/969.6\ \mathrm{K})\ \mathrm{cm}^2$ (in Menningen et al., 1995). Based on the remeasured absorption cross-section of Davidson et al. (Hirose & Kondo, 1988), $\sigma = 2.03 \times 10^{-17} \times \exp(-T/1675\ \mathrm{K})\ \mathrm{cm}^2$, Cappelli and coworkers used the method of broadband UV absorption at 216 nm for quantitative detection of the methyl radical in plasmas of a supersonic arc jet (Loh & Cappelli, 1997) and of an MW bell-jar reactor (Cappelli et al., 2000), both used for diamond deposition. Applying CRDS, Zalicki and Zare (1995); Zalicki et al. (1995a) performed CH_3 concentration measurements with UV radiation at 216 nm, using the cross-section of Davidson et al. (1995), and at 213.9 nm (Wahl et al., 1997; Zalicki et al., 1995b), using the cross sections of Hwang, Rabinowitz, and Gardiner (1993), in a HF reactor.

A highly important study for quantifying the densities of methyl radicals by IR absorption techniques was the determination of the line strength of the $Q(8,8)$ line of the $\nu 2$-band of methyl at 608.3 cm^{-1} by Wormhoudt & McCurdy (1989) using TDLAS in 1989. The only pressure-broadening coefficients for CH_3 lines have been determined for the $Q(6,6)$ line of the $\nu 2$-band at 607.024 cm^{-1} in two gases—argon and nitrogen—for pressure values of up to about 53 mbar by Robinson, Zahniser, Freedman, & Nelson (1996), also using TDLAS. For diagnostic studies in plasmas containing HCs, the IR TDLAS technique has proven to be the most useful because it can also measure the densities of related species, providing they are IR active. In the decade, this flexibility has been demonstrated by measuring the density of CH_3 and various related stable molecules in several types of nonequilibrium molecular plasmas (Röpcke, Revalde, Osiac, Li, & Meichsner, 2002; Wormhoudt, 1990). Celii et al. were the first to detect the absorption spectrum of the methyl radical in a HF CVD reactor using TDLAS (Yamada, Hirota, & Kawaguchi, 1981; Yamada & Hirota, 1983) and made rough estimates of the densities of CH_3, C_2H_2, CH_4, and C_2H_4 near the filament (Celii et al., 1988).

In LSPM, both spectroscopic approaches (UV and IR techniques) have been compared to verify the applicability of the absorption cross-sections or line strengths for the conditions under study (Lombardi, Stancu, et al., 2004). This comparison was important since the limitations of the validity of the line parameters are directly related to the accuracy of calculated methyl densities and in turn to the quality assessment of related plasma chemical modeling. IR TDLAS was seen to be a powerful diagnostic, which allows high spectral resolution (typically $10^{-4}\ \mathrm{cm}^{-1}$), high selectivity (up to 10^{-5} as the detection limit) and time-resolved diagnostics (up to 1 μs) (Ropcke et al., 2000). The reader is invited to consult Lombardi, Stancu, et al. (2004), Lombardi, Hassouni, et al. (2004).

Besides comparing the UV and IR absorption methods, LSPM, in collaboration with the INP group headed by J. Röpcke, investigated a relatively wide range of experimental conditions, with typical pressure/power ranging from 25 hPa/600 W to 120 hPa/2 kW. For these conditions, the maximum gas temperature ranged from 2200 to 2800 K. Since TDLAS is a line-of-sight averaged technique, the analysis of the experimental data has required the use of a one-dimensional nonequilibrium transport model that provides species density and gas-temperature variations along the optical beam that is along the reactor diameter (Lombardi, 2003; Lombardi et al., 2005b).

3.10.4 Analysis of the Plasma Operating at High Power Density: Identification of the Main Production and Loss Processes for H Atoms and CH_3 Radicals

Owing to the important role of H atoms for diamond deposition, the control of their density and of their production and consumption governing parameters is crucial. The main elementary processes responsible for their production and destruction in the plasma and at the plasma/surface interface have been partially discussed above. The H-atom production rate is a function, in plasma reactors, of both the electron temperature and the gas temperature, which respectively control the electron impact dissociation and the thermal dissociation of molecular hydrogen. However, as shown before, while at low power density ($<15\ \mathrm{W\ cm}^{-3}$), the electron impact dissociation plays a significant role, at high power density ($>15\ \mathrm{W\ cm}^{-3}$), thermal dissociation remains the only channel for dissociation of molecular hydrogen as well as methane.

The H atoms strongly participate to methane dissociation and CH_3 radicals production in volume via $H + CH_x \Leftrightarrow CH_{x-1} + H_2$ ($x = 3,4$) or $H + CH_3 + M \rightarrow CH_4 + M$ very fast set of collisional reactions (Angus, 1994; Angus et al., 1993; Goodwin, 1993b; Rayar, Supiot, Veis, & Gicquel, 2008), that occurs at relatively high temperature. These reactions may participate to H-atom loss, in competition to volume recombination reaction such as $H + H + H_2 \Leftrightarrow 2\,H_2$ as well as to surface reactions such as catalytic recombination, etching and abstraction processes (Frenklach & Wang, 1991; Goodwin, 1993a; Harris & Belton, 1992).

The estimation of the importance of the different phenomena is the subject of next section, in particular for the conditions of very high power density. The stainless-steel reactor and the experimental setup used to perform OES and TALIF measurements are shown in **Figure 7**.

Although the electron impacts with molecular hydrogen do not participate, at high power density, to the H-atom production, the electrons remain the reactor engine for heating the gas. Let us then first analyze the electron density and electron temperature behavior inside the plasma. Electron temperature profiles obtained from simulation and from OES measurements (from $I_{H\alpha}/I_{H\beta}$ emission intensity ratios measurements) are presented in **Figure 6(a)**. A rather constant electron temperature is observed in the plasma phase excepted at the plasma/surface interface, where a slight increase followed by a decrease at the surface is observed. While the spatial distribution of electron temperature is well described by the model, the latter is however seen to underestimate the value of electron temperature. This fact indicates that an improvement of the electron kinetics of the model must be done for treating high-power density plasmas. In **Figure 6(b)** is shown the calculated electron density axial profile for typical experimental conditions. Note that after 2.5 cm from the surface, due to the strong decrease of the electron density that lowers the emission intensities, emission spectroscopic measurements are difficult to realize. This implies that OES measurements are expected to be scattered at these locations.

3.10.4.1 H-Atom Production and Loss

3.10.4.1.1 H-Atom Density Spatial Analysis

The control of the diamond quality and growth rate needs mastering the gas phase processes responsible for the production and loss of the species governing the surface reactions, as well as the surface temperature. As a matter of fact, the latter controls the surface chemistry dynamics such as adsorption, desorption and abstraction reaction yields, as well as the surface mobility, and then, together with the H-atom and CH_3 densities at the surface, governs the species supersaturation and the growth mechanisms (1D or 2D) (Spitsyn, Bouilov, & Alexenko, 2000; Spitsyn, Bouilov, & Derjaguin, 1981).

As already discussed in different papers, and illustrated in **Figure 3**, the H-atom production, for power densities higher than $15\ \mathrm{W\,cm^{-3}}$, is entirely governed by thermal processes, i.e. by the gas temperature. The latter strongly increases with the pressure/power, i.e. the power density, as reported in **Figure 8** where experimental measurements show an increase of gas temperature from 2200 K at 25 hPa–600 W up to 3200 K at 400 hPa–3000 W.

The increase in gas temperature clearly appears stronger in the domain from low to medium power density than at high power density. As a matter of fact, at low power density, most of the power is channelled to heat up the gas, while at high power density, it is mainly channelled for dissociating molecular hydrogen and HC-containing species.

Simulations of the axial distribution variations of gas temperature and of H-atom mole fraction for low, moderate and high power densities are presented in **Figure 8** for the stainless-steel reactor configuration (Derkaoui, 2012; Gicquel et al., 2012). In the upper part of the reactor ($z > 6$ cm), the gas temperature is lower than 1000 K, and then a strong increase in the gas temperature is observed as the plasma approaches. The maximum gas temperature is reached inside the plasma that is followed by a decrease due to energy transfer from the plasma to the surface (**Figure 9(a)**). H-atom density is also seen to increase first in the plasma phase and then to decrease at the plasma/surface interface (**Figure 9(b)**) (Gicquel et al., 2012). Experimental measurements confirm the simulation results as seen in **Figure 9(c) and (d)** (gas temperature and H-atom density).

It is worth noting that the comparisons between experiments and simulations offer a rather good agreement, confirming that the 1D H_2–CH_4 model is relevant even at relatively high power density (200 hPa–3000 W). In particular, the excellent agreement between H-atom mole fraction obtained from (1) OES (through emission intensity ratio $I_{H\alpha}/I_{Ar7}$), (2) TALIF and (3) calculations, both in shape and values, makes us confident.

For the conditions of high power density (pressure > 100 hPa and power > 2 kW), i.e. when the gas temperature controls the dissociation, we can distinguish, as a function of z (the axial coordinate), three zones: the heating/diffusive zone expending from approximately $z = 6$ cm to $z = 3$–4 cm from the substrate surface, the

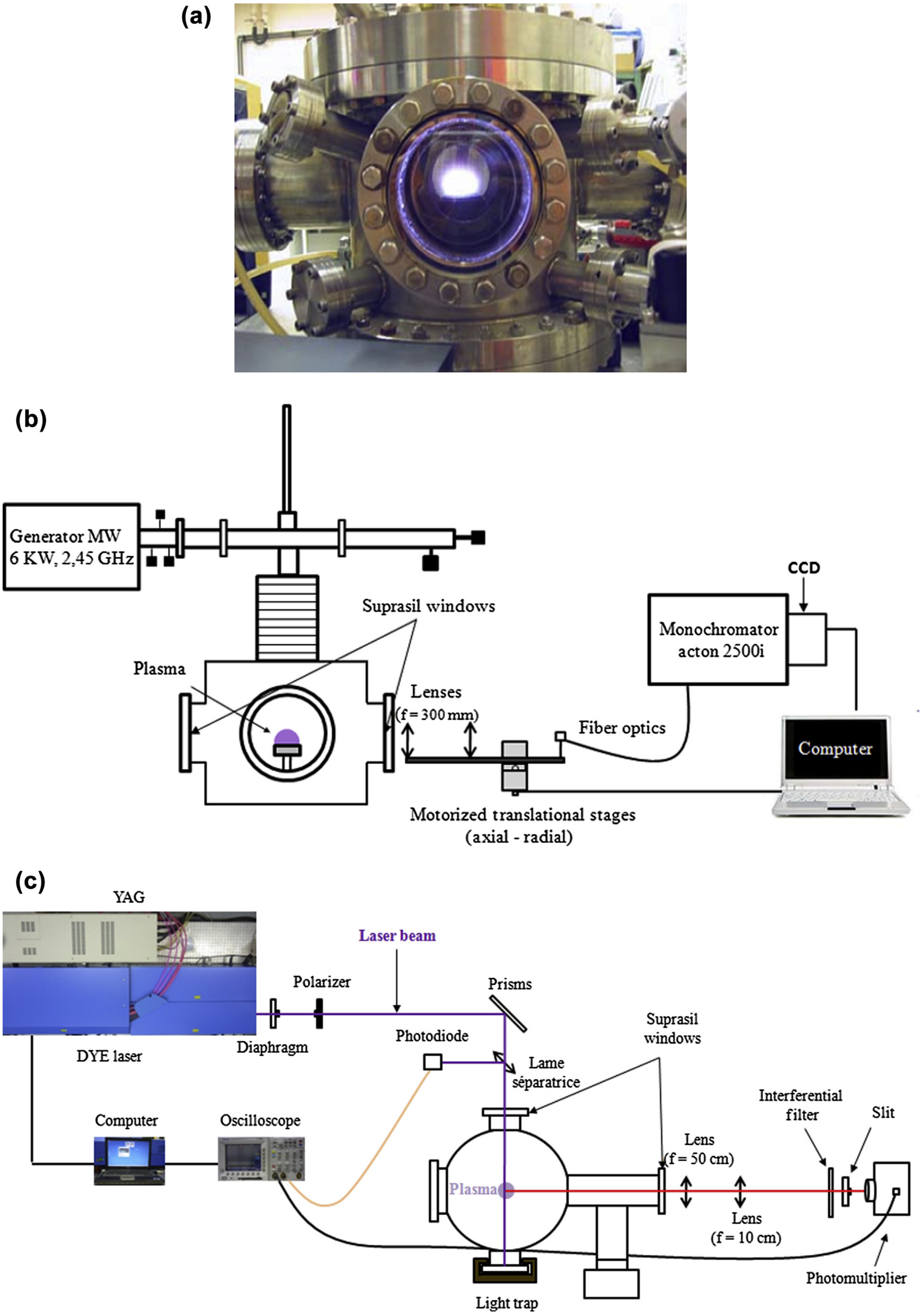

Figure 7 (a) Stainless steel microwave plasma reactor designed at LSPM; (b) OES experimental set up and (c) TALIF experimental set up (Derkaoui, 2012; Gicquel, Hassouni, et al., 1996; Wartel et al., work in progress).

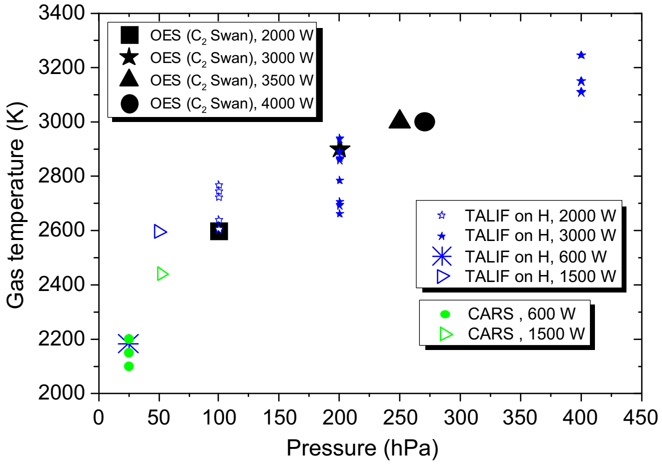

Figure 8 Variations of TH (TALIF), line-of-sight THα (OES) (both from Doppler broadening), and T_{H2} (from CARS) measured at distances of 15 (for high power densities) to 20 mm (low power densities) from the substrate as a function of pressure for different powers (Derkaoui, 2012; Gicquel, Hassouni, et al., 1996; Wartel et al., work in progress).

H-atom production zone characterized by a gas temperature higher than 2600 K that expands from $z = 3$–4 cm to $z = 0.2$–0.5 cm, and finally the plasma/surface interface ($z < 0.5$ cm) where a high energy transfer occurs leading to the decrease of the gas temperature and the H-atom density. The region of high H-atom density ($[n_H > 6 \times 10^{15}$ cm^{-3}), that we will call the "active plasma volume," is larger than the H-atom production zone, since it expands from $z = 4.7$ cm to less than $z = 0.1$–0.2 cm (Figures 9(e) and 9(f)). The estimation of the thicknesses of the different plasma regions is given in Table 3. We can note that except for two couples 250 hPa/3500 W and 270 hPa/4000 W, varying simultaneously pressure and power in the range (25–400 hPa; 600–3000 W) lead to a rather constant plasma volume. For the related conditions, the accessible surface for diamond deposition will then be rather similar. However, we must be conscientious that due to the highly nonuniform spatial distribution of H-atom density, the film thickness is expected to be nonuniform in particular as pressure increases. For the conditions 250 hPa/3500 W and 270 hPa/4000 W, we can note an increase in the plasma volume associated to higher gas temperatures and higher H-atom densities, than that observed at 3000 W.

Furthermore, the observation of Figure 9(e) and (f) clearly reveals that the maximum of both the gas temperature and the H-atom mole fraction is shifted toward the diamond surface as the power density is increased. This behavior leads to a rather strong increase in H-atom flux to the surface since both the maximum value and the gradient are boosted as power density is raised.

As seen above, another important process variable is the methane percentage that is introduced into the discharge. As a matter of fact, growing fast diamond requires increasing CH_3 radical density. Although it has been shown that increasing the methane percentage does not modify electron behavior, let us analyze its effect on the H-atom density profiles. As the percentage of methane is increased into the gas phase, no sensitive variation, neither in shape nor in value, is observed on the H-atom mole fraction spatial distribution is observed (Figure 10).

3.10.4.1.2 Influence of the Power Density

The variations of the electron temperature, the electron density and the H-atom mole fraction/density, at their maximum values in the plasma core ($z = 1.2$–1.7 cm) as a function of the power density are shown in Figure 11. (Derkaoui, 2012; Gicquel et al., 2012).

The electron temperature is seen to strongly decrease as a function of the pressure/power (Figure 11(a)), due to enhanced collision frequency, while the electron density is shown to increase (Figure 11(b)). The comparison between experimental and theoretical results confirms the underestimation of the electron temperature by simulations and reveals a discrepancy in the variation of the electron density as a function of power density. This confirms the need to further improve the electron kinetics of the model, for these conditions of high power density.

The experimental H-atom densities measured by actinometry and TALIF as a function of the pressure for different powers and for 1 and 4% of methane are reported in Figure 11(c). From actinometry, the H-atom density is seen to strongly increases from 5×10^{14} cm^{-3} to 5×10^{17} cm^{-3} (around two orders of magnitude)

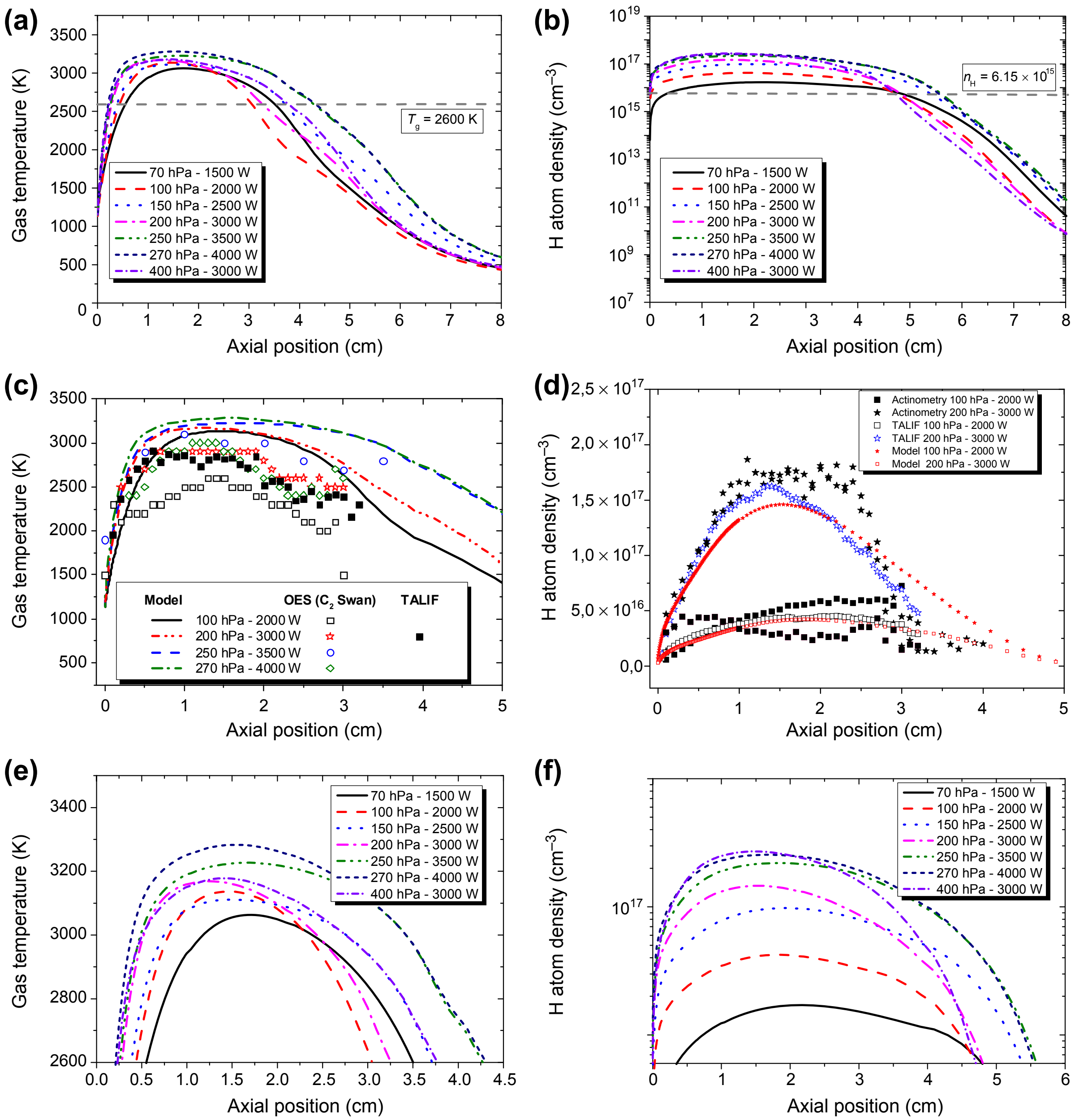

Figure 9 (a) Calculated spatial distribution of gas temperatures and (b) H-atom density for different couples (pressure, power)): 70 hPa, 1500 W, 100 mbar -2000W, 150 hPa-2500 W; 200 hPa – 3000 W; 250 hPa – 3500 W; 400 hPa – 3000 W; 270 hPa, 4000 W; (c) comparison between calculated (lines) and experimental gas temperature. Experimental measurements were obtained by OES from the rotational spectrum on the Swan system and by TALIF (black squares). (d) Comparison between calculated and experimental H atom density axial profiles for two conditions: H_2/CH_4 at 200 hPa, 3000 W, 4 % of CH_4, 500 sccm and at 100 hPa, 2000 W, 4 % of CH_4, 500 sccm. Experimental measurements were carried out either by OES, or by TALIF. (e) Calculated Tg profiles corresponding to the H atom production zone (Tg > 2600 K), and (f) calculated n_H profiles corresponding to high n_H ($n_H > 6.15\ 10^{15}\ \text{cm}^{-3}$), *i.e.* of the active plasma zone. The same conditions as in **Figure 9a** are considered (Derkaoui, 2012; Derkaoui et al., work in progress; Spitsyn et al., 1981; Wartel et al., work in progress).

when the pressure and power couple increases from (25 hPa–600 W) up to (400 hPa–3000 W), the corresponding H-atom mole fraction increases from 1% to almost 60%.

It is worth noting that the H-atom densities measured by actinometry at high pressure are always much higher than those calculated and those measured by TALIF. As a matter of fact, the calculated H-atom density increases from 0.5 to 1 × 10^{15} cm^{-3} to 2.8 × 10^{17} cm^{-3}. We may mention that at high power density, the calculated values

Table 3 Variations as a function of pressure and power of some plasma characteristics thicknesses corresponding to the heating/diffusive section, the H-atom production section (Tg > 2600 K) and the H-atom section where $n_H > 6\ 10^{15}\ cm^{-3}$.

Pressure (hPa)	*Power (W)*	$e_{heating/diffusive}$ *(cm) 1000* K $< T <$ *2600* K	e_{prod} *(cm)*	e_H *(cm)* $n_H > 6 \times 10^{15}\ cm^{-3}$
70	1500	2.4	2.9	4.4
100	2000	2.6	2.5	4.7
150	2500	2.8	3.4	5.3
200	3000	2.6	2.9	4.7
250	3500	2.5	4.0	5.6
270	4000	2.5	4.1	5.5
400	3000	1.8	3.4	4.7
400 without any recombination on reactor walls	3000	7	7	6.5

underestimate the H-atom density by construction, since in the 1D model is considered a radial loss of H atom due to recombination on the walls similar whatever the conditions of pressure. We will see later that this is not correct since at high pressure, volume recombination consumes H-atom which will not reach the walls. As a consequence, the radial term due to wall H-atom recombination has to be lowered as pressure increases. A 2D approach is necessary to take into account precisely this effect. To explain now the discrepancy between measurements from actinometry and TALIF, we may recall that actinometry measurements are based, on the one hand, on the use of quenching cross-sections that are unfortunately not very well known. When moving from low to high power density, the plasma progressively goes from almost pure molecular hydrogen plasma toward a 50% molecular –50% (or more) atomic hydrogen plasma. As a consequence, the respective importance of the cross-sections (those corresponding to collisions with molecular hydrogen and atomic hydrogen) are modified, inducing an effect on the absolute values. On the other hand, H-atom and krypton TALIF measurements depend of the fluorescence life times of the two species. At high pressure, H-atom fluorescence life times (around 5 ns) are shorter than the laser pumping time, leading to an uncertainty on the H-atom life time measurements and then to the H-atom absolute density. Finally, at high pressure–high power, when performing TALIF measurements, we have noticed laser beam absorption by the gas phase (when adding methane). Although this effect seems to be negligible in the absence of methane, a deeper analysis is in progress today at LSPM.

Note furthermore that the OES measurements obtained at high-power-density conditions appeared more dispersed than the TALIF measurements. It is partly attributed to the strong decrease in the argon line emission intensity due to the low electron temperature at high pressure that increases the error made on the emission intensities, and partly to the fact that experiments have been realized over a long period of time (around 2 years), with a consequence of possible changes in the MW coupling parameters. On the opposite, TALIF measurements have been carried out on a restricted period of time (6 months) without any change in the MW coupling parameters.

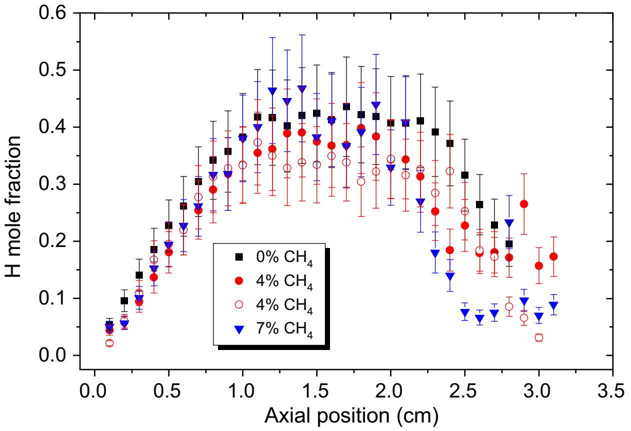

Figure 10 H atom mole fraction experimental (OES) axial profiles for three percentages of methane: 0 %, 4 %, and 7 % at 200 hPa, 3000 W, and 500 sccm (Derkaoui, 2012).

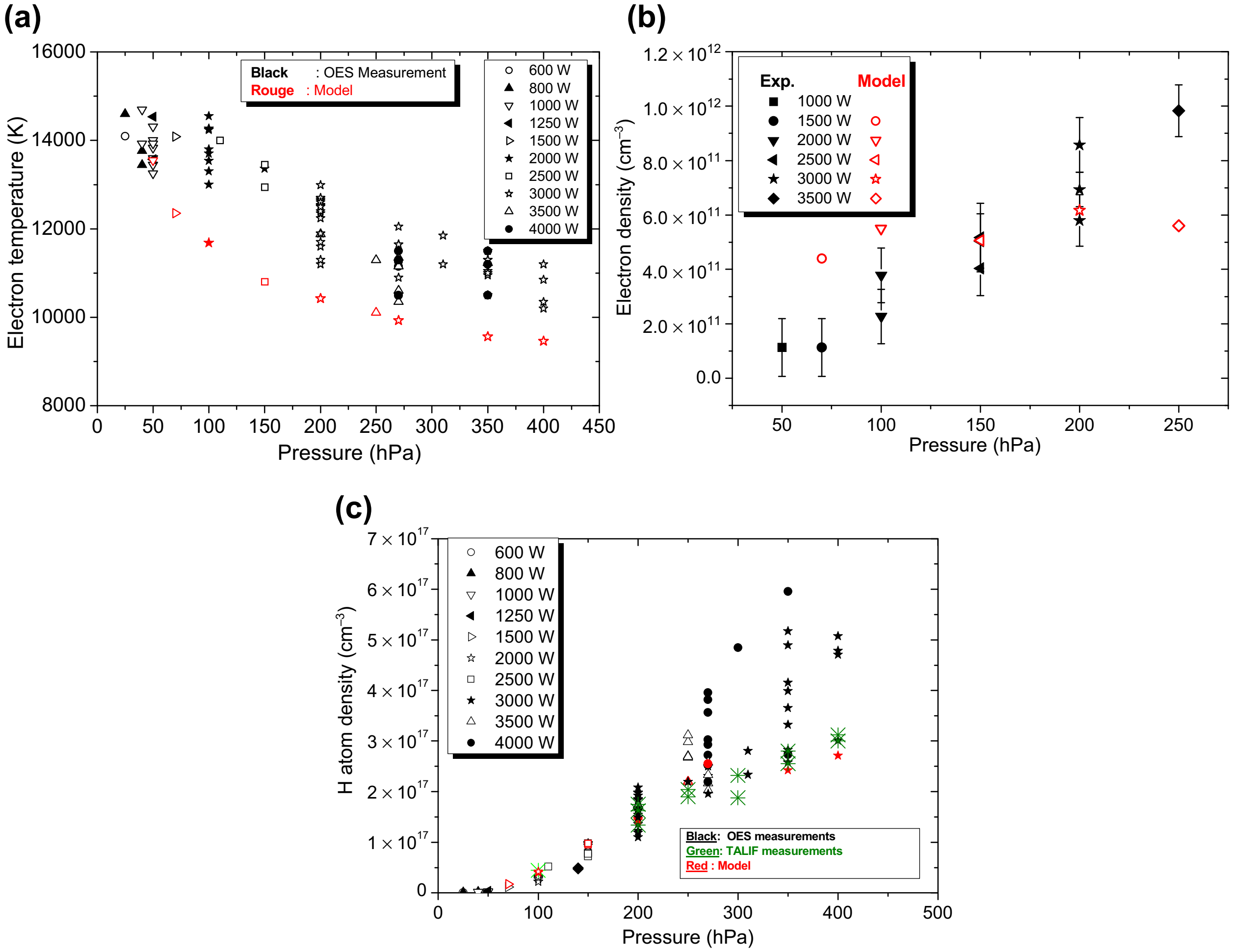

Figure 11 (a) Measured (OES) and calculated electron temperature variation as a function of pressure for different microwave powers, at 15 mm from the substrate. Measurements were performed from $I_{H\alpha}/I_{H\beta}$ ratio measurements. Conditions: H_2/CH_4 with 4 % CH_4 and 500 sccm. (b) Variation of the measured and calculated electron density as a function of pressure for different microwave powers. The volume-of-sight measurements were performed by microwave interferometry. Conditions : H_2/CH_4 with 4 % CH_4 and 500 sccm.(c) Maximal plasma bulk measured and calculated H-atom density as a function of pressure for different microwave powers. The measurements were obtained from actinometry and from TALIF. The measurements performed at 4 % and 7 % of methane are plotted (flow rate = 500 sccm) (Derkaoui, 2012; Gicquel et al., 2012).

Whatever the absolute value, all the tendencies obtained by TALIF, modeling and OES remain the same. For the following pages, we have opted to base our approach on the measurements made by OES (actinometry) although we are conscientious that they are probably slightly overestimated.

The strong increase in H-atom density as the gas temperature increases and as the electron temperature decreases confirms that at high power density, dissociation is only carried out through heavy–heavy collisional reactions that are activated by rotational–vibrational excitation. Since the vibrational temperature is in equilibrium with the translational one (Hassouni et al., 1999), the whole process appears to be governed by the gas temperature.

Finally, the influence of increasing the power from 3000 to 4000 W, for a constant pressure of 270 hPa, is such that the H-atom density is raised from 2.2×10^{17} cm^{-3} to 3.5×10^{17} cm^{-3} due to the increase in the gas temperature (Figure 9(e)).

3.10.4.1.3 Production and Loss Processes and Boundary Layers behavior

The net H-atom production yields for different reactions as a function of the power density (pressure/power) are shown in Figure 12. As already mentioned, the thermal dissociation of molecular hydrogen clearly dominates at high power density. Two processes are responsible for the production of H atoms: $H_2 + H_2 \rightarrow 2H + H_2$, and

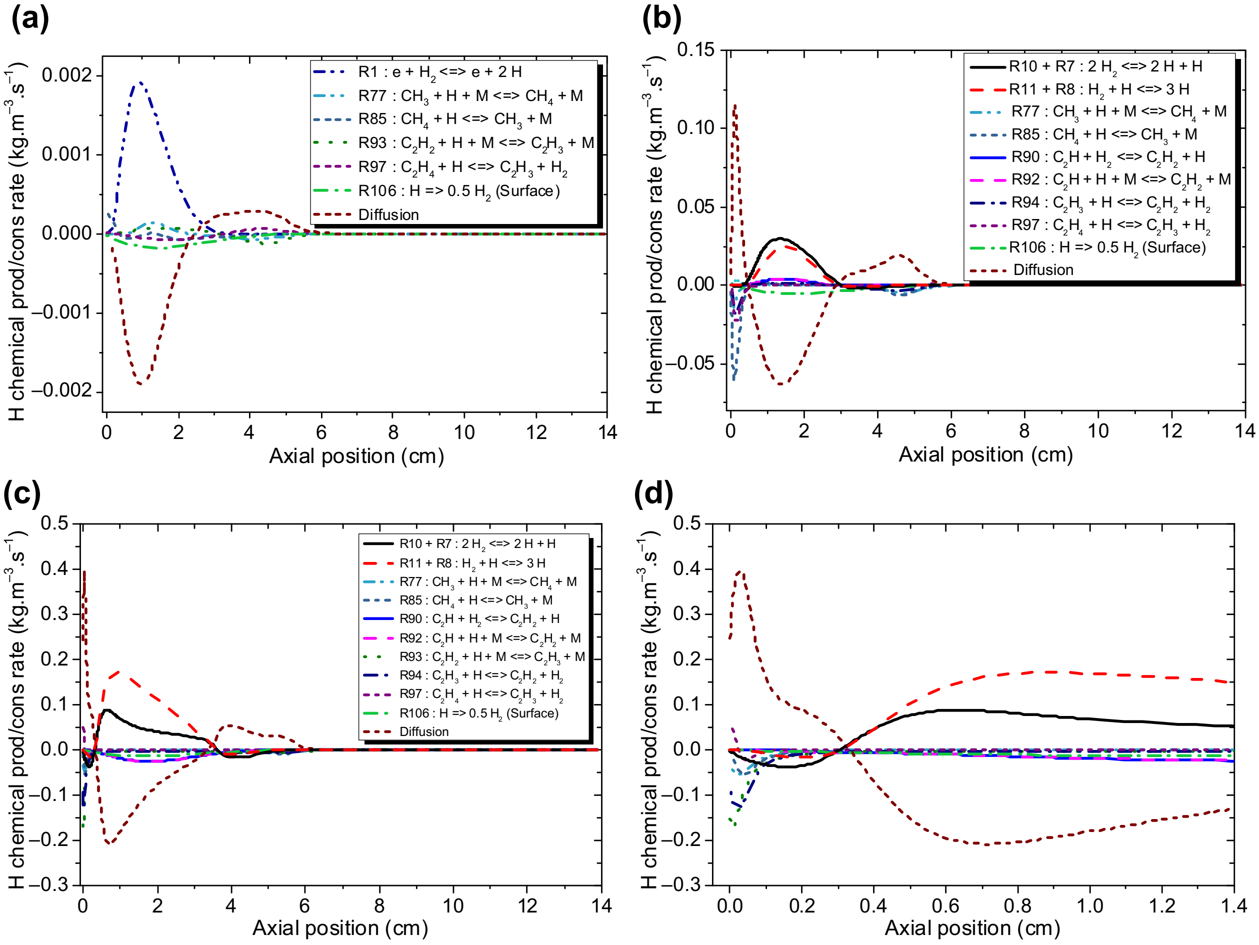

Figure 12 Profiles of net production yields for H-atom at different couples (pressure and power): (a) 25 hPa / 600 W; (b) 100 hPa / 2000 W; (c) 270 hPa / 4000 W; (d) details of (c) at the near vicinity of the surface. The percentage of methane is kept constant at 5 % (Derkaoui, 2012; Rond et al., work in progress).

$H_2 + H \rightarrow 3H$. Under conditions of high H-atom density, the second process dominates. At 9 W cm^{-3} (25 hPa/600 W) (Figure 12(a)), atomic hydrogen is mainly produced by electron collisional dissociation process, the gas temperature being not high enough to ensure high molecular hydrogen vibrational excitation, and the consequent thermal dissociation due to successive inelastic collisions. At 270 hPa/4000 W (Figure 12(c)), molecular hydrogen electronic dissociation is totally inefficient versus the thermal dissociation. Diffusion toward locations of lower H-atom density ensures an efficient transport of H-atom through the surface boundary layer until the diamond surface, where they recombine.

At low power density, the H-atom density is low and the surface recombination reaction at the reactor stainless-steel walls is seen to contribute to the decrease of H atoms in gas phase (Reaction (106) in Figure 12(a)). At high power density (270 hPa for instance), this process becomes negligible and volume recombination becomes significant even in the near-surface vicinity (Figure 12(d)).

At the plasma/surface interface, the diffusion process, driven by the high H-atom density gradient, is the process responsible for extraction of H atoms from the gas phase. The H-atom consumption at the surface acts as a well for H-atom and diffusion constitutes its supplier.

In order to estimate the importance of diffusion relatively to volume recombination, let us analyze their corresponding characteristic times. Once the H atoms are produced, the H-atom spatial evolution is given by the continuity equation. In one dimension, it is written as follows:

$$u(\partial n_H/\partial z) + \mathrm{d}n_H/\mathrm{d}t = D_H\left(\partial^2 n_H/\partial z^2\right) + R_H \tag{14}$$

where u is the gas velocity, n_{H}, the H-atom mole fraction, and R_{H}, the H-atom loss rate due to reaction in volume. The associated boundary condition is

$$D_{\mathrm{H}}(\partial n_{\mathrm{H}}/\partial z) = R_{\mathrm{SH}} \tag{15}$$

where R_{SH} is the total H-atom surface consumption reaction rate.

At the steady state and without any convective flux (stagnation point condition), it comes,

$$D_{\mathrm{H}}\left(\partial^2 n_{\mathrm{H}}/\partial z^2\right) + R_{\mathrm{H}} = 0 \tag{16}$$

The diffusion characteristic time is given by

$$\tau_{\mathrm{diff}} = \delta_{\mathrm{H}}^2/\mathrm{D_H} \tag{17}$$

where D_{H} is the atomic hydrogen diffusivity ($\mathrm{m^2\ s^{-1}}$), while the volume recombination characteristic time for H atoms is given by

$$\tau_{\mathrm{Rec\ vol}} = \frac{1}{2.76 \times 10^{-31} T_{\mathrm{g}}^{-0.6} n_{\mathrm{H_2}} \cdot n_{\mathrm{H}}} \tag{18}$$

In **Table 4** are reported the values of τ_{diff} and $\tau_{\text{rec-vol}}$ obtained, at the plasma/surface interface, in LSPM MW reactors for different conditions of pressure and power. In addition, are reported values corresponding to HF reactor and also two conditions simulated by Goodwin (1993a): one simulates a hydrogen–methane medium heated at 3000 K, the other a fully dissociated medium interacting with a surface with a velocity gradient of $10^5\ \mathrm{s^{-1}}$.

For all the systems reported here, the plasma/surface interfaces are H diffusion limited. Transport by diffusion takes much less time than volume recombination reaction does.

In **Table 5** are reported τ_{diff} and $\tau_{\text{rec-vol}}$ corresponding to the "heating/diffusive zone" for the LSPM MW reactors. The results clearly show that while at low pressure this zone is dominated by the diffusion transport, the volume recombination processes become to play a significant role when pressure reaches 200 hPa. Note that these simple calculations do not include recombination processes with HC.

Table 4 Comparison between H atom diffusion characteristic times and H atom volume recombination characteristic times for different gas phase conditions, at the plasma / surface interface.

Reactor and Conditions	*Pressure (hPa)*	δ_H *(exp or model) (m) See* **Table 6**	T_g *(Boundary Layer) (K)*	τ_{diff} *for H (s)*	$\tau_{Rec\ vol}$ *for H at 1500 K) (s)*	*Ratio* $\tau_{volRec}/\tau_{diff}$
Hot filament Goodwin/Chen	20	0.60	Fil temp 2600	36×10^{-3}	>4	>100
LSPM 25 hPa–600 W	25	0.017	1100	9×10^{-4}	40	43×10^3
LSPM 70 hPa–1500 W	70	0.0145	1100	1.2×10^{-3}	2	1670
LSPM 100 hPa–2000 W	100	0.008	1100	4.2×10^{-4}	0.6	1430
LSPM 150 hPa–2500 W	150	0.011	1100	1.2×10^{-3}	0.264	210
LSPM 200 hPa–3000 W	200	0.008	1100	8.4×10^{-4}	0.12	142
LSPM 270 hPa–4000 W	270	0.007	1100	8×10^{-4}	0.066	80
LSPM 400 hPa–3000 W	400	0.005	1100	7.3×10^{-4}	0.04	55
Gas @ 3000 K From Goodwin	1000	0.007	1100	2.5×10^{-3}	$2.8\ 10^{-3}$	1
Fully dissociated flow interacting surf @ of $10^5\ \mathrm{s^{-1}}$ From Goodwin	2000	0.0001	1100	5×10^{-7}	6	1.2×10^7

Table 5 Comparison between H atom diffusion characteristic times and H atom volume recombination characteristic times for different gas phase conditions, at the plasma heating / diffusive section (2 cm< z <4 cm).

Microwave Reactors	BL$_H$ *Thickness (m)*	$T_{g_{\max}}$ *(K)*	*Pressure (hPa)*	τ_{diff} *for* H *(s)*	$\tau_{Rec\ vol}$ *for* H *(s)*	*Ratio* $\tau_{volRec}/\tau_{diff}$
LSPM 25 hPa–600 W	0.03	2200	25	3.5×10^{-3}	5	2200
LSPM 70 hPa–1500 W	0.03	2200	25	6.4×10^{-3}	0.194	30
LSPM 100 hPa–2000 W	0.025	2800	100	5×10^{-3}	4.7	11
LSPM 150 hPa-2500 W	0.025	2900	150	8×10^{-3}	0.0144	1.84
LSPM 200 hPa–3000 W	0.022	3000	200	7.15×10^{-3}	7.35×10^{-3}	1
LSPM 270 hPa–4000 W	0.022	5000	1000	7×10^{-3}	3.3×10^{-3}	0.46
LSPM 400 hPa–3000 W	0.015	3200	400	1.1×10^{-2}	1.5×10^{-3}	0.14

As a conclusion, we can state that at the plasma/surface interface, the MW reactors operating up to 400–500 hPa remain dominated by the diffusion transport.

At the plasma/surface interface, the continuity equation becomes

$$D_{\mathrm{H}}\left(\partial^2 n_{\mathrm{H}}/\partial z^2\right) = 0 \tag{19}$$

$$\text{with the boundary condition}: D_{\mathrm{H}}(\partial n_{\mathrm{H}}/\partial z) = R_{\mathrm{SH}} \tag{20}$$

At the diamond surface, the H atoms recombine and/or participate to surface reactions, such as abstraction for instance. In principle, to calculate R_{SH}, one should identify the main processes, together with their reaction rates to obtain an expression for R_{HS}. However, using the global parameter H-atom recombination coefficient γ_{H} allows one simulating all the processes with only one parameter.

On diamond surface, γ_{H} has been determined by different authors (Goodwin, 1993b; Krasnoperov et al., 1993; Rousseau, Cartry & Duten, 2001), and Goodwin proposed the following expression as a function of the surface temperature:

$$\gamma_H = 410^{-4} + 1.95\ \exp(-3025/T) \tag{21}$$

At 1100 K, $\gamma_{\mathrm{H}} = 0.12$.

Note that γ_{H} is also defined for recombination on quartz surfaces and water-cooled stainless-steel walls. The corresponding values have been taken at 10^{-3}–10^{-4} (Kim & Boudart, 1991) and 10^{-2} (Tserepi & Miller, 1994), respectively.

Equation (15) allows us obtaining the H-atom mole fraction (and density) at the surface:

$$D_{\mathrm{s}} \vec{\nabla}\, n_{\mathrm{s}} \cdot \vec{n}\big|_{\mathrm{wall}} = R_{\mathrm{HS}} = \gamma_{\mathrm{s}} \frac{v_{\mathrm{s}}^*}{4} n_{\mathrm{s-w}} \quad \text{for} \quad \mathrm{H-atoms} \tag{22}$$

Written in one dimension, it comes

$$n_{\mathrm{H}}\big|_{\mathrm{s}} = \left(1 + \gamma_{\mathrm{s}} \frac{\delta_{\mathrm{H}} v_{\mathrm{s}}^*}{4D_{\mathrm{H}}}\right)^{-1} n_{\mathrm{HMax}} = \left(1 + \gamma_s \frac{\delta_{\mathrm{H}} v_{\mathrm{s}}^*}{4D_{\mathrm{H}}}\right)^{-1} n_{\mathrm{H}\infty} \tag{23}$$

where $n_{\mathrm{H}}|_{\mathrm{s}}$ and $n_{\mathrm{H}\infty} = n_{\mathrm{HMax}}$ represent the H-atom mole fraction at the diamond surface and in the plasma at their maximum value, respectively.

In **Figure 13(a)** is reported the variation of $n_{\mathrm{H}}|_{\mathrm{s}}$ as a function of pressure for different powers: in agreement with what is observed in the gas phase, a strong increase of $n_{\mathrm{H}}|_{\mathrm{s}}$ occurs as the power density increases. In **Figure 13(b)** is reported the variation of $n_{\mathrm{H}}|_{\mathrm{s}}$ as a function of the maximum of n_{H} into the plasma bulk. A quasi-linear variation is observed and an increase from 2.5×10^{15} to 2.4×10^{16} cm^{-3} is observed for an increase of n_{H}

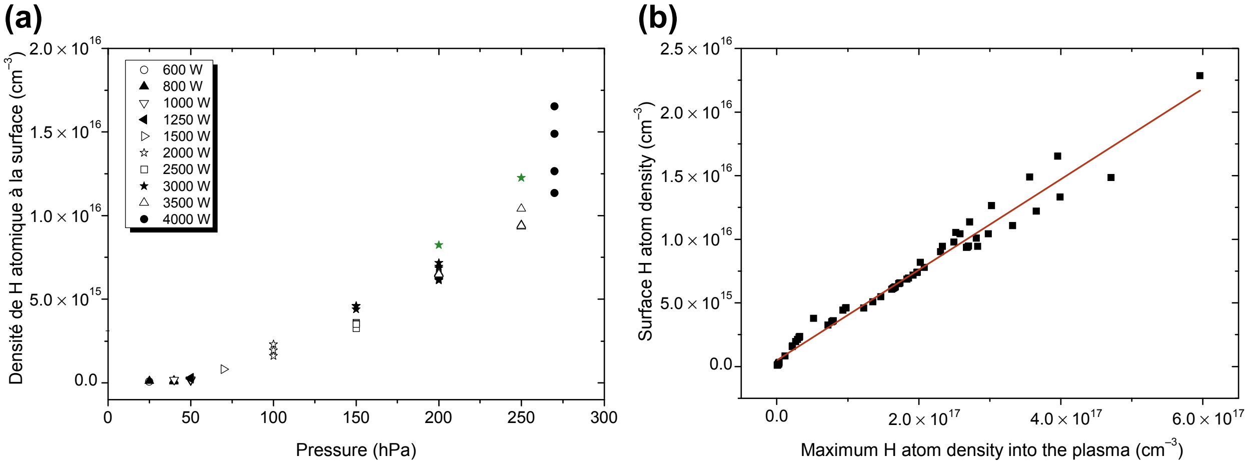

Figure 13 (a) Variations of the surface H-atom density as a function of pressure for some different powers; (b) H-atom density of the diamond surface as a function of the maximum of H-atom density in the plasma bulk (Derkaoui, 2012; Derkaoui et al., work in progress).

from 0.5×10^{17} to $6 \times 10^{17} \times \text{cm}^{-3}$, i.e. when the couple (pressure, power) varies from (100 hPa–2000 W) to (350 hPa–4000 W).

$n_H|_s$ values reported here must be compared to the maximal value at the surface (6×10^{17} cm^{-3}) predicted by Goodwin et al. for a fully dissociated gas flowing at 5000 K and 2 atm, arriving at the stagnation point with a stagnation-point velocity gradient of 10^5 s^{-1} (quasi-absence of boundary layer). We observe a difference of more than one order of magnitude with our maximal experimental values (0.04).

From the spatial distributions of T_g (gas temperature) and n_H (H-atom density), the thermal and mass boundary layer thicknesses, defined by the following relationships, can be estimated by

$$\delta_T = \frac{T_\infty - T_0}{(\mathrm{d}T/\mathrm{d}z)|_{z=0}} \tag{24}$$

and

$$\delta_H = \frac{X_{H\infty} - X_{H0}}{(\mathrm{d}X_H/\mathrm{d}z)|_{z=0}} \tag{25}$$

The experimental and numerical estimations are reported in Table 6. The experimental values always appear higher than the calculated ones: at 25 hPa and 600 W, the experimental δ_H referred to x_H is 16 mm while the calculated one gives only 5 mm; at 3 kW and 200 hPa, the corresponding values are 8 and 4, respectively. As the power density is increased, both experimental and calculated δ_H and δ_T decrease due to on the one hand the location where the MW energy is mainly absorbed (Figure 14(a)) and on the other hand to the reduction of the thermal and mass diffusivity at high pressure. Indeed, as shown on the measurements of the emission argon line intensity profile (IAr_7), the maximum of the IAr_7 is displaced toward the surface as the pressure and power increases,

Table 6 Thicknesses of the thermal and mass boundary layers at the plasmas / surface interface, for different conditions of pressure and power.

Pressure (hPa)	Power (W)	δ_{T_g} (mm) Calculated	δ_H(mm) exp(Model)
70	1500	4.4	17(5.2)
100	2000	4	8(4.3)
150	2500	3.1	(4.1)
200	3000	2.6	8(4)
250	3500	2.4	6.8(3.7)
270	4000	1.9	(3)
400	3000	2.1	4.9

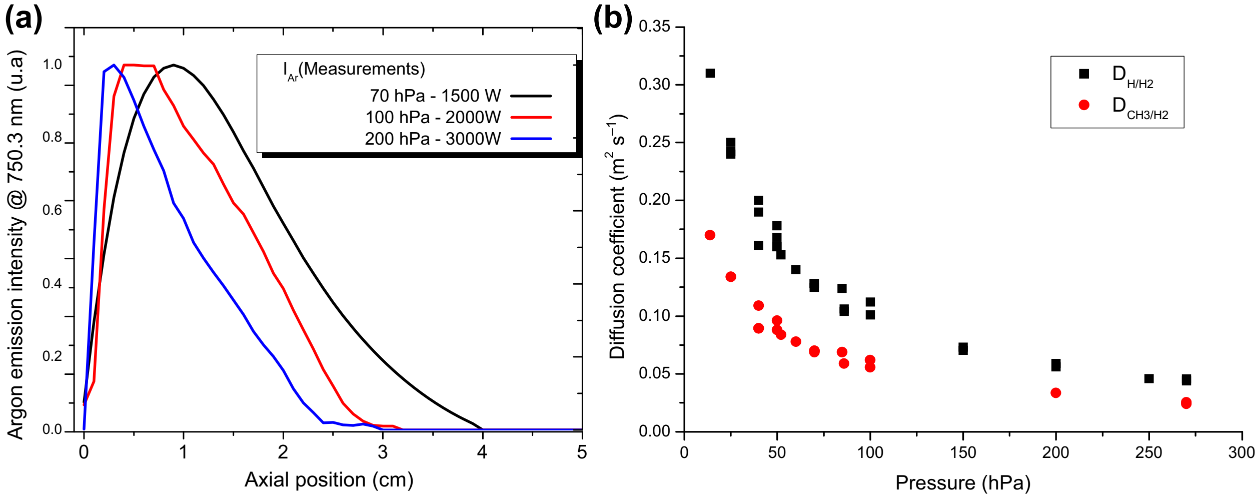

Figure 14 (a) I_{Ar7} Emission intensity axial profiles for three sets of power-pressure (Dearkaoui, 2012). (b) H-atom and CH_3 radical diffusion coefficients as a function of the pressure (Hassouni et al., 1998; Gicquel et al., 2012).

evidencing that the higher the power density, the closer to the surface, the power is absorbed (**Figure 14(a)**). The decrease in δ_H is attributed to that of δ_T; and to the decrease of the H-atom diffusivity (**Figure 14(b)**).

From this analysis, it comes that high surface H-atom densities can be obtained under conditions of very high gas temperature with a gas temperature peak located very close to the surface. This can be obtained by an increase in power density coupled to the plasma (high pressure and/or power values). However, in order to reach values much higher than 6×10^{16} cm^{-3} for H-atom density, one needs to use very high flow velocity to decrease the boundary layer thicknesses.

3.10.4.2 CH_3 Radical Production and Loss

The axial distributions of CH_3 radical density simulated for different pressure/power sets are shown in **Figure 15(a)**. Details in the surface vicinity are also presented in **Figure 15(b)**. These figures clearly confirm the role of the gas temperature and the H-atom density on the CH_3 radical density behavior. The production/loss net balance in the gas phase is governed by the well-known in-equilibrium set of very fast reactions (**Table 2**). The fast equilibrium reaction set $CH_4 + H \Leftrightarrow CH_3 + H_2$ is largely predominant in volume to produce and consume CH_3 radicals, for both low and high power conditions (**Figure 16**). Far from the surface (outside the plasma) and in the vicinity of the diamond surface, CH_3 density peaks for high-power-density conditions. For low power density conditions, the CH_3 density maximum is observed in the plasma bulk (Cappelli et al., 2000). At high power densities, the high gas temperature into the discharge (>2600 K) implies a complete disappearance of CH_3 radicals, its production occurs either outside the discharge (5–6 cm from the substrate) or at the plasma/surface interface, where the gas temperature is in the range 1400–2200 K, with a peak of net production at 1650 K. Thus, for high-power conditions, the set of fast equilibrium reactions is displaced toward the production of CH_3 at the plasma/surface interface and in a shell just outside the plasma. In addition, clearly, the CH_3 density is linked to the CH_4 amount available at the location of adequate range of gas temperature for the CH_3 radical existence (**Table 7**). As a matter of fact, CH_3 density is much higher in the outside shell, where CH_4 is dominant, than at the near diamond surface vicinity, where C_2H_2 is dominant (**Figure 15(c) and (d)**). As already discussed by Ma, Cheesman, et al. (2009), CH_4 is the stable HC content dominant in the regions of gas temperature <1400 K, while C_2H_2 is the dominant stable HC species for gas temperature in the range 1400–2200 K.

From this analysis, an important finding is that increasing fresh CH_4 by an appropriate injection into the boundary layer is a potential way to increase surface CH_3 density, and thus the diamond growth rates.

The surface CH_3 density is seen to vary linearly with the maximum of CH_3 produced at the plasma/surface interface (**Figure 17(a)**). As well, a quasi-linear relationship is observed between surface CH_3 density and the maximum H-atom density (**Figure 17(b)**).

As a conclusion, at the plasma/surface interface, the CH_3-radical density maximum is located at the position where the gas temperature reaches around 1650 K. The higher the power density, the closer to the diamond

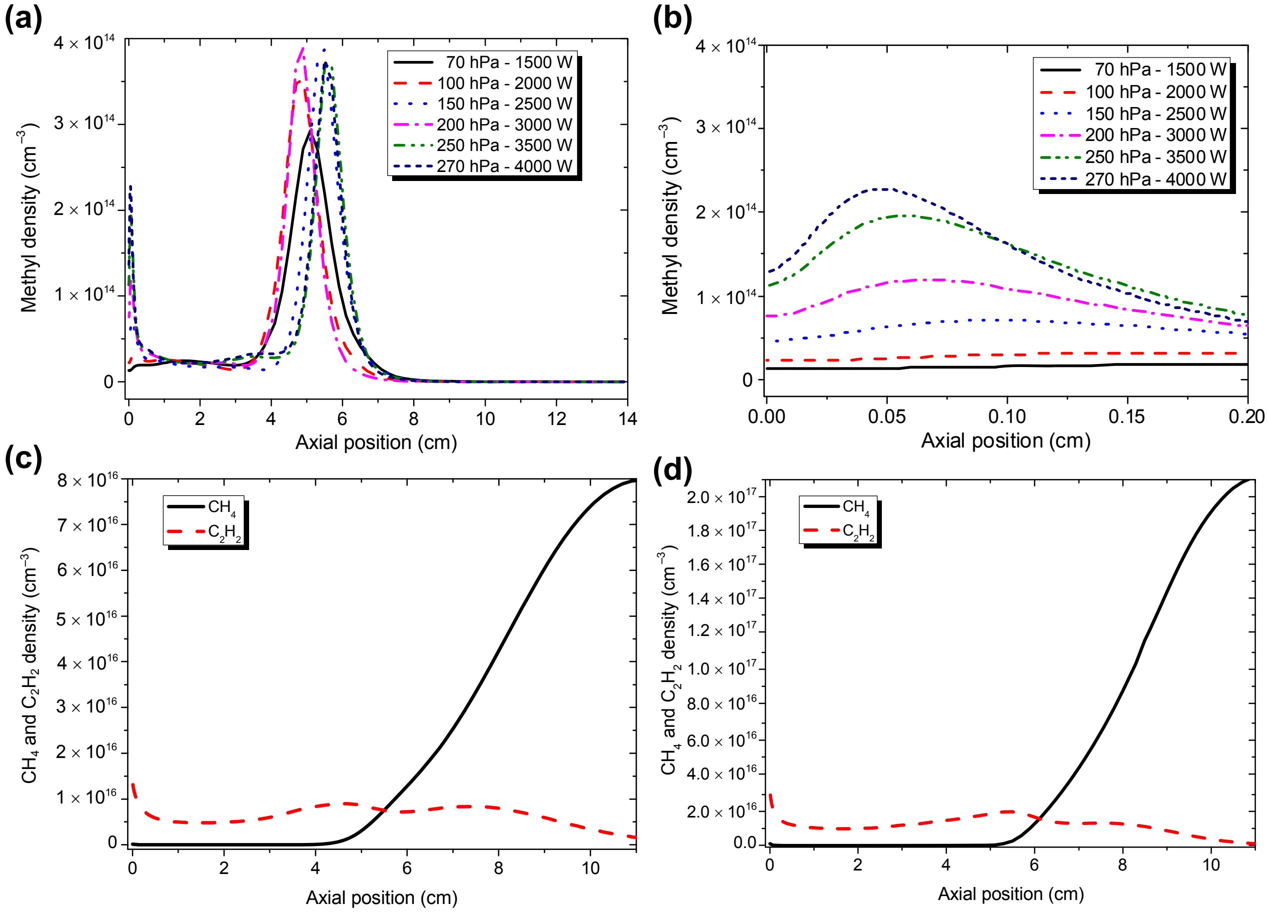

Figure 15 (a) Simulated CH_3 density axial profiles for different sets of pressure/power. (b) Zoom at the plasma / surface interface, Conditions: 4% of CH_4 in the H_2/CH_4 gas discharge and substrate temperature of 1100 K; 70 hPa, 1500 W, 100 mbar -2000W, 150 hPa-2500 W; 200 hPa – 3000 W; 250 hPa – 3500 W; 400 hPa – 3000 W; 270 hPa, 4000 W; (c) C_2H_2 and CH_4 axial profiles for 100 hPa and 2000 W and (d) C_2H_2 and CH_4 density axial profiles for 270 hPa and 4000 W (Derkaoui, 2012; Gicquel et al., 2012; Rond et al., work in progress).

surface is this particular gas temperature value, and then the maximum of CH_3 density. In addition, at this location, the maximum value for CH_3-radical density is proportional to the H-atom density in the plasma bulk. Thus, the higher the power density coupled to the plasma, the closer to the surface and the higher the maximum of CH_3-radical density is. As a consequence, the higher is the surface CH_3 density. It is worth remembering that the maximum of CH_3 density at the surface (obtained at 1650 K) also depends on the CH_4 available at the plasma–surface interface and is depending on its injection location.

Let us now analyze how the CH_3 radicals are living when they are transported to the surface after they have been produced (Figure 16). At low power density, CH_3 is produced from CH_4 in the plasma bulk by reverse reaction R77 and direct reaction R85 (at 2 cm from the substrate for 25 hPa/600 W), it is then consumed by

Table 7 Densities and locations of the peak CH_3 radical density into the reactor, at the plasma/ surface interface and at the plasma frontier, for different conditions of pressure and power. The peak CH_3 radical density occurs at 1650 K.

Pressure – Power	*n_{CH_3} Frontier (cm^{-3})*	*n_{CH_3} Plasma/Surface (cm^{-3})*	*z_{max} Frontier (cm)*	*z_{max} Frontier (cm)*	*Ratio Interface/Frontier*
70 hPa–1500 W	2.9×10^{14}	0.19×10^{14}	5	0.365	0065
100 hPa–2000 W	3.5×10^{14}	0.3×10^{14}	4.9	0.155	0.085
150 hPa–2500 W	3.8×10^{14}	0.7×10^{14}	4.9	0.095	0.18
200 hPa–3000 W	3.9×10^{14}	1×20^{14}	4.9	0.065	0.3
270 hPa–4000 W	3.75×10^{14}	2.28×10^{14}	6	0.05	0.6

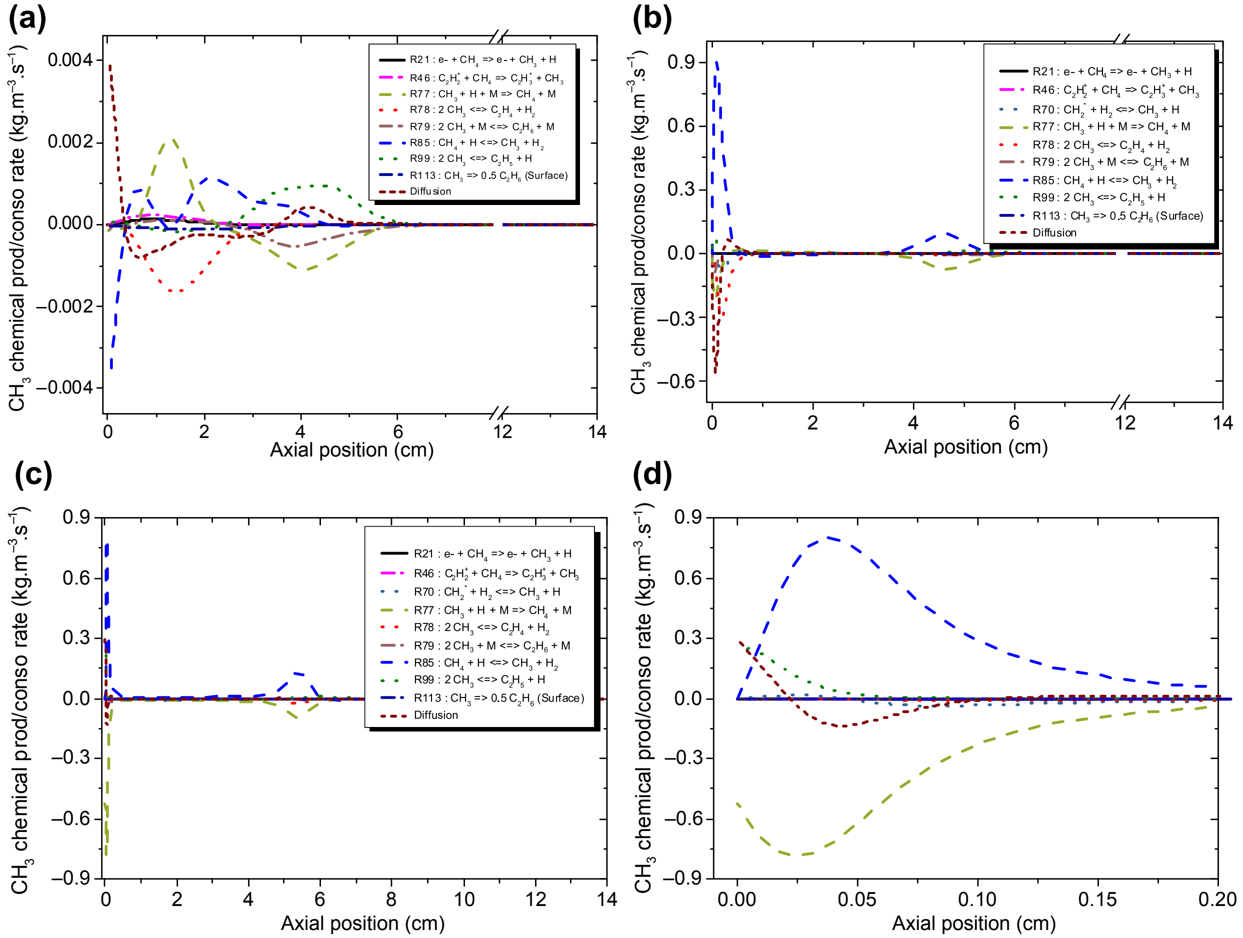

Figure 16 Axial profiles for net production yields of CH_3 for the three couples (pressure, power) considered: (a) 25 hPa/600W, (b) 100 hPa/ 2000 W, (c) 270 hPa/4000 W, (d) 270 hPa/4000 W zoom in the near surface vicinity (Derkaoui, 2012; Gicquel et al., 2012; Rond et al., work in progress).

the direct reaction R78 and diffusion as well as by direct reaction R77 and reverse reaction R85 forming CH_4. In the near vicinity of the surface, diffusion brings CH_3 while reverse reaction R85 consumes it. At 100 hPa/ 2000 W, the maximum production is seen at 0.1 cm from the substrate. Reverse reaction (R85) consumes almost totally CH_3 in gas phase before producing it again with direct reaction (R85) at 0.1 cm from the surface, at this location CH_4 is produced mostly from C_2H_2 which is the domianant species. Finally at high power density, as seen before, CH_3 is produced in an outside shell, it is then totally absent in the plasma bulk, due to high gas temperature. In the last millimeter from the surface, CH_3 is produced by direct reaction (R85) and reverse reaction (R77). It is then consumed by direct reaction (R77) and diffusion. In the near-surface vicinity diffusion process and reactions (R99) and reverse (R77) bring CH_3 radicals to the surface.

It is worth noting that the increase in pressure lowers the diffusion coefficient for both H atoms and CH_3 radicals in the mixture (**Figure 14(b)**). Although it does not affect so much the transport of H atoms at the plasma/surface interface even at pressure as high as 300 hPa, it affects the transport of CH_3. A high power density, part of CH_3 appears to be consumed by collisional reactions in volume before it can reach the surface.

Finally, the variations of the maximum of CH_3 radical density close to the heating/diffusive zone, at the plasma/surface interface and at the surface as a function of the amount of methane introduced in the mixture are presented in **Figure 18**. At the plasma/surface interface, the square-root function proposed by the Bristol group for the CH_3-radical density variation as a function of methane percentage (Butler et al., 2009) fit rather well, note however that the range of methane percentage tested here is limited.

As a conclusion, the density variation of CH_3 radical due to chemistry mainly originates from the higher H-atom density at the plasma/surface interface which enhances the kinetics of $C_2H_2 \rightarrow CH_4$ back-conversion.

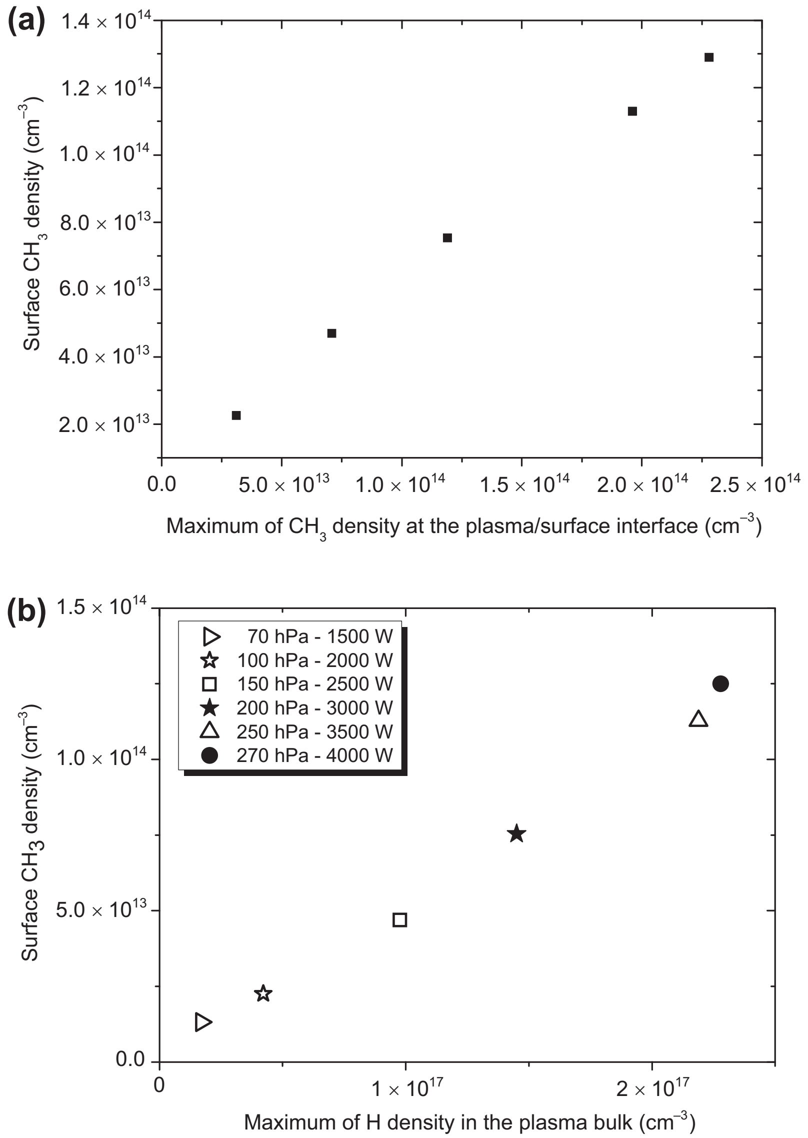

Figure 17 Variations of the surface methyl density: (a) as a function of the maximum of CH_3 density at the plasma / surface interface; (b) as a function of the maximum H atom density in the plasma bulk with increased methane percentage in the feed-gas. Conditions: 200 hPa/ 3000 W (Derkaoui, 2012; Gicquel et al., 2012).

All this supports the idea that most of the improvement potential of the deposition process relies on H-atom density. It also relies on the ability in making CH_4 available into the plasma/surface interface, by a proper injection.

3.10.5 How Can We Increase the Growth Rates

Increasing growth rate keeping very high the diamond crystalline quality and purity is obviously an important challenge if one wants to increase the capacity of development of diamond applications in the world, in particular in the domain of high-power electronics.

As seen before, the densities of the key species for diamond are governed by the local conditions at the plasma/surface interface, i.e. the H-atom density and CH_3-radical density at the growing surface, and the substrate temperature. An enhanced energy deposited in the bulk of the discharge strongly increases the H-atom density produced into the gas phase which is then transported to the surface. This also strongly affects the CH_3

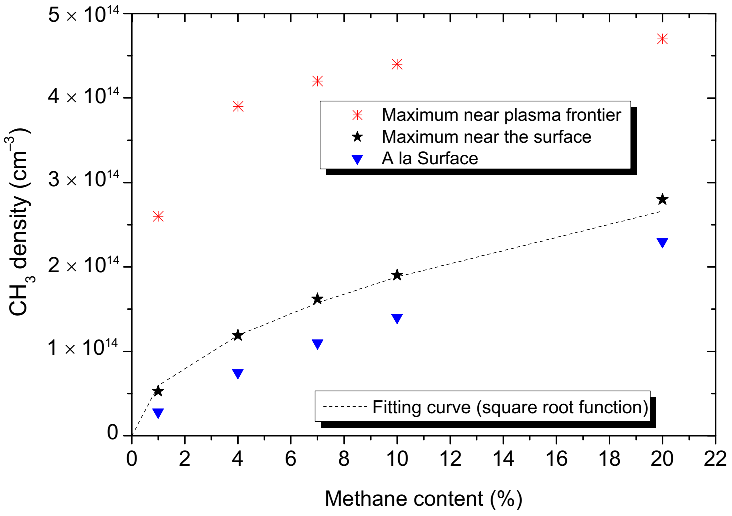

Figure 18 Variation of CH_3 density as a function of the percentage of methane, 200 hPa et 3000 W, and for three locations into the gas phase: in the near entry of the plasma where Tg equal to 1650 K ($z > 4$ cm), at the plasma / surface interface plasma / surface (Tg $= 1650$ K) and at the diamond surface (Brinza et al., 2008; Derkaoui, 2012; Gicquel et al., 2012).

density at the diamond surface since the latter is a strong function of the H-atom density and gas temperature gradients at the plasma/surface interface. On the basis of the understanding of how works a diamond-deposition MW plasma reactor, some possibilities exist to push forward their limits. Among them, increasing the power density and increasing as much as possible the carbon-containing source at the plasma/surface interface are possible means.

In this section, we propose to discuss these options, but also others, at the condition to maintain the use of the subatmospheric pressure MW cavity-based plasma reactor, and to keep the gas purity without any impurity that can incorporate into the diamond crystal lattice such as nitrogen or boron (Tallaire et al., 2006). It is worth mentioning that the issue for development of diamond will also come from the ability to grow larger single-crystal and larger polycrystalline diamond substrates, and then from the ability in developing very energetic and large surface diamond deposition reactors. This is a real challenge that implies an important knowledge on the MW cavity-based reactors coupled to thermal and vacuum managements (Asmussen & Zhang, 1994; Funer, Wild, & Koidl, 1998; Grotjohn et al., 2005; Silva, Achard, et al., 2009).

Our discussion will be focused on (1) the change in the precursor giving rise to CH_3-radical species production and (2) the physical ways to increase gas temperature and to concentrate these high values as much as possible toward the diamond surface (Naito et al., 1993). As far as the physical ways are concerned, we will analyze (1) the hydrodynamics, (2) adding a rare gas with a lower thermal diffusivity, (3) increasing the power density coupled to the plasma, (4) working with a pulse MW excitation mode instead of a continuous mode, and (5) changing the MW cavity design, and even the frequency.

3.10.5.1 Influence of the HC Precursor and CH_4 Injection Location

As far as the precursor is concerned, many studies have been carried out on this subject in the 90′ (Frenklach & Spear, 1987; Frenklach & Spear, 1988). However, in order to keep high the diamond purity, the only precursors that can be used are HCs only composed of hydrogen and carbon. Modeling (Hassouni et al., 2010) as well as experimental (Ma, Cheesman, et al., 2009) works allowed us establishing that due to the high temperatures involved in these kinds of plasma, whatever the type of HC used, C_2H_2 and CH_4 are the dominant species, the importance of which depends on the location and gas temperature into the plasma. For an injection of the gas realized far from the diamond surface, when working under energetic conditions, CH_4 is seen to be present only in the heating/diffusive zone while C_2H_2 is dominant at the plasma/surface interface (Figures 15(c) and 15(d)). Therefore, no effect of the precursor will be observed in this case and the CH_3 density will always appear rather low at the plasma/surface interface.

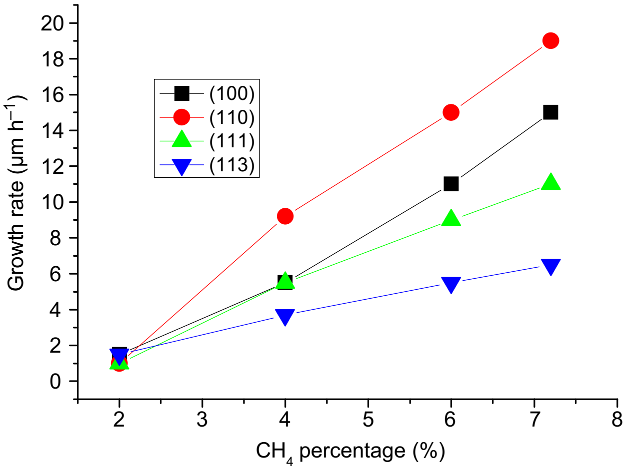

Figure 19 Influence of the percentage of methane on the growth rate on different diamond orientations. Conditions: 200 hPa, 3000 W, Ts = 850 °C (Brinza et al., 2008).

On the opposite, an influence of the precursor is expected in the case where HC is directly injected at the plasma/surface interface, and light HC such as CH_4 will be obviously preferred. As a consequence, we can state that if someone finds a mean to introduce directly CH_4 at the plasma/surface interface, an increase in the growth rate will certainly be observed.

3.10.5.2 Influence of the Gas Velocity

To reduce the thermal and mass boundary layers and increase the Peclet number higher than 1, very high gas velocity must be used. In addition, HC chemistry, including soot formation, is sensitive to the residence time and to the flow distribution. Analyzing deeply the effects of flow rate, methane injection location, instabilities of the discharge requires the development of a 2D or 3D code involving Navier–Stokes equations. Work in this field is under progress in LSPM.

3.10.5.3 Influence of the Methane Percentage

Keeping constant the quality and purity (nitrogen content <0.2 ppb) of the diamond crystals, a strong increase in the growth rate is observed as a function of the methane percentage (**Figure 19**) (Brinza et al., 2008). For the couple 200 hPa/3000 W, the growth rate is seen to increase by a factor of 8 as the methane percentage is increased by a factor of 3.5. The same kind of results has been obtained for other conditions of high power density.

Thus, increasing growth rate by increasing the HC source content in the gas mixture may constitute an interesting solution. However, at low power density, a decrease in the diamond quality is generally observed as the percentage of CH_4 is increased (Silva & Gicquel, 1998). On the opposite, at high power density and reasonable HC percentages, the quality is not decreased as a function of methane percentage. In addition, when working at very high power density, high percentages of methane must be used in order to compensate the loss of growth due to the increase in diamond etching rate (H-atom density dependent). However, at high power density, the maximum of HC content that can be introduced is limited by soot formation that occurs in the outside shell of the plasma as seen in **Figure 20** for percentage of methane higher than 10%. Soot deposits on the quartz windows, provoking their heating and their destruction. In addition, soot may affect the diamond quality. As already mentioned, the formation of soot appears to be linked to hydrodynamics.

As a conclusion, although an interesting parameter for increasing growth rate, increasing the percentage of HC must be done sensitively.

3.10.5.4 Argon Addition

Other effects can be attempted to increase the production of H atoms. For instance, addition of argon into the mixture is known to increase gas temperature. Indeed, in $Ar/CH_4/H_2$ mixtures used for depositing

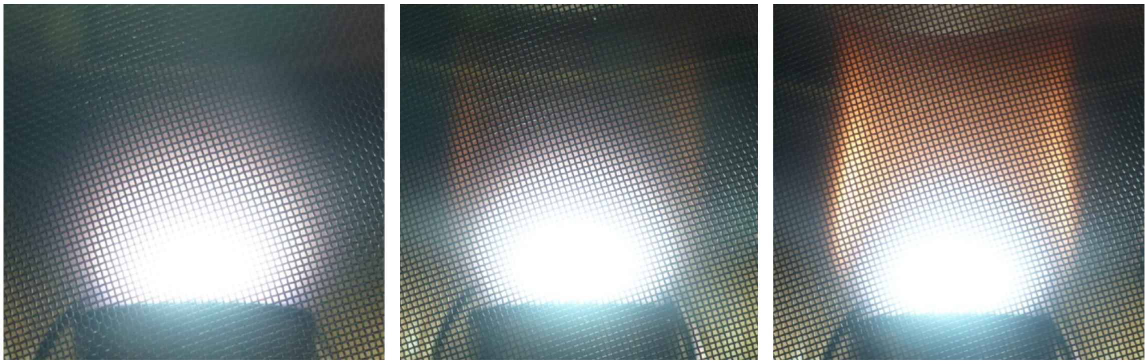

$4\%\ CH_4$ $10\%\ CH_4$ $20\%\ CH_4$

Figure 20 Formation of soot particles in a LSPM stainless steel metallic diamond deposition plasma reactor at a working pressure of 200 hPa and power of 3000 W (Derkaoui, 2012).

nanocrystalline diamond, much higher gas temperature than those measured in conventional H_2–CH_4 mixtures have been reported (Monéger, 2009).

In LSPM, up to 40% of argon has been added to the H_2–CH_4 gas flow. Measurements of volume-of-sight gas temperatures on the C_2 swan system have been made simultaneously to the measurements of the (100) diamond growth rates (Tallaire et al., 2011). The results clearly showed a strong increase in both the gas temperature and the growth rate when adding argon: they increase from around 2800 to 3200 K and from 5.5 to 11 $\mu m\ h^{-1}$, respectively, when argon increase from 0 to 40% (**Figure 21(a) and (b)**). The effect of increasing the gas temperature is the consequence of lowering the thermal conductivity due to argon addition.

As a conclusion, adding some argon in the gas mixture to increase growth rates may be an interesting option.

3.10.5.5 Influence of the Power Density

The ability in coupling very high MW power densities to the plasma is one of the best ways to increase gas temperature and H-atom density, and to reduce boundary layer thicknesses.

A strong increase in the diamond (100)-face growth rate as a function of the pressure for different power is shown in **Figure 22**, where the results are given for two conditions of methane (4 and 7%).

A picture of the single crystal grown at 70 $\mu m\ h^{-1}$ obtained at 400 hPa and 3000 W and its associated photoluminescence spectrum are shown in **Figure 23(a) and (b)**, respectively. Electronic paramagnetic resonance (EPR) analysis (Silva, Achard, et al., 2009) clearly evidenced a very low level of nitrogen contamination (0.2 ppb) for this diamond single crystal.

The corresponding variations of the H-atom density in the plasma have been already shown in **Figure 11(c)**. The value of H-atom density corresponding to the growth rate of 70 $\mu m\ h^{-1}$ obtained with 7% of methane and at 400 hPa and 3000 W reaches $5 \times 10^{17}\ cm^{-3}$.

Since obviously growth rate is driven by H-atom density, let us now analyze the relationship between these two parameters.

For a given methane percentage, the linearity between the CH_3 density at the diamond surface and that of H-atom density in the plasma bulk allow us to express the growth rate as a function of the only H-atom density. Indeed,

$$\text{Growth rate} = \tag{26}$$

can be transformed, and it comes

$$\text{Growth rate} = k(T_s)[CH_3]_s\left(1+\frac{5\times10^{-9}}{[H]_s}\right)^{-1} = k(T_s)k'\left(1+\frac{5\times10^{-9}}{[H]_s}\right)^{-1}[H]_\infty \tag{27}$$

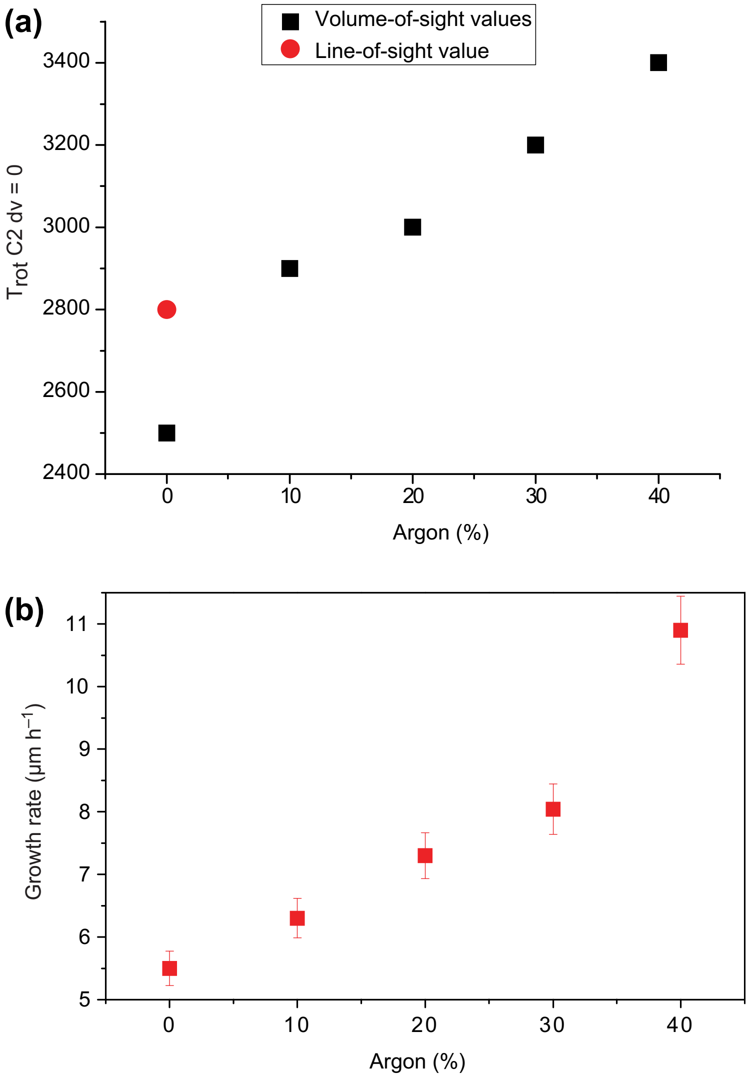

Figure 21 (a) Volume-of-sight averaged gas temperature as a function of Ar content measured from the optical emission of C2 Swan system. Line-of-sight averaged Tg at 0% of argon. (b) Growth rates of single crystal diamond films grown with increasing amounts of argon in the gas phase. Typical conditions: 2800 W; 200 hPa, Ts = 880°C, 4 % CH4 (Tallaire et al., 2011).

where k' is a constant that takes into account for the proportionality between the surface CH_3 density and the H-atom density in the plasma bulk, for a given CH_4 percentage considered, as shown above (**Figure 17(b)**). $[H]_\infty$ in mol cm^{-3} corresponds to $n_{H\infty}$ the maximum of n_H in the plasma bulk (in cm^{-3}).

Remarks:

- First, from **Figure 13(a)**, we can note that the surface H-atom density n_{Hs} is higher than 3×10^{15} cm^{-3} (i.e. $[H]_s < 5 \times 10^9$ mol cm^{-3}) once the couples pressure/power are higher than 100 hPa–2000 W. This allows us to define a lower limit for the growth rate: for these conditions, the minimum of the form $(1 + 5 \times 10^{-9}/[H]_s)^{-1}$ is equal to $^1/_2$.
- Second, at very high power density, the H-atom density increases very much and at a certain point, the form $5 \times 10^{-9}/[H]_s$ will become negligible relatively to 1. As a consequence, an upper limit for growth rate exists, at high power density.

Then, for a given percentage of methane, growth rates can be framed between a lower and an upper limit function that only depends on the maximum H-atom density, this being directly accessible by actinometry or TALIF.

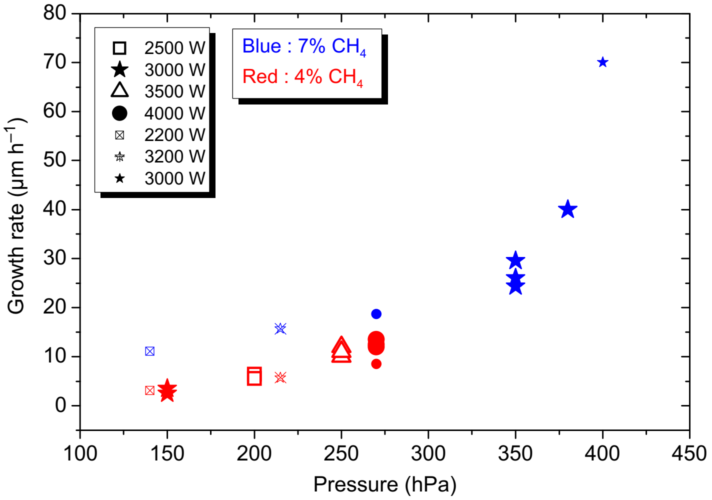

Figure 22 Growth rates as a function of pressure for different powers. The points in blue correspond to 7 % of methane, while those in red and black correspond to 4 % of methane (Derkaoui, 2012; Gicquel et al., 2012).

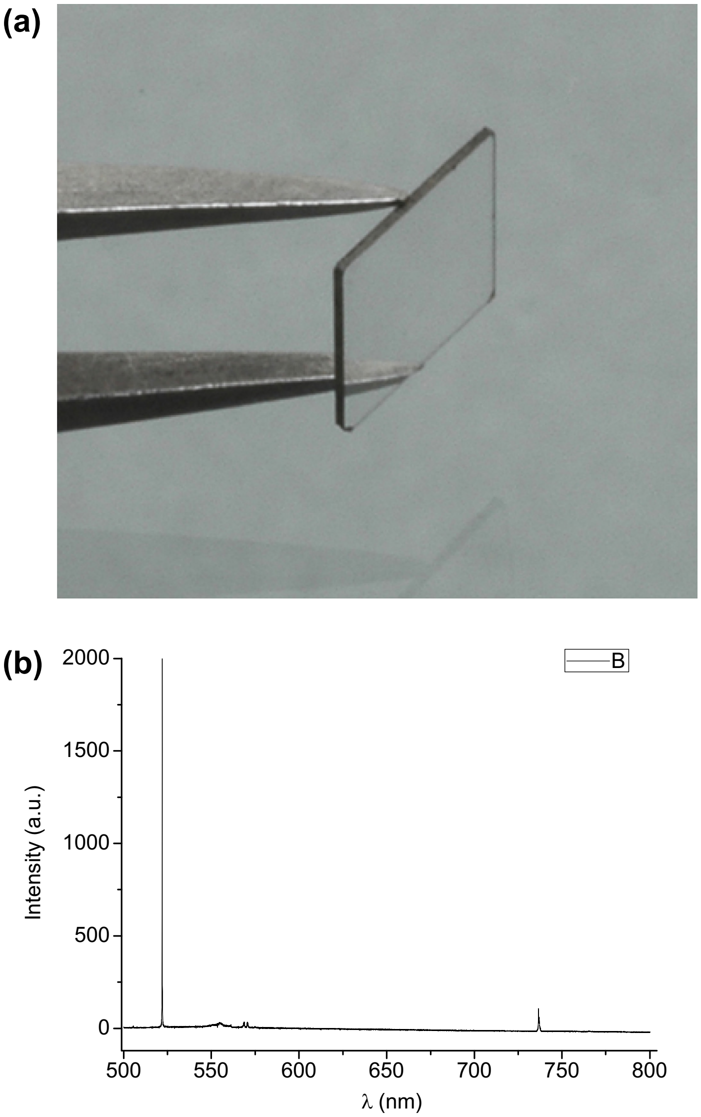

Figure 23 (a) Photography of a 350 µm thick diamond single crystal grown at 70 µm/h in a water cooled stainless steel reactor. (b) Photoluminescence spectrum of the film shown in Figure 21a obtained at 77K showing an intense Raman peak and a luminescence originating from SiV impurities at 737 nm (Silva, Hassouni, et al., 2009).

The frame inequality is written as it follows

$$k(T_s)\frac{k'}{2}[H]_\infty < \text{Growth rate} < k(T_s)k'[H]_\infty \tag{28}$$

Replacing k' by its value 5.5×10^{-4} for 4% of CH_4 and 6.3×10^{-4} for 7% de CH_4, inequalities 28 become

4% CH_4:

$$k(T_s)2.75 \times 10^{-4}[H]_\infty < \text{Growth rate} < k(T_s)5.5 \times 10^{-4}[H]_\infty$$

7% CH_4:

$$k(T_s)3.15 \times 10^{-4}[H]_\infty < \text{Growth rate} < k(T_s)6.3 \times 10^{-4}[H]_\infty$$

Experimental and calculated growth rates together with the lower and the upper limits of growth rates are presented in Figure 24(a) and (b) for the two percentages of methane. A strong increase in the growth rate is observed once the volume H-atom density ($n_{H\infty}$) is higher than 10^{17} cm^{-3} (i.e. $[H]_\infty > 16 \times 10^{-8}$ mol cm^{-3}) and the surface H-atom density (n_{Hs}) higher than around 3×10^{15} cm^{-3}.

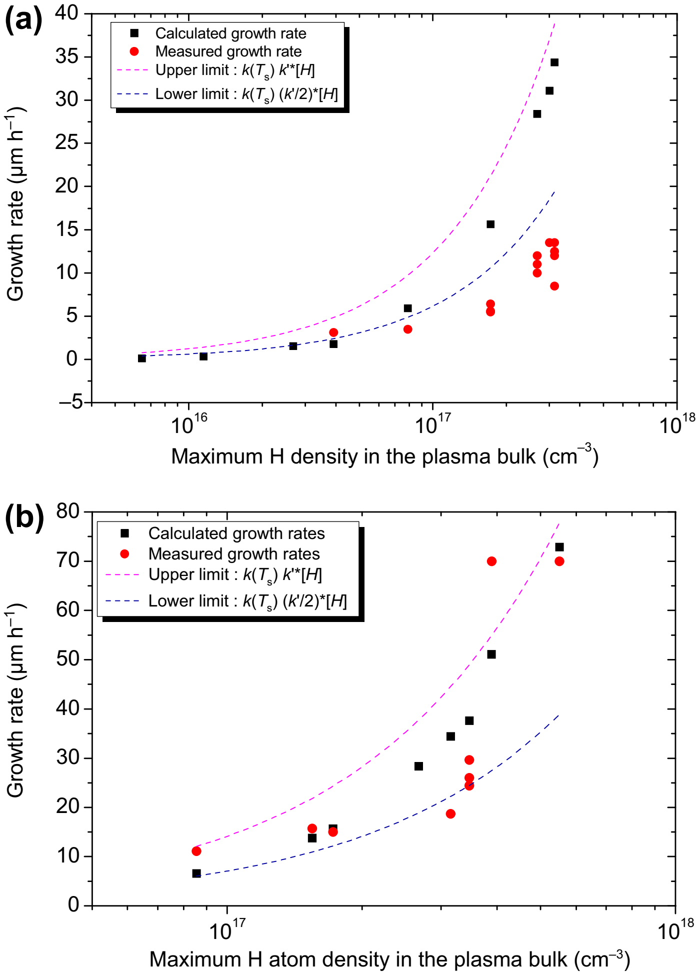

Figure 24 (a) Variation of the growth rate with 4 % of methane added in the feed gas as a function of the maximum H-atom density in the gas phase for pressure and power couples higher than (70 hPa and 1500 W). Diamonds for calculated values and points for measured values. (b) Variation of the growth rate with 7 % of methane added in the feed gas as a function of the maximum H-atom density in the gas phase for pressure and power couples higher than (70 hPa and 1500 W). Diamonds for calculated values and points for measured values. (Derkaoui, 2012; Gicquel et al., 2012).

We can note the following:

- The calculated growth rates based on the H-atom density determined through experiments fit well within the lower limit and the upper limit predicted for the growth rate once the couples of power and pressure are higher than (100 hPa, 2000 W).
- The experimental values obtained at 4% of methane are all lower than the lowest limit. We attribute this behavior to the etching of diamond by H atoms due to the high H-atom density (high etching rate). For these conditions, the methane percentage (CH_3 density at the surface) is not high enough relatively to the H-atom density to totally compensate the diamond etching rate. Higher percentage of methane must be used. It is worth noting that for percentage of methane that does not allow compensating etching, the growth rate relationship predicted by Goodwin is not valid.
- The experimental values obtained at 7% of methane fit perfectly into the lower and the upper values, validating our approach. Under these conditions, enough CH_4 amount was introduced into the gas phase, and the relationship predicted by Goodwin is valid.

Considering the very limit of H-atom density predicted by Goodwin for the fully dissociated flow impinging the surface at very high velocity and a tenuous boundary layer thickness, for this condition, we can estimate the very limit of growth rate at around 350 μm h^{-1}. This value is higher by a factor of 9 than our highest values. This factor is a result not only due to the difference in H-atom density but also of the difference in thickness of the boundary layers due to the gas velocity at the surface. Obviously, our plasma reactors do not have the ability in working neither at such high pressure nor at high speed (to remove the boundary layer). As a consequence, the maximum growth rates expected cannot overpass a factor of 2 relatively to the highest value obtained today (70 μm h^{-1}).

Let us recall here that to take into account for the variation of methane percentage, one needs to apply a square-root variation of CH_3 with CH_4 percentage as this has been shown in **Figure 18**. This method must be however taken with caution when varying the CH_4 injection location.

As a conclusion, although the MW cavity-based reactors can still be improved, the remaining progression margin is not so large. Increasing gas temperature is still achievable and will lead to an increase in n_{Hs}; however, high power densities require an increase in HC content to prevent etching. Soot formation will limit the HC enhancement except if an optimal management between CH_4 injection location and flow is found. In addition, we must recall that pressure higher than 500 hPa may lead to H-atom loss in the boundary layer due to volume recombination (except if very thin boundary layers are reached). Furthermore, we must add that filamentation of the discharge may also occur. Finally, growing at very high power density may also lead to contamination of the diamond films by silicon due to quartz windows etching that heat up, as this has been observed in LSPM, except if pulsed plasmas are used.

3.10.5.6 Pulsed Plasmas

When working at very high power density, if the quartz windows are not enough cooled down, the presence of silicon contamination can be observed as shown on the photoluminescence spectra of diamond crystals grown at high power density, presented in **Figure 25**.

To solve this problem, either the quartz windows allowing coupling the MW to the plasma must be drastically cooled down using air convection or silicon oil cooling, or one can make use of a pulsed plasma (Hassouni et al., 2001; Tallaire, Achard, Silva, & Gicquel, 2005). Indeed, this procedure is known allowing coupling higher powers to the plasma while reducing the reactor wall overheating (Duten, 2000; Vikharev et al., 2003).

This solution allowed us growing CVD-diamond films at 22 μm h^{-1}, with a peak power of 3000 W with a pressure of 200 hPa and 7% of methane, free of silicon contamination as shown in **Figure 26**. Pulsed plasma advantages have been deeply studied by means of modeling and experiments.

The use of pulsed mode was mainly motivated by the existence of an additional degree of freedom for the control of the chemical kinetic and energy dissipation in the plasma, and its capability in lowering the wall temperature, and consequently the contamination of the films when working at very high power density. The production of the active species, and especially H-atom, was seen to be enhanced, compared with a continuous discharge with the same average power by an optimal choice of the duty cycle δ_c. This parameter represents the ratio of the pulse duration, t_{on}, to the time between two successive pulses, i.e. the pulse period, T. Beside this chemical aspect, the effective reduction of the thermal load on the reactor wall and the substrate was seen to improve the stability of the deposition process especially at high pressure (Gicquel et al., 2003).

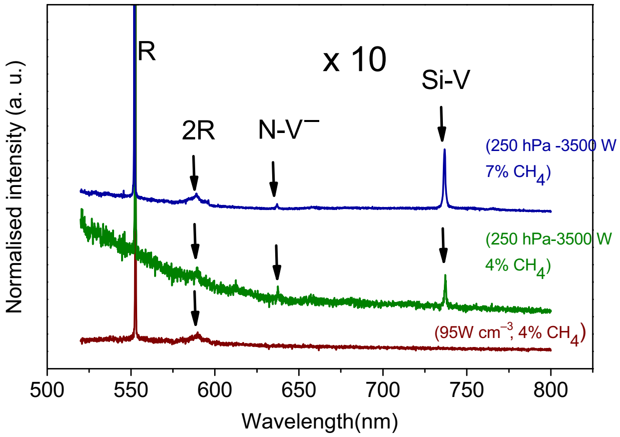

Figure 25 Photoluminescence spectra obtained at liquid nitrogen temperature of diamond single crystals growth at different power densities and different methane percentage (Tallaire, Achard, Silva, & Gicquel, 2005).

As far as MW excited plasmas are concerned, pulsed mode was considered for the deposition of diamond since the mid-1990s. Pulsed H_2/CH_4 discharges used for diamond films deposition were first investigated by Laimer and Matsumoto (1994) who used emission spectroscopy and reported a large enhancement of H_α to argon emission line intensities ratio (I_H/I_{Ar}), which would indicate an enhancement of H-atom production under pulsed discharge conditions. However, these authors did not observe any change in the diamond quality or growth rate with respect to deposition processes using continuous wave plasmas. This first work was followed by others, where comparison between pulsed and continuous H_2/CH_4 MW discharges in terms of diamond growth rate and Raman quality were discussed (Brinza et al., 2007; Chatei et al., 1997; Ring, Mantei, Tlali, & Jackon, 1995). The main conclusions resulting from the major part of these investigations indicate that the use of pulsed discharges leads to an increase of the Raman film quality while the growth rate remains rather constant.

The analysis of the difference between pulsed and continuous plasma modes used in diamond deposition processes required a quantitative investigation of the chemistry and energy transfer occurring in moderate-pressure H_2/CH_4 pulsed discharges. For this purpose, we present some modeling results that show how the time variations of the chemical species and plasma temperatures take place in pulsed discharges. We also propose to discuss how time variations and space variations of the plasma characteristics affect the average key species densities *seen* by the substrate surface. These are strongly related to the frequency and duty cycle used. We will mainly focus on gas temperature, H atom and CH_3 radical.

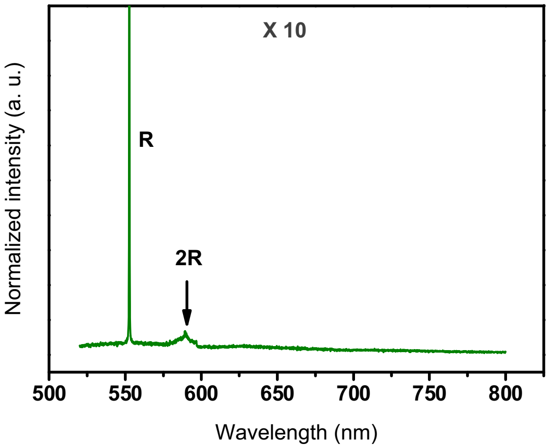

Figure 26 Photoluminescence spectra of a 660 μm thick diamond crystals grown in a stainless steel reactor in pulsed mode with a peak power of 190 W.cm^{-3}. Others conditions: 7% CH_4, duty cycle 50%, average power density of around 95 W.cm^{-3} (3000 W and 200 hPa) (Tallaire, Achard, Silva, & Gicquel, 2005).

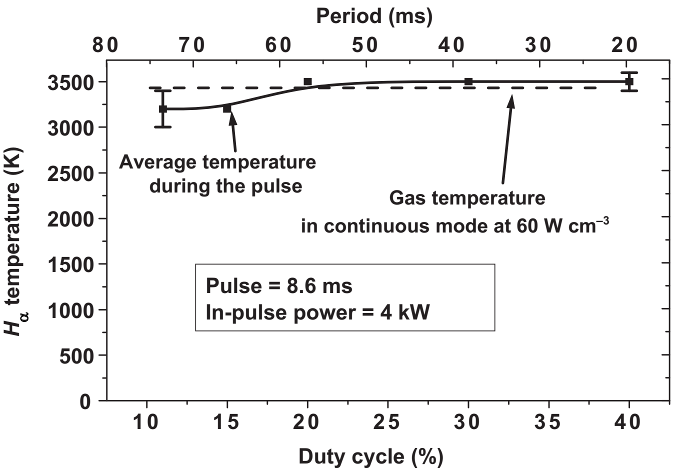

Figure 27 Averaged gas temperature and substrate temperature (at 12 W.cm^{-3}) as a function of the duty cycle. Pressure 40 hPa // power 800 W (Duten, 2000).

One of the major questions that arise when working on pulsed plasma is whether this mode allows the improvement of active species production while keeping a constant time-averaged power. This question is linked to the possibility of an oriented or selective power deposition offered by the pulsed mode. The first answer has been provided by the result showing that for a peak power density identical to the power density in continuous mode, the gas temperature is kept constant (Duten, 2000). This is illustrated in **Figure 27**, where the variation of the gas temperature as a function of the duty cycle is shown. Are also indicated the surface temperature measured. Clearly, the gas temperature only depends on the peak power density while the surface temperature depends on the average power density coupled to the plasma. An additional degree of freedom for controlling reactors is obviously provided by using pulsed plasmas.

The variations of the growth rate as a function of different pulse mode parameters (t_{on} and t_{off}) are reported in **Figure 28** (Brinza et al., 2007). Choosing a t_{on} of 15 ms and a t_{off} of 2 ms allows increasing the growth rate by a factor of 27% while the average power coupled to the plasma is 12% lower (2650 W/200 hPa) than in continuous mode (3000 W/200 hPa). It is worth noting that the purity and quality of all the samples were identical for all the diamond crystals.

The dynamic of a plasma working at a power of 3000 W and a pressure of 200 hPa generated under a pulsed mode has been studied with the help of the 1D model presented above, in the bell-jar reactor configuration. A square pulse waveform is considered for these simulations, and the instantaneous spatial distribution of the

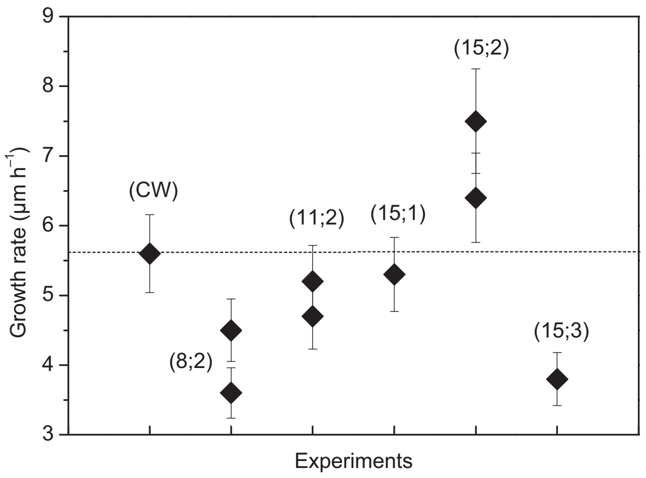

Figure 28 Growth rate of the different samples for different t_{on} and t_{off}. The dotted line represents a guide for the eyes corresponding to the growth rate obtained in continuous mode. 4 % methane, Ts = 850 °C, 200 hPa. Reference power in continuous mode 3000 W (Tallaire, Achard, Silva, & Gicquel, 2005).

relative power density is assumed to be similar to that obtained in continuous mode at the steady state. This assumption must be considered as a first approximation since the change in electron density distribution during the power pulse is likely to result in a change in the spatial distribution of the relative plasma dielectric constant and of the relative power distribution.

In pulsed plasmas, H-atom and CH_3-radical production and loss depend not only on the axial position (due to the axial gas-temperature profile) but also on the time since the gas temperature varies as a function of the time. A periodic stop of the plasma favors the CH_3 production at the beginning of the pulse as well as during t_{off}, in particular at high MW power. Indeed, during the steady state, the gas temperature reaches high values leading to a strong production of H atoms, while during t_{off} as well as during the beginning of t_{on}, the gas temperature reached the range of 1400–2200 K, favorable for CH_3-radical production. The tradeoff leading to optimal local conditions for diamond growth is then a function of the characteristic times of the different phenomena involved including reactions and transport (diffusion and convection). In particular, if one wants to produce CH_3 radical during the step of the plasma heating, H atom must be kept in life. As a consequence, the off plasma phase must be less than its recombination characteristic time. At 200 hPa, the best compromise found was to be around 2 ms.

In **Figure 29(a)** are shown the time variations of H-atom density and CH_3-radical density at the growing substrate surface for several values of pulse and postdischarge durations. The dynamic of CH_3 density is different as compared with that of H-atom density. H-atom density reaches its maximum (*steady state*) value more than 8 ms after the beginning of the pulse, it decreases by more than factor 5, 3 ms after the end of the discharge pulse, due to recombination processes (**Figure 29(b)**). For a t_{off} of 2 ms, CH_3 density reaches its steady-state value around 2 ms after the starting of the pulse, and is produced again at the plasma shut down. It is worth noting that the steady-state value of CH_3 radical at 900 μm from the substrate is much higher than that in continuous mode.

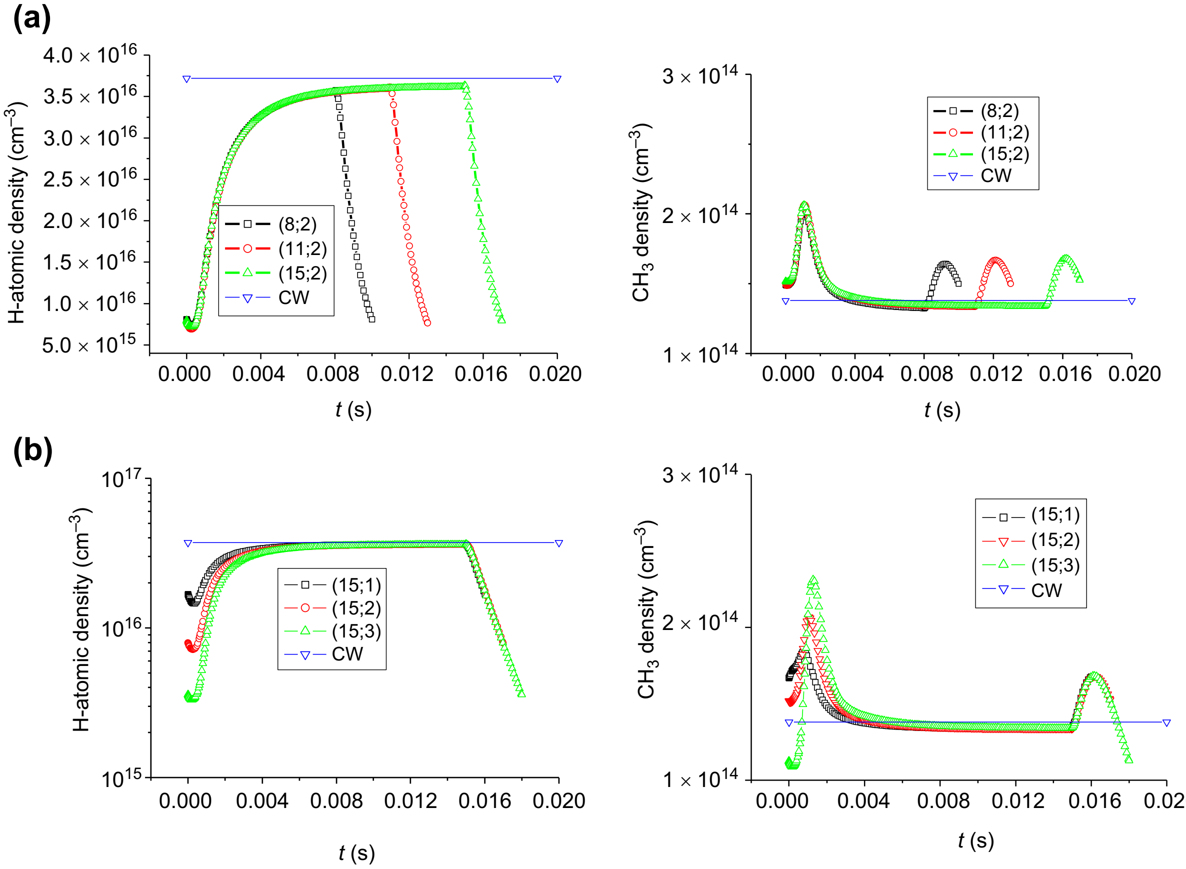

Figure 29 Temporal evolution of [H] and [CH_3] at a distance of 900 μm from the substrate during the pulse for different t_{on} and a t_{off} of 2 ms. (b) Time variations of H-atom (left) and CH_3 radical (right) densities at 900 μm from the substrate surface calculated with the 1D model for different t_{off}. Discharge conditions are a pressure of 200 hPa, a pulse power of 3 kW and a feed gas with 4% CH_4 (Tallaire, Achard, Silva, & Gicquel, 2005).

The temporal evolution of [*H*] for t_{on} varying from 8 to 15 ms [at constant t_{off} equal to 2 ms] shows that [*H*] needs around 4 ms to reach 80% of its steady-state value. As a consequence, for $t_{\mathrm{on}} = 8$ ms, only 50% of the on-state presents the steady-state hydrogen density while for $t_{\mathrm{on}} = 15$ ms, 75% of the on-state allows to obtain the highest hydrogen density.

The analysis of the temporal evolution of [*H*] and [CH_3] during t_{on} allowed then highlighting experimental results obtained on growth rates. Thus, the highest growth rates obtained for ($t_{\mathrm{on}} = 15$ and $t_{\mathrm{off}} = 2$), can be attributed to the higher production of both CH_3 radicals and H atoms for ($t_{\mathrm{on}} = 15$ and $t_{\mathrm{off}} = 2$), than for other conditions. Moreover, it is worth noting that the time during which the sample is exposed to the plasma varies as a function of the duty cycle: for $t_{\mathrm{on}} = 8$ ms and $t_{\mathrm{off}} = 2$ ms, the exposure time of the sample to the plasma is only 80% while this time reaches 88% for $t_{\mathrm{on}} = 15$ ms and $t_{\mathrm{off}} = 2$ ms. This may play a role on the observed gap between the growth rates obtained in these two experimental conditions.

3.10.5.7 Improvement of the Microwave Cavity

Keeping constant the excitation wave giving rise to the plasma ignition, one may also optimize the plasma cavity in order to improve the H-atom density. However the MW cavity improvement cannot be made to the disadvantages to either thermal management or vacuum limit. Some groups around the world have dedicated works on this purpose, in particular reactor supplier such as Wavemat, Michigan State University and Astex, but also the Fraunhofer group led by Koidl, P. as well as the Brazilian group led by Trava-Airoldi, V.

In LSPM, EM simulations using the commercial Microwave Studio® software coupled to the LSPM 2D self-coherent code allowed us proposing two new configurations of cavity. Two goals were searched for (1) to be able to couple the highest power as possible in our current reactors, and (2) to move away as much as possible the reactor walls to prevent H-atom loss by recombination at the walls. The simulation of the plasma obtained for a new metallic configuration is compared to that of our current stainless-steel reactor in Figure 30(a) and (b) Figures 30a and 30b. Clearly, the H-atom density has been increased by a factor of three and its radial

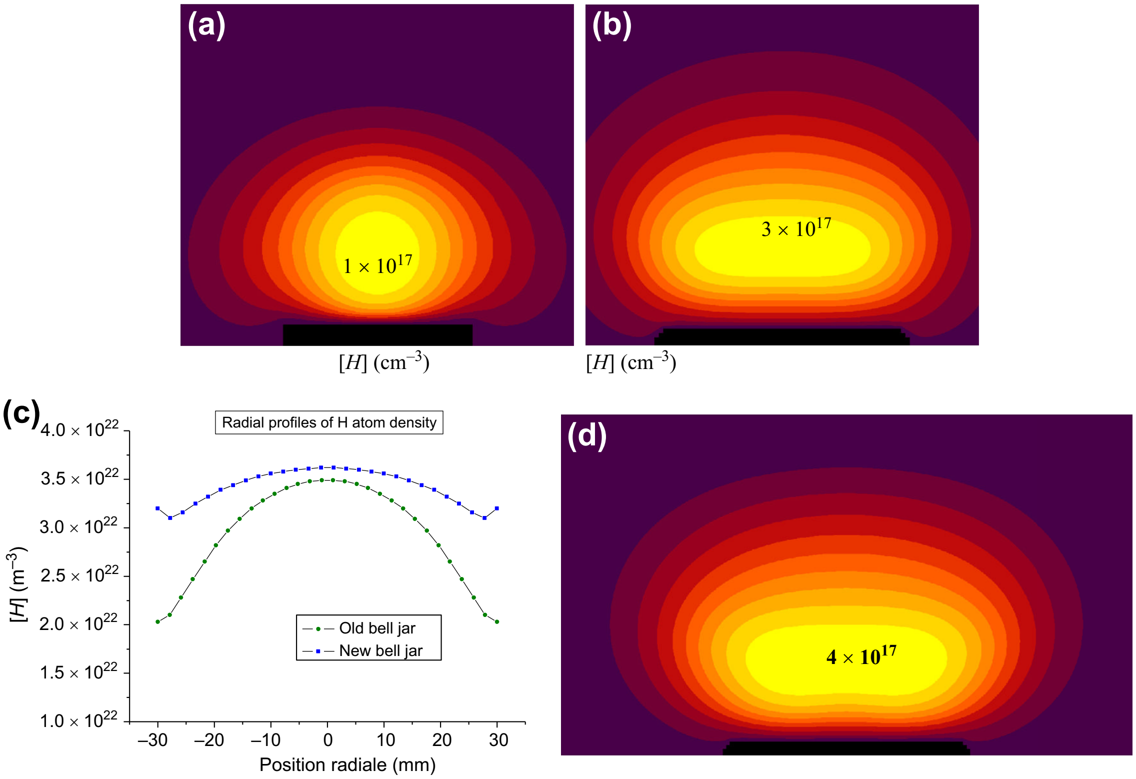

Figure 30 (a) 2D self-consistent simulation of H atom density for an excitation frequency of 2.45 GHz in the current stainless steel reactor; (b) new configuration of metallic reactor (2.45 GHz); (c) new bell jar configuration (2.45 GHz); (d) 2D self-consistent simulation of H atom density for an excitation frequency of 915 MHz. Equivalent of a power density coupled to the plasma of 80 W/cm^3 (Silva, Hassouni, et al., 2009).

distribution is improved compared to the current stainless-steel reactor. The second configuration of reactor (a quartz bell-jar reactor) is shown in **Figure 30c**, where the H-atom distribution is compared with that of our first bell-jar reactor (of the 90 years). Although the H-atom density remained rather identical, its distribution is flatter. That is crucial for improving the uniformity of polycrystalline films or to grow several diamond single crystals at once, with identical properties (Silva, Hassouni, et al., 2009).

To end up, lets us introduce the interest in lowering the excitation frequency from 2.45 GHz to 915 MHz to form larger plasma interacting with a substrate of more than 4 in. This option has been already reported in the literature (Funer et al., 1998; Funer, Wild, & Koidl, 1999). This group had designed an ellipsoid reactor called the *egg reactor*.

In LSPM, another configuration has been hold back, and the H-atom density distribution on top of a 4 in substrate is shown in **Figure 30c**. An increase in H-atom density can be obtained compared to the cavity working at 2.45 GHz, but more interesting, the H-atom radial distribution at the substrate vicinity is pretty flat over at least 3 in.

3.10.6 Conclusion

The purpose of this chapter was to discuss the way to improve synthetic diamond growth rate with the objective to reach ultrafast deposition keeping very high the quality and the purity of the layers. In order to draw some relevant conclusions, we have then limited our study to gas mixtures containing species preventing contamination of diamond, i.e. H_2–C_xH_y molecule content, although we considered the possibility of adding argon, a rare gas. Furthermore, we have limited our purpose on growth of diamond single crystals with (100) exact faces since the influence of the growth rate on the face orientation as well as on misorientation is well known (Janssen & Giling, 1995; Tallaire, Achard, Silva, Sussmann, & Gicquel, 2005).

Our choice was to analyze in detail how work the worldly diamond MW cavity-based plasma reactors by means of modeling and of plasma diagnostics since these are studied in LSPM (ex-LIMHP) since 1990. We have however included in the discussion plasma reactors running at high gas velocity and HF reactors in order to make some comparisons and to position the reactors among them.

Our analysis was focused on the understanding of the production, loss and transportation of the diamond deposition key species, i.e. first of all H atoms and CH_3 radicals. The key parameters for these processes have been identified and the way to improve them in order to produce the right species at the right location into the plasma has been discussed. We have shown that H is produced in the plasma bulk where the gas temperature is maximal and that it is then transported by diffusion to the surface where it is consumed. At least up to 400 hPa, no consumption of H atoms occurs in the plasma volume. Once H-atom density has been optimized, then we established that for a couple of pressure and pressure higher than (100 hPa, 2000 W), CH_3-density profiles present two maxima, one in a shell just outside the plasma and the other one at the plasma/surface interface. The game is obviously to increase the maximum located in the near vicinity of the surface.

We have shown that a numerical approach coupled with experiments is a powerful tool to put forward the limit of the actual State of the Art on these reactors. We have drawn the limits that we can expect in terms of growth rate with these reactors without making use of high gas velocity that would strongly decrease their flexibility. However, we are conscious that increasing the power density at very high value needs to ensure thermal, vacuum, MW injection and carbon-containing injection management all together. This constitutes a difficult technological challenge.

The self-consistent model of pure H_2 plasma made possible the optimization and the scale-up of MW cavity systems that are used for diamond deposition, while one-dimensional transport models for H_2/CH_4 plasmas allowed understanding how the populations of key species at the substrate surface change with the process controlling parameters. The transport model was also used to investigate how the dynamic effects generated when using pulsed mode can be used with a benefit to improve the deposition process from the film quality and growth rate, as well as energy cost points of view. On the basis of these models that have been validated not only at low power density but more recently at high power density although there is still discrepancies to be solved, and on the basis of direct measurements, spatial profiles of H-atom density, CH_3 density, average electron temperature and gas temperature as a function of power and pressure, while keeping as much as possible the ratio of the injected power over the total gas density were obtained. The analysis of the production and loss reaction yields as well as of the diffusion efficiency has been made.

We clearly confirmed that the plasma/surface interface of MW cavity-based reactor is H-atom diffusion limited as the HF reactors and most of the high-velocity reactors, but we have shown even without the use of increasing flow rates that the boundary layer thicknesses can be decreased. As a matter of fact, the deposition of MW energy occurs in the near-surface vicinity, and as the power density increases, partly due to the increase in the gas temperature this is displaced closer to the surface. The consequence is a strong increase in the temperature gradient at the surface that moves closer to the surface the production of hydrogen atoms and increases its flux at the surface. The consumption reactions of H atoms at the surface, that include diamond growth, are then increased.

Concerning CH_3 radicals at the plasma/surface interface, the formation of which is totally controlled by H-atom density and the gas temperature that must be in the range of 1400–2000 K, and ideally of 1650 K, the highest the power density, the closer to the surface it is formed with the highest density. Also, we have shown that the surface CH_3 density is diffusion limited in the last micrometers from the surface, however, in the last millimeter from the surface, we have observed the important effect of the very fast equilibrium reaction set activated by the steep temperature gradient, in producing methyl radicals. We have shown that the surface CH_3-radical density is a linear function of the maximum of H-atom density into the gas phase, for a given percentage of CH_4 introduced in the feed gas.

From this analysis, it is clear that the most interesting variable to increase growth rates is the power density (simultaneous change in pressure and power) that provokes strong increase in gas temperature and then in growth rates. However, this process variable increases strongly the difficulty of the thermal management.

We have furthermore established that the maximum of CH_3 at the plasma/surface interface is linked, through a square-root relationship, to the CH_4 available in this region that has been produced back through the fast equilibrium set of reactions between H atoms and CH_x radicals. The plasma/surface interface is actually the location where C_2H_2 is the dominant stable carbon-containing species while the outside shell of the plasma is the seat of predominance of CH_4. Finding a way to inject fresh CH_4 directly at the plasma/surface interface appears to be able to bring improved growth rates.

Increasing methane percentage in the feed gas obviously allows increasing growth rates, however, percentages $>8\%$ provoke formation of soot, prohibiting long-time depositions.

Pulsed plasmas were seen to add some flexibility for managing the dynamic of production of the key species and increasing growth rates while lowering the temperature of the walls of the reactor. It allows then preventing contamination of the diamond films at very high power density due to plasma etching.

Argon addition was seen to increase the gas temperature and then the growth rates.

Our coupled theoretical and experimental analysis allowed us to rely, for a given methane percentage introduced in the feed gas, directly the growth rate to the maximum H-atom density in the plasma bulk. From measurements by OES actinometry and TALIF, and calculations, we have access to a relevant estimation of the growth rate. This is extremely interesting to optimize the plasma conditions.

Although the model still need improvement in particular to better describe the electron kinetics, we believe that the plasma composition at the growing substrate surface predicted with the existing H_2/CH_4 transport model is rather accurate to be used in detailed surface models. Combining these H_2/CH_4 plasma models with a diamond growth model may clearly help not only in identifying the deposition process conditions that allows an enhancement of the film growth rate without quality degradation, but also in finding out process conditions that favor a given crystal morphology (Silva et al., 2008) as well as a polycrystalline layer texture.

Finally, complex flow patterns that are probably linked to thermoconvective instabilities resulting from the very high temperature gradients in the deposition plasma as well as soot formation when working at high methane percentage appear at high power density. These instabilities affect the convective mass and energy fluxes, and then the space distributions of the electron density and the gas temperature which could in turn affect the plasma dielectric permittivity and, consequently, the electric field distribution in the cavity. The improvement of the deposition process at high power density would require understanding and controlling these flow instabilities. A research program on this aspect is currently going on in LSPM today. This is an important issue that has to be addressed to make the deposition process very stable in these conditions, and to allow a further enhancement of diamond quality and growth rate. It is also necessary to understand and control the formation of carbon-containing particles at high methane concentration in diamond-deposition plasmas. A first attempt of modeling particle formation was already made in the case of argon/hydrogen/methane discharges used for nanocrystalline diamond film deposition (Hassouni, Mohasseb, Benedic, Lombardi, & Gicquel, 2006). Extension of this work for diamond single crystal and polycrystalline layers is planned in the near future.

We compared the efficiency of the MW cavity-based reactors to those working at very high flux, since they have an additional degree of freedom, i.e. the possibility in decreasing the boundary layer thicknesses. We have positioned the MW cavity-based plasma reactors in regards of the upper limit of H-atom density proposed by Goodwin for a fully dissociated plasma flowing at 2 atm at very high speed (10^{-6} mol cm^{-3}), that gives an upper limit of growth rate of around 350 μm h^{-1} for deposition on a 10 cm in diameter substrate. We have shown that we cannot expect growth rates greater than around 50% of the upper value even for fully dissociated plasma, working at 500 hPa. Thus, while our MW cavity-based reactors are already efficient and flexible to use, they only gave rise today to growth rates up to 70 μm h^{-1} for a high diamond quality. As a consequence, there is obviously still a margin to increase the growth rate.

Acknowledgments

CNRS, University Paris 13, DGA (Direction Générale de l'Armement) together with ANR (Agence Nationale de la Recherche) and CGI (Commissariat à l'Investissement d'Avenir) are gratefully acknowledged for their financial support of this work in particular through different contracts and through the Labex SEAM (Science and Engineering for Advanced Materials and devices) (ANR10-LABX-0096_SEAM-IDEX-0005-02) and the project Diamond n° ANR-06-BLAN-0173.

References

Achard, J., Silva, F., Tallaire, A., Bonnin, X., Lombardi, G., Hassouni, K., et al. (2007). High quality MPACVD diamond single crystal growth: high microwave power density regime. *Journal of Physics D: Applied Physics, 40*(20), 6175–6188.

Amano, T., Bernath, P. F., Yamada, C., Endo, Y., & Hirota, E. (1982). Difference frequency laser spectroscopy of the nu$_3$ band of the CH_3 radical. *The Journal of Chemical Physics, 77*(11), 5284–5287.

Ando, S., Shinohara, M., & Takayama, K. (1998). Detection of CH_3 radicals in an RF CH_4/H_2 plasma by photoionization mass spectrometry. *Vacuum, 49*(2), 113–120.

Angus, J. C. (1994). Development of low pressure diamond growth in the united states. In J. P. Dismukes, & Karl E. Spear (Eds.), *The electrochemical societies: 21. Synthetic diamond*.

Angus, J. C., Argoitia, A., Gat, R., Li, Z., Sunkara, M., Wang, L., et al. (1993). Chemical vapour deposition of diamond. *Philosophical Transactions: Physical Sciences and Engineering, 342*(1664), 195–208.

Arthur, N. L. (1986). Methyl-radical absorption cross-section at 216.4 nm and rate constant for methyl-radical recombination. *Journal of the Chemical Society, Faraday Transactions 2: Molecular and Chemical Physics, 82*(3), 331–336.

Asmussen, J., & Zhang, J. (1994). *Apparatus for the coating of material on a substrate using a microwave or UHF plasma*. East Lansing, MI: USA, Board of Trustees operating Michigan State University.

Bachmann, P. K., & van Enckevort, W. (1992). Diamond deposition technologies. *Diamond and Related Materials, 1*(10–11), 1021–1034.

Bachmann, P. K., Leers, D., & Lydtin, H. (1991). Towards a general concept of diamond chemical vapour deposition. *Diamond and Related Materials, 1*(1), 1–12.

Bird, R. B., Stewart, W. E., & Lightfoot, E. N. (1960). *Transport phenomena* (New York).

Bittner, J., Kohse-höinghaus, K., Meier, U., & Just, T. (1988). Quenching of two-photon-excited H(3s, 3d) and O(3p 3P2,1,0) atoms by rare gases and small molecules. *Chemical Physics Letters, 143*(6), 571–576.

Brinza, O., Achard, J., Silva, F., Bonnin, X., Barroy, P., De Corte, K., et al. (2008). Dependence of CVD diamond growth rate on substrate orientation as a function of process parameters in the high microwave power density regime. *Physica Status Solidi (A), 205*(9), 2114–2120.

Brinza, O., Achard, J., Silva, F., Duten, X., Michau, A., Hassouni, K., et al. (2007). Improvement of energetic efficiency for homoepitaxial diamond growth in a H_2/CH_4 pulsed discharge. *Physica Status Solidi (A), 204*(9), 2847–2853.

Butler, J. E. (1990). Optical probing of diamond chemical vapor-deposition. *Carbon, 28*(6), 809.

Butler, J. E., Mankelevich, Y. A., Cheesman, A., Jie Ma, & Ashfold, M. N. R. (2009). Understanding the chemical vapor deposition of diamond: recent progress. *Journal of Physics: Condensed Matter, 21*(36), 4201.

Butler, J. E., Celii, F. G., Oakes, D. B., Hanssen, L. M., Carrington, W. A., & Snail, K. A. (1989). Studies of diamond chemical vapor-deposition. *High Temperature Science, 27*, 183–197.

Butler, J. E., & Windischmann, H. (1998). Developments in CVD-diamond synthesis during the past decade. *MRS Bulletin (USA), 23*(9), 22–27.

Cacciatore, M. A., Capitelli, M., & Celiberto, R. (1992). Dissociative and energy transfer reactions involving vibrationally excited H_2/D_2 molecules. *Atomic and Plasma Material Interaction Data for Fusion, 2*, 65–74.

Capitelli, M., Colonna, C., Gicquel, A., Gorse, C., Hassouni, K., & Longo, S. (1996). Maxwell and non-Maxwell behavior of electron energy distribution function under expanding plasma jet conditions: the role of electron-electron, electron-ion, and superelastic electronic collisions under stationary and time-dependent conditions. *Physical Review E, 54*(2), 1843–1849.

Capitelli, M., Colonna, G., Hassouni, K., & Gicquel, A. (1994). Electron energy distribution functions in non-equilibrium H_2 discharges. The role of superelastic collisions from electronically excited states. *Chemical Physics Letters, 228*(6), 687–694.

Capitelli, M., Gorse, C., Berlemont, P., Skinner, D. A., & Bacal, M. (1991). Theoretical non-equilibrium electron energy and vibrational distributions of H_2 in magnetic multicusp plasmas: and analysis of the input cross-section data. *Chemical Physics Letters, 179*(1–2), 48–52.

Cappelli, M. A., & Loh, M. H. (1994). In-situ mass sampling during supersonic arcjet synthesis of diamond. *Diamond and Related Materials, 3*(4–6), 417–421.

Cappelli, M. A., Owano, T. G., Gicquel, A., & Duten, X. (2000). Methyl concentration measurements during microwave plasma-assisted diamond deposition. *Plasma Chemistry and Plasma Processing, 20*(1), 1–12.

Celii, F. G., & Butler, J. E. (1989). Hydrogen atom detection in the filament-assisted diamond deposition environment. *Applied Physics Letters, 54*(11), 1031–1033.

Celii, F. G., & Butler, J. E. (1992). Direct monitoring of CH_3 in a filament-assisted diamond chemical vapor deposition reactor. *Journal of Applied Physics, 71*(6), 2877–2883.

Celii, F. G., Pehrsson, P. E., Wang, H. T., & Butler, J. E. (1988). Infrared detection of gaseous species during the filament-assisted growth of diamond. *Applied Physics Letters, 52*(24), 2043–2045.

Celii, F. G., Thorsheim, H. R., Butler, J. E., Plano, L. S., & Pinneo, J. M. (1990). Detection of ground-state atomic-hydrogen in a DC-plasma using 3rd-Harmonic generation. *Journal of Applied Physics, 68*(8), 3814–3817.

Chatei, H., Bougdira, J., Remy, M., Alnot, P., Bruch, C., & Krüger, J. K. (1997). Combined effect of nitrogen and pulsed microwave plasma on diamond growth. *Diamond and Related Materials, 6*, 505–510.

Chen, K.-H., Chuang, M.-C., Penney, C. M., & Banholzer, W. (1992). Temperature and concentration distribution of H_2 and H atoms in hot-filament chemical-vapor deposition of diamond. *Journal of Applied Physics, 71*(3), 1485–1493.

Chenevier, M., Cubertafon, J. C., Campargue, A., & Booth, J. P. (1994). Measurement of atomic hydrogen in a hot filament reactor by two-photon laser-induced fluorescence. *Diamond and Related Materials, 3*(4–6), 587–592.

Childs, M. A., Menningen, K. L., Chevako, P., Spellmeyer, N. W., Anderson, L. W., & Lawler, J. E. (1992). Detection of CH_3 during CVD growth of diamond by optical absorption. *Physics Letters A, 171*(1–2), 87–89.

Cohen, N., & Westberg, K. R. (1983). Chemical kinetic data sheets for high-temperature chemical reactions. *Journal of Physical and Chemical Reference Data, 12*(3), 531–590.

Connell, L. L., Fleming, J. W., Chu, H. N., Vestyck, D. J., Jensen, E., & Butler, J. E. (1995). Spatially-resolved atomic-hydrogen concentrations and molecular-hydrogen temperature profiles in the chemical-vapor-deposition of diamond. *Journal of Applied Physics, 78*(6), 3622–3634.

Corat, E. J., & Goodwin, D. G. (1993). Temperature dependence of species concentrations near the substrate during diamond chemical vapor deposition. *Journal of Applied Physics, 74*(3), 2021–2029.

Davidson, D. F., Chang, A. Y., Di Rosa, M. D., & Hanson, R. K. (1993). A cw laser absorption diagnostic for methyl radicals. *Journal of Quantitative Spectroscopy and Radiative Transfer, 49*(5), 559–571.

Davidson, D. F., Di Rosa, M. D., Chang, E. J., & Hanson, R. K. (1995). An improved determination of the 216.615 nm absorption coefficient for methyl radicals. *Journal of Quantitative Spectroscopy and Radiative Transfer, 53*(5), 581–583.

Davies, P. B., & Martineau, P. M. (1992a). Infrared laser diagnostics in methane chemical-vapor-deposition plasmas. *Journal of Applied Physics, 71*(12), 6125–6135.

Davies, P. B., & Martineau, P. M. (1992b). Diagnostics and modeling of silane and methane Plasma CVD Processes. *Advanced Materials, 4*(11), 729–736.

Derkaoui, N. (2012). *Étude des plasmas micro-ondes à haute densité de puissance en systèmes H2-CH4 et H2-CH4-B2H6 pour le dépôt de diamant*. Université Paris 13.

Derkaoui, N., Rond, C., Gicquel, A., Gries, T., & Henrion, G., (Submitted). Electronic properties of H_2/CH_4 microwave plasma for diamond deposition.

Derkaoui, N., Rond, C., Wartel, M., & Gicquel, A., (work in progress).

Duten, X. (2000). *Etude spectroscopique et modélisation de réacteurs de dépôt de films de diamant par plasma micro-onde, fonctionnant en régime continu et impulsionel*. Orsay, France: Université de Paris 11.

Duten, X., Rousseau, A., Gicquel, A., Hassouni, K., & Leprince, P. (2002). Time-resolved measurements of the gas temperature in a H_2/CH_4 medium pressure microwave 915 MHz pulsed plasma. *Journal of Physics D: Applied Physics, 35*(16), 1939–1945.

Erickson, C. J., Jameson, W. B., Watts-Cain, J., Menningen, K. L., Childs, M. A., Anderson, L. W., et al. (1996). High-sensitivity absorption spectroscopy on a microwave plasma-assisted chemical vapour deposition diamond growth facility. *Plasma Sources, Science and Technology, 5*(4), 761–764.

Fan, W. Y., Knewstubb, P. F., Käning, M., Mechold, L., Röpcke, J., & Davies, P. B. (1999). *Journal of Physical Chemistry, 103*, 4118.

Ferreira, C. M. (1992). In C. M. Ferreira, & M. Moisan (Eds.), *Microwave discharges: fundamentals and applications* (313–338). New York – London: Plenum Press.

Frenklach, M., & Spear, K. E. (1988). Growth mechanism of vapor-deposited diamond. *Journal of Materials Research, 3*(1), 133–140.

Frenklach, M., & Wang, H. (1991). Detailed surface and gas-phase chemical kinetics of diamond deposition. *Physical Review B, 43*(2), 1520–1545.

Funer, M., Wild, C., & Koidl, P. (1998). Novel microwave plasma reactor for diamond synthesis. *Applied Physics Letters, 72*(10), 1149–1151.

Funer, M., Wild, C., & Koidl, P. (1999). Simulation and development of optimized microwave plasma reactors for diamond deposition. *Surface and Coatings Technology, 116–119*, 853–862.

Gicquel, A. (1996). *Le diamant métastable: matériau stratégique? Procédés de production, applications optiques et opto-électroniques*. Institut d'expertise et de prospective de l'école normale supérieure.

Gicquel, A., Chenevier, M., & Lefebvre, M. (1998). Spatially resolved spectroscopic analysis of the plasma. In G. P. M. A. prelas, & L. K. Bigelow (Eds.), *Handbook of industrial diamond and diamond films* (739).

Gicquel, A., Chenevier, M., Breton, Y., Petiau, M., Booth, J. P., & Hassouni, K. (1996). Ground state and excited state H-atom temperatures in a microwave plasma diamond deposition reactor. *Journal de physique, III*(6), 1167–1180.

Gicquel, A., Chenevier, M., Hassouni, K., Tserepi, A., & Dubus, M. (1998). Validation of actinometry for estimating relative hydrogen atom densities and electron energy evolution in plasma assisted diamond deposition reactors. *Journal of Applied Physics, 83*(12), 7504–7521.

Gicquel, A., Derkaoui, N., Rond, C., Benedic, F., Cicala, G., Moneger, D., et al. (2012). Quantitative analysis of diamond deposition reactor efficiency. *Chemical Physics, 398*(0), 239–247.

Gicquel, A., Hassouni, K., Breton, Y., Chenevier, M., & Cubertafon, J. C. (1996). Gas temperature measurements by laser spectroscopic techniques and by optical emission spectroscopy. *Diamond and Related Materials, 5*(3–5), 366–372.

Gicquel, A., Hassouni, K., Farhat, S., Breton, Y., Scott, C. D., & Lefebre, M. (1994). Spectroscopic analysis and chemical kinetics modeling of a diamond deposition plasma reactor. *Diamond and Related Materials, 3*(4), 581–586.

Gicquel, A., Hassouni, K., Silva, F., & Achard, J. (2001). CVD diamond films: from growth to applications. *Current Applied Physics, 1*(6), 479–496.

Gicquel, A., Silva, F., & Hassouni, K. (2000). Diamond growth mechanisms in various environments. *Journal of the Electrochemical Society, 147*(6), 2218–2226.

Gicquel, A., Silva, F., Duten, X., Hassouni, K., Lombardi, G. & Rousseau, A. (2003). High-speed diamond growth using a microwave plasma in pulsed mode France, extension Europe, USA, USPTO US 7,662,441 B2 (2010). FR0300254.

Girshick, S. L., Li, C., Yu, B. W., & Han, H. (1993). Fluid boundary layer effects in atmospheric-pressure plasma diamond film deposition. *Plasma Chemistry and Plasma Processing, 13*(2), 169–187.

Girshick, S. L. (1998). Diamond CVD using radio-frequency plasmas. In G. P. M. A. Prelas, & L. K. Bigelow (Eds.), *Handbook of industrial diamonds and diamond films* (851).

Girshick, S. L., Yu, B. W., Li, C., & Han, H. (1993). Diamond deposition by atmospheric pressure induction plasma: effects of impinging jet fluid mechanics on film formation. *Diamond and Related Materials, 2*(5–7), 1090–1095.

Glänzer, K., Quack, M., & Troe, J. (1977). High temperature UV absorption and recombination of methyl radicals in shock waves. *Symposium (International) on Combustion, 16*(1), 949–960.

Glass, J. T., Williams, B. E., & Davis, R. F. (1988). Chemical vapor deposition and characterization of diamond films grown via microwave plasma enhanced CVD. *Proceedings of the SPIE The International Society for Optical Engineering, 877*, 56–63.

Goodwin, D. G. (1993a). Scaling laws for diamond chemical-vapor deposition. I. Diamond surface chemistry. *Journal of Applied Physics, 74*(11), 6888–6894.

Goodwin, D. G. (1993b). Scaling laws for diamond chemical-vapor deposition. II. Atomic hydrogen transport. *Journal of Applied Physics, 74*(11), 6895–6906.

Gordon, M. H., Duten, X., Hassouni, K., & Gicquel, A. (2001). Energy coupling efficiency of a hydrogen microwave plasma reactor. *Journal of Applied Physics, 89*(3), 1544–1549.

Gordon, M., Owano, T. G., Kruger, C. H., & Cappelli, M. A. (1989). *Proceedings of GEC, 35*.

Gray, K. J., & Windischmann, H. (1999). Free-standing CVD diamond wafers for thermal management by d.c. arc jet technology. *Diamond and Related Materials, 8*(2–5), 903–908.

Green, M., Jennings, K., Linnett, J., & Schoffield, D. (1959). *Transactions of the Faraday Society, 55*, 2152.

Green, D. S., Owano, T. G., Williams, S., Goodwin, D. G., Zare, R. N., & Kruger, C. H. (1993). Boundary layer profiles in plasma chemical vapor deposition. *Science, 259*(5102), 1726–1729.

Grotjohn, T., Liske, R., Hassouni, K., & Asmussen, J. (2005). Scaling behavior of microwave reactors and discharge size for diamond deposition. *Diamond and Related Materials, 14*(3–7), 288–291.

Harris, S. J. (1989). Gas-phase kinetics during diamond growth: CH_4 as-growth species. *Journal of Applied Physics, 65*(8), 3044.

Harris, S. J. (1990). Mechanism for diamond growth from methyl radicals. *Applied Physics Letters, 56*(23), 2298–2300.

Harris, S. J., & Belton, D. N. (1992). Diamond growth on a (100)-type step. *Thin Solid Films, 212*(1–2), 193–200.

Harris, S. J., & Weiner, A. M. (1993). Reaction kinetics on diamond: measurement of H atom destruction rates. *Journal of Applied Physics, 74*(2), 1022–1026.

Hassouni, K., Duten, X., Rousseau, A., & Gicquel, A. (2001). Investigation of chemical kinetics and energy transfer in a pulsed microwave H_2/CH_4 plasma. *Plasma Sources Science and Technology, 10*, 61–75.

Hassouni, K., Silva, F., & Gicquel, A. (2010). Modelling of diamond deposition microwave cavity generated plasmas. *Journal of Physics D: Applied Physics, 43*(15), 153001.

Hassouni, K., Farhat, S., & Scott, C. D. (1997). Flow modeling for plasma assisted diamond deposition reactor. In G. P. M. A. Prelas, & L. K. Bigelow (Eds.), *Handbook of industrial diamond and diamond films* (653–672). New York – Basel – Hong Kong: Marcel Dekker.

Hassouni, K., Farhat, S., Scott, C. D., & Gicquel, A. (1996). Modeling species and energy transport in moderate pressure diamond deposition H_2 plasmas. *Journal of Physics III France, 6*, 1229–1243.

Hassouni, K., Grotjohn, T. A., & Gicquel, A. (1999). Self-consistent microwave field and plasma discharge simulations for a moderate pressure hydrogen discharge reactor. *Journal of Applied Physics, 86*(1), 134–151.

Hassouni, K., Leroy, O., Farhat, S., & Gicquel, A. (1998). Modeling of H_2 and H_2/CH_4 moderate-pressure microwave plasma used for diamond deposition. *Plasma Chemistry and Plasma Processing, 18*(3), 325–362.

Hassouni, K., Mohasseb, F., Benedic, F., Lombardi, G., & Gicquel, A. (2006). Formation of soot particles in $Ar/H_2/CH_4$ microwave discharges during nanocrystalline diamond deposition: a modeling approach. *Pure and Applied Chemistry, 78*(6), 1127–1145.

Hassouni, K., Scott, C. D., & Farhat, S. (1997). *Flow modeling for a plasma assisted diamond deposition reactor. Handbook of industrial diamond and diamond films.* New York: GPMA Prelas and LK Bigelow.

Hassouni, K., Scott, C. D., Farhat, S., Gicquel, A., & Capitelli, M. (1997). Non-Maxwellian effect on species and energy transport in moderate pressure H_2 plasmas. *Surface and Coatings Technology, 97*(1–3), 391–403.

Hay, S. O., Roman, W. C., & Colket, M. B. (1990). CVD diamond deposition processes investigation: CARS diagnostics/modeling. *Journal of Materials Research, 5*(11).

Hirmke, J., Glaser, A., Hempel, F., Stancu, G. D., Röpcke, J., Rosiwal, S. M., et al. (2007). Improved flow conditions in diamond hot filament CVD–Promising deposition results and gas phase characterization by laser absorption spectroscopy. *Vacuum, 81*(5), 619–626.

Hirose, Y., & Kondo, N. (1988). *Japanese Journal of Applied Physics*.

Hsu, W. L. (1992). Gas-phase kinetics during microwave plasma-assited diamond deposition: is the hydrocarbon product distribution dictated by neutral-neutral interaction? *Journal of Applied Physics, 72*(7), 3102–3109.

Hwang, S. M., Rabinowitz, M. J., & Gardiner, W. C., Jr. (1993). Recombination of methyl radicals at high temperatures. *Chemical Physics Letters, 205*(2–3), 157–162.

Janev, R. K., & Reiter, D. (2004). Collision processes of $C_{2,3}H_y$ and $C_{2,3}H_y^+$ hydrocarbons with electrons and protons. *Physics of Plasmas, 11*(2), 780–829.

Janev, R. K. L., William, D., Post, D. E., Jr., & Evans, K., Jr. (1987). Elementary processes in hydrogen-helium plasmas: cross sections and reaction rate coefficients. *Springer-Verlag (Springer Series on Atoms and Plasmas), 4*, 335.

Janssen, G., & Giling, L. J. (1995). "Mosaic." growth of diamond. *Diamond and Related Materials, 4*(7), 1025–1031.

John, P., Rabeau, J. R., & Wilson, J. I. B. The cavity ring-down spectroscopy of C_2 in a microwave plasma. *Diamond and Related Materials, 11*(3–6), 608–611.

Karpasb, Z., Anicich, V., & Huntress, J. W. T. (1979). An ion cyclotron resonance study of reactions of ions with hydrogen atoms. *The Journal of Chemical Physics, 70*(6), 2877–2881.

Kaminski, C., & Ewart, P. (1995). Absolute concentration measurements of C_2 in a diamond CVD reactor by laser-induced fluorescence. *Applied Physics B: Lasers and Optics, 61*(6), 585–592.

Kaminski, C. F., & Ewart, P. (1997). Multiplex H_2 CARS thermometry with a modeless laser. *Applied Optics, 36*(3), 731–734. doi:10.1364/AO.36.000731.

Kamo, M., Takamura, F., & Sato, Y. (1990). In O. Fukunaga, S. Saito, & M. Yoshikawa (Eds.), *Science and technology of new diamond*.

Kim, Y. C., & Boudart, M. (1991). Recombination of oxygen, nitrogen, and hydrogen atoms on silica: kinetics and mechanism. *Langmuir, 7*(12), 2999–3005.

King, D., Yaran, M. K., Schuelke, T., Grotjohn, T. A., Reinhard, D. K., & Asmussen, J. (2008). Scaling the microwave plasma-assisted chemical vapor diamond deposition process to 150–200 mm substrates. *Diamond and Related Materials, 17*(4–5), 520–524.

Koemtzopoulos, C. R., Economou, D. J., & Pollard, R. (1993). Hydrogen dissociation in a microwave discharge for diamond deposition. *Diamond and Related Materials, 2*(1), 25–35.

Konov, V. I. (1996). 4th Int. Conf. and Exh. of the Gorham Advanced Materials Institute.

Krasnoperov, L. N., Kalinovski, I. J., Chu, H. N., & Gutman, D. (1993). Heterogeneous reactions of H atoms and CH_3 radicals with a diamond surface in the 300–1133 K temperature range. *Journal of Physical Chemistry, 97*(45), 11787–11796.

Laimer, J., & Matsumoto, S. (1994). Atomic hydrogen concentrations in pulsed microwave discharges used for diamond synthesis. *Plasma Chemistry and Plasma Processing, 14*(2), 117–130.

Lavrov, B. P., Osiac, M., Pipa, A. V., & Ropcke, J. (2003). On the spectroscopic detection of neutral species in a low-pressure plasma containing boron and hydrogen. *Plasma Sources Science and Technology, 12*(4), 576.

Lehfaoui, L., Rebrion-Rowe, C., Laubé, S., Mitchell, J., & Rowe, B. (1997). *Journal of Chemical Physics, 106*(1).

Lieberman, M. A., & Lichtenberg, A. J. (1994). *Principle of plasma discharges and material processing*. New York: John Wiley and Sons, Inc.

Lin, L., Shibing, T., Sun, W., Wuxia, L., Junjie, L. & Changzhi, G. (to be published). Reducing edge effect of temperature-field for large-area thin film deposition in hot filament chemical vapor deposition system. *Surface and Coatings Technology*.

Loh, M. H., & Cappelli, M. A. (1992). Diamond synthesis in supersonic direct-current arcjet plasma at subtorr pressures. *Surface and Coatings Technology, 54–55*(Part 2), 408–413.

Loh, M. H., & Cappelli, M. A. (1997). CH_3 detection in a low-density supersonic arcjet plasma during diamond synthesis. *Applied Physics Letters, 70*(8), 1052–1054.

Lombardi, G. (2003). *Diagnostics spectroscopiques d'espèces carbonées et modélisation physico-chimique de plasmas micro-ondes dans les mélanges H_2/CH_4 et $Ar/H_2/CH_4$ utilisés pour le dépôt de diamant*. Université Paris Sud - Paris XI.

Lombardi, G., Benedic, B., Mohasseb, F., Hassouni, K., & Gicquel, A. (2004). Determination of gas temperature and C_2 absolute density in $Ar/H_2/CH_4$ microwave discharges used for nanocrystalline diamond deposition from the C_2 Mulliken system. *Plasma Sources Science and Technology, 13*(3), 375.

Lombardi, G., Hassouni, K., Benedic, F., Mohasseb, F., Ropcke, J., & Gicquel, A. (2004). Spectroscopic diagnostics and modeling of $Ar/H_2/CH_4$ microwave discharges used for nanocrystalline diamond deposition. *Journal of Applied Physics, 96*(11), 6739–6751.

Lombardi, G., Hassouni, K., Stancu, G. D., Mechold, L., Ropcke, J., & Gicquel, A. (2005a). Modeling of microwave discharges of H_2 admixed with CH_4 for diamond deposition. *Journal of Applied Physics, 98*(5), 053303–053312.

Lombardi, G., Hassouni, K., Stancu, G. D., Mechold, L., Röpcke, J., & Gicquel, A. (2005b). Study of an H_2/CH_4 moderate pressure microwave plasma used for diamond deposition: modelling and IR tuneable diode laser diagnostic. *Plasma Sources Science and Technology, 14*(3), 440–450.

Lombardi, G., Stancu, G. D., Hempel, F., Gicquel, A., & Roepcke, J. (2004). Quantitative detection of methyl radicals in non-equilibrium plasmas: a comparative study. *Plasma Sources Science and Technology, 13*(1), 27–38.

Lommatzsch, U., Wahl, E. H., Owano, T. G., Kruger, C. H., & Zare, R. N. (2000). Spatial concentration and temperature distribution of CH radicals formed in a diamond thin-film hot-filament reactor. *Chemical Physics Letters, 320*(3–4), 339–344.

Loureiro, J., & Ferreira, C. M. (1989). Electron and vibrational kinetics in the hydrogen positive column. *Journal of Physics D Applied Physics, 22*(11), 1680–1691.

Lu, Z. P., Heberlien, J., & Pfender, E. (1992a). Process study of thermal plasma chemical vapor deposition of diamond, part II: pressure dependence and effect of substrate pretreatment. *Plasma Chemistry and Plasma Processing, 12*(1), 55–69.

Lu, Z. P., Heberlien, J., & Pfender, E. (1992b). Process study of thermal plasma chemical vapor deposition of diamond, part I. *Plasma Chemistry and Plasma Processing, 12*(1), 35–53.

Ma, J., Cheesman, A., Ashfold, M. N. R., Hay, K. G., Wright, S., Langford, N., et al. (2009). Quantum cascade laser investigations of CH_4 and C_2H_2 interconversion in hydrocarbon/H_2 gas mixtures during microwave plasma enhanced chemical vapor deposition of diamond. *Journal of Applied Physics, 106*(3), 033305–033315.

Ma, J., Richley, J. C., Ashfold, M. N. R., & Mankelevich, Y. A. (2008). Probing the plasma chemistry in a microwave reactor used for diamond chemical vapor deposition by cavity ring down spectroscopy. *Journal of Applied Physics, 104*(10), 103305–103309.

Ma, J., Ashfold, M. N. R., & Mankelevich, Y. A. (2009). Validating optical emission spectroscopy as a diagnostic of microwave activated $CH_4/Ar/H_2$ plasmas used for diamond chemical vapor deposition. *Journal of Applied Physics, 105*(4), 043302–043312.

Mankelevich, Y. A., Ashfold, M. N. R., & Ma, J. (2008). Plasma-chemical processes in microwave plasma-enhanced chemical vapor deposition reactors operating with C/H/Ar gas mixtures. *Journal of Applied Physics, 104*(11), 113304–113311.

Mankelevich, Y. A., Ashfold, M. N. R., & Orr-Ewing, A. J. (2007). Measurement and modeling of $Ar/H_2/CH_4$ arc jet discharge chemical vapor deposition reactors II: modeling of the spatial dependence of expanded plasma parameters and species number densities. *Journal of Applied Physics, 102*(6), 063310–063311.

Mankelevich, Y. A., & May, P. W. (2008). New insights into the mechanism of CVD diamond growth: single crystal diamond in MW PECVD reactors. *Diamond and Related Materials, 17*(7–10), 1021–1028.

Mankelevich, Y. A., Rakhimov, A. T., & Suetin, N. V. (1995). Two-dimensional model of reactive gas flow in a diamond film CVD reactor. *Diamond and Related Materials, 4*(8), 1065–1068.

Massey, H. S. W. (1969). *Electronic and ionic impact phenomena*.

Matsumoto, S., Kobayashi, T., & Hino, M. (1987). *Proceedings of the International Symposium on Plasma Chemistry, 8*(4), 2453.

Mechold, L., Ropcke, J., Duten, X., & Rousseau, A. (2001). On the hydrocarbon chemistry in a H_2 surface wave discharge containing methane. *Plasma Sources Science and Technology, 10*(1), 52.

Menningen, K. L., Childs, M. A., Chevako, P., Toyoda, H., Anderson, L. W., & Lawler, J. E. (1993). *Chemical Physics Letters, 204*(573).

Menningen, K. L., Childs, M. A., Toyoda, H., Ueda, Y., Anderson, L. W., & Lawler, J. E. (1995). CH_3 and CH densities in a diamond growth DC discharge. *Contributions to Plasma Physics, 35*(4–5), 359–373.

Mitsuda, Y., Tanaka, K., & Yoshida, T. (1990). In situ emission and mass spectroscopic measurement of chemical species responsible for diamond growth in a microwave plasma jet. *Journal of Applied Physics, 67*(8), 3604–3608.

Moisan, M., & Pelletier, J. (1992). *Microwave excited plasma.* Amsterdam, London, New York, Tokyo: Elsevier.

Monéger, D. (2009). *Étude d'un procede de depot de films de diamant nanocristallin par CVD assistee par plasma micro-onde en regimes continu et pulse – Application a la realisation de filtres a ondes acoustiques de surface.* Université Paris 13.

Naito, S., Ikeda, M., Ito, N., Hattori, T., & Goto, T. (1993). Effect of rare gas dilution on CH_3 radical density in rf-discharge CH_4 plasma. *Japanese Journal of Applied Physics, 32*(12A), 5721–5725.

Ohtake, N., Tokura, H., Kuriyama, Y., Mashino, Y., & Yoshikawa, M. (1989). Diamond and diamond like films proceedings. *Electrochemical Society, 89*(12), 93.

Osiac, M., Lavrov, B. P., & Röpcke, J. (2002). Intensity distributions in R and P branches of (0-0) band of the A1[Pi]–>X1[Sigma]+ electronic transition of the BH molecule and determination of gas temperature in non-equilibrium plasmas. *Journal of Quantitative Spectroscopy and Radiative Transfer, 74*(4), 471–491.

Oskam, J. (1958). Microwave investigation of disintegrating gaseous discharge plasmas. *Philips Research Reports*, 335.

Owano, T. G., Kruger, C. H., & Cappelli, M. A. (1991). *Proceedings of the International Symposium on Plasma Chemistry, 10*(3).

Owano, T. G., Kruger, C. H., Green, D. S., Williams, S., & Zare, R. N. (1993). Degenerate four-wave mixing diagnostics of atmospheric pressure diamond deposition. *Diamond and Related Materials, 2*(5–7), 661–666.

Preppernau, B. L., Pearce, K., Tserepi, A., Wurzberg, E., & Miller, T. A. (1995). Angular momentum state mixing and quenching of n = 3 atomic hydrogen fluorescence. *Chemical Physics, 196*(1–2), 371–381.

Ralchenko, V. G., Smolin, A. A., Konov, V. I., Sergeichev, K. F., Sychov, I. A., Vlasov, I. I., et al. (1997). Large-area diamond deposition by microwave plasma. *Diamond and Related Materials, 6*(2–4), 417–421.

Rayar, M., Veis, P., Foissac, C., Supiot, P., & Gicquel, A. (2006). Gas temperature determination using BH (0â€"0) A 1 Î â†' X 1 Î£ + emission spectrum in a B 2 H 6 containing plasma for doped diamond deposition. *Journal of Physics D: Applied Physics, 39*(10), 2151.

Rayar, M., Supiot, P., Veis, P., & Gicquel, A. (2008). *Journal of Applied Physics, 104*(3).

Rebrion-Rowe, C., Lehfaoui, L., Rowe, B. R., & Mitchell, J. B. A. (1998). The dissociative recombination of hydrocarbon ions. II. Alkene and alkyne derived species. *The Journal of Chemical Physics, 108*(17), 7185–7189.

Reeve, S. W. W., & Weimer, W. A. (1995). Plasma diagnostics of a direct-current arcjet diamond reactor. II. Optical emission spectroscopy. *Journal of Vacuum Science & Technology A: Vacuum, Surfaces, and Films, 13*(2), 359–367.

Rennick, C. J., Smith, J. A., Ashfold, M. N. R., & Orr-Ewing, A. J. (2004). Cavity ring-down spectroscopy measurements of the concentrations of C2(X1[Sigma] g+) radicals in a DC arc jet reactor used for chemical vapour deposition of diamond films. *Chemical Physics Letters, 383*(5–6), 518–522.

Rennick, C. J., Ma, J., Henney, J. J., Wills, J. B., Ashfold, M. N. R., Orr-Ewing, A. J., et al. (2007). Measurement and modeling of Ar/H_2/CH_4 arc jet discharge chemical vapor deposition reactors. I. Intercomparison of derived spatial variations of H atom, C_2, and CH radical densities. *Journal of Applied Physics, 102*(6), 063309–063313.

Ring, Z., Mantei, T. D., Tlali, S., & Jackon, H. E. (1995). Low-temperture diamond growth in a pulsed microwave plasma. *Journal of Vacuum Science and Technology A, 13*(3), 1617–1618.

Robinson, G. N., Zahniser, M. S., Freedman, A., & Nelson, J. D. D. (1996). Pressure-broadened linewidth measurements in the [nu]2band of the CH_3 radical. *Journal of Molecular Spectroscopy, 176*(2), 337–341.

Rond, C., Derkaoui, N., Michau, A., Hassouni, K., & Gicquel, A., (work in progress).

Röpcke, J., & Ohl, A. (1994). Temperature distributions across the plasma layer of planar low pressure microwave plasmas — a comparative investigation by optical emission spectroscopy. *Contributions to Plasma Physics, 34*(4), 575–586.

Röpcke, J., Mechold, L., Käning, M., Fan, W. Y., & Davies, P. B. (1999). Tunable diode laser diagnostic studies of N_2-Ar-O_2 microwave plasmas containing methane. *Plasma Chemistry and Plasma Processing, 19*(3), 345–419.

Ropcke, J., Mechold, L., Kaning, M., Anders, J., Wienhold, F. G., Nelson, D., et al. (2000). IRMA: a tunable infrared multicomponent acquisition system for plasma diagnostics. *Review of Scientific Instruments, 71*(10), 3706–3710.

Röpcke, J., Revalde, G., Osiac, M., Li, K., & Meichsner, J. (2002). *Plasma Chemistry and Plasma Processing, 22*, 137.

Rousseau, A., Cartry, G., & Duten, X. (2001). Surface recombination of hydrogen atoms studied by a pulsed plasma excitation technique. *Journal of Applied Physics, 89*(4), 2074–2078.

Rousseau, A., et al. (1994). Microwave discharge in H_2: influence of H-atom density on the power balance. *Journal of Physics D: Applied Physics, 27*(7), 1412.

Schafer, L., Klages, C.-P., Meier, U., & Kohse-Hoinghaus, K. (1991). Atomic hydrogen concentration profiles at filaments used for chemical vapor deposition of diamond. *Applied Physics Letters, 58*(6), 571–573.

Schelz, S., Campillo, C., & Moisan, M. (1998). Characterization of diamond films deposited with a 915-MHz scaled-up surface-wave-sustained plasma. *Diamond and Related Materials, 7*(11–12), 1675–1683.

Schulz-von der Gathen, V., Röpcke, J., Gans, T., Käning, M., Lukas, C., & Döbele, H. F. (2001). Diagnostic studies of species concentrations in a capacitively coupled RF plasma containing CH_4-H_2-Ar. *Plasma Sources Science and Technology, 10*(3), 530.

Schwärzler, C. G., Schnabl, O., Laimer, J., & Störi, H. (1996). On the plasma chemistry of the C/H system relevant to diamond deposition processes. *Plasma Chemistry and Plasma Processing, 16*(2), 173.

Scott, C. D., Farhat, S., Gicquel, A., Hassouni, K., & Lefebvre, M. (1996). Determining electron temperature and temperature and density in a hydrogen microwave plasma. *Journal of Thermophysics and Heat Transfer, 10*, 426–435.

Sevillano, E. (1998). Microwave-plasma deposition of diamond. In B. Dischler, & C. Wild (Eds.), *Low-pressure synthetic diamond: Manufacturing and applications* (11–39). Berlin: Springer.

Silva, F., & Gicquel, A. (1998). Structural characteristics of CVD diamond films versus nitrogen impurities coupled to other deposition parameters. Proceedings of the fifth-International Symposium on Diamond Materials *Journal of Electrochemical Society, 97-32*, 99–125.

Silva, F., Achard, J., Brinza, O., Bonnin, X., Hassouni, K., Anthonis, A., et al. (2009). High quality, large surface area, homoepitaxial MPACVD diamond growth. *Diamond and Related Materials, 18*(5–8), 682–697.

Silva, F., Bonnin, X., Achard, J., Brinza, O., Michau, A., & Gicquel, A. (2008). Geometric modeling of homoepitaxial CVD diamond growth: I. The {100}{111}{110}{113} system. *Journal of Crystal Growth, 310*, 187–203.

Silva, F., Hassouni, K., Bonnin, X., & Gicquel, A. (2009). Microwave engineering of plasma-assisted CVD reactors for diamond deposition. *Journal of Physics: Condensed Matter, 21*(36), 364202.

Smith, J. A., Cameron, E., Ashfold, M. N. R., Mankelevich, Y. A., & Suetin, N. V. (2001). On the mechanism of CH_3 radical formation in hot filament activated CH_4/H_2 and C_2H_2/H_2 gas mixtures. *Diamond and Related Materials, 10*(3–7), 358–363.

Spitsyn, B. V., Bouilov, L. L., & Alexenko, A. E. (2000). Origin, state of the art and some prospects of the diamond CVD. *Brazilian Journal of Physics, 30*(3), 471.

Spitsyn, B. V., Bouilov, L. L., & Derjaguin, B. V. (1981). Vapor growth of diamond on diamond and other surfaces. *Journal of Crystal Growth, 52*(Part 1), 219–226.

St-Onge, L., & Moisan, M. (1994). Hydrogen atom yield in RF and microwave hydrogen discharges. *Plasma Chemistry and Plasma Processing, 14*(2), 87–116.

Sugai, H., & Toyoda, H. (1992). Appearance mass spectrometry of neutral radicals in radio frequency plasmas. *Journal of Vacuum Science & Technology A, 10*(4), 1193–1200.

Sugai, H., Kojima, H., Ishida, A., & Tiyida, H. (1990). Spatial distribution of CH_3 and CH_2 radicals in a methane rf discharge. *Applied Physics Letters, 56*(26), 2616–2618.

Tachibana, T., Ando, Y., Watanabe, A., Nishibayashi, Y., Kobashi, K., Hirao, T., et al. (2000). Diamond films grown by a 60kW microwave plasma chemical vapor deposition system. *Diamond and Related Materials, 10*(9–10), 1569–1572.

Tachibana, K., Nishida, M., Harima, H., & Urano, Y. (1984). Diagnostics and modelling of a methane plasma used in the chemical vapour deposition of amorphous carbon films. *Journal of Physics D: Applied Physics, 17*(8), 1727.

Tahara, H., Minami, K. I., Murai, A., Yasui, T., & Yoshikawa, T. (1995). *Japanese Journal of Applied Physics, 34*(1972).

Tallaire, A., Achard, J., Silva, F., & Gicquel, A. (2005). Effect of increasing the microwave density in both continuous and pulsed wave mode on the growth of monocrystalline diamond films. *Physica Status Solidi (A), 202*(11), 2059–2065.

Tallaire, A., Achard, J., Silva, F., Sussmann, R. S., & Gicquel, A. (2005). Homoepitaxial deposition of high-quality thick diamond films: effect of growth parameters. *Diamond and Related Materials, 14*(3–7), 249–254.

Tallaire, A., Rond, C., Benedic, F., Brinza, O., Achard, J., Silva, F., et al. (2011). Effect of argon addition on the growth of thick single crystal diamond by high-power plasma CVD. Submitted to Physica Status Solidi A.

Tallaire, A., Collins, A. T., Charles, D., Achard, J., Sussmann, R., Gicquel, A., et al. (2006). Characterisation of high-quality thick single-crystal diamond grown by CVD with a low nitrogen addition. *Diamond and Related Materials, 15*(10), 1700–1707.

Tan, W., & Grotjohn, T. A. (1994). Modeling the electromagnetic excitation of a microwave cavity plasma reactor. *Journal of Vacuum Science and Technology A, 12*(4), 1216–1220.

Tan, W., & Grotjohn, T. A. (1995). Modeling of the electromagnetic field and the plasma discharge in a microwave plasma diamond deposition reactor. *Diamond and Related Materials, 4*, 1145–1154.

Tawara, H., Nishimura, H., Tanaka, H., & Nakamura, Y. (1990). *NIFS-DATA Research Report, 6*(1–112).

Tawara, H., Nishimura, H., & Yoshino, M. (1990). Cross sections and related data for electron collisions with hydrogen molecules and molecular ions. *Journal of Physical and Chemical Reference Data, 19*(3), 617–636.

Tserepi, A. D., & Miller, T. A. (1994). Two-Photon absorption laser-induced fluorescence of H atoms: a probe for heterogeneous processes in hydrogen plasmas. *Journal of Applied Physics, 75*(11), 7231–7236.

Vetterhöffer, J., Campargue, A., Chenevier, M., & Stoeckel, F. (1993). Temperature measurement of atomic hydrogen produced by hot-filament dissociation in a CH_4–H_2 mixture. *Diamond and Related Materials, 2*(2–4), 481–485.

Vikharev, A. L., Gorbachev, A. M., Koldanov, V. A., Akhmedzhanov, R. A., Radishchev, D. B., Grotjohn, T. A., et al. (2003). Comparison of pulsed and CW regimes of MPACVD reactor operation. *Diamond and Related Materials, 12*(3–7), 272–276.

Wahl, E. H., Owano, T. G., Kruger, C. H., Ma, Y., Zalicki, P., & Zare, R. N. (1997). Spatially resolved measurements of absolute CH_3 concentration in a hot-filament reactor. *Diamond and Related Materials, 6*(2–4), 476–480.

Wahl, E. H., Owano, T. G., Kruger, C. H., Zalicki, P., Ma, Y., & Zare, R. N. (1996). Measurement of absolute CH_3 concentration in a hot-filament reactor using cavity ring-down spectroscopy. *Diamond and Related Materials, 5*(3–5), 373–377.

Wang, H., & Frenklach, M. (1997). A detailed kinetic modeling study of aromatics formation in laminar premixed acetylene and ethylene flames. *Combustion and Flame, 110*(1–2), 173–221.

Wartel, M., Derkaoui, N., Rond, C., Duluard, C., & Gicquel, A., (work in progress).

Whitfield, M. D., Jackman, R. B., & Foord, J. S. (2000). Spatially resolved optical emission spectroscopy of the secondary glow observed during biasing of a microwave plasma. *Vacuum, 56*(1), 15–23.

Woodin, R. L., Bigelow, L. K., & Cann, G. L. (1991). In M. Y, Y. Tzeng, M. Murakawa, & A. feldman (Eds.), *Applied of diamond films and related materials* (439–444).

Wormhoudt, J. (1990). Radical and molecular product concentration measurements in CF_4 and CH_4 radio frequency plasmas by infrared tunable diode laser absorption. *Journal of Vacuum Science and Technology A, 8*(3), 1722–1725.

Wormhoudt, J., & McCurdy, K. E. (1989). A measurement of the strength of the [nu]2 band of CH_3. *Chemical Physics Letters, 156*(1), 47–50.

Yamada, C., & Hirota, E. (1983). The transition dipole moment of the nu_2 band of the methyl radical. *The Journal of Chemical Physics, 78*(2), 669–671.

Yamada, C., Hirota, E., & Kawaguchi, K. (1981). Diode laser study of the nu [sub 2] band of the methyl radical. *The Journal of Chemical Physics, 75*(11), 5256–5264.

Yos, J. M. (1963). NASA Technical Memorandum RAD TM-63–7.

Yu, C. L., & Bauer, S. H. (1998). Thermochemistry of the boranes. *Journal of Physical and Chemical Reference Data, 27*(4), 807–835.

Yu, B. W., & Girshick, S. L. (1994a). Atomic carbon vapor as a diamond growth precursor in thermal plasmas. *Journal of Applied Physics, 75*(8), 3914–3923.

Yu, B. W., & Girshick, S. L. (1994b). Atomic carbon vapor as a diamond growth precursor in thermal plasmas. *Journal of Applied Physics, 75*(8).

Zalicki, P., Ma, Y., Zare, R. N., Wahl, E. H., Dadamio, J. R., Owano, T. G., et al. (1995a). Methyl radical measurement by cavity ring-down spectroscopy. *Chemical Physics Letters, 234*(4–6), 269–274.

Zalicki, P., Ma, Y., Zare, R. N., Wahl, E. H., Dadamio, J. R., Owano, T. G., et al. (1995b). Measurement of the methyl radical concentration profile in a hot-filament reactor. *Applied Physics Letters, 67*(1), 144.

Zalicki, P., & Zare, R. N. (1995). Cavity ring-down spectroscopy for quantitative absorption measurements. *The Journal of Chemical Physics, 102*(7), 2708–2717.

Zarrabian, M., Leteinturier, C., & Turban, G. (1998). Mass spectrometric investigations on CH_4 plasmas obtained from a dual electron cyclotron resonance-radio frequency discharge. *Plasma Sources Science and Technology, 7*(4), 607.

3.11 Single Crystal Diamond Growth on Iridium

Matthias Schreck, Universität Augsburg, Institut für Physik, Augsburg, Germany

Glossary

AFM atomic force microscopy
c-AFM conductive AFM
BEN bias enhanced nucleation
CVD chemical vapor deposition
CTE coefficient of thermal expansion
ELO epitaxial lateral overgrowth
ERD elastic recoil detection analysis
FET field effect transistor
FWHM full width at half maximum
HFCVD hot filament chemical vapor deposition
HPHT high-pressure, high-temperature synthesis
HREELS high-resolution electron energy loss spectroscopy
HRTEM high-resolution transmission electron microscopy
HRXRD high-resolution X-ray diffraction
IBAD ion beam assisted deposition
LEED low energy electron diffraction
LFM lateral force microscopy
MWPCVD microwave plasma chemical vapor deposition
RHEED reflection high energy electron diffraction
SEM scanning electron microscopy
XANES X-ray absorption near edge structure
X-PEEM X-ray photoemission electron microscopy
XPD X-ray photoelectron diffraction

http://dx.doi.org/10.1016/B978-0-08-096527-7.00048-9

3.11.1 Introduction

Diamond exhibits a unique combination of material properties of which ultrahardness, the highest thermal conductivity of all solid materials (at room temperature), and a wide range of optical transparency from the infrared to the ultraviolet are only the most well known. In 1954, the high-pressure high-temperature (HPHT) method for diamond synthesis was invented (Nassau, 1993). This technique mimicked the natural formation process by applying extremely high pressure–temperature conditions in the phase diagram under which diamond is the stable phase of carbon. Even 50 years later, the constraints imposed by these extreme growth environments still limit the size of HPHT crystals to a volume of about 1 cm^3 (Abbaschian, Zhu, & Clarke, 2005). Chemical vapor deposition (CVD) techniques work far from thermodynamic equilibrium conditions at moderate temperatures in a low-pressure gas phase. As a consequence, they offered the possibility to grow thin films on large-area substrates. In the meantime polycrystalline diamond films entered the market as commercial products in different application areas (Prelas, Popovici, & Bigelow, 1998).

With the advancing development of the field, new applications such as electronic devices and radiation detectors have come into focus. They require the highest structural perfection and chemical purity, that is, demands that can only be met by single crystals in which the influence of grain boundaries is absent.

Homoepitaxial layers grown by CVD on HPHT single crystals can apparently fulfill these quality requirements as proved by the ultimate electron and hole mobility values that have recently been measured (Isberg et al., 2002). Under α-particle irradiation, excellent energy resolution and charge collection efficiencies have been demonstrated (Berdermann et al., 2010).

Various modified concepts based on the enlargement of single crystal substrates by homoepitaxial growth are currently under evaluation. They include the increase of the growth rate using nitrogen (Yan, Vohra, Mao, & Hemley, 2002), the sequential application of many high rate growth steps in specifically designed sample holders (Mokuno, Chayahara, Soda, Horino, & Fujimori, 2005), the use of multiple seeds, that is, mosaic growth (Yamada et al., 2010), and the lift-off by ion implantation combined with sequential side surface growth (Mokuno, Chayahara, Yamada, & Tsubouchi, 2009). With the latter techniques first samples with a size of 1 in. have been demonstrated. Further work has to show whether this complex procedure can form the base for a robust industrial technology.

For other materials like GaN suffering from a similar lack of large single crystals, heteroepitaxy has turned out to be a viable alternative (Edgar, Strite, Akasaki, Amano, & Wetzel, 1999; Liu & Edgar, 2002). Heteroepitaxy means oriented growth of one crystalline material on the surface of another one. The orientation relationship is usually given by designating for both crystals (1) the lattice planes that form the interface and (2) two coinciding lattice vectors within these planes. Early work on heteroepitaxy was based on the assumption that oriented growth is only possible below a certain misfit in the lattice parameters (Pashley, 1975). In the meantime, many epitaxial systems with a huge misfit have been demonstrated, which proves that this parameter does not yield a serious criterion for exclusion. Nevertheless, the usual aim is to minimize the mismatch since it controls the misfit dislocation network at the interface and thus influences the defect structure and mosaic spread of the grown layer.

While searching for an appropriate diamond growth substrate, several aspects have to be considered:

1. stability in the diamond growth environment;
2. chemistry, that is, binding between carbon and substrate material, carbide formation, and solubility of carbon in the substrate material;
3. geometry, that is, crystal structure and lattice mismatch;
4. availability in high quality and as large-area samples.

Concerning diamond heteroepitaxy it turned out that completely different materials can provide a template for oriented growth. They span from insulators (Al_2O_3; Yoshimoto et al., 1999) over elemental (Si; Jiang, Klages, Zachai, Hartweg, & Füsser, 1993) and compound semiconductors (β-SiC; Stoner & Glass, 1992) to carbide forming (TiC; Wolter, McClure, Glass, & Stoner, 1995) and non-carbide-forming metals (Ir; Ohtsuka, Suzuki, Sawabe, & Inuzuka, 1996).

This chapter starts with a brief summary of the different nucleation procedures for diamond on foreign substrates and of the various substrate materials that have been tested for diamond heteroepitaxy. For more details, the reader is referred to Schreck (2009). The focus is on iridium as a unique heteroepitaxial growth substrate that is currently the only material that combines the ability to generate single crystal heteroepitaxial diamond films with realistic concepts for scaling up to wafer dimensions.

3.11.2 Diamond Nucleation

3.11.2.1 General Aspects

The deposition of a solid film from the gas phase proceeds through nucleation and growth stages. Depending on the relative strength of the forces inside the condensed phase as compared to the forces between deposit and substrate three different growth modes can be distinguished:

1. layer by layer (Frank–van der Merwe),
2. layer plus island (Stranski–Krastanov),
3. island (Volmer–Weber).

In a thermodynamic description, the surface energies of deposit γ_D, substrate γ_S and the interface energy γ_{DS} between D and S are considered. In the case of $\gamma_D + \gamma_{DS} > \gamma_S$, 3D island growth is energetically preferred, for $\gamma_D + \gamma_{DS} < \gamma_S$, 2D layer growth is expected (Ickert & Schneider, 1983; Venables, Spiller, & Hanbrücken, 1984).

The thermodynamics of the nucleation process comprises the change in Gibbs energy ΔG of the bulk phase ($\propto r^3$) and the surface energy contributions ($\propto r^2$) with r as the radius of a spherical nucleus. For positive supersaturation, the first is negative, that is, condensation of particles is energetically favorable. The surface terms are positive. The critical radius given by the maximum in $\Delta G(r)$ defines the nucleus size.

In deposition experiments on foreign substrates (excluding the special case of c-BN) without any specific pretreatment, a low density of diamond crystals is found ($<10^6$ cm^{-2}). This points to a high nucleation barrier and stimulated the development of different nucleation techniques. After the nucleation on heterosubstrates, Volmer–Weber type growth is observed.

In diamond, breaking bonds and forming a free surface cost a high amount of energy: Field (1979) specifies a fracture surface energy of 6 J m^{-2}. However, under CVD process conditions, different carbon phases (sp^2 versus sp^3) compete with each other, the surface shows reconstruction, and the majority of bonds are terminated by hydrogen. As a consequence, the complexity of the process hinders a simple calculation of nucleation barriers.

For most technical applications, nucleation densities of 10^9–10^{11} cm^{-2} are indispensable. They can only be obtained by additional nucleation enhancement procedures. While a large variety of pretreatment methods (Liu & Dandy, 1995; Pehrsson, Celii, & Butler, 1993) have been studied, two methods turned out to be the most efficient: the treatment with diamond powder, for example, by mechanical or ultrasonic scratching, and the bias enhanced nucleation (BEN) procedure. Due to their relevance, this chapter is mainly restricted to these two methods.

Mechanical scratching of substrate surfaces with diamond powder or paste and ultrasonic treatment with a diamond powder suspension can increase the nucleation density up to the 10^{11} cm^{-2} range. The particle size of the powder ranges from several nanometers (Williams et al., 2007) to several microns. It is applied for the deposition of polycrystalline diamond on technical surfaces, for example, tools, or for the conformal coating of surfaces with pinhole-free films of an extremely low thickness. A careful investigation of the correlation between the density of nanoscopic diamond particles on the surface after the pretreatment and the density of diamond crystals in the subsequent growth step could identify seeding as the principal “nucleation” mechanism (Ihara, Komiyama, & Okubo, 1994).

3.11.2.2 Nucleation by Ion Bombardment

In 1991, Yugo et al. introduced a new method, later termed BEN, in a microwave plasma (MWPCVD) setup (Yugo, Kanai, Kimura, & Muto, 1991). The authors applied bias voltages between +100 and −200 V for 2–15 min to an unscratched silicon substrate using methane concentrations between 1 and 40% in hydrogen. They observed nucleation enhancement with particle densities up to 10^{10} cm^{-2} for negative bias voltages and found threshold values of −70 V and 5% methane. Weaker effects were later also reported for positive bias voltages. In subsequent experiments, threshold values down to ±20 V were found (Katoh, Aoki, & Kawarada, 1994). Furthermore, diamond nucleation by BEN on silicon at CH_4 concentrations of only 1% contradicted the existence of a strict threshold value for the methane concentration (Thürer, Schreck, & Stritzker, 1998).

In further work, biasing with AC voltage (Wolter, Borst, Vescan, & Kohn, 1996) and repetitive pulse bias (Flöter et al., 1998) were introduced as means to increase the fraction of oriented diamond crystals and to improve the homogeneity of epitaxial diamond films on silicon, respectively. Among all these technological variants, negative DC biasing using moderately increased methane concentrations represents the most established technique.

Thermal excitation of the gas phase by a hot filament (HF) does not generate sufficient charge carriers to allow a significant current flow under low bias voltage. At higher voltages, a discharge is ignited and under careful control of the process conditions it is possible to nucleate heteroepitaxial diamond (Stubhan, Ferguson, Füsser, & Behm, 1995; Chen, Yang, & Lin, 1995). The technique has been refined by introducing a grid above the filament. It allowed the generation of a defined stable discharge by applying a second bias voltage between filament and grid (Zhou et al., 2000).

Sawabe et al. combined a DC-plasma CVD setup with a second DC biasing discharge for nucleation of diamond on iridium (Ohtsuka, Suzuki, Sawabe, & Inuzuka, 1996).

Applying a negative voltage in HF, MWP, or DC-plasma CVD is always accompanied by a localized discharge above the substrate. The simplest way to achieve this nucleation promoting discharge is to use only the DC voltage and increase it until a self-sustaining glow discharge is ignited. This promising technique was successfully applied for the epitaxial nucleation of diamond on Ir/MgO substrates (Ando, Kuwabara, Suzuki, & Sawabe, 2004).

Triggered by the awareness that the bombardment with positive ions may be the key mechanism of diamond nucleation by BEN, pure low energy ion beams were also employed to deposit carbon films and to generate diamond nuclei (Zhang et al., 2000). In principle, this technique should allow a much better control of the local bombarding parameters like ion energy, ion-to-neutral ratio, and particle fluxes. However, the experimental results reported up to now could neither reach the nucleation density nor the epitaxial alignment that can be readily obtained by BEN in MWPCVD.

3.11.3 Oriented Diamond Deposition on Heterosubstrates

All the nucleation techniques described above were at first developed to deposit polycrystalline films. In order to obtain oriented nucleation, it was necessary to implement the following modifications:

1. For the seeding technique, for example, on Co, Ni, and Pt, a careful control of the deposition conditions (Sato, Yashima, Fujita, Ando, & Kamo, 1991; Shintani, 1996; Tachibana et al., 1996) and the application of specific posttreatment procedures (Liu, Tucker, Yang, & Glass, 1995; Yang, Zhu, & Glass, 1993; Zhu, Yang, & Glass, 1993) facilitated the transformaton of the initially at random oriented seeds into heteroepitaxial diamond grains.
2. The key parameter to obtain oriented nucleation by BEN on Si turned out to be the duration of the biasing procedure. Epitaxial diamond crystallites are only observed within a well-defined process time window (Schreck, Thürer, & Stritzker, 1997).
3. For all nucleation and deposition techniques—even for systems that do not require a surface pretreatment—it is important to choose textured growth conditions adapted for the specific growth surface, for example, (001) or (111). Otherwise, renucleation and twinning create polycrystalline films by overgrowth of the initially oriented nuclei.

Figure 1 shows a summary of different growth substrates for the heteroepitaxial diamond deposition. It comprises the lattice matched c-BN (**Figure 1(a) and (b)**), the oxide Al_2O_3 (**Figure 1(c)**), the metals Ni (**Figure 1(d) and (e)**), Pt (**Figure 1(f)**), Ir (**Figure 1(i)**), the elemental semiconductor Si (**Figure 1(g)**), and the compound semiconductor SiC (**Figure 1(h)**). The different diamond films were nucleated without specific treatment ((a)−(c)), by seeding ((d)−(f)), and by biasing ((g)−(i)).

Further materials proved capable of acting as a template for oriented diamond growth: Co (Liu, Tucker, Yang, & Glass, 1995), Re (Bauer, Schreck, Gsell, Hörmann, & Stritzker, 2003), Cu (Sato et al., 1991), BeO (Argoitia, Angus, Wang, Ning, & Pirouz, 1993), Ni_3Si (Tucker et al., 1995), Ni_3Ge (Haubner, Lux, Gruber, & Schuster, 1999), graphite and 6H-SiC (Suzuki, Yagi, & Shibuki, 1994).

Only sparse information, for example, without any texture data, is available for the majority of the investigated systems. **Table 1** compares the most promising candidates that have been studied in detail. Diamond's presumably excellent alignment on c-BN does not provide a route to obtain diamond wafers due to the

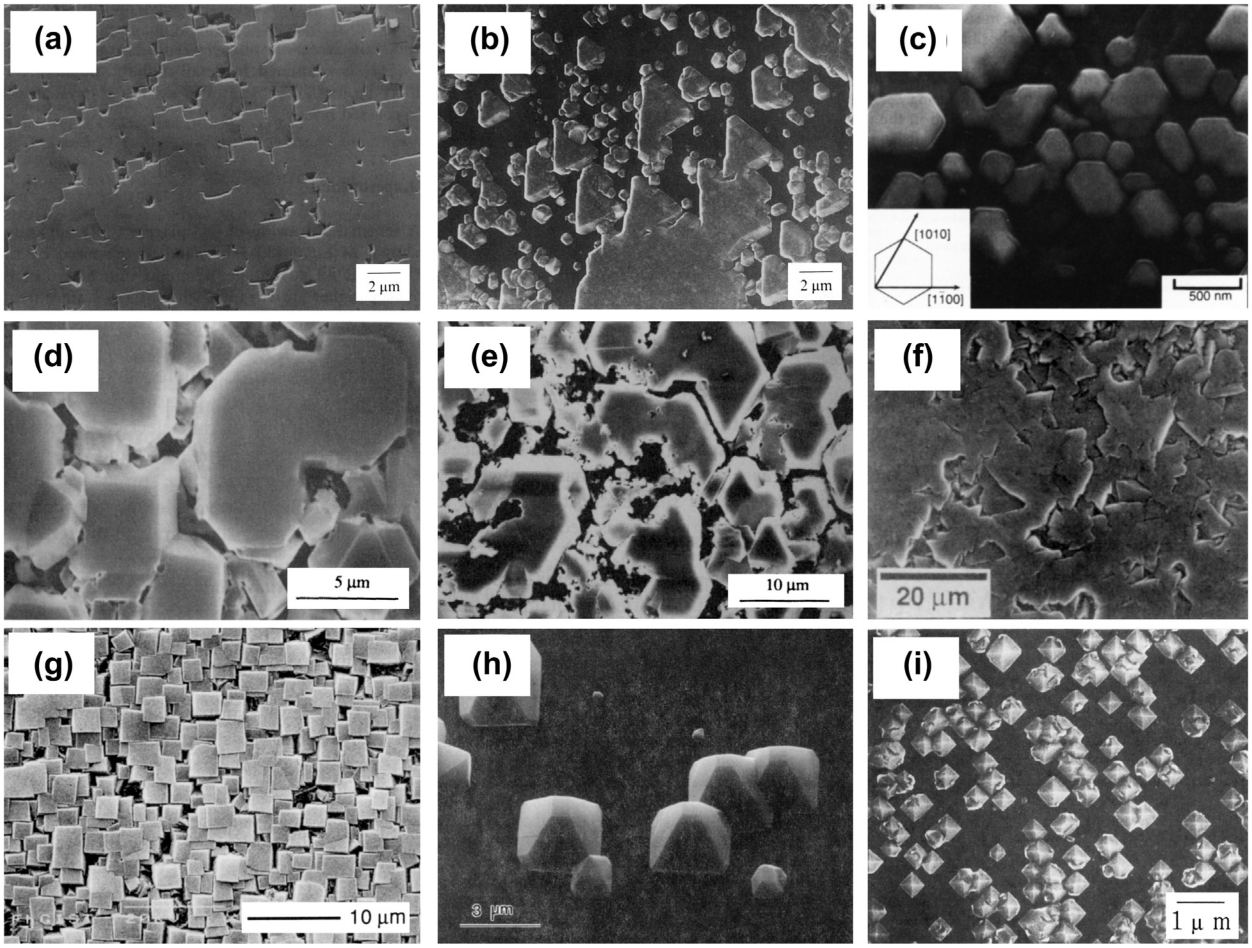

Figure 1 Heteroepitaxial diamond growth on different substrate materials: (a) c-BN(001), (b) c-BN(111), (c) Al_2O_3(0001), (d) Ni(001), (e) Ni(111), (f) Pt(111), (g) Si(001), (h) β-SiC(001), and (i) Ir/MgO(001). (Schreck, 2009).

negligible size of available substrates. The films on Pt suffer from the disadvantages of growth on {111} sectors, the high mosaic spread, and the complex seeding technique. The best epitaxial orientation was obtained with the BEN technique on Si, β-SiC, and Ir. As the next sections will show, iridium combines the lowest mosaic spread with a beneficial behavior in the biasing procedure.

Table 1 Mosaic spread of heteroepitaxial diamond on different substrates. The values of the lattice misfit are related to the lattice constant of diamond.

Substrate	*Lattice misfit (%)*	*Orientation*	*First publication*	*Current state of the art*	*Reference*
Si	+52.2	(001), (111), (110)	Jiang et al. (1993)	Tilt: ~2° Twist: ~4° For (001)	Jiang et al. (1998) Thürer et al. (1998)
β-SiC	+22.2	(001)	Stoner and Glass (1992)	Tilt: 0.6° Twist: ~1.5°	Kawarada et al. (1997) Kawarada (1998)
Pt	+11	(111)	Shintani (1996)	Tilt: 1.1°	Tachibana, Yokota, Hayashi, and Kobashi (2001)
Ir	+7.6	(001), (111)	Ohtsuka et al. (1996)	Tilt: ~0.06° Twist: ≥0.1 For (001)	Sawabe et al. (2011)

3.11.4 Heteroepitaxy of Diamond on Iridium

3.11.4.1 Unique Properties of the Nucleation Process by BEN on Iridium

3.11.4.1.1 BEN on Si and Related Materials

In a microwave plasma CVD discharge the negative bias voltage is applied directly to the substrate with the chamber walls defining the grounded reference. As an alternative, the substrate may be at ground potential and a positive voltage is applied to the plasma ball via an electrode, for example, a metal ring as reported in Schreck & Stritzker (1996). The latter arrangement can avoid technical problems with heating and temperature measurement of a substrate holder at a DC voltage of −200 … −300 V.

Figure 2(a) and (b) schematically show the change in the shape of the plasma ball above the substrate when the bias voltage is applied. Few millimeters above the cathode a localized luminous layer separated by a dark space from the plasma ball is observed. It resembles the negative glow emission in the classical glow discharge. A detailed analysis of the optical emission intensity and the Stark splitting of the hydrogen Balmer lines show that the similarity is not only ostensible: The field strength of several kilovolts per centimeter above the substrate confirms that nearly the complete externally applied bias voltage drops within the thin boundary layer (Schreck, Baur, & Stritzker, 1995). As a consequence, positive ions can be accelerated appreciably: Kátai, Kováts, Maros, and Deák (2000) measured kinetic energies up to >100 eV for a bias voltage of −200 V in spite of a gas kinetic mean free path in the range of 1−10 μm for the studied pressure of 25 mbar. The process is schematically described in **Figure 2(c)**.

Hyperthermal particles hitting the surface can induce three major effects:

1. ion-induced electron emission,
2. activation of surface processes due to energy transfer,
3. shallow implantation of the accelerated ions and subsurface particle displacements.

Process (1) is crucial for the sustainment of a glow discharge. In the cathode fall, the electrons released from the surface by impingement of the hyperthermal particles are accelerated and multiplied by electron impact ionization. The emission coefficient γ strongly depends on the type of gas and the cathode material. It is exceptionally high (Ternyak et al., 2007) for hydrogen-terminated diamond. This has important consequences for the temporal development of the bias current. On substrate materials like Si and β-SiC, after the application of the bias voltage, the bias current first stays nearly constant. This induction time, which depends on the applied conditions (voltage, gas composition, etc.), is followed by a steep increase. For long-time biasing, the current turns into a plateau with a current density that can be up to a factor of 10 higher than on the pristine substrate. Scanning electron micrographs of the sample in the different stages show that the surface is successively covered by diamond grains. During the whole biasing procedure, the diamond nuclei that form by the treatment immediately start to grow. The higher emission coefficient γ of diamond results in a field enhancement and increase in current density as observed experimentally.

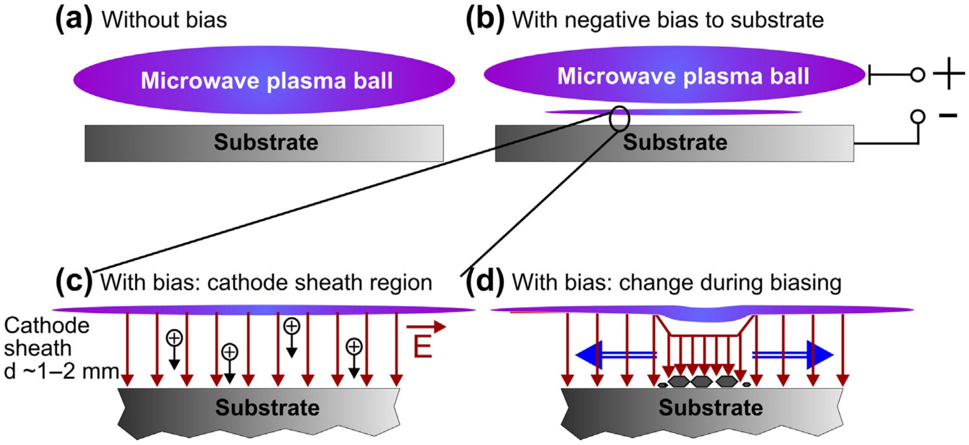

Figure 2 Schema of a microwave plasma discharge and its modification during BEN. The local field enhancement due to growing diamond crystals in (d) is observed for typical nucleation conditions on Si but not on Ir.

Figure 2(d) shows a further implication of this feedback of the growing diamond grains on the biasing current: At the transition between the high field area above the diamond covered surface and the low field area above the pristine substrate, the field strength is enhanced and the nucleation is accelerated. As a consequence, nucleation starts at a fixed point in the center (or at the edges of the substrate if placed on a diamond coated substrate holder) followed by a radial spreading of a nucleation front across the substrate.

Processes (2) and (3) are crucial for the generation of diamond nuclei by BEN. While the local changes in the gas phase activation were initially considered as one possible mechanism (Stoner, Ma, et al., 1993), biasing on micropatterned silicon wafers later clearly revealed the crucial role of directional ion bombardment: nucleation was only obtained on planar areas while the side walls, parallel to the preferential direction of accelerated ions, remained free of nuclei (Jiang, Paul, Klages, & Jia, 1995).

Enhanced surface diffusion induced by process (2) was claimed by Jiang, Schiffmann, and Klages (1994) as the crucial step in the nucleation of diamond by BEN. The majority of alternative models are based on process (3). It is well established that carbon and hydrocarbon ions with energies above a threshold of several tens of electron volts are capable of penetrating the surface of a carbon layer (15−20 eV) (Robertson, 1993), to displace atoms in graphite (15−20 eV) and also in a diamond lattice (30−48 eV) (Zaiser, Lyutovich, & Banhart, 2000). In brief, they can induce all the elementary processes that play a role in the deposition of hard amorphous carbon films with high sp^3 fraction. According to the subplantation model, carbon atoms that are shallowly implanted, densify the carbon matrix. Driven by compressive stress and/or preferential displacement processes (carbon atoms bound in graphite can be more easily displaced than those in a diamond environment) sp^2 bonded carbon is transformed into sp^3. Spontaneous bulk nucleation of diamond embryo clusters that are able to grow continuously by ion bombardment-induced preferential displacement processes was suggested as an explanation for diamond nucleation under these conditions (Lifshitz et al., 2002). The ion bombardment-induced growth mechanism is supported by the direct experimental observation of transformation processes from fullerene and graphite to diamond under particle irradiation as reported by Zaiser et al. (2000).

Displacement of atoms in a carbon matrix by ion bombardment also has a negative aspect: lattice defects are generated, mosaic spread can develop, and for prolonged BEN treatment the epitaxial orientation will be lost completely (Thürer et al., 1998). Thus, a process time window exists that defines the conditions for epitaxial diamond nucleation on silicon. This is summarized in Figure 3.

Appearance of epitaxial grains and subsequent loss of epitaxial orientation during BEN also limit the homogeneity of the diamond films: during the lateral spread of the nucleation front as sketched in Figure 2(d), the substrate may finally be covered completely with diamond but only a limited (typically annular) area will have experienced the optimum biasing conditions.

3.11.4.1.2 BEN on Ir: Nucleation under Etching Conditions

On iridium, the situation is quite different. In order to obtain diamond nucleation, slightly higher bias voltages are required, for example, −250 V instead of −200 V. During the BEN treatment, the variation of the current with time is much lower than on Si. The successful nucleation can be easily checked by adding a short growth step after switching off the bias voltage.

This observation suggested two alternative explanations: either the secondary electron emission coefficients γ (Raizer, 1991) for diamond and iridium are similar or—other than on Si—growth of diamond and coverage of the substrate is inhibited during BEN on Ir. A conclusive decision between these two options was possible after exposing an iridium film with a small number of microscopic diamond crystals to the BEN process. Figure 4 shows the scanning electron micrographs of a selected spot on the sample (a) before and (b) after a 60-min BEN step (Hörmann, Schreck, & Stritzker, 2001). The diamond crystals with an initial size of up to 0.5 μm have nearly completely disappeared. Since the conditions were typical for diamond nucleation on iridium, the result proved that nucleation by BEN on iridium proceeds under conditions for which bulk diamond is etched.

Thus, nucleation apparently proceeds under conditions for which the bulk phase of diamond is unstable. Nucleation under etching conditions is incompatible with classical nucleation theory (Section 3.11.2.1), where a positive supersaturation ensures that clusters after having overcome the nucleation barrier can grow without further limitation.

The suppression of diamond growth under BEN on Ir can account for the absence of a process time window as found on Si (Schreck, Thürer, & Stritzker, 1997). According to the considerations in Figure 2(d), this behavior could also be beneficial for homogeneous large-area nucleation.

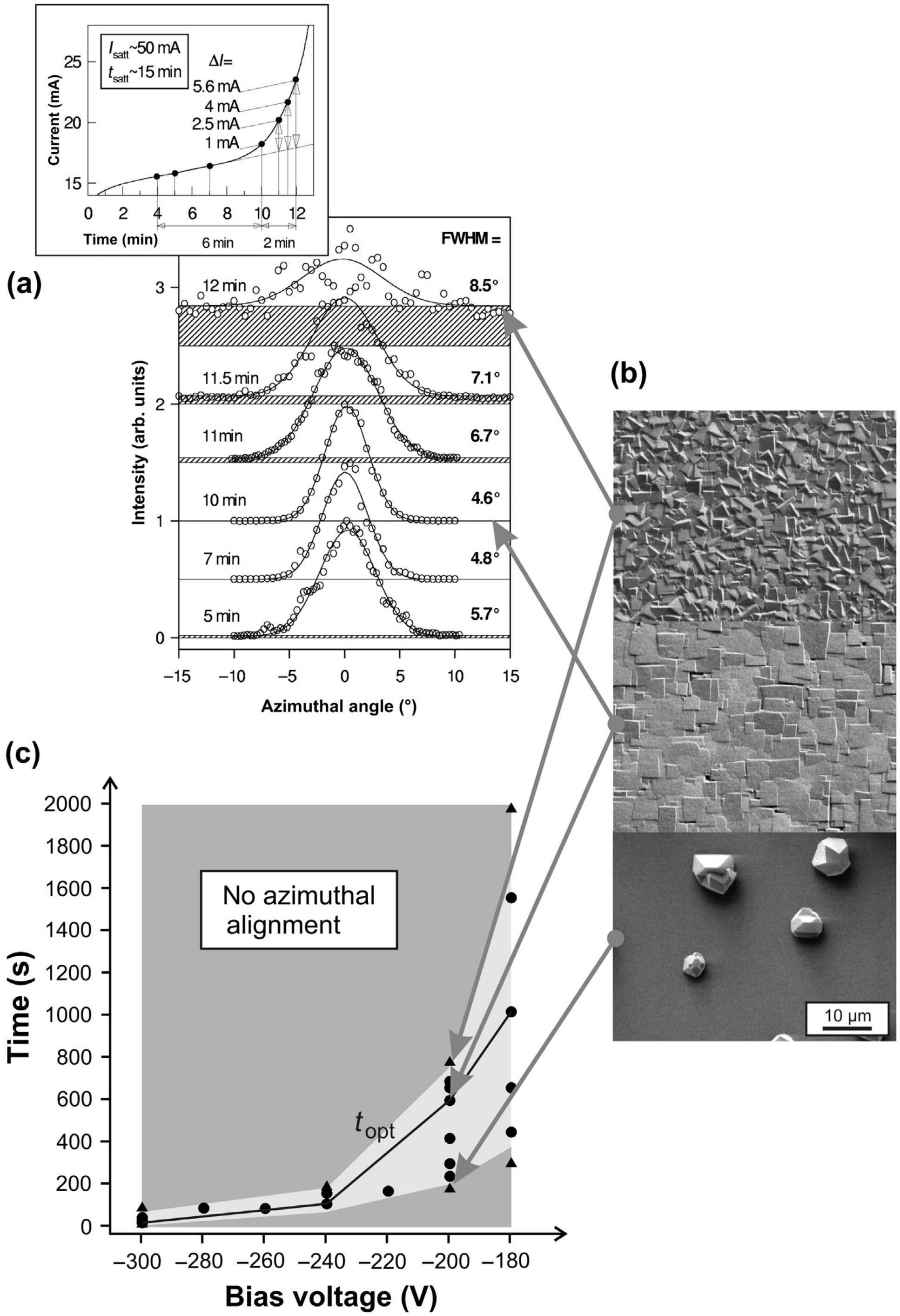

Figure 3 The process time window of epitaxial diamond nucleation on silicon. (a) Biasing current and XRD azimuthal scans of diamond films after BEN and 20 h growth. (b) SEM micrographs of the corresponding diamond films that were grown after different durations of the BEN process. (c) Map of the biasing time–bias voltage parameter space. Epitaxial alignment is only observed within the light gray area (Schreck, Hörmann, Roll, Bauer, & Stritzker, 2001).

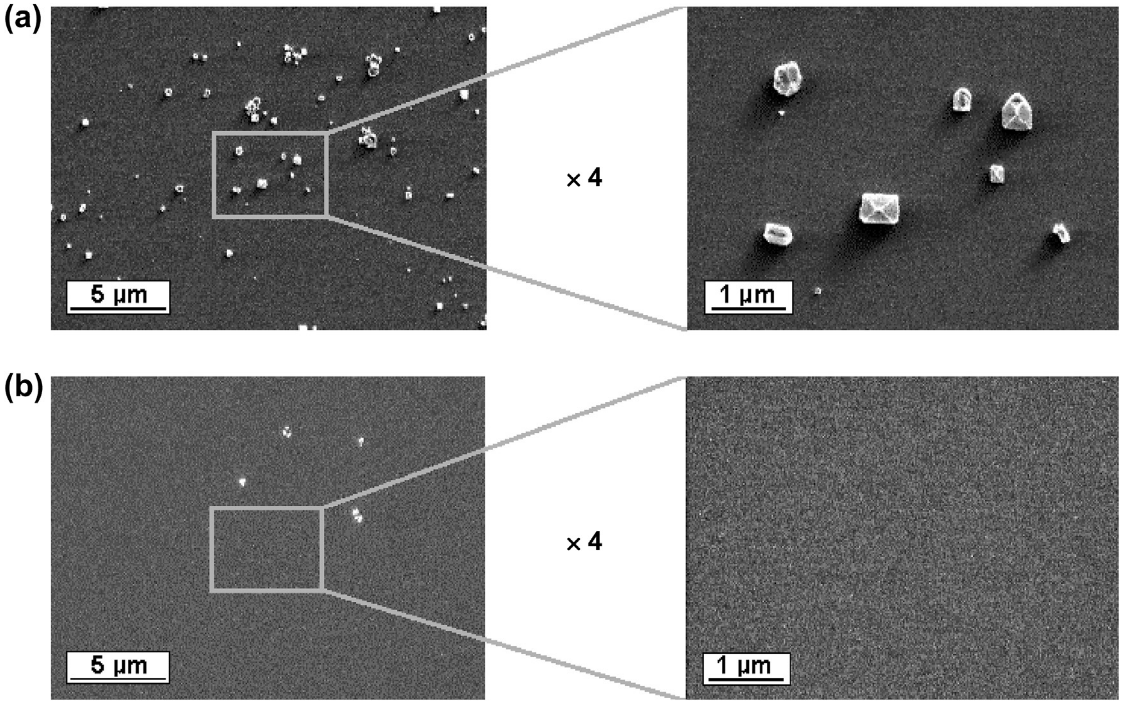

Figure 4 Scanning electron micrographs of an ensemble of small isolated diamond grains on Ir/SrTiO$_3$(001) (a) before and (b) after exposure to 60 min BEN conditions (Hörmann et al., 2001).

3.11.4.1.3 BEN on Ir: Pattern Formation

In order to study the modifications that have been induced by the BEN treatment on iridium, it is necessary to switch off bias voltage and microwave simultaneously. Three major observations are typically made:

1. surface roughening,
2. presence of a carbon layer with a thickness of about 1 nm,
3. patterns consisting of extended islands that show a bright contrast in scanning electron microscopy (SEM).

Ir surface roughening has been reported by several groups (Hörmann et al., 2001; Sawabe, Yamada, Okamura, Katagiri, & Suzuki, 2002; Tsubota et al., 2000). The grooves with a depth of typically 3 nm are aligned along the low index crystal directions of the iridium. Depending on the process parameters, the preferential orientation can switch between <110> and <100> (Bauer, Gsell, Hörmann, Schreck, & Stritzker, 2004) (**Figure 5**). Some transmission electron microscopy (TEM) work suggests that diamond nucleates on top of the roughened structures (Sawabe, Fukuda, Suzuki, Ikuhara, & Suzuki, 2000). However, the less common case of successful nucleation without roughening exists beside the observation of a pronounced Ir surface roughening without successful diamond nucleation. The role of Ir surface roughening in the diamond nucleation process and in particular its meaning for the alignment of the films is still unclear.

After BEN the iridium surface is covered by a thin carbon layer. First measurements by elastic recoil detection (ERD) analysis of BEN layers deposited using isotopically enriched ^{13}C methane in the gas phase yielded a value of 0.7 nm for the thickness of the carbon films assuming the atomic density of diamond (Bauer et al., 2002). The coverage showed only a weak variation with biasing time. Measurements of the carbon coverage by X-ray photoelectron spectroscopy (Kono et al., 2005) and of the geometric carbon film thickness by TEM (Brescia, Schreck, Gsell, Fischer, & Stritzker, 2008; Schreck, Hörmann, Gsell, Bauer, & Stritzker, 2006) gave similar results on the order of 1–2 nm.

The most striking peculiarity of the nucleation layer on iridium is reflected in the formation of characteristic patterns (Fujisaki, Tachiki, Taniyama, Kudo, & Kawarada, 2003; Golding, Bednarski-Meinke, & Dai, 2004; Saito et al., 1998; Schreck et al., 2003; Tsubota et al., 2000): Monitoring the surface by SEM with the in-lens detector allows one to distinguish bright islands of homogeneous contrast with clear border lines (**Figure 6**). Imaging the same area with the standard secondary electron detector, which is more sensitive to topographic features, yields an extremely weak (or often no) contrast. The initial presumption that diamond nuclei are located within

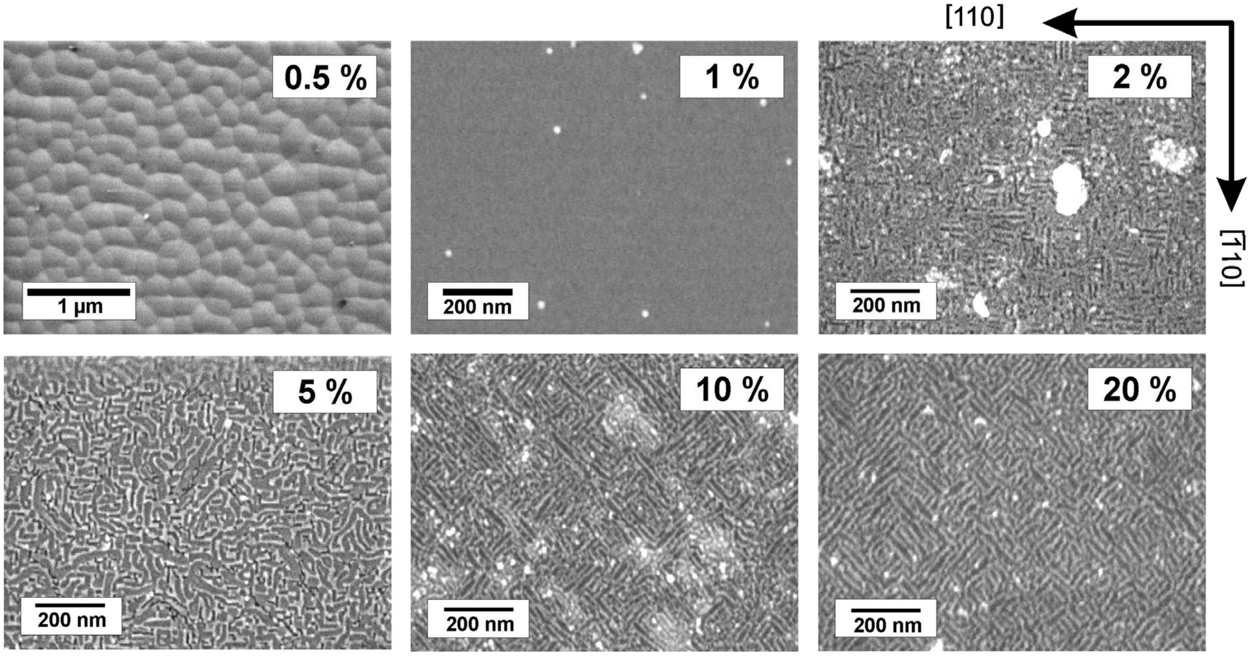

Figure 5 Scanning electron micrographs of the surface structures formed during BEN on Ir/SrTiO$_3$(001). The CH$_4$ concentration during the 45 min of BEN treatments was varied between 0.5 and 20% (Bauer et al., 2004).

the bright areas was confirmed by measuring one and the same spot immediately after BEN and after a subsequent growth step (**Figure 6(b) and (c)**). As in **Figure 6(c)**, the epitaxial grains are located in the former bright islands with negligible or no grains outside. In rare cases, the epitaxial regions were surrounded by nonepitaxial areas (**Figure 7(b)**) which motivated the expression "domain formation" for this phenomenon.

3.11.4.1.4 Topography, Internal Structure, and Temporal Development of the BEN Layer

In SEM images, the domains are not associated with any detectable topographic contrast. In atomic force microscopy (AFM) studies, the 3-nm-deep surface roughening hampered an unequivocal correlation of surface structures with domains. Kono et al. (2005) described nanometer size dots forming a regular pattern

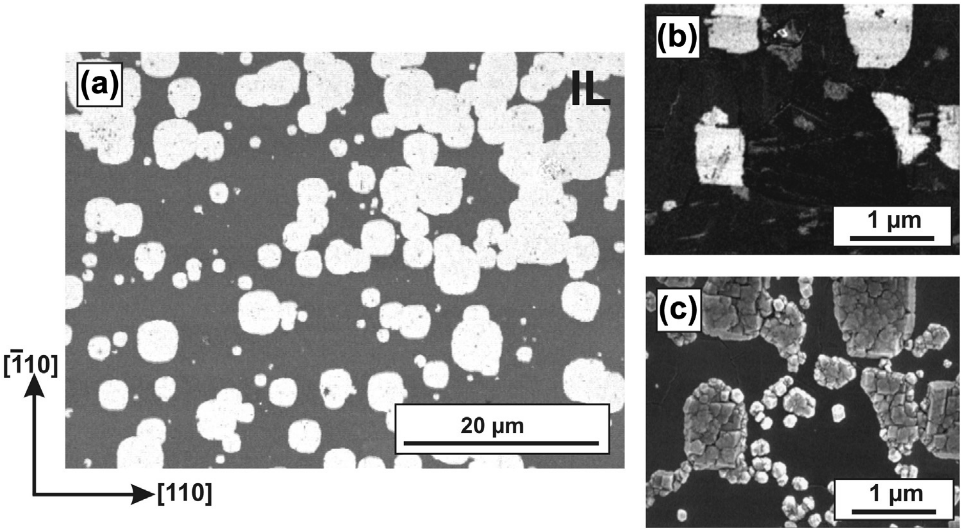

Figure 6 (a) SEM image of the iridium surface after BEN treatment taken with the in-lens detector. (b) Local spot imaged by SEM after BEN and (c) after a subsequent growth step (Schreck et al., 2003).

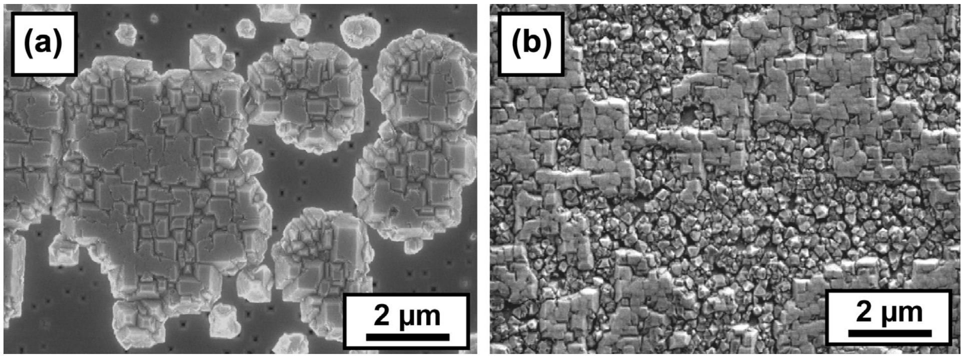

Figure 7 SEM images of two different samples of diamond on Ir/SrTiO$_3$(001) after nominally identical BEN treatment and (a) 1 h and (b) 2 h growth, respectively. The epitaxial areas are surrounded by (a) areas without nucleation and (b) nonepitaxial grains. In both cases the transition at the border of the domains is abrupt (Schreck, Hörmann, Roll, Bauer, et al., 2001).

with close-packed arrangement that they attributed to epitaxial diamond crystals. In our AFM studies, we could identify domains for the first time on a BEN layer without surface roughening (Gsell, Schreck, Benstetter, Lodermeier, & Stritzker, 2007) (**Figure 8**). The topographic image in **Figure 8(c)** shows a downward step of about 1 nm when crossing the sharp borderline between the nucleation-free area and the inner part of the domains in contrast to the intuitive expectation. In comparative experiments, imaging identical spots by SEM and AFM, a similar height contrast was also found on roughened iridium films (Gsell, Schreck, et al., 2007).

Since the observation of the bright domains by SEM could be used as an unequivocal proof for the presence of diamond nuclei, a wide range of surface-sensitive tools as well as high-resolution transmission

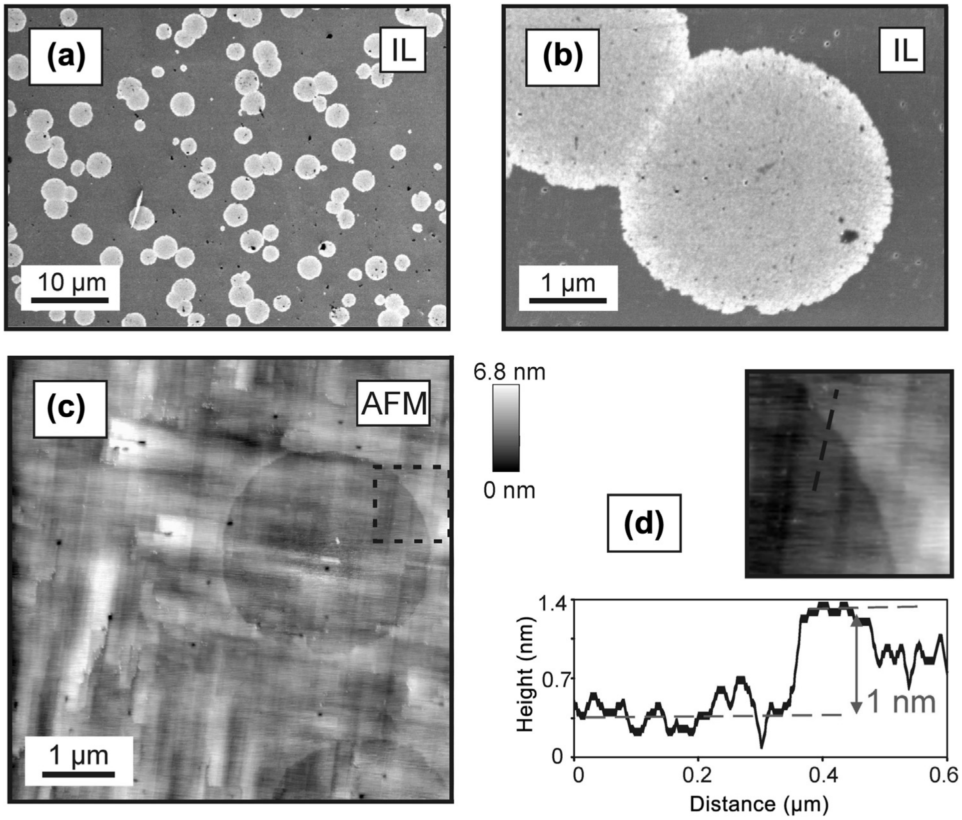

Figure 8 (a) Low and (b) high magnification SEM images of the domains on an Ir(001) surface after BEN. The negligible roughening of the Ir substrate allows the direct identification of the domains in the AFM images (c) and (d) (Gsell, Schreck, et al., 2007).

electron microscopy (HRTEM) were applied to clarify the internal structure of the 1-nm-thick BEN layer, to identify, and—if possible—image the diamond nuclei. In conductive AFM measurements, it turned out that the surface is apparently completely covered by a continuous film that is highly resistive outside and inside the domains (Gsell, Schreck, et al., 2007). Lateral force microscopy (LFM) images yielded a clear friction contrast, which indicated a higher elastic modulus for the carbon matrix inside the domains (**Figure 9**) (Schreck et al., 2009).

For the HRTEM studies, the nucleation layer formed by BEN was additionally coated by 10-nm Ir in order to protect it during TEM sample preparation. The TEM image in **Figure 10(a)** shows the carbon nucleation layer sandwiched between the Ir substrate and the 10-nm-thick protecting Ir film. The high-resolution image in **Figure 10(b)** shows lattice resolution in both Ir layers, but only amorphous structures in between. Neither in this nor in many further samples spots have been found where the diamond lattice could be resolved. This observation is in accordance with the absence of diamond-related spots in reflection high-energy electron diffraction (RHEED) (Gsell, Berner, et al., 2008; Ohtsuka et al., 1996; Sawabe et al., 2002) and low-energy electron diffraction (LEED) (Gsell, Berner, et al., 2008; Kono et al., 2004) measurements of the BEN layer.

The following four methods facilitated the detection of diamond structures within the BEN layer:

1. In laterally resolved X-ray absorption near edge structure (XANES) combined with an X-ray photoemission electron microscope (X-PEEM) the spectra taken within the domains feature a dip around 303 eV, which is a fingerprint for diamond (Bernhard et al., 2006).
2. In Auger spectra, the carbon signal showed a clear signature of diamond within the domains and more graphitic structures outside (Schreck et al., 2009).
3. In high-resolution electron energy loss spectroscopy, the spectra of samples with successful diamond nucleation (i.e., showing domains) contained overtone peaks stemming from diamond's optical phonons (Hoffman et al., 2009).
4. X-ray photoelectron diffraction (XPD) yielded clear patterns in the C 1s photoelectron signal only for samples with successful diamond nucleation.

XPD is currently the only scattering technique that allows for the reliable detection of the crystalline order due to the diamond nuclei in a BEN layer (Aoyama et al., 2007; Gsell, Berner, et al., 2008; Kono et al., 2004, 2005). **Figure 11** shows the XPD patterns of two BEN layers on Ir/$SrTiO_3$(001) (Gsell, Berner, et al., 2008). (a), (c), and (e) are the patterns of Ir 4f electrons of a native Ir film, a sample after unsuccessful BEN treatment ("A") and after a successful BEN step ("B"), respectively. Similarly, (b), (d), and (f) are C 1s patterns of a diamond reference sample (a 13-µm-thick heteroepitaxial film), and samples "A" and "B". The C 1s pattern of sample "A" does not show any feature that could be correlated with ordered structures within the carbon layer. In contrast, apart from less fine structure, the C 1s pattern of sample "B" is identical to that of the reference diamond.

The pattern formation in XPD is mainly based on the forward scattering of photoelectrons by atoms that are neighbors of the emitter. While most other electron diffraction techniques or HRTEM require an ordered lattice

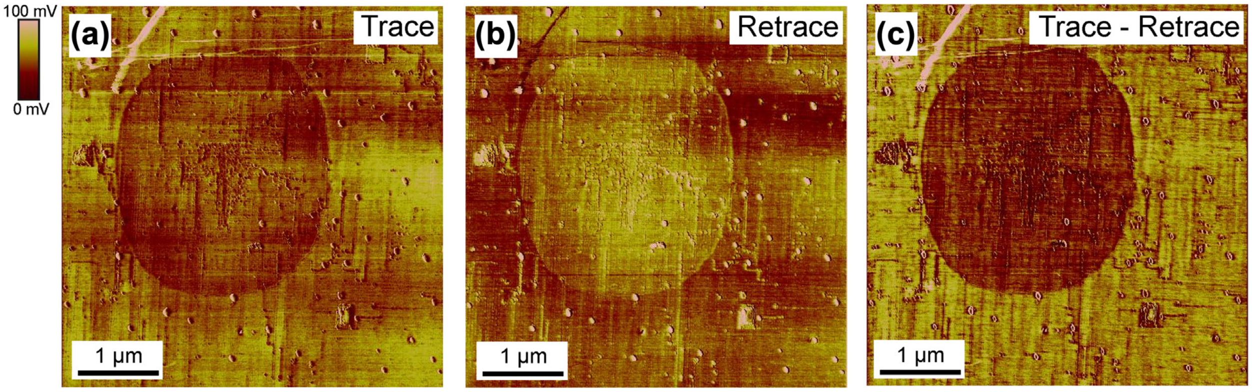

Figure 9 LFM images of a domain on a nonroughened Ir film after BEN: (a) forward scan, (b) backward scan, and (c) difference signal (Schreck et al., 2009).

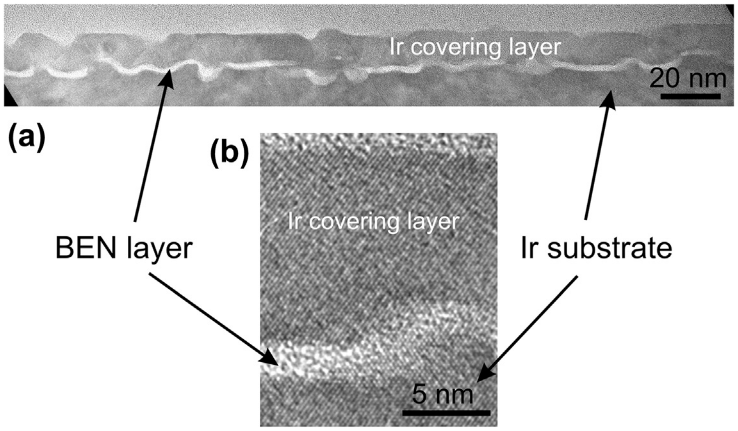

Figure 10 Cross-section TEM images of a BEN layer on Ir. The sample showed the typical 3-nm deep roughening. Before TEM sample preparation, an additional 10-nm-thick Ir layer was deposited, which protected the carbon film during ion milling and improved its visibility in TEM (Schreck et al., 2006).

over at least several lattice constants, XPD patterns can be formed without a long-range crystalline order. Quantitative evaluation of XPD patterns for a specific sample allowed the estimation that about one fourth of the carbon atoms resides in an ordered crystalline diamond environment (Gsell, Berner, et al., 2008). The lower fine structure in the pattern as compared to the single crystal reference (**Figures 11 (f) and (b)**) and the absence of diamond structures in the LEED, RHEED, and TEM studies suggests that the crystalline structures are highly defective and exhibit only a short range order. Orientational spread may also contribute to some extent to the blurring in the pattern.

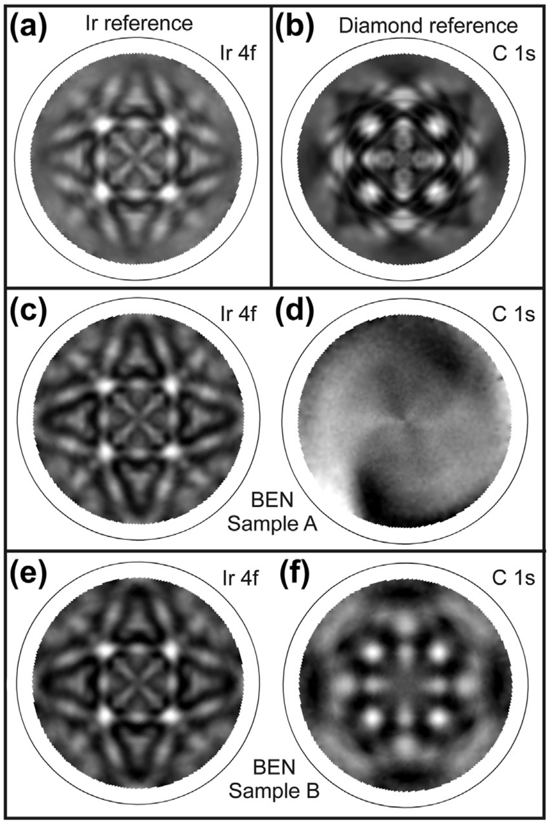

Figure 11 XPD patterns of Ir 4f and the C 1s core levels taken for (a) the Ir reference, (b) the diamond reference (c), (d) sample A after unsuccessful BEN, and (e), (f) sample B after successful BEN treatment (Gsell, Berner, et al., 2008).

Topography and internal structure of the BEN layer can only be studied ex situ after the termination of the bias treatment. However, a convincing model that explains diamond nucleation on Ir has to include a mechanism that describes the formation of the domains. Important information on this pattern formation process was deduced from an experiment in which the temporal development of the domain shape was studied by exposing a BEN layer after imaging the patterns by SEM to a second biasing step (Gsell, Schreck, et al., 2007). Two different spots—5 mm apart—were chosen. At the first spot, the shape of the domains was nearly identical before and after the second BEN treatment having only increased in size (**Figure 12**). At the second spot (not shown here), the size had decreased and small domains had vanished. As a crucial conclusion from this experiment, growth of the domains (or shrinkage, when the local biasing conditions are not appropriate) is a continuous process. The suggestion of Golding et al. (2004) that nucleation and pattern formation is a spontaneous event that emerges not before the bias voltage is switched off can be ruled out.

3.11.4.1.5 Growth of Diamond Crystallites after BEN

After the failure to directly image the epitaxial diamond nuclei formed during BEN, efforts were made to detect the earliest appearance of diamond crystallites and monitor their growth during the first minute after termination of the biasing procedure. For the cross-section TEM analysis, the samples were again coated by a 10-nm-thick iridium protection layer. **Figure 13** shows the first 60 s after termination of BEN (Brescia et al., 2008). After 5 s, the diamond grains have reached a vertical size of 2 nm and the crystalline structure is clearly resolvable in HRTEM. The continuous—in TEM amorphous—carbon film seen immediately after BEN has completely

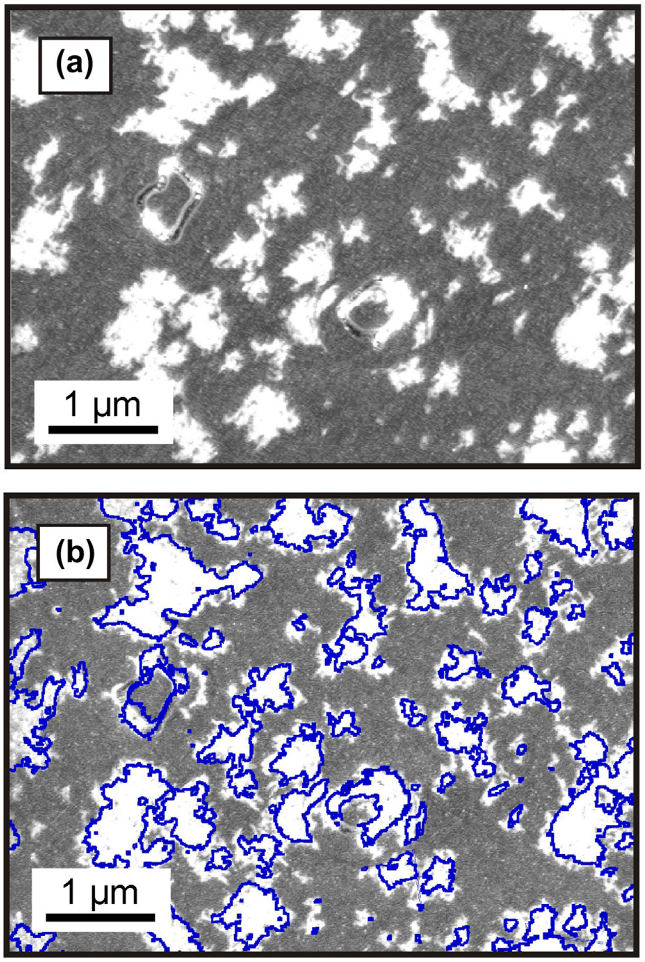

Figure 12 (a) IL-SEM images of an Ir/SrTiO$_3$(001) sample after 60 min BEN. (b) SEM image of the same spot after 15 min of additional BEN treatment under identical conditions. The blue contour lines in (b) correspond to the former boundaries of the domains in (a) (Gsell, Schreck, et al., 2007).

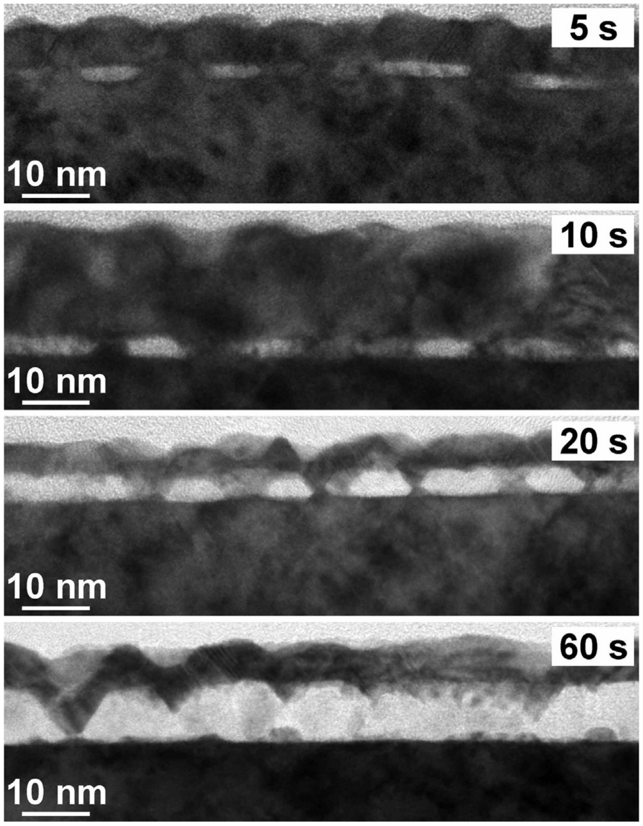

Figure 13 Cross-section TEM images of samples prepared by BEN and subsequent short growth steps. The biasing time was 30–45 min. The growth time after BEN varied between 5 and 60 s (Brescia et al., 2008).

vanished within the first 5–10 s. Thus, the amorphous carbon layer that is deposited and stabilized by the ion bombardment is immediately etched under standard growth conditions even with the increased methane concentration that is still present in the chamber during the first minutes of growth.

The distance of the individual grains as deduced also from SEM and AFM images is about 18 nm corresponding to a nucleation density of 3×10^{11} cm^{-2}. These grains are all epitaxially oriented. Afterward the grains continue vertical and lateral growth until they start to merge before the end of the first minute.

3.11.4.1.6 The Mechanism of Diamond Nucleation on Iridium

The experimental results described in Sections 3.11.4.1.2–3.11.4.1.5 suggest the following mechanism for the nucleation of diamond on iridium by BEN:

1. Applying the bias voltage causes an ion bombardment that results in the deposition of carbon on the iridium surface. Due to the low solubility of carbon in iridium, atoms implanted in the metal (Bauer et al., 2002) immediately diffuse out again. The amount of carbon at the surface quickly reaches a saturation value that is controlled by a dynamic equilibrium between deposition and etching. The thickness is about 1 nm. It is an amorphous, highly resistive (hydrogenated) carbon layer without crystalline structures or inclusions.
2. Spontaneous nucleation of crystalline diamond structures occurs. This may be described by a mechanism suggested by Lifshitz et al. (2002) for the nucleation of diamond from energetic particles. According to this model first an amorphous hydrogenated carbon phase is deposited by bombardment of a surface by energetic particles as in a BEN process. The density of the a-C:H phase is increased by subplantation of particles. Spontaneous nucleation of diamond embryo clusters occurs with a very low probability. Under the harsh bombardment conditions on Ir the probability is even lower. The exceptionally high fraction of epitaxial grains observed in subsequent growth experiments on Ir, indicates that the nucleation event takes place at the iridium/carbon layer interface.

3. The nuclei immediately try to grow in the same way as on other substrates. Due to the higher bias voltage (as compared to BEN on Si), the growth perpendicular to the surface is suppressed. However, lateral crystal growth close to the iridium interface is apparently still possible.
4. The lateral growth occurs under a permanent harsh ion bombardment. This ion bombardment can contribute to the lateral growth. In combination with stress effects resulting from the lattice misfit (Brescia, Schreck, Michler, Gsell, & Stritzker, 2007), it can cause the splitting of the laterally growing film into subunits that later represent the nuclei. The higher density of the carbon matrix within the domains as compared to the surrounding a-C:H layer might explain the step at the edge of the domains.
5. After switching off the bias voltage, the highly defective crystalline matrix between the nuclei is completely etched away within 10 s (Brescia et al., 2008). It has been formed and was stabilized by the ion bombardment. Simultaneously, the nuclei start to grow as isolated diamond crystals that coalesce when their size reaches a value equal to their lateral distance. For domains with a lateral size of the order of 1 μm, one can estimate that only one or very few nuclei are created in real nucleation events. More than 99% are formed by 2-dimensional lateral growth followed by a splitting process. The density of real nucleation events is usually only 10^8–10^9 cm^{-2}.

3.11.4.2 Growth of Heteroepitaxial Diamond Layers on Ir(001)

3.11.4.2.1 Epitaxial Orientation Relationship and Mosaic Spread of Thin Diamond Layers

For the orientation of the diamond layer on the iridium (001) surface, the following relationship has been observed consistently by Ohtsuka et al. (1996) and Schreck, Roll, and Stritzker (1999):

$$\mathrm{diamond}(001)[100]||\mathrm{Ir}(001)[100]. \tag{1}$$

A similar cube-on-cube geometry had also been reported for growth on Ir(111) (Section 3.11.4.4) and was characteristic of the diamond deposition on Si (Jiang et al., 1993) and β-SiC (Stoner & Glass, 1992).

Already in the first report on diamond heteroepitaxy on iridium using Ir/MgO(001) as a substrate (Ohtsuka et al., 1996) it was noticed that essentially all diamond grains were oriented epitaxially. This observation was later confirmed by other authors in many deposition experiments and holds even for the high grain densities of 3×10^{11} cm^{-2} described in Section 3.11.4.1.5. For the grains within a domain, this observation may be easily explained by the fact that the majority of them are formed in a lateral epitaxial growth process.

On silicon and also on β-SiC, maximum nucleation densities of the order of 10^{11} cm^{-2} can also be obtained. However, typically only a small fraction of the grains is epitaxially oriented, for example, 10^8–10^9 cm^{-2} for diamond nucleation on β-SiC (Suesada, Nakamura, Nagasawa, & Kawarada, 1995) and Si (Jiang et al., 1993). The majority of the grains are nonepitaxial. The possible reasons for this difference are the high lattice misfit between diamond and Si or β-SiC (**Table 1**), which could favor the competing nucleation of nonepitaxial grains or the immediate growth of diamond grains during BEN which causes a loss of the orientation under the ion bombardment.

A low density of oriented grains is not necessarily a disadvantage as long as their alignment is perfect. X-ray diffraction (XRD) analysis is a very accurate and sensitive method that allows one to determine the mosaic spread for thin and thick films quantitatively. The total angular spread can be decomposed into an out-of-plane component (tilt $\Delta\omega$) and an in-plane component (twist $\Delta\varphi$). They are deduced from the full width at half maximum (FWHM) of rocking curves and azimuthal scans (for details of the evaluation of the pure twist component see Thürer et al., 1998).

Values of the mosaic spread for a comparable film thickness yield a huge difference between Ir and Si substrates:

1. Mosaic spread of a 600-nm-thick diamond film on Si(001): $\Delta\omega \sim 10^\circ$, $\Delta\varphi \sim 5$–6°,
2. Mosaic spread of a 600-nm-thick diamond film on Ir/SrTiO$_3$(001): $\Delta\omega$, $\Delta\varphi \sim 1^\circ$.

The corresponding pole figures are shown in **Figure 14(a) and (b)**.

3.11.4.2.2 Variation of Surface and Film Structure with Thickness

Figure 15 shows the SEM images of 0.6-, 8-, and 34-μm-thick diamond films on iridium. The corresponding TEM micrographs are given in **Figure 16** (Hörmann, Bauer, Schreck, Gsell, & Stritzker, 2003). In the SEM images

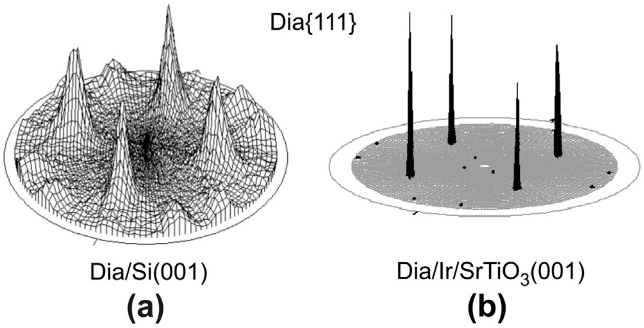

Figure 14 Diamond {111} XRD pole figures of 0.6-μm-thick diamond films on (a) Si(001) and (b) Ir/SrTiO$_3$(001).

of the 0.6-μm film, individual grains can be distinguished. At a thickness of 34 μm, the surface is very flat. The only surface structures of this film are some fine grooves preferentially oriented along [100] or [010], that is, at 45° to the crystallite edges of the 0.6-μm sample.

The grain structure of the thin films is also visible in the TEM image Figure 16(a). At a thickness of 8 μm (Figure 16(b)) nearly dislocation-free single crystal areas with a typical diameter of 1 μm are surrounded by a closed network of grain boundaries consisting of dislocations—a nice example for the textbook model of a fully polygonized mosaic crystal. At 34 μm, this grain boundary network has disintegrated into short defect bands consisting of clusters of dislocations. As in the SEM image, the alignment of the bands has changed.

SEM and TEM have shown a continuous increase in the grain size followed by a transition to a defective single crystal in which individual grains cannot be identified any more. Concomitantly, the dislocation density has decreased significantly. For the 34-μm sample, it is estimated to be $5-10 \times 10^8$ cm^{-2}.

The change in the defect structure can also be monitored by Raman spectroscopy. For layers of 1 μm the FWHM is typically of the order of 15 cm^{-1} (Ohtsuka, Fukuda, Suzuki, & Sawabe, 1997; Schreck, Roll, Michler, Blank, & Stritzker, 2000). At a thickness of several 100 μm, the value decreases to below 3 cm^{-1}. The high initial peak width results only partially from the limited grain size. In fact, it reflects the high stress fluctuations caused by the coalescence of neighboring grains and the presence of a high density of dislocations (Section 3.11.4.2.4).

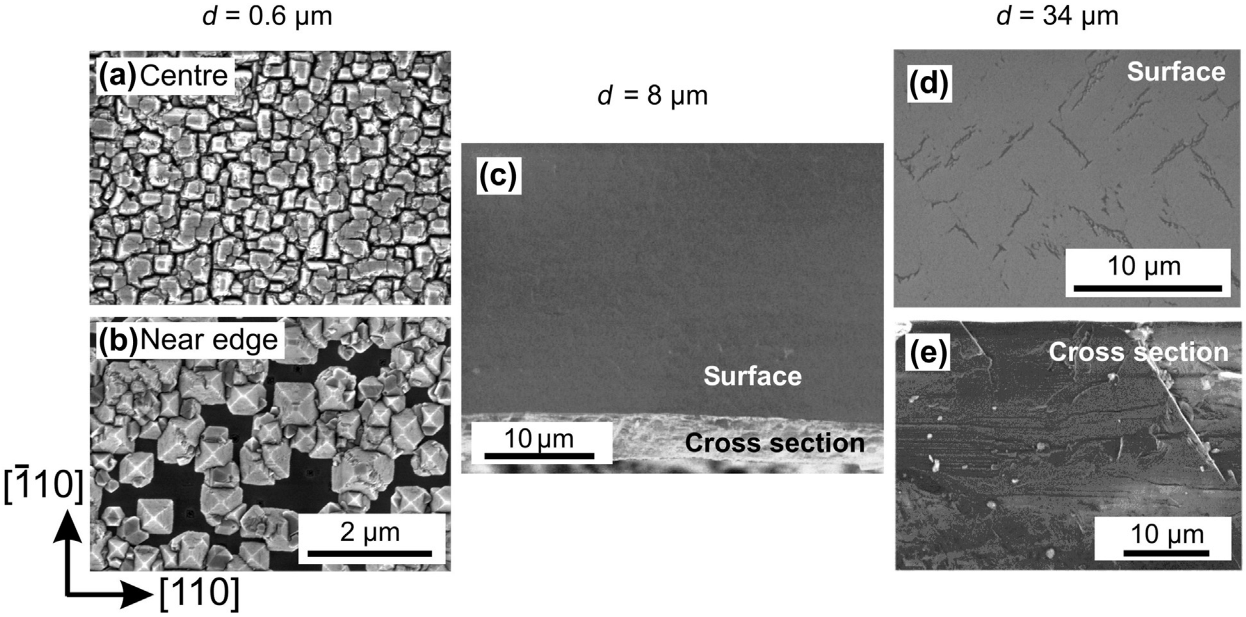

Figure 15 Scanning electron micrographs of heteroepitaxial diamond layers on Ir/SrTiO$_3$(001) with a thickness of (a), (b) 0.6 μm, (c) 8 μm, and (d), (e) 34 μm.

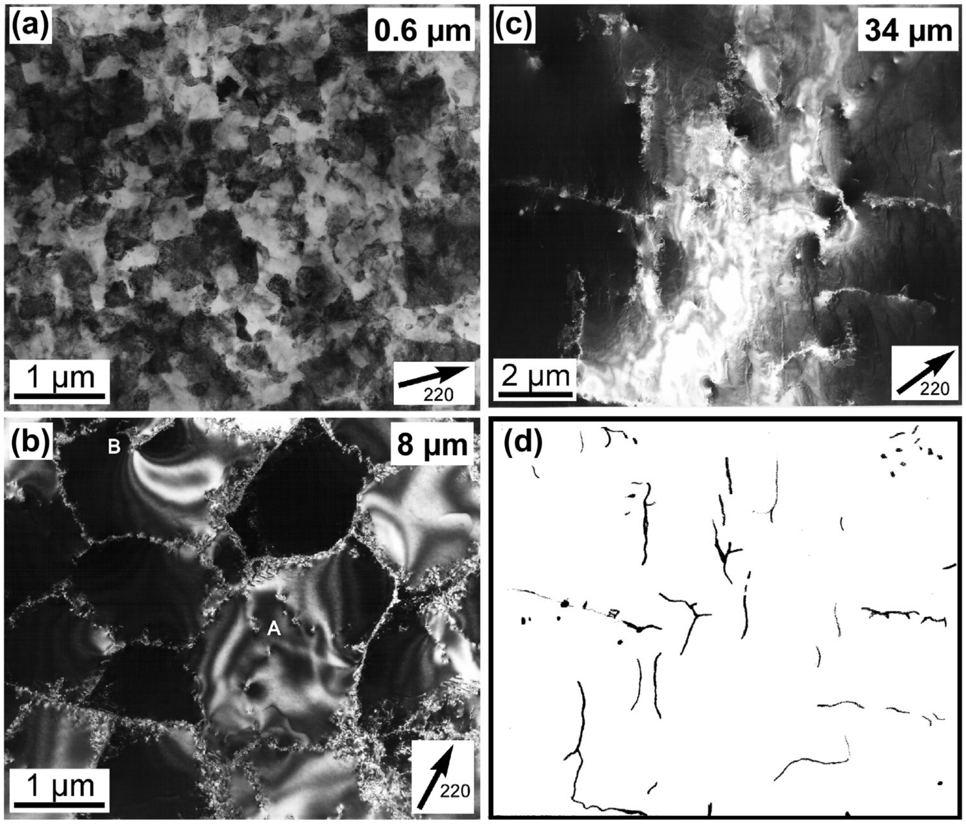

Figure 16 (a)—(c) Plan-view TEM images of epitaxial diamond layers grown on Ir/$SrTiO_3$(001) with different thickness. (d) Schematic drawing of the defect lines in the TEM image shown in (c) (Schreck, Hörmann, Roll, Lindner, & Stritzker, 2001).

3.11.4.2.3 Variation of the Mosaic Spread with Film Thickness

With respect to their epitaxial alignment, thin diamond films on Ir outperform the films on the other heterosubstrates as shown in the previous section. However, due to the mosaic spread of 1° and the high density of grain boundaries (see below) they are still far from being monocrystalline.

The further development of the film texture is controlled by the selection of the growth conditions. If they are chosen inappropriately, twins can appear (Wild, Kohl, Herres, Müller-Sebert, & Koidl, 1994) and overgrow even a perfect single crystal surface so that epitaxial orientation is lost gradually.

For the choice of appropriate process parameters, the concept of evolutionary selection turned out to be very helpful (Van der Drift, 1967; Wild et al., 1993). In diamond CVD crystals are normally bounded by {100} and {111} growth faces. A growth parameter $\alpha = \sqrt{3}\,\frac{v_{100}}{v_{111}}$ with v_{100}, and v_{111} being the growth rates perpendicular to the corresponding faces was defined, which nicely allowed one to predict the formation of fiber textures from randomly oriented seed crystals. Within the range between 1 and 3, α close to 3 means that <100> is the direction of fastest growth and a near <100> fiber texture forms after prolonged growth. In the same way, near <111> fiber textures are formed for α close to 1. Any intermediate value with a corresponding fiber axis may be realized by tuning the process parameters. The power of the concept was shown by the report of fiber textures with an FWHM of the polar angular spread of only 0.8° (Locher, Wild, Müller-Sebert, Kohl, & Koidl, 1993).

Selection of α close to 3 was also applied for the growth of thick heteroepitaxial diamond films on silicon or β-SiC. A large number of nonepitaxial crystallites typical for these substrates were quickly overgrown. Moreover, the mosaic spread of the epitaxially oriented fraction showed a pronounced narrowing.

A detailed analysis of the change in mosaic spread requires the decomposition of the angular spread into tilt and twist. Figure 17 shows the evolution of tilt and twist for diamond on Si(001) and diamond on Ir/$SrTiO_3$(001). The direct comparison between the two substrates yields a valuable insight into the underlying mechanisms. In the diamond films on Si(001), the tilt starts at 10° and continuously decreases with thickness. For prolonged growth values down to 2° have been reported. In contrast, the twist starts at 5—6° and changes only marginally. In extended parameter studies, a minimum value of 3.9° has been measured.

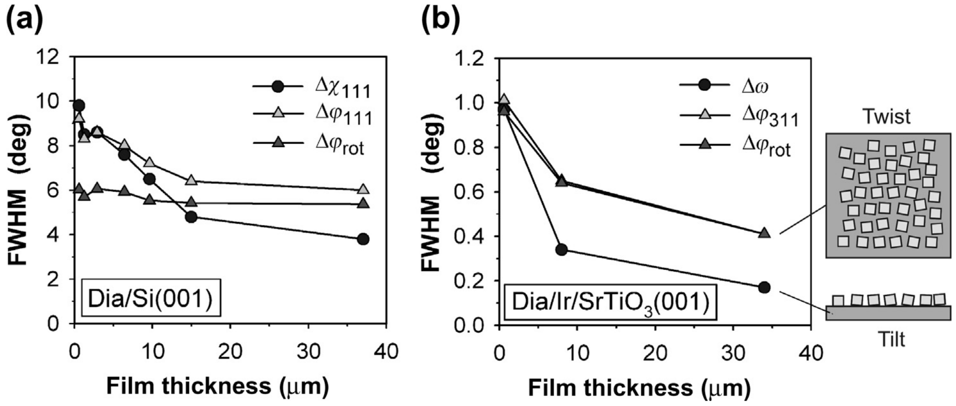

Figure 17 The reduction in mosaic spread with increasing thickness for heteroepitaxial diamond films on (a) silicon and (b) Ir/ $SrTiO_3(001)$. $\Delta\chi_{111}$ and $\Delta\omega$ correspond to the polar spread in orientation, $\Delta\varphi_{rot}$ is the measure of the pure azimuthal spread (Schreck, Hörmann, Roll, Lindner, et al., 2001).

On Ir, the initial mosaic spread (measured at a thickness of 0.6 μm) is about one order of magnitude lower, that is, ~1° (**Figures 14 (b)** and **17 (b)**). In the following film growth, both, tilt and twist, experience a significant reduction with film thickness.

Using the simple geometric α-parameter concept with constant growth rates on the {100} and {111} facets for the description of the mosaic spread reduction shown in **Figure 17 (a) and (b)** yields pronounced inconsistencies. In order to obtain a fiber texture with a width below 4°, growth with $\alpha > 2.8$ would be required. However, the tilt $\Delta\chi_{111}$ of about 4° for the 37-μm film on Si(001) was obtained with an α-parameter of about 2.5 (Schreck & Stritzker, 1996). With similar arguments, the thickest diamond films on iridium with a minimum tilt below 0.2° would require $\alpha \sim 2.99$, which is also far from the experimental observation (Schreck, Schury, Hörmann, Roll, & Stritzker, 2002).

Two alternative mechanisms have been suggested by Jiang and Jia (1996): a modified overgrowth-by-step-flow model and merging of neighboring, initially individual grains. These grains with a slight difference in orientation continue their growth as a single crystal and leave back a crystal defect, which is called a disclination (**Figure 18**). The energy aspects of this process were later analyzed by Michler, von Kaenel, Stiegler, and Blank (1998). They found that only small grains with low misorientation can merge by the formation of disclinations.

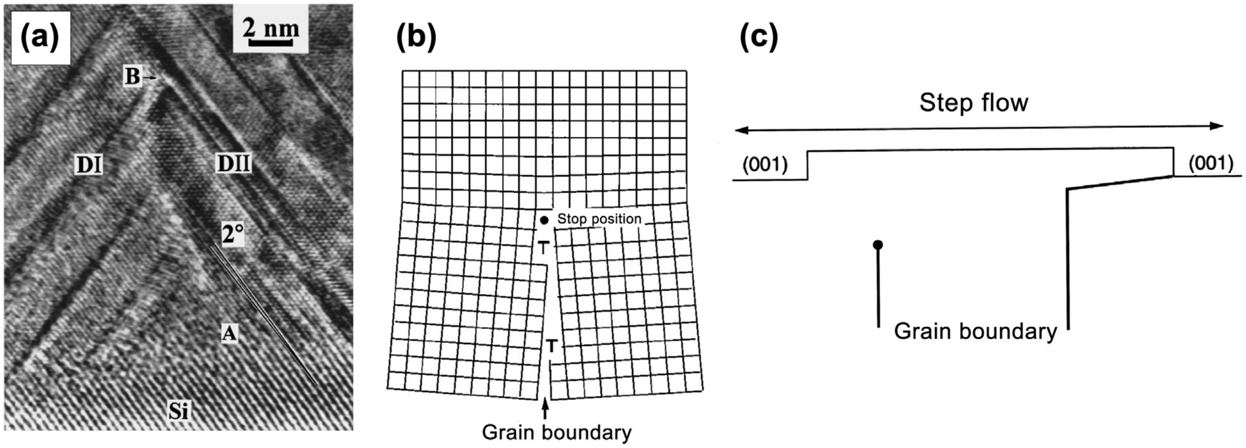

Figure 18 (a) Cross-section TEM image of the grain boundary region between two diamond grains on silicon. The 2° low-angle grain boundary disappears toward the upper edge of the image. (b) Schematic representation of the stopping of the grain boundary by introduction of a disclination. (c) Schematic representation of the lateral overgrowth by the step-flow growth mechanism (Jiang & Jia, 1996).

3.11.4.2.4 Disclination Formation: A Driving Force for Reduction of the Mosaic Spread in Diamond Layers on Ir

The disclination concept was successfully applied to explain quantitatively the fundamental difference in the texture development of diamond on Si and diamond on Ir shown in **Figure 17** (Schreck et al., 2002). In **Figure 19(a)–(d)**, the structure of a low-angle grain boundary and of a partial wedge disclination in a cubic primitive lattice model are sketched schematically. Here, the disclination corresponds to an incomplete tilt boundary. The schema makes it already clear that the partial substitution of the grain boundary implies a strong deformation of the crystal lattice and far-ranging elastic fields.

The elastic energy E of complete low-angle grain boundaries "gb" and a partial wedge disclinations "dis" (Hirth & Lothe, 1992; Michler et al., 1998; Romanov & Vladimirov, 1992; Schreck et al., 2002) vary with the grain boundary angle ω as follows:

$$E^{\mathrm{gb}} = \frac{Gb\omega}{4\pi(1-\nu)}\left(\ln\left(\frac{\beta}{2\pi\omega}\right)+1\right)2Rl \tag{2}$$

and

$$E^{\mathrm{dis}} = \frac{G}{16\pi(1-\nu)}\omega^2 R^2 l \tag{3}$$

with the shear module $G = 533$ GPa, Poisson's ratio $\nu = 0.07$, the core parameter $\beta = 2$, the radius R of the cylindrical grain, and the Burgers vector $\mathbf{b} = a/2<110>$ assuming a = 0.35 nm for the lattice constant as in Michler et al. (1998).

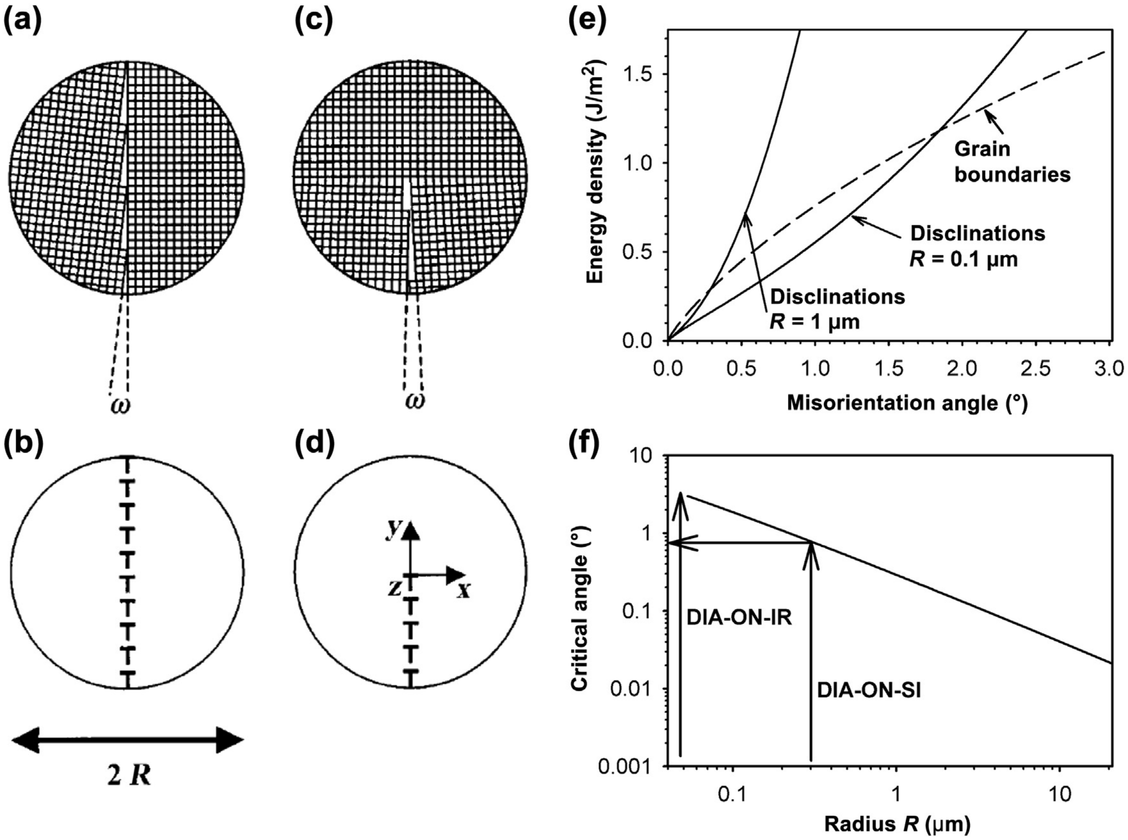

Figure 19 Schematic view of (a), (b) a grain boundary separating two slightly misaligned grains and (c), (d) its substitution by a wedge disclination, i.e. an incomplete low-angle grain boundary that ends in the centre of the grain (Michler et al., 1998). (e) Energy density of a grain boundary and of disclinations for two different particle sizes (0.1 and 1 μm) versus the misorientation angle (Schreck et al., 2002). The intersection between the curve for grain boundary and disclination defines a critical angle. Below this value, grain merging by disclination formation is energetically preferred. (f) Critical angle versus particle size.

In Eqn (3), the core energy of the disclination built up of dislocations is neglected. Its contribution can be taken into account approximately by adding 1/2 E^{gb}. For $E_{\mathrm{tot}}^{\mathrm{dis}}$ we obtain

$$E_{\mathrm{tot}}^{\mathrm{dis}} = E^{\mathrm{dis}} + \frac{1}{2}E^{\mathrm{gb}}. \tag{4}$$

The product $2Rl$ corresponds to the area of the grain boundary. Dividing Eqn (2) by $2Rl$ yields an interface energy density $E^{\mathrm{gb}}/2Rl$, which is independent of the dimensions of the grains. In contrast, the expression $E_{\mathrm{tot}}^{\mathrm{dis}}/2Rl$ is still a function of R, that is, the energy density for the disclination increases with the radius of the grains. In simple words, for larger grains, the elastic bending becomes energetically more and more unfavorable. **Figure 19(e)** shows the variation of the energy densities $E^{\mathrm{gb}}/2Rl$ and $E_{\mathrm{tot}}^{\mathrm{dis}}/2Rl$ with the angle ω. For the disclinations, two curves with $R = 0.1$ and 1 μm have been plotted. The graph shows that disclinations are energetically favored for low misorientation angles. The points of intersection given by the condition

$$E^{\mathrm{gb}} - E_{\mathrm{tot}}^{\mathrm{dis}} = 0 \tag{5}$$

define a critical angle ω_{crit} which moves from 1.85° for small grains with $R = 0.1$ μm down to 0.29° for larger grains with $R = 1$ μm. As a consequence, the probability for the substitution of a grain boundary by a disclination rapidly decreases not only with an increasing misorientation angle but also with the increasing size of the grains.

Combining Eqns (2)–(5), a general relationship between R and ω_{crit} can be deduced:

$$R = \frac{4b}{\omega_{\mathrm{crit}}}(1 - \ln \pi\omega_{\mathrm{crit}}). \tag{6}$$

The result for $\omega_{\mathrm{crit}}(R)$ is plotted in **Figure 19(f)**. Note that Eqn (6) only contains b, a pure geometric quantity, but no material parameters of diamond. As a consequence, it should directly apply to other crystalline materials, too.

The two vertical arrows in **Figure 19(f)** indicate the lateral size R of epitaxial grains when they meet and start to merge. For diamond on silicon, though nucleation densities of 10^{11} cm^{-2} can be obtained by BEN, the maximum density of epitaxial grains is about 10^{9} cm^{-2}, which corresponds to an R of 300 nm. Thus, misorientation angles below 1° would be required to favor substitution of grain boundaries by disclinations. As shown in **Figure 17 (a)**, the angular spread is well >5° so that very few grains will merge by this mechanism. Lateral overgrowth of grains (**Figure 18(c)**) should therefore control the grain coarsening as it is experimentally observed during growth of thick films. The negligible variation of the twist with film thickness (**Figure 17(a)**) yields a strong confirmation for these arguments.

In contrast, for the epitaxial diamond grains on Ir, similar arguments suggest that disclination formation is the dominant mechanism of grain coarsening.

3.11.4.2.5 Simulation of Texture Development

As deduced from **Figures 15** and **16**, grain coarsening accompanies the texture development process during the first several 10 μm. In the previous section, the reduction of the grain boundary energies in the films has been identified as the driving force for the merging of grains. A simple geometric model was developed to qualitatively simulate the reduction in mosaic spread caused by the merging process. The schema in **Figure 20(a)** shows two neighboring grains C1 and C2, which merge to form C3. The orientation of every grain is given by three angles χ, φ, φ_t, which were chosen with correspondence to the angles used in pole figure measurements. When C1 and C2 merge, the orientation of C3 is calculated as the intermediate between the orientations of C1 and C2 (for details see Schreck et al., 2002). In a Monte Carlo-type simulation, an initial ensemble of $n = 2 \times 10^{5}$ grains with an orientation distribution of $\Delta\chi$, $\Delta\varphi = 1°$ (mimicking the 600 nm film in **Figure 14(b)**) was subject to $n/2$ merging processes after stochastically selecting always two grains as coalescing neighbors. After every simulation step, the number of grains has decreased by 50%. Simultaneously, the orientation distribution has narrowed $\propto \sqrt{n}$.

Figure 20(c) shows a comparison between the simulation and the experimentally observed decrease of tilt and twist. While the twist runs roughly in accordance with the simulation, the decrease in tilt is approximately 50% slower. It was suggested that this difference can be explained in terms of every second grain coarsening process being due to lateral overgrowth, which should not influence the twist distribution (as seen for diamond

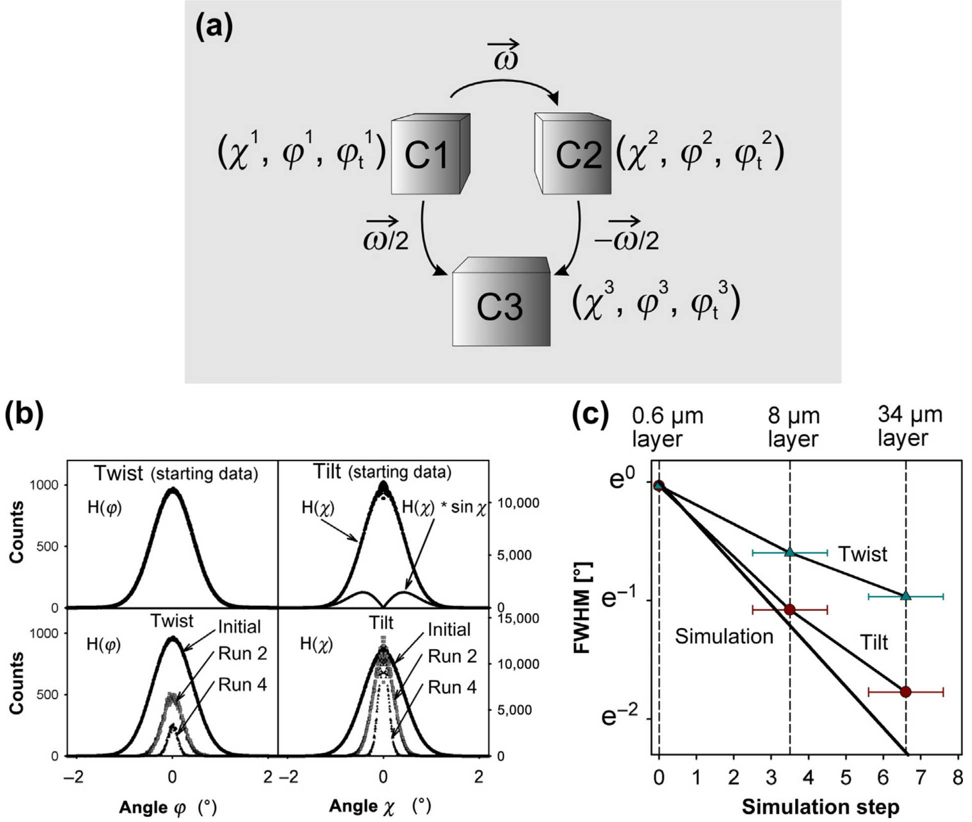

Figure 20 (a) Schema outlining the calculation of the orientation of crystal C3 that is formed by coalescence of C1 and C2 in the simulation. (b) Development of the tilt and twist distribution after several runs of the simulation. (c) Comparison of the results of the simulation with the experimental data derived from **Figure 17** (Schreck et al., 2002).

on Si). As a surprising consequence, growth conditions that avoid an early closure of the film surface (i.e., which favor small {001} growth sectors and preserve the {111} facets) could avoid grain coarsening by lateral overgrowth and thus enhance the reduction of the azimuthal mosaic spread.

3.11.4.2.6 Reduction of Dislocation Density by Patterned Growth

Due to the extreme nucleation densities, the initial amount of dislocations that are located even in small angle grain boundaries is very high. A single dislocation line cannot simply terminate within a crystal. Instead it must thread to the free surface or an interface, fuse with annother dislocation or form a loop (Romanov, Pompe, Beltz, & Speck, 1996). It was suggested that during the coalescence of grains and the formation of disclinations, dislocations are shifted from the top {001} growth sectors to the {111} sectors which form grooves in the films and which are often populated by twins (**Figure 21**). Some of the dislocations can annihilate when they meet a dislocation with an opposite Burgers vector or react with other dislocations if the reaction is energetically favored. Many of them may be buried when the grooves are filled during the lateral growth of the {001} growth sectors similar to the process in epitaxial lateral overgrowth (ELO).

A controlled way to perform patterned growth was described by Sawabe's team (Ando et al., 2004; Ando & Sawabe, 2008). **Figure 22** shows a diamond film on Ir that had been patterned as a narrow line after the BEN treatment. In the subsequent growth step, a highly anisotropic growth rate has been observed experimentally. The process yielded a significant reduction of the dislocation density (Sawabe et al., 2011; Ando, Kamano, Suzuki, & Sawabe, 2012).

Exploratory experiments with ELO structures have also been done in the author's group (Bauer, Schreck, & Stritzker, 2007). While these experiments were not primarily intended to reduce the dislocation density as is normally the case for heteroepitaxial semiconductor materials (Jain, Willander, Narayan, & Van Overstraeten, 2000; Zheleva, Nam, & Davis, 1999), the experiments showed that a thin iridium grid pattern can be overgrown epitaxially by diamond. In addition, the experiments indicated that wing tilt, a common phenomenon in ELO

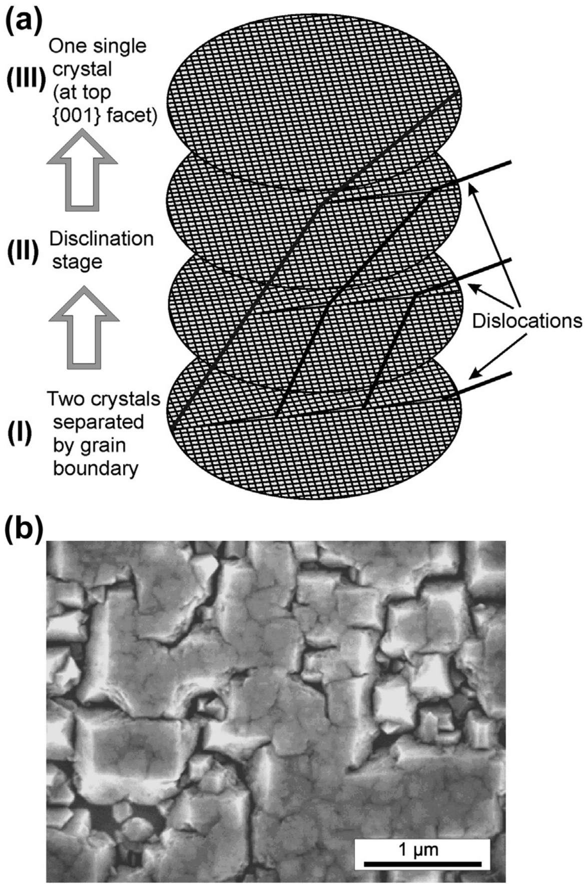

Figure 21 (a) Schema showing how dislocations are shifted out of a grain when two grains separated by a grain boundary merge to form a single crystal. (b) The grooves bounded by {111} facets provide the heterogeneity that allows the gathering, mutual reaction, partial annihilation, and overgrowth of the dislocations (Schreck et al., 2002).

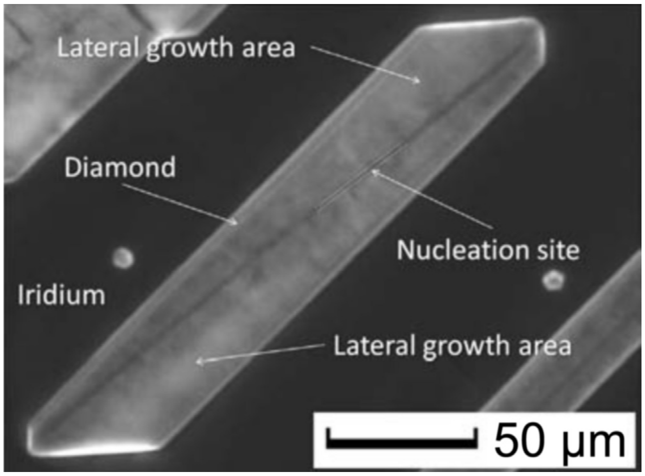

Figure 22 ELO of diamond on Ir(001). The initial nucleation area is a narrow line with 3-μm width and 200-μm length. Growth time is 1 h (Ando & Sawabe, 2008).

of other material systems, also plays a role in lateral overgrowth experiments with diamond. Further experiments in this field are required to explore the potential of ELO for the structural improvement, that is, reduction of the dislocation density, in single crystal diamond films.

3.11.4.3 Diamond Deposition on Off-Axis Substrates

Growth on vicinal crystal planes is a very common concept in materials science to optimize homoepitaxial and heteroepitaxial growth. Slight off-axis angles can promote the step-flow growth resulting in an improved crystal structure and can modify the incorporation of impurities or doping atoms.

In diamond homoepitaxy, it has been shown that off-axis growth can effectively suppress nonepitaxial crystallites (Bauer, Schreck, Sternschulte, & Stritzker, 2005). Moreover, experiments with diamond heteroepitaxy on vicinal Ir have also been performed using $SrTiO_3(001)$ single crystals with off-axis angles of 3° toward [110] or 5° toward [100] (Gsell, Schreck, & Stritzker, 2004). The iridium layers grew on the vicinal $SrTiO_3(001)$ with a perfect cube-on-cube registry. Epitaxial diamond films could be successfully nucleated by BEN on these stepped surfaces. However, the crystal lattice of the diamond experienced a strong additional tilting, that is, the off-axis angle of the diamond film was higher than that of the subjacent substrate.

Figure 23 shows the texture data for two samples of each type. In (a) and (b), two crucial regions around the four pole density maxima of the epitaxial component in the Dia$\{111\}$ and Ir$\{111\}$ pole figures of a 3° off-axis sample have been plotted in a common diagram, respectively. The positions of the maxima do not coincide. A careful analysis for all maxima in the pole figure yields an off-angle that is 1° higher than that of the Ir film and the $SrTiO_3$ substrate. In **Figure 23(c) and (d)**, rocking curves have been measured after azimuthal alignment of a diamond/Ir/$SrTiO_3(001)$ sample with a 5° off-axis angle toward [100] of the oxide substrate. The rocking curves have been measured twice—at azimuthal angles of 0 and 180°. An additional tilt angle of 2° was deduced from the data.

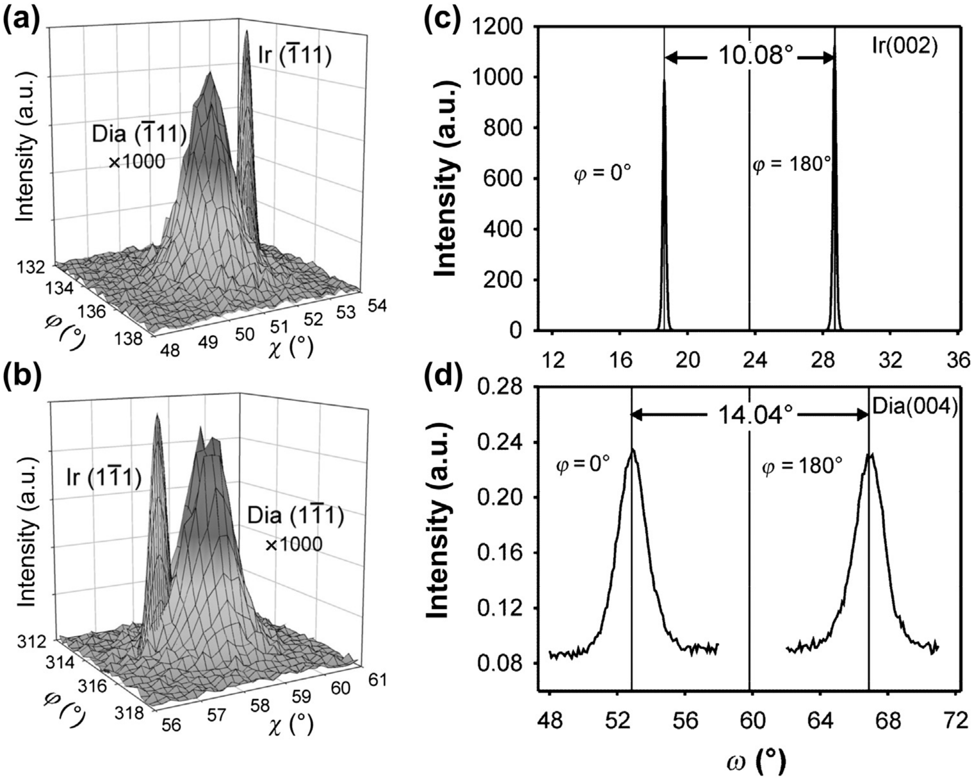

Figure 23 Dia{111} and Ir{111} pole density maxima near the (a) ($\bar{1}11$) and (b) ($1\bar{1}1$) poles measured for a diamond/Ir/$SrTiO_3(001)$ sample with a 3° off-axis angle toward [110] for the oxide substrate. In each case, both maxima are plotted in the same graph. The broader peaks stem from diamond. From the position of all four maxima the additional tilt toward [110] can be deduced. (c), (d) Rocking curves of Ir and diamond measured at $\varphi = 0°$ and after rotation by 180° for a diamond film on an Ir/$SrTiO_3(001)$ 5° off-axis sample (off-angle toward [100]) (Gsell, Schreck, & Stritzker, 2004).

A model was proposed that explains the additional tilt by the preferential incorporation of misfit dislocations due to the stress anisotropy on the vicinal plane substrate taking into account the lattice misfit and the island-like growth mode of diamond.

3.11.4.4 Heteroepitaxy of Diamond on Ir(111)

The {100} faces provide by far the best growth surface which permits the highest structural quality for single crystal diamond synthesis by CVD as shown in many homoepitaxial growth experiments. Deposition experiments on Ir(111) were motivated (a) by the basic interest to study the BEN process on an alternative face of Ir and (b) by potential applications of (111)-oriented diamond films for n-type doping studies with phosphorous (Koizumi, Kamo, Sato, Ozaki, & Inuzuka, 1997; Koizumi, Watanabe, Hasegawa, & Kanda, 2001) and as growth substrate for wurtzite-type semiconductor materials in order to produce heterojunction devices (Hirama, Taniyasu, & Kasu, 2011).

Ir/yttria-stabilized zirconia (YSZ)/Si(111) multilayers, the growth substrates that have been used for the nucleation and growth experiments on Ir(111), will be described in detail in Section 3.11.5. BEN on Ir(111) yields domain patterns similar to the case on (001) substrates (Fischer, Brescia, et al., 2008). Cross-section TEM images confirm that again a 1- to 2-nm-thick carbon layer has been deposited during BEN. As for the carbon layer on Ir(100), a clear XPD pattern is obtained for the C 1s electrons (**Figure 24**). One of the most intriguing features is the threefold symmetry of the pattern that is nearly identical to that of the single crystal reference without noticeable contribution of carbon atoms residing in a twin orientation environment. This is rather surprising since twinning poses severe limitations on the crystal quality in homoepitaxy on diamond (111) and double positioning of several 10% was typically reported for heteroepitaxy on Pt(111) (Tachibana, Yokota, Kobashi, & Shintani, 1997; Tachibana, Yokota, Miyata, et al., 1997).

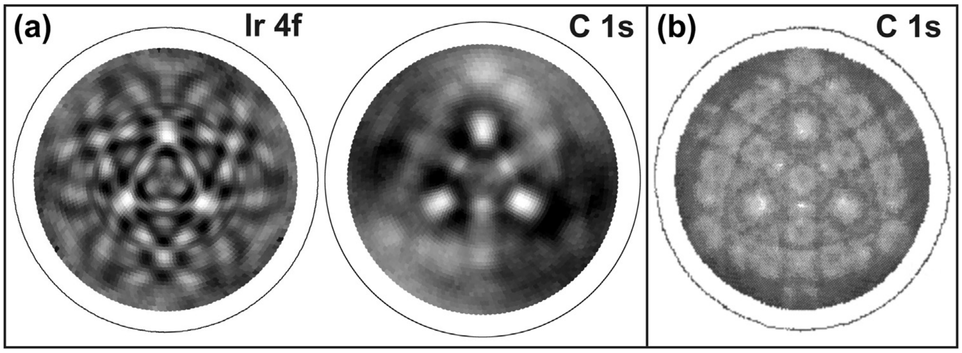

Figure 24 XPD patterns of (a) the Ir $4f_{7/2}$ and C 1s core levels of an Ir/YSZ/Si(111) sample after BEN treatment. (b) C 1s XPD pattern of a diamond (111) single crystal surface taken as a reference from the literature (Fischer, Brescia, et al., 2008).

After 3 h growth, a 1.5-µm-thick epitaxial diamond film was formed. The pole figures of all components of the multilayer structure are plotted in **Figure 25**. Diamond, Ir, and YSZ are in a perfect cube-on-cube orientation relationship. In contrast to the situation on Si(001), YSZ is rotated by 60° with respect to the Si(111) substrate. Azimuthal XRD scans prove that at this stage of film growth the twin fraction is still <1%. Tilt and twist for the 1.5-µm film are 0.96 and 1.85°, respectively. They are somewhat higher than for the corresponding (001) oriented diamond films. It has been shown in the meantime that textured growth can also reduce the mosaic spread for heteroepitaxial diamond films with (111) orientation to values below 1°.

3.11.5 Different Concepts for a Scaling-up: Ir on Large Oxide Single Crystals versus Silicon-Based Multilayer Structures

Diamond deposition on iridium always means deposition on iridium layers grown epitaxially on another substrate. Bulk single crystals of this precious metal have no technological relevance as substrates. Most Ir films up to now have been deposited on oxide single crystals like MgO (Ohtsuka et al., 1996), $SrTiO_3$ (Bednarski, Dai, Li, & Golding, 2003; Schreck et al., 1999), and sapphire (Dai, Bednarski-Meinke, Loloee, & Golding, 2003). Size,

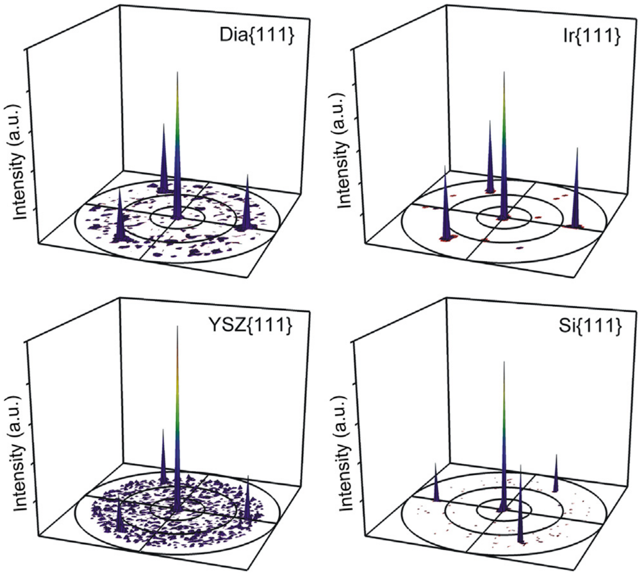

Figure 25 XRD pole figures of Si, YSZ, Ir, and diamond {111} reflections measured for a 1.5-μm-thick heteroepitaxial diamond film on Ir/YSZ/Si(111) (Fischer, Brescia, et al., 2008).

quality, and price are important criteria for the selection of an Ir growth substrate. For $SrTiO_3$ and MgO at least 2-in. wafers, and for sapphire up to 8-in. samples are available (Rubicon, 2011).

Besides the dimension of the single crystal substrate, its coefficient of thermal expansion (CTE) is of similar importance. Figure 26(a) compares the thermal stress induced in a thin diamond layer on a thick substrate after cooling down from deposition temperature (Gsell, Bauer, Goldfuβ, Schreck, & Stritzker, 2004). The vertical line and the numbers on the right side indicate the values for a rather low deposition temperature of 700 °C. Nevertheless, the compressive stress for oxide single crystal substrates varies from −4 GPa for sapphire to more than −8 GPa for MgO. Diamond layers thicker than some micrometers are therefore prone to delamination. In contrast, with −0.68 GPa, the thermal stress on silicon is comparatively low. It even decreases for higher deposition temperatures.

Deposition of iridium directly on silicon seems unrealistic due to the chemical reactivity of the two elements forming a variety of iridium silicides with different crystal structures of low symmetry, some of them with a low

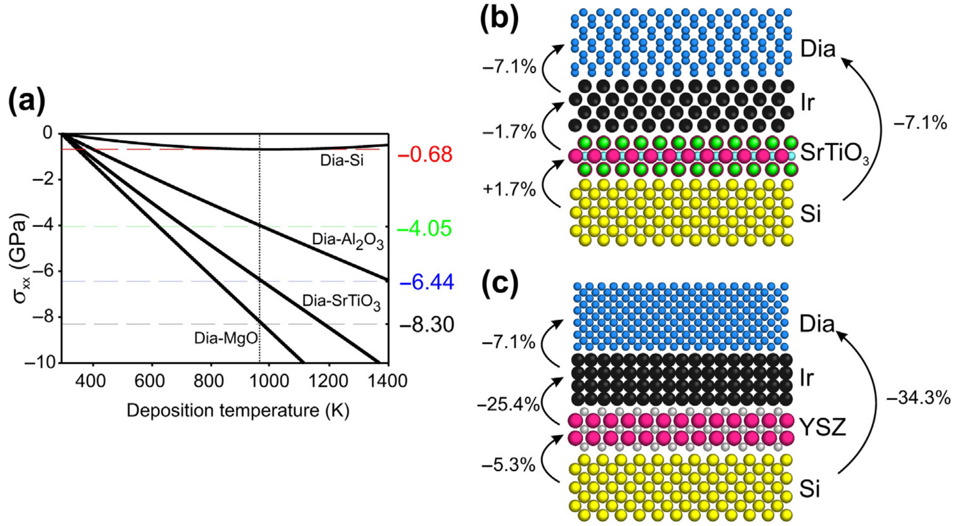

Figure 26 (a) Thermal stress σ_{xx} in diamond layers on different substrates versus deposition temperature (Gsell, Bauer, Goldfuß, Schreck, & Stritzker, 2004). Schematic view of the epitaxial multilayer structures (b) diamond/Ir/$SrTiO_3$/Si(001) and (c) diamond/Ir/YSZ/Si(001).

melting point (Maex & van Rossum, 1995). A first attempt with CaF_2 buffer layers between Ir and Si yielded oriented Ir films and diamond grains (Wu et al., 2003) but the insufficient thermal stability of the fluoride films turned out to be a drawback.

Oxide buffer layers are a viable alternative. Two multilayer structures based on $SrTiO_3$ (Bauer, Gsell, et al., 2005) and YSZ (Gsell, Bauer, Goldfuβ, Schreck, & Stritzker, 2004) have been explored successfully. They are schematically shown in **Figure 26(b) and (c)**.

The epitaxial deposition of stable oxides like YSZ on silicon has formerly been studied in the context of HTc superconductor (Lubig et al., 1992) and ferroelectrics (Ramesh et al., 1993) research. The mosaic spread of these oxide buffer layers is typically >1° (FWHM). Nevertheless, it was possible to grow high-quality single crystal iridium films on top of $SrTiO_3$/Si(001) and YSZ/Si(001) substrates by the use of a novel two-step growth process (Gsell, Fischer, et al., 2007). **Figure 27(a)** shows the cross-section TEM image of a 20-nm-thick Ir film on YSZ/Si(001). The corresponding rocking curves (Ir(002) and YSZ(002) reflections) and azimuthal scans (Ir(311) and YSZ(111) reflections) were taken for a multilayer sample with a 150-nm-thick Ir film (**Figure 27(b) and (c)**). According to the profiles, the mosaic spread of the oxide buffer layers is one order of magnitude higher than that of the iridium layer on top. This is even more surprising against the background of a 25% lattice mismatch.

To study the underlying mechanism, the development of the mosaic spread was monitored for the first 20 nm growth, that is, the first part of the two-step process that is distinguished by an extremely small deposition rate of 0.004 nm s^{-1}. The first data points in **Figure 28** correspond to a mosaic spread of the Ir layer that is higher than that of the YSZ buffer layer. With increasing thickness, the angular spread drops well below that of the YSZ. After having reached a thickness of 20 nm, the process was reversed and the metal film was successively etched. It turned out that the low mosaic spread is preserved, which is a clear hint that the mosaic reduction process implies a complete rearrangement of the Ir islands. The orientation averaging mechanism of an ensemble of grains whose alignment scatters around a preferred orientation as described by the simulation in Section 3.11.4.2.5. can yield a nice model for the present mosaic reduction, too. As a basic difference, the present process involves a complete rearrangement of the metal islands during merging while in the diamond film the improvement only applies to the newly forming crystal lattice planes directly at the growth front. In contrast to the ductile metal, the brittle diamond normally impedes an internal rearrangement due to the high activation energy for the movement of dislocations.

The Ir films grown via high-mosaic-spread oxide buffer layers on Si(001) have minimum FWHMs for the tilt and twist of 0.1° comparable with the best values that have been measured in the author's laboratory for Ir on

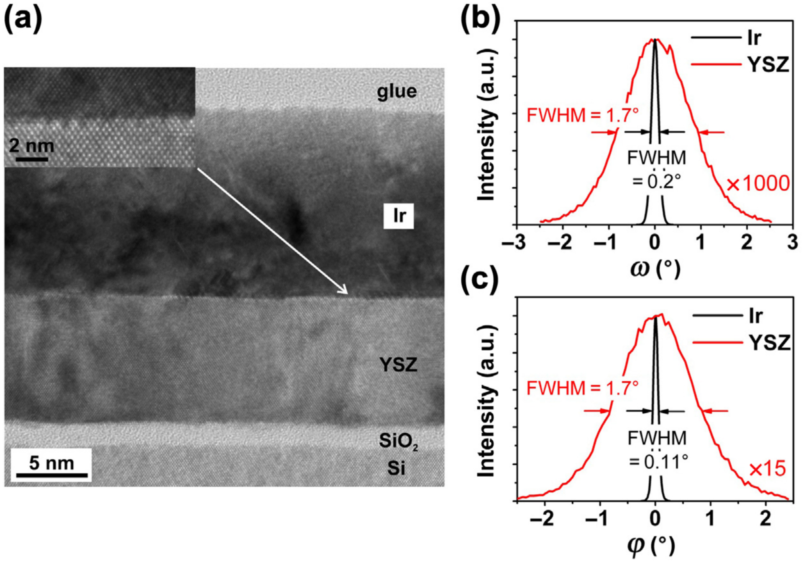

Figure 27 (a) Cross-section TEM image of an Ir(20 nm)/YSZ/Si(001) sample taken along the [110] zone axis (Gsell, Fischer, et al., 2007). (b) Ir(002) and YSZ(002) rocking curves and (c) Ir(311) and YSZ(111) azimuthal scans of a 150-nm-thick Ir layer on YSZ/Si(001) (Fischer, Gsell, Schreck, Brescia, & Stritzker 2008).

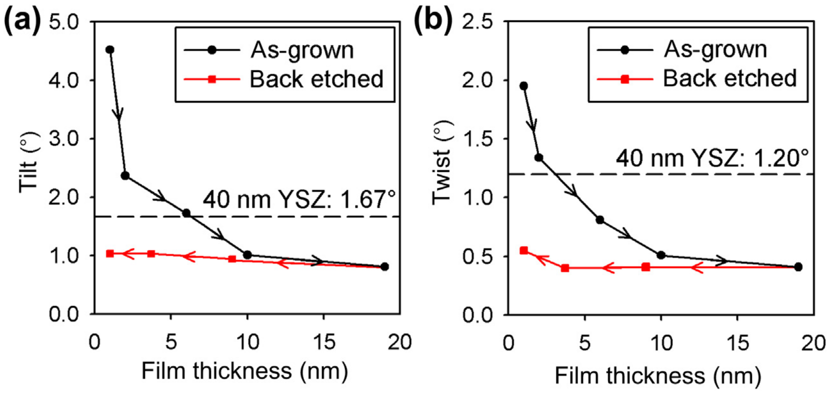

Figure 28 Variation of the mosaic spread of iridium on YSZ/Si(001) with film thickness. The circles correspond to the improvement with increasing film thickness. The square shaped data points were acquired after progressively thinning the 19-nm-thick iridium film by ion sputtering. The mosaic spread (tilt and twist) of the YSZ buffer layer is included in the graphs for comparison (Gsell, Schreck, et al., 2008).

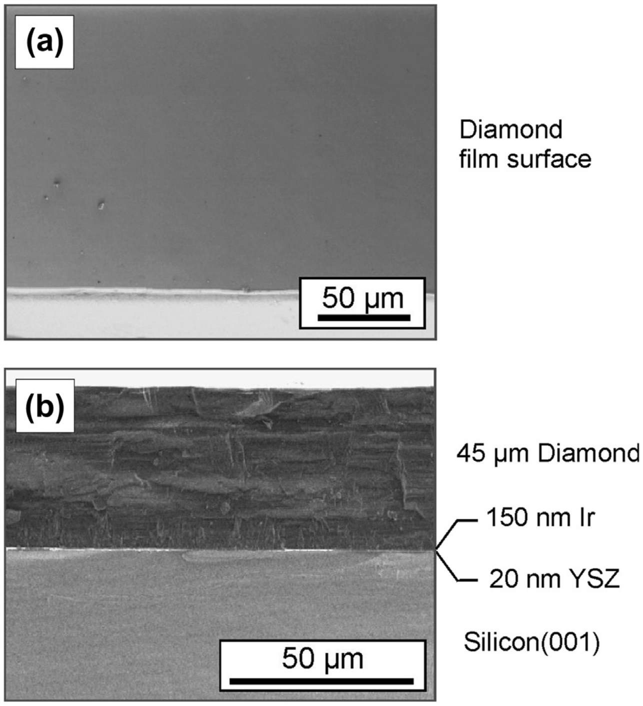

Figure 29 (a) Surface and (b) cross-section SEM images of a diamond/Ir/YSZ/Si(001) sample (Gsell, Bauer, et al., 2004).

$SrTiO_3$ single crystals. It was later shown that the process is also applicable to (111)-oriented Ir (Section 3.11.4.4.) and to various other metals (Gsell, Fischer, Schreck, & Stritzker, 2009).

In the BEN treatment and diamond growth step, the whole layer system diamond/Ir/YSZ/Si(001) stays intact up to thicknesses of 1 mm. Film surface and cross-section of the whole multilayer structure for a 45-μm-thick diamond film are shown in Figure 29.

3.11.6 Single Crystal Diamond Deposition on Arbitrary Substrates

Biaxially textured oxide films are an important topic in the field of high-Tc superconductors. Since the early days of research, it was observed that large angle grain boundaries in the oxide superconductor materials form weak

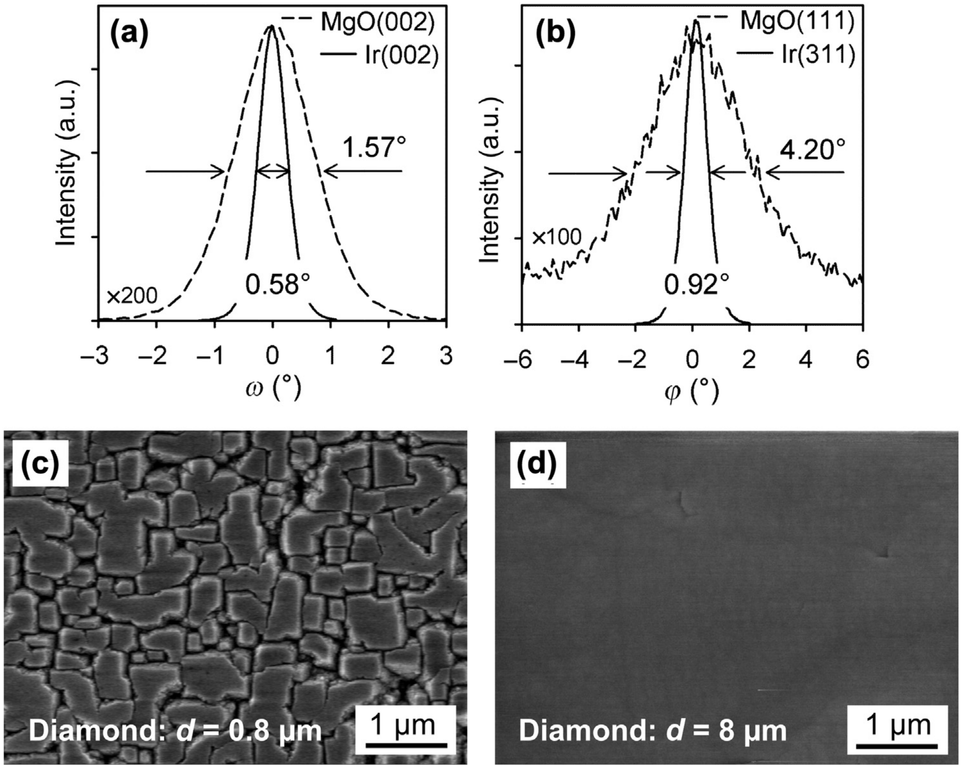

Figure 30 Rocking curves and azimuthal scans for MgO and iridium reflections measured on the multilayer system Ir/IBAD–MgO/amorphous-Y_2O_3/Si. (c), (d) SEM micrographs of two diamond films epitaxially nucleated by BEN on the Ir/IBAD–MgO stacks (Gsell, Schreck, et al., 2008).

links that drastically reduce the critical current densities (Dimos, Chaudhari, Mannhart, & Legoues, 1988). Development of cables therefore required a technique of depositing *c*-axis-oriented films with small grain boundary angles on polycrystalline steel tapes. The narrow mosaic spread of several degrees was finally achieved by the application of biaxially textured oxide buffer layers deposited by ion beam assisted deposition (IBAD) (Arendt et al., 2004). In this technique, an oxide (MgO) is deposited, for example, by sputtering while the growing film is simultaneously bombarded with 700 eV Ar^+ ions under a well-defined angle of 45° to the surface. The preferred contact face MgO/substrate and the direction of ion incidence define a lattice plane and a crystal axis so that the orientation of the MgO crystal is completely determined. Currently, the best IBAD samples have a mosaic spread of around 4°.

State-of-the art biaxially textured IBAD oxide layers were applied to grow Ir with the parameters of the two-step growth process and subsequently nucleate and grow diamond (Gsell, Schreck, et al., 2008). **Figure 30** summarizes the results of this study. The XRD rocking curves and azimuthal scans show the broad orientation distribution of the IBAD-MgO layer and the significantly narrower Ir profiles with a width of <1°. Texture narrowing as described in the previous section apparently also works on oxide layers with several degrees of mosaic spread. SEM images of the diamond layers grown on top are shown in **Figure 30(c) and (d)**.

Since IBAD-textured oxides can be deposited on polycrystalline or amorphous substrates that can be chosen, for example, to meet CTE requirements or to coat real device structures, the described experiments offer an exciting strategy for deposition of (near) single crystal films on arbitrary substrates.

3.11.7 Present State-of-the-Art Heteroepitaxial Diamond Films

Currently, diamond on Ir films have reached thicknesses of 1–2 mm (Freund et al., 2011) and sample areas of 1 in. in diameter (Yokota et al., 2007). With respect to structural quality, Sawabe's group (Sawabe et al., 2011) reported FWHM values for the mosaic spread of around or below 0.1° on Ir/oxide single crystals, which is similar to values obtained on Ir/YSZ/Si in our group. The width of the rocking curves competes well with values measured for typical IIa single crystals (Fujii, Nishibayashi, Shikata, Uedono, & Tanigawa, 1995). Dislocation densities for the ELO samples in the 10^7-cm^{-2} range have been reported (Sawabe et al., 2011).

Scaling-up of the Ir/YSZ/Si(001) substrates to 4-in. wafer dimensions has successfully been shown (Fischer, Gsell, Schreck, Brescia, & Stritzker, 2008) (**Figure 31**) and the transfer of the BEN step and diamond growth process to 4-in. substrates is in progress.

3.11.8 Applications of Heteroepitaxial Diamond Crystals

The potential of the early heteroepitaxial diamond layers on iridium was explored in different areas. In electron emission experiments, they revealed a higher homogeneity and a lower turn-on voltage than comparable polycrystalline layers (Yamada, Maede, & Sawabe, 1999). Hall effect measurements on boron-doped diamond films yielded mobility values of 340 $\mathrm{cm}^2\ \mathrm{V}^{-1}\ \mathrm{s}^{-1}$ (Kusakabe, Sobana, Sotowa, Imato, & Tsubota, 2003). These are higher than the 165 $\mathrm{cm}^2\ \mathrm{V}^{-1}\ \mathrm{s}^{-1}$ (Stoner, Kao, Malta, & Glass, 1993) measured at room temperature for heteroepitaxial layers on silicon but still by a factor of five below the typical values for high-quality homoepitaxial diamond. In another study, p-type surface channel field effect transistors have been successfully fabricated on a diamond quasisubstrate grown on Ir/$\mathrm{SrTiO_3}$ (Kubovic et al., 2003). Finally, diamond-on-iridium films were investigated as detector material for heavy ion tracking (Stolz, Behravan, Regmi, & Golding, 2006). While the relative energy resolution of 18% could not reach the minimum values measured for the homoepitaxial layers, their excellent time resolution close to 10 ps qualified them as promising candidates for timing applications.

In the following chapters, two examples are described in more detail. In both cases sample quality has reached a level that an early application in scientific areas looks very promising.

3.11.8.1 Diamond Mosaic Crystals for Neutron Monochromators

Neutrons are an important probe in solid-state physics. In contrast to photons or electrons, they can only be provided in an extremely inefficient generation process. In a typical fission reactor, the generation of two to three neutrons is accompanied by a heat generation of 200 MeV. The energetic neutrons are then slowed down in the moderators to generate cold, thermal, or hot neutrons with energies between 1 and 1000 meV (Furrer, Mesot, & Strässle, 2009). With a typical energy efficiency of $<10^{-8}$ even the powerful 60-MW neutron reactor at the Institute-Laue-Langevin (ILL, Grenoble, France) is a worse source for neutrons than a 60-W light bulb is for photons.

For diffraction and scattering experiments, the neutrons have to be monochromatized. Using a perfect single crystal as is usually done for synchrotron radiation would result in unacceptably low intensities. As a

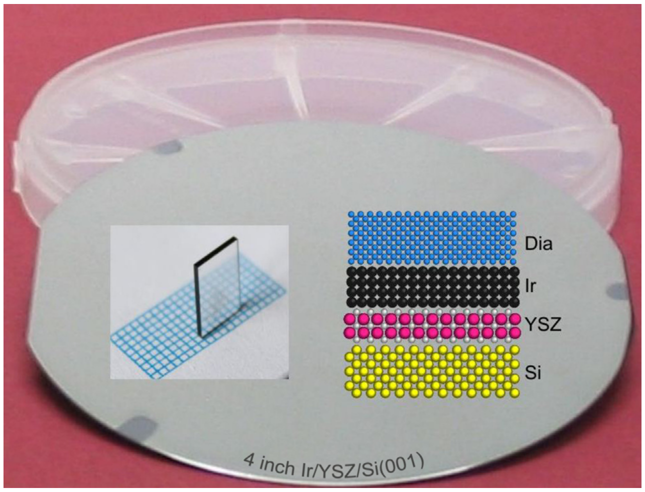

Figure 31 The 4-in. Ir/YSZ/Si(001) wafer. The inset shows a $6 \times 8 \times 1\text{-mm}^3$ diamond crystal that has been grown on this type of substrates.

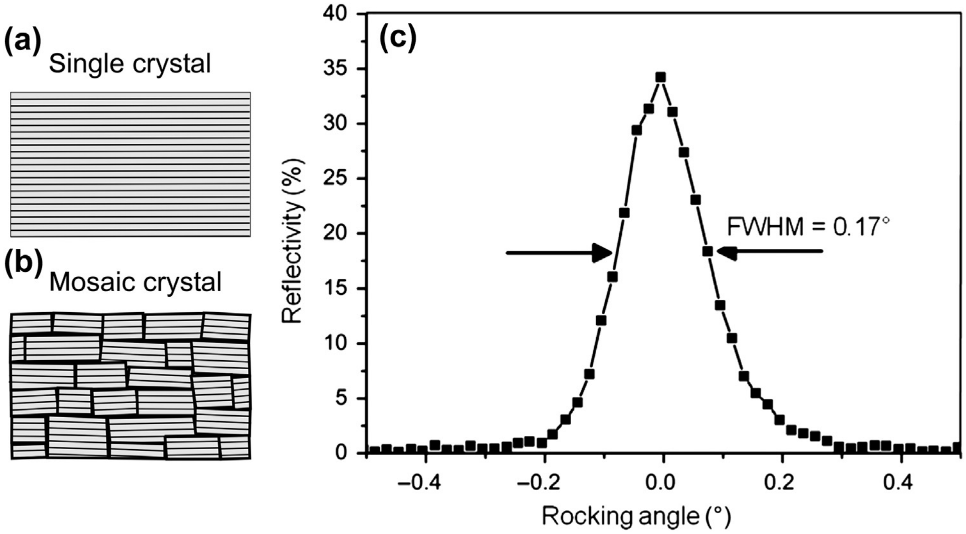

Figure 32 Schema of (a) a single crystal and (b) a mosaic crystal. (c) Neutron rocking curve obtained from a 1-mm-thick diamond sample (diamond(004) reflection, $2\Theta_B = 73.5°$, $\lambda = 0.1067$ nm) grown on Ir/YSZ/Si(001) (Freund et al., 2011).

compromise between intensity and resolution, in real and reciprocal space, mosaic crystals with an angular reflectivity distribution that matches the beam divergence of 0.2–1° are chosen. The internal structure of an ideally imperfect crystal (Warren, 1990) consists of slightly disoriented mosaic blocks that are small enough to avoid primary extinction (**Figure 32(a) and (b)**).

Current monochromators use Si, Ge, Cu, Be, or highly oriented pyrolytic graphite (HOPG). All except HOPG are initially high-quality crystals that underwent a plastic deformation to produce the mosaic spread. A full monochromator with a typical area of 20 × 20 cm^2 consists of dozens of square-centimeter-size crystals with individual alignment facilities.

Recent calculations revealed that diamond mosaic crystals would have the highest performance of all materials for neutron monochromators exceeding currently used materials by factors between 1.5 and 4 (Freund, 2009). Synthesizing perfect diamond crystals and then deforming them is not a reasonable option for easily comprehensible reasons. However, the mosaic spread of several-micrometer-thick diamond layers on Ir is just in the desired range (**Figure 17**). So the technological challenge consists in the growth of mm-thick diamond with a homogeneous mosaic spread and an internal defect structure that avoids or at least minimizes primary extinction. In the meantime, diamond mosaic crystals with a thickness of up to 2 mm have been grown on Ir/YSZ/Si(001) substrates (Freund et al., 2011). Absolute values and uniformity of the mosaic spread of these samples have been characterized by X- and γ-rays and finally neutron reflectivity curves have been measured. **Figure 32(c)** shows a neutron rocking curve of a 1-mm-thick diamond sample. The peak reflectivity of 34% at a neutron FWHM of 0.17° is about 28% below the theoretical predictions. On the one hand, this indicates that the structure of the samples still requires some further improvements toward a perfect mosaic crystal. On the other hand, even currently used materials typically reach only 90% of the theoretical values (Courtois, 2011) so that the result already represents a convincing proof of concept for neutron monochromators made of diamond mosaic crystals grown by CVD. Further improvements have been achieved in the meantime.

3.11.8.2 Heteroepitaxial Diamond as a Detector for High-Energy Ionizing Radiation

The main interest of particle physicists in diamond is based on their need for fast, low noise, and radiation-hard detectors. For sensors in radiotherapy, the tissue equivalence of carbon represents an additional beneficial feature.

In the past years, homoepitaxial CVD growth has reached a perfection that allows the synthesis of diamond samples with nearly 100% charge collection efficiency and an energy resolution of 0.3% comparable with the best single crystal silicon detectors (Berdermann et al., 2010). Due to the very nature of the heteroepitaxial nucleation process on Ir, the initial dislocation density is extremely high. Concepts for its reduction during the subsequent growth step have been discussed extensively in this article. In the medium term, it is not expected that the heteroepitaxial layers will reach the ultimate quality of homoepitaxial samples necessary for the energy resolution in spectroscopy applications. However, they offer the potential for timing and tracking devices with a higher homogeneity than polycrystalline material.

First experiments at GSI in Darmstadt with heteroepitaxial diamond films grown on Ir/YSZ/Si(001) have revealed charge collection efficiencies well above 90% with an energy resolution of 3–4% and an intrinsic time resolution of 18 ps. Details on this work will be given in the chapter of E. Berdermann in this book.

3.11.9 Summary and Outlook

This chapter summarized the most important steps of epitaxial diamond growth on Ir since its discovery in 1996 (Ohtsuka et al., 1996). The uniqueness of iridium was revealed in the aftermath, step by step, in many experimental studies. In different exploratory experiments with other comparable materials (e.g., Re and Rh) none could be identified that showed comparable properties and a similar potential for diamond heteroepitaxy.

The distinctiveness of Ir is based on the mechanism of lateral spreading of the diamond grains during the biasing which results in the frequently described nucleation patterns ("domains") rather than on a very effective nucleation process. Real nucleation appears to be a comparatively rare event. Iridium is a non-carbide-forming metal with a negligible solubility for carbon. Nevertheless it forms strong bonds with diamond. The lattice misfit of 7.6% between the two is apparently in an acceptable range for heteroepitaxy. The combination of these properties facilitates the unique processes occurring during the BEN treatment.

Strong bonding forces are also of high technological importance in order to guarantee a stable multilayer structure in the harsh CVD process. Establishing reliable and reproducible biasing treatments over the whole wafer size areas is one of the major challenges for the near future. Additionally, growth processes on the large areas have to be developed. The processes responsible for the reduction of the mosaic spread during the first 20–30 μm have been studied. The potential and the limits for the reduction of dislocation densities during the growth of millimeter-thick samples are under investigation.

The use of diamond crystals as neutron monochromators and as detectors for particle tracking and timing in high-energy physics are promising developments. Nevertheless, they represent niche applications. Further work is required to identify industrial fields that offer a technological and economic perspective for heteroepitaxial diamond.

Acknowledgments

Many former and current coworkers and students participated with great enthusiasm and commitment in the heteroepitaxy studies on Ir. I would like to thank H. Roll, A. Schury, F. Hörmann, H. Sternschulte, T. Bauer, J. Goldfuβ, P. Huber, R. Brescia, D. Reuber, S. Dunst, and C. Stehl. I am especially indebted to S. Gsell and M. Fischer, who strongly pushed ahead the technological developments, and Prof. B. Stritzker for his continuous support. Many external partners contributed, of whom E. Berdermann in the detector project and the collaborators from the neutron sources shall be mentioned. Financial support from DFG, BMBF, EU, AMU Augsburg, Bayerische Forschungsstiftung and from the neutron centres ILL (Grenoble), FRMII (Munich), and HZB (Berlin) is highly appreciated.

References

Abbaschian, R., Zhu, H., & Clarke, C. (2005). High pressure–high temperature growth of diamond crystals using split sphere apparatus. *Diamond and Related Materials, 14*, 1916–1919.

Ando, Y., Kuwabara, J., Suzuki, K., & Sawabe, A. (2004). Patterned growth of heteroepitaxial diamond. *Diamond and Related Materials, 13*, 1975–1979.

Ando, Y., & Sawabe, A. (2008). Heteroepitaxy of diamond. In S. Koizumi, C. E. Nebel, & M. Nesladek (Eds.), *Physics and applications of CVD diamond* (pp. 77–92). Weinheim: Wiley-VCH.

Ando, Y., Kamano, T., Suzuki, K., & Sawabe, A. (2012). Epitaxial lateral overgrowth of diamonds on iridium by patterned nucleation and growth method. *Japanese Journal of Applied Physics, 51*, 090101-1–1-090101-5.

Aoyama, T., Amano, N., Goto, T., Abukawa, T., Kono, S., Ando, Y., et al. (2007). Characterization of planar-diode bias-treatment in DC-plasma heteroepitaxial diamond growth on Ir(001). *Diamond and Related Materials, 16*, 594–599.

Arendt, P. N., Foltyn, S. R., Civale, L., DePaula, R. F., Dowden, P. C., Groves, J. R., et al. (2004). High critical current YBCO coated conductors based on IBAD MgO. *Physica C, 412*, 795–800.

Argoitia, A., Angus, J. C., Wang, L., Ning, X. I., & Pirouz, P. (1993). Diamond grown on single-crystal beryllium oxide. *Journal of Applied Physics, 73*, 4305—4312.

Bauer, T., Gsell, S., Hörmann, F., Schreck, M., & Stritzker, B. (2004). Surface modifications and first stages of heteroepitaxial diamond growth on iridium. *Diamond and Related Materials, 13*, 335—341.

Bauer, T., Gsell, S., Schreck, M., Goldfuß, J., Lettieri, J., Schlom, D. G., et al. (2005). Growth of epitaxial diamond on silicon via iridium/$SrTiO_3$ buffer layers. *Diamond and Related Materials, 14*, 314—317.

Bauer, T., Schreck, M., Gsell, S., Hörmann, F., & Stritzker, B. (2003). Epitaxial rhenium buffer layers on Al_2O_3(0001): a substrate for the deposition of (111)-oriented heteroepitaxial diamond films. *Physica Status Solidi (A), 199*, 19—26.

Bauer, T., Schreck, M., Hörmann, F., Bergmaier, A., Dollinger, G., & Stritzker, B. (2002). Analysis of the total carbon deposition during the bias enhanced nucleation of dia mond on Ir/$SrTiO_3$(001) using ^{13}C-methane. *Diamond and Related Materials, 11*, 493—498.

Bauer, T., Schreck, M., Sternschulte, H., & Stritzker, B. (2005). High growth rate homoepitaxial diamond deposition on off-axis substrates. *Diamond and Related Materials, 14*, 266—271.

Bauer, T., Schreck, M., & Stritzker, B. (2007). Epitaxial lateral overgrowth (ELO) of homoepitaxial diamond through an iridium mesh. *Diamond and Related Materials, 16*, 711—717.

Bednarski, C., Dai, Z., Li, A.-P., & Golding, B. (2003). Studies of heteroepitaxial growth of diamond. *Diamond and Related Materials, 12*, 241—245.

Berdermann, E., Pomorski, M., de Boer, W., Ciobanu, M., Dunst, S., Grah, C., et al. (2010). Diamond detectors for hadron physics research. *Diamond and Related Materials, 19*, 358—367.

Bernhard, P., Ziethen, C., Schoenhense, G., Schreck, M., Bauer, T., Gsell, S., et al. (2006). Structural properties of the diamond nucleation layer on iridium analyzed by laterally resolved X-ray absorption spectroscopy. *Japanese Journal of Applied Physics Part 2—Letters & Express Letters, 45*, L984—L986.

Brescia, R., Schreck, M., Gsell, S., Fischer, M., & Stritzker, B. (2008). Transmission electron microscopy study of the very early stages of diamond growth on iridium. *Diamond and Related Materials, 17*, 1045—1050.

Brescia, R., Schreck, M., Michler, J., Gsell, S., & Stritzker, B. (2007). Interaction of small diamond islands on iridium: a finite element simulation study. *Diamond and Related Materials, 16*, 705—710.

Chen, Q., Yang, J., & Lin, Z. (1995). Synthesis of oriented textured diamond films on silicon via hot filament chemical vapor deposition. *Applied Physics Letters, 67*, 1853—1855.

Courtois, P., (2011) ILL, Grenoble, personal communication.

Dai, Z., Bednarski-Meinke, C., Loloee, R., & Golding, B. (2003). Epitaxial (100) iridium on A-plane sapphire: a system for wafer scale diamond heteroepitaxy. *Applied Physics Letters, 82*, 3847—3849.

Dimos, D., Chaudhari, P., Mannhart, J., & Legoues, F. K. (1988). Orientation dependence of grain-boundary critical currents in $YBa_2Cu_3O_{7-\delta}$ bicrystals. *Physical Review Letters, 61*, 219—222.

Edgar, J. H., Strite, S., Akasaki, I., Amano, H., & Wetzel, C. (Eds.). (1999). In *Emis datareviews series no. 23: properties, processing and applications of gallium nitride and related semiconductors*. London: Inspec.

Field, J. E. (1990). Strength and fracture properties of diamond. In J. E. Field (Ed.), *The properties of diamond* (pp. 281—324). London: Academic Press.

Fischer, M., Brescia, R., Gsell, S., Schreck, M., Brugger, T., Greber, T., et al. (2008). Growth of twin-free heteroepitaxial diamond on Ir/YSZ/Si(111). *Journal of Applied Physics, 104*, 123531-1—123531-5.

Fischer, M., Gsell, S., Schreck, M., Brescia, R., & Stritzker, B. (2008). Preparation of 4-inch Ir/YSZ/Si(001) substrates for the large-area deposition of single crystal diamond. *Diamond and Related Materials, 17*, 1035—1038.

Flöter, A., Güttler, H., Schulz, G., Steinbach, D., Lutz-Elsner, C., Zachai, R., et al. (1998). The nucleation and growth of large area, highly oriented diamond films on silicon substrates. *Diamond and Related Materials, 7*, 283—288.

Freund, A. K. (2009). Single-crystal diamond: a potential gem in neutron instrumentation. *Journal of Applied Crystallography, 42*, 36—42.

Freund, A. K., Gsell, S., Fischer, M., Schreck, M., Andersen, K. H., Courtois, P., et al. (2011). Diamond mosaic crystals for neutron instrumentation: first experimental results. *Nuclear Instruments and Methods in Physics Research A, 634*, S28—S36.

Fujii, S., Nishibayashi, Y., Shikata, S., Uedono, A., & Tanigawa, S. (1995). Characterization of diamond single crystals by means of double-crystal X-ray diffraction and positron annihilation. *Applied Physics A, 61*, 331—333.

Fujisaki, T., Tachiki, M., Taniyama, N., Kudo, M., & Kawarada, H. (2003). Initial growth of heteroepitaxial diamond on Ir(001)/MgO(001) substrates using antenna-edge-type microwave plasma assisted chemical vapor deposition. *Diamond and Related Materials, 12*, 246—250.

Furrer, A., Mesot, J., & Strässle, T. (2009). *Neutron scattering in condensed matter physics*. In *Series on neutron techniques and applications* (Vol. 4). New Jersey: World Scientific.

Gsell, S., Bauer, T., Goldfuß, J., Schreck, M., & Stritzker, B. (2004). A route to diamond wafers by epitaxial deposition on silicon via iridium/yttria-stabilized zirconia buffer layers. *Applied Physics Letters, 84*, 4541—4543.

Gsell, S., Berner, S., Brugger, T., Schreck, M., Brescia, R., Fischer, M., et al. (2008). Comparative electron diffraction study of the diamond nucleation layer on Ir(001). *Diamond and Related Materials, 17*, 1029—1034.

Gsell, S., Fischer, M., Brescia, R., Schreck, M., Huber, P., Bayer, F., et al. (2007). Reduction of mosaic spread using iridium interlayers: a route to improved oxide heteroepitaxy on silicon. *Applied Physics Letters, 91*, 061501-1—061501-3.

Gsell, S., Fischer, M., Schreck, M., & Stritzker, B. (2009). Epitaxial films of metals from the platinum group (Ir, Rh, Pt and Ru) on YSZ-buffered Si(111). *Journal of Crystal Growth, 311*, 3731—3736.

Gsell, S., Schreck, M., Benstetter, G., Lodermeier, E., & Stritzker, B. (2007). Combined AFM—SEM study of the diamond nucleation layer on Ir(001). *Diamond and Related Materials, 16*, 665—670.

Gsell, S., Schreck, M., Brescia, R., Stritzker, B., Arendt, P. N., & Groves, J. R. (2008). Iridium on biaxially textured oxide templates: a concept to grow single crystals on arbitrary substrates. *Japanese Journal of Applied Physics, 47*, 8925—8927.

Gsell, S., Schreck, M., & Stritzker, B. (2004). Crystal tilting of diamond heteroepitaxially grown on vicinal Ir/$SrTiO_3$(001). *Journal of Applied Physics, 96*, 1413—1417.

Golding, B., Bednarski-Meinke, C., & Dai, Z. (2004). Diamond heteroepitaxy: pattern formation and mechanisms. *Diamond and Related Materials, 13*, 545—551.

Haubner, R., Lux, B., Gruber, U., & Schuster, J. C. (1999). Diamond deposition on Ni_3Ge single- and polycrystalline substrates. *Diamond and Related Materials, 8*, 246–250.

Hirama, K., Taniyasu, Y., & Kasu, M. (2011). Electroluminescence and capacitance-voltage characteristics of single crystal n-type AlN (0001)/p-type diamond (111) heterojunction diodes. *Applied Physics Letters, 98*, 011908-1–011908-3.

Hirth, J. P., & Lothe, J. (1992). *Theory of dislocations.* Malabar: Krieger.

Hörmann, F., Bauer, Th., Schreck, M., Gsell, S., & Stritzker, B. (2003). TEM analysis of nanometer-size surface structures formed by bias enhanced nucleation of diamond on iridium. *Diamond and Related Materials, 12*, 350–355.

Hörmann, F., Schreck, M., & Stritzker, B. (2001). First stages of diamond nucleation on iridium buffer layers. *Diamond and Related Materials, 10*, 1617–1621.

Hoffman, A., Michaelson, Sh., Akhvlediani, R., Hangaly, N. K., Gsell, S., Brescia, R., et al. (2009). Comparison of diamond bias enhanced nucleation on Ir and 3C-SiC: a high resolution electron energy loss spectroscopy study. *Physica Status Solidi (A), 206*, 1972–1977.

Ickert, L., & Schneider, H. G. (1983). *Wachstum einkristalliner Schichten.* Leipzig: VEB Deutscher Verlag für Grundstoffindustrie (in German).

Ihara, M., Komiyama, H., & Okubo, T. (1994). Correlation between nucleation site density and residual diamond dust density in diamond film deposition. *Applied Physics Letters, 65*, 1192–1194.

Isberg, J., Hammersberg, J., Johansson, E., Wikström, T., Twitchen, D. J., Whitehead, A. J., et al. (2002). High carrier mobility in single-crystal plasma-deposited diamond. *Science, 297*, 1670–1672.

Jain, S. C., Willander, M., Narayan, J., & Van Overstraeten, R. (2000). III-nitrides: growth characterization and properties. *Journal of Applied Physics, 87*, 965–1006.

Jiang, X., & Jia, C. L. (1996). The coalescence of [001] diamond grains heteroepitaxially grown on (001) silicon. *Applied Physics Letters, 69*, 3902–3904.

Jiang, X., Klages, C.-P., Zachai, R., Hartweg, M., & Füsser, H.-J. (1993). Epitaxial diamond thin films on (001) silicon substrates. *Applied Physics Letters, 62*, 3438–3440.

Jiang, X., Paul, M., Klages, C. P., & Jia, C. L. (1995). Studies of heteroepitaxial nucleation and growth of diamond on silicon. In K. K. Ravi, & J. P. Dismukes (Eds.), *Diamond materials IV: Vol. 95-4. Electrochemical society proceedings* (pp. 50–60). Pennington, NJ: The Electrochemical Society, Inc.

Jiang, X., Schiffmann, K., & Klages, C.-P. (1994). Nucleation and initial growth phase of diamond thin films on (100) silicon. *Physical Review B, 50*, 8402–8410.

Jiang, X., Schiffmann, K., Klages, C.-P., Wittorf, D., Jia, C. L., Urban, K., & Jäger, W. (1998). Coalescence and overgrowth of diamond grains for improved heteroepitaxy on silicon (001). *Journal of Applied Physics, 83*, 2511–2518.

Kátai, S., Kováts, A., Maros, I., & Deák, P. (2000). Ion energy distributions and their evolution during bias-enhanced nucleation of chemical vapor deposition of diamond. *Diamond and Related Materials, 9*, 317–321.

Katoh, M., Aoki, M., & Kawarada, H. (1994). Plasma enhanced diamond nucleation on Si. *Japanese Journal of Applied Physics Part 2-Letters, 33*, L194–L196.

Kawarada, H. (1998). Heteroepitaxy and highly oriented diamond deposition. In B. Dischler, & C. Wild (Eds.), *Low-pressure synthetic diamond: manufacturing and applications* (pp. 139–162). Berlin: Springer.

Kawarada, H., Wild, C., Herres, N., Locher, R., Koidl, P., & Nagasawa, H. (1997). Heteroepitaxial growth of highly oriented diamond on cubic silicon carbide. *Journal of Applied Physics, 81*, 3490–3493.

Koizumi, S., Kamo, M., Sato, Y., Ozaki, H., & Inuzuka, T. (1997). Growth and characterization of phosphorous doped {111} homoepitaxial diamond films. *Applied Physics Letters, 71*, 1065–1067.

Koizumi, S., Watanabe, K., Hasegawa, M., & Kanda, H. (2001). Ultraviolet emission from a diamond pn junction. *Science, 292*, 1899–1901.

Kono, S., Shiraishi, M., Plusnin, N. I., Goto, T., Ikejima, Y., Abukawa, T., et al. (2005). X-ray photoelectron diffraction study of the initial stages of CVD diamond heteroepitaxy on Ir(001)/$SrTiO_3$. *New Diamond and Frontier Carbon Technology, 15*, 363–371.

Kono, S., Takano, T., Goto, T., Ikejima, Y., Shiraishi, M., Abukawa, T., et al. (2004). Effect of bias treatment in the CVD diamond growth on Ir(001). *Diamond and Related Materials, 13*, 2081–2087.

Kubovic, M., Aleksov, A., Schreck, M., Bauer, T., Stritzker, B., & Kohn, E. (2003). Field effect transistor fabricated on hydrogen-terminated diamond grown on $SrTiO_3$ substrate and iridium buffer layer. *Diamond and Related Materials, 12*, 403–407.

Kusakabe, K., Sobana, A., Sotowa, K.-I., Imato, T., & Tsubota, T. (2003). Electrical properties of boron-doped diamond films synthesized by MPCVD on an iridium substrate. *Diamond and Related Materials, 12*, 1396–1401.

Lifshitz, Y., Köhler, Th., Frauenheim, Th., Guzmann, I., Hoffman, A., Zhang, R. Q., et al. (2002). The mechanism of diamond nucleation from energetic species. *Science, 297*, 1531–1533.

Liu, H., & Dandy, D. S. (1995). Studies on nucleation process in diamond CVD – an overview of recent developments. *Diamond and Related Materials, 4*, 1173–1188.

Liu, L., & Edgar, J. H. (2002). Substrates for gallium nitride epitaxy. *Materials Science and Engineering R – Reports, 37*, 61–127.

Liu, W., Tucker, D. A., Yang, P., & Glass, J. T. (1995). Nucleation of oriented diamond particles on cobalt substrates. *Journal of Applied Physics, 78*, 1291–1296.

Locher, R., Wild, C., Müller-Sebert, W., Kohl, R., & Koidl, P. (1993). Optical reflection and angle-resolved light scattering from textured polycrystalline diamond films. *Diamond and Related Materials, 2*, 1248–1252.

Lubig, A., Buchal, Ch., Schubert, J., Copetti, C., Guggi, D., Jia, C. L., et al. (1992). Epitaxial growth of $YBa_2Cu_3O_{7-x}$ thin films on Si(100) with zirconia buffers of varying crystalline quality and structure. *Journal of Applied Physics, 71*, 5560–5564.

Maex, K., & van Rossum, M. (Eds.). (1995). In *Properties of metal silicides.* London: INSPEC.

Michler, J., von Kaenel, Y., Stiegler, J., & Blank, E. (1998). Complementary application of electron microscopy and micro-Raman spectroscopy for microstructure, stress, and bonding defect investigation of heteroepitaxial chemical vapor deposited diamond films. *Journal of Applied Physics, 83*, 187–197.

Mokuno, Y., Chayahara, A., Soda, Y., Horino, Y., & Fujimori, N. (2005). Synthesizing single-crystal diamond by repetition of high rate homoepitaxial growth by microwave plasma CVD. *Diamond and Related Materials, 14*, 1743–1746.

Mokuno, Y., Chayahara, A., Yamada, H., & Tsubouchi, N. (2009). Improving purity and size of single-crystal diamond plates produced by high-rate CVD growth and lift-off process using ion implantation. *Diamond and Related Materials, 18*, 1258–1261.

Nassau, K. (1993). Synthesis of bulk diamond: history and present status. In R. F. Davis (Ed.), *Diamond films and coatings* (pp. 31–67). Park Ridge: Noyes Publications.

Ohtsuka, K., Fukuda, H., Suzuki, K., & Sawabe, A. (1997). Fabrication of epitaxial diamond thin film on iridium. *Japanese Journal of Applied Physics Part 2-Letters, 36*, L1214–L1216.

Ohtsuka, K., Suzuki, K., Sawabe, A., & Inuzuka, T. (1996). Epitaxial growth of diamond on iridium. *Japanese Journal of Applied Physics Part 2-Letters, 35*. L1072–L1074.

Pashley, D. W. (1975). A historical review of epitaxy. In J. W. Matthews (Ed.), *Epitaxial growth Part A* (pp. 1–27). New York: Academic Press.

Pehrsson, P. E., Celii, F. G., & Butler, J. E. (1993). Chemical mechanisms of diamond CVD. In R. F. Davis (Ed.), *Diamond films and coatings* (pp. 68–146). Park Ridge: Noyes Publications.

Prelas, M. A., Popovici, G., & Bigelow, L. K. (Eds.). (1998). In *Handbook of industrial diamonds and diamond films*. New York: Marcel Dekker.

Raizer, Y. P. (1991). *Gas discharge physics*. Berlin: Springer.

Ramesh, R., Gilchrist, H., Sands, T., Keramidas, V. G., Haakenaasen, R., & Fork, D. K. (1993). Ferroelectric La–Sr–Co–O/Pb–Zr–Ti–O/La–Sr–Co–O heterostructures on silicon via template growth. *Applied Physics Letters, 63*, 3592–3594.

Robertson, J. (1993). Deposition mechanisms for promoting sp^3 bonding in diamond-like carbon. *Diamond and Related Materials, 2*, 984–989.

Romanov, A. E., & Vladimirov, V. I. (1992). Disclinations in crystalline solids. In F. R. N. Nabarro (Ed.), *Dislocations in solids* (Vol. 9; pp. 191–402). Amsterdam: North Holland.

Romanov, A. E., Pompe, W., Beltz, G., & Speck, J. S. (1996). Model of threading dislocation reduction in heteroepitaxial layers. *Physica Status Solidi (B), 198*, 599–613.

Rubicon (2011). Rubicon Technology Inc., Illinois, US, http://rubicon-es2.com/index.php.

Saito, T., Tsuruga, S., Ohya, N., Kusakabe, K., Morooka, S., Maeda, H., et al. (1998). Epitaxial nucleation of diamond on an iridium substrate by bias treatment, for microwave plasma-assisted chemical vapor deposition. *Diamond and Related Materials, 7*, 1381–1384.

Sato, Y., Yashima, I., Fujita, H., Ando, T., & Kamo, M. (1991). Epitaxial growth of diamond from the gas phase. In R. Messier, J. T. Glass, J. E. Butler, & R. Roy (Eds.), *New diamond science and technology, proceedings of the second international conference* (pp. 371–376). Pittsburg, PA: Materials Research Society.

Sawabe, A., Fukuda, H., Suzuki, T., Ikuhara, Y., & Suzuki, T. (2000). Interface between CVD diamond and iridium films. *Surface Science, 467*, L845–L849.

Sawabe, A., Kodama, H., Washiyama, S., Hitaka, M., Suzuki, K., & Kono, S. (2011). Recent progress in heteroepitaxial growth of diamond on Ir, invited talk at Hasselt Diamond Workshop, Feb. 21–23, 2011, Hasselt, Belgium.

Sawabe, A., Yamada, T., Okamura, H., Katagiri, M., & Suzuki, K. (2002). Epitaxial growth of diamond thin films on Ir(001)/MgO(001) stacking by two-step dc plasma chemical vapor deposition and their characterization. *New Diamond and Frontier Carbon Technology, 12*, 343–353.

Schreck, M. (2009). Heteroepitaxial Growth. In R. S. Sussmann (Ed.), *CVD diamond for electronic devices and sensors* (pp. 125–161). Chichester: Wiley.

Schreck, M., Bauer, Th., Gsell, S., Hörmann, F., Bielefeldt, H., & Stritzker, B. (2003). Domain formation in diamond nucleation on iridium. *Diamond and Related Materials, 12*, 262–267.

Schreck, M., Baur, T., & Stritzker, B. (1995). Optical characterization of the cathode plasma sheath during the biasing step for diamond nucleation on silicon. *Diamond and Related Materials, 4*, 553–558.

Schreck, M., Gsell, S., Brescia, R., Fischer, M., Bernhard, P., Prunici, P., et al. (2009). Diamond nucleation on iridium: local variations of structure and density within the BEN layer. *Diamond and Related Materials, 18*, 107–112.

Schreck, M., Hörmann, F., Gsell, S., Bauer, Th., & Stritzker, B. (2006). Transmission electron microscopy study of the diamond nucleation layer on iridium. *Diamond and Related Materials, 15*, 460–464.

Schreck, M., Hörmann, F., Roll, H., Bauer, T., & Stritzker, B. (2001b). Heteroepitaxial diamond films on silicon substrates and on iridium layers: analogies and differences in nucleation and growth. *New Diamond and Frontier Carbon Technology, 11*, 189–205.

Schreck, M., Hörmann, F., Roll, H., Lindner, J. K. N., & Stritzker, B. (2001). Diamond nucleation on iridium buffer layers and subsequent textured growth: a route for the realization of single-crystal diamond films. *Applied Physics Letters, 78*, 192–194.

Schreck, M., Roll, H., Michler, J., Blank, E., & Stritzker, B. (2000). Stress distribution in thin heteroepitaxial diamond films on Ir/$SrTiO_3$ studied by X-ray diffraction, Raman spectroscopy and finite element simulations. *Journal of Applied Physics, 88*, 2456–2466.

Schreck, M., Roll, H., & Stritzker, B. (1999). Diamond/Ir/$SrTiO_3$, a material combination for improved heteroepitaxial diamond films. *Applied Physics Letters, 74*, 650–652.

Schreck, M., Schury, A., Hörmann, F., Roll, H., & Stritzker, B. (2002). Mosaicity reduction during growth of heteroepitaxial diamond films on iridium buffer layers: experimental results and numerical simulations. *Journal of Applied Physics, 91*, 676–685.

Schreck, M., & Stritzker, B. (1996). Nucleation and growth of heteroepitaxial diamond films on silicon. *Physica Status Solidi (A), 154*, 197–217.

Schreck, M., Thürer, K.-H., & Stritzker, B. (1997). Limitations of the process time window for the bias enhanced nucleation of heteroepitaxial diamond films on silicon in the time domain. *Journal of Applied Physics, 81*, 3092–3095.

Shintani, Y. (1996). Growth of highly (111)-oriented, highly coalesced diamond films on platinum (111) surface: a possibility of heteroepitaxy. *Journal of Materials Research, 11*, 2955–2956.

Stolz, A., Behravan, M., Regmi, M., & Golding, B. (2006). Heteroepitaxial diamond detectors for heavy ion beam tracking. *Diamond and Related Materials, 15*, 807–810.

Stoner, B. R., & Glass, J. T. (1992). Textured diamond growth on (001) β-SiC via microwave plasma chemical vapor deposition. *Applied Physics Letters, 60*, 698–700.

Stoner, B. R., Kao, C. T., Malta, D. M., & Glass, R. C. (1993). Hall effect measurements on boron-doped, highly oriented diamond films grown on silicon via microwave plasma chemical vapour deposition. *Applied Physics Letters, 62*, 2347–2349.

Stoner, B. R., Ma, G. H., Wolter, S. D., Zhu, W., Wang, Y.-C., Davis, R. F., et al. (1993). Epitaxial nucleation of diamond on β-SiC via bias-enhanced microwave plasma chemical vapor deposition. *Diamond and Related Materials, 2*, 142–146.

Stubhan, F., Ferguson, M., Füsser, H.-J., & Behm, R. J. (1995). Heteroepitaxial nucleation of diamond on Si(001) in hot filament chemical vapor deposition. *Applied Physics Letters, 66*, 1900–1902.

Suesada, T., Nakamura, N., Nagasawa, H., & Kawarada, H. (1995). Initial growth of heteroepitaxial diamond on Si(001) substrates via β-SiC buffer layers. *Japanese Journal of Applied Physics, 34*, 4898–4904.

Suzuki, T., Yagi, M., & Shibuki, K. (1994). Growth of oriented diamond particles on 6H-type of SiC and graphite flakes. In S. Saito, N. Fujimori, O. Fukunaga, M. Kamo, K. Kobashi, & M. Yoshikawa (Eds.), *Advances in new diamond science and technology* (pp. 271–274). Tokyo: MYU.

Tachibana, T., Yokota, Y., Hayashi, K., & Kobashi, K. (2001). Growth of {111}-oriented diamond on Pt/Ir/Pt substrate deposited on sapphire. *Diamond and Related Materials, 10*, 1633—1636.

Tachibana, T., Yokota, Y., Kobashi, K., & Shintani, Y. (1997). X-ray diffraction pole figure measurements of diamond films grown on platinum (111). *Journal of Applied Physics, 82*, 4327—4330.

Tachibana, T., Yokota, Y., Miyata, K., Onishi, T., Kobashi, K., Tarutani, M., et al. (1997). Diamond films heteroepitaxially grown on platinum (111). *Phys Rev. B, 56*, 15967—15981.

Tachibana, T., Yokota, Y., Nishimura, K., Miyata, K., Kobashi, K., & Shintani, Y. (1996). Heteroepitaxial diamond growth on platinum (111) by the Shintani process. *Diamond and Related Materials, 5*, 197—199.

Ternyak, O., Cheifetz, E., Shchemelinin, S., Breskin, A., Chechik, R., Zhang, H., et al. (2007). Ion-induced electron emission (IIEE) from undoped and B-doped diamond films induced by 1—10 KeV H^+ and Ar^+. *Diamond and Related Materials, 16*, 861—866.

Thürer, K.-H., Schreck, M., & Stritzker, B. (1998). Limiting processes for diamond epitaxial alignment on silicon. *Physical Review B, 57*, 15454—15464.

Tsubota, T., Ohta, M., Kusakabe, K., Morooka, S., Watanabe, M., & Maeda, H. (2000). Heteroepitaxial growth of diamond on an iridium (100) substrate using microwave plasma-assisted chemical vapor deposition. *Diamond and Related Materials, 9*, 1380—1387.

Tucker, D. A., Seo, D.-K., Whangbo, M.-H., Sivazlian, F. R., Stoner, B. R., Bozeman, S. P., et al. (1995). Comparison of silicon, nickel, and nickel silicide (Ni_3Si) as substrates for epitaxial diamond growth. *Surface Science, 334*, 179—194.

Van der Drift, A. (1967). Evolutionary selection, a principle governing growth orientation in vapour-deposited layers. *Philips Research Reports, 22*, 267—288.

Venables, J. A., Spiller, G. D. T., & Hanbrücken, M. (1984). Nucleation and growth of thin films. *Reports on Progress in Physics, 47*, 399—459.

Warren, B. E. (1990). *X-ray diffraction*. New York: Dover Publications.

Wild, C., Kohl, R., Herres, N., Müller-Sebert, W., & Koidl, P. (1994). Oriented CVD diamond films: twin formation, structure and morphology. *Diamond and Related Materials, 3*, 373—381.

Wild, C., Koidl, P., Müller-Sebert, W., Walcher, H., Kohl, R., Herres, N., et al. (1993). Chemical vapor deposition and characterization of smooth {100}-faceted diamond films. *Diamond and Related Materials, 2*, 158—168.

Williams, O. A., Douheret, O., Daenen, M., Haenen, K., Osawa, E., & Takahashi, M. (2007). Enhanced diamond nucleation on monodispersed nanocrystalline diamond. *Chemical Physics Letters, 445*, 255—258.

Wolter, S. D., McClure, M. T., Glass, J. T., & Stoner, B. R. (1995). Bias enhanced nucleation of highly oriented diamond on titanium carbide (111) substrates. *Applied Physics Letters, 66*, 2810—2812.

Wolter, S. D., Borst, T. H., Vescan, A., & Kohn, E. (1996). The nucleation of highly oriented diamond on silicon via an alternating current substrate bias. *Applied Physics Letters, 68*, 3558—3560.

Wu, Y., Qi, J., Lee, C. H., Hung, L. S., Zhang, W. J., Bello, I., et al. (2003). Diamond growth on Ir/CaF_2/Si substrates. *Diamond and Related Materials, 12*, 1675—1680.

Yamada, H., Chayahara, A., Mokuno, Y., Umezawa, H., Shikata, S., & Fujimori, N. (2010). Fabrication of 1 inch mosaic crystal diamond wafers. *Applied Physics Express, 3*, 051301-1—051301-3.

Yamada, T., Maede, J., & Sawabe, A. (1999). Electron emission from a heteroepitaxial diamond planar emitter. *Japanese Journal of Applied Physics Part 2-Letters, 38*, L902—L903.

Yan, C. S., Vohra, Y. K., Mao, H. K., & Hemley, R. J. (2002). Very high growth rate chemical vapor deposition of single-crystal diamond. *Proceedings of the National Academy of Sciences of the United States of America, 99*, 12523—12525.

Yang, P. C., Zhu, W., & Glass, J. T. (1993). Nucleation of oriented diamond films on nickel substrates. *Journal of Materials Research, 8*, 1773—1776.

Yokota, Y., Kawakami, N., Maeda, S., Ando, Y., Tachibana, T., Kobashi, K., & Sawabe, A. (2007). Device operation of p+-i-p+ diamond metal-insulator-semiconductor field-effect transistors on heteroepitaxial diamond films grown on Ir(001)/MgO(001). *New Diamond and Frontier Carbon Technology, 17*, 211—217.

Yoshimoto, M., Yoshida, K., Maruta, H., Hishitani, Y., Koinuma, H., Nishio, S., et al. (1999). Epitaxial diamond growth on sapphire in an oxidizing environment. *Nature, 399*, 340—342.

Yugo, S., Kanai, T., Kimura, T., & Muto, T. (1991). Generation of diamond nuclei by electric field in plasma chemical vapor deposition. *Applied Physics Letters, 58*, 1036—1038.

Zaiser, M., Lyutovich, Y., & Banhart, F. (2000). Irradiation-induced transformation of graphite to diamond: a quantitative study. *Physical Review B, 62*, 3058—3064.

Zhang, W. J., Sun, X. S., Peng, H. Y., Wang, N., Lee, C. S., Bello, I., et al. (2000). Diamond nucleation enhancement by direct low-energy ion-beam deposition. *Physical Review B, 61*, 5579—5586.

Zheleva, T. S., Nam, O.-H., & Davis, R. F. (1999). Lateral epitaxy and microstructure in selectively grown GaN on SiC substrates. In J. H. Edgar, S. Strite, I. Akasaki, H. Amano, & C. Wetzel (Eds.), *Properties, processing and applications of gallium nitride and related semiconductors. EMIS datareviews series no. 23* (pp. 447—453). London: INSPEC.

Zhou, X. T., Lai, H. L., Peng, H. Y., Sun, C., Zhang, W. J., Wang, N., et al. (2000). Heteroepitaxial nucleation of diamond Si(001) via double bias-assisted hot filament chemical vapor deposition. *Diamond and Related Materials, 9*, 134—139.

Zhu, W., Yang, P. C., & Glass, J. T. (1993). Oriented diamond films grown on nickel substrates. *Applied Physics Letters, 63*, 1640—1642.

3.12 Conductivity and Impurity Doping on Single Crystal Diamond

Hiromitsu Kato, Energy Technology Research Institute, AIST, Japan

Glossary

Compensation ratio Ideal semiconductor has only one type of carrier, i.e. electrons or holes, whereas general semiconductor has both carriers, which is called a “compensated semiconductor”. The electron density N_D is larger than the hole density N_A, i.e. $N_D - N_A > 0$, and the semiconductor shows the n-type conductivity, whereas it shows p-type conductivity when $N_A - N_D > 0$. The compensation ratio η is given by the ratio N_A/N_D for an n-type material and by N_D/N_A for a p-type, which should be quite less than 1.

Hall effect measurement Most important tool to identify the semiconductor properties of carrier type, carrier concentration, and mobility. The direction of current flow under the applied magnetic field identifies whether the major carrier is hole or electron according to the Lorentz force. The voltage is proportional to the current and the field and inversely proportional to the thickness in the direction of the magnetic field. $V \sim RIH/t$, where I is the current, H is the magnetic field, t is the thickness, V is the Hall voltage, and R is the Hall coefficient.

Plasma-enhanced chemical vapor deposition A major process to deposit thin films from a gas mixture (vapor) to a solid state on a substrate. Chemical reactions of source gas mixtures are enhanced by plasma, which effectively creates reacting gases of radicals and deposits several materials such as semiconductor, insulator, and metals. Microwave plasma of 2.45 GHz is generally used for diamond growth from hydrocarbon gas mixtures.

3.12.1 Homoepitaxial Growth of Single Crystal Diamond

Homoepitaxial diamond growth is usually obtained via plasma-enhanced chemical vapor deposition (PECVD) using 2.45 GHz microwaves and a source gas mixture of hydrogen H_2 and methane CH_4. Commercially available high-pressure and high-temperature (HPHT)-synthesized single-crystal diamond plates are used as the substrate. A typical PECVD system with a schematic description focusing on the plasma during chemical vapor deposition (CVD) diamond growth is shown in Figure 1. Methane is introduced into the hydrogen plasma and is decomposed to active radicals for diamond growth. Some of these radicals covalently bond on surface of the diamond substrate giving rise to homoepitaxial diamond growth. The typical growth temperature is approximately 800 °C (700–900 °C), using a methane to hydrogen ratio (CH_4/H_2) ranging from 1% to 5%. The majority of the plasma contains hydrogen-related species, which make the microwave plasma uniform and remove graphitic sp^2 bonds from the surface of the deposited diamond. Hydrogen is essential for diamond growth by PECVD, while the precursors for diamond growth have been identified to be CH_3 radicals (Lombardi, Hassouni, Stancu, Mechold, Ropcke, et al., 2005). The formation ratio of CH_3 radicals strongly depends on plasma density, which is defined by the input power of microwaves divided by the volume of the plasma. A larger plasma density is preferable to obtain a higher growth rate with good crystallinity (Achard, Tallaire, Sussmann, Silva, & Gicquel, 2005).

http://dx.doi.org/10.1016/B978-0-08-096527-7.00049-0

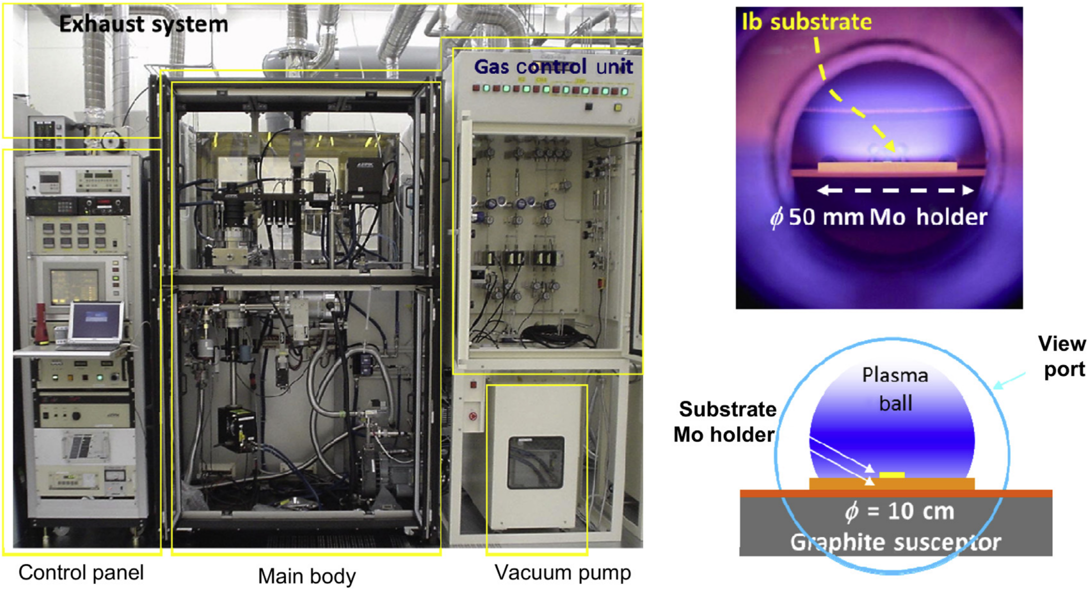

Figure 1 Pictures and schematic descriptions of a typical PECVD machine. The reactor consists of a 6-inch stainless-steel chamber, microwave generator with maximum output power of 1.5 kW, waveguide, tuner, and vacuum setup. The base pressure of the system can be decreased to 1×10^{-8} Torr by a turbo molecular pump with an oil-free scroll pump. An oil-free scroll pump is also equipped for CVD process. The gas flow rate is controlled independently by mass flow controllers. The substrate temperature is measured by optical pyrometer from the top quartz window through the plasma and the plasma conditions were monitored by optical emission spectroscopy (OES). The temperature and the plasma emission were confirmed to be stable during CVD growth.

The microwave plasma can be characterized by optical emission spectroscopy (OES). Figure 2 shows the OES spectra obtained for two different plasma densities of 5 W/cm^3 (a) and 50 W/cm^3 (b). In the case of low plasma density in Figure 2(a), the plasma mainly consists of hydrogen-related lines of Hα, Hβ, and H_2 molecules, since the decomposition of the gas mixtures proceeds weakly. Few components, with low intensities, related to methane can be detected. On the other hand, the plasma components are drastically changed in case of high-density conditions as shown in Figure 2(b). The carbon-related peaks of CH and C_2 lines become sharp and strong, and the peaks of H_2 molecules disappear. CH_3 unfortunately is a nonradiative radical. While the increments of CH and C_2 peaks support the enhancement of CH_4 decomposition by higher plasma density, the resultant growth rate is around several micrometers per hour, which is roughly ten times higher than that in low plasma density around 5 W/cm^3.

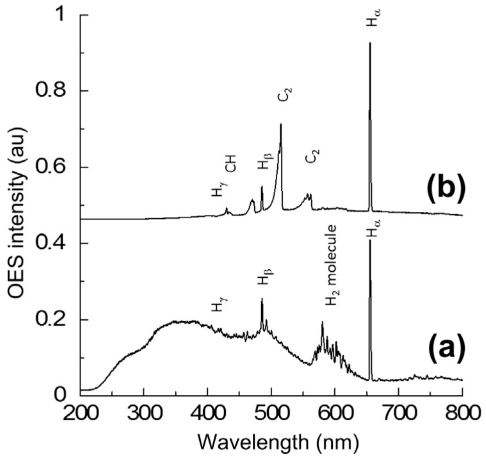

Figure 2 Optical emission spectra from microwave plasma during homoepitaxial diamond growth: (a) plasma density of 5 W/cm^3 and (b) 50 W/cm^3. Hydrogen atomic lines Hα (656.3 nm), Hβ (486.1 nm), and Hγ (434.0 nm) and H_2 molecular lines (570–620 nm), CH (430 nm), and C_2 swan lines (470, 517, and 558 nm) are observed. All peaks are identified by Pearse and Gaydon (1976).

The surface morphology of the deposited diamond varies with the plasma and substrate conditions. Nonepitaxial crystallites (NCs) and pyramidal hillocks (PHs) are typical growth defect structures on homoepitaxial CVD diamond. The origin of NCs is considered to be particles in the plasma. Therefore, they can be suppressed by enhancing the decomposition of gas mixtures using high-power plasma conditions or a decrease in the methane ratio to less than 0.1% at low-power conditions. The surface contamination of the initial substrate also influences NC formation. The following pretreatment is effective to obtain a well-defined surface. First, the substrate is boiled in an acid mixture ($H_2SO_4/H_2O_2/H_2O = 3/1/1$) at 220 °C for 15 min to remove organic and metallic contaminations, followed by a HF treatment for 5 min to remove SiO_2 and related contaminations, and then the substrate is again boiled in SC1 ($NH_4OH/H_2O_2/H_2O = 1/1/5$) at 75 °C for 15 min and washed in deionized water to finish the cleaning procedure.

PHs arise from spiral growth at structural defects, including initial crystal defects and/or those created by mechanical polishing. Polishing damage can be removed by oxygen plasma etching before the initiation of CVD deposition. For intrinsic diamond growth, the formation of PHs is prevented by oxygen plasma etching (Tallaire, Achard, Silva, Sussmann, Gicquel, et al, 2004) and higher carrier mobility can be observed in CVD n-type diamond film (Tavares, Koizumi, & Kanda, 2005). However, not all substrate defects can be removed by such plasma treatments. Spiral growth starts at surface defects, which are atomic steps and therefore growth sites. This enhances vertical diamond growth, resulting in the formation of PHs on the (001) substrate. One possibility to suppress the formation of hillocks is the enhancement of lateral growth along the crystal orientation which is faster than the vertical growth by application of higher plasma densities and/or high misorientation angles of the initial substrate. The precise optimization of both plasma and substrate conditions are essential for realizing good homoepitaxial diamond growth, as shown in Figure 3(c). The impurity doping is no exception.

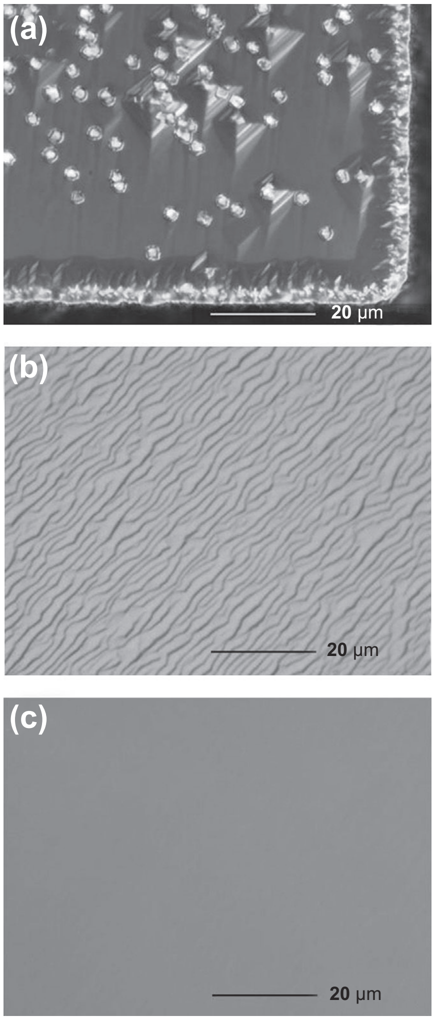

Figure 3 Surface morphologies of homoepitaxial grown diamond. (a) Nonepitaxial crystallites and pyramidal hillocks, (b) macrobunching steps, and (c) well-defined surface without macroscopic structures.

3.12.2 Impurity Doping by PECVD

3.12.2.1 Progress in Impurity Doping

In the case of standard semiconductors represented by silicon, Si, impurity doping is usually applied by ion implantation with postannealing processing. This doping process enables doping density variations over orders of magnitudes, with different depth profiles and areas, simply by controlling the acceleration voltage of the source ion beam and the operation time. On the other hand, impurity doping by ion implantation has not been well established in diamond, since carbon sp^3 bonds (diamond bonds) are metastable; therefore, the created defects tends to reconstruct to the stable graphite phase (sp^2 bonds) by postannealing processing. However, cold implantation and rapid annealing processes such as Cold Implantation Rapid Annealing (CIRA) (Kalish, 1997; Prins, 2002) and HPHT (Ueda & Kasu, 2008) processes can activate the implanted boron atoms in diamond; the activation ratio of dopants by these methods have been reported to be much smaller than that for doping during the growth of diamond.

In the 1980s, the CVD of diamond using microwave plasmas (Kamo, Sato, Matsumoto, & Setaka, 1983) was invented. Since then, many studies have been carried out on intrinsic diamond growth and on p- and n-type doping by PECVD. For p-type diamond, the impurity boron, B, is easily incorporated into both natural and synthetic diamond by PECVD without any restriction with respect to crystal orientation. The boron acceptor level was determined to be ~0.37 eV above the top of the valence band. The quality of boron-doped CVD diamond has now reached a maximum mobility of ~1800 cm^2/Vs at room temperature as determined by Hall effect measurements (Yamanaka, Watanabe, Masai, Takeuchi, Okushi, et al., 1998).

On the other hand, n-type diamond is not present in nature, and controlled n-type doping had been considered almost impossible until 1997. Among the group V elements, nitrogen was one of the candidates for n-type doping because of its similar covalent bond length (0.74 Å) to diamond (0.77 Å). However, unfortunately, nitrogen forms a deep defect level at ~1.7 eV below the bottom of the conduction band, due to its structural distortion from the substitutional position in the diamond lattice (Farrer, 1969).

Phosphorus, P, has long been considered as another candidate for n-type doping. In the 1990s, considerable efforts of phosphorus doping were reported by hot-filament CVD (Okano, Kiyota, Iwasaki, Nakamura, Akiba, et al., 1990) and PECVD (Saito, Kameta, Kusakabe, Morooka, Maeda, et al., 1998), but all doping experiments failed, including those on polycrystalline diamond. Even in the case of partial incorporation of phosphorus, films showed very high resistivity due to coincorporation of hydrogen along with phosphorus atoms. Hydrogen atoms are negatively charges in n-type diamond and easily form complexes with positively charged phosphorus donors (Goss, Jones, Heggie, Ewels, Briddon, et al., 2002). Since P–H complexes are electrically inactive, coincorporation of hydrogen must be suppressed to achieve n-type doping. In addition, as phosphorus atoms are incorporated into the substitutional site, structural distortions should occur due to degradation of the site symmetry caused by the difference in covalent bond length between phosphorus (1.10 Å) and carbon (0.77 Å). Such size mismatch indicates that some native defects and structural displacement will accompany phosphorus incorporation, which was also an argument used to prevent diamond n-type doping for a long time.

In 1997, Koizumi et al. (Koizumi, Kamo, Sato, Ozaki, & Inuzuka, 1997) experimentally demonstrated the growth of n-type diamond on (111)-oriented diamond substrates by PECVD using a mixture of PH_3, CH_4, and H_2 gases. Following this success, much effort was devoted to growing high-quality phosphorus-doped n-type diamond films, and in 2005, n-type diamond on (001)-oriented diamond as well as on (111)-oriented diamond (Kato, Yamasaki, & Okushi, 2005a, 2005b) were achieved. The phosphorus donor level was determined to be ~0.57 eV below the bottom of the conduction band. The quality of phosphorus-doped diamond has now reached a maximum mobility of around 700 cm^2/Vs at room temperature as determined by Hall effect measurements (Katagiri, Isoya, & Kanda, 2004; Kato, Makino, Yamasaki, & Okushi, 2008; Kato, Umezawa, Tokuda, Takeuchi, Okushi, et al., 2008).

Phosphorus doping (n-type doping) without any restriction with respect to substrate orientation has finally been achieved. A search for shallower donor dopants than phosphorus (0.57 eV) is, however, still ongoing. Arsenic and antimony are candidates for n-type shallow dopant, which has been calculated to be ~0.3 and ~0.2 eV below the conduction band, respectively (Sque, Jones, Goss, & Briddon, 2004). The covalent bond lengths of these atoms (As: 1.21 Å, Sb: 1.41 Å) are much larger than those of carbon, resulting in low solubility. The reported donor level of arsenic is about 0.95 eV below the conduction band, which is much deeper than expected (Kasu & Kubovic, 2010).

Another possibility to achieve shallow doping is the utilization of interstitial doping with Li or Na atoms (Kajihara, Antonelli, & Bernholc, 1993). The calculated donor levels are ~0.1 eV for Li and ~0.2 eV for Na.

These atoms are, however, not so easy to use in PECVD. There have been some experimental results from Li and Na ion implantations; however the origin of conductivity has not been identified up to now. Codoping is also an important candidate, for example, boron–sulfur codoping, oxygen–nitrogen pairs, nitrogen–aluminum–nitrogen or nitrogen–silicon–nitrogen clusters, etc. (Anderson, Grantscharova, & Angus, 1996). Theoretical calculations indicated several possibilities to achieve shallow doping; however, most are not applicable experimentally. In addition, the formation energy of these complexes needs to be considered. The boron–hydrogen and boron–deuterium complexes have shown interesting phenomena, where boron-doped p-type diamond converted to n-type diamond by the formation of hydrogen or deuterium complexes (Saguy, Kalish, Cytermann, Teukamb, Chevallier, et al., 2004). Although the estimated donor level of 0.34 eV is shallower than that of phosphorus-doped diamond, the experimental results remain questionable. The most reliable acceptor and donor states in diamond are still boron and phosphorus, respectively.

3.12.2.2 Process Window of p- and n-Type Diamond

In order to achieve doped diamond with p- or n-type conductivity by PECVD, a dopant gas is introduced into the gas mixtures of H_2 and CH_4 during the homoepitaxial growth. The dopant gas is decomposed by the H_2 plasma and partially incorporated into the growing diamond. The decomposition and the reaction depend on the dopant gas. The selection of a suitable dopant gas is one of the important topics in CVD doping technology. Diborane (B_2H_6) or trimethylboron (TMB) diluted by H_2 gas and phosphine (PH_3), tertiary-butylphosphine (TBP:$P(C_4H_9)H_2$), or trimethylphosphine (TMP:$P(CH_3)_3$) diluted by H_2 gas are candidates for p- and n-type, respectively.

Chemical properties of TBP, TMP, and phosphine are summarized in **Table 1**. The molecular structure of TBP is asymmetrical with respect to phosphorus, whereas that of TMP is symmetrical, similar to PH_3. Such a difference is expected to produce a difference in decomposition and the doping incorporation ratio of phosphorus atoms. TBP and TMP are usually in liquid phase at room temperature and their vapor pressure is significantly lower than that of PH_3. Comparing the decomposition kinetics between organic (TBP and TMP) and hydride (PH_3) molecules, the most obvious difference is the lower decomposition temperature of organophosphorus (Hill, Gedridge, Groshens, Stringfellow, & Sadwick, 1996). The purity of organic sources is usually inferior to that of hydrides.

The incorporation efficiency and electrical and optical properties of phosphorus-doped diamond films have been investigated using these three different doping gases. The results show that there is almost no difference among them (Kato et al., 2005a, 2005b). This indicates that for diamond growth and phosphorus doping, the plasma-induced decomposition of TBP, TMP, and PH_3 is comparable, giving rise to comparable doping

Table 1 Chemical properties of tertiary-butylphosphine, trimethylphosphine, and phosphine

Chemical name	Tertiary-butylphosphine	Trimethylphosphine	Phosphine
Formula	t-$P(C_4H_9)H_2$	$P(CH_3)_3$	PH_3
Appearance	Colorless liquid	Colorless liquid	Colorless gas
Melting point	4.0 °C	−85 °C	−133 °C
Boiling point	56.1 °C	37.8 °C	−87 °C
Decomposition temp.	~800 K	–	~1200 K
Toxicity (LC_{50})	~1100 ppm/4 h	–	~11ppm/4 h
Impurity content	~1 ppm	~1 ppm	<1 ppm (Detection Lim)
	Asymmetry	Symmetry	Symmetry
	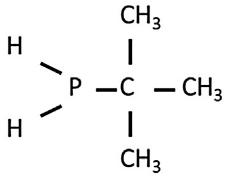	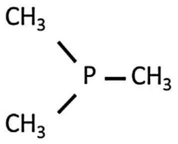	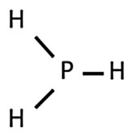
	Organic	Organic	Hydride

properties. Usually, the gas temperature is a key parameter for the molecular decomposition process. It has been reported that the gas temperature, which means neutral and ionized molecule temperatures, exceeds ~2000 K during the growth of CVD diamond (Hassouni, Grotjohn, & Gicquel, 1999). The thermal decomposition of TBP was reported to start at about 800 K and that of TMP is as low as that of TBP. Even for PH_3, it was reported to start about 1200 K. Thermal decomposition temperatures of three gases are much lower than gas temperature during CVD growth. This comparison between gas temperature and decomposition temperatures supports the presented results. That is also the case for boron doping using diborane or TMB.

Since phosphine and diborane are generally used in the field of semiconductor technology and/or fabrication of III–V semiconductors, their purity is higher than that of organic dopant gases. Therefore, hydride dopant source gases are favorably used for high-quality doping of CVD diamond films. On the other hand, TBP and TMP are usually in the liquid phase at room temperature and their vapor pressure is significantly lower than that of PH_3. This means that TBP and TMP have a safety advantage over PH_3 due to several orders of magnitude lower toxicity. However, organic source are difficult to supply with high phosphorus concentration in the gas phase because of their lower vapor phase pressure. With this point of view, PH_3 and B_2H_6 gases would be suitable as dopant gases due to their higher purity and possible higher dopant concentration.

Figure 4 shows the typical CVD process cycles for p- and n-type doping of CVD diamond using PH_3 and B_2H_6 dopant gases for differently oriented diamond substrates like (001) and (111). It shows the relation of dopant gas concentration for p- and n-type doping as a function of CH_4/H_2 ratio for (001) and (111)-oriented diamonds. It is noteworthy that the plasma power is constant at 750 W. The parameters for (111) phosphorus and boron doping are quite similar, whereas only (001) phosphorus doping requires unique parameters. The incorporation efficiencies for (111) phosphorus and boron doping, which is the ratio [P]/[C] in the diamond film to [dopant]/[CH_4] in the gas phase, is estimated to be 10^{-2}, whereas for (001)-oriented diamond the phosphorus incorporation is 10^{-4}, which is two orders of magnitude smaller than for (111) substrates.

According to numerical calculations, the formation energy of substitutional phosphorus atoms on the surface is much smaller than that in the bulk, which suggests that phosphorus atoms have a tendency of segregation close to the surfaces (Miyazaki, Kato, Ri, Ogura, Tokuda, et al., 2006), like, for example, antimony doping in silicon. This tendency on (001) surfaces is much stronger than on (111). Segregation arises from the difference in covalent bond length between phosphorus and carbon. The temperature dependence of phosphorus flux in addition reveals interesting information. The flux represents the ratio of phosphorus atoms propagating through the surface of the growing film per unit area and per time. For (111) doping, the temperature dependence of the flux is weaker, while for (001), the flux decreases significantly with increasing growth temperature. This means that the thermal stability of adsorbed phosphorus atoms on (001) surface is weaker than that on (111). The surface segregation effect and low thermal stability are responsible for the low incorporation efficiency of (001)-oriented diamond for phosphorus doping.

The impurity concentration in the film increases proportionally to the dopant density in the gas phase. The range of boron doping varies between 10^{15} and 10^{21} cm^{-3} without any restriction due to substrate orientation.

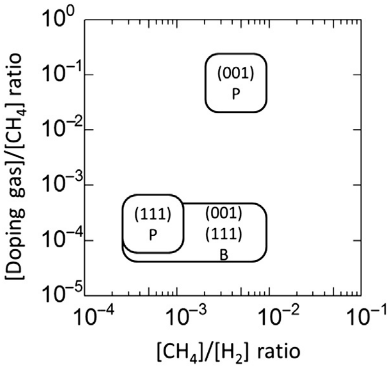

Figure 4 CVD process for phosphorus and boron doping of CVD diamond, focusing on relationship between CH_4/H_2 ratio and doping gas concentration (PH_3/CH_4, B_2H_6/CH_4). These parameters represent values that give rise to carrier conduction in the conduction or valence bands, where carries are generated by thermal excitation from donor or acceptor state as shown in **Figure 8**. It is important to note that for an extremely high doping level ("metallic doping regime"), which results in optimized hopping conduction in the donor or acceptor state, different parameters must be implemented.

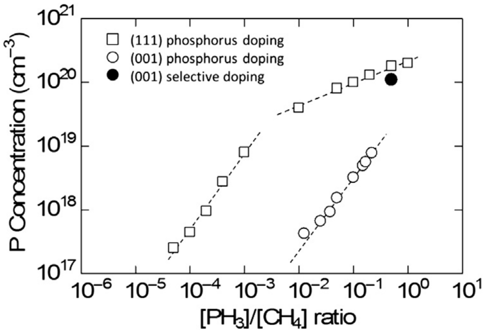

Figure 5 The controllable doping level of phosphorus both for (001) and (111)-oriented diamond. Open circles and rectangles represent data obtained for phosphorus doping on (001) and (111), respectively. The solid circles indicate the data for (001) phosphorus-doped diamond grown by selective growth technique. The broken lines are the results of the least-squares fitting to the data with $y \sim ([PH_3]/[CH_4])^x$.

This is not the case for phosphorus doping. Figure 5 shows changes in phosphorus concentrations in the diamond films as a function of the [PH$_3$]/[CH$_4$] ratio in the gas phase. The controllable range of phosphorus incorporation in (111) diamond is between $\sim 5 \times 10^{17}$ and $\sim 2 \times 10^{20}$ cm^{-3}, whereas for (001)-oriented diamond, it is smaller and between $\sim 5 \times 10^{17}$ and $\sim 8 \times 10^{18}$ cm^{-3}. In the lower regime up to $\sim 10^{19}$ cm^{-3}, phosphorus incorporation follows proportionally to the increase in [PH$_3$]/[CH$_4$] ratio in the gas phase as detected both for (001) and (111) diamond. For doping higher than $\sim 10^{19}$ cm^{-3}, the increase is sublinear with a gentle slope around $x \sim 0.35$. Such a tendency has also been reported for phosphorus doping of silicon. This saturation effect of incorporation as well as the lower incorporation efficiency prevents (001) diamond from being heavily doped with phosphorus.

To overcome the lower incorporation efficiency of phosphorus in (001)-oriented diamond, a selective growth technique using patterned (001) diamond has been proposed. In this approach, the growth and doping are controlled by using patterned surface morphologies of (001)-oriented diamond, which gives rise to growth along the ⟨111⟩ direction. This gives rise to heavily doped diamond directly on (001) n-type diamond film (Kato, Makino, Ogura, Tokuda, Okushi, et al., 2009).

Figure 6 shows the detailed procedures for fabricating n$^+$ diamond on (001) n-type diamond. First, a conventional phosphorus-doped n-type diamond is deposited on a (001)-oriented Ib substrate by CVD. Square trench structures with line-and-space patterns along the ⟨110⟩ direction were then fabricated on the

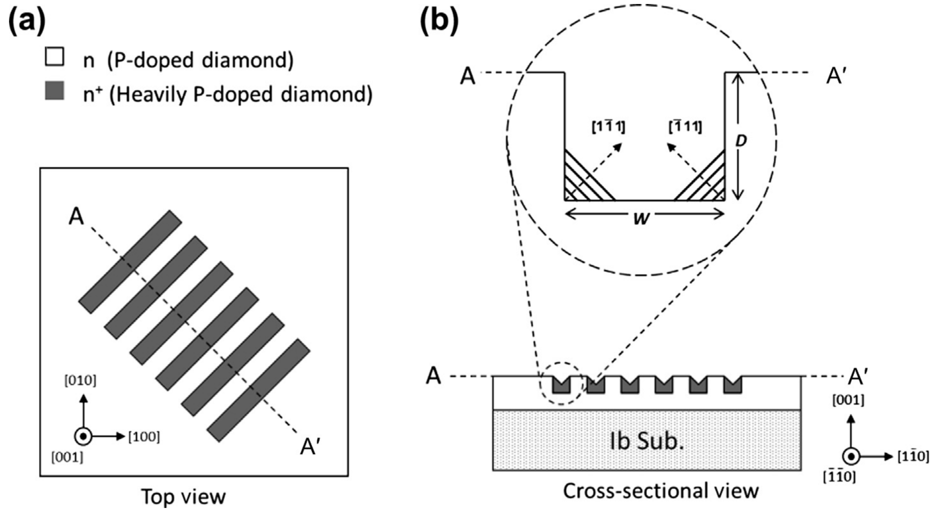

Figure 6 Schematic top (left) and cross-sectional (right) views of the selective growth process. First, conventional phosphorus-doped n-type diamond is grown on a (001)-oriented Ib substrate followed by the fabrication of a line-and-space trench structure. The selective growth of buried n$^+$ diamond starts at the bottom corners of fabricated trenches. A detailed image of the trench structure and ⟨111⟩ selective growth are shown in the dashed circle.

surface of (001) n-type diamond by the Inductive Coupled Plasma (ICP) etching process. Selective ⟨111⟩ direction growth was then performed by using the optimized (111) growth conditions, which resulted in the formation of a buried n^+ diamond. The selective growth begins at crossing lines between trench bottom and trench side, i.e. trench corners. The ⟨111⟩ growth dominates and enables high-efficiency phosphorus doping even of (001) diamond. The depth profile of the selectively grown (001) phosphorus-doped diamond film was evaluated by Secondary Ion Mass Spectroscopy (SIMS) analysis. The depth distribution of phosphorus is not uniform, but the phosphorus concentration is about 1×10^{20} cm^{-3} as expected.

Heavily doping on (001) diamond has been a major issue owing to its much lower phosphorus incorporation efficiency, which is two orders of magnitude lower than that on (111). Namba et al. proposed a phosphorus doping process using (111) faces fabricated on the (001)-oriented substrate (Namba, Tatsumi, Yamamoto, Nishibayashi, & Imai, 2005). In their process, phosphorus doping was performed on the buffer layer of fabricated (111) faces, but not directly on the (001) surface. This selective growth method as shown in **Figure 6**, enables high-efficiency phosphorus doping directly on (001) diamond and is one of the solutions without any buffer layers.

3.12.3 Electronic Properties

The covalent bond length of boron, carbon, nitrogen, and phosphorus are 0.80, 0.74, 0.77, and 1.10 Å, respectively. As phosphorus atoms are incorporated, substitutional, structural distortions should occur due to the degradation of the site symmetry caused by such difference in covalent bond length between phosphorus and carbon. Even nitrogen, which has almost similar covalent bond length compared to diamond, structural distortions occur along the ⟨111⟩ directions due to the Jahn–Teller effect. The electronic structure of phosphorus in the diamond lattice has been investigated by theoretical calculation and experimental studies using electron spin resonance (ESR) analysis. The calculations indicate that the site symmetry of phosphorus is trigonal $C^3{}_V$ due to the Jahn–Teller effect or tetrahedral T_d, whereas tetragonal $D^2{}_d$ is revealed by the ESR studies of (111) phosphorus-doped diamond (Katagiri, et al., 2004; Katagiri, Isoya, Koizumi, & Kanda, 2004). The phosphorus donor level in diamond was experimentally detected to be 0.57 eV below the conduction band. This is much deeper than the calculated values of 0.2–0.4 eV. The difference might relate to the model of structural distortion as mentioned above.

Spectroscopic characterization of diamond has been used to identify the electronic fine structure of dopants at very low concentrations. From constant photocurrent and optical absorption spectroscopy in the infrared regime, typical absorption bands related to acceptor and donor levels in diamond are observed. The main absorption features of boron-doped diamond are a boron-induced one-phonon absorption around 160 meV, followed by a series of three lines at 300, 350, and 360 meV due to transitions of electrons from the ground to excited state (Gheeraert, Koizumi, Teraji, Kanda, & Nesladek, 1999). Each absorption has a linear relationship to the boron concentration in the films. A strong increase in the photoionization cross-section for boron concentration above 5×10^{18} cm^{-3} is observed.

The absorption features of phosphorus-doped diamond show four excited states around 523, 565, 575, and 584 meV obtained by the quasi-steady-state photocurrent technique and photothermal ionization spectroscopy (Nesladek, 2005). These peaks can be reproduced by numerical calculations using the longitudinal optical (LO) phonon values of 155 meV, which corresponds to phonons at the conduction band minimum, positioned along the *d*-axis of the diamond band structure in ⟨100⟩ direction (Haenen, Meykens, Nesladek, Knuyt, Stals, et al., 2000).

Figure 7 shows typical cathodoluminescence spectra of the near-band-edge region measured at 80 K for phosphorus- and boron-doped diamond films. The phosphorus and boron concentrations are $\sim 8 \times 10^{17}$ and 5×10^{17} cm^{-3}, respectively. Strong sharp excitonic emission lines are clearly observed. The peak at 235 nm (FE_{TO}) is due to the Free-Exciton (FE) emission associated with a transverse optical (TO) phonon. The other peaks are due to the bound-exciton (BE) emissions of phosphorus donors (P-BE) or of boron acceptors (B-BE), and are associated with nonphonon (NP), transverse acoustic (TA) phonons, TO phonons, LO phonons, and TO phonon replica (TO + O). The binding energy of excitons bound to neutral phosphorus donors is 90 meV calculated from the energy difference between FE_{TO} and P-BE_{TO}. This is larger than the binding energies of 80 meV for free excitons and 55 meV for bound excitons to neutral boron acceptors. Considering binding energies, the NP radiation can be identified in p- and n-type diamond, which is important evidence of the existence of bound excitons. Since the transition rate from free to bound exciton depends on the density of states

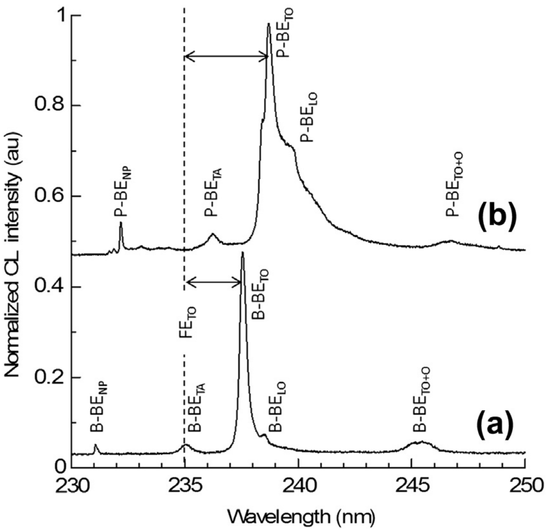

Figure 7 Typical cathodoluminescence spectra of the near-band-edge region measured at 80 K for phosphorus- and boron-doped diamond films. (a) Peaks around 232.6, 236.5, 238.8, 239.5, and 246.5 nm are due to the phosphorus bound excitons of P-BE$_{NP}$, P-BE$_{TA}$, P-BE$_{TO}$, P-BE$_{LO}$, and P-BE$_{TO+O}$, respectively. (b) Peaks around 231.1, 235.2, 237.4, 238.5, and 245.4 nm are due to the boron bound excitons of B-BE$_{NP}$, B-BE$_{TA}$, B-BE$_{TO}$, B-BE$_{LO}$, and B-BE$_{TO+O}$, respectively.

for donors or acceptors, the density of donor or acceptor can be estimated from the ratio of peak intensity between free and bound excitons.

3.12.4 Electrical Properties

Hall effect measurement is the most straightforward method for characterizing electrical conduction mechanisms in semiconductors. Figure 8 shows typical results of carrier concentrations measured as a function of temperature from 300 to 1000 K. Open and closed circles indicate the data for phosphorus-doped diamond with $\sim 8 \times 10^{17}$ cm^{-3} and for boron-doped diamond with $\sim 5 \times 10^{17}$ cm^{-3}, respectively. Both films show Hall signals over a wide temperature range, indicating that dopants are thermally activated. The carrier concentration increases exponentially with increasing temperature, which indicates that the carrier conduction is dominated by free carriers in the conduction or valence band.

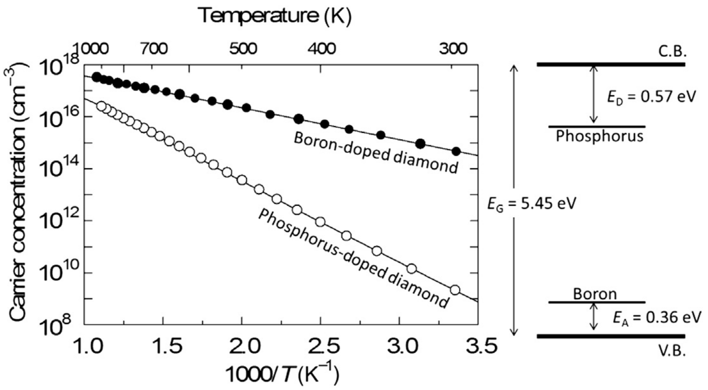

Figure 8 Temperature dependence of carrier concentration obtained for the p-type boron-doped and n-type phosphorus-doped diamond films grown on Ib (001)-oriented substrates. Open and closed circles are the data for phosphorus- and boron-doped diamond, respectively. The solid lines are the results of the least-squares fitting to the data using Eqn (1). The schematic is the energy diagram with donor and acceptor levels.

In the case of n-type semiconductors, the electron concentration, n, can be calculated by taking into account the donor states, N_D, and compensating acceptor states, N_A, which may originate from impurity atoms and/or defects:

$$\frac{n(n+N_A)}{N_D-N_A-n}=\frac{N_C}{g}\exp\left(-\frac{E_D}{k_BT}\right) \tag{1}$$

where k_B is the Boltzmann constant, T is the temperature, g is the degeneration of the donor level E_D ($=2$ for diamond) and N_C is the effective density of states in the conduction band as expressed by the following:

$$N_C = 2M_C\left(\frac{2\pi m^*_{dos}k_BT}{h^2}\right) \tag{2}$$

where M_C is the number of equivalent minima in the conduction band ($=6$ for diamond) and h is the Planck constant. The density of state effective mass of electrons m^*_{dos} is given by $m^*_{dos} = (m^*_l\ m^*_t\ m^*_t)^{1/3}$, where m^*_l and m^*_t are the longitudinal and transverse effective masses of electrons, respectively. We assumed $m^*_l = 1.4\ m_0$ and $m^*_t = 0.36\ m_0$, where m_0 is the free electron mass (Nava, Canali, Jacoboni, Reggiani, & Kozlov, 1980). For the boron-doped p-type case, the effective mass of holes is usually given by $0.74\ m_0$. The solid lines shown in **Figure 8** are the least-square fit as calculated by Eqn (1). The donor level is estimated to be 0.57 eV in phosphorus-doped diamond and the acceptor level to be 0.37 eV in boron-doped diamond.

To attain a more thorough understanding of the electrical conduction properties, the effect of carrier compensation due to impurities and/or defects should be taken into account. The compensation ratio η is given by N_A/N_D in n-type semiconductor, which should be significantly less than 1. **Figure 9** shows changes in carrier concentration at room temperature as a function of compensation ratio η calculated using Eqns (1) and (2). The carrier concentrations at room temperature strongly depend on the carrier compensation and significantly decrease with an increase in the compensation ratio. The hole and electron concentrations are estimated to be 10^{12}–10^{15} cm^{-3} and 10^{8}–10^{14} cm^{-3} due to the deep accepter and donor levels, respectively. The carrier compensation ratio in CVD boron-doped diamond has been reported to be less than 1%, in which the hole concentration can increase with an increase in the acceptor density N_A. On the other hand, the compensation ratio of phosphorus-doped diamond has been reported to be several percent in (111) and about 50% in (001) diamond. The carrier concentration at room temperature mainly depends on the compensation ratio and is insensitive to the donor density.

Until now, however, the identification of compensating centers in phosphorus-doped diamond is missing. Hydrogen has been reported to occupy bond center sites and form acceptor properties H(0/−) at ~2 eV below the conduction band (Goss et al., 2002). This hydrogen could trap electrons very efficiently, but it has not been clarified experimentally whether or not its incorporation depends on phosphorus doping. On the other hand, the P–H complex is also stable in n-type diamond, while this hydrogen only passivates phosphorus donors and forms an electrically inactive complex. The calculated (0/+) transition energy of the P–H

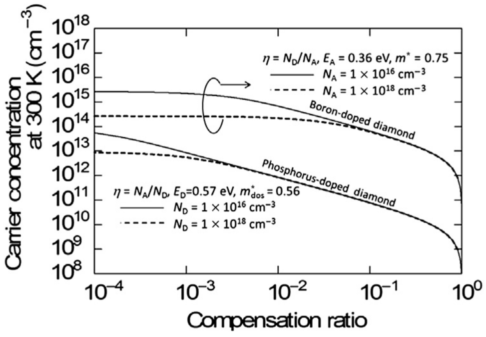

Figure 9 Changes in carrier concentration at room temperature as a function of compensation ratio calculated using Eqns (1) and (2). For phosphorus-doped diamond, the carrier concentration at room temperature was calculated using donor level of 0.57 eV, electron effective mass of 0.56, donor density of 1×10^{16} cm^{-3} (solid curve) and 1×10^{18} cm^{-3} (broken curve). The concentration for boron-doped diamond was calculated using acceptor level of 0.36 eV, effective mass of 0.74, acceptor density of 1×10^{16} cm^{-3} (solid curve) and 1×10^{18} cm^{-3} (broken curve).

complex is ~3.3 eV below the conduction band, which is very deep and does not contribute to conductivity (Wang & Zunger, 2002). One possibility could be the phosphorus–vacancy (P–V) complexes suggested by Jones et al. (Jones, Lowther, & Goss, 1996). Here, phosphorus lies at the midpoint between two neighboring vacancies. This complex introduces an acceptor state ~2.7 eV below the conduction band. In addition, the estimated binding energy of the P–V complex is ~7.1 eV for dissociation into neutral constituents, which is much larger than that of the P–H complex of ~2.6 eV, indicating that the P–V complex is more stable in phosphorus-doped diamond (Miyazaki et al., 2006). The compensation centers, calculated by assuming that donor concentration is equal to phosphorus concentration, increase with an increase in phosphorus concentration. If some of the incorporated phosphorus atoms in (001)-oriented diamond induce such P–V complexes, it would explain the detected features.

On the other hand, H1′ centers, often observed in CVD diamond by ESR, are candidates for donor compensation. The H1′ centers are possibly hydrogen–vacancy complexes, where the carbon dangling bond is near a hydrogen atom. Since this defect is observed not only in nondoped but also in B-doped CVD diamond, it has been suggested that its electronic state, D(0/+), lies between the top of the valence band and boron acceptor level (Mizuochi, Ogura, Watanabe, Isoya, Okushi, et al., 2004). However, in (001) P-doped diamond, such defects were not observed by ESR. This result indicates two possibilities: (1) these defects are not generated in n-type diamond and (2) the defects of H1′ centers are generated even in n-type diamond, but their charge is changed from D(0/+) to D(−/0) by compensating donor electrons, where the D(−/0) state is located below the phosphorus donor level and therefore cannot be detected by ESR analysis.

3.12.5 Ohmic Contact Issue in n-Type Diamond

Ohmic metallization is an important subject for attaining high-performance electronic devices. It should be able to supply the required current without any voltage drop at the contact of the electronic device. For boron-doped p-type diamond, a low-resistivity contact has been almost achieved by TiC contact, which reduces the specific contact resistance ρ_c to less than $10^{-5}\ \Omega\text{cm}^2$. On the other hand, for phosphorus-doped n-type diamond, a reliable contact with low resistance had not been achieved yet. Various methods, such as graphite formation by Ga or Ar ion implantation, selection of low-work-function metals, and control of doping level, have been used to make a good contact on n-type diamond films; however, the ρ_c obtained was quite high around 10^3–$10^6\ \Omega\text{cm}^2$ (Teraji, Koizumi, & Kanda, 2000).

Based on the simple theory of metal/n-type semiconductor contacts, the resistance ρ_c varies exponentially with the factor $\phi_b/N_D{}^{(1/2)}$, where ϕ_b is Schottky barrier height and N_D donor concentration. Therefore, to lower ρ_c, it is basically necessary to reduce ϕ_b and narrow the barrier width by increasing N_D. According to previous reports on capacitance–voltage properties of n-type Schottky barrier diodes (Suzuki, Koizumi, Katagiri, Ono, Sakuma, et al., 2006), the Fermi level at the metal/n-type diamond interface is strongly pinned at 4.3 eV below the bottom of the conduction band, which makes it difficult to control ϕ_b. Thus, the only realistic solution for lowering ρ_c in n-type diamond is to increase N_D. Moreover, even in the case of an n-type film with a phosphorus concentration of $1 \times 10^{19}\ \text{cm}^{-3}$, the contact resistance has been reported to be $10^3\ \Omega\text{cm}^2$, indicating that a much higher phosphorus concentration of over $10^{20}\ \text{cm}^{-3}$ would be required.

The specific contact resistance was evaluated by circular-type transfer length method (c-TLM) as shown in **Figure 10**, which allows a precise evaluation of the contact scheme. When the radius $r_1 + r_2$ is constant, the total resistance R_T between two electrodes depends linearly on the contact spacing $d = r_2 - r_1$. The resistance R_T can be expressed by

$$R_{\text{Total}} = \frac{R_{\text{SH}}}{2\pi}\left[L_T\left(\frac{1}{a_2}+\frac{1}{a_1}\right)+\ln\frac{a_2}{a_1}\right] \tag{3}$$

where R_{SH} is the sheet resistance of the semiconductor layer, r_1 and r_2 are the radii of each circular electrode edge, and L_T is the transfer length. The transfer length can be thought of as the distance over which most of the current transfers from the semiconductor into the metal or from the metal into the semiconductor and can be expressed by $L_T = \rho_c/R_{\text{SH}}$, where ρ_c is specific contact resistance in Ωcm^2. Fitting the R_T value of different spacings to the appropriate formula Eqn (3) yields the free parameters R_{SH} and L_T, and then ρ_c can be calculated from $\rho_c = R_{\text{SH}} L_T^2$.

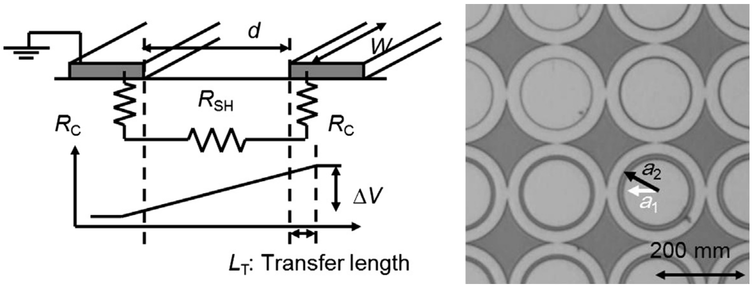

Figure 10 Schematic picture of TLM analysis and optical microscopic image of circular-type TLM patterns on a (111) heavily phosphorus-doped diamond film. The c-TLM pattern was fabricated by conventional electron-beam lithography and lift-off process. Electrodes (Ti 30 nm)/(Pt 30 nm)/(Au 100 nm) were deposited by electron-beam evaporation followed by thermal annealing in Ar atmosphere at 420 °C for 30 min. The measurements were performed in a vacuum chamber with background pressure of 2×10^{-7} Torr.

Typical current–voltage, *I–V*, characteristics corresponding to different contact spacings of metal/ phosphorus-doped diamond Ti/n$^+$ contacts at room temperature are shown in **Figure 11**. An ideal Ohmic property was not obtained, while the *I–V* characteristics clearly depend on the contact spacing. Each inter-electrode resistance, estimated from the linear region in the *I–V* characteristics, was plotted as a function of the contact spacing *d*. The data show a good linear relationship between *d* and resistance. The film resistivity is estimated using Eqn (3) to be 80 Ωcm, which agrees well with that obtained by Hall effect measurements of 70 Ωcm. The specific contact resistance of Ti/n$^+$ is deduced to be 2×10^{-3} Ωcm^2 at room temperature, which is six orders of magnitude lower than the reported values (Kato, Makino, et al., 2008; Kato, Umezawa, et al., 2008). The barrier width would be sufficiently narrow for tunneling through the barrier to take place by heavy doping of over 10^{20} cm^{-3}.

The transport mechanism at a metal/semiconductor interface can be considered in terms of the relationship between temperature and doping level using the parameter E_{00}, which is defined as

$$E_{00} = \frac{qh}{2}\sqrt{\frac{N_D}{m^* \varepsilon_s}} \tag{4}$$

where h is the Planck constant, m^* the effective mass of an electron, ε_s the dielectric constant, and N_D donor concentration. E_{00} is a parameter which plays an important role in tunneling theory. A rough categorization can be set by comparing the thermal energy k_BT and E_{00}. When $k_BT \gg E_{00}$, thermionic emission dominates and the original Schottky barrier prevails without tunneling. When $k_BT \ll E_{00}$, field emission (FE), which is a pure tunneling process, dominates. When $k_BT \sim E_{00}$, thermionic field emission (TFE) dominates, which is a tunneling of thermally excited carriers. The calculated value for the present n$^+$ layer is 130 meV, i.e. 1400 K, and the tunneling process will be the dominant transport mechanism. Even at heavy doping levels of over 10^{20} cm^{-3}, the resistivity still shows temperature dependence. Accordingly, the contact resistance also depends

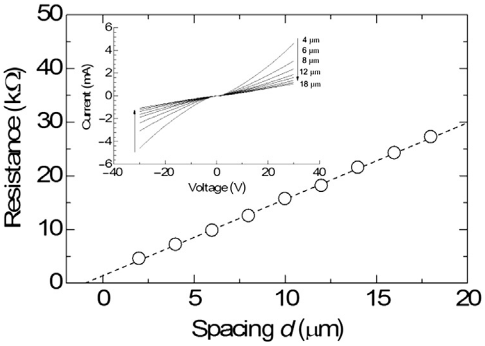

Figure 11 Resistances between two neighboring contacts as a function of the spacing *d* of circular-type TLM patterns. The dashed line indicates a least-square fit. The insert shows current–voltage (*I–V*) characteristics between two neighboring contact pads corresponding to different contact spacing of Ti/n$^+$ contacts at room temperature.

on the temperature, and the value of ρ_c decreases down to 10^{-4} Ωcm^2 with an increase in the measurement temperature. Such temperature dependence is evidence for TFE, while the roughness of Ti/n$^+$ interface and/or the effective carrier concentration as well as doping level will also affect the carrier transport. The detailed mechanism at the Ti/n$^+$ interface is currently under investigation.

3.12.6 Diamond Bipolar Applications

Based on recent progress in diamond growth and doping, research on p–n junction applications has increased rapidly. Diamond possesses excellent physical and electrical properties such as wide band gap of 5.47 eV, highest breakdown voltage of 2.7×10^7 V/cm and thermal conductivity of 22 W/cmK, resulting in a high attainable power density. In addition, exciton-related devices, electron emitters with negative electron affinity (NEA), and single photo source with excellent spin characteristic including long coherence time are also considered to be future applications utilizing the unique properties of diamond semiconductor.

It is also a candidate for ultraviolet (UV) light-emitting applications because of its stable exciton properties, although diamond is an indirect semiconductor. The exciton binding energy of 80 meV and the small Bohr radius of 1.57 nm due to its lower dielectric constant allow the formation of high-density excitons around 10^{18}–10^{19} cm^{-3} even at room temperature (Okushi, Watanabe, Yamasaki, & Kanno, 2006). This unique advantage is considered to be utilized for high-efficiency deep UV light sources, which would be comparable to other luminescence semiconductors which emit light by electron–hole recombination such as III–V compounds. The peak wavelength is 235 nm and therefore in the deep UV region. Research on diamond light-emitting diode (LED) started with a simple p–n junction structure and improved to a p–i–n structure. Currently p$^+$–i–n$^+$ are typically fabricated with thick intrinsic layers of 15 μm. Heavily doped p$^+$ and n$^+$ layers enhance the carrier injection to the intrinsic layer, giving rise to the formation of even higher amount of exciton densities in the thick intrinsic layer. The reported maximum output power and external quantum efficiency of diamond UV-LED are 0.1 mW and 0.006%, respectively. The sterilization of bacterial *Escherichia coli* has been demonstrated by irradiation using the diamond UV-LED (Makino, Yoshino, Sakai, Uchida, Koizumi, et al., 2011).

A diamond electron emitter based on p–n junction diodes has been developed. It is well known that p-type hydrogen-terminated diamond surfaces show NEA features. This means that electrons injected into the conduction band of H-terminated p-type diamond can be emitted into vacuum. Using the n$^+$ contact metallization, the p–i–n$^+$ emitter device can operate at room temperature with an emission efficiency of 0.1% and an emission current of 10 μA (Takeuchi, Makino, Kato, Ogura, Tokuda, et al., 2011). A new type of high-voltage DC vacuum switch utilizing this p–i–n$^+$ emitter and a high-voltage switching device of 10 kV has recently been demonstrated.

The bipolar junction transistor (BJT) is currently one of the major power switching devices. BJTs may offer benefits in high-power applications, due to a lower on-resistance from conductivity modulation arising from minority carrier injection and the absence of a gate insulator. Considering several candidates of wide-band-gap semiconductors suitable for high-power BJT applications, it is expected that diamond BJTs will exhibit superior performance as a switching power device with high current amplification and low conduction loss. Current amplification at room temperature has been achieved in diamond BJTs fabricated on (111)-oriented substrates. Improved current amplification properties were achieved by utilizing optimized phosphorus-doped diamond for reducing the series resistance of the n-type base layer. Further enhancement of characteristics including operation current, blocking voltage and reproducibility is required; however, the developed diamond bipolar transistor that works at room temperature is considered to be the first step toward realizing a high-performance power device (Kato, Oyama, Makino, Ogura, Takeuchi, et al., 2012).

Single-photon sources from single defects in diamond have recently attracted strong attention for quantum cryptography applications because of their outstanding photostability at room temperature. The nitrogen–vacancy (NV) center exhibits excellent spin characteristics, including long coherence time and fast manipulation rates, and allows implementation of few-qubit quantum registers. Mizuoch et al. have recently developed an electrically driven single-photon source device by utilizing a novel diamond p$^+$–i–n$^+$ junction structure with NV centers (Mizuochi, Makino, Kato, Takeuchi, Ogura, et al., 2012). From photo- and electroluminescence mapping analysis, it has been shown that NV centers emit both by photo- and electroluminescence. The detailed emission mechanisms of NV centers is currently under investigation.

Although the acceptor and donor levels are relatively deep in the band gap of diamond, the use of heavily doped layers with impurity concentration over 10^{20} cm^{-3}, which can reduce the resistivity and contact resistance, is considered to be a realistic solution for several applications driven at room temperature. The future for diamond applications is therefore promising and will attract increasing attention in the coming years.

References

Achard, J., Tallaire, A., Sussmann, R., Silva, F., & Gicquel, A. (2005). The control of growth parameters in the synthesis of high-quality single crystalline diamond by CVD. *Journal of Crystal Growth, 284*, 396–405.

Anderson, A. B., Grantscharova, E. J., & Angus, J. C. (1996). Molecular-orbital theory of monatomic and diatomic substitutional defects as shallow n-type dopants in diamond. *Physical Review B, 54*, 14341–14348.

Farrer, R. G. (1969). On the substitutional nitrogen donor in diamond. *Solid State Communications, 7*, 685–688.

Gheeraert, E., Koizumi, S., Teraji, T., Kanda, H., & Nesladek, M. (1999). Electronic states of boron and phosphorus in diamond. *Physica Status Solidi (A), 174*, 39–51.

Goss, J. P., Jones, R., Heggie, M. I., Ewels, C. P., Briddon, P. R., et al. (2002). Theory of hydrogen in diamond. *Physical Review B, 65*, 115207-1-13.

Haenen, K., Meykens, K., Nesladek, M., Knuyt, G., Stals, L. M., et al. (2000). Temperature dependent spectroscopic study of the electronic structure of phosphorus in n-type CVD diamond films. *Diamond and Related Materials, 9*, 952–955.

Hassouni, K., Grotjohn, T. A., & Gicquel, A. (1999). Self-consistent microwave field and plasma discharge simulations for a moderate pressure hydrogen discharge reactor. *Journal of Applied Physics, 86*, 134–151.

Hill, C. W., Gedridge, R. W., Groshens, T. J., Stringfellow, G. B., & Sadwick, L. P. (1996). Low-pressure pyrolysis studies of a new phosphorus precursor: tertiarybutylbis(dimethylamino)phosphine. *Journal of Electronic Materials, 25*, 1434–1438.

Jones, R., Lowther, J. E., & Goss, J. P. (1996). Limitations to n-type doping in diamond: the phosphorus–vacancy complex. *Applied Physics Letters, 69*, 2489–2491.

Kajihara, S. A., Antonelli, A., & Bernholc, J. (1993). Impurity incorporation and doping of diamond. *Physica B, 185*, 144–149.

Kalish, R. (1997). Ion-implantation in diamond and diamond films: doping, damage effects and their applications. *Applied Surface Science, 117/118*, 558–569.

Kamo, M., Sato, Y., Matsumoto, S., & Setaka, N. (1983). Diamond synthesis from gas phase in microwave plasma. *Journal of Crystal Growth, 62*, 642–644.

Kasu, M., & Kubovic, M. (2010). Arsenic-doped n-type diamond grown by microwave-assisted plasma chemical vapour deposition. *Japanese Journal of Applied Physics, 49*, 110209-1-3.

Katagiri, M., Isoya, J., & Kanda, H. (2004). Electron spin resonance characterization of phosphorus-doped CVD diamond films. *Physica Status Solidi (A), 201*, 2451–2456.

Katagiri, M., Isoya, J., Koizumi, S., & Kanda, H. (2004). Lightly phosphorus-doped homoepitaxial diamond films grown by chemical vapor deposition. *Applied Physics Letters, 85*, 6365–6367.

Kato, H., Makino, T., Ogura, M., Tokuda, N., Okushi, H., et al. (2009). Selective growth of buried n^{+} diamond on (001) phosphorus-doped n-type diamond film. *Applied Physics Express, 2*, 055502-1-3.

Kato, H., Makino, T., Yamasaki, S., & Okushi, H. (2008). n-type diamond growth by phosphorus doping. *Material Research Society Symposium Proceedings, 1039*, 39–48.

Kato, H., Oyama, K., Makino, T., Ogura, M., Takeuchi, D., et al. (2012). Diamond bipolar junction transistor device with phosphorus-doped diamond base layer. *Diamond and Related Materials, 27–28*, 19–22.

Kato, H., Umezawa, H., Tokuda, N., Takeuchi, D., Okushi, H., et al. (2008). Low specific contact resistance of heavily phosphorus-doped diamond film. *Applied Physics Letters, 93*, 202103-1-3.

Kato, H., Yamasaki, S., & Okushi, H. (2005a). n-type doping of (001)-oriented single-crystalline diamond by phosphorus. *Applied Physics Letters, 86*, 222111-1-3.

Kato, H., Yamasaki, S., & Okushi, H. (2005b). Growth and characterization of phosphorus-doped diamond using organophosphorus gases. *Physica Status Solidi (A), 202*, 2122–2128.

Koizumi, S., Kamo, M., Sato, Y., Ozaki, H., & Inuzuka, T. (1997). Growth and characterization of phosphorous doped {111} homoepitaxial diamond thin films. *Applied Physics Letters, 71*, 1065–1067.

Lombardi, G., Hassouni, K., Stancu, G.-D., Mechold, L., Ropcke, J., et al. (2005). Modeling of microwave discharges of H_2 admixed with CH_4 for diamond deposition. *Journal of Applied Physics, 98*, 053303-1-12.

Makino, T., Yoshino, K., Sakai, N., Uchida, K., Koizumi, S., et al. (2011). Enhancement in emission efficiency of diamond deep-ultraviolet light emitting diode. *Applied Physics Letters, 99*, 061110-1-3.

Miyazaki, T., Kato, H., Ri, S. G., Ogura, M., Tokuda, N., et al. (2006). Energetics of dopant atoms in subsurface positions of diamond semiconductor. *Superlattices and Microstructures, 40*, 574–579.

Mizuochi, N., Ogura, M., Watanabe, H., Isoya, J., Okushi, H., et al. (2004). EPR study of hydrogen-related defects in boron-doped p-type CVD homoepitaxial diamond films. *Diamond and Related Materials, 13*, 2096–2099.

Mizuochi, N., Makino, T., Kato, H., Takeuchi, D., Ogura, M., et al. (2012). Electrically driven single-photon source at room temperature in diamond. *Nature Photonics, 6*, 299–303.

Namba, A., Tatsumi, N., Yamamoto, Y., Nishibayashi, Y., & Imai, T. (2005). Synthesis of phosphorus-doped diamond semiconductor and application to electron emitters. *Sumitomo Electric Technical Review, 166*, 38–44.

Nava, F., Canali, C., Jacoboni, C., Reggiani, L., & Kozlov, S. F. (1980). Electron effective masses and lattice scattering in natural diamond. *Solid State Communications, 33*, 475–477.

Nesladek, M. (2005). Conventional n-type doping in diamond: state of the art and recent progress. *Semiconductor Science and Technology, 20*, R19–R27.

Okano, K., Kiyota, H., Iwasaki, T., Nakamura, Y., Akiba, Y., et al. (1990). Synthesis of n-type semiconducting diamond film using diphosphorus pentoxide as the doping source. *Applied Physics A, 51*, 344–346.

Okush, H., Watanabe, H., Yamasaki, S., & Kanno, S. (2006). Emission properties from dense exciton gases in diamond. *Physica Status Solidi (A), 203*, 3226–3244.

Pearse, R. W. B., & Gaydon, A. G. (1976). *The identification of molecular spectra* (4th ed.). London: Chapman and Hall Ltd.

Prins, J. F. (2002). Implantation-doping of diamond with B^+, C^+, N^+ and O^+ ions using low temperature annealing. *Diamond and Related Materials, 11*, 612–617.

Saguy, C., Kalish, R., Cytermann, C., Teukamb, Z., Chevallier, J., et al. (2004). n-type diamond with high room temperature electrical conductivity by deuteration of boron doped diamond layers. *Diamond and Related Materials, 13*, 700–704.

Saito, T., Kameta, M., Kusakabe, K., Morooka, S., Maeda, H., et al. (1998). Synthesis and electrical properties of phosphorus-doped homoepitaxial diamond (111) by microwave plasma-assisted chemical vapor deposition using triethylphosphine as a dopant source. *Japanese Journal of Applied Physics, 37*, L543–L546.

Sque, S. J., Jones, R., Goss, J. P., & Briddon, P. R. (2004). Shallow donors in diamond: chalcogens, pnictogens, and their hydrogen complexes. *Physical Review Letters, 92*, 017402-1-4.

Suzuki, M., Koizumi, S., Katagiri, M., Ono, T., Sakuma, N., et al. (2006). Electrical characteristics of n-type diamond Schottky diodes and metal/diamond interfaces. *Physica Status Solidi (A), 203*, 3128–3135.

Takeuchi, D., Makino, T., Kato, H., Ogura, M., Tokuda, N., et al. (2011). Electron emission from CVD diamond p–i–n junctions with negative electron affinity during room temperature operation. *Diamond and Related Materials, 20*, 917–921.

Tallaire, A., Achard, J., Silva, F., Sussmann, R. S., Gicquel, A., et al. (2004). Oxygen plasma pre-treatments for high quality homoepitaxial CVD diamond deposition. *Physica Status Solidi (A), 201*, 2419–2424.

Tavares, C., Koizumi, S., & Kanda, H. (2005). Effects of RIE treatments for {111} diamond substrates on the growth of P-doped diamond thin films. *Physica Status Solidi (A), 202*, 2129–2133.

Teraji, T., Koizumi, S., & Kanda, H. (2000). Ohmic contact for phosphorus-doped n-type diamond. *Physica Status Solidi (A), 181*, 129–139.

Ueda, K., & Kasu, M. (2008). High-pressure and high-temperature annealing effects of boron-implanted diamond. *Diamond and Related Materials, 17*, 502–505.

Wang, L. G., & Zunger, A. (2002). Phosphorus and sulphur doping of diamond. *Physical Review B, 66*, 161202-1-4.

Yamanaka, S., Watanabe, H., Masai, S., Takeuchi, D., Okushi, H., et al. (1998). High-quality B-doped homoepitaxial diamond films using trimethylboron. *Japanese Journal of Applied Physics, 37*, L1129–L1131.

3.13 Single-Ion Implantation in Diamond with a High Lateral Resolution: A Key Technology for the Fabrication of Quantum Devices

Sébastien Pezzagna and Jan Meijer, Nuclear Solid State Physics, University Leipzig, Leipzig, Saxony, Germany

3.13.1 Introduction

The development of quantum devices for electronic, optoelectronic, or photonic applications has become more and more in focus in the last decade. Diamond, as a host material, plays an increasing role taking advantage of its remarkable overall physical properties and of some recent technological breakthroughs. For example, the reproducible growth of extremely pure diamond substrates is now possible with impurity levels as low as 1 ppb (Bogdan et al., 2005; Markham et al., 2011; Tallaire et al., 2006) or even with an isotopic control of the carbon atoms constituting the diamond (Balasubramanian et al., 2009; Ishikawa et al., 2012). As a consequence, some optically active centers (among the hundreds of centers already known in diamond) can now be artificially produced (Meijer et al., 2005), observed (Gruber et al., 1997), and manipulated (Jelezko, Gaebel, Popa, Gruber, & Wrachtrup, 2004) at the single level. Nitrogen-vacancy (NV) and the silicon-vacancy defects are such centers, which possess unique properties for the development of new quantum devices (Ladd et al., 2010). Moreover, besides the strong isolating character of diamond (band gap of 5.5 eV), p-type (Vogel, Meijer, & Zaitsev, 2004) and maybe also n-type doping (Chernyshev et al., 2008; Kato, Yamasaki, & Okushi, 2005), are possible, as well as 3-dimensional structuration with conductive graphite (Olivero et al., 2005).

Although active optical centers can be intentionally produced during the growth of diamond, ion implantation is the best way to spatially control the position at which such a center should be created. Meanwhile, ion implantation techniques have kept improving both in terms of spatial resolution of implantation (almost at the nanometer level) (Pezzagna, Wildanger et al., 2010; Spinicelli et al., 2011; Toyli, Weiss, Fuchs, Schenkel, & Awschalom, 2010) and in control of the number of implanted ions (aiming at the deterministic implantation of single ions). Till recently, single centers could only be optically imaged with a resolution limited by diffraction (typically ∼300 nm). However, new optical microscopy techniques breaking the diffraction barrier have emerged and the imaging of single optical centers in diamond with a resolution of <10 nm has been demonstrated (Hell & Winchmann, 1994; Rittweger, Han, Irvine, Eggeling, & Hell, 2009).

These "nanoscopy" tools give a new and invaluable insight into material or living objects, and we have used them to determine the resolution of the different ion implantation techniques. The procedure consists of implanting nitrogen atoms using focused or collimated ion beams to produce NV centers and to image them optically.

The NV center consists of a substitutional nitrogen atom associated with a carbon vacancy as a first neighbor. After implantation of nitrogen atoms, it can be formed by annealing above 800 °C, which enables the mobility of carbon vacancies and thus the formation of the N–V bonds (Allers, Collins, & Hiscock, 1998; Iakoubovskii & Adriaenssens, 2001; Pezzagna, Naydenov, Jelezko, Wrachtrup, & Meijer, 2010). The NV center has unique optical and spin properties (Jelezko & Wrachtrup, 2006; Manson, Harrison, & Sellars, 2006). It is highly photo and temperature stable. The electron spin associated with the negatively charged NV center can be optically polarized and read out a room temperature, which makes it one of the most promising solid-state quantum bits. Moreover, the coherence time of the electron spin can reach milliseconds in isotopically engineered ^{12}C diamond samples with reduced spin impurities (Balasubramanian et al., 2009; Ishikawa et al., 2012). NV^- centers in diamond offer all the necessary properties to fabricate a future room-temperature quantum computer. Indeed, quantum registers (Neumann, Kolesov et al., 2010) and entanglement (Dolde, Jakobi, Naydenov, et al., 2013; Neumann et al., 2008; Pfaff et al., 2013) based on coupled NV centers have already been demonstrated. The single-shot readout of the nuclear spin state is also possible (Dréau, Spinicelli, Maze, Roch, & Jacques, 2013; Maurer et al., 2012; Neumann, Beck et al., 2010). NV centers can be found in different charge states (NV^-, NV^0, and possibly NV^+), and the controlled switching from one to the other has recently been shown (Grotz et al., 2012; Hauf et al., 2011). This offers another degree of freedom in the individual addressing capabilities of single NV centers. A quantum computer is yet still missing, and one of the main challenges lies in the possibility to build scalable structures involving several coupled NV centers, which would all be individually addressable.

The spin properties of the NV^- are also suitable for applications in magnetic sensing (Balasubramanian et al., 2008; Degen, 2008; Maze et al., 2008) with a high resolution, high sensitivity and an almost nonperturbative behavior. Different approaches have emerged to image magnetic fields, as scanning probe (Maletinsky et al., 2012; Rondin et al., 2012) or as wide field (Acosta et al., 2009; Maertz, Wijnheijmer, Fuchs, Nowakowski, & Awschalom, 2010; Maurer et al., 2010; Pham et al., 2011; Steinert et al., 2010) magnetometers. Nuclear magnetic resonance at the nanoscale has also been shown recently (Mamin et al., 2013; Staudacher et al., 2013). Diamond also possesses a large transparency window that makes it an ideal host matrix for (single-photon) light emission as regards the hundreds of optically active defects known (Zaitsev, 2001). Single-photon sources at room temperature have already been realized with, for example, NV or SiV centers (Aharonovich et al., 2011; Kurtsiefer, Mayer, Zarda, & Weinfurter, 2000; Neu et al., 2011; Pezzagna, Rogalla, Wildanger, Meijer & Zaitsev, 2011). Moreover, electrically driven emission of the defects is also possible (Lohrmann et al., 2011; Mizuochi et al., 2012). In biology and medicine, the fluorescence and stability properties of these color centers are now used for biolabeling and drug delivery (Faklaris et al., 2008; Fu et al., 2007; Mohan, Chen, Hsieh, Wu, & Chang, 2010).

In the first part of this chapter, we will describe the main physical effects that impose an intrinsic limit for the placement of atoms by ion implantation. In the second part, we will mainly focus on the resolution of ion implantation in a large range of ion kinetic energies from keV to MeV. Different ion implantation setups will be reviewed. Particular attention will be given to the "nanoimplanter" system with which a lateral resolution of 15 nm has already been demonstrated. The nanoimplanter combines a low-energy (5 kV) ion beam with the tip of an atomic force microscope (AFM) in which a nanohole is drilled and used as a movable mask. Furthermore, a technique able to deterministically implant single ions will be presented. The last part will be dedicated to some promising applications that become achievable thanks to the engineering and addressing of single NV centers with a high spatial resolution. A proposal to build a fully scalable quantum computer based on diamond material will be discussed.

3.13.2 Physical Effects Limiting the Spatial Resolution

In the process of ion implantation, spatial resolution is defined as the precision in the final position (in three dimensions) of an implanted ion in a target material. Whereas the lateral placement depends on masking capabilities or focusing of the ions, the depth is fixed by the velocity of the ions. The uncertainties in the depth and in the lateral resolution are also directly related to the velocity of the ions, and the intrinsic physical limitations will be first considered in this part. We can assume that for all the implantation techniques presented in the following, the ion kinetic energy E is well known and that an uncertainty due to $\Delta E/E$ is negligible in comparison with ion straggling or ion channeling.

The lateral resolution is intrinsically limited due to ion–matter interactions. However, the technical limitations related to the focusing capabilities of the implantation setup are in most cases predominant. In this section, the intrinsic limitations will be first reviewed while the techniques to obtain the best focus will be presented in detail and discussed in Section 3.13.3.

The depth of an ion implantation depends on the ion species, on its kinetic energy, and on the target material. It has been already shown that Stopping and Range of Ions in Matter (SRIM) simulations (Ziegler, 2008) give suitable results, even for low energies (Hönicke et al., 2010). The program requires the knowledge of some important parameters such as lattice binding energy (Guzmán de la Mata, Dowsett, & Palitsin, 2005). Additionally, these parameters should be unchanged during the implantation procedure. Fortunately, this is the case for the low fluence implantations performed in the following. However important effects are not considered in this program like ion channeling, aperture scattering, or vacancy saturation (Fairchild et al., 2012). Moreover, in the case of implantation of molecules or clusters, the implantation depth is affected, and it has to be taken into account.

3.13.2.1 Ion Straggling

After having been accelerated, a kinetic ion first hits the target surface, then propagates through the material (crystalline or not), and loses energy being scattered several times until it stops. This results in a broadening of the ion beam focus, which can be defined as the uncertainty in the final position of each single implanted ion. The scatterings can be due to collisions with the electrons or with the nucleus of the atoms. The collisions with the electrons reduce the velocity mainly, whereas collisions with the nuclei change the direction of the impinging ion and could produce crystal defects such as point defects. The straggling is defined as the square root of the variance of the ion distribution and depends on several parameters such as the mass and the velocity of the ion as well as the nature of the target.

Figure 1 is an SRIM simulation that illustrates the trajectories of nitrogen ions implanted into diamond at two different kinetic energies of 5 keV and 1 MeV. It clearly evidences how the ion straggling increases with ion energy and as a consequence that low energies (few keV or less) are required for high-resolution implantation. Defects are created along the whole ion trajectory, mainly vacancies and interstitials, but mostly at the end of

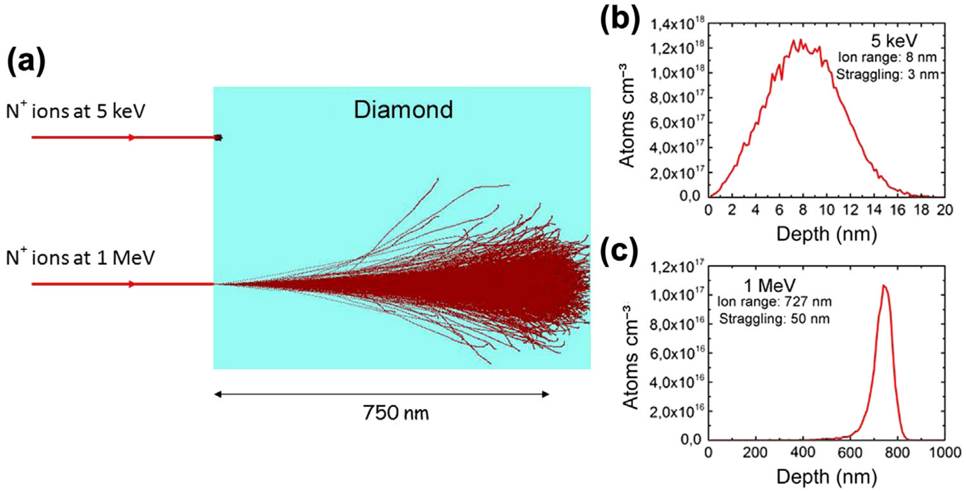

Figure 1 (a) SRIM simulation (trajectories) of nitrogen atoms implanted into diamond with kinetic energies of 5 keV and 1 MeV. It evidences the need to use low ion energies to ensure low straggling and therefore high-resolution implantation. (b) Depth profile of the concentration of 5-keV nitrogen atoms calculated for a fluence of 1×10^{12} cm^{-2}. (c) Depth profile of the concentration of 1-MeV nitrogen atoms calculated for the same fluence of 1×10^{12} cm^{-2}.

range. Indeed, it is short before the ion stops that the interaction with the nuclei of the target reaches a maximum (end of range defects).

3.13.2.2 Ion Channeling

Ion channeling is another effect that may add uncertainty in the depth. This effect leads to an underestimation of the implantation depth for ions implanted into any crystalline target material (Derry, Fearick, & Sellschop, 1982; Smith & Webb, 1991; Toyli et al., 2010). Ion channeling can happen in crystalline samples in case the incident direction of an ion beam is aligned with a particular axis of the crystal. The ions can travel through channels between atom rows or planes driven by the interaction between the charged ion and the potential induced by the arrangement of the target atoms. This results in a decrease in the number of collisions and an increase in the implantation depth. SRIM simulations do not take ion channeling into account. Figure **1**(b) and 1(c) show typical results for the depth profiles of nitrogen ions implanted into diamond. The simulations are performed with a displacement energy of 28 eV, surface binding energy of 7.4 eV, and lattice binding energy of 3 eV (Guzmán de la Mata et al., 2005). As previously mentioned, the deceleration of the ions is due to collisions with electrons (electron stopping) and nuclei of the target atoms (nuclear stopping). For low energy ions, the nuclear stopping power dominates.

The relevant parameters while considering ion channeling are the angle of the ion tray with respect to the crystal orientation and the ion energy. For a particular crystalline axis, only ions incoming within a certain angle can penetrate the channeling rows. This angle is called the critical angle. If the ion velocity is reduced, channeling also does not happen anymore below the so-called critical ion energy. The channeling effect has been well known for decades and is described by a large number of theoretical models and simulations (Cho, Allen, Finstad, & Chu, 1985; Courant, 1951; Hobler, 1995; Hobler, 1996; Lindhard, 1964; Redinger, Standop, Rosandi, Urbassek, & Michely, 2011; Smith & Webb, 1991). The first model was developed by Lindhart (Lindhard, 1964). This model has been modified several times but still gives the basic results (Redinger et al., 2011). The theory is based on a continuum potential and predicts that the fraction of channeled ions is given by the average distance of the atoms in a row. In the case of axial channeling, the distance d_R can be found in Hoble (1996):

$$d_R = K_R a_{lat} \sqrt{h^2 + k^2 + l^2}$$

with the structure constant K_R:

$$K_R = 1 \quad \text{if one Miller index is odd}$$

$$K_R = 0.5 \quad \text{else.}$$

a_{latt} defines the lattice distance, and the Miller indices are given by <hkl>. The fraction of the channeled ions f_{chan} and nonchanneled ions f_{dechan} is found by

$$f_{chan} = 1 - f_{dechan},$$

$$f_{chan} = N d_R r_{cri}^2 \pi$$

with N being the atomic density and r_R the average critical distance to the row of atoms:

$$r_{crit} = d_R \ \psi_{cri}.$$

The critical angle ψ_{cri} for low energetic ion beams is given by

$$\psi_{cri} = \sqrt[4]{\frac{2Z_1 Z_2 e^2 a^2}{4\pi\varepsilon_0 d_R^3 E}}$$

with the atomic numbers being Z_1 for the ion and Z_2 for the target; ε_0 is the dielectric constant, E the ion energy, and a is the Thomas Fermi Screening length.

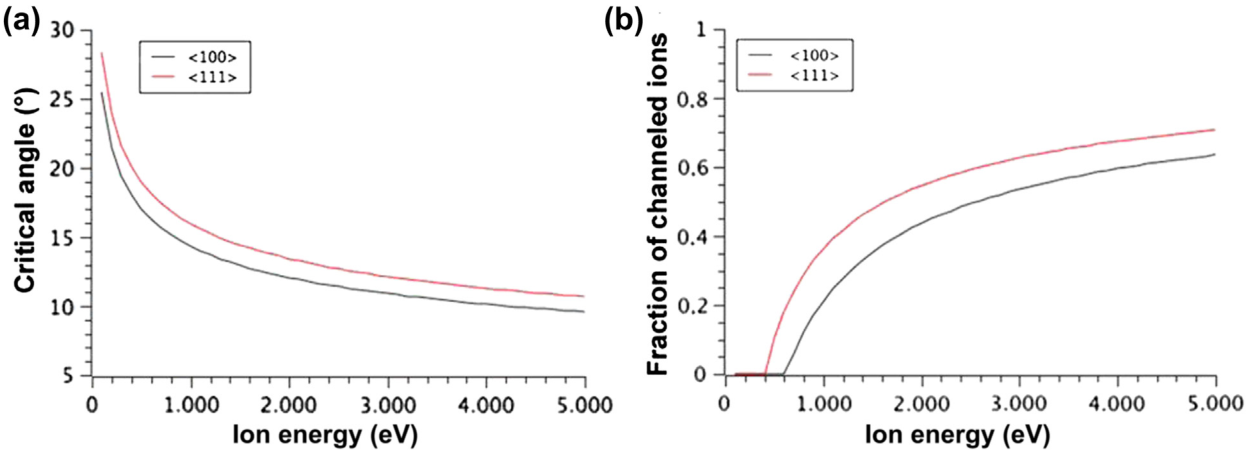

Figure 2 (a) Critical angle for low energetic nitrogen ions in (100) and (111) diamond. The calculation is based on the Lindhart model (Lindhard, 1964). (b) Fraction of channeled ions in (100) and (111) diamond. The critical ion energy is found to be 700 and 400 eV for ions in (100) and (111) crystal direction, respectively.

Figure 2(a) shows the critical angle for nitrogen ions into diamond, for (100) and (111) surface orientations. It can be seen that the critical angle becomes very large at low energy. Therefore, a large fraction of channeled ions is expected at these energies, even for high misalignments between the ion beam and the target. For an even lower kinetic ion energy, channeling does not occur anymore; thus, a critical angle does not give suitable results (Hobler, 1995). **Figure 2(b)** shows the expected fraction of channeled ions in the case of nitrogen in (001) and (111) diamond. It is found that the critical ion energies for channeling are 700 and 400 eV, respectively. For 5-keV ion energy, the theory gives a channeling fraction of $>50\%$. Molecular dynamics (MD) simulations show that this value is overestimated by a factor of ≥ 2 (Redinger et al., 2011). Moreover, MD assumes a target temperature of 0 K, a perfect crystal structure, and no surface contamination. For realistic models (Cho et al., 1985), it can be shown that the values are further reduced.

It can be concluded that the ion channeling effect does not occur for ion energies below 700 eV. For energies between 0.7 and 2 keV, the channeling effect has to be taken into account. However, not a large difference due to the ideal conditions used in the theoretical models is expected. For ion energies higher than 2 keV, channeling indeed could produce a large error in the calculation of the ion depth. **Figure 3** is a crystal-SRIM simulation (Posselt, 2004) of 5 keV nitrogen atoms implanted into (110) diamond at different incident angles. It shows indeed how the implantation depth profile is affected by channeling. Such a behavior is experimentally shown in Toyli et al. (2010).

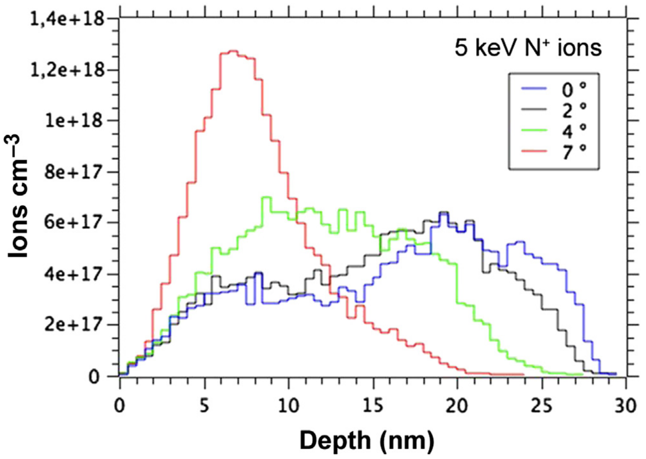

Figure 3 C-TRIM simulation of 5-keV nitrogen ions implanted into diamond at different angles with respect to the normal to the (110) surface.

Another possible effect is that, due to the large critical angle, ions may channel into different crystal axes. In the case of a (100) diamond surface, low energetic ions may channel in the <110> directions and lead to a lateral displacement (Hobler, 1995).

A defined noncrystalline coating deposited on the diamond surface allows one to avoid channeling effects (Redinger et al., 2011).

3.13.2.3 Diffusion

Due to the damage induced by ion implantation, the samples generally need to be annealed in order to restore the crystal lattice. In the case of NV centers in diamond, the N–V bonds form during the annealing taking advantage of the mobility of the carbon vacancies, which can then be eventually "trapped" by a nitrogen atom (Iakoubovskii & Adriaenssens, 2001). The heating process may as well lead to the diffusion of the implanted species and therefore to a broadening of the implanted volume and a loss in the resolution. In the case of diamond, the diffusion of impurity atoms is extremely small (Craven, Harte, Fisher, & Schulze, 2009; Harte, Taniguchi, & Chakraborty, 2009), and the implanted nitrogen atoms do not diffuse under the annealing conditions that we use (2 h at 800 °C). This is an important point since the determination of the ion implantation resolution will be measured in diamond samples that are annealed after having been implanted.

3.13.2.4 Other Factors

First, in the case of insulating samples such as diamond, the surface can charge up during ion implantation. This phenomenon may lead to high potentials, which can be especially detrimental in the case of low-energy ions that can be deviated from their initial trajectory. This possible loss of resolution can be avoided by depositing a thin conductive layer on the sample before implantation, by exposing the sample to an electron shower or by terminating the diamond surface with hydrogen (giving rise to surface conductivity).

The second factor is the implantation of molecules or clusters, which is a widely used method in the semiconductor industry to increase the throughput for shallow implanted dopants such as boron (Liang, Chiang, Chen, Niu, & Tseng, 2002). Molecules immediately dissociate while hitting the target surface, and the energy of each atom is given by the mass ratio of the accelerated molecule. For N_2 molecules, it is simply half of the implantation energy, and the implantation depth is comparable to monomer ion implantation (Liang et al., 2002). However, it is known that cluster implantation reduces the channeling tail but increases the damage (Liang et al., 2002).

Finally, proximity effects due to scattered ions on a mask are a well-known problem in the semiconductor industry. The scattered ions do not only reduce the lateral resolution, but they also have a lower implantation depth due to the fact that their kinetic energy is reduced by scattering. In the case of a focusing system (no use of mask), ion scattering produces a halo. The fraction of scattered ions depends on the aperture size, material, shape, ion species, and energy. Theoretical models and simulations have been performed to calculate the expected straggling with different types of apertures (Adamczewski, Meijer, Stephan, Bukow, & Rolfs, 1996). Fortunately, the effect is very small for low energetic (keV) ion beams. The implantation depth of 5 keV nitrogen in Pt is only 4 nm. The fraction of scattered ions can be approximated by

$$f_{\mathrm{Scatt}} = \frac{\left(R_{\mathrm{App}} + \Delta R\right)^2 - R_{\mathrm{App}}^2}{R_{\mathrm{App}}^2}$$

with R_{App} being the radius of the aperture and ΔR the enlargement due to ions that could penetrate the aperture and be scattered.

In the case of the nanoimplantation shown in Section 13.3.4.2, we use an object aperture of 25 µm in diameter. An electrostatic lens further forms the image of the aperture to a 25-µm beam spot (Meijer et al., 2008). To avoid any scattering, a 200-µm diameter aperture is installed after the electrostatic lens. By assuming that the aperture shape is curved of about 30°, ΔR is found to be 5.8 nm. This approximation leads to a fraction $f_{\mathrm{scatt}} = 10^{-3}$, which is even reduced due to the divergence aperture. The scattered ions eventually reaching the diamond have a reduced energy and therefore a reduced penetration depth.

3.13.3 Ion Implantation Setups to Create Single NV Centers

In this section, different ion implantation techniques to create NV centers are presented. They cover a wide ion energy range from keV to MeV and therefore implantation depths from the very first nanometers to several micrometers or tens of micrometers. For each of these techniques, we will show and discuss their capabilities in terms of resolution. Note that the optical imaging (with stimulated emission depletion (STED) microscopy) of NV centers created by nitrogen implantation is the method we chose to determine the spatial resolution of the different ion implantation techniques.

3.13.3.1 MV Electrostatic Accelerator

Megavolt (MV) electrostatic accelerators (single ended or Tandem) can provide nitrogen ions in the energy range from 300 keV to a few MeV. Ion currents up to 100 μA can be reached. These systems are suitable for deep implantation of ions in the so-called bulk conditions, generally far from the surface influence. For the implantation of large structures in a short time, the system is equipped with an ion projection setup (not presented here). For the implantation of fine structures or of single ions, we use two different techniques: either directly focusing the beam to the sample using a strong magnetic field or implanting through a mica mask containing nanochannels with a high aspect ratio.

3.13.3.1.1 Focusing with Single-Lens Superconductive Solenoid

A maskless and focused ion implantation below 1 μm can be achieved using megaelectron microprobe systems. Microprobe systems are mainly developed for proton induced X-ray emission application. These systems are mainly based on magnetic quadrupole lenses and are optimized to focus a 3-MeV proton beam. However, a few of these systems are also able to focus heavy ions. We developed a single-lens system based on a superconductive 14-T solenoid without any ferromagnetic core (Meijer & Stephan, 2002). With its focusing power of 100 MeV a.m.u., it is possible to focus any ion in the energy range from 500 keV to more than 20 MeV. Moreover, the ion species and ion energy can be easily changed within 30 min. The chromatic aberration is comparable to the one of quadrupole systems; however, the spherical aberration is reduced to about one order of magnitude. The smallest spot size of the system is about 400 nm, which corresponds to the demagnification of the "object" aperture with respect to the distance aperture lens (Meijer et al., 1999). Till recently, this focused implantation of MeV nitrogen ions has been chosen in order to produce pairs of coupled NV centers used as quantum registers. High energy was preferred due to the fact that the coherence time of the electron spin of the NV^- centers is in most cases longer than for shallow NV centers (Naydenov et al., 2010; Ofori-Okai et al., 2012; Staudacher et al., 2012). Note that the conversion yield from N to NV also increases with the implantation depth of the N atoms (Pezzagna, Naydenov et al., 2010). However, the severe requirement on the distance between the two NV centers (<30 nm due to the $1/r^3$ strength of magnetic dipolar coupling) makes this production method not scalable. The probability to find a suitable pair of NV centers is low as regards the ion straggling and the focusing capabilities of the system. Despite these difficulties, and implanting a high number of pairs (showing a poissonian distribution of distances between the two NVs), a quantum register has been demonstrated with a pair of NV centers produced in this way with an NV–NV distance of 9 nm (Neumann, Kolesov et al., 2010).

3.13.3.1.2 Collimating through Nanochannels in Mica

Another possibility to obtain high-resolution implantation using MeV ions is to use a mask. The mask should be thick enough to stop energetic MeV ions while having small collimation apertures. Here, we describe a technique with which the ion implantation resolution has been improved by almost one order of magnitude, so that it reaches the straggling limit. The idea is to use mica foils irradiated with GeV ions to produce tracks through the whole thickness of the foils. These tracks can then be easily etched using hydrofluoric acid. We demonstrated that by following this method (Khan, Khan, & Spohr, 1981; Pezzagna, Rogalla et al., 2011), one can produce channels with sizes below 30 nm in a 5-μm-thick mica layer (**Figure 4**). The aspect ratio of these channels reaches values of >100. Using such masks to collimate an ion beam therefore requires an exact alignment between the ion beam and the channels.

Figure 4(d) shows the result of the implantation of 1 MeV nitrogen ions in diamond through such a mica layer with nanochannels. The fluorescence scan of the diamond after annealing reveals the creation of NV centers. Each bright spot corresponds to the fluorescence of one or several NV centers. High-resolution

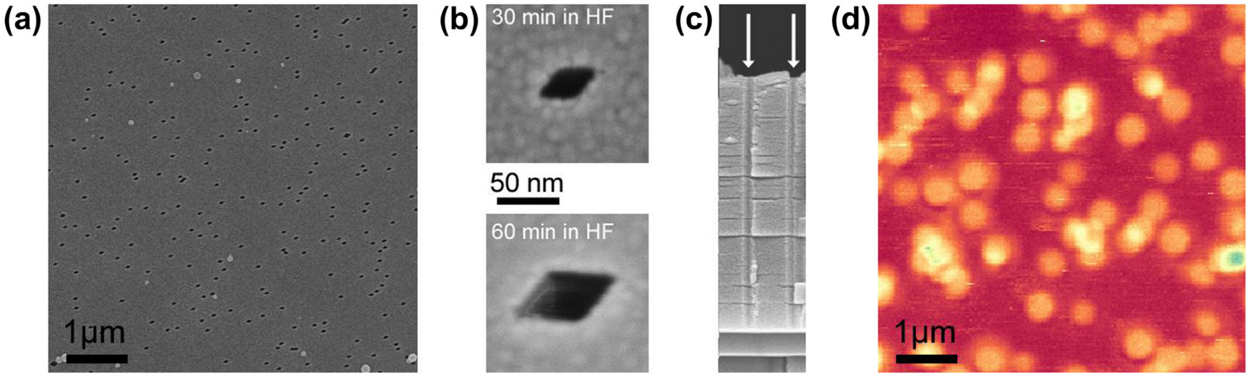

Figure 4 (a) Mica layer with nanochannels after irradiation with 1.6-GeV Sm ions and subsequent etching in a 10% HF solution (etching time of 30 min). (b) Aperture of the channels for 30 and 60 min etching times. (c) Section image showing two nanochannels through a 2-μm depth in mica. (d) Confocal fluorescence scan of an ultrapure synthetic diamond implanted with 1-MeV nitrogen ions through a mica layer. Each spot has been produced by the implantation of nitrogen ions through a nanochannel and corresponds to one or more NV centers.

microscopy reveal (data not shown here) that the interdistance between NV centers within one spot (i.e., implanted through the same channel) is in the range of a few tens of nanometers as expected due to the channel size (Dolde et al., in press). Details of the experiment can be found in Pezzagna, Rogalla et al. (2011). Apart from the incident angle of the ion beam, the transmission factor of the ions depends on the channel size and mica thickness; it has been evaluated to be between 1 and 10% for 30-nm-wide channels. Moreover, an energy loss of the transmitted ions is observed in the case of a misalignment between ion beam and mica channels. Scattering at the walls of the channels and charging up of the mica layer may contribute to limit the transmission. Despite these technical considerations, this method offers an implantation resolution for MeV ions approaching the straggling limit. Further developments concern the isolation of single nanochannels that could be mounted on piezotranslational stages.

3.13.3.2 Shallow Collimated Ion Implantation

Although the use of nanochannels in mica brings the resolution of high-energy ions close to the straggling limit, it is still in the order of several tens of nanometers. The only possibility to further improve it toward nanometer resolution is to reduce the energy of the ions to a few keV or less. This implies however a shallow implantation depth. Most of the focused ion beams (FIBs) work with Ga ions at 30 keV and can reach a beam focus of <10 nm. They are generally used to etch fine structures in materials or to prepare thin samples for transmission electron microscopy. They rely on a liquid metal ion source (LMIS). Nitrogen ions can be accelerated using gas or plasma sources, but the beam focus is much worse than for LMIS, especially at a few keV or less, due to chromatic aberration.

Some of the most promising and challenging applications in diamond require a precise placement of engineered point defects. For example, a quantum computer scheme based on coupled NV centers requires nanometer resolution to make it scalable. The creation of a single optical center in the heart of a photonic structure by ion implantation also requires high resolution and addressing with respect to the photonic structure.

Here, we present a method that demonstrates the targeted implantation of nitrogen ions at better than 20 nm, for the creation of single NV centers. The setup relies on the combination of a low energy ion beam (between 0.2 and 10 keV) and of an AFM. The tip of the AFM is pierced and has a nanohole used to collimate the beam, as seen in Figure 5(a).

The holes are previously drilled with an FIB system. The size of the hole and the position at which it is drilled in the tip are well controlled: Figure 5(b) shows a 60-nm hole pierced in a facet and Figure 5(c) a 20-nm hole pierced directly at the sumit. The advantages of this nanoimplanter are that a maskless implantation is possible, and that with the help of the AFM, the ion beam can be precisely addressed at any place of the sample. The low-energy beam ensures a straggling of a few nanometers, and the resolution depends only on the nanohole diameter and the distance at which it can be approached to the surface. The distance is controlled by the AFM

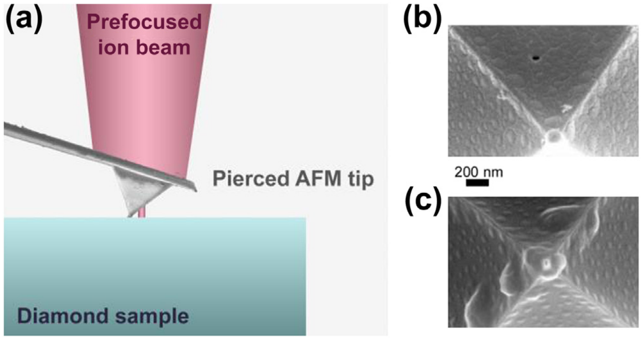

Figure 5 (a) Scheme of the implantation setup combining a low energy ion beam and an AFM with a pierced tip. The sample position is controlled by the piezostage of the AFM. The ion beam is prefocused and aligned with the tip. The implantation is performed in contact mode. (b) Fifty-nanometer hole pierced by FIB milling in a facet. (c) Twenty-nanometer hole pierced directly at the summit of the tip.

approach, and the implantation is performed in the contact mode. More details can be found in Meijer et al. (2008).

Although nitrogen ions are used in the following, the nanoimplanter is versatile, and the gas source can be replaced by an LMIS to extend the implantation possibilities to other atoms. A typical example of collimated implantation with this technique can be found in **Figure 6**. Here, 5-keV nitrogen ions have been implanted at a fluence of 1×10^{13} cm^{-2} through a 100-nm diameter hole (measured by electron microscopy) to create a hexagonal pattern. The distance between each implantation spot is 500 nm.

Figure 6(a) shows a fluorescence scan of this pattern, measured with a confocal microscope. Due to the diffraction-limited resolution, it is not possible to see single NV centers. The scan of the same structure in **Figure 6(b)** is realized using the STED microscopy technique, which is not diffraction limited. Here, single NV centers are imaged with a 10-nm optical resolution and can be recognized in each implantation spot. The spot diameter is in the range of 100 nm, in good agreement with the size of the hole in the tip. We show in Pezzagna, Wildanger et al. (2010) the same implantation with a hole diameter <20 nm, that is, at a resolution suitable for the creation of NV center arrays for quantum applications. Moreover, using the ion sculpting technique (Li et al., 2001), it is possible to further reduce and control the size of the nanoholes.

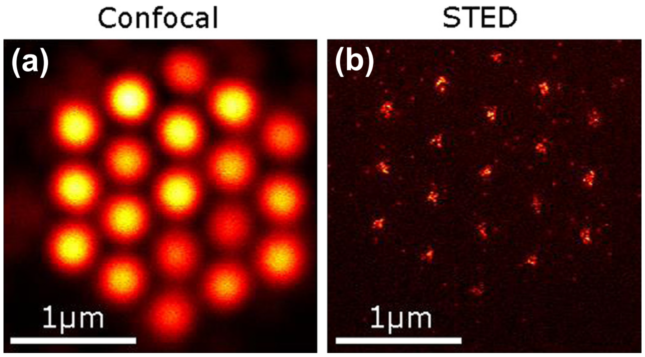

Figure 6 Fluorescence imaging of an array of shallow NV centers created by implantation of 5-keV nitrogen ions through a pierced AFM tip. (a) confocal fluorescence scan with resolution limited by diffraction. (b) STED scan that reveals the details of implantation through the hole of a diameter of approximately 100 nm. (Courtesy of D. Wildanger (MPI Göttingen)).

3.13.3.3 Can Single Ions be Deterministically Implanted?

It has been shown that the spatial resolution of ion implantation is now approaching the nanometer level. However, when a few or a few tens of atoms have to be implanted, fluctuations in the number of implanted ions start playing a role. It is therefore necessary to improve the implantation techniques to, ideally, reach a deterministic implantation of single ions (Meijer et al., 2005). Two approaches are then possible: on the one hand to detect the event of a single ion being implanted and then stop the ion beam or on the other hand to make sure that only one ion is extracted out of the accelerator. The first idea has been implemented in silicon either by detecting secondary electrons created at the ion impact (Schenkel et al, 2002) or by collecting electron–hole pairs with the help of a p–i–n structure (Jamieson et al., 2005). Both of those are however difficult to implement with diamond as it would require to use highly charged ions or to fabricate a p–i–n structure at each place where a single ion has to be implanted. The second method is more promising and versatile; it is based on a Paul trap. Schnitzler et al. show that deterministic single Ca^+ ions can be shot out of such a trap and detected by an electron multiplier (Schnitzler et al, 2009). Nanometer focusing can theoretically be obtained if the ions in the trap can be previously cooled down to their motional ground state. The energy range can be extended to the keV range and extraction rates of a few kilohertz are possible.

3.13.4 Scheme of Individual Addressing of NV Centers

One of the main challenges to build a quantum computer or a magnetometer based on an architecture of coupled NV centers is to individually manipulate and read out the spin of each single NV center. In order to have a sufficient dipolar magnetic coupling, the NV centers have to be close enough (within a few nanometers or tens of nanometers) which makes the addressing particularly difficult. For two or three qubits, it may be possible to manipulate the electron spins individually if the NVs are oriented differently in the diamond. In such a case, applying a magnetic field leads to a different Zeeman splitting for each NV center and therefore to different resonance frequencies. However, this scheme is not scalable. Nevertheless, the imaging of single NVs and the optical detection of electron spin resonance are possible well below the diffraction limit with STED microscopy (Rittweger et al., 2009; Wildanger, Maze, & Hell, 2011). However, the phase of adjacent spin states cannot be preserved due to the intense optical fields, the size of which is diffraction limited (Wildanger et al., 2011).

Here, we propose a new approach to solve this problem, combining the NV centers with conventional electronic devices via electrical connectors; in other words by "wiring" the NV centers. The idea is to control the quantum components and switch them from active to passive with an individual electrical addressing. The NV centers can be found in different charge states in diamond, and it seems today that the ability to switch on demand between these charge states may make possible the individual addressing of NV centers at the nanoscale. Neutral NV^0 and negatively charged NV^- states are well known, and a recently observed unknown state was suggested to be positively charged NV^+ (Grotz et al., 2012). The NV^- center enables an easy manipulation and readout of the electron spin at room temperature with suitable coherence time. It has been proposed that the NV^0 center could also be used as a qubit (Gali, 2009); however, the scheme has not been implemented yet. The NV^+ center is optically dark (Grotz et al., 2012). This center provides no electron spin and therefore does not affect the nuclei at all.

Our proposed pathway for a quantum computer scheme is to selectively and individually use NV^- as active qubits for initialization, operation, and readout, and to use NV^+ (or NV^0) as inactive qubits, transparent to the laser and microwave pulses only working on NV^-. Such a scheme offers the possibility to store the information into nuclear spins (in the order of seconds) but it requires the previous transfer of the spin state from the electron to the nitrogen nuclei before the charge state is switched. This has been recently demonstrated in Dolde et al., in press; the authors do swap the entangled state between two electron spins to the two nitrogen nuclear spins (where the entanglement is "stored") and swap it back to the electrons.

This should allow an individual addressing of NV centers and could lead to a fully scalable quantum computer. The key feature in this scheme is the ability to control reversibly and at a high speed the charge state of the NV centers. In this view, we will recall the first successful experiments that demonstrate passive and active charge state control, and then we will present our approach for a selective electrical addressing of single NV centers.

3.13.4.1 Passive Charge State Control of NV Centers

It has been shown recently that a passive control of the charge state of shallow NV centers is possible through the surface termination of diamond (Hauf et al., 2011). In the case of a Hydrogen-terminated surface, a two-dimensional hole gas forms at the surface, leading to p-type surface conductivity of diamond. This is responsible for the switching of the charge state of shallow NVs to the neutral NV^0 state. This can be seen in **Figure 7** for an ensemble of shallow NV centers created by nitrogen implantation (5 keV, fluence between 1×10^{11} and 1×10^{14} N cm^{-2}) in an as-grown high-purity chemical vapour deposition (CVD) diamond (Tallaire et al., 2006).

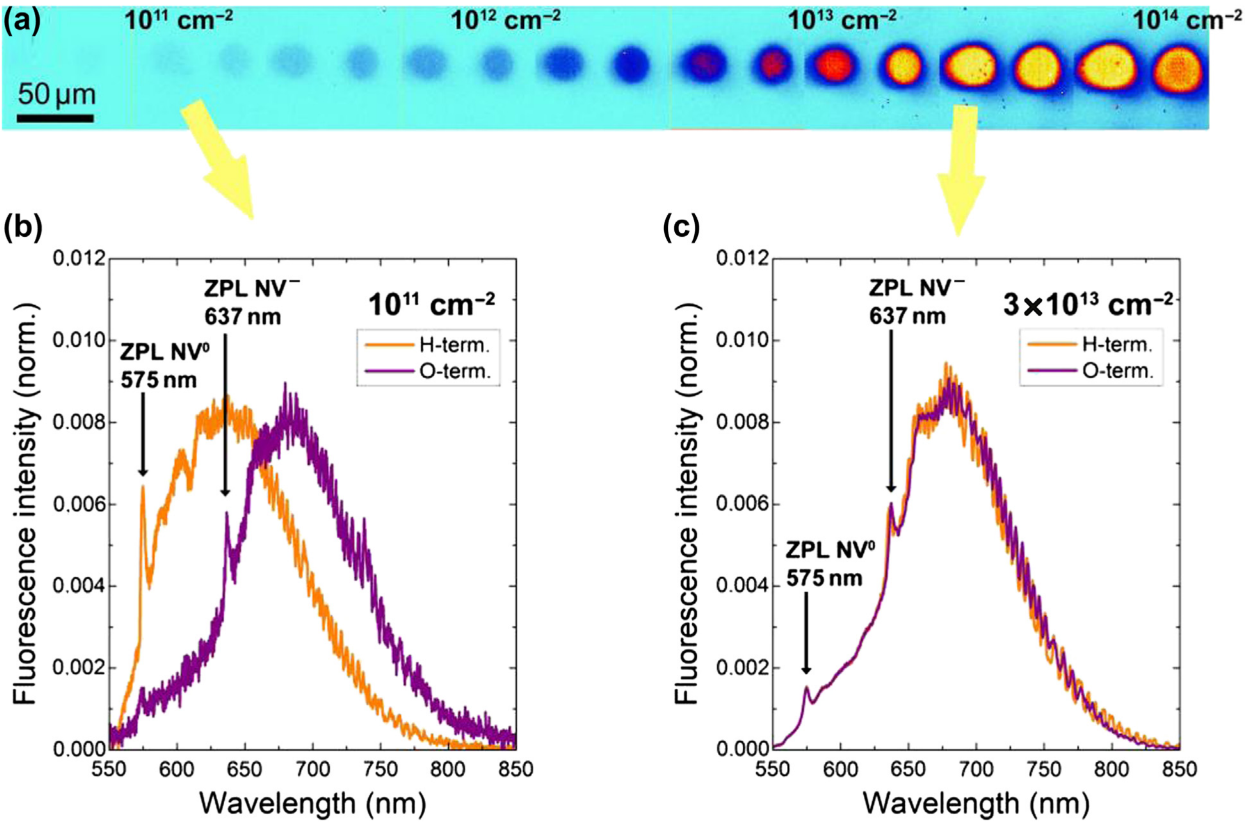

Figure 7 Surface termination-induced charge state control of an ensemble of shallow implanted NV centers. (a) Fluorescence image of a diamond implanted with a 25-µm focused beam of 5-keV N$^+$ ions at different fluences from 6×10^{10} to 1×10^{14} cm^{-2}. (b) Fluorescence spectra taken from the region at 1×10^{11} cm^{-2} with either a hydrogen (orange) or oxygen (violet) surface termination. The charge state is changed from NV^0 to NV$^-$ when the surface termination is modified from H to O. (c) Fluorescence spectra taken from the region at 3×10^{13} cm^{-2} with either a hydrogen (orange) or oxygen (violet) surface termination. At such a high fluence, the surface termination does not influence the charge state anymore.

The fluorescence spectra for H- and O-terminated surface are compared. The diamond surface is H-terminated after the growth and keeps getting H-terminated after annealing in vacuum (800 °C, 2 h). In order to obtain an O-terminated surface, the diamond is boiled in a (1:1:1) mixture of sulfuric, perchloric, and nitric acids for several hours. The fluorescence spectra of the ensemble corresponding to the 1×10^{11} N cm^{-2} fluence clearly shows NV^0 emission (orange curve in Figure 7(b)) while it turns out to be clearly NV$^-$ after the acid bath (purple curve in Figure 7(b)). However, this switching effect is not observed for the ensemble implanted with a higher fluence of 3×10^{13} N cm^{-2} (Figure 7(c)) where most NVs are negatively charged. This may be due to the higher amount of NV centres (with respect to the limited amount of available surface holes) and to the higher amount of nitrogen atoms that act as donators and overcompensate the surface hole gas (Figure 8).

Note that the nitrogen concentration surrounding each NV center from the ensemble in the implanted area corresponds to 0.6 and to 170 ppm (to be compared with the intrinsic concentration of the sample below 5 ppb). Such an effect of the nitrogen concentration has also been experimentally shown and simulated in Hauf et al. (2011). In diamond, unlike in other standard semiconductors, point defects can be found in different charge states, and the Fermi level should be defined locally, depending on the close environment of the defects (Collins, 2002). As a consequence, the implantation of dopants (e.g., phosphorus, boron, or lithium) in the vicinity of NV centers may be another way to passively control the charge of single defects. First experiments on ensemble of NV centers are promising, showing that the coimplantation of phosphorous or boron atoms are able to modify the charge state of NV centers toward NV$^-$ or NV^0, respectively (Groot-Berning, Raatz, Dobrinets, et al., in press). Beside the charge state consideration, the surrounding of the NV centers used as qubits or magnetic sensors has to be kept clean enough not to be detrimental to the fluorescence rate or to the coherence time. This has to be further investigated.

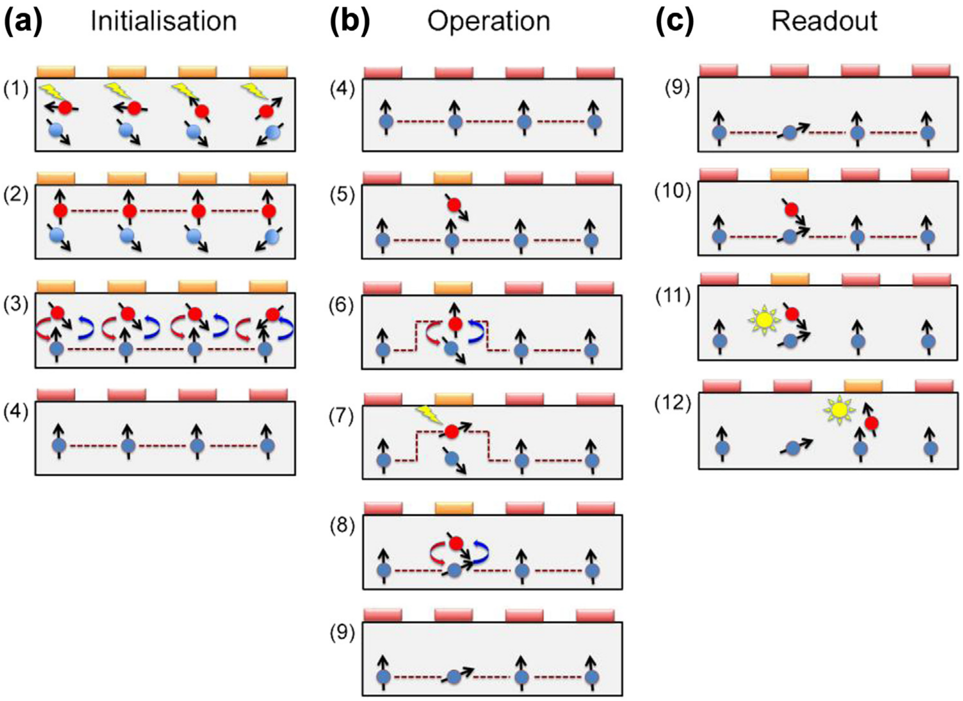

Figure 8 Scheme of the proposed operation sequence for a diamond quantum computer. (a) Initialization: (1) all NV centers are switched to NV$^-$ and a laser pulse is applied to polarize all electron spins that are then brought to the up state with microwave π pulses and then (2) become entangled. (3) A swap operation is used to transfer the spin states to the nuclear spins. The nuclear spins are then now entangled. (4) The last step consists of applying a voltage to the gates in order to ionize the NV centers (from NV$^-$ to NV$^+$). This last step should be done at a high speed to preserve the nuclear spin states. (b) Operation: one qubit or two qubits gate operations are realizable in this scheme using the following process steps: (4) Starting from an entangled system of nuclear spins, (5) a single NV center can be switched from NV$^+$ to NV$^-$ by addressing the corresponding gate. Then, after a spin swap (6), the gate operation can be performed (7). The state is then swop back to the nuclear spin (8) and the voltage applied to the gate can be released (9) to ionize the NV again and finish the gate operation. (c) Readout: the measurement process is achieved by first switching the charge state of the target NV center from NV$^+$ to NV$^-$ (10) and then applying a single-shot readout process (11). This will destroy the entanglement of the system. By changing the gate voltage, the state of the next qubit can be measured using a similar process.

3.13.4.2 Active Charge State Control of NV Centers

It has been recently shown that using an electrolytic gate electrode on an H-terminated surface allows an active and reversible control of the charge state of NV centers. For an ensemble of shallow NVs, the population can be shifted reversibly from NV^0 to NV$^-$ by changing the gate voltage. Single centers can be switched from a nonfluorescent state (still unknown, probably NV$^+$) into the neutral charge state (Grotz et al., 2012). In these experiments, the number of surface holes is controlled by the applied gate voltage. The nitrogen concentration in the direct vicinity of the NV centers appears to shift the population of NV centers toward negatively charged, that is, to pin the local Fermi level upward.

Besides, it is shown in Hirama et al. (2006) that an H-terminated diamond can be successfully covered by an aluminum oxide layer without losing the properties of the hole gas. The authors use a metal gate to fabricate a field effect transistor. This experiment further proves that the Fermi level can also be tuned by using a solid gate. Therefore, this method also seems to be suitable for the charge state switching of NV centers. We propose to implement it at the single level, and to associate such a gate on each single NV of the future quantum device.

3.13.4.3 Quantum Computer (QC) scheme by separation of active and passive quantum elements

A "good" quantum device should have both a very long coherence (T_2) time and be easy to manipulate. However, this is difficult to achieve: either the coherence time is long, meaning that the quantum device is well separated from the environment and can be hardly manipulated, or it is easily manipulated but then shows a short coherence time. With the NV centers, it is possible to satisfy both, taking advantage of the different charge states in which a same single NV can be found. The electron spin associated with the negatively charged NV^- can be manipulated easily. On the contrary, when positively charged, it turns out that the NV center is completely "dark" and cannot be manipulated at all; this promises a very long T_2 time for the nuclear spin. Therefore, the controlled switching between the charge states together with the swapping of the quantum state from the electron to the nuclear spin (forth and back) should provide both a very long T_2 time as well as an optimal manipulation and readout of the quantum device.

The idea of this scheme is to use an array of electron spins, to initialize it, and entangle a given register. The next step is to swap and store the states onto the nuclear spins of the NV centers as a kind of long-term memory and then to switch the NV^- to NV^+ in order to make the array dark and to separate it from the environment. This last step is critical, in order to preserve the coherent state of the nuclei, the charge state has to be switched faster than the hyperfine coupling rate (e.g., >3.3 MHz for ^{15}N). Now the computer is initialized and ready to operate.

In this scheme, gate operations can be realized by the addressing of the qubits by the controlled charge state manipulation of one or two NV centers. One (to perform a single qubit gate operation) or a pair of NV centers (two qubit gate operation) can be controlled and switched back to NV^-, the information of the nuclear spin is swop back to the electron spin and manipulated with the usual techniques.

Once the gate operations are complete, the information will be swop back to the nuclei spin and the charge state of the center will be transferred back to NV^+. To switch the charge state in a controlled way, electronic contacts are necessary. In reference (Grotz et al., 2012) a gate voltage is applied on top of an H-terminated surface using a drop of electrolyte. The idea here to reach a charge state control of individual NVs implies to considerably reduce the size of the electronics by using solid-state gates based on transparent Indium–TinOxide stripes. These stripes should allow an individual switching of the charge state of any of the NV centers, thus allowing a scalable addressing of the NVs.

The readout of the nuclei spins (measurement) can be performed using the single-shot readout method as already shown in Neumann, Beck et al. (2010). The type of array and the number of the applied registers can be freely configured depending on the requirements of the application.

However, to realize this scheme, some technical problems have to be solved so far: (1) an array of single NV centers close to the surface is necessary, (2) the transfer of the quantum information from the electron to the nuclear spin has to be achieved with very high fidelity, (3) the high speed charge switching of individual NV centers from NV^- to NV^+ has to be solved, and (4) a single-shot readout with a high frequency is necessary.

A large number of the necessary properties like single-shot readout have been successfully shown. Not yet shown is the charge state switching from NV^- to NV^+ using solid-state gates and the large coherence time of the nuclear spin for NV^+. However, if this would turn out to be complicated, the switching from NV^- to NV^0 and the storing to ^{13}C spins is also a possible scheme.

3.13.5 Conclusions

NV centers in diamond are among the most interesting objects to produce quantum elements that fulfill the Di Vincenzo's criteria at room temperature. The production of artificial NV centers is feasible using ion implantation. Low kinetic energy single-ion beam implantation enables to address atoms within a few nanometers in all three dimensions. This technique is at the moment the only way to produce an array of, for example, NV centers with a suitable precision as needed to fabricate a quantum array. But the requirements and pitfalls are large: care must be taken regarding the surface roughness, channeling effect, or charging up of the surface. Besides technical limitations, the main intrinsic limitation factor is ion beam straggling. Ion beam straggling depends on the ion species and the target atoms and increases strongly with the ion energy, for example, kinetic ion energies <5 keV for nitrogen ions in diamond are necessary to achieve a lateral resolution aiming at 1 nm. The addressing of ions requires a mask or a focusing technique. At low ion energies, the mask technique is preferable due to the high chromatic aberration of the ion lens systems. We developed an AFM nanomask method that combines a high-resolution AFM with a nanocollimation implantation technique. With this method, the addressing of ions that are <20 nm has been demonstrated and can be further improved. The number of implanted ions is controlled by the implantation time at a fixed ion current. In this way, the error on the implanted ions is given by the Poisson statistics. A deterministic implantation of countable ions can be achieved using a single-ion source developed at the university in Mainz, or by counting the impinging ions with a measurement of secondary electrons. The last technique requires ion energies >30 keV and limits the lateral resolution.

However, ion implantation is only the first step toward the creation of quantum devices based on NV centers in diamond. To produce artificial NV optical centers using nitrogen implantation also requires repairing the crystal implantation defects, creating the N–V bonds and stabilizing the NV charge state. This is commonly done by annealing the samples in a vacuum furnace at a temperature between 800 and 1000 °C. Unfortunately, the creation yield of NV centers is small for low ion energies (a few percent or less). Possible solutions to increase it are a postirradiation and annealing process, a subsequent overgrowth to bury the shallow NV centers, or a surface treatment to find a suitable termination of the surface.

Besides the production of the NV, the charge state of the center has to be controlled. A passive charge state manipulation is possible either by using an appropriate surface termination or by bringing dopant atoms in the vicinity of the NV centers (by implantation or during the growth of the diamond layer). But an active control is also feasible by using a gate structure as used in diamond field effects transistors. This further enables to switch the charge state and promises a new route toward individual addressing of NV centers. There are still a large number of open questions; however, ion implantation seems to be a key feature in the production of quantum devices.

Acknowledgments

The authors acknowledge the financial support of the Volkswagen Foundation, the Deutsche ForschungsGemeinschaft (FOR1493) and the European project QINVC 01BQ1105. The authors acknowledge fruitful collaborations with the groups of Prof. Jörg Wrachtrup (Stuttgart University, Germany), Prof. Jean-François Roch (Ecole Normale Supérieure de Cachan, France), Prof. Fedor Jelezko (Ulm University, Germany), Prof. Stefan W. Hell (Max Planck Institute Göttingen, Germany), Prof. Alexander Zaitsev (Staten Island University, USA), and with the LSPM laboratory (Villetaneuse, France).

References

Acosta, V. M., Bauch, E., Ledbetter, M. P., Santori, C., Fu, K.-M. C., Barclay, P. E., et al. (2009). Diamonds with a high density of nitrogen-vacancy centers for magnetometry applications. *Physical Review B, 80*, 115202.

Adamczewski, J., Meijer, J., Stephan, A., Bukow, H. H., & Rolfs, C. (1996). Optimization of material and shape for nuclear microprobe apertures. *Nuclear Instruments & Methods in Physics Research Section B, 114*, 172.

Aharonovich, I., Castelletto, S., Simpson, D. A., Su, C.-H., Greentree, A.-D., & Prawer, S. (2011). Diamond-based single-photon emitters. *Reports on Progress in Physics, 74*, 076501.

Allers, L., Collins, A. T., & Hiscock, J. (1998). The annealing of interstitial-related optical centres in type II natural and CVD diamond. *Diamond and Related Materials, 7*, 228.

Balasubramanian, G., Chan, I. Y., Kolesov, R., Al-Hmoud, M., Tisler, J., Shin, C., et al. (2008). Nanoscale imaging magnetometry with diamond spins under ambient conditions. *Nature, 455*, 648–652.

Balasubramanian, G., Neumann, P., Twitchen, D., Markham, M., Kolesov, R., Mizuochi, N., et al. (2009). Ultralong spin coherence time in isotopically engineered diamond. *Nature Materials, 8*, 383.

Bogdan, G., Nesládek, M., D'Haen, J., Maes, J., Moshchalkov, V. V., Haenen, K., et al. (2005). Growth and characterization of near-atomically flat, thick homoepitaxial CVD diamond films. *Physica Status Solidi A: Applications and Materials Science, 202*, 2066.

Chernyshev, V. A., Meijer, J., Grambole, D., Herrmann, F., Dagkaldiran, Ü., & Wieck, A. D. (2008). n-type diamond produced by MeV lithium implantation in channeling direction. *Diamond and Related Materials, 17*, 1933.

Cho, K., Allen, W. R., Finstad, T. G., & Chu, W. W. (1985). Channeling effect for low energy ion implantation in Si. *Nuclear Instruments & Methods in Physics Research Section B, 7/8*, 265.

Collins, A. T. (2002). The Fermi level in diamond. *Journal of Physics: Condensed Matter, 14*, 3743.

Courant, E. D. (1951). Multiple scattering corrections for collimating slits. *Review of Scientific Instruments, 22*, 1003.

Craven, J. A., Harte, B., Fisher, D., & Schulze, D. J. (2009). Diffusion in diamond. I. Carbon isotope mapping of natural diamond. *Mineralogical Magazine, 73*, 193.

Degen, C. L. (2008). Scanning magnetic field microscope with a diamond single-spin sensor. *Applied Physics Letters, 92*, 243111.

Derry, T. E., Fearick, R. W., & Sellschop, J. P. F. (1982). Ion channeling in natural diamond. II. Critical angles. *Physical Review B, 26*, 17.

Dolde F., Jakobi I., Naydenov B., Zhao N., Pezzagna S., Trautmann C., et al. (2013). Room temperature entanglement between single defect spins in diamond. *Nature Physics 9*,1393.

Dréau, A., Spinicelli, P., Maze, J., Roch, J.-F., & Jacques, V. (2013). Single-shot readout of multiple nuclear spin qubits in diamond under ambient conditions. *Physical Review Letters, 110*, 060502.

Fairchild, B. A., Rubanov, S., Lau, D. W. M., Robinson, M., Suarez-Martinez, I., Marks, N., et al. (2012). Mechanism for the amorphisation of diamond. *Advanced Materials, 24*, 2024.

Faklaris, O., Garrot, D., Joshi, V., Druon, F., Boudou, J.-P., Sauvage, T., et al. (2008). Detection of single photoluminescent diamond nanoparticles in cells and study of the internalization pathway. *Small, 4*, 2236.

Fu, C.-C., Lee, H.-Y., Chen, K., Lim, T.-S., Wu, H.-Y., Lin, P.-K., et al. (2007). Characterization and application of single fluorescent nanodiamonds as cellular biomarkers. *Proceedings of the National Academy of Sciences of the United States of America, 104*, 727.

Gali, A. (2009). Theory of the neutral nitrogen-vacancy center in diamond and its application to the realization of a qubit. *Physical Review B, 79*, 235210.

Groot-Berning K., Raatz N., Dobrinets I., Tallaire A., Achard J., Meijer J. et al. (in press). Passive charge state control of nitrogen-vacancy centres in diamond using phosphorous and boron doping.

Grotz, B., Hauf, M. V., Dankerl, M., Naydenov, B., Pezzagna, S., Meijer, J., et al. (2012). Charge state manipulation of qubits in diamond. *Nature Communications, 3*, 729.

Gruber, A., Dräbenstedt, A., Tietz, C., Fleury, L., Wrachtrup, J., & von Borczyskowski, C. (1997). Scanning confocal optical microscopy and magnetic resonance on single defect centers. *Science, 276*, 2012.

Guzmán de la Mata, B., Dowsett, M. G., & Palitsin, V. (2005). Ultra-low energy SIMS study of ultra-shallow boron implants in HPHT diamond. *Physica Status Solidi A: Applications and Materials Science, 202*, 2148.

Harte, B., Taniguchi, T., & Chakraborty, S. (2009). Diffusion in diamond. II. High-pressure-temperature experiments. *Mineralogical Magazine, 73*, 201.

Hauf, M. V., Grotz, B., Naydenov, B., Dankerl, M., Pezzagna, S., Meijer, J., et al. (2011). Chemical control of the charge state of nitrogen-vacancy centers in diamond. *Physical Review B, 83*, 081304.

Hell, S. W., & Winchmann, J. (1994). Breaking the diffraction resolution limit by stimulated emission: stimulated-emission-depletion fluorescence microscopy. *Optics Letters, 19*, 780.

Hirama, K., Miyamoto, S., Matsudaira, H., Yamada, K., Kawarada, H., Chikyo, T., et al. (2006). Characterization of diamond metal–insulator–semiconductor field-effect transistors with aluminium oxide gate insulator. *Applied Physics Letters, 88*, 112117.

Hoble, G. (1996). Critical angles and low-energy limits to ion channeling in silicon. *Radiation Effects and Defects in Solids, 139*, 21.

Hobler, G. (1995). Monte Carlo simulation of two-dimensional implanted dopant distributions at mask edges. *Nuclear Instruments & Methods in Physics Research Section B, 96*, 155.

Hobler, G. (1996). Theoretical estimate of the low-energy limit to ion channeling. *Nuclear Instruments & Methods in Physics Research Section B, 115*, 323.

Hönicke, P., Beckhoff, B., Kolbe, M., Giubertoni, D., van den Berg, J., & Pepponi, G. (2010). Depth profile characterization of ultra shallow junction implants. *Analytical and Bioanalytical Chemistry, 396*, 2825.

Iakoubovskii, K., & Adriaenssens, G. J. (2001). Trapping of vacancies by defects in diamond. *Journal of Physics: Condensed Matter, 13*, 6015.

Ishikawa, T., Fu, K.-M. C., Santori, C., Acosta, V. M., Beausoleil, R. G., Watanabe, H., et al. (2012). Optical and spin coherence properties of nitrogen-vacancy centers placed in a 100 nm thick isotopically purified diamond layer. *Nano Letters, 12*, 2083.

Jamieson, D. N., Yang, C., Hopf, T., Hearne, S. M., Pakes, C. I., Prawer, S., et al. (2005). Controlled shallow single-ion implantation in silicon using an active substrate for sub-20-kV ions. *Applied Physics Letters, 86*, 202101.

Jelezko, F., Gaebel, T., Popa, I., Gruber, A., & Wrachtrup, J. (2004). Observation of coherent oscillations in a single electron spin. *Physical Review Letters, 92*, 076401.

Jelezko, F., & Wrachtrup, J. (2006). Single defect centres in diamond: a review. *Physica Status Solidi A: Applications and Materials Science, 203*, 3207.

Kato, H., Yamasaki, S., & Okushi, H. (2005). n-type doping of (001)-oriented single-crystalline diamond by phosphorus. *Applied Physics Letters, 86*, 222111.

Khan, H. A., Khan, N. A., & Spohr, R. (1981). Scanning electron microscope analysis of etch pits obtained in a muscovite mica track detector by etching in hydrofluoric acid and aqueous solutions of NaOH and KOH. *Nuclear Instruments & Methods in Physics Research Section B, 189*, 577.

Kurtsiefer, C., Mayer, S., Zarda, P., & Weinfurter, H. (2000). Stable solid-state source of single photons. *Physical Review Letters, 85*, 290.

Ladd, T. D., Jelezko, F., Laflamme, R., Nakamura, Y., Monroe, C., & O'Brien, J. L. (2010). Quantum computers. *Nature, 464*, 45.

Li, J., Stein, D., McMullan, C., Branton, D., Aziz, M. J., & Golovchenko, J. A. (2001). Ion-beam sculpting at nanometre length scales. *Nature, 412*, 166.

Liang, J.-H., Chiang, S.-L., Chen, C.-T., Niu, H., & Tseng, M.-S. (2002). Depth profiles of cluster-ion-implanted BSi in silicon. *Nuclear Instruments & Methods in Physics Research Section B, 190*, 767.

Lindhard, J. (1964). Motion of swift charged particles, as influenced by strings of atoms in crystals. *Physics Letters, 12*, 126.

Lohrmann, A., Pezzagna, S., Dobrinets, I., Spinicelli, P., Jacques, V., Roch, J.-F., et al. (2011). Diamond based light-emitting diode for visible single-photon emission at room temperature. *Applied Physics Letters, 99*, 251106.

Maertz, B. J., Wijnheijmer, A. P., Fuchs, G. D., Nowakowski, M. E., & Awschalom, D. D. (2010). Vector magnetic field microscopy using nitrogen vacancy centers in diamond. *Applied Physics Letters, 96*, 092504.

Maletinsky, P., Hong, S., Grinolds, M. S., Hausmann, B., Lukin, M. D., Walsworth, R. L., et al. (2012). A robust scanning diamond sensor for nanoscale imaging with single nitrogen-vacancy centres. *Nature Nanotechnology, 7*, 320.

Mamin, H. J., Kim, M., Sherwood, M. H., Rettner, C. T., Ohno, K., Awschalom, D. D., et al. (2013). Nanoscale nuclear magnetic resonance with a nitrogen-vacancy spin sensor. *Science, 339*, 557.

Manson, N. B., Harrison, J. P., & Sellars, M. J. (2006). Nitrogen-vacancy center in diamond: model of the electronic structure and associated dynamics. *Physical Review B, 74*, 104303.

Markham, M. L., Dodson, J. M., Scarsbrook, G. A., Twitchen, D. J., Balasubramanian, G., Jelezko, F., et al. (2011). CVD diamond for spintronics. *Diamond and Related Materials, 20*, 134.

Maurer, P. C., Kucsko, G., Latta, C., Jiang, L., Yao, N. Y., Bennett, S. D., et al. (2012). Room-temperature quantum bit memory exceeding one second. *Science, 336*, 1283.

Maurer, P. C., Maze, J. R., Stanwix, P. L., Jiang, L., Gorshkov, A. V., Zibrov, A. A., et al. (2010). Far-field optical imaging and manipulation of individual spins with nanoscale resolution. *Nature Physics, 6*, 912.

Maze, J., Stanwix, P. L., Hodges, J. S., Hong, S., Taylor, J. M., Cappelaro, P., et al. (2008). Nanoscale magnetic sensing with an individual electronic spin in diamond. *Nature, 455*, 644.

Meijer, J., Burchard, B., Domhan, M., Wittmann, C., Gaebel, T., Popa, I., et al. (2005). Generation of single color centers by focused nitrogen implantation. *Applied Physics Letters, 87*, 261909.

Meijer, J., Pezzagna, S., Vogel, T., Burchard, B., Bukow, H. H., Rangelow, I. W., et al. (2008). Towards the implanting of ions and positioning of nanoparticles with nm spatial resolution. *Applied Physics A, 91*, 567.

Meijer, J., & Stephan, A. (2002). Prospects of ion projection techniques for maskless implantation at high ion energies. *Nuclear Instruments & Methods in Physics Research Section B, 188*, 9.

Meijer, J., Stephan, A., Adamczewski, J., Röcken, H., Weidenmüller, U., Bukow, H. H., et al. (1999). Microprobe as implanter for semiconductor devices. *Nuclear Instruments & Methods in Physics Research Section B, 158*, 39.

Mizuochi, N., Makino, T., Kato, H., Takeuchi, D., Ogura, M., Okushi, H., et al. (2012). Electrically driven single-photon source at room temperature in diamond. *Nature Photonics, 6*, 299.

Mohan, N., Chen, C.-S., Hsieh, H.-H., Wu, Y.-C., & Chang, H.-C. (2010). In vivo imaging and toxicity assessments of fluorescent nanodiamonds in Caenorhabditis elegans. *Nano Letters, 10*, 3692.

Naydenov, B., Reinhard, F., Lämmle, A., Richter, V., Kalish, R., D'Haenens-Johansson, U. F. S., et al. (2010). Increasing the coherence time of single electron spins in diamond by high temperature annealing. *Applied Physics Letters, 97*, 242511.

Neu, E., Steinmetz, D., Riedrich-Möller, J., Gsell, S., Fischer, M., Schreck, M., et al. (2011). Single photon emission from silicon-vacancy colour centres in chemical vapour deposition nano-diamonds on iridium. *New Journal of Physics, 13*, 025012.

Neumann, P., Beck, J., Steiner, M., Rempp, F., Fedder, H., Hemmer, P. R., et al. (2010). Single-shot readout of a single nuclear spin. *Science, 329*, 542.

Neumann, P., Kolesov, R., Naydenov, B., Beck, J., Rempp, F., Steiner, M., et al. (2010). Quantum register based on coupled electron spins in a room-temperature solid. *Nature Physics, 6*, 249.

Neumann, P., Mizuochi, N., Rempp, F., Hemmer, P., Watanabe, H., Yamakasi, S., et al. (2008). Multipartite entanglement among single spins in diamond. *Science, 320*, 1326.

Ofori-Okai, B. K., Pezzagna, S., Chang, K., Loretz, M., Schirhagl, R., Tao, Y., et al. (2012). Spin properties of very shallow nitrogen vacancy defects in diamond. *Physical Review B, 86*, 081406.

Olivero, P., Rubanov, S., Reichart, P., Gibson, B. C., Huntington, S. T., Rabeau, J., et al. (2005). Ion-beam-assisted lift-off technique for three-dimensional micromachining of freestanding congle-crystal diamond. *Advanced Materials, 17*, 2427.

Pezzagna, S., Rogalla, D., Becker, H.-W., Jakobi, I., Dolde, F., Naydenov, B., et al. (2011). Creation of colour centres in diamond by collimated ion-implantation through nano-channels in mica. *Physica Status Solidi A: Applications and Materials Science, 208*, 2017.

Pezzagna, S., Rogalla, D., Wildanger, D., Meijer, J., & Zaitsev, A. (2011). Creation and nature of optical centres in diamond for single-photon emission—overview and critical remarks. *New Journal of Physics, 13*, 035024.

Pezzagna, S., Naydenov, B., Jelezko, F., Wrachtrup, J., & Meijer, J. (2010). Creation efficiency of nitrogen-vacancy centres in diamond. *New Journal of Physics, 12*, 065017.

Pezzagna, S., Wildanger, D., Mazarov, P., Wieck, A. D., Sarov, Y., Rangelow, I., et al. (2010). Nanoscale engineering and optical addressing of single spins in diamond. *Small, 6*, 2117.

Pfaff, W., Taminiau, T. H., Robledo, L., Bernien, H., Markham, M., Twitchen, D. J., et al. (2013). Demonstration of entanglement-by-measurement of solid-state qubits. *Nature Physics, 9*, 29.

Pham, L. M., Le Sage, D., Stanwix, P. L., Yeung, T. K., Glenn, D., Trifonov, A., et al. (2011). Magnetic field imaging with nitrogen-vacancy ensembles. *New Journal of Physics, 13*, 045021.

Posselt, M. (2004) in http://www.hzdr.de/db/Cms?pNid=310&pOid=21576, Helmoltz Zentrum Dresden/Rossendorf.

Redinger, A., Standop, S., Rosandi, Y., Urbassek, H. M., & Michely, T. (2011). Making channeling visible: keV noble gas ion trails on Pt(111). *New Journal of Physics, 13*, 013002.

Rittweger, E., Han, K. Y., Irvine, S. E., Eggeling, C., & Hell, S. W. (2009). STED microscopy reveals colour centres with nanometric resolution. *Nature Photonics, 3*, 144.

Rondin, L., Tetienne, J.-P., Spinicelli, P., Dal Savio, C., Karrai, K., Dantelle, G., et al. (2012). Nanoscale magnetic field mapping with a single spin scanning probe magnetometer. *Applied Physics Letters, 100*, 153118.

Schenkel, T., Persaud, A., Park, S. J., Meijer, J., Kingsley, J. R., McDonald, J. W., et al. (2002). Single ion implantation for solid state quantum computer development. *The Journal of Vacuum Science and Technology B, 20*, 2819.

Schnitzler, W., Linke, N. M., Fickler, R., Meijer, J., Schmidt-Kaler, F., & Singer, K. (2009). Deterministic ultracold ion source targeting the Heisenberg limit. *Physical Review Letters, 102*, 070501.

Smith, R., & Webb, R. P. (1991). Long-range channeling in low energy ion implantation into silicon. *Philosophical Magazine Letters, 64*, 253.

Spinicelli, P., Dréau, A., Rondin, L., Silva, F., Achard, J., Xavier, S., et al. (2011). Engineered arrays of nitrogen-vacancy color centers in diamond based on implantation of CN- molecules through nanoapertures. *New Journal of Physics, 13*, 025014.

Staudacher, T., Shi, F., Pezzagna, S., Meijer, J., Du, J., Meriles, C. A., et al. (2013). Nuclear magnetic resonance spectroscopy on a (5 nm)^3 sample volume. *Science, 339*, 561.

Staudacher, T., Ziem, F., Häussler, L., Stöhr, R., Steinert, S., Reinhard, F., et al. (2012). Enhancing the spin properties of shallow implanted nitrogen vacancy centers in diamond by epitaxial overgrowth. *Applied Physics Letters, 101*, 212401.

Steinert, S., Dolde, F., Neumann, P., Aird, A., Naydenov, B., Balasubramanian, G., et al. (2010). High sensitivity magnetic imaging using an array of spins in diamond. *Review of Scientific Instruments, 81*, 043705.

Tallaire, A., Collins, A. T., Charles, D., Achard, J., Sussmann, R., Gicquel, A., et al. (2006). Characterisation of high-quality thick single-crystal diamond grown by CVD with a low nitrogen addition. *Diamond and Related Materials, 15*, 1700.

Toyli, D. M., Weiss, C. D., Fuchs, G. D., Schenkel, T., & Awschalom, D. (2010). Chip-scale nanofabrication of single spins and spin arrays in diamond. *Nano Letters, 10*, 3168.

Vogel, T., Meijer, J., & Zaitsev, A. (2004). Highly effective p-type doping of diamond by MeV-ion implantation of boron. *Diamond and Related Materials, 13*, 1822.

Wildanger, D., Maze, J., & Hell, S. W. (2011). Diffraction unlimited all-optical recording of electron spin resonances. *Physical Review Letters, 107*, 017601.

Zaitsev, A. M. (2001). *Optical properties of diamond. A data handbook.* Springer, ISBN 3-540-66582-X.

Ziegler, J. (2008). *The stopping range of ions in matter*. SRIM-2008. online at http://srim.org.

SECTION V

SELECTED PROPERTIES OF DIAMOND AND APPLICATIONS

3.14 Surface Electronic Properties of Diamond

3.15 Polycrystalline CVD Diamond for Industrial Applications

3.16 Diamond Nanoparticles: Surface Modifications and Applications

3.17 Diamond for Particle and Photon Detection in Extreme Conditions

3.18 Single Color Centers in Diamond: Materials, Devices, and Applications

3.19 Electrochemical Application of Diamond Electrodes

3.14 Surface Electronic Properties of Diamond

Christoph E. Nebel, Fraunhofer-Institute for Applied Solid State Physics, Freiburg, Germany

3.14.1 Introduction

Diamond exhibits considerable potential for a variety of applications on account of its outstanding mechanical, optical, and electronic properties (Dischler & Wild, 1998). Especially, two features of diamond are unique among all semiconductors (Bandis & Pate, 1995; Ristein, Stein, & Ley, 1997). One is the true negative electron affinity (NEA) of the hydrogen-terminated diamond surface. Second, diamond shows under special circumstances a high p-type surface conductivity (Landstrass, & Ravi, 1989a,b), which may be utilized in a variety of electronic devices (Geis & Twichell, 1995; Gluche, Aleksov, Ebert, & Kohn, 1997; Tsugawa, Kitatani, Noda, et al., 1999). The electron affinity χ is the energy difference between the conduction-band minimum E_{CBM} and the vacuum level E_{VAC} (Mönch, 1995):

$$\chi = E_{\mathrm{VAC}} - E_{\mathrm{CBM}}$$

It can be modified by surface dipole effects that are intentionally or unintentionally generated on the surface of diamond. Diamond therefore shows great potential for cold electron emitters (Geis & Twichell, 1995), optimized molecular interfaces (Nebel, 2007; Hoffmann et al., 2011), pH and biosensors due to the combination of surface conductivity, biocompatibility, and chemical stability (Nebel, Rezek, Shin, Uetsuka, & Yang, 2007).

This chapter is organized as follows: First, we will introduce the effects of dipoles on diamond surfaces (part II), then we will discuss the surface conductivity of undoped diamond in air (part III), followed by a description of surface electronic properties of diamond covered with adsorbates (part IV). A summary of features related to surface electronic properties in electrolytes will be given in part V and a summary in part VI.

3.14.2 Dipole Effects on Diamond Surfaces

The diamond surface can be terminated by a variety of elements such as H, O, F, and Cl (Miller & Brown, 1996) or organic molecules such as OH, phenyl, and long-chain amines (Nebel, Rezek, et al., 2007, Nebel, Shin, et al., 2007), giving rise to new phenomena and applications. Surface terminations affect the electron affinity χ. For example, oxygen (O) termination causes an increase in the positive electron affinities (PEAs), while

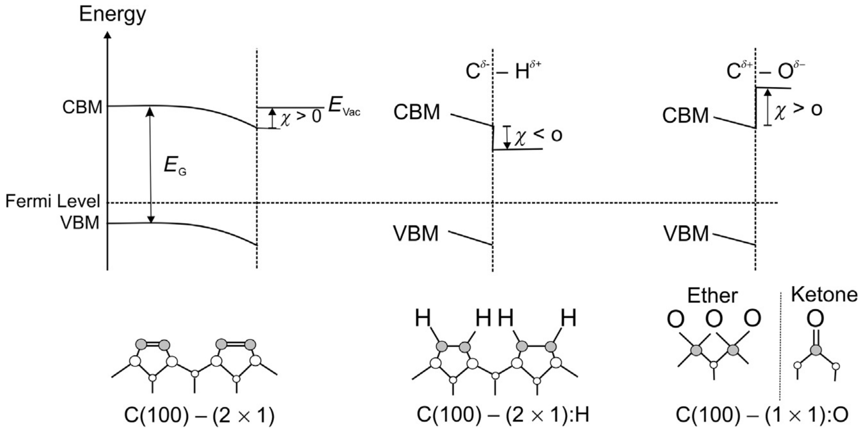

Figure 1 Top: Band scheme and electron affinity χ for the bare, the hydrogenated, and the oxidized diamond (100) surface. Bottom: Sketch of the atomic arrangement of the bare, the hydrogenated, and the oxidized (100) diamond surface.

hydrogen (H) gives rise to an NEA (Bandis & Pate, 1995; Cui, Ristein, & Ley, 1998; Maier, Ristein, & Ley, 2001; Ristein, Maier, Riedel, Cui, & Ley, 2000). This is shown schematically in **Figure 1**. The variation of the electron affinity can be discussed taking into account the electronegativity, δ, of atoms (Mönch, 1995). The δ is a chemical property that describes the tendency of an atom to attract electrons toward it. The higher the associated electronegativity number, the more an atom attracts electrons. The electronegativity of atoms has been calculated and is given as a dimensionless quantity, the Pauling units (Pauling, 1939/1960, pp. 88–107). Carbon has an electronegativity of 2.55 and hydrogen 2.2. Pauling correlated the amount of ionic character or the iconicity of single bonds in diatomic molecules A–B with the different δ_A–δ_B of the atomic electronegativities of the atoms forming the molecule. A revised version of the relation originally proposed by Pauling is that of Hanney and Smith (1946):

$$\Delta q_1 = 0.16|\delta_A - \delta_B| + 0.035|\delta_A - \delta_B|^2 \tag{1}$$

In a simple point-charge model, such atoms are charged by $+\Delta q_1 e$ and $-\Delta q_1 e$ where the more electronegative atom becomes negatively charged ("e" is the elementary charge). Diatomic molecules with $|\delta_A - \delta_B| \neq 0$ thus possess dipole moments. By using the simple point-charge model, they may be written as

$$p = \Delta q_1 ed \tag{2}$$

where d is the bond length of the diatomic molecule.

Considering the hydrogen-terminated diamond surface diatomic surface dipoles $^-$C–H$^+$ are formed. In the case of oxygen termination (electronegativity of O is 3.44), the dipole reverses to $^+$C–O$^-$. Such dipoles cause potential steps ΔV perpendicular to the surface over the distance of the C–H bond length of $d_{CH} = 1.1$ Å or over the spacing between C–O (ether configuration of O) of about $d_{CO} = 0.7$ Å. This potential step gives rise to a lowering (H-termination) or enlargement (O-termination) of the vacuum level, E_{VAC}, with respect the conduction-band minimum, E_{CM}, given by $\Delta E = e\Delta V$ compared to its value without the dipole layer.

The reduction of the electron affinity χ from χ_{max} depends on the areal density, n, and on the magnitude p of the dipoles (Maier et al., 2001; Cui et al., 1998; Kawarada, 1996):

$$\chi - \chi_{max} = -e\Delta V = -\frac{epn}{\varepsilon_o} f(n) \tag{3}$$

where ε_o is the dielectric constant. The function $f(n)$, which depends on n takes the interaction of dipoles into account with the result that the contribution of each dipole to ΔV is reduced for high dipole densities. An expression for $f(n)$ with the polarizability α of the dipoles as a parameter can be obtained according to the calculation of Topping (1927):

$$f(n) = \left(1 + \frac{9\alpha n^{3/2}}{4\pi\varepsilon_o}\right)^{-1} \tag{4}$$

Table 1 Electron affinities of (100) and (111) oriented diamond surfaces with different reconstructions

Diamond surface	*Electron affinity* χ *(eV)*	*Dipole moment* p *(eÅ)*
(111)-(2 × 1)	+0.38	
(111)-(2 × 1):H	−1.27	+0.09
(100)-(2 × 1)	+0.50	
(100)-(2 × 1):H	−1.30	+0.08
(100)-(1 × 1):O	+1.73	−0.10

Data from Maier et al. (2001); and Cui et al. (1998).

Maier et al. (2001) and Cui et al. (1998) have discussed these properties in detail, and their results are summarized in **Table 1**:

Instead of using fully hydrogen- or oxygen-terminated diamond surfaces with data summarized in **Table 1**, there is the possibility to apply partially terminated surfaces generated, for example, by the thermal evaporation of hydrogen or oxygen. Considering first-order desorption kinetics of hydrogen from the diamond surface, the dipole density as a function of isothermal annealing time t is given Maier et al. (2001) and Cui, Ristein, and Ley (1998):

$$n(t) = n_0 e^{-t/\tau} \tag{5}$$

where n_0 is the areal density of the H atoms at the start of the annealing and thus equals the surface density of C atoms of 1.81×10^{15} cm^{-2} for the (111) surface and 1.57×10^{15} cm^{-2} on (100). For thermal desorption experiments on H-terminated diamond at 1000 K, τ is about 1850 s. A typical result of the variation of the electron affinity as measured by photoemission experiments on H-terminated diamond is shown in **Figure 2**. The electron affinity χ versus annealing time (at $T = 1000$ K) is continuously changing from −1.3 eV (fully hydrogen terminated) to +0.3 eV for a bare carbon surface. The dashed line through the date points is a result of a fit calculation using Eqns (3)–(5) (for details see Maier et al., 2001 and Cui et al., 1998). To investigate the effect of increasing PEA, thermal annealing experiments in combination with photoemission measurements and X-ray photoelectron spectroscopy have been performed on an initially oxidized diamond surface with (100) orientation. With decreasing oxygen coverage, the electron affinity decreases from +1.7 to 0.3 eV for a bare diamond surface as shown in **Figure 3**.

These experiments demonstrate that the electron affinity on diamond can be tuned between −1.3 and +1.7 eV over about 3 eV using fractional H and O terminations. This means that the vacuum energy level can be

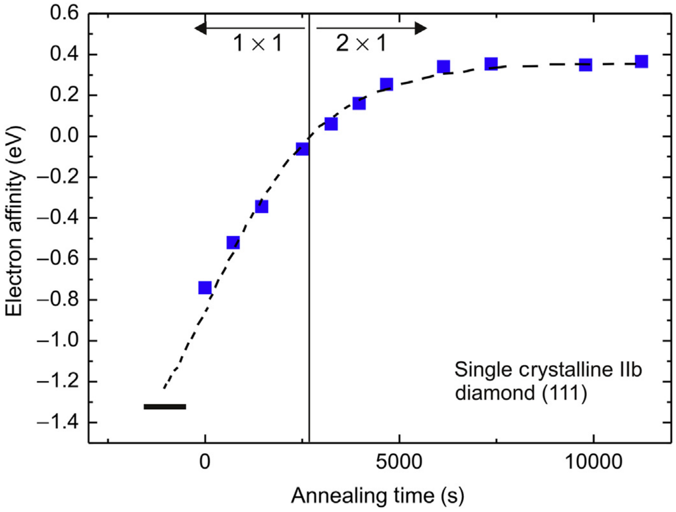

Figure 2 The electron affinity χ (solid squares) as a function of the annealing time at 1000 K. The dashed line through the data points for χ is the result of a fit assuming first-order desorption kinetics of hydrogen. The full line marks the transition from NEA to PEA.

adjusted by surface treatments thereby adjusting energy levels (highest unoccupied molecular orbital, lowest unoccupied molecular orbital) of molecular layers on diamond for the optimization of electron transfer rates in electrochemical devices or at biomimetic diamond/protein interfaces.

3.14.3 Surface Conductivity of Undoped Diamond in Air

Insulating ("undoped") hydrogen-terminated diamond exhibits a surface conductivity in air (Gi, Mizumasa, Akiba, et al., 1995; Maier, Riedel, Mantel, Ristein, & Ley, 2000). Hall effect experiments revealed the p-type nature of the surface conductivity (Hayashi, Yamanaka, Okushi, & Kajimura, 1996; Maki et al., 1992), with typical hole sheet-densities between 10^{10} and 10^{13} cm^{-2}, and Hall mobilities between 1 and 100 $cm^2 V^{-1} s^{-1}$ (Gi, Tashiro, Tanaka, et al., 1999; Looi, Jackman, & Foord, 1998). A summary of the data is shown in **Figure 4** (Nebel, Rezek, Shin, & Watanabe, 2006). There is an overall trend toward lower mobilities with increasing hole sheet densities.

The surface conductivity is related to hydrogen termination in combination with an adsorbate coverage. As the most plausible model for the formation of the surface conductivity, a "transfer doping model" has been proposed (Chakrapani, Angus, Anderson, et al., 2007; Gi et al., 1995; Maier et al., 2000; Shirafuji & Sugino, 1996). In this model, valence-band electrons tunnel into electronic empty states of an adjacent adsorbate layer as shown schematically in **Figure 5**. In order to act as sink for electrons, the adsorbate layer must have its lowest unoccupied electronic level below the valence band maximum (VBM) of diamond. Maier et al. (2000) proposed that for standard atmospheric conditions, the pH value of water is about 6 due to CO_2 content or other ionic contaminations. They calculated the chemical potential μ_e for such an aqueous wetting layer to be about −4.26 eV below the vacuum level. To calculate the VBM, E_{VBM}, of H-terminated diamond with respect to the vacuum level, E_{VAC}, we take into account the band gap of diamond, E_G of 5.47 eV, and the NEA χ of −1.1 to −1.3 eV (Maier et al., 2000, Takeuchi et al., 2005). This results in a gap between the vacuum level and VBM of −4.17 to −4.37 eV if we refer to the vacuum level as zero. The Fermi-level E_F at the electrolyte/diamond interface is therefore either slightly in (~90 meV) or close to the VBM (110 meV above E_{VBM}). A generalized summary of chemical potentials with respect to hydrogen- and oxygen-terminated diamond is given in **Figure 6** (Angus, Pleskov, & Eaton, 2004). This shows that for well-defined pH liquids, the chemical potential μ(pH) may indeed be below E_{VBM}. In such a case, a hole accumulation layer at the surface of diamond is generated by transfer doping. However, as the pH value of adsorbate layers cannot be detected experimentally, a discussion based on assumptions will not elucidate the real features.

In the following, a summary of surface electronic properties of H-terminated diamond is given for (1) diamond/adsorbate and (2) diamond/electrolyte combinations based on the Hall effect, contact potential

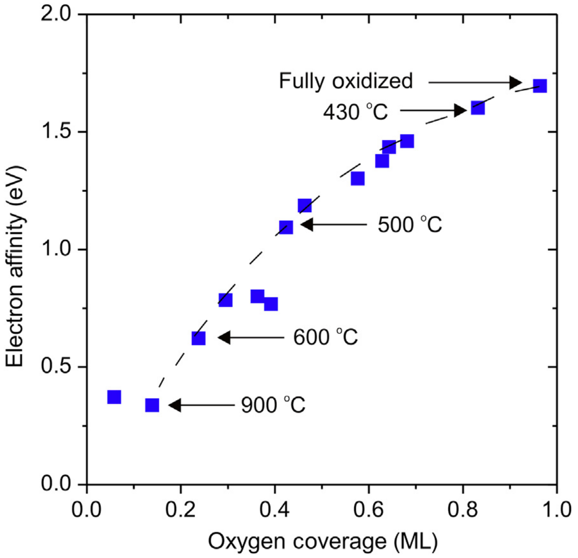

Figure 3 Electron affinity χ versus oxygen coverage: the solid line is a fit to the data with a dipole moment $p_z = -0.10$ e Å and a polarizability $\alpha = -2.0 \times 10^{-30}$ Asm^2 V^{-1} (for details, see Maier et al. (2001)).

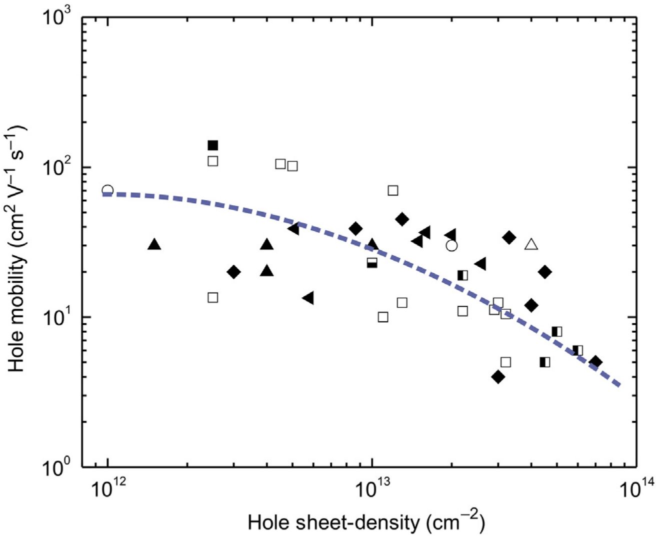

Figure 4 Summary of hole mobilities and sheet densities as detected at room temperature on a variety of films (the dashed line is "guiding the eyes") (Data from Nebel, Rezek, Shin, & Watanabe (2006)).

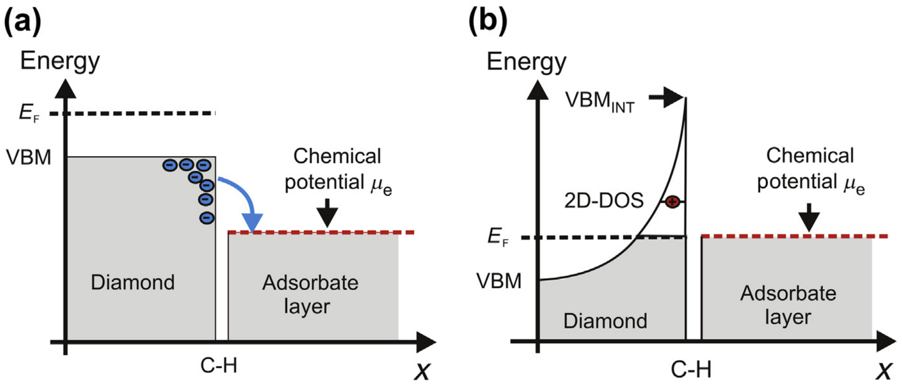

Figure 5 Schematic description of the diamond/adsorbate heterojunction (a) nonequilibrated and (b) equilibrated. Electrons from the valence-band tunnel into empty electronic states of the adsorbate layer as long as the chemical potential μ_e is lower than the Fermi energy E_F.

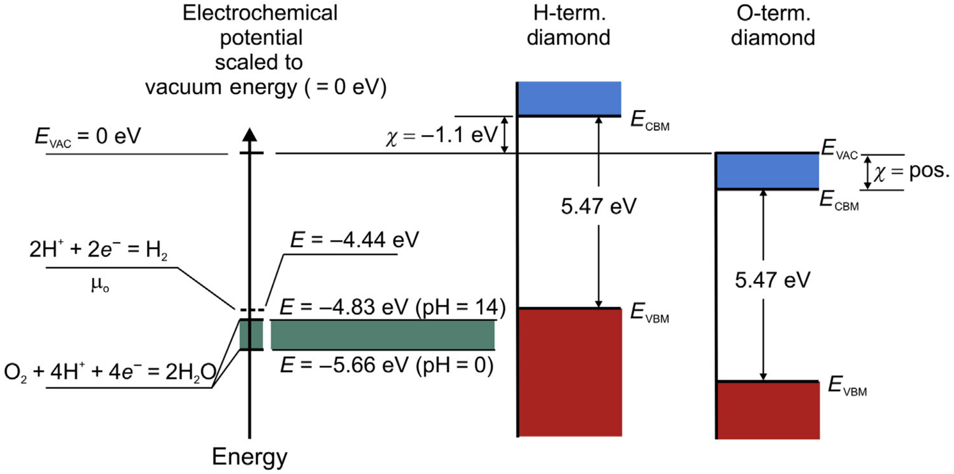

Figure 6 Chemical potentials referred to the standard hydrogen electrode and semiconductor energies referred to the vacuum level. The electron energies for the couple $O_2 + 4H^+ + 4e^- = H_2O$ at pH 0 and 14 are shown along with the band edges for hydrogen-terminated and oxidized diamond. The NEA has been assumed to be −1.1 eV on H-terminated diamond (Angus et al., 2004).

difference ("Kelvin force", "CPD"), Schottky junction characterizations, cyclic voltammetry, and field effect measurements using ion-sensitive field effect transistors (ISFETs). In addition, the electronic properties of such interfaces have been calculated using one-dimensional (1D) (Nebel, 2005) numerical solutions of the Schrödinger and Poisson equations.

3.14.4 Surface Electronic Properties of Diamond Covered with Adsorbates

3.14.4.1 Contact Potential Difference Experiments

For contact potential difference (CPD) experiments on diamond, Au is used as a reference metal (Rezek, Shin, Watanabe, & Nebel, 2007). However, the work function χ of Au exposed to air as measured by total photoyield experiments is typically 4.3 (±0.1) eV, which is significantly smaller than the values reported in the literature for Au of 4.9–5.1 eV (Sze, 1981, p. 251). A typical scanning electron microscopy (SEM) image and a related CPD result as detected on Au (region A), hydrogen-terminated diamond surface (region B), and on a surface that has been exposed to oxygen plasma (regions C) are shown in **Figures 7(a) and (b)**. In **Figure 7(c)**, a line scan in units of potential (millivolts) (white line in **Figure 7**) is shown, which shows no difference between Au and H-terminated diamond. The oxidized area is dark in the SEM photograph, which is a result of the lower electron backscattering from the PEA surface. The hydrogen-terminated surface appears bright due to its NEA. **Figure 5** summarizes the result schematically, taking into account an NEA of −1.2 eV (±0.1 eV) (Cui et al., 1998, Nebel, Rezek, & Zrenner, 2004a,b) and surface energies as detected with respect to the work function χ_{Au} of Au.

CPD measurements on Al contacts on H-terminated diamond result in a surface potential difference of +588 mV. The work function of Al, χ_{Al}, is therefore about 588 meV smaller than the work function of Au, which results in $\chi_{Al} = 3.7$ eV. We assume that this result is governed by the partial oxidation of the Al surface as the χ_{Al} reported in the literature is 4.3 eV (Sze, 1981, p. 251). **Figure 8** summarizes the results schematically. Based on the CPD data, the Fermi level of H-terminated diamond covered with an adsorbate layer is slightly in the valence

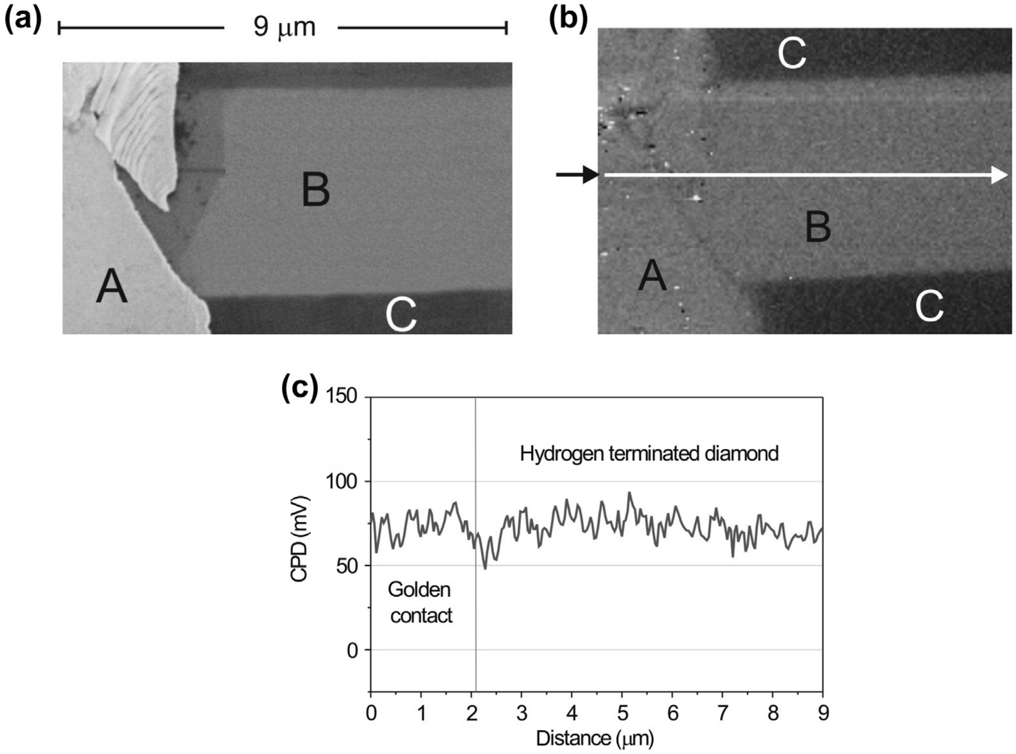

Figure 7 (a) SEM image of diamond that has been partially covered with Au (A), and that is hydrogen terminated (B) and oxidized (C). (b) The 2D contact potential measurement (CPD) on the same sample as shown in **Figure 7(a)**. (c) The white line in **Figure 7(b)** indicates the scan position of the spatial CPD profile shown here. Note, within experimental accuracy, no contact potential difference between Au and H-terminated diamond can be detected.

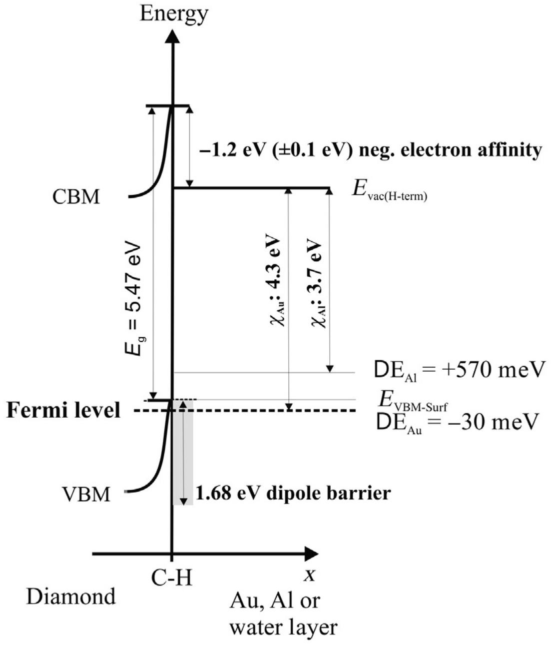

Figure 8 Schematic energy band diagram of the interface of H-terminated diamond covered with Au or Al. The ΔE_{Al} and ΔE_{Au} refer to the VBM at the surface, $E_{VBM\text{-}Surf}$.

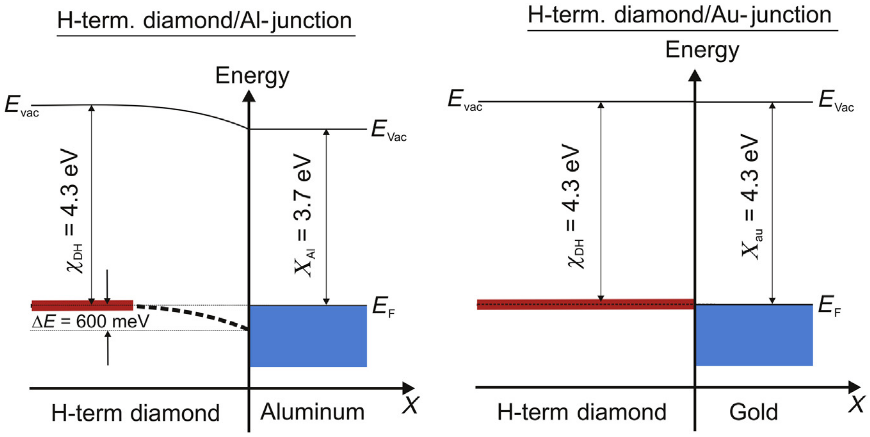

Figure 9 Schematic surface energy diagrams of H-terminated diamond covered with an adsorbate layer that is in contact with aluminum and with gold. The data were calculated using contact potential difference experiments and assuming an NEA of −1.1 eV.

band (in this case, ~30 meV). Obviously, no band bending is generated by Au contacts on H-terminated diamond resulting in "Ohmic" contact properties. This is different for Al where a band bending of about 570 meV is expected as shown in Figure 9.

3.14.4.2 Current–Voltage (IV) Properties

The current voltage characteristics of Al on H-terminated diamond, as measured at 300 K, are shown in Figure 10 (Al size: 250 × 250 μm) measured on two different junctions. They show Schottky properties with an ideality factor n of about 1. Applying negative voltages of >0.6 V (threshold voltage) to the Al contacts give rise to an exponential increase in the current over seven orders of magnitude. The threshold voltage of 600 meV is reasonably well in agreement with the detected energy barrier of 570 meV by CPD experiments.

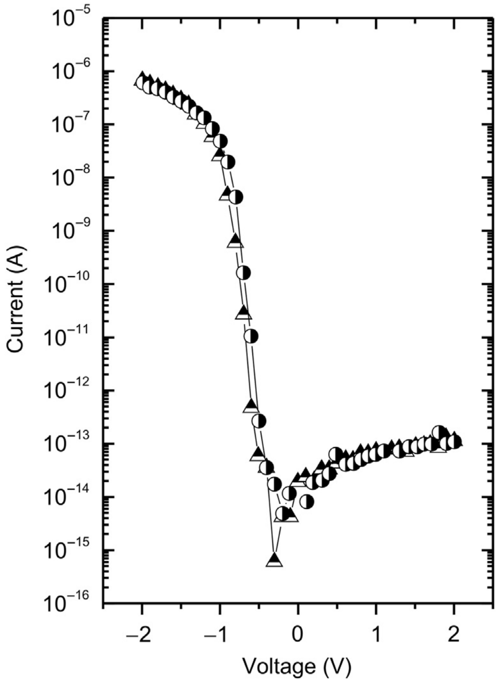

Figure 10 Two IV characteristics measured on Al/H-terminated diamond Schottky junctions in air at $T = 300$ K with a 250×250 μm 2contact size.

Positive voltages result in minor current variations (reverse currents) in the range of 10^{-13} A (note, the current has not been normalized by contact areas, as it is an in-plane current, flowing at the surface of diamond between Al and Au).

3.14.4.3 Capacitance–Voltage Experiments

Capacitance–voltage (CV) experiments on these contacts measured at $T = 300$ K are shown in **Figure 11** (Garrido, Nebel, Stutzmann, Snidero, & Bergonzo, 2002). It is important to note that the capacitance, C, is ≤ 1 pF in the regime $-3\ \mathrm{V} \leq V \leq 0\ \mathrm{V}$. If a three-dimensional (3D) parallel-plate capacitor is assumed, the capacitance C can be calculated by

$$C = \varepsilon_{\mathrm{o}}\varepsilon_{\mathrm{r}}(A/d) \tag{6}$$

where ε_{o} is the dielectric constant, ε_{r} is the relative dielectric constant of diamond ($\varepsilon_{\mathrm{r}} = 5.7$), A is the area of the Al contact, and d is the depletion layer width or the distance between the Al top contact and the doping layer. For an Al contact with 250×250-μm^2 area and a spatial distance of 10 nm between the Al contact and the H-induced doping layer, the capacitance would be about 310 pF. Experimentally, C is ≤ 1 pF on all contacts realized and follows an approximate linear relationship with the length of the periphery of the Al contact as shown in **Figure 12**. This indicates that no hole accumulation layer is present below the Al layer. The diode characteristics are governed by in-plane properties, where a p-type channel exists at the surface of hydrogen-terminated diamond, which connects to Al or Au. Unfortunately, 2D and 3D Schottky junctions generate nearly comparable IV and CV properties as discussed in detail by Petrosyan and Shik (1989) and by Gelmont and Shur (1992).

3.14.4.4 Two-Dimensional Properties of a Perfectly H-Terminated Diamond Surface

Figure 5 shows a schematic view of the electronic properties at the surface of H-terminated diamond, where valence-band electrons can tunnel into the empty electronic states of an adsorbate layer. Tunneling gives rise to band bending, which decreases in diamond with increasing distance to the surface. To calculate the width and bending of the valence band, one has to take into account light hole (LH), heavy hole (HH), and split-off (SO)

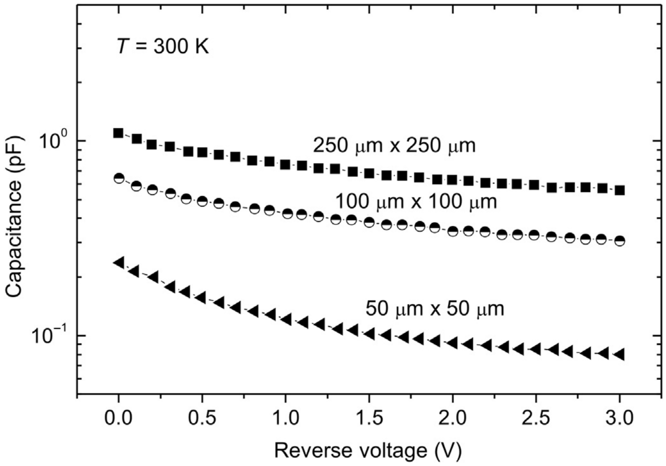

Figure 11 CV data detected on three contact configurations with Al areas 250 × 250, 100 × 100, and 50 × 50 μm^2.

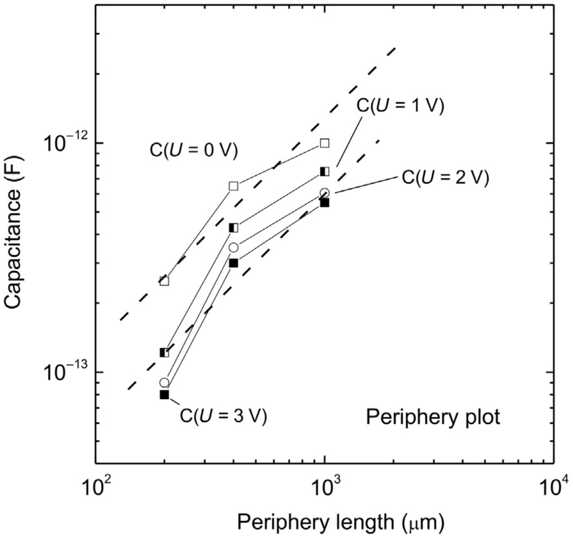

Figure 12 Capacitance of the Al contacts with sizes 50 × 50, 100 × 100, and 250 × 250 μm^2 plotted for $U = 0$, 1, 2, and 3 V as a function of periphery length (dashed line is guiding the eyes of a linear dependence).

bands. The band structure of diamond is described by Luttinger parameters and has been discussed by Willatzen, Cardona, and Christensen (1994). They derived $\gamma_1 = 2.54$, $\gamma_2 = -0.1$, and $\gamma_3 = 0.63$.

To calculate the band bending in the vicinity of the surface of diamond, a numeric approach has been used, optimized for solving the Schrödinger and Poisson equations simultaneously to calculate the energy levels and the electron wave functions in narrow GaAs/$Ga_{1-x}Al_xAs$ heterojunctions. Details can be found in Stern & DasSarma (1984). In the case of band bending over a distance that is shorter than the De Broglie wavelength of about 100 Å for holes (in diamond), the 3D density-of-state (DOS) changes to a two-dimensional (2D) DOS as shown schematically in Figure 5(b). For this calculation, the heterojunction effect is modeled using a graded interface in which the barrier height, as well as the effective mass, is assumed to change smoothly in a transition layer whose thickness is specified. Holes move in an effective potential given by

$$V(x) = e\phi(x) + V_h(x)$$

where $\phi(x)$ is the electrostatic potential, $V_h(x)$ is the effective potential energy associated with the heterojunction discontinuity, which we assume to be 1.68 eV. The normalized envelope function $\zeta_i(x)$ for the hole subband i is given by the Schrödinger equation of the BenDaniel–Duke form:

$$-\frac{\hbar^2}{2}\frac{\mathrm{d}}{\mathrm{d}x}\frac{1}{m_n(z)}\frac{\mathrm{d}\zeta_i(x)}{\mathrm{d}x}+V(x)\zeta_i(x) = E_i\zeta_i(x) \tag{7}$$

where $m_n(x)$ is the position-dependent effective mass (n stands for HH, LH, SO) and E_i is the energy of the bottom of the ith subband. The Poisson equation for the electrostatic potential takes the form

$$\frac{\mathrm{d}}{\mathrm{d}z}\varepsilon_o\varepsilon_r(x)\frac{\mathrm{d}\phi(x)}{\mathrm{d}x} = e\sum N_i\zeta_i^2(x) - \rho_I(x) \tag{8}$$

with

$$N_i = \frac{m_n kT}{\pi\hbar^2}\ln\left[1+\exp\left(\frac{E_i - E_F}{kT}\right)\right] \tag{9}$$

where $\varepsilon_r(x)$ is the position-dependent dielectric constant, assumed to be constant in diamond ($\varepsilon_r = 5.7$). For the adsorbate layer, we varied ε_r between 1 and 5.7. The calculations show that ε_r does not affect the energy levels in the quantum well but does affect the width of the wave function of holes extending out of the diamond into the water layer. In the following, we show results deduced for $\varepsilon_r = 5.7$. N_i is the number of holes per unit area in the subband i, E_F is the Fermi energy, and m_n represents the mass of holes (HH, LH, and SO). As a first-order approximation, we neglect impurities ($\rho_I(x) = 0$). Calculations have been performed for hole sheet densities in the range 5×10^{12} to 5×10^{13} cm^{-2} (Nebel et al., 2004a,b).

A typical result is shown in **Figure 13**. In diamond at the interface to the H-terminated surface, three discrete energy levels for holes govern the electronic properties, namely, the first subbands of the LH, HH, and SO holes. For a hole sheet density of 5×10^{12} cm^{-2}, levels at 221 meV (HH), 228 meV (SO), and 231 meV (LH) below the VBM at the surface (VBM$_S$) are deduced. The Fermi energy is 237 meV below the VBM$_S$. Also shown are normalized hole wave functions labeled LH, HH, and SO. In thermodynamic equilibrium, the chemical potential of the adsorbate layer and the Fermi level of diamond are in equilibrium. Our calculations reveal an energy gap between electrons in the adsorbate layer and holes in the quantum well. In the case of 5×10^{12} cm^{-2}, holes must overcome $\geq$6 meV to recombine with electrons. The wave function of holes extends about 5 Å into the adsorbate layer calculated for a dielectric constant ε_r of 5.7. For a hole sheet density of

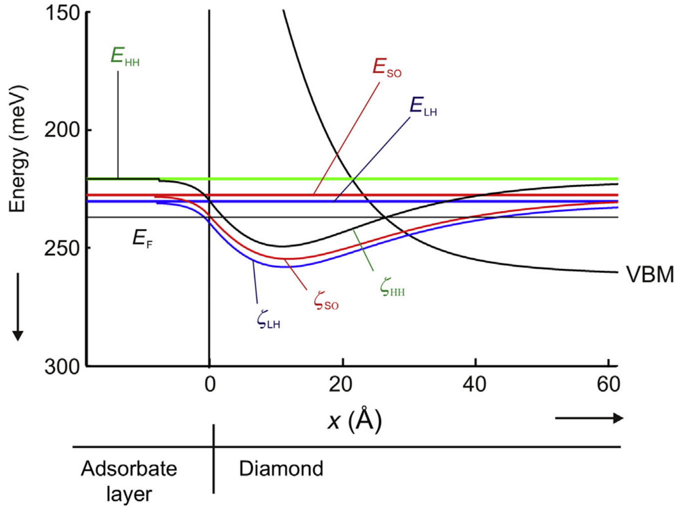

Figure 13 Energy band diagrams at the interface of hydrogen-terminated diamond and an adsorbate layer calculated for a hole sheet-density of 5×10^{12} cm^{-2}. The energies refer to the VBM at the interface (VBM$_{INT}$). The figure shows the calculated energy levels of the first subbands of the LH, HH, and split-off band (SO). Also shown are the normalized wave functions ζ of holes (LH, SO, and HH).

5×10^{13} cm^{-2}, three discrete energy levels are calculated, namely, 770 meV (HH), 786 meV (SO), and 791 meV (LH) below the VBM$_S$. The first three sublevels are occupied by holes, and recombination is prevented by a gap of 90 meV.

Such 2D properties can be expected only theoretically as the real surface is governed by several additional properties such as (1) Surface and bulk defects that may pin the surface Fermi level. (2) Surface roughness. (3) Ions in the Helmholtz layer of the adsorbate film in close vicinity to the hole channel. These parameters may cause a broadening of the 2D levels so that a continuous, semimetallic DOS may be a better description (Nebel et al., 2002; Sauerer et al., 2001).

3.14.4.5 In-Plane CV Properties of Al on H-Terminated Diamond

The CV data shown in **Figures 11** and **12** indicate that a peripheral depletion layer is present between Al and H-terminated diamond that is covered with an adsorbate layer to generate transfer doping. This is schematically displayed in **Figure 9**. Toward the Al contact, the accumulation layer is depleted as the work function of Al relative to H-terminated diamond is misaligned. This depletion region generates an in-plane capacitance, which can be detected experimentally and which scales approximately with the length of the periphery (**Figure 12**). As the contacts were squares, some deviations from a perfect fit can be expected. The data indicate that in-plane Schottky-junction (2D) properties of Al on H-terminated diamond dominate the electronic properties.

General features of a junction between a 2D electron gas and a metal contact with Schottky properties have been discussed by Petrosyan and Shik (1989) and by Gelmont and Shur (1992). Following their arguments, the capacitance of a metal in contact with a 2D gas is well described by

$$C = \frac{\varepsilon_o \varepsilon_r L}{\pi} \ln\left\{\frac{\left(d_{Al}^2 + x_{dep}^2\right)^{0.5} + d_{Al}}{\left(d_{Al}^2 + x_{dep}^2\right)^{0.5} - d_{Al}}\right\} \tag{10}$$

where L is the length of the metal periphery, d_{Al} is the thickness of Al, and x_{dep} is the width of the space-charge region. Taking into account the thickness of Al as 600 nm, $\varepsilon_r = 5.7$, and the detected variation of the capacitance, the variation of the depletion width in our experiments is in the range of 10–300 nm (**Figure 14**). The shortness of the depletion layer is a result of the high hole sheet-carrier density, which is in the range 10^{12}–10^{14} cm^{-2}. Petrosyan and Shik (1989) calculated an inverse proportional relationship between the width of the depletion layer and the sheet carrier density, given by

$$x_{dep} \propto \frac{\varepsilon_o \varepsilon_r}{2\pi e} \frac{V}{p_{sh}} \tag{11}$$

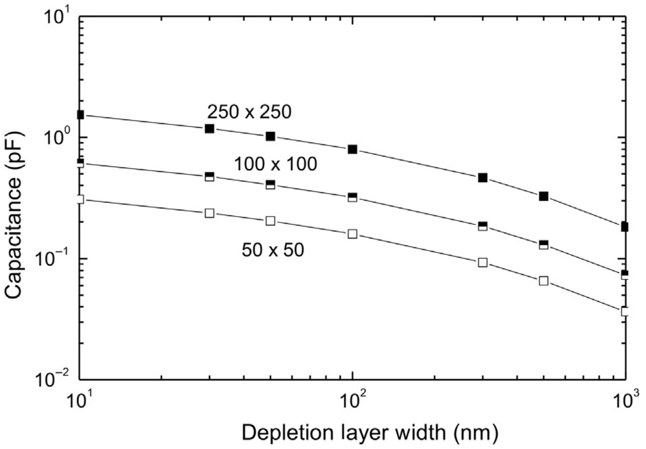

Figure 14 Calculated capacitance variations as a function of width of the depletion layer. Experimentally, the capacitance is in the range 0.06–1 pF, which shows that the depletion layer width varies between 10 and 300 nm.

where V is the applied voltage, e is the elementary charge, and p_{sh} the sheet hole density. It is interesting to note that such an in-plane (2D) junction also follows the exponential law given by

$$j \approx j_{\mathrm{rev}}\left[\exp\left(\frac{eU}{kT}\right) - 1\right] \tag{12}$$

where j_{rev} is the contact-specific reverse current. The summary of these results is as follows: The detected absolute values of the capacitance are orders of magnitude too small to be discussed using a parallel plate model. The most reasonable model is an in-plane Schottky model. Unfortunately, such junctions show comparable characteristics to 3D (conventional) Schottky junctions and are therefore not distinguishable if only IV experiments are applied. Only a combination of CV and IV helps to elucidate the detailed properties.

3.14.4.6 Hole Carrier Propagation and Scattering in the Surface Layer

To elucidate the transport properties of holes in the surface channel of diamond without scattering by grain boundaries and surface roughness, several undoped single crystalline chemical vapor deposition (CVD) diamond films of a 1-μm thickness have been grown homoepitaxially on 3-mm × 3-mm (100) oriented synthetic Ib substrates, using microwave plasma CVD. Typical deposition parameters were sample temperature 800 °C, power 750 W, gas pressure 25 Torr, hydrogen flow 398 sccm, and methane flow 2 sccm. To achieve H termination after growth, the CH_4 is switched off, and diamond is exposed to a pure hydrogen plasma for 5 min with an otherwise identical parameter. Samples are then cooled down to room temperature in an H_2 atmosphere. Temperature ramping, gas flow, and plasma switching are shown schematically as functions of time in **Figure 15**. A detailed discussion of growth and sample properties is given in (1) Watanabe et al. (1999), (2) Okushi (2001); Okushi, Watanabe, Ri, Yamanaka, and Takeuchi (2002), and (3) Watanabe, Ri, Yamanaka, Takeuchi, and Okushi (2002). The high quality of these films is demonstrated by cathode-luminescence (CL) measurements and atomic force microscopy (AFM). In CL free-exciton emission is detected at 300 K at 5.27 and 5.12 eV, which is only the case for ultrapure diamond (negligible extrinsic contaminations and intrinsic defects). In addition, AFM shows atomically flat surface properties so that the effect of surface roughness on carrier propagation should be negligible.

The samples were then characterized by Hall effect measurements (for details, see Rezek, Watanabe, & Nebel, 2006), which have been performed in ambient air at 300 K. Then, the samples were annealed at 400 K at 1 Torr in argon gas for a given period of time. After that, temperature-dependent Hall experiments have been performed.

At room temperature, the mobility increased after 1-h annealing at 400 K from the original 114 to about 223 $\mathrm{cm}^2\,\mathrm{V}^{-1}$. The sheet carrier concentration was strongly affected by thermal annealing: It decreased from 7×10^{12} to $6 \times 10^{11}\,\mathrm{cm}^{-2}$. The sheet conductivity decreased from 1×10^{-4} to $2 \times 10^{-5}\,(\Omega/\mathrm{sq})^{-1}$. Obviously, the increasing carrier mobility is accompanied by a decrease in the carrier density and increase in the resistivity.

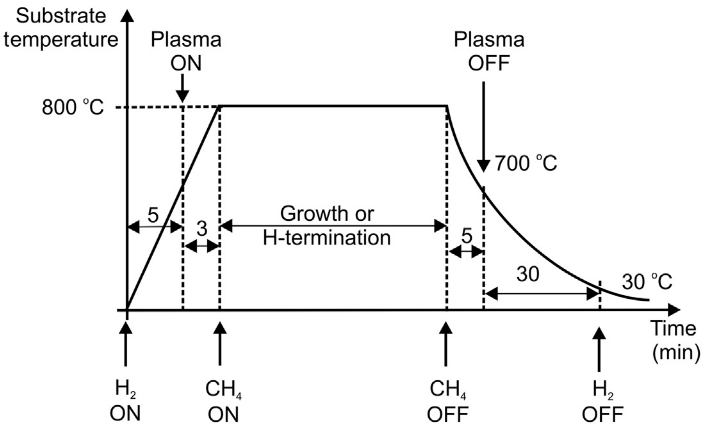

Figure 15 Temperature and gas flow variations, plasma switching cycles for growth or H-termination of CVD diamond.

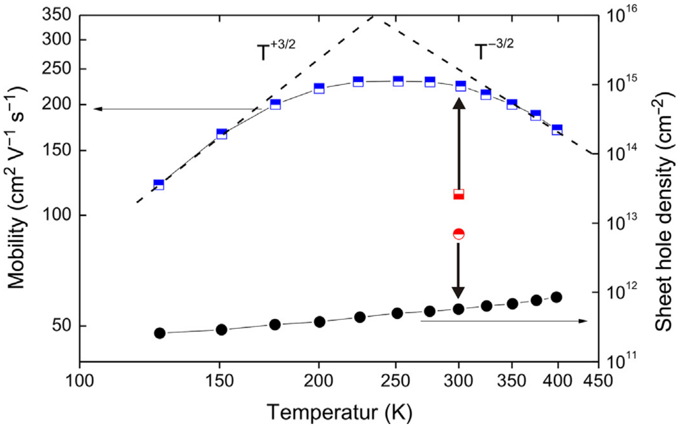

Figure 16 Temperature-dependent Hall mobility (squares) and sheet hole concentrations (dots) as measured on diamond surface in 1-Torr vacuum after 1 h of annealing at 400 K. Original values measured in air at 300 K are also shown.

Figure 16 shows the detected variation of mobility and sheet hole density as a function of temperature. The mobility shows a maximum around 240 K, decreasing toward lower and higher temperatures. The sheet carrier concentration exhibits a monotonous increase toward high temperatures over the whole temperature range, with an activation energy of (9–23) meV. This is in good agreement with previously reported data, which showed that transport properties of holes at hydrogenated diamond surfaces are near to metallic (Nebel et al., 2002; Nebel, Sauerer, Ertl, et al., 2001).

The time evolution of the mobility and sheet carrier concentration at the annealing temperature of 400 K is shown in **Figure 17**. During annealing, the carrier concentration decays exponentially as $\sim\exp(-t/\tau)$ (full line in **Figure 17** "sheet hole density") with a time constant τ of (6.8 ± 0.3) h. At the same time, the mobility increases, which is well fitted by an exponential increase of $\mu \sim (1-\exp(\ t/\tau))$ (dashed line in **Figure 17** "mobility") using the same time constant.

Figure 18 shows mobilities and carrier concentrations as measured at 300 K after annealing at 400 K for 1–16 h. Compared to the data at 400 K (**Figure 17**), a more pronounced increase of mobility (squares) with annealing time is detected with values reaching up to 328 $\text{cm}^2\ \text{V}^{-1}\ \text{s}^{-1}$ after 16 h. The sheet carrier concentration (dots) decays in correlation with the increase in mobility.

Exposing the samples to air for several days results in a complete recovery of the original values of mobility, hole concentration, and conductivity. The recovery indicates that the annealing did not degrade the diamond surface H termination but rather modified the properties of the adsorbate layer on the diamond surface.

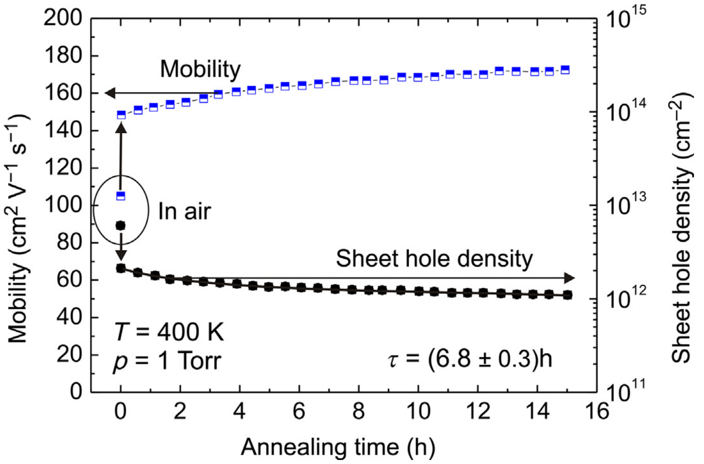

Figure 17 Hall mobility and sheet hole density as measured in a vacuum at the annealing temperature 400 K as a function of time. Curves represent a fit of the exponential decay of carrier concentration (full line in sheet hole density) and an exponential increase of carrier mobility (the dashed line in mobility).

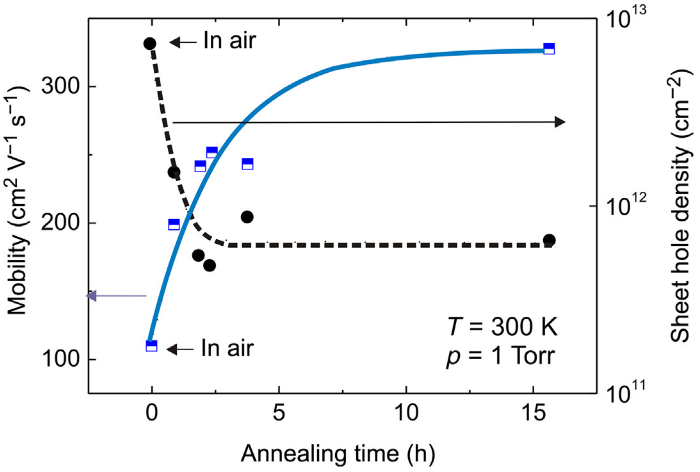

Figure 18 Hall mobility and sheet hole density as measured in vacuum (1 Torr) at 300 K as a function of annealing time. Curves are for guiding the eyes.

The most pronounced increase in mobility was enabled by a mechanical cleaning step on hydrogenated surfaces. Prior to cleaning, the mobility of holes at room temperature was 92 cm^2 V^{-1} s^{-1} in air and increased to 115 cm^2 V^{-1} s^{-1} after 1 h of annealing in vacuum. Using mechanical cleaning, the mobility was typically 114 cm^2 V^{-1} s^{-1} in air and increased further to 223 cm^2 V^{-1} s^{-1} after 1 h of annealing in vacuum. The sheet carrier concentration decreased after cleaning by about a factor of 1.5.

As illustrated in **Figure 1**, the mobility decreases toward lower or higher temperatures from a maximum centered at about 240 K. The decrease is remarkably close to the tendencies corresponding to ionized impurity scattering $\sim T^{+3/2}$ toward lower temperatures and phonon scattering $\sim T^{-3/2}$ toward higher temperatures (Seeger, 1999). These power-law tendencies were introduced for bulk 3D scattering processes. Yet, even in 2D systems, the carrier transport is dominated by 3D effects if carrier mobilities are relatively low and typically $<$1000 cm^2 V^{-1} s^{-1} (Ando, Fowler, & Stern, 1982).

Considering the transfer doping model of hydrogenated diamond, the exponential decay of carrier concentration with annealing time indicates thermal desorption of surface adsorbates. Since the time constant of the desorption process is expressed as $\tau = (1/\nu_o)\exp(E_d/kT)$, the desorption energy can be calculated by

$$E_d = kT\ln(\tau\nu_o) \qquad 13$$

Using $\tau = 6.8$ h and typical attempt-to-escape frequency prefactor $\nu_o = 10^{13}$ s^{-1}, Eqn (1) yields $E_d = 1.1$ eV. This is about 2 times larger than typical desorption energies that are in the range of 0.5 eV, typical for physisorbed water molecules (Chakarov, Österlund, & Kasemo, 1995). The additional energy may arise from the fact that the decrease of hole concentration in the surface channel requires not only desorption but also transfer of electrons from the adsorbate layer back into diamond via an electrochemical reaction (Maier et al., 2000).

Based on our data, we assume that due to the small separation of few Angstroms between holes in the surface conductive channel and ions in the adsorbate layer on the surface (Nebel et al., 2004a,b), holes are scattered by electrostatic interaction with ions. Thus, the annealing leads to higher mobilities by reducing the concentration of ionized adsorbates at the surface.

3.14.5 Surface Electronic Properties of Diamond in Electrolyte Solutions

3.14.5.1 Redox Couple Interactions with Undoped H-Terminated CVD Diamond

Electrochemical experiments on H-terminated diamond are suited to investigate transfer doping properties as the electrolyte solutions are well defined with respect to pH and redox couple chemical potentials (Nebel, Kato, et al., 2006; Nebel, Rezek, Shin, Watanabe, & Yamamoto, 2006; Shin, Watanabe, & Nebel, 2005; Shin, Watanabe, & Nebel, 2006). To characterize these properties, the same undoped hydrogen-terminated CVD diamond substrate has been applied as electrode as discussed above in the Hall effect experiments. The contact

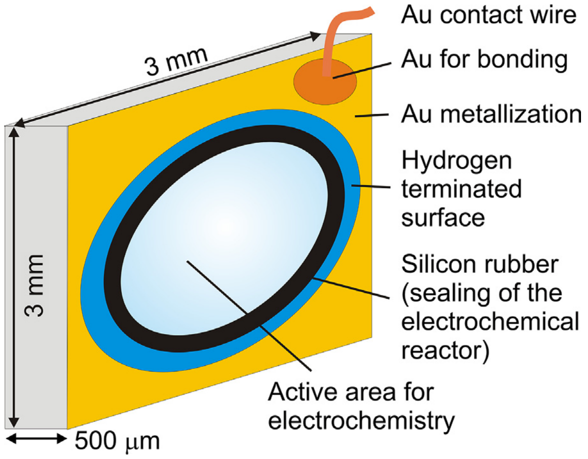

Figure 19 Contact configuration applied to characterize undoped H-terminated diamond by electrochemical experiments. The geometry is in-plane where Au is evaporated on H-terminated diamond to generate an Ohmic contact on a 1-μm intrinsic CVD diamond grown on a Ib diamond substrate.

arrangement, shown in Figure 19, has been optimized for the electrochemical experiments. Au films that are 200 nm thick have been evaporated on the H-terminated surface with rotational symmetry. The electrochemical active area is about 0.8 mm^2. Pt is used as the counterelectrode, a saturated calomel electrode (Hg/Hg_2Cl_2) as the reference electrode, and a voltammetric analyzer is applied for cyclic voltammetry experiments. The scan rate is 100 mV s^{-1}. To calculate the RC-time limitation of the experiments, the active area of 0.8 mm^2, the experimentally detected series resistance of the surface conductive film of $10^5\ \Omega$, and the typical double layer capacitance of 5 μF cm^{-2} as also detected by Granger, Xu, Strojek, and Swain (1999) have been taken into account. Using $\tau = RC$, results in a time constant of about 4 ms. This is two to three orders of magnitude faster than our potential scan rate of 100 mV s^{-1}. We exclude therefore RC-limited effects in our cyclic voltammetry experiments.

Redox analyte of a 10 mM concentration has been mixed with the supporting 0.1 M Na_2SO_4 electrolyte solution. As redox analytes we used well-characterized molecules such as $Fe(CN)_6^{3-/4-}$ (formal potential ($U_{FE}{}^{o}$) is +0.46 V versus Standard Hydrogen Electrode (SHE), chemical potential $\mu_{Fe} = -4.9$ eV below the vacuum level), $Ru(NH_3)_6^{2+/3+}$ ($U_{Ru}{}^{o} = +0.025$ V versus SHE, $\mu_{Ru} = -4.46$ eV), methyl viologen $MV^{2+/1+}$ ($U_{MV2}{}^{o} = -0.48$ V versus SHE, $\mu_{MV2} = -3.96$ eV), $MV^{+1/0}$ ($U_{MV1}{}^{o} = -0.81$ V versus SHE, $\mu_{MV2} = -3.63$ eV), and $Co(sep)^{2+/3+}$ ($U_{Co} = -0.38$ V versus SHE, $\mu_{Co} = -4.06$ eV) (Granger et al., 2000). The redox energy levels with respect to vacuum and to H-terminated diamond are shown in Figure 20.

Cyclic voltammetry can be used to gather information about diamond films and surface qualities. In particular, this method can be applied to detect nondiamond carbon that is present at grain boundaries or graphitic ("sp2") deposits at the surface. It is known that sp2 gives rise to catalytic effects on hydrogen and oxygen evolution, which reduces the working potential window significantly. Figures 21 and 22 shows background cyclic voltammetry IV curves as detected in 0.1 M H_2SO_4 (pH = 1) on our sample (DRC, full line in Figure 21). The data are compared with two high-quality polycrystalline boron-doped diamond films from the literature (Granger et al., 1999, 2000).

On our undoped, H-terminated CVD diamond, the electron exchange reaction between the hole accumulation layer and the electrolyte reveals distinct features. A large chemical potential window extends from less than −3 V (detection limit of our setup) to +1.6 V (for pH 1). In this regime, the background current density is in the microamperes per square centimeter range, as can be seen in the inset of Figure 21 where the background current is plotted in log scale. The general feature is comparable to a diode. We attribute the large window and the small current density first to the absence of an sp^2 carbon as no grain boundaries are at the surface (Angus et al., 2004; Fujishima, Einaga, Rao, & Tryk, 2005; Granger et al., 2000; Swain, 2004). Hydrogen evolution cannot be detected down to −3 V, which is the limit of our setup. Second, we attribute this to the fact that for negative potentials, applied to the diamond film, the surface conductivity disappears (see the next chapter) as the hole-accumulation layer becomes depleted.

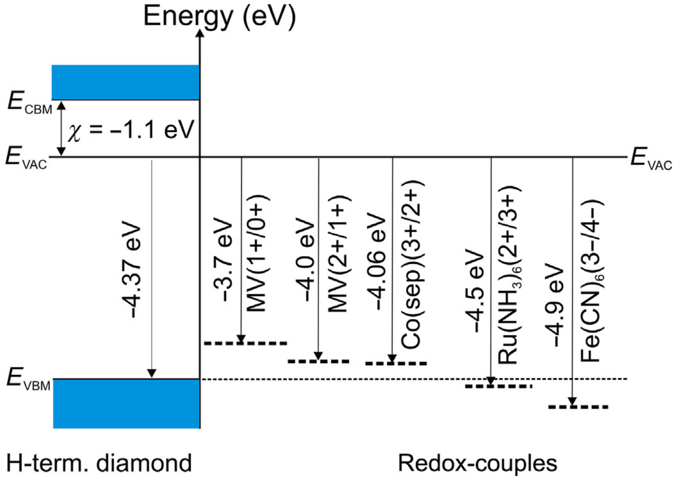

Figure 20 Redox chemical potentials of different redox couples with respect to the vacuum level. We assumed an NEA of −1.1 eV. Only $Fe(CN)_6^{3-/4-}$ and $Ru(NH_3)_6^{2+/3+}$ have levels below E_{CBM}.

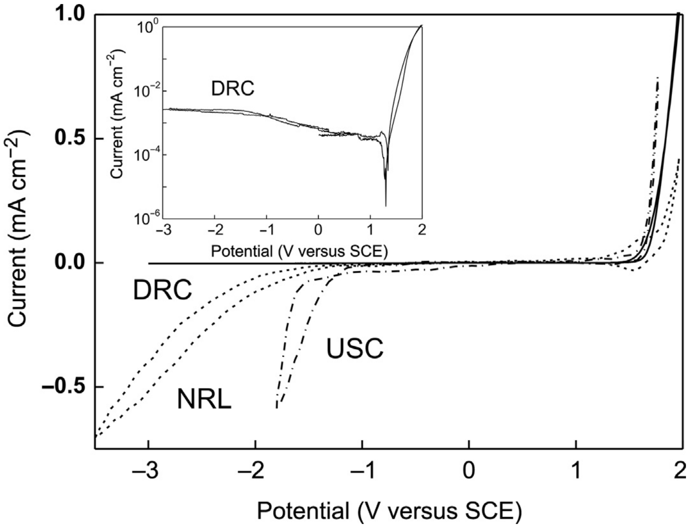

Figure 21 Background cyclic voltammetry IV curves as detected in 0.1 M H_2SO_4 (pH = 1) on a hydrogen-terminated undoped single crystalline CVD diamond film (DRC, full line). The data are compared with two high-quality polycrystalline boron doped diamond films (U.S. Naval Research Laboratory (NRL) and Uta Sate Univ., Dep. of Chemistry (USC)) from the literature (Granger et al., 1999). The inset shows the DRC data in a log scale. The chemical window if DRC is >4.6 V.

For positive potentials, the surface conductivity remains. Therefore, the diamond surface can be oxidized at potentials larger than +1.6 V at pH 1, which removes hydrogen from the surface but does not produce any morphological damage to the surface.

A summary and comparison of redox reactions with H-terminated diamond is shown in Figure 21. For $Fe(CN)_6^{3-/4-}$ and $Ru(NH_3)_6^{2+/3+}$, electron transfer from the redox couple into the diamond electrode (oxidation peak) and from the diamond to the redox couple (reduction peak) can be clearly detected. For methyl viologen $MV^{2+/1+}/MV^{+1/0}$ and $Co(sep)^{2+/3+}$, the result indicates no redox interaction.

To discuss these in a more general context, we compare our data with the data published in the literature for H-terminated highly boron doped (10^{19}–10^{20} cm^{-3}) diamond (Granger et al., 1999). These films are 3D electrodes in contrast to our in-plane contact geometry. Cyclic voltammetry experiments on these polycrystalline films have been performed using a 1 M KCl electrolyte solution and 0.05 V s^{-1}. To overcome problems that arise by comparison in absolute terms, we discuss in the following normalized data as shown in Figure 23 (a: $Fe(CN)_6^{3-/4-}$, b: $Ru(NH_3)_6^{2+/3+}$, c: $Co(sep)^{3+/2+}$, d: $MV^{2+/1+}/MV^{+1/0}$).

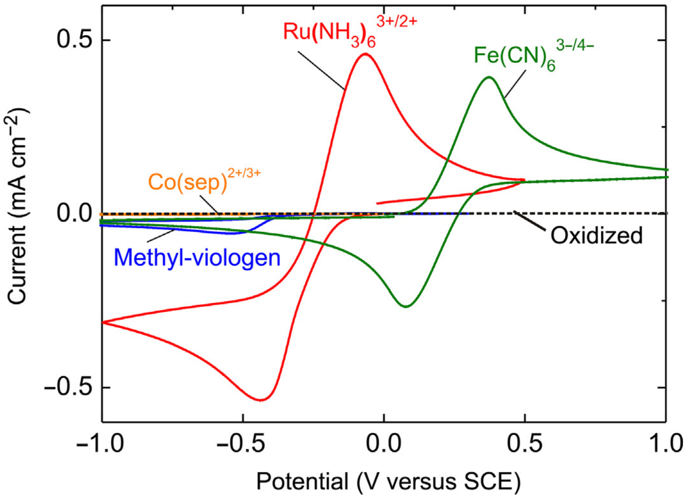

Figure 22 Cyclic voltammetric I–V curves for $Fe(CN)_6^{3-/4-}$, $Ru(NH_3)_6^{2+/3+}$, $Co(sep)^{3+/2+}$, and methyl viologen $MV^{2+/1+/}MV^{+1/0}$. After anodic oxidation, the current decreased to zero (dashed line). Pt was used as the counterelectrode, a saturated calomel electrode (Hg/Hg_2Cl_2) as the reference electrode, and cyclic voltammetry experiments have been performed with scan rates of 0.1 V s^{-1}. Redox analyte of 10 mM concentration has been mixed with the supporting 0.1 M Na_2SO_4 electrolyte solution.

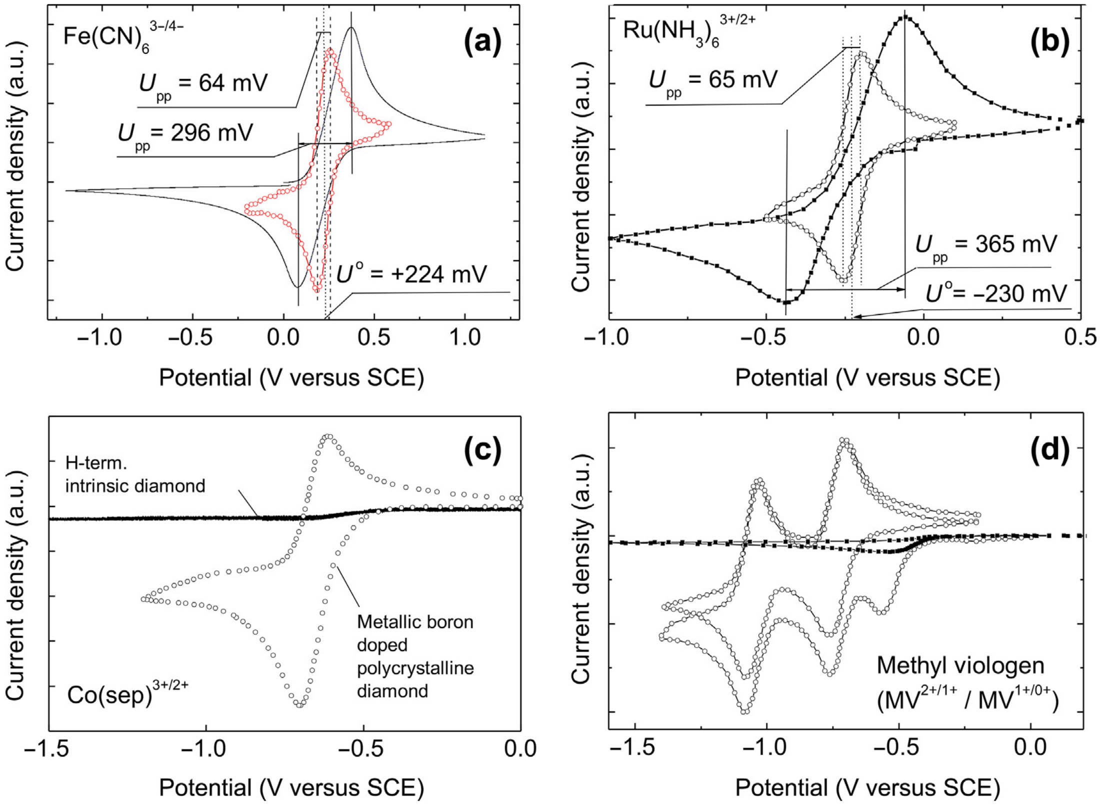

Figure 23 Normalized I–V curves for $Fe(CN)_6^{3-/4-}$ (a), $Ru(NH_3)_6^{3+/2+}$ (b), $Co(sep)^{3+/2+}$ (c), and methyl viologen (d) as detected on intrinsic H-terminated diamond (full squares) and on boron-doped (metallic) H-terminated polycrystalline CVD diamond (open circles) (Granger et al., 1999, 2000). In (d), the open circles show cyclic voltammetric IV curves as measured on boron-doped diamond using methyl viologen. The cycles are slightly changing and are discussed in detail in Granger et al. (1999).

For $Fe(CN)_6^{3-/4-}$ and for $Ru(NH_3)_6^{2+/3+}$, hydrogen-terminated intrinsic diamond acts like a metal electrode, with oxidation peak amplitudes of about 0.37 mA cm^2 ($Fe(CN)_6^{3-/4-}$) and 0.46 mA cm^{-2} ($Ru(NH_3)_6^{2+/3+}$). ΔU_{pp} for $Fe(CN)_6^{3-/4-}$ is 296 mV and for $Ru(NH_3)_6^{2+/3+}$ 365 mV compared to 64 and 65 mV as detected for metallic polycrystalline diamond (Granger et al., 1999). The oxidation/reduction currents are reversible. The peak shift and broadening indicate rate-limited electron transfer as we exclude RC-time constant effects. This is well described in the literature based on the Marcus–Gerischer model (Marcus, 1956). For $Fe(CN)_6^{3-/4-}$ and $Ru(NH_3)_6^{2+/3+}$, the reduction and oxidizing currents are symmetrically centered around the formal potential U° of +224 mV ($Fe(CN)_6^{3-/4-}$) and −230 mV ($Ru(NH_3)_6^{2+/3+}$). This is in good agreement with the data of Granger et al. (1999) who detect +220 mV for $Fe(CN)_6^{3-/4-}$ and −217 mV for $Ru(NH_3)_6^{2+/3+}$. Taking into account the relation between electrode potential and electron energy with respect to the vacuum level, we use (Angus et al., 2004):

$$\varepsilon = (-e)U^\circ - 4.44\ \text{eV} \tag{14}$$

where ε is the energy of electrons with respect to the vacuum level, e is the elementary charge, U° is the formal potential (versus SHE), and 4.44 eV is the scaling parameter between electrode potential and electron energy. The chemical potential of redox couples $Fe(CN)_6^{3-/4-}$ and $Ru(NH_3)_6^{2+/3+}$ are calculated to be −4.9 eV ($Fe(CN)_6^{3-/4-}$) and −4.45 eV ($Ru(NH_3)_6^{2+/3+}$), which results in Fermi level positions of about 530 and 80 meV below the valence-band maximum at the surface, assuming an NEA of about −1.1 eV (**Figure 20**). For these two redox couples transfer doping conditions are fulfilled, which gives rise to the insulator–metal transition of intrinsic diamond.

Cyclic voltammetry experiments on methyl viologen ($MV^{2+/1+}/MV^{+1/0}$) and $Co(sep)^{3+/2+}$ show distinct differences. The redox activities are shifted deep into negative potentials (with respect to diamond electrode). Here, the surface conductive layer is depleted, and diamond becomes an insulator.

Application of potentials larger than +1.6 V gives rise to the oxidation of hydrogen-terminated diamond surfaces. To characterize to electronic properties in the transition region from perfectly hydrogen terminated to fully oxidized, we have performed a sequence of voltammetric experiments using 10 mM $Fe(CN)_6^{3-/4-}$ as redox couple in 0.1 M Na_2SO_4 electrolyte solution (pH = 6). The scan rate of the voltammetric experiment was 0.1 V s^{-1} in the regime −1.2 to +1.6 V. The results are shown in **Figure 24**. The application of a sequence of short time anodic oxidation can be summarized as follows:

1. The reduction peak marked by "a" in **Figure 24** decreases rapidly, while the oxidizing peak remains nearly stable (steps 1–4).

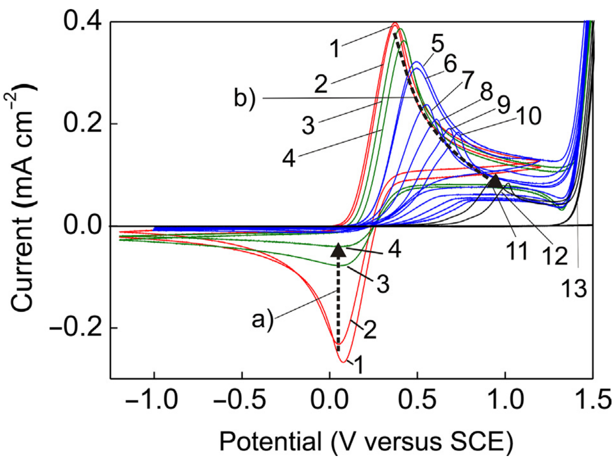

Figure 24 Electronic properties in the transition region from perfectly hydrogen terminated to fully oxidized. A sequence of voltammetric experiments using 10 mM $Fe(CN)_6^{3-/4-}$ as a redox couple in 0.1 M Na_2SO_4 electrolyte solution (pH = 6) has been applied (indicated by: 1–13).

2. After the disappearance of the reduction peak, the oxidizing peak, marked "b" in **Figure 24**, decreases and shifts to higher potentials (steps five–12).
3. Finally, the redox interaction completely disappears but oxygen evolution can still be detected. We attribute this to the chemical reaction:

$$2H_2O \Rightarrow O_2 + 4H^+ + 4e^-$$

which has an energy level at −5.3 eV below the vacuum (Angus et al., 2004). This is significantly deeper than for $Fe(CN)_6^{3-/4-}$ (energy level: −4.9 eV).

4. After prolonged anodic oxidation, the current approaches zero due to the complete removal of hydrogen and of the surface conductivity.

3.14.5.2 Electrochemical Exchange Reactions of H-Terminated Diamond with Electrolytes and Redox Couples

CVD diamond films under discussion are perfect insulators if measured in vacuum with a clean surface. In this case, the Fermi level is in the band gap of diamond. The same films become metallic if immersed into redox-electrolyte solutions with chemical potentials below the VBM. This can be ascribed to the alignment of Fermi level and redox potential or chemical potential at the interface. It is a remarkable phenomenon, which requires "defect-free" bulk properties and perfect hydrogen termination of the surface carbon dangling bonds to unpin the Fermi level. Both conditions seem to be fulfilled for these samples. Obviously, optimized growth and hydrogen termination of diamond generate high-quality subsurface and surface electronic properties. It is also certain that the insulator metal transition is related to the presence of hydrogen at the surface as the electrochemical currents vanish after anodic oxidation.

A comparison with metallic boron-doped polycrystalline diamond shows that the current voltage variations are broader and that the maxima are shifted to higher (oxidation) or lower potentials (reduction) with respect to the formal potential. Based on arguments given above, we exclude RC limitations as the origin for the shifts and broadening. We assume that these variations are generated by limited electron transfer rates at the interface. This is schematically illustrated in **Figure 25**. Metallic properties are established by occupied and empty electronic states in the valence band, separated by E_F. In the case of metals, the DOS distribution $\rho(E)$ is approximately constant around E_F whereas for diamond $\rho(E)$ is a function of energy. The application of external potentials shifts E_F, either up (negative potential) by the filling of empty electronic levels or down (positive potential) by the emptying of valence-band states. External potentials will, however, not change the confinement of holes (band bending) significantly, as potentials are applied parallel to the conductive layer (perpendicular to the band bending).

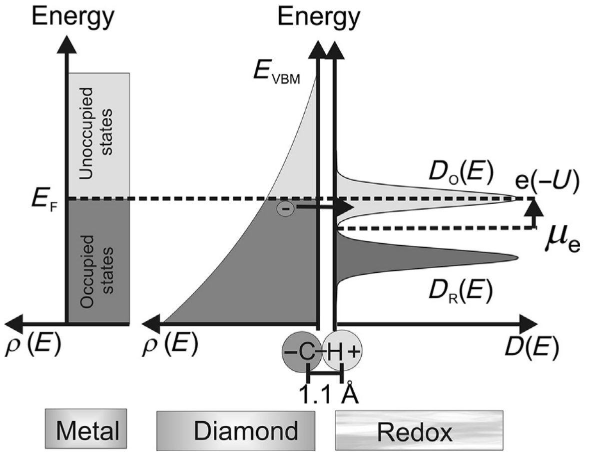

Figure 25 Schematic comparison of a metal and a diamond electrode in contact with a redox system with chemical potential μ_e below E_{VBM}. We show the situation for a negative voltage applied to diamond that shifts the Fermi level E_F up compared to μ_e. This gives rise to a reduction electron flow into empty states of the redox couple.

The interaction of metal and semiconducting electrodes with redox couples has been described in the literature using the Marcus–Gerischer model (Bard & Faulkner, 2002, pp. 124–132), where the oxidizing DOS ($D_O(E)$) above the chemical potential μ and the reduction states ($D_R(E)$) below μ are Gaussian shaped. An upward shift of the Fermi energy, E_F, gives rise to electron transfer from the electrode into empty D_O states and vice versa. The local rate of reduction $r_R(E)$ or oxidation $r_O(E)$ are given by

$$r_R(E) = A\{f(E)\rho(E)\varepsilon_{\text{red}}(E)D_O(E)\text{d}E\}/\Delta t \tag{15}$$

$$r_O(E) = A\{[1-f(E)]\rho(E)\varepsilon_{\text{ox}}(E)D_R(E)\text{d}E\}/\Delta t \tag{16}$$

where A is the electrode area, Δt a given time interval, $f(E)$ the Fermi distribution, $\rho(E)$ the DOS distribution of the metal or semiconductor, $D_O(E)$ the DOS of the oxidizing redox states, $D_R(E)$ the DOS of the reduction states, $\varepsilon_{\text{red}}(E)$ and $\varepsilon_{\text{ox}}(E)$ the proportionality functions for reduction (red) and oxidation (ox), and dE the energy interval under discussion. The exchange rates are proportional to the DOS of the electrode $\rho(E)$.

The transition rate equations contain $\varepsilon_{\text{red}}(E)$ and $\varepsilon_{\text{ox}}(E)$. These parameters are governed by the wave-function overlap of electrons in the valence band of diamond with empty D_O states and of electrons in the D_R states with empty states in the valence band of diamond. Here, the hydrophobic properties of H-terminated diamond may play an important role as the gap between the redox-electrolyte molecules and the diamond surface will be a function of wetting characteristics. Holes in the surface-conducting channel are confined by a dipole energy barrier of about 1.7 eV (Ristein et al., 2000). This conductive layer is very thin (10–20 Å), the continuous DOS distribution may therefore be transformed into a 2D (2D) system with discrete energy levels. It is however very likely that the 2D states are broadened by disorder due to ionic interface scattering and surface roughness.

The experiments show that for two redox couples with chemical potential below the valence-band maximum, oxidation and reduction currents can be detected with formal potentials as for H-terminated metallic polycrystalline boron-doped diamond. This indicates that the electrochemical interaction of boron-doped diamond is also governed by energy alignment properties that are dominated by hydrogen termination and related negative electron affinities. The conductivity of a 3D electrode (metallic boron doped diamond) is, however, significantly higher than that of a conductive surface layer of a 10- to 20-Å thickness. It affects the dynamic properties of cyclic voltammetry experiments as shown in **Figures 23** and **24**. In the case of a 3D metallic boron-doped film, the peaks are narrow and separated only by about 65 mV. We attribute the different results detected for methyl viologen and Co(sep)$^{3+/2+}$ to the depletion of the surface hole accumulation layer at potentials where the redox activity is expected.

Finally, we want to address the oxidation phenomena as detected by cyclic voltammetry. It is known that H-terminated diamond has an NEA in the range −1.1 to −1.3 eV, and oxidized diamond shows a PEA. We expect therefore a vacuum level shift at the surface of diamond of more than $\Delta E \geq 1.1$ eV. Our data indicate that partial oxidation generates a partial shift of the vacuum level, which gives rise to a redox-level shift as shown schematically in **Figure 26**. After the first partial oxidation, the "reduction peak" (electron flow from the diamond to the redox-couple) disappears. This indicates that electrons in the surface conducting layer of diamond cannot be transferred into the redox couple as only occupied $D_R(E)$ states are aligned with the conductive layer. Further, oxidation shifts the redox levels even higher, so that the "oxidizing peak" also decreases and finally vanishes. The redox couple and the electronic levels of the valence band are approaching a situation that normally prevents the formation of a conductive layer as the redox energetic layers are higher than the VBM of diamond. As the redox couple is dissolved in an electrolyte of 0.1 M of Na_2SO_4 with pH 6, the chemical potential of the oxygen evolution at −5.3 eV, given by the reaction

$$2H_2O \Leftrightarrow O_2 + 4H^+4e^-$$

can accommodate electrons ("formation of surface conductivity") if O_2 is in the electrolyte. This is the case in our experiments as we applied anodic oxidation potentials (>+1.6 V). **Figure 26** shows the energy diagram schematically. As long as this level is below the VBM E_{VBM}, surface conductivity can be expected. Prolonged oxidation gives rise to insulating surface properties, as all H is chemically removed from the surface. As a result, the PEA misaligns energy levels significantly, which prevents transfer doping and redox activity. It is interesting to note that a similar result has been reported by Cui et al. (1998). They applied photoelectron emission experiments on hydrogen-terminated diamond and removed the hydrogen termination partially by a sequence of annealing steps. They also find a continuous shift of the vacuum level from −1.3 to +0.38 eV for a hydrogen-free surface. This is in good agreement with our electrochemical results where we removed hydrogen by a sequence of oxidizing steps.

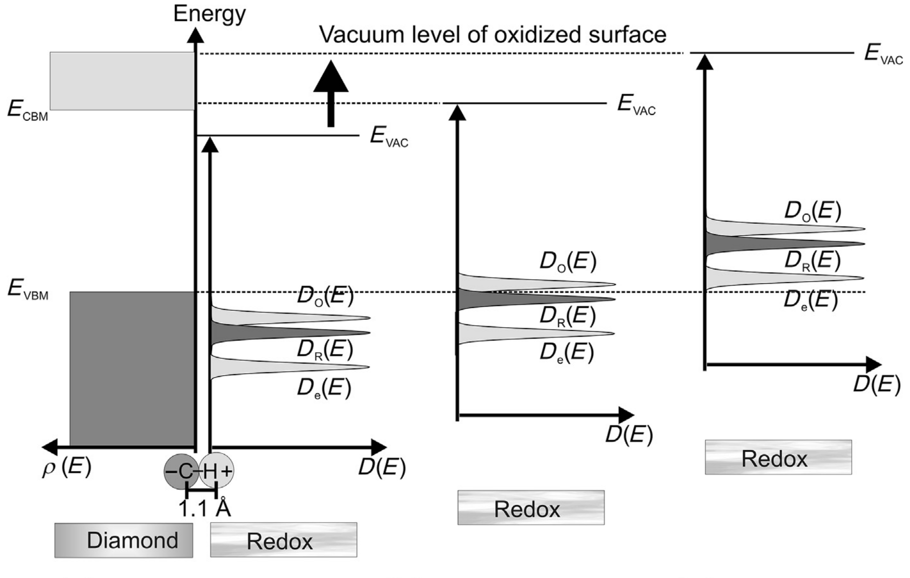

(a) H-terminated **(b)** Partially oxidized **(c)** Fully oxidized

Figure 26 Diamond and redox-couple interaction ($D_O(E)$ and $D_R(E)$) as a function of (a) hydrogen termination, (b) partially oxidized, and (c) fully oxidized. $D_e(E)$ is the chemical potential of the reaction $2H_20 < > O_2 + 4H^+ + 4e^-$ the 0.1 M Na_2SO_4 electrolyte solution (pH = 6) which has an energy level of −5.3 eV below the vacuum.

3.14.5.3 ISFET from Undoped CVD Diamond

In the following, we address the pH sensitivity of the surface-conducting layer as the last part of the transfer doping phenomena. To measure the variation of surface conductivity in different pH liquids, we manufactured ion-sensitive field effect (ISFET) structures (Kawarada, Araki, Sakai, Ogawa, & Umezawa, 2001; Rezek, Watanabe, Shin, Yamamoto, & Nebel, 2006). The geometric properties are shown in **Figure 27** where a hydrogen-terminated surface area of 100 × 500-μm size connects two Au contacts of 130 × 130 μm, which have been thermally evaporated on to diamond. Au wires are bonded to these pads and insulated by a resistive lacquer from contact to electrolyte solution.

The outer part has been oxidized by a soft oxygen plasma to generate insulating surface properties. The schematic arrangement of ISFET in electrolyte solution is shown in **Figure 28**. Platinum is used as "semi-reference" electrode. The level of pH was varied between 2 and 12 by the use of a Britton–Robinson buffer (0.04 M $H_3BO_3 + H_3PO_4 + CH_3COOH$, titrated with NaOH (0.2 M)).

Variations of the drain–source currents with pH, measured at constant drain–source potentials of 0.2 V are shown in **Figure 29**. The currents show transistor characteristics with increasing amplitude for decreasing pH. For positive gate potentials, the current is pinched off with thresholds, dependent on pH. This supports the results of Chapter 3.14 where the redox activity of Co(sep) and Methyl Viologen has been quenched. To prevent degradation by partial oxidation, the maximum applied negative gate voltage was limited to −0.5 V. At this gate

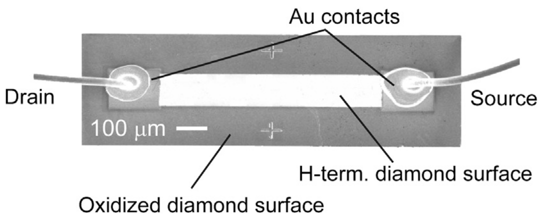

Figure 27 Top view of a realized ISFET structure as measured by electron microscopy. The length of the sensitive H-terminated area 2is 500 μm and the width is 100 μm. On both ends, Au contacts have been thermally evaporated, which act as drain and source electrodes, contacted by wire bonding. The H-terminated area is electrically insulated from the surrounding by an oxidized diamond surface. The Au contacts and wires are covered by a lacquer, which cannot be seen in this figure.

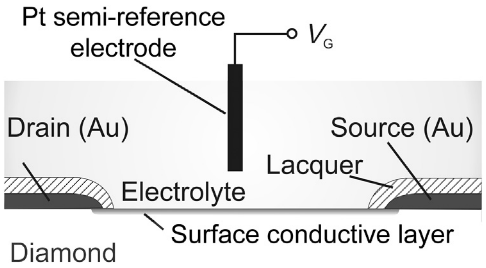

Figure 28 Schematic arrangement of an ISFET from diamond. Due to hydrogen termination of diamond, a thin surface conductive layer is formed at the interface of the electrolyte. Au contacts serve as drain and source electrodes. Both are covered for insulation in the electrolyte solution by a lacquer.

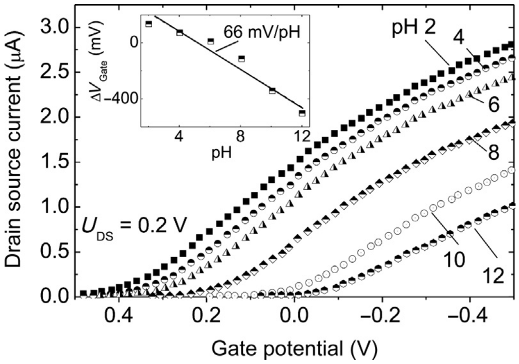

Figure 29 Drain–source currents as a function of gate voltage of an ISFET structure on H-terminated diamond, measured in electrolyte solutions with pH in the regime 2–12. The pH sensitivity is shown in the inset for $I_{DS} = 1$ μA, which results in a pH sensitivity of 66 mV/pH.

potential, the drain–source resistance is in the range (7–13) × 10^4 Ω. Defining 1-μA drain–source current as the reference, a pH sensitivity of 66 mV/pH is calculated as shown in the inset of Figure 29. This is slightly higher than expected by the Nernst law (59 mV/pH). From the leakage current of the ISFET (current flow from surface channel of diamond into the electrolyte), which is about 3 μA cm^{-2} at −3 V, we calculate a gate resistance of 10^8 Ω. The drain–source resistance is in the range of 10^5 Ω (Nebel, Rezek, et al., 2006).

The gate properties can be best described by diode characteristics. Below a critical gate/channel voltage, there is only a small leakage current flowing. Above the threshold voltage, the diode opens, and exponentially increasing currents can be detected. The electronic circuit of a diamond ISFET is summarized in Figure 30. Gate leakage threshold voltages are shown in Figure 31 for different pHs, measured in 0.1 M $HClO_4$ (A) (pH 1), 0.1 M

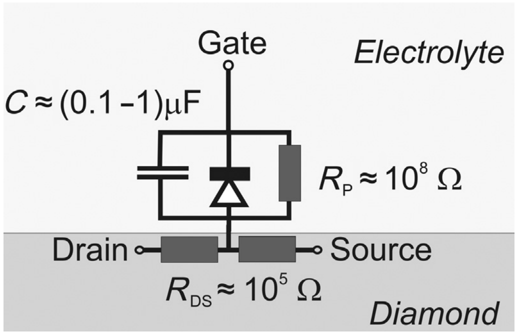

Figure 30 The diamond/electrolyte interface described in electronic terms. The interface is dominated by the Helmholtz capacitance, a leakage resistance in the range of 10^8 Ω, and diode properties if a critical threshold voltage for anodic oxidation is applied. The drain–source resistance is in the range of 10^5 Ω.

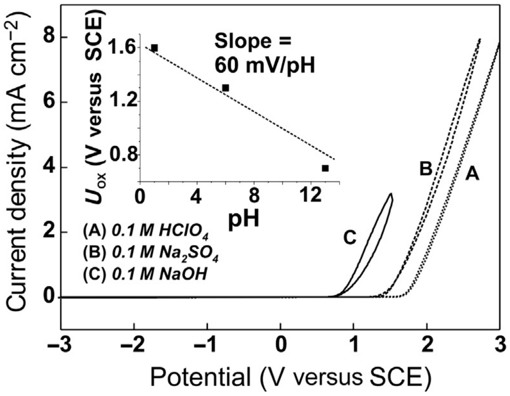

Figure 31 Cyclic voltammograms as detected on an H-terminated undoped diamond electrode in (A) 0.1 M $HClO_4$, (B) 0.1 M Na_2SO_4, and (C) 0.1 NaOH. The oxidizing threshold shifts with increasing pH to lower potentials with about 60 mV/pH.

Na_2SO_4 (B) (pH 6), and 0.1 NaOH (C) (pH 13). The threshold voltage of oxygen evolution at positive potentials (U_{OX}) shifts from +0.7 V (versus Standard Calomel Electrode (SCE)) at pH 13 to about +1.6 V at pH 1. The shift is about 60 mV/pH, which is in reasonable agreement with the Nernst prediction. Oxidation of H termination occurs for potentials larger than U_{OX}, which limits the application of pH sensors to gate potentials <0.7 V.

3.14.6 Conclusions

The combination of results from ISFET characterization and from cyclic voltammetry experiments on the very same samples show that a surface-conducting layer is generated in all investigated pH electrolytes, ranging from 2 to 12. The drain–source currents of H-terminated single crystalline diamond ISFETs show a high pH sensitivity, with about 66 mV/pH. The basic mechanism behind this phenomenon is the alignment of chemical potential and Fermi level of diamond ("transfer doping model") as shown schematically in **Figure 32(a)**. In the case of a low pH, the chemical potential with respect to the vacuum is large, and therefore, the Fermi level is deep in the valence band, giving rise to a high drain–source current (**Figure 32(a)**), which is in agreement with our findings. With increasing pH, the chemical potentials shift up in energy as well as E_F and the drain–source current decreases. For the site-binding model, where a partially oxidized surface is required (Kawarada et al., 2001; Madou & Morrison, 1989), opposite characteristics are detected (**Figure 32(b)**). We therefore conclude that our pH sensitivity favors the transfer-doping model.

The formation of surface conductivity in diamond requires electron transitions from occupied valence-band states into empty states of the electrolyte. This is possible if we follow the arguments of Angus et al. (2004) and Ristein, Riedel, and Ley (2004) who assume that electrons will trigger the reduction of atmospheric oxygen or

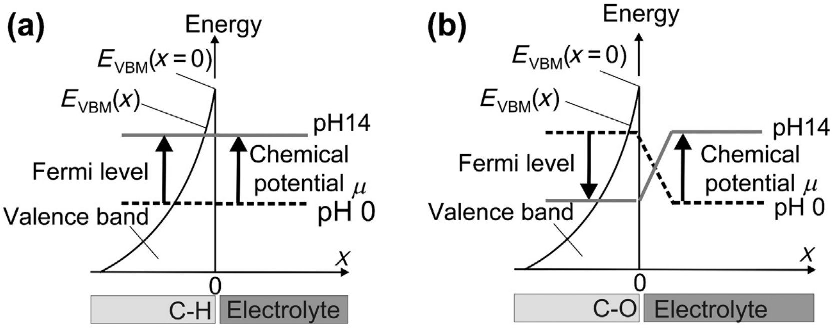

Figure 32 Schematic comparison of transfer doping (a) and site-binding (b) model. In the case of (a), the shift of the chemical potential deeper in energy with decreasing pH gives rise to an increase in the surface conductivity, because the Fermi level also moves deeper into the valence band. For the site-binding model (b), the opposite is expected ($E_{VBM\text{-}Surf}$ = valence-band maximum at the surface, $E_{VBM}(x)$ = valence-band maximum in diamond).

other atmospheric contaminants in the electrolyte, described by $O_2 + 2H_2O + 4e^- \rightarrow 4OH^-$. If we discuss this phenomenon like a redox couple interaction (O_2/OH^-), the O_2 is the empty state of the couple and energetically slightly above OH^-. As the energy level of OH^-, and therefore of O_2, for all pH values is below the valence-band maximum, the formation of a surface conducting film will take place in all electrolytes. The reaction will be limited either by a complete consumption of O_2 and/or by the electric field that builds up at the surface and that prevents unlimited electron flow. The consumption argument is of minor importance if we take into account absolute numbers. Considering data from Hall effect experiments, we know that the typical sheet hole density is in the range of 10^{12} cm^{-2} for drain–source conductivities as in our experiments. The ISFET sensor area is 4×10^{-4} cm^2, which results in about 10^8 electrons, which are exchanged at the interface to reduce O_2. This is a small number that may not generate saturation effects.

In summary, the formation of a conductive layer at the surface of undoped diamond has been detected and characterized by Hall effect, conductivity, contact potential difference (CPM), SEM, and cyclic voltammetry experiments. The revealed data show that due to electron transfer from the valence band into empty states of an electrolyte or adsorbate, a highly conductive surface layer is generated. Holes propagate in the layer with mobilities up to 350 $cm^2\,V^{-1}$. The sheet hole density in this layer is in the range 10^{11}–5×10^{12} cm^{-2}, and dependent on the pH of the electrolyte or adsorbate. This can been utilized to manufacture ISFETs, where the drain–source conductivity is pH dependent, with about 66 mV/pH. Application of potentials larger than the oxidation threshold of +0.7 V (pH 13) to +1.6 V (pH 1) gives rise to exponentially increasing currents between diamond and electrolyte and to partial surface oxidation. In general, the electronic interaction of diamond with redox couples and pH electrolyte solutions is well described by the transfer-doping model.

Theoretical calculations of the "ideal surface electronic properties" of H-terminated diamond in contact with an electrolyte reveal 2D properties, with discrete energy levels. The calculated energies are in reasonable agreement with contact potential difference experiments applied. Extended energy bands with 2D properties could be expected for atomically smooth diamond surfaces on ultrapure CVD diamond. However, ions in the Helmholtz layer of the adsorbate film will cause strong Coulomb scattering as they are only a few Angströms away from the hole-accumulation layer.

Acknowledgments

The author likes to thank Dr B. Rezek, Dr D. Shin, and Dr H. Watanabe for their scientific contributions. He also wants to acknowledge the help of T. Yamamoto for fabricating ISFET structures and greatly appreciated discussions with Dr Okushi, Dr Yamasaki, and with all members of the Diamond Research Center at AIST, Japan. Special thanks goes to Dr Park who supported these activities with the donation of an electrochemical analyzer. The authors also thank Elsevier, New Diamond and Frontier Carbon Technology, Wiley, and American Physical Society to grant copyright permission for several figures published in related journals.

References

Ando, T., Fowler, A. B., & Stern, F. (1982). Electronic properties of two-dimensional systems. *Review of Modern Physics, 54*(2), 437–672.

Angus, J. C., Pleskov, Y. V., & Eaton, S. C. (2004). In C. E. Nebel, & J. Ristein (Eds.), *Semiconductors and semimetals: Vol. 77. Thin film diamond II* (97–119). Elsevier.

Bandis, C., & Pate, B. B. (1995). Electron-emission due to exciton breakup from negative electron affinity diamond. *Physical Review Letters, 74*, 777–780.

Bard, A. J., & Faulkner, L. R. (2002). *Electrochemical methods, fundamentals and applications*. John Wiley & Sons, ISBN 0-471-40521-3, 124–132.

Chakarov, D. V., Österlund, L., & Kasemo, B. (1995). Water-adsorption on graphite (0001). *Vacuum, 46*, 1109–1112.

Chakrapani, V., Angus, J. C., Anderson, A. B., Wolter, S. D., Stoner, B. R., & Sumanasekera, G. U. (2007). Charge transfer equilibria between diamond and an aqueous oxygen electrochemical redox couple. *Science, 318*, 1424–1430.

Cui, J. B., Ristein, J., & Ley, L. (1998). Electron affinity of the bare and hydrogen covered single crystal diamond (111) surface. *Physical Review Letters, 81*, 429–432.

Dischler, B., & Wild, C. (1998). In *Springer series in materials processing: Low-pressure synthetic diamond*. Berlin: Springer.

Fujishima, A., Einaga, Y., Rao, T. N., & Tryk, D. A. (2005). *Diamond electrochemistry*. Elsevier/BKC-Tokyo.

Garrido, J. A., Nebel, C. E., Stutzmann, M., Snidero, E., & Bergonzo, P. (2002). Capacitance–voltage studies of Al-Schottky contacts on hydrogen-terminated diamond. *Applied Physics Letters, 81*, 637–639.

Geis, M. W., & Twichell, J. C. (1995). Electron field emission from diamond and other carbon materials after H_2, O_2 and Cs treatment. *Applied Physics Letters, 67*, 1328–1330.

Gelmont, B., & Shur, M. (1992). Theory of junction between 2-dimensional electron-gas and p-type semiconductor. *IEEE Transaction on Electron Devices, 39*(5), 1216–1222.

Gi, R. S., Mizumasa, T., Akiba, Y., Hirose, H., Kurosu, T., & Iida, M. (1995). Formation mechanism of p-type surface conductive layer on deposited diamond films. *Japanese Journal of Applied Physics, 34*, 5550–5555.

Gi, R. S., Tashiro, K., Tanaka, S., Fujisawa, T., Kimura, H., Kurosu, T., et al. (1999). Hall effect measurements of surface conductive layer on undoped diamond films in NO_2 and NH_3 atmospheres. *Japanese Journal of Applied Physics, 38*, 3492–3496.

Gluche, P., Aleksov, A., Ebert, W., & Kohn, E. (1997). Diamond surface-channel FET structure with 200 V breakdown voltage. *IEEE Electron Device Letters, 18*, 547–549.

Granger, M. C., Witek, M., Xu, J., Wang, J., Hupert, M., Hanks, A., et al. (2000). Standard electrochemical behavior of high-quality, boron-doped polycrystalline diamond thin-film electrodes. *Analytical Chemistry, 72*, 3739–3804.

Granger, M. C., Xu, J., Strojek, J. W., & Swain, G. W. (1999). Polycrystalline diamond electrodes: basic properties and applications as amperometric detectors in flow injection analysis and liquid chromatography. *Analytical Chimica Acta, 397*, 145–161.

Hanney, N. B., & Smith, C. P. (1946). The dipole moment of hydrogen fluoride and the ionic character of bonds. *Journal of the American Chemical Society, 68*, 171–173.

Hayashi, K., Yamanaka, S., Okushi, H., & Kajimura, K. (1996). Study of the effect of hydrogen on transport properties in chemical vapor deposited diamond films by Hall measurements. *Applied Physics Letters, 68*, 376–378.

Hoffmann, R., Kriele, A., Obloh, H., Tokuda, N., Smirnov, W., Yang, N., et al. (2011). The creation of a biomimetic interface between boron-doped diamond and immobilized proteins. *Biomaterials, 32*, 7325–7332.

Kawarada, H. (1996). Hydrogen-terminated diamond surfaces and interfaces. *Surface Science Reports, 26*, 205–259.

Kawarada, H., Araki, Y., Sakai, T., Ogawa, T., & Umezawa, H. (2001). Electrolyte-solution-gate FETs using diamond surface for biocompatible ion sensors. *Physica Status Solidi (A), 185*, 79–83.

Landstrass, M. I., & Ravi, K. V. (1989a). Resistivity of chemical vapor-deposited diamond films. *Applied Physics Letters, 55*, 975–977.

Landstrass, M. I., & Ravi, K. V. (1989b). Hydrogen passivation of electrically active defects in diamond. *Applied Physics Letters, 55*, 1391–1393.

Looi, H. J., Jackman, R. B., & Foord, J. S. (1998). High carrier mobility in polycrystalline thin film diamond. *Applied Physics Letters, 72*, 353–355.

Madou, M. J., & Morrison, S. R. (1989). *Chemical sensing with solid-state devices*. Boston: Academic Press.

Maier, F., Riedel, M., Mantel, B., Ristein, J., & Ley, L. (2000). Origin of surface conductivity in diamond. *Physical Review Letters, 85*, 3472–3475.

Maier, F., Ristein, J., & Ley, L. (2001). Electron affinity of plasma-hydrogenated and chemically oxidized diamond (100) surfaces. *Physical Review B, 64*, 165411.

Maki, T., Shikama, S., Komori, M., Sakaguchi, Y., Sakuta, K., & Kobayashi, T. (1992). Hydrogenating effect of single-crystal diamond surface. *Japanese Journal of Applied Physics, 31*, L1446–L1449.

Marcus, R. A. (1956). On the Theory of Oxidation-Reduction Reactions Involving Electron Transfer. I. *The Journal of Chemical Physics, 24*(5), 966.

Miller, J. B., & Brown, D. W. (1996). Photochemical modification of diamond surfaces. *Langmuir, 12*, 5809–5817.

Mönch, W. (1995). *Semiconductor surfaces and interfaces*. Berlin: Springer.

Nebel, C. E. (2005). Surface transfer-doping of H-terminated diamond with adsorbates. *New Diamond and Frontier Carbon Technology, 15*, 247–264.

Nebel, C. E. (2007). Surface conducting diamond. *Science, 318*, 1391–1392.

Nebel, C. E., Ertl, F., Sauerer, C., Stutzmann, M., Graeff, C. F. O., Bergonzo, P., et al. (2002). Low temperature properties of the p-type surface conductivity of diamond. *Diamond and Related Materials, 11*, 351–354.

Nebel, C. E., Kato, H., Rezek, B., Shin, D., Takeuchi, D., Watanabe, H., et al. (2006). Electrochemical properties of undoped hydrogen terminated CVD diamond. *Diamond and Related Materials, 15*(2–3), 264–268.

Nebel, C. E., Rezek, B., Shin, D., Uetsuka, H., & Yang, N. (2007). Diamond for biosensor applications. *Journal of Physics D: Applied Physics, 40*, 6443–6466.

Nebel, C. E., Rezek, B., Shin, D., & Watanabe, H. (2006). Surface electronic properties of H-terminated diamond in contact with adsorbates and electrolytes. *Physica Status Solidi (A), 203*(13), 3273–3298.

Nebel, C. E., Rezek, B., Shin, D., Watanabe, H., & Yamamoto, T. (2006). Electronic properties of H-terminated diamond in electrolyte solutions. *Journal of Applied Physics, 99*(3), 033711.

Nebel, C. E., Rezek, B., & Zrenner, A. (2004a). Electronic properties of the 2D-hole accumulation layer on hydrogen terminated diamond. *Diamond and Related Materials, 13*, 2031–2036.

Nebel, C. E., Rezek, B., & Zrenner, A. (2004b). 2D-hole accumulation layer in hydrogen terminated diamond. *Physica status solidi (A), 11*, 2432–2438.

Nebel, C. E., Shin, D., Nakamura, T., Rezek, B., Tokuda, N., Watanabe, H., et al. (2007). Diamond and biology. *Journal of the Royal Society Interface, 4*, 439–461.

Okushi, H. (2001). High quality homoepitaxial CVD diamond for electronic devices. *Diamond and Related Materials, 10*, 281–288.

Okushi, H., Watanabe, H., Ri, R. S., Yamanaka, S., & Takeuchi, D. (2002). Device-grade homoepitaxial diamond film growth. *Journal of Crystal Growth, 237–239*, 1269–1276.

Pauling, L. (1939/1960). *The nature of the chemical bond*. Cornell University Press, ISBN 0801403332.

Petrosyan, S. G., & Shik, A. Y. (1989). Contact phenomena in a two-dimensional electron-gas. *Soviet physics: Semiconductors, 23*(6), 696–697.

Rezek, B., Shin, D., Watanabe, H., & Nebel, C. E. (2007). Intrinsic hydrogen-terminated diamond as ion-sensitive field effect transistor. *Sensors and Actuators B-Chemical, 122*(2), 596–599.

Rezek, B., Watanabe, H., & Nebel, C. E. (2006). High carrier mobility on hydrogen terminated (100) diamond surfaces. *Applied Physics Letters, 88*, 042110.

Rezek, B., Watanabe, H., Shin, D., Yamamoto, T., & Nebel, C. E. (2006). Ion-sensitive field effect transistor on hydrogenated diamond. *Diamond and Related Materials, 15*(4–8), 673–677.

Ristein, J., Maier, F., Riedel, M., Cui, J. B., & Ley, L. (2000). Surface electronic properties of diamond. *Physica status solidi (A), 181*, 65–67.

Ristein, J., Riedel, M., & Ley, L. (2004). Electrochemical surface transfer doping: the mechanism behind the surface conductivity of hydrogen-terminated diamond. *Journal of the Electrochemical Society, 151*, E315–E321.

Ristein, J., Stein, W., & Ley, L. (1997). Defect spectroscopy and determination of the electron diffusion length in single crystal diamond by total photoelectron yield spectroscopy. *Physical Review Letters, 78*, 1803–1806.

Sauerer, C., Ertl, F., Nebel, C. E., Stutzmann, M., Bergonzo, P., Williams, O. A., et al. (2001). Low temperature surface conductivity of hydrogenated diamond. *Physica status solidi (A), 186*, 241–247.

Seeger, K. (1999). *Semiconductor physics*. Berlin: Springer.

Shin, D., Watanabe, H., & Nebel, C. E. (2005). Insulator–metal transition of intrinsic diamond. *Journal of the American Chemical Society, 127*(32), 11236–11237.

Shin, D., Watanabe, H., & Nebel, C. E. (2006). Redox-couple interactions with undoped single crystalline CVD diamond. *Diamond and Related Materials, 15*, 121–128.

Shirafuji, J., & Sugino, T. (1996). Electrical properties of diamond surfaces. *Diamond and Related Materials, 5*, 706–713.

Stern, F., & DasSarma, S. (1984). Electron-energy levels in GaAs-Ga 1-x AlxAs heterojunctions. *Physical Review B, 30*, 840–848.

Swain, G. M. (2004). In C. E. Nebel, & J. Ristein (Eds.), *Semiconductors and semimetals: Vol. 77. Thin film diamond II* (121). Elsevier.

Sze, S. M. (1981). *Physics of semiconductor devices*. John Wiley & Sons.

Takeuchi, D., Kato, H., Ri, G. S., Yamada, T., Vinod, P. R., Hwang, D., et al. (2005). Direct observation of negative electron affinity in hydrogen-terminated diamond surfaces. *Applied Physics Letters, 86*, 152103.

Topping, J. (1927). On the mutual potential energy of a plane network of doublets. *Proceedings of the Royal Society of London A, 114*, 67–72.

Tsugawa, K., Kitatani, K., Noda, H., Kokazono, A., Hirose, K., Tajima, M., et al. (1999). High-performance diamond surface-channel field-effect transistors and their operation mechanism. *Diamond and Related Materials, 8*, 927–933.

Watanabe, H., Ri, S. G., Yamanaka, S., Takeuchi, D., & Okushi, H. (2002). High-quality homoepitaxial diamond film growth. *New Diamond and Frontier Carbon Technology, 12*, 369–379.

Watanabe, H., Takeuchi, D., Yamanaka, S., Okushi, H., Kajimura, K., & Sekiguchi, T. (1999). Homoepitaxial diamond film with an atomically flat surface over a large area. *Diamond and Related Materials, 8*, 1272–1276.

Willatzen, M., Cardona, M., & Christensen, N. E. (1994). Linear-muffin-tin-orbital and k-center-dot-p calculations of effective masses and band-structure of semiconducting diamond. *Physical Review B, 50*, 18054–18059.

3.15 Polycrystalline CVD Diamond for Industrial Applications

Eckhard Wörner and Christoph Wild, Diamond Materials GmbH, Freiburg, Germany

3.15.1 Introduction

The advent of gas-phase deposition (chemical vapor deposition (CVD)) techniques for the synthesis of diamond in the 1980s was the beginning of a remarkable hype in this field. Inspired by the extraordinary properties of diamond and by expectations about future markets with turnovers in the multibillion dollar range, many research groups and companies started programs on the CVD growth of diamond and the development of applications. From today's view, one can state that these expectations were mostly not realistic and led to some disappointment in this field. Apart from that, CVD diamond has found its way in many new industrial applications, and there are a couple of successful companies doing business with CVD diamond. In many cases, CVD diamond has been an enabling material, i.e. it is often the only material that meets the requirements of extreme applications involving high-power levels, high thermal loads or abrasive wear.

3.15.2 CVD of Diamond

A variety of diamond deposition techniques have been developed since the first discovery that diamond can be deposited from the gas phase. A common feature of all these techniques is the activation of the process gas, which consists usually of hydrogen and a hydrocarbon such as methane. The main purpose of the gas activation is the generation of atomic hydrogen, i.e. the dissociation of the hydrogen molecules. Atomic hydrogen is known to play a key role during diamond growth as it suppresses the formation of graphite and stabilizes the formation of diamond. Usually the gas is activated by a plasma (microwave, DC discharge, plasma torch, arc discharge, etc.), thermally, e.g. by a hot filament, or using a combustion flame. All these techniques are different with respect to growth rate, deposition area or diamond quality. For commercial diamond synthesis mainly two techniques became most established: microwave plasma deposition for high-quality diamond films or disks and hot filament CVD for thin films on large areas.

As the growth rate is usually in the micrometer per hour range and the energy consumption of these techniques is rather high, diamond CVD is not a really cheap source for synthetic diamond. For example, high-pressure/high-temperature diamond can be produced at much lower costs. However, diamond CVD is the only technique that provides diamond in the shape of extended disks or films, i.e. in the shape needed by many

http://dx.doi.org/10.1016/B978-0-08-096527-7.00052-0

optical, thermal, or mechanical applications. Furthermore, the most perfect diamond crystals that have been analyzed so far were synthetic diamonds grown by microwave plasma CVD.

3.15.3 CVD Diamond Radiation Windows

In the past, physicists used to say that diamond would be the ideal window material. Very seldom, however, natural diamond windows were actually used for exceptional applications such as the 18.2-mm detector window of the Pioneer spacecraft that flew to Venus in 1978 (Seal, 1992). Nowadays, large area diamond windows are commercially available. Outstanding properties such as wide spectral range of transparency, high stiffness, chemical inertness, little change of refractive index with temperature, and last but not the least, its extraordinarily high thermal conductivity and low atomic number make diamond an ideal choice for many window applications.

Figure 1 shows the transmission spectrum of polycrystalline CVD diamond compared to other optical materials such as sapphire and ZnSe. Diamond is extraordinary in being transparent from the ultraviolet to the infrared (IR) and effectively to infinite wavelengths. With a bandgap of 5.4 eV diamond becomes transparent at 225 nm. Near the bandgap and in the visible part of the spectrum, diffuse scattering at grain boundaries reduces the transmission by some percentage. For wavelengths above 1 μm, light scattering is—for most applications—no problem anymore. Between 3 and 7 μm, intrinsic multiphonon absorption reduces the transmission. The maximum absorption coefficient of 14 cm^{-1} is measured at 4.62 μm. In contrast to most other materials where one-phonon absorption leads to an extinction of the transmission at longer wavelengths, perfect diamond remains transparent due to its lattice symmetry. Defects such as incorporated nitrogen and boron, however, break the lattice symmetry and give rise to one-phonon absorption between 7.5 and 11 μm. Most natural stones contain such defects and show one-phonon absorption. Only about 2% of natural diamonds are of type IIa, i.e. are free of defects and show a transmission spectrum comparable to the one of optical-grade CVD diamond.

Diamond has a refractive index of 2.4 in the visible region. Therefore, only about 70% of the incident radiation is transmitted (see Figure 1) and the remaining 30% is reflected. Antireflection coatings or mounting of windows at Brewster angle are possible approaches to overcome this problem.

Diamond is one of the most universal materials with respect to its spectral properties. No other material is employed like diamond in different regions of the electromagnetic spectrum. The applications cover the range from long wavelength microwave to high-energy X-ray radiation. In Table 1, some of the spectral applications of diamond are listed together with the corresponding specific properties of diamond. In particular, if the application takes advantage of two or more properties, diamond is often the only material that meets the requirements of the specific application.

The following sections will describe some applications in more detail.

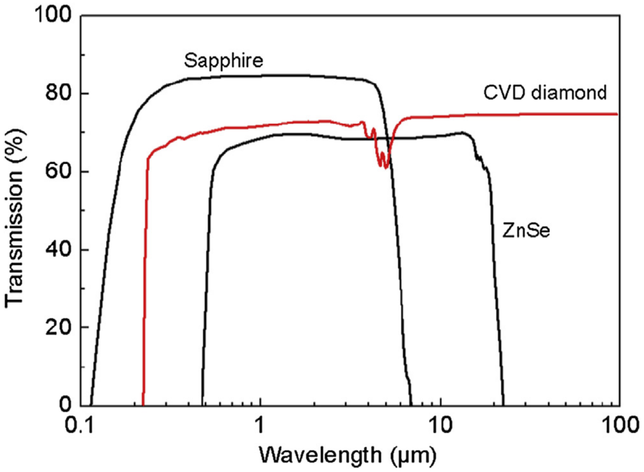

Figure 1 Transmission spectra of optical materials.

Table 1 Application of diamond as radiation transparent material and properties exploited

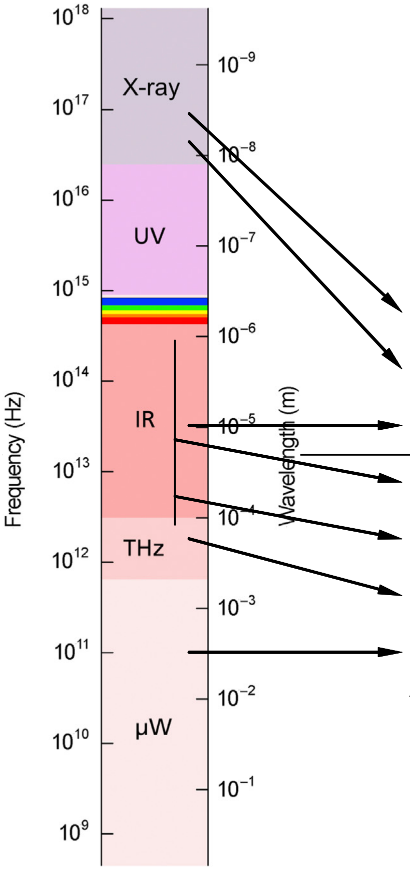

	Hardness	High thermal conductivity	Broadband transparency	Low dispersion	Low-Z	Low dielectric losses	Low d*n*/d*t*	High *n*
X-ray windows	X				X			
X-ray targets		X	X		X			
Laser windows	X	X	X				X	
ATR inserts	X		X					X
Infrared windows	X		X					
THz windows			X	X		X		
Gyrotron windows	X	X				X		

3.15.3.1 Diamond Windows for Spectroscopy

There are lots of possible applications for diamond windows in spectroscopy. Only its price has, of course, been a major deterrent to its use in optics. This partially changed with the advent of CVD techniques to produce synthetically extended diamond windows. Nevertheless, diamond is expensive and only used for applications that really take advantage of its extraordinary properties.

Typical examples are cryostat windows for academic research, IR windows for synchrotron beamlines, and beam splitters for space applications. Such windows are normally used without an antireflection coating, since that would be in conflict with the large transparency range. A possibility to reduce reflection losses without coating is windows mounted in Brewster geometry. Because of the high refractive index, the Brewster angle of diamond is with 68° very oblique. Mounting at Brewster angle is awkward in practice, expensive in diamond, and only used for cutting-edge applications such as the IR beamline window shown in Figure 2.

For spectroscopic applications that cover a large frequency range, the undulated variation of transparency due to wavelength-dependent thickness interferences may be a problem. Such interferences can be suppressed by wedge-shaped windows. Since a typical diamond window is seldom thicker than 1 mm, the wedge angle is limited to values between 0.5° and 1°.

The planarity of the window surfaces is of critical importance for applications that require a low wave front distortion such as CO_2 laser windows and beam splitters. The flatness of these windows is normally specified to be better than one-tenth of the wavelength they are used for. Values better than $\lambda/10$ measured at 633 nm have recently been demonstrated (see Section 3.15.3.2).

Figure 3 shows a 60-mm diamond beam splitter developed for NASA's composite infrared spectrometer (CIRS)-lite Fourier transform infrared (FTIR) spectrometer. This FTIR spectrometer is the lightweight successor model of the 43 kg heavy CIRS that observes the Saturnian system in NASA/ESA's Cassini mission since 2004. CIRS is heavy partly because it was impossible to cover the full spectral range between 7 and 1000 μm with a single beam splitter.

Figure 2 Ultra-high vacuum (UHV) window in Brewster geometry for a synchrotron infrared (IR) beamline.

The successor model uses only one beam splitter—this, however, made of diamond. Its broad transparency range opens the possibility to use a single Fourier transform spectrometer (FTS) architecture instead of a dual one, thus saving precious payload and reducing the total mass of the spectrometer to about 14 kg.

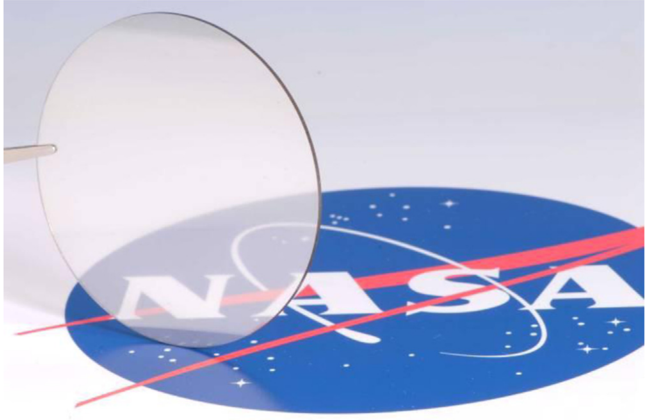

Figure 3 A 60-mm beam splitter produced by *Diamond Materials GmbH* for NASA's CIRS-lite FTIR spectrometer.

To manufacture a diamond beam splitter is a challenging task. In order to obtain a good spectral resolution, a wedge of precisely 0.17° and a flatness at least one-tenth of the shortest wavelength is required (Brasunas, Flasar, & Jennings, 2009; Pasquale, Brasunas, Hagopian, & Gong, 2010).

3.15.3.2 CO_2 Laser Windows

CO_2 lasers are next to solid-state lasers the most common and most powerful and hard-wearing industrial lasers used. With a ratio of up to 20% between output power and pump power, they are also very efficient. Currently, they are available with powers ranging from a few watts to tens of kilowatts.

CO_2 lasers typically emit at 10.6 μm. When taking a look at materials that are transparent at that wavelength, one comes across either diamond or ZnSe. ZnSe is the material of choice for low-power applications. The absorption of ZnSe is below 0.0005 cm^{-1} at 10.6 μm and therefore two orders of magnitude lower than that of diamond (about 0.05 cm^{-1}) (Wild, 1998, p. 189). However, radiation is not only absorbed in the material but also in the antireflection coating. The power absorbed in the coating (about 0.2% i.e. 20 W for a 10-kW CO_2 laser) yields in ZnSe—due to its low thermal conductivity—a significant temperature variation between the water-cooled edge of the window and its center. This temperature gradient results in a strong thermal lens, i.e. the focal length varies with time and output power. Diamond absorbs even more radiation but due to its excellent thermal conductivity, low expansion coefficient and low change of refractive index with temperature, diamond does hardly show any thermal lensing. As a consequence, CO_2 lasers with an output power exceeding 5 kW are generally equipped with diamond windows.

There are basically two types of high-power CO_2 lasers. *Axial flow lasers* circulate the gas through the arc tube and cool the gas to ambient temperatures externally. *Diffusion-cooled lasers* work with radio-frequency (RF) plasma excitation in a narrow gap between two extended electrodes. The electrodes both generate the RF plasma and cool the gas by diffusion. From the window manufacturer's point of view, these types of laser differ a lot. In the case of *diffusion-cooled lasers*, the window is not part of the laser resonator. Therefore, it must not influence the transmitted wave front, i.e. it has to be homogeneous in thickness but not necessarily very stiff. For such a laser system, typically a 400-μm-thick diamond window that is coated on both sides with an antireflective is used. *Axial flow lasers*, on the other hand, are operated with windows that act as an output coupler. Being part of the laser cavity, they have to be planar and also stay planar in operation. Such windows have to be about twice as thick and are usually coated with a semireflective coating.

High-power CO_2 lasers have been used for welding and cutting of up to 50-mm-thick stainless-steel plates for many years; however, quite recently, a challenging new application arose from a completely different field of applications.

Driven by Gordon Moore's law that anticipates a doubling of transistors per chip area every 18–20 mounts, scientists all over the world search for new techniques to increase integration density of ICs. It is agreed that argon fluoride laser emission at 193 nm, which is used in today's deep ultraviolet immersion lithography with a resolution of 38 nm, will not meet the future demands anymore. Lithography with higher resolution needs light sources with shorter wavelengths.

A way to extend the resolution of photolithography is to use the extreme ultraviolet (EUV) light that is emitted by a tin plasma (13.5 nm). Such small wavelengths are expected to have the potential to reduce the resolution below 10 nm (Wagner & Harned, 2010).

Currently, there are two competing concepts to generate such a tin plasma. Companies like Ushido (Japan) use an electrical discharge system, whereas Cymer (USA) and Gigapjoton (Japan) produce the plasma by targeting small droplets of molten tin with a pulsed, high-power CO_2 laser. This technology has to face and solve many new challenges. About 13.5 nm radiation is absorbed in air; consequently the whole system has to be operated in a vacuum environment. Refractive optics such as lenses cannot be used anymore for the same reason. In addition, each focusing mirror, and there are at least six of them in projection lens assembly, absorbs at least 28% of the incident EUV radiation (Wagner & Harned, 2010). Consequently, there has to be a very powerful laser to generate a bright tin plasma at first place to guarantee that enough light reaches the wafer to ensure cost-effective wafer throughput.

At the time of this writing, Cymers EUV light source (HVM I) uses a 20-kW CO_2 laser system consisting of a master oscillator and four amplifier stages. This laser vaporizes 30 μm molten tin droplets that are produced at a typical frequency of 50 kHz to generate about 100 W of raw light (Fomenkov et al., 2009).

The good news for the diamond manufacturers is that at these power levels there is no other competing material anymore. They have to face, however, extreme specifications for their optical windows both with respect to material quality and geometrical accuracy. Typical specifications request an absorption coefficient below 0.05 cm^{-1} and a planarity and wave front distortion below one fringe at 633 nm over the entire clear aperture.

Figure 4 shows a 1.5″ diamond window with a planarity better than $\lambda/10$ at 633 nm that meets these specifications.

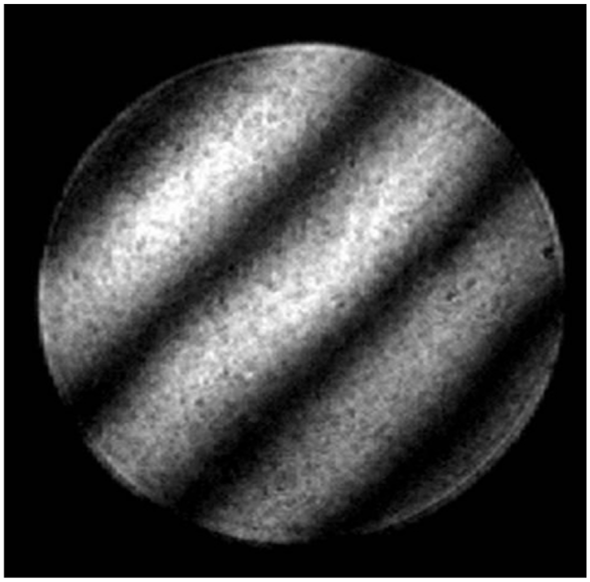

Figure 4 1.5″ CVD diamond CO_2 laser window with a planarity better than $\lambda/10$ at 633 nm.

3.15.3.3 Gyrotron Windows

The largest diamond windows are used for gyrotrons. Gyrotrons are vacuum tubes that generate millimeter waves with an output power in the megawatt range. Many of these devices are going to be used to heat up the plasma in future nuclear fusion plants such as the *International Thermonuclear Experimental Reactor* that is currently under construction in Cadarache in southern France. In Greifswald, Germany, the experimental stellarator *Wendelstein 7-X* uses 10 gyrotrons with 1 MW output power each to heat up its fusion plasma. These gyrotrons and the stellarator torus use diamond windows that are 106 mm in diameter and 1.81 mm thick (Heidinger, Dammertz, Meier, & Thumm, 2002).

The property that makes diamond attractive for millimeter-wave gyrotrons is its low absorption coefficient for microwaves ($\tan \delta < 2 \times 10^{-5}$ at 145 GHz) (Heidinger et al., 2002). The low absorption together with the extremely high thermal conductivity prevents a thermal runaway and a thermal crack formation in diamond windows. Latest measurements on state-of-the-art water-cooled diamond windows revealed an absorbed power of only 55 W at a power level of 500 kW. This promising result emphasizes the intention to reach 1–2 MW transmitted power in the near future (Scherer, Meier, Strauss, & Schreck, 2011).

3.15.3.4 X-ray Windows and Anodes

Diamond is a low-Z material ($Z = 6$). Only beryllium has a lower atomic number ($Z = 4$). As a result, these materials are relatively transparent to X-ray radiation. **Figure 5** shows the X-ray transmission coefficient of diamond depending on energy and thickness. At typical thicknesses for free-standing diamond windows (>100 μm), diamond is well transparent for X-ray energies above 5 keV. The absorption of soft X-rays is dominated by the carbon k-edge at 280 eV. Here, only very thin diamond membranes with thicknesses in the submicron range exhibit reasonable transparency values.

3.15.3.5 High-Power X-ray Windows

The potential of CVD diamond disks as window material for high-power X-ray beams has been recognized in the early 1990s (Khounsarya & Kuzaya, 1992). In particular, synchrotron light sources like wigglers and undulators produce very intense broadband electromagnetic radiation beams and therefore require high-power filters and windows to select and transmit the spectral ranges to be used in X-ray beamlines. **Figure 6** shows a diamond window assembly consisting of a large water-cooled copper body with a central tapered hole and an embedded diamond window that separates the vacuum of the synchrotron storage ring from the ambient air.

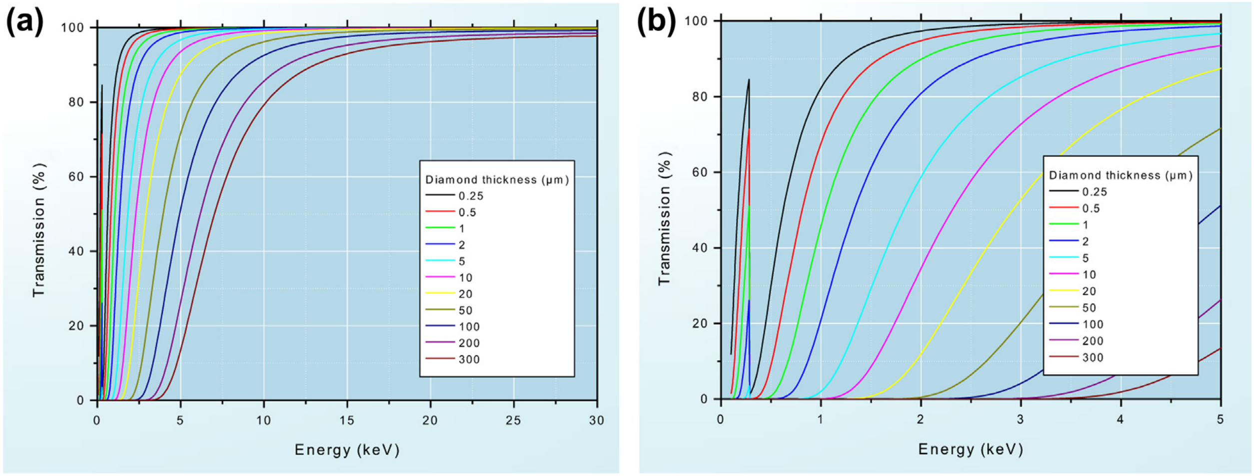

Figure 5 X-ray transmission of CVD diamond for various thicknesses. (a) 0–30 keV and (b) 0–5 keV.

Figure 6 Ultra-high vacuum compatible diamond window for high-power X-ray beamlines.

The window is directly brazed to copper to obtain maximum cooling and therefore maximum power handling capability. As an example, the window shown in Figure 6 is 150 μm thick and can handle power loads up to 400 W (Figure 7).

3.15.3.6 X-ray Beam Monitors

The control of the X-ray beam in synchrotron radiation facilities is an important issue for the proper focusing and alignment of the X-ray and for obtaining well-defined and reproducible experimental conditions (Smith, 2006). Ideally, a beam-monitoring device yields information about the beam properties like the beam position, direction, profile and intensity. Furthermore, an ideal beam monitor can handle high intensities and can be left in the beam during the experiment without affecting its properties such allowing real-time monitoring of the beam properties. In this context, thin polycrystalline diamond fluorescence screens have been found to be very

Figure 7 CVD diamond fluorescence monitors with engraved cross-hair.

useful. The irradiation of these diamond screens by X-rays leads to the formation of electron–hole pairs, which recombine thereby emitting visible light that can be detected by a conventional charge-coupled device camera. By an appropriate doping of the diamond with dopants that form optically active centers, the intensity of the fluorescence signal can be adjusted to the specific requirements.

3.15.3.7 X-ray Transmission Targets

In microfocus X-ray tubes, the electron beam is focused on an X-ray transparent window coated with the target material (typically tungsten). A schematic setup is shown in Figure 8. Due to the small focal spot size of the electron beam and its close proximity to the object under investigation, very high magnification and resolution values can be achieved. In modern radioscopic devices, a sophisticated movement of the object offers the possibility of computed tomography, giving a three-dimensional (3D) view into the object.

In this application, diamond windows coated with the appropriate target material have been proved to be very useful and to improve the performance of the microfocus tube considerably. Here they have a triple function: they act as an X-ray-transparent vacuum window, a metal-coated target, and a heat sink for the heat generated by the electron beam. Indeed, the thermal load at the focal spot of the electron beam is extremely high: a 10-W electron beam focused on an area of 1 μm diameter corresponds to power flow of 1 billion Watt on 1 cm^2. The high thermal conductivity of diamond improves the heat dissipation considerably and offers the possibility to increase the power of the X-ray tube or to further decrease the spot size. Figure 9 shows a comparison between two radiographic images taken with a diamond (a) and a beryllium (b) transmission target. The images show 20-μm bond wires placed behind a 3-mm-thick metal plate. Obviously, the image taken with the diamond target is considerably sharper and less noisy.

In Figure 10, diamond X-ray transmission targets as offered by Diamond Materials are depicted. They are coated with 6-μm tungsten. In spite of the fact, that a considerable amount of electrons pass the tungsten layer and are stopped in the diamond window, no deterioration of the diamond due to radiation defects can be observed, indicating the superior radiation resistance of diamond.

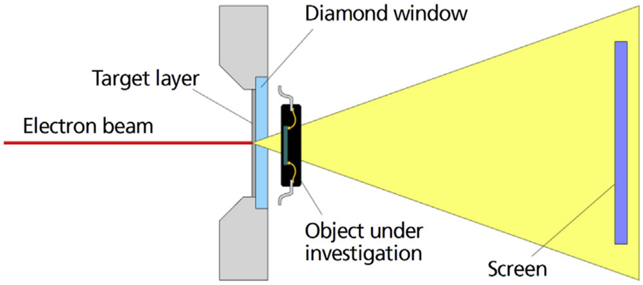

Figure 8 Schematic setup of a microfocus X-ray tube using a diamond transmission target and of the imaging geometry used for the inspection of small objects.

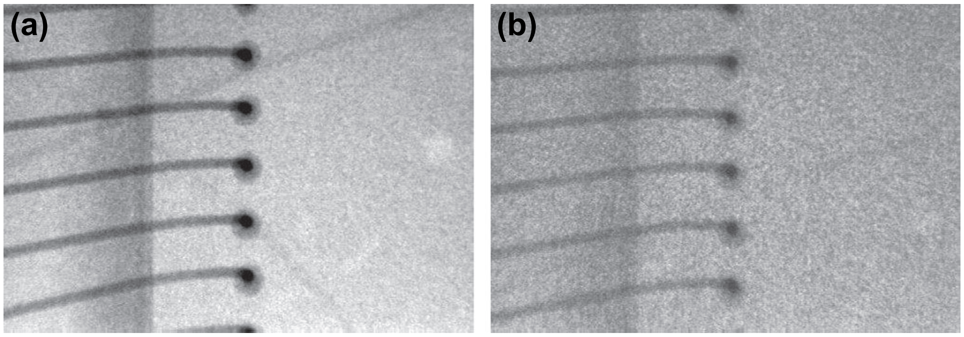

Figure 9 X-ray image taken from gold bond wires. (a) Tube with diamond target and (b) tube with beryllium target. Images courtesy of Feinfocus GmbH (now Yxlon International).

Figure 10 X-ray transmission targets used in open X-ray tubes.

3.15.4 Thermal Management Applications

Diamond is the material with the highest thermal conductivity at room temperature. This is all the more surprising since diamond is an electrical insulator. As a rule of thumb, materials with a good electrical conductivity also have a high thermal conductivity. This rule, however, is only true for metals, in which conduction electrons carry most of the heat. In electrical insulators, heat is conducted by lattice vibrations (phonons). At low temperatures, the thermal conductivity is governed by phonon scattering at surfaces and extended defects such as grain boundaries, whereas at high temperatures, phonon–phonon interaction (Umklapp-scattering) is the main source for thermal resistance. At about one-twentieth of the Debye temperature, the thermal conductivity reaches its maximum. Diamond with its unsurpassed atomic density, its light carbon atoms and the strong bonds between them has the highest Debye temperature of all materials (2220 K). As a consequence, the maximum of the thermal conductivity is shifted to higher temperatures and the room-temperature value is, with about 2000 W $(\mathrm{mK})^{-1}$, still five times higher than that of copper.

Before it was possible to synthesize CVD diamond in the form of extended disks, the technical use of diamond as a heat spreader was limited to applications such as laser or microwave diodes (Seal, 1992) that require only very tiny volumes. Nowadays, heat spreaders in different thermal grades with thermal conductivities from about 800 to 2000 W $(\mathrm{mK})^{-1}$ are available from a number of suppliers. They are still used not only for the efficient cooling of all kinds of laser diodes and laser diode arrays but also for the mounting of large-area neodymium:yttrium-aluminum-garnet laser disk laser crystals.

3.15.5 3D CVD Diamond Components

Diamond is the hardest material known. Therefore, it is generally a difficult task to prepare 3D diamond components by cutting and polishing bulk diamond. One may object that cut and polished brilliants are 3D shapes made of diamond, which is true. But when manufacturing brilliants, diamond cutters avoid polishing in crystallographic hard directions by all means. Nevertheless, with considerable effort it is also possible to polish hard orientations as is needed, for example, to prepare diamond lenses. First lenses were already made in 1824 by Andrew Pritchard (Nuttall & Frank, 1972). In those days, diamond lenses were needed for microscopes (Davis, 1984), making use of the large refractive index of diamond. Nowadays, polishing techniques have improved significantly and even spheres made of single and polycrystalline diamond (Biener et al., 2009) have been reported.

It is much easier, however, to take advantage of the fact that a CVD diamond is a perfect copy of the substrate that is used to grow on. Molding techniques that use preshaped substrate enable a large variety of 3D components. Examples are lenses (Wörner, Wild, Müller-Sebert, & Koidl, 2001), Atomic force microscope (AFM) tips (Niedermann, Hänni, Blanc, & Christoph, 1996) and moth-eye structures (Ralchenkov et al., 1999) that can be used as durable antireflection coatings in the IR frequency range.

3.15.5.1 Diamond Loudspeaker Cones for High-End Audio Components

Loudspeaker membranes are one of the prominent examples where 3D diamond components have actually entered the market in significant number.

Early suggestions to use diamond as a tweeter membrane date back to 1987 (Japanese Patent Office). However, no further development was done until in 1999 when the Fraunhofer Institute for Applied Solid State Physics and Thiel & Partner GmbH, an audio equipment manufacturer specialized in hard material loudspeaker membranes, entered a cooperation aiming to develop a novel high-frequency tweeter with a diamond membrane. This cooperation succeeded in launching the first commercial tweeter system in the year 2000. With its extreme hardness, paired with low density and high velocity of sound, diamond is the ideal material for tweeters. Unlike diamond membranes, conventional ones made of metal or synthetic material such as fabric, ceramics or plastics suffer from nonlinearities and cone breakup modes at fairly low audio frequencies. Due to their mass, inertia and limited mechanical stability, the speaker membranes made of conventional materials cannot follow highest frequency excitations of the actuating voice coil causing phase shift and sound pressure losses due to interference effects (Wörner, Wild, Müller-Sebert, Koidl, & Bankewitz, 2006). Dome-shaped diamond membranes that are available from several suppliers are prepared using the molding technique. They are 20–65 mm in diameter and only about 50 μm thick. These lightweight membranes can easily been accelerated and generate a high sound pressure level (SPL).

Figure 11 shows the simulated SPL of 20-mm membranes made of aluminum, diamond and an imaginary infinitely stiff material (Wörner et al., 2006). With 24 kHz, the aluminum membrane shows its cone breakup, the first significant membrane resonance, slightly above the audible range, causing harmonic distortions in the audible. The diamond membrane, on the other hand, shows an almost linear SPL up to values of about 60 kHz, which is confirmed by measurements (Wörner et al., 2006). Surprising at first sight is the fact that the infinitely stiff membrane shows a pronounced dip in the response around 90 kHz. This extinction is a result of the

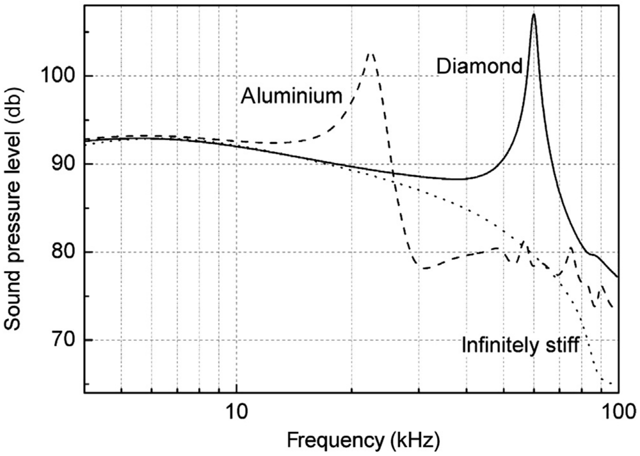

Figure 11 Sound pressure level versus frequency for an aluminum, a diamond and an infinitely stiff membrane, all of the same mass (Wörner et al., 2006).

dome-shaped geometry of the membrane causing phase interferences between sound emitted at the center and at the rim of the membrane (Figure 12).

3.15.5.2 Diamond Spheres and Hollow Shells

Diamond spheres prepared by coating a spherical mandrel with a thick diamond layer followed by subsequent grinding and polishing have found significant interest during recent years. The applications are twofold:

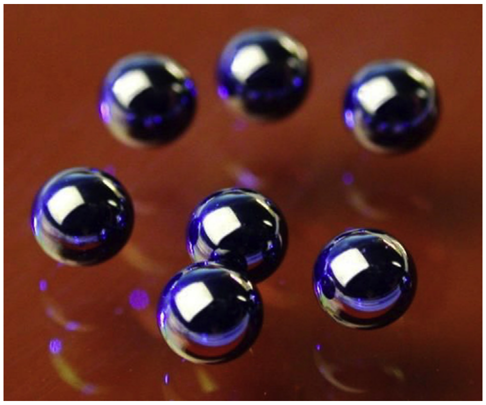

Figure 12 CVD diamond spheres with polished surface finish.

1. Hollow diamond shells for nuclear fusion research

By drilling a micron-sized hole into the diamond layer and by removing the mandrel using wet- or dry-etching techniques, hollow diamond shells can be prepared that are ideally suited to be used as an ablator for inertial confinement fusion (Ultra-high precision diamond shells). These diamond shells offer a nearly perfect spherical surface. Indeed, the deviation from an ideal spherical shape can be as low as 10 nm. Figure 13 shows the result of measurement obtained with a sphere mapper confirming the nearly perfect sphericity. For nuclear fusion, the shells are filled with nuclear fuel (deuterium and tritium), and an extremely intense megajoule laser pulse is used to compress the shell. Thereby, the volume shrinks by about four orders of magnitude leading to high pressure and temperature levels that are sufficient to ignite a self-sustained nuclear reaction. The perfectly

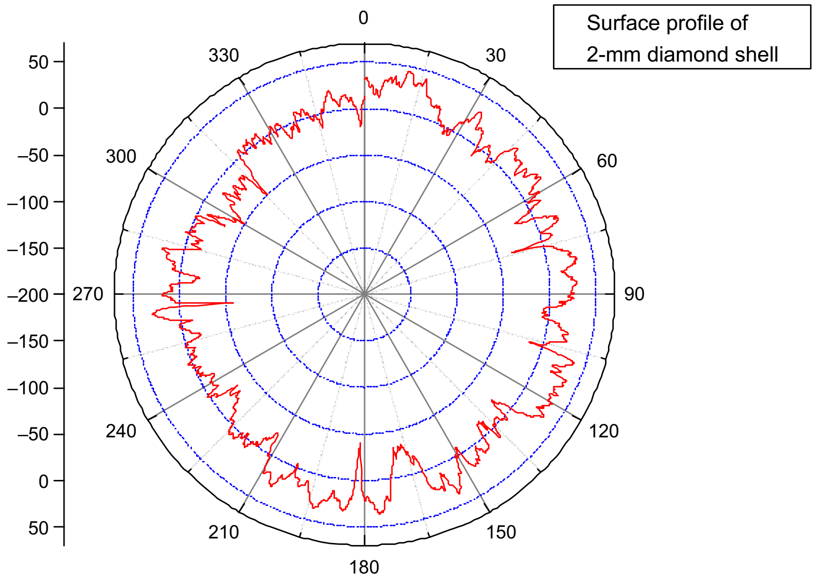

Figure 13 Surface profile as measured with a high-precision sphere mapper. The red curve shows the deviation from a perfect sphere.

spherical surface of the diamond shells is an important prerequisite to avoid Raleigh–Taylor instabilities that would deform the shell during compression.

2. Diamond spheres for metrology

The application of diamond spheres as stylus tip of length gauges takes advantage of the hardness, wear resistance and low friction properties provided by diamond surfaces. Diamond spheres are used in metrical applications, where conventional materials like sapphire fail due to pronounced abrasion, for example, in cases where the tip is in contact with an abrasive or sliding surface. The perfect sphericity mentioned above is, of course, a prerequisite for high-accuracy measurements. In addition, it was found that diamond spheres do not show the problem of galling (material transfer or material buildup), which is presumably the result of the low friction coefficient.

3.15.6 Conclusion

In 1992, Michael Slack concluded that although CVD diamond deposition had been developed, "almost all diamond products sold for high technology applications are made from natural or high pressure synthetic diamond" (Seal, 1992). This was attributed to low growth rate, difficulties in polishing and internal stress.

This situation changed completely.

These days, polycrystalline CVD diamond can be deposited with properties comparable to those of perfect type IIa natural stones. The rate at which high-quality diamond grows is still low and as a consequence such material is still not really cheap. Nevertheless, many applications that take advantage of the exceptional properties of diamond have found their way into the market. Prominent examples are diamond windows that shifted the power level of CO_2 lasers to values exceeding 20 kW or diamond gyrotron windows that can handle power levels of up to 1 MW. But X-ray windows with a membrane thickness below 1 μm that are transparent to photon energies as low as 1 keV have also opened up a complete new range of applications. Last but not the least, diamond tweeter domes that are used up to 70 kHz in high-end audio systems are an example of CVD diamond entering the consumer market.

Up to now, many fascinating products were made with CVD diamond and most probably plenty of new and challenging problems are going to be solved with it the future.

Acknowledgments

The authors want to thank Prof. Peter Koidl for valuable comments. Unless otherwise indicated, the figures are reproduced with permission from *Diamond Materials GmbH*.

References

Biener, J., Ho, D. D., Wild, C., Woerner, E., Biener, M. M., El-dasher, B. S., et al. (2009). *Nuclear Fusion, 49*, 112001, 5 pp.

Brasunas, J. C., Flasar, F. M., & Jennings, D. E. CIRS-lite: a Fourier transform spectrometer for a future mission to Titan. In *Fourier transform spectroscopy*, OSA Technical Digest (CD) (Optical Society of America, 2009), paper FTuA1.

Davis, G. (1984). *Diamond*. Bristol, UK: Adam Hilger Ltd.

Fomenkov, I. V., Brandt, D. C., Bykanov, A. N., Ershov, A. I., Partlo, W. N., Myers, D. W., et al. (2009). Laser-produced plasma light source for EUVL. *Proceedings of SPIE, 7271*, 727138.

Heidinger, R., Dammertz, G., Meier, A., & Thumm, M. K. (2002). *IEEE Transactions on Plasma Science, 30*, 800.

Japanese Patent Office: JP63226197A.

Khounsarya, A. M., & Kuzaya, T. M. (August 1, 1992). *Nuclear Instruments and Methods in Physics Research Section A: Accelerators, Spectrometers, Detectors and Associated Equipment, 319*(1–3), 233–239.

Niedermann, Ph., Hänni, W., Blanc, N., Christoph, R., & Burger, J. (1996). *Journal of Vacuum Science and Technology A, 14*, 1233.

Nuttall, R., & Frank, A. (1972). *New Scientist, 53*, 92.

Pasquale, B., Brasunas, J., Hagopian, J., & Gong, Q. Optical design for the composite InfraRed spectrometer lite (CIRS-Lite). In *International optical design conference*, OSA Technical Digest (CD) (Optical Society of America, 2010), paper JMB42.

Ralchenkov, V., et al. (1999). In M. Yoshikawa, et al. (Eds.), *Proc. applied diamond conference/Frontier carbon Technology'99* (pp. 128). Tsukuba, Japan.

Scherer, T. A., Meier, A., Strauss, D., & Schreck, S. (2011). In *Proceedings of 36th international conference in infrared, millimeter, and terahertz waves.*

Seal, M. (1992). High technology applications of diamond. In J. E. Field (Ed.), *The properties of natural and synthetic diamond* (pp. 608–616). Academic Press.

Smith, S. J. (2006). *Front end x-ray beam position monitors at the CLS* (Master thesis). Saskatoon, Canada: University of Saskatchewan.

Ultra-high precision diamond shells have been developed within a cooperation between Fraunhofer IAF, Lawrence Livermore National Laboratory and Diamond Materials in the framework of the National Ignition Facility project.

Wagner, C., & Harned, N. (2010). *Nature Photonics, 4*, 24–26.

Wild, C. (1998). In B. Dischler, & C. Wild (Eds.), *CVD diamond for optical windows, low pressure synthetic Diamond: Manufacturing and application.* Heidelberg, Germany: Springer.

Wörner, E., Wild, C., Müller-Sebert, W., & Koidl, P. (2001). *Diamond and Related Materials, 10*, 557.

Wörner, E., Wild, C., Müller-Sebert, W., Koidl, P., & Bankewitz, A. (2006). *Advances in Science and Technology, 48*, 142–150.

3.16 Diamond Nanoparticles: Surface Modifications and Applications

Anke Krueger, Institute for Organic Chemistry, Julius-Maximiliaus University of Würzburg, Am Hubland, 97074 Würzburg, Germany

3.16.1 Introduction

The nanoscale version of diamond has only recently been "rediscovered". Although the first reports of its production (see Chapter 3.07) date back to the 1960s, significant global efforts to investigate their properties did not begin till over 30 years later. However, research activities have been tremendously intensified in the last few years fueled by discoveries such as the stable luminescence from lattice defects (Fu et al., 2007; Greentree et al., 2010; Markham et al., 2011). Additionally, ease of availability and favorable properties such as chemical inertness and biocompatibility, among others, make nanoscale diamond an ideal material for a variety of applications (Holt, 2007; Krueger, 2008a; Krueger, 2011; Schrand, Ciftan Hens, & Shenderova, 2009; Vaijayanthimala & Chang, 2009). Then again, other forms of diamond, e.g. bulk material and microcrystalline forms of diamond as well as diamond films, have already been used for a long time (Auciello & Sumant, 2010; May, 2010; Sussmann, 2009; Williams, 2011).

One of the major aspects for the application of a new material is the possibility to control its surface. Along this line surface termination, especially of diamond films produced by chemical vapor deposition (CVD), always played an important role not only for the film properties but also for the respective applications (Lud et al., 2006; Maier, Ristein, & Ley, 2001; Stavis et al., 2011). Typically, the surface of an as-grown diamond films is terminated with hydrogen which also ensures the absence of sp^2 carbon on the film's surface (for more details, refer to the chapters on CVD diamond) (Fox, 1997). Air oxidation (at elevated temperature) or oxygen plasma treatment increases the hydrophilicity of the diamond surface. It is afterward terminated either with different ketone-related groups (either with C═O or the related bridging –O– moieties) or with carboxylic acids (Ghodbane et al., 2010; Kulisch et al., 2010). Other transformations involving reactive gases can also be used to control the surface of diamond films. For instance, in 1998, Ohtani et al. reported the chlorination and subsequent formation of quaternary pyridinium salts on a CVD diamond surface (Ohtani et al., 1998). But not only reactions with gaseous reactants but also conventional organic transformations can be applied. Important achievements include the covalent grafting of alkyl chains with additional terminal groups onto hydrogenated CVD diamond by the photochemical grafting of terminal alkenes (Nichols, Butler, Russell, & Hamers, 2005; Zhuang et al., 2010), the fluorination of diamond films (Ray et al., 2007), radical reactions on diamond films (Nakamura, 2010) as well as the application of other techniques derived from silicon technology (Lud et al.,

http://dx.doi.org/10.1016/B978-0-08-096527-7.00053-2

2010; Remes, Choukourov, Stuchlik, Potmesil, & Vanecek, 2006). More complex transformations include the immobilization of bioactive moieties. Nebel and coworkers achieved the structured binding of DNA strands onto the hydrogenated areas of a diamond film after patterned surface oxidation (Rezek, Shin, Nakamura, & Nebel, 2006). Such biofunctionalized films can be employed, e.g. in sensor architectures or for lab on a chip applications.

In addition to covalent surface modification, diamond films with different surface termination can also adsorb organic compounds such as small molecules like allyl alcohol (Loh, Lim, Gao, Qi, & Wee, 2006) or complex structures such as DNA or enzymes. These materials can be used, for example, for the fabrication of sensing devices or the delivery of therapeutic agents (Bijnens et al., 2009; Garguilo, Davis, Buddie, Kock, & Nemanich, 2004; Huang et al., 2009; Xu, Jeedigunta, & Kumar, 2007).

A similar approach has to be taken for the control of the surface of nanoscale diamond. Only with total control of its properties resulting from a well-defined surface termination will the full potential of its applications be realized. This chapter discusses the surface termination of nanodiamond (ND), efficient methods for the well-controlled surface modification and different options for the application of suitably functionalized ND.

3.16.2 The Surface of Nanoscale Diamond

As there are different ways for the production of nanoscale diamond, there are as many characteristic surface structures and terminations. Besides the powders produced by detonation or shockwave synthesis since the early days of ND in the 1960s, there are several other methods to obtain diamond in the form of nanocrystals (Dolmatov, 2001; Krueger, 2008b; Osawa, 2007). The production of nanoparticles starting from high-pressure high-temperature (HTHP) synthesis diamond and CVD diamond opens the way for ND powders with distinctly different properties. Although the general crystal structure (except for the density of twins, dislocations or other lattice defects) is basically identical for all diamond nanoparticles, the size and surface of the particles resulting from the various production processes differ depending on the applied method (Cheng, Chen, Shaio, Tsai, & Chen, 2005; Donnet et al., 1997; Yin et al., 2001). The most usual surface termination of commercially available ND is an oxygenated surface. It results from, for example, the employment of water or ice for the cooling in the detonation process, which results in the reaction with highly reactive hydroxyl species (stemming from the decomposition of water molecules in the extremely harsh environment). Besides, the purification of nanoscale diamond of all origins is usually carried out using oxidizing mineral acids and/or air oxidation (Butenko et al., 2006; Mitev, Dimitrova, Spassova, Minchev, & Stavrev, 2007; Osswald, Yushin, Mochalin, Kucheyev, & Gogotsi, 2006; Pichot et al., 2008; Tyurina, Apolonskaya, Kulakova, Kopylova, & Obraztsov, 2010). Such treatment leads to the formation of carbonyl and carboxyl groups on the diamond surface. The only ND material with a hydrogenated surface would result from the destruction of CVD films into nanoparticles as the feed gas for the deposition of the diamond films consists of a carbon source and a significant amount of hydrogen gas to ensure the continued sp^3 hybridization of the deposited carbon by saturation with hydrogen atoms (Fox, 1997; Landstrass & Ravi, 1989a, 1989b). However, the subsequent treatment of the initial material (coarsely crushed into clusters of nanocrystals) for the isolation of single particles from continuous films (such as washing with acids or milling processes) usually yields materials with an oxidized surface (Neu et al., 2011).

In general, the main surface groups found on ND particles include carboxylic acids (COOH) and keto groups (C=O) in addition to different alcohol functions (tertiary, secondary, and primary) and ether groups (these are strongly related to C=O groups as they represent another variant of the oxygen-terminated diamond surface) (Comet, Pichot, Siegert, Britz, & Spitzer, 2010; Jiang & Xu, 1995; Mochalin, Osswald, & Gogotsi, 2009; Skorik, Krivozubov, Karzhenevskii, & Spitsyn, 2011; Tu, Perevedentseva, Chung, & Cheng, 2006; Zou, Wang, & Li, 2010). However, other structural elements, e.g. involving sp^2 carbon of different nature (isolated double bonds, extended areas with π-conjugation up to graphene-like or graphitic structures), are also present on ND (**Figure 1**). The different surfaces of ND exhibit different zeta potentials ranging from -50 to $+50$ mV depending on their termination with those groups. Typically, carboxylated surfaces exhibit negative potentials, whereas hydroxylated material shows positive values and sp^2-terminated particles exhibit rather weak zeta potentials. Accordingly, the agglomeration behavior of ND of different origin varies significantly. The agglomeration behavior not only depends on the surface termination, though. Particle size, shape and the existence of graphitic carbon influence the tendency of aggregate formation. While nanoparticles derived from HTHP or CVD materials show only a moderate tendency toward agglomeration, detonation nanodiamond

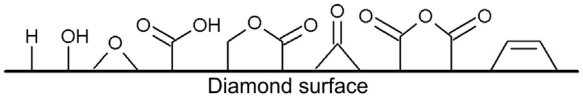

Figure 1 Surface termination of diamond depends on the production method and the postproduction treatment. For CVD films, the hydrogenated surface is most common, whereas diamond nanoparticles often carry an inhomogeneously oxygenated surface. For all materials, the presence of sp^2 carbon at the diamond surface is the result of surface reconstruction or annealing.

(DND) usually occurs in strongly bound agglomerates if no counteraction is taken (Avdeev et al., 2009; Krüger et al., 2005; Spitsyn et al., 2005). In recent years, several techniques have been developed to produce fully dispersed diamond nanoparticles in different solvents using mostly mechanochemical approaches (Hsin et al., 2011; Li & Huang, 2010; Liang, Ozawa, & Krueger, 2009; Niu et al., 2011; Ozawa et al., 2007; Pentecost, Gour, Mochalin, Knoke, & Gogotsi, 2010).

Starting with these different ND materials, it becomes obvious that reproducible results in applications can only be obtained with reproducible material. Hence, the nanoparticles' surface should be as homogeneous as possible. It is therefore decisive to fully control the surface termination in order to control the quality of the final functionalized material and its applicability.

3.16.3 Modifications to the Initial Surface Termination of ND

3.16.3.1 Hydrogenated ND

Although a hydrogenated diamond surface is the simplest surface termination from the structural point of view, it turned out that a postproduction hydrogenation of ND is quite demanding. Of course, CVD diamond produced in a hydrogen atmosphere carries a hydrogenated surface from the beginning. But all oxidized forms of diamond have to be treated under rather harsh conditions to completely replace the oxygen-containing groups by hydrogen atoms. This is due to the fact that typical reducing agents do not actually lead to the pure hydrocarbon (which is the molecular analog of the hydrogen-terminated diamond surface) but rather to the formation of different types of hydroxyl functions (Chapter 3.02). Therefore, other ways to transform the surface into its most reduced state are required. The simplest hydrogen source for reactions is the element itself. Experimentally, ND samples can be heated in a hydrogen atmosphere. Main reaction pathways during the treatment of DND in hydrogen (either at high temperatures or in plasma) include decarbonylation and decarboxylation (Jiang, Xu, & Ji, 1996). The thermal hydrogenation at 850 °C was, for example, applied by Spitsyn et al. (2010). However, it was found that only a fraction of the surface carbon atoms carried hydrogens. The remainder was terminated with OH groups. Other diamond particles can be hydrogenated in a similar manner as Tsubota and coworkers showed with the hydrogenation of submicron diamond at ∼900 °C. Here (probably due to the less oxidized initial surface), the resulting materials are hydrophobic and the IR data clearly reveal the existence of significant amounts of hydrogen-bound sp^3 carbon (Ida, Tsubota, Hirabayashi, et al., 2003). Such high temperatures pose, however, a danger to very small diamond nanoparticles (well below 100 nm) as those have an increased tendency toward graphitization. Some of the resulting sp^2 carbon is surely resaturated, but most likely at the expense of crystalline perfection at the surface of the particles (the formed alkyl groups will not reintegrate into the diamond lattice). Of course, it is an option to simply work at lower temperatures for the hydrogenation. Indeed this leads to partially hydrogenated ND and hydrophobic behavior of the products (Obraztsova & Eremenko, 2008; Williams et al., 2010). Another method for the increase of reactivity in hydrogenation reactions (usually a rather high activation barrier is responsible for low reactivity under mild conditions) is to apply a catalyst. In synthetic chemistry, hydrogenations are typically carried out using metal catalysts, such as palladium, platinum, rhodium or sometimes nickel-based catalysts (Ager, 2011; Smith & March, 2007). Experimental difficulties have probably so far hampered the application of this approach for the hydrogenation of ND. Homogeneous hydrogenation catalysts are often sensitive toward moisture or oxygen. Other, less-sensitive catalyst versions are applied as preadsorbed materials on solid supports. Namely those catalysts that are prepared on activated charcoal are the most difficult to remove when used with ND. And if the removal of the catalyst and/or support requires the use of oxidizing mineral acids, the diamond surface would be immediately reoxidized.

The function of the catalyst is to yield more active hydrogen by splitting the H_2 molecules, e.g. upon chemisorption on the catalyst's surface. Hence one has to look for other ways to generate hydrogen atoms.

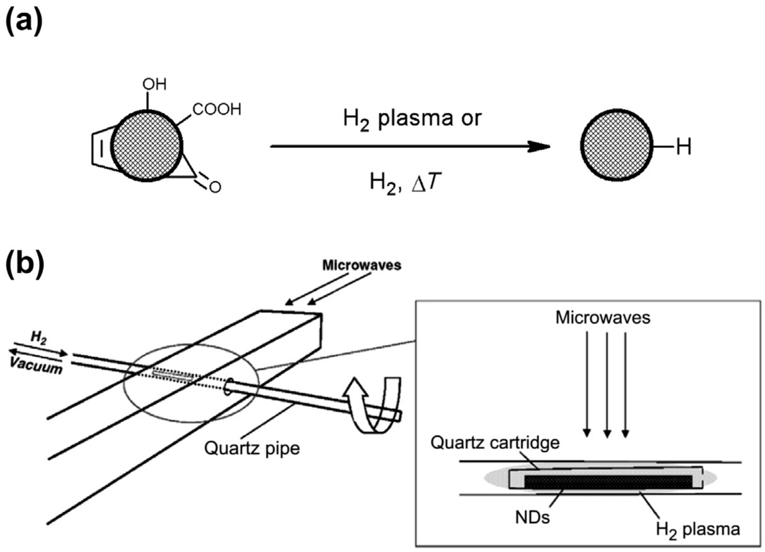

Figure 2 (a) Hydrogenation of nanodiamond can be achieved using hydrogen plasma or hydrogenation with H_2 at elevated temperature. (b) Plasma hydrogenation leads to homogeneous results when a rotating tube containing the ND powder is introduced into the plasma zone. Copyright Elsevier, image reproduced with permission from Girard et al. (2010).

Under the conditions in a hydrogen plasma, this requirement is met as the hydrogen molecules are broken apart and highly reactive species in a reductive atmosphere ensure the desired attack on the diamond surface. For diamond films, the surface hydrogenation in a plasma reactor is a well-established technique (Fox, 1997; Ghodbane et al., 2010; Kulisch et al., 2010). However, some technical problems have to be overcome when applying this technique to powder-like targets. The actual particle surface is at least to some extent hidden within larger agglomerates of the crystallites and thick powder layers might hamper the uniform access of the reactant to the surface. Repeating the hydrogenation after mixing the sample after an initial hydrogenation step ensures a more homogeneous termination. This was reported by Loh and co-workers who repeated the hydrogenation of air-oxidized detonation diamond in a microwave plasma reactor at 800 °C twice for 60 min (Yeap, Chen, & Loh, 2009). Atomic hydrogen can also be produced on a hot filament. It can react, e.g. with graphitized ND under addition to the π-bonds (Yeganeh et al., 2007). For large-scale production, a semicontinuous process has been conceived by Girard and colleagues. They constructed a special reactor with a rotating quartz tube as its core piece. By placing it into a microwave plasma reactor, they achieved the homogeneous hydrogenation of the ND powder (**Figure 2**) (Arnault et al., 2011; Girard et al., 2010; Girard et al., 2011).

3.16.3.2 Hydroxylated ND

In the range of different oxidation states of the functionalized surface atoms of the diamond particle, hydroxylated ND stands in between the hydrogenated and the carboxylated (and carbonylated) surfaces. It should be therefore accessible by both reduction and oxidation of the respective starting materials. Furthermore, hydroxyl functions enable a broad variety of subsequent reactions. Therefore, the homogeneous termination of the ND's surface with a high amount of OH groups is a highly appreciated objective. Several approaches have been successful (**Figure 3**). In 2006, we reported the reduction of existing oxygenated surface groups carrying C═O moieties (such as ketones and acids) with borane (Krueger et al., 2007; Krüger, Liang, Jarre, & Stegk, 2006). Hydroxylated diamond with up to 0.5 mmol g^{-1} of OH groups was obtained. These hydroxyl groups could then be used for different grafting reactions using trialkoxysilanes or acid chlorides reactions (see below). However, the borane reduction is not always fully successful. The main parameter for the reduction efficiency is the nature of the initial surface groups on the ND. Especially esters or lactones cannot be easily reduced by borane (and can still be identified after the borane reduction, e.g. in Fourier transform infrared spectroscopy (FTIR) spectra). But the reaction with borane also has its advantage: in a reaction related to the well-known hydroborination, sp^2 carbon (i.e. from disordered and graphitic material) will be hydrogenated in the

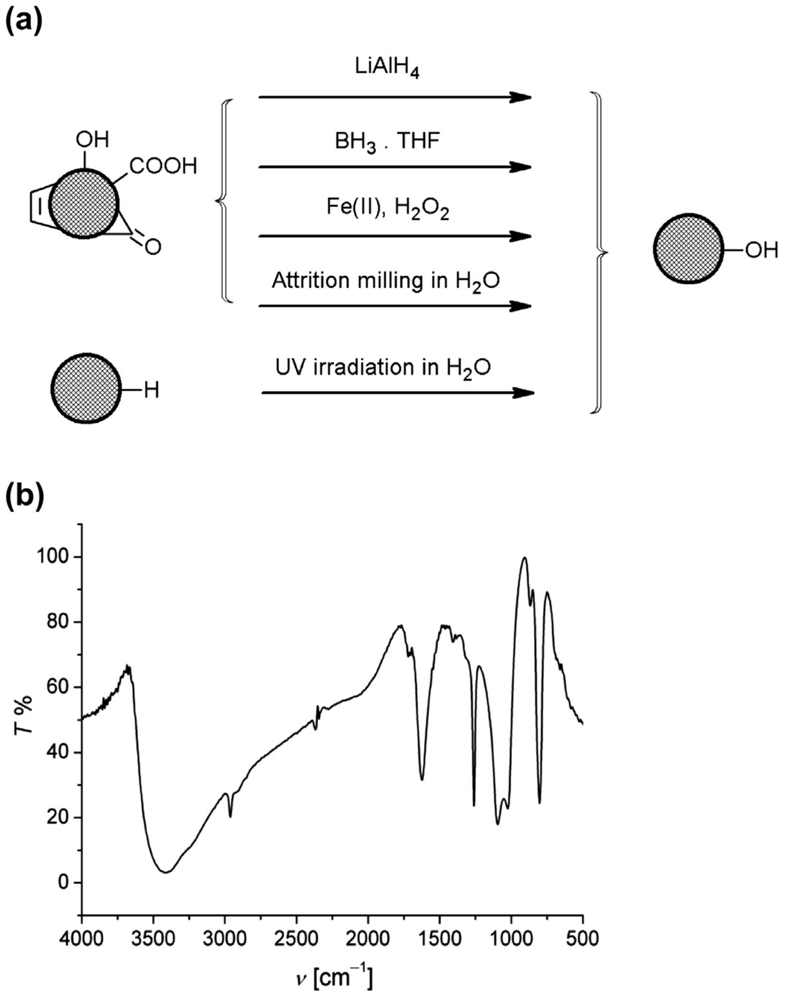

Figure 3 (a) The termination of ND with hydroxyl functions can be achieved either by the reduction of carbonyl and carboxyl groups or by the partial oxidation of hydrogenated ND. (b) The ND surface can be also terminated with OH using mechanochemical processes occurring during attrition milling in water. The FTIR spectrum shows the large amount of OH groups in the milled ND sample.

subsequent acidic workup. Therefore, the reaction of ND with borane not only produces the desired OH groups but also reduces the amount of unsaturated fragments such as double bonds (this is also a very simple way to introduce C–H bonds without using gaseous hydrogen). Other reducing agents can be employed if the complete reduction of all carbonyl species is required. Namely highly reactive complex hydrides such as LiAlH$_4$ can be used. It reduces all types of carbonyl groups to alcohol moieties. In contrast to borane, it cannot saturate sp^2 carbon by hydrogenation, though. The reduction with LiAlH$_4$ has been reported, e.g. by Ida, Tsubota, Nagata, et al. (2003), Zheng et al. (2009) and Ciftan Hens et al. (2008) for the hydroxylation of different types of diamond. In our hands, it showed that utmost care should be taken that all side products (i.e. aluminum oxide hydroxides) are removed. Simple acidic workup using hydrochloric acid does not suffice; complexing agents such as citrate are necessary to fully remove the inorganic compounds from the diamond sample.

The introduction of surface OH groups is also possible by reacting ND with in situ generated OH radicals. These can be formed either photochemically, in a chemical reaction or by mechanochemistry. All these ways have been used to hydroxylate ND. Girard et al. reported on the photochemical hydroxylation of hydrogenated ND (Girard et al., 2011). In their experiment, water vapor in a quartz ampoule was irradiated with ultraviolet (UV) light in the presence of ND carrying a hydrogen termination. In situ generated OH radicals bind to the diamond surface yielding ND–OH.

The chemical synthesis of OH radicals can be achieved by the reaction of FeSO$_4$ and hydrogen peroxide in acidic solution. This mixture is called the *Fenton* reagent, a well-known oxidizing agent. The mixture has been applied by Garcia and co-workers leading to the successful oxidation of DND (Martín, Álvaro, Herance, & García, 2010; Martín, Heydorn, Alvaro, & García, 2009). An additional advantage consists in the oxidative removal of nondiamond carbon (leading to the formation of CO_2). Such highly hydroxylated ND can be used for a variety of covalent and noncovalent interactions with larger functional moieties (see below).

Mechanical energy can also be used to generate hydroxyl radicals from water if the process enables the breaking of covalent bonds by sufficient energy input. We have used this method to graft OH groups on fully dispersed primary particles of ND by mechanochemical treatment of the initial agglomerates in water. When dispersing detonation diamond slurries by attrition milling (Krüger et al., 2005) or beads-assisted sonic disintegration (BASD) (Ozawa et al., 2007), the particles become significantly more hydrophilic, and are well stabilized in colloidal solutions as the zeta potential rises to ~+40 mV (at neutral pH). Spectroscopic data such as FTIR support the increase of the amount of OH groups (**Figure 3(b)**). These colloidal aqueous solutions of hydroxylated ND can contain high concentrations of ND of up to 10 wt% ND. Above this value, strong noncovalent interactions by hydrogen bonding induce the formation of gels. A word of warning has to be given about the full hydroxylation of oxidized diamond samples. Typically, all methods for the reduction or radical hydroxylation do not lead to the complete absence of C=O structures when pristine ND material is treated. If this is desired, the removal of oxygen-containing surface groups is recommended prior to hydroxylation by a method involving OH radicals (Fenton, BASD or attrition milling in water, and photochemical hydroxylation).

Nevertheless, hydroxylated ND is a very useful derivative of nanoscale ND. Its surface is hydrophilic (suitable for bioapplications) with typical zeta potentials of ~+40 mV at neutral pH, the particles can be easily dispersed in aqueous solution or other polar solvents and can be used for the grafting of functional moieties by adsorption or covalent bonds (see below).

3.16.3.3 Carboxylated ND

The highest oxidation state of the surface carbon atoms is achieved by termination with carboxyl functions (those are connected by only one C–C bond to the actual ND crystal) or keto groups (which can be directly bound to lattice atoms).

The carboxyl or keto groups saturate the otherwise dangling bonds on the diamond core (which would be located, e.g. on the apices of the adamantane units). When the complete carboxylation of the ND surface is required, it is necessary to achieve maximum oxidation. This comes at a price: as carbon in general and hence also diamond are prone to complete oxidation to CO_2, the surface carboxylation is inevitably accompanied by material loss and size reduction of the ND core (Turner et al., 2009). This effect becomes more pronounced the smaller the ND particles are as reactivity of diamond is depending on the crystal size. Typical reagents for harsh oxidation include mixtures of strongly oxidizing mineral acids (**Figure 4**). Reagents frequently used for ND oxidation at elevated temperatures (of up to >200 °C!) consist of equal amounts of concentrated sulfuric, nitric and perchloric acids or HCl, HNO_3, and H_2SO_4 (both reagent mixtures to be handled with utmost care!) (Butenko et al., 2006; Mitev et al., 2007; Osswald et al., 2006; Pichot et al., 2008; Tyurina et al., 2010; Xie, Yu, & Li, 2006). Other authors report the oxidation of carbonaceous material by the so-called "piranha water" (a mixture of sulfuric acid and hydrogen peroxide) (Rondin et al., 2010), pure concentrated hydrogen peroxide solution (Mitev et al., 2007) or a mixture (3:1)

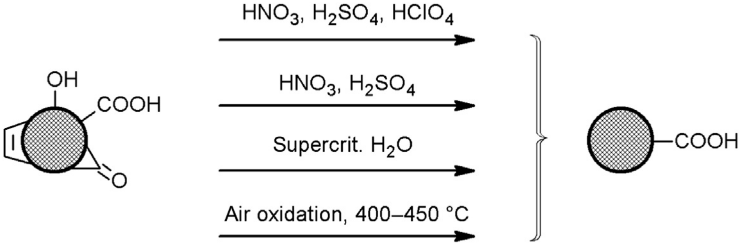

Figure 4 Carboxyl groups are the result of oxidation under harsh conditions. Typically, these reactions are accompanied by a significant loss of diamond material as it is "burned" by the reagents. Simultaneously, the amount of sp^2 carbon is efficiently reduced as its reactivity toward oxidation is higher than for sp^3 carbon.

of concentrated sulfuric and nitric acids (Cheng, He, Li, & Yang, 2008; Tu et al., 2006). The oxidative power of all these reagents cannot only terminate the ND surface with highly oxidized groups but helps also to get rid of undesired nondiamond carbon. The reactivity of sp^2 and sp^3 carbon toward oxidation differs and a certain selectivity for the complete oxidation of the graphitic carbon can be achieved (Pichot et al., 2008). However, complete phase purity is paid by huge losses of diamond! Another reagent for the selective oxidation of nondiamond components is supercritical water, a strong oxidant (the nature of the resulting oxygen-containing surface groups after the hydrothermal treatment requires further study, though) (Anikeev & Zaikovskii, 2010; Kruger, Osawa, & Kataoka, 2002). Both acids and supercritical water help also to remove other, e.g. metallic impurities by solubilizing them. For many applications, it is important not only to know the type of surface termination but also to obtain quantitative data on the density of these surface groups. To quantify the surface loading with COOH groups, several methods are applicable. The adsorption of dodecylamine (Cheng et al., 2008) on the carboxylated diamond by zwitterion formation and the subsequent gravimetric determination of the amount of active acid groups have been used for this purpose. Another excellent method to quantify the amount of acid groups on the diamond particles uses the *Boehm* titration (Comet et al., 2010). When using this wet-chemical quantification, care has to be taken to ensure the complete removal of dissolved CO_2 immediately before the titration (Goertzen, Thériault, Oickle, Tarasuk, & Andreas, 2010). Otherwise, the obtained results overestimate the actual amount of COOH moieties. Due to the different acidity of the oxygenated surface groups, the technique can be also used to distinguish between those moieties when a careful stepwise titration is employed.

Besides the wet-chemical oxidation, the reaction with oxidizing gases (air or elemental oxygen) is yet another way to introduce oxygen-containing surface groups on ND. Air oxidation at elevated temperatures can be even used to control the sp^3/sp^2 ratio on ND surfaces as Gogotsi and coworkers have reported (Osswald et al., 2006). It turned out that the reaction temperature is key to the selective oxidation of nondiamond carbon. A minimum temperature of typically ~400 °C is required for the onset of the oxidation. However at more than 450 °C, all kinds of nanoscale carbon undergo oxidation, leading to the simultaneous burning of diamond and sp^2 material. In the quite narrow-temperature window around 425 °C, the sp^2 carbon is selectively etched and a high amount of oxygenated surface groups is established on the remaining ND. This method has been used by Smith et al. to remove sp^2 carbon from nanoscale diamond of different size and to improve the luminescence properties of inherent N–V centers in these diamonds (which are not visible when strongly absorbing graphitic carbon is hindering both excitation and emission) (Smith, Gruber, & Plakhotnik, 2010). There are also reports on air oxidation using significantly higher temperatures (obviously resulting in more ND loss) for the complete removal of sp^2 carbon and the oxidation of the diamond surface (Tyurina et al., 2010). However, such treatment with air at high temperatures not necessarily leads to a fully homogeneous surface. Most likely, the majority of the existing surface groups after air treatment are COOH groups, but other groups such as ketones and aldehydes, ethers and alcohols are found as well. Further work to elucidate the true termination of such materials and to improve the termination homogeneity is needed. Additionally, air oxidation has also been used to deliberately reduce the size of ND particles. Already in 2004, Gordeev and Korchagina reported on the different reactivity (and the resulting size reduction) of ND of different origin toward the oxidation with air (Gordeyev & Korchagina, 2004). Recently, Gaebel and colleagues succeeded in the size reduction of luminescent ND by careful air oxidation. The smallest ND particles still exhibiting a stable luminescence from N–V centers had a size of 8 nm (Gaebel et al., 2012). This comes close to the limit where ND crystallites are not stable in hot air anymore. Particles smaller than ~4 nm transform into sp^2 carbon easily when heated (in air). In that size range, stability of sp^2 and sp^3 carbon is quite similar and phase transformations can be induced by rather small changes in the environmental conditions (temperature and pressure). Additionally, surface oxidation is an exothermic process and hence locally provides thermal energy also contributing to this transformation. As small NDs are also more reactive in oxidations than larger crystallites (Gordeev & Korchagina, 2007), the smallest particles will be etched away during air oxidation together with sp^2 carbon. Therefore, in some experiments, an apparent size increase has been observed during surface oxidation. However, the removal of the smaller fractions is at the basis of this finding. For each particle, the diameter is reduced by thorough oxidative treatment. In summary, oxidative treatment can be used to control the size of the nanocrystallites while improving the material's phase purity at the same time (Osswald, Havel, Mochalin, Yushin, & Gogotsi, 2008). The resulting oxidized ND samples (whether air oxidized or treated with mineral acids) possess a highly hydrophilic character, typically zeta potentials of −30 to −50 mV and can be dispersed in polar media even in the presence of salts (as typically found in buffer solutions for cell culture).

3.16.3.4 ND Terminated with sp^2 Carbon

For diamond films, the phenomenon of surface reconstruction is well known (Frauenheim et al., 1993; Le Huu, Zaidi, Paulmier, & Voumard, 1996; Ristein, 2006). Patterns of π-bonds are formed upon thermal annealing of the diamond films. These result from the recombination of dangling bonds which are generated by the removal of noncarbon surface atoms or groups after thermally induced bond breakage. The arrangement of the π-bonds is controlled by the lattice orientation of the surface (Schwartz et al., 2005; Wang et al., 1999). The same transformation should occur on diamond nanoparticles (Okada, 2009; Raty & Galli, 2005). And indeed the partial or even complete conversion of ND particles into "bucky diamonds" (ND with a multilayer graphitic shell) or carbon onions (multishell fullerene-like objects) has been reported in the past. The transformation can be achieved by thermal annealing (Kuznetsov & Butenko, 2005; Kuznetsov, Chuvilin, Butenko, Mal'kov, & Titov, 1994; Mykhaylyk, Solonin, Batchelder, & Brydson, 2005) or by electron irradiation with high-energy electrons beams, e.g. in a transmission electron microscope (Hiraki et al., 2005; Qin & Iijima, 1996; Roddatis, Kuznetsov, Butenko, Su, & Schloegl, 2002). As electron irradiation is not easily available for the transformation of large samples, thermal treatment is the method of choice for the surface annealing of macroscopic amounts of ND. However, conditions of this treatment have to be chosen carefully according to the thickness of the desired graphitic layer. Typically, a very thin layer of sp^2 carbon, mostly one graphene layer or less, is required as this preserves the inherent properties of the ND particle but still provides sufficient sp^2 carbon for further surface chemistry (see below). Parameters that influence the resulting sample structure include temperature, annealing duration and the vacuum quality (pressure and residual reactive species in the gas phase). On the other side, the reactivity of the ND particles depends on their size (smaller particles are more reactive), their crystal shape ($\sim$spherical ND is usually more reactive than material with pronounced facets as more steps and reactive crystal edges are available from where the transformation will start) and the already existing amount of sp^2 carbon on the ND's surface (the latter can serve as a "nucleation center" for the further transformation of sp^3 into sp^2 carbon). Hwang and coworkers carried out a thermal treatment of air-oxidized submicron diamond ($d < 0.25$ μm) at 1200 °C for 1–3 h and used the generated sp^2 carbon for a subsequent radical reaction on the particles' surface (Chang et al., 2010). They reported on the generation of well-ordered graphitic material which showed a behavior like the sidewalls of carbon nanotubes. For diamond with significantly smaller particle size, e.g. DND, the annealing temperature has to be much lower. Otherwise the graphitization leads to particles with thick graphitic layers (the so-called "bucky diamonds") or at higher temperatures to the formation of carbon onions. We found that for detonation diamond thermal treatment at 750 °C for 2 h in vacuum of 10^{-3} mbar is suitable for the formation of sufficient amounts of reactive sp^2 carbon (**Figure 5**) (Liang et al., 2011; Krueger & Lang, 2012). Higher temperatures always lead to the formation of multilayered graphitic structures. It should be taken into consideration that such large amounts of graphitic material will govern the properties of the bucky diamond particle. A very detailed study of the early stages of surface annealing of DND has been reported by Petit et al. very recently (Petit, Arnault, Girard, Sennour, & Bergonzo, 2011). They followed the thermal annealing process by XPS (X-ray photoelectron spectroscopy) and basically found exactly the same temperature ranges for the possible transformation steps as with the observation of the reactivity of the annealed surface (see below): for initial sp^2 formation $\sim$700–900 °C, beginning core transformation (>900 °C) and thorough graphitization of the ND particles and formation of ordered sp^2 carbon (>1100 °C).

Originally it was thought that better vacuum would improve the formation of partially graphitized ND. However, this was not the case. We found that for a certain annealing time, higher amounts of surface groups remain on the ND surface (e.g. by persisting signals of carbonyl functions in the FTIR spectra). It seems that a residual amount of oxygen is useful for the removal of less reactive surface groups (they need to be oxidized first before being desorbed from the surface). The reaction with the residual oxygen can be considered as an initial etching step before the actual annealing and formation of sp^2 carbon sets in. Carboxylic groups are easily removed as CO_2 and can be removed by the breaking of one single bond. Arnault and coworkers reported that ND spin coated onto silicon substrates covered with silicon nitride survives higher temperatures before desorption of surface groups and surface annealing sets in. This might be due to the stabilizing effect of the silicon nitride layer. But as the experiment was carried out in high vacuum, the proposed initial etching step is also not possible due to the lack of oxygen (Zeppilli, Arnault, Gesset, Bergonzo, & Polini, 2010). As already mentioned above, mechanochemical treatment can be used for the induction of surface modification on ND. Milling will eventually leads to the formation of dangling bonds and if no suitable reaction partner (such as water) is present in the vicinity, dangling bonds may recombine to form π-bonds on the diamond surface (Liang et al., 2009).

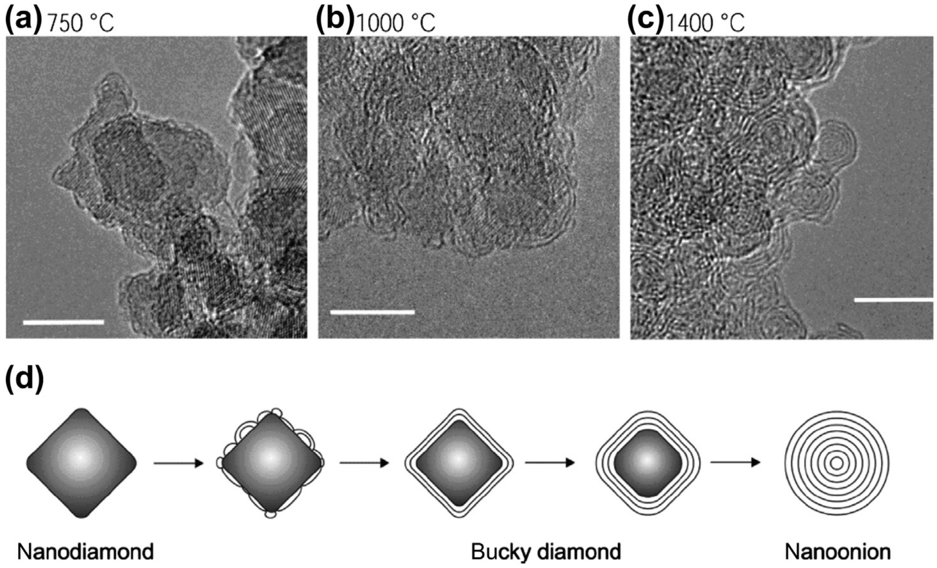

Figure 5 Surface annealing of nanodiamond leads to the formation of sp^2 carbon. Depending on the reaction conditions, the nondiamond layer is very thin (less than a closed shell) or can dominate the properties of the particles as in bucky diamond and carbon nanoonions. One method to control the amount of sp^2 carbon is the vacuum annealing at suitable temperatures. At moderate temperatures, only small caps of graphitic carbon form (a), with increasing temperature the amount and order of the graphitic material increases (b, c) as can be seen in high-resolution transmission electron microscopic images (all scale bars 5 nm). The schematic stages of ND annealing are shown in (d). Copyright Wiley-VCH, with kind permission from Krueger and Lang (2012).

When investigating the surface composition of commercially available ND, it turns out that some of these materials already contain varying amounts of nondiamond carbon. This is resulting from graphitization processes during their production, e.g. in the detonation synthesis (Dubois et al., 2009; Fang, Mao, Levin, & Schmidt-Rohr, 2009; Panich et al., 2006). Unfortunately, the amount and structure of that sp^2 carbon is not always the same and the amount and structure cannot be fully controlled under the harsh production conditions and in the purification process. Therefore, a rather irreproducible composition of the pristine material is usually observed. It is hence recommended to remove such disordered nondiamond carbon first, even if an sp^2-terminated diamond surface is to be generated. The removal of sp^2 carbon from ND soots can be achieved with different reagents. As already mentioned in Chapter 3.03, the treatment with supercritical water can be used to selectively etch away nondiamond carbon (Anikeev & Zaikovskii, 2010). Oxidation using ozone (Cunningham, Panich, Shames, Petrov, & Shenderova, 2008; Shenderova et al., 2011), mixtures of oxidizing acids such as HF/HNO_3 or HNO_3/H_2O_2 (Pichot et al., 2008) (see also Chapter 3.03) or boric anhydride (Chiganov, 2004) can be applied as well. When gas-phase oxidation is chosen for the etching process, careful control of the temperature and oxygen content of the gas flow is crucial in order to not burn the diamond (Osswald et al., 2006). Actually, most published purification protocols for the production of ND with reproducible surface quality include an oxidation step in order to remove nondiamond carbon. Even for the surface termination with controlled amounts of sp^2 carbon, such purified and homogenized ND is the preferred starting material.

3.16.4 Surface Functionalization of ND

Having the choice now between different initial surface terminations of the ND particles, the next step is the grafting of more complex moieties onto the surface of ND. This can be done either by noncovalent adsorption or by the formation of covalent bonds between the diamond surface and the functional moiety.

3.16.4.1 Noncovalent Surface Functionalization of ND

The noncovalent adsorption of more complex moieties (biomolecules, polymers and others) is a very flexible and rather facile technique to modify different types of nanoparticles. This technique is also very valuable for the

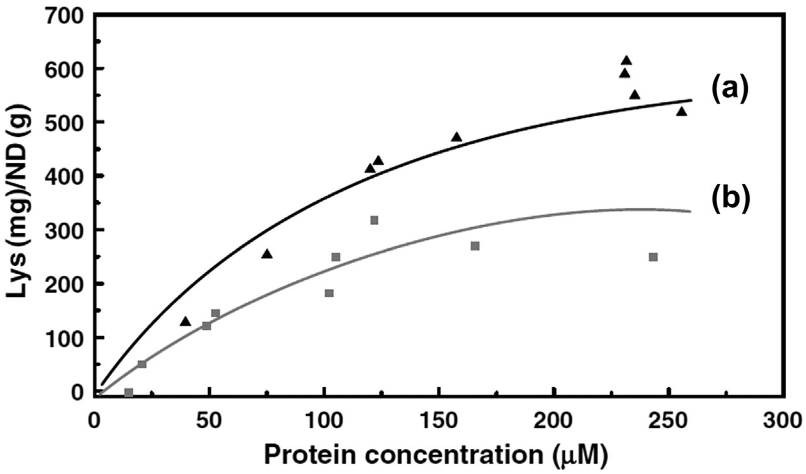

Figure 6 The adsorption isotherm of lysozyme on detonation nanodiamond and different pH values: (a) adsorption from PBS buffer solution at pH 6.5; (b) adsorption from bidistilled water at pH 4.5. The different adsorption behavior correlates with the concentration of carboxylate (COO^-) groups on the surface. With higher pH their number increases, thus facilitating the adsorption of highly polar (bio)molecules by electrostatic interaction. Copyright Elsevier, with kind permission from Chung et al. (2006).

functionalization of diamond nanoparticles. The actual adsorption properties are governed by the available surface area and its curvature but even more by the termination of the ND surface. A suitable termination would allow for the formation of a multitude of noncovalent interactions (H-bonds, π–π- or hydrophobic interaction) and strongest binding forces are observed when the nanoparticle surface and the adsorbed compound possess complementary properties. Most of the available ND samples exhibit a hydrophilic surface with quite large amounts of different oxygen-containing functional groups, e.g. after oxidative or acid treatment (see above). Therefore, the particles in these samples are able to undergo the interaction via a large number of hydrogen bonds with polar molecules. The strength of a single H-bond is obviously much lower than a covalent bond (Grimme, Antony, Schwabe, & Mueck-Lichtenfeld, 2007), however, in a typical case, several or even large numbers of these bonds are formed between the surface and the adsorbed molecule. The overall binding strength is the result of the individual noncovalent interactions and sum up to considerable overall bond strength. This is especially useful for the interaction with larger biomolecules, as the molecules can be used in their unaltered, natural state if only noncovalent binding is used for their immobilization. Ho and colleagues have immobilized bovine insulin on DND using the noncovalent interaction between the hydrophilic ND surface and the polar biomolecule (Shimkunas et al., 2009). Other biomolecules that have been immobilized on ND include cytochrome c (Huang & Chang, 2004), lysozyme (**Figure 6**) (Chao et al., 2007; Chung, Perevedentseva, Tu, Chang, & Cheng, 2006; Nguyen, Chang, & Wu, 2007; Perevedentseva, Cai, Chiu, & Cheng, 2011) and apoobelin (Bondar, Pozdnyakova, & Puzyr, 2004). In all cases, the functionality of the immobilized molecule has been proven, but some reduction in activity was observed in many cases most likely due to slight alterations of the natural 3D structure.

Not only biomolecules but also bioactive compounds such as drug molecules can be bound by noncovalent adsorption on the surface of ND particles. Applications of these conjugates include drug delivery or the solubilization of lipophilic compounds (see also Chapter 3.06 on applications). A frequently studied drug is doxorubicin which has been immobilized on ND by Ho and coworkers. They applied the ND–drug conjugate for the controlled release of the antitumor substance (Huang, Pierstorff, Osawa, & Ho, 2007; Lam et al., 2008). Other antitumor compounds that have been noncovalently bound to ND include 10-hydroxycamptothecin (HCPT) (Li et al., 2010) and paclitaxel (Liu et al., 2010).

The formation of core–shell particles with a diamond core and an organic shell (typically polymer substances are used) is another field of application for the noncovalent immobilization of large molecules. These composite particles either can be directly applied or can be used to establish special functional groups on the outer surface of the coated ND particle (this is often necessary when the direct bonding of these groups on the ND surface is not possible or difficult). Chang and coworkers coated ND particles with L-polylysine to produce an ND conjugate with a high number of primary amino groups. In a subsequent step, these groups can be used for further covalent functionalization, e.g. by amide formation. Similarly, ND–polyarginine conjugates have been

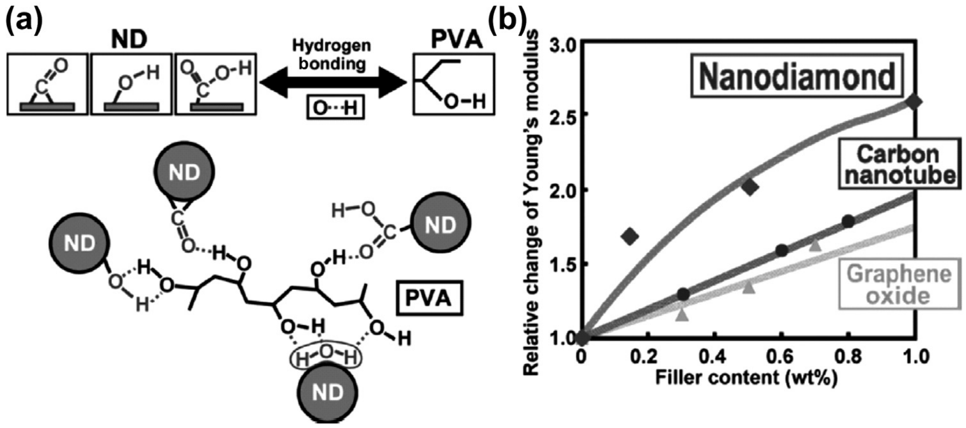

Figure 7 The formation of hydrogen bonds enables, e.g. the formation of composites between nanodiamond and polyvinyl alcohol (PVA). Typically, the incorporation of ND into polymer matrices results in a significant improvement of the mechanical properties as shown by the Young's modulus (b). Copyright ACS, with kind permission from Morimune et al. (2011).

produced (Chang, Wu, et al., 2008; Vaijayanthimala, Tzeng, Chang, & Li, 2009). Artificial proteins are not the only polymers that can be used to coat ND particles. Other composite particles have been fabricated from ND and PANI (polyaniline) (Gomez, Ram, Alvi, Stefanakos, & Kumar, 2010; Kovalenko, Bucknall, & Yushin, 2010), ND and polyethyleneimine (Zhang et al., 2009) or ND and poly(lactic acid) (PLLA) (Zhang et al., 2011). Such composites, e.g. the biodegradable ND–PLLA conjugate, can be used for the production of improved biodegradable (bone) implants. In general, the noncovalent formation of composites of ND with polymers is increasingly studied. The properties of such composites are very beneficial (Comet et al., 2010; Hsin et al., 2011; Mochalin et al., 2011; Morimune, Kotera, Nishino, Goto, & Hata, 2011; Neitzel, Mochalin, Knoke, Palmese, & Gogotsi, 2011). For instance, the noncovalent incorporation of ND into polymer matrices usually results in improved mechanical strength of the composite. One example for this is shown in **Figure 7** with the composite of polyvinyl alcohol and ND (Morimune et al., 2011). Such materials are interesting not only for implants but also as sturdy and light-weight materials for construction and similar applications. Another interesting property of diamond is its high thermal conductivity without the usually also observed electrical conductivity (this is the case for all metallic heat transmitters). ND–polymer composites with a certain ND concentration exhibit better thermal conductivity than the neat polymer.

In conclusion, the noncovalent surface modification of ND is a versatile method for the formation of even complex conjugates. Some of the features of this immobilization method such as low bond strength of individual interactions and rather undefined stoichiometry have to be taken into consideration. For some applications (e.g. drug delivery), they come in handy, though.

3.16.4.2 Covalent Surface Functionalization of ND

3.16.4.2.1 Modification of the Initial Surface Termination by Halogenation, Amination and Thiolation

The previously discussed surface termination with hydrogen or oxygenated groups can be replaced by other atoms (**Figure 8**). Such substitutions include the halogenation and amination of the diamond surface that will be described prior to the grafting of larger molecules.

Halogenations, especially fluorination, are very useful for the further modification of ND particles as they enable reactions with a variety of reagents. Fluorine can be grafted in a gas-phase reaction of ND powder with F_2/H_2 mixtures at elevated temperatures. As reported by Khabashesku and coworkers, high surface loadings with fluorine atoms are possible. Afterward they successfully reacted the ND–$(F)_x$ with different kinds of nucleophiles (see below) (Liu, Gu, Margrave, & Khabashesku, 2004). Instead of using elemental fluorine, it is also possible to generate reactive fluorine species in an atmospheric pressure plasma with CF_4 as Ray et al. reported for the grafting of fluorine atoms at the surface of different ND samples (Ray et al., 2007). The termination with higher halogens has been investigated with much effort. They represent better leaving groups for subsequent substitution reactions and reagents are much safer to handle than for fluorination. Several approaches for the chlorination of ND have been taken. The most successful is so far the photochemical chlorination of

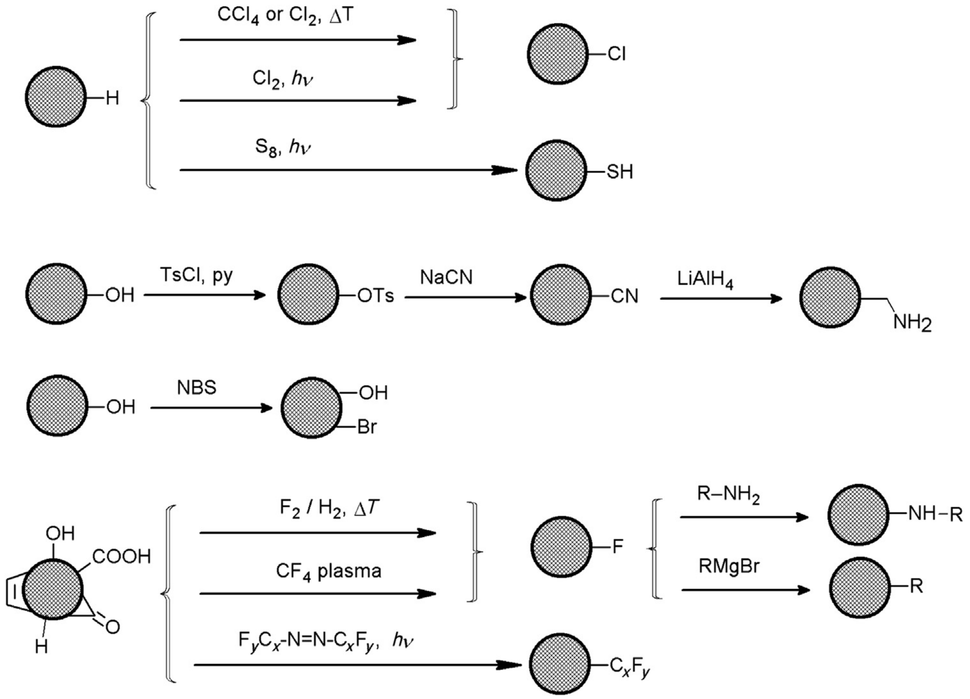

Figure 8 Nanodiamond with different initial surface terminations can serve as a starting material for subsequent transformations. Typically, photochemical reactions and reactions using gaseous reactants at elevated temperature proved to be very efficient.

hydrogenated ND (Sotowa, Amamoto, Sobana, Kusakabe, & Imato, 2004). This reaction relies on the attack of the photo-induced chlorine radicals on the C–H bonds of the ND surface. For hydrocarbons, the reaction is well established and works on the "giant diamondoid" (the ND), too. Other reactions include the thermal chlorination with Cl_2 or CCl_4, which are most likely radical processes as well (Spitsyn et al., 2010). The bromination with elemental bromine has not been successful so far, probably due to insufficient reactivity of the bromine radicals. Only the partial bromination of ND was achieved by Garcia and coworkers employing a wet-chemical reaction of hydroxylated BD with *N*-bromosuccinimide in CCl_4 (Martín et al., 2009). No reports on the direct grafting of iodine have been given so far. This is probably due to the low reactivity of iodine radicals and the weak C–I bonds (see below).

For the higher halogens (Cl, Br), it turned out that the bond strength of the C–X bond is not very high. Chlorinated (or partially brominated) ND samples are sensitive toward air and humidity. Upon exposure to ambient air, they form at least partially hydroxylated surfaces (as in halohydrines). As chlorine and bromine are known to be good leaving groups and most of them are bound to tertiary carbon atoms (and hence the generated tertiary cations are well stabilized), it is rather easy to cleave the C–X bond. Any kind of nucleophile (including water) can enter a substitution reaction with such a reactive diamond species. For fluorine, the situation is somewhat different: it is not considered a good leaving group due to the considerable strength of the C–F bond. Only strong nucleophiles such as amines or metal organic compounds can react with the fluorinated diamond surface. Therefore, ND–$(F)_x$ can be stored under ambient conditions without the formation of surface OH groups.

Another very useful termination of ND is nitrogen-based. Amino groups are versatile starting points for subsequent coupling reactions and much sought after. Therefore, the direct amination of the ND surface is of high interest as it would enable the straightforward binding of a large variety of functional molecules such as bioactive compounds or polymer building blocks by amide formation, reductive amination, nucleophilic attack or direct condensation reactions. However, the direct amination of the ND surface turned out to be rather difficult and was so far not fully successful. There has been a report on the substitution of chlorine atoms on the surface of submicron diamond (~0.5 μm) using gaseous ammonia at elevated temperature (Sotowa et al., 2004). As for diamond films, several methods for the direct amination are known, such as the reaction with photochemically activated ammonia (Zhang et al., 2006) or in an ammonia plasma (Koch et al., 2011), it should be eventually possible to aminate nanoscale diamond particles directly with ammonia. For the time being, other methods for the establishment of NH_2 groups on the ND particles' surface are applied.

Typically, these techniques establish the amino function somewhat farther away from the ND surface by binding, e.g. aminated silanes (Krueger et al., 2007; Krüger et al., 2006), aminated aromatic moieties (Yeap et al., 2009) (see also Section 3.16.4.2.2.4 for covalent attachment of aromatic rings), or the formation of aminomethyl groups. The latter moiety comes closest to the direct surface amination as only a methylene spacer is bound between the lattice atoms and the nitrogen. The multistep reaction has been reported by Shenderova and colleagues. Starting from hydroxylated ND, they transform the OH group into a better leaving group by tosylation followed by the substitution of the OTs (tosylate) group by nitrile moieties. The cyanide groups which are directly bound to the ND surface are then reduced to aminomethyl groups using lithium aluminum hydride (Ciftan Hens et al., 2008). In the further grafting step for the immobilization of biotin, it was shown that sufficient amounts of NH_2 groups can be immobilized on ND using this reaction sequence. The mechanism of this reaction remains, however, somewhat unclear. The substitution of the tosylate should take place in an S_N2 reaction, which cannot occur here due to the structural situation (the diamond particle is blocking the backside where the nucleophilic attack of the cyanide would occur). On the other hand, reaction mechanisms including the formation of an intermediate carbenium ion or the stepwise elimination–addition process could be discussed.

Especially for the interaction of ND with gold and other noble metals (e.g. for the construction of plasmonic structures, where luminescent lattice defects of the ND interact with nanostructures such as antennas or cavities (Schietinger, Barth, Aichele, & Benson, 2009)), the termination of the diamond surface with thiol groups (and other groups with the sulfur in a negative oxidation state) is of great interest. An efficient method to graft sulfur on the ND surface was reported by Nakamura and coworkers (Nakamura, Ohana, Hagiwara, & Tsubota, 2009). The reactive species was generated photochemically from elemental sulfur S_8. Although the exact nature of the groups (whether SH or with additional S–S bonds) is not known, their interaction with gold surfaces was demonstrated and indicates the formation of thiols or at least closely related moieties. As for the amination, indirect methods for the grafting of SH groups on ND have been studied. After such a surface transformation, the thiol groups are bound to the tip of a short linker. These can be aromatic structures, which can be used for the establishment of sulfonic acids or (after suitable reduction) of thiols (Liang et al., 2011).

3.16.4.2.2 Additional Surface Modification of ND by Grafting Moieties to the Initial Surface Termination

In the preceding chapters, several methods for the modification of the initial surface termination have been presented. These groups enable now the flexible modification of the ND particles using additional grafting steps. Covalent bonding is for many applications the method of choice due to the comparatively high bond strength and the possibility to control, e.g. stoichiometry or ratios of immobilized units. Depending on the molecule to be immobilized, a suitably terminated ND material can be chosen which enables the specific and preferentially site-selective binding of enzymes or other bioactive compounds. Such selective grafting is necessary when noncovalent immobilization by adsorption hampers the proper function of these moieties. The latter can arise from a high number of binding sites on the diamond surface and their strong interaction with such molecules over large fractions of their surface. Potentially, this modifies the three-dimensional structure or induces an unfavorable orientation of the compound on the surface of the ND. Covalent binding in the nonfunctional periphery of the molecule overcomes this problem. If concurrent noncovalent interactions prevail, a stiff linker molecule can ensure sufficient distance from the ND surface and hence the absence of nonspecific interactions between the ND and the immobilized molecule. And indeed, in many cases, spacer moieties are used in the covalent grafting of larger functional molecules onto the ND surface.

As ND can be considered as a giant hydrocarbon of the “polymantane” family (molecules consisting of multiple adamantane units), its reactivity is expected to be comparable to its lower homologs like adamantane, diamantane, etc. (Schwertfeger, Fokin, & Schreiner, 2008). Indeed, conventional organic reactions take place on the ND surface. However, structural differences (e.g. surface irregularities), electronic differences, steric hindrance and the already existing surface groups on the ND particles modify their actual behavior to some extent. Still, ND can be seen as an at least moderately reactive “molecule,” whatever its surface termination. In the following chapters, an overview of the transformations of different surface groups of ND will be given. Some reactions can take place on ND with different surface termination (e.g. the arylation using aromatic diazonium salts) and will therefore appear in several contexts.

3.16.4.2.2.1 Grafting onto Hydrogenated ND

The simplest surface termination, the one with hydrogen atoms, is not necessarily the one to be modified in the easiest way. Nevertheless, several methods to graft larger moieties onto hydrogenated ND have been reported. They are related to wet-chemical transformations on diamond films employing photochemical and electrochemical reactions.

A recent review by Zhong and Loh discusses the possible grafting reactions on diamond films in great detail (Zhong & Loh, 2010). Many of these reactions are also possible on diamond nanoparticles. Examples include the already mentioned photochemical thiolation of hydrogenated submicron diamond powder using UV light as reported by Nakamura et al. (2009). The irradiation of S_8 initially generates polysulfide radicals which abstract hydrogen atoms from the ND surface. The resulting unsaturated bonding sites are highly reactive and recombine with other radicals (polysulfide of SH directly) to form SH groups on the ND particles.

In general, the substitution of hydrogen atoms on the ND surface proceeds as a radical process. One other option to graft molecules onto diamond surfaces in a radical reaction was reported by Komatsu and coworkers. They immobilized ω-amino carboxylic acids using benzoyl peroxide as thermal radical starter. The resulting surface grafting is proposed to be established by ester functions leaving the primary amino groups available for further reactions such as the bonding of fluorescent dyes (Takimoto et al., 2010).

The reactions mentioned so far result in the formation of carbon–heteroatoms bonds. However, the immobilization of organic moieties on ND via heteroatoms (i.e. O, N and S) can be an issue in further applications in terms of the required stability against, e.g. enzymes. Therefore, the grafting via less unstable covalent bonds is helpful in respective cases. A good candidate is the carbon–carbon single bond as it possesses the required inertness against enzymes. In recent years, several methods for the formation of C–C bonds directly linked to the diamond lattice have been conceived (**Figure 9**).

One of them is the photochemical grafting of ω-alkenes onto hydrogen-terminated ND. This reaction type has been known for diamond films for quite long time. As expected, the radical reaction leads to the substitution of the hydrogen atom by the alkyl residue (Yang et al., 2002). Nakamura et al. successfully applied this technique for submicron diamond powder. They grafted an optically active amide and used it for the recognition of the components of racemic compounds (Nakamura, Ohana, Hagiwara, & Tsubota, 2010). In the meantime, grafting of alkenes onto hydrogenated ND promoted by UV irradiation has been achieved by Girard et al. (2011).

The aromatic diazonium salts give another class of reagents for the formation of C–C bonds on hydrogenated ND. When the diamond film is conductive, e.g. if boron-doped, the electrochemical grafting of aromatic diazonium salts is an efficient way to arylate the diamond surface without the application of additional reagents. Unfortunately, this strategy has not yet been used for ND particles, mainly due to the unavailability of electrically conducting ND particles. Instead, wet-chemical reactions have to be employed.

The diazonium compound can be generated in situ from the respective amines if the isolation of the actual diazonium salt, e.g. tetrafluoroborate, turns out to be difficult (Girard et al., 2010; Girard et al., 2011). In both cases, the hydrogenated diamond surface is most likely attacked in a radical reaction. However, the detailed mechanism of this reaction has not been fully elucidated yet.

3.16.4.2.2.2 Grafting onto Hydroxylated ND

Similar to the hydrogenated diamond surface, the hydroxylated diamond termination represents a reduced state compared to the carboxylated one. It has an intermediate position concerning oxidation level and reactivity. Organic alcohols are useful substrates for a variety of transformations and so are hydroxylated ND particles. They are probably among the most studied ND species with a focus on the formation of homogeneously and

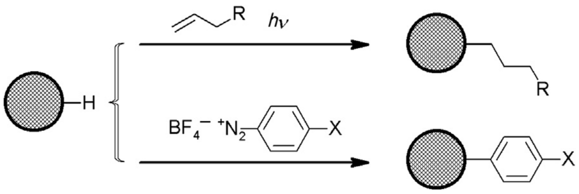

Figure 9 Hydrogenated nanodiamond is an ideal starting material for the grafting of more complex moieties by direct bonding to the diamond lattice. The resulting C–C single bonds are chemically rather inert.

densely covered hydroxylated surfaces. Details on the formation of OH groups on ND can be found in Chapter 3.02. The resulting hydroxylated ND is a very useful derivative of nanoscale ND and can be modified with a great variety of chemical reactions (**Figure 10**).

This includes the formation ethers, a grafting method that Cheng and colleagues successfully applied for the reaction with alkyl chlorides in the presence of NaH (similar to a Williamson ether synthesis) (Liu et al., 2010; Zheng et al., 2009). It turned out that NaH deprotonates the hydroxyl functions on the ND surface. The alcoholates then act as nucleophiles and attack the alkyl halide to form an ether.

The hydroxyl groups on ND behave more or less like a normal alcohol and hence can be used to open the epoxides such as in glycidol. In consequence, they initiate the polymerization of the glycidol resulting in very hydrophilic core–shell particles with a diamond core. The product shows a very high solubility in various solvents (e.g. up to 20 mg ml^{-1} in water). It can be even eluted from a size-exclusion chromatography column and characterization by solution nuclear magnetic resonance (NMR) spectroscopy is possible (Zhao et al., 2011). Komatsu et al. noted that the employed ND carries not only OH but also COOH groups. Therefore, the polymer might be also connected to the ND surface by ester bonds. However, this is not detrimental for properties such as hydrophilicity and solubility.

The formation of esters with carboxylic acids or their halides is another possible reaction of alcohols. When long-chain acid chlorides are employed for the ND–OH esterification, the obtained products exhibit an increased solubility in rather nonpolar, aprotic solvents such as dichloromethane and tetrahydrofuran (Krueger & Boedeker, 2008). The particles can be dispersed and stored in those solvents without decomposition, and precipitation occurs only slowly. An interesting finding is the fact that the esters of ND–OH show very limited stability against hydrolysis or alcoholysis. When dispersed in water or short-chained alcohols like methanol and ethanol, the acyl groups are removed from the ND surface yielding the hydroxylated ND again. In higher alcohols, such as isopropanol or *tert*-butanol, this effect is not observed to the same extent. The reason for this behavior might be the nature of the existing OH groups. Many of them are tertiary or neopentyl alcohols and their esters are thus prone to transesterification reactions.

The OH functions of ND–OH also react with oxophilic compounds like trialkoxysilanes. The alkyl residue can be terminated with a large variety of functional groups, e.g. amines, acrylates, epoxides, thiols, etc. For instance, in the product of the reaction of ND–OH with (3-aminopropyl) trimethoxysilane, the terminal amino groups of the surface layer can be subsequently bound to the C-terminus of peptides or other biomolecules (Krüger et al., 2006).

Especially at pH values below 7, the bridge between the diamond and the siloxane is quite sensitive to hydrolysis. This property limits the application of these ND derivatives in bioapplications. Instead, peptides can be grafted onto benzoquinone-modified ND (Purtov, Petunin, Burov, Puzyr, & Bondar, 2010).

Additionally, there is another problem to be addressed when working with silanized ND (but not restricted to it): during the surface functionalization, multiple graftings and intermolecular condensations reactions take place. This induces an increase in agglomerate size and an organic shell consisting of more than one layer of

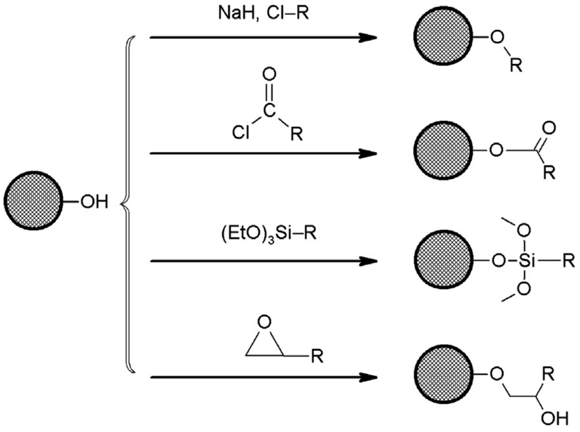

Figure 10 Hydroxylated nanodiamond is the starting point for ether and acyl bond formation. It can also participate in condensation reactions with trialkoxysilanes. The resulting ND derivatives can be easily controlled in their hydrophilicity by the choice of a suitable residue R.

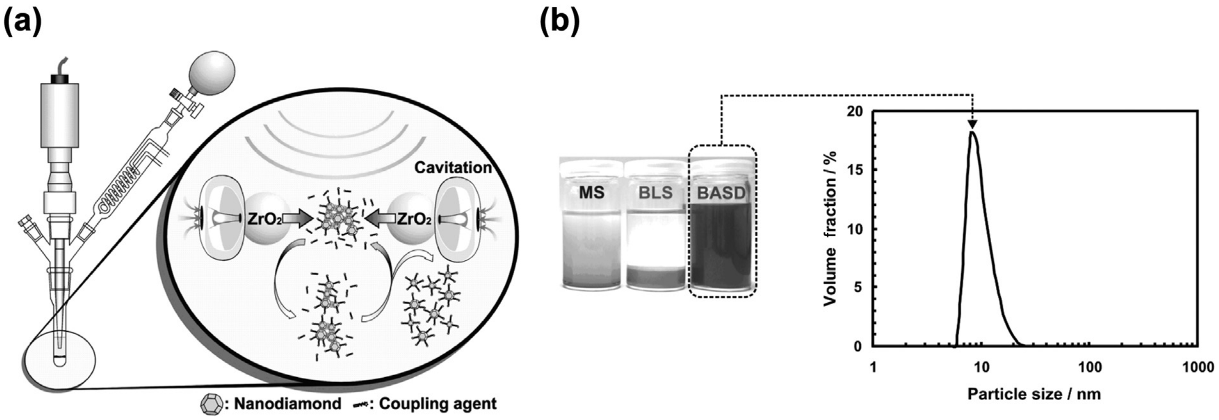

Figure 11 When reagents are used that lead to the formation of covalently bound agglomerates, e.g. by the formation of oxygen bridges in condensation reactions the application of a mechanochemical deagglomeration technique such as the beads-assisted sonic disintegration (BASD) proved to be beneficial. (a) Fresh surface for the functionalization is formed continuously and in a kind of circle process, the particles become well dispersed and fully functionalized. (b) This effect is not observed with simple magnetic stirring (MS) or beadless sonication (BLS). Copyright ACS, with kind permission from Liang et al. (2009).

organic molecules. This is due to the fact that usually not all of the alkoxy groups of a trialkoxysilane react with the surface of the same ND particle (e.g. due to geometric hindrance and insufficient OH group density on the ND particle). To overcome the covalent agglomeration of the functionalized ND particles, several approaches can be taken. The simplest variation consists in the replacement of the trialkoxysilane with mono- or dialkoxysilanes which are less prone to such cross-linking side reactions. An alternative technique is the immediate destruction of existing and/or emerging agglomerates using a mechanical procedure like the BASD setup (see above). Such simultaneous milling/functionalization process avoids the formation of large, irregular clusters of silanized ND particles. As the BASD technique produces continuously a large amount of fresh diamond surface, the procedure can be optimized to yield functionalized primary ND particles. With a suitable functionalization (i.e. sufficient hydrophobicity), the ND derivatives are soluble in nonpolar solvents (where the initial ND–OH cannot be stabilized as a colloidal solution) (Liang et al., 2009). In the case of silanization, the ultrasound treatment also supports the closure of the siloxane shell by condensation reactions of neighboring silanes. Such "curing" of the particles' shell further improves the colloidal stability and prevents the formation of multilayer shells (**Figure 11**).

As already mentioned in Chapter 3.02, ND–OH is also a suitable starting material for the termination with NH_2, Cl and Br moieties. Such modification opens the road to more complex surface transformations (Martín et al., 2009; Martín et al., 2010).

3.16.4.2.2.3 Grafting onto Carboxylated ND

It has been shown for carbon nanotubes that carboxylic groups at the end or the sidewalls of the tubes are easily grafted to proteins by amide formation with amino groups, e.g. in the side chains of the peptide. The same reaction can be carried out on COOH groups located at the surface of ND particles leading to an amide link (**Figure 12**). Of course, other substances with reactive amino groups can be coupled to ND–COOH

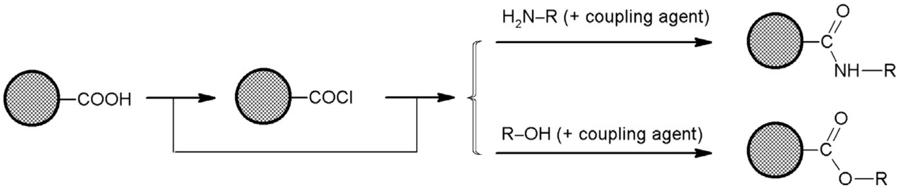

Figure 12 The immobilization of larger moieties by amide or ester linkages onto carboxylated ND proceeds either via the more reactive acid chloride or via the in situ generation of activated species using coupling agents such as *N*-ethoxycarbonyl-2-ethoxy-1,2-dihydroquinoline or EDC (1-ethyl-3-(3-dimethylaminopropyl)carbodiimide).

particles using efficient peptide coupling techniques. Typically, coupling agents such as *N*-ethoxycarbonyl-2-ethoxy-1,2-dihydroquinoline or the well-known carbodiimides have to be used for the reaction of the COOH groups with amines (otherwise a simple acid–base reaction will yield the carboxylate and an ammonium cation) (Goyal, 2010). If coupling agents are not to be used, the respective acid chloride with its high carbonyl reactivity can be used for the reagent-free amide formation. Gogotsi et al. transformed oxidized ND first into the acid chloride using thionyl chloride. In the second step, they immobilized dodecylamine via an amide bond (Mochalin & Gogotsi, 2009; Zhang et al., 2011). The hydrophobicity of the long alkyl residues improves the dispersibility of the ND derivative in nonpolar solvents. Furthermore, the authors observed a blue fluorescence of this ND derivative when exciting with light at 410 nm. So far, the origin of this luminescence remains unknown. Lee and coworkers produced ND where an imidazolinium bromide is immobilized via an amide linkage. As an ionic species, the ND conjugate was found to be soluble in ionic liquids and may be the starting point for new diamond-based composite materials (Park, Jee, Lee, & Lee, 2009). Amide bonds can be formed also on aminated ND. See Section 3.16.4.2.2.6 for the details of further surface modifications.

The carboxylic group on the ND surface reacts not only with amines but also with alcohols leading to ester linkages. Either the COOH group itself (using acid catalysis) or the corresponding acid chloride can be used to immobilize alcohols by esterification. Compared to amides, the resulting ND–esters possess a limited stability against hydrolysis under both acidic and basic conditions. Esterification of ND–COOH using polymers carrying epoxy units in the side chain (which are opened and form an ester bond between the ND–COOH and the polymer) has been shown by Cheng et al. (2008).

3.16.4.2.2.4 Grafting on sp^2-Terminated ND

Not only hydrogen-terminated ND can be used to immobilize organic moieties by formation of C–C single bonds. The thermally annealed ND surface is accessible in a similar manner and enables even more diverse reaction schemes as the sp^2 carbon can participate in reactions similar to those at fullerenes and carbon nanotubes. The π-bonds on ND are strained to some extent as the bonds to the diamond surface are bent away from the preferred planar arrangement. Furthermore, they exhibit behavior related to electron-poor π-systems, which is in correspondence with the observations made for fullerenes (**Figure 13**) (Hirsch & Brettreich, 2005).

Similar to hydrogen-terminated ND, the sp^2-terminated analog can be reacted with aromatic diazonium salts. As already reported for carbon nanotubes, sp^2 carbon reacts readily with diazonium salts (Bahr et al., 2001). As the surface on annealed ND resembles fragments of graphene-like structures, a similar reactivity toward aromatic diazonium salts is expected. Indeed it was reported that especially aromatic diazonium salts carrying electron withdrawing groups in *para*-position to the diazonium moiety (which increase the reactivity of the supposed reactive species) undergo efficient reaction with the π-bonds on ND (Liang et al., 2011). The aryl groups are bound by a single C–C bond to the diamond surface resulting in rehybridization of the carbon

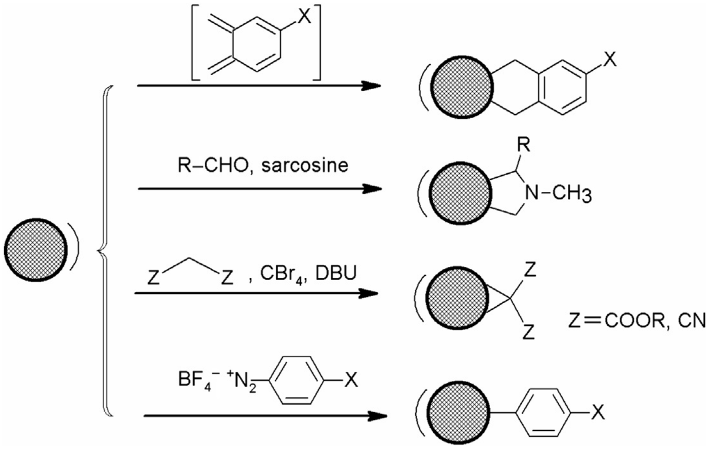

Figure 13 Nanodiamond with a certain amount of sp^2 carbon at its surface can be regarded as an analog to fullerenes and carbon nanotubes concerning its reactivity. Especially those reactions leading to C–C bonds are valuable as the resulting ND derivatives possess high stability.

surface atoms to sp^3, the bonding scheme is thus very similar to arylated ND produced from ND–H. Only the further surface termination of incompletely arylated particles differs in both cases: either residual π-bonds or sp^3-hybridized, hydrogen-terminated structures will be present and are responsible for somewhat different properties of the arylated materials (like overall hydrophilicity, zeta potential, etc.). Depending on the actual requirements for the sample's properties, the starting material for arylated ND derivatives has to be chosen accordingly.

As the thermally annealed diamond surface contains a significant amount of sp^2 carbon arranged in more or less conjugated π-bonds, it cannot only be modified using reactions forming single C–C bonds. A versatile strategy is the consideration of all types of reactions that are possible on large, electron-poor π-systems such as fullerenes and carbon nanotubes. Among these transformations, the class of cycloadditions deserves special attention as these reactions usually proceed without any further reagents and typically with high yields. The necessary π-systems (isolated double bonds or even extended (conjugated) π-systems) on the diamond surface resemble fullerene-like structures. Such motifs have been proposed for sp^2-terminated ND by computational methods (Raty, Galli, Bostedt, van Buuren, & Terminello, 2003).

Among the most popular cycloaddition reactions is the Diels–Alder reaction. We carried this reaction out on thermally annealed ND. In the case of C_{60}, the reaction is well understood. The curvature and the high electron affinity of the fullerene induce an electron deficiency in the carbon cage. Hence the fullerenes do not undergo Diels–Alder reaction as the diene component. A similar observation is made for partially graphitized diamond. The surface participates as the dienophile in [4+2] cycloadditions, e.g. with *ortho*-quinodimethanes (generated in situ). The advantage of the *ortho*-quinodimethanes lies in their special structure. Upon ring closure in the cycloaddition, an aromatic ring is formed, preventing the otherwise occurring *retro*-Diels–Alder reaction (Jarre, Liang, Betz, Lang, & Krueger, 2011). As with conventional dienes, only low yields of the addition products have been obtained, this strategy turned out to be very useful also for π-bonds on ND.

Not only [4+2] cycloadditions as the Diels–Alder reaction require the presence of suitable π-bonds. In a very similar fashion, other kinds of cycloadditions may be used to functionalize the surface of thermally annealed ND. So far, the Prato reaction of azomethine ylides with double bonds on the diamond surface has been reported. Such reactions belong to the type of 1,3-dipolar cycloaddition. The reactive species, i.e. the azomethine ylides are generated in situ from aldehydes and amino acids as for the reactions of carbon nanotubes (Tasis, Tagmatarchis, Bianco, & Prato, 2006). Depending on the chosen aldehydes and amino acids, the resulting diamond–pyrrolidine conjugates can be terminated with a large variety of functional groups (Lang & Krueger, 2011).

Besides the cycloaddition reactions other transformations leading to C–C-bonded rings on the diamond surface are of great interest. One of them is the so-called Bingel–Hirsch reaction. This transformation has been developed for the very efficient grafting of single or multiple addends onto C_{60} and higher fullerenes (Bingel, 1993; Bingel & Schiffer, 1995). Starting from malonic acid derivates (malonates or nitriles or related keto compounds), the respective bromomalonate is formed in the first step. By adding a base, the acidic proton in the bis-α-position is removed resulting in a nucleophile that can react especially with electron-poor double bonds resulting in the transfer of the nucleophilic properties to one of the former sp^2 carbons. The latter attacks then the same α-carbon atom resulting in ring closure upon the exit of the bromide leaving group. The reaction sequence leads to an effective cyclopropanation of the π-bond. This reaction can be used to introduce a variety of electron-withdrawing functional groups onto the surface of ND (Betz & Krueger, 2012). As these can be used for a variety of further grafting steps and due to the easy and fast procedure, the Bingel–Hirsch reaction is a valuable method for the surface functionalization of ND.

3.16.4.2.2.5 Grafting onto Halogenated ND

As for organic compounds, halogenated diamond can be a versatile starting material for the covalent grafting of complex functional units. Concerning the leaving group character, brominated ND should be the best precursor followed by chlorinated and then fluorinated material (ND with iodine at its surface has so far not been reported, the bond strength seems to be too low). However, it turned out that fluorinated diamond nanoparticles can be submitted to a variety of nucleophilic substitutions. Typically, organometallic compounds (e.g. Grignard compounds or lithium organyls) or amines are used as reagents (**Figure 8**). Hence C–C coupling or bonding via heteroatom bridges is achieved (Liu et al., 2004).

However, the fluorination of ND requires harsh reaction conditions. Therefore, other reactions resulting in the same or similar surface termination are in many cases preferred.

Chlorinated ND can be reacted with gaseous ammonia. This reaction leads to the replacement of chlorine atoms by amino groups (Sotowa et al., 2004). For (partially) brominated ND, no extensive study on further reactions has been reported so far. This is most probably due to the increased reactivity of the bromine derivate. It seems that even in ambient air reaction with air humidity occurs rather quickly.

3.16.4.2.2.6 Further modification of Prefunctionalized ND

In many cases, the surface functionalization of a nanoparticle does not stop at the homogeneous termination with a certain functional group. More complex architectures with multiple functionalities for the selective binding of different moieties or the grafting of large biomolecules or drugs are envisaged. To successfully apply such transformations, their effect on the particle size, colloidal stability, and surface charge of the ND particles has to be studied very carefully. Depending on the chosen reaction scheme, surprisingly different behavior of the resulting particle may result. Generally spoken, all reactions known to an organic chemist can be carried out on suitably terminated ND which behaves more or less like a giant (and obviously carbon-rich) hydrocarbon with distinct peripheral functional groups. However, some specific issues occur upon reacting ND with complex organic moieties. These are typically related to problems with purification from insoluble or adsorbed side products, steric hindrance for the actual reactive attack or the inhomogeneity or incompleteness of the coupling reaction. The following chapter will give some examples for how functionalized ND can be used to bind complex molecules.

In a further step to C–C-bonded derivatives of ND, the continuation of the coupling reactions can be envisaged. Loh and coworkers coupled arylboronic acids with arylbromides by a Suzuki reaction. Beforehand, the bromoaromatic compound had been bound onto ND by diazonium chemistry (Yeap et al., 2009). Boronic acids can also react with the multiple hydroxyl functions of carbohydrates or glycoproteins. In this way, it is possible to immobilize these biomolecules by the formation of multiple covalent bonds. However, especially glycoproteins are prone to nonspecific interaction with the hydrophilic surface of ND particles. Typically, spacer moieties help to prevent these undesired interactions. In the present case, alkyl chains were employed to elongate the boronic acid (i.e. the capturing site) from the diamond surface and hence hinder the back binding by noncovalent interactions (Yeap, Tan, & Loh, 2008).

Besides the formation of stable carbon–carbon bonds, other types of ligation lead also to very stable conjugates. Many of the respective coupling reactions belong to the class of the so-called “click reactions” (Kolb, Finn, & Sharpless, 2001). By definition, a reaction qualifies as “click” when it can be carried out under mild (aqueous) conditions, leads to quantitative conversion in short time and does not yield side products. The archetypical click reaction is the Cu(I)-catalyzed coupling of azides with alkynes. For the application on ND, either the alkyne or the azide can be immobilized on the nanoparticle. They react with the complementary agent (azide or alkyne) to form a stable triazol ring carrying on one side the ND particle, while on the other the immobilized organic moiety (Barras, Szunerits, Marcon, Monfilliette-Dupont, & Boukherroub, 2010; Meinhardt, Lang, Dill, & Krueger, 2011). The reaction is efficient in aqueous media and tolerates the majority of possible other functional groups and can therefore be applied to the coupling of larger biomolecules even under quasi-physiological conditions. As a standard method for the establishment of alkyne or azide groups on ND, the arylation with respective diazonium salts can be used. Mixing these reagents with, for example, a carboxyl terminated aromatic diazonium salt (or its amino precursor) enables the statistical orthogonal functionalization of ND. The resulting ND derivative can be independently coupled to two different functional moieties such as fluorescent dyes, antibodies or drugs. For future (bio)applications, this strategy is of high interest as it permits the simultaneous delivery and tracking of, for example, drugs (Meinhardt et al., 2011).

A major strategy to bind biomolecules onto ND is the generation of amides. These are formed if the diamond surface exhibits amino groups which react with carboxylic acids usually with the help of a coupling agent. One example for this approach is the modification of aminomethylated ND by Boukherroub and coworkers. They applied 4-azidobenzoic acid and DCC: dicyclohexylcarbodiimide to graft azide-containing groups onto the prefunctionalized ND (Barras et al., 2010). Amides can also be formed by the reaction of carboxylated ND–COOH with amines as shown by Gogotsi and coworkers. They reacted the COOH surface groups with octadecylamine and used the resulting material as a component for biodegradable implant materials (Zhang et al., 2011). Amides belong to the more stable derivatives of carboxylic acids and are not too quickly hydrolyzed even under moderately basic conditions. Nevertheless, amides can be decomposed using suitable enzymes (i.e. proteases). This class of enzymes is ubiquitously present in all kinds of organisms and tissues. Therefore, the stability of amide-bound ND conjugates might be limited in vivo (Radzicka & Wolfenden, 1996).

The limitation, however, could be a virtue on the other hand if the release of biomolecules is desired in applications such as drug delivery.

Among the bioactive molecules that have been covalently immobilized on ND are the carbohydrates. This class of molecules exercises a variety of functions in the living organism such as energy source, structural polymer and recognition moiety, e.g. for cell–cell interaction. ND carrying such recognizable moieties can mimic cell surfaces and can be used for the study of complex phenomena related to infection processes as was shown by us. The respective sugar motifs have been immobilized using the efficient coupling between a surface thiol of the ND with a terminal alkene on the carbohydrate side (sometimes called the "thiol–ene reaction") (Hartmann et al., 2012).

Fabrication of complex conjugates of ND includes also the binding of ND onto a variety of polymers. Several approaches have been taken including the immobilization of initiators for atom transfer radical polymerization (ATRP) reactions as reported by Lukehart (Li, Davidson, & Lukehart, 2006) or Mangeney (Dahoumane et al., 2009) and coworkers. Others have conjugated the diamond to reactive groups in side chains of polymers such as epoxides (Cheng et al., 2008) or amines (Huang & Chang, 2004). The latter conjugation, however, relies on electrostatic interaction between ND–COO$^-$ and protonated amino groups. Earlier reports on noncovalently bound polymer composites are quite abundant and show a significant increase in mechanical strength and hardness of the composites (Shenderova, Zhirnov, & Brenner, 2002). More examples can be found in Section 3.16.4.1 on noncovalent surface modification.

Besides the production of composites, the immobilization of catalysts and enzymes has found some interest as the resulting conjugates might show higher stability or better recycling properties, etc. Recently, the covalent immobilization of a proline-based, enantioselective catalyst on ND was used for asymmetric aldol reactions. So far, the results are not fully convincing with 10% overall yield and 60–80% ee (Zheng et al., 2009). However, as a starting point, this study proved the applicability of such conjugates. In analogy to organocatalysts, enzymes play a similar role as highly efficient catalysts for chemical transformation and their immobilization on inert supports promises great advantages concerning their stability and reusability. Immobilized alcohol dehydrogenase shows high immobilization efficiencies and enantioselectivities (both >99%) as well as satisfactory reaction efficiencies (50% compared to the free enzyme) for the reduction of acetophenone to the enantiomerically pure phenylethanol (Goldberg et al., 2008). The reduction of enzyme activity has been observed for a variety of solid supports and is most likely due to shape modifications of the enzyme by agglomeration and noncovalent interaction with the nanoparticle surface.

Another way to combine prefunctionalized ND with more complex moieties is the combination of covalent functionalization and noncovalent adsorption.

In addition to enzymes, other bio(active) molecules can be coupled to prefunctionalized ND. Martín et al. reported the electrostatic immobilization of a plasmid containing the gene for green fluorescent protein (GFP) onto triethylammonium functionalized ND. They were able to transfect HeLa cells with this construct, and to observe the expressed GFP by fluorescence microscopy (Martín et al., 2010). Such approach can in principle be used for the delivery of various genes into living cells and organisms.

In many cases, ND particles have to be prepared with a complex shell architecture to exclude undesired bonding modes and to gain control over the actual link between the nanoparticle and the biomolecule. Those structures typically contain a spacer unit to prevent nonspecific adsorption of the usually hydrophilic (and protic) proteins, etc. by increasing the distance between the particle surface and the periphery of the biomolecule or drug. The antitumor drug paclitaxel immobilized using an alkyl spacer yields diamond conjugates which show anticancer activity in human lung carcinoma cells (Liu et al., 2010). Dahoumane et al. employed diamond nanoparticles carrying bromoethylphenyl groups and subjected them to ATRP (atom transfer radical polymerization). The latter reaction generates a spacer shell with a large number of binding sites for bovine serum albumin (Dahoumane et al., 2009).

Besides nonpolar alkyl chains, more hydrophilic spacers can be employed to improve the solubility of the conjugates while still preventing nonspecific interaction with the ND surface. Among possible compounds, polyethylene glycol (PEG) is one of the most prominent. Komatsu and coworkers conjugated a PEG derivative onto prefunctionalized ND carrying terminal amino groups by reacting them with COOH groups of the polymer. In a further step, the PEG shell could be labeled with fluorescent dyes opening the way to imaging applications as the resulting conjugates showed increased water solubility (Takimoto et al., 2010).

Many more reactions have been reported for the synthesis of complex ND conjugates. All of them rely on a highly reproducible surface chemistry and classical organic chemistry. A sound knowledge of the latter is therefore the best way to conceive more and better ways to expose the unique features of suitably functionalized ND.

3.16.5 Applications of ND

In this chapter, only a short look on the numerous and diverse applications of different ND materials is possible. Basically, several fields of applications have emerged in recent years. They can be classified as ″materials applications″ and ″biomedical applications″. The following paragraphs present a selection of recent developments. A large variety of applications have been either been reviewed concisely (Shenderova et al., 2002) or are in the stage of emergence.

3.16.5.1 Materials Applications of ND

A frequent use of ND is the application as seeds for the growth of new diamond films. Here, the diamond nanoparticles induce the nucleation of further diamond growth when deposited onto suitable substrates. As the production of uniform diamond films with controlled purity has high priority, it is necessary to pay attention to each step of the diamond film growth. One major parameter to achieve high-quality films is the quality and homogeneity of the nucleation seeds. In order to avoid the contamination with foreign materials (when using nondiamond seeds), diamond is the first choice as nucleation seed. However, to qualify as a superior seeding material, several requirements such as the purity of the ND (e.g. no sp^2 carbon in the seeding material), the absence of agglomerates in the seeding suspension, etc. have to be met. Therefore, techniques to produce pure and well-dispersed primary particles of ND are of high importance. There are several approaches available for the production of isolated ND particles. These include purely mechanical methods such as milling (Krüger et al., 2005; Pentecost et al., 2010) and ultrasound (Ozawa et al., 2007), as well as chemical methods such as the separation of ND particles by surface functionalization (Liang et al., 2009). The resulting slurries have been used for the nucleation of film growth, e.g. by Williams and colleagues (Williams, Douheret, Daenen, Haenen, & Osawa, 2007). It was also found that the surface charge and choice of coating solvent (although dried away before growing the diamond film) play an important role (**Figure 14**) (Shenderova, Hens, & McGuire, 2010).

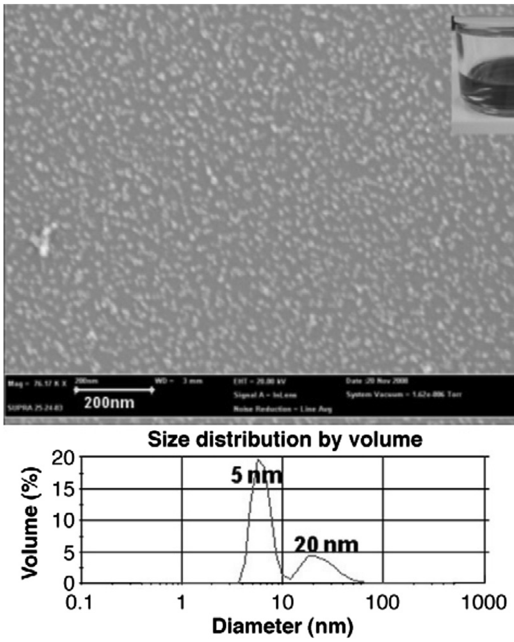

Figure 14 Seeding with colloidal solutions of ND produces very homogeneous and nonagglomerated seeding layers for CVD growth of diamond films. Here, a colloidal solution of 0.5 wt.% ND in DMSO/MeOH (1:3) was used to deposit the nucleation seeds. Copyright Elsevier, with kind permission from Shenderova et al. (2010).

Different types of seeding procedures have been reported, from simple dip coating to electrostatic grafting of ND nanoparticles onto polymer-coated substrates (where the success of the seeding becomes independent of the nature of the actual substrate) (Girard et al., 2009). The surface of substrates can be seeded in a homogeneous manner or in a structured way. The latter can be achieved by inkjet printing the stable colloidal solutions onto the substrate (Chen et al., 2009).

Another materials application makes use of the superior mechanical properties of diamond. Namely in composite materials, ND particles can contribute significantly to the overall properties of otherwise soft polymers. Several approaches including the noncovalent incorporation of the nanoparticles up to different covalent techniques have been reported. The latter include the "grafting from" approach using ND particles carrying initiator units for ATRP or the immobilization of monomers which can be connected covalently to the polymer matrix (Dahoumane et al., 2009; Li et al., 2006). These particles act as a kind of cross-linking agent in the polymer and can significantly enhance its mechanical properties. Among the polymer composites, those for biomedical applications deserve special attention. ND can help to improve the mechanical strength of biodegradable implant materials such as PLLA (Zhao et al., 2010). Besides organic matrices, the formation of ND inorganic composites with Pt (Bian, Wang, Zang, et al., 2010; La-Torre-Riveros, Soto, Scibioh, & Cabrera, 2010), Pd (Vershinin et al., 2011) and titanium dioxide (Bian, Wang, Lu, et al., 2010) has been reported for applications such as powder electrodes or electrocatalytic oxidation.

Diamond nanoparticles carrying controlled lattice defects are an ideal material for quantum applications, for single photon sources (Cuche et al., 2009) or nanoscopic magnetometers (Balasubramanian et al., 2008). For these applications, not only the number and quality of the respective lattice defects (typically N–V centers, but recently other defects such as Si–V, nickel and chromium-related structures have shown their suitability) is important. Another requirement for these applications is the reliable emission of single photons without bleaching or blinking of the light source. When the particle size is sufficiently small, refraction issues are overcome (Greentree et al., 2010) and luminescent ND particles with, for example, negatively charged N–V centers are an ideal candidate for such uses. They can be placed in photonic and plasmonic nanostructures (Barth, Schietinger, Schroeder, Aichele, & Benson, 2010; Stewart et al., 2009), or can be fixed to the tip of an optical fiber (Schroeder, Schell, Kewes, Aichele, & Benson, 2011).

As a member of the nanocarbon family, ND should be also a suitable material for some catalytic applications. Two different types of application in catalysis have to be distinguished: the actual use as a catalyst, thus applying the catalytic activity of the ND surface, and the application as an inert support for the immobilization of the catalytic species. In the second sense, the immobilization of noble metal nanoparticles such as platinum, palladium or gold represents a promising approach. Applications for the catalysis of hydrogenation reactions (Pd) (Turova et al., 2011) or the Fenton reaction (Au) (Navalon, de Miguel, Martin, Alvaro, & Garcia, 2011) have been reported (**Figure 15**). Besides such inorganic nanoparticles, biological catalysts, i.e. enzymes, can be bound to the ND surface. They retain their activity at least to a major extent and can be recycled easily. There have been reports on the immobilization and application of trypsin (Wei, Zhang, Lu, & Yang, 2010), lysozyme (Chung et al., 2006; Perevedentseva et al., 2011) and alcohol dehydrogenase (Goldberg et al., 2008). Another

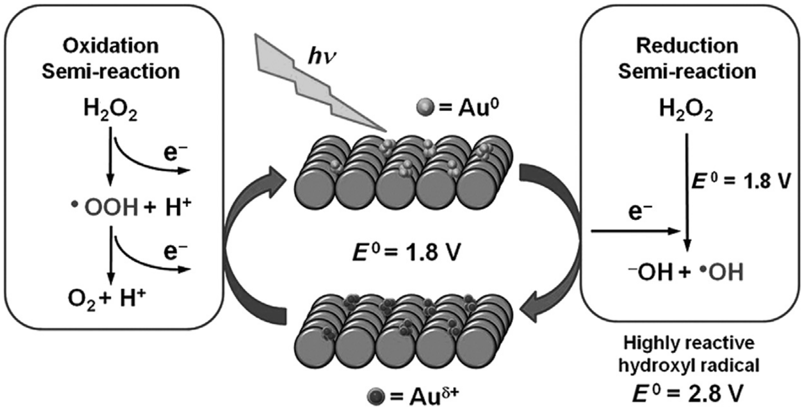

Figure 15 ND particles can be used as a support for catalytically active metal nanoparticles. Here, gold nanoparticles are not only immobilized on the ND surface but the catalytic process (i.e. the photocatalytic Fenton degradation of e.g. phenol) is improved by the presence of ND. Copyright ACS, with kind permission from Navalon et al. (2011).

class of catalysts, the so-called organocatalysts (typically chiral organic compounds) have been recently of great interest due to their potential impact on sustainability of chemical syntheses. However, the examples for ND-immobilized organocatalysts for, e.g. aldol reaction show so far an inferior performance concerning the selectivity and yield compared to the free catalysts (Zheng et al., 2009). Nevertheless, some stereoselectivity has already been observed.

Furthermore, the ND surface exhibits some catalytic activity on its own. It can be applied for the dehydrogenation of ethylbenzene to styrene (Zhang et al., 2010). It seems that the typical inhomogeneous surface structure of DND with its mixture of sp^3 and sp^2 carbon and the presence of a variety of surface groups is beneficial for this catalytic process.

The surface of ND can also promote electrochemical reactions when applied in powder-electrode setups. The large surface area, the unique surface structure and the high electrochemical stability even at rather high potentials are attractive features of such diamond electrodes (Zang, Wang, Zhao, Bian, & Lu, 2007). One example of an electrochemical reaction on ND is the oxidation of nitrite (Chen, Zang, Wang, & Bian, 2008). One issue related to ND is the required electric conductivity, which is naturally very low in defect-free diamond. Residual sp^2 carbon or the introduction of lattice defects (boron doping) can help to overcome this technical problem. Swain and colleagues improved the electrochemical characteristics of diamond electrode materials by coating of submicron particles with a thin layer of boron-doped diamond. This approach lead to superior corrosion resistance and improved electrode activity compared to other carbon electrodes (Ay, Swope, & Swain, 2008). A coating with titanium dioxide nanoparticles yields a similar result (Bian, Wang, Lu, et al., 2010).

3.16.5.2 Biomedical Applications of ND

Diamond with its proverbial inertness is a perfect material for biological environments. This makes it also a prospective candidate for biomedical applications (Grichko & Shenderova, 2006; Schrand et al., 2009). Among the carbon materials, it shows the lowest and often negligible toxicity and behaves inoffensively in cell culture and organisms. For details on the biocompatibility, see for instance Krueger (2011). Several applications of ND can be envisaged making use of its unique properties and inertness. These include the fabrication of biocompatible materials, the delivery of drugs or other molecules on ND as a carrier, the use in biotesting systems and the application as a highly inert and stable label.

The small particle size and the resulting large, specific surface make ND a good candidate for the adsorption of, e.g. drugs. Compared to other nanoparticles or activated charcoal, a major advantage of ND is its rather hydrophilic (and tunable) surface termination with polar groups (e.g. OH and COOH). This improves the solubility of the conjugates in physiological media and enables strong interactions also with highly polar (bio) molecules. Several examples for the successful delivery of drugs and other substances have been reported. One of the widely used chemotherapeutics called doxorubicin has been immobilized and efficiently applied in animal models for the therapy of malignant tumors (Huang et al., 2007; Lam et al., 2008). The toxicity of the drug was significantly reduced and enabled higher efficiency resulting in rapid reduction of tumor size and higher survival rates. Other antitumor agents such as (HCPT) (Li et al., 2010) paclitaxel (Liu et al., 2010) have been immobilized and delivered. The latter was used to study its effect on A549 human lung carcinoma cells where it induced mitotic arrest as well as apoptosis.

Also (therapeutic) proteins have been delivered to cells and organisms using ND. In some cases, the surface of the ND was prefunctionalized, e.g. Hui and co-workers modified the surface of ND with N,O-carboxymethyl chitosan (Wang, Yang, & Niu, 2010). In an analogous fashion, bovine insulin has been noncovalently grafted onto DND and its release could be controlled, e.g. by changes in pH value (Shimkunas et al., 2009).

In addition to drugs and proteins, nucleic acid derivatives can be immobilized and delivered. In these cases, the ND particle acts as a kind of biocompatible, nonviral vector. For instance, small interfering RNA—a powerful tool for the analysis and therapy of gene-related diseases—can be delivered using ND (Chen et al., 2010). Entire genes, such as the one for the GFP, can be delivered to cells. Martin et al. used hydroxylated ND (OH groups by reaction with Fenton's reagent) as a platform for gene delivery. In their study, the gene was successfully transferred into the nuclei of HeLa cells initiating the green fluorescence of the treated cells (Martin, Alvaro, Herance, & Garcia, 2010).

Another important field of application for ND is the study of biological processes. The outstanding luminescences of lattice defects in diamond coupled with its biological inertness make it an ideal candidate for the application as a biolabel. The observation of the luminescence has been reported for cell cultures as well as for entire organisms using the stable, nonbleaching and nonblinking luminescence of the so-called N–V center

(Fu et al., 2007; Neugart et al., 2007). For an example of blinking in very small ND particles and the influence of different surface termination, see the reference Bradac et al. (2010). In general, the photophysical phenomena related to this lattice defect are well understood (Jelezko & Wrachtrup, 2006). Furthermore, the "mass" production of such luminescent diamond particles can be managed using semicontinuous techniques (Chang, Lee, et al., 2008). It was shown that fluorescent ND (fND) particles with a diameter of <20 nm can be produced using helium ion irradiation and subsequent centrifugation (Mohan, Tzeng, et al., 2010). Besides He ions, the irradiation is successful with high-energy electrons or protons (Sonnefraud et al., 2008; Vlasov et al., 2010). But not only the generation of the luminescent defects is of importance, efficient uptake of the nanoparticles into the cells is a mandatory prerequisite for the application as a label. Treussart and colleagues studied the uptake of fND into mammalian cells (Faklaris et al., 2009). They found that the NDs enter the cells by clathrin-mediated endocytosis by excluding alternative pathways in blocking experiments. Chang and co-workers reported on the observation of fND particles on their way through an animal, the worm *Caenorhabditis elegans* after ingestion or injection and found fND to be a fully biocompatible, easily visible label (**Figure 16**) (Mohan, Chen, et al., 2010).

In addition to the frequently used N–V center, other lattice defects in diamond show attractive luminescence properties, too. One of these centers is the so-called H3 (N–V–N) center with an emission maximum at ~550 nm (Mkandawire et al., 2009; Wee et al., 2009). So far, the structural characteristics of the

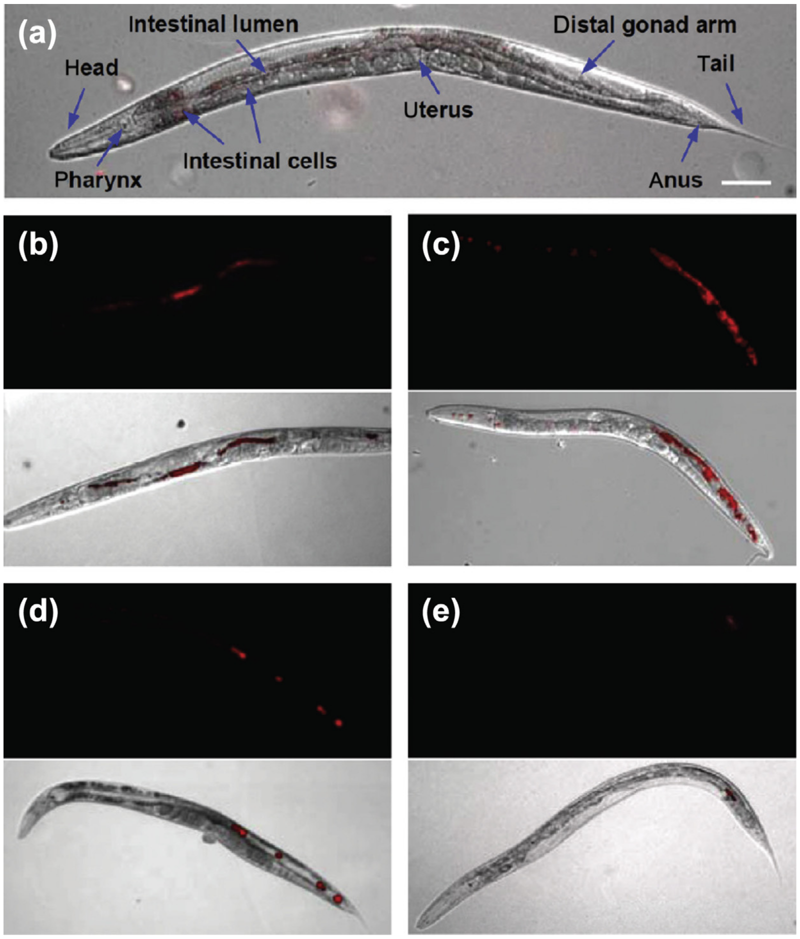

Figure 16 Epifluorescence and epifluorescence/DIC-merged images of wild-type *C. elegans*. (a) An untreated young adult. (b, c) Worms, fed with bare fNDs for 2 h (b) and 12 h (c). The fluorescent NDs (fND) stayed inside the gut and were not excreted out when the worms were deprived of food. Excretion of fNDs occurred upon feeding with *Escherichia coli*. (d, e) Worms were provided with *E. coli* for 20 min (d) and 40 min (e), after being fed with bare fNDs for 2 h. Almost, if not all, fNDs were excreted out within 1 h. The upper panels in (b–e) show the epifluorescence images; (a) and the lower panels in (b–e) show the epifluorescence/DIC-merged images. Anterior is left and dorsal is up in all figures. Scale bar is 50 μm. Copyright ACS, with kind permission from Mohan, Chen, et al. (2010).

luminescent center are unknown. In this and other cases, lattice defects may be the origin of the luminescence; however, the participation of residual nondiamond carbon has not yet been excluded. In the same manner as N–V–diamond, these other luminescent diamond samples can be used for labeling purposes as was shown by Wee et al. and Mkandawire et al. These authors reported on the application of green fND for the targeting of cell components and sensing (Mkandawire et al., 2009; Wee et al., 2009). A blue luminescence was observed for carboxylated ND functionalized with octadecylamine. Such hydrophobic ND could be used for the visualization of cell membranes or other lipophilic components of biological systems (Mochalin & Gogotsi, 2009). But not only optical detection can be used with ND as a label. The material shows a characteristic Raman resonance (Cheng et al., 2007) in an area where biological material is typically "silent". Furthermore, ND can be used as a scattering label (Smith, Niebert, Plakhotnik, & Zvyagin, 2007). The use of these physical properties does not require the existence of controlled lattice defects, hence, all kinds of ND particles can be used, provided their size is sufficiently big. Typically, a diameter of 50–100 nm is required for the application as Raman or scattering label, whereas luminescent ND particles are visible even with a single-digit nanometric size.

3.16.6 Summary

As shown in this chapter the surface chemistry of nanoscale diamond is surprisingly rich and diverse. Besides typical gas-phase reactions to control the surface termination of the ND particle, a broad portfolio of organic reactions can be used to control the oxidation state of the diamond surface, establish all kinds of functional groups (OH, keto, COOH, amines, halogens, etc.) and to couple even large (bio) molecules to the surface of the diamond nanoparticles. Such immobilization can occur either covalently or by adsorption. The envisaged application decides on the suitability of the different approaches. Depending on the accomplished surface modification, the resulting ND derivatives exhibit a wide range of properties (concerning solubility, surface charge, biocompatibility, etc.). Therefore, a chemical transformation of ND should always be adapted to the requirements resulting from a specific application.

The variety of applications of ND conjugates is as broad as the possibilities for surface modification. Among the uses for ND are the seeding of substrates for CVD diamond growth, the function as solid support for biotesting systems, catalysts or drugs, as carriers in drug delivery and as solid phase in chromatography. Also composite materials containing ND have a bright future in biomedical or technical applications.

References

Ager, D. (2011). Hydrogenation of carbon-carbon double bonds. In J. G. De Vries, G. A. Molander, & P. A. Evans (Eds.), *Science of synthesis, stereoselective synthesis* (Vol. 1; pp. 185).

Anikeev, V. I., & Zaikovskii, V. I. (2010). *Russian Journal of Applied Chemistry, 83*, 1202.

Arnault, J.-C., Petit, T., Girard, H., Chavanne, A., Gesset, C., Sennour, M., et al. (2011). *Physical Chemistry Chemical Physics, 13*, 11481.

Auciello, O., & Sumant, A. V. (2010). *Diamond and Related Materials, 19*, 699.

Avdeev, M. V., Rozhkova, N. N., Aksenov, V. L., Garamus, V. M., Willumeit, R., & Osawa, E. (2009). *Journal of Physical Chemistry C, 113*, 9473.

Ay, A., Swope, V. M., & Swain, G. M. (2008). *Journal of the Electrochemical Society, 155*, B1013.

Bahr, J. L., Yang, J., Kosynkin, D. V., Bronikowski, M. J., Smalley, R. E., & Tour, J. M. (2001). *Journal of the American Chemical Society, 123*, 6536.

Balasubramanian, G., Chan, I. Y., Kolesov, R., Al-Hmoud, M., Tisler, J., Shin, C., et al. (2008). *Nature, 455*, 648.

Barras, A., Szunerits, S., Marcon, L., Monfilliette-Dupont, N., & Boukherroub, R. (2010). *Langmuir, 26*, 13168.

Barth, M., Schietinger, S., Schroeder, T., Aichele, T., & Benson, O. (2010). *Journal of Luminescence, 130*, 1628.

Betz, P., & Krueger, A. (2012). *Chemical Physics and Physical Chemistry. 13*, 2578.

Bian, L. Y., Wang, Y. H., Lu, J., & Zang, J. B. (2010). *Diamond and Related Materials, 19*, 1178.

Bian, L. Y., Wang, Y. H., Zang, J. B., Yu, J. K., & Huang, H. (2010). *Journal of Electroanalytical Chemistry, 644*, 85.

Bijnens, N., Vermeeren, V., Daenen, M., Grieten, L., Haenen, K., Wenmackers, S., et al. (2009). *Physica Status Solidi A, 206*, 520.

Bingel, C., & Schiffer, H. (1995). *Liebigs Annalen*, 1551.

Bingel, C. (1993). *Chemische Berichte, 126*, 1957–1959.

Bondar, V. S., Pozdnyakova, I. O., & Puzyr, A. P. (2004). *Physics of the Solid State, 46*, 758.

Bradac, C., Gaebel, T., Naidoo, N., Sellars, M. J., Twamley, J., Brown, L. J., et al. (2010). *Nature Nanotechnology, 5*, 345.

Butenko, Yu. V., Kuznetsov, V. L., Paukshtis, E. A., Stadnichenko, A. I., Mazov, I. N., Moseenkov, S. I., et al. (2006). *Fullerenes, Nanotubes, and Carbon Nanostructures, 14*, 557.

Chang, Y.-R., Lee, H.-Y., Chen, K., Chang, C.-C., Tsai, D.-S., Fu, C.-C., et al. (2008). *Nature Nanotechnology, 3*, 284.

Chang, C.-K., Wu, C.-C., Wang, Y.-S.-, & Chang, H.-C. (2008). *Analytical Chemistry, 80*, 3791.

Chang, I. P., Hwang, K. C., Ho, J.-A. A., Lin, C.-C., Hwu, R. J.-R., & Horng, J.-C. (2010). *Langmuir, 26*, 3685.

Chao, J.-I., Perevedentseva, E., Chung, P.-H., Liu, K.-K., Cheng, C.-Y., Chang, C.-C., et al. (2007). *Biophysical Journal, 93*, 2199.

Chen, L. H., Zang, J. B., Wang, Y. H., & Bian, L. Y. (2008). *Electrochimica Acta, 53*, 3442.

Chen, Y.-C., Tzeng, Y., Cheng, A.-J., Dean, R., Park, M., & Wilamowski, B. M. (2009). *Diamond and Related Materials, 18*, 146.

Chen, M., Zhang, X.-Q., Man, H. B., Lam, R., Chow, E. K., & Ho, D. (2010). *Journal of Physical Chemistry Letters, 1*, 316.

Cheng, C.-L., Chen, C.-F., Shaio, W.-C., Tsai, D.-S., & Chen, K.-H. (2005). *Diamond and Related Materials, 14*, 1455.

Cheng, C.-Y., Perevedentseva, E., Tu, J.-S., Chung, P.-H., Cheng, C.-L., Liu, K.-K., et al. (2007). *Applied Physics Letters, 90*, 163903.

Cheng, J., He, J., Li, C., & Yang, Y. (2008). *Chemistry of Materials, 20*, 4224.

Chiganov, A. S. (2004). *Physics of the Solid State, 46*, 620.

Chung, P.-H., Perevedentseva, E., Tu, J.-S., Chang, C. C., & Cheng, C.-L. (2006). *Diamond and Related Materials, 15*, 622.

Ciftan Hens, S., Cunningham, G., Tyler, T., Moseenkov, S., Kuznetsov, V., & Shenderova, O. (2008). *Diamond and Related Materials, 17*, 1858.

Comet, M., Pichot, V., Siegert, B., Britz, F., & Spitzer, D. (2010). *Journal of Nanoscience and Nanotechnology, 10*, 4286.

Cuche, A., Drezet, A., Sonnefraud, Y., Faklaris, O., Treussart, F., Roch, J.-F., et al. (2009). *Optics Express, 17*, 19969.

Cunningham, G., Panich, A. M., Shames, A. I., Petrov, I., & Shenderova, O. (2008). *Diamond and Related Materials, 17*, 650.

Dahoumane, S. A., Nguyen, M. N., Thorel, A., Boudou, J.-P., Chehimi, M. M., & Mangeney, C. (2009). *Langmuir, 25*, 9633.

Dolmatov, V. Yu. (2001). *Russian Chemical Reviews, 70*, 607.

Donnet, J.-B., Lemoigne, C., Wang, T. K., Peng, C.-M., Samirant, M., & Eckhardt, A. (1997). *Bulletin de la Societe Chimique de France, 134*, 875.

Dubois, M., Guerin, K., Petit, E., Batisse, N., Hamwi, A., Komatsu, N., et al. (2009). *Journal of Physical Chemistry C, 113*, 10371.

Faklaris, O., Joshi, V., Irinopoulou, T., Tauc, P., Sennour, M., Girard, H., et al. (2009). *ACS Nano, 3*, 3955.

Fang, X. W., Mao, J. D., Levin, E. M., & Schmidt-Rohr, K. (2009). *Journal of the American Chemical Society, 131*, 1426.

Fox, B. A. (1997). Diamond films. In A. Elshabini-Riad, & F. D. Barlow, III (Eds.), *Thin film technology handbook*. New York: McGraw Hill Professional (and references cited therein).

Frauenheim, Th., Stephan, U., Blaudeck, P., Porezag, D., Busmann, H.-G., Zimmermann-Edling, W., et al. (1993). *Physical Review B, 48*, 18189.

Fu, C.-C., Lee, H.-Y., Chen, K., Lim, T.-S., Wu, H.-Y., Lin, P.-K., et al. (2007). *Proceedings of the National Academy of Sciences, 104*, 727.

Gaebel, T., Bradac, C., Chen, J., Say, J. M., Brown, L., Hemmer, P., et al. (2012). *Diamond and Related Materials, 21*, 28.

Garguilo, J. M., Davis, B. A., Buddie, M., Kock, F. A. M., & Nemanich, R. J. (2004). *Diamond and Related Materials, 13*, 595.

Ghodbane, S., Haensel, T., Coffinier, Y., Szunerits, S., Steinmuller-Nethl, D., Boukherroub, R., et al. (2010). *Langmuir, 26*, 18798.

Girard, H. A., Perruchas, S., Gesset, C., Chaigneau, M., Vieille, L., Arnault, J.-C., et al. (2009). *ACS Applied Materials and Interfaces, 1*, 2738.

Girard, H. A., Arnault, J. C., Perruchas, S., Saada, S., Gacoin, T., Boilot, J.-P., et al. (2010). *Diamond and Related Materials, 19*, 1117.

Girard, H. A., Petit, T., Perruchas, S., Gacoin, T., Gesset, C., Arnault, J. C., et al. (2011). *Physical Chemistry Chemical Physics, 13*, 11517.

Goertzen, S. L., Thériault, K. D., Oickle, A. M., Tarasuk, A. C., & Andreas, H. A. (2010). *Carbon, 48*, 1252.

Goldberg, K., Krueger, A., Meinhardt, T., Kroutil, W., Mautner, B., & Liese, A. (2008). *Tetrahedron Asymmetry, 19*, 1171.

Gomez, H., Ram, M. K., Alvi, F., Stefanakos, E., & Kumar, A. (2010). *Journal of Physical Chemistry C, 114*, 18797.

Gordeev, S. K., & Korchagina, S. B. (2007). *Journal of Superhard Materials, 29*, 124.

Gordeyev, S. K., & Korchagina, S. B. (2004). *Journal of Superhard Materials, 26*, 32 (Transl. from Sverkhtverdye Materialy 2004, 26, 34).

Goyal, N. (2010). *Synlett*, 335.

Greentree, A. D., Aharonovich, I., Castelletto, S., Doherty, M. W., McGuinness, L. P., & Simpson, D. A. (2010). *Optics Photonics News, 21*, 20.

Grichko, V., & Shenderova, O. A. (2006). In O. A. Shenderova, & D. M. Gruen (Eds.), *Ultrananocrystalline diamond* (pp. 529–558). Norwich: William Andrew Inc.

Grimme, S., Antony, J., Schwabe, T., & Mueck-Lichtenfeld, C. (2007). *Organic and Biomolecular Chemistry, 5*, 741.

Hartmann, M., Betz, P., Sun, Y., Gorb, S. N., Lindhorst, T. K., & Krueger, A. (2012). *Chemistry, a European Journal. 18*, 6485.

Hiraki, J., Mori, H., Taguchi, E., Yasuda, H., Kinoshita, H., & Ohmae, N. (2005). *Applied Physics Letters, 86*, 223101.

Hirsch, A., & Brettreich, M. (2005). *Fullerenes*. Weinheim: Wiley-VCH, 73.

Holt, K. B. (2007). *Philosophical Transactions of the Royal Society of London, Series B, 365*, 2845.

Hsin, Y. L., Chu, H.-Y., Jeng, Y.-R., Huang, Y.-H., Wang, M. H., & Chang, C. K. (2011). *Journal of Materials Chemistry, 21*, 13213.

Huang, L.-C. L., & Chang, H.-C. (2004). *Langmuir, 20*, 5879.

Huang, H., Pierstorff, E., Osawa, E., & Ho, D. (2007). *Nano Letters, 7*, 3305.

Huang, H., Chen, M., Bruno, P., Lam, R., Robinson, E., Gruen, D., et al. (2009). *Journal of Physical Chemistry B, 113*, 2966.

Ida, S., Tsubota, T., Nagata, M., Matsumoto, Y., Uehara, M., & Hojo, J. (2003). *Hyomen Gijutsu, 54*, 764.

Ida, S., Tsubota, T., Hirabayashi, O., Nagata, M., Matsumoto, Y., & Fujishima, A. (2003). *Diamond and Related Materials, 12*, 601.

Jarre, G., Liang, Y., Betz, P., Lang, D., & Krueger, A. (2011). *Chemical Communications, 47*, 544.

Jelezko, F., & Wrachtrup, J. (2006). *Physica Status Solidi A, 203*, 3207 (and references cited therein).

Jiang, T., & Xu, K. (1995). *Carbon, 33*, 1663.

Jiang, T., Xu, K., & Ji, S. (1996). *Journal of the Chemical Society, Faraday Transactions, 92*, 3401.

Koch, H., Kulisch, W., Popov, C., Merz, R., Merz, B., & Reithmaier, J. P. (2011). *Diamond and Related Materials, 20*, 254.

Kolb, H. C., Finn, M. G., & Sharpless, K. B. (2001). *Angewandte Chemie, International Edition, 40*, 2004.

Kovalenko, I., Bucknall, D. G., & Yushin, G. (2010). *Advanced Functional Materials, 20*, 3979.

Krueger, A., & Boedeker, T. (2008). *Diamond and Related Materials, 17*, 1367.

Krueger, A., & Lang, D. (2012). *Advanced Functional Materials, 22*, 890.

Krueger, A., Ozawa, M., Jarre, G., Liang, Y., Stegk, J., & Lu, L. (2007). *Physica Status Solidi A, 204*, 2881.

Krueger, A. (2008a). *Advanced Materials, 20*, 2445.

Krueger, A. (2008b). *Journal of Materials Chemistry, 18*, 1485–1492.

Krueger, A. (2011). *Journal of Materials Chemistry, 21*, 12571–12578.

Kruger, A., Osawa, E., & Kataoka, F. (2002). Jpn. Patent App. 2002–205973.

Krüger, A., Ozawa, M., Kataoka, F., Fujino, T., Suzuki, Y., Aleksenskii, A. E., et al. (2005). *Carbon, 43*, 1722.

Krüger, A., Liang, Y., Jarre, G., & Stegk, J. (2006). *Journal of Materials Chemistry, 16*, 2322.

Kulisch, W., Popov, C., Gilliland, D., Ceccone, G., Rossi, F., & Reithmaier, J. P. (2010). *Surface and Interface Analysis, 42*, 1152.
Kuznetsov, V. L., & Butenko, Yu. V. (2005). Ultrananocrystalline diamond: Synthesis, properties and applications. In *NATO science series* (vol. 192; pp. 199).
Kuznetsov, V. L., Chuvilin, A. L., Butenko, Yu. V., Mal'kov, I. Yu., & Titov, V. M. (1994). *Chemical Physics Letters, 222*, 343.
Lam, R., Chen, M., Pierstorff, E., Huang, H., Osawa, E., & Ho, D. (2008). *ACS Nano, 2*, 2095.
Landstrass, M. I., & Ravi, K. V. (1989a). *Applied Physics Letters, 55*, 975.
Landstrass, M. I., & Ravi, K. V. (1989b). *Applied Physics Letters, 55*, 1391.
Lang, D., & Krueger, A. (2011). *Diamond and Related Materials, 20*, 101.
La-Torre-Riveros, L., Soto, K., Scibioh, M. A., & Cabrera, C. R. (2010). *Journal of the Electrochemical Society, 157*, B831.
Le Huu, T., Zaidi, H., Paulmier, D., & Voumard, P. (1996). *Thin Solid Films, 290–291*, 126.
Li, C.-C., & Huang, C.-L. (2010). *Colloids Surfaces A, 53*, 52.
Li, L., Davidson, J. L., & Lukehart, C. M. (2006). *Carbon, 44*, 2308.
Li, A. J., Zhu, Y., Li, W., Zhang, X., Peng, Y., & Huang, Q. (2010). *Biomaterials, 31*, 8410.
Liang, Y., Ozawa, M., & Krueger, A. (2009). *ACS Nano, 3*, 2288.
Liang, Y., Meinhardt, T., Jarre, G., Ozawa, M., Vrdoljak, P., Schöll, A., et al. (2011). *Journal of Colloid and Interface Science, 354*, 23.
Liu, Y., Gu, Z., Margrave, J. L., & Khabashesku, V. N. (2004). *Chemistry of Materials, 16*, 3924.
Liu, K.-K., Zheng, W.-W., Wang, C.-C., Chiu, Y.-C., Cheng, C.-L., Lo, Y.-S., et al. (2010). *Nanotechnology, 21*, 315106.
Loh, K. P., Lim, C. W., Gao, X., Qi, D., & Wee, A. T. S. (2006). *Diamond and Related Materials, 15*, 711.
Lud, S. Q., Steenackers, M., Jordan, R., Bruno, P., Gruen, D. M., Feulner, P., et al. (2006). *Journal of the American Chemical Society, 128*, 16884.
Lud, S. Q., Neppl, S., Richter, G., Bruno, P., Gruen, D. M., Jordan, R., et al. (2010). *Langmuir, 26*, 15895.
Maier, F., Ristein, J., & Ley, L. (2001). *Physical Reviews B, 64*, 165411.
Markham, M. L., Dodson, J. M., Scarsbrook, G. A., Twitchen, D. J., Balasubramanian, G., Jelezko, F., et al. (2011). *Diamond and Related Materials, 20*, 134.
Martín, R., Heydorn, P. C., Alvaro, M., & García, H. (2009). *Chemistry of Materials, 21*, 4505.
Martin, R., Alvaro, M., Herance, J. R., & Garcia, H. (2010). *ACS Nano, 4*, 6523.
Martín, R., Álvaro, M., Herance, J. R., & García, H. (2010). *ACS Nano, 4*, 65.
May, P. W. (2010). *Materials Science Foundations, 65–66*, 145.
Meinhardt, T., Lang, D., Dill, H., & Krueger, A. (2011). *Advanced Functional Materials, 21*, 494.
Mitev, D., Dimitrova, R., Spassova, M., Minchev, Ch., & Stavrev, S. (2007). *Diamond and Related Materials, 16*, 776.
Mkandawire, M., Pohl, A., Gubarevich, T., Lapina, V. A., Appelhans, D., Roedel, G., et al. (2009). *Journal of Biophotonics, 2*, 596.
Mochalin, V. N., & Gogotsi, Y. (2009). *Journal of the American Chemical Society, 131*, 4594.
Mochalin, V., Osswald, S., & Gogotsi, Y. (2009). *Chemistry of Materials, 21*, 273.
Mochalin, V. N., Neitzel, I., Etzold, B. J. M., Peterson, A., Palmese, G., & Gogotsi, Y. (2011). *ACS Nano, 5*, 7494.
Mohan, N., Chen, C.-S., Hsieh, H.-H., Wu, Y.-C., & Chang, H.-C. (2010a). *Nano Letters, 10*, 3692.
Mohan, N., Tzeng, Y.-K., Yang, L., Chen, Y.-Y., Hui, Y. Y., Fang, C.-Y., et al. (2010b). *Advanced Materials, 22*, 843.
Morimune, S., Kotera, M., Nishino, T., Goto, K., & Hata, K. (2011). *Macromolecules, 44*, 4415.
Mykhaylyk, O. O., Solonin, Yu. M., Batchelder, D. N., & Brydson, R. (2005). *Journal of Applied Physics, 97*, 074302.
Nakamura, T., Ohana, T., Hagiwara, Y., & Tsubota, T. (2009). *Physical Chemistry Chemical Physics, 11*, 730.
Nakamura, T., Ohana, T., Hagiwara, Y., & Tsubota, T. (2010). *Applied Surface Science, 257*, 1368.
Nakamura, T. (2010). *Diamond and Related Materials, 19*, 374.
Navalon, S., de Miguel, M., Martin, R., Alvaro, M., & Garcia, H. (2011). *Journal of the American Chemical Society, 133*, 2218.
Neitzel, I., Mochalin, V., Knoke, I., Palmese, G. R., & Gogotsi, Y. (2011). *Composites Science and Technology, 71*, 710.
Neu, E., Arend, C., Gross, E., Guldner, F., Hepp, C., Steinmetz, D., et al. (2011). *Applied Physics Letters, 98*, 243107.
Neugart, F., Zappe, A., Jelezko, F., Tietz, C., Boudou, J.-P., Lu, L., et al. (2007). *Nano Letters, 7*, 3588.
Nguyen, T.-T.-B., Chang, H.-C., & Wu, V. W.-K. (2007). *Diamond and Related Materials, 16*, 872.
Nichols, B. M., Butler, J. E., Russell, J. N., Jr., & Hamers, R. J. (2005). *Journal of Physical Chemistry B, 109*, 20938.
Niu, K. Y., Zheng, H. M., Li, Z.-Q., Yang, J., Sun, J., & Du, X.-W. (2011). *Angewandte Chemie, International Edition, 50*, 4099.
Obraztsova, I. I., & Eremenko, N. K. (2008). *Russian Journal of Applied Chemistry, 81*, 603.
Ohtani, B., Kim, Y.-H., Yano, T., Hashimoto, K., Fujishima, A., & Uosaki, K. (1998). *Chemistry Letters*, 953.
Okada, S. (2009). *Chemical Physics Letters, 483*, 128.
Osawa, E. (2007). *Diamond and Related Materials, 16*, 2018.
Osswald, S., Yushin, G., Mochalin, V., Kucheyev, S. O., & Gogotsi, Y. (2006). *Journal of the American Chemical Society, 128*, 11635.
Osswald, S., Havel, M., Mochalin, V., Yushin, G., & Gogotsi, Y. (2008). *Diamond and Related Materials, 17*, 1122.
Ozawa, M., Inakuma, M., Takahashi, M., Kataoka, F., Krueger, A., & Osawa, E. (2007). *Advanced Materials, 19*, 1201.
Panich, A. M., Shames, A. I., Vieth, H.-M., Osawa, E., Takahashi, M., & Vul, A. Ya. (2006). *European Physical Journal B, 2*, 397.
Park, C.-L., Jee, A. Y., Lee, M., & . Lee, S. G. (2009). *Chemical Communications*, 5576.
Pentecost, A., Gour, S., Mochalin, V., Knoke, I., & Gogotsi, Y. (2010). *ACS Applied Materials and Interfaces, 2*, 3289.
Perevedentseva, E., Cai, P. J., Chiu, Y.-C., & Cheng, C.-L. (2011). *Langmuir, 27*, 1085.
Petit, T., Arnault, J.-C., Girard, H. A., Sennour, M., & Bergonzo, P. (2011). *Physical Review B, 84*, 233407.
Pichot, V., Comet, M., Fousson, E., Baras, C., Senger, A., Le Normand, F., et al. (2008). *Diamond and Related Materials, 17*, 13.
Purtov, K. V., Petunin, A. I., Burov, A. E., Puzyr, A. P., & Bondar, V. S. (2010). *Nanoscale Research Letters, 5*, 631.
Qin, L. C., & Iijima, S. (1996). *Chemical Physics Letters, 262*, 252.
Radzicka, A., & Wolfenden, R. (1996). *Journal of the American Chemical Society, 118*, 6105.
Raty, J.-Y., & Galli, G. (2005). *Journal of Electroanalytical Chemistry, 584*, 9.
Raty, J.-Y., Galli, G., Bostedt, C., van Buuren, T. W., & Terminello, L. J. (2003). *Physical Review Letters, 90*, 037401.
Ray, M. A., Tyler, T., Hook, B., Martin, A., Cunningham, G., Shenderova, O., et al. (2007). *Diamond and Related Materials, 16*, 2087.
Remes, Z., Choukourov, A., Stuchlik, J., Potmesil, J., & Vanecek, M. (2006). *Diamond and Related Materials, 15*, 745.

Rezek, B., Shin, D.-C., Nakamura, T., & Nebel, C. E. (2006). *Journal of the American Chemical Society, 128*, 3884.
Ristein, J. (2006). *Applied Physics A, 82*, 377.
Roddatis, V. V., Kuznetsov, V. L., Butenko, Yu. V., Su, D. S., & Schloegl, R. (2002). *Physical Chemistry Chemical Physics, 4*, 1964.
Rondin, L., Dantelle, G., Slablab, A., Grosshans, F., Treussart, F., Bergonzo, P., et al. (2010). *Physical Reviews B, 82*, 115449.
Schietinger, S., Barth, M., Aichele, T., & Benson, O. (2009). *Nano Letters, 9*, 1694.
Schrand, A. M., Ciftan Hens, S. A., & Shenderova, O. A. (2009). *Critical Reviews in Solid State and Materials Sciences, 34*, 18.
Schroeder, T., Schell, A. W., Kewes, G., Aichele, T., & Benson, O. (2011). *Nano Letters, 11*, 198.
Schwartz, M. P., Barlow, D. E., Russell, J. N., Jr., Butler, J. E., D'Evelyn, M. P., & Hamers, R. J. (2005). *Journal of the American Chemical Society, 127*, 8348.
Schwertfeger, H., Fokin, A. A., & Schreiner, P. R. (2008). *Angewandte Chemie, International Edition, 47*, 1022.
Shenderova, O. A., Zhirnov, V. V., & Brenner, D. W. (2002). *Critical Reviews in Solid State and Materials Sciences, 27*, 227.
Shenderova, O., Hens, S., & McGuire, G. (2010). *Diamond and Related Materials, 19*, 260.
Shenderova, O., Koscheev, A., Zaripov, N., Petrov, I., Skryabin, Y., Detkov, P., et al. (2011). *Journal of Physical Chemistry C, 115*, 9827.
Shimkunas, R. A., Robinson, E., Lam, R., Lu, S., Xu, X., Zhang, X.-Q., et al. (2009). *Biomaterials, 30*, 5720.
Skorik, N. A., Krivozubov, A. L., Karzhenevskii, A. P., & Spitsyn, B. V. (2011). *Protection of Metals and Physical Chemistry of Surfaces, 47*, 54.
Smith, M. B., & March, J. (2007). *March's advanced organic chemistry* (6th ed.). Hoboken: John Wiley & Sons.
Smith, B. R., Niebert, M., Plakhotnik, T., & Zvyagin, A. V. (2007). *Journal of Luminescence, 127*, 260.
Smith, B. R., Gruber, D., & Plakhotnik, T. (2010). *Diamond and Related Materials, 19*, 314.
Sonnefraud, Y., Cuche, A., Faklaris, O., Boudou, J.-P., Sauvage, T., Roch, J.-F., et al. (2008). *Optics Letters, 33*, 611.
Sotowa, K.-I., Amamoto, T., Sobana, A., Kusakabe, K., & Imato, T. (2004). *Diamond and Related Materials, 13*, 145.
Spitsyn, B. V., Gradoboev, M. N., Galushko, T. B., Karpukhina, T. A., Serebryakova, N. V., Kulakova, I. I., et al. (2005). *NATO Science Series, II: Mathematics, Physics and Chemistry, 192*, 241.
Spitsyn, B. V., Denisov, S. A., Skorik, N. A., Chopurova, A. G., Parkaeva, S. A., Belyakova, L. D., et al. (2010). *Diamond and Related Materials, 19*, 123.
Stavis, C., Clare, T. L., Butler, J. E., Radadia, A. D., Carr, R., Zeng, H., et al. (2011). *Proceedings of the National Academy of Sciences, 108*, 983.
Stewart, L. A., Zhai, Y., Dawes, J. M., Steel, M. J., Rabeau, J. R., & Withford, M. J. (2009). *Optics Express, 17*, 18044.
Sussmann, R. S. (Ed.). (2009), *Wiley series in materials for electronic and optoelectronic applications, CVD diamond for electronic devices and sensors*. Chichester: Wiley (and references cited therein).
Takimoto, T., Chano, T., Shimizu, S., Okabe, H., Ito, M., Masaaki, M., et al. (2010). *Chemistry of Materials, 22*, 3462.
Tasis, D., Tagmatarchis, N., Bianco, A., & Prato, M. (2006). *Chemical Reviews, 106*, 1105.
Tu, J.-S., Perevedentseva, E., Chung, P.-H., & Cheng, C.-L. (2006). *Journal of Chemical Physics, 125*, 174713.
Turner, S., Lebedev, O. I., Shenderova, O., Vlasov, I. I., Verbeeck, J., & Van Tendeloo, G. (2009). *Advanced Functional Materials, 19*, 2116.
Turova, O. V., Starodubtseva, E. V., Vinogradov, M. G., Sokolov, V. I., Abramova, N. V., Vul', A. Ya., et al. (2011). *Catalysis Communications, 12*, 577.
Tyurina, A. V., Apolonskaya, I. A., Kulakova, I. I., Kopylova, P. G., & Obraztsov, A. N. (2010). *Poverkhnost*, 106.
Vaijayanthimala, V., & Chang, H.-C. (2009). *Nanomedicine, 4*, 47.
Vaijayanthimala, V., Tzeng, Y.-K., Chang, H.-C., & Li, C.-L. (2009). *Nanotechnology, 20*, 425103.
Vershinin, N. N., Efimov, O. N., Bakaev, V. A., Aleksenskii, A. E., Baidakova, M. V., Sitnikova, A. A., et al. (2011). *Fullerenes, Nanotubes, and Carbon Nanostructures, 19*, 63.
Vlasov, I. I., Shenderova, O., Turner, S., Lebedev, O. I., Basov, A. A., Sildos, I., et al. (2010). *Small, 6*, 687.
Wang, Y. M., Wong, K. W., Lee, S. T., Nishitani-Gamo, M., Sakaguchi, I., Loh, K. P., et al. (1999). *Physical Review B, 59*, 10347.
Wang, H.-D., Yang, Q., & Niu, C. H. (2010). *Diamond and Related Materials, 19*, 441.
Wee, T.-L., Mau, Y.-W., Fang, C.-Y., Hsu, H.-L., Han, C.-C., & Chang, H.-C. (2009). *Diamond and Related Materials, 18*, 567.
Wei, L., Zhang, W., Lu, H., & Yang, P. (2010). *Talanta, 80*, 1298.
Williams, O. A., Douheret, O., Daenen, M., Haenen, K., & Osawa, E. (2007). *Chemical Physics Letters, 445*, 255.
Williams, O. A., Hees, J., Dieker, C., Jäger, W., Kirste, L., & Nebel, C. E. (2010). *ACS Nano, 4*, 4824.
Williams, O. A. (2011). *Diamond and Related Materials, 20*, 621.
Xie, H., Yu, W., & Li, Y. (2006). *Journal of Physics D, 42*, 095413.
Xu, Z., Jeedigunta, S., & Kumar, A. (2007). *Journal of Nanoscience and Nanotechnology, 7*, 2092.
Yang, W., Auciello, O., Butler, J. E., Cai, W., Carlisle, J. A., Gerbi, J. E., et al. (2002). *Nature Materials, 1*, 253.
Yeap, W. S., Tan, Y. Y., & Loh, K. P. (2008). *Analytical Chemistry, 80*, 4659.
Yeap, W. S., Chen, S., & Loh, K. P. (2009). *Langmuir, 25*, 185.
Yeganeh, M., Coxon, P. R., Brieva, A. C., Dhanak, V. R., Šiller, L., & Butenko, Yu. V. (2007). *Physical Review B, 75*, 155404.
Yin, L.-W., Li, M.-S., Cui, J.-J., Song, Y.-S., Li, F.-Z., & Hao, Z.-Y. (2001). *Applied Physics A, 73*, 653.
Zang, J. B., Wang, Y. H., Zhao, S. Z., Bian, L. Y., & Lu, J. (2007). *Diamond and Related Materials, 16*, 16.
Zeppilli, S., Arnault, J. C., Gesset, C., Bergonzo, P., & Polini, R. (2010). *Diamond and Related Materials, 19*, 846.
Zhang, G.-J., Chong, K.-S., Nakamura, Y., Ueno, T., Funatsu, T., Ohdomari, I., et al. (2006). *Langmuir, 22*, 3728.
Zhang, X.-Q., Chen, M., Lam, R., Xu, X., Osawa, E., & Ho, D. (2009). *ACS Nano, 3*, 2609.
Zhang, J., Su, D. S., Blume, R., Schloegl, R., Wang, R., Yang, X., et al. (2010). *Angewandte Chemie, International Edition, 49*, 8640.
Zhang, Q., Mochalin, V. N., Neitzel, I., Knoke, I. Y., Han, J., Klug, C. A., et al. (2011). *Biomaterials, 32*, 87.
Zhao, Y.-Q., Lau, K.-T., Kim, J.-K., Xu, C.-L., Zhao, D.-D., & Li, H.-L. (2010). *Composites, Part B, 41*, 646.
Zhao, L., Takimoto, T., Ito, M., Kitagawa, N., Kimura, T., & Komatsu, N. (2011). *Angewandte Chemie, International Edition, 123*, 1424.
Zheng, W.-W., Hsieh, Y.-H., Chiu, Y.-C., Cai, S.-J., Cheng, C.-L., & Chen, C. (2009). *Journal of Materials Chemistry, 19*, 8432.
Zhong, Y. L., & Loh, K. P. (2010). *Chemistry, an Asian Journal, 5*, 1532.
Zhuang, H., Srikanth, V. V. S. S., Jiang, X., Aronov, I., Wenclawiak, B. W., Luo, J., et al. (2010). *Chemistry of Materials, 22*, 4414.
Zou, Q., Wang, M. Z., & Li, Y. G. (2010). *Journal of Experimental Nanoscience, 5*, 319.

3.17 Diamond for Particle and Photon Detection in Extreme Conditions

Eleni Berdermann, GSI Helmholtzzentrum für Schwerionenforschung GmbH, Darmstadt, Germany

http://dx.doi.org/10.1016/B978-0-08-096527-7.00054-4

3.17.1 Introduction

Diamond is a material combining the distinct thermal, optical and electronic properties needed for radiation detection in hostile environments. This is, however, a persistent belief and a way of speaking that disregard the numerous radiation-induced defects in diamond (Mitchel, 1959; Clark, Ditchburn & Dyer, 1956; Clark & Walker, 1973; Sellshop in Field, 1979, p. 107; Prins in Field, 1992, p. 301; Davies, Lawson, Collins, Mainwood, & Sharp, 1992; Pu, Avalos & Dannefaer, 2001; Davies et al., 2001; Bruzzi, Menichelli, & Sciortino, 2002), which lead to a notable degradation of the detection properties of diamond radiation sensors (Benny & Champion, 1954; Behnke et al., 2003; Oh et al., 2000) (The RD42 Collaboration (RD42) 2006; de Boer et al., 2007). Indeed, we experience that diamond detectors operate longer at high temperatures and under intense irradiation as compared to any other known solid-state sensor. This chapter is dedicated to the evaluation of the above statements based on the performance of chemical vapor deposition (CVD)-diamond detectors under severe conditions, i.e. where the classical detector devices fail.

Interestingly, we do not have a clear-cut rational theory, which predicts that diamond ought to be more radiation tolerant than other semiconductors. We do have solely some working hypotheses confirming some positive experimental results. The origin of the famous properties of diamond is the close distance of neighbor carbon atoms in the diamond unit cell and the resulting strong covalent tetrahedral (sp^3) bonding of the carbon atoms in the diamond lattice. The extreme indentation hardness of diamond is of minor importance for radiation sensors. There are the wide band gap (5.5 eV), high displacement energy (42 eV), and extreme thermal conductivity (2000 W m^{-1} K^{-1}), the characteristics that are most likely responsible for the observed radiation and temperature resistance of diamond sensors. A variety of further consequences defines diamond as a unique detector material of all-time unrivaled properties: intrinsic diamond sensors do not need darkness, pn-junction or cooling for high-performance operation. They reveal usually low dark conductivity and—in conjunction with the low nuclear charge Z—they enable a low-noise low-background implementation. The high drift velocity of electrons and holes and the extreme ohmic resistivity of the material support an ultrafast collection of charge, hence, the realization of diamond radiation sensors of highest single-particle count-rate capability.

Detector tests bear the opportunity to combine basic solid-state research with a realistic technological task. By investigating a diamond timing detector with ionizing particles, we can determine charge-carrier mobilities, trapping, recombination, and charge-collection distance (CCD). This is the reason why the progress in the synthesis of artificial-diamond materials is throughout the centuries inseparably linked to the research and development of diamond detectors for nuclear physics purposes. Sellschop (1992, p. 82) stated that the diamond characterization data obtained with “nuclear probes” had been unique in the sense that “no other techniques are able to address the problems, either at all, or with comparable sensitivity”.

The focus of this report will be on three types of CVD diamond known to be well suited for detector applications. They are in the order of their appearance: (1) polycrystalline CVD (pcCVD) diamond grown on silicon wafers; (2) homoepitaxial single-crystal CVD (scCVD) diamond grown on high-pressure–high-temperature (HPHT) Ib diamond substrates; and (3) “quasi single-crystal” CVD diamond on iridium (DoI) grown on multilayer substrates of an iridium top layer. DoI materials are presently not commercially available but they are developed at academic institutions in Japan (Aoyama Gakuin University: Ohtsuka, Suzuki, Sawabe et al., 1996; Sawabe, JP Patent 2009), in Europe (University of Augsburg: Schreck, Roll, and Stritzker, 1999) and the USA (Mitchigan State University: Bednarski, Dai, Li, and Golding, 2003).

The detector physics pertinent to diamond sensors is discussed in Sections 3.17.3 and 3.17.4. Section 3.17.5 is a review of theoretical considerations and of experimental data on the radiation tolerance of diamond sensors in actual particle physics experiments performed with high-luminosity/high-intensity beams, and Section 3.17.6 is a selection of present CVD-diamond detector applications in extreme conditions.

3.17.2 Historical Outline

Diamond has been one of the prominent materials used for fundamental investigations on the photoconductivity of isolating crystals (Gudden & Pohl, 1920, 1923a, 1923b). As early as the beginning of the twentieth century, an amazing bulk of knowledge about diamond as an active device has been collected. Tapper (2000) stated that it was probably this pioneering work on natural samples “representing the earliest observations of the physical effects, which underlie the use of diamond as a radiation detector” (p. 1279). The effects of “memory and polarization”, “trapping and release” as well as what we call today “pumping” or “priming” have been known. Robert Wichard Pohl, who according to Hughes and Du Bridge (1932, p. 313) has been the leader in this field, formulated the first Ansatz to the (later understood) number of electron–hole (e–h) pairs created by ionizing radiation. Together with Bernhard Gudden, Pohl postulated the "quantum equivalent $N = Q/h\nu$" as the number of electrons N generated in a crystal by light of frequency ν after absorption of light energy Q. This was required in order to fulfill Einstein's suggestion (Einstein, 1905) that the energy of the photoelectrons can be in best case equal to Planck's energy quantum $h\nu$, and in addition to explain the "mysterious independency of the energy of photoelectrically separated electrons from the light intensity" observed by Lenard (1902). Karl Hecht (1932, pp. 240–241) developed an absorption model describing the collection of photoelectrons in AgCl crystals in the presence of trapping and recombination centers (Section 3.17.4.3.4). He knew to treat the crystals with red light preserving the same field conditions over the whole measurements. Robertson Sir, Fox, and Martin (1934) classified the quality of diamond materials with respect to their transparency to ultraviolet (UV) photons and denominated the samples as type I or type II diamonds (transparent and nontransparent, respectively).

3.17.2.1 The First Crystal Counters

Hofstadter (1949a, 1949b) reported that "it appeared the urgent requirement to develop an instrument capable of counting individual particles in order to fulfill the increased demands of modern nuclear physics". The potential of the commonly used gaseous radiation chambers seemed to be rather overstressed. The first who suggested a "particle-induced conductivity" and the use of a crystal as an ionization chamber was Stetter (1941). At the end, however, it was Piet van Heerden (1945), who—during his Ph.D. thesis—demonstrated that it was possible to build a realistic apparatus for particle counting. AgCl crystals at low temperatures have been used also in that case. However, in the following years, the work on crystal counters was increasingly focused on the investigation of natural diamond detectors. Curtiss and Brown (1947) explored their potential for γ-ray counting, whereas McKay (1948) looked into its "bombardment conductivity" by using 14 keV electrons. McKay achieved a reduction of space–charge effects by applying an alternating external field method and developed a theoretical model for a "space–charge free crystal". In addition, he described for the first time the peculiarities of the space-charge limited current (SCLC) flow saying that the induced charge in a crystal affected by space charge may be accelerated beyond the drift velocity expected at that electric field.

Notwithstanding the fact that there were some significant achievements, the progress in the development of diamond counters was slow. The reasons have been manifold: the irreproducible properties of natural stones, the difficulties in postprocessing of suitable plates for characterization, and, nonetheless, the lack of appropriate electronics. It was about the same time when the discovery of the pn-junction by Russel Ohl (1940, 1941) awaked the scientific community. Riordan and Hoddeson appointed the finding of this "unsung hero of semiconductor history" as "one of the three or four fundamental structures without which the modern semiconductor industry would not exist" (Riordan & Hoddeson, 1997). Among the numerous applications arisen out of the triumphal procession of the pn-junction in science and technology, it was the pn-type radiation sensor, which dominated henceforward the development of crystal counters. Two of the most important types of particle and radiation sensors in nuclear physics were born: the silicon-diode detector for the measurement of charged particles and soft X-rays, and the germanium diode for the detection of hard γ-rays. It was no more urgent to battle with quirky diamond crystals. The silicon-diode sensor is up to the present day the most established and extremely successful crystal counter for charged-particle detection in nuclear and high-energy physics (HEP), and therefore the most serious contender of diamond detectors in these and related fields.

3.17.2.2 Natural Diamond Detectors in the 1970s

In this period, the development of diamond counters was mainly pushed by Russian scientists around Konorova and Kozlov. This group reviewed the general properties of advanced diamond sensors of that time (Kozlov, Stuck, Hage-Ali, & Siffert, 1975), and developed prototype detectors for fast neutron spectrometry (Kozlov, Konorova, Barinov, & Jarkov, 1975), immersed alpha-counters for the research on radioactive solutions (Kozlov, Konorova, Krapivin, Nadein, & Yudina, 1977) as well as sensors for X- and δ-ray dosimetry (Kozlov, Konorova, Kuznetsov, et al., 1977). They proposed furthermore a method to prepare polarization-free contacts by "making the back contact injecting under the influence of the applied field" and defined the energy needed to create an e–h pair in diamond to $\varepsilon_{\mathrm{Dia}} = (13.07 \pm 0.07)$ eV (Konorova & Kozlov, 1970), which is still the most accepted value in the community.

Italian scientists published an important paper on "the drift velocities, the mobilities, and the mean free drift time in natural diamond in a wide temperature and electric field range" (Nava, Canali, Artuso, Gatti, & Manfredi, 1979). They concluded that diamond behaves better than any other known detector up to temperatures of ~ 500 K, and confirmed that the best (lowest) values for $\varepsilon_{\mathrm{Dia}}$ and for the energy resolution $\delta E/E$ appear at room temperature (RT). Nava et al. obtained an $\varepsilon_{\mathrm{Dia}} = 13.25$ eV for $T \sim 300$ K, which was only 1% higher compared to the estimate of Konorova and Kozlov. However, they observed a decreasing $\varepsilon_{\mathrm{Dia}}$ value with increasing quality of the samples and noticed that this trend is expected to hold for any new generation of diamond materials (see also Sections 3.17.3.2.1 and 3.17.3.2.2).

3.17.2.3 CVD-Diamond Sensors in the 1990s

Spitsyn was the first who applied for a patent (Spitsyn & Derjaguin, 1956) "on the production of diamond by plasma-assisted CVD processes on nondiamond substrates". Unfortunately, this patent was "forgotten," and this was probably the reason why the CVD-diamond growth began years later, when a group of scientists at NIRIM in Tsukuba (Kamo, Sato, Matsumoto, & Setaka, 1983; Matsumoto, Sato, Kamo, & Setaka, 1982) "seized" Spitsyn's proposal (Spitsyn, Bouilov, & Derjaguin, 1981).

In the 1990s, large-area pcCVD diamond plates became available, which showed promising detection properties and radiation tolerance. The positive results obtained from the first studies on high-energy sensors (Franklin et al., 1992; Pan et al., 1992) reactivated worldwide the interest on diamond for radiation detection, which prior to that was somehow in the background, especially after the enthusiastic work of previous generations. The same spirit supported now the rapid progress in the CVD-diamond growth (Butler, Cheesman & Ashfold, 2009) for detector applications. There was again a serious concern that the conditions expected at the modern high-energy, high-luminosity hadron colliders, the Superconducting Super Collider (SSC) in the USA and the Large Hadron Collider (LHC) at CERN would overtax the capabilities of classical sensors. The anticipated physics aims connected with the LHC were not less than "to smash protons moving at 99.999999% of the speed of light into each other and to recreate conditions a fraction of a second after the Big Bang". In 10 years of LHC operation, integral fluencies as high as 10^{15} particles cm^{-2} were expected on the silicon sensors placed for particle tracking near the interaction points (IPs) of the colliding beams. Large-area, radiation-hard and fast detector systems were urgently required for the innermost detector parts of the coaxial multishell spectrometers.

Similar considerations initiated the development of CVD-diamond detectors at GSI Darmstadt, the Helmholtz Center for Heavy-Ion Research in Germany (GSI). The intensities of the ion beams (protons to uranium) extracted from the heavy-ion synchrotron SchwerIonenSynchrotron (SIS) are in the range of 10^6–10^{10} ions per spill, respectively. Even higher intensities and beams of unrivaled brilliance are foreseen for the upcoming Facility for Antiproton and Ion Research (FAIR). Assuming a useful synchrotron extraction cycle of 10^4 spills per day, one can estimate that a uranium beam of an intensity of 10^{10} ions per spill deposits approximately a dose of 27 Gy per day in a diamond detector of thickness $d_{\mathrm{D}} = 150$ µm and of an area of 1 cm^2. It appeared evident to consider CVD diamond for a possible replacement of so far successfully applied gas counters (ionization chambers (ICs), multiwire proportional counters (MWPCs) or parallel-plate counters). Severe problems were anticipated for the silicon-diode sensors used for spectroscopic beam monitoring as well as for the plastic scintillation detectors implemented for high-rate ion counting and timing. Plastic sensors operate at maximum rates of 10^6–10^8 ions per second and become "blind" with time in high-radiation environments. The signals of the radiation-resistant gaseous detectors saturate due to the transient space charge at ion rates of and beyond 1 and 100 kHz for ICs and MWPCs, respectively.

The first comprehensive overview on pcCVD diamond sensors was published by Tapper (2000), who described the first detector applications of those days for minimum-ionizing particles (MIP), electrons, protons, alphas, heavy ions, neutrons as well as X- and γ-rays. Bergonzo and Jackmann (2004) reviewed the behavior of diamond detectors under UV light and X-ray irradiation and investigated the crystal structure and the charge-collection efficiency (CCE) of pcCVD diamond using X-rays, alpha particles, and short-wavelength lasers. Stolz, Behravan, Regmi, and Golding (2006) demonstrated, for the first time, the suitability of as-grown DoI samples for heavy-ion beam tracking at MSU, East Lansing, and by this encouraging result, they fired the hope of wafer-scale diamond sensors approaching the properties of homoepitaxial diamond. In 2009, Sussmann edited the book *CVD diamond for Electronic Devices and Sensors* (Sussmann, 2009) comprising the actual status of CVD-diamond material research and electronic applications including radiation detectors for UV and far-UV photons described by (Collins, 2009, p. 165) radiotherapy detectors described by (Bruzzi, 2009, p. 185) sensors in ultrarelativistic HEP by (Kagan & Trischuk, 2009, p. 205) detectors for hadrons, nuclei and atoms by (Berdermann & Ciobanu, 2009, p. 227), as well as diamond neutron detectors reported by (Verona-Rinati, 2009, p. 257). Shorter review articles concerning diamond detectors for heavy-ion and hadron physics research have been published by Berdermann, Blasche, Daues et al. (2001), Berdermann (2009), Berdermann, Pomorski, et al. (2010).

3.17.3 Detector Physics

3.17.3.1 Interactions of Particles and Photons with Diamond Matter

When diamond is exposed to either corpuscular or electromagnetic radiation, a chain of phenomena starts which depend on the species and the energy of the impinging radiation. The group of particles considered in modern nuclear physics is very large. It comprises the stable elements from protons to uranium including their stable and unstable isotopes as well as exotic nuclei, in which one or more atomic constituents are replaced by other particles of the same charge (for instance myons, pions or kaons, or any baryon containing strange quarks). The energy of the particles varies from a few keV/A to several hundred GeV/A (with A the atomic mass number of the nuclei). Slow ions undergo inelastic nucleus–nucleus collisions and stop within a few tenths of micrometers diamond, while depositing the highest amount of their kinetic energy at the end of their path ("Bragg peak," after Sir William Henry Bragg). In contrast, swift ions traversing the samples deposit approximately the same amount of kinetic energy in consecutive steps over the whole diamond thickness. With high probability, they undergo peripheral elastic collisions, in which the incoming and the outgoing particles are identical. At higher projectile velocities (relativistic ions), both elastic and inelastic nuclear reactions with the carbon nuclei take place. Projectile and target (carbon) fragmentation occur, and all particles out of the element range $1 \leq Z \leq Z_{\text{projectile}}$ are simultaneously created and emitted with projectile velocity in forward direction. They are accompanied by a swarm of δ-electrons, fast neutrons, X- and γ-rays. In fact, the heaviest projectile fragments are ejected in a small solid angle of $\pm 3°$ around the beam direction, while lighter projectile fragments and protons occupy the forward 2π solid angle. An isotropic emission of the target fragments (in 4π) is observed. The fragmentation processes of projectile and target nuclei and the following dramatic increase of displacements due to these (slowed down) secondary ions are responsible for the serious damage of solid-state sensors in heavy-ion experiments.

The above picture changes completely in ultrarelativistic nuclear physics environments—as they are for instance, the ALICE experiment at LHC (http://aliceinfo.cern.ch) or the future CBM experiment at FAIR (http://www.gsi.de/forschung/fair_experiments/CBM/index_e.html). The central mission of the ALICE Collaboration is to study the physics of strongly interacting matter at extreme energy densities, where the formation of a new state of matter, the "quark-gluon plasma" (Braun-Munzinger & Stachel, 2007), is predicted by quantum chromodynamics. For this purpose, Pb–Pb collisions at TeV energies are performed, and the produced hadrons, electrons, muons, and photons are the subjects of detection and research. The existence and the properties of this new state of matter are key issues for the understanding of the confinement of quarks in hadrons and of chiral-symmetry restoration. Moreover, it is believed that this was the state of matter of the young universe immediately after the Big Bang.

The reaction products of relativistic heavy-ion collisions are similar to that of the classical particle physics experiments, which are usually performed with colliding proton, antiproton or electron beams. In some cases, all charged particles to detect are moving approximately with light velocity and have atomic number $Z = 1$. Diamond sensors exposed to such MIP (Section 3.17.3.2) have to cope with relatively low damage. However, due to the large momentum transfer to the diamond lattice, numerous knock-on carbon atoms and fragments are created also in that case, which are eventually responsible for the observed degradation of high-energy diamond sensors. The actual status of diamond irradiation studies is discussed in Section 3.17.5.

Photon beams become "attenuated" in diamond either by real photoelectric absorption or by scattering. In real photoelectric absorption, the photons of energies $E\gamma = h\nu < 1$ MeV ionize one shell electron per absorbed photo quantum. Photon scattering is a nonionizing process, by which the photons change their incident direction without excitation of the carbon atoms. Medium-energy photons ($E\gamma$ between 100 keV and 10 MeV) transfer a part of their energy to a shell electron emitting a "softer" photon (Compton scattering). Energetic γ-rays have a significant probability to interact with the carbon nucleus producing "internal pairs"—being nuclear systems consisting of a particle and its antiparticle. The process of "internal-pair conversion" needs the initial γ-energy to be greater than twice the rest mass energy of the particle. For the production of an electron–positron pair, photons of $E\gamma > (2 \times 511)$ keV are needed as the rest mass energy of the electron corresponds to 511 keV.

Since the "real absorption" coefficient decreases with the nuclear charge of the detector material as well as with increasing photon energy, high-Z materials are preferable for the detection of high-energy γ-rays, while diamond ($Z = 6$) is most advantageous for in-situ, distortion-free monitoring of intense X-ray beams (Section 3.17.6.1). Charged particles and photons belong to the category of ionizing radiation, by which a significant part of the energy lost in the diamond is spent in ionization of the carbon atoms. The remaining nonionizing part of the energy loss is released to the diamond lattice (phonon creation). Neutral particles, such as neutrons, do not interact with the shell electrons but with the nuclei of the sensor material. Thermal neutrons ($E_{\mathrm{n}}^{\mathrm{Th}} \approx 0.025$ eV) are easily captured by the nuclei creating nonstable carbon isotopes (^{13}C). They do not damage the lattice since the displacement energy in diamond ($E_{\mathrm{C}}^{\mathrm{Dis}} \approx 45$ eV) is much higher than $E_{\mathrm{n}}^{\mathrm{Th}}$. After elastic scattering with neutrons of 1 MeV $\leq E_{\mathrm{n}}^{\mathrm{Fast}} \leq$ 5 MeV (fast neutrons), the recoiling carbon atoms create vacancies and interstitials but ionization is scarce. In contrast, high-energy neutrons of $E_{\mathrm{n}}^{\mathrm{HE}} > 5$ MeV trigger nuclear reactions leading to the creation of charged secondary particles of appreciable ionization potential, which in turn can be exploited for neutron detection (Section 3.17.6.4).

3.17.3.2 Detector Response to Charged Particles

Ionized electrons are excited from the valence into the conduction band creating an unoccupied energy level (a "hole") in the valence band. The main part of the kinetic energy deposited by ionizing radiation in a diamond crystal is converted to a number of free electron–hole (e–h) pairs along its path (electronic part of the energy loss). A much smaller amount is lost by energy transfer to the carbon nuclei (nuclear part of the energy loss) and by releasing energy to the diamond lattice in form of phonons. The nuclear part of the energy loss is responsible for the radiation damage processes, whereas the electronic part for the detector signal generation, respectively. The ionized e–h pairs can be manipulated by an external electric field overlaid to the internal field of the crystal. Under its influence, the pairs separate and the released electrons and holes move apart toward the detector electrodes, each time in a direction given by the spatial superposition of the external and the actual internal field components. A biased diamond crystal senses that moving charge.

The signal processing applied for timing or spectroscopy measurements is explained in Section 3.17.4.1. The signal size is defined by the electronic part of the specific energy loss (dE/dx) of swift charged particles in matter, which is characteristic for both the impinging ion and the detector material. The parameter dE/dx is also denominated the "stopping power" of the target material for a certain ion. Hans Bethe (1930) and later on Felix Bloch (1933) developed the theory of the slow down of swift charged particles in matter and provided a computation formula for the parameter$-$dE/dx given in Eqn (1):

$$-\frac{\mathrm{d}E}{\mathrm{d}x} = \frac{4\pi}{m_{\mathrm{e}}c^2}\cdot\frac{nZ^2}{\beta^2}\cdot\left(\frac{e^2}{4\pi\varepsilon_0}\right)^2\cdot\left(\ln\frac{2m_{\mathrm{e}}c^2\beta^2}{I\cdot\left(1-\beta^2\right)} - \beta^2\right) \tag{1}$$

with E, the kinetic energy of the particle; $Z\cdot e = Z_{\mathrm{eff}}$, the charge state of the ion; $\beta = v/c$, the ion velocity v related to the velocity c of light; e and m_{e}, the electron charge and mass, respectively; n, the electron density; I, the mean excitation potential of the target; and ε_0, the vacuum permittivity.

Figure 1 shows the stopping power of diamond for randomly selected ions versus the ion energy, given in the typical units of MeV/A, with A, the atomic mass number $A = N_{\mathrm{Protons}} + N_{\mathrm{Neutrons}}$. The physical dimension of MeV/A corresponds to the square of the ion velocity (β^2). The dE/dx data shown in **Figure 1** have been calculated with a recent SRIM code and plotted on the y-axis normalized to the stopping power of diamond for protons. At low ion energies, at which the ions become rapidly neutralized by electron capture ($Z^{\mathrm{eff}} \ll Z$), the specific energy loss increases proportional to β^2. The varying atomic charge state of the ions (as they travel through matter) is the reason for the deviation of the maximum (dE/dx) values from the proton curve. At high velocities, the ions become fully ionized ($Z_{\mathrm{eff}} \sim Z$) and the normalized curve shapes come together up to a complete overlap in the velocity ranges $E/A \geq 1$ GeV at which all shell electrons are stripped ($Z_{\mathrm{eff}} = Z$). The energy loss scales there with Z^2 only.

In a simplified approach, the total kinetic energy loss ΔE of a particle is the integral over the individual dE values calculated for infinitesimal dx steps. Note that concerning the interaction of very slow ions of $E < 300$ keV or that of the very heavy particles over the available energy range, several high-order corrections of

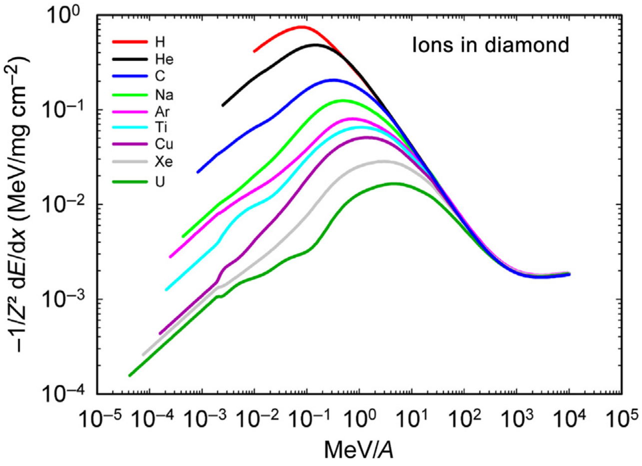

Figure 1 Stopping power of diamond for various ions normalized to the proton data versus E/A, which is proportional to the square of the ion velocity (β^2).

Eqn (1) (not explicitly discussed here) have meanwhile been introduced (Lindhard & Sørensen, 1996; Mikkelsen & Sigmund, 1989). The expected number of e–h pairs is given by the ratio $\Delta E/\varepsilon_{\mathrm{Dia}}$, with $\varepsilon_{\mathrm{Dia}}$ denoting the energy consumed per generated e–h pair. The value of $\varepsilon_{\mathrm{Dia}}$ decreases for better specimens (Alig, Bloom, & Struck, 1980; Gabrysch et al, 2008; Konorova & Kozlov, 1970; Nava et al., 1979)—a finding, which inherently indicates an increasing trend of this parameter for sensors damaged by radiation.

3.17.3.2.1 Energy Needed to Create an Electron–Hole Pair (in Diamond)

The importance of this fundamental quantity in seeking new physics demands specific attention. The first calculations to a theoretical determination of ε have been performed by Niels Bohr (1916). Almost two decades later, Bethe (1930) estimated the average ionization energy I with the help of his formulae describing the stopping power of target materials (Eqn (1)). Bethe's work was followed by a more accurate estimation of Bagge (1937) based on the formulae of Bloch (1933) but showing better experimental evidence. However, the results obtained for different gases have been inconsistent and this inconsistency has been later also found for solids (Mohler & Taylor, 1934, p. 659). The discrepancy between theory and experiment concerning the correlation of ε with the ionization potential I of the detector material motivated Ugo Fano to enter the field. Eventually, Fano demonstrated (in contradiction to the expectation and the theories of Bethe and Bragge) that "the greater the ionization potential, the greater is the share of the absorbed energy which is actually spent in ionization" (Fano, 1946, p. 44). He concluded that "this explains why the ionization potential of a substance has little influence upon the amount of energy that must be absorbed by that substance per each pair of ions actually produced". Fano claimed that first of all, the energy ε must be greater than the ionization potential I since a part of the absorbed energy is always "wasted" for other purposes, in particular "into excitation of optical levels and thus in the production of light". He suggested that most of the energy absorbed by gas molecules does induce dipole oscillations of their electronic charge. Lower frequency oscillations would lead to excitation, those of higher frequency to ionization of the molecules. The sum of the oscillator strengths of all excitation processes in a material would correspond to the "wasted" energy disabled for ionization. By comparing the calculated total oscillator strengths to the ionization potential of selected substances (H, He, and Li), he found a critical inverse correlation, and therefore, the "waste" energy (ε–I) to be an inverse function of I.

Lappe observed a remarkable correlation between ε and the band gap energy E_{G} (Lappe, 1961). At least for the semiconductor materials (Ge, Si, GaAS, CdS, and PbO) investigated at that time, he obtained all ε values to be three times the band gap energy ($\varepsilon_{\mathrm{x}} \sim 3E_{\mathrm{Gx}}$). He suggested that "this observation might have a very general meaning"—which in fact has not been disclosed up to the present day. Shockley (1961) proposed a threshold energy E_{th} below which no pairs can be created; impinging swift particles force then all states below E_{th} to be ultimately populated uniformly. In that case, the average kinetic energy E_{K} lost to the lattice is the average energy of the subthreshold states. In the free-particle approximation, this energy is $E_{\mathrm{K}} = 3E_{\mathrm{th}}/5$, and consequently, ε is twice this loss plus the band gap energy: $\varepsilon = 6E_{\mathrm{th}}/5 + E_{\mathrm{G}}$. Klein (1968) observed a $\varepsilon = 2.8E_{\mathrm{G}}$ assuming

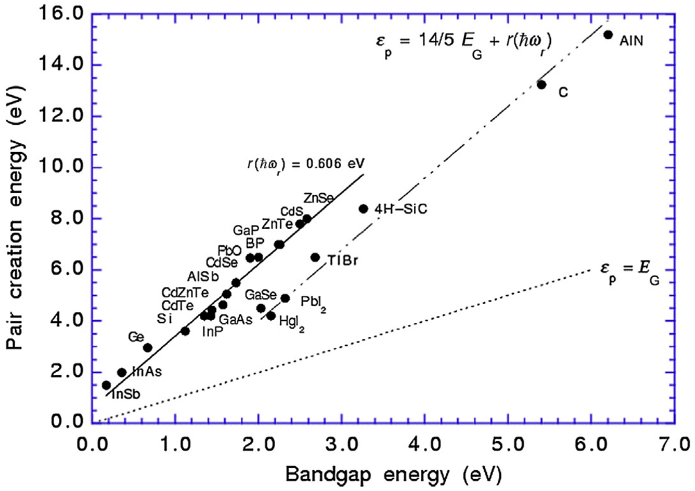

Figure 2 The average energy to create an electron–hole pair as a function of the band gap energy for a selection of semiconductors. Two main bands are evident: the main branch found by Klein (1968) (solid line) and the second one (dashed-dotted line) which fits to the diamond value as well as to the values of other wide band gap semiconductors such as 4H–SiC ($E_G = 3.3$ eV) or AlN (6.28 eV). The dotted line denotes the limiting case when $\varepsilon_p = E_G$ (copyright ESA 2007).

$E_{th} = 1.5E_G$ and noticed that this threshold value is "the most appropriate one". After all, Klein proposed the still used relation given in Eqn (2):

$$\varepsilon = 14/5 \cdot E_G + r(\hbar\omega) \quad \text{with} \quad 0 < r(\hbar\omega) < 1 \tag{2}$$

where $r(\hbar\omega)$ is an adjustable parameter representing the Raman-phonon energies. For various semiconductors, $r(\hbar\omega)$ had been estimated to about 0.5 eV.

Figure 2 shows the largest collection of actual ε values of various semiconductors as published by European Space Agency (ESA, 2007). The data split in two groups, the main branch found by Klein (1968) (solid-line fit) and a second one (dashed-dotted line) fitted with a free parameter $r(\hbar\omega) > 1$, which however is in contradiction to the range predicted by Klein. The quest for an explanation of this striking deviation of ε_{Dia} from the common rule is ongoing. The second branch of the plot suggests another systematic, probably inherent to wide-band-gap materials. At least, the ε values (here ε_p) of several semiconductors with energy gaps larger than 2 eV (e.g. 4H–SiC and aluminum nitride (AlN)) fit also to this line.

3.17.3.2.2 Interdependence of ε and the Fano Factor F

The ionization produced by a swift charged particle in a sensor corresponds to its total kinetic energy loss in the detector, which can be used further for particle identification (PID) (Z and E measurements). The significant contribution of Fano with respect to radiation detectors is the theoretical description of the stochastic nature of the ionization process and the resulting theoretical limits for the best possible energy resolution, which eventually defines "the accuracy limits of that measurement method" (Fano, 1947). Fano postulated a correlation of the consecutive ionization events for the case in which the total kinetic energy loss ΔE of a particle of energy E is constant. This condition is always fulfilled when ions are stopped in a sensor ($\Delta E = E$), and never, in the case of relativistic ions flying through the sensor while losing only a small part of their kinetic energy in the counter. If the energy lost by an ion was completely converted to ionization in totally correlated consecutive steps, the fluctuation of the number of generated electrons would be zero $\langle (N - N_0)^2 \rangle = 0$ (for $N = N_0$) and ε would obey the simple equation $\varepsilon = \Delta E / N_0$. In the other extreme case, in which the competing energy-loss mechanisms contributing to ΔE are completely uncorrelated, Poisson statistics apply. In that case, the corresponding variance of N changes to $\langle (N - N_0)^2 \rangle_{AV} = N_0$. However, the energy and momentum conservation correlates the lattice excitations (phonon creation) with the ionization; in other words, no one of these two pictures describes the case of a real detector. The different competing processes modify the fluctuation of N. If all impacts J occur under the same conditions, both the average number of ionizations (n_{AV}) and the average energy loss ΔE_{AV} would be equal in each impact. The total number of ionizations is then given by the sum over all impacts, and the sum of the energy-loss contributions of each step yields the total energy loss ΔE. For a constant number of single-particle impacts $J = N_0/n_{\mathrm{AV}} = \Delta E/\Delta E_{\mathrm{AV}}$, the variance of N is given by

$$\left\langle \left(N - \frac{\Delta E}{\varepsilon}\right)^2 \right\rangle_{\mathrm{AV}} = J \cdot \left\langle \left(n - \frac{\Delta E}{\varepsilon}\right)^2 \right\rangle_{\mathrm{AV}} = F \cdot N_0 \qquad (3)$$

$$\text{with } F = \frac{\left\langle \left(n - \frac{\Delta E}{\varepsilon}\right)^2 \right\rangle_{\mathrm{AV}}}{n_{\mathrm{AV}}} \qquad (4)$$

where F is denominated the "Fano factor". It defines the variance-to-yield ratio, which varies from 0 to 1 for perfect to highly defective sensors, respectively. F and ε are the correlated parameters (Eqn (4)) predicting the spectroscopic properties of a crystal counter; both are decreasing with improving crystal quality.

To our knowledge, no experimental value of the Fano factor of CVD-diamond sensors has been established up to present. This is most likely due to the correlation of F and $\varepsilon_{\mathrm{Dia}}$ and the varying $\varepsilon_{\mathrm{Dia}}$ values observed for different sample qualities. In an extended theoretical study with various semiconductors (including natural IIa diamond), Alig et al. (1980) compared the calculated and the experimental values of ε and F for 16 different solid-state materials. The theoretical parameters obtained for diamond have been $\varepsilon_{\mathrm{Dia}} = 11.6$ eV and $F_{\mathrm{Dia}} = 0.08$, respectively. The authors confirmed the earlier experimental results of Konorova and Kozlov (1970), who anticipated that the measured values of $\varepsilon_{\mathrm{Dia}}$ decrease along with the improvement of the CCE of the newer samples tested. Accordingly, the $\varepsilon_{\mathrm{Dia}}$ and F_{Dia} values published by Alig et al. belong to diamond samples of excellent quality. In fact, more recent data obtained from Element Six scCVD diamond samples showed also a steady decrease of $\varepsilon_{\mathrm{Dia}}$ with every new batch of production: March 2005, $\varepsilon_{\mathrm{Dia}} \sim 17$ eV (Pernegger et al., 2005); September 2005, $\varepsilon_{\mathrm{Dia}} = (12.84 \pm 0.04)$ eV (Pomorski et al., 2005); March 2008, $\varepsilon_{\mathrm{Dia}} = (11.81 \pm 0.59)$ eV (Gabrysch et al., 2008).

3.17.4 Basic Diamond Assemblies

The potential of a diamond detector depends in equal shares on the crystal quality of the sensing diamond and on the characteristics and performance of the front-end electronics (FEE) used for the signal processing. One has therefore to consider rather the behavior of the "assemblies"' consisting of the sensor setup and the FEE and not solely the properties of a single diamond sample. In the following, we discuss the crucial components and the operation principles of the two basic categories of diamond assemblies: the timing and the spectroscopy setups. Strip and pixel assemblies operate according to the same principles. However, instead of the single-channel FEE presented in the next paragraph, application-specific integrated circuits (ASICs) have to be used for the multichannel readout.

The radiation parameters to be measured are defined by the aspired physics goals of the particular envisaged experiment. These can be one or all of the following quantities: the kinetic energy E and the nuclear charge Z of an impinging particle, the time and position in which the particle (or a group of particles) passes the sensor, and the total number of particles impinging on the sensor in a given time interval. Sensors used for charge, energy or position measurements based on charge-sharing techniques belong to the category of "spectroscopy detectors". All others are regarded as "fast" detectors, belonging to the category of applications for which the precise measurement of the radiation-induced charge is not of particular importance. These are the detectors used for particle counting and timing. The proper quality and thickness of the diamond sensor has to be optimized with respect to the acceptable material budget, the anticipated signal strength at that sample thickness, and the noise of the appropriate FEE required.

3.17.4.1 Front-end Electronics and Signal Processing

Figures 3 and 4 show the schematics of single-channel assemblies used for timing and spectroscopy, respectively. In both cases, the sensing diamonds are represented by the detector capacitance C_{D} and a current source I_{tr} (dashed boxes). The peculiarities of each type of amplifier will be described later on. For the moment, we assume a detector circuit consisting of a defect-free diamond sensor of parallel-plate geometry and thickness d_{D}, biased with constant voltage V_{b} through a bias resistor R_{b}. In the equilibrium state, the internal electric field is constant and equal to the external field $E_{\mathrm{D}} = V_{\mathrm{b}}/d_{\mathrm{D}}$. Under the influence of the internal field, the e–h pairs generated along the path of the impinging ionizing radiation in the diamond sensor separate and the liberated

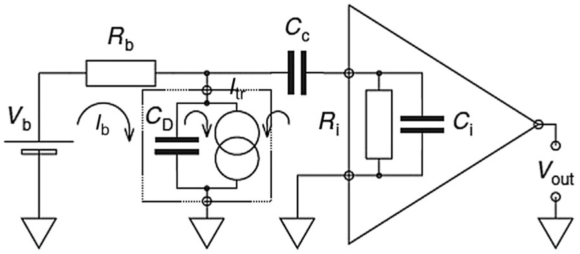

Figure 3 Schematics of a single-channel diamond broadband assembly for particle timing and counting. The sensing diamond is illustrated by the detector capacitance C_D and a current source I_{tr} (dashed box). Whenever an ionizing particle impinges the diamond sample, a transient current $I_{tr}(t)$ flows through the circuit and into the voltage/current amplifier. Reprinted from Berdermann and Ciobanu (2009).

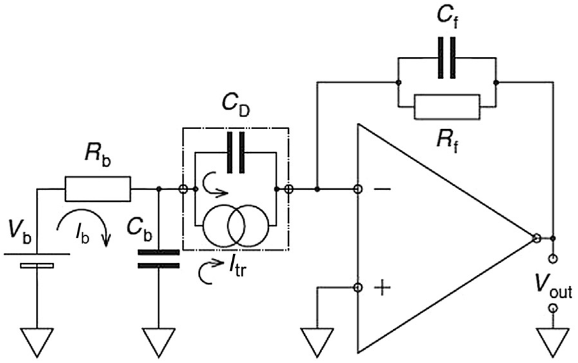

Figure 4 Schematics of a charge-sensitive diamond assembly as it is used for high-resolution energy spectroscopy. As in **Figure 3**, the diamond sensor is replaced by an equivalent circuit, consisting of the detector capacitance C_D fed by a current source $I_{tr}(t)$. The particle-induced current $I_{tr}(t)$ is fully integrated at the feedback circuit (R_f--C_f) connecting the output with the input of the amplifier. Reprinted from Berdermann and Ciobanu (2009).

electrons and holes drift apart to the corresponding attractive electrode. According to the Shockley–Ramo theorem (Shockley, 1938; Ramo, 1939), a charge Q_G which moves with constant velocity v_{Dr} in a homogeneous electric field between two parallel-plate electrodes at distance d_D induces a constant current $I_0 = Q_G \cdot v_{Dr}/d_D$. The detector capacitance C_D discharges with the separation of the e–h pairs (at $t \approx 0$) and the pulse $dQ_C(t)/dt = I_{tr}(t)$ sensed by the electrodes rises to its maximum value (signal amplitude I_0). At the end of the charge drift ($t = t_{tr}$), C_D slowly recharges (signal decay). The power supply compensates the consumed charge by feeding a current I_b until the excited circuit has returned to its equilibrium state.

The transient current pulse $I_{tr}(t)$ appearing at the amplifier input is given by the following equations (Spieler, 1982):

$$\begin{aligned} I_{tr}(t) &= I_0 \cdot \left(1 - e^{-t/RC}\right); \quad \text{for} \quad 0 \le t \le t_{tr} \\ I_{tr}(t) &= I_0 \cdot \left(e^{t_{tr}/RC} - 1\right) \cdot e^{-t/RC}; \quad \text{for} \quad t_{tr} \le t \le \infty \end{aligned} \tag{5}$$

with $I_{tr}(t)$, the total transient current sensed by the electrodes in the time between circuit excitation and relaxation, t_{tr}, the charge transit time, and RC the time constant of the measurement system.

The parameter $C = C_D + C_i + C_P$ represents the sum of all circuit capacitances and $R = R_b \cdot R_i/(R_b + R_i)$ the sum of R_b and R_i. C_p (not shown in the schematics) is the contribution of the parasitic capacitances of the assemblies. The ultrafast original diamond signal is composed of a continuous frequency-dependent amplitude spectrum dominated by very high frequencies. The characteristic of the readout is defined by the relation of the charge transit time t_{tr} to the time constant RC of the circuit (Eqn (5)). Aiming at best time resolution and rate capability, a time constant $RC \ll t_{tr}$ is needed to reproduce the original rise time and width of the diamond signals. Peter Moritz (1998, 2001) developed an appropriate diamond broadband amplifier (DBA) as an AC-coupled low-noise low-impedance (50 Ω) device with a large bandwidth (BW) ranging from 1 MHz to 2.3 GHz. The DBA has a relatively low capacitance $C_i \sim 2$–5 pF, which provides input time constants R_iC_i from

100 to 250 ps. The capacitor C_C couples the transient current pulse $I_{tr}(t)$ to the amplifier and blocks in addition possible DC current components (for instance, dark currents). The DBA output signal is the voltage drop $v_i(t)$ over the amplifier's input impedance R_i, amplified by a (voltage) gain G_A, which can be tuned from 1 to 140: $v_{out}(t) = G_A \cdot I_{tr}(t) \cdot R_i$. The subsequent pulse height selection for time measurements is performed with fast "leading edge (LE)" discriminators, capable of processing high particle rates. In order to achieve high-detection efficiency and to minimize the significant time walk of signals disturbing the time resolution, the discriminator threshold of inhomogeneous detectors showing large variation of signal pulse-heights (Section 3.17.4.3.8) has to be set "just above noise".

For precise energy measurements with diamond detectors, "charge-sensitive amplifiers" (CSA, **Figure 4**) are used, which have been originally developed for silicon-diode detectors. In contrast to the broadband amplifiers, the bias loop of a CSA consists of a high-bias resistor R_b (between 100 MΩ and 1 GΩ) and a large capacitor $C_b \gg C_D$ transferring the noise of R_b to the ground. An operational (op) amplifier performs integration of the induced current $I_{tr}(t)$ at a feedback circuit ($R_f - C_f$) connected between the output and the input of the op-amplifier. Such devices are high-gain high-input-impedance amplifiers with an open loop gain A_0, which is the gain obtained without feedback circuit. Note that an ideal op-amplifier would have infinite A_0 but the feedback circuit reduces the total gain of the device to a reasonable value. The (still) very high gain of the op-amplifiers is advantageous for the amplifier sensitivity and therefore, for the general performance of the detector assembly. The equivalent amplifier input parameters can be calculated from the equations: $R_i = R_f/(1 - A_0)$ and $C_i = C_f(1 - A_0)$, respectively (Johns & Martin, 1997). Using for instance realistic parameters of state-of-the- art spectroscopy amplifiers ($R_f = 1$ GΩ, $C_f = 1$ pF, and $A_0 = -10{,}000$), one can estimate an $R_i = 100$ kΩ and a $C_i = 10$ nF. The resulting time constant $R_iC_i = 1$ ms is then much longer than the transition time t_{tr}, which is usually in the nanosecond range. The induced current is fully integrated at the feedback capacitance C_f and the amplitude of the output signal obeys Eqn (6):

$$v_{out-peak} = \frac{\int I_{Tr}(t)\mathrm{d}t}{C_f} = \frac{Q_C^{(e,h)}}{C_f} \tag{6}$$

In order to proceed for energy/energy-loss/charge measurements, the CS preamplifier signals have to be post-amplified and shaped. The output signals of the shaping amplifiers have no similarity with the original transient current signal shape. However, the analysis of the signal amplitudes with high-resolution peak-sensing ADCs provides (after adequate calibration) a precise measurement of the ion energy/energy-loss spectra corresponding to the ion-induced charge distributions.

3.17.4.2 Time and Energy Resolution—the Signal-to-Noise (S/N) Ratio

The time and the energy resolution of an assembly are strongly affected by the ratio of the particle-induced signal (S) to the noise signal (N) of the setup. There are mainly two types of noise to consider: "thermal noise," produced by the movement of electrons in the resistive elements of the detector circuit and "shot noise," appearing in an active device when a fluctuating number of charge carriers traverse a pn-junction. Both noise types are nonimportant for diamond sensors: due to the wide band gap of diamond, the dark current (thermal noise) is negligible over a wide temperature range, and due to the absence of a pn-junction, the shot noise is negligible as well. Consequently, the S/N ratio of diamond assemblies is usually limited by the noise of the FEE.

Based on the early work of Spieler (1982), recent extended analytical calculations as well as new simulations have been published by Ciobanu et al. (2011), which concern the optimization of the S/N ratio and of the time resolution of CVD-diamond detectors for fast MIP timing.

The time resolution (σ_t) of an assembly is given by Eqn (7):

$$\sigma_t = \frac{\sigma_n}{\mathrm{d}v/\mathrm{d}t} \tag{7}$$

where $\sigma_n = \sqrt{(k \cdot T \cdot C)}$ is the dispersion of the noise voltage; dv/dt, the slope of the signal's LE at discriminator threshold, k, the Boltzmann constant, T, the temperature and C_D, the detector capacitance.

Since the charge generation in diamond is much faster than the time constant of any actual amplifier, the maximum slope at the amplifier output can be estimated to $\mathrm{d}v/\mathrm{d}t = 0.8 \times S/t_{r\_A}$, with t_{r_A} the amplifier rise time (10–90% amplitude level). The rise time of an amplifier of bandwidth BW_A is estimated by $t_{r\_A} = 0.35/BW_A$ and hence, $\mathrm{d}v/\mathrm{d}t = 2.28 \cdot Q_C \cdot BW_A/C_D$. By inserting $\mathrm{d}v/\mathrm{d}t$ in the formalism giving the time resolution (Eqn (7)), one obtains Eqn (8):

$$\sigma_t = \frac{\sqrt{k \cdot T \cdot C_D}}{2.28 \cdot Q_C \cdot BW_A}. \tag{8}$$

The absolute energy resolution is defined by the line width (δE) of the pulse-height distribution of a monoenergetic charged particle, measured with charge-sensitive assemblies of a low bandwidth, and thus, of significantly lower noise compared to the timing setups. The inherent narrow Gaussian lines broaden due to the influence of different parameters. The total width (δE_{Sum}) measured includes contributions due to crystal structure defects and due to the FEE noise

$$\delta E_{Sum} = \sqrt{\delta E_G^2 + \delta E^2 + \delta E_{Dia}^2 + \delta E_{noise}^2} \tag{9}$$

with δE_G representing the statistical fluctuations in the charge-generation processes, δE, the energy-loss straggling caused by different impact parameters, δE_{Dia}, the term related to the diamond crystal quality, and δE_{noise}, the FEE contribution.

The fluctuations in the charge-generation contribute very little to the spectral width; this is due to the relation $\delta E_G = \sqrt{F \cdot \varepsilon_{Dia} \cdot \Delta E}$, where F and ε_{Dia} are the Fano factor and the energy to create an e–h pair in diamond. Spectral lines revealing after subtraction of the noise contribution and width in the order of the tabulated energy-loss straggling δE indicate excellent spectroscopic properties of the detector material. The energy resolution is one of the most sensitive figures of merit for the characterization of a detector material. A narrow width postulates defect-free crystal structure, which implies a high drift velocity of the charge carriers as well (Berdermann et al., 2008).

Homoepitaxial scCVD diamond is presently the only sensor material capable of serving both fast timing and precise energy-loss spectroscopy applications. In case of MIP measurements, however, the FEE has to cope with very small signals, which is a consequence of the high energy needed to create one e–h pair in diamond (about four times higher as compared to the silicon value). Vice versa, in heavy-ion measurements, the FEE has to support a fast collection of charge in order to avoid pulse-height defects, which are a crucial unavoidable drawback of the silicon detectors.

3.17.4.3 The Sensing Diamond

The majority of diamond-radiation sensors consist of intrinsic diamond films providing the opportunity to utilize the inherent electronic and optical properties of undoped diamond (Field, 1979, 1992; Kania, Landsrass, Plano, Pan, & Han, 1993; Manfredotti, 1998). A low atomic mass number ($A = 12$) and nuclear charge ($Z = 6$) predestinate diamond sensors for low-background implementations in complex spectrometers, while the almost equally high drift velocities of electrons and holes (Section 3.17.4.3.6) in conjunction with the low dielectric constant and a high breakdown field enable unrivaled high-speed counters.

The crystal structure of a diamond sample predicts its potential for a specific application category. Whereas, in time measurements, detectors with structural defects or rest impurities are acceptable (as long as the S/N ratio is sufficiently high), only the ultrapure, homoepitaxial diamond plates can be used for energy-loss spectroscopy or for any other application, in which the amplitude of the detector signal is used to discriminate different particles.

3.17.4.3.1 Crystal Structure

The images shown in **Figure 5** reveal the peculiarities of the crystal structure of the three types of CVD diamond considered for detector applications. On the left-hand side are shown the images of homoepitaxial scCVD diamond samples, in particular a birefringence image obtained by cross-polarizer microscopy on the top-left and a white-beam X-ray topograph on the bottom-left picture respectively. The birefringence images displayed on the right-hand side of the figure have been obtained from a heteroepitaxial film grown on an iridium substrate (Schreck, 2009) (top-right) and from a standard heteroepitaxial sample grown on silicon (bottom-right). The cross-polarizer images are directly comparable since they have been recorded at the same

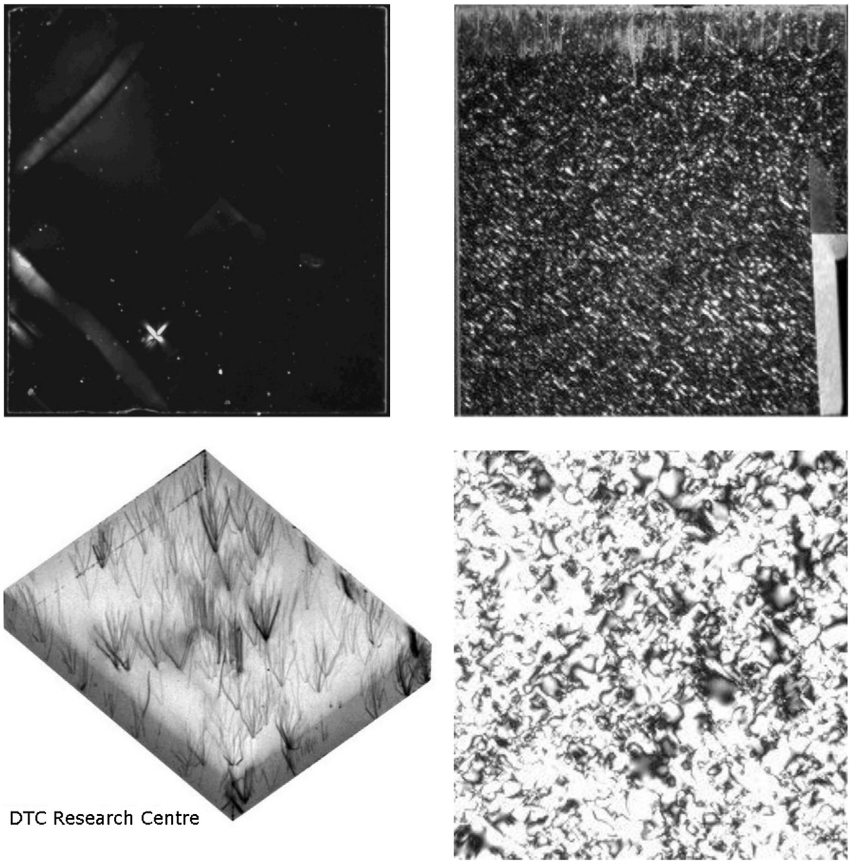

Figure 5 Crystal structure of typical CVD-diamond sensors. (a) Birefringence image and (b) white-beam Laue topograph of scCVD diamond samples. A dangerous threading dislocations (bright-cross structure) become clear in high-resolution X-ray topographs, where the diamonds are tilted relatively to the beam axis (Gaukroger et al., 2008) Birefringence images of (c) DoI and (d) pcCVD diamond, respectively.

magnification with the same optical system. Hereby, the dark areas indicate optically isotropic material, whereas the bright features point to extended structural defects. In contrast to the birefringence images, in X-ray topographs, the structural defects are reproduced as dark motives (bottom-left picture) and perfect crystal regions as bright areas.

The birefringence image of the scCVD diamond (top-left) confirms an almost defect-free single-crystal structure of little stress and strain. However, the striking bright cross-like defect at the bottom-left part of the image is the fingerprint of a bundle of threading edge dislocations (Pinto & Jones, 2009), the peculiarities of which are illustrated in more detail by high-resolution X-ray topography (bottom-left picture). Martineau et al. (2004) were the first addressing legitimate concerns about these kinds of isolated structural defects in scCVD diamond, which appear mostly along the 001 crystal direction and (actually) in concentrations up to $10^5/\text{cm}^2$. Threading dislocations are the prolongation of surface imperfections of the HPHT substrates used for the epitaxial growth. They act as nonradiative recombination centers (Martineau, Gaukroger, Khan, & Evans, 2009 as cited in Pinto & Jones, 2009) and contain nitrogen impurities (Mora et al., 2005). However, most dangerous for detector applications are the erratic currents observed from such defects (Yang et al., 2005). An increased susceptibility to a sudden detector breakdown has been suggested in conjunction with rough sample surfaces (Morse, Salomé, Berdermann et al., 2008).

The cross-polarizer image of present DoI material (top-right) reveals a homogeneously distributed high dislocation density, which is a consequence of the otherwise advantageous dense nucleation of DoI. The relatively dark coloration of the image indicates less birefringence strength of DoI films compared to that of heteroepitaxial diamond grown on silicon (bottom-right). The structure of the latter is a typical polycrystalline texture consisting of single-crystal grains surrounded by grain boundaries. It is not clear (at present) whether the DoI dislocations behave electrically like highly oriented grain boundaries as in pcCVD diamond or as nonthreading edge dislocations as in homoepitaxial scCVD diamond. However, they contribute very little to the dark conductivity of DoI samples, as will be demonstrated later on.

Nowadays, one can classify as of "spectroscopic grade" quality selected natural diamonds or homoepitaxial scCVD diamond plates. Since a perfect crystal structure does not mask the disadvantage of impurities, nonselected HPHT materials cannot be used for particle detection (Berdermann et al., 2004). It can be assumed that improved DoI sensors of reduced dislocation density will also be approaching the performance required for ion spectroscopy. Contrary to this believe, even best "detector-grade" pcCVD diamond samples will definitely not be considered for such measurements. This conclusion applies also for MIP-timing applications (Section 3.17.6.3) as well as for experiments with highly focused beams (either particles or X-rays), where the presence of grain boundaries leads to "dead" regions of significantly reduced detection efficiency.

3.17.4.3.2 Contact Issues

An ideal detector electrode blocks the injection of charge into the diamond bulk while providing an effective and fast extraction of the charge generated by the impinging particle. Theoretical predictions concerning the best choice of metals and procedures for the contact preparation of diamond sensors have been not always experimentally confirmed or they have been seldom realized. Undesirable contact effects arise from space charges accumulated in the diamond surface–contact interface (Nebel, Münz, Stutzmann, Zachai, & Güttler, 1996). The width and polarity of the space–charge layer depends on the type and quality of the diamond material. The charge accumulation seems pronounced in measurements of short-range radiation (such as ^{241}Am-α-particles or UV photons), in which the charge generation occurs close to the irradiated contact.

In praxis, it is difficult to distinguish bulk polarization from contact effects. Nebel, Stutzmann, Lacher, Koidl, and Zachai (1998) depicted the space–charge generation in the bulk as shown in **Figure 6(a)**. They claimed that a space charge is generated due to the partial extraction of the radiation-induced charge and the subsequent charge trapping of the moving charge carriers in bulk defects. However, if a charge-trapping barrier has been built beneath the contact–diamond surface interface, a space–charge layer can be accumulated in this region—even in the case of a defect-free diamond bulk. The built-in field is opposed to the external field and can be easily detected in the short-circuit mode sketched in **Figure 6(b)**.

Figure 7 shows the two typical photocurrent transients generated by laser excitation in a pcCVD diamond sensor: signal (a) has been recorded at an electric field $F = 1.2 \times 10^3\ \mathrm{V\,cm^{-1}}$ and signal (b) 1 s after signal (a) with the sensor at zero bias, respectively. About 20% of the laser induced charge was trapped, which is an extremely large amount of space charge pointing rather to a low-bulk quality than to a contact effect.

Homoepitaxial single-crystal detectors of intrinsic bulk and surface quality (Ristein, 2004) are almost free of space charge and their performance is not influenced from the metal used for the electrodes (Berdermann, Pomorski, et al., 2010). It is anticipated that carbide-forming metals lead to an ohmic behavior and non-carbide-forming metals to a blocking characteristic, respectively. However, in most of the cases, the result is unpredictable. Nonetheless, as long as the high-field stability of the detector is preserved, its general detection properties are dominated by the bulk and not the contact properties.

Tachibana, Williams, and Glass (1992, 1992a) investigated non-carbide-forming (gold) and carbide-forming (titanium) metals on pcCVD diamond surfaces cleaned by different procedures including a step of argon glow

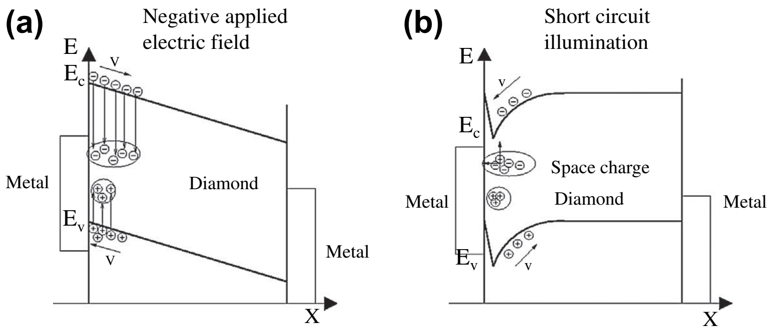

Figure 6 (a) Space–charge generation and (b) detection in the short-circuit mode. Due to charge generation in the vicinity of the irradiated contact one type of carriers (holes) is partially extracted, whereas the other is driven deeper into the bulk and trapped, giving rise to immobile space charge. Reprinted from Nebel (1998).

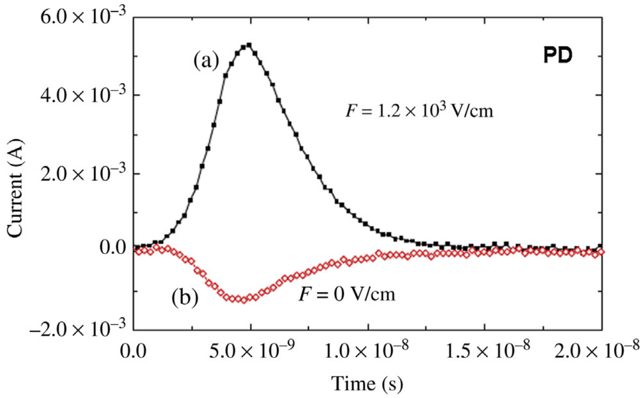

Figure 7 Deep trapping of carriers in undoped pcCVD diamond in undoped pcCVD diamond (in plot: PD). Transient photocurrents at $T = 300$ K with (a) applied electric field and (b) in short-circuit mode (at zero bias) 1 s after signal A. Reprinted from Nebel (1998).

discharge. Independent of the surface pretreatment, the application of "as-deposited" gold contacts led reproducibly to ohmic *I*–*V* characteristics, whereas a rectifying behavior of the gold contacts was measured after glow discharge with subsequent annealing. It was concluded that the argon bombardment creates a graphitic layer on the diamond surface, which once annealed disappears—probably due to absorption into the gold film. Omitting the argon treatment, the "as-deposited" titanium contacts were rectifying, most likely due to the weak interaction with the diamond surface. They became ohmic after annealing with and without previous glow discharge. In this case, the carbide formation at the interface layer creates electrically active defects, which lower the barrier height of the metal and increase the leakage current. In fact, a decrease of the Schottky barrier height from 1.3 to 0.8 eV was observed after annealing.

A further property that influences the behavior of the electrodes and the sample conductivity is the atomic reconstruction of the diamond surface (Ristein, 2004) and the resulting surface density of states. A group leaded by Milos Nesladek tested the application of pure aluminum on both oxygen-terminated (Deferme, Tanasa, Amir et al., 2006) and hydrogen-terminated (Nesladek, Bogdan, Deferme, Tranchant, & Bergonzo, 2008) scCVD diamond surfaces. The *I*–*V* curves measured in this study are shown in **Figure 8**. An extreme ohmic behavior was measured in the case of an O-termination of the sample (blue triangles) and a complete blocking characteristic after H-termination (red solid line). The authors concluded that O-termination creates more defect states in the surface band gap compared to the clean H-reconstruction and suggested that the lower density of states prevents the tunneling of charges to the surface states.

The extended studies on contact issues found in literature are still not conclusive. Moreover, they are a source of confusion when evaluating differently a single case. For example, several authors describe the Cr–Au contact

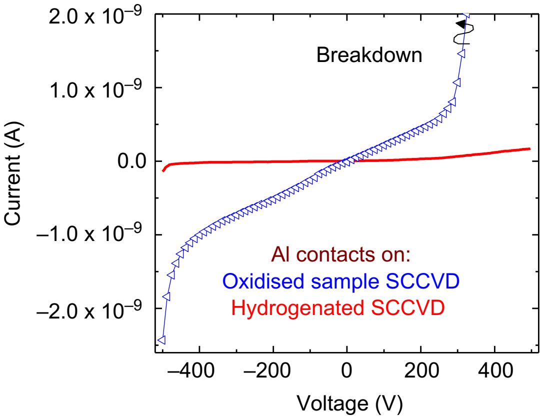

Figure 8 I–V characteristics of an IMOMEC scCVD diamond sample with hydrogenated (red data) and oxidized surfaces (blue data) as discussed in the text. The expected blocking behavior of aluminum on the H-terminated diamond surfaces is convincingly demonstrated in this measurement. Reprinted from Nesladek, Bogdan, Deferme, Tranchant, and Bergonzo (2008).

on diamond as of Schottky behavior with a barrier height of 3.8 eV (e.g. Nebel et al., 1998). Other authors, however, stated an ohmic characteristic (Mainwood, 2000; Galbiati, 2009). In most reports, ohmic contacts are recommended for radiation detectors. In contrast, the above study of Nesladek and coworkers showed that, although the oxidezed sample of more defective surface behaved "more ohmic" than the "clean" H-reconstructed diamond of complete blocking characteristics, the latest showed less charge trapping.

Fact is that diamond sensors have to be of high bulk and surface resistivity enabling high-field operation at negligible leakage current. No capacitance decrease (characterized by the decrease of the rms noise of charge-sensitive preamplifiers by increasing the detector bias) is detectable for intrinsic diamond sensors with any contact—which would be the ultimate confirmation of an active junction. Pomorski et al. (2005), Pomorski (2008) was (at that time) probably the first who characterized more than 30 excellent scCVD diamond sensors from Element Six, metalized with a variety of different electrodes on O-terminated surfaces. He tested Ti/Pt/Au and Cr/Au contacts, the pure metals Al and Pd as well as nominally mixed (Schottky/ohmic) electrodes. All samples were first treated with wet chemistry and afterward they were exposed to oxygen plasma and argon glow discharge before metallization (sputtering). Where appropriate (e.g. for Ti/Pt/AU; Cr/Au contacts), an annealing step after the sputtering was applied in addition. Pomorski detected neither different dark current characteristics of the diamond sensors nor significantly varying charge-collection and timing properties.

3.17.4.3.3 Dark Conductivity

In order to exploit the extraordinary physical properties of pure diamond, the majority of present sensors consist of intrinsic diamond plates. Based on the wide band gap energy of diamond ($E_G^{Dia} = 5.45$ eV) and the corresponding constraints $T_{\text{Ionization}} \sim 30.000$ K and $E\gamma > 3.27$ eV, respectively, it is possible to operate diamond detectors at RT and in natural daylight. However, as Nebel (2003) noticed "no truly intrinsic diamond with conductivity activation energies of about 2.5 eV expected for the large band gap is available". The dark conductivity of the sensing films generates a DC current in the circuit of biased samples, which affects the particle-induced signal and increases the electronic noise. The absolute values of the dark currents measured are low (tens of picoamps) and usually of minor importance. However, a high breakdown field is required for good detector operation, which is not always provided. The structural defects described in the previous paragraph may limit significantly the resistivity of the intrinsic diamond crystals and may therefore be responsible for increasing dark currents at relatively low detector bias. It is known that electric fields of $E \approx \pm 1$ V/μm are sufficient to (almost) saturate the charge-carrier drift velocities during the detection of MIPs (Weilhammer, Adam, Bauer et al., RD42 1998). In contrast, such values are considered as rather low for the operation of heavy-ion sensors, which have to cope with the strong signals generated by heavy charged particles in solid matter (Berdermann et al., 1999). Due to a temporary field screening, the performance of both spectroscopy and timing assemblies at low bias is highly deteriorated. Ultrafast collection of charge is required, which can only be provided at very high electric fields.

Figures 9–11 show the RT dark current–electric field characteristics $I_D(E_D)$ of arbitrary electronic grade pc, sc, and DoI CVD-diamond sensors, respectively. All samples are prepared with sandwich electrodes on oxygen-terminated surfaces (wet chemistry followed by an additional oxygen plasma treatment). In order to study the influence of the diamond surface and of the contact properties to the detector performance, different finishing processes were tested (mechanical polishing or ion-beam milling plus etching). In addition, different single-metal or metal multilayers sputtered on both sides have been probed for the electrodes. The unpolished "as grown" pcCVD-diamond sensors of **Figure 9** were metalized with Cr–Au (50/100 nm) contacts, annealed for 10 min at 500 °C in an argon atmosphere. All scCVD diamond films (**Figure 10**) were covered with "as-deposited" pure aluminum (100 nm) on ion-beam polished, resin-wheel polished, or scaife polished surfaces.

The DoI sensor was equipped with annealed Ti/Pt/Au (50/50/100 nm) electrodes, which nominally form ohmic contacts due to the creation of a carbide interface layer.

The $I(E_D)$ characteristics were measured using sensitive Keithley electrometers, while the samples were kept in the dark within electrically shielding boxes floated with nitrogen (to avoid humidity). The dark currents obtained from the three types of detector-grade CVD diamond differ by several orders of magnitude, showing similar values ($\sim 10^{-12}$ A) for the scCVD diamond and the DoI samples, and about two to three orders of magnitude higher currents for the pcCVD-diamond sensors ($\sim 10^{-9}$ A). However, similar undesirable features are obvious in all cases. Both the asymmetric shapes of the curves at reversed bias polarity and the breakdown fields seem to be arbitrary, suggesting another source but the contacts as the origin of these phenomena. Deeply trapped charge is more or less evident in most of the presented measurements, which is revealed through the characteristic hysteretic behavior in the corresponding data. Asymmetric $I_{\text{Dark}}(\pm E_D)$ curves indicate inhomogeneously distributed donor and acceptor defects or lopsided Schottky contacts. The detector-grade DoI layer

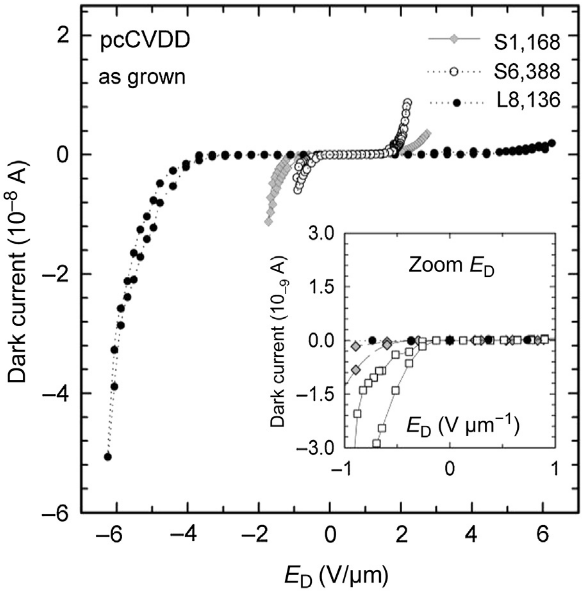

Figure 9 $I_D(E_D)$ characteristics of arbitrary pcCVD-diamond detectors supplied by DDL. The samples are metalized with Cr–Au electrodes on as-grown (unpolished), oxygen-terminated diamond surfaces. Reprinted from Berdermann et al. (2010).

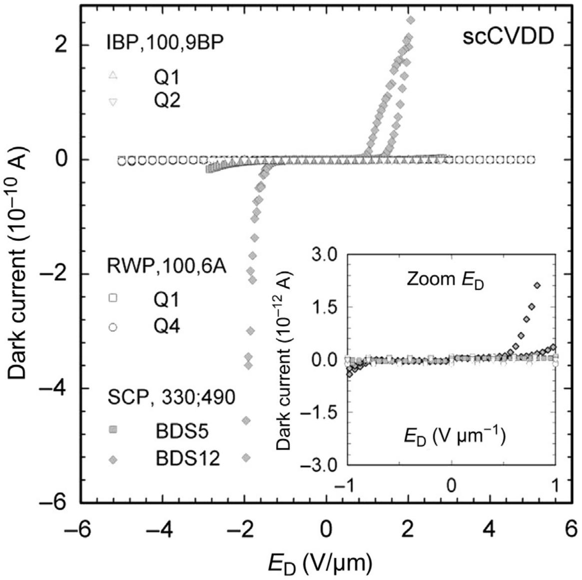

Figure 10 $I_D(E_D)$ characteristics of arbitrary scCVD diamond sensors supplied by DDL. The oxidized samples are postprocessed with different protocols (see text) and metalized with pure aluminum Schottky contacts. Reprinted from Berdermann et al. (2010).

was grown on top of a ~1-mm-thick DOI substrate. After growth, the substrate was separated by laser cutting from the detector film by removing simultaneously several tens of micrometers DOI matter from the nucleation side. It has been suggested that the relatively low dark conductivity found in the DOI sensors is most likely due to the compensation of shallow traps by electron injection through the ohmic contacts (Berdermann, Pomorski, et al., 2010). However, this statement has to be confirmed with more recent samples.

The behavior of the dark resistivities of various nominally intrinsic diamond samples obtained in the temperature range $10\,°C < \Delta T < 1000\,°C$ is plotted in **Figure 12** (Nebel, 2003).

There are compared data of two HPHT diamonds, types IIa and Ib, respectively, to the behavior of two pcCVD films noticed in the figure as “PCD”. As expected, the IIa sample reveals a higher resistivity. Surprisingly however, at sufficient high temperatures, the activation energies (E_{act}) of both HPHT samples (of quite different

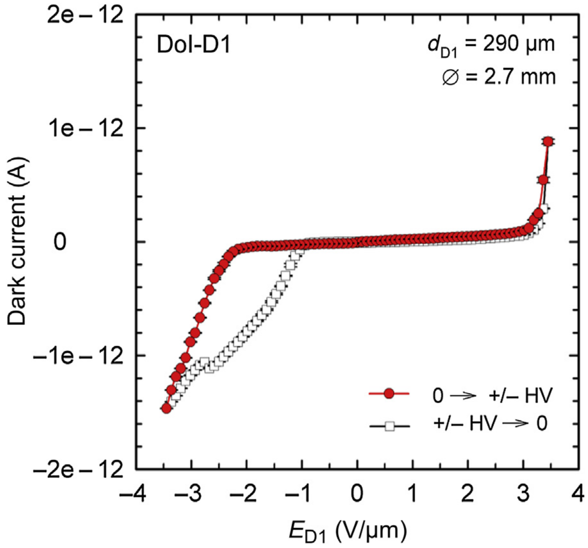

Figure 11 $I_D(E_D)$ characteristics of a CVD-diamond sensor grown on an Ir/YSZ/Si(001) substrate and metalized with annealed Ti–Pt–Au electrodes. Both, the *I–E* hysteresis at negative bias and the order of magnitude of the measured currents are similar features to that obtained occasionally also from scCVD diamond films.

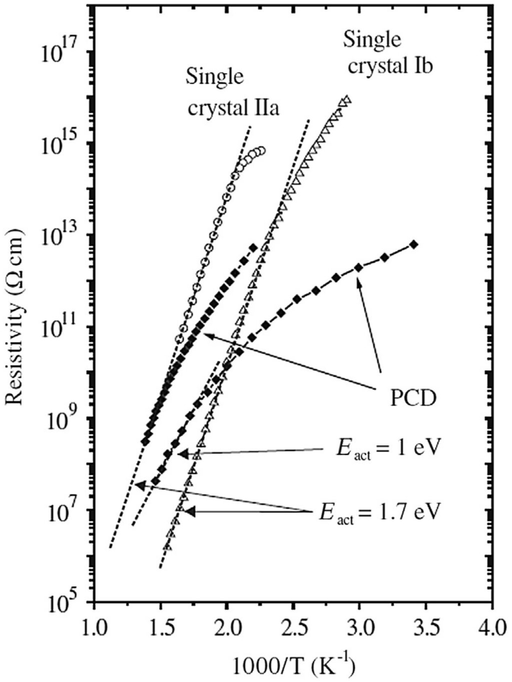

Figure 12 Temperature-dependent dark resistivities of two polycrystalline CVD-diamond films (PCD), and of two synthetic single-crystal Ib (Borst & Weis, 1996) and IIa (Vandersande & Zoltan, 1991) diamonds. Despite the different purity of IIa and Ib samples, the same activation energy has been obtained in this specific case. PCD films show significantly lower resistivity but similar activation energies for better specimens. Reprinted from Nebel (2003).

purity) are equal and amounting to $E_{act} = 1.7$ eV. This energy corresponds to the photo ionization energy of substitutional nitrogen acting as a deep donor (Farrer, 1969), which had been previously confirmed for Ib diamonds (Dyer, Raal, du Preez, & Loubser, 1965) containing typically ~300 ppm single-substitutional nitrogen. Nebel (2003) attributed the indicated n-type conductivity of the IIa sample to be specific to that probe and not reflecting the general conductivity of IIa diamonds. Nevertheless, this result suggested that even a small amount of substitutional nitrogen is sufficient to dominate the conductivity of otherwise perfect crystals.

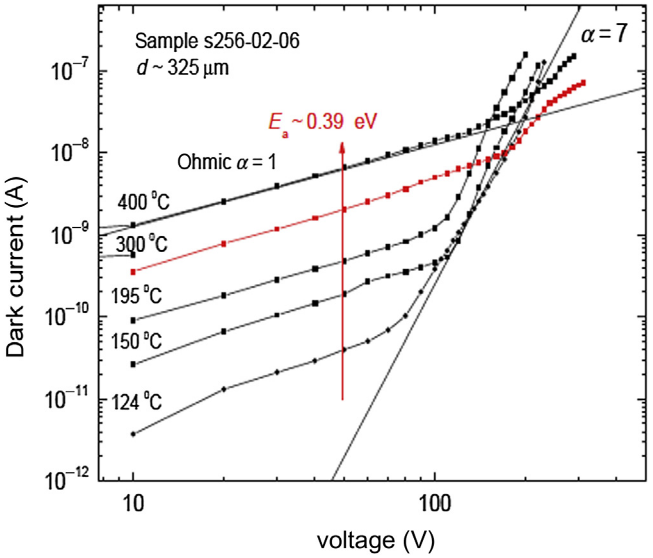

Figure 13 Typical thermally activated dark currents of scCVD diamond samples supplied by Element Six. An activation energy $E_a \sim 0.39$ eV (indicating the ionization of boron acceptors) has been determined for a variety of E6 samples, confirming commonly a residual p-conductivity for CVD diamond of impurity concentrations $N < 10^{14}/\mathrm{cm}^3$ and $B \sim 10^{15}/\mathrm{cm}^3$. Reprinted from Pomorski, 2008, p. 36.

For selected IIa specimens, Redfield (1954) demonstrated a hole-dominated photoconductivity by photo Hall experiments. Pomorski (2008) obtained similar results from scCVD diamond detectors. He extracted activation energies in the range of 0.37–0.39 eV for a variety of films, which indicated strongly the dominance of boron acceptor ionization. An example of his studies is displayed in **Figure 13**.

Thermally activated dark currents were measured in the temperature range $\sim 120\,°\mathrm{C} \leq T \leq 400\,°\mathrm{C}$ confirming that Element Six samples reveal nitrogen concentrations below the detection limit (i.e. $\sim N < 10^{14}/\mathrm{cm}^3$) but still detectable boron concentrations of $B \sim 10^{15}/\mathrm{cm}^3$. In pcCVD-diamond films, amorphous carbon-like absorption has been found by photothermal deflection spectroscopy (Nesladek, Meykens, Stals et al., 1996). This speculation was supported by the shift of spectrally resolved photoresponse spectra to energies as small as 0.6 eV, confirming the opinion that the dark conductivity of polycrystalline samples is governed by impurity transport in grain boundaries (Nebel, Waltenspiel, Stutzmann et al., 2000). However, the influence of nitrogen seems to be stronger: despite their defective crystal structure, the pcCVD diamond films of better quality show increased activation energies at high temperatures approaching that of Ib samples (**Figure 12**).

3.17.4.3.4 Charge-Collection Efficiency, Schubweg, and Charge-Collection Distance

In realistic diamond sensors, the number of the particle-generated e–h pairs is greater than the number of separated electrons and holes measured. As noticed in the historical part, Karl Hecht (1932) irradiated AgCl crystals polarized with an external field E_x with a collimated ionizing light source at different distance x from the anode, and measured for each distance x, the number of photoelectrons N_x arriving at the anode. He observed an exponential decrease of N_x with increasing source distance from the anode and described the charge $Q_C = q \cdot N_x$ measured ("collected") by the electrometer with the help of the absorption constant $1/w_x(E_x)$. Thereby q is the elementary charge and $w_x(E_x)$ is the field-dependent material parameter denominated the "Schubweg," since it describes the average electron drift distance in x-direction, within which the number of the collected electrons (N_x) has decreased to the $1/e$ part of the particle-generated number of electrons (N_0). However, the detector-relevant parameter is the CCE(E_x), which is the ratio of the collected charge Q_C over the generated charge $Q_G = q \cdot N_0$, defined by Hecht as given in Eqn (10):

$$\mathrm{CCE}(E_x) = \frac{Q_C(E_x)}{Q_G} = \frac{w_x(E_x)}{d_D} \cdot \left(1 - e^{\frac{-x}{w_x(E_x)}}\right); \quad 0 \leq x \leq d_D \tag{10}$$

with Q_C and Q_G being the collected and the generated charges, respectively, d_D, the crystal thickness, and $w_x(E_x)$, the "Schubweg".

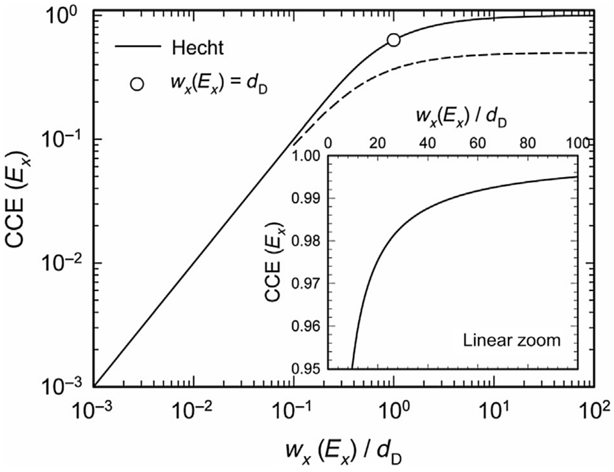

Figure 14 Log–log plot of Eqn (10). For $w_x(E)$ much smaller than the detector thickness the CCE(E) increases linearly with $w_x(E)$ up to a CCE(E) value of 63.2% for $w_x(E) = d_D$. The highest E_x-field range is shown in linear scale as the inset of the figure. A CCE(E) of 95% is reached for $w_x(E) = 10\ d_D$, while for $w_x(E) > 100d_D$, the still increasing CCE(E) remains less than unity.

The important conclusion for diamond detectors derived from Hecht's equation (Berdermann & Ciobanu, 2009) becomes obvious by plotting Eqn (10) in a double-logarithmic scale (**Figure 14**). The message is that a CCE(E_x) equal to unity is impossible. The CCE increases proportional to E_x for small $w_x(E_x)$ values and achieves a figure of ~63% for $w_x(E) = d_D$ (open circle). An approximately loss-less collection of the particle generated charge would only be possible in perfect crystals polarized with a very high electric field, in which the carrier drift velocities would be almost saturated and $w_x(E_x)$ much larger as compared to the detector thickness d_D. Exclusively in such cases, a bending CCE(E_D) characteristic indicates the real saturation of the collected charge—on the contrary to the case of pcCVD-diamond samples, for which the bent curves measured delude saturation (**Figure 15**). Even at relatively low fields, apparent saturation may be observed in polycrystalline diamond of a Schubweg $w_x(E_{max}) \ll d_D$ and thus, of highly reduced collection efficiency—which is in contradiction to Hecht's equation.

The Schubweg parameter was conceived to describe the "single-carrier drift" case, as it is initiated in diamond by short-range ^{241}Am-α-particle (range$^{\alpha}_{\text{Dia}}$ = 13.4 μm), low-energy heavy ions (range$_{\text{HI}}$ ≈ a few to tenths of micrometers) or UV photons (range$^{\text{UVP}}_{\text{Dia}} \leq$ 11 μm). Long-range radiation on the other hand, for instance, relativistic ions or high-energy gamma rays, triggers "dual-carrier drift" by each ionization step along their path

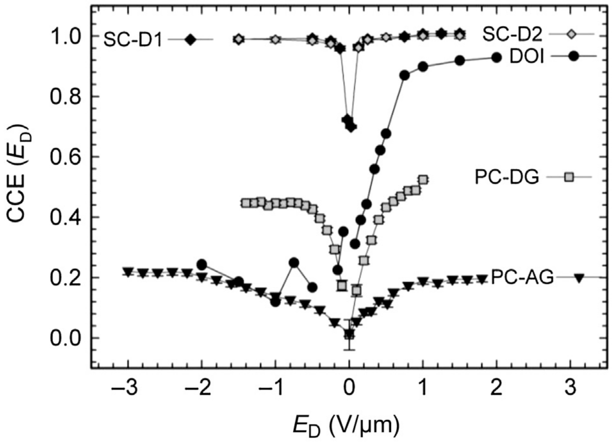

Figure 15 CCE(E) characteristics of various detector-grade CVD-diamond sensors. Two single-crystal samples (SC-D1, SC-D2, and diamond symbols) are compared with a PC detector-grade sensor (squares) and to an as-grown polycrystalline diamond detector (triangles), respectively. Both polycrystalline sensors were tested in the primed state. (pcCVD and scCVD diamond data, reproduced from Berdermann & Ciobanu, 2009. DOI data unpublished).

within a diamond sensor. In such cases, the detector signal consists of two indistinguishable contributions from both carrier types. The CCD parameter was introduced to define the average distance, which separated charge carriers drift apart before being trapped (Zhao, 1994). Eqn (10) and **Figure 14** enable the estimation of the CCD of high-quality scCVD diamond samples (for which $\mathrm{CCD}(E_x) \gg d_\mathrm{D}$) from the measured CCE at field E_x, and by taking into account the corresponding ratio $w_x(E_\mathrm{max})/d_\mathrm{D}$. The plot illustrates that at very high efficiencies the accurate estimation of the CCD error is difficult, since a small uncertainty in the measurement of the collected charge leads to a large error of the collection distance.

The thickness-independent CCD at $E_\mathrm{D} = 1$ V/μm is used as the figure of merit of diamond samples. However, the CCE is the parameter evidencing the ratio of "high-quality = collecting" to the "defective = noncollecting" volumes of the detector material. This ratio is essential with respect to the requirement of minimized material budget of all front-end detector components of the complex spectrometers. It is important to avoid dead matter in the trajectories of the reaction products contributing nothing but background to the experiments.

A routine test is the measurement of the "detector-plateau" characteristics $Q_\mathrm{C}(E)$ or the corresponding $\mathrm{CCE}(E)$. The aim is to define the safe detector operation field E_D within which the variation of the detector amplitudes can be neglected. In the laboratory, the measurements are performed either with alpha particles (single-carrier drift case) or with ^{90}Sr electrons of $E_\beta > 1$ MeV (dual-carrier drift), both simulating the small-signal case of stopped light ions and of MIP particles, respectively. The pulse-height "saturation" for traversing swift heavy ions has to be determined in online beam tests. **Figure 15** shows the plateau characteristics of CVD-diamond sensors of rather different crystal quality. They were measured on-line and in the laboratory, using α-particles and swift ^{134}Xe ions of 400 AMeV kinetic energy for all the heteroepitaxial CVD-diamond samples and the homoepitaxial single-crystal diamonds, respectively. The collected charge was determined from event-by-event measurements of the corresponding energy-loss spectra by calibrating the voltage amplitudes of the shaped signals with spectroscopy pulse generators and capacitor standards of high precision. The generated charge Q_G was calculated with the ATIMA code (ATIMA) of the ion stopping powers in carbon by extrapolating the carbon ($\rho_{12\mathrm{C}} = 2.26/\mathrm{g\ cm}^3$) to the diamond density. For the energy to create an e–h pair, an $\varepsilon_\mathrm{Dia} = (12.86 \pm 0.02)$ eV was considered (Pomorski et al, 2005).

The general shape of the curves is the same for both drift modes. The experimental details, and the results obtained at highest possible electric field (i.e. at operation bias) are listed in **Table 1**. Traditionally, diamond data are compared at $E_\mathrm{D} = 1$ V/μm, arguing that this field is enough to achieve saturation velocity in measurements of MIPs. However, this field is too low for fast applications (including MIP timing) as well as for any kind of heavy-ion measurement, where a huge amount of transient space charge is created in the sensors—even at low ion rates (Berdermann et al., 1999).

The two "spectroscopic grade" homoepitaxial diamonds (SC-D1 and SC-D2) show at relatively low fields $E_\mathrm{D} < 0.3$ V/μm, a saturating behavior, which confirms the high quality of the samples. However, the CCE values obtained at 1.5 V/μm equal and exceeding unity need to be explained. The most probable uncertainties suggested are an underestimation of the stopping power of diamond for the xenon ions, a lower ε_Dia value for the specific samples, and/or charge injection from the contacts (Berdermann & Ciobanu, 2009). The DoI sensor as well as both polycrystalline samples was tested in the primed state. The "detector-grade" (PC-DG) film is a heteroepitaxial diamond, which had been first grown to a thickness of about 1 mm, and afterward, it was thinned down to a final thickness of 500 μm by removing several hundreds of micrometers from the substrate side. The best CCE achieved at present with such kind of pcCVD diamond sensors amounts to about 65%. For the actual sample, a $\mathrm{CCE}(E+) = 52.4\%$ and a $\mathrm{CCE}(E-) = 44.7\%$ have been measured at positive and negative external field, respectively.

The results obtained so far with alpha particles from first heteroepitaxial "quasi single-crystal" DoI samples are rather new and have to be studied in more detail in order to draw general conclusions. The characteristic

Table 1 Experimental details and charge-collection properties of the three types of detector-grade CVD diamond

Sample	d_D *(μm)*	*Contacts*	*Radiation*	*CCE* $(+E_{max}; -E_{max})$	*CCD* $(+E_{max}; -E_{max})$
SC-D1	400	Cr/Au	Xe, 650 AMeV	1.000; 0.989	(2.45; 1.80) cm
SC-D2	400	Cr/Au	Xe, 650 AMeV	1.002; 0.990	(3.27; 2.45) cm
DOI	290	Ti/Pt/Au	α, $E_\alpha \sim 5.5$ MeV	0.929; 0.244	(1950; 71.1) μm
PC-DG	500	Al	β, $E_\beta > 1$ MeV	0.524; 0.447	(342.5; 260.5) μm
PC-AG	350	Al	β, $E_\beta > 1$ MeV	0.195; 0.221	(68.3; 76.3) μm

plotted in **Figure 15** levels out at a CCE > 93% at $E_D \geq 1$ V/μm in the hole-drift case, showing an unexpected low CCE ≈ 22% for the electron drift, that is similar to the value obtained from the as-grown pcCVD diamond (PC-AG) at both polarities. However, considering the early status of research and development on the electronic properties of DoI films for detector applications (Berdermann, Pomorski, et al., 2010), the encouraging results measured for holes are very promising for future large-area detector projects.

3.17.4.3.5 Drift Velocity, Mobility, and Deep-Trapping Lifetime of Ionized Charge Carriers

Another approach to discuss the charge collection in diamond sensors is the dynamics of the charge transport initiated by ionizing radiation in a sample polarized with constant field E. The drift velocity of the charge carriers is composed by a thermal and a field-related component, respectively. At RT and very low electric field (including zero field), the (isotropic) thermal velocity is dominating the average drift velocity. At moderately increasing (low) fields, $v_{Dr}(E)$ increases linearly with E, and the "ohmic" mobility parameter (μ) is used to describe the low-field behavior

$$v_{\mathrm{Dr}}(E) = \mu \cdot E. \tag{11}$$

In polycrystalline diamond samples, the average drift distance of the generated electrons and holes is significantly shorter than the detector thickness. The drift velocity is expressed by

$$v_{\mathrm{Dr}}^{\mathrm{e,h}}(E) = \frac{\mathrm{CCD}(E)}{\tau_{\mathrm{DT}}^{\mathrm{e,h}}} \tag{12}$$

and the collection distance by

$$\mathrm{CCD}(E) = \mu \cdot \tau_{\mathrm{DT}} \cdot E \tag{13}$$

with μ, the ohmic mobility and $\tau_{\mathrm{DT}}^{\mathrm{e,h}}$, the deep-trapping lifetime, i.e. the time which the ionized charge carriers spend in the conduction band before being trapped.

Hecht's Eqn (10) can then be described by the $\mu \cdot \tau_{\mathrm{DT}}$ product, as given in Eqn (14):

$$\mathrm{CCE}(E) = \frac{\mu \cdot \tau_{\mathrm{DT}} \cdot E}{d_{\mathrm{D}}} \cdot \left(1 - e^{\frac{-d_{\mathrm{D}}}{\mu \cdot \tau_{\mathrm{DT}} \cdot E}} \right). \tag{14}$$

In praxis, the CCD of polycrystalline sensors is estimated by the relation CCD = CCE$\cdot d_{\mathrm{D}}$ (Meier, 1999).

By increasing the electric field, the drift velocity of the charge carriers in semiconductors begin to saturate on the steady rise of scattering with crystal defects, impurity atoms, phonons or other charge carriers (Isberg, 2009; Lutz, 1999; Nava et al., 1979). The proportionality of v_{Dr} and E is disturbed, and instead of the constant "ohmic" mobility $\mu = v_{\mathrm{Dr}}/E_{\mathrm{D}}$, the "field-dependent drift mobility" $\mu_{\mathrm{e,h}}^{*}(E)$ has been introduced to describe the drift velocity over the full electric-field range. The first who discussed the concept of "effective drift mobility" were Caughey and Thomas (1967). Several empirical formulas used in later years to determine the experimentally inaccessible parameters zero-field mobility (μ_0) and saturation velocity (v_{Sat}) are based on the original Caughey–Thomas expressions (Jacoboni, Canali, Ottaviani, Alberigi-Quaranta, 1977; Lutz, 1999). The most frequently used is given in Eqn (15) (Jacoboni et al., 1977). The μ_0 and v_{Sat} values are extracted by fitting this equation to the measured drift velocity data $v_{\mathrm{Dr}}(E)$.

$$v_{\mathrm{Dr}}(E) = \frac{\mu_0 \cdot E}{1 + \frac{\mu_0 \cdot E}{v_{\mathrm{Sat}}}} \tag{15}$$

As a matter of fact, a saturated carrier velocity in diamond would be of particular interest from the detector/device application point of view. While a weak but steady increase of v_{Dr} with E is commonly observed in realistic samples up to very high fields, Jacoboni, Canali, Ottaviani, & Alberigi Quaranta (1977) stated that "there is a tendency to consider v_{Dr} saturated at high fields when its variation is so small as to approach constancy within the experimental uncertainties" (p. 84). The authors mentioned furthermore that velocity saturation in the case of holes (in silicon) is "neither predicted theoretically nor found experimentally". The latest statement may not apply for the fast holes in diamond; it emphasizes, however, the difficulty to define a real saturation of the carrier velocity in semiconductors. After all, a noncompletely saturating drift velocity is also consistent with Hecht's postulate of a CCE < 1, valid for all times and for all electric fields applied. When the CCE and the transition time $t_{\mathrm{tr}}^{\mathrm{e,h}}$ of electrons and holes is known over a large electric field range, the charge-carrier lifetime $\tau_{\mathrm{DT}}^{\mathrm{e,h}}$ can be extracted by fitting Hecht's equation in its modified form given in Eqn (16) to the experimental data:

$$\frac{Q_{\mathrm{C}}(E)}{Q_{\mathrm{G}}} = \mathrm{CCE}(E) = \frac{\tau_{\mathrm{DT}}^{\mathrm{e,h}}}{t_{\mathrm{tr}}^{\mathrm{e,h}}}\left(1 - e^{\frac{-t_{\mathrm{tr}}^{\mathrm{e,h}}}{\tau_{\mathrm{DT}}^{\mathrm{e,h}}}}\right). \tag{16}$$

3.17.4.3.6 The Time-of-Flight Experiment or the Transient Current Technique (TCT)

The charge–transport parameters described above are measured performing the "time-of-flight (TOF) experiment," which is also denominated the "transient current technique" (TCT). In 1957, W. E. Spear developed this method aiming at the characterization of the conductivity properties of isolating crystals. Using pulsed lasers of photon energy $E\gamma \sim 220$ nm and a range in diamond of $R\gamma \sim 11$ µm (i.e. much smaller compared to the standard thickness of particle detectors $d_{\mathrm{D}} = 100$–500 µm), he excited the samples by injecting a small amount of photons just under the irradiated semitransparent contact. According to the bias polarity, one type of the generated charge carriers was quickly absorbed into that electrode, whereas the other carrier type moved through the diamond bulk in the direction of the opposite electrode. This method allows for studying separately the drift of electrons and holes in semiconductors.

The particular advantage of the laser-TOF technique is the possibility to pulse and to synchronize the diamond excitation with the power supply. This protects in particular the defective samples from polarization and space–charge accumulation during the measurements, which falsify the results of the transport parameter measurements. Many authors characterized with this method both pcCVD diamond and scCVD diamond (Deferme, Bogdan, Bogdan, Haenen, & De Ceuninck, 2007; Isberg et al., 2002; Isberg, Majdi, Gabrysch, Friel, & Balmer, 2009; Isberg, Gabrysch, Tajani, & Twitchen, 2006; Nebel et al., 1998; Nebel, 1998; Nesladek et al., 2008; Tranchant et al., 2007 and references therein). With the appearance of high-quality scCVD diamonds on the market, the use of short-range alpha particles for the same purposes has been successfully demonstrated by Pernegger et al. (2005), Pernegger (2008). This method has been well appreciated from particle detector physicists since it connects the material characterization with the routinely performed detector alpha-tests prior to each physics experiment. The energy of the main ^{241}Am-α-line is $E_{\alpha} = 5.486$ MeV and the corresponding α-range in diamond is $R_{\alpha} = 13$ µm. Weak calibration α-sources (α-rate ~ 1 kHz) ensure a "single-carrier drift" in the "small-signal case" soustaing a homogeneous internal electric field at all times equal to the externally applied field. The "small-signal case" is given when the generated charge is significantly smaller compared to the "bias-induced" charge $Q_{\mathrm{BI}} = C_{\mathrm{D}} \cdot V_{\mathrm{b}}$. The other extreme case is the "space–charge-limited current (SCLC) transport," where Q_{G} is greater than Q_{BI} (Juška, Viliunas, Klíma, Šípek, & Kočka, 1994). Note that the rather different longitudinal irradiation profiles (i.e. an exponential decay in the laser-excitation case and a broad Bragg peak for alpha excitation) do not alter the TCT results.

The particular merit of Pernegger was the adaptation of the data analysis applied for the characterization of silicon pn-junction detectors (Eremin, Strokan, Verbitskaya, and Li, 1996) to the conditions of intrinsic diamond sensors. In addition to the transport parameters, this method allows for the estimation of trapped charge, the deep-trapping lifetimes as well as for the calculation of the effective net concentration of ionized charges (N_{eff}) in the "space–charge region" (for diamond sensors, in the "diamond bulk"). Pernegger characterized one of the first scCVD diamond samples produced by Element Six, which was of a thickness $d_{\mathrm{D}} = 470$ µm and metalized with Cr–Au contacts. The principle schematic of the α-TCT setup used was similar to the broadband assembly showed in **Figure 3**. A collimated ^{241}Am-α-source irradiated the front electrode, which was connected to a low-noise, fast-broadband amplifier developed by Frais-Kölbl, Griesmayer, Pernegger, and Kagan (2004). Both, the α-source and the amplifier were on the front-side electrode, which was connected through a bias resistor to ground, while the high-voltage potential was applied on the rear electrode. With this configuration, hole drift occurs for negative and electron drift for positive bias voltage, respectively. The α-induced current pulses obtained at different voltage settings (**Figure 16**) were recorded with a digital scope of 1 GHz bandwidth. As discussed at the beginning of this section, the shape of an induced current pulse in a defect-free sensor of

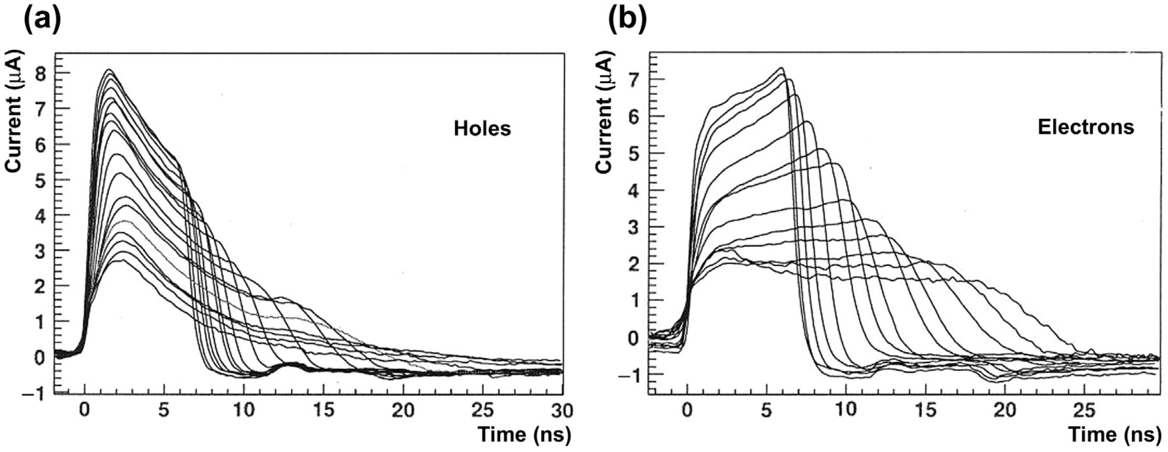

Figure 16 ^{241}Am-α-induced current pulses in a scCVD diamond sensor of thickness $d_D = 470$ μm, for hole drift (a) and for electron drift (b), respectively. The α-source and the broadband amplifier had been mounted on the front electrode, whereas the HV was applied at the rear electrode; in fact, negative HV for hole drift and positive for electron drift, respectively. Reprinted from Pernegger et al. (2005).

parallel-plate geometry (Eqn (5)) is a rectangular signal of amplitude $I_0 = (Q_C \cdot v_{Dr})/d_D$ and of a full width at half maximum (FWHM) corresponding to the charge transit time at constant drift velocity v_{Dr}. When a sample contains uniformly distributed space charge in the bulk, the internal field changes. The field gradient which the drifting electrons or holes are faced depends on the sign of the net effective space charge. Moving holes are repelled from positive space charge and became therefore accelerated toward the cathode, whereas vice versa, electrons moving in the environment of negative space charge are accelerated toward the anode. Below a critical bias voltage (V_c) compensating that space charge ("depleting the bulk"), no drift signals can be obtained. Assuming the realistic case of an additional (small) concentration of bulk traps, the induced current is described by Eqn (17):

$$I_{tr}^{e,h}(t) = \frac{Q_G \cdot v_{Dr}}{d_D} \cdot e^{\frac{t}{\tau_{eff}^{e,h}} - \frac{t}{\tau^{e,h}}} \tag{17}$$

with Q_G, the generated charge; $d_D/v_{Dr} = t_{tr}$, the charge transition time at constant drift velocity v_{Dr}; $\tau_{e,h}$, the deep-trapping lifetime, and $\tau_{eff}^{e,h}$, the effective carrier lifetime of electrons and holes given by Eqn (18):

$$\tau_{eff}^{e,h} = \frac{\varepsilon\varepsilon_0}{e_0 \cdot \mu_{e,h} \cdot |N_{eff}|} \approx \frac{\varepsilon\varepsilon_0 \cdot t_{tr} \cdot V}{e_0 \cdot d_D^2 \cdot |N_{eff}|} \tag{18}$$

with ε_0 and ε are the vacuum permittivity and the dielectric constant of diamond, respectively, e_0, the electron charge, $\mu_{e,h}$, the drift mobility of electrons and holes, N_{eff}, the effective space–charge concentration in the bulk, and t_{tr}, the transit time of the charge through the bulk at an applied voltage V.

The average current pulses shown in **Figure 16** were obtained in the external field ranges: (a) -0.085 V/μm $\leq E_D \leq -0.798$ V/μm (hole-drift signals) and (b) 0.149 V/μm $\leq E_D \leq 1.468$ V/μm (electron-drift signals), respectively. The long decay time of the signals at low bias was attributed to increased charge diffusion as the drift time increases beyond ~10 ns. The systematically broader width of the electron signals indicated a higher drift velocity of the holes in CVD diamond, which was never reported for natural diamond films (Field, 1979, 1992). In both cases, the induced current showed first a steep rise, followed by a decreasing trend for holes drift and an increasing behavior for electron drift.

Pernegger et al. (2005) interpreted this observation as the convolution of deep trapping with effects arisen from a net negative space charge in the bulk. Hole trapping enhances the effect of the negative space charge, leading to a faster decrease of the hole current compared to the increase of the current in the case of electron drift. If electron traps exist in the bulk, the trapping effect is overcompensated by the steady increase of the internal field toward the anode. At a negative voltage $|V_c| \approx 70$–80 V, the hole signals begin to show the characteristic falling edge which indicate the arrival of the positive charge carriers to the opposite electrode. No electron signals could be measured for any positive bias setting below ≈70 V, suggesting an almost "field-free region" for electrons in this positive bias range, where no detectable drift occur. These results confirm a negative net space charge in this specific scCVD diamond sample. The relation between N_{eff} and V_c is given by

$$N_{\text{eff}} = \frac{2\varepsilon\varepsilon_0 \cdot V_c}{e_0 \cdot d_D^2} \tag{19}$$

with V_c, the bias voltage needed to compensate the negative space–charge concentrations in the diamond bulk. V_c is analog to the "full-depletion voltage" of pn-junction sensors.

An average effective negative space charge $N_{\text{eff}} = 2.8 \times 10^{11}\ \text{cm}^{-3}$ was estimated for the actual sample.

The total induced charge is proportional to the broadband signal area and can be estimated by the numerical integration of the average current pulse,

$$Q_C^{e,h}(V_b) = \int_0^\infty I_{Tr}^{e,h}(V_b, t)\,dt. \tag{20}$$

Figure 17 shows the measured charge obtained from the signal areas shown in Figure 16, actually, for electrons (solid markers) and holes (open markers), respectively. The data show charge saturation for both charge carriers at $V_b \geq 200$ V. However, according to Hecht's statements, a "real" saturation of the collected charge appears doubtful in that case.

The reasons are on one hand, the rather low field $E_D \geq 0.4$ V/μm and on the other hand, the low amount of charge collected from each ^{241}Am-α-particle. Instead of the expected 68 fC, only ~49 fC were measured. By taking into account Kozlov's $\varepsilon_{\text{Dia}} \approx 13$ eV/e–h pair, this charge corresponds to a CCE ≈ 72% and confirms the relatively high charge loss indicated by the "missing areas" of the induced-current signals in Figure 16. Moreover, the extremely high value of $\varepsilon_{\text{Dia}} = (17.6 \pm 2.7)$ eV, obtained by Pernegger et al., points in addition to a rather moderate quality of this homoepitaxial scCVD diamond sample. As the authors noticed, however, this does not affect the estimation of the transport parameters by TCT, for which only the measured charge transit time and relative changes of the amplitudes have to be considered.

Figure 18 shows the development of average α-TOF signals at increasing bias voltage, obtained from a scCVD diamond plate supplied in 2007 from the same commercial diamond producer. The sample of a thickness $d_D = 393$ μm was characterized using the broadband circuit presented in Figure 3. The high-voltage potential was applied to the irradiated electrode, which was also connected to the amplifier. The output signals of the DBA were recorded with a digital storage oscilloscope (DSO) of 3 GHz bandwidth and 20 GS/s resolution (50 ps sampling). The fine ripples overlaid to the traces appear due to a weak mismatching of the circuit

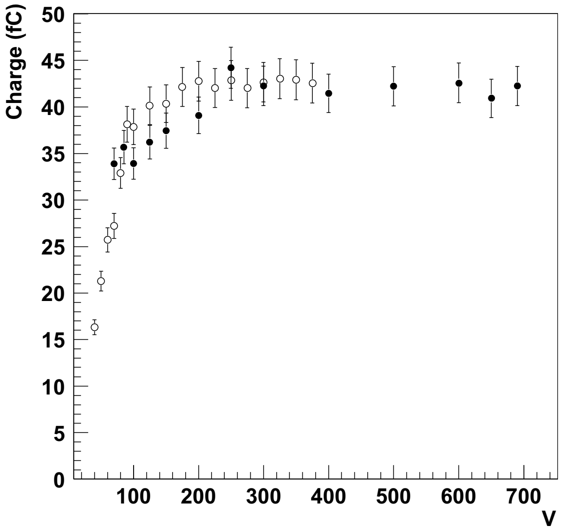

Figure 17 Total induced charge for electrons (solid markers) and holes (open markers) as a function of the applied drift voltage. Reprinted from Pernegger et al. (2005).

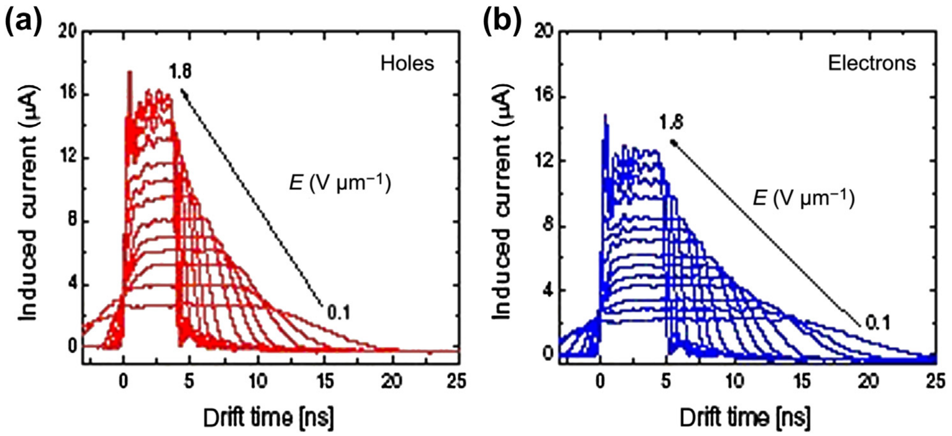

Figure 18 ^{241}Am-α-induced transient current signals measured with a fast scCVD diamond assembly at various electric fields. The sensing sample has a thickness $d_{\mathrm{D}} = 393$ μm. (a) The hole-drift and (b) the electron-drift signals are obtained by polarizing the α-irradiated electrode with positive and negative potential, respectively. Reprinted from Pomorski (2008).

impedances, and have therefore no physical meaning for the detector evaluation. It is in particular the flat top of the current signals, which illustrate impressively the rapid progress of the quality of scCVD diamond within a few years. In contrast to the sample produced in 2004, negligible trapping and no space charge are visible. The internal field is homogeneous and equal to the external field. Where charge diffusion is restricted due to a dominant forward component of $v_{\mathrm{Dr}}(E_{\mathrm{D}})$, the decay time of the signals is approximately equal to the signal rise time. A prompt circuit relaxation indicates in addition a space–charge-free diamond–contact interface. For both, hole (left-hand graph) and electron drift (right-hand graph), a clear arrival of the drifting charge to the opposite electrode occurs at a field $|E_{\mathrm{D}}| \leq 0.1$ V/μm, which is similar to the value observed from Pernegger with the old sample. Also, in "spectroscopic grade," samples are the widths of the electron pulse broader compared to the widths of the hole-drift signals, indicating a higher drift velocity of holes in the measured detector bias range.

Figures 19 and 20 show the electric-field dependence of the drift velocity and the effective drift mobility in the ⟨100⟩ crystal direction of scCVD diamond samples. The data were obtained by α-TCT from 15 scCVD diamond films and were fitted with the Caughey–Thomas expressions. In the wide field range $0.1\ \mathrm{V}/\mu\mathrm{m} \leq E_{\mathrm{D}} \leq 10\ \mathrm{V}/\mu\mathrm{m}$, the hole drift velocity was reproducibly higher than the electron drift velocity.

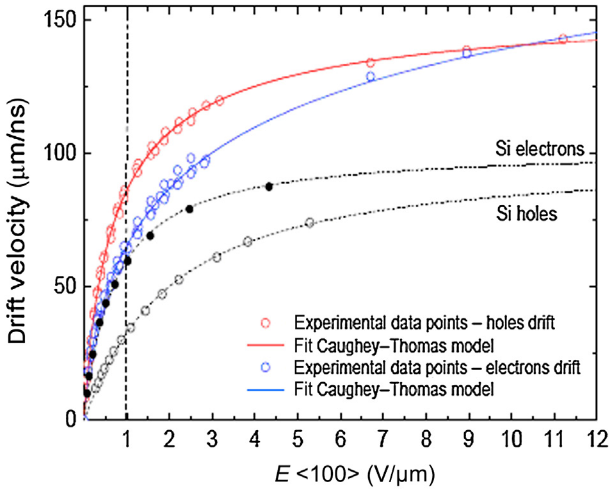

Figure 19 Charge-carrier drift velocities in the ⟨100⟩ crystal direction of scCVD diamond samples as a function of the electric field applied in parallel to the crystallographic direction. The CaugheyThomas expressions (1967) have been fitted to the data of 15 spectroscopic grade scCVD diamond detectors measured by TCT. Reprinted from Pomorski et al. (2006).

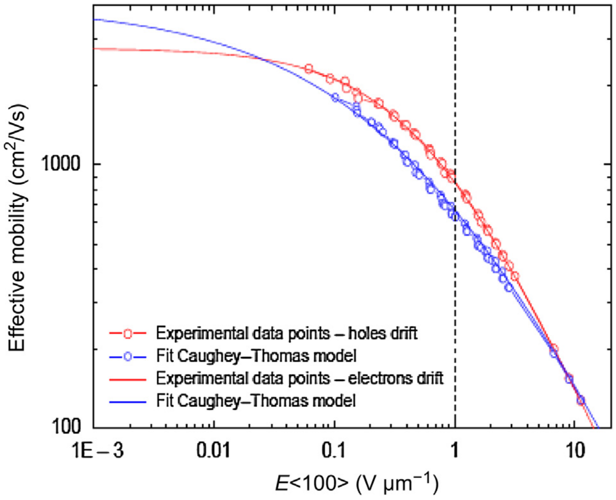

Figure 20 Effective drift mobilities of 15 spectroscopic grade scCVD diamond detectors as a function of the electric field applied in the ⟨100⟩ crystallographic direction, in particular, electron data in blue and hole data in red symbols, respectively. The experimental data are fitted with the original empirical expressions developed by Caughey and Thomas (1967). Reprinted from Pomorski (2008).

Furthermore, the electron data showed a spread on the order of 6%. However, the extrapolated fits to the data reveal higher zero-field mobility (μ_0^e) as well as a higher saturation velocity (v_{sat}^e) for the electrons. The measured electron and hole velocity curves cross each other at a field $E_D \sim 11$ V/μm, at which the carrier velocities are both equal to $v_{Dr}^{e,h} = 1.43 \times 10^7 \text{cm/s}$. Similar results have been obtained from more than 30 scCVD diamond films, confirming the electron data to illustrate a general feature of homoepitaxial CVD diamond. This property has been attributed to the multivalley band structure of diamond and the field-dependent valley repopulation effect, which results in a varying effective conductivity mass $m*$ for the electrons in diamond (Pomorski, 2008). More about the theory of the electron transport in many-valley semiconductors can be found in the works of Tschulena (1972) and Liu, Xing, Ting, & Xu (1988).

Reconsidering the data of **Figure 20**, vested doubts come up concerning the denomination "high-mobility diamonds," which has been used from different authors (Nesladek et al., 2008; Pernegger, 2008) to describe intrinsic CVD-diamond detector materials. As described previously, any particle sensor operates with best performance at highest possible electric field. The long experience with realistic diamond detectors showed that in at operation bias range, the drift mobility of both charge carriers has decreased to $\mu_{e,h} \sim 700 \text{ cm}^2/\text{V s}$ at $E_D = 1$ V/μm and to $\mu_{e,h} \sim 130 \text{ cm}^2/\text{V s}$ at $E_D = 10$ V/μm.

The temperature dependence of the carrier drift mobility in scCVD diamond and natural IIa diamond is shown in **Figure 21** (Nesladek et al., 2008). There are compared drift mobilities in samples produced at CEA-LIST to that measured for commercial (E6) scCVD diamond samples, investigated/published for the first time by Isberg et al. (2002).

The trend of the mobility is decreasing with increasing temperature, in fact according to the relation $\mu(T) \propto T^\alpha$. The exponent α in the temperature range of 300–340 K amounts to about -1.5 for holes and to -1.4 for electrons. At higher temperatures, the slope changes to values of -3.2 for holes and of -2.5 for electrons. These numbers are in agreement with theoretical calculations for IIa diamonds, which predict at RT acoustic phonon scattering and at higher temperatures optical (holes) or intervalley (electrons) phonon scattering. Nesladek et al. concluded that for high-quality laboratory and commercial CVD-diamond samples, the mobilities are consistent with theoretical and experimental data known from IIa diamond.

The deep-trapping lifetimes $\tau_{DT}^{e,h}$ of the charge carriers in scCVD diamond are obtained by fitting the measured CCE(E, t_{tr}) data to Eqn (16). The results obtained from four scCVD diamond sensors are presented in **Figure 22** with the extracted deep-trapping lifetimes indicated in the plots. The collected charge was measured with high-precision charge-sensitive electronics whereas the charge transition time $t_{tr}^{e,h}(E_D)$ was determined previously by α-TCT.

A summary of typical scCVD diamond parameters obtained by α-TCT are listed in **Table 2** (Pomorski et al, 2006; Pomorski, 2008). The data are in good agreement with the very first results from this type of diamond material published by Isberg et al. (2002).

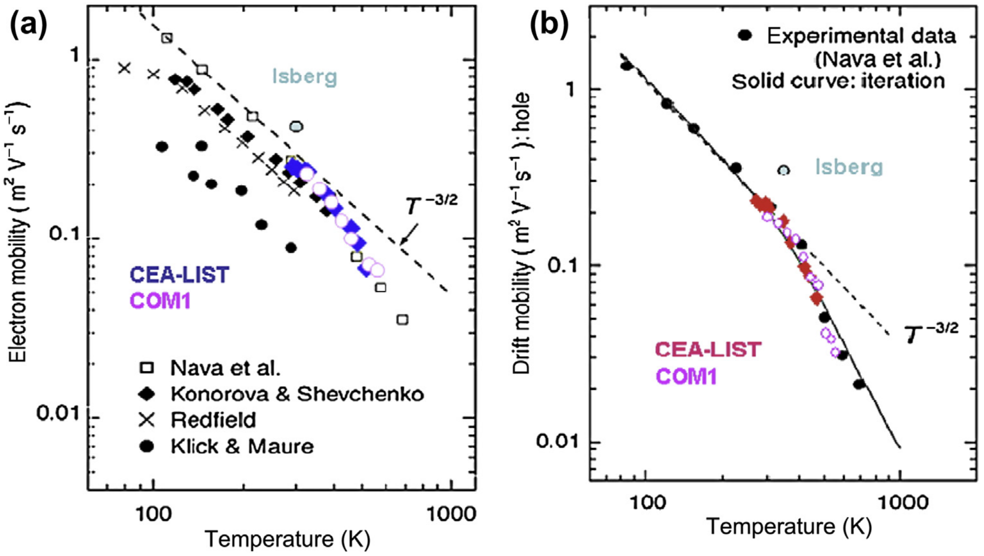

Figure 21 Temperature dependence of (a) electron and (b) hole drift mobilities of commercial scCVD diamond and of samples produced at CEA/Saclay. Both data sets are conform with theoretical and experimental data obtained from natural type IIa diamonds revealing at RT acoustic phonon scattering and at higher temperatures optical scattering for holes and intervalley phonon scattering for electrons, respectively. Reprinted from Nesladek et al., 2008.

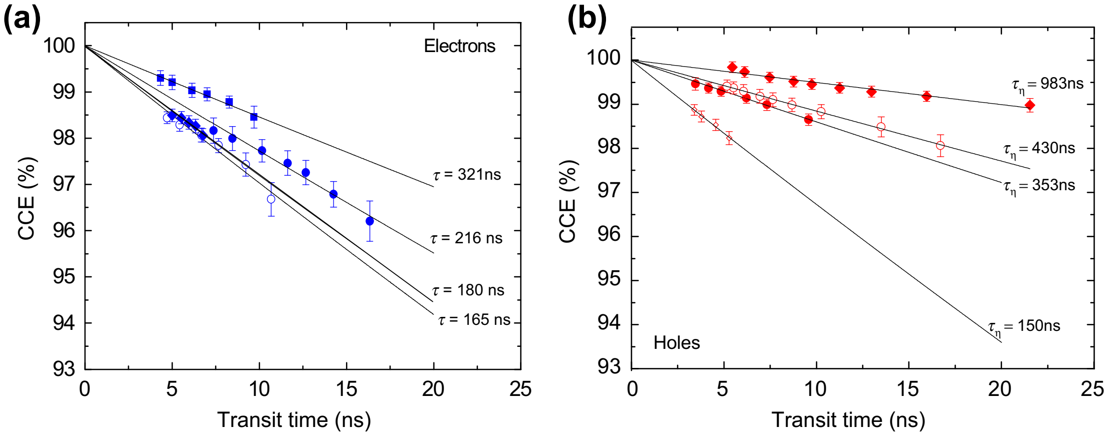

Figure 22 The CCE of four scCVD diamond samples as a function of the charge transition time estimated by TCT: (a) electron drift data (b) hole drift data. The indicated lifetimes are extracted by fitting the data with Hecht's Eqn (20). Reprinted from Pomorski et al. (2006).

3.17.4.3.7 Electric Field Profiling

The shape of the laser-TOF as well as of the α-TCT signals $I_{\mathrm{tr}}(t)$ reproduces quite well the shape of the internal field profile. The numerical calculation of the lateral profile $E(x)$ for $0 \leq x \leq d_{\mathrm{D}}$ can be performed under several assumptions: (1) one-dimensional charge drift of constant carrier drift velocity, (2) negligible initial width and additional carrier diffusion of the carrier distribution, and (3) homogeneous distributed space charge. In that case, the internal field is proportional to the induced current I measured at the electrodes, and the distance x traveled by the charge carriers in a time t is given by the actual integral of the drift velocity (Isberg, Gabrysch, Tajani, & Twitchen, 2006):

$$I = \frac{Q_{\mathrm{C}} \cdot v_{\mathrm{Dr}}}{d_{\mathrm{D}}}; \quad E_{\mathrm{D}} = \frac{I \cdot d_{\mathrm{D}}}{\mu \cdot Q_{\mathrm{C}}} \quad \text{and} \quad x = \int_0^t v\mathrm{d}t = \frac{d_{\mathrm{D}}}{Q_{\mathrm{C}}} \int_0^t I\mathrm{d}t \qquad (21)$$

Table 2 Summary of characterization results obtained from recent spectroscopic grade scCVD diamond detectors by α-TCT, with the electric field applied in the ⟨100⟩ crystallographic direction

	μ_0 ($cm^2/V\,s$)	v_{Sat} (cm/s)	v_{Dr} (cm/s) @ $E_D = 2\ V/\mu m$	τ_{DT} (ns)
Electrons	4551 ± 500	$(2.6 \pm 0.2) \times 10^7$	$\sim 9 \times 10^6$	150–320
Holes	2750 ± 70	$(1.6 \pm 0.1) \times 10^7$	$\sim 1 \times 10^7$	150–1000

The electric field as a function of the distance from the anode is then obtained by plotting E_D versus x from Eqn (21). The mobility and the collected charge are determined by TOF.

3.17.4.3.8 Correlation between Spectroscopy and TCT

Figure 23 shows the α-spectra measured with three spectroscopy assemblies in the hole-drift mode, consisting of CVD-diamond sensors of quite different quality. The almost perfect α-spectrum (green data) has been obtained using a scCVD diamond sensor. It shows the main α-line at $E_\alpha = 5.484$ MeV and the two well-known low-energy α-satellite lines of the ^{241}Am isotope. The red spectrum on the left shows a broader line at a reduced energy $E_\alpha \approx 5.1$ MeV; it has been acquired using a DoI sensor of slightly worse CCE (∼93%). The broad bump (blue spectrum) of a mean value at $E_\alpha \approx 1.3$ MeV was measured with a pcCVD-diamond sensor. The event statistics in all three spectra was comparable.

The energy resolution values $\delta E/E$ given in the plot have been estimated by the ratio of the width δE of the main alpha line over the measured energy E. The dramatically different values obtained illustrate impressively the different crystal structure of "detector-grade" diamonds. A narrow line indicates a complete position-independent charge collection, which can only be disturbed (broaden) by impurities or by structural defects of the sensor material. Both lead to charge losses, hence, to statistical fluctuations of the detector signal. The resolution of present DoI samples is affected by the still high dislocation density of the material, which however has potential to be improved in the future. Due to its polycrystalline structure are diamonds grown on silicon unthinkable for any application aiming to use the collected charge as a decisive parameter. The deviation of the measured peak values and widths from the expected tabulated numbers is a global measure of the trap concentrations and of the structural defect densities in crystal counters (Berdermann et al., 2008).

The corresponding average α-TOF signals are shown in Figure 24. Note that hole-drift measurements are shown in both figures from the scCVD and the DoI CVD diamond samples (green and blue lines, respectively), in contrast to the case of the pcCVD-diamond sensor, for which the (empirically better) electron-drift data are presented (blue traces). As expected, the induced-current pulse in the scCVD diamond sensor (and with some restrictions also in the DoI sample) is of trapezoidal shape confirming the complete holes drift to the opposite

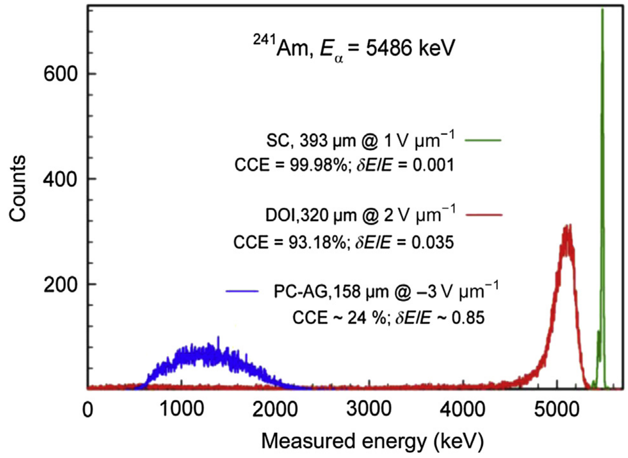

Figure 23 A comparison of the ^{241}Am-α-spectra measured with spectroscopy assemblies using a scCVD diamond sensor (green line), a DoI sample (red line), and a PC-AG sensor (blue line), respectively. The extremely different line widths and positions of the main americium line in the calibrated spectra of the three types of "detector-grade" CVD diamond illustrate the extremely different crystal structure as well as the variation of the charge–transport parameters.

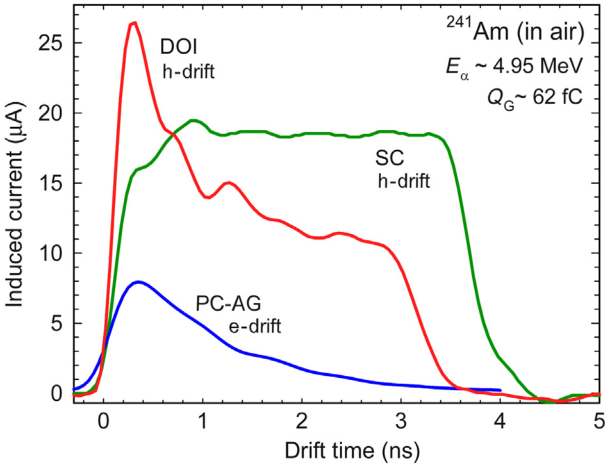

Figure 24 Average α-TOF signals obtained with the diamond samples used for the study shown in **Figure 23**. The current pulses are recorded with a DBA amplifier and a 6 GHz–20 GS/s DSO. The extremely different shapes and widths mirror the different crystal structures of electronic grade CVD diamond, which lead to excellent energy resolution in the case of the single-crystal sensor and in space–charge concentration and/or trapping in the case of the DOI and the PC-AG samples.

electrode. In contrast, the rapid charge quenching in pcCVD diamond leads to triangular signal shapes of varying amplitudes and widths, which are depicted in a broad bump distribution.

In this case, only lower and upper limits of the drift parameters can be estimated by TCT and the deep-trapping lifetimes usually estimated are on the order of 1–2 ns (Berdermann et al., 1999). The "quasi single-crystal" DOI sample shows high collection efficiency (similar signal area than the homoepitaxial sample), the arrival of the drifting charge to the opposite electrode, and a high drift velocity of about $v_{\mathrm{Dr}}^{\mathrm{DOI}}(2\ \mathrm{V}/\mu\mathrm{m}) \approx 9 \times 10^6$ cm/s, which is similar to the value estimated for electrons in homoepitaxial diamond (**Table 2**). However, in this case is the homogeneity of the single α-pulses worse than for the single-crystal samples and this property is demonstrated by the broader α-line width of the DoI spectrum.

The FWHM of the current transients obtained from relativistic heavy ions decreases due to the dual-carrier drift to <3 ns for a sample of a thickness $d_{\mathrm{D}} = 400\ \mu\mathrm{m}$ (Berdermann et al., 2008). At the same time, the signal decay time increases. The reason is the extended detector relaxation time caused by the longer time needed to extract the huge amount of charge produced by single ions. However, due to the high carrier drift velocity, the excess charge can be expelled from the crystal in a time of about 10 ns, which is still much shorter than the integration time of at least 1 μs used in high-precision energy-loss spectroscopy. It is eventually that high carrier drift velocity in conjunction with the high breakdown fields the features which prevent pulse-height defects in diamond sensors—which are a serious well-known problem of heavy-ion silicon detectors.

3.17.5 On the Radiation Tolerance of Diamond Detectors

The radiation hardness of an assembly is understood as the nuclear dose or fluence at which one or more of the following detector parameters incurred inacceptable degradation: the detection efficiency, the time, the energy or the position resolution. All these properties are in the broadest sense dominated by the degradation of the S/N ratio, which however affects differently the broadband and the spectroscopy signals (Section 3.17.5.3). The acceptable damage threshold depends on the specific application envisaged.

3.17.5.1 The Quest for the Origin of the Radiation Tolerance of Diamond

A detectable degradation of the sensor properties by impinging radiation appears after significant distortion of the diamond lattice. Several series of displaced carbon atoms in a row may change the electronic parameters of the diamond material, thus the performance of the diamond detectors. Impinging particles or photons transfer successively their kinetic energy to the carbon atoms of the crystal lattice. Depending on the particle's energy, the displaced atoms either remain permanently separated from the created lattice vacancy or (if the separation was less than a few interatomic distances) bounce back (recombine) to their initial lattice position. No damage occurs in that case. However, high-energetic particles transfer enough energy to the displaced atoms, forcing them to move on (knock-on atoms) generating a cascade of vacancies and interstitials along their path through the crystal. Davies et al. (1992) reported that in relatively pure diamonds (e.g. type IIa and scCVD diamond) and in diamonds containing large concentrations of nitrogen (e.g. type I or pcCVD diamond), almost all radiation-induced vacancies appear in their neutral (V^0) and their negative (V^-) charge states. Both of these states of the monovacancy in diamond act as deep donors, which can compensate acceptor impurities (Dyer & Ferdinando, 1966; Prins, 1993). Dannefaer & Jakoubovskii (2008) performed positron annihilation experiments and extracted an estimate of the energy levels of the radiation-induced monovacancy in diamond. For the V^{0+} vacancy, they obtained $\sim$0.6 eV above the valence band edge, which is well below the value measured for the V^{0-} vacancy at $\sim$2.5 eV.

Wu and Fahy (1994) wanted to understand whether the higher displacement energy (also called the "damage threshold" energy) confirmed for diamond results exclusively from the high binding energy of the carbon atoms in the crystal lattice. They applied molecular dynamics simulations using 1 MeV electrons in order to simulate "microscopically" the basic damage process, which is the permanent displacement of one carbon atom when all other neighbor atoms are initially at rest. They simulated the interaction of the impinging electron with the diamond lattice by a sudden localized input of kinetic energy to one atom. They obtained the threshold kinetic energy of $E_\mathrm{d} = 47$ eV for displacing one atom for motion in the $\langle 100 \rangle$ direction, $E_\mathrm{d} = 50$ eV for motion in the $\langle 110 \rangle$ direction, and $E_\mathrm{d} = 54$ eV for motion in the $\langle 111 \rangle$ direction, which is in accordance with the experimental results of irradiations with high-energy electrons performed by Clark and Mitchell (1977). The displacement energies seemed to be constant in a wide temperature range from 0 K to RT and in addition, weakly dependent on the irradiation species. Prins, Derry, and Sellschop (1986) estimated a value of 55 eV from ion-implantation studies. The remarkable result, however, was that all these energies were about twice as large as the estimate, based on the sum of bond breaking and crystal-strain energies (Bourgoin & Massarani, 1976). Wu and Fahy interpreted this discrepancy as due to the rapid transfer of kinetic energy from the displaced atom to incoherent vibrations of the surrounding crystal (heat) before the atom reaches the energy barrier for defect formation. They assumed that the energy is transported at a speed comparable to the sound velocity, and concluded that "the exceptional radiation hardness of diamond is not only due to its large binding energy but also due to its extremely high velocity of sound". The required condition for this fast energy transfer is a similar velocity of the displaced atom to the velocity of sound in diamond, which is easily achieved in the physics experiments considered in this report. The hypothesis of Wu and Fahy is in agreement with the actual experimental results. The radiation tolerance of the tested semiconductors come along with the corresponding velocities of sound:

1. GaAs: $v_{\mathrm{Sound}}^{\mathrm{GaAs}} \sim 0.5 \times 10^4$ m/s; $F_{\mathrm{p,24\ GeV}} \sim 8.3 \times 10^{13}$ p/cm^2 (Braunschweig et al., 1996).
2. Si: $v_{\mathrm{Sound}}^{\mathrm{Si}} \sim 0.7 \times 10^4$ m/s; $F_{\mathrm{p,24\ GeV}} \leq 1 \times 10^{15}$ p/cm^2 (M. Moll on behalf of the RD50 Collaboration, 2009).
3. SiC: $v_{\mathrm{Sound}}^{\mathrm{SiC}} \sim 1.2 \times 10^4$ m/s; $\mathrm{F}_{\mathrm{p,24\ GeV}} > 1 \times 10^{15}$ p/cm^2 (Nava et al., 2008; Sciortino et al., 2005).
4. CVD diamond, $v_{\mathrm{Sound}}^{\mathrm{Dia}} \sim 1.8 \times 10^4$ m/s, $F_{\mathrm{p,24\ GeV}} > 1 \times 10^{16}$ p/cm^2 (Kagan et al., RD42 2008).

Lebedev, Kozlovski, Davydov, et al. (2002) pursued another approach. They evaluated the specific features of wide-gap semiconductors with respect to radiation hardness. They compared the wide-gap materials SiC ($E_{\mathrm{G\_SiC}}^{300\mathrm{K}} = 3.3$ eV) and diamond ($E_{\mathrm{G\_Dia}}^{300\mathrm{K}} = 5.45$ eV) with the narrow-gap semiconductors Si ($E_{\mathrm{G\_Si}}^{300\mathrm{K}} = 1.11$ eV) and GaAs ($E_{\mathrm{G\_GaAs}}^{300\mathrm{K}} = 1.43$ eV). Lebedev et al. considered the "carrier removal rate" caused by radiation as the best parameter to determine the radiation hardness of semiconductors. Majority carriers are captured by (radiation-induced) deep defects of the opposite nature and the corresponding decrease of the free-carrier concentration causes an increase of the resistivity. Clark, Kemmey and Mitchell (1961) had previously commented on the same topic that "a semiconductor may become an insulator at large irradiation doses". On the other hand, the carrier removal rate increases dramatically in narrow-gap semiconductors at high temperatures. Lebedev et al. estimated the resistivity of 4H–SiC at $T = 450$ K and found it equal to the maximum value obtained for GaAs at RT. The conclusion of this study was that wide-band-gap materials, such as diamond, are predestined for operation in extreme radiation environments, where deep defects become compensated and for hot temperatures, since they do not affect the carrier removal rates as it is the case of narrow-band semiconductors.

3.17.5.2 Numerical Calculations and New Simulations of the Radiation Damage in Diamond

Campbell and Mainwood (2000) used a displacement energy of $E_\mathrm{d} = 40$ eV and applied Monte Carlo simulations to model the lateral distribution of the total vacancy production due to electrons and photons in the energy range 0.25–10 and 1–15 MeV, respectively. The data of the generated knock-on atoms were transferred to TRIM for the calculation of the subsequent damage. The range of 1 MeV electrons in diamond (~1.3 mm) is larger than the standard thickness of radiation sensors while about 80% of the 1 MeV photons pass 5 mm diamond without causing any damage. That means that both these nuclear probes traverse a standard diamond detector. The estimated total rates of the Frenkel pairs (vacancy–interstitial pairs) predominantly formed by both nuclear probes vary over the investigated energy ranges between 0.74 and 3.42 vacancies per incident electron and centimeter diamond, and between 0.03 and 0.84 vacancies per incident photon and centimeter diamond, respectively.

The solid-state sensors applied in HEP experiments are mainly subjected to hadron (protons, neutrons, and pions) and lepton (electron) beams. The radiation damage in silicon sensors as well as the comparison of the irradiation results between different damaging nuclear probes was evaluated based on the so-called "NIEL scaling hypothesis," which assumes that the damage cross-section increases proportional to the nonionizing energy loss (NIEL)—independently of the nature and the specific interactions of the impinging radiation with the detector material. The NIEL is determined by the energy dependent, flux-weighted displacement cross-section $D(\Phi, E)$, which describes the average displacement kinetic energy released in matter (KERMA) given in Eqn (22):

$$D(\Phi, E) = \frac{\int_E \frac{\mathrm{d}\Phi(E)}{\mathrm{d}E} D(E)\mathrm{d}E}{\int_E \frac{\mathrm{d}\Phi(E)}{\mathrm{d}E}\mathrm{d}E} \tag{22}$$

with $D(E)$ the damage function given in Eqn (23) representing the sum of the macroscopic cross-sections $\sigma_i(E)$ for a specific particle interaction with the crystal:

$$D(E) = \sum_i \sigma_i(E) \int \mathrm{d}E_\mathrm{r} f_i(E, E_\mathrm{r}) \cdot P(E_\mathrm{r}) \tag{23}$$

where $f_i(E, E_\mathrm{r})$ gives the probability that an incident particle of energy E creates a recoil of energy E_r, and $P(E_\mathrm{r})$ is the "Lindhard partition function" giving the ratio of the ionizing energy loss over the total energy loss.

The NIEL damage cross-section of 1 MeV neutrons is used as reference, and its normalized ASTM value is specified to 95 MeV mb. The damage efficiency of any flux Φ_i of particles of type i, and kinetic energy E_i applied to any silicon detector can be described by the hardness factor k

$$k(\Phi_i) = \frac{D(\Phi_i)}{D_{1\ \mathrm{MeV\ n}(95\ \mathrm{MeV\ mb})}} \tag{24}$$

with $D(\Phi_i)$ and $D_{1\ \mathrm{MeV\ n}}$ the NIEL of a particle fluence Φ_i of arbitrary particles of given energy E_i and the NIEL of 1 MeV neutrons, respectively.

However, this normalization was proved for silicon detectors only, and even in that case, it was valid for nonmodified sensor materials. Impurities like oxygen may reduce the signal losses by forming stable non-trapping defects with the vacancies (ROSE Collaboration, 2001), leading therefore to a deviation from the NIEL scaling hypothesis.

The first radiation-hardness experiments with low-energy protons of 26 MeV and high-energy neutrons of 20 MeV showed that the signal of scCVD diamond sensors decreased surprisingly fast with fluence. This observation triggered (for the first time) extended studies on the validity of the "NIEL scaling hypothesis" for diamond sensors (de Boer et al., 2007). The NIEL damage cross-sections of diamond and silicon are compared in **Figure 25**. The damage cross-sections for diamond (right-hand graph) are throughout lower compared to the silicon damage (left-hand graph, Huhtinen, 2002). At low incident particle energies, the NIEL cross-section is dominated by long-range Rutherford scattering, which creates many small-scale displacements that quickly recombine at RT (self-annealing). At intermediate energies around and above 1 MeV, the elastic nucleus–nucleus Rutherford scattering causes predominately displacements due to the created primary knock-on atoms. The particular advantage of diamond is obvious at particle energies higher than 100 MeV, where the inelastic reaction cross-section is almost energy independent but significantly increasing with increasing nuclear charge Z of the target material. The "nuclear fragmentation" process in the silicon case leads to a much higher number of heavy fragments and secondary particles. The ratio of the damage functions of silicon over that of diamond ranges from about 10 at 24 GeV to about 3 at 20 MeV.

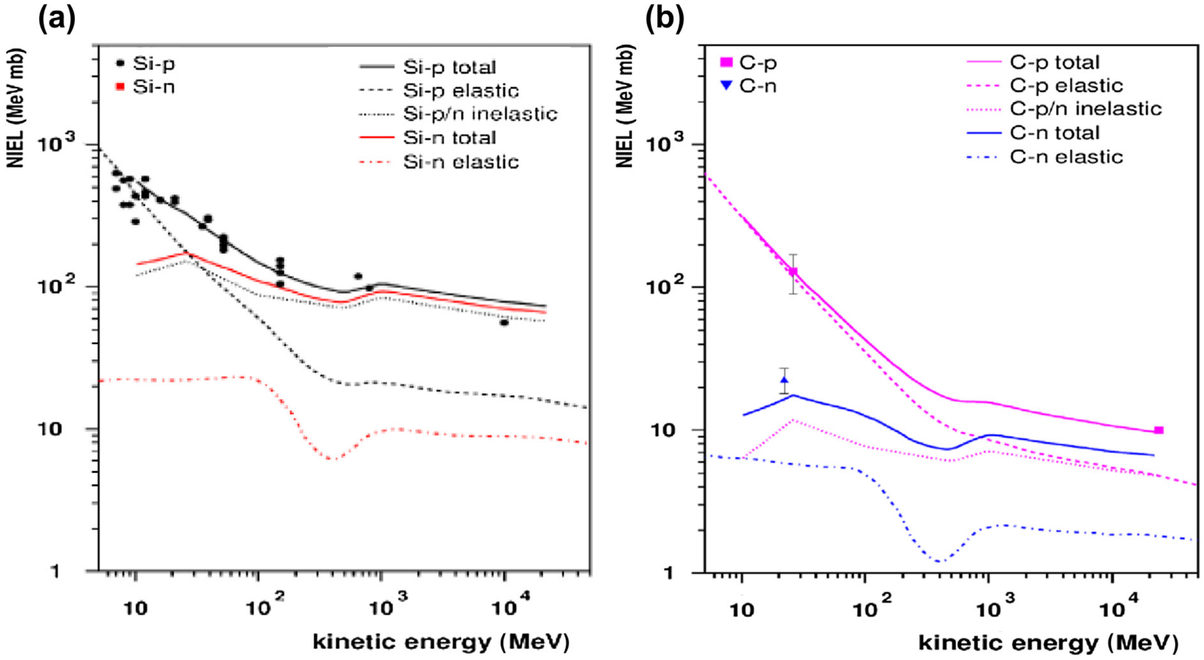

Figure 25 NIEL calculations for protons and neutrons in (a) silicon (Huhtinen, 2002) and (b) diamond. Reprinted from de Boer et al. (2007).

A disadvantage of the NIEL hypothesis is the overestimation of radiation damage due to the inclusion of phonon creation and of other nondamaging processes. A new simulation study on the radiation hardness of diamond, which is an update of the paper of de Boer et al. (2007), has been worked out in the dissertation thesis of Steffen Müller (Müller, 2011). Instead of the NIEL, the displacement per atom (DPA) is used as a measure of damage and a new NIEL has been computed. The DPA value states how often a carbon atom is on average displaced by the incident particles. For example, a DPA of two means that each atom of a detector sample is displaced two times from its lattice site. The DPA is therefore independent of the sample density and volume—in other words, it is directly related to the production of Frenkel pairs.

As expected, the DPA distribution follows the characteristic shape of the specific energy loss along the path through the irradiated sample. The graphs of Figure 26 show the distributions of the DPA for the two extreme

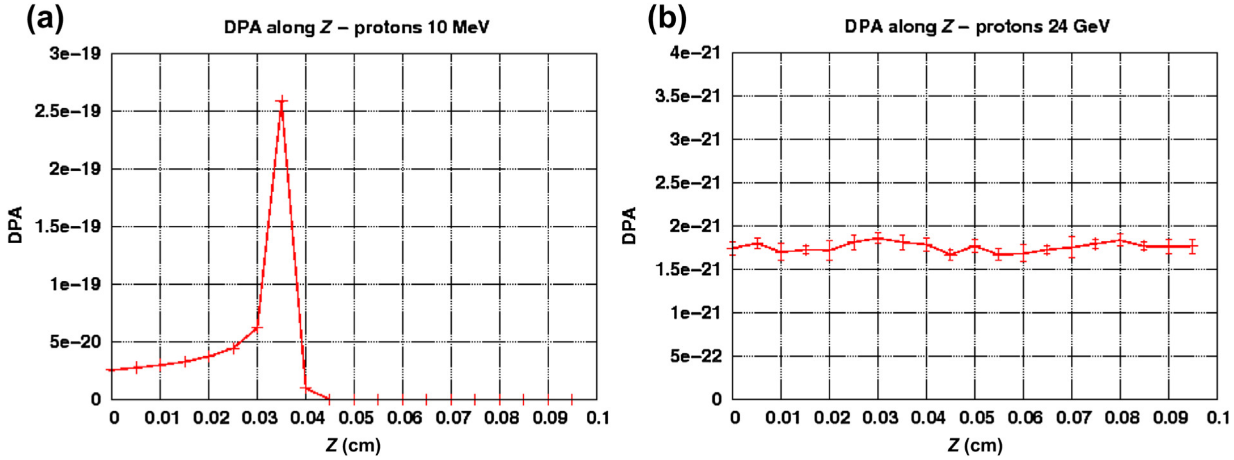

Figure 26 DPA as a function of penetration depth in diamond. (a) 10 MeV protons; (b) 24 GeV protons. Both distributions follow the behavior of the specific energy loss: a clear Bragg-peak in the case of stopped ions and a constant ΔE per unit path in the case of relativistic ions. Reprinted from Müller (2011).

cases considered: low-energy particles (here protons of 10 MeV) stopped within the sensor (left-hand graph) and relativistic ions (here protons of 24 GeV) (right-hand graph), loosing only 1% to 1‰ of their kinetic energy in the counter. The left-hand graph reveals a classical Bragg-peak behavior while the right-hand one shows a constant (low) energy loss per unit path within the diamond bulk.

The recalculated NIEL curves for diamond and silicon are shown in **Figure 27**. This new computation was necessary aiming at the comparison of the DPA with the pure NIEL. **Figure 28** shows the DPA curves for silicon (upper curves) and diamond (lower curves) for protons, neutrons, and pions (π^+). In the case of diamond, the mean displacement energy of 42 eV was taken into account. For easier comparison with existing proton data of RD42, the DPA values were normalized so that the DPA of a 24 GeV proton equals 10. Whereas the new NIEL values of silicon and diamond are of the same order of magnitude, the trends of the DPA deviate significantly.

Following the behavior of the d*E*/d*x* distribution, the radiation damage shows a flat characteristic for relativistic particles, while for particles of energy below 200 MeV, a significant increase of the DPA is obvious for both protons and neutrons. The new calculation reveals a higher ratio of the damage functions of silicon over diamond, in particular at 24 GeV a factor of about 15 (compared to previously 10) and at 20 MeV a factor 6.7 (instead of previously 3). However, Müller warns against the conclusion that in high-energy experiments, diamond detectors were 15 times "harder" than silicon sensors. It was shown that for some cases of modern silicon

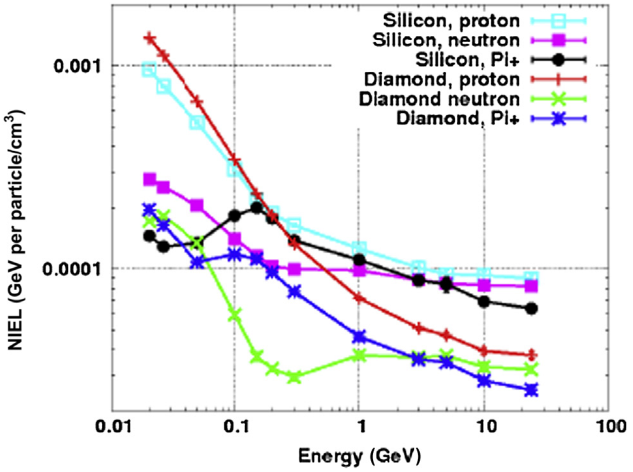

Figure 27 New NIEL simulations for diamond (red, green, blue data) and silicon (cyan, magenda, black data) exposed to protons, neutrons, and pions, respectively. Reproduced from Müller (2011).

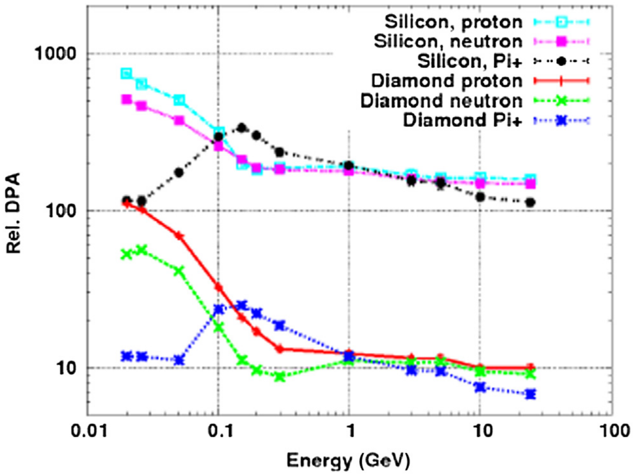

Figure 28 DPA simulations for diamond (red, green, blue data) and silicon (cyan, magenda, black data) exposed to protons, neutrons, and pions, respectively. The relative DPA is scaled so that DPA($p_{24\ \mathrm{GeV}}$) = 10. Reproduced from Müller (2011).

detectors (such as 3D or oxygen-enriched devices), the above simulations do not apply; such novel silicon detectors are harder than predicted (Hartmann, 2010).

A universal parameterization (Eqn (25)) was introduced to determine the radiation hardness factor k based on the degradation of the CCD after irradiation with fluence Φ:

$$\mathrm{CCD}(\Phi) = \mathrm{CCD}_0(1 + k \cdot \Phi \cdot \mathrm{CCD}_0) \tag{25}$$

where CCD_0 is the charge-collection distance before irradiation, k, the radiation damage constant of a given radiation, and $\mathrm{CCD}(\Phi)$, the collection distance after irradiation with fluence Φ of the respective radiation.

The higher the radiation damage produced by a certain radiation, the higher the corresponding k value. Kagan (2010) stated that a "larger CCD_0 performs better at any fluence". However, from Eqn (25), one can derive that the relative change of the collection distance is proportional to the initial collection distance—which may sound contradictory to the above statement. Fact is that the induced defect concentration in scCVD diamond is large compared to that of its virgin state, whereas the additional degradation of the inherently defective polycrystalline sensors is less.

In timing applications, other detector signal parameters are more important than the collected charge. According to Eqn (7) and assuming constant electronic noise after irradiation, the time resolution is determined through the slope of the broadband signal amplitude ($\mathrm{d}v/\mathrm{d}t$) at discriminator threshold. Pomorski (2008) observed that the TCT signal amplitudes and widths were less affected by irradiation than the broadband signal areas corresponding directly to the collected charge. This result can be interpreted as a higher radiation tolerance of diamond timing detectors as compared to spectroscopy assemblies operating under similar conditions.

3.17.5.3 Experimental Results

3.17.5.3.1 Dark Conductivity of Irradiated Sensors

One important property of all types of intrinsic diamond sensors is that of decreasing dark conductivity with irradiation. This behavior is in agreement with the theoretical models described in the previous section, according to which the radiation-induced defects compensate intrinsic shallow traps located prevalent in grain boundaries, dislocations and other structural defects. The dominating process is the compensation of ionized acceptor levels by different states of the created neutral monovacancies acting as deep donors. Gonon, Prawer, Nugent, and Jamieson (1996) obtained unchanged dark currents in pcCVD-diamond sensors after irradiation with 2 MeV α-particles at fluencies of $\Phi_\alpha \leq 10^{16}\ \alpha/\mathrm{cm}^2$, whereas an increase in conductivity was observed at a $\Phi_\alpha = 3 \times 10^{16}\ \alpha/\mathrm{cm}^2$. Husson et al. (RD42, 1997) confirmed a decreased conductivity of pcCVD-diamond sensors after irradiation at the ISIS facility (Rutherford Appleton Laboratory) with fast neutrons of a spectrum peaking at 1 MeV. Beyond a $\Phi_\mathrm{n} > 10^{14}\ \mathrm{n/cm}^2$, the dark current almost vanished. Meier (RD42, 1999) observed unchanged dark currents of the order of picoamps after 500 MeV and 24 GeV/c proton irradiations up to $\Phi_\mathrm{p} = 1 \times 10^{15}\ \mathrm{p/cm}^2$. The behavior of spectroscopic grade scCVD diamond sensors metalized with different contacts has been studied before and after irradiation with 26 MeV (low-energy) protons and 20 MeV (high-energy) neutrons (Pomorski, 2008). The irradiation conditions applied are listed in **Table 3** and the resulting I–E characteristics obtained before (black data) and after (red data) the irradiations are plotted in **Figure 29** left and right-hand graphs, respectively.

Table 3 (a) 26 MeV proton irradiation (b) 20 MeV neutron irradiation

Sample	*d_D (μm)*	*Contacts*	*E-field condition*	*Integral fluence Φ (particle cm^{-2})*
(a)				
BDS 14	490	Cr/Au	No field	6.4×10^{13}
EBS 3	377	Cr/Au	No field	6.1×10^{14}
BDS 13	473	Cr/Au	No field	1.2×10^{16}
(b)				
BDS 12	460	Al	Biased	2.0×10^{14}
s014-06	328	Al	Biased	5.9×10^{14}
s014-09	320	Al	Biased	1.3×10^{15}

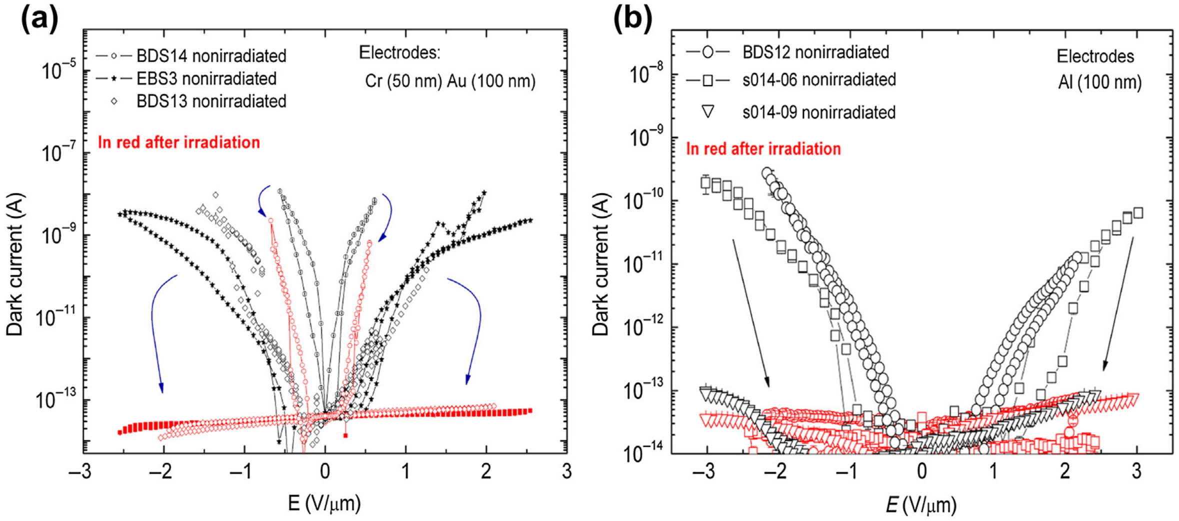

Figure 29 The dark current behavior of scCVD diamond sensors before (black symbols) and after (red symbols) irradiation with (a) 26 MeV protons and (b) 20 MeV neutrons. In both cases, a strong suppression of the dark conductivity has been observed after irradiation. Reprinted from Pomorski (2008).

A successive decrease of the dark current with increasing proton irradiation is obvious (**Figure 28**, left-hand graph, red data). Whereas at a proton fluence $\Phi \approx 6 \times 10^{13}$ p/cm^2, this effect is just indicated—for instance, in the characteristics of sample BDS 14 (open circles, left-hand graph), the currents measured for the heavier damaged samples EBS3 (dots) and BDS 13 (diamonds) decreased down to the measurement limit of the Keithley electrometers used. Similar behavior was found for the samples irradiated with high-energy neutrons of 20 MeV (**Figure 28**, right-hand graph).

The activation energy of sample S014-09 was found changed after irradiation with 1.3×10^{15} $n_{20\ \mathrm{MeV}}/\mathrm{cm}^2$ from initially 0.37 to 0.56 eV. This result was interpreted as a further indication of compensated residual boron impurities in excess of neutral mono vacancies V^{0+}. Accordingly, the dark current of scCVD diamond almost vanished after irradiation (**Figure 29**, right-hand graph, red data) (Pomorski, 2008)—as it was previously confirmed for pcCVD-diamond samples (Daniel Husson, on behalf of RD42, 1997).

3.17.5.3.2 Degradation of the Charge-Collection Properties

Particle physicists need to evaluate and to relate the performance of irradiated sensors consisting of various diamond types in measurements with different particles of different kinetic energies. The most extended studies of this kind have been performed by RD42. **Figure 30** shows a summary of the CCD data measured by RD42 for pcCVD- and scCVD diamond sensors after irradiation with ultrarelativistic protons of 24 GeV/c up to fluencies $\Phi = 1.8 \times 10^{16}$ p/cm^2 (Kagan, Gan, & Kass, 2008). The energy loss of a single ~24 GeV proton in a diamond sensor of thicknesses ~450 μm is about 230 keV, corresponding at highest fluence Φ to an absorbed dose of ~ 4 MGy.

The CCD of the pcCVD (solid squares) and scCVD (open circles) films are plotted versus the proton fluence Φ, so that zero of the *x*-axis corresponds to the CCD of nonirradiated pcCVD-diamond samples. A shift of the scCVD strip sensor data by a fluence $\Delta\Phi = -3.8 \times 10^{15}$ p/cm^2 allows for fitting all results with Eqn (25). Kagan et al. interpreted this plot as a demonstration of a common damage rate for both CVD-diamond types. They stated that "unirradiated pcCVD diamond has as many trapping centers as scCVD diamond after a proton dose $\Phi \approx 3.8 \times 10^{15}$ p/cm^2". An additional data set was obtained from a pcCVD diamond with 70 MeV protons, which however showed a different (much steeper) decrease (**Figure 30**, right-hand plot).

Müller (2011, p. 181) fitted all available data to the parameterization function (Eqn (25)) and determined the relative radiation damage factor *k* normalized to the damage factor of 24 GeV protons. The results are listed in the legends of **Figure 31** for pcCVD diamond (upper plot) and scCVD diamond (bottom plot) sensors, respectively, with the colored lines representing the corresponding fit to each data set given by the colored symbols. The qualitative conclusion from these figures is similar for both diamond detector types: as expected, low-energy particles damage more than high-energy particles. Conformity is achieved between the pcCVD and the scCVD diamond curves shifting the pcCVD data sets to higher fluencies by $\Delta\Phi_{p24\ \mathrm{GeV}} = 30.5 \times 10^{14}$ p/cm^{-2} and by $\Delta\Phi_{n21\ \mathrm{MeV}} = 9.1 \times 10^{14}$ n/cm^{-2}, respectively. However, the 26 MeV proton data are incompatible for

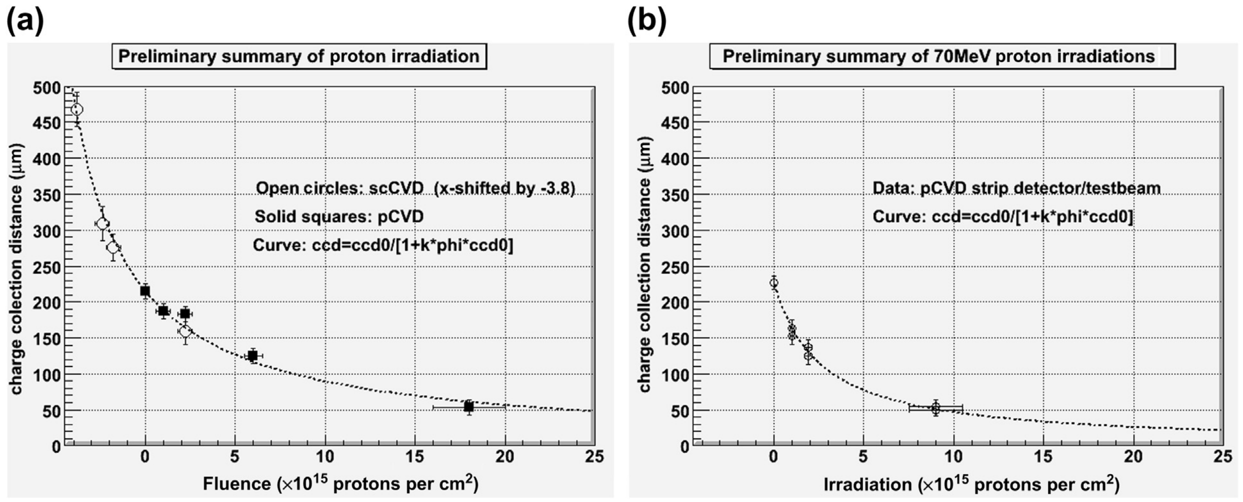

Figure 30 Results of RD42. (a) Summary of the high-energy proton irradiation results for pcCVD (solid squares) and scCVD (open circles) diamond strip sensors up to a fluence $\Phi = 1.8 \times 10^{16}$ p/cm^2. The CCD values plotted on the *y*-axis have been obtained at an electric field of 1 V/µm. By shifting the scCVD diamond data by an amount $-\Delta\Phi = 3.8 \times 10^{15}$ p/cm^2, all data can be fitted by a single damage curve of the same decay (damage) parameter *k*. (b) A steeper decrease is obvious in a data set obtained with 70 MeV protons from a pcCVD diamond sample, which are presented at positive (lower values) and negative (upper values) bias, respectively. Reprinted from Kagan et al. (RD42 2008).

any shift. The scCVD diamond results obtained with 60 MeV protons show a completely different behavior suggesting another source than bulk damage as the reason of the highly reduced efficiency.

A significant improvement of the old NIEL data is achieved due to the new DPA-based calculations. The simulated and the experimental *k*-factors are in good qualitative agreement. The results demonstrate that indeed diamond is more radiation hard than silicon—although however, the total signal yield after irradiation is lower. The RD42 hypothesis that pcCVD diamond behaves as irradiated scCVD diamond could not be confirmed for all available data sets—and this is in accordance with the theoretical studies saying that radiation hardness results cannot be extrapolated between pcCVD diamond and scCVD diamond materials (Mainwood, Newton, & Campbell, 2001).

3.17.5.3.3 Thickness Dependence of the CCE Degradation

Figure 32 (left-hand plot, Pomorski, 2008, p. 125) is a calculation describing the expected CCE (*z*-axis) of irradiated scCVD diamond samples as a function of the applied particle fluence (*x*-axis) and the distance between the electrodes (*y*-axis). The borderline of the violet area (cyan curve) indicates the 1/*e* drop of the CCE. Motivated by these calculations, Sergej Schuwalow and a group of DESY around Wolfgang Lohmann investigated the dependence of the CCE degradation on the sample thickness. They obtained a higher radiation tolerance for thin sensors as it is demonstrated by the right-hand graph of **Figure 32** (Sergej Schuwalow et al., 2010; unpublished). Note that the prospect of a higher radiation tolerance of 3D detectors (being actually on vogue for silicon and diamond detector devices (CERN Courier, January 2003; Alexander Oh (2013)) is based on that simple result.

3.17.5.3.4 α-TOF Studies with Irradiated scCVD Diamond Sensors

Pomorski applied α-TCT on proton-irradiated samples and stated a predominant creation of neutral vacancies (V^0). He argued with the almost unchanged carrier drift velocities (corresponding to the signal widths) obtained up to fluencies $\Phi_{\text{p26 MeV}} \geq 1.1 \times 10^{14}/\text{cm}^2$. Optical absorption spectroscopy performed in addition confirmed the detector test results (Pomorski, 2008). **Figure 33** shows the results of the samples BDS 14, s256-05-06, and EBS3 obtained in the depumped state after proton irradiation with fluencies $\Phi = 6.4 \times 10^{13}$, 1×10^{14}, and 6×10^{14} $\text{p}_{26\ \text{MeV}}/\text{cm}^2$, respectively.

The damaged electron (left-hand plots, thin blue curves) and hole-drift signals (right-hand plots, thin red lines) reproduce nicely the transient current signals before irradiation (black traces) after correction for charge trapping (thick colored lines). The almost equal signal widths after irradiation indicate that the radiation-induced effective space charge is neutral and that the excess carriers exhibit negligible scattering with these

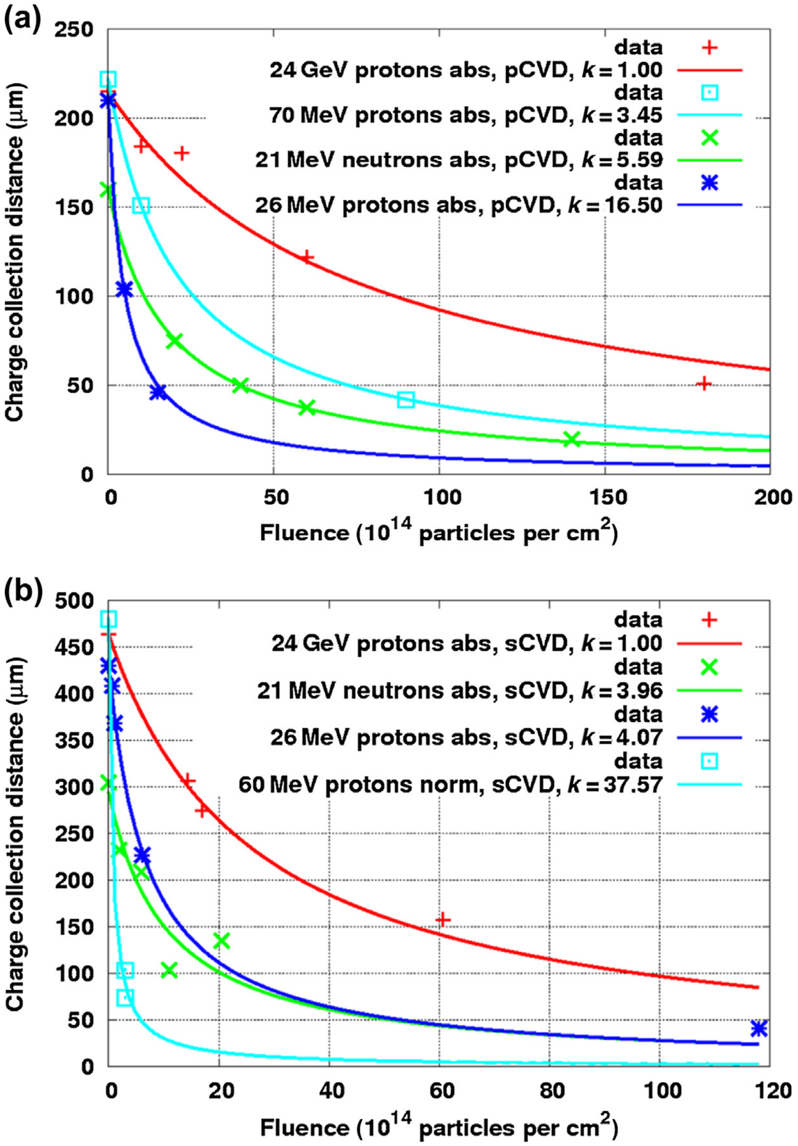

Figure 31 Fits of the measured CCD(Φ) data to Eqn (25) giving the damage factors *k* for (a) pcCVD and (b) scCVD diamond, respectively. Reprinted from Müller (2011).

defects. Beyond a fluence $\Phi_{\mathrm{p26\ MeV}} > 6 \times 10^{14}/\mathrm{cm}^2$ (EBS3, bottom graphs) the CCD becomes much smaller than the detector thickness and almost all the alpha-generated charge is trapped within the diamond bulk.

The behavior of the neutron-irradiated samples metalized with pure Al electrodes was different. Figure 34 illustrates the results of an α-TCT study performed with a sample after irradiation with $\Phi_{\mathrm{n20\ MeV}} \approx 10^{14}\ \mathrm{n/cm}^2$. The hole-drift signals were strongly deteriorated (a, d), whereas no electron-drift signals were obtained for positive bias (b). Pomorski quoted a process denominated "DC bias induced polarization" as a possible explanation. This effect, which was previously observed with cryogenic silicon detectors (Borer et al., 2001) and CdTl sensors (Fink, Krüger, Lodomez, & Wermes, 2006), causes rapid reconfiguration of the internal field after applying bias to the detector. For both bias polarities, a strong enhancement of the field appears near the anode (hole drift in (a) and (d)), which can be interpreted as a partial depletion of the detector bulk. It is most likely a result of charge injection from the cathode with subsequent expansion of the negative space charge toward the anode, where the electrons cannot be efficiently expelled. Within a few seconds after applying positive bias, the field close to the cathode vanishes (a, b), whereas successive polarization occurs with time for negative bias (c, d). After switching off the electric field, the polarization is neutralized but the experiment can be reproduced.

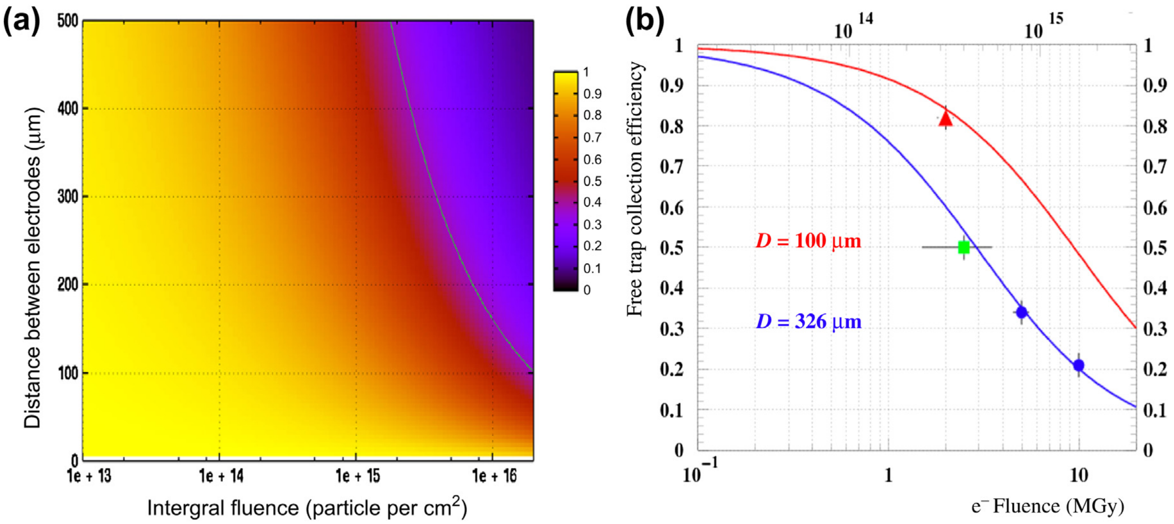

Figure 32 (a) The expected CCE of primed scCVD diamond detectors as a function of the electrodes interspacing and the integral fluence applied. The cyan curve indicates the 1/*e* drop of the CCE. The sensors are "harder" for smaller interspacing. Reprinted from Pomorski (2008). (b) Experimental confirmation of Pomorski's calculations: two scCVD diamond detectors of similar initial CCE but different thickness (*D*) were irradiated with 10 MeV electrons. The CCE of the thin sample was systematically higher after irradiation. Courtesy of Sergej Schuwalow, DESY, unpublished.

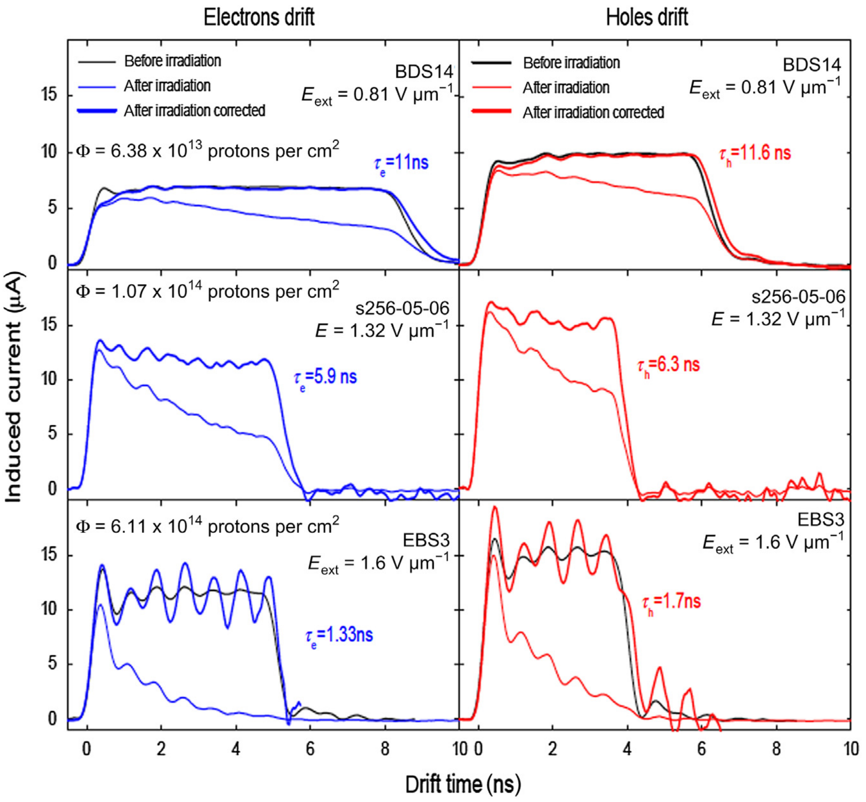

Figure 33 ^{241}Am-α-TCT signals of high-quality scCVD-diamond sensors metalized with Cr–Au electrodes after irradiation with 26 MeV protons each up to the indicated fluence Φ. The black curves are the TCT signals before irradiation, and the thick-colored traces the reproduced signals of the irradiated samples after correction for charge trapping. Reprinted from Pomorski (2008).

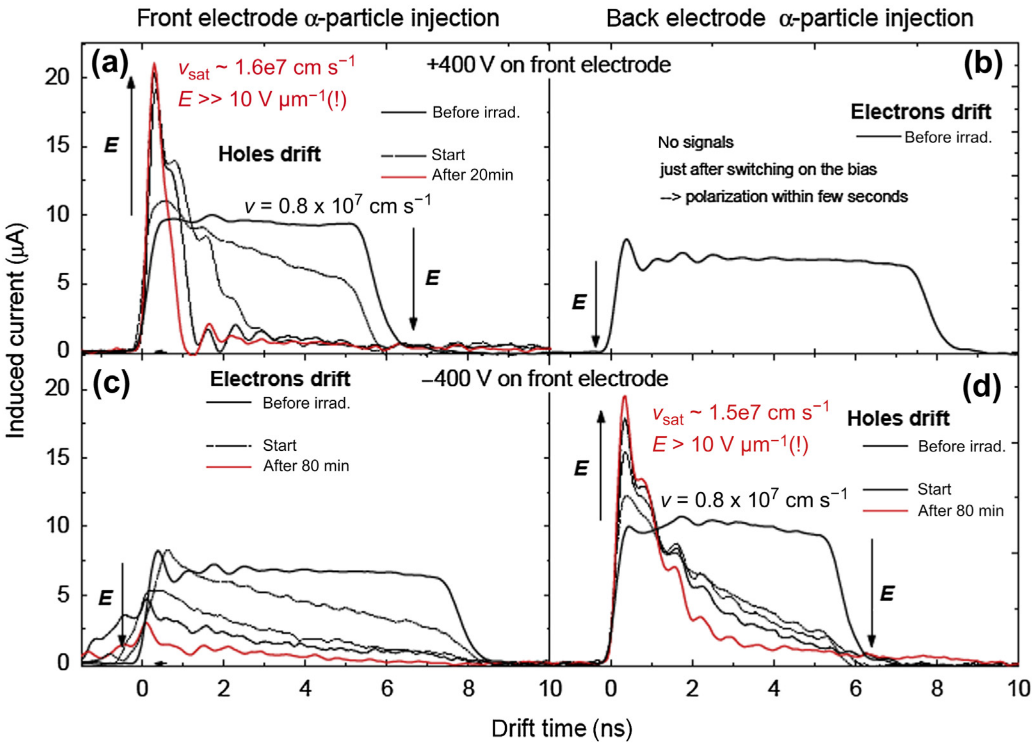

Figure 34 ^{241}Am-α-TCT signals of a scCVD diamond sensor irradiated with 20 MeV neutrons up to $\Phi_{\text{n20 MeV}} \approx 10^{14}/\text{cm}^2$. The samples were metalized with aluminum electrodes. The trapezoidal black curves are the TCT signals before irradiation. For positive bias, no electron drift can be observed, whereas a strongly asymmetric internal field profile appears for both polarities with a strong enhancement in the vicinity of the anode. Reprinted from Pomorski (2008).

3.17.5.3.5 *Miscellaneous Radiation Damage Results*

Grah, Afanaciev, Emeliantchik, et al. (2009) tested the radiation hardness of pcCVD and scCVD diamond for electrons of 10 MeV. A total fluence of an equivalent dose of 10 MGy was applied to the samples. The authors stated unchanged operation up to an absorbed dose of relativistic electrons equivalent to ~7 MGy of electromagnetic radiation. Above this dose, the performance significantly deteriorated.

Systematic data concerning the damage of diamond sensors by high-energy heavy ions are missing. In particular, there exist no data describing the Z and E dependence of the damage processes over the whole available range of particle species and energies. Some knowledge was derived from ion-implantation studies performed on natural or HPHT-type diamonds by Derry, Fearick and Sellshop, (1975), Sellshop (summary in Field, 1979, p. 107), Kalisch, Bernstein, Shapiro, and Talmi (1980), Kalisch (1993, 2003), Prins et al. (1986), Prins (1993, 2000, 2002), Prins and Derry (2000). However, these authors investigated the influence of stopped heavy ions of $A \leq 30$ and $Z \leq 15$, which were suggested to be suitable for diamond doping. Almost unchanged detector signals were observed after bombardment of pcCVD-diamond samples with relativistic ^{238}U ions of 1 AGeV up to $\Phi_{\text{U}, Z=92} > 5 \times 10^{10}$ ions/cm^2 (Berdermann et al., 1999). However, the irradiation of pcCVD diamond with slow ^{131}Xe ions of 8.3 AMeV, which "stop" in the sensor, led to a complete loss of the diamond response after $F_{\text{xe}, Z=54} \sim 10^{13}$ ions/cm^2. Stopped heavy ions in any solid-state detector are the most damaging nuclear particles. They destroy the crystal lattice and strongly polarize sensors with structural defects—a rather serious problem in atomic physics experiments dealing with the heaviest low-energy particles. Instead of pcCVD-diamond sensors, expensive and small scCVD diamond samples have to be used to avoid polarization. Alternatively, very thin polycrystalline membranes ($d_{\text{D}} < 30$ μm) enable the transmission of the heavy particles. As far as small detector systems are concerned, the usual techniques of in situ irradiation with light of certain frequencies or the production of polarization-free contacts by charge injection, etc. may be suggested as a possible solution. However, for large-area composite devices, these are nonviable solutions.

Polycrystalline diamond neutron sensors in nuclear reactor operation were found unchanged up to a neutron fluence of $\Phi_{\text{n}} \approx 3 \times 10^{15}/\text{cm}^2$ and photon irradiation of 250 Mrad (Bergonzo, et al., 2001). The single-crystal diamond detectors implemented at the Joint European Torus (JET) run reliably after irradiation with 14 MeV high-energy neutrons beyond $\Phi_n > 5 \times 10^{14}$ n/cm^2 (Almaviva et al., 2008). Similar devices are foreseen for the International Thermonuclear Experimental Reactor (ITER).

3.17.5.4 Radiation Hard Electronics

The optimum performance of an assembly requires usually short (low capacitance) connections between sensor and FEE. This implies that in most high beam-intensity/luminosity experiments, the radiation load on the sensors and the FEE is similar. However, the immediate consequences of the radiation-induced defects on the ICs of the FEE are rather different than those happened to the radiation sensors. A relatively high integral dose on usually much larger active areas is required to degrade consecutively with time the performance of a particle detector. In contrast, the functionality of an electronic device of the FEE may deteriorate after a single damaging event. Such single-event effects (SEE) are important and dangerous for all sensor applications in extreme conditions, including to the above space experiments and avionics, automotive, medical, and information technology applications. SEEs occur after head-on collision of charged particles or high-energy neutrons of $E_n > 1$ MeV with the sensitive part of an IC, disrupting its correct operation (Normand, 1996). Thousands of electrons may knocked out, producing noise and signal spikes in analog circuits, or, inaccurate and unintelligible results in digital circuits. In general, lattice displacements creating an increased number of recombination centers cause a depletion of the minority carriers, which worsens the analog properties of the affected semiconductor junctions. Counterintuitively, higher doses over short time cause partial annealing of the damaged lattice, which eventually lead to lower damage than the same dose delivered over a long time. Ionization effects cause "soft errors" but on the other hand, they can destroy a device by triggering the creation of short-circuit paths of low impedance leading to erratic currents. All the above is strongly device specific. The annihilation of minority carriers is especially important for bipolar transistors, while it is the gradual accumulation of holes in the oxide layers initiating a progressive worsening of metal-oxide-semiconductor field-effect transistors.

Since the development of dedicated radiation-hard ASICs is a very expensive and time-consuming endeavor, one can presently profit from the developments foreseen for the silicon-vertex devices. However, the fastest chip foreseen for these applications has a shaping of 25 ns (matched to the LHC extraction cyclus (LHC, Technical Design Report)). Concerning the fast-timing assemblies, no radiation-hard broadband ASICs for diamond detectors exist so far.

3.17.6 Diamond Applications in Hot Environments

3.17.6.1 Diamond in Ultrarelativistic Particle Physics—MIP Sensors

As described in the introductory sections, solid-state detectors for high-luminosity experiments at present and future high-energy particle collider accelerators have to be capable of withstanding extreme doses of both ionizing and nonionizing radiation. The inner layers of the tracking detectors of LHC experiments at CERN have to survive typically a dose of 50 Mrad of ionizing radiation and the damage due to the NIEL of $\sim 10^{15}$ particles/cm^2, expected to accumulate over the 10 years of LHC operation (Pernegger, 2008). The LHC upgrade to the super LHC (sLHC) foresees the increase of the luminosity by another order of magnitude. The compact construction of the complex collider spectrometers and the large number of the detector channels involved intensify the problematic. Pernegger refers to an area of 61 m^2 and 6 millions of detector channels for the tracking detectors of the ATLAS silicon tracker and to even higher numbers for the compact muon solenoid (CMS) tracking area covering 220 m^2 and 10 millions of individual detector channels. Maintenance or replacement of damaged samples becomes extremely difficult. Moreover, only one regular shut down of the LHC was initially foreseen, scheduled 5 years after the routine start of the machine operation.

3.17.6.1.1 Beam-Condition Monitors

Over the last decade, an appreciable number of scCVD and pcCVD diamond beam diagnostics and control monitors have been implemented at several large accelerator facilities for HEP research (**Figure 35**). The general task of these devices is to protect the important sensitive parts of the experiment detectors by monitoring and control of the beam intensity and quality near these locations.

The Beam condition and Radiation Monitoring (BRM) system of CMS (Bell, 2008) is a modular setup comprising a number of different slow (current-integrating) and fast detector components. The slow systems are

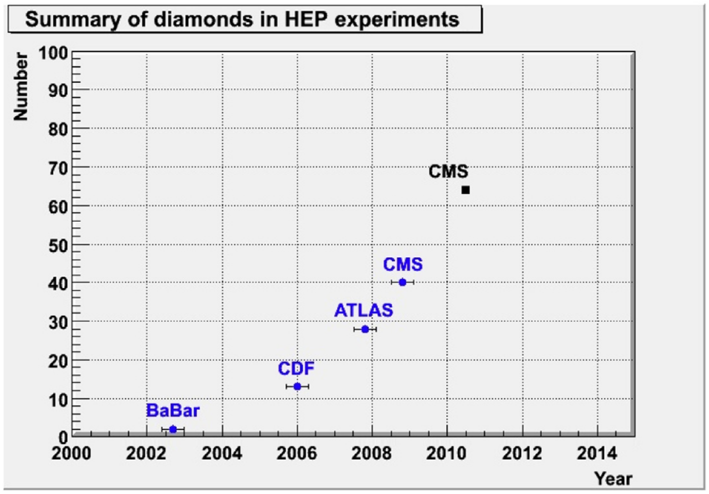

Figure 35 Summary of CVD-diamond samples in high-energy experiments. Courtesy of Harris Kagan, RD42.

used "to measure the accumulated dose near the volume of all subdetectors," which is "necessary to understand the potential long-term damage to detector elements" (Bell et al., 2010). Two of these particle flux monitors consist of pcCVD sensors (BCM1L) placed close to the beam-pipe "to measure the integral particle flux over half an orbit or over a bunch train". The beam-induced current signal in the diamonds is integrated over 40 and 5 μs, respectively. Such fluence measurements assist beam tuning, indicate critical beam halo conditions for the inner detectors, and initiate LHC beam aborts when conditions "are such that detectors might be endangered".

A pair of scCVD diamond Fast Beam Conditions Monitors (BCM1F) is positioned in a plane perpendicular to the beam-pipe (Figure 36, indicated by red arrows) at both sides of the CMS beam IP. Each module consists of

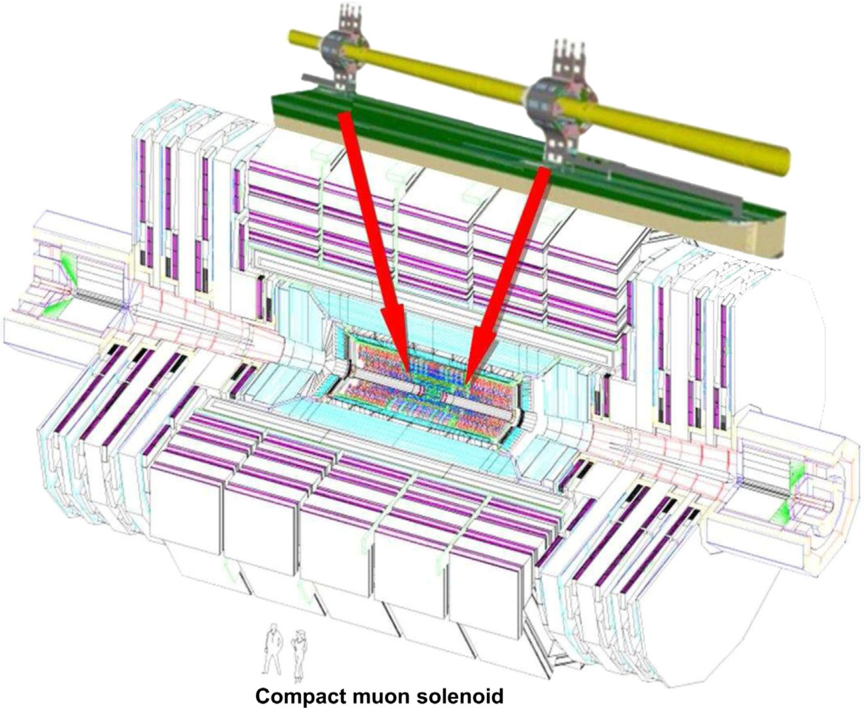

Figure 36 Overview schematic of the CMS spectrometer. The red arrows indicate the position of the diamond BCM1F monitor modules, which are mounted in a carbon fiber structure (shown in the upper part of the figure) at both sides of the IP in front of the silicon pixel detector and inside the volume of the silicon tracker. Reprinted from Bell, Castro, Hall-Wilton (2010).

four scCVD diamond sensors mounted in a carbon fiber structure shown on top of the figure, and in more detail, on the left-hand picture of **Figure 37**. Each diamond sensor has a volume of $5 \times 5 \times 0.5$ mm^3. The samples are located inside the silicon-vertex device at a distance $Z = \pm 1.8$ m from the IP and a radius $r < 5$ cm from the beam axis. The flight distance of a MIP from the IP to one of the sensor planes corresponds to a flight time of ~6.3 ns. At nominal LHC luminosity, the expected flux of charge particles at BCM1F position will be 3×10^8 cm^{-2} s^{-1}.

Radiation-hard FEE and analog optical transmission lines are used for the signal readout (**Figure 37**, right side).

The BCM1F detects beam halo particles and collision products with a time resolution of ~1 ns, which is much shorter than the 25 ns time period between the bunch crossings. It is therefore sensitive to very fast changes of the beam conditions—including the sudden "beam-loss bursts," which are anticipated to be the most serious source of damage for the CMS detector components. **Figure 38** is shown to demonstrate the successful commissioning of the BCM1F detectors during the first proton runs of the LHC. At the third CARAT Workshop, Maria Hempel (2011) reported that the diamond sensors turned out to be extremely useful for the daily safe operation of the CMS detector. BCM1F data are routinely used to validate the performance of the whole BRM system "working in a reliable mode since the start of the LHC in 2008". The device became a key tool to measure collision products, the beam halo rate, and instantaneous luminosity. Encouraged by this success, the LHC ring has been equipped with additional BCM1F modules all along the beam orbit.

3.17.6.1.2 MIP Tracking Devices in LHC Experiments

Two categories of diamond tracking detectors are considered: "beam-luminosity tracking" devices and "reaction-particles tracking" detectors. The advantage of diamond for the first category is obvious and has been

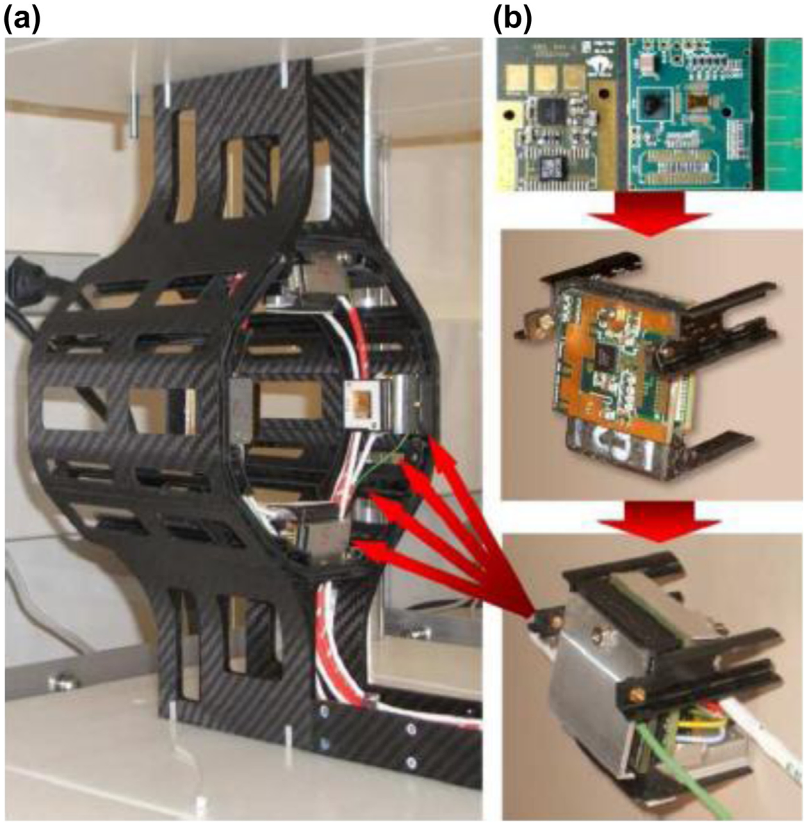

Figure 37 (a) The four scCVD diamond modules of the BCM1F (indicated by red arrows) installed in the carbon fiber carrier structure of the BCM1. A pcCVD-diamond BCM1L module is also visible on the left-hand side to the single-crystal sensors. (b) Each BCM1F module consists of a diamond sensor and the preamplifier board with radiation-hard FEE (top left and right, respectively) combined to a sandwich (central), connected with optical fibers to the subsequent electronic chain. The assemblies are protected by an aluminum cage (bottom). Reprinted from Bell et al. (2010).

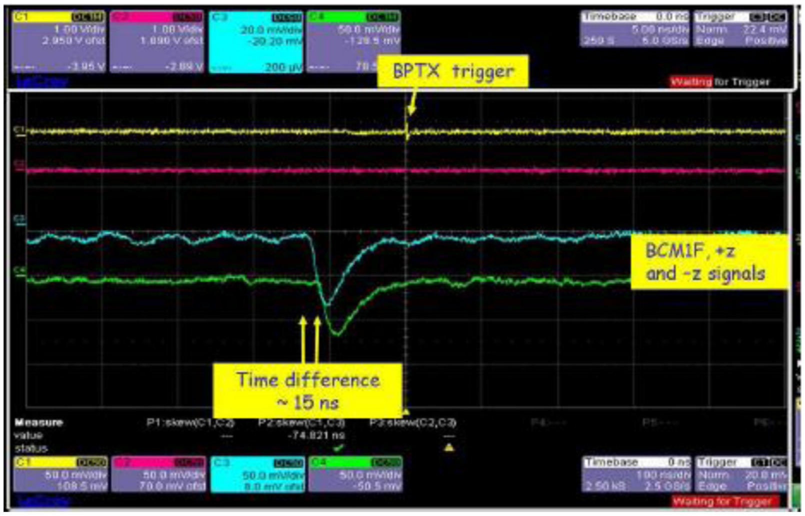

Figure 38 First proton signals from the LHC in BCM1F (blue and green traces), which were triggered by a bunch pickup detector BPTX (yellow line) and recorded during commissioning in September 2008. The blue and green traces are the sum of the BCM1F signals of each side. The time difference of ~15 ns measured between these two signals corresponds roughly to the time of flight of a MIP between both sensor planes. Reprinted from Bell et al. (2010).

frequently addressed earlier. The Pixel Luminosity Telescope (PLT) is a dedicated luminosity monitor for the CMS experiment consisting of eight scCVD diamond sensor telescopes of three planes each (three-plane beam tracking). It is ready for installation at the next opening opportunity of CMS. Two identical systems will be mounted at both ends of the CMS beamline. Figure 39 illustrates the one half of the PLT detector (right-hand side, green/magenta arrangement) and its position relative to the beam pipe and the IP. The main characteristics of the setup are indicated in the legends of the figure. The diamonds are bump bonded to the same pixel readout chip used for the silicon pixel system of CMS. The final hardware and software components have been assembled at CERN. Successful beam tests have been performed at both the CERN SPS and the test beam facility at Fermilab. The current R&D status and the first beam test results have been presented at the IEEE NSS 2011 (Hall-Wilton et al., 2012).

"Particle tracking devices" are used to "track" the path of the collision products. The deflection of charged particles in a magnetic field is exploited for PID (momentum definition) and for vertex reconstruction. The outer tracker layers of high-energy experiments are mounted at larger radial distances from the IP (20–120 cm), where radiation load and particle occupancy are relatively low. Without exception, silicon strip detectors are throughout successfully used at these places. In contrast, the survival of silicon pixel devices is doubtful at designed sLHC luminosities (10^{35} $\mathrm{cm}^{-2}\,\mathrm{s}^{-1}$, LHC Technical Design Report) and at distances <20 cm as

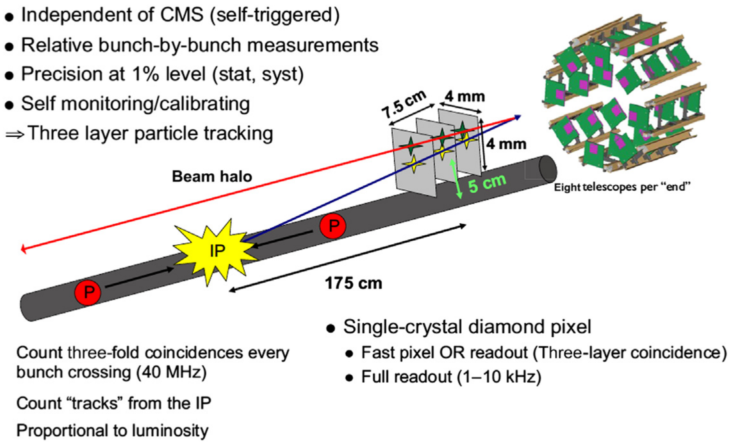

Figure 39 The Pixel Luminosity Telescope of the CMS spectrometer. Courtesy of Richard Hall-Wilton.

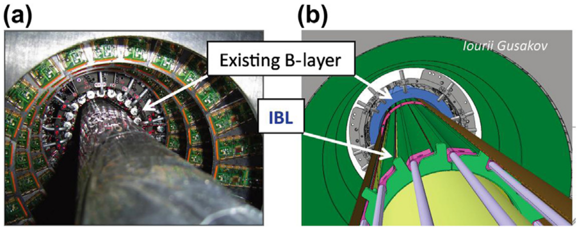

Figure 40 Insertable B-layer (IBL) of the upcoming ATLAS pixel upgrade: (a) Photo of the Pixel Detector with the inserted beam pipe during the integration of the present detector; (b) rendering of the insertion of the IBL with the smaller beam pipe. The pixel sensors mounted on the inner side of 14 staves surrounding the beam pipe (green ladders) will consist optional of planar silicon, full 3D silicon or pcCVD diamond samples. Reprinted from Hügging (2011).

required for vertexing. Fact is that vertex detectors of LHC experiments are large-area pixel sensors, arranged around the IP in two to three zylindrical layers roughly 1 m long ($\sim$7 m with services), comprising a huge number of individual detector channels (approaching order 10^8). Among the important detector components of HEP experiments, the vertex pixel detectors are the most challenging. No one of the novel wide band gap materials (including diamond) will attain silicon status, before one of the large HEP experiments will establish this material for its vertex device (present author's opinion).

At the 2011 Europhysics Conference on High Energy Physics, William Trishuk concluded confidently "diamond trackers should start to appear in the next few years" (Trischuk, 2011). RD42 collected diamond-pixel data up to integral fluencies $F > 10^{16}$ MIP/cm^2, which have been published in Asner, Barbero, Bellini, et al. (2011). The ATLAS Collaboration included also diamond as one among the three options considered for the sLHC pixel upgrade: planar Si, 3D silicon, and pcCVD diamond. A new pixel layer, called "Insertable B-Layer" (IBL), is being prepared to be inserted at a radius of $\sim$3.2 cm between the existing silicon-pixel detector and a new beam-pipe of smaller radius (**Figure 40**). The radial distance of the IBL to the IP will be <20 cm. This upgrade is scheduled for 2014 and will provide ATLAS with a "four-layer" pixel tracker.

At VERTEX 2011, various authors presented the different aspects of the IBL project, on behalf of the ATLAS IBL Collaboration, for instance Pernegger (2011), Hügging (2011), and others. Concerning the study of the three options of sensor materials, Wermes (2011) claimed that "the S/N ratio of diamond after irradiation is, in fact, very competitive to silicon". Although diamond detectors respond with a three times smaller signal than Si of same thickness, "they offer zero-leakage currents even after strong irradiation and smaller pixel capacitances—hence, lower noise". He concluded, "As of today the question remains if one can produce diamond detectors, especially single-crystal CVD diamond, in sufficient quantity on a reasonable time scale".

3.17.6.2 Diamond in High-Energy Nuclear Physics—Relativistic Heavy Ion and Proton Detectors

High-energy nuclear physics comprises experiments with projectile energies in the range 10 AMeV $< E_{\text{proj}} <$ 90 AGeV. In relativistic heavy-ion collisions, both projectile ions and target atoms disintegrate into their constituent parts. Depending on the collision energy, a number of light heavy charged particles are simultaneously created with a swarm of hadrons (protons and neutrons) as well as of elementary particles (electrons, muons, neutrinos, and quarks). This picture illustrates an important difference between relativistic heavy-ion and ultrarelativistic (HEP) high-energy physics. In HEP experiments, all reaction products are minimum ionizing and of $Z = 1$, therefore, inducing signals of equal strength in the detectors and the FEE. In contrast, the assemblies implemented in nuclear physics experiments are facing a very large dynamic range of signals. A particle-induced charge variation of $\sim$1:9000 is easily achieved in a single collision event, assuming, for instance, uranium ($Z = 92$) projectiles impinging any solid target.

We selected for presentation in this report the heavy-ion "spectroscopy" detectors used for the identification of ions of mass $A > 40$ (Berdermann et al., 2008, Berdermann, de Boer, et al., 2010) as well as the important "start" (i.e. "time-zero") detectors (Ciobanu et al., 2007), in particular, the extremely challenged in-beam "start" detectors for minimum-ionizing protons (Pietraszko, Fabbietti, Koenig, & Weber, 2010; Ciobanu et al., 2011).

3.17.6.2.1 Heavy-Ion Spectroscopy Detectors

The high ionization density produced by heavy ions in solid-state detectors is challenging for the sensors used for PID via energy-loss spectroscopy. Gaseous MUltiple-Sampling-Ionization-Chambers (MUSIC detectors) are the radiation-hard, low-mass, state-of-the-art detectors for this purpose (Hans Sann, 1997). However, such devices are rather complex and not easy to handle. They consist of a large gas volume, requiring accurate pressure and temperature stabilization, a high-bias voltage, and permanent maintenance. Where space is restricted, compact silicon detectors are successfully used—as far as the particles' atomic number and mass are not too high.

The performance of silicon sensors suffers by "pulse-height defects" resulting from a delayed charge collection within the temporarily reduced electric field, screened due to the high density of the induced transient charge clouds. The corresponding transient current signals are deteriorated revealing wide widths, which are longer than the time constant of the shaping amplifiers used for spectroscopy (>500 ns), and thus, incompletely integrated in the spectra. The transient current signals of diamond sensors do also moderately broaden. However, the measured signal widths are of the order of 10 ns (**Figure 41**, left-hand plot). The particle-induced charge is fully integrated by the electronics. There are two reasons for this behavior: (1) the amount of charge produced in diamond is three times lower, and (2) electrons and holes in diamond drift faster than that in silicon.

The potential of CVD diamond in heavy-ion spectroscopy measurements has been evidenced in a fragmentation experiment performed at the high-resolution magnetic system fragment separator (FRS) of GSI (Berdermann et al., 2008). ${}^{136}_{54}\mathrm{Xe}$ projectiles of 680 AMeV disintegrate after collision with the atoms of a fixed ${}^{9}_{4}\mathrm{Be}$ target in all stable ions of the periodic system lighter than xenon. The Z-spectrum of the emitted fragments was measured with the standard MUSIC detector of the FRS (40 cm gas layer in beam direction) and a scCVD diamond sensor of 400 μm thickness, placed in air close behind the MUSIC. The fragmentation spectrum has been measured in a shortly followed, independent measurement with a silicon pin-diode detector of same thickness, replacing the diamond. The electronic chain used for the pin diode was the same as for the diamond. In front of the above sensors, two ToF systems consisting of plastic scintillation counters served for background suppression, in particular, the elimination of isotopes of same fragment rigidity reaching the test samples.

The fragment distributions obtained from the three sensors—MUSIC, diamond, and silicon detector—have been overlaid in the right-hand plot of **Figure 41** (red, blue, and green data, respectively). Three individual groups of fragments were focused consecutively onto the small areas of the solid-state detectors (4 mm × 4 mm each). The actual settings of the FRS magnets defined the transmission profiles, leading finally to a modulation of the measured fragment intensity in the merged spectra. In reality, the number of fragments produced in the total Z-range ($Z_{\mathrm{xenon}} \geq \Delta Z_{\mathrm{frag}} \geq Z_{\mathrm{proton}}$) increases exponentially with decreasing atomic number Z of the fragments. Note that the MUSIC spectrum has been corrected for background, whereas both the diamond and the silicon data are raw distributions.

Already after the measurement of the first fragment group ($54 \geq \Delta Z_{\mathrm{frag}} \geq 50$), the performance of the silicon sensor (green spectrum) was destroyed. In contrast, excellent Z-resolution for the scCVD diamond detector was demonstrated during the whole experiment (blue spectrum)—despite the (small) contamination by isotopes of

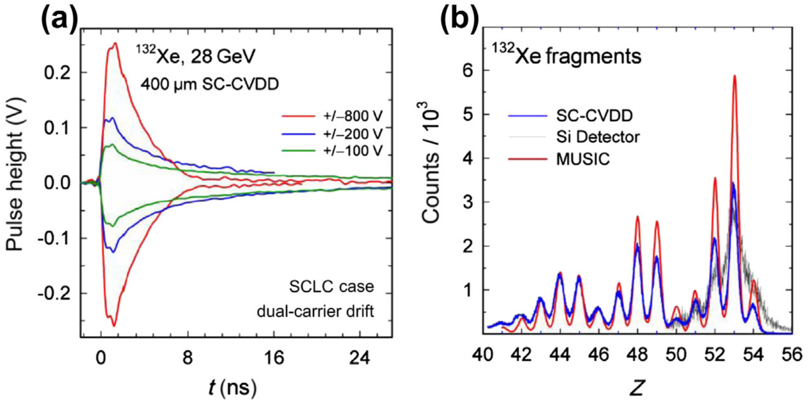

Figure 41 (a) Original (non-amplified) transient current signals of ^{136}Xe ions of 230 AMeV measured with a scCVD diamond sensor of 400 μm thickness at different positive and negative bias. The basis width of the signals is slightly broaden to ∼10–13 ns due to the high ionization density in the sensor, but the complete ion-generated charge is easily integrated within the 1 μs shaping of the spectroscopy amplifier. (b) Overlaid fragmentation spectra measured with MUSIC (red line), a diamond (blue line), and silicon detector (green line). The absence of pulse-height defects in diamond provides excellent energy resolution and PID potential to high-quality homoepitaxial samples. Reprinted from Berdermann (2009).

same rigidity and "border" events, which appear due to a spatial fragment distribution broader than the area of the sensors. The measured line widths (δE) correspond to the theoretical energy-loss straggling, while the energy resolution $\delta E/\Delta E = 0.013$ obtained is, unexpectedly, rather similar to the brilliant resolution of the MUSIC chamber. The insensitivity of diamond heavy-ion sensors (and MUSIC chambers) for photons and δ-electrons created in such experiments might be an additional advantage. Diamond sensors with spectroscopic properties are capable of replacing silicon devices in energy spectroscopy and target-thickness monitoring as well as in any similar application which get along with small-area devices.

3.17.6.2.2 The Start-Veto Device of the HADES Spectrometer

The slow extracted beams from the synchrotron SIS at GSI are pulsed with a spill-on duration adjustable between 0.5 and 10 s. The spill intensities achieve values $\geq 10^{12}$ for light heavy ions up to 10^9 for the heaviest projectiles. In order to minimize the chance-coincidence rates, the most experiments prefer the use of long spills. In-beam "start detectors" are required to select the interesting events out of all beam-particle collisions with target nuclei. They are important multitasking devices of nuclear physics experiments, providing simultaneously the time-zero (T_0) for the TOF measurements (stopped by an associated TOF wall), a fast trigger signal for the data acquisition as well as beam intensity and position monitoring. The uncertainty of T_0 affects directly the TOF resolution, and hence, velocity and mass identification of the particles. Ciobanu et al. (2011) claimed that the time resolution of a start detector have to be "less than the half of the eventually required TOF resolution". Needless to say, the high beam intensities applied for the investigation of rare processes demand for radiation-hard, ultrafast assemblies capable of handling the corresponding ion rates.

The high acceptance di-electron spectrometer (HADES) is a detector system for lepton pair spectroscopy built up at GSI by a large European collaboration (Agakichiev, 2009). Since leptons do not undergo strong interactions, they are considered penetrating probes of compressed hadronic matter, formed within the collision zone of relativistic heavy-ion reactions. The HADES detector (**Figure 42**, right-hand plot) provides a very large acceptance and an excellent mass resolution for comprehensive studies of the in-medium properties of light vector mesons produced in such collisions, such as ρ, ω, and Φ particles. The decay of these mesons is the predominant dilepton source for invariant masses $e^+e^- > 500$ MeV/c^2, which can be reconstructed from the lepton momenta.

A pair of segmented polycrystalline diamond sensors, denominated in the literature the "HADES Start-Veto device" (**Figure 42** left-hand plot), is located in the primary ion beam at 75 cm upstream (Start) and 75 cm downstream (Veto) the HADES target. The ensemble shown in the figure was designed for heavy-ion reactions in 1997. It consists of identical, octagonally shaped pcCVD diamonds of a thickness of 100 μm and an area of

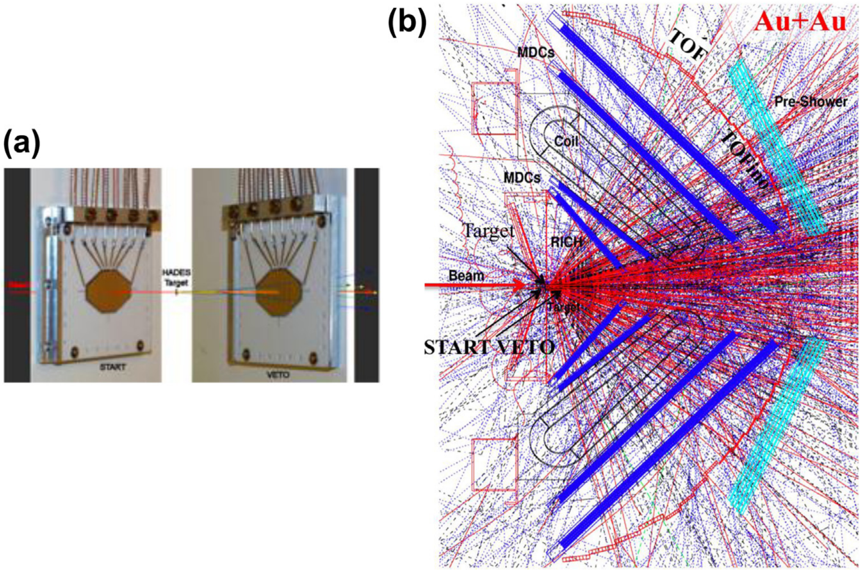

Figure 42 (a) The first heavy-ion "start-veto" device of the HADES spectrometer, was consisting of two independent, identically formed and segmented pcCVD-diamond sensors, each of a thickness $d = 100$ μm (b) The start and veto detector at experiment position. A simulated Au–Au event has been overlaid to the schematic of the HADES detector.

$\sim$300 mm^2 used "as grown". Both front electrodes are metalized with eight stripes of variable width, optimized for constant ion rate. The downstream detector "vetoes" all ions triggered by the upstream (Start) detector which have not reacted with the target (veto multiplicity 1). The output signal of the Start-Veto device triggers the TOF measurement, which is here stopped either in the inner part of the HADES TOF wall called TOFino (24 scintillators in front of the Pre-Shower detector) or in the outer wall called TOF (**Figure 42**, right-hand picture). The intrinsic time resolution of the device for relativistic ions heavier than carbon has been routinely measured below $\sigma_t = 30$ ps. σ_t showed an increasing trend ($\sigma_t \leq 50$ ps) at beam intensities increased up to 10^8/s—which is still an excellent result.

This performance changes completely in measurements of relativistic light ions and protons. The incompatibility between the high e–h pair production energy of diamond and the required wide bandwidth of timing electronics is fatal for the S/N ratio of MIP timing signals. All new Start-Veto devices consist of scCVD diamond samples, integrated together with the first stage of the broadband amplifiers, on a common pcb (Pietraszko & Koenig, 2011). In 2009, a resolution $\sigma_t = 32$ ps was measured with ^{6}Li ions of 1.8 AGeV using an assembly of minimized capacitances (Berdermann, de Boer, et al., 2010). Ciobanu et al. (2011) published extensive analytical calculations and simulations concerning the dependence of the S/N ratio and the time resolution of diamond "proton assemblies" on the collected charge, the detector capacitance, the temperature as well as the noise contribution and bandwidth of the front-end amplifier.

3.17.6.3 Diamond in Nuclear Fusion Science—Neutron Detectors

Fusion is an exothermic reaction releasing thermal energy in form of kinetic energy of the reaction products. In agreement with $E = \Delta mc^2$, the fusion energy corresponds to the amount of the mass changing Δm, which is the difference of the rest mass of the fused particle to the sum of the individual rest masses of the initial particles. The sun (and most of the stars of the galaxy) consists of hydrogen atoms, which lose their electrons due to the enormous temperatures prevailing. The bare hydrogen nuclei (pure protons) collide and "fuse" forming the heavier hydrogen isotopes: Deuterium $\mathrm{D} = \mathrm{p} + \mathrm{n}$ and tritium $\mathrm{T} = \mathrm{p} + 2\mathrm{n}$. An enormous amount of fusion energy is released by such processes throughout the universe. Based on that, scientists try to exploit the potential of fusion power on earth as a safe, clean, and virtually limitless energy source for future generations. The challenge is to create "sun plasma conditions" on an earthly scale.

The JET in Culham, UK (JET home page) is the only current experiment capable of producing controlled thermonuclear fusion power. It is presently used to prepare and optimize the instrumentation of ITER which will be the successor of JET providing 100 times more power than achievable with JET (EFDA home page). A mixture of deuterium and tritium is used, which is the most efficient fuel releasing 17.6 MeV of fusion energy per event. The hot plasma is confined with magnetic fields within a ring-shaped metallic vacuum vessel (Tokamak), in a safe distance from the wall of the toroidal chamber. A temperature between 100 and 200 million °C and a plasma density $\rho_{\text{plasma}} \approx 1\ \text{mg m}^{-3} \approx 10^{-6}\ \rho_{\text{air}}$ are the fusion conditions to maintain for as long as possible. The reaction D+T leads to the emission of a relatively slow, double-charged helium nucleus ($^4_2\mathrm{He} = \alpha$-particle) of 3.5 MeV and a high-energy neutron (n) of 14.1 MeV. The α-particles cannot escape the magnetic field but the released neutrons provide excellent probes for the indirect diagnostics of the hot fusion plasma.

However, the diagnostic detectors prepared for ITER will face severe problems due to both the extreme high-temperature environment and the huge amount of neutrons and gammas expected from the ITER plasma. Presently used detection techniques based on silicon or scintillation materials cannot be used. Instead, scCVD diamond sensors have been developed from Italian scientists of the University Rome "Tor Vergata" in close cooperation with the European Institutions for energy research ENEA, EURATOM, and EFDA. Three scCVD diamond sensors have been installed at JET in 2007, where they are working with good performance during continuous operation after the restart in 2008 (Lattanzi et al., 2009). The goal was to detect simultaneously both thermal (mV range) and 14 MeV neutrons and to record the time-dependent neutron emission of each single JET pulse.

The principle schematic of these devices, originally developed for high-flux neutron monitoring in fission reactors (Almaviva et al., 2008), is shown in **Figure 43**. The active scCVD diamond sensor is grown on a thin, boron-doped diamond layer previously deposited by CVD on an HPHT diamond substrate. The boron-doped film forms the ground electrode, whereas the anode is made of an aluminum contact covered by an evaporated ^{6}LiF layer. Fast neutrons, which easily penetrate the ^{6}LiF film, interact with the carbon atoms of the active sensor volume according to reactions of the kind $^{12}_6\mathrm{C}(\mathrm{n},\alpha)^9_4\mathrm{Be}$ and $^{12}_6\mathrm{C}(\mathrm{n},\mathrm{n}')3\alpha$, whereas the thermal neutrons not

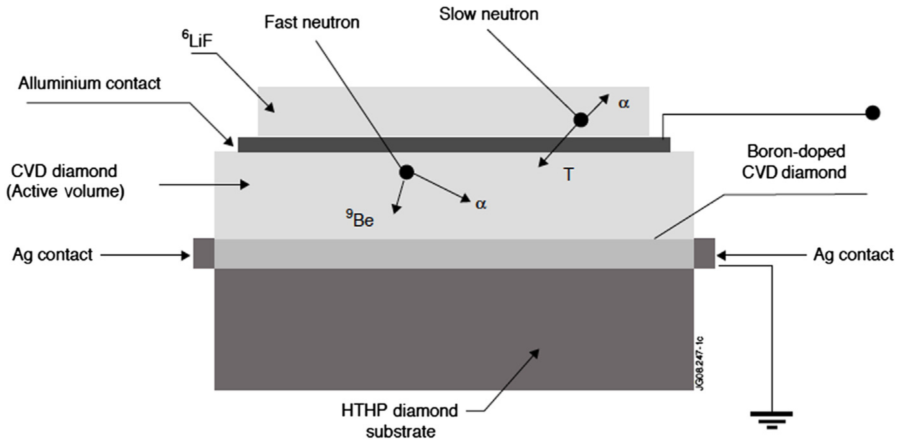

Figure 43 Schematic of scCVD diamond detectors developed at the University Rome "Tor Vergata" for the simultaneous detection of thermal and fast neutrons. The active scCVD diamond sensor has been grown on a thin, boron-doped diamond layer realized on an HPHT diamond substrate and serving for the ground electrode. The anode is an aluminum contact covered by a thin ^{6}LiF layer. Fast neutrons penetrate the ^{6}LiF film and react with the carbon atoms of the active sensor volume, whereas slow neutrons react with the ^{6}Li atoms of the top layer. Reprinted from Lattanzi, Angelone, Pillon et al. (2008).

reaching the diamond react with the ^{6}Li atoms of the coating layer by the reaction $^6_3\mathrm{Li}(n,\alpha)\mathrm{T}$. **Figure 44** shows the spectra of both neutron-energy ranges measured from Almaviva et al. (2008). The "monoenergetic" products emitted in both reactions are clearly identified.

The first of the three sensors currently installed at JET (SCD-236, $d = 200\ \mu\mathrm{m}$) is metalized with an Al electrode of 4 mm diameter and embedded in paraffin. The second (SCD-234, $d = 104\ \mu\mathrm{m}$) as well as the third sample (SCD-242, $d_\mathrm{D} = 75\ \mu\mathrm{m}$) are identically prepared. In both cases, the electrodes consist of aluminum dots of 3 mm diameter covered by a ^{6}LiF (95% ^{6}Li enriched) layer of 3 μm thickness; both samples are shielded with polyethylene of 25 mm thickness. Paraffin has been used "to enhance the 14 MeV response through the recoiling protons" (of a cross-section = 1 b) and polyethylene, in order to "enhance the thermal neutron response". The authors reported that this preparation was necessary because JET was operating with D + D fuel (instead of D + T) during this campaign.

The signals of samples SCD-236 and SCD-234 are amplified with a classical spectroscopy chain consisting of a modified ORTEC 142A preamplifier (mounted close by) and a shaping amplifier. Sensor SCD-242 is locally separated from its broadband amplifier (DBA, Moritz, Berdermann, Blasche, Stelzer, & Voss, 2001) but electrically connected to the FEE via a low capacitance, superscreened cable, enabling installation outside the JET Torus Hall. The results of the latter setup will be used to optimize diamond neutron detectors of upcoming Tokamaks (for instance, ITER), where the huge neutron and gamma fluxes expected prohibit the operation of detector assemblies in the Torus Hall.

The diamond signals are acquired by means of the JET CODAS acquisition system—worth mentioning to demonstrate the high integration status. Each of the ~900 JET pulses accumulated corresponds to an integral

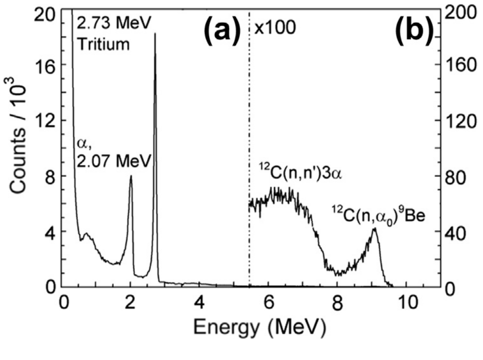

Figure 44 Detection of (a) thermal and (b) 14 MeV neutrons via the nuclear reactions $^6_3\mathrm{Li}(n,\alpha)\mathrm{T}$ and $^{12}_6\mathrm{C}(n,\alpha)^9_4\mathrm{Be}$ or $^{12}_6\mathrm{C}(n,n')3\alpha$, respectively. Reprinted from Almaviva et al. (2008).

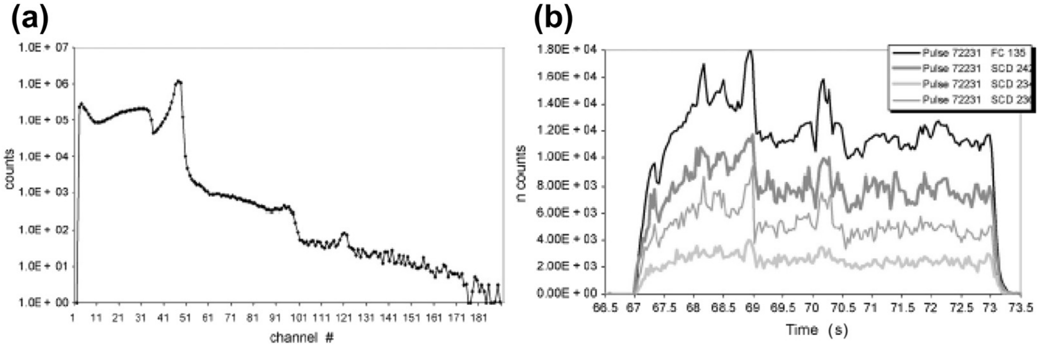

Figure 45 (a) Sum of more than 800 JET pulse spectra (total neutrons) as measured by SCD-234. (b) A typical JET pulse showing the matching between a fission chamber and the three scCVDD detectors (normalized counts). Pulse duration 6.2 s; neutron yield $= 1.109 \times 10^{16}$. Both reprinted from Lattanzi et al. (2008).

neutron yield in the range 4.9 E^{13}–7.2 E^{16}. All three counters have not been calibrated yet as for the neutron yields. Lattanzi et al. mentioned that the results reported in **Figure 45** "concern the comparison of the SCDs with the standard detectors presently used at JET". The right-hand graph of the figure shows a typical single-JET pulse as seen from the three diamond detectors, compared to the signal recorded from a classical ^{235}U fission chamber (FC) used for total n-yield measurements. A high linearity over the whole neutron yield range has been reported, which was evidenced, for all ~900 JET shots analyzed, by the linear correlation between the neutron count rate in all three diamond sensors and the neutron numbers registered in the FC.

Due to the low count rate of 14 MeV neutrons provided by the $D + D$ reaction, a reliable comparison with the Si diodes was so far not possible (Lattanzi et al., 2009). However, the left-hand graph of **Figure 45** demonstrates that sample SCD-234 is a rather good neutron spectrometer. Note that the total n-energy spectrum displayed represents the sum of individual spectra obtained from more than 800 JET pulses. Two peaks are measured at channel no. 33 and channel no. 47, which have been identified as the 2.07 MeV (α) and the 2.73 MeV (T) lines from ^{6}Li(n_{th},α)T reactions (Lattanzi et al., 2009). The structures of low statistics observed on the high-energy side of the spectrum need, however, further analysis. The authors concluded "the fabrication of highly reliable single-crystal diamonds as neutron detectors in future Tokamaks has proven to be feasible almost in a routine basis".

3.17.6.4 Diamond in Synchrotrons and Solar Space Experiments—Photon Detectors

3.17.6.4.1 Beam Position Monitors for Synchrotron Radiation and Free-Electron Laser X-ray Beams

Following the rapid progress of nanoscience, X-ray synchrotron beams are now routinely focused down to submicrometer spots with the target figure being 10 nm (Morse, Solar, & Graafsma, 2010). The required position stability of the beam is ~10% of the beam size varying in the range 0.1–50 μm. This is especially challenging at synchrotron facilities owing to the long source–optics–sample distances involved which can reach up to 100 m or more. Accuracy and linearity of the beam intensity have to be below 0.1%. The ionizing radiation loads exceeds 10^4 Gray/s while the maximum absorbed X-ray power from monochromatic beams is less than a few milliwatts. "White beams" achieve easily 100 MW, however, at a larger beam size of ~1 mm^2. None of the traditional detector materials can cope with the thermal load and the ablation energies of such radiation.

Single-crystal diamond is an outstanding material for the fabrication of semitransparent X-ray photon beam position monitors (XBPM) capable of in-situ monitoring of highly focused synchrotron and free-electron laser beams. It provides low X-ray absorption combined with radiation hardness and excellent thermomechanical properties, in addition to submicrometer spatial resolution and real-time information for beam-position control. Early tests revealed already device sensitivities to beam movements ≤20 nm (Morse, Salomé, Berdermann et al., 2008). When readout with broadband electronics, an XBPM can simultaneously measure beam position and intensity as well as the time structure of bunched photon beams.

Diamond quadrant monitors of a very compact detector design (**Figure 46**, left-hand picture) have been realized at the ESRF (ESRF Home page). The homoepitaxial CVD-diamond samples have areas of the order 4 mm × 4 mm and thicknesses ranging from 30 to 100 μm. They are mounted on a multilayer glass-ceramic pcb

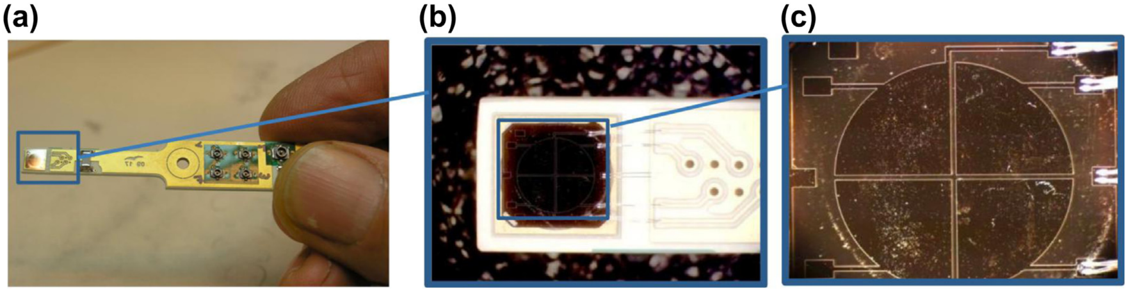

Figure 46 The compact X-ray Beam Position Monitor (XBPM) developed at ESRF (a). The diamond sensor is mounted on a glass-ceramic multilayer pcb (b) and the layout of the electrodes is a quadrant design with a 50 μm isolating cross-gap (c). The rear electrode is a single contact pad of same diameter, not visible in this image. Courtesy of John Morse, ESRF & Harris Kagan, RD42.

and connected to the FEE via microcoax wire lead outs (Figure 46 central picture). The isolating cross-gap of the sector electrodes (Figure 46, right-hand picture) is 50 μm wide, enabling monitoring of beam sizes between 0.1 and 50 μm.

The beam position is obtained by the simple algorithms given on the right-hand sketch of Figure 47, which considers the beam-induced currents in the four sectors (*A*, *B*, *C* and *D*) measured with slow, sensitive elecrometers. The left-hand picture of the figure illustrates the installation conditions of such an XBPM at the fluorescence microscopy beamline ID21 of the ESRF. On the top left of the figure, the indicated scale of 10 mm demonstrates the extremely limited available space. The diamond XBPM devices operate in dirty vacuum or in air, permanently placed into the intense focused X-ray beam.

In the case of free-electron X-ray lasers, the distances between source and sample are even larger than at synchrotrons (about several hundred meters). The required stability for source and optics are even harder to reach. Angular movement of the beam upstream can translate into very large position variations at the sample under investigation. Since many applications will have to use single shots (Graafsma, 2009), pulse-by-pulse position information is required. At the same time, the data acquisition cyclus, now ranging from milliseconds to a second, demand photon beam position monitors (pBPM) operating at comparable frequencies. The devices developed for DESY have been tested by "signal readout at synchrotron radiofrequency" using an "I-Tech Libera Brilliance" readout system originally designed for beam position measurements and feedback control of the electron beam in synchrotron storage rings. The Libera apparatus is in principle a narrow-passband RF voltmeter providing X and Y position information derived from four input voltage pulses, which correspond to the photon-induced currents in the four sectors.

Morse et al. (2010) have been the first confirming a Libera Brilliance system capable of monitoring beam-induced currents in a diamond quadrant pBPM. They tested this approach at DORIS III with a pBPM

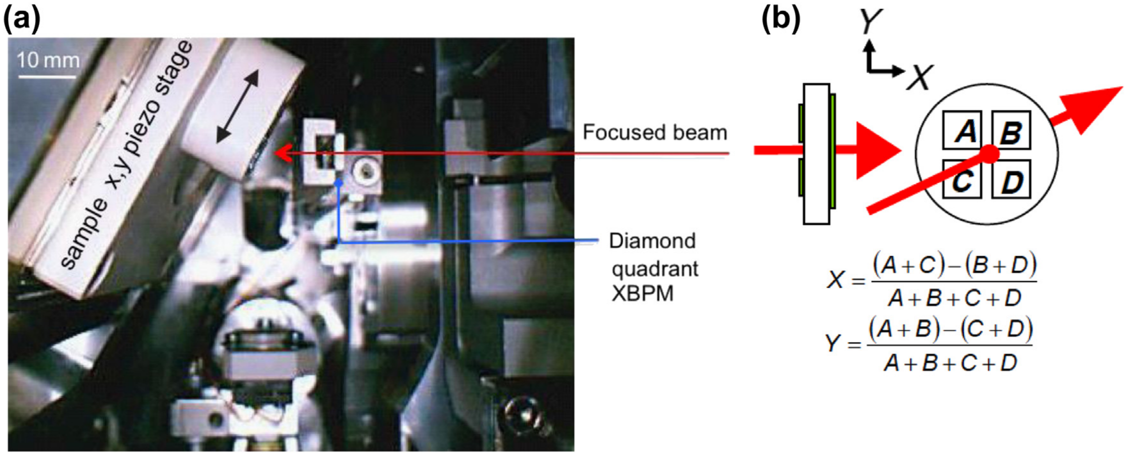

$$X = \frac{(A+C)-(B+D)}{A+B+C+D}$$

$$Y = \frac{(A+B)-(C+D)}{A+B+C+D}$$

Figure 47 (a) Diamond quadrant XBPM installed at beamline ID21 of the ESRF. The sensor is mounted in air perpendicular to the highly focused intense photon beam. The indicated 10 mm scale illustrates the restricted place available. (b) Principle of operation of XBPMs. Both, courtesy of John Morse, ESRF.

quadrant device impinged from an X-ray beam collimated to a diameter of 25 μm. The center of gravity position of the X-ray beam was obtained with the diamond signal output digitally sampled by the Brilliance system at a rate of 130 M samples per second. The measured position noise was below 50 nm (rms) for a bandwidth of 10 Hz—even after averaging of the position signals. The authors concluded that "it was not possible to clearly separate the noise contribution of the measurement system (including diamond) from the real movement of the beam position". John Morse summarized the status of the above developments at a recent Joint Users' Meeting at the National Synchrotron Light Source (NSLS home page) as follows: "the potential of diamond XBPMs with electrometer readout has been now established by several groups and for widely varying beam conditions. The deployment of such devices is ongoing at ESRF and SOLEIL (SOLEIL Home page). Sensors operating with improved LiberaRF readout will be installed at PETRA III" (Morse, 2012).

3.17.6.4.2 Beam Diagnostics Detectors for High-Intensity Synchrotron White Beams

In the following, the white-beam position monitors (wBPM) are described, which have been developed at the NSLS for the difficult task to monitor a range of power densities up to a maximum of ~90 W/mm^2, at spot sizes focused down to a 0.5 mm-diameter spot, and with a broad energy range from 5 to 15 keV (Bohon, Muller, & Smedley, 2010). The thermal effects that occur at these power densities turn out to be serious issues for many state-of-the-art synchrotron beamlines. The authors reported that prior to the installation of diamond sensors, "no device other than a fluorescent screen was available for the diagnosis of white beams"—and this was the case at any beamline of the NSLS.

Encouraged by the measurements performed with diamond sensors under modest beam conditions (Keister & Smedley, 2009), novel transmission-mode diamond wBPMs have been developed for simultaneous monitoring of flux, position, angle and timing of intense white beams (Muller et al., 2012). Two such cooled monitors were installed at the facility beamline X25 of the NSLs. They are placed at a distance of 13.5 m upstream and 15.82 m downstream the source center of a miniature-gap undulator, delivering 4.6×10^{11} photons per second across an energy range of 5–20 keV.

The four 100-μm-thick electronic grade scCVD diamond samples (grown by Element Six and supplied by DDL) used were selected from a batch of eight after white-beam X-ray topography screening, performed to ensure the absence of photoconductive gain or, at least, to identify the samples containing fewer defects responsible for gain in such devices (Keister & Smedley, 2009). After a standard acid cleaning followed by UV illumination for several hours, platinum electrodes of 30 nm thickness were sputtered, two on each incident surface of the samples. By this, a diamond pair completed a quadrant (Muller et al., 2012). **Figure 48(a)** shows the diagram of the electrical and thermal contacts to the diamonds as well as the dimensions of the platinum metallization and the overlap with the cupper block. The mechanical layout of the wBPMs is shown in **Figure 48(b)**. Each wBPM is constructed around two horizontally tiled single-crystal diamonds separated by an unavoidable small gap ≤50 μm. Phosphor–bronze clamps press the diamonds against a copper mount with a 1 mm overlap, providing both structural support and heat sinking. The electrical contact to the platinum pads is made with opposing phosphor–bronze clips.

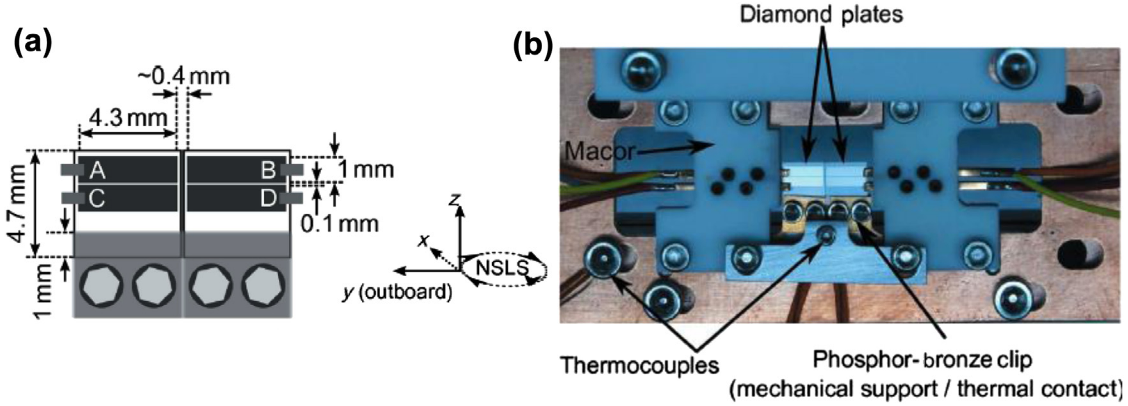

Figure 48 (a) Diagram of the electrical and thermal contacts to the diamonds as well as the dimensions of the platinum metallization. The overlap of the diamonds with the copper block is nominally 1 mm, clamped by a phosphor–bronze clip. (b) An overview photograph of the upstream water-cooled diamond wBPM, showing the intermediate electrical contacts and the Macor electrical isolation. Reprinted from Muller et al. (2012).

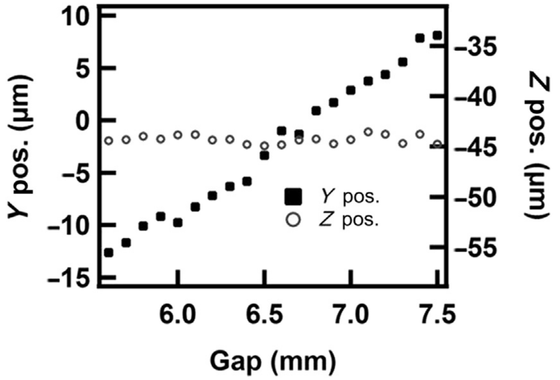

Figure 49 Dependence of the photon beam position versus the undulator gap separation. Reprinted from Muller et al. (2012).

Two thermocouples are used to monitor the temperature of the detector, one placed just below the diamonds on the phosphor–bronze clamp and the other several centimeters away on the copper housing, respectively. Both monitors are installed on a manipulator stage with horizontal and vertical motions for alignments. The upstream wBPM is rather "bulky," because it is mounted on a water-cooled copper block, which however ensures very high temperature stability. The downstream wBPM is designed without water cooling and is therefore more compact. A reasonable temperature stability is achieved by heat dissipation from the copper block and a copper rod support. In fact, the temperature drop of the downstream wBPM amounts only to a few degrees Kelvin, when the X-rays are impinging with the bias turned off (Muller et al., 2012).

The position, angle and flux of a white beam, focused to a spot of 3 mm × 1 mm, was monitored in real time with a position resolution of 500 nm in horizontal and 100 nm in vertical directions. The first diamond wBPM has been in operation for more than 1 year without any observable degradation in performance. The installation of the second (downstream) diamond, which followed about 6 months later, enabled the measurement of the angular trajectory of the photon beam.

Up to 748 mA total current was measured in the diamonds when the apertures were opened and the undulator gap adjusted to 5.68 mm. In **Figure 49**, the photon beam position measured with wBPMs is plotted versus the opening of the undulator gap (usually adjusted between 5.7 and 7 mm).

This study has been initiated after one of the first observations using wBPMs. In some cases, the diamond monitors revealed a photon beam movement by changing the undulator gap. Moreover, it was observed that a misalignment of the synchrotron electron beam resulted in a photon beam position that depends on the value of the undulator gap. This example demonstrates the usefulness of the diamond wBPM beyond the standard beam position monitoring. The authors concluded "The wBPM has proven to be reliable and robust, showing no degradation after more than one year in use. Such devices represent a new type of beamline diagnostic, allowing inline optimization of the undulator and calibration of the front-end apertures during commissioning of new beamlines or during normal operation".

3.17.6.4.3 Diamond in Solar Space Experiments—The Diamond Sensors of the LYRA Radiometer

Wide band gap semiconductors are the primary choice of photosensitive materials for photon detection in the VUV range. BenMoussa et al. (2009) tested diamond UV-photon sensors together with AlN and cubic boron nitride devices for the use of them in space experiments. They concluded, "The presented figure of merit of all tested materials is several orders of magnitude higher compared to silicon semiconductors, since they provide high radiation hardness, low dark signal at room temperature, solar-blindness, and chemical as well as thermal stability". The particular advantage of solar-blindness is that it allows for omitting some of the filters blocking the unwanted visible light, which, at the same time, seriously attenuate the desired UV radiation. The effective area and, due to this, the signal-to-noise ratio are increased.

The following paragraph is dedicated to the diamond VUV sensors of the large yield radiometer (LYRA) (BenMoussa et al., 2003; BenMoussa et al., 2006), which is one of the two scientific instruments on board of the ESA spacecraft PROBA-2 (PRoject for On-Board Autonomy 2), launched in November 2, 2009. The second apparatus (SWAP) is an imaging telescope operating on PROBA-2 next to LYRA. Together, they enable high-performance solar monitoring for space weather nowcasting and research. The PROBA satellites are "among the smallest spacecrafts ever flown by ESA, conceived for demonstrating new technologies on orbit" (ESA).

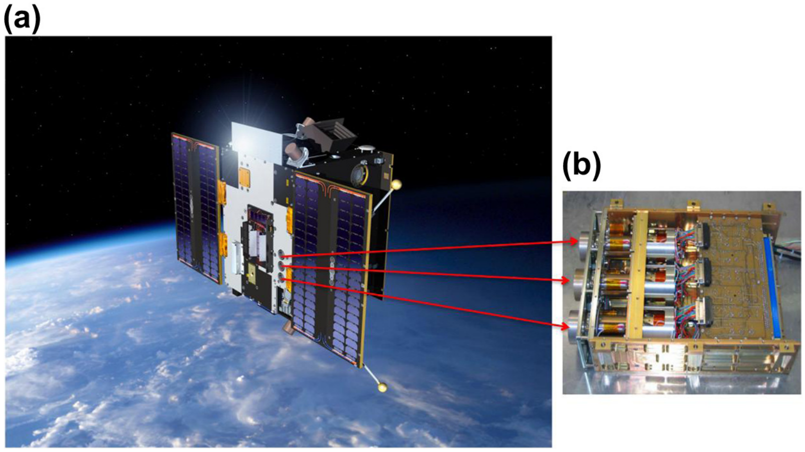

Figure 50 (a) Proba-2 satellite flying in a 720 km orbit is the second in ESA's Project for Onboard Autonomy series, capable of flying itself with minimal support from the ground. Its purpose is flight-test new technologies and it carries a total of 17 technology payloads. It also carries four scientific instruments focused on the sun and space weather. (b) The LYRA instrument (reprinted from Stockman et al., 2010). The arrows indicate the position of LYRA on board of PROBA-2. Reprinted from ESA web pages.

LYRA demonstrates technologies important for future missions such as the ESA Solar Orbiter. **Figure 50** shows on the left-hand side PROBA-2 and on the right-hand side LYRA, (reprinted from Stockman et al. (2010)), being "the first space assessment of a pioneering UV diamond detectors program" (BenMoussa et al., 2009). The red arrows indicate the position of LYRA on board of PROBA-2.

In 2006, Hochedez et al. (2006) described the LYRA instrument in *Advances in Space Research*. LYRA is a compact solar VUV radiometer, designed, manufactured and calibrated by a Belgian–Swiss–German consortium with additional international collaborations. The goal is to observe solar irradiance (the radiative output of the Sun) at highest possible cadence (>20 Hz). LYRA comprises three units, each being sensitive in four UV wavelength ranges relevant to aeronomy, space weather and solar physics applications: (1) 1–20 nm (zirconium), (2) 17–70 nm (aluminum), (3) 115–125 nm (lyman α), and (4) 200–220 nm (herzberg). Most likely because of the lyman-α range, the LYRA acronym is sometimes also derived in the literature from LYman RAdiometer.

Figure 51 is an exploded view of a single LYRA channel, consisting of a collimator and a head with a precision aperture, a spectral filter, a detector and two LED light sources. The solar-blind scCVD diamond detectors (hidden by the head) have been designed and fabricated at IMOMEC, Belgium, with the collaboration of the National Institute for Materials Science (NIMS), Tsukuba, Japan.

Two types of diamond sensors are investigated with LYRA: PiN photodiodes, and MSM (metal–semiconductor–metal) photoresistor structures with interdigitated Ti/Pt/Au electrodes. The PiN devices are used in the Herzberg channels, which offer (only in that range) excellent sensitivity and linearity and, at the same time, maximum solar-blindness. They have been meanwhile confirmed superior to Si in terms of spectral purity and signal-to-noise ratio. Although the MSM devices are less solar-blind and less linear than PiN diodes, they are used for the Lyman-α, the Al, and the Zr channels, because of possible uncontrolled photoemissions, which prevent the use of sensitive PiNs (Hochedez et al., 2006).

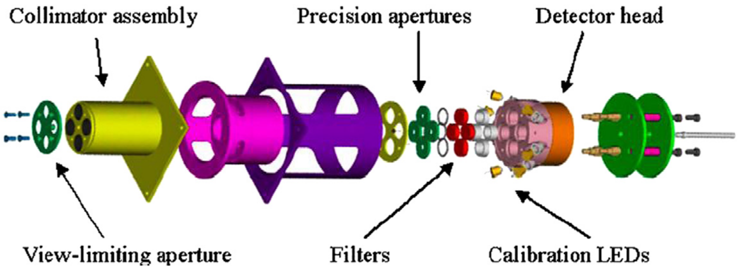

Figure 51 Exploded view of one of the three identical LYRA units. The collimator, the filters, the LEDs and the head can be seen. The detectors are hidden by the head. Reprinted from Hochedez et al., 2006.

LYRA has been switched on in space for the first time on November 16, 2009. The solar output in the different UV bands is sampled at least once every 50 ms, enabling to pursue how energy is released during solar events. After a prolonged period of low activity, "the sun awakens and the solar intensity measurements from LYRA are now available to the scientific community" (ESA). We refer to the ESA home pages (and references therein) for detailed information on the actual scientific results of the PROBA-2 mission and for many beautiful images of "the sun in action" delivered from SWAP.

3.17.7 Concluding Remarks

The operation of CVD-diamond detectors in stringent experimental conditions has been discussed. We addressed the limitations and constraints faced by diamond sensors in each of the main application fields comprised within the framework of particle and radiation physics on earth and space. After all, one can conclude that diamond sensors are capable of withstanding both high temperatures and high-radiation environments of levels, unreachable for comparable detector materials. Diamond detectors are unbeatable in beam diagnostics as well as timing applications, in particular, in experiments performed with high-intensity particle or photon beams. The conclusion concerning MIP tracking at large collider accelerators is not that clear. It has to be individually decided, whether it is preferable to apply a sensor material which deteriorates less than others under long-term heavy irradiation (such as diamond), or it is eventually more advantageous to use that material, which, at the end of the experiment, provides sensors of higher amplitudes and better S/N ratio (such as silicon).

All types of CVD-diamond detectors investigated show rather similar properties with respect to radiation hardness, temperature and breakdown stability or the fast collection of charge. However, the corresponding, most appropriate application fields are rather different since these are strongly dependent on the quality of the crystal structure of the sensing samples. The most difficult tasks for diamond detectors have been identified at the two opposite ends of the available particle energy and mass ranges: (1) the detection of heavy, low-energy ions, which are stopped in the diamond bulk (extremely polarizing defective sensors) and (2) the timing of relativistic particles of $Z = 1$ with a time resolution below 100 ps. The highest potential is currently attributed to the homoepitaxial scCVD diamond sensors, fulfilling the requirements of both timing and spectroscopy detectors. Moreover, they are almost free of polarization, and hence, the optimum choice over the whole energy range. However, where large detector areas are required, scCVD diamond fails. In spite of deficient operation, pcCVD diamond has to be used. It is expected that in the upcoming years, these applications will profit from the availability of large-area "quasi single-crystal" diamond plates grown by heteroepitaxy on iridium. Hitherto unexpectedly good energy resolution was obtained, which is currently worse than the resolution of homoepitaxial samples but unrivaled if compared to the heteroepitaxial samples grown on silicon. At the same time, DoI detectors show similar timing properties as confirmed for polycrystalline and single-crystal diamond sensors. From the present point of view, it will be solely the high-resolution energy/energy-loss spectroscopy remaining the exclusive domain of homoepitaxial diamond. Fortunately, diamond sensors for "slow" applications, such as ion spectroscopy or particle tracking, profit from the electronics originally developed for silicon detectors. However, the lack of suitable multichannel broadband electronics for large diamond timing sensors is still a serious problem in many upcoming large nuclear physics experiments. The ultimate improvement of low-noise diamond broadband assemblies for extreme radiation conditions will be conceivable when electronic devices based on diamond will appear on the market.

The last remaining to express is the hope that the diamond industry will continue with the development and the production of "detector-grade" CVD diamond. About 17 years after the formation of RD42 (Nazarè, Foster, Gilmore, Llewellyn, Tapper, et al., 1994), we experience an increasing interest on diamond detectors and the use of CVD diamond in important fields. However, the anticipated aims concerning the ultimate quality improvement of the detector materials, the enlargement of the active area of single-crystal diamond plates, and the standardization of reliable procedures for the diamond detector surface reconstruction before metallization are still not reached.

Acknowledgments

The author is grateful and indebted to all individual scientists as well as to all academic and industrial groups, which contributed over the centuries—up to present—to this exciting field of diamond science and technology and, therefore, to this comprehensive review on diamond detectors. In particular, we acknowledge the teams growing and supplying "detector-grade" CVD-diamond materials—without them this field could not and would not exist. We would like to extend our gratitude to the local national and to the European agencies for their financial support and to all colleagues and scientific publishers for the provision of published data and for the permission to use them for this report. We appreciate the increasing interest of the scientific diamond-detector user-community, with its continuous contribution of new ideas for novel challenging applications. Finally, we keep in mind all the nonlisted members of diverse laboratories and accelerator operating crews all over the world for their tireless support in many technical and mental aspects. The author is grateful to C. Kozhuharov, C. Schmidt, and M. Träger for their comments to this manuscript as well as for the daily discussions concerning diamond work, and more.

References

Adam, W., Boer, W., de, Borchi, E., et al. RD42. (2006). Radiation hard diamond sensors for future tracking applications. *Nuclear Instruments & Methods A, 565*, 278–283.

Agakichiev, G., For the HADES Collaboration. (2009). The high-acceptance dielectron spectrometer HADES. *European Physical Journal A, 41*, 243–277.

ALICE, A large ion collider experiment, http://aliceinfo.cern.ch/Public/Welcome.html.

Alig, R. C., Bloom, S., & Struck, C. W. (1980). Scattering by ionization and phonon emission in semiconductors. *Physical Review B, 22*(12), 5565–5582.

Almaviva, S., Marinelli, M., Milani, E., Prestopino, G., Tucciarone, A., Verona, C., et al. (2008). Thermal and fast neutron detection in chemical vapor deposition single-crystal diamond detectors. *Journal of Applied Physics, 103*, 054501.

Asner, D., Barbero, M., Bellini, V., Belyaev, V., Brom, J-M., Bruzzi, M., et al. RD42. (2011). Diamond pixel modules. *Nuclear Instruments & Methods A, 636*, S125–S129.

ATIMA. http://www-linux.gsi.de/weick/atima/.

ATLAS. http://atlas.web.cern.ch/Atlas/Collaboration/.

Bagge, E. (1937). Über die Berechnung der mittleren Ionisierungsenergie der Gase. *Annalen der Physik, 30*, 72, 5. Folge.

Barbero, M., Bellini, V., Belayaev, V., Berdermann, E., Bergonzo, P., Bruzzi, M., et al. RD42. (2008). *Development of Diamond Tracking detectors for High Luminosity Experiments at the LHC.* Status Report/RD42, CERN/LHCC 2008–005.

Barnes. J.J. (1972). *Surface threshold displacement energy measurement of silicon* (thesis). UCRL-51194, LB Laboratory, University of California.

Braun-Munzinger, P., & Stachel, J. (2007). The quest for the quark-gluon plasma. *Nature, 448*, 302–309.

Behnke, T., Douceta, M., Ghodbane, N., & Imho, A. (2003). Radiation hardness and linearity studies of CVD diamonds. *Nuclear Physics B, Proceedings Supplements, 125*, 263–266 (Innovative particles and radiation detectors).

Bell, A., Castro, E., Hall-Wilton, R., Lange, W., Lohmann, W., Macpherson, A., et al. (2010). Fast beam conditions monitor BCM1F for the CMS experiment. *Nuclear Instruments & Methods A, 614*, 433–438.

Bell, Alan. J., & On behalf of the CMS Beam & Radiation Monitoring Group (2008) Beam & Radiation Monitoring for CMS. (2008). *IEEE Nuclear Science Symposium Conference Record*, 2322–2325. http://ieeexplore.ieee.org.

BenMoussa, A., Hochedeza, J. F., Schmutz, W. K., Schühle, U., Nesladek, M., Stockman, Y., et al. (2003). Solar-blind diamond detectors for LYRA, the solar VUV radiometer on board PROBA II. *Experimental Astronomy, 16*, 141–148 (Berlin: Springer, 2005).

BenMoussa, A., Hochedeza, J. F., Schühle, U., Schmutz, W., Haenen, K., Stockman, Y., et al. (2006). Diamond detectors for LYRA, the solar VUV radiometer on board PROBA2. *Diamond & Related Materials, 15*(4–8), 802–806.

BenMoussa, A., Soltani, A., Schühle, U., Haenen, K., Chong, Y. M., Zhang, W. J., et al. (2009). Recent developments of wide-bandgap semiconductor based UV sensors. *Diamond & Related Materials, 18*, 860–864.

Benny, A. H., & Champion, F. C. (1954). Some effects of neutron irradiation of diamond. *Nature, 4414*, 1087.

Berdermann, E. (2009). Advanced diamond particle detectors. *Nuclear Physics News, 19*(2), 25–31 (London: Taylor & Francis).

Berdermann, E., Blasche, K., Moritz, P., Stelzer, H., Voss, B., & Zeytouni, F. (1999). First applications of CVD-diamond detectors in heavy-ion experiments. In E. Borchi, J. Huston, S. Majewski, A. Penzo, & P. G. Rancoita (Eds.), *Nuclear physics B: Vol. 78. Proc. 6th int. conf. on advanced technology and particle physics* (pp. 533–539). Elsevier.

Berdermann, E., Blasche, K., Moritz, P., Stelzer, H., & Voss, B. (2001). The use of CVD-diamond for heavy-ion detection. *Diamond & Related Materials, 10*, 1770–1777.

Berdermann, E., Blasche, K., Daues, H. W., Moritz, P., Stelzer, H., & Voss, B. (2001). The diamond project at GSI - Perspectives. In M. Barone, E. Borchi, J. Huston, C. Leroy, P. G. Rancoita, P. Riboni, et al. (Eds.), *Proc. 7th int. conf. on advanced technology & particle physics* (pp. 246–251). World Scientific Publishing Co. Pte. Ltd.

Berdermann, E., Caragheorgheopol, A., Ciobanu, M., Pomorski, M., Pullia, A., Riboldi, S., et al. (2008). Ion spectroscopy – a diamond characterization tool. *Diamond & Related Materials, 17*, 1159.

Berdermann, E., & Ciobanu, M. (2009). CVD-diamond detectors for experiments with hadrons, nuclei, and atoms. In R. S. Sussmann (Ed.), *CVD diamond for electronic devices and sensors* (1st ed.). (pp. 227–256) Chichester: John Wiley & Sons Ltd. ISBN: 978-0-470-06532-7 (HB).

Berdermann, E., Ciobanu, M., Connell, S. H., da Costa, A. M. O. D., Fernandet-Hernando, L., Oh, A., et al. (2004). Charged particle detectors made of single-crystal diamond. *Physica Status Solidi (A), 201*(11), 2521–2528.

Berdermann, E., Ciobanu, M., Herrmann, N., Hildenbrand, K. D., Kiš, M., Koenig, W., et al. (2009). Diamond start detectors. In *Proceedings IEEE NSS-MIC, Orlando*.

Berdermann, E., de Boer, W., Ciobanu, M., Dunst, S., Kiš, M., Koenig, W., et al. (2010). CVD-diamond detectors – R&D status and new results. In *Proc. XIVIII international winter meeting on nuclear physics – BORMIO2010, Bormio, Italy, January 25–29, 2010.* PoS(BORMIO2010)040.

Berdermann, E., Pomorski, M., de Boer, W., Ciobanu, M., Dunst, S., Grah, C., et al. (2010). Diamond detectors for hadron physics research. *Diamond & Related Materials, 19*, 358–367.

Bergonzo, P., Brambilla, A., Tromson, D., Marshall, R. D., Jany, C., Foulon, F., et al. (1999). Diamond-based semi-transparent beam-position monitor for synchrotron radiation applications. *Journal of Synchrotron Radiation, 6*, 1–6.

Bergonzo, P., Tromson, D., Mer, C., Guizard, B., Foulon, F., & Brambilla, A. (2001). *Physica Status Solidi (A), 185*(1), 167181.

Bergonzo, P., & Jackmann, R. B. (2004). In C. E. Nebel (Ed.), *Thin-Film Diamond II, by C.* San Diego: Academic Press.

Bethe, H. (1930). *Annalen der Physik, 5*, 325.

Bloch, F. (1933). *Annalen der Physik, 5*, 285.

de Boer, W., Bol, J., Furgeri, A., Müller, S., Sander, C., Berdermann, E., et al. (2007). Radiation hardness of diamond and silicon sensors compared. *Physica Status Solidi (A), 204*(9), 3004–3010.

Bohon, J., Muller, E., & Smedley, J. (2010). Development of diamond-based X-ray detection for high-flux beamline diagnostics. *Journal of Synchrotron Radiation, 17*, 711–718.

Bohr, N. (1916). *Philosophical Magazine, 30*, 606.

Borer, K., Janos, S., Li, Z., Dezillie, B., Da Viá, C., Granata, V., et al. (2001). Charge collection efficiency of an irradiated cryogenic double-p silicon detector. *Nuclear Instruments & Methods A, 462*(3), 474–483.

Borst, T. H., & Weis, O. (1996). *Physica Status Solidi (A), 154*, 423.

Bourgoin, J. C., & Massarani, B. (1976). *Physical Review B, 14*, 3690.

Braun-Munzinger, P., & Stachel, J. (2007). The quest for the quark-gluon plasma. *Nature, 448*, 302–309.

Braunschweig, W., Chu, Z. H., Karpinski, W., Kubicki, Th., Lübelsmeyer, K., Rente, C., et al. (1996). Time structure of charge signals and noise studies of GaAs detectors irradiated by neutrons and protons. *Il Nuovo Cimento, 109A*(9), 1289–1302.

Bruzzi, M. (2009). Diamond radiation sensors for radiotherapy. In R. S. Sussmann (Ed.), *CVD diamond for electronic devices and sensors* (pp. 185–206). Chichester: John Wiley & Sons. ISBN: 978-0-470-06532-7 (HB).

Bruzzi, M., Menichelli, D., & Sciortino, S. (2002). Deep levels and trapping mechanisms in chemical vapor deposited diamond. *Journal of Applied Physics, 91*(9), 5765–5774.

Butler, J. E., Cheesman, A., & Ashfold, M. N. R. (2009). Recent progress in the understanding of CVD growth of diamond. In R. S. Sussmann (Ed.), *CVD diamond for electronic devices and sensors* (pp. 103–124). John Wiley & Sons Ltd., 978-0-470-06532-7 (HB).

Campbell, B., & Mainwood, A. (2000). Radiation damage of diamond by electron and gamma irradiation. *Physica Status Solidi (A), 181*, 99.

Caughey, D. M., & Thomas, R. E. (1967). Carrier mobilities in silicon empirically related to doping and field. *Proceedings of the IEEE, 55*, 2192.

Ciobanu, M., Berdermann, E., Herrmann, N., Hildenbrand, K. D., Kis, M., Koenig, W., et al. (2011). In-beam diamond start detectors. *IEEE Transactions on Nuclear Science, 58*(4), 2073–2083.

Ciobanu, M., Schuettauf, A., Cordier, E., Herrmann, N., Hildenbrand, K. D., Kim, Y. J., et al. (2007). A front-end electronics card comprising a high gain/high bandwidth amplifier and a fast discriminator for time-of-flight measurements. *IEEE Transactions on Nuclear Science, 54*, 1201–1206.

Clark, C. D., Ditchburn, R. W., & Dyer, H. B. (1956). The absorption spectra of irradiated diamonds after heating. *Proceedings of the Royal Society A, 237*(1208), 75–89.

Clark, C. D., Kemmey, P. J., & Mitchell, E. W. J. (1961). Optical and electrical effects of radiation damage in diamond. *Discussions of the Faraday Society, 31*, 96–106.

Clark, C. D., & Mitchell, E. W. J. (1977). Radiation effects in semiconductors. In N. B. Urli, & J. W. Corbett (Eds.), *IOP conf. proc. 31* (pp. 45).

Clark, C. D., & Walker, J. (1973). The neutral vacancy in diamond. *Proceedings of the Royal Society of London A., 334*, 241–257.

CMS, Compact muon solenoid, http://cms.web.cern.ch/.

Collins, A. T. (2009). Detectors for UV and far UV radiation. In R. S. Sussmann (Ed.), *CVD diamond for electronic devices and sensors* (1st ed.). (pp. 165–183) Chichester: John Wiley & Sons Ltd. ISBN: 978-0-470-06532-7 (HB).

Curtiss, L. F., & Brown, B. W. (1947). Diamond as a gamma-ray counter. *Physical Review Letters, 72*, 643.

Dabrowski, W. (1989). Transport equations and Ramo's theorem: applications to the impulse response of a semiconductor detector and to the generation-recombination noise in a semiconductor junction. *Progress in Quantum Electronics, 13*, 233.

Dannefaer, S., & Jakoubovskii, K. (2008). Defects in electron irradiated boron-doped diamonds investigated by positron annihilation and optical absorption. *Journal of Physics: Condensed Matter, 20*(23), 235225.

Davies, G., Campbell, B., Mainwood, A., Newton, M., Watkins, M., Kanda, H., et al. (2001). Interstitials, vacancies and impurities in diamond. *Physica Status Solidi (A), 186*(2), 187–198.

Davies, G., Lawson, S. C., Collins, A. T., Mainwood, A., & Sharp, S. (1992). Vacancy-related centers in diamond. *Physical Review B, 46*(20), 13157–13170.

DDL, Diamond Detectors Ltd, 16 Fleetsbridge Business Centre, Upton Road, Poole, Dorset, BH17 7AF.

Deferme, W., Bogdan, A., Bogdan, G., Haenen, K., & De Ceuninck, W. (2007). Electrical transport measurements and emission properties of freestanding single crystalline CVD diamond samples. *Physica Status Solidi (A), 204*(9), 3017–3022.

Deferme, W., Tanasa, G., Amir, J., Haenen, K., Nesládek, M., & Flipse, C. F. J. (2006). The role of (sub)-surface oxygen on the surface electronic structure of hydrogen terminated (100) CVD diamond. *Diamond & Related Materials, 15*, 687–691.

Derry, T. E., Fearick, R. W., & Sellshop, J. P. F. (1975). *NPRU publication series: NPRU 75/12.* DESY: Deutsches Electron Synchrotron. http://www.desy.de.

Dyer, H. B., & Ferdinando, P. (1966). The optical absorption of electron-irradiated semiconducting diamond. *British Journal of Applied Physics, 17*, 419–420.

Dyer, H. B., Raal, F. A., du Preez, L., & Loubser, J. H. N. (1965). *Philosophical Magazine, 11*, 763.

EFDA, European Fusion Development Agreement, http://www.efda.org/.

Einstein, A. (1905, March 17). *Annalen der Physik, 4*, 132. § 8.

Element Six Ltd., Kings Ride Park, Ascot, Berkshire, SL5 8BP, UK, http://www.e6.com.

ENEA, Italian National Agency for new technologies, Energy and sustainable economic development, http://www.enea.it/it.

Eremin, V., Strokana, N., Verbitskaya, E., & Li, Z. (1996). Development of transient current and charge techniques for the measurement of effective net concentration of ionized charges in the space charge region of p-n junction detectors. *Nuclear Instruments & Methods A, 372*, 388–398.

ESRF, European Synchrotron Radiation Source, http://www.esrf.fr.

EURATOM, The European Atomic Energy Community, http://ec.europa.eu/energy/nuclear/euratom/.

FAIR, Facility for Antiproton and Ion Research, Darmstadt, Germany, http://www.gsi.de/portrait/fair.html.

Fano, U. (1946). On the theory of ionization yield of radiations in different substances. *Physical Review, 70*(1 and 2), 44–52.

Fano, U. (1947). Ionization yield of radiations. II, the fluctuations of the number of ions. *Physical Review, 72*, 26–29.

Farrer, R. G. (1969). *Solid State Communications, 7*, 686.

Field, J. E. (Ed.). (1979). *The properties of diamond*. London: Academic Press.

Field, J. E. (Ed.). (1992). *The properties of natural and synthetic diamond*. London: Academic Press.

Fink, J., Krüger, H., Lodomez, P., & Wermes, N. (2006). Characterization of charge collection in CdTe and CZT using the transient current technique. *Nuclear Instruments & Methods A, 560*(2), 435.

Frais-Kölbl, H., Griesmayer, E., Pernegger, H., & Kagan, H. (2004). A fast low-noise charged-particle CVD diamond detector. *IEEE Transactions on Nuclear Science., 51*(6), 3833–3837.

Franklin, M., Fry, A., Gan, K. K., Han, S., Kagan, H., Kanda, S., et al. (1992). *Nuclear Instruments & Methods A, 315*, 39–42.

Gabrysch, M., Marklund, E., Hajdu, J., Twitchen, D. J., Rudati, J., Lindenberg, A. M., et al. (2008). Formation of secondary electron cascades in single-crystalline plasma-deposited diamond upon exposure to femtosecond X-ray pulses. *Journal of Applied Physics, 103*, 064909.

Galbiati, A., Lynn, S., Oliver, K., Schirru, F., Nowak, T., Marczewska, B., Dueñas, J. A., Berjillos, R., Martel, I., & Lavergne, L. (2009). Performance of Monocrystalline Diamond Radiation Detectors Fabricated Using TiW, Cr/Au and a Novel Ohmic DLC/Pt/Au Electrical Contact. *IEEE Transactions of Nuclear Science, 56*, 1863.

Gaukroger, M. P., Martineau, P. M., Crowder, M. J., Friel, I., Williams, S. D., & Twitchen, D. J. (2008). X-Ray topography studies of dislocations in single crystal CVD Diamond. *Diamond & Related Materials, 17*(3), 262.

Gonon, P., Prawer, S., Nugent, K. W., & Jamieson, D. N. (1996). Radiation damage induced by MeV alpha particles in polycrystalline diamond films. *Journal of Applied Physics, 80*(9), 5006–5013.

Graafsma, H. (2009). Requirements for and development of 2 dimensional X-ray detectors for the European X-ray free electron laser in Hamburg. *Journal of Instrumentation, 4*, 12011.

Grah, C., Afanaciev, K., Emeliantchik, I., Harder, U., Henschel, H., Ignatenko, A., Kouznetsova, E., Lange, W., Lohmann, W., Ohlerich, M., & Schmidt, R. (2009). *IEEE Transactions on nuclear science, 56*, 462–467. http://dx.doi.org/10.1109/TNS, 2009.2013853.

GSI, Helmholtz Zentrum für Schwerionenforschung GmbH, http://www.gsi.de/.

Gudden, B., & Pohl, R. (1920). Über lichtelektrische Fähigkeit von Diamanten. *Zeitschrift für Physik Bd., III*, 123–129.

Gudden, B., & Pohl, R. (1923a). Über lichtelektrische Wirkung und Leitung in Kristallen. *Zeitschrift für Physik, 16*(1), 170–182.

Gudden, B., & Pohl, R. (1923b). Das Quantenäquivalent bei der lichtelektrischen Leitung. *Zeitschrift für Physik, 17*(1), 331–346.

Hall-Wilton, R., Gastal, M., Loos, R., Ryjov, V., Pernicka, M., Steininger, H., et al. (2012). Studies of PLT-type single-crystal diamond pixel detectors. In *IEEE NSS 2011 Conference Record 6154592* (pp. 1150–1155).

Hartmann, F. (2010). Semiconductor sensors. In *Proc. of the 12th Vienna conference on instrumentation – VCI 2010*.

He, Z. (2001). Review of the Shockley-Ramo theorem and its application in semiconductor gamma-ray detectors. *Nuclear Instruments & Methods A, 463*, 250.

Hecht, K. (1932). Zum Mechanismus des lichtelektrischen Primärstromes in isolierenden Kristallen. *Zeitschrift für Physik, 77*, 235–246.

van Heerden, P. J. (1945). *The crystal counter – a new instrument in nuclear physics* (thesis). University of Utrecht.

Hempel, M. (2011), http://www-carat.gsi.de/CARAT03/CARAT03Talks/Lohmann_CARAT03.pdf.

Hochedez, J.-F., Schmutz, W., Stockman, Y., Schühle, U., BenMoussa, A., Koller, S., et al. (2006). LYRA, a solar UV radiometer on Proba2. *Advances in Space Research, 37*, 303–312.

Hofstadter, R. (April 1949a). Crystal counters-I. *Nucleonics*.

Hofstadter, R. (May 1949b). Crystal counters-II. *Nucleonics*.

Hügging, F., & On behalf of the ATLAS Collaboration. (2011). The ATLAS Pixel Insertable B-Layer (IBL). *Nuclear Instruments and Methods A, 650*, 45–49.

Hughes, A. L., & Du Bridge, L. A. (1932). *Photoelectric phenomena*. New York: McGraw Hill Book Co. Inc.

Huhtinen, M. (2002). Simulation of non-ionising energy loss and defect formation in silicon. *Nuclear Instruments & Methods A, 491*, 194.

Husson, D., Bauer, C., Baumann, I., et al., RD42. (1997). Neutron irradiation of CVD diamond samples for tracking detectors. *Nuclear Instruments & Methods A, 388*, 421–426.

IMOMEC, Belgium, http://www.uhasselt.be/IMO.

Isberg, J. (2009). Transport properties of electrons and holes in diamond. In R. S. Sussmann (Ed.), *CVD diamond for electronic devices and sensors* (1st ed.). (pp. 29–48) Chichester: John Wiley & Sons Ltd. ISBN: 978-0-470-06532-7 (HB).

Isberg, J., Gabrysch, M., Tajani, A., & Twitchen, D. (2006). Transient current electric field profiling of single crystal CVD diamond. *Semiconductor Science and Technology, 21*, 1193–1195.

Isberg, J., Hammersberg, J., Johansson, E., Wikström, T., Twitchen, D. J., Whitehead, A. J., et al. (2002). *Science, 297*(5587), 1670–1672.

Isberg, J., Majdi, S., Gabrysch, M., Friel, I., & Balmer, R. S. (2009). A lateral time-of-flight system for charge transport studies. *Diamond & Related Materials, 18*, 1163–1166.

ITER, http://www.iter.org/proj.

Jacoboni, C., Canali, C., Ottaviani, G., & Alberigi Quaranta, A. (1977). A review of some charge transport properties of silicon. *Solid-State Electronics, 20*, 77–89.

JET (Joint European Torus), http://www.ccfe.ac.uk/JET.aspx.

Johns, D., & Martin, K. (1997). *Analog integrated circuit design*. New York: John Wiley and Sons Inc.

Juška, G., Viliunas, M., Klíma, O., Šípek, E., & Kočka, J. (1994). New features in space-charge-limited-photocurrent transients. *Philosophical Magazine Part B, 69*(2), 277–289.

Kagan, H., Gan, K. K., & Kass, R. (2008). *Development of single crystal chemical vapour deposition diamonds for detector applications*. Final report for Ohio State University Grant DE-FG02–06ER41432.

Kagan, H., & Trischuk, W. (2009). Radiation sensors for high energy physics experiments. In R. S. Sussmann (Ed.), *CVD diamond for electronic devices and sensors* (1st ed.). (pp. 207–226) Chichester: Wiley & Sons. ISBN: 978-0-470-06532-7 (HB).

Kagan, H., & for RD42. (2010). *Diamond for High Energy Radiation and Particle Detection. Presentation at the RESMDD 2010*. Italy: Florence.

Kalisch, R. (1993). Ion beam modification of diamond. *Diamond & Related Materials, 2*(5–7), 621–633.

Kalisch, R. (2003). Doping diamond by ion-implantation. In C. E. Nebel, & J. Ristein (Eds.) (1st ed.).*Series semiconductors and semimetals: Vol. 76. Thin-film diamond I* (pp. 145–181) Elsevier Academic Press. (Chapter 3).

Kalisch, R., Bernstein, T., Shapiro, B., & Talmi, A. (1980). *Radiation Effects, 52*, 153.

Kamo, M., Sato, Y., Matsumoto, S., & Setaka, N. (1983). *Journal of Crystal Growth, 62*, 642.

Kania, D. R., Landsrass, M. I., Plano, M. A., Pan, L. S., & Han, S. (1993). Diamond radiation detectors. *Diamond & Related Materials, 2*, 1012–1019.

Keister, J. W., & Smedley, J. (2009). *Nuclear Instruments & Methods A, 606*, 774–779.

Klein, C. A. (1968). Bandgap dependence and related features of radiation ionization energies in semiconductors. *Journal of Applied Physics, 39*(4), 2029.

Konorova, E. A., & Kozlov, S. F. (1970). *Fizika i Tekhnika Poluprovodnikov, 4*, 1865.

Kozlov, S. F., Konorova, E. A., Barinov, A. L., & Jarkov, V. P. (1975). Neutron spectrometer by diamond detector for nuclear radiation. *IEEE Transactions on Nuclear Science, NS-22*, 171–172.

Kozlov, S. F., Konorova, E. A., Krapivin, M. I., Nadein, V. A., & Yudina, V. G. (1977). Usage of diamond detectors as immersed alpha counters. *IEEE Transactions on Nuclear Science, NS-24*(1), 242–243.

Kozlov, S. F., Konorova, E. A., Kuznetsov, Y. A., Salikov, Y. A., Redko, V. I., Grinberg, V. R., et al. (1977). Diamond dosimeter for X-ray and d-radiation. *IEEE Transactions on Nuclear Science, NS-24*(1), 235–237.

Kozlov, S. F., Stuck, R., Hage-Ali, M., & Siffert, P. (1975). Preparation and characteristics of natural diamond radiation detectors. *IEEE Transactions on Nuclear Science, NS-22*, 160–170.

Lappe, F. (1961). The energy of electron-hole pair formation by X-rays in PbO. *Journal of Physics and Chemistry of Solids, 20*(3/4), 173–176.

LHC, Technical Design Report. https://edms.cern.ch/file/445830/5/Vol_1_Chapter_2.pdf.

Lattanzi, D., Angelone, M., Pillon, M., Almaviva, S., Marinelli, M., & JET EFDA contributors. (2008). *Single Crystal CVD Diamonds as Neutron Detectors at JET.* EFDA–JET–CP(08)04/04.

Lattanzi, D., Angelone, M., Pillon, M., Almaviva, S., Marinelli, M., Milani, E., et al. (2009). Single crystal CVD diamonds as neutron detectors at JET. *Fusion Engineering and Design, 84*, 1156–1159.

Lebedev, A. A., Kozlovski, V. V., Strokan, N. B., Davydov, D. V., Ivanov, A. M., Strel'chuk, A. M., et al. (2002). *Semiconductors, 36*, 1270–1275.

Lenard, P. (1902). *Annalen der Physik, 4*(8), 149. § 26.

LHC, http://lhc-machine-outreach.web.cern.ch/lhc-machine-outreach/.

Lindhard, J., & Sørensen, A. H. (1996). *Physical Review A, 53*, 2443.

Liu, M., Xing, D. Y., Ting, C. S., & Xu, W. T. (1988). Hot-electron transport for many-valley semiconductors by the method of nonequilibrium statistical operators. *Physical Review B, 37*(6), 2997.

Lutz, G. (1999). *Semiconductor radiation detectors.* Berlin, Heidelberg: Springer-Verlag. ISBN 3-540-64859-3, pp.102-105.

Mainwood, A. (2000). Recent developments of diamond detectors for particles and UV radiation. *Semiconductor Science & Technology, 15*. R55.

Mainwood, A., Newton, M., & Campbell, B. (2001). http://ssd-rd.web.cern.ch/ssd-rd/rd/talks/mainwood-rd-2001.pdf.

Manfredotti, C., Polesello, P., Truccato, M., Vittone, E., Giudice, A Lo, & Fizzotti, F. (1998). CVD diamond detectors. *Nuclear Instruments & Methods A, 410*, 96–98.

Martineau, P. M., Lawson, S. C., Taylor, A. J., Quin, S. J., Evans, D. J. F., & Crowder, M. J. (2004). *Gems & Gemology, 40*, 2.

Martini, M., & Ottaviani, G. (1969). Ramo's theorem and the energy balance equations in evaluating the current pulse from semiconductor detectors. *Nuclear Instruments & Methods, 67*, 177.

Matsumoto, S., Sato, Y., Kamo, M., & Setaka, N. (1982). Vapor deposition of diamond particles from methane. *Japanese Journal of Applied Physics, 21*, L183.

McKay, K. G. (1948). Electron bombardment conductivity in diamond. *Physical Review, 74*(11), 1606–1621.

Meier, D. (1999). *CVD diamond sensors for particle detection and tracking* (thesis). Heidelberg: Ruprecht-Karls Universität.

Mikkelsen, H. H., & Sigmund, P. (1989). Barkas effect in electronic stopping power: rigorous evaluation for the harmonic oscillator. *Physical Review A, 40*, 101–116.

Mitchell, E. W. J. (1959). A review of recent work on diamond. *Journal of Physics and Chemistry of Solids, 8*, 444–449.

Mohler, F., & Taylor, J. (1934). *Journal of Research of the National Bureau of Standards, 13*, 659.

Moll, M., & The RD50 Collaboration. (2009). Recent advances in the development of radiation tolerant silicon detectors for the super-LHC. In *ICATPP conf. Villa Olmo, Italy, 5–9 October*.

Mora, A. E., Steeds, J. W., Butler, J. E., Yan, C.-S., Mao, H. K., Hemley, R. J., et al. (2005). *Physical Status Solidi (A), 202*, 2943.

Moritz, P., Berdermann, E., Blasche, K., Stelzer, H., & Voss, B. (2001). Broadband electronics for diamond detectors. *Diamond & Related Materials, 10*, 1770–1777.

Moritz, P., Berdermann, E., Blasche, K., Stelzer, H., & Zeytouni, F. (1998). Diamond detectors for beam diagnostics in heavy-ion accelerators. In *AIP conference proceedings, 3rd European workshop on beam diagnostics and instrumentation for particle accelerators, DIPAC III, Stanford CA*.

Morse, J. (2012). *X-ray beam position Monitors: hardware and experience.* Presentation at the 2012 NSLS/CFN joint users' meeting, Brookhaven, NY.

Morse, J., Salomé, M., Berdermann, E., Pomorski, M., Grant, J., O'Shea, V., et al. (2008). Single crystal CVD diamond detectors: position and temporal response measurements using a synchrotron microbeam probe. In , *Materials Research Society symposium proceedings series: Vol. 1039. Diamond electronics – fundamentals to applications II*. Warrendale, PA: Materials Research Society. pp. P06–P02.

Morse, J., Solar, B., & Graafsma, H. (2010). Diamond X-ray beam-position monitoring using signal readout at the synchrotron radiofrequency. *Journal of Synchrotron Radiation, 17*(4), 456–464.

Muller, E. M., Smedley, J., Bohon, J., Yang, X., Gaowei, M., Skinner, J., et al. (2012). Transmission-mode diamond white-beam position monitor at NSLS. *Journal of Synchrotron Radiation, 19*, 381–387.

Müller, S. (2011). *The beam condition monitor 2 and the radiation environment of the CMS detector at the LHC.* PhD Thesis. University of Karlsruhe.

Nava, F., Canali, C., Artuso, M., Gatti, E., & Manfredi, P. F. (1979). Transport properties of natural diamond used as nuclear particle detector for a wide temperature range. *IEEE Transactions on Nuclear Science, NS-26*(1), 308–316.

Nava, F., Bertuccio, G., Cavallini, A., & Vittone, E. (2008). Silicon carbide and its use as a radiation detector material. *Measurements Science and Technology, 19*, 102001 (25pp).

Nava, F., Bertuccio, G., Cavallini, A., & Vittone, E. (2008). *Measurement Science & Technology, 19*, 102001.

Nazarè, M. H., Foster, B., Gilmore, R. S., Llewellyn, T. J., Tapper, R. J., et al., RD42. (1994). *Development of diamond tracking detectors for high luminosity experiments at the LHC.* CERN-LHCC Proposal.

Nebel, C. E. (1998). *Optische und elektronische Eigenschaften von CVD-Diamant* (Habilitation thesis). Technische Universität München.

Nebel, C. E. (2003). Electronic properties of CVD diamond. *Semiconductor Science and Technology, 18*, S1–S11.

Nebel, C. E., Münz, J., Stutzmann, M., Zachai, R., & Güttler, H. (1996). Electronic properties of CVD and synthetic diamond. *Physical Review B, 55*(15), 9786–9791.

Nebel, C. E., Stutzmann, M., Lacher, F., Koidl, P., & Zachai, R. (1998). Carrier trapping and release in CVD-diamond films. *Diamond & Related Materials, 7*, 556–559.

Nebel, C. E., Waltenspiel, A., Stutzmann, M., Paul, M., & Schäfer, L. (2000). Persistent photocurrents in CVD diamond. *Diamond & Related Materials, 9*, 404–407.

Nesládek, M., Meykens, K., Stals, L. M., Quaeyhaegens, C., D'Olieslaeger, M., Wu, T. D., Vaněček, M., & Rosa, J. (1996). Investigation of n-doping in CVD diamond using gap states spectroscopy. *Diamond and Related Materials, 5*, 1006–1011.

Nesladek, M., Bogdan, A., Deferme, W., Tranchant, N., & Bergonzo, P. (2008). Charge transport in high mobility single crystal diamond. *Diamond & Related Materials, 17*, 1235.

Normand, E. (1996). Single event upset at ground level. *IEEE Transactions on Nuclear Science, 43*, 2742–2750.

NSLS, National Synchrotron Light Source, http://www.nsls.bnl.gov/.

Oh, A., Moll, M., Wagner, A., & Zeuner, W. (2000). Neutron irradiation studies with detector grade CVD diamond. *Diamond & Related Materials, 9*(11), 1897–1903.

Oh, A., Caylar, B., Pomorski, M., & Wengler, T. (2013). A novel detector with graphitic electrodes in CVD diamond. *Diamond & Related Materials, 38*, 9–13.

Ohl, R. (1940) in http://www.computerhistory.org/semiconductor/timeline/1940-Discovery.html. Discovery of the pn-junction.

Ohl, R. (1941) in http://www.computerhistory.org/semiconductor/timeline/1941-semiconductor.html. Semiconductor diode rectifiers serve in WW II.

Ohtsuka, K., Suzuki, K., Sawabe, A., & Inuzuka, T. (1996). Epitaxial growth of diamond on Iridium. *Japanese Journal of Applied Physics, 35*, L1072–L1074.

Pan, L. S., Kania, D. R., Han, S., Ager, J. W., III, Landsrass, M., Landen, O. L., et al. (1992). Electrical transport properties of undoped CVD diamond films. *Science, 255*, 830–833.

Pernegger, H. (2008). High-mobility diamonds and particle detectors. In S. Koizumi, C. E. Nebel, & M. Nesládek (Eds.), *Physics and applications of CVD diamond* (pp. 309–328). Wiley-VCH Verlag GmbH & CoKG, ISBN 978-3-527-40801-6.

Pernegger, H., & On Behalf of the ATLAS Collaboration. (2011). ATLAS insertable B-layer overview. In *Proc. VERTEX 2011, June 19–24, 2011, Rust, Lake Neusiedl, Austria*.

Pernegger, H., Roe, S., Weilhammer, P., Eremin, V., Frais-Kolbl, H., Griesmayer, E., et al. (2005). Measurement of charge carrier properties in single-crystal CVD diamond using the transient-current technique. *Journal of Applied Physics, 97*, 073704.

Pietraszko, J., Fabietti, L., Koenig, W., Weber, M., & On Behalf of the HADES Collaboration. (2010). Diamonds as timing detectors for minimum-ionizing particles: the HADES proton-beam monitor and start signal detectors for time of flight measurements. *Nuclear Instruments & Methods A, 618*, 121–123.

Pietraszko, J. & Koenig, W. (2011). *Diamond based detectors for timing applications at HADES*. Presentation 3rd CARAT Workshop, December 11–13, 2011, Darmstadt, Germany. Available online. http://www-carat.gsi.de/CARAT03/CARAT03Talks/Pietraszko_CARAT03.pdf.

Pinto, H., & Jones, R. (2009). Theory of the birefringence due to dislocations in single crystal CVD diamond. *Journal of Physics: Condensed Matter, 21*, 364220 (7pp).

Pomorski, M. (2008). *Electronic properties of CVD diamond and its suitability for particle detection in hadron physics experiments* (thesis). Goethe Universität Frankfurt.

Pomorski, M., Berdermann, E., Caragheorgheopol, A., Ciobanu, M., Kiš, M., Martemiyanov, A., et al., On Behalf of the NoRHDia Collaboration. (2006). Development of single-crystal CVD-diamond detectors for spectroscopy and timing. *Physica Status Solidi (A), 203*(12), 3152–3160.

Pomorski, M., Berdermann, E., Ciobanu, M., Martemiyanov, A., Moritz, P., Rebisz, M., et al. (2005). Characterization of single crystal CVD diamond particle detectors for hadron physics experiments. *Physica Status Solidi (A), 202*(11), 2199–2205.

Prins, J. F. (1993). Ion beam modification and dopant activation in diamond. *Nuclear Instruments & Methods B, 80/81*, 1433–1440.

Prins, J. F. (2000). The nature of radiation damage in diamond: activation of oxygen donors. *Diamond & Related Materials, 9*, 1275–1281.

Prins, J. F. (2002). Implantation-doping of diamond with B^+, C^+, N^+ and O^+ ions using low temperature annealing. *Diamond & Related Materials, 11*, 612.

Prins, J. F., & Derry, T. E. (2000). Radiation defects and their annealing behaviour in ion-implanted diamonds. *Nuclear Instruments & Methods B, 166-167*, 364–373.

Prins, J. F., Derry, T. E., & Sellschop, J. P. F. (1986). Volume expansion of diamond during ion implantation. *Physical Review B, 34*, 8870.

Pu, A., Avalos, V., & Dannefaer, S. (2001). Negative charging of mono-and divacancies in IIa diamonds by monochromatic illumination. *Diamond & Related Materials, 10*, 586.

Ramo, S. (1939). Currents induced by electron motion. *Proceedings of the IRE, 27*(9), 584–585.

Redfield, A. G. (1954). Electronic Hall Effect in Diamond. *Physical Review, 94*, 526–537.

Riordan, M., & Hoddeson, L. (June 1997). Excerpts from the book 'Crystal Fire – the Birth of the Information Age'. *IEEE Spectrum*.

Ristein, J. (2004). Structural and electronic properties of diamond surfaces. In C. E. Nebel, & J. Ristein (Eds.), *Series semiconductors and semimetalsThin-film diamond II* (pp. 37–96). San Diego, CA, USA: Elsevier Inc.

Robertson Sir, R., Fox, J. J., & Martin, A. E. (1934). *Philosophical Transactions of the Royal Society, 232*, 463.

ROSE Collaboration (2001). http://rd48.web.cern.ch/rd48/technical-notes/rosetn.htm#2001.

Sann, H. (1997). Position sensitive detectors in heavy ion physics at GSI. *Nuclear Instruments & Methods A, 392*, 433.

Sawabe, A. (JP Patent 2009). *Base Substrate for Epitaxial diamond film, Method for Producing the Base Substrate for Epitaxial Diamond Film, and Method for Producing the Epitaxial Diamond Film*. Kanagawa JP Appl. No. 20090176114.

Schreck, M., Roll, H., & Stritzker, B. (1999). Diamond/Ir/SrTiO3: A material combination for improved heteroepitaxial diamond films. *Applied Physics Letters, 74*, 650–652.

Sciortino, S., Hartjes, F., Lagomarsino, S., Nava, F., Brianzi, M., Cindro, et al.. (2005). Effect of heavy proton and neutron irradiations on epitaxial 4H-SiC Schottky diodes. *Nuclear Instruments & Methods A, 552*, 138–145.

Schreck, M. (2009). Heteroepitaxial growth. In R. S. Sussmann (Ed.), *CVD diamond for electronic devices and sensors* (pp. 125–161). John Wiley & Sons Ltd. ISBN: 978-0-470-06532-7 (HB).

Sellschop, J. P. F. (1979). In J. E. Field (Ed.), *The properties of diamond*. London: Academic Press.

Sellschop, J. P. F. (1992). In J. E. Field (Ed.), *The properties of natural and synthetic diamond*. San Diego: Academic Press.

Shockley, W. (1938). Currents to conductors induced by moving point charge. *Journal of Applied Physics, 9*(10), 635.

Shockley, W. (1961). Problems related to pn-junctions in silicon. *Solid-State Electronics, 2*(1), 35–60.

SOLEIL, French National Synchrotron Facility, http://www.synchrotron-soleil.fr/.

Spear, W. E. (1957). *Proceeding of the Physical Society, London, Section B, 70*, 669.

Spieler, H. (1982). Fast timing methods for semiconductor detectors. *IEEE Transactions on Nuclear Science, NS-29*, 1142–1158.

Spitsyn, B. V., Bouilov, L. L., & Derjaguin, B. V. (1981). *Journal of Crystal Growth, 52*, 219.

Spitsyn, B. V. & Derjaguin, B. V. (1956). Patent application July 10 1956. USSR Patent No. 339,134, May 5 1980.

SRIM code, http://www.srim.org.

Stetter, G. (1941). Durch Korpuskularstrahlen in Kristallen hervorgerufene Elektronenleitung. *Verhandlungen der Deutschen Physikalischen Gesellschaft, 1*, 13.

Stolz, A., Behravan, M., Regmi, M., & Golding, B. (2006). Heteroepitaxial diamond detectors for heavy ion beam tracking. *Diamond and Related Materials, 15*, 807–810.

Stockman, Y., BenMoussa, A., Dammasch, I., Defise, J.-M., Dominique, M., Halain, J.-P., Hochedez, J.-F., Koller, S., Schmutz, W., & Schühle, U. (2010). *In-flight performance of the solar UV radiometer LYRA on PROBA-2*. Greece: Proc. International Conference on Space Optics ICSO 4–8 October 2010 Rhodes.

CVD diamond for electronic devices and sensors. In Sussmann, R. S. (Ed.), *Series materials for electronic & optoelectronic applications*. Chichester: John Wiley & Sons. ISBN: 978-0-470-06532-7 (HB).

Tachibana, T., Williams, B. E., & Glass, J. T. (1992). Correlation of the electrical properties of metal contacts on diamond films with the chemical nature of the diamond-metal interface. I. Gold contacts: a non-carbide-forming metal; II. Titanium contacts: a carbide-forming metal. *Physical Review B, 45*(20), 11 968-1011 973; 11 975-1011 981.

Tachibana, T., Williams, B. E., & Glass, J. T. (1992a). Correlation of the electrical properties of metal contacts on diamond films with the chemical nature of the diamond-metal interface. II. Titanium contacts: A carbide-forming metal. *Physical Reviews B, 45*(20), 11 968–11 973, 11 975–11 981.

Tapper, R. J. (2000). Diamond detectors in particle physics. *Reports on Progress in Physics, 63*, 1273–1316.

Tranchant, N., Nesladek, M., Tromson, D., Remes, Z., Bogdan, A., & Bergonzo, P. (2007). Time of flight study of high performance CVD diamond detector devices. *Physica Status Solidi (A), 204*(9), 3023–3029.

Trischuk, W., & On Behalf of RD42. (2011). Diamond for high energy radiation and particle detection. In *Europhysics conference on high-energy physics 2011*. Available online http://indico.in2p3.fr/conferenceDisplay.py?confId=5116.

Tschulena, G. R. (1972). Anisotropy of warm electrons in germanium and silicon. *Zeitschrift für Physik, 256*, 113.

Vandersande, J. W., & Zoltan, L. D. (1991). *Surface Coating Technology, 47*, 392.

Verona-Rinati, G. (2009). Neutron detectors. In R. S. Sussmann (Ed.), *CVD diamond for electronic devices and sensors* (pp. 257–274). John Wiley & Sons Ltd.. ISBN: 978-0-470-06532-7 (HB).

Weilhammer, P., Adam, W., Bauer, C., et al. RD42. (1998). Recent results on CVD diamond radiation sensors. *Nuclear Instruments & Methods A, 409*, 264–270.

Wermes, N. (2011). Pixel 2010 – a resume. *Nuclear Instruments & Methods A, 650*, 245–252.

Wu, W., & Fahy, S. (1994). Molecular-dynamics study of single-atom radiation damage in diamond. *Physical Review B, 49*, 3030.

Yang, J., Huang, W., Chow, T. P., & Butler, J. E. (2005). Diamond single-crystal film for electronics applications. In *Proceedings Materials Research Society*, 0905-DD06-09.

Zhao, S. (1994). *Characterization of the electrical properties of polycrystalline diamond films* (Thesis). Ohio State University.

This page intentionally left blank

3.18 Single Color Centers in Diamond: Materials, Devices, and Applications

Igor Aharonovich, School of Physics and Advanced Materials, University of Technology Sydney, Ultimo, New South Wales, Australia
Thomas Babinec, Departments of Electrical Engineering and Applied Physics, Stanford University, CA, USA

List of Acronyms

AFM Atomic force microscope	**FWHM** Full width at half maximum
CVD Chemical vapor deposition	**NIR** Near infrared
ESR Electron spin resonance	**PCC** Photonic crystal cavity
HPHT High pressure high temperature	**PL** Photoluminescence
ISC Intersystem crossing	**ZPL** Zero phonon line

3.18.1 Introduction

We live in a society driven by information. We are constantly seeking new ways to share, communicate, store, and process that information. Our capacity to compute and to communicate is crudely captured by the familiar Moore's law, which says that the number of transistors in an integrated circuit doubles (roughly) every 18 months, as well as trends in speed and bandwidth in optical communication systems. Other demand includes that these computations and communications be done securely, and with protection from eavesdroppers who would contaminate and misuse access to confidential information. As a result, radically new approaches to information processing are required.

An important example, and one that we will discuss merging field of "solotronics", or solitary dopant optoelectronics, where novel forms of information storage, computation, and communication are engineered at the level of a single solid-state impurity. Nanoscale and quantum science and engineering are essential ingredients for the development of such "solotronic" devices. As the "natural" size of the devices we use progresses to the nanoscale—where critical dimensions can approach the size of some billionths of a meter—these familiar and "classical" information processing devices may be controlled at the level of a single, solitary impurity. Here, however, quantum mechanical properties and effects of this system are manifest. These quantum mechanical effects, moreover, may allow for radically new functionality desired.

In this spirit, we present in this book's chapter several topics in photonic nanostructures for, and based upon, individual luminescent centers (color centers) in single crystal diamond. Special emphasis is placed upon the nitrogen-vacancy (NV) center in diamond, which possesses additional spin (matter) degrees of freedom in its electronic structure that are coupled to optics. The main application of the devices lies in quantum communication and information processing, which promise computational speed and communication security eclipsing that offered in classical systems as well as high-resolution, room-temperature magnetometry—surpassing most of the current techniques (e.g. commercial magnetic resonance imaging (MRI)). The key merits to utilize single defects in diamond for quantum photonic applications include (1) "natural" scalability and large-scale manufacturing of solid-state devices compared to many alternative approaches such as trapped atoms; (2) efficient quantum networking compared to other existing solid-state approaches such as linear optical computing and neutral quantum dots, which lack the suitable quantum memory for information storage and distribution; and (3) integration of solid-state emitters into photonic device architectures offering efficient and single mode photon collection, weak- and strong-cavity effects, and photon distribution on- and off-chip.

These ambitious ends are certainly motivated by recent progress in other solid-state photonic quantum information-processing systems such as InGaAs/GaAs quantum dots (Hennessy et al., 2007; Michler et al., 2000). Here, molecular beam epitaxy allows for the growth of sophisticated semiconductor structures such as an optically thin ($\sim$150 nm) device layer containing quantum dots on a sacrificial substrate. This material is readily patterned with a high-quality factor (Q) and small mode volume (V) cavities, waveguide, etc., and this forms the basis of cavity quantum electrodynamics approaches to quantum information and even proposals for explorations of many-body physics in coupled-cavity systems (Ellis et al., 2011; Imamoglu et al., 1999; Kimble, 2008; O'Brien, Furusawa, & Vuckovic, 2009; Vahala, 2003).

While it remains (as it was, originally) tempting to map this well-established template for a research program on to the emerging NV-diamond material system, this approach is manifestly insufficient: the diamond system possesses its own unique set of material properties and challenges, and its application space within quantum photonics extends beyond the existing quantum dot technology. In any case, the state-of-the-art "device" for color centers in single crystal diamond at the start of this thesis included a bulk diamond sample. No "diamond-on-insulator" material, in analogy to "silicon-on-insulator" material in classical silicon photonics or such InGaAs/GaAs materials in quantum photonics, was originally available for device processing. Optically thin nanocrystalline diamond films on silicon dioxide were available at the start, though these are unfortunately of a poor optical quality and single color centers have still not been observed in this material. Considering these substantial material challenges, the approach recently taken by the community has been flexible and exploratory.

It is well established that the optical properties of light emitters in the solid state are not fixed. Rather, the structure on a scale which is comparable to the emission wavelength alters the electromagnetic environment and hence the emitter's fluorescent properties. Regardless of the specific device geometry or nature of the light emitter, this feature size approaches the nanoscale level of approximately 200 nm for the visible wavelength of approximately 600–700 nm and a solid-state host of modest refractive indices $n \sim 2$–3. Applications of this general principle have led to landmark experiments with light emitters such as fluorescent dye molecules, colloidal and epitaxial quantum dots, and optically active defects (color centers) in wide band-gap semiconductors. In some cases, these systems may be isolated and individually addressed, and incorporation into advanced devices based on micropillar cavities, photonic crystals cavities and waveguides, plasmonic antenna, and whispering gallery mode resonators, to name a few.

Single crystal diamond possesses a unique combination of exquisite material properties, mature growth processes for bulk crystals, and now widespread availability of samples that make it a heretofore underdeveloped material system for diverse and multifunctional nanoscale systems. For example, diamond possesses high thermal conductivity, low coefficient of thermal expansion, large breakdown field, and high carrier mobility for applications in electronics. It can be doped n- and p-type, thus allowing for realization of optoelectronic devices (Balmer et al., 2009). Diamond is also an ultrahard material with a large Young's modulus, which is advantageous for high-frequency electromechanical and optomechanical systems. In the field of photonics, devices may benefit from diamond's modest refractive index ($n = 2.4$), large band gap (5.5 eV), and wide transparency window (ultraviolet (UV) to infrared (IR) wavelengths). As a member of the "carbon family" with nanotubes and graphene, diamond device platforms are naturally extended to biological and chemical contexts where the toxicity of some alternative semiconductor materials is an issue.

Significant advances have been made in the past few decades in the large-scale synthesis of high-purity diamond crystals via high-pressure high-temperature (HPHT) and chemical vapor deposition (CVD) growth techniques. An approximately $4 \times 4 \times 1$-mm bulk diamond sample could be purchased from commercial vendors such as Element Six at a modest price for research purposes. Over time, it seems likely that progress will continue to be made resulting in an increase of available sample size, improvements in doping and composition control, reduction in overall cost, etc. But we must pick a first application area to demonstrate the utility of diamond nanotechnology, and for the purposes of this thesis we consider the case of nanoscale optical devices based on luminescent centers in diamond.

3.18.1.1 A Brief History of Color Centers in Optoelectronics

Color centers are ubiquitous features of all crystalline materials. Color centers are defects or impurities—often a foreign atom, a vacancy or a combination of the above. Color centers give coloration to crystals and gemstones such as the Emerald or the Ruby. Ruby is a form of alumina and the red color originates due to the chromium incorporation in its crystal lattice. One of the chromium defects, the R1 line is a substitutional Cr^{3+}, with a doublet centered at approximately 700 nm. This color center plays a central role in optoelectronics as it was the first solid-state optical laser, realized over 50 years ago (Maiman, 1960).

Doping semiconductors with impurities can significantly modify their photoluminescence (PL) properties. For instance, doping GaN with In or Al shifts the emission wavelength and was demonstrated to produce white light emitting diodes and lasers at various visible wavelengths. Erbium-doped silica fibers are playing a central role in modern communication technologies—mainly as fiber amplifiers.

3.18.1.2 An Overview of Diamond Color Centers

Diamond being one of the most valuable stones in nature, its coloration has been studied for many decades. Although diamonds, which are used for gems, are often colorless, some of the most valued stones have bright, fancy colors (**Figure 1**) (Kitawaki, 2007). The colors originate from defects within the matrix such as a missing atom (e.g. a vacancy), an impurity atom, or a cluster of imperfections. Diamond possesses a very high optical band gap ($\sim$5.5 eV), much larger than the energy gap of the transition from the impurity band. Hence, the emission from the defect will not be absorbed and therefore can be visible. Diamond hosts >500 luminescent centers (Zaitsev, 1998). Although these color centers emit across the spectrum from the deep UV to the far IR,

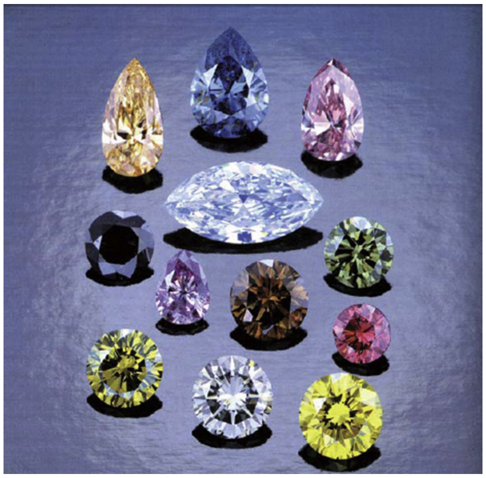

Figure 1 Diamond crystals with various colorations. The yellow color is associated with the presence of nitrogen, while the blue coloration originates due to boron impurities. The origin of the pink coloration is still under discussion. Reprinted from Kitawaki (2007).

the gemological imperatives have led to those in the visible being most studied. The yellow coloration of natural diamonds, for instance, originates from the nitrogen-related clusters (N3, N2) while the popular and rare blue color mostly referred to boron or hydrogen containing stones. Some stones have a brown or green hue due to the irradiation effects and HPHT annealing effects. Irradiation and annealing are also often used to modify diamond coloration and activation of luminescent defects. Plastic deformation underground is believed to be the cause for the formation of the most valuable and rare pink diamonds.

Despite the fact that diamond can be found naturally in a plethora of colors, assigning a particular line to a specific impurity is a challenging task. Interpreting their PL spectra is not a straightforward task. A combination of a number of characterization techniques (such as electron magnetic resonance, absorption and stress measurements) is required to understand the defect chemical composition and the associated level structure of a defect. Indeed the chemical structure of only very few diamond color centers is well understood, with most being unidentified or subject to conflicting structures.

Remarkably, however, some of the color centers in diamond can be observed and addressed individually, at room temperature and studied as an independent quantum system that is capable of generating single photons on demand (Aharonovich et al., 2011; Gruber et al., 1997). Such confined systems emit only one photon per excitation and relaxation cycle. This chapter will focus on these types of defects and provide an overview of single emitters (color centers) in diamond—their generation, characterization, and the applications.

3.18.1.3 Overview

With the increasing importance of photons in modern technologies, this chapter will only focus on single photon emitters (quantum emitters) and their suitability for photonics, spintronics, and other quantum applications. The chapter is arranged as follows: In the first part of the chapter, various single photon emitters in diamond will be described including their photophysical properties, fabrication, and characterization routes. Particular attention will be given to the NV center as the most promising emitter for quantum photonic applications. In the second part, we will provide the reader with a brief introduction to light matter interactions and the fundamental of photonic devices. Then we will review the recent developments in the field of diamond photonics—mainly coupling diamond emitters to optical cavities utilizing the hybrid approach and the "all diamond" approach. Finally, the chapter will be concluded, and an outlook exploring future applications and directions will be discussed.

3.18.2 Materials Science of Artificial Atoms in Diamond

3.18.2.1 Single Photon Emitters in Diamond

Diamond is an indirect wide band-gap semiconductor (5.5 eV), which leads to its capacity to accommodate a large variety of optically active defects. Due to its high Debye temperature ($\sim$1850 K), and the good separation of the defects in its rigid lattice, some of the color centers can be addressed individually by an excitation laser. A hand full of emitters so far have been identified as bright, stable single photon emitters (Aharonovich et al., 2011; Pezzagna, Rogalla, Wildanger, Meijer, & Zaitsev, 2011). This section describes the chemical, physical, and optical properties of the most common diamond single photon emitters. Their fabrication methods are also highlighted.

3.18.2.1.1 NV Center

The NV defect center is one of the most common and studied defect centers in diamond (Davies, 1976). It is formed through the incorporation of a single substitution nitrogen atom in the diamond lattice located adjacent to a vacant carbon lattice site in one of the (111) crystallographic orientations (Smith, Sorokin, Gelles, & Lasher, 1959). The schematic illustration of this defect is shown in **Figure 2(a)**. The defect can exist in two known charge states: a neutral state referred to as NV^0, and a negatively charged state commonly known as NV^-. The PL of the NV^0 center exhibits a zero phonon line (ZPL) at 575 nm with a characteristic broad phonon side band that extends from 580 to 650 nm. The NV^- defect has a ZPL centered at 637 nm and a phonon side band extended to 800 nm. Most quantum-based applications utilize the fluorescence properties of the NV^- center, but in many instances, both charge states can be found within the same defect center (Gaebel et al., 2006; Iakoubovskii, Adriaenssens, & Nesladek, 2000). Detailed time-resolved experiments show that switching from NV^0 to NV^- is photoinduced, whereas the reverse photochromic transformation from NV^- to NV^0 occurs under dark

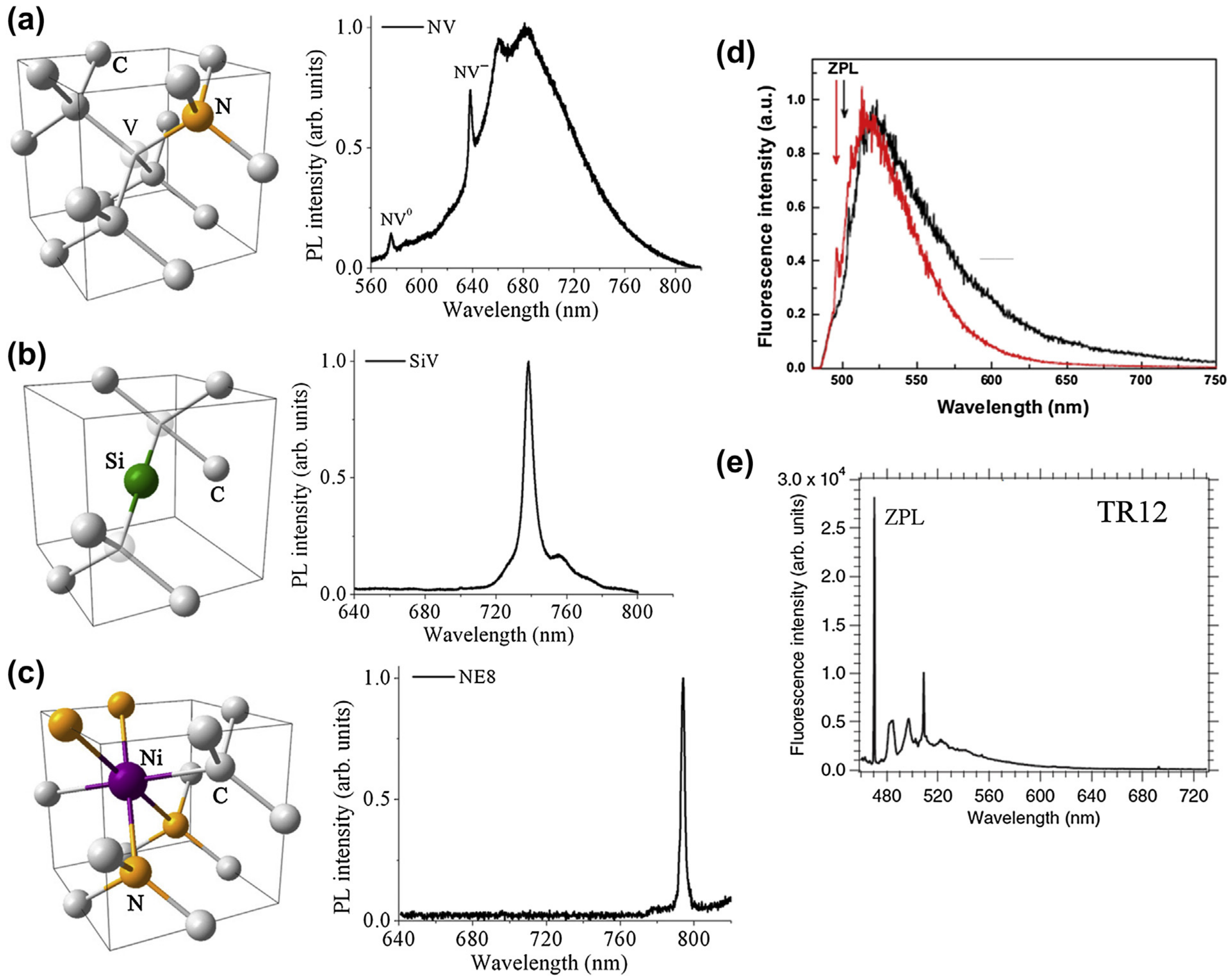

Figure 2 Crystal structures and the emission properties of various color centers that demonstrated single photon emission. (a) The NV center, (b) the silicon vacancy (SiV) center, (c) the NE8 center, (d) the H3/H4 (red/black) center, and (e) the TR12 center. Reprinted from Aharonovich et al. (2011), Naydenov et al. (2009), and Hsu, Su, Yang, Tzeng, & Chang (2011).

conditions with a time constant between 0.3 and 3.6 μs and irreversible transformation can occur under intense femtosecond illumination (Dumeige et al., 2004). The mechanism that gives rise to this interconversion is at the present time unclear. Many recent experiments proved that NV centers that are located in a closed proximity to the surface (~10 nm) can be influenced by the surface chemistry of the diamond. For instance, oxygen termination promotes the formation of NV$^-$ while hydrogen termination results in a dominant concentration of NV^0 (Fu, Santori, Barclay, & Beausoleil, 2010; Hauf et al., 2011; Rondin et al., 2010). Active switching of the emitters by immersing the diamond in an electrolyte has also been shown (Grotz et al., 2012). Although the quest for a promising recipe to generate stable NV$^-$ centers is ongoing, experimentally these emitters can be found deep in an ultrapure material with <1 ppb nitrogen defects.

3.18.2.1.1.1 NV$^-$ Level Structure

The NV$^-$ center has a C_3v symmetry with six unpaired electrons—five from the neighboring carbon and intrinsic nitrogen, plus an additional electron trapped at the defect (Doherty et al., 2011; Doherty et al., 2012; He, Manson, & Fisk, 1993a, 1993b). The ground and the excited states (Fu et al., 2009; Fuchs et al., 2008; Neumann et al., 2009) form the spin triplet states ($^3A_2$ and ^3E), while the metastable states are the singlet states (1E and 1A1). The optical ZPL transition at 637 nm of the $^3A_2 \rightarrow {}^3E$ transition and the ordering of the triplet states are now established. Recently, an IR transition between the two singlet states was also demonstrated (Rogers, Armstrong, Sellars, & Manson, 2008). The detailed and the simplified level structure of the NV$^-$ center is depicted in **Figure 3**.

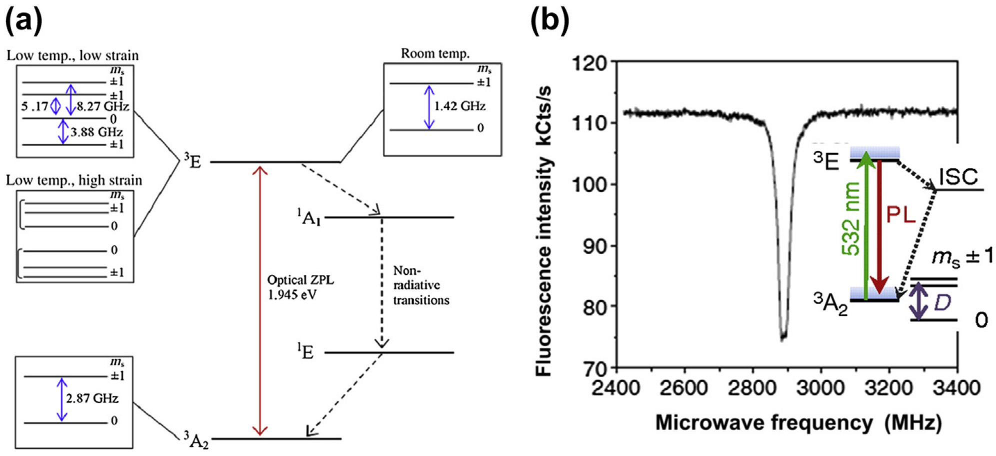

Figure 3 (a) Detailed level structure of the NV$^-$ center. (b) A typical optically detected magnetic resonance spectrum of a single NV center. Inset, simplified level structure of the NV$^-$, showing the green excitation and the red emission along with the ISC and the splitting in the ground state. Reprinted from Aharonovich et al. (2011); Gruber et al. (1997).

The electronic fine structure of NV arises due to spin–orbit interaction and electronic spin–spin interactions. The ground $^3A_2$ triplet exhibits a zero-field splitting of approximately 2.87 GHz between the spin sublevels, and this transition can be coherently driven with microwave fields. This feature is key to the observed optical spin polarization of the ground triplet state of the NV$^-$, which constitutes its remarkable properties. Under green illumination, the population is transferred from the $m_s = \pm 1$ spin sublevels to the $m_s = 0$ spin sublevel of the ground triplet state, so that the center is rapidly prepared in the $m_s = 0$ state with a high probability. This same spin-dependent pumping also gives rise to different fluorescence rates from the ground states, so that fluorescence from the $m_s \pm 1$ states is significantly less than that from the $m_s = 0$ state. This mechanism allows for room-temperature, single-spin readout, which has made NV so important for quantum applications (Hanson, Gywat, & Awschalom, 2006; Hanson, Mendoza, Epstein, & Awschalom, 2006; Jelezko et al., 2004; Jelezko & Wrachtrup, 2004; Santori et al., 2006; Tamarat et al., 2008). **Figure 3(c)** shows an example of an optically detected magnetic resonance spectrum, recorded from a single NV.

To achieve a significant difference in the optical emission from the excited triplet spin sublevels, there must be competing transitions that preferentially depopulate the $m_s = \pm 1$ states. The strongest competing nonradiative transition is believed to involve an intersystem crossing (ISC) from the excited triplet to the $^1A_1$ state, which subsequently decays radiatively and nonradiatively to the ^1E state. Given this decay of the $m_s = \pm 1$ population to the ^1E state, there must be a final nonradiative transition that also involves an ISC from the ^1E to the $m_s = 0$ sublevel of the ground $^3A_2$ state for the ground triplet state to spin polarize. Hence, the population is transferred from the $m_s = \pm 1$ to the $m_s = 0$ sublevels of the ground triplet state via the intermediate singlet states. Given the nature of the ISCs, these processes are expected to be both strain and electric field dependent, as has been observed in single crystal studies. Researchers are now striving to understand the exact mechanism for this spin-polarization phenomenon, to be able to engineer similar systems in other materials.

The fine structure of the excited ^3E state depends on both temperature and strain. At room temperature, the fine structure of the excited triplet mimics that of the ground triplet state with a single zero-field splitting of 1.42 GHz. At low temperatures, the fine structure of the excited triplet is highly dependent on crystal strain. In the low strain limit, it exhibits four fine structure levels corresponding to different combinations of orbital and spin sublevels. The excited triplet fine structure shows pronounced Stark shifts (Acosta et al., 2012; Batalov et al., 2009; Fu et al., 2009; Fuchs et al., 2008; Neumann et al., 2009; Tamarat et al., 2006).

The realization of room-temperature readout of an electron spin immediately sparked a comprehensive research into coherent manipulation of single spins. Through an improvement of the material and introduction of various pulse schemes, coherence times of up to almost 2 ms were measured at room temperature (Balasubramanian et al., 2009; de Lange, Wang, Riste, Dobrovitski, & Hanson, 2010; Hodges et al., 2012; Pfaff et al.; Robledo, Bernien, van Weperen, & Hanson, 2010; Robledo et al., 2013; van der Sar et al., 2012). For the realization of practical quantum information processing, storage and readout are realized by coupling the NV$^-$ spin to the nearby nuclear spin of ^{13}C or an additional N atom. For more detailed information, we refer the

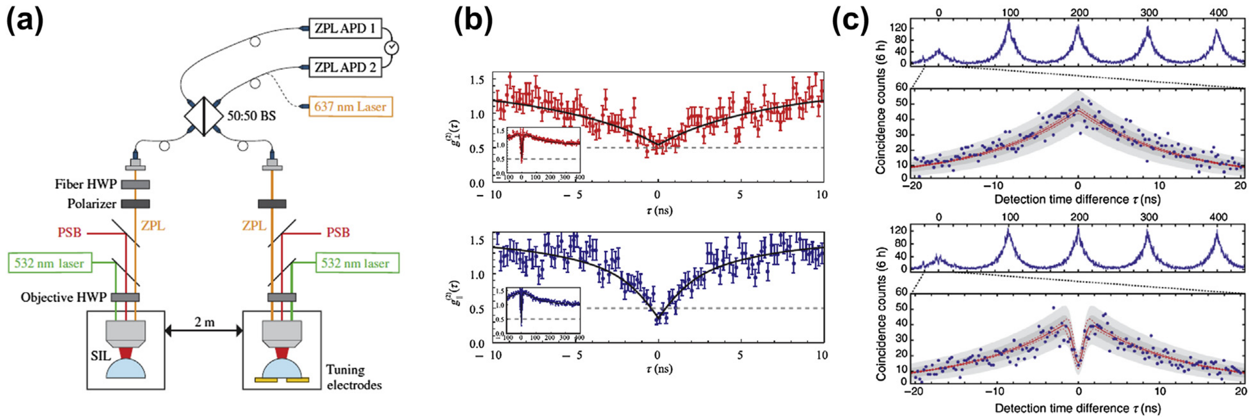

Figure 4 (a) Experimental setup for the demonstration of two photon interference from two remote NV centers. The setup includes two separate excitation and collection paths that recombine on a beam splitter. (b, c) Results of the experiment, showing in both continuous and pulsed excitation wavelengths that two separate NV centers emit indistinguishable photons. Reprinted from Sipahigil et al. (2012); Bernien et al. (2012).

reader to the works done by the groups of Neil Manson (ANU), Jeorg Wrachtrup (Stuttgart), Fedor Jelezko (Ulm), Ronald Hanson (Delft), and David Awschalom (UCSB), and Michail Lukin (Harvard).

Although the majority of research into the NV center is motivated due to its spin system, one should also consider its use for quantum photonic applications (Aharonovich, Greentree, & Prawer, 2011; Greentree, Fairchild, Hossain, & Prawer, 2008). For realization of linear quantum computing or entanglement, indistinguishable photons are required. Achieving indistinguishable photons from NV centers was nonetheless challenging due to a relatively low photon flux from the ZPL. In 2012, two groups achieved this goal independently, by increasing the collection efficiency using solid immersion lenses (Bernien et al., 2012; Sipahigil et al., 2012). Although the visibility was still poor, this marked the first realization of indistinguishable photons from a color center in diamond. **Figure 4** shows the schematic illustration of the experimental setup of the experiment and the obtained results. Note that the excitation was done either in a pulsed or in a continuous wavelength regime.

3.18.2.1.2 Silicon-Vacancy Center

Silicon defects are very common in CVD-grown diamond due to the routine use of silicon substrates and quartz bell jars. The most common silicon-related defect is the SiV center, which has a ZPL centered at 738 nm (**Figure 2(b)**) with a negligible phonon side band (Feng & Schwartz, 1993; Goss, Jones, Breuer, Briddon, & Oberg, 1996). The narrow line and the emission in the near infrared (NIR) makes this defect very attractive for sensing and tagging applications. The SiV can be observed by an intentional addition of silicon to the diamond growth cell or by silicon implantation into pristine diamond. The structure of the ZPL is complicated and consists of many lines, originating from the split ground and excited states as well as different silicon isotopes. The atomic structure of the SiV defect consists of a silicon atom splitting two vacancies, as was recently confirmed by electron paramagnetic resonance (EPR) measurements (Edmonds, Newton, Martineau, Twitchen, & Williams, 2008). **Figure 2(b)** shows the crystallographic structure and the associated emission spectrum of the SiV center. There was a disagreement in the literature regarding the charge state of the complex; however, recent results suggest a negative charge state for this center. The SiV center possesses a very short excited state lifetime (~1 ns) but exhibits a QE as low as 0.05 that varies with temperature and between samples grown under different conditions.

Single SiV centers were engineered by Wang et al. (Wang, Kurtsiefer, Weinfurter, & Burchard, 2006) in a monolithic crystal diamond using the ion implantation technique. The observed single SiV exhibited extremely low count rates due to fast nonradiative decay channels and low QE. Incorporating single silicon emitters into nanodiamonds is technically challenging. If diamonds are grown on silicon or silica substrate, silicon atoms diffuse simultaneously into the growing crystals, forming large clusters of SiV centers that cannot be isolated. This approach is therefore not suitable for preparing isolated single SiV centers.

Despite these apparent shortcomings, new results have emerged to show that single SiV emitters embedded in nanodiamonds grown on iridium substrate, exhibited ultrabright single photon emission

(Neu, Agio, & Becher, 2012; Neu et al., 2011a). The reported count rate of approximately 5×10^6 counts/s is more than three orders of magnitude higher than that reported in single crystal diamond. Neu et al. showed that the ZPL of the SiV can be shifted by >5 nm. The SiV emitter is fully polarized in both absorption and emission channels and shows strong bunching, characteristic of a three-level system. Employing cross-correlation measurements, it was shown that the SiV has another line in the NIR at approximately 822 nm, which originates from an additional electronic transition from/to the shelving state of the same defect (Neu et al., 2012).

Low-temperature spectroscopy measurements show that the lines of individual SiV centers are still broadened to at least 25 GHz, most likely due to spectral diffusion. Phonon broadening was proposed to dominate, and the temperature dependence measurements show a T^3 trend (Dr Neu). Further stress measurements on SiV defects should be carried out to fully understand this defect.

Although the bright emission from the SiV was only measured when the nanodiamonds are grown on iridium, techniques now exist to transfer these nanodiamonds to other substrates by techniques such as bead assisted sonic disintegration. Utilizing this method, standalone nanodiamonds containing single, bright SiV emitters were produced (Neu et al., 2011b).

3.18.2.1.3 Nickel-Related Complexes

Transition metals, in particular nickel, are often present in synthetic HPHT diamonds due to their role as catalysts. Their vast abundance in natural diamonds has attracted major interest in the scientific community and significant research has been carried out to map out their optical and physical properties.

The most common nickel-related defect shows a PL doublet around 883/885 nm (Kupriyanov, Gusev, Borzdov, Kalinin, & Pal'yanov, 1999; Nadolinny et al., 2000; Nazare, Neves, & Davies, 1991; Orwa et al., 2010). The center has a trigonal symmetry, and the doublet structure is a result of the spin orbit interaction splitting the ground state of the center. A fine structure of the ZPL resolves the components associated with stable nickel isotopes. This signature is often observed in synthetic diamonds grown in the presence of a nickel catalyst. However, single photon emission from this center has not been observed.

In high nitrogen content diamonds, a family of nickel nitrogen complexes (NEx, $1 \leq x \leq 8$) is formed, as has been confirmed by EPR measurements. It was also shown that the NE4 defect, ascribed to a nickel atom in a divacancy, acts as a nucleus for the aggregation of nitrogen atoms. Once the NE4 defect is formed, up to four nitrogen atoms can be captured consecutively in different configurations to form the rest of the NEx family. Most of the NEx complexes were also observed optically, with the NE1 centered in the UV (ZPL at 472 nm) and NE8 centered in the NIR (ZPL at 793 nm). The structure of the NE8 is depicted in **Figure 2(c)** consisting of four nitrogen atoms neighboring a nickel atom. This center is of particular interest owing to its narrow emission in the NIR. It is the only center from the NEx family that has demonstrated single photon emission (Gaebel et al., 2004; Rabeau et al., 2005; Wu et al., 2006).

The first observation of single photon emission from the NE8 center was reported by Gaebel et al. (Gaebel et al., 2004). The schematic and the PL of the center are shown in **Figure 2(c)**. The center was observed in a type IIA natural diamond. This discovery ignited further research into the NE8 defect, and it was subsequently observed in nanodiamond films and individual nanodiamonds. The Debye–Waller factor of the NE8 center is 0.7 as most of the emission is concentrated within the ZPL. The NE8 center exhibits a three-level emission behavior, and its fluorescence QE is estimated to be approximately 0.7. Pulsed excitation measurements revealed the typical times during which the emitter is active ($T_{\mathrm{on}} = 9.1\ \mu\mathrm{s}$) and a time during which it is trapped in its metastable state ($T_{\mathrm{off}} = 7\ \mu\mathrm{s}$) (Wu et al., 2007). **Figure 2(c)** shows the crystallographic structure and the associated emission spectrum of the NE8 center.

Besides the NE8 center, there are other reports on single photon emission from nickel-related centers in the NIR. The Ni/Si complex is one example. Single photon emission from this defect was first reported by Aharonovich et al., who investigated CVD-grown nanodiamond crystals implanted with nickel (Aharonovich et al., 2009a), and then independently confirmed by Steinmetz et al. (Steinmetz, Neu, Meijer, Bolse, & Becher, 2010). The latter coimplanted nickel and silicon into type IIA single crystal diamond. The Ni/Si defect has a ZPL centered around 770 nm and a short excited state lifetime of approximately 3 ns. Further investigation to identify the exact structure of these defects is currently underway.

Other Nickel-related defects were observed in nanodiamonds grown by the CVD method from a slurry containing Nickel and nanodiamond seeds and by the addition of nickel through the gas phase (Wolfer et al., 2009). The ZPLs of the emitters were scattered at the spectral region of 700–800 nm and most of them are still unidentified (Castelletto, Edmonds, Gaebel, & Rabeau, 2012).

3.18.2.1.4 Other Color Centers

Since diamond hosts >500 color centers, it is expected that several defects would be isolated to a single level. Indeed, during the last few years numerous new single defects were isolated and controllably created in diamond. A carbon-related single photon source, the TR12 center, was engineered by high energy implantation of carbon ions into low nitrogen concentration (<0.1 ppb) CVD single crystal diamond (Naydenov et al., 2009). The TR12 center contains an interstitial carbon atom, has a ZPL centered at 470 nm, an excited state lifetime of 3.6 ns and exhibits single photon emission (**Figure 2(e)**). This is the first diamond-based emitter in the blue spectral region. An advantageous property of this center is that it consists solely of carbon atoms and vacancies and can be potentially engineered in a spin free environment by employing ^{12}C-enriched diamond. The theoretical and experimental work to establish the level structure of this center is therefore crucial.

Single photon emitters in the green spectra range were also observed. The H3 defect—a complex consisting of an N–N aggregate trapping a vacancy forming an NVN structure and the H4 defect (VNNV complex) (Hsu et al., 2011) (**Figure 2(d)**). The defects have a ZPL at 496 and 503 nm, respectively, with a broad phonon side band extending all the way to the red spectral range. The emitters also exhibit a relatively long lifetimes of approximately 40 ns. The single photon emission from the H3 and the H4 defects was observed in type IA nanodiamonds.

The last family of single emitters to be discussed here is the Chromium-related emitters (Aharonovich, Castelletto, Simpson, Greentree, & Prawer, 2010; Aharonovich et al, 2009b; Aharonovich et al., 2010). The emitters were first discovered by growing nanodiamond crystals on a sapphire substrate. Chromium is a common impurity in sapphire, which can be incorporated into a diamond crystal during the CVD growth. The new class of chromium emitters show narrow luminescence lines in the NIR region (~80% of the emission is concentrated in the ZPL), ultrabright single photon emission with the brightest emitter reaching rates of 3.2×10^6 counts/s, short excited state lifetime of approximately 1–4 ns and fully polarized excitation and emission behavior. Remarkably, some of the emitters are well described by a two-level model that was confirmed by the absence of photon bunching in the $g^{(2)}(\tau)$ function for excitation powers beyond saturation.

Chromium emitters were also fabricated by ion implantation of chromium into a monolithic single crystal diamond. Subsequent research showed that the best methodology to fabricate these emitters is by coimplanting chromium with a donor (e.g. oxygen) into type IIA ([N] <1 ppm, [B] <0.05 ppm) diamond. Polarization measurements showed that the absorption dipole lies along one of the main crystallographic directions in the diamond lattice. By imaging the excitation dipole intensity distribution, it was determined that the emission dipole is oriented nearly orthogonal to the diamond–air interface.

Another striking property of these emitters is their large linear and quadratic stark shift under electric field. Tenability of more than a nanometer was demonstrated (Muller et al., 2011), a very important tool for quantum optics experiments. The photon coherence of chromium emitters in the bulk was approximately 700 ps while in nanodiamonds the emitters exhibited a much shorter coherence time of approximately 60 ps.

In addition to the known color centers in diamond, which were identified as single emitters, photon antibunching was recorded from a number of unknown defects. A defect ZPL at 532 nm has been observed in a CVD-grown diamond (Smith et al., 2011). It has a narrow FWHM and a short excited state lifetime of approximately 3.5 ns. The center has a visible phonon side band with a Huang–Rhys factor of 2.48 at 77 K. Another diamond defect exhibited an intense and narrow spectral emission line with a ZPL at 734 nm, and a Debye–Waller factor of 0.8 was observed in nanodiamonds (NDs) (Simpson et al., 2009). The reported lifetime of the emitter was 13.6 ns with a measured photon count rate of 1.6×10^6 counts/s. The high fluorescence efficiency of the center was attributed to its two-level structure.

Table 1 summarizes the optical properties of single emitters in diamond.

Single defects in diamond sparked a lot of attention in the solid-state photonics community and initiated the search for single emitters in other systems. Unsurprisingly, therefore, single emission has been recently reported from defects in ZnO, SiC, and Pr-doped YAG (Dr Castelletto; Kolesov et al., 2012; Morfa et al., 2012). Each system offers advantages and drawbacks in fabrication, photophysical properties, and integration. The selection of a specific source will depend on the particular application—but what is important is the availability of materials and the emitting wavelengths.

3.18.3 Applications and Devices Based on Color Centers

In this chapter, the main applications proposed for diamond color centers will be discussed. The primary focus will be on photonic devices and magnetic sensing, as these applications are central in the field of single

Table 1 Summary of various single photon emitters and their optical properties

	ZPL (nm)	*Maximum count rate*	*Excited state lifetime (ns)*
NV	637	~50 kcounts/s*	~11–22
SiV	738	~4.8 Mcounts/s	~1
H3	503	Not reported	~27
TR12	470	Not reported	~3.6
Chromium defects	740–780	~0.1–3.2 Mcounts/s	~1–14
NE8	780–810	~80 kcounts/s	~2
Other nickel-related defects	700–800	~20–100 kcounts/s	~1–4

**Without external enhancement by plasmonic or photonic means.*

diamond emitters. Other applications such as quantum cryptography (also known as quantum key distributions) will not be covered here, and we refer the reader to the recent research papers and review articles (Gisin, Ribordy, Tittel, & Zbinden, 2002; Intallura et al., 2007).

3.18.3.1 Magnetic and Electric Field Sensing

3.18.3.1.1 Magnetometry

The unique spin properties of the NV center are employed in what the majority of the researchers in the field are most intrigued about—nanoscale magnetometry (Acosta et al.; Acosta et al., 2009; Balasubramanian et al., 2008; de Lange et al.; Mamin, Sherwood, & Rugar, 2012; Maze et al., 2008; Rondin et al., 2012; Taylor et al., 2008; Tetienne et al., 2012). Imagine a probe capable of detecting information simultaneously with atomic level magnetic fields, at ambient conditions at room temperature. Such a system may sense single electron and nuclear spins, chemical molecules attached on the surface, detect nanoscale magnetic fields and paramagnetic defects, and eventually atom-scale MRI (Degen, 2008; Taylor et al., 2008).

An NV containing diamond can be attached to a scanning device (e.g. atomic force microscope (AFM)), with an available optical path to drive the optical transitions and optically detect the magnetic resonance signal. Scanning various substrates, the NV will feel the presence of any local magnetic fields causing a shift of its electron spin resonance (ESR) frequency. This shift is detected by exciting an ESR transition with a microwave field and monitoring the change in the PL of the probe spin. Alternatively, the probe NV can be embedded in an ultrapure diamond and sense external magnetic fields. Using various echo-based techniques, sensing of both a.c. and d.c. magnetic fields is possible.

The spin Hamiltonian of the NV ground state (neglecting electron–nuclear spin coupling) can be expressed as

$$H_{\mathrm{gs}} = hD_{\mathrm{gs}}S_z^2 + g\mu_{\mathrm{B}}B\cdot S$$

where h is the Planck constant, g is the electron g-factor ($g \sim 2$), μ_{B} is the Bohr magneton. D is the zero-field splitting parameter, which in the case of the NV center corresponds to the splitting between the $m_{\mathrm{s}} = 0$ and $m_{\mathrm{s}} = \pm 1$ and equals to $D = 2.88$ GHz, as is evident by the single resonance line appears at the NV ESR spectrum at a zero magnetic field. An external magnetic field lifts the degeneracy of $m_{\mathrm{s}} = \pm 1$, leading to the appearance of multiple lines. By measuring the positions of the ESR resonances, it is possible to calculate the magnitude of the external field B.

The noise limited minimum detectable magnetic field can be expressed as

$$\delta B_{\min} \approx \frac{\hbar}{g\mu_{\mathrm{B}}\sqrt{T_2 T}}$$

where T_2 is the electronic spin coherence time, T is the measurement. In principle, for typical values of $T_2 < 0.1$–1 ms, sensitivity of the order of a few nT Hz$^{-1/2}$ can be achieved with a single NV center. This condition clearly emphasizes two of the most important conditions for employing NVs for magnetometry: long coherence time and proximity to the surface (localization).

Figure 5 shows the initial results on magnetometry with NV centers (Balasubramanian et al., 2008; Maze et al., 2008). One approach shows a d.c. magnetometer based on a diamond nanocrystal, which was attached to an AFM tip. A scan over a magnetic nanostructure is demonstrated. The sensitivity of the NV nanocrystal

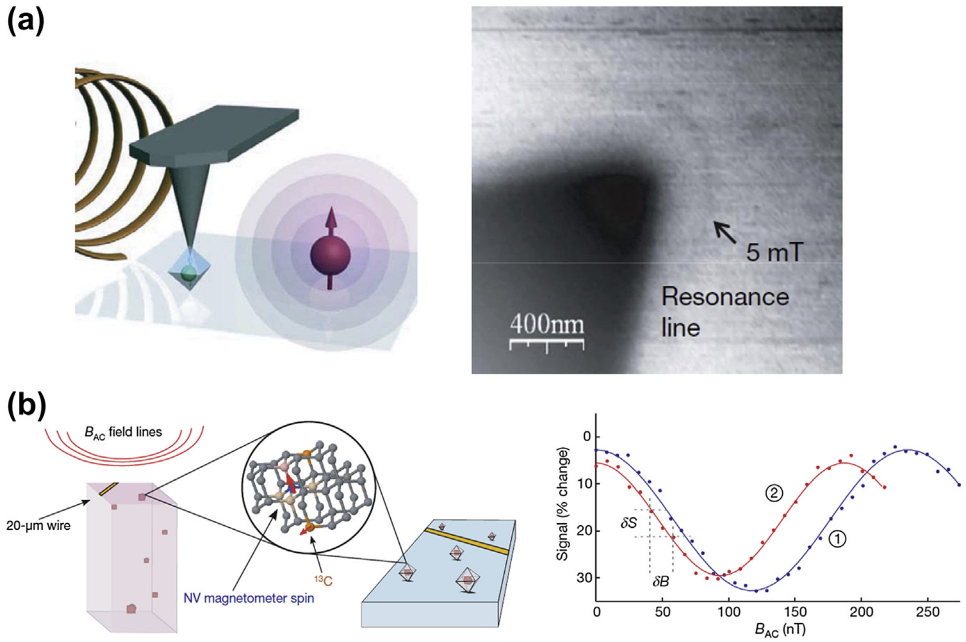

Figure 5 Realization of diamond magnetometry with single NV centers. (a) A magnetometer based on a diamond nanocrystal that is attached to an AFM tip. A scan over a magnetic nanostructure is demonstrated. (b) A magnetometer based on an embedded NV center close to the surface of a bulk single crystal diamond. This configuration measures ambient magnetic fields with a high resolution. Reprinted from Taylor et al. (2008) and Balasubramanian et al. (2008).

magnetometer is determined by the line width of the ESR transition—which is on the order of a few MHz. The measurement resolution was about 5 mT (the magnetic field gradient is $\sim 25\ \mu\mathrm{T\ nm}^{-1}$). Another limiting factor here is oscillatory motion of the nanodiamond attached to the AFM tip. The other approach depicts an a.c. magnetometer based on NVs embedded in a high purity single crystal diamond close to the surface. In this case, a detection limit of 3-nT magnetic fields at kilohertz frequencies after 100 s of averaging is demonstrated.

To achieve a high-resolution scanning magnetometer, the group of A Yacoby realized a scanning tip with an attached high-purity single crystal diamond nanopillars, containing a single NV center (Grinolds et al., 2011; Maletinsky et al., 2012). This solution addressed both the low coherence times of the NVs in nanodiamonds as well as inefficient far field collection from the nanodiamond. The mechanical robustness of the device over week long scans in conjunction with long spin coherence times of approximately 75 μs and the close proximity of the NV to the surface, 25-nm magnetic domains were imaged with a sensitivity of approximately 50-nT $\mathrm{Hz}^{-1/2}$ at a frequency of 33 kHz.

Although the magnetometry results were unprecedented—the fabrication of such a magnetometer is extremely challenging. First, diamond nanopillars have to be etched out of a single crystal diamond membrane. Then, shallow implantation of nitrogen atoms to generate NVs has to be done. Finally, focused ion beam (FIB) liftoff and assembly of the diamond pillar onto an AFM tip is carried out. The fabrication process and the magnetometry results are depicted in **Figure 6**. Panel (a) shows the various fabrication steps while (b) shows the results of scanning magnetic bits.

A complimentary scheme of broadband magnetometry—employing an ensemble of NV centers rather than a single NV, was also proposed (Acosta et al.; Acosta et al., 2009; Pham et al., 2011). Realization of such a magnetomer will rely on the reliable production of high concentration of NV centers with reduced defects that can contribute to spin relaxation. Preliminary results show that 10 ppm of NV centers can have a reasonable benchmark for 100 μm scale magnetometry at approximately 100 fT $\mathrm{Hz}^{-1/2}$.

3.18.3.1.2 Sensing of Biological Materials

One of the most important applications in diamond magnetometry is the ability to sense biological processes at the nanoscale (Hall, Cole, Hill, & Hollenberg, 2009; Hall et al., 2010). So far, orientation and tracking of

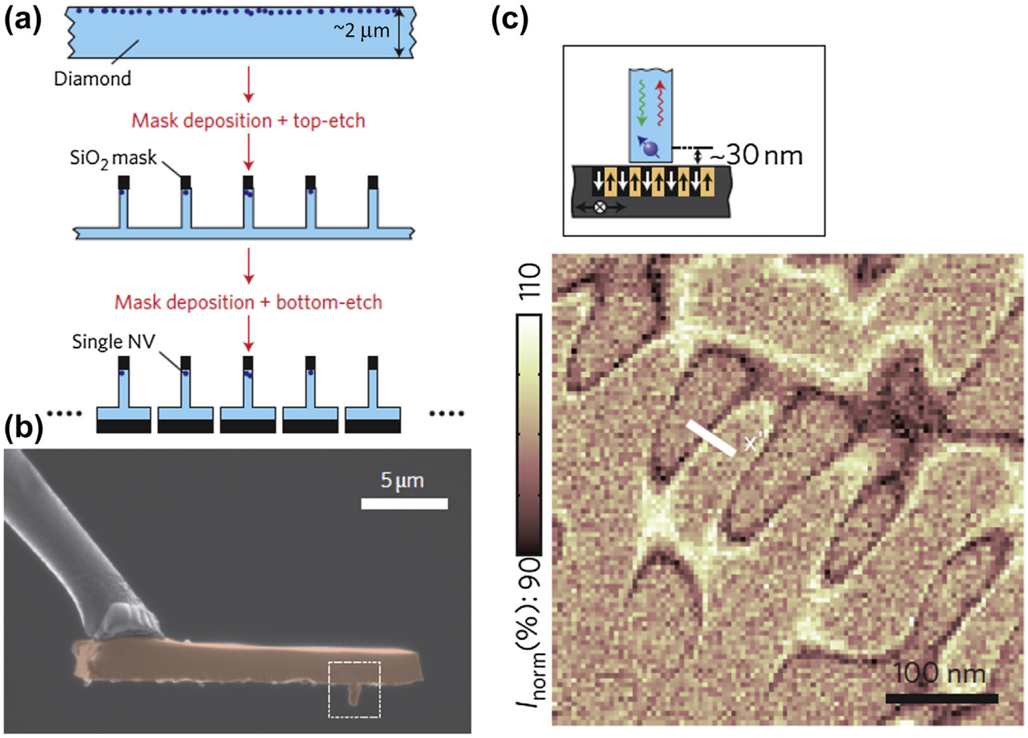

Figure 6 The high-resolution diamond magnetometer with a diamond nanopillar. (a) Fabrication steps of the pillar include patterning, reactive ion etching (RIE), ion implantation, liftoff, and attachment of the pillar to an AFM tip. (b) SEM image of the diamond nanopillar attached to a probe. (c) Scanning results of the pillar magnetometer, where the NV is embedded 30 nm from the tip of the pillar. Reprinted from Maletinsky et al. (2012).

fluorescent nanodiamonds have been demonstrated (Chang et al., 2008; Faklaris et al., 2009; Mochalin, Shenderova, Ho, & Gogotsi, 2012). Recently, an additional, spin, dimension was added and a full quantum measurement of a nanodiamond inside a cell was performed (McGuinness et al., 2011; Tisler et al., 2009). The idea is based on the simultaneous identification of quantum spin levels of the NV, which serve as a fingerprint of the local spin environment, and its fluorescence, which allows to track the three dimensional position of the nanocrystal. By measuring the quantum coherence and the Rabi oscillations, one can further gain information about the rotational motion of the nanodiamond. The millisecond time resolution is on the order of the intercellular processes. Therefore, this noninvasive technique can be potentially used to monitor and observe, in vivo, intercellular processes.

Another application of diamond magnetometry utilized an ensemble of NV centers in conjunction with wide-field imaging (Hall et al., 2012; Pham et al., 2011). This architecture can be used for instance to image neural activities. Employing an NV-rich layer close to the surface, a sensitivity of approximately 100 nT $Hz^{-1/2}$ can be achieved over a 140-mm^2 region. A separation of approximately 1 mm between the neurons and the NV centers, the magnitude of the magnetic field generated by a single firing axon is expected to be at the range of 1–100 nT, depending on the species and the type of the neurons. Simulation of neural activities on top of an NV-rich diamond samples enabled simultaneously high temporal and spatial resolution of extracellular field potentials in regimes beyond those obtained by current methodologies. To bring this imaging concept to reality, one must assemble all the individual and nontrivial components, such as sufficiently dense near-surface NV layer structures in high-grade diamond material, neuron growth on these diamond surfaces, and microwave quantum control and optical wide-field readout commensurate with long term integrity and function of the biological structure.

Beyond the improvement in materials, pulse sequencing plays a central role in detecting weak magnetic fields. Indeed, recent work by Zhao and coworkers (Zhao et al., 2012) realized for the first time a detection of a single, remote nuclear spin (^{13}C) embedded in nuclear spin batch. Although the single detected spin is located only approximately 3 nm from the NV center, the technique is promising to sense external spins in single molecules and solids.

3.18.3.1.3 Electric Field Sensing

In addition to its role in high-resolution magnetic sensing, it was demonstrated that employing the NV center, electric fields can be sensed too (Dolde et al., 2011). The electric field sensing is based on the Stark effect and the Zeeman shifts in the ground state of the NV. An a.c. electric-field sensitivity reaching approximately $200\ \mathrm{V cm^{-1}\ Hz^{-1/2}}$ has been achieved, allowing the detection of an electrostatic field produced by a single elementary charge located at a distance of 150 nm from the sensing NV spin. The NV technique compliments the current existing techniques, including scanning capacitance microscopy, scanning Kelvin probe, and electric field-sensitive atomic force microscopy. Although the NV sensitivity still falls short from the state-of-the-art single electron transistors, the key advantage here is the accessibility to an atomic-scale sensor that can potentially perform precision sensing at distances as close as a few nanometers under ambient conditions.

3.18.3.2 Diamond Photonic Devices

The interaction of single photons with single atoms in an optical cavity is a rich field of fundamental science with major applications in photonic quantum technologies. Implementation of quantum photonics with diamond therefore constitutes the necessity to couple single emitters with photonic resonators. Optimizing the emission from color centers into defined radiative modes through coupling to optical structures including waveguides and cavities will improve their optical properties and allow manipulation and routing of single photons. In the scope of this chapter, we will only discuss the weak coupling regime.

The enhancement of the spontaneous emission of an emitter coupled to a microresonator (assuming same emission rates in uniform dielectric medium and outside the cavity mode) is given by

$$F_{\mathrm{i}} = F_{\mathrm{cav}}\left(\frac{E(r_{\mathrm{i}})\cdot\mu_{\mathrm{i}}}{|E(r_{\mathrm{i}})||\mu_{\mathrm{i}}|}\right)^2 \frac{1}{1+4Q^2(\lambda_{\mathrm{i}}/\lambda_{\mathrm{cav}}-1)^2}$$

where μ_{i} is the dipole moment, $E(r_{\mathrm{i}})$ is the local electric field at the emitter location r_{i}, λ_{cav} is the cavity wavelength, λ_{i} is the emitter wavelength, and |Emax| is the maximum value of the electric field in the resonator. If the dipole is resonant with the cavity and also ideally positioned and oriented with respect to the local electric field, the expression is shortened to

$$F_{\mathrm{cav}} = \frac{3}{4\pi^2}\frac{(\lambda_{\mathrm{cav}})^3}{n}\frac{Q}{V_{\mathrm{mode}}}$$

where n is the refractive index, Q is the quality factor, and V is the cavity mode volume. This expression is also known as the Purcell effect, after Edward Purcell, who studied the modifications of spontaneous emission of radiofrequencies in resonators, and first derived this expression.

Q/V is an important figure of merit for cavity design that clearly emphasizes the need for a high Q and low V. Ultrahigh Q values were achieved in high finesse Fabry–Perot cavities or at a whispering gallery modes of silica spheres or microdisks—both have relatively high modal volumes. In 1987, Yablonovitch introduced the photonic crystal cavities to modify the spontaneous emission (Yablonovitch, 1987). These possess a much lower modal volume and since then a great effort was devoted to engineer photonic band-gap cavities. Understandably, fabrication of high Q cavities requires unprecedented control over the material fabrication.

The initial work on realizing photonic crystal cavities and microdisk cavities from diamond was pioneered by Evelyn Hu at UCSB in 2007 (Wang, Choi, et al., 2007; Wang et al., 2007). Since thin single crystal diamond membranes were not available, nanocrystalline diamond films were used to fabricate the first resonators. An example of a microdisk cavity and a photonic crystal cavity (PCC) made from a polycrystalline material is shown in **Figure 7**. Despite the successful fabrication of microdisk cavities and PCCs, the quality factors of these devices were extremely low, <1000. The reasons for such low Qs are the multiple grain boundaries and the relatively high content of sp2 material, which cause absorption and scattering, which in turn degrades the Q. Although the initial results were not ground breaking in terms of optical performance, it certainly initiated the quest toward the most promising route to fabricate photonic devices out of diamond and avenues to realize coupling of diamond emitters to optical cavities. In the following sections, we will highlight these efforts and describe the two main approaches for diamond photonics—the hybrid approach and the single crystal diamond approach.

3.18.3.2.1 The Hybrid Approach

The hybrid approach underlies coupling single emitters in diamond nanocrystals to optical cavities made out of traditional semiconductors (e.g. GaAs and Si) (Benson, 2011). To achieve best refractive index matching with

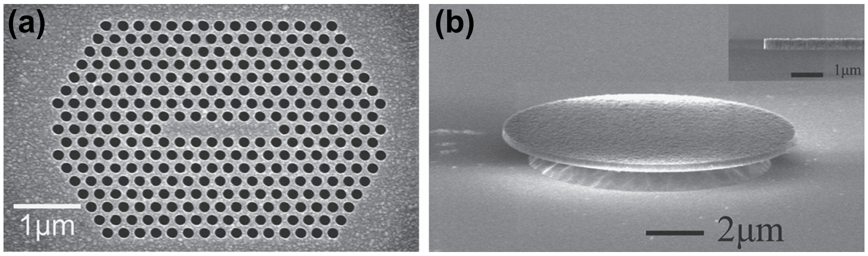

Figure 7 Photonic devices fabricated from polycrystalline diamond material. (a) PCC and (b) microdisk cavity. Reprinted from Wang et al. (2007) and Wang, Choi, et al. (2007).

diamond ($n = 2.4$), the most appropriate candidate is GaP ($n = 3.18$) and indeed most of the initial work on the hybrid approach were demonstrated with GaP (Barclay, Fu, Santori, & Beausoleil, 2009a, 2009b; Fu et al., 2008; Santori et al., 2010; Wolters et al., 2010). The hybrid approach has therefore obvious advantages: the knowledge and the expertise of processing traditional semiconductors are mature and techniques are known to fabricate high-quality optical resonators out of these materials. Furthermore, nanodiamonds hosting single defects are also readily available. The main challenge remains to manipulate the single nanocrystal and put it in the high-energy field of the optical resonator.

Manipulating diamond nanocrystals was pioneered in 2009 by using nanomanipulators and fiber tapers (Ampem-Lassen et al., 2009; Barclay, Santori, Fu, Beausoleil, & Painter, 2009; Van der Sar et al., 2009). A selected nanocrystal hosting a single emitter was first identified by using a traditional confocal microscope, and then selectively picked up and positioned onto a location of choice—such as an optical fiber. **Figure 8** a,b show examples of positioning the nanodiamonds onto photonic resonators made out of GaP and SiO_2. Further improvement and mastering this elegant technique resulted in a controlled nanopositioning of nanodiamonds containing single NV centers in the center of a PCC or photonic crystal fiber, and hot spots of a bow tie nanoantenna (Alaverdyan et al., 2011; Schietinger, Schroder, & Benson, 2008). Despite the poor optical properties of the emitters within the nanocrystals, their spectral broadening and instability, scattering losses and imperfect orientation of the emission dipole with respect to the cavity field, quantum optics effects were demonstrated using the hybrid approach. An enhancement of the NV ZPL was achieved as well as mapping the plasmonic fields of nanoantennas. Transmission measurements through a fiber maintaining the quantum nature of the emitters were also shown (Schröder, Engel, Schmidt, & Benson, 2012).

Another approach toward the demonstration of hybrid systems is to grow nanodiamonds on top of an optical fiber (Rabeau, Huntington, Greentree, & Prawer, 2005) or to embed nanocrystals directly into the optical fiber (Henderson et al., 2011). The latter is done in the early stage, before the fibers are extruded. A mixture of nanodiamonds and the preform are formed into a billet, which is then pulled into a fiber. By controlling the nanodiamond concentration, single emitters within the optical fibers can be isolated.

The hybrid approach extends beyond the use of nanocrystals. A promising method is to use the near-surface optical emitters and couple them to a cavity fabricated on the surface of a single crystal diamond (Barclay et al., 2009b; Fu et al., 2008). **Figure 8(c) and (d)** exemplifies this approach, which was pioneered by the Hewlett Packard (HP) group. Coupling of near-surface emitters to a GaP waveguide and then to GaP microdisk and microring cavities was demonstrated. Employing single crystals rather than nanodiamonds offers the potential to access optically stable NV centers and even controllably generate single emitters by methods of ion implantation. Resonant enhancement of the ZPL and spontaneous emission lifetime reduction was demonstrated using this approach.

3.18.3.2.2 Single Crystal Diamond Approaches

Fabrication of photonic devices out of single crystal diamond has a tremendous potential for integrated nanophotonics. Comparing the single crystal approach with the hybrid approach, the former has a number of advantages. First, the emitters embedded in single crystal diamond exhibit superior photophysical properties in terms of spin coherence and spectral stability. Second, there is no scattering loses due to the nanocrystal and there is no difference in the refractive index, which all together minimizes the losses. Third, only by employing the all diamond approach can one achieve maximum spectral and lateral overlap with the cavity field. Finally, the all diamond approach offers the potential for scalability and eventually a demonstration of a diamond

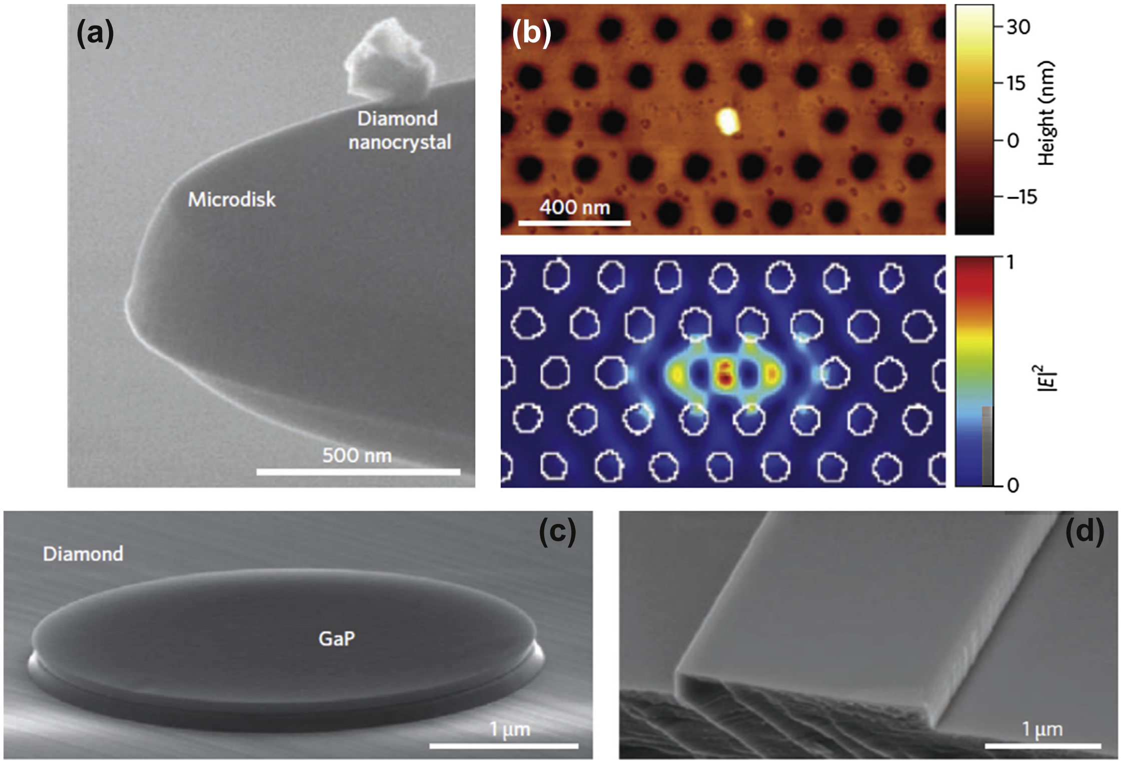

Figure 8 Hybrid approach for diamond photonics. (a) Positioning of diamond nanoparticles on a SiO_2 microdisk. (b) Manipulation of nanodiamonds on the top of a GaP PCC. (c) GaP microdisk and (d) GaP waveguide fabricated on top of a single crystal diamond. Reprinted from Fu et al. (2008), Barclay et al. (2009b), Wolters et al. (2010), and Barclay et al. (2009).

photonic network. In this chapter, we will highlight the recent developments in fabrication of photonic entitles out of single crystal diamond.

3.18.3.2.3 Sculpting Photonic Elements Out of Diamond: Pillars and Solid Immersion Lenses

As was mentioned earlier, one of the main drawbacks of the NV center is its broad phonon line and fairly modest emission rate. Combining this with the refractive index of diamond (2.4), an efficient collection of the emitted photons from the NV becomes challenging. To overcome this problem, two solutions were proposed and efficiently demonstrated. The first includes a pure optical approach, which involves improvement in the collection efficiency by means of geometrical optics. The second approach involves a quantum regime, where by coupling an emitter to an optical cavity, one can increase the radiative decay time, thereby increasing the photon flux. From the obvious reasons of the ease of fabrication, the first approach was realized first, and is discussed in the following paragraphs.

Babinec et al. have realized diamond pillars by employing RIE (Babinec et al., 2010). The pillars were etched out of a single crystal diamond that contained native NV centers. Statistically, some of the pillars therefore had single NV centers. The count rate from these embedded NVs exhibited a factor of 10 in brightness, due to the enhanced collection efficiency out of the nanowire. Further experiments demonstrated the fabrication of pillars out of an ultrapure diamond, followed by a controlled generation of NV centers by ion implantation. The nanowire platform offers a unique platform to engineer single photon sources on demand with an enhanced collection efficiency. The nanopillars are shown in **Figure 9(a)**.

A solid immersion lens (SIL) is another attractive option to enhance the collection efficiency of an emitter. The hemispherical SILs geometrically avoid any refraction at the diamond–air interface. If a color center is placed at the origin of a hemispherical diamond surface, the fluorescent light coming out is perpendicular to the surface over the full 2π solid angle of the hemisphere. Therefore, no refraction occurs, and the collection is effectively increased by the refractive index of diamond (~2.4). The orientation of the emitting dipole must be located in the centroid of the SIL to maximize the collection. This can be done by performing high-energy ion implantation of nitrogen into the SIL, or precharacterizing a diamond sample to locate the emitters deep into

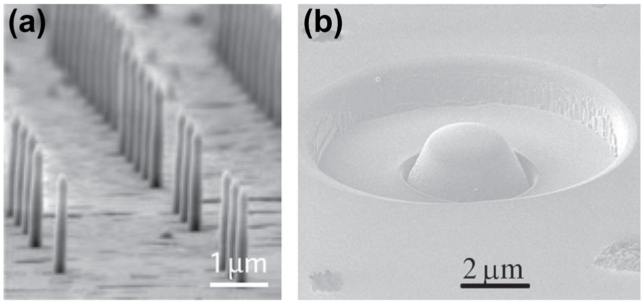

Figure 9 Photonic structures to enhance light emission from diamond. (a) Diamond pillars and (b) solid immersion lens fabricated from a single crystal diamond. Reprinted from Babinec et al. (2010) and Hadden et al. (2010).

the crystal, and deterministically curve an SIL around them. Both techniques were demonstrated (Hadden et al., 2010; Siyushev et al., 2010).

Integrated microlenses have previously been fabricated in diamond using inductively coupled plasma etching (Karlsson & Nikolajeff, 2003); however, they have not been used to improve the collection of defect center emission. The newer generation of diamond SILs was fabricated in diamond using FIB—an example is shown in **Figure 9(b)**. Since the SIL has a relatively large dimension (~2–10 μm), the residual ion damage is not as detrimental to the SIL performance. Indeed, the usage of SILs was instrumental in the very recent demonstration of photon entanglement from NV centers.

3.18.3.2.4 Generation of Devices by Ion Implantation

Ion implantation is a common technique to modify physical, chemical, and optical properties of a material by introducing external impurities into the crystalline lattice. To perform an implantation, atoms are ionized, accelerated with an electric field and "bombarded" into the target material. The end of a range of the implanted ions is determined by the acceleration energy of the ions (typically ranging from few kiloelectron volts to megaelectron volts), the mass of the ion, and the target material. Due to an introduction of external atoms by bombardment, ion beam-induced damage is always associated with the implantation. Therefore, a thermal annealing sequence is usually applied after the implantation to allow the material to recover and to allow the activation of the implants into their energetically favorable location.

To predict the profile of the implanted ions in the implanted matrix, Monte Carlo-based modeling packages are routinely employed. The most commonly known is stopping and range of ions in matter. The software is based on the estimation of different probabilities of collisions among the implanted ions while taking into account lattice parameters such as density and lattice spacing. The output provides a useful prediction regarding the stopping range of the implanted ions and its distribution, damage events, and concentration of the created vacancies.

Ion implantation in diamond can be used to create color centers for electronic and photonic applications (Kalish et al., 1997; Prawer & Kalish, 1995). In recent years, this technique has been used to achieve thin diamond membranes (Fairchild et al., 2008; Olivero et al., 2005; Olivero et al., 2006; Parikh et al., 1992). First, the bulk diamond crystal is implanted with high dose (~10^{16}), high-energy He^+ ions (~1–2 MeV) to generate an amorphous layer at the end of the range of the ion. After annealing, this layer can be selectively etched leaving behind a thin (typically a few hundreds nanometers to several microns thick) diamond membrane. Since diamond does not have native etchable oxides and high-quality heteroepitaxy of single crystal diamond on dissimilar substrates have not been shown, the ion implantation and liftoff route is currently the only way to generate large area single crystal diamond membranes.

Indeed, employing this approach, the first prototypes of diamond microring resonators and waveguides were demonstrated (**Figure 10**). Furthermore, this technique served as a foundation to the first devices patterned by FIB. The FIB method offers the direct patterning of photonic structures without the necessity of e-beam lithography and hard masking of the sample (Babinec, Choy, Smith, Khan, & Loncar, 2011; Bayn et al., 2011; Bayn, Meyler, Salzman, & Kalish, 2011). One approach using the FIB for diamond devices was as follows: first, a suspended membrane was generated by double implantation of He into diamond lattice, and etching away of the graphitized regions. Then, a PCC was patterned into the membrane using FIB. In an alternative, more creative approach, FIB was used to directly remove diamond from the side and from the

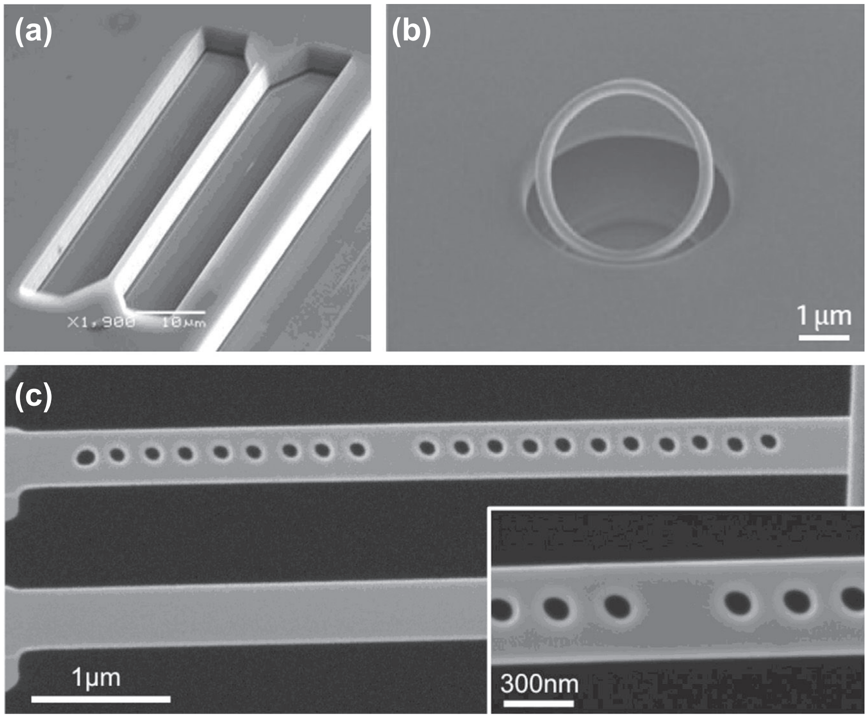

Figure 10 Initial results on diamond photonic resonators fabricated by FIB and liftoff. (a) Diamond waveguide, (b) diamond microring, (c) FIB made PCC nanobeam cavity. Reprinted from Olivero et al. (2005), Fairchild et al. (2008), and Babinec et al. (2011).

top, leaving behind a suspended nanobeam structure. Recently, angle etching of triangular nanobeam cavities was also realized using an FIB milling process (Bayn, Meyler, et al., 2011). FIB was also used to sculpt nanocavities from micron-sized CVD diamond crystals grown on iridium. This approach was used to demonstrate the coupling of SiV emitters to photonic crystal cavities, although the quality factors were extremely low (Riedrich-Moller et al., 2012). Despite the considerable effort to sculpt diamond devices with FIB, every FIB procedure is associated with severe damage from the Ga ion beam. Multiple annealing sequences and chemical treatments in acids did not prove to be useful. The residual built-in strain as a result of the high ion damage significantly limits the performance of diamond devices fabricated in this manner (**Figure 10**).

Recently, the ion implantation method has been reviewed and an additional fabrication step was introduced. Rather than fabricating the devices straight out of the lifted-off diamond membranes, the membranes were used as templates for a short overgrowth of a thin layer of single crystal diamond (Aharonovich et al., 2012; Lee, Aharonovich, Magyar, Rol, & Hu, 2012; Magyar et al., 2011). The overgrowth process gives the flexibility to intentionally dope the diamond device layer with color centers such as NV or SiV centers that were not present in the original diamond template. The structure can then be flipped and the original damaged material thinned away, leaving behind a pristine, high-quality diamond membrane. This method proved to be successful and devices with high-quality factors ($Q \sim 3000$) were fabricated. **Figure 11** illustrates the experimental procedure for this approach and shows an SEM image of a diamond PCC fabricated in this manner.

3.18.3.3.5 Generation of Optical Cavities from Commercial Diamond Material

With the recent availability of commercial, thin (~10–20 μm thick) diamond membranes (e6cvd), the field of diamond photonics had a fresh start. Engineering simple photonic devices, such as microring cavities, were now viable with high-quality material. Indeed, in 2011, the HP team was the first to demonstrate a Purcell enhancement from an emitter coupled to a microring resonator—all made out of a single crystal diamond (Faraon, Barclay, Santori, Fu, & Beausoleil, 2011).

The fabrication of the microring resonators first involved an RIE the diamond membrane to a thickness of a few hundreds nanometers. Then, by employing e-beam lithography, a microring pattern was defined, and the

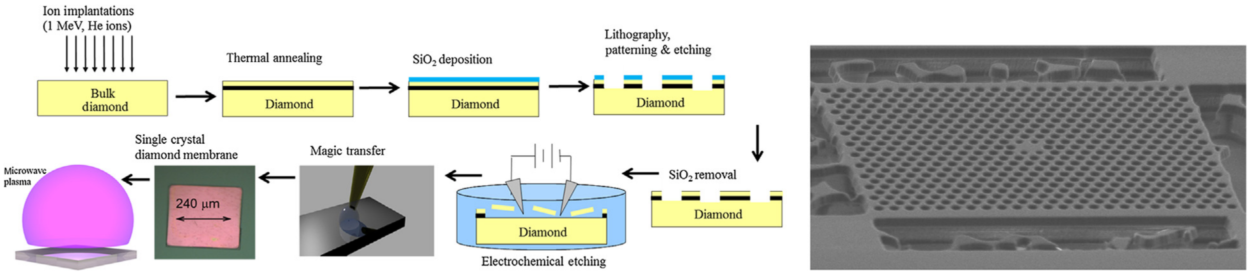

Figure 11 Schematic illustration of the fabrication of diamond photonic devices from an ion-implanted material. The process involved ion implantation, lithography, liftoff of a thin diamond membrane, and regrowth of a pristine diamond crystal on top of the membrane. The original material is then etched away and a photonic cavity is fabricated—as shown in the SEM. Image courtesy of Jonathan C. Lee

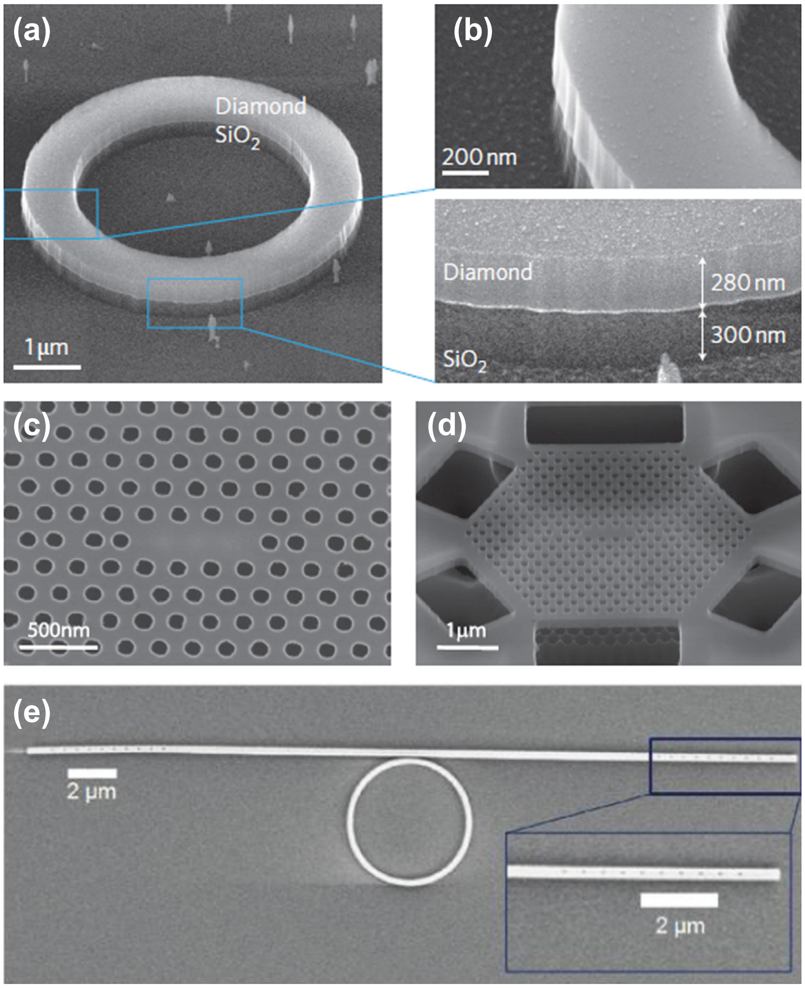

Figure 12 Photonic resonators fabricated from a pristine single crystal diamond membrane. (a,b) Diamond microring cavity positioned on top of a SiO_2 substrate. (c,d) PCC fabricated from a similar membrane. (e) Integrated device consisting of a single microring resonator coupled to an optical waveguide—all are made out of single crystal diamond positioned on top of a SiO_2 substrate. Reprinted from Faraon et al. (2011), Faraon et al. (2012), and Hausmann et al. (2012).

device was finalized. The device is shown in Figure 12(a) and (b). Since the starting material was of type IIA, electronic grade diamond, NV centers were randomly distributed in the sample, and were easily accessible in the final device. Resonant excitation of the NVs embedded in the microring in conjunction with lifetime measurements resulted in the first demonstration of a Purcell enhancement of approximately 13.

As expected, the follow-up device was a PCC, fabricated in a very similar manner. The diamond photonic crystal is shown in **Figure 12(c) and (d)**. In this case, however, due to the lower modal volume compared to the microring device, the Purcell enhancement was approximately 70 (Faraon, Santori, Huang, Acosta, & Beausoleil, 2012). Faraon and colleagues also recorded an antibunching curve from the single emitter located inside the cavity, unambiguously demonstrating that single emitters were addressed. In their results, 70% of the emission was directed into the ZPL, allowing practical applications into integrated diamond photonics. Although the NV centers in this particular case were inside the diamond, a priori, one could fabricate a PCC from a pristine, ultrapure material and generate the emitters deterministically at the high cavity energy field. Other parameters that have to be considered are the misalignment of the NV dipole with respect to the cavity field.

Although the quality factors in the current resonators are not as high as the reported values for GaAs or Silicon, one should remember that the resonant emission is in the visible range and not in the IR. Furthermore, it was shown that a Q of approximately $10–20 \times 10^3$ is required for realization of various quantum protocols, which is certainly within reach.

The success in the fabrication of optical cavities was immediately followed by a modest though neat demonstration of an integrated photonic network (**Figure 12(e)**) (Hausmann et al., 2012), where both the cavity (microring resonator) and the waveguide were etched down from a single membrane. Once again, employing low nitrogen diamond membranes, single photon emission routing through the waveguide to the cavity and vice versa, was demonstrated.

3.18.4 Conclusions and Future Outlook

Diamond quantum photonics and single emitters in diamond have seen tremendous progress in the last decade. From the discovery of new bright, quantum emitters through a rigorous understanding of the photophysics of the NV center, to the realization of high-resolution diamond magnetic and electric sensors and diamond optical resonators. With more groups joining this fascinating field, the research avenues expand and new challenges are constantly addressed. Highlighted below are some key items that are considered essential for new developments in the future:

1. The interface of plasmonics and photonics, employing single emitters and silver (or gold) nanostructures is emerging. Initial results showed an enhancement in photon collection by coupling emitters to plasmonic cavities (Barth et al., 2010).
2. For integrated photonics, an electrical excitation of single emitters should be possible. Preliminary experiments demonstrated that the neutral NV center can be electrically excited, while an electrically triggered NV^- defect is yet to be showed (Lohrmann et al., 2012; Mizuochi et al., 2012).
3. Stability of emitters and long coherence times in single emitters located at a close proximity to the surface. This is arguably the most crucial goal in both sensing and photonics as proximity of the emitters to the surface is unavoidable for high-performance devices. Preliminary results include surface functionalization and stabilization using electric fields (Acosta et al., 2012; Naydenov et al., 2010; Stacey et al., 2012).
4. Availability of high-quality, thin diamond membranes. The recent commercial availability of thin diamond membranes was certainly a boost to the fabrication of diamond devices. However, amelioration of diamond processing (including regrowth approach and angle etch) can be further optimized and new fabrication paths should be introduced.
5. Employment of diamond devices in life science application. Experiments in drug delivery, biomarking, and in vivo imaging are already on the way. Further improvements in the generation of long coherence NVs in nanodiamonds may eventually lead to the sensing of neural activities and ion channels and in vivo imaging of biological processes inside living cells.
6. Optomechanics. Diamond possesses excellent mechanical properties. The new fabrication development to demonstrate excellent suspended nanostructures made of single crystal diamond may pave the way to a whole new branch of optomechanics with diamond (Burek et al., 2012; Kolkowitz et al., 2012; Liao, Hishita, Watanabe, Koizumi, & Koide, 2010; Ovartchaiyapong, Pascal, Myers, Lauria, & Jayich, 2012). Furthermore, combining the NV spin properties with mechanical motion will enhance our understanding in the hybrid mechanical-spin systems, enabling new sensors and devices. Research in this direction is already undergoing, with the initial coherent quantum control of a single spin driven by the motion of a mechanical resonator being demonstrated (Hong et al., 2012).

References

Acosta, V. M., Bauch, E., Jarmola, A., Zipp, L. J., Ledbetter, M. P., & Budker, D. Broadband magnetometry by infrared-absorption detection of nitrogen-vacancy ensembles in diamond. *Applied Physics Letters*, *97*(3).

Acosta, V. M., et al. (2009). Diamonds with a high density of nitrogen-vacancy centers for magnetometry applications. *Physical Review B, 80*.

Acosta, V. M., et al. (2012). Dynamic stabilization of the optical resonances of single nitrogen-vacancy centers in diamond. *Physical Review Letters, 108*.

Aharonovich, I., Castelletto, S., Simpson, D. A., Greentree, A. D., & Prawer, S. (2010). Photophysics of chromium-related diamond single-photon emitters. *Physical Review A, 81*, 043813.

Aharonovich, I., Castelletto, S., Simpson, D. A., Su, C. H., Greentree, A. D., & Prawer, S. (2011). Diamond-based single-photon emitters. *Reports on Progress in Physics, 74*, 076501.

Aharonovich, I., et al. (2009a). Enhanced single-photon emission in the near infrared from a diamond color center. *Physical Review B, 79*, 235316.

Aharonovich, I., et al. (2009b). Two-level ultrabright single photon emission from diamond nanocrystals. *Nano Letters, 9*, 3191–3195.

Aharonovich, I., et al. (2010). Chromium single-photon emitters in diamond fabricated by ion implantation. *Physical Review B, 81*, 121201 (R).

Aharonovich, I., et al. (2012). Homoepitaxial growth of single crystal diamond membranes for quantum information processing. *Advanced Materials, 24*, OP54–OP59.

Aharonovich, I., Greentree, A. D., & Prawer, S. (2011). Diamond photonics. *Nature Photonics, 5*, 397–405.

Alaverdyan, Y., Vamivakas, N., Barnes, J., Lebouteiller, C., Hare, J., & Atature, M. (2011). Spectral tunability of a plasmonic antenna with a dielectric nanocrystal. *Optics Express, 19*, 18175–18181.

Ampem-Lassen, E., et al. (2009). Nano-manipulation of diamond-based single photon sources. *Optics Express, 17*, 11287–11293.

Babinec, T. M., Choy, J. T., Smith, K. J. M., Khan, M., & Loncar, M. (2011). Design and focused ion beam fabrication of single crystal diamond nanobeam cavities. *Journal of Vacuum Science and Technology B, 29*, 010601.

Babinec, T. M., et al. (2010). A diamond nanowire single-photon source. *Nature Nanotechnology, 5*, 195–199.

Balasubramanian, G., et al. (2008). Nanoscale imaging magnetometry with diamond spins under ambient conditions. *Nature, 455*, 648–652.

Balasubramanian, G., et al. (2009). Ultralong spin coherence time in isotopically engineered diamond. *Nature Materials, 8*, 383–387.

Balmer, R. S., et al. (2009). Chemical vapour deposition synthetic diamond: materials, technology and applications. *Journal of Physics: Condensed Matter, 21*, 364221.

Barclay, P. E., Fu, K. M., Santori, C., & Beausoleil, R. G. (2009a). Hybrid photonic crystal cavity and waveguide for coupling to diamond NV-centers. *Optics Express, 17*, 9588–9601.

Barclay, P. E., Fu, K. M. C., Santori, C., & Beausoleil, R. G. (2009b). Chip-based microcavities coupled to nitrogen-vacancy centers in single crystal diamond. *Applied Physics Letters, 95*, 191115.

Barclay, P. E., Santori, C., Fu, K. M., Beausoleil, R. G., & Painter, O. (2009). Coherent interference effects in a nano-assembled diamond NV center cavity-QED system. *Optics Express, 17*, 8081–8097.

Barth, M., et al. (2010). Nanoassembled plasmonic-photonic hybrid cavity for tailored light-matter coupling. *Nano Letters, 10*, 891–895.

Batalov, A., et al. (2009). Low temperature studies of the excited-state structure of negatively charged nitrogen-vacancy color centers in diamond. *Physical Review Letters, 102*, 195506.

Bayn, I., et al. (2011). Processing of photonic crystal nanocavity for quantum information in diamond. *Diamond and Related Materials, 20*, 937–943.

Bayn, I., Meyler, B., Salzman, J., & Kalish, R. (2011). Triangular nanobeam photonic cavities in single-crystal diamond. *New Journal of Physics, 13*, 025018.

Benson, O. (2011). Assembly of hybrid photonic architectures from nanophotonic constituents. *Nature, 480*, 193–199.

Bernien, H., Childress, L., Robledo, L., Markham, M., Twitchen, D., & Hanson, R. (2012). Two-photon quantum interference from separate nitrogen vacancy centers in diamond. *Physical Review Letters, 108*.

Burek, M. J., et al. (2012). Free-standing mechanical and photonic nanostructures in single-crystal diamond. *Nano Letters*.

Castelletto, S., Edmonds, A., Gaebel, T., & Rabeau, J. (2012). Production of multiple diamond-based single-photon sources. *IEEE Journal of Selected Topics in Quantum Electronics, 18*, 1792–1798.

Chang, Y. R., et al. (2008). Mass production and dynamic imaging of fluorescent nanodiamonds. *Nature Nanotechnology, 3*, 284–288.

Davies, G. (1976). A-nitrogen aggregate in diamond-its symmetry and possible structure. *Journal of Physics C: Solid State Physics, 9*, L537–L542.

Degen, C. L. (2008). Scanning magnetic field microscope with a diamond single-spin sensor. *Applied Physics Letters, 92*, 243111.

de Lange, G., Riste, D., Dobrovitski, V. V., & Hanson, R. Single-spin magnetometry with multipulse sensing sequences. *Physical Review Letters*, *106*.

de Lange, G., Wang, Z. H., Riste, D., Dobrovitski, V. V., & Hanson, R. (2010). Universal dynamical decoupling of a single solid-state spin from a spin bath. *Science, 330*, 60–63.

Doherty, M. W., et al. (2012). Theory of the ground-state spin of the NV-center in diamond. *Physical Review B, 85*.

Doherty, M. W., Manson, N. B., Delaney, P., & Hollenberg, L. C. L. (2011). The negatively charged nitrogen-vacancy centre in diamond: the electronic solution. *New Journal of Physics, 13*, 025019.

Dolde, F., et al. (2011). Electric-field sensing using single diamond spins. *Nature Physics, 7*, 459–463.

Dumeige, Y., Treussart, F., Alleaume, R., Gacoin, T., Roch, J. F., & Grangier, P. (2004). Photo-induced creation of nitrogen-related color centers in diamond nanocrystals under femtosecond illumination. *Journal of Luminescence, 109*, 61–67.

e6cvd www.e6cvd.com.

Edmonds, A. M., Newton, M. E., Martineau, P. M., Twitchen, D. J., & Williams, S. D. (2008). Electron paramagnetic resonance studies of silicon-related defects in diamond. *Physical Review B, 77*, 245205.

Ellis, B., et al. (2011). Ultralow-threshold electrically pumped quantum-dot photonic-crystal nanocavity laser. *Nature Photonics, 5*, 297–300.

Fairchild, B. A., et al. (2008). Fabrication of ultrathin single-crystal diamond membranes. *Advanced Materials, 20*, 4793.

Faklaris, O., et al. (2009). Comparison of the photoluminescence properties of semiconductor quantum dots and non-blinking diamond nanoparticles. Observation of the diffusion of diamond nanoparticles in living cells. *Journal of the European Optical Society: Rapid Publications, 4*.

Faraon, A., Barclay, P. E., Santori, C., Fu, K. M. C., & Beausoleil, R. G. (2011). Resonant enhancement of the zero-phonon emission from a colour centre in a diamond cavity. *Nature Photonics, 5*, 301–305.

Faraon, A., Santori, C., Huang, Z. H., Acosta, V. M., & Beausoleil, R. G. (2012). Coupling of nitrogen-vacancy centers to photonic crystal cavities in monocrystalline diamond. *Physical Review Letters, 109*.

Feng, T., & Schwartz, B. D. (1993). Characteristics and origin of the 1.681 eV luminescence center in chemical-vapor-deposited diamond films. *Journal of Applied Physics, 73*, 1415–1425.

Fuchs, G. D., et al. (2008). Excited-state spectroscopy using single spin manipulation in diamond. *Physical Review Letters, 101*.

Fu, K. M. C., et al. (2008). Coupling of nitrogen-vacancy centers in diamond to a GaP waveguide. *Applied Physics Letters, 93*, 203107.

Fu, K. M. C., Santori, C., Barclay, P. E., & Beausoleil, R. G. (2010). Conversion of neutral nitrogen-vacancy centers to negatively charged nitrogen-vacancy centers through selective oxidation. *Applied Physics Letters, 96*.

Fu, K. M. C., Santori, C., Barclay, P. E., Rogers, L. J., Manson, N. B., & Beausoleil, R. G. (2009). Observation of the dynamic Jahn–Teller effect in the excited states of nitrogen-vacancy centers in diamond. *Physical Review Letters, 103*, 256404.

Gaebel, T., et al. (2006). Photochromism in single nitrogen-vacancy defect in diamond. *Applied Physics B: Lasers and Optics, 82*, 243–246.

Gaebel, T., Popa, I., Gruber, A., Domhan, M., Jelezko, F., & Wrachtrup, J. (2004). Stable single-photon source in the near infrared. *New Journal of Physics, 6*, 98–104.

Gisin, N., Ribordy, G. G., Tittel, W., & Zbinden, H. (2002). Quantum cryptography. *Reviews of Modern Physics, 74*, 145–195.

Goss, J. P., Jones, R., Breuer, S. J., Briddon, P. R., & Oberg, S. (1996). The twelve-line 1.682eV luminescence center in diamond and the vacancy-silicon complex. *Physical Review Letters, 77*, 3041–3044.

Greentree, A. D., Fairchild, B. A., Hossain, F. M., & Prawer, S. (2008). Diamond integrated quantum photonics. *Materials Today, 11*, 22–31.

Grinolds, M. S., Maletinsky, P., Hong, S., Lukin, M. D., Walsworth, R. L., & Yacoby, A. (2011). Quantum control of proximal spins using nanoscale magnetic resonance imaging. *Nature Physics, 7*, 687–692.

Grotz, B., et al. (2012). Charge state manipulation of qubits in diamond. *Nature Communications, 3*, 729.

Gruber, A., Drabenstedt, A., Tietz, C., Fleury, L., Wrachtrup, J., & von Borczyskowski, C. (1997). Scanning confocal optical microscopy and magnetic resonance on single defect centers. *Science, 276*, 2012–2014.

Hadden, J. P., et al. (2010). Strongly enhanced photon collection from diamond defect centers under microfabricated integrated solid immersion lenses. *Applied Physics Letters, 97*, 241901.

Hall, L. T., Cole, J. H., Hill, C. D., & Hollenberg, L. C. L. (2009). Sensing of fluctuating nanoscale magnetic fields using nitrogen-vacancy centers in diamond. *Physical Review Letters, 103*, 4.

Hall, L. T., et al. (2010). Monitoring ion-channel function in real time through quantum decoherence. *Proceedings of the National Academy of Sciences of the United States of America, 107*, 18777–18782.

Hall, L. T., et al. (2012). High spatial and temporal resolution wide-field imaging of neuron activity using quantum NV-diamond. *Scientific Reports, 2*.

Hanson, R., Gywat, O., & Awschalom, D. D. (2006). Room-temperature manipulation and decoherence of a single spin in diamond. *Physical Review B, 74*.

Hanson, R., Mendoza, F. M., Epstein, R. J., & Awschalom, D. D. (2006). Polarization and readout of coupled single spins in diamond. *Physical Review Letters, 97*.

Hauf, M. V., et al. (2011). Chemical control of the charge state of nitrogen-vacancy centers in diamond. *Physical Review B, 83*, 081304(R).

Hausmann, B. J. M., et al. (2012). Integrated diamond networks for quantum nanophotonics. *Nano Letters, 12*, 1578–1582.

He, X. F., Manson, N. B., & Fisk, P. T. H. (1993a). Paramagnetic-resonance of photoexcited N-V defects in diamond. 1. Level anticrossing in the (3)A ground-state. *Physical Review B, 47*, 8809–8815.

He, X. F., Manson, N. B., & Fisk, P. T. H. (1993b). Paramagnetic-resonance of photoexcited N-V defects in diamond. 2. Hyperfine interaction with the N-14 nucleus. *Physical Review B, 47*, 8816–8822.

Henderson, M. R., et al. (2011). Diamond in tellurite glass: a new medium for quantum information. *Advanced Materials, 23*, 2806.

Hennessy, K., et al. (2007). Quantum nature of a strongly coupled single quantum dot-cavity system. *Nature, 445*, 896–899.

Hodges, J. S., et al. (2012). Long-lived NV − spin coherence in high-purity diamond membranes. *New Journal of Physics, 14*, 093004.

Hong, S. K., Grinolds, M. S., Maletinsky, P., Walsworth, R. L., Lukin, M. D., & Yacoby, A. (2012). Coherent, mechanical control of a single electronic spin. *Nano Letters, 12*, 3920–3924.

Hsu, J.-H., Su, W.-D., Yang, K.-L., Tzeng, Y.-K., & Chang, H.-C. (2011). Nonblinking green emission from single H3 color centers in nanodiamonds. *Applied Physics Letters, 98*, 193116–193119.

Iakoubovskii, K., Adriaenssens, G. J., & Nesladek, M. (2000). Photochromism of vacancy-related centres in diamond. *Journal of Physics: Condensed Matter, 12*, 189–199.

Imamoglu, A., et al. (1999). Quantum information processing using quantum dot spins and cavity QED. *Physical Review Letters, 83*, 4204–4207.

Intallura, P. M., et al. (2007). Quantum key distribution using a triggered quantum dot source emitting near 1.3 μm. *Applied Physics Letters, 91*, 161103.

Jelezko, F., Gaebel, T., Popa, I., Domhan, M., Gruber, A., & Wrachtrup, J. (2004). Observation of coherent oscillation of a single nuclear spin and realization of a two-qubit conditional quantum gate. *Physical Review Letters, 93*.

Jelezko, F., & Wrachtrup, J. (2004). Read-out of single spins by optical spectroscopy. *Journal of Physics: Condensed Matter, 16*, R1089–R1104.

Kalish, R., et al. (1997). Nitrogen doping of diamond by ion implantation. *Diamond and Related Materials, 6*, 516–520.

Karlsson, M., & Nikolajeff, F. (2003). Diamond micro-optics: microlenses and antireflection structured surfaces for the infrared spectral region. *Optics Express, 11*, 502–507.

Kimble, H. J. (2008). The quantum internet. *Nature, 453*, 1023–1030.

Kitawaki, H. (2007). Gem diamonds: causes of colors. *New Diamond and Frontier Carbon Technology, 17*, 119–126.

Kolesov, R., et al. (2012). Optical detection of a single rare-earth ion in a crystal. *Nature Communications, 3*.

Kolkowitz, S., et al. (2012). Coherent sensing of a mechanical resonator with a single-spin qubit. *Science, 335*, 1603–1606.

Kupriyanov, I. N., Gusev, V. A., Borzdov, Y. M., Kalinin, A. A., & Pal'yanov, Y. N. (1999). Photoluminescence study of annealed nickel- and nitrogen-containing synthetic diamond. *Diamond and Related Materials, 8*, 1301–1309.

Lee, J. C., Aharonovich, I., Magyar, A. P., Rol, F., & Hu, E. L. (2012). Coupling of silicon-vacancy centers to a single crystal diamond cavity. *Optics Express, 20*, 8891–8897.

Liao, M., Hishita, S., Watanabe, E., Koizumi, S., & Koide, Y. (2010). Suspended single-crystal diamond nanowires for high-performance nanoelectromechanical switches. *Advanced Materials*.

Lohrmann, A., et al. (2012). Diamond based light-emitting diode for visible single-photon emission at room temperature. *Applied Physics Letters, 99*.

Magyar, A., et al. (2011). Fabrication of thin, luminescent, single-crystal diamond membranes. *Applied Physics Letters, 99*, 081913.

Maiman, T. H. (1960). Stimulated optical radiation in ruby. *Nature, 187*, 493–494.

Maletinsky, P., et al. (2012). A robust scanning diamond sensor for nanoscale imaging with single nitrogen-vacancy centres. *Nature Nanotechnology, 7*, 320–324.

Mamin, H. J., Sherwood, M. H., & Rugar, D. (2012). Detecting external electron spins using nitrogen-vacancy centers. *Physical Review B, 86*, 195422.

Maze, J. R., et al. (2008). Nanoscale magnetic sensing with an individual electronic spin in diamond. *Nature, 455*, 644–648.

McGuinness, L. P., et al. (2011). Quantum measurement and orientation tracking of fluorescent nanodiamonds inside living cells. *Nature Nanotechnology, 6*, 358–363.

Michler, P., et al. (2000). A quantum dot single-photon turnstile device. *Science, 290*, 2282.

Mizuochi, N., et al. (2012). Electrically driven single-photon source at room temperature in diamond. *Nature Photonics, 6*, 299–303.

Mochalin, V. N., Shenderova, O., Ho, D., & Gogotsi, Y. (2012). The properties and applications of nanodiamonds. *Nature Nanotechnology, 7*, 11–23.

Morfa, A. J., et al. (2012). Single-photon emission and quantum characterization of zinc oxide defects. *Nano Letters, 12*, 949–954.

Muller, T., et al. (2011). Wide-range electrical tunability of single-photon emission from chromium-based colour centres in diamond. *New Journal of Physics, 13*.

Nadolinny, V. A., et al. (2000). Mechanisms of nitrogen aggregation in nickel- and cobalt-containing synthetic diamonds. *Diamond and Related Materials, 9*, 883–886.

Naydenov, B., et al. (2009). Engineering single photon emitters by ion implantation in diamond. *Applied Physics Letters, 95*, 181109.

Naydenov, B., et al. (2010). Increasing the coherence time of single electron spins in diamond by high temperature annealing. *Applied Physics Letters, 97*, 242511.

Nazare, M. H., Neves, A. J., & Davies, G. (1991). Optical studies of the 1.40-eV Ni center in diamond. *Physical Review B: Condensed Matter, 43*, 14196–14205.

Neu, E., Agio, M., & Becher, C. (2012). Photophysics of single silicon vacancy centers in diamond: implications for single photon emission. *Optics Express, 20*, 19956–19971.

Neu, E., Albrecht, R., Fischer, M., Gsell, S., Schreck, M., & Becher, C. (2012). Electronic transitions of single silicon vacancy centers in the near-infrared spectral region. *Physical Review B, 85*.

Neu, E., et al. (2011a). Single photon emission from silicon-vacancy centres in CVD-nano-diamonds on iridium. *New Journal of Physics, 13*, 025012.

Neu, E., et al. (2011b). Narrowband fluorescent nanodiamonds produced from chemical vapor deposition films. *Applied Physics Letters, 98*.

Neumann, P., et al. (2009). Excited-state spectroscopy of single NV defects in diamond using optically detected magnetic resonance. *New Journal of Physics, 11*, 013017.

O'Brien, J. L., Furusawa, A., & Vuckovic, J. (2009). Photonic quantum technologies. *Nature Photonics, 3*, 687–695.

Olivero, P., et al. (2005). Ion-beam-assisted lift-off technique for three-dimensional micromachining of freestanding single-crystal diamond. *Advanced Materials, 17*, 2427.

Olivero, P., et al. (2006). Characterization of three-dimensional microstructures in single-crystal diamond. *Diamond and Related Materials, 15*, 1614–1621.

Orwa, J. O., et al. (2010). Nickel related optical centres in diamond created by ion implantation. *Journal of Applied Physics, 107*, 093512.

Ovartchaiyapong, P., Pascal, L. M. A., Myers, B. A., Lauria, P., & Jayich, A. C. B. (2012). High quality factor single-crystal diamond mechanical resonators. *Applied Physics Letters, 101*, 505–508.

Parikh, N. R., et al. (1992). Single-crystal diamond plate liftoff achieved by ion-implantation and subsequent annealing. *Applied Physics Letters, 61*, 3124–3126.

Pezzagna, S., Rogalla, D., Wildanger, D., Meijer, J., & Zaitsev, A. (2011). Creation and nature of optical centres in diamond for single-photon emission—overview and critical remarks. *New Journal of Physics, 13*, 035024.

Pfaff, W., et al. Demonstration of entanglement-by-measurement of solid-state qubits. *Nature Physics*, *9*, 29–33.

Pham, L. M., et al. (2011). Magnetic field imaging with nitrogen-vacancy ensembles. *New Journal of Physics, 13*.

Prawer, S., & Kalish, R. (1995). Ion-beam induced transformation of diamond. *Physical Review B, 51*, 15711–15722.

Private communication with Dr Castelletto, S.

Private communication with Dr Neu, E.

Rabeau, J. R., Chin, Y. L., Prawer, S., Jelezko, F., Gaebel, T., & Wrachtrup, J. (2005). Fabrication of single nickel-nitrogen defects in diamond by chemical vapor deposition. *Applied Physics Letters, 86*, 131926.

Rabeau, J. R., Huntington, S. T., Greentree, A. D., & Prawer, S. (2005). Diamond chemical-vapor deposition on optical fibers for fluorescence waveguiding. *Applied Physics Letters, 86*, 134104.

Riedrich-Moller, J., et al. (2012). One- and two-dimensional photonic crystal microcavities in single crystal diamond. *Nature Nanotechnology, 7*, 69–74.

Robledo, L., Bernien, H., van Weperen, I., & Hanson, R. (2010). Control and coherence of the optical transition of single nitrogen vacancy centers in diamond. *Physical Review Letters, 105*.

Robledo, L., Childress, L., Bernien, H., Hensen, B., Alkemade, P. F. A., & Hanson, R. (2013). High-fidelity projective read-out of a solid-state spin quantum register. *Nature, 477*, 574–578.

Rogers, L. J., Armstrong, S., Sellars, M. J., & Manson, N. B. (2008). Infrared emission of the NV centre in diamond: Zeeman and uniaxial stress studies. *New Journal of Physics, 10*, 103024.

Rondin, L., et al. (2010). Surface-induced charge state conversion of nitrogen-vacancy defects in nanodiamonds. *Physical Review B, 82*.

Rondin, L., et al. (2012). Nanoscale magnetic field mapping with a single spin scanning probe magnetometer. *Applied Physics Letters, 100*.

Santori, C., Barclay, P. E., Fu, K. M. C., Beausoleil, R. G., Spillane, S., & Fisch, M. (2010). Nanophotonics for quantum optics using nitrogen-vacancy centers in diamond. *Nanotechnology, 21*, 274008.

Santori, C., et al. (2006). Coherent population trapping of single spins in diamond under optical excitation. *Physical Review Letters, 97*.

Schietinger, S., Schroder, T., & Benson, O. (2008). One-by-one coupling of single defect centers in nanodiamonds to high-Q modes of an optical microresonator. *Nano Letters, 8*, 3911–3915.

Schröder, T., Engel, P., Schmidt, E., & Benson, O. (2012). Integrated and compact fiber-coupled single-photon system based on nitrogen-vacancy centers and gradient-index lenses. *Optics Letters, 37*, 2901–2903.

Simpson, D. A., et al. (2009). A highly efficient two level diamond based single photon source. *Applied Physics Letters, 94*, 203107.

Sipahigil, A., et al. (2012). Quantum interference of single photons from remote nitrogen-vacancy centers in diamond. *Physical Review Letters, 108*.

Siyushev, P., et al. (2010). Monolithic diamond optics for single photon detection. *Applied Physics Letters, 97*, 241902.

Smith, J. M., Grazioso, F., Patton, B. R., Dolan, P. R., Markham, M. L., & Twitchen, D. J. (2011). Optical properties of a single-colour centre in diamond with a green zero-phonon line. *New Journal of Physics, 13*.

Smith, W. V., Sorokin, P. P., Gelles, I. L., & Lasher, G. J. (1959). Electron-spin resonance of nitrogen donors in diamond. *Physical Review, 115*, 1546–1552.

Stacey, A., et al. (2012). Near-surface spectrally stable nitrogen vacancy centres engineered in single crystal diamond. *Advanced Materials, 24*, 3333–3338.

Steinmetz, D., Neu, E., Meijer, J., Bolse, W., & Becher, C. (2010). Single photon emitters based on Ni/Si related defects in single crystalline diamond. *Applied Physics B: Lasers and Optics*.

Tamarat, P., et al. (2006). Stark shift control of single optical centers in diamond. *Physical Review Letters, 97*, 083002.

Tamarat, P., et al. (2008). Spin-flip and spin-conserving optical transitions of the nitrogen-vacancy centre in diamond. *New Journal of Physics, 10*, 045004.

Taylor, J. M., et al. (2008). High-sensitivity diamond magnetometer with nanoscale resolution. *Nature Physics, 4*, 810–816.

Tetienne, J. P., et al. (2012). Magnetic-field-dependent photodynamics of single NV defects in diamond: an application to qualitative all-optical magnetic imaging. *New Journal of Physics, 14*.

Tisler, J., et al. (2009). Fluorescence and spin properties of defects in single digit nanodiamonds. *ACS Nano, 3*, 1959–1965.

Vahala, K. J. (2003). Optical microcavities. *Nature, 424*, 839–846.

Van der Sar, T., et al. (2009). Nanopositioning of a diamond nanocrystal containing a single nitrogen-vacancy defect center. *Applied Physics Letters, 94*, 173104.

van der Sar, T., et al. (2012). Decoherence-protected quantum gates for a hybrid solid-state spin register. *Nature, 484*, 82–86.

Wang, C. F., Choi, Y. S., Lee, J. C., Hu, E. L., Yang, J., & Butler, J. E. (2007). Observation of whispering gallery modes in nanocrystalline diamond microdisks. *Applied Physics Letters, 90*.

Wang, C. F., et al. (2007). Fabrication and characterization of two-dimensional photonic crystal microcavities in nanocrystalline diamond. *Applied Physics Letters, 91*, 201112.

Wang, C. L., Kurtsiefer, C., Weinfurter, H., & Burchard, B. (2006). Single photon emission from SiV centres in diamond produced by ion implantation. *Journal of Physics B: Atomic Molecular and Optical Physics, 39*, 37–41.

Wolfer, M., Kriele, A., Williams, O. A., Obloh, H., Leancu, C. C., & Nebel, C. E. (2009). Nickel doping of nitrogen enriched CVD-diamond for the production of single photon emitters. *Physica Status Solidi (A) Applied Research, 206*, 2012–2015.

Wolters, J., et al. (2010). Enhancement of the zero phonon line emission from a single nitrogen vacancy center in a nanodiamond via coupling to a photonic crystal cavity. *Applied Physics Letters, 97*, 141108.

Wu, E., et al. (2007). Room temperature triggered single-photon source in the near infrared. *New Journal of Physics, 9*, 434.

Wu, E., Jacques, V., Treussart, F., Zeng, H., Grangier, P., & Roch, J. F. (2006). Single-photon emission in the near infrared from diamond colour centre. *Journal of Luminescence, 119*, 19–23.

Yablonovitch, E. (1987). Inhibited spontaneous emission in solid-state physics and electronics. *Physical Review Letters, 58*, 2059–2062.

Zaitsev, A. M. (1998). *Optical properties of a diamond*.

Zhao, N., et al. (2012). Sensing single remote nuclear spins. *Nature Nanotechnology, 7*, 657–662.

3.19 Electrochemical Application of Diamond Electrodes

Yasuaki Einaga, Department of Chemistry, Keio University, Yokohama, Japan

3.19.1 Introduction

Conductive boron-doped diamond (BDD) is an alternative to traditional carbon electrodes that provide superior chemical and dimensional stability, low background currents, and a very wide potential window of water stability. Recently, electrochemical applications using BDD electrodes are attracting attention not only in electrochemistry, but also in fields such as functional materials science, analytical chemistry, environmental science, biomedical or biological science to name a few. In fact, wastewater treatment systems and ozone generation systems using BDD electrodes have already become commercially available, and the number of publications involving BDD electrochemistry research is drastically increasing year by year. Several review articles and books on diamond electrodes have been published (Alfaro, Ferro, Martínez-Huitle, & Vong, 2006; Brillas & Martinez-Huitle, 2011; Chailapakul, Siangproh, & Tryk, 2006; Compton, Foord, & Marken, 2003; Fujishima, Einaga, Rao, & Tryk, 2005; Kraft, 2007; McCreery, 2008; Luong, Male, & Glennon, 2009; Panizza & Cerisola, 2005; Swain, Anderson, & Angus, 1998; Xu et al., 1997). This chapter covers a brief overview of the current development on BDD electrochemistry such as water treatment, ozone generation, electrochemical organic synthesis, and features especially on electrochemical analysis applications.

3.19.2 Preparation of BDD Electrodes

Normally, BDD electrodes are deposited on conducting substrates by chemical vapor deposition (CVD) system. The deposition by CVD can be achieved by hot filaments or by microwave plasma (Fryda et al., 2003; Schäfer, Höfer, & Kröger, 2006; Yano, Tryk, Hashimoto, & Fujishima, 1998). For example, BDD electrodes have been deposited on Si wafers (flat electrodes) or on tungsten wires (microelectrodes) in a microwave plasma-assisted CVD system. The vapor of liquid mixtures of acetone and trimethoxyborane ($B(OCH_3)_3$) as the source gases was introduced into the reactor by bubbling with hydrogen gas. The liquid mixtures were prepared with appropriate mixing ratios based on Raoult's law so that the boron/carbon (B/C) ratios in the reactor were controlled. Typical grain size of the resulting BDD thin films was up to ~ 5 μm, with a thickness of ~ 20 μm for a deposition time of 7 h using 5 kW of plasma power (**Figure 1**).

http://dx.doi.org/10.1016/B978-0-08-096527-7.00056-8

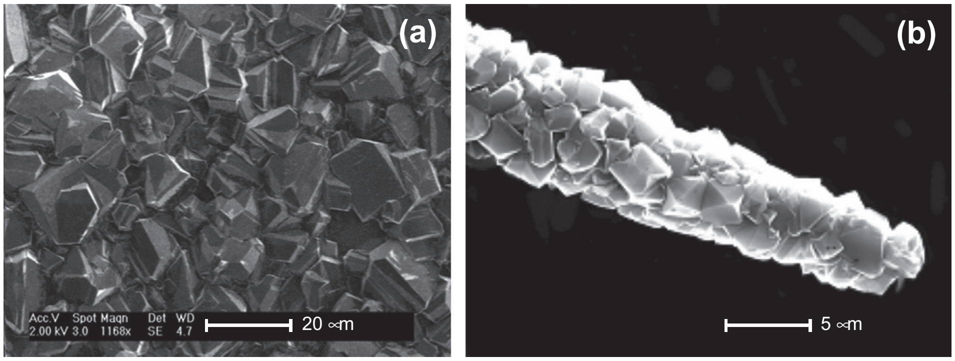

Figure 1 SEM image of BDD electrodes: (a) macroelectrode (flat) and (b) microelectrode.

3.19.3 Electrochemical Properties of BDD as Electrode Materials

BDD electrodes have an extremely wide potential window of water stability, low background currents (Figure 2), chemical and mechanical stability, resistance to fouling, lack of a surface oxide film, and controllable surface termination. These characteristics have led to the application of BDD electrodes in electrochemical sensing, in electroanalysis, in electrochemical synthesis, and for the anodic destruction of organic wastes. BDD also can be used as a transparent, conducting medium for analytical chemistry and photoelectrochemical applications.

3.19.4 Applications

3.19.4.1 Water Treatment

One of the early applications of BDD electrodes was the water treatment by anodic destruction of organic compounds. Advanced oxidation processes (AOPs) or advanced oxidation technologies can be defined (Comninellis et al., 2008) as aqueous phase oxidation methods based on the intermediacy of highly reactive species such as hydroxyl radicals in the mechanisms leading to the destruction of the target pollutant. It is believed that BDD electrodes generate not only oxygen (O_2) but also strong oxidants such as hydroxyl radicals (OH•), ozone (O_3), and hydrogen peroxide (H_2O_2) (Farrell, Martin, Martin, O’Grady, & Natishan, 2005; Marselli, Garcia-Gomez, Michaud, Rodrigo, & Comninellis, 2003; Michaud et al., 2003). Especially, hydroxyl radicals are stronger oxidants (2.80 V) than ozone (2.08 V) and hypochlorite ion (ClO^-) (1.49 V). Therefore, the electrochemical production of hydroxyl radicals is an alternative AOP, which is called electrochemical advanced oxidation process (EAOP) (Tröster et al., 2002; Tröster, Schäfer, Fryda, Matthée, 2004). The EAOPs can be possible to mineralize organic compounds in water to CO_2 and H_2O.

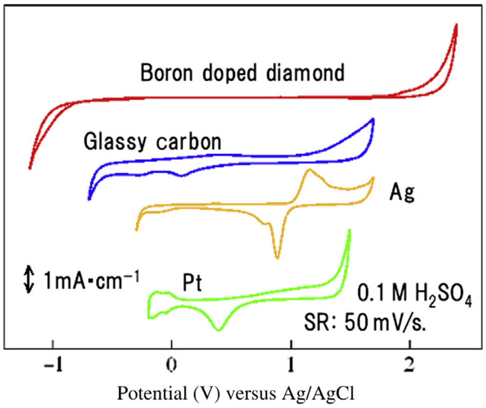

Figure 2 Electrochemical properties of various electrodes.

From 1999, extensive series of papers on basic discussion including proposed reaction mechanisms and generated species were published (Alfaro et al., 2006; Martinez-Huitle & Brillas, 2008; Kapalka, Foti, & Comninellis, 2007; Kapalka, Foti, & Comninellis, 2008a, 2008b; Kapalka, Lanova, Baltruschat, Foti, & Comninellis, 2008; Kapalka, Lanova, Baltruschat, Foti, & Comninellis, 2009; Panizza, Kapalka, & Comninellis, 2008; Suffredini, Machado, & Avaca, 2004; Tissot et al., 2012; Kapalka, Foti, & Comninellis, 2009). Recently, many other groups reported anodic oxidation of organic compounds such as 1, 4-dioxane (Choi, Lee, Shin, & Yang, 2010), sinapinic acid (Elaoud, Panizza, Cerisola, & Mhiri, 2011), atenolol (Murugananthan, Latha, Raju, & Yoshihara, 2011), textile dyehouse effluents (Tsantaki, Velegraki, Katsaounis, & Mantzavinos, 2012), bisphenol A (Pereira, Rocha-Filho, Bocchi, & Biaggio, 2012), tetracycline (Brinzila, Pacheco, Ciriaco, Ciobanu, & Lopes, 2012), dye (Costa, Montilla, Morallón, & Olivi, 2009; Hmani, Samet, & Abdelhedi, 2012; Panizza, Barbucci, Ricotti, & Cerisola, 2007), and others (Comninellis & Nerini, 1995; Martínez-Huitle, Ferro, & De Battisti, 2005; Sirés et al., 2006; Yoshihara & Murugananthan, 2009; Zhang, Fu, & Gu, 2009) by BDD electrodes, and theoretical modeling of the oxidation was also discussed (Scialdone, Galia, & Randazzo, 2012).

3.19.4.2 Ozone Generation

Ozone dissolved in water can be also powerful chemicals for water treatment. Moreover, ozone water is very friendly not only to environment but also to organism and living body because the residual spontaneously decomposes to oxygen, rendering post washing unnecessary. Therefore, ozone water is used for hand washing and some medical treatment for disinfection in hospitals. Here, BDD electrodes are well suited for the ozone production due to the high-oxygen overvoltage in aqueous electrolytes (Franco, Jardim, Boodts, & Silva, 2008).

In 1982, anodic ozone evolution was characterized for several different anode materials (except BDD) and electrolyte combinations (Foller & Tobias, 1982). Ozone generation by BDD anodes were reported in 1998 (Katsuki et al., 1998), then, several reports on ozone production including discussion on the mechanisms were shown (Silva, Santana, & Boodts, 2003). Recently, improved systems for ozone generation by preparing modified (freestanding perforated and vertically aligned whiskers) BDD electrodes (Arihara, Terashima, & Fujishima, 2007; Terashima et al., 2011) were reported. Furthermore, ozone sensor is also developed (Ochiai, Arihara, Terashima, & Fujishima, 2006).

3.19.4.3 Organic Synthesis

In the field of organic synthesis including drug developments, electrochemical organic synthesis has some advantages as environmental friendly methods because chemicals-free oxidation can be possible. For the electrochemical organic synthesis, carbon electrodes are used because they are the most cost-effective ones. However, in the last years, BDD electrodes for electrochemical organic synthesis are attracting increasing attention due to their mechanical, thermal and chemical stability.

From 2004, Comninellis et al. reported a methoxylation of *p*-tert-butyltoluenes by BDD electrodes and showed several other examples (Zollinger, Griesbach, Putter, & Comninellis, 2004a, 2004b). From 2006, Waldvogel et al. showed several advantages of BDD electrodes compared to that of other carbon electrode materials. For example, highly chemoselective anodic *ortho*-coupling reaction of 2,4-dimethylphenol (Kirste et al., 2009; Malkowsky, Griesbach, Putter, & Waldvogel, 2006) and phenol-arene cross-coupling reaction of 4-methyulguaiacol (Kirste, Elsler, Schnakenburg, & Waldvogel, 2012; Kirste, Schnakenburg, Stecker, Fischer, & Waldvogel, 2010). Furthermore, we have confirmed the methoxy radical formation as oxidation mediator by X-ray photoelectron spectroscopy (XPS) and synthesized licarin A (Sumi et al., 2012), and review article is also published (Waldvogel & Elsler, 2012).

3.19.4.4 Electrochemical Analysis and Sensors

As mentioned in the introduction section, BDD electrodes have much superior electrochemical properties. The wide potential window between oxygen and hydrogen evolution in aqueous electrolytes offers a large potential range for electroanalytical measurements, and low background current (low charging current) can realize high sensitivity due to the high signal-to-background ratios (Xu et al., 1997). Surface inertness of diamond has also shown advantages due to the absence of the formation and reduction of surface oxides, etc. Based on the properties, many examples for electrochemical analysis have been reported (Einaga et al., 2004; Lawrence et al., 2006; Einaga, 2010; Granger, Xu, Strojek, & Swain, 1999; Jolley, Koppang, Jackson, & Swain, 1997; Strojek, Granger, Swain, Dallas, & Holtz, 1996) especially for environmental analysis (Banks, Hyde, Tomčõk, Jacobs, & Compton, 2004; Chatterjee et al., 2002; Fierro, Comninellis, & Einaga, 2013; Fierro, Watanabe, Akai, & Einaga, 2012; Fierro, Watanabe, Akai, Yamanuki, & Einaga, 2011a, 2011b; Ivandini et al., 2010; Ivandini, Saepudin, Wardah, Dewangga, & Y. Einaga, 2012; Ivandini, Sato, Makide, Fujishima, & Einaga, 2006; Koppang, Witek, Blau, & Swain, 1999; Langeloth, Chiku, & Einaga, 2010; Lee, Einaga, Fujishima, & Park, 2004; Manivannan, Seehra, & Fujishima, 2004; Murata et al., 2008; Nagaoka et al., 2010; Prado, Wilkins, Gründler, Marken, & Compton, 2003; Prado, Wilkins, Marken, & Compton, 2002; Rao, Loo, Sarada, Terashima, & Fujishima, 2002; Saterlay, Foord, & Compton, 1999; Seehraa, Ranganathana, & Manivannan, 2008; Song & Swain, 2007; Sugitani, Watanabe, Ivandini, Iguchi, & Einaga, 2013; Wei, Zhou, et al., 2008; Yamada, Ivandini, Komatsu, Fujishima, & Einaga, 2008) and bio-related analysis (Adams, Puchades, & Ewing, 2008; Batchelor-McAuley, Banks, Simm, Jones, & Compton, 2006; Boonsong, Chuanuwatanakul, Wangfuengkanagul, & Chailapakul, 2005; Chatterjee & Foord, 2009; Chiku et al., 2008; Chiku, Horisawa, Doi, Yanagawa, & Einaga, 2010; Chiku, Nakamura, Fujishima, & Einaga, 2008; Chiku, Watanabe, & Einaga, 2010; Fierro et al., 2012; Fierro, Mitani, Comninellis, & Einaga, 2011; França, Oliveira, Pedrosa, & Codognoto, 2012; Fujishima et al., 1999; Gopalan, Lee, & Komathi, 2010; Halpern et al., 2006; Hason, Pivonkova, Vetterl, & Fojta, 2008; Hoffman et al., 2012; Ivandini, Honda, Rao, Fujishima, & Einaga, 2007; Ivandini, Naono, Nakajima, & Einaga, 2005; Ivandini, Rao, Fujishima, & Einaga, 2006; Ivandini, Sato, Makide, Fujishima, & Einaga, 2004a, 2004b, 2005; Janegitz, Medeiros, Rocha-Filho, & Fatibello-Filho, 2012; Karuwan et al., 2006; Kato et al., 2011; Kato, Fierro, Watanabe, Yoshimi, & Einaga, 2012; Kondo et al., 2008; Lima-Neto et al., 2009; McEvoy & Foord, 2005; Medeiros, Carvalho, Rocha-Filho, & Fatibello-Filho, 2007, 2008; Mitani & Einaga, 2009; Musilová, Barek, & Pecková, 2011; Paleček & Bartošík, 2012; Prado et al., 2002; Preechaworapun et al., 2006, 2008; Racaud, Groenen-Serrano, & Savall, 2010; Sarada, Rao, Tryk, & Fujishima, 2000; Singh, Sawarynski, Dabiri, Choi, & Andrews, 2011; Spătaru, Sarada, Popa, Tryk, & Fujishima, 2001; Suryanarayanan, Zhang, Yoshihara, & Shirakashi, 2005; Suzuki, Ivandini, Kamiya, et al., 2007; Suzuki, Ivandini, Yoshimi, et al., 2007; Treetepvijit et al., 2006; Treetepvijit, Chuanuwatanakul, Einaga, Sato, & Chailapakul, 2005; Trouillon, Passarelli, Wang, Kurczy, & Ewing, 2013; Wangfuengkanagul & Chailapakul, 2002; Watanabe & Einaga, 2009; Watanabe, Ivandini, Makide, Fujishima, & Einaga, 2006; Wei, Sun, et al., 2008; Xie, Shafer, Wilson, & Martin, 2006; Xu & Swain, 1998; Yang, Hoffmann, Smirnov, Kriele, & Nebel, 2010; Yoshimi et al., 2011; Zhao, Qi, & Tian, 2006; Zhou & Zhi, 2006; Zhou, Zhi, Zou, Zhang, & Lee, 2008).

3.19.4.4.1 For Environmental Monitoring

3.19.4.4.1.1 Free Chlorine (Murata et al., 2008)

Chlorine is a strong oxidizing agent and is the conventional chemical used for the continuous disinfection of drinking water, water in swimming pools and wastewater. The exact determination and continuous on-line monitoring of residual water disinfectant is a necessary requirement.

The general detection methods for free chlorine include the colorimetric method, the amperometric titration method, and the iodometry. However, these methods are unsuitable for continuous on-line monitoring because they each have a number of disadvantages, such as the requirement for many types of reagents that may produce greater toxicity, a high detection limit, the difficulty of operation, and so on.

Electroanalytical methods require fewer reagents, promote easy handling and can provide high sensitivity as well as long-term response stability. Reduction of HClO and ClO^- has mainly been reported for the electrochemical determination of free chlorine. However, there are some problems which should be considered when using this method, such as inefficiency due to a similar reduction potential to the dissolved oxygen, metal deposition from the sample solution at the electrode, and the effect of trace metal ions. On the other hand, there have been a few investigations on quantitative determination based on the anodic reaction of free chlorine, which should be superior because it is not subjected to the above problems.

In this chapter, the quantitative determination and the possibility of continuous on-line monitoring of free-chlorine oxidation using BDD electrodes are highlighted. Cyclic voltammograms for various concentrations of NaClO in a 0.1 M $NaClO_4$ obtained using an as-deposited BDD electrode were shown in **Figure 3**. A well-defined irreversible oxidation peak was observed at a potential of ~1.3 V (versus Ag/AgCl). This is the typical advantage of wide potential window because the observation of oxidation current at such high potential (1.3 V) is impossible in the case of other conventional electrodes due to the narrow potential window. The inset in **Figure 3** shows a plot of the oxidation peak current versus the free-chlorine concentration. A linear calibration curve obtained in the concentration range of 20–100 mg Cl l^{-1}, indicating that determination of free chlorine can be performed at ad-BDD electrodes. A slope of 0.744 μA cm^{-2} mg^{-1} l shows the sensitivity. This sensitivity

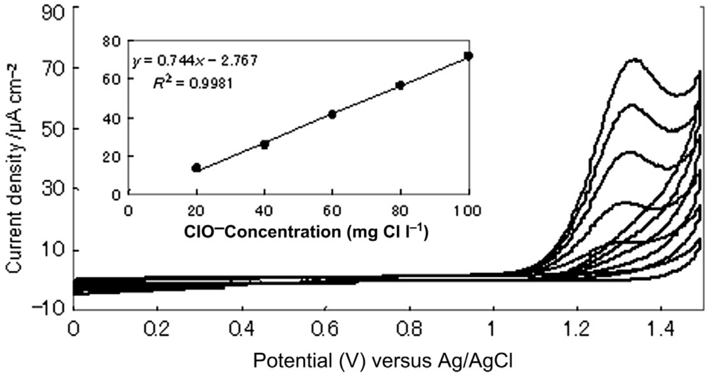

Figure 3 Cyclic voltammograms of a 0.1 M $NaClO_4$ solution in the presence of various concentrations of free chlorine (2–100 mg Cl l^{-1}) at as-deposited BDD electrodes. Linear calibration plots are shown in the inset.

was 3–4 times higher in comparison with those at conventional electrodes, suggesting the superiority of using ad-BDD for chlorine oxidation. It is known that BDD electrodes have a small background current due to the inert surface of BDD. The small background current can give rise to a very low detection limit due to the decrease in the noise. Furthermore, excellent stability was also shown for repetitive voltammograms.

3.19.4.4.1.2 Heavy Metals

3.19.4.4.1.2.1 Arsenic (III) Detection by Ir-Implanted BDD (Ivandini, Sato, et al., 2006)

Many arsenic compounds are known to be toxic. Their direct exposure to especially humans and animals and the side effect to the ecosystem remain international problems. Arsenic exists in many different chemical forms in nature; particularly, in groundwater, they are found almost exclusively as arsenite (AsO_2^-, As^{3+}) and arsenate ($HAsO_4^{2-}$, As^{5+}). Arsenite can be converted to arsenate under oxidizing conditions. However, the conversion in either direction is difficult. The reduced species can be found in both oxidized environments and vice versa. Typical targets of arsenic toxicity are the respiratory system, the circulatory system, and the reproductive system.

However, arsenic compounds could not be detected directly by BDD because BDD does not have electrochemical catalytic activities due to the surface inertness. On the other hand, metal electrodes such as Ir have electrochemical catalytic properties even though the sensitivities are not good due to the large background currents.

Modification of BDD electrodes with redox active particle/compounds offers significant advantages in the design and development of electrochemical sensors. Although electrochemical deposition is a convenient method to prepare metal deposits on substrate, it is not suitable for metal deposition at BDD because the nonuniform doping of boron in diamond crystals causes surface conductivity to be inhomogeneous. Furthermore, the stability of the deposited metal is not good.

Since its inception, ion implantation has been considered as the most feasible method to change the electrical properties of a diamond substrate. The method modifies the near-surface structure of a target by heavy ions bombardment. Here, BDD electrodes modified with implanted iridium ions were investigated for arsenic (III) detection by using cyclic voltammetry (CV) and flow injection analysis (FIA). BDD electrodes were implanted with 800 keV Ir^+ by using iridium metal powder as the targets.

CV (**Figure 4**) and FIA with amperometric detection were used to study the electrochemical reaction. The electrodes exhibited high catalytic activity toward As (III) oxidation with the detection limit ($S/N = 3$), sensitivity, and linearity are 20 nM (1.5 ppb), 93 nA μM^{-1} cm^{-2}, and 0.999, respectively. The precision for 10 replicate determinations of 50 μM As (III) was 4.56% of relative standard deviation. The advantage properties of the electrodes were their inherent stability with a very low background current. The electrode was applicable for analysis of spiked arsenic in tap water containing a significant amount of various ion elements. These results indicate that metal-implanted method could be a promising method for controlling the electrochemical properties of diamond electrodes.

3.19.4.4.1.2.2 Selective Detection of Arsenic (As^{3+}, As^{5+}) by Stripping Voltammetry (Yamada et al., 2008)

Electrochemical detection of mixture solutions of As^{3+} and As^{5+} has been investigated by stripping voltammetry at gold-modified diamond electrodes. The method was performed based on stripping oxidation of

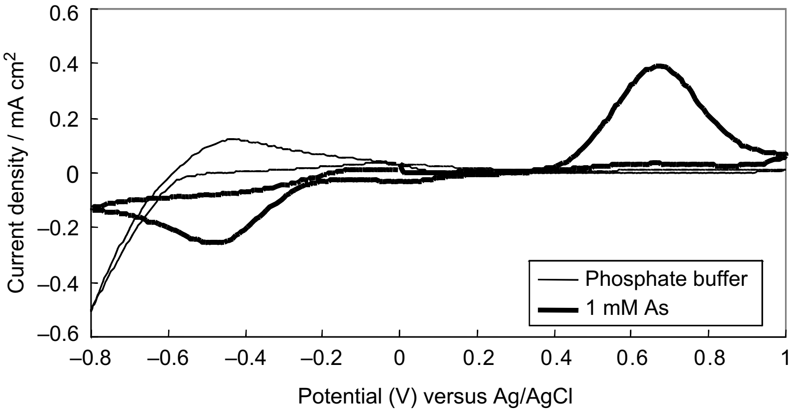

Figure 4 Cyclic voltammograms of 0.1 M phosphate buffer solution in the absence and presence of 1 mM As(III) at Ir-implanted diamond electrodes.

As^0 deposited at the electrode surface. Whereas As^{3+} can be deposited by simple electrochemical reduction of As^{3+} to As^0 at -0.4 V (versus Ag/AgCl), much higher potential is required to overcome the activation energy of As^{5+} reduction. However, in such high potential, hydrogen evolution also occurs. Consequently, one more step should be added to release the hydrogen gas adsorbed at the electrode surface during the reduction step. During the deposition of As^{5+}, As^{3+} species was also simultaneously deposited. Therefore, to differentiate As^{3+} and As^{5+} quantification in a mixture solution, both stripping voltammetry methods should be performed and calculated mathematically. Comparison of stripping voltammograms of both methods for As^{3+} solution in the absence of As^{5+} demonstrated similar peak shapes and current intensities, and confirmed that error calculation of As^{5+} concentration in the mixture solution with As^{3+} can be avoided. Good linear responses were observed for each standard solution of As^{3+} and As^{5+}. Linear calibration curve could also be achieved for a series concentrations of 100–1000 ppb As^{5+} in a mixture solution with 100 ppb As^{3+} ($r^2 = 0.99$) and for a series concentrations of 5–30 ppb As^{3+} in a mixture solution with 100 ppb As^{5+}. Detection limits of 5 and 100 ppb can be achieved for As^{3+} and As^{5+} in a mixture solution, respectively. The reproducibility was shown for stripping voltammetry of As^{3+} and As^{5+} with an Relative Standard Deviation (RSD) ($n = 8$) of 7.5% and 8.4%, respectively. Good stability of gold-modified diamond electrodes before and after arsenic detection was also evaluated by SEM image. Application of the method for real sample analysis was performed for arsenic detection in Yokohama tap water.

3.19.4.4.1.2.3 Other Species

Not only the above examples but also some other heavy metals and other important species have been investigated by our group (**Table 1**).

3.19.4.4.1.3 Prototype of BDD Electrochemical Sensor for Heavy Metals (by Collaboration with HORIBA Ltd)

In 2010, the future potential of diamond electrochemical sensors was greatly enhanced with the development of the first prototype of sensitive heavy metal sensors using diamond electrodes (**Figure 5**) by HORIBA Ltd (Kyoto, Japan).

3.19.4.4.2 For Medical or Biosensors

3.19.4.4.2.1 Oxalic Acid (Ivandini, Rao, et al., 2006)

Oxalic acid, naturally occurs in many plants (spinach, ginger, chocolate, etc.), combines with Ca, Fe, Na, Mg or K to form less soluble salts known as oxalates. High levels in diets lead to irritation of the digestive system, and particularly of the stomach and kidneys. It is also known to contribute the formation of kidney stones. The urinary level of oxalic acid has long been recognized as an important indicator for the diagnosis of renal stone formation.

CV and FIA with amperometric detection were used to study the electrochemical reaction. In this case, the oxidation current was observed at $\sim$1.35 V (versus Ag/AgCl) (high potential), which could not be observed by conventional electrodes. A good linear response was observed for a concentration range from 50 nM to 10 μM with the estimated detection limit of $\sim$0.5 nM (S/N = 3).

Table 1 Electrochemical sensor application using BDD reported by Einaga's group (for environment)

Heavy metals			
As^{3+}, As^{5+}	Oxidation	Ir-implanted BDD	(Ivandini et al., 2006)
	Stripping voltammetry	Gold-modified BDD	(Yamada et al., 2008)
	Stripping voltammetry	BDD (addition of gold ions)	(Nagaoka et al., 2010)
Zn^{2+}	Stripping voltammetry		(Langeloth et al., 2010)
Se^{4+}	Stripping voltammetry	Gold-modified BDD	(Fierro et al., 2011a)
Cd^{2+}	Stripping voltammetry		(Fierro et al., 2011b)
	Stripping voltammetry	Four-electrode system (selective detection)	(Sugitani et al., 2013)
Cr^{6+}	Stripping voltammetry		(Fierro et al., 2012a)
Others			
Free chlorine	Oxidation	BDD	(Murata et al., 2008)
BOD	Reduction	Gold-modified BDD	(Ivandini et al., 2012)
I^-, I_2	Oxidation	BDD	(Fierro, Comninellis, & Einaga, 2013)
AsH_3	Oxidation	BDD	(Ivandini et al., 2010)
Acid	Oxidation	BDD	(Mitani & Einaga, 2009)
pH	Reduction	BDD	(Fierro et al., 2011c)

3.19.4.4.2.2 Selective Detection of Glucose by Cu-Implanted BDD (Watanabe et al., 2006)

Highly sensitive and simple glucose detection is very desirable for the diagnosis and management of diabetes mellitus. However, glucose is normally undetectable using bare BDD electrodes, the same as the above example of arsenic detection. The glucose oxidation is a complex process that requires a catalytic reaction using an enzyme or active metal surfaces. Although Au, Pt, Ni and Cu metal electrodes are known for showing electrocatalysis for the glucose oxidation, BDD electrode does not have the catalytic properties. Electrochemical detection of glucose using Cu-modified BDD electrode (Cu-BDD) has been investigated. A simple method of selective glucose detection using the Cu-BDD is presented.

Not only the detection of glucose using Cu-implanted BDD electrodes but also selectivity was derived from the differences in the diffusion processes for interfering species such as ascorbic acid (AA) and uric acid (UA) (linear diffusion on BDD) and for glucose (spherical diffusion on implanted copper). Each dispersed copper particle of the Cu-BDD act as an ultra microelectrode because glucose react only at copper surface but not BDD

Figure 5 Prototype of electrochemical sensor for heavy metals using diamond electrodes (Horiba Ltd).

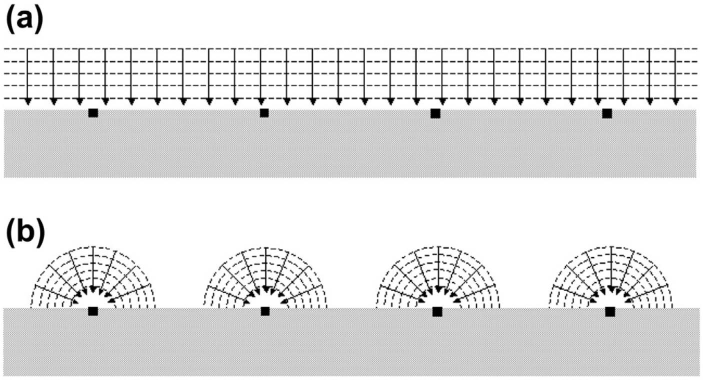

Figure 6 Illustration of the diffusion profiles at Cu-implanted diamond electrodes for (a) ascorbic acid and uric acid and (b) glucose.

surface (Figure 6). On the other hand, interfering substances react at both of the two electrodes. Eventually, the difference of diffusion leads to dependence or independence of the Faradic current on time, and a steady-state component of the current reflects only glucose concentration. That is, the time dependence of the observed current should be followed by the Eqns (1) and (2), respectively.

$$\text{Interfering species(linear diffusion)}: I = nFACD(1/\pi Dt) \tag{1}$$

$$\text{Glucose(spherical diffusion)}: I = nFACD(1/\pi Dt + 4/\pi r) \tag{2}$$

By using the differences of the diffusion profiles, electrochemical quantitative analyses of glucose at Cu-BDD electrodes were carried out by chronoamperometry at 0.6 V versus Ag/AgCl. The Cottrell plots of 6 mM glucose solution and a mixed solution containing 6 mM glucose and interfering species (0.5 mM AA and 0.5 mM UA) showed almost the same y-intercept values (data not shown). According to the above discussions, similar values for both intercepts reflect the concentration of glucose (6 mM) only. It implies that the simple and novel methodology using Cu-BDD is promise for selective glucose sensor.

3.19.4.4.2.3 Proteins

3.19.4.4.2.3.1 Detection of Protein (Including Cancer Markers) (Chiku et al., 2008)

The detection of proteins, including cancer markers, has been attracting increasing attention. The direct, unmediated electron transfer between proteins and electrodes has been investigated for many different combinations of proteins and electrode surfaces in recent years. These studies have received much attention because of the requirement in understanding the fundamental reactions of biomolecules, from the viewpoint of developing a direct detection method of the protein at the electrode, or in order to develop new materials by combinations between the protein and the electrode surface. In general, direct electrochemical oxidation of proteins is based on the electrooxidation of metal ions or electroactive amino acids in the protein structure. The proteins studied in this manner range from small, water-soluble redox proteins, to large, sometimes multiredox enzyme-centered proteins. However, it can be said that the cytochromes, the blue-copper proteins, and the iron–sulfur proteins are as familiar to electrochemical analysts as they are to biochemists. In contrast, the electrochemical detection of the larger non-metalated proteins (e.g. albumin) is reported much less frequently. The limited number of reports is due not only to the complexity of the protein structure but also to the strong adsorption of the proteins on the electrode surface, which can lead to signal depression, resulting in a lack of predictability and reproducibility.

On the other hand, other superior properties of BDD hydrogen-terminated diamond films are that they are well faceted, hydrophobic, and have a low surface energy. Therefore, it is expected that even proteins can be directly detected electrochemically using BDD because of the surface inertness.

Cyclic voltammogram of 300 mg dl^{-1} bovine serum albumin (BSA) in 0.1 M phosphate buffered saline pH 10 at the BDD electrode showed three peaks. It is known that BSA contains 20 types of amino acids, including cysteine, tryptophan and tyrosine, as well as 17 disulfide bonds which are known to be electroactive at BDD electrodes. In order to confirm the active sites of BSA at the BDD electrode, comparison was made between the CVs of BSA and several amino acids. The oxidation peaks can be observed separately at different potentials at pH 10. Thus, it is suggested that the oxidation peaks of BSA correspond to the oxidation peaks of cysteine, tyrosine and tryptophan.

Further, FIA was used to minimize the adsorbing effects of the protein and to obtain calibration curves. The peak current shows good linearity in the concentration range of 5–3000 mg dl^{-1} of BSA, with an experimental detection limit of 5 mg dl^{-1}. The stability of the current response is also shown for five injections of each concentration in the concentration range of 5–3000 mg dl^{-1}. Reproducibility was also confirmed. As an example of cancer maker detection, the possibility of using H-terminated BDD for the direct electrochemical detection of other proteins was also investigated for immunosuppressive acidic protein (IAP). The amperometric FIA responses of IAP showed the possibility of the direct electrochemical detection. A linear detection range of 200–800 μg ml^{-1} was observed. Since the normal human serum IAP level is ∼355 μg ml^{-1} ml, the detectable range should be suitable for cancer screening.

3.19.4.4.2.3.2 Detection of Conformational Change in Nonmetalloproteins (Chiku, Nakamura, et al., 2008)

Since direct electrochemical detection of protein was possible, a new electrochemical method for the detection of conformational changes in large, nonmetalloproteins such as BSA, using FIA coupled with hydrogen-terminated BDD electrodes has been established.

Protein folding/unfolding is the most fundamental and universal example of biological self-assembly. The sequences of natural proteins have emerged through evolutionary processes such that their unique native states can be found very efficiently even in the complex environment inside a living cell. However, under some conditions, proteins fail to fold correctly in living systems, and this failure can result in a wide range of diseases, known as *amyloidoses*, which includes Alzheimer's disease and Parkinson's disease. Plaques that contain misfolded peptides called amyloid beta are formed in the brain of Alzheimer's disease patients over many years. This protein fold is shared by other peptides such as prions associated with protein misfolding diseases. All known prions induce the formation of an amyloid fold, in which the protein polymerizes into an aggregate consisting of tightly packed beta sheets. Prions cause a number of diseases in a variety of mammals, including bovine spongiform encephalopathy (mad cow disease) in cattle and Creutzfeldt–Jakob disease in humans. Anyway, the detection of denaturation of proteins is very important. For the purpose, denaturation of proteins has been extensively investigated by a number of techniques including nuclear magnetic resonance, ultraviolet (UV) absorption, electron spin resonance, circular dichroism, birefringence and fluorescence spectroscopy.

The results of an investigation into the detection of conformational changes in a nonmetalloprotein (albumin) by direct electrochemical oxidation using BDD electrodes are discussed.

Urea-induced unfolding of BSA has been studied previously by monitoring the change of its intrinsic fluorescence. Here, to validate our new method, urea-induced denaturation of BSA was monitored by both fluorescence and FIA.

To make a better comparison between fluorescence and electrochemistry, the reciprocal of the oxidation current is used as an indicator for the state of protein unfolding and is plotted. **Figure 7** shows the changes of fluorescence intensities and reciprocals of oxidation currents by FIA using BDD electrodes at several oxidation potentials as a function of urea concentration. That is, direct electrochemical detection of conformation changes of proteins using BDD electrodes can be performed with advantages in terms of simplicity and sensitivity.

3.19.4.4.2.3.3 Detection of Protein Tyrosine Kinase Activity (Chiku, Horisawa, et al., 2010)

Recently, as a detection of protein function, protein tyrosine kinase (PTK) activity in human epidermoid carcinoma cells (A431) was also determined by employing a novel electrochemical method using BDD electrodes. A BDD electrode enables the electrochemical oxidation of tyrosine (Tyr), phosphorylated Tyr (Tyr-P) and sulfated Tyr (Tyr-S) in water-based solutions because of the wide potential window. More so, for the detection of kinase activity, poly (Glu–Tyr)-modified magnetic beads were used. Linear-sweep voltammograms for the electrochemical detection of PTK activity were carried out using BDD electrodes consisting of peptide-modified magnetic beads. Without phosphorylation of the peptide-modified magnetic beads using PTKs, we observed clear oxidation peaks for Tyr oxidation and no significant electrochemical responses for Tyr-P oxidation at 1.4 V for the background. On the other hand, with phosphorylation of the beads using PTK, the peak oxidation current at 1.4 V clearly increased, while the peak oxidation current for Tyr oxidation decreased. This indicates that PTKs activity could be successfully detected by using electrochemical methods employing BDD electrodes.

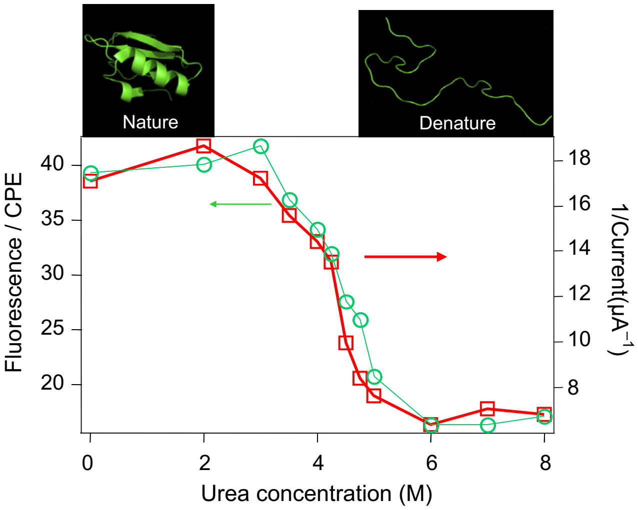

Figure 7 (○) Intrinsic fluorescence emission intensity of 50 μg/ml BSA in 0.1 M phosphate buffer solution (pH 7.4) as a function of urea concentration. Excitation wavelength: 280 nm. Emission wavelength: 290–500 nm. (□) Reciprocal of the oxidation current of 50 μg/ml BSA in 0.1 M phosphate buffer solution (pH 7.4) as a function of urea concentration. The current is corrected by FIA using BDD electrodes. Oxidation potential is 1300 mV versus Ag/AgCl. Flow rate is 1 ml/min.

This method was utilized for the in vitro kinase activity detection of human cell lysate, and the electrochemical measurements were compatible with the enzyme-linked immunosorbent assay based method. Our results indicate that the electrochemical method can be applied to real samples such as cell lysate.

3.19.4.4.2.4 Amperometric Immunosensor (Preechaworapun et al., 2008)

In order to realize the selectivity of the protein detection, surface modification can be useful. As one example, a poly-o-ABA-modified BDD was developed for a protein immunosensor. The amperometric sensing of mouse IgG (MIgG) was selected as the model at the poly-o-ABA-modified BDD to compare to the poly-o-ABA-modified glassy carbon (GC) at the same condition. An antimouse IgG from goat (GaMIgG) was covalently immobilized at a poly-o-ABA-modified BDD electrode, which used a sandwich-type alkaline phosphatase (ALP) catalyzing amperometric immunoassay with 2-phospho-L-ascorbic acid as a substrate. The ALP enzyme conjugated at the immunosensor can generate the electroactive AA, which can be determined by amperometric detection. The signal was found to be proportional to the quantity of MIgG. The limit of detection of 0.30 ng ml^{-1} (3SD) and 3.50 ng ml^{-1} (3SD) for MIgG at BDD and GC electrodes was obtained. It also was found that the dynamic range of three orders of magnitude (1–1000 ng ml^{-1}) was obtained at BDD, while at GC, the dynamic range was narrower (10–500 ng ml^{-1}). The method was applied to a real mouse serum sample that contained MIgG.

3.19.4.4.2.5 Dopamine (In Vivo Detection Using BDD Microelectrodes) (Suzuki, Ivandini, Yoshimi, et al., 2007)

BDD microelectrode has gotten much attention as an electrochemical sensor, especially in vivo sensor. By using this promising electrode, in vivo electrochemical detection of dopamine (DA) was investigated. DA is one of the neurotransmitters, and thought to act as a trigger of many vital activities. Therefore, in vivo DA monitoring is important. However, in case of carbon fiber which is a conventional in vivo sensor, it is a long-standing problem to separate from some interfering substances, particularly AA. To overcome this issue, BDD microelectrodes (Figure 1(b)) were used. Anodically oxidized BDD (ao-BDD) has a property to recognize DA and AA separately by investigating their specificity of oxidation potential. This useful property for in vivo analysis with microelectrode was used. Finally, good separation between DA and AA could be obtained not only in vitro but also in vivo. Moreover, some advantages over the conventional carbon fiber electrode were demonstrated. Therefore, it was concluded that BDD microelectrodes are really promising for future in vivo analysis.

Here, ao-BDD microelectrode was utilized for the in vivo measurements (Figure 8). BDD was put into striatum in mouse brain, and Medial Forebrain Bundle (MFB) stimulations were applied to induce DA release. Clear signals were recorded for each stimulation, and it indicated that in vivo monitoring of DA was successfully

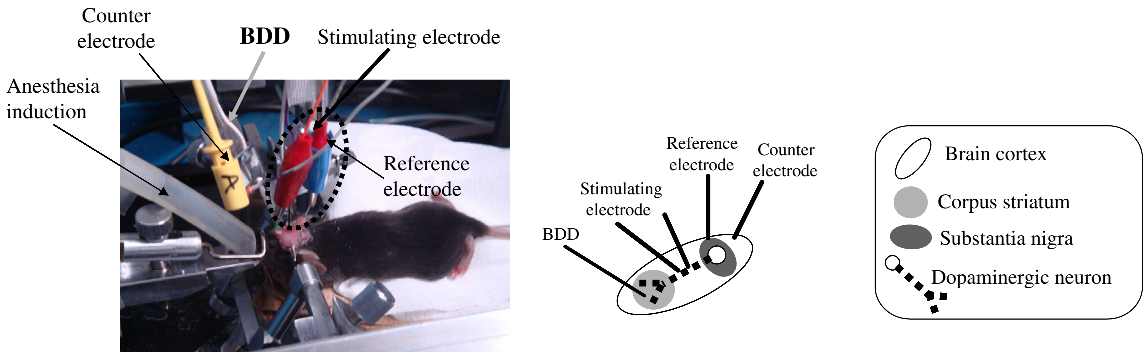

Figure 8 Photo image and schematic drawing of in vivo mouse brain experimental setup.

achieved at ao-BDD microelectrode. Moreover, correlation diagram for in vivo analysis showed very similar feature of that for in vitro DA. These results confirmed that these signals certainly came from DA oxidation.

3.19.4.4.2.5.1 Reward-Induced Burst Firing of Dopaminergic Neurons (Monkey Brain) (Yoshimi et al., 2011)

Reward-induced burst firing of dopaminergic neurons has mainly been studied in the primate midbrain. Voltammetry allows high-speed detection of DA release in the projection area. Although voltammetry has revealed presynaptic modulation of DA release in the striatum, to date, reward-induced release in awakened brains has been recorded only in rodents. To make such recordings, it is possible to use conventional carbon fibers in monkey brains but the use of these fibers is limited by their physical fragility. In this study, constant-potential amperometry was applied to novel diamond microelectrodes for high-speed detection of DA. In primate brains during Pavlovian cue-reward trials, a sharp response to a reward cue was detected in the caudate of Japanese monkeys. Overall, this method allows measurements of monoamine release in specific target areas of large brains, the findings from which will expand the knowledge of reward responses obtained by unit recordings (**Figure 9**).

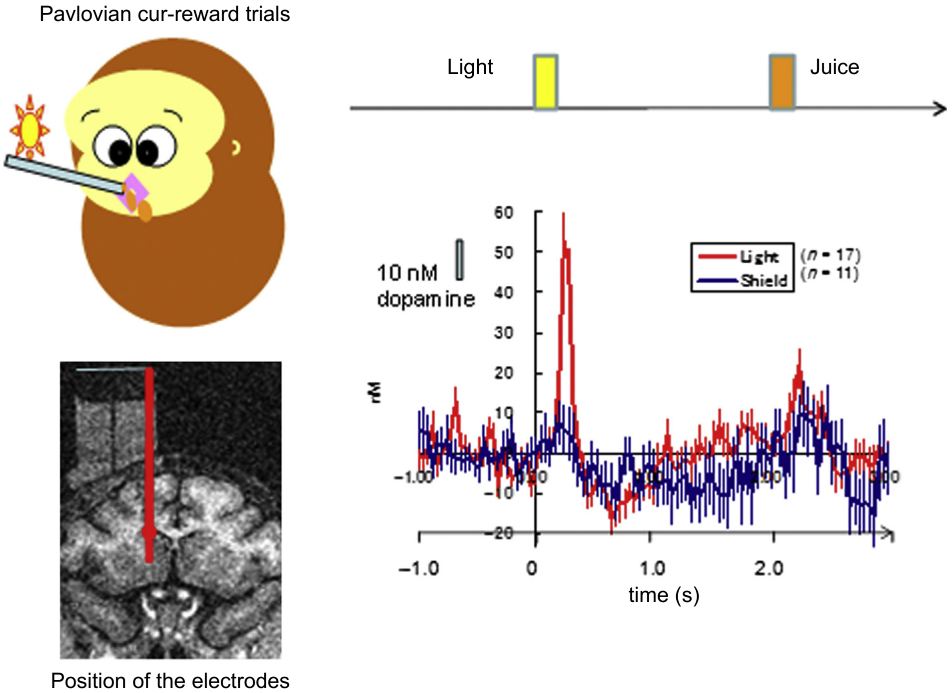

Figure 9 In vivo recording in the caudate of monkey during the behavioral tasks. Time 0 is aligned to the onset of the light cue, and the juice was delivered 2.0 s later. Light without juice (red line) and juice without light (blue line).

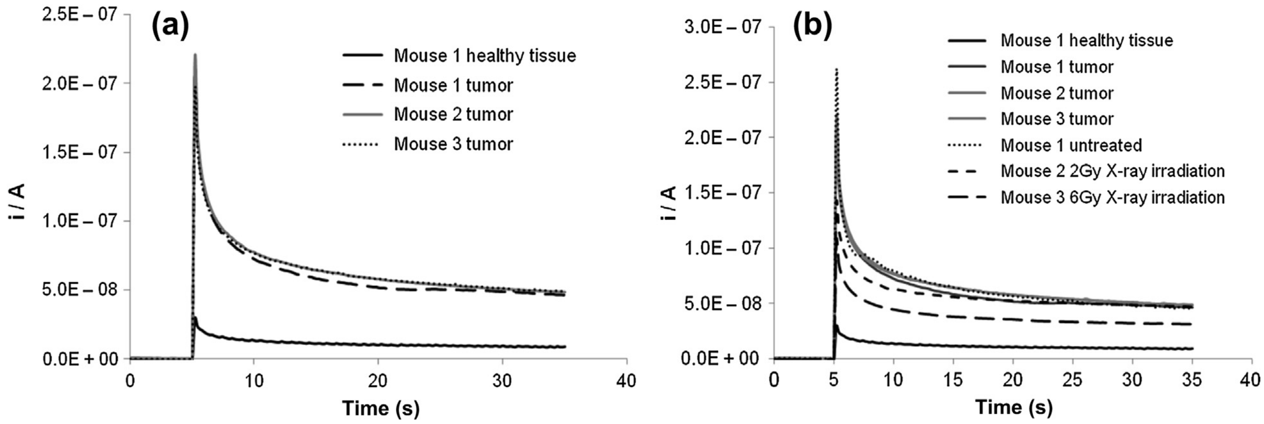

Figure 10 (a) Assessment of the biological features of HSC-2-derived xenograft tumor: difference between normal and tumorous tissue. (b) Assessment of the biological features of HSC-2-derived xenograft tumor before and after X-ray treatment.

3.19.4.4.2.6 Cancerous Tumors (In Vivo Assessment) (Fierro et al., 2012)

The in vitro and in vivo electrochemical detection of the reduced form of glutathione (L-γ-glutamyl-L-cysteinyl-glycine, GSH) using BDD microelectrode for potential application in the assessment of cancerous tumors is presented. Accurate calibration curve for the determination of GSH could be obtained by the in vitro electrochemical measurements. Additionally, it was shown that it was possible to separate the detection of GSH from the oxidized form of glutathione (GSSG) using chronoamperometry measurements.

So far, conventional methods are based on column derivatization followed by fluorimetric detection or on the conversion to their phenyl or pyridine derivatives followed by UV detection. Therefore, these methods require expensive equipment and time-consuming procedures in order to measure GSH concentration. Additionally, these techniques are not suited for in vivo GSH detection and thus require tissue samples obtained through biopsy, which is an invasive procedure for the patient.

Here, in vivo GSH detection measurements have been performed in human cancer cells inoculated in immunodeficient mice. These measurements have shown that the difference of GSH level between cancerous and normal tissues can be detected. Moreover, GSH detection measurements carried out before and after X-ray irradiation have proved that it is possible to assess in vivo the decrease in GSH concentration in the tumor after a specific treatment (**Figure 10**).

3.19.4.4.3 Trend in Other Groups

Reports on electrochemical sensor application of bio-related species by our group are summarized in **Table 2**. Many reports on the detection by BDD electrodes of these target compounds have been published. For example, these are selective assay for cysteine (Nekrassova, Lawrence, & Compton, 2004), lincomycin (Boonsong et al., 2005), blue-copper proteins (McEvoy & Foord, 2005), tryptophan and tyrosine (Zhao et al., 2006), aspartame

Table 2 Electrochemical sensor application using BDD reported by Einaga's group (for biomedical)

Glucose	Cu-implanted BDD	Selective detection	(Watanabe et al., 2006)
	Ni-modified BDD	Selective detection	(Watanabe & Einaga, 2009)
Oxalic acid	Gold-modified BDD		(Ivandini et al., 2006b)
Dopamine	BDD microelectrodes	in vivo (brain of mouse)	(Suzuki, Ivandini, Yoshimi, et al., 2007)
		in vivo (brain of monkey)	(Yoshimi et al., 2011)
Protein	BDD	BSA	(Chiku, Ivandini, et al., 2008)
		Structure change monitoring	(Chiku, Nakamura, et al., 2008)
		Kinase activity detection	(Chiku, Horisawa, et al., 2010)
Antigen	Antibody-modified BDD		(Preechaworapun et al., 2008)
Glutathione (GSH)	BDD microelectrodes	in vivo (healthy and cancerous tissues)	(Fierro, Yoshikawa, et al., 2012)

(Medeiros et al., 2007), cytochrome c (Yang et al., 2010; Zhou et al., 2008), aspartame and cyclamate (Medeiros et al., 2008), riboflavin (Chatterjee & Foord, 2009), nitrofurantoin (Lima-Neto et al., 2009), critical micellar concentration of surfactants (Racaud et al., 2010), nitrite ions (Gopalan et al., 2010), carbendazim and fenamiphos (França et al., 2012), tyrosinase and phenol (Janegitz et al., 2012).

As one of the application field of BDD with promising future, in vivo analysis (in living systems) especially using BDD microelectrodes are increasing attention.

Neurotransmitter is one of the important targets for the in vivo detection. The trends into these directions are summarized in by Patel (Brillas & Martinez-Huitle, 2011), and Trouillon reviewed the very recent trends by 2012 (Trouillon, 2012; Trouillon, Svensson, Berglund, Cans, & Ewing, 2012). For example, serotonin (5-HT) release from the guinea pig mucosa was monitored by BDD microelectrodes by Swain (Zhao, Bian, Galligan, & Swain, 2010). Martin also studied neurodynamism in *Aplysia californica* by BDD microelectrodes (Halpern et al., 2006). Furthermore, importance of the BDD microelectrodes is also discussed (Chan, Aslam, Wiler, & Casey, 2009; Cooper, Pang, Albin, Zheng, & Johnson, 1998; Park et al., 2008; Patel, Galligan, Swain, & Bian, 2008). Basic properties such as fouling properties of the electrode surfaces, which can be limitations for the application, are also important by comparison with carbon fiber electrodes (Trouillon, O'Hare, & Einaga, 2011).

3.19.5 Modified BDD Electrodes with Functions

In order to improve the electrochemical properties of BDD electrodes or to add some functions, preparation of modified BDD electrodes is promising (Foord, Hao, & Hurst, 2007; Szunerits & Boukherroub, 2008). These include chemical surface modification and micro- or nanofabrication of BDD electrodes. Concerning chemical surface modification, it is well known that basic electrochemical properties are depending on the surface termination of BDD electrodes such as hydrogen and oxygen (Notsu, Fukazawa, Tatsuma, Tryk, & Fujishima, 2001; Yagi, Notsu, Kondo, Tryk, & Fujishima, 1999). Not only the termination but also some functional groups such as halogens, nitrogen, and sulfur can be modified (Ando et al., 1996; Ikeda et al., 1998; Kealey, Klapötke, McComb, Robertson, & Winfield, 2001). Functional organic molecules or metal nanoparticles also can be modified on the surface by electrochemically and/or photochemically (Hoffmann et al., 2011; Hoffmann, Obloh, Tokuda, Yang, & Nebel, 2012; Kondo et al., 2007; Kondo, Taniguchi, Yuasa, & Kawai, 2012; Nakamura, Ohana, Hasegawa, & Koga, 2007; Wang et al., 2010). The surface-modified BDD electrodes can be applied to more sensitive electrochemical detection of certain analytes, e.g. oxalic acid, DA, hydrogen peroxide, glucose (Hoffmann et al., 2012; Kondo et al., 2012; Kondo, Tamura, Fujishima, & Kawai, 2008; Wang et al., 2010).

Furthermore, recently, many studies on micro- or nanofabrication of BDD are also reported (Colley et al., 2006; Hees et al., 2011; Lawrence et al., 2006; Luo & Zhi, 2009; Luo, Wu, & Zhi, 2009; Smirnov, Kriele, Yang, & Nebel, 2010; Soh et al., 2008; Terashima et al., 2011; Yang, Uetsuka, & Nebel, 2009; Yang, Uetsuka, Osawa, & Nebel, 2008; Yang, Uetsuka, Williams, et al., 2009). For example, vertically aligned BDD nanorod forest electrodes for biofuctionalization (Smirnov et al., 2010; Yang et al., 2008; Yang, Uetsuka, & Nebel, 2009; Yang, Uetsuka, Williams, et al., 2009), nanoelectrode arrays (Hees et al., 2011; Lawrence et al., 2006; Soh et al., 2008), nanorod forest electrodes for glucose sensor (Luo & Zhi, 2009; Luo et al., 2009), vertically aligned whiskers (Terashima et al., 2011), and so on.

3.19.6 Basic Study on Boron-Doped Diamond Electrodes

The importance of the basic studies on doped diamond materials as electrode materials has been increasing more and more (Chakrapani et al., 2007; Chane-Tune et al., 2006; Charrier, Lévy, Vigneron, Etcheberry, & Simon, 2011; Denisenko, Pietzka, Romanyuk, El-Hajj, & Kohn, 2008; Gerger & Haubner, 2005; Girard, Simon, Ballutaud, & Etcheberry, 2008; Granger et al., 2000; Latto, Pastor-Moreno, & Riley, 2004; Patten et al., 2012; Petrini & Larsson, 2007; Pietzka et al., 2010; Pleskov et al., 2012; Ristein, Riedel, & Ley, 2004; Simon et al., 2005; Torz-Piotrowska, Wrzyszczyński, Paprocki, & Staryga, 2009; Watanabe et al., 2010; Zhang, Yoshihara, Shirakashi, & Kyomen, 2005). It is well known that the inclusion of dopants during diamond crystal growth expands the possibility of creating new wide bandgap semiconductors. Anyhow, the electrochemical properties of BDD electrodes may have been influenced on several factors such as electronic states (related to the doping type (Gerger & Haubner, 2005; Zhang et al., 2005; Torz-Piotrowska et al., 2009), distribution, and level (Chane-Tune et al., 2006; Latto et al., 2004; Watanabe et al., 2010)), chemical surfaces (Charrier et al., 2011; Denisenko et al.,

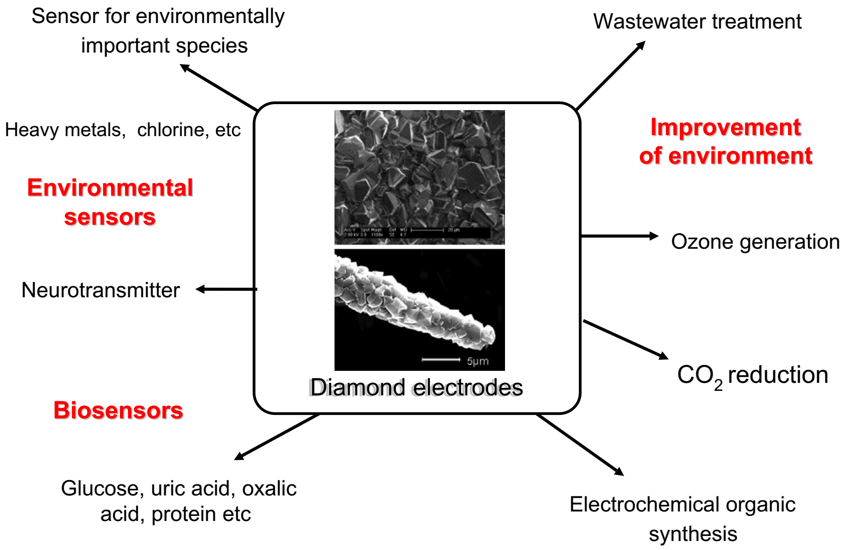

Figure 11 Application of diamond electrodes in the future.

2008; Girard et al., 2008; Patten et al., 2012; Pietzka et al., 2010; Ristein et al., 2004; Simon et al., 2005), morphology (Pleskov et al., 2012), sp^2 impurity contents (Watanabe et al., 2010), and so on. The studies on the relationship between these factors and electrochemical properties are increasing the importance year by year.

3.19.7 Summary

Recently BDD electrodes have attracted increasing attention as novel electrode materials in many areas. In the near future, the use of BDD electrodes is projected in a spectrum of applications such as environmental analysis, medical analysis, wastewater treatment systems, drug discovery, ozone generation systems, and CO_2 reduction systems. In other words, this technology can widely contribute to the safety and health of mankind (Figure 11).

References

Adams, K. L., Puchades, M., & Ewing, A. G. (2008). In vitro electrochemistry of biological systems. *Annual Review of Analytical Chemistry, 1*, 329–355.

Alfaro, M. A. Q., Ferro, S., Martínez-Huitle, C. A., & Vong, Y. M. (2006). Boron doped diamond electrode for the wastewater treatment. *Journal of the Brazilian Chemical Society, 17*(2), 227–236.

Ando, T., Yamamoto, K., Matsuzawa, M., Takamatsu, Y., Kawasaki, S., Okino, F., et al. (1996). Direct interaction of elemental fluorine with diamond surfaces. *Diamond and Related Materials, 5*(9), 1021–1025.

Arihara, K., Terashima, C., & Fujishima, A. (2007). Electrochemical production of high-concentration ozone-water using freestanding perforated diamond electrodes. *Journal of the Electrochemical Society, 154*(4), E71–E75.

Banks, C. E., Hyde, M. E., Tomčõk, P., Jacobs, R., & Compton, R. G. (2004). Cadmium detection via boron-doped diamond electrodes: surfactant inhibited stripping voltammetry. *Talanta, 62*(6), 279–286.

Batchelor-McAuley, C., Banks, C. E., Simm, A. O., Jones, T. G. J., & Compton, R. G. (2006). The electroanalytical detection of hydrazine: a comparison of the use of palladium nanoparticles supported on boron-doped diamond and palladium plated BDD microdisc array. *Analyst, 131*, 106–110.

Boonsong, K., Chuanuwatanakul, S., Wangfuengkanagul, N., & Chailapakul, O. (2005). Electroanalysis of lincomycin using boron-doped diamond thin film electrode applied to flow injection system. *Sensors and Actuators B, Chemical, 108*(1–2), 627–632.

Brillas, E., & Martinez-Huitle, C. A. (Eds.), (2011). *Synthetic diamond films*. Wiley.

Brinzila, C. I., Pacheco, M. J., Ciriaco, L., Ciobanu, R. C., & Lopes, A. (2012). Electrodegradation of tetracycline on BDD anode. *Chemical Engineering Journal, 209*, 54–61.

Chailapakul, O., Siangproh, W., & Tryk, D. A. (2006). Boron-doped diamond-based sensors: a review. *Sensor Letters, 4*, 99–119.

Chakrapani, V., Angus, J. C., Anderson, A. B., Wolter, S. D., Stoner, B. R., & Sumanasekera, G. U. (2007). Charge transfer equilibria between diamond and an aqueous oxygen electrochemical redox couple. *Science, 318*, 1424–1430.

Chan, H., Aslam, D. M., Wiler, J. A., & Casey, B. (2009). A novel diamond microprobe for neuro-chemical and -electrical recording in neural prosthesis. *Journal of Microelectromechanical Systems, 18*(3), 511–521.

Chane-Tune, J., Petit, J., Szunerits, S., Bouvier, P., Delabouglise, D., Marcus, B., et al. (2006). Using scanning electrochemical microscopy to determine the doping level and the flatband potential of boron-doped diamond electrodes. *European Journal of Chemical Physics and Physical Chemistry, 7*(1), 89–93.

Charrier, G., Lévy, S., Vigneron, J., Etcheberry, A., & Simon, N. (2011). "Electroless oxidation of boron-doped diamond surfaces: comparison between four oxidizing agents; Ce4+, MnO4−, H2O2 and S2O82−. *Diamond and Related Materials, 20*(7), 944–950.

Chatterjee, A., & Foord, J. S. (2009). Biological applications of diamond electrodes; electrochemical studies of riboflavin. *Diamond and Related Materials, 18*(5–8), 899–903.

Chatterjee, A., Wiltshire, R., Holt, K. B., Compton, R. G., Foord, J. S., & Marken, F. (2002). Abrasive stripping voltammetry of silver and tin at boron-doped diamond electrodes. *Diamond and Related Materials, 11*(3–6), 646–650.

Chiku, M., Horisawa, K., Doi, N., Yanagawa, H., & Einaga, Y. (2010). Electrochemical detection of tyrosine derivatives and protein tyrosine kinase activity using boron-doped diamond electrodes. *Biosensors and Bioelectronics, 26*, 235–240.

Chiku, M., Ivandini, T. A., Kamiya, A., Nakamura, J., Fujishima, A., & Einaga, Y. (2008). Direct electrochemical oxidation of proteins at conductive diamond electrodes. *Journal of Electroanalytical Chemistry, 612*, 201–207.

Chiku, M., Nakamura, J., Fujishima, A., & Einaga, Y. (2008). Conformational change detection in non-metal proteins by direct electrochemical oxidation using diamond electrodes. *Analytical Chemistry, 80*, 5783–5787.

Chiku, M., Watanabe, T., & Einaga, Y. (2010b). Fabrication of Cu-modified boron-doped diamond microband electrodes and their application for selective detection of glucose. *Diamond and Related Materials, 19*, 673–379.

Choi, J. Y., Lee, Y.-J., Shin, J., & Yang, J.-W. (2010). Anodic oxidation of 1,4-dioxane on boron-doped diamond electrodes for wastewater treatment. *Journal of Hazardous Materials, 179*, 762–768.

Colley, A. L., Williams, C. G., Johansson, U. D., Newton, M. E., Unwin, P. R., Wilson, N. R., et al. (2006). Examination of the spatially heterogeneous electroactivity of boron-doped diamond microarray electrodes. *Analytical Chemistry, 78*(8), 2539–2548.

Comninellis, Ch., Kapalka, A., Malato, S., Parsons, S. A., Poulios, I., & Mantzavinos, D. (2008). Advanced oxidation processes for water treatment: advances and trends for R&D. *Journal of Chemical Technology and Biotechnology, 83*, 769–776.

Comninellis, Ch., & Nerini, A. (1995). Anodic oxidation of phenol in the presence of NaCl for wastewater treatment. *Journal of Applied Electrochemistry, 25*, 23–28.

Compton, R. G., Foord, J. S., & Marken, F. (2003). Electroanalysis at diamond-like and doped-diamond electrodes. *Electroanalysis, 15*(17), 1349–1363.

Cooper, J. B., Pang, S., Albin, S., Zheng, J., & Johnson, R. M. (1998). Fabrication of boron-doped CVD diamond microelectrodes. *Analytical Chemistry, 70*, 464–467.

Costa, C. R., Montilla, F., Morallón, E., & Olivi, P. (2009). Electrochemical oxidation of acid black 210 dye on the boron-doped diamond electrode in the presence of phosphate ions: effect of current density, pH, and chloride ions. *Electrochimica Acta, 54*(27), 7048–7055.

Denisenko, A., Pietzka, C., Romanyuk, A., El-Hajj, H., & Kohn, E. (2008). The electronic surface barrier of boron-doped diamond by anodic oxidation. *Journal of Applied Physics, 103*, 014904.

Einaga, Y., Sato, R., Olivia, H., Shin, D.-C., Ivandini, T. A., & Fujishima, A. (2004). Modified diamond electrodes for electrolysis and electroanalysis application. *Electrochimica Acta, 49*, 3989–3995.

Einaga, Y. (2010). Diamond electrodes for electrochemical analysis. *Journal of Applied Electrochemistry, 40*, 1807–1816.

Elaoud, S. C., Panizza, M., Cerisola, G., & Mhiri, T. (2011). Electrochemical degradation of sinapinic acid on a BDD anode. *Desalination, 272*, 148–153.

Farrell, J., Martin, F. J., Martin, H. B., O'Grady, W. E., & Natishan, P. (2005). Anodically generated short-lived species on boron-doped diamond film electrodes. *Journal of the Electrochemical Society, 152*(1), E14–E17.

Fierro, S., Comninellis, C., & Einaga, Y. (2013). Simultaneous detection of iodine and iodide on boron doped diamond electrodes. *Talanta, 103*, 33–37.

Fierro, S., Mitani, N., Comninellis, C., & Einaga, Y. (2011). pH sensing using boron doped diamond electrodes. *Physical Chemistry Chemical Physics, 13*, 16795–16799.

Fierro, S., Watanabe, T., Akai, K., Yamanuki, M., & Einaga, Y. (2011a). Anodic stripping voltammetry of Se4+ on gold modified boron doped diamond electrodes. *International Journal of Electrochemistry, 2012*, 1–5.

Fierro, S., Watanabe, T., Akai, K., Yamanuki, M., & Einaga, Y. (2011b). Highly sensitive detection of Cd2+ using boron doped diamond electrodes. *Journal of the Electrochemical Society, 158*, F173–F178.

Fierro, S., Watanabe, T., Akai, K., & Einaga, Y. (2012). Highly sensitive detection of Cr6+ on boron doped diamond electrodes. *Electrochimica Acta, 82*, 9–11.

Fierro, S., Yoshikawa, M., Nagano, O., Yoshimi, K., Saya, H., & Einaga, Y. (2012). In vivo assessment of cancerous tumors using boron doped diamond microelectrode. *Scientific Reports, 2*, 901.

Foller, P. C., & Tobias, C. W. (1982). The anodic evolution of ozone. *Journal of the Electrochemical Society, 129*(3), 506–515.

Foord, J. S., Hao, W., & Hurst, S. (2007). Studies of the chemical functionalisation of diamond electrodes. *Diamond and Related Materials, 16*, 877–880.

França, R. F., Oliveira, H. P. M., Pedrosa, V. A., & Codognoto, L. (2012). Electroanalytical determination of carbendazim and fenamiphos in natural waters using a diamond electrode. *Diamond and Related Materials, 27–28*, 54–59.

Franco, D. V., Jardim, W. F., Boodts, J. F. C., & Silva, L. M. D. (2008). Electrochemical ozone production as an environmentally friendly technology for water treatment. *Clean, 36*(1), 34–44.

Fryda, M., Matthée, Th, Mulcahy, S., Hampel, A., Schäfer, L., & Tröster, I. (2003). Fabrication and application of Diachem® electrodes. *Diamond and Related Materials, 12*, 1950–1956.

Fujishima, A., Rao, T. N., Popa, E., Sarada, B. V., Yagi, I., & Tryk, D. A. (1999). Electroanalysis of dopamine and NADH at conductive diamond electrodes. *Journal of Electroanalytical Chemistry, 473*(1–2), 179–185.

Fujishima, A., Einaga, Y., Rao, T. N., & Tryk, D. A. (Eds.), (2005). *Diamond electrochemistry*. BKC Inc. and Elsevier.

Gerger, I., & Haubner, R. (2005). Cyclic voltammetry measurements on boron- and nitrogen-doped diamond layers. *Diamond and Related Materials, 14*(3–7), 369–374.

Girard, H. A., Simon, N., Ballutaud, D., & Etcheberry, A. (2008). Correlation between flat-band potential position and oxygenated termination nature on boron-doped diamond electrodes. *Comptes Rendus Chimie, 11*(9), 1010–1015.

Gopalan, A. I., Lee, K. P., & Komathi, S. (2010). Bioelectrocatalytic determination of nitrite ions based on polyaniline grafted nanodiamond. *Biosensors and Bioelectronics, 26*(4), 1638–1643.

Granger, M. C., Xu, J., Strojek, J. W., & Swain, G. M. (1999). Polycrystalline diamond electrodes: basic properties and applications as amperometric detectors in flow injection analysis and liquid chromatography. *Analytica Chimica Acta, 397*(1–3), 145–161.

Granger, M. C., Witek, M., Xu, J., Wang, J., Hupert, M., Hanks, A., et al. (2000). Standard electrochemical behavior of high-quality, boron-doped polycrystalline diamond thin-film electrodes. *Analytical Chemistry, 72*(16), 3793–3804.

Halpern, J. M., Xie, S., Sutton, G. P., Higashikubo, B. T., Chestek, C. A., Lu, H., et al. (2006). Diamond electrodes for neurodynamic studies in *Aplysia californica. Diamond and Related Materials, 15*(2–3), 183–187.

Hason, S., Pivonkova, H., Vetterl, V., & Fojta, M. (2008). Label-free sequence-specific DNA sensing using copper-enhanced anodic stripping of purine bases at boron-doped diamond electrodes. *Analytical Chemistry, 80*, 2391–2399.

Hees, J., Hoffmann, R., Kriele, A., Smirnov, W., Oblo, H., Glorer, K., et al. (2011). Nanocrystalline diamond nanoelectrode arrays and ensembles. *ACS Nano, 5*(4), 3339–3346.

Hmani, E., Samet, Y., & Abdelhedi, R. (2012). Electrochemical degradation of auramine-O dye at boron-doped diamond and lead dioxide electrodes. *Diamond and Related Materials, 30*, 1–8.

Hoffman, J. M., Tyler, K., MacEachern, S. J., Balemba, O. B., Johnson, A. C., Brooks, E. M., et al. (2012). Activation of colonic mucosal 5-HT(4) receptors accelerates propulsive motility and inhibits visceral hypersensitivity. *Gastroenterology, 142*(4), 844–854.

Hoffmann, R., Kriele, A., Obloh, H., Tokuda, N., Smirnov, W., Yang, N., et al. (2011). The creation of a biomimetic interface between boron-doped diamond and immobilized proteins. *Biomaterials, 32*(30), 7325–7332.

Hoffmann, R., Obloh, H., Tokuda, N., Yang, N., & Nebel, C. E. (2012). Fractional surface termination of diamond by electrochemical oxidation. *Langmuir, 28*(1), 47–50.

Ikeda, Y., Saito, T., Kusakabe, K., Morooka, S., Maeda, H., Taniguchi, Y., et al. (1998). Halogenation and butylation of diamond surfaces by reactions in organic solvents. *Diamond and Related Materials, 7*(6), 830–834.

Ivandini, T. A., Honda, K., Rao, T. N., Fujishima, A., & Einaga, Y. (2007). Simultaneous detection of purine and pyrimidine at highly boron-doped diamond electrodes by using liquid chromatography. *Talanta, 71*, 648–655.

Ivandini, T. A., Naono, Y., Nakajima, A., & Einaga, Y. (2005). Gold nanoparticles dispersed boron-doped diamond electrodes for electrochemical oxidation of oxalic acid. *Chemistry Letters, 34*, 1086–1087.

Ivandini, T. A., Rao, T. N., Fujishima, A., & Einaga, Y. (2006). Electrochemical oxidation of oxalic acid at highly boron-doped diamond electrodes. *Analytical Chemistry, 78*, 3467–3471.

Ivandini, T. A., Saepudin, E., Wardah, H., Dewangga, N., & Einaga, Y. (2012). Development of a biochemical oxygen demand sensor using gold-modified boron doped diamond electrodes. *Analytical Chemistry, 84*(22), 9825–9832.

Ivandini, T. A., Sato, R., Makide, Y., Fujishima, A., & Einaga, Y. (2004a). Electroanalytical application of modified diamond electrodes. *Diamond and Related Materials, 13*, 2003–2008.

Ivandini, T. A., Sato, R., Makide, Y., Fujishima, A., & Einaga, Y. (2004b). Pt-implanted boron doped-diamond electrodes for electrochemical oxidation of hydrogen peroxide. *Chemistry Letters, 33*, 1330–1331.

Ivandini, T. A., Sato, R., Makide, Y., Fujishima, A., & Einaga, Y. (2005). Pt-implanted boron doped-diamond electrodes and the application for electrochemical detection of hydrogen peroxide. *Diamond and Related Materials, 14*, 2133–2138.

Ivandini, T. A., Sato, R., Makide, Y., Fujishima, A., & Einaga, Y. (2006). Electrochemical detection of arsenic (III) using iridium-implanted boron-doped diamond electrodes. *Analytical Chemistry, 78*, 6291–6298.

Ivandini, T. A., Yamada, D., Watanabe, T., Matsuura, H., Nakano, N., Fujishima, A., et al. (2010). Development of amperometric arsine gas sensor using gold-modified diamond electrodes. *Journal of Electroanalytical Chemistry, 645*, 58–63.

Janegitz, B. C., Medeiros, R. A., Rocha-Filho, R. C., & Fatibello-Filho, O. (2012). Direct electrochemistry of tyrosinase and biosensing for phenol based on gold nanoparticles electrodeposited on a boron-doped diamond electrode. *Diamond and Related Materials, 25*, 128–133.

Jolley, S., Koppang, M., Jackson, T., & Swain, G. M. (1997). Flow injection analysis with diamond thin-film detectors. *Analytical Chemistry, 69*(20), 4099–4107.

Kapalka, A., Foti, G., & Comninellis, Ch. (2007). Investigation of electrochemical oxygen transfer reaction on boron-doped diamond electrodes. *Electrochimica Acta, 53*, 1954–1961.

Kapalka, A., Foti, G., & Comninellis, Ch. (2008a). Determination of the Tafel slope for oxygen evolution on boron-doped diamond electrodes. *Electrochemistry Communications, 10*, 607–610.

Kapalka, A., Foti, G., & Comninellis, Ch. (2008b). Kinetic modeling of the electrochemical mineralization of organic pollutants for wastewater treatment. *Journal of Applied Electrochemistry, 38*, 7–16.

Kapalka, A., Lanova, B., Baltruschat, H., Foti, G., & Comninellis, Ch. (2008). Electrochemically induced mineralization of organics by molecular oxygen on boron-doped diamond electrode. *Electrochemistry Communications, 10*, 1215–1218.

Kapalka, A., Foti, G., & Comninellis, Ch. (2009). The importance of electrode material in environmental electrochemistry formation and reactivity of free hydroxyl radicals on boron-doped diamond electrodes. *Electrochimica Acta, 54*, 2018–2023.

Kapalka, A., Lanova, B., Baltruschat, H., Foti, G., & Comninellis, Ch. (2009). A DEMS study of methanol and formic acid oxidation on boron-doped diamond electrode. *Journal of the Electrochemical Society, 156*(11), E149–E153.

Karuwan, C., Mantim, T., Chaisuwan, P., Wilairat, P., Grudpan, K., Jittangprasert, P., et al. (2006). Pulsed amperometry for anti-fouling of boron-doped diamond in electroanalysis of beta-agonists: application to flow injection for pharmaceutical analysis. *Sensors, 6*, 1837–1850.

Kato, D., Goto, K., Fujii, S., Takatsu, A., Hirono, S., & Niwa, O. (2011). Electrochemical DNA methylation detection for enzymatically digested CpG oligonucleotides. *Analytical Chemistry, 83*(20), 7595–7599.

Kato, T., Fierro, S., Watanabe, T., Yoshimi, K., & Einaga, Y. (2012). Dopamine detection on boron doped diamond electrodes using fast cyclic voltammetry. *Chemistry Letters, 41*, 224–226.

Katsuki, N., Takahashi, E., Toyoda, M., Kurosu, T., Iida, M., Wakita, S., et al. (1998). Water electrolysis using diamond thin-film electrodes. *Journal of the Electrochemical Society, 145*(7), 2358–2362.

Kealey, C. P., Klapötke, T. M., McComb, D. W., Robertson, M. I., & Winfield, J. M. (2001). Fluorination of polycrystalline diamond films and powders. An investigation using FTIR spectroscopy, SEM, energy-filtered TEM, XPS and fluorine-18 radiotracer methods. *Journal of Materials Chemistry, 11*, 879–886.

Kirste, A., Nieger, M., Malkowsky, I. M., Stecker, F., Fischer, A., & Waldvogel, S. R. (2009). ortho-Selective phenol-coupling reaction by anodic treatment on boron-doped diamond electrode using fluorinated alcohols. *Chemistry – A European Journal, 15*, 2273–2277.

Kirste, A., Schnakenburg, G., Stecker, F., Fischer, A., & Waldvogel, S. R. (2010). Anodic phenol-arene cross-coupling reaction on boron-doped diamond electrodes. *Angewandte Chemie International Edition, 49*, 971–975.

Kirste, A., Elsler, B., Schnakenburg, G., & Waldvogel, S. R. (2012). Efficient anodic and direct phenol-arene C, C cross-coupling: the benign role of water or methanol. *Journal of the American Chemical Society, 134*, 3571–3576.

Kondo, T., Aoshima, S., Honda, K., Einaga, Y., Fujishima, A., & Kawai, T. (2007). Fabrication of covalent SAM/Au nanoparticle/boron-doped diamond configurations with a sequential self-assembly method. *Journal of Physical Chemistry C, 111*(34), 12650–12657.

Kondo, T., Niwano, Y., Tamura, A., Ivandini, T. A., Einaga, Y., Tryk, D. A., et al. (2008). Sensitive electrochemical detection of oxalate at a positively charged boron-doped diamond surface. *Electroanalysis, 20*, 1556–1564.

Kondo, T., Tamura, A., Fujishima, A., & Kawai, T. (2008). High sensitivity electrochemical detection of hydrogen peroxide at a cobalt phthalocyanine-modified boron-doped diamond electrode. *ECS Transactions, 16*(11), 465–473.

Kondo, T., Taniguchi, Y., Yuasa, M., & Kawai, T. (2012). Polyoxometalate-modified boron-doped diamond electrodes. *Japanese Journal of Applied Physics, 51*, 090121.

Koppang, M. D., Witek, M., Blau, J., & Swain, G. M. (1999). Electrochemical oxidation of polyamines at diamond thin-film electrodes. *Analytical Chemistry, 71*(6), 1188–1195.

Kraft, A. (2007). Doped diamond: a compact review on a new, versatile electrode material. *International Journal of Electrochemical Science, 2*, 355–385.

Langeloth, M., Chiku, M., & Einaga, Y. (2010). Anodic stripping voltammetry of zinc at boron-doped diamond electrodes in ammonia buffer solution. *Electrochimica Acta, 55*, 2824–2828.

Latto, M. N., Pastor-Moreno, G., & Riley, D. J. (2004). The influence of doping levels and surface termination on the electrochemistry of polycrystalline diamond. *Electroanalysis, 16*(6), 434–440.

Lawrence, N. S., Pagels, M., Meredith, A., Jones, T. G. J., Hall, C. E., Pickles, C. S. J., et al. (2006). Electroanalytical applications of boron-doped diamond microelectrode arrays. *Talanta, 69*(4), 829–834.

Lee, J.-W., Einaga, Y., Fujishima, A., & Park, S.-M. (2004). Electrochemical oxidation of Mn2+ on boron-doped diamond electrodes with Bi3+ used as an electron transfer mediator. *Journal of the Electrochemical Society, 151*, E265–E270.

Lima-Neto, P., Correia, A. N., Portela, R. R., Julião Mda, S., Linhares-Junior, G. F., & Lima, J. E. (2009). Square wave voltammetric determination of nitrofurantoin in pharmaceutical formulations on highly boron-doped diamond electrodes at different boron-doping contents. *Talanta, 80*(5), 1730–1736.

Luo, D., & Zhi, J. (2009). Fabrication and electrochemical behaviour of vertically aligned boron-doped diamond nanorod forest electrodes. *Electrochemistry Communications, 11*(6), 1093–1096.

Luo, D., Wu, L., & Zhi, J. (2009). Fabrication of boron-doped diamond nanorod forest electrodes and their application in nonenzymatic amperometric glucose biosensing. *ACS Nano, 3*(8), 2121–2128.

Luong, J. H., Male, K. B., & Glennon, J. D. (2009). Boron-doped diamond electrode: synthesis, characterization, functionalization and analytical applications. *Analyst, 134*(10), 1965–1979.

Malkowsky, I. M., Griesbach, U., Putter, H., & Waldvogel, S. R. (2006). Unexpected highly chemoselective anodic ortho-coupling reaction of 2,4-dimethylphenol on boron-doped diamond electrodes. *European Journal of Organic Chemistry*, 4569–4572.

Manivannan, A., Seehra, M. S., & Fujishima, A. (2004). Detection of mercury at the ppb level in solution using boron-doped diamond electrode. *Fuel Processing Technology, 85*(6–7), 513–519.

Marselli, B., Garcia-Gomez, J., Michaud, P.-A., Rodrigo, M. A., & Comninellis, Ch (2003). Electrogeneration of hydroxyl radicals on boron-doped diamond electrodes. *Journal of the Electrochemical Society, 150*(3), D79–D83.

Martinez-Huitle, C. A., & Brillas, E. (2008). Electrochemical alternatives for drinking water disinfection. *Angewandte Chemie International Edition, 47*, 1998–2005.

Martínez-Huitle, C. A., Ferro, S., & De Battisti, A. (2005). Electrochemical incineration in the presence of halides. *Electrochemical and Solid-State Letters, 8*(11), D35–D39.

McCreery, R. L. (2008). Advanced carbon electrode materials for molecular electrochemistry. *Chemical Reviews, 108*, 2646–2687.

McEvoy, J. P., & Foord, J. S. (2005). Direct electrochemistry of blue copper proteins at boron-doped diamond electrodes. *Electrochimica Acta, 50*(14), 2933–2941.

Medeiros, R. A., Carvalho, A. E., Rocha-Filho, R. C., & Fatibello-Filho, O. (2007). Square-wave voltammetry determination of aspartame in dietary products using a boron-doped diamond electrode. *Analytical Letters, 40*(17), 3195–3207.

Medeiros, R. A., Carvalho, A. E., Rocha-Filho, R. C., & Fatibello-Filho, O. (2008). Simultaneous square-wave voltammetric determination of aspartame and cyclamate using a boron-doped diamond electrode. *Talanta, 76*(3), 685–689.

Michaud, P.-A., Panizza, M., Ouattara, L., Diaco, T., Foti, G., & Comninellis, Ch. (2003). Electrochemical oxidation of water on synthetic boron-doped diamond thin film anodes. *Journal of Applied Electrochemistry, 33*, 151–154.

Mitani, N., & Einaga, Y. (2009). The simple voltammetric analysis of acids using highly boron-doped diamond macroelectrodes and microelectrodes. *Journal of Electroanalytical Chemistry, 626*, 156–160.

Murata, M., Ivandini, T. A., Shibata, M., Nomura, S., Fujishima, A., & Einaga, Y. (2008). Electrochemical detection of free chlorine at highly boron-doped diamond electrodes. *Journal of Electroanalytical Chemistry, 612*, 29–36.

Murugananthan, M., Latha, S. S., Raju, G. B., & Yoshihara, S. (2011). Role of electrolyte on anodic mineralization of atenolol at boron doped diamond and Pt electrodes. *Separation and Purification Technology, 79*, 56–62.

Musilová, J., Barek, J., & Pecková, K. (2011). Determination of nitrophenols in drinking and river water by differential pulse voltammetry at boron-doped diamond film electrode. *Electroanalysis, 23*(5), 1236–1244.

Nagaoka, Y., Ivandini, T. A., Yamada, D., Fujita, S., Yamanuki, M., & Einaga, Y. (2010). Selective detection of As(V) with high sensitivity by as-deposited boron-doped diamond electrodes. *Chemistry Letters, 39*, 1055–1057.

Nakamura, T., Ohana, T., Hasegawa, M., & Koga, Y. (2007). Photochemical modification of diamond films with sulfur-containing functionalities. *Japanese Journal of Applied Physics, 46*(1), 348–350.

Nekrassova, O., Lawrence, N. S., & Compton, R. G. (2004). Selective electroanalytical assay for cysteine at a boron doped diamond electrode. *Electroanalysis, 16*(16), 1285–1291.

Notsu, H., Fukazawa, T., Tatsuma, T., Tryk, D. A., & Fujishima, A. (2001). Hydroxyl groups on boron-doped diamond electrodes and their modification with a silane coupling agent. *Electrochemical and Solid-State Letters, 4*(3), H1–H3.

Ochiai, T., Arihara, K., Terashima, C., & Fujishima, A. (2006). Electrochemical reduction of ozone dissolved in perchloric acid solutions at boron-doped diamond electrodes. *Chemistry Letters, 35*(9), 1018–1019.

Paleček, E., & Bartošík, M. (2012). Electrochemistry of nucleic acids. *Chemical Reviews, 112*(6), 3427–3481.

Panizza, M., & Cerisola, G. (2005). Application of diamond electrodes to electrochemical processes. *Electrochimica Acta, 51*, 191–199.

Panizza, M., Barbucci, A., Ricotti, R., & Cerisola, G. (2007). Electrochemical degradation of methylene blue. *Separation and Purification Technology, 54*(3), 382–387.

Panizza, M., Kapalka, A., & Comninellis, Ch. (2008). Oxidation of organic pollutants on BDD anodes using modulated current electrolysis. *Electrochimica Acta, 53*, 2289–2295.

Park, J., Quaiserová-Mocko, V., Patel, B. A., Novotný, M., Liu, A., Bian, X., et al. (2008). Diamond microelectrodes for in vitro electroanalytical measurements: current status and remaining challenges. *Analyst, 133*(1), 17–24.

Patel, B. A., Galligan, J. J., Swain, G. M., & Bian, X. (2008). Electrochemical monitoring of nitric oxide released by myenteric neurons of the guinea pig ileum. *Neurogastroenterol Motility, 20*, 1243–1250.

Patten, H. V., Meadows, K. E., Hutton, L. A., Iacobini, J. G., Battistel, D., McKelvey, K., et al. (2012). Electrochemical mapping reveals direct correlation between heterogeneous electron-transfer kinetics and local density of states in diamond electrodes. *Angewandte Chemie International Edition, 51*(28), 7002–7006.

Pereira, G. F., Rocha-Filho, R. C., Bocchi, N., & Biaggio, S. R. (2012). Electrochemical degradation of bisphenol A using a flow reactor with a boron-doped diamond anode. *Chemical Engineering Journal, 198–199*, 282–288.

Petrini, D., & Larsson, K. (2007). A theoretical study of the energetic stability and geometry of hydrogen- and oxygen-terminated diamond (100) surfaces. *Journal of Physical Chemistry C, 111*(2), 795–801.

Pietzka, C., Denisenko, A., Romanyuk, A., Schäfer, P. J., Kibler, L. A., Scharpf, J., et al. (2010). Electronic surface barrier properties of boron-doped diamond oxidized by plasma treatment. *Diamond and Related Materials, 19*(2–3), 213–216.

Pleskov, Y. V., Krotova, M. D., Elkin, V. V., Varnin, V. P., Teremetskaya, I. G., Saveliev, A. V., et al. (2012). Benzene oxidation at diamond electrodes: comparison of microcrystalline and nanocrystalline diamonds. *European Journal of Chemical Physics and Physical Chemistry, 13*(12), 3047–3052.

Prado, C., Wilkins, S. J., Marken, F., & Compton, R. G. (2002). Simultaneous electrochemical detection and determination of lead and copper at boron-doped diamond film electrodes. *Electroanalysis, 14*(4), 262–272.

Prado, C., Flechsig, G., Gründler, P., Foord, J. S., Marken, F., & Compton, R. G. (2002). Electrochemical analysis of nucleic acids at boron-doped diamond electrodes. *Analyst, 127*, 329–332.

Prado, C., Wilkins, S. J., Gründler, P., Marken, F., & Compton, R. G. (2003). Electrodeposition of lead at boron-doped diamond film electrodes: effect of temperature. *Electroanalysis, 15*(12), 1011–1016.

Preechaworapun, A., Chuanuwatanakul, S., Einaga, Y., Grudpan, K., Motomizu, S., & Chailapakul, O. (2006). Electroanalysis of sulfonamides by flow injection system/high-performance liquid chromatography coupled with amperometric detection using boron-doped diamond electrode. *Talanta, 68*, 1726–1731.

Preechaworapun, A., Ivandini, T. A., Suzuki, A., Fujishima, A., Chailapakul, O., & Einaga, Y. (2008). The development of amperometric immunosensor using boron-doped diamond with poly (o-aminobenzoic acid). *Analytical Chemistry, 80*, 2077–2083.

Racaud, C., Groenen-Serrano, K., & Savall, A. (2010). Voltammetric determination of the critical micellar concentration of surfactants by using a boron doped diamond anode. *Journal of Applied Electrochemistry, 40*(10), 1845–1851.

Rao, T. N., Loo, B. H., Sarada, B. V., Terashima, C., & Fujishima, A. (2002). Electrochemical detection of carbamate pesticides at conductive diamond electrodes. *Analytical Chemistry, 74*(7), 1578–1583.

Ristein, J., Riedel, M., & Ley, L. (2004). Electrochemical surface transfer doping: the mechanism behind the surface conductivity of hydrogen-terminated diamond. *Journal of the Electrochemical Society, 151*(10), E315–E321.

Sarada, B. V., Rao, T. N., Tryk, D. A., & Fujishima, A. (2000). Electrochemical oxidation of histamine and serotonin at highly boron-doped diamond electrodes. *Analytical Chemistry, 72*(7), 1632–1638.

Saterlay, J., Foord, J. S., & Compton, R. G. (1999). Sono-cathodic stripping voltammetry of manganese at a polished boron-doped diamond electrode: application to the determination of manganese in instant tea. *Analyst, 124*, 1791–1796.

Schäfer, L., Höfer, M., & Kröger, R. (2006). The versatility of hot-filament activated chemical vapor deposition. *This Solid Films, 515*, 1017–1024.

Scialdone, O., Galia, A., & Randazzo, S. (2012). Electrochemical treatment of aqueous solutions containing one or many organic pollutants at boron-doped diamond anodes. Theoretical modeling and experimental data. *Chemical Engineering Journal, 183*, 124–134.

Seehraa, M. S., Ranganathana, S., & Manivannan, A. (2008). Electrochemical quantification of mercury in solutions using boron-doped diamond electrodes: electrode regeneration and role of gold and impurities. *Analytical Letters, 41*(12), 2162–2170.

Silva, L. M. D., Santana, M. H. P., & Boodts, J. F. C. (2003). Electrochemistry and green chemical processes: electrochemical ozone production. *Quimica Nova, 26*(6), 880–888.

Simon, N., Girard, H., Ballutaud, D., Ghodbane, S., Deneuville, A., Herlem, M., et al. (2005). Effect of H and O termination on the charge transfer of moderately boron doped diamond electrodes. *Diamond and Related Materials, 14*(3–7), 1179–1182.

Singh, Y. S., Sawarynski, L. E., Dabiri, P. D., Choi, W. R., & Andrews, A. M. (2011). Head-to-Head comparisons of carbon fiber microelectrode coatings for sensitive and selective neurotransmitter detection by voltammetry. *Analytical Chemistry, 83*(17), 6658–6666.

Sirés, I., Cabot, P. L., Centellas, F., Garrido, J. A., Rodríguez, R. M., Arias, C., et al. (2006). Electrochemical degradation of clofibric acid in water by anodic oxidation: comparative study with platinum and boron-doped diamond electrodes. *Electrochimica Acta, 52*(1), 75–85.

Smirnov, W., Kriele, A., Yang, N., & Nebel, C. E. (2010). Aligned diamond nano-wires: fabrication and characterisation for advanced applications in bio- and electrochemistry. *Diamond and Related Materials, 19*, 186–189.

Soh, K. L., Kang, W. P., Davidson, J. L., Wong, Y. M., Cliffel, D. E., & Swain, G. M. (2008). Ordered array of diamond ultramicroband electrodes for electrochemical analysis. *Diamond and Related Materials, 17*(3), 240–246.

Song, Y., & Swain, G. M. (2007). Development of a method for total inorganic arsenic analysis using anodic stripping voltammetry and a Au-coated, diamond thin-film electrode. *Analytical Chemistry, 79*, 2412–2420.

Spãtaru, N., Sarada, B. V., Popa, E., Tryk, D. A., & Fujishima, A. (2001). Voltammetric determination of l-cysteine at conductive diamond electrodes. *Analytical Chemistry, 73*(3), 514–519.

Strojek, J. W., Granger, M. C., Swain, G. M., Dallas, T., & Holtz, M. W. (1996). Enhanced signal-to-background ratios in voltammetric measurements made at diamond thin-film electrochemical interfaces. *Analytical Chemistry, 68*(13), 2031–2037.

Suffredini, H. B., Machado, S. A. S., & Avaca, L. A. (2004). The water decomposition reaction on boron-doped diamond electrodes. *Journal of the Brazilian Chemical Society, 15*(1), 16–21.

Sugitani, A., Watanabe, T., Ivandini, T. A., Iguchi, T., & Einaga, Y. (2013). Controlling the diffusion profile of electroactive species for selective anodic stripping voltammetry of cadmium at boron-doped diamond electrodes. *Physical Chemistry Chemical Physics, 15*(1), 142–147.

Sumi, T., Saitoh, T., Natsui, K., Yamamoto, T., Atobe, M., Einaga, Y., et al. (2012). Anodic oxidation on a boron-doped diamond electrode mediated by methoxy radicals. *Angewandte Chemie International Edition, 51*, 5443–5446.

Suryanarayanan, V., Zhang, Y., Yoshihara, S., & Shirakashi, T. (2005). Voltammetric assay of naproxen in pharmaceutical formulations using boron-doped diamond electrode. *Electroanalysis, 17*(11), 925–932.

Suzuki, A., Ivandini, T. A., Kamiya, A., Nomura, S., Yamanuki, M., Matsumoto, K., et al. (2007). Direct electrochemical detection of sodium azide in physiological saline buffers using highly boron-doped diamond electrodes. *Sensors and Actuators B, Chemical, 120*, 500–507.

Suzuki, A., Ivandini, T. A., Yoshimi, K., Fujishima, A., Oyama, G., Nakazato, T., et al. (2007). Fabrication, characterization, and application of boron-doped diamond microelectrodes for in vivo dopamine detection. *Analytical Chemistry, 79*, 8608–8615.

Swain, G. M., Anderson, A. B., & Angus, J. C. (1998). Applications of diamond thin films in electrochemistry. *MRS Bulletin, 23*(9), 56–60.

Szunerits, S., & Boukherroub, R. (2008). Different strategies for functionalization of diamond surfaces. *Journal of Solid State Electrochemistry, 12*, 1205–1218.

Terashima, C., Arihara, K., Okazaki, S., Shichi, T., Tryk, D. A., Shirafuji, T., et al. (2011). Fabrication of vertically aligned diamond whiskers from highly boron-doped diamond by oxygen plasma etching. *ACS Applied & Materials Interfaces, 3*(2), 177–182.

Tissot, G. B., Anglada, A., Dimitriou-Christidis, P., Rossi, L., Arey, J. S., & Comninellis, Ch (2012). Kinetic experiments of electrochemical oxidation of iohexol on BDD electrodes for wastewater treatment. *Electrochemistry Communications, 23*, 48–51.

Torz-Piotrowska, R., Wrzyszczyński, A., Paprocki, K., & Staryga, E. (2009). Application of N- and B-doped CVD diamond layers for cyclic voltammetry measurements. *Optical Materials, 31*(12), 1870–1872.

Treetepvijit, S., Chuanuwatanakul, S., Einaga, Y., Sato, R., & Chailapakul, O. (2005). Electroanalysis of tetracycline using nickel-implanted boron-doped diamond thin film electrode applied to flow injection system. *Analytical Science, 21*, 531–535.

Treetepvijit, S., Preechaworapun, A., Praphairaksit, N., Chuanuwatanakul, U., Einaga, Y., & Chailapakul, O. (2006). Use of nickel implanted boron-doped diamond thin film electrode coupled to HPLC system for the determination of tetracyclines. *Talanta, 68*, 1329–1335.

Tröster, I., Fryda, M., Herrmann, D., Schäfer, L., Hänni, W., Perret, A., et al. (2002). Electrochemical advanced oxidation process for water treatment using DiaChem® electrodes. *Diamond and Related Materials, 11*, 640–645.

Tröster, I., Schäfer, L., Fryda, M., & Matthée, T. (2004). Electrochemical advanced oxidation process using DiaChem® electrodes. *Water Science and Technology, 49*(4), 207–212.

Trouillon, R., O'Hare, D., & Einaga, Y. (2011). Effect of doping level on the biological stability of hydrogenated boron doped diamond electrodes. *Physical Chemistry Chemical Physics, 13*, 5422–5429.

Trouillon, R. (2012). Biological applications of the electrochemical sensing of nitric oxide: fundamentals and recent developments. *Biological Chemistry, 394*(1), 17–33.

Trouillon, R., Svensson, M. I., Berglund, E. C., Cans, A., & Ewing, A. G. (2012). Highlights of selected recent electrochemical measurements in living systems. *Electrochimica Acta, 84*, 84–95.

Trouillon, R., Passarelli, M. K., Wang, J., Kurczy, M. E., & Ewing, A. G. (2013). Chemical analysis of single cells. *Analytical Chemistry, 85*(2), 522–542.

Tsantaki, E., Velegraki, T., Katsaounis, A., & Mantzavinos, D. (2012). Anodic oxidation of textile dyehouse effluents on boron-doped diamond electrode. *Journal of Hazardous Materials, 207–208*, 91–96.

Waldvogel, S. R., & Elsler, B. (2012). Electrochemical synthesis on boron-doped diamond. *Electrochimica Acta, 82*, 434–443.

Wang, M., Schneider, A., Niedziółka-Jönsson, J., Marcon, L., Ghodbane, S., Steinmüller-Nethl, D., et al. (2010). Covalent modification of boron-doped diamond electrodes with an imidazolium-based ionic liquid. *Electrochimica Acta, 55*(5), 1582–1587.

Wangfuengkanagul, N., & Chailapakul, O. (2002). Electrochemical analysis of d-penicillamine using a boron-doped diamond thin film electrode applied to flow injection system. *Talanta, 58*(6), 1213–1219.

Watanabe, T., & Einaga, Y. (2009). Design and fabrication of nickel micordisk-arrayed diamond electrodes for a non-enzymatic glucose sensor based on control of diffusion profiles. *Biosensors and Bioelectronics, 24*, 2684–2689.

Watanabe, T., Ivandini, T. A., Makide, Y., Fujishima, A., & Einaga, Y. (2006). A selective detection method derived from controlled diffusion process at metal-modified diamond electrodes. *Analytical Chemistry, 78*, 7857–7860.

Watanabe, T., Shimizu, T. K., Tateyama, Y., Kim, Y., Kawai, M., & Einaga, Y. (2010). Giant electric double-layer capacitance of heavily boron-doped diamond electrode. *Diamond and Related Materials, 19*, 772–777.

Wei, M., Zhou, Y., Zhi, J., Fu, D., Einaga, Y., Fujishima, A., & et al. (2008). Comparison of boron-doped diamond and glassy carbon electrodes for determination of procaine hydrochloride. *Electroanalysis, 20*, 137–143.

Wei, M., Sun, L., Xie, Z., Zhi, J., Fujishima, A., Einaga, Y., & et al. (2008). Selective determination of dopamine on a boron-doped diamond electrode modified with gold nanoparticle/polyelectrolyte-coated polystyrene colloids. *Advanced Functional Materials, 18*, 1–8.

Xie, S., Shafer, G., Wilson, C. G., & Martin, H. B. (2006). In vitro adenosine detection with a diamond-based sensor. *Diamond and Related Materials, 15*(2–3), 225–228.

Xu, J., & Swain, G. M. (1998). Oxidation of azide anion at boron-doped diamond thin-film electrodes. *Analytical Chemistry, 70*(8), 1502–1510.

Xu, J., Granger, M. C., Chen, Q., Strojek, J. W., Lister, T. E., & Swain, G. M. (1997). Boron-doped diamond thin-film electrodes. *Analytical Chemistry News & Features*, 591A–597A.

Yagi, I., Notsu, H., Kondo, T., Tryk, D. A., & Fujishima, A. (1999). Electrochemical selectivity for redox systems at oxygen-terminated diamond electrodes. *Journal of Electroanalytical Chemistry, 473*, 173–178.

Yamada, D., Ivandini, T. A., Komatsu, M., Fujishima, A., & Einaga, Y. (2008). Anodic stripping voltammetry of inorganic species of As3+ and As5+ at gold-modified boron doped diamond electrodes. *Journal of Electroanalytical Chemistry, 615*, 145–153.

Yang, N., Hoffmann, R., Smirnov, W., Kriele, A., & Nebel, C. E. (2010). Direct electrochemistry of cytochrome c on nanotextured diamond surface. *Electrochemistry Communications, 12*(9), 1218–1221.

Yang, N., Uetsuka, H., & Nebel, C. E. (2009). Biofunctionalization of vertically aligned diamond nanowires. *Advanced Functional Materials, 19*(6), 887–893.

Yang, N., Uetsuka, H., Osawa, E., & Nebel, C. E. (2008). Vertically aligned diamond nanowires for DNA sensing. *Angewandte Chemie International Edition, 47*(28), 5183–5185.

Yang, N., Uetsuka, H., Williams, O. A., Osawa, E., Tokuda, N., & Nebel, C. E. (2009). Vertically aligned diamond nanowires: fabrication, characterization, and application for DNA sensing. *Physica Status Solidi (A), 206*(9), 2048–2056.

Yano, T., Tryk, D. A., Hashimoto, K., & Fujishima, A. (1998). Electrochemical behavior of highly conductive boron-doped diamond electrodes for oxygen reduction in alkaline solution. *Journal of the Electrochemical Society, 145*(6), 1870–1876.

Yoshihara, S., & Murugananthan, M. (2009). Decomposition of various endocrine-disrupting chemicals at boron-doped diamond electrode. *Electrochimica Acta, 54*(7), 2031–2038.

Yoshimi, K., Naya, Y., Mitani, N., Kato, T., Inoue, M., Natori, S., et al. (2011). Phasic reward responses in the monkey striatum as detected by voltammetry with diamond microelectrodes. *Neuroscience Research, 71*, 49–62.

Zhang, Y., Yoshihara, S., Shirakashi, T., & Kyomen, T. (2005). Electrochemical characteristics of boron-doped, undoped and nitrogen-doped diamond films. *Diamond and Related Materials, 14*(2), 213–219.

Zhang, C., Fu, D., & Gu, Z. (2009). Degradation of microcystin-RR using boron-doped diamond electrode. *Journal of Hazardous Materials, 172*, 847–853.

Zhao, H., Bian, X., Galligan, J. J., & Swain, G. M. (2010). Electrochemical measurements of serotonin (5-HT) release from the guinea pig mucosa using continuous amperometry with a boron-doped diamond microelectrode. *Diamond and Related Materials, 19*(2–3), 182–185.

Zhao, G., Qi, Y., & Tian, Y. (2006). Simultaneous and direct determination of tryptophan and tyrosine at boron-doped diamond electrode. *Electroanalysis, 18*(8), 830–834.

Zhou, Y., & Zhi, J. (2006). Development of an amperometric biosensor based on covalent immobilization of tyrosinase on a boron-doped diamond electrode. *Electrochemistry Communications, 8*(12), 1811–1816.

Zhou, Y., Zhi, J., Zou, Y., Zhang, W., & Lee, S. T. (2008). Direct electrochemistry and electrocatalytic activity of cytochrome c covalently immobilized on a boron-doped nanocrystalline diamond electrode. *Analytical Chemistry, 80*(11), 4141–4146.

Zollinger, D., Griesbach, U., Putter, H., & Comninellis, Ch (2004a). Electrochemical cleavage of 1,2-diphenylethanes at boron-doped diamond electrodes. *Electrochemistry Communications, 6*, 605–608.

Zollinger, D., Griesbach, U., Putter, H., & Comninellis, Ch. (2004b). Methoxylation of p-tert-butyltoluene on boron-doped diamond electrodes. *Electrochemistry Communications, 6*, 600–604.

SECTION VI

OTHER CARBON PHASES

3.20 Superhard Materials Based on Fullerenes and Nanotubes

Michail Popov, Boris Kulnitskiy, and Vladimir Blank, Technological Institute for Superhard and Novel Carbon Materials, Moscow, Russia

Glossary

Superhard materials These include materials with hardness from cubic boron nitride to diamond

Ultrahard materials These include materials with hardness exceeding the diamond hardness

3.20.1 Introduction

Quantitatively, hardness is defined as the load on the indenter divided by the indentation area produced. Hardness H is associated with yield strength τ^*; for most materials, τ^* is approximately equal to $0.33H$ (Gilman, 1975a, 1975b). Hardness can be measured by both indentation and sclerometry (Mohs technique) methods. Both methods have been shown (Grigorovich, 1976) to agree well with each other. Sclerometry tests impose higher plastic strain than the indentation technique. Although there are several indenter shape options, such (Vickers, Knoop, Berkovich, etc.) results obtained by different indenters are nevertheless close to each other (Grigorovich, 1976).

Superhard materials include the materials with hardness from cubic boron nitride (c-BN) to diamond (Wentorf, DeVries, et al., 1980) while the ultrahard class of materials has been defined on the basis of studies (Blank, Buga, et al., 1994a, 1994b; Blank, Buga, et al., 1995a, 1995b, 1995c; Blank, Buga, et al., 1996a, 1996b, 1996c; Blank, Buga, et al., 1997; Blank, Buga, et al., 1998a, 1998b, 1998c, 1998d, 1998e; Blank, Buga, et al., 2001; Blank, Buga, et al., 2002; Blank, Denisov, et al., 1998; Blank, Popov, et al., 1994; Blank, Popov, et al., 1997a, 1997b; Blank, Popov, et al., 1998; Blank, Popov, et al., 1999a, 1999b; Blank, Popov, et al., 1993; Blank, Serebryanaya, et al., 1995; Popov & Koga, 2002; Popov, Koga, et al., 2002; Popov, Kyotani, et al., 2000; Popov, Kyotani, et al., 2001a, 2001b; Popov, Kyotani, et al., 2002a, 2002b, 2002d, 2002e; Serebryanaya, Blank, et al., 1995) of fullerites, exceeding the diamond hardness.

Obviously, indenter hardness should be higher than the hardness of the test material. For many years, this requirement has been a major obstacle to measure the hardness of diamond since there was no material harder than diamond. Diamond hardness measurement problems have been discussed in great detail

http://dx.doi.org/10.1016/B978-0-08-096527-7.00057-X

(Blank, Popov, et al., 1997a, 1997b; Blank, Popov, et al., 1998; Blank, Popov, et al., 1999a, 1999b; Field, 1992; Novikov & Dub, 1996; Sumiya, Toba, et al., 1997; Westbrook & Conrad, 1973; Wilks & Wilks, 1991). In investigations where a diamond indenter was used to measure the hardness of diamond, the resultant hardness values ranged from 56 to 257 GPa, clearly indicating problems associated with the indenter. In comparison, the hardness of c-BN hardness, which is in the class of superhard materials (Wentorf, DeVries, et al., 1980), ranged from 60 to 72 GPa (Blank, Popov, et al., 1997a, 1997b; Popov, Kyotani, et al., 2001a, 2001b; Popov, Kyotani, et al., 2002a, 2002b, 2002c, 2002d; Popov, Kyotani, et al., 2003a, 2003b) depending on the so-called hardness anisotropy (Blank, Popov, et al., 1999a, 1999b; Grigorovich, 1976; Sumiya, Toba, et al., 1997). As is well established, single-crystal hardness depends on the crystallographic planes and directions, and other crystal characteristics. Problems with the measurement of the hardness of diamond have been solved by using an ultrahard fullerite tip (which exceeds the hardness of diamond) as an indenter (Blank, Popov, et al., 1997a, 1997b; Blank, Popov, et al., 1998; Blank, Popov, et al., 1999a, 1999b; Field, 1992; Novikov & Dub, 1996; Sumiya, Toba, et al., 1997; Westbrook & Conrad, 1973; Wilks & Wilks, 1991). The hardness of a nitrogen-free (0.3 ppm nitrogen impurity) diamond, depending on hardness anisotropy, is between 139 and 175 GPa, while for a diamond with nitrogen content of 200 ppm, it is between 115 and 151 GPa.

It should be noted that the hardness of diamond and c-BN was specifically measured to calibrate this new methodology and to correctly measure the hardness of ultrahard fullerite and other superhard fullerite phases (Blank, Popov, et al., 1997a, 1997b; Blank, Popov, et al., 1998; Blank, Popov, et al., 1999a, 1999b; Popov, Koga, et al., 2002).

The elastic properties of the materials are related to their structure, along with other parameters such as hardness, and help determine their application area as structural materials. Additionally, high elastic modulus may indicate substantial strength (Sung & Sung, 1996; Teter & Hemley, 1996), although there is no direct correlation between these parameters (Gilman, 1993). Therefore, while developing a new material, it is desirable to obtain some information on its mechanical properties, even at a diamond cell research stage.

3.20.2 Harder than Diamond Carbon Materials Synthesis Possibilities

3.20.2.1 Strength Properties Variations for Materials with Similar Elastic Moduli

Superhard materials (materials with hardness from c-BN to diamond (Wentorf, DeVries, et al., 1980)) can be conditionally divided into intrahard and extrahard. According to Veprek (1999), an approximately linear dependence of the strength to the elastic modulus is typical of the intrahardness materials; while for materials with extrahardness, strength depends more on the nanostructuring effect than on the elastic modulus. In the materials with an extrahardness effect, strength can be controlled by changing the plastic deformation mechanisms in the nanostructured materials. Thus, material strength can be increased by 3–7 times, as shown in the case of superhard nanocrystalline composites (Nesladek & Veprek, 2000; Veprek, 1999). This division is somewhat conventional since material strength in both cases is determined by the plastic deformation mechanism. For example, the bulk modulus of osmium, according to various sources, is 395 ± 15 (Takemura, 2004), 411 ± 6 (Occelli, Farber, et al., 2004) of 462 GPa (Cynn, Klepeis, et al., 2002), and is comparable to that of diamond, but Os is not even classified as a hard material. However, for covalently bonded materials, a linear dependence of hardness on the elastic modulus can be accepted, at least, as an empirical relationship for materials with intrahardness, and can be used to predict the mechanical properties of the new materials (Clerc & Ledbetter, 1998; Lowther, 2000; Teter & Hemley, 1996; Veprek, 1999).

The problem of differences between materials with similar elastic moduli has been investigated. The criterion to evaluate the accepted limit to which a material can be hardened is usually based on a theoretical strength model (theoretical limit shear stress model), proposed by Frenkel (1926). He estimated the shear stress τ^*_{theor} required to shift a single atomic plane of a crystal relative to the neighboring plane. Assuming the transfer energy sinusoidal dependence per unit length and the level of the strain under which Hooke's law works, he obtained the following estimate for the theoretical limit shear stress:

$$\tau^*_{\text{theor}} = Gb/2\pi d \tag{1}$$

where G is the shear modulus, b, the lattice vector transmission value, and d, the interplanar distance. A more precise consideration of the interatomic attraction forces and inclusion of different stable configurations in the lattice reduce the estimate of the theoretical limit shear stress (Hirt & Lote, 1972). In the end, after some modifications to the Frenkel model, the theoretical limit shear stress value was set as (Dieter, 1986; Šandera & Pokluda, 1993)

$$\tau^*_{\text{theor}} \approx G/10 \tag{2}$$

It is noteworthy that the shear modulus of aluminum and copper is almost the same as that of silicon, but their single-crystal samples hardness is 30 times less than that of the silicon hardness due to different plastic deformation mechanisms (Gilman, 1993). The plastic deformation mechanism for metals is well described by a dislocation theory, including the temperature dependence of yield stress (Hirt & Lote, 1972). Typically, the resistance to dislocation motion in metals is a thermally activated process, and the yield stress for a single crystal is conditioned by such factors as resistance to dislocation motion exerted by the lattice, the dislocations interaction, the alloy addition impact, dispersion hardening, the interaction with point defects, and so on.

Strength of polycrystalline materials can be controlled by changing the plastic deformation mechanisms (the extrahardness effect). The Hall–Petch relation empirically linked yield strength σ_s with grain size d: $\sigma_s = \sigma_0 + K \cdot d^{-1/2}$, where σ_0 and K are constants (Hall, 1951; Petch, 1953). There are various dislocation models describing this relation, in particular, Veprek (1999). With decreasing grain size to <10–50 nm, the intergrain sliding factor has a significant effect on the strength, and in some cases that may lead to a decrease in strength (Veprek, 1999). With material structure optimization, superplasticity effect can be observed, while maintaining the high-strength properties (Valiev, 2004). Creating nanocomposites can suppress the intergrain sliding mechanism, thereby greatly increasing the strength (Koehler, 1970; Veprek, 1999). Thus, the strength of aluminum, nanostructured and modified by a C_{60} fullerene (Popov, Medvedev, et al., 2010), approaches the theoretical limit shear stress of aluminum.

3.20.2.2 Diamond and Other Covalent Crystals Strength and Theoretical Strength

The dislocation plasticity mechanism developed for metals poorly describes the covalent crystals behavior (Gilman, 1993, 2002). The main difference is that the covalent bond has a pronounced directional property (the potential energy depends essentially on the bond angle change) (Madelung, 1996). In covalent crystals (such as germanium, silicon, and diamond), plastic deformation caused by dislocation motion is observed mainly at temperatures above the Debye temperature (Gilman, 1993; Brookes, Comins, et al., 2000).

Plastic deformation of diamond, at room temperature, was first observed in a high-nitrogen diamond anvil at a pressure of 170 GPa (Mao, Bell, et al., 1979), but its strength was not reported. A limited number of studies are known where diamond plasticity was observed at room temperature and quantitative strength measurements were made at the same time (Blank, Popov, et al., 1997a, 1997b; Blank, Popov, et al., 1998; Blank, Popov, et al., 1999a, 1999b; Field, 1992; Novikov & Dub, 1996; Sumiya, Toba, et al., 1997; Westbrook & Conrad, 1973; Wilks & Wilks, 1991). Initially measurements via indentation of diamond with an indenter made of the material harder than diamond (ultrahard fullerite) were carried out by (Blank, Popov, et al., 1997a, 1997b; Blank, Popov, et al., 1998; Blank, Popov, et al., 1999a, 1999b). In particular, it was shown that diamond plasticity deformation at the indentation, and for the nitrogen-free IIa-type diamond, hardness H is 150–175 GPa, for the faces (100) and (111), respectively. In this case, the yield stress τ^* could be estimated from the hardness value $\tau^* = 0.33H$ (Gilman, 1975a, 1975b), and was about 54 GPa. The value obtained agreed well with the direct measurement of the maximal shear stress of 55 GPa (Popov, 2010) identified in the study of attainable pressure in a shear diamond cell. Upon reaching a shear stress of 55 GPa, a phase transition into a new phase was observed, which indicates lattice stability loss before initiation of plastic deformation via the dislocation mechanism. The diamond lattice instability which manifests itself in a phase transition was also observed in the experiments on the diamond indentation with a diamond indenter (Gogotsi, Kailer, et al., 1997; Gogotsi, Kailer, et al., 1998; Gogotsi, Kailer, et al., 1999). For comparison, in experiments with ultrahard fullerite indentation, although plastic deformation occurred, it was not accompanied by a phase transition. Model studies (from the first principles) on the dependence of shear stress on deformation show that the diamond lattice instability occurs almost immediately after reaching the theoretical limit shear stress (Roundy & Cohen, 2001). Most likely, this explains the observations that at similar values of critical shear stress, in some cases, plastic deformation is observed, while in other cases, there is a phase transition.

Maximum shear stress of 65–70 GPa was estimated (Eremets, Trojan, et al., 2005) based on the experiment results when a superhard material (c-BN) was compressed between diamond anvils to pressures of about 200 GPa. However, in the latter case, the stress tensor spherical part (pressure) was significantly higher which likely led to an increase in τ^* (τ^* grows with increasing pressure (Chua & Ruoff, 1975)). Thus, the diamond yield stress at room temperature measured in various experiments was $\tau^* = 55$ GPa (Blank, Popov, et al., 1997a, 1997b; Blank, Popov, et al., 1998; Blank, Popov, et al., 1999a, 1999b; Popov, 2010).

To assess covalent crystals strength, Gilman designed a "chemical theory of dislocation mobility" (Gilman, 1993, 2002). In the proposed model, for materials formed by covalently bonded atoms, the dislocations activation energy is so high that the difference between the theoretical limit shear stress and the plasticity dislocation model virtually disappears, and the plastic deformation is accompanied by the breaking of bonds (Gilman, 1968, 1975a, 1975b). For covalent crystals, the model explains, in particular, the linear dependence of hardness on the shear modulus in the glide plane. In the case of crystals with other type of bonds (metals and ionic crystals), such dependence also exists, but it quantitatively differs by 10–100 times from the covalent crystals hardness with the same shear modulus values (Sirdeshmukh, Sirdeshmukh, et al., 2006), as mentioned above.

Interest in the Gilman model was focused on diamond strength evaluations which amounted to $\tau^* = 54$ GPa (shear stress required for dislocation motion) and were comparable to the theoretical limit shear stress (2). Indeed, the diamond shear modulus in the (111) G_{111} plane (Gilman, 2002) was defined as:

$$G_{111} = \frac{3C_{44}(C_{11} - C_{12})}{4C_{44} + (C_{11} - C_{12})} \tag{3}$$

and was equal to 507 GPa ($C_{11} = 108$ GPa, $C_{12} = 125$ GPa, and $C_{44} = 577$ GPa). Thus, diamonds theoretical limit shear stress (2) is equal to 51 GPa and practically coincides with the stress required to move the dislocation kink in the diamond (Gilman, 2002). To estimate the theoretical limit shear stress, the (111) plane was chosen as it is well known both from experiments and from simulation results that this plane provides the easiest cleavage in the diamond crystal and it is along these planes that the atom layers are most distant from each other.

The theoretical limit shear stress of diamond, silicon and germanium has been calculated from the first principles (Chacham & Kleinman, 2000; Ogata, Li, et al., 2004; Roundy & Cohen, 2001) and values of 95, 6.5 and 4.5 GPa, respectively, were reported. Herewith, the Peierls stresses calculated by the Peierls–Nabarro dislocation model were 7 GPa for Si and 6 GPa for Ge. In the case of silicon and germanium, the calculated data agreed well with the experimental fact that indentation in these materials showed some phase transitions, i.e. the lattice becomes unstable instead of plastic deformation (Kailer, Gogotsi, et al., 1977): Peierls stress is comparable to the theoretical limit shear stress, as it is for diamond. Perhaps, the theoretical limit shear stress of diamond, silicon and germanium, calculated from first principles, is somewhat overestimated. Ogata, Li, et al. (2004) estimated data analyzed in terms of their conformity with the classical Frenkel model. A good conformity was observed, and if a periodic lattice potential sinusoidal dependence was taken into account, higher values of the theoretical limit shear stress were obtained, as mentioned above.

Indeed, experimental data are lower than the data calculated from first principles (for silicon—on the average around 15%). Thus, the yield stress τ^*, estimated from the hardness value $\tau^* = 0.33H$, is 5.3 GPa for silicon. The theoretical limit shear stress, calculated by Formula (2), is equal to 5.8 GPa (silicon $C_{11} = 167$ GPa, $C_{12} = 65$ GPa, $C_{44} = 80$ GPa, and $G_{111} = 58$ GPa (Ogata, Li, et al., 2004)). As in the case of diamond, indentation experimental data are in good agreement with the theoretical limit shear stress calculated by Formula (2).

Based on the experimental and theoretical studies, it can be concluded that for materials formed by covalently bonded carbon atoms, the dislocations activation energy is so high that the difference between the concept of the theoretical limit shear stress and the plasticity dislocation model virtually disappears. This implies, in particular, that nanostructuring of diamond will not lead to an increase in strength. This assertion can be proved experimentally.

Indeed, in Sumiyaa and Irifune's (2004) investigation, the hardness of nanostructured nitrogen-free polycrystalline diamond with grain sizes of 10–20 nm was measured (Irifune, Kurio, et al., 2003), and was found to be the same as that of singe-crystal diamond measured under identical conditions (Sumiya, Toba, et al., 1997). Basically Hall–Petch dependence and accordingly the hardening mechanisms associated with dislocation motion characteristics, in the case of diamond, are not significant which confirms this assertion. For comparison, nanostructuring or amorphization in silicon does not also lead to an increase in hardness (Danesh, et al., 2011; Williams, Haberl, et al., 2005).

Thus, the mechanical properties of the materials formed by covalently bonded carbon atoms can be accurately evaluated with their elastic moduli.

3.20.2.3 Covalent Materials with Elastic Modulus Higher than Diamond

Elastic moduli in a general case are defined by both the interatomic interaction force constants (the second derivatives of the binding energy) and the relative atom position (in the crystal primitive lattice) (Born & Huang, 1954; Harrison, 1970; Peierls). For covalent crystals with diamond and zinc sulfide structure in the approximation of interatomic interaction only with the nearest neighbors and assuming a covalent bond cylindrical shape (Cohen, 1985) resulted in the following elastic modulus evaluation [GPa]:

$$B = 1761 d^{-3.5} \tag{4}$$

where d is the distance between the nearest neighbors [A]. Based on this relation, it was suggested that a hypothetical material based on C–N bonds could have a higher bulk modulus than diamond. Teter and Hemley (1996) using first principle calculations modeled a cubic C_3N_4 structure with a bulk modulus of 496 GPa—exceeding that of diamond. Bulk modulus of the latter, in accordance with similar calculations, was 468 GPa (experimental value 443 GPa). This material has not been synthesized although there were a number of studies on the C–N films synthesis with disordered structure, with hardness values reaching 60 GPa (Veprek, 1999), as well as graphite-like C_3N_4 (Montigaud, Tanguy, et al., 2000).

It is possible to obtain material substantially harder than diamond if its elastic properties are largely determined by the carbon atoms sp^2 bonds. Indeed, the interatomic distances in graphene layers (0.142 nm) are smaller than in diamond (0.154 nm). Accordingly, the speed of sound along the graphite layers (26.3 km/s) exceeds the speed of sound in diamond (19.6 km/s). However, for a material with properties mainly determined by sp^2 bonds between the carbon atoms, the model conditions in which Relation (4) has been achieved, will not work (Cohen, 1985), and an estimation based on already defined structures of the new material is required.

One possible sp^2 bonds three-dimensional distribution example is C_{60}, the fullerene molecule. In this molecule, the interatomic distance of 0.144 nm is close to the interatomic distances in a graphite layer. As in graphene, each atom in fullerene is bonded to three neighboring atoms with sp^2 bonds. As the molecule is mostly formed by hexagons (20 hexagons and 12 pentagons), this gives grounds for considering C_{60} as a graphene sheet folded in a sphere (Dresselhaus, Dresselhaus, et al., 1996). Meanwhile, there are slight differences between the atomic bonds in graphene and C_{60} [100], [101], and [102]. The bonds between the pentagons and hexagons are single with a 0.146 nm distance, and for hexagons, they are double with the distance 0.139–0.140 nm. Since, unlike graphite, sp^2 trigonal σ bonds in C_{60} do not lie in one plane, the C_{60} molecule is often regarded as formed by sp^2 bonds, with an admixture of sp^3 bonds (Dresselhaus, Dresselhaus, et al., 1996).

Extrapolating C_{60} by the folded graphene sheets allows accurate estimation of the single molecule bulk modulus $B_0 = 843$ GPa, using experimental data of the mechanical properties of graphite (in the planes formed by the graphene layers). According to the calculations in Ruoff and Ruoff (1991a, 1991b),

$$B_0 = \frac{2}{3}\frac{1.088}{(S_{11} + S_{12})}\frac{h}{R} \tag{5}$$

where S_{ij} is the elastic compliances in the graphite layer, R, the sphere radius, h, the graphene layer thickness and the coefficient of 1.088 takes into account that C_{60} has a shape of an icosahedron, not a sphere (in case of a sphere, this coefficient would be 1).

The calculation performed in Ruoff and Ruoff (1991a, 1991b) using the force constants for C–C interaction in a C_{60} molecule gave the following formula for B_0:

$$B_0 = 0.449(k/R) \tag{6}$$

where k is the average force constant, $k = 2/3\, k_1 + 1/3\, k_2$. Here, k_1 is the force constant for a bond along the pentagon edge and k_2, the force for a bond between the two hexagons; $k = 6.60$ mdyn/A (660 N/m), which gives $B_0 = 842$ GPa. For comparison, the force constant for graphite $k_G = 7.08$ mdyn/A, which is close to the average C_{60} value.

Studies of Ruoff and Ruoff (1991a, 1991b) provided bulk modulus estimation for a hypothetical material formed by noninteracting C_{60} molecules under 20 GPa pressure when the graphene layers connected by weak Van der Waals bonds became much closer (Yagi, et al., 1992). Therefore, the hypothetical material bulk modulus, if the molecules in it were packed into a dense face-centered cubic (fcc) lattice (with a filling factor 0.74), using additive fractions rule would be $B = 843 \times 0.74 = 624$ GPa. A more complex model that includes simulation from first principles (Wang, Tománek, et al., 1991) gives qualitatively the same result: with increasing pressure, the bulk modulus of a C_{60} hypothetical material exceeds that of diamond at pressures above 70 GPa (taking into account the fact that the diamond modulus increases with pressure as well).

3.20.2.4 Bulk Modulus and Hardness of the Materials Formed by Polymerized Carbon Nanoclusters

In fullerites, under conditions of controlled shear deformation under pressure, intermolecular covalent sp^3 bonds form, and that allows synthesis of three-dimensional fullerite polymers (Blank, Buga, et al., 1998a, 1998b, 1998c, 1998d, 1998e; Blank, Popov, et al., 1994; Popov, Koga, et al., 2002). In this case, contribution of the bonds formed must also be considered as the materials' elastic modulus is determined by all the interatomic interaction of force constants and the relative positions of all atoms. Calculations from first principles (Adams, Page, et al., 1994) have shown several options for a possible C_{60} polymerization. The first variant, the so-called $2+2$ cycloaddition mechanism, is well known and was first investigated in the C_{60} dimers formation during photopolymerization (Adams, Page, et al., 1994; Blank, Buga, et al., 1998a, 1998b, 1998c, 1998d, 1998e; Porezag & Frauenheim, 1999; Porezag, Pederson, et al., 1995; Rao et al., 1993). In this case, two covalent bonds and a four-member ring occur between the two C_{60} molecules. Both dimers and linear chains may be formed by this mechanism as well as polymerized C_{60} two- and three-dimensional structures (Blank, Buga, et al., 1998a, 1998b, 1998c, 1998d, 1998e).

There are also options when there are six bonds between two hexagons (6 +6) or five bonds between two pentagons. The latter option, however, is less favorable from an energy point of view (Adams, Page, et al., 1994).

O'Keeffe (1991) proposed the variant of a body-centered cubic (bcc) structure formed by C_{60} molecules connected by a (6 +6) mechanism. Such 3D polymerization leads to the fact that some smaller sized polyhedra of fragments of C_{60} and four-member rings connecting the neighboring C_{60} form between the C_{60}. At each bcc cell of this structure, there are six distorted truncated octahedrons (consisting of 8 hexagons and 6 squares, 24 atoms, with a diameter of about 4.5 A) and six 12-hedra (consisting of four hexagons, four pentagons and four squares, the diameter is about 4 A).

Based on X-ray data, and using the possibility of forming six bonds between two hexagons, an ultrahard fullerite structure element has been proposed consisting of four C_{60} molecules mutually linked by six covalent bonds (6 +6) and forming a tetrahedron (Blank, Buga, et al., 1998a, 1998b, 1998c, 1998d, 1998e; Blank, Buga, et al., 2001). In this case, a polyhedron with a diameter of about 4 A, consisting of 22 carbon atoms, forms between the molecules.

The bulk modulus of the 3D polymerized by a (6 +6) mechanism structure is relatively simple to estimate since the material bulk is occupied by the C_{60} molecules (0.68 of a volume for a bcc lattice or 0.74 for an fcc-lattice). Therefore, the possible error of estimation will be reduced by a relatively small contribution (according to the additivity fractions rule) of the newly formed bonds.

Clusters with a diameter of about 4–4.5 A formed between the C_{60}, in both cases, are a closed surface formed by covalently bonded carbon atoms. C_{20}, C_{24} and C_{36}, unlike that described in the literature (Iqbal, Zhang, et al., 2003; Park, Srivastava, et al., 2001; Piskoti, Yarger, et al., 1998), they contain four-member rings. Nevertheless, the atom surface density for C_{20}–C_{22} and C_{60} (about 2.5 Å/atom) are close. Therefore, for the first approximation, the bulk modulus for C_{60} can be scaled by substituting the cluster radius by 2–2.2 Å in Formula (5) or (6). We should also take into account that such a cluster is formed by sp^3 bonds that are weaker than sp^2 bonds in C_{60}. To roughly estimate the elastic compliance ratios S_{sp^3}/S_{sp^2} of surfaces formed by sp^3 and sp^2 bonds, respectively, the k_{sp^3}/k_{sp^2} force constants ratio can be used where the force constants are proportional to the phonon frequencies squares (Born & Huang, 1954). To estimate the sp^2 bonds frequencies, it is possible to choose $E_{2g}(2)$ mode 1580 cm^{1} for a graphite plane. As discussed in detail (Ferrari & Robertson, 2000), this mode is a bond-stretching mode of a pair of sp^2-bonded carbon atoms. Accordingly, to assess the sp^3 frequencies, a 1333 cm^{-1} diamond mode is chosen. Both of these modes are close to the maximum possible for graphite and diamond. Thus, $S_{sp^3}/S_{sp^2} = k_{sp^2}/k_{sp^3} = (1581/1333)^2 = 1.4$ and the bulk modulus calculated by Formula (5) or (6) as estimated for clusters C_{20-22} is $B_{C20-22} \approx 1000$ GPa.

Thus, in the case of C_{60} three-dimensional polymerization, forming the maximum possible number of sp^3 bonds between the molecules, the 3D fullerite bulk modulus is around 900 GPa as the entire volume is filled with C_{60} molecules with an 843 GPa modulus and C_{20-22} clusters with a 1000 GPa modulus.

According to the bulk modulus obtained, the ultrahard fullerite hardness can be estimated. Based on the pure diamond module of 443 GPa, and its average hardness of 160 GPa (150 and 175 GPa, respectively, for the nitrogen-free IIa-type diamond faces (100) and (111) (Blank, Popov, et al., 1999a, 1999b)), the ultrahard fullerite hardness will be about 320 GPa. As shown below, the modulus and hardness calculated within the model comply with the experimental values with good accuracy.

In fact, the structures considered, as in any model, can be somewhat idealized: in the experiments for the 3D C_{60} phases, distorted bcc and fcc structures are observed (Blank, Buga, et al., 1998a, 1998b, 1998c, 1998d, 1998e; Blank, Kulnitskiy, et al., 2005; Blank, Zhigalina, et al., 1997). Apparently, this is due to the fact that C_{60} does not have the fourth-order rotation axes (Dresselhaus, Dresselhaus, et al., 1996). Thus, the obtained elastic modulus assessment of 900 GPa can be regarded as the maximum possible for 3D C_{60}.

Depending on the bonds between the C_{60} distribution, which in turn depends on the synthesis parameters (stress tensor, plastic strain and temperature), polymerized 3D C_{60} phases with smaller modules can be obtained. For example, the bulk modulus was estimated by numerical simulation for the case of 3D fullerite formed by $(2+2)$ and $(3+3)$ cycloaddition mechanisms along the different crystallographic axes (Chernozatonskii, Serebryanaya, et al., 2000; Serebryanaya, Blank, et al., 2001). Depending on the C_{60} packing, the modulus values were 530 and 800 GPa, as can be expected with a smaller number of intermolecular bonds below the value obtained for the case of six bonds between the two hexagons discussed above. As shown below, the hardness of such materials also reduced in proportion to their modules, which complies with the presented concept.

The maximum possible density of 3D C_{60} is 2.5 g/cm^3. However, experimentally anomalously high bulk modulus (>1000 GPa) is observed for the amorphous structures (we conditionally call them 3D C_n), synthesized from C_{60} in the toroid cell at a pressure of 13 GPa and a temperature of 1770 K has a density of 3.3 g/cm^3 (Levin, Blank, et al., 2000; Prokhorov, Blank, et al., 1999) (for comparison, the density of diamond, which has a smaller bulk modulus of 442 GPa, is 3.51 g/cm^3). Transmission electron microscope (TEM) and X-ray studies have shown that 3D C_n structures have no nanocrystalline or amorphous diamond in them. Moreover, the formation of diamond-like areas in the 3D C_{60} samples would reduce the hardness (as the diamond strength is equal to its theoretical strength, which is less than the 3D C_{60} strength) and the bulk modulus. Reduction in hardness is in fact observed with an increase in the synthesis temperature to 2100 K, followed by diamond formation in the samples (Blank, Buga, et al., 1998a, 1998b, 1998c, 1998d, 1998e).

Raman analysis (Blank, Buga, et al., 1998a, 1998b, 1998c, 1998d, 1998e; Blank, Popov, et al., 1994; Popov, Koga, et al., 2002) show that 3D C_n structure formation is not accompanied by a noticeable change in Raman spectra compared to 3D C_{60}, indicating the structural elements preservation in the form of curved covalently bound planes.

The structural elements having a greater modulus and density than the C_{60} are partly present in 3D C_{60}. As discussed earlier, these are C_{20-22} clusters with the bulk modulus of 1000 GPa. Therefore, such clusters can formally be considered as the new phase nuclei, and an increase in pressure, temperature, or an additional sample deformation during the synthesis can lead to a rearrangement of C_{60} in the smaller sized clusters (C_{14}–C_{24}), which will connect the existing clusters, i.e. will complete the structure initially defined by the polyhedra formed at C_{60} polymerization. The covalent bond angle in the C_{14}–C_{24} fullerene clusters is close to the tetrahedral sp^3 arrangement (Iqbal, Zhang, et al., 2003; Park, Srivastava, et al., 2001; Piskoti, Yarger, et al., 1998). Therefore, to describe the amorphous 3D C_n structure, a hard sphere random close packing model can be used (Suzuki, Fujimori, et al., 1982). In this model, space can be filled with Bernal polyhedra, which contain an atomic sphere at each vertex. Half of the amorphous material cavities space falls on the octahedral and tetrahedral cavities in the 1:2.5 ratio and the other half, on the complex polyhedra. Thus, space in an amorphous carbon material can be filled by sp^3-bonded atoms and the structure element will not be an amorphous diamond, but some more stringent fullerene-like clusters with the bulk modulus, as shown above, of about 1000 GPa. Accordingly, the amorphous 3D C_n bulk modulus will also be about 1000 GPa.

For a comprehensive analysis of possibilities to synthesis of ultrahard materials, carbon nanotubes should be considered. Nanotubes are accurately described by a graphene plane rolled into a cylinder, which has been confirmed by numerous experiments and simulation studies. In particular, an adding zones method was applied to calculate the nanotubes phonon spectra (Dresselhaus, Dresselhaus, et al., 1996; Jishi, Venkataraman, et al., 1995) using data for graphene layers (AI-Jishi & Dresselhaus, 1982). Even ignoring the graphene layer curvature in a nanotube, a good agreement between the calculated and the observed Raman modes for nanotubes was obtained (Dresselhaus, Dresselhaus, et al., 1996; Jorio, Saito, et al., 2001; Pimenta, Jorio, et al., 2001; Rao, Richter, et al., 1997; Rinzler, Liu, et al., 1998). Using molecular dynamics (Chernozatonskii, Menon, et al., 2001; Chernozatonskii, Richter, et al., 2002) has investigated the possibility to synthesize polymerized (linked by sp^3 bonds) nanotubes with a diameter of 1 nm with different chirality. The polymerized nanotubes bulk modulus of 420 GPa was also estimated. The value obtained complies well with experimental data presented below (the bulk modulus of 465 GPa and hardness at the diamond level).

3.20.3 Mechanical Properties Research under Pressure in Shear Diamond Anvil Cells on Ultrahard Fullerite and Superhard Nanotubes

3.20.3.1 Hardness and Yield Stress

It has been observed (Blank, Popov, et al., 1994) that C_{60} fullerene at a pressure of 18 GPa in a shear diamond anvil cell (SDAC) goes into phase V, which is ultrahard, i.e. exceeds the diamond hardness. To initiate this transition, controlled shear deformation was applied to the loaded sample under a pressure of 20 GPa by rotating one of the anvils around the load axis. The sample was loaded in a gasket. When rotating the anvils, the sample started slipping along one of the anvils' culet, leaving the tracks of ploughing with 1–2 μm width on the diamond surface. The tracks were located along the arcs, the lengths of which corresponded to the anvil rotation angle (10°). The tracks are formed by plastic deformation of the diamond, without cracking.

Ploughing the diamond with an ultrahard fullerite sample is possible only when the ultrahard fullerite hardness exceeds the hardness of diamond. It is this experiment that served as the first and direct evidence of ultrahard fullerite hardness exceeding that of the diamond.

The very fact that the sample slips over the anvil at a pressure of 20 GPa (regardless of whether there is ploughing) indicates that the yield stress of ultrahard fullerite exceeds 20 GPa. Indeed, at high compressive loads, the friction becomes adhesive and the friction coefficient is equal to 1 (Bridgman, 1935; Johnson, 1985); i.e. the friction force is equal to the normal stress (20 GPa in the experiment). To exceed the friction force and begin sliding instead of internal plastic deformation, the samples yield stress must be >20 GPa. In the experiments by Popov and Koga (2002), Popov, Koga, et al. (2002) and Popov, Kyotani, et al. (2003a, 2003b), sample sliding, followed by ploughing of the diamond, was observed at a pressure of 55 GPa. Therefore, ultrahard fullerite yield τ^* exceeds 55 GPa, i.e. as shown above, the maximal shear stress of diamond τ^* is just equal to 55 GPa.

3.20.3.2 Bulk Modulus

The bulk modulus of a material can be defined by the phonon frequency dependence on the pressure, for example, by Raman scattering or the infrared spectra absorption (Weinstein & Zallen, 1984), recorded under pressure in a diamond anvil cell, if one knows the corresponding Gruneisen coefficient. For the ω_i phonon frequency, the Gruneisen coefficient is defined as

$$\gamma_i = -\frac{\partial \ln \omega_i}{\partial \ln V} = \frac{1}{\beta}\frac{\partial \ln \omega_i}{\partial P} \tag{7}$$

where β is the isothermal bulk compressibility and γ_i, the Gruneisen coefficient for the quasi-harmonic mode with ω_i frequency (Weinstein & Zallen, 1984; Grimvall, 1999).

In single-walled nanotubes (SWNTs) and C_{60} fullerene polymerization process research, data on high-frequency Raman spectra dependence on pressure were obtained (Popov, Koga, et al., 2002; Popov, Kyotani, et al., 2002a, 2002b, 2002c, 2002d; Popov, Kyotani, et al., 2003a, 2003b). For superhard polymerized nanotubes (SP-SWNTs), it is the dependence for the 1594 cm^{-1} mode, and for the ultrahard fullerite (Phase V), it is the dependence for the 1570 cm^{-1} mode. As discussed in detail in Ferrari and Robertson (2000), these modes relate to the bond-stretching mode of a pair of sp^2-bonded carbon atoms. The appearance of this mode in the material phonon spectrum does not require any graphene structures, and it lies in the 1500–1630 cm^{-1} frequency range. Moreover, it is these bonds that determine the polymerized 3D structures stiffness based on carbon nanoclusters (C_{60}, nanotubes).

To calculate the bulk modulus, some assumptions on the materials structure are required. For group IV semiconductors covalent bonds, $\gamma \approx 1$ (Weinstein & Zallen, 1984) are characteristic and, in particular, for a graphene plane, according to various sources $\gamma = 1.06$ (Hanfland, Beister, et al., 1989) to 1.11 (Goncharov & Andreev, 1991) and for a diamond, $\gamma = 0.96$ (Hanfland, Syassen, et al., 1985). For SWNTs, the Gruneisen coefficient $\gamma = 1.24$ was calculated (Reich, Jantoljak, et al., 2000). The average experimental value of $\gamma = 1.1$ for both (SP-SWNT and ultrahard fullerite) 3D polymerized structures based on carbon nanoclusters was assumed.

In principle, one could directly use the experimental dependencies ω_i (P) (Popov, Kyotani, et al., 2002a, 2002b, 2002c, 2002d) and Formula (7) to directly determine the corresponding bulk modulus. However, it is possible to significantly increase the accuracy and reliability of the modulus values (Popov, Kyotani, et al., 2003a, 2003b). The fact is that the sample is in essentially nonhydrostatic conditions, namely, the difference between the maximum and minimum principal stresses in the superhard materials samples compressed between the diamond anvil cells, can be substantial and determined by the materials yield strength. As shown above, the ultrahard fullerite yield stress (equal to half the difference between the maximum and minimum principal stresses) exceeds 55 GPa. In addition, as discussed in detail in Popov (2004), only the normal stress in the sample can be measured correctly. It is therefore more precise to consider the phonon mode shift toward a piezoelectric sensor (sample) with known properties, located in close stress conditions.

Such a piezoelectric sensor is always available in experiments carried out in diamond anvils (Popov, 2004). Raman spectra of stressed diamond anvils shift to higher frequencies of the spectrum and split into a ω_s singlet and a ω_d doublet mode. Herewith, the mode splitting is proportional to the stress tensor deviator part (pure shear) and the split mode centroid displacement $\omega_c = (\omega_s + 2\omega_d)/3$ is proportional to the stress tensor spherical part. If the sample is isotropic, there is one line and its displacement is proportional to the stress tensor spherical part. In the case of a superhard sample, as the sample and the anvil mechanical properties are similar, their stress tensors are also close.

Figure 1 shows the SP-SWNTs 1594 cm^{-1} frequency mode and ultrahard fullerite (Phase V) 1570 cm^{-1} mode relative displacement $\Delta\omega/\omega_0 = (\omega - \omega_0)/\omega_0$ dependencies on the relative centroid displacement $\Delta\omega_c/\omega_0$ (ω_0—the mode frequency ω_i at $P = 0$). At the sample Raman spectra registration, the strained diamond anvil Raman spectrum is always recorded simultaneously. Therefore, it is always possible to compare the sample Raman spectrum to the centroid from the anvil.

To study the displacement of the sample phonon mode with respect to the piezospectroscopy sensor, Relation (7) can be represented as follows:

$$\frac{B_{sample}}{B_{diamond}} = \frac{\gamma_{sample}}{\gamma_{diamond}} \cdot \frac{(\Delta\omega/\omega_0)_{diamond}}{(\Delta\omega/\omega_0)_{sample}} \tag{8}$$

where B is the bulk modulus and ω_0 is the mode frequency ω_i at $P = 0$.

The least squares dependency for SP-SWNT:

$$\Delta\omega_{\text{sample}}/\omega_0\big|_{\text{SP-SWNT}} = 1.09\Delta\omega_c/\omega_0$$

The least squares dependency for the ultrahard fullerite:

$$\Delta\omega_{\text{sample}}/\omega_0\big|_{\text{phaseV}} = 0.87\Delta\omega_c/\omega_0$$

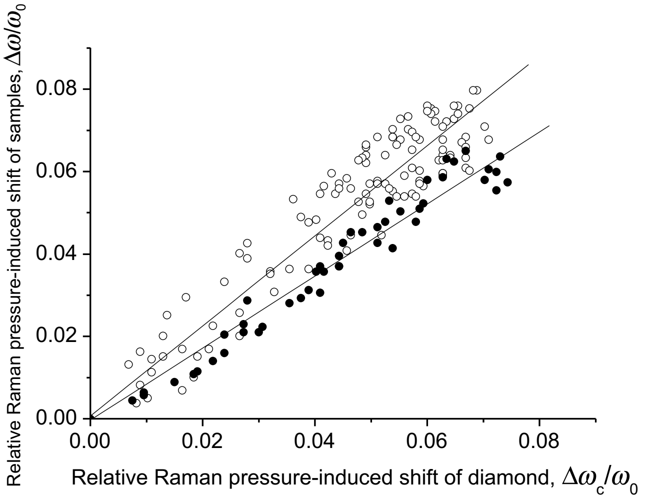

Figure 1 The relative Raman ($(\omega - \omega_0)/\omega_0$) pressure-induced shifts are plotted against the relative diamond Raman pressure-induced shift of the centroid $\Delta\omega_c/\omega_0$ (Popov, Kyotani, et al., 2003a, 2003b).

Single-crystal bulk modulus of diamond is 443 ГПа (Prokhorov, Blank, et al., 1999) and as noted above, $\gamma_{\text{diamond}} = 0.96$ and $\gamma_{\text{sample}} = 1.1$. Thus, the corresponding SP-SWNT bulk modulus calculated by Formula (8) (Popov, Kyotani, et al., 2003a, 2003b) is

$B_{\text{SP-SWNT}} = 465$ GPa (close to diamond)

And 3D C_{60} phase V bulk modulus (Popov, Kyotani, et al., 2003a, 2003b) is

$B_{\text{3D C60-V}} = 585$ GPa (exceeds the diamond by 30%)

Module values obtained correspond to the estimates made within the outlined above concept of the materials formed by polymerized carbon nanoclusters. In addition, the high 3D C_{60} bulk modulus value, higher than diamond, correlates with the fact that its strength and hardness are also superior to the diamond.

3.20.4 The Superhard and Ultrahard Carbon Materials Mechanical Properties Comparative Analysis

3.20.4.1 Sclerometry Hardness Testing

The sclerometry hardness measurement technique using a scanning probe microscope NanoScan (Blank, Popov, et al., 1997a, 1997b; Blank, Popov, et al., 1998; Blank, Popov, et al., 1999a, 1999b) was developed specifically to study the superhard and ultrahard materials. The device enables indentation or scratching the surface with the indenter load up to 0.1 N. The surface is scanned before and after the indentation/scratching. The indenter is made with either diamond or ultrahard fullerite.

As discussed above, the indenter material must be harder than the test material as described in the previous section for the SDAC-synthesized ultrahard fullerite. However, for ultrahard fullerite samples synthesized in toroid-type cells (Blank, Buga, et al., 1998a, 1998b, 1998c, 1998d, 1998e; Popov, Koga, et al., 2002) that were used to manufacture NanoScan indenters, the hardness was not determined. Using the simplest Moos method of visual observation of scratches with an optical microscope did not give a definite answer. The diamond surface was scratched by both the diamond and the ultrahard fullerite sample, and the scratch images were not as sharp as those obtained in SDAC. Increase in load led to the macroscopic cracks formation and test samples destruction. The IIa-type diamond hardest face (111) was tested.

The problem was resolved by observing scratches via NanoScan. Figure 2 shows the image of the scratches on the (111) diamond plane made by a diamond indenter. No traces of plastic deformation were observed, but multiple cracks systems were clearly visible, including ring cracks that are typically observed in diamond wear,

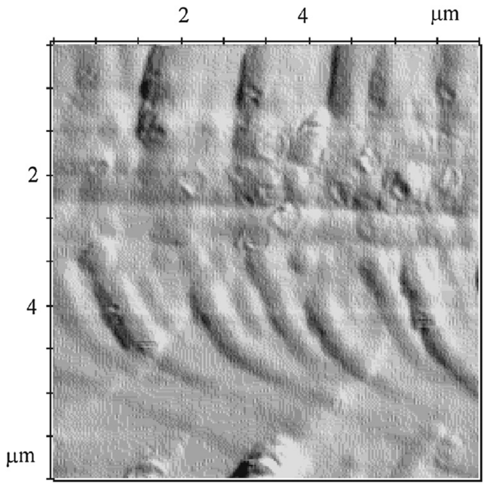

Figure 2 An image of the scratches on a diamond plane (111) made with a diamond indenter. In the picture, there are no traces of plastic deformation, but the multiple cracks systems are clearly visible (including ring cracks, which are usually regarded as a diamond wear mechanism). The result (formation of numerous cracks, their morphology, and no traces of plastic deformation) did not depend on the type of diamond used for the indenter: IIa or carbonado (Blank, Popov, et al., 1997a, 1997b).

which is characteristic (Wilks & Wilks, 1991). The result (formation of numerous cracks, their morphology, and no traces of plastic deformation) did not depend on the type of diamond indenter used namely IIa or carbonado (Vereschagin & Slesarev 1969 (3)).

Essentially a different result was obtained when scratching the (111) diamond plane with an ultrahard fullerite indenter (**Figure 3**). The scratch formed via plastic deformation of the diamond without cracking, i.e. the ultrahard fullerite hardness is sufficient to intrude a diamond, in contrast to a diamond indenter, and its hardness exceeded the hardness of a diamond.

The possibility plastic deformation of diamond at room temperature is of separate scientific interest and is also essential to the correct measurement of hardness with an ultrahard fullerite indenter. The plastic deformation of diamond, at room temperature, was for the first time observed in a high-nitrogen diamond anvil at a pressure of 170 GPa (Mao, Bell, et al., 1979). Typically, the plastic deformation was observed only at temperatures above 1200–1400 K (Wilks & Wilks, 1991).

In sclerometry measurements (Grigorovich, 1976), hardness H is

$$H = kP/b^2 \tag{9}$$

where k is the indenter form-factor, P, the load on the indenter, and b, the width of the scratches. The indenter form-factor is an important parameter influencing the test results, especially at the submicron scale (Mencik & Swain, 1995). However, indenter production of the ultrahard fullerite with repeatable accuracy sufficient for measurements is a relatively difficult task: the material, as shown below, is hard to process. Therefore, a special technique for calibrating the indenter was developed. In the standard procedure, there is a given load on the indenter P and if the measured scratch width is b, then in the proposed technique, b is kept constant (0.6 μm in this case), P_{sample} is measured, and the form factor k can be determined from the calibration sample of known hardness H_{calibr}. When calibrating, width of the scratches should be the same as test standard (0.6 μm). Thus, the form factor is excluded from Formula (9) and the sample hardness H_{sample} is determined from

$$H_{\text{sample}}/H_{\text{calibr}} = P_{\text{sample}}/P_{\text{calibr}}$$

where P_{calibr} is the indenter load at calibration and P_{sample}, the indenter load at sample test. The calibration sample hardness should be as close as possible to the test sample hardness. In this study, we used a sapphire sample as the calibration sample. Scratching is made under the "edge forward" scheme. The indenter load rise time before scratching is 10 s, scratching time is 2 s, and the scratch length is 2.5 μm.

To simplify the procedure, it is possible to vary the scratch width in the range of 0.5–0.7 mm, followed by interpolation by Formula (9). For this purpose, a series of scratches (usually five scratches) are made on the calibration sample under different loads.

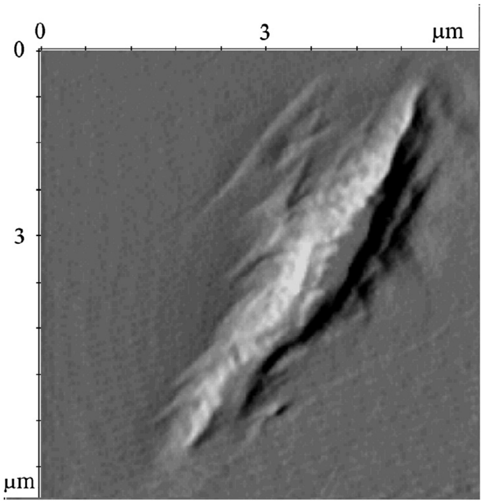

Figure 3 An image of a diamond plane (111) scratched with an ultrahard fullerite indenter. The scratch is formed by diamond plastic deformation without cracking (Blank, Popov, et al., 1997a, 1997b).

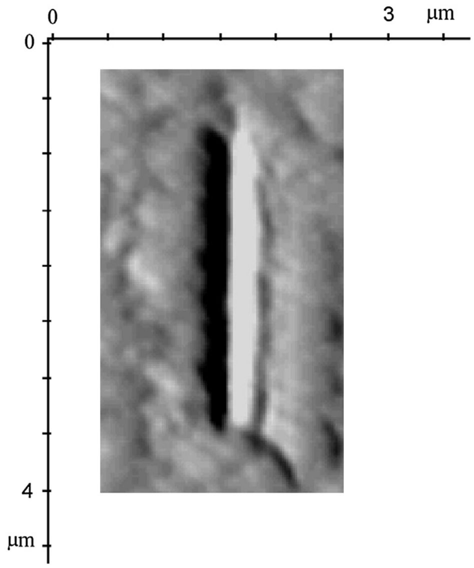

Figure 4 A calibration scratch image made and scanned by the NanoScan device on the sapphire surface. At the end of the scratch (image bottom), a characteristic pile is visible formed by the material plastic flow, and also there are some small plastic piles-ups on the sides of the scratch (Blank, Popov, et al., 1999a, 1999b).

Study by Grigorovich (1976) shows that the indentation method and the sclerometry method conform well with each other. There are various indenter options for the indentation method (Vickers, Knoop, Berkovich, etc.), which, however, give similar results. The Vickers method was chosen for calibration. The measurements were made with a PMT-3 hardness tester. The samples were prepared for the measurements according to the requirements set in study (Grigorovich, 1976).

The technique was tested on a number of materials. There is good agreement between the developed technique and the standard indentation methods. About 15 ultrahard fullerite indenters for NanoScan were used. The indenter form-factor, calculated by Formula (9), ranged from 1.5 to 3.5, which is typical of such measurements (Mencik & Swain, 1995).

The method described was applied to measure the diamond hardness. In the experiments, the synthetic nitrogen-free diamonds (0.3 ppm of nitrogen impurity), produced by FSI TISNCM, and diamonds with a 200 ppm nitrogen content produced by Almazot (Belarus), were used. We measured the (111) and (100) diamond planes hardness. The scratching direction on the (100) plane was carried out in the crystallographic directions ⟨100⟩ and ⟨110⟩. At (111) plane, the crystallographic scratching direction was not monitored since it was not expected to face strong mechanical properties anisotropy (Wilks & Wilks, 1991). **Figure 4** shows an image of the gauge scratches made and scanned by the NanoScan device on the sapphire surface. At the end of the scratch (image bottom), a characteristic pile is visible formed by the material plastic flow, and also there are some small plastic piles-ups on the sides of the scratch. **Figure 5** shows the image of scratches made on the diamond surface (with a nitrogen content of 200 ppm) at (100) plane in the ⟨110⟩ direction. At the end of the scratch (see image bottom), a characteristic pile is also visible, formed by the material plastic flow, and also there are some small plastic piles-ups on the sides of the scratch, similar to the macroscratch tests (**Figure 3**).

If a diamond indenter is applied instead of an ultrahard fullerite indenter for NanoScan, diamond measurements become impossible. As with macrotests (**Figure 2**), an attempt to scratch a diamond with a diamond indenter only leads to cracking (**Figure 6**) without an indent made by plastic deformation.

The different diamond-type hardness measurements results by sclerometry made by an ultrahard fullerite indenter in the NanoScan are shown in **Table 1**.

As **Table 1** shows, a nitrogen-free diamond has the greatest hardness. The hardness anisotropy of nitrogen-containing and nitrogen-free diamonds is different: at (100) plane, ⟨100⟩ is the most solid direction for a diamond with 200 ppm of nitrogen, and for a diamond with 0.3 ppm, it is ⟨110⟩. Qualitatively, this trend to the diamond hardness increases with decreasing nitrogen impurities concentration, including the inverse hardness anisotropy for the nitrogen-containing and nitrogen-free diamonds, was discovered experimentally on the diamond indentation with a diamond Knoop indenter (Sumiya, Toba, et al., 1997), despite the fact that

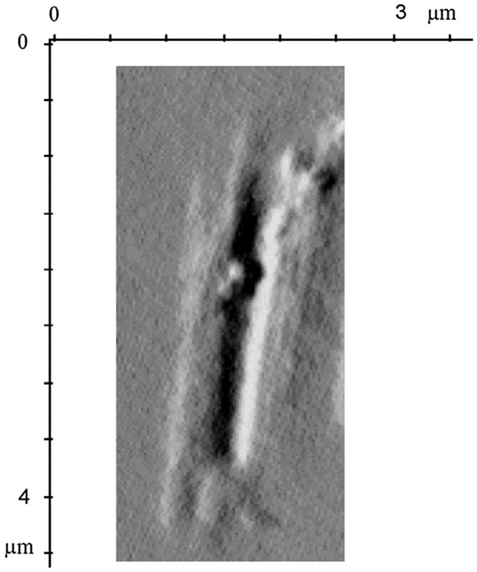

Figure 5 An image of a scratch made on the diamond surface (with a nitrogen content of 200 ppm) at (100) plane in the ⟨110⟩ direction. At the end of the scratch (see image bottom), a characteristic pile is also visible, formed by the material plastic flow, and also there are some small plastic piles-ups on the sides of the scratch (Blank, Popov, et al., 1999a, 1999b).

cracking is the dominant diamond indentation mechanism in case of applying a diamond Knoop indenter (Wilks & Wilks, 1991).

After testing the sclerometry hardness measurement by an ultrahard fullerite indenter in the NanoScan device technique on a diamond, we measured the ultrahard and superhard fullerite samples hardness, synthesized in the toroid-type cell at different pressures and temperatures. The hardness of these samples is shown in Figure 7. The samples are synthesized at pressures of 9.5 and 13 GPa. The highest hardness measured in these

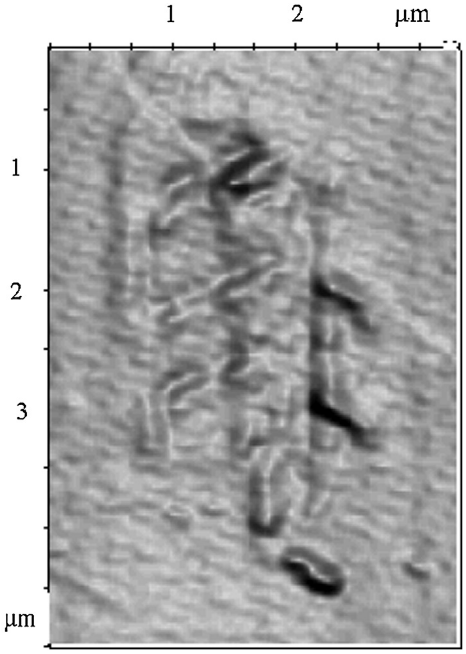

Figure 6 An image of a scratch made and scanned by the NanoScan device on the diamond surface (with a nitrogen content of 0.3 ppm) with a diamond indenter. An attempt to scratch a diamond with a diamond indenter only leads to cracking without an indentation made by plastic deformation (Blank, Popov, et al., 1997a, 1997b; Blank, Popov, et al., 1998).

Table 1 The different diamond-type hardness measurements results by sclerometry method made by an ultrahard fullerite indenter in the NanoScan

	Hardness (GPa)		
Nitrogen content (ppm)	*(111)*	(100)⟨100⟩	(100)⟨110⟩
200	151 ± 5	131 ± 2	115 ± 10
0.3	175 ± 5	139 ± 7	160 ± 3

experiments is 310 ± 40 GPa. Herewith, the most solid ultrahard fullerite samples were not measured because, as shown above in the example of a diamond, it is incorrect to measure the hardness with an indenter having the same hardness as the test material. To illustrate the above concept that the hardness of materials formed by covalently bonded carbon atoms is determined by their elastic moduli, the data on the hardness and bulk modulus were presented in one diagram (Blank, Buga, et al., 1998a, 1998b, 1998c, 1998d, 1998e). According to the estimate made earlier in the model of an ultrahard material consisting of carbon nanoclusters, the highest hardness for the 3D C_{60} is 320 GPa, and for the 3D C_n, it is about 360 GPa.

Vickers indenters made of ultrahard fullerite enable diamond hardness measurement with loads up to 13 N (Blank, Buga, et al., 2002). The ultrahard fullerite indenter was manufactured by the method similar to the diamond treatment with diamond powder: crushed ultrahard fullerite sample powder was used for the indenter treatment. (111) plane hardness was measured at indenter loads from 2 to 13 N and was 167 ± 7 GPa, which is close to the value obtained under a load of about 0.1 N in NanoScan. The test sample was made in a plane plate shape with parallel faces (111), which allowed controlling the indentation process from the opposite side. The indent size measured under load, within the experimental error, was consistent with the size measured after unloading the indenter.

3.20.4.2 Nanoindentation Hardness Testing

There is another superhard materials hardness measurement method by elastic deformation of the indenter and the test surface, described in detail in Richter, Ries, et al. (2000). This technique involves a careful indenter shape assessment, followed by a numerical simulation of elastic contact. This method allowed to measure the relative difference in hardness of the diamond faces (111) and (100), which corresponds to the data in **Table 1**. However, the intermediate steps, including determining the indenter shape and the simulation, can be omitted if we apply the mechanical properties comparative analysis of the unknown material with the materials with known parameters and similar properties. This approach was implemented in Popov, Koga, et al. (2002), Popov, Kyotani, et al. (2002a, 2002b, 2002c, 2002d) and Popov, Kyotani, et al. (2003a, 2003b) to assess the hardness of SP-SWNT synthesized in SDAC.

The measurements were performed in the Nanoindentation System device equipped with a Berkovich indenter. A nitrogen-free IIa-type diamond (plane (100)) and c-BN single crystals ((100) and (111) planes) and amorphous

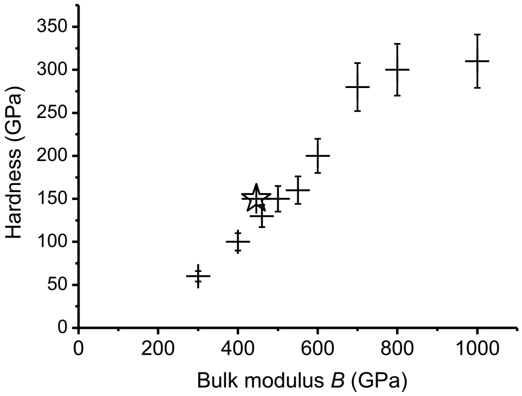

Figure 7 The superhard and ultrahard fullerites hardness and bulk modulus (Blank, Popov, et al., 1998; Blank, Buga, et al., 1998a, 1998b, 1998c, 1998d, 1998e; Popov, Koga, et al., 2002). The IIa diamond hardness is marked by a star.

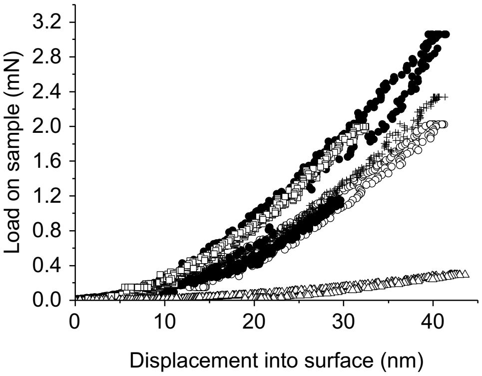

Figure 8 The elastic-indentation curves of SP-SWNT samples (filled circles), nitrogen-free IIa-type diamond (face (100), nonfilled squares), cubic-BN single crystals ((100) face, circles; (111), crosses) and amorphous silica (triangles). Reproduced from Popov, Kyotani, et al. (2002a, 2002b, 2002c, 2002d) and Popov, Kyotani, et al. (2003a, 2003b).

silica were used as the calibration samples. The elastic indentation curves (load–displacement of the indenter) for the listed samples and SP-SWNT samples are shown in **Figure 8**. Both load and unload loops are given.

The c-BN hardness was measured by the same device in some experiments at a 1 μm indentation depth, and the indentation was accompanied by a plastic imprint formation. The c-BN hardness is for (111) from 66 ± 1 to 73 ± 1 GPa, depending on the indenter orientation from the sample crystallographic axes (the hardness anisotropy effect), for (100), 62 ± 1 (at this plane, the trihedral Berkovich indenter anisotropy is not so strongly expressed). To assess the diamond plane (100) hardness, the data from **Table 1** were used. An average value of 150 GPa was chosen, because as in the case of the c-BN (100) plane, this pyramid should not have a significant hardness anisotropy effect on the diamond plane (100) as well.

All measurements were performed on the samples with an optical-quality polishing. As the SP-SWNT sample was pressed between the polished anvil surfaces, there was no additional sample preparation.

Loading curves for the calibration samples are well reproduced, while for the SP-SWNT samples, a large spread is observed. **Figure 8** shows the curves corresponding to the minimum and maximum SP-SWNT hardness values. This spread can be explained by the presence of cracks in the sample formed during unloading. The lower curve for SP-SWNT (lowest hardness) is virtually identical to the c-BN (100) curve (62 GPa hardness), the upper curve (maximum hardness) corresponds to a nitrogen-free diamond (100)—the hardness of 150 GPa. Thus, the SP-SWNT hardness is in the range of 62–150 GPa and the SP-SWNT belong to a class of superhard materials.

Similar to the ultrahard fullerite, the experimentally measured hardness values correlate with the bulk modulus measured values in accordance with the concept of the mechanical properties of superhard and ultrahard materials based on the carbon nanoclusters.

3.20.4.3 Wear-Resistance Research

Wear resistance is an important material mechanical properties characteristic, which depends on the hardness and fracture toughness (Evans & Charles, 1976; Liu & Li, 2001). To have the more reliable data, as in the case of hardness, the wear-resistance studies for novel superhard and ultrahard materials were conducted in comparison with known materials (Blank, Popov, et al., 1998; Blank, Popov, et al., 1999a, 1999b). Wear resistance was determined from the wear tracks made by a rotating brass disc with diamond powder (Wilks & Wilks, 1982; Wilks & Wilks, 1987; Blank, Popov, et al., 1998). The brass disk (Ø 9.25 mm and thickness of 0.13 mm) rotating at 250 rpm was slipping over the test-material surface in a drop of olive oil containing 16 wt% diamond powder of 10–14 μm fraction. The load on the disk was 0.1 N. The dimensionless quantity $J = \pi Dn/\Delta$ (D, disk diameter; n, number of disk rotations; Δ, wear track depth) was chosen as a wear-resistance parameter. All tests were conducted so that the wear track length was 1.15 mm. Thus, the number of disk rotations was the only variable parameter by which we calculated the wear resistance. The wear-resistance values for the novel superhard materials, polycrystalline carbonado diamond and sapphire are given in **Figure 9** depending on their hardness.

Thus, the wear-resistance study results once again confirmed that the ultrahard fullerite greatly exceeds the diamond in mechanical properties. As in the hardness and elastic modules research, the investigation was

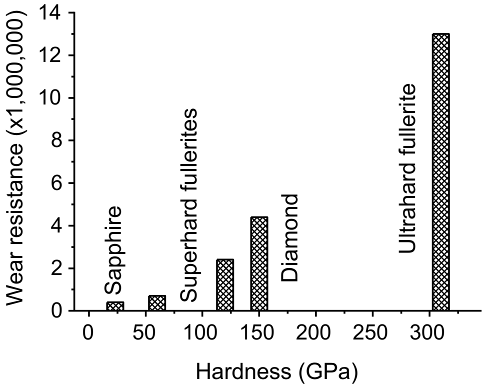

Figure 9 The wear-resistance values for the novel superhard and ultrahard materials, polycrystalline carbonado diamond and sapphire are given in the picture depending on their hardness. The data are taken from the studies of Blank, Popov, et al. (1998) and Popov, Koga, et al. (2002).

carried out in comparison with the known materials, including diamond, which significantly increases the results reliability.

3.20.5 The Structural Transition Sequence in C_{60} at Thermobaric Treatment

Structural studies of fullerenes are being actively conducted since the receipt of these unusual materials (Kroto, 1988). Under normal conditions, C_{60} has a fcc-lattice with parameter $a = 1.417$ nm. C_{60} pressure treatment at high temperatures leads to crystalline and disordered structures with high mechanical properties, comparable and sometimes superior to the diamond mechanical properties (Blank, Buga, et al., 1994a, 1994b; Blank, Popov, et al., 1994). These features of the new structural states attract great interest to them. There is some evidence on the amorphous state and the large number of crystalline phases. The following trend is characteristic of the crystalline states: the temperature and pressure growth leads to a sequence of fcc-lattices, the parameter of which is monotonically decreasing (Blank, Serebryanaya, et al., 1995; Duclos, Brister, et al., 1991; Iwasa, Arima, et al., 1992). In addition to fcc-lattice, the electron microscopy showed two crystalline phases with slightly distorted fcc-lattices in the samples treated with pressure of 9 GPa at 750 K (Blank, Kulnitskiy, et al., 1995; Blank, Zhigalina, et al., 1997). In the researched samples, as a rule, several crystalline phases were observed, each of which had a differently distorted lattice. Such crystal structures are found in the samples in small quantities, and X-ray analysis does not allow detecting them.

3.20.5.1 C_{60} Research after 13 GPa Pressure Treatment in a 900–1300 K Temperature Range

In general, the structural condition of most samples can be represented as a combined amorphous–crystalline. In some locations in the amorphous matrix, there are the monocrystalline areas with a characteristic size of several micrometers. These crystalline formations have no visible borders—there is a smooth transition from an amorphous to a crystalline state. Figure 10 presents a set of three electron diffraction patterns and their transcript results made from such a crystal section of the sample after pressure treatment. The electron diffraction patterns are obtained by an electron microscopic study by rotating the sample around the selected axis.

The sequence of these diffraction patterns with zone axes [001], $[\bar{1}\,11]$ and $[\bar{1}\,10]$ corresponds to the fcc-lattice. At the same time, the angles in the reciprocal lattice (as seen from the microdiffraction pattern) are slightly different from the angles of the fcc-lattice. For example, **Figure 10(b)** shows that the angle between the directions [200] and [020] differs by 5° from a straight one. **Figure 10(d)** also indicates that the angles between the directions of the $\langle 220 \rangle$ type are different from 60°. Measuring the distances between the reflections suggests that two out of the three values $\{200\}$ are the same. It should be noted that the interplanar distances experimental determination accuracy in electron microscopic studies is less than the x-ray analysis accuracy. With this regard, a gold film was deposited on the samples as a reference point. This allowed us to refine the interplanar distances measured values, but the error for the values given is still around 0.01 nm.

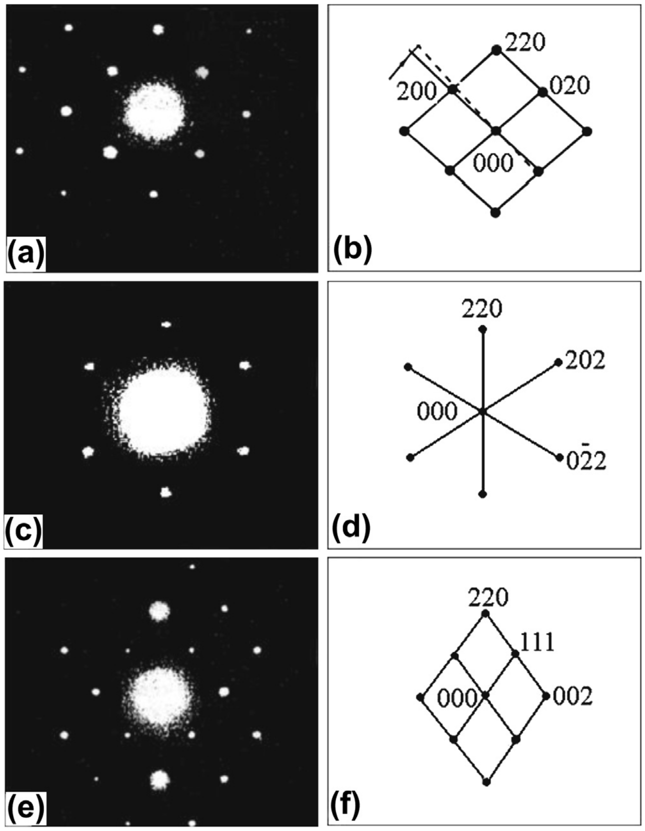

Figure 10 A set of electron diffraction patterns and their transcripts made from a sample crystal section by rotating it around the [220] axis. Slope angles are 0, 54° and 90°. The axis of zones [001], $[\bar{1}\,11]$ and $[\bar{1}\,10]$, respectively.

Thus, from these microdiffraction patterns, we can directly obtain the values of three parameters for the desired crystal lattice **a**, **b**, and **c**, since we know the values d_{200}, d_{020} and d_{002}, as well as one of the angles between [200] and [020]. It remains to find the two missing angles and to refine the **a**, **b**, and **c**, parameters since the angles are different from the straight ones. The analysis shows that a triclinic crystal lattice with parameters: $\mathbf{a} = \mathbf{b} = 1.225$ nm, $\mathbf{c} = 1.175$ nm, $\alpha = 89°$, $\beta = 91{,}5°$, $\gamma = 85°$ best corresponds to the given electron diffraction patterns. In the sample treated with a 13 GPa pressure at a temperature of 1100 K, a similar method was used to determine the another crystal lattice parameters: $\mathbf{a} = \mathbf{b} = 1.23$ nm, $\mathbf{c} = 1.12$ nm, $\alpha = \beta = \gamma = 92.5°$.

The given triclinic lattices are not the only possible ones under the given experimental conditions. There are also other microdiffraction patterns from single-crystal fragments, which are the fcc-lattice distorted sections, not corresponding to the shown triclinic phases. Analyzing a large number of such lattices, formed in the 900–1100 K temperature range at pressures of 13 GPa, showed that the parameters **a**, **b**, and **c** vary within a wide range from 1.12 to 1.3 nm, while the α, β, and γ angles differ from a straight one by no more than 6°. The triclinic structures occurrence can be explained as follows. The thermobaric treatment leads to molecules going closer, accompanied by a consistent decrease in the number of degrees of freedom associated with the rotation. Convergence of the molecules with increasing pressure leads to the fact that molecules can connect. There is a rupture in one of the double bonds between the hexagons in the molecule. At a single-bond rupture, the whole molecule can be destructed. Freed bonds in the neighboring molecules close, an intermolecular bond forms. Table 2 contains some details of the C_{60} phases detected by electron microscopic analysis. As follows from the tabular data, increasing pressure and temperature leads to a decrease in the parameters and the distortion of the fcc-lattice caused by reducing the shortest distances between the molecules along the [110] direction, as well as to an increase in the calculated density of detected phases from 1.68 at the initial phase to 2.98 (g/cm^3) in the most dense distorted fcc-lattice with a 1.17 nm parameter. Several phases in X-ray of the samples lead to line splitting, changes in intensity, and given the dominating amorphous state—to the great difficulties in the x-ray diffraction pattern interpretation. The obtained results fit into the general trend-consistent decrease in crystal structure parameters at the fullerene samples thermobaric treatment. Previously, TEM discovered small

Table 2 Crystalline structures found in C_{60} by transmission electron microscopy after thermobaric treatment

Lattice parameters, nm, angles in degrees		*Distances (nm) in [110] direction*	*Density g/cm^3*	*Treatment conditions*	
				P, *GPa*	T, *K*
$\mathbf{a} = 1.417$	$\alpha = \beta = \gamma = 90$	1.02	1.68	9	750
$\mathbf{a} = 1.30$	$\alpha = \beta = \gamma = 87.5$	0.919	2.17	9	750
$\mathbf{a} = 1.29$	$\alpha = \beta = \gamma = 90$	0.930, 0.892	2.23	13	900
$\mathbf{a} = \mathbf{b} = 1.225$, $\mathbf{c} = 1.175$	$\alpha = 89$, $\beta = 91.5$, $\gamma = 85$	0.856, 0.841, 0.837	2.71	13	900
$\mathbf{a} = \mathbf{b} = 1.23$ $\mathbf{c} = 1.12$	$\alpha = \beta = \gamma = 92.5$	0.813, 0.850, 0.888	2.82	13	1100
$\mathbf{a} = 1.17$	≈ 90	0.828	2.98	13	1300

quantities of crystal structure with a lattice close to the fcc, and with the parameter of about 1.17 nm. Given the accuracy of microscopic analysis, we can assume that in this case, such a combination of molecules occurred in which the distance between their centers is 0.827 nm. As seen from **Table 2**, a lower intermolecular distance value is observed: 0.813 nm. The intermolecular bond type becomes important for explaining the shortest distances between the molecules. In Xu and Scuseria (1995) and Blank, Buga, et al. (1998), as a result of theoretical consideration, the bond length between the C_{60} molecules is proposed to be 0.164 nm. Apparently, we cannot exclude an intermolecular bond corresponding to the bond in graphite (0.142 nm). In all these cases, the effective diameter of connected molecules (0.651–0.673 nm) is less than the actual C_{60} diameter. According to the literature, the C_{60} diameter is considered equal to 0.68–0.71 nm (Xu & Scuseria, 1995; Blank, Buga, et al., 1998a, 1998b, 1998c, 1998d, 1998e). This suggests that the molecules are joined, turning the edges of the respective faces to each other. Herewith, they formed some chains, and the molecules in each are aligned and linked the same way. A linear chain of such molecules corresponds to one of the $\langle 110 \rangle$ directions observed in the triclinic structure. The molecule chains received can vary by type of bonds between the molecules. This leads to the fact that in the $\{111\}$ planes, the distances between the molecules in the $\langle 110 \rangle$ direction are different, which leads to a change in the angles and fcc-lattice distortion. It is obviously hard to get an ideal fcc structure at small distances between the molecules (rigid bonds between the molecules) because the molecule symmetry incompletely complies with the fcc structure. For example, the hexagons in a free molecule have an angle between the normal of $<70.5°$, characteristic for the angle between the fcc-lattice planes $\{111\}$, which should probably lead to different bond length in different directions [110] with tends to the same package in all $\{111\}$ planes (the threefold axis in the molecule must necessarily coincide with the [111] direction in an ideal fcc structure). Since the formation of linear chains leads to a further material hardening, it is expected that implementation of such a case can lead to getting a material with higher mechanical properties. Large values of the shortest intermolecular distances may not meet the joined molecules. The distance value "discreteness" in this case is connected with the C_{60} orientational transition, and the molecules are connected according to the Van der Waals law.

3.20.5.2 C_{60} Research after 15 GPa Pressure Treatment at 1800 K: The Onion-like Structures

In this chapter, we studied C_{60} samples after thermobaric treatment with higher values of temperature and pressure. In the previous section, we used the pressure of 13 GPa. Therefore, we chose an intermediate range of pressures and temperatures. TEM studies of C_{60} samples after thermobaric treatment at pressures up to 15 GPa and temperatures up to 1800 K were carried out in the present study. We used the TEMs: JEM-2010 and JEM-200CX.

The minimum parameter values for the fcc-lattice and distorted fcc-lattice, as defined above, did not exceed 1.17 nm. Further reducing the fcc-lattice parameter is problematic. Indeed, the shortest distance between the C_{60}-molecule centers corresponds to the [110] direction and is equal to 1 nm. When the lattice parameter is 1.17 nm, this distance is already 0.827 nm. If we consider that the molecule diameter is 0.7 nm and a minimum bond between the carbon atoms varies from 0.164 to 0.154 nm, it is clear that the molecule must be either deformed or destroyed. For a 1.17 nm lattice parameter, d_{111} equals 0.67 nm. We did not find our images any distances even close to these values. Some interesting images for these samples are presented in **Figures 11** and **12**.

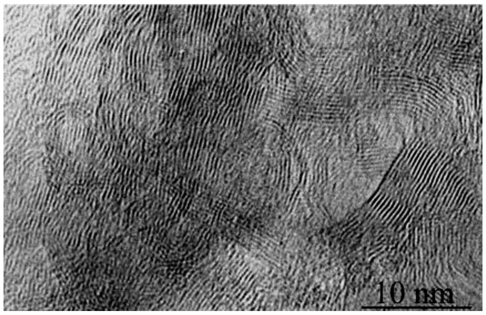

Figure 11 Distorted (002) graphite planes. There is an onion-like structure on the left.

Figure 11 shows the distorted lines, and the distance between them is close to the distance between (002) graphite planes (0.335 nm). As seen in the figure, sometimes these planes form a closed curved surface. **Figure 11** also presents some spherical structures—the onions. Apparently, the curved-graphite surfaces formed from the damaged molecules. Chains of C_{60} molecules in a one-dimensional polymerization elongate along the $\langle 110 \rangle$.

Volume intersections of these chains may happen further, i.e. the bulk polymerization in big volume, and as a consequence, such surfaces can form. Such a durable surface, consisting of sp^2 and sp^3 bonds, may be a hard nucleus, to which the following graphite layers will attach as a result of continuing pressure treatment. The onion shown in **Figure 12** may have been formed this way. This onion contains many defects in spherical shells and differs from the classical one composed of regular spheres. In addition, it was possible to detect the reduction in the interplanar distances along the onions radius, similar to that noted in Banhart (1997).

The minimal shell diameter for a nearly spherical shape, which may be internal to an onion, can be smaller than the C_{60} molecule diameter, since it can be formed from the C_{28} or C_{32} molecules. Such a molecule can form inside a tetrahedron composed of four C_{60} molecules, and can be regarded as a nucleus around which there will be the new shells.

This design forms an onion-like structure. Polymerized crystalline structures are characterized as linear (1D), with two dimensions (flat) (2D) and bulk-polymerized (3D). For small values of processing parameters, when some distorted fcc structures are observed (Blank, Kulnitskiy, et al., 1995; Blank, Zhigalina, et al., 1997), their occurrence can be explained by the formation of linearly polymerized chains of C_{60} molecules along the $\langle 110 \rangle$ in a distorted fcc-lattice. Perhaps the linear chain contains the sp^3 bonds between the atoms. Anyway, this is indirectly confirmed by the high hardness values of these new phases. In Blank, Kulnitskiy, et al. (1995) and Blank, Tatyanin, et al. (1997), the possible links between the two C_{60} molecules are considered: pentagon–pentagon, hexagon–hexagon, pentagon–hexagon, hexagon–edge, etc. The literature

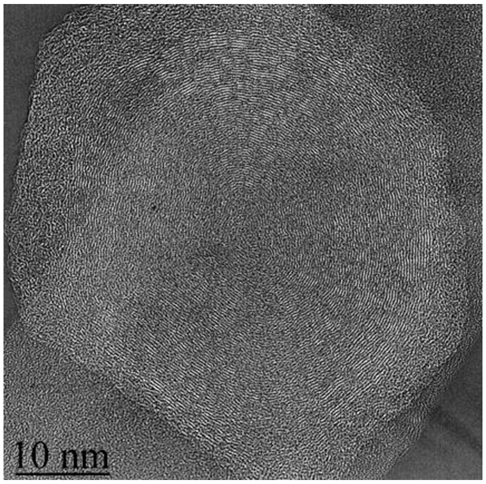

Figure 12 A big onion formed at 15 GPa and 2100 K.

Table 3 The sequence of C_{60} structures at thermobaric treatment

1	*2*	*3*	*4*	*5*	*6*	*7*
C_{60}	C_{60}	C_{60}	C_{60} and C atoms	C atoms	C atoms	C atoms
Initial fcc $a = 14.17$ A	Fcc phases with decreasing parameters	Distorted fcc-phases of ~3–5 μm (linear polymerization)	Metastable bulk-polymerized crystalline phases of size <100 A	Onions, ellipsoids, etc.	~70° distorted structures	Diamond

also contains the different bond types, such as "2 + 2". In Sundqvist, Eklund, et al. (1998), the structural and dynamical C_{60} properties at low pressure and temperature are discussed, and it is suggested that the polymerized crystalline phase distortion arise from the nuclei of molecular chains, which, in turn, reflect the random positions in a quasi-free molecular rotation in an fcc-lattice. In Moret, Launois, et al. and Launois, Moret, et al. (1998), it was proved that such chains in the $\langle 110 \rangle$ direction exceed the length of 200 A. Keita, Nadjo, et al. (1995) investigated the C_{60} after the thermobaric treatment (9.5 GPa, 623–773 K) and concluded that the polymerization mechanism is carried out by the partial consolidation of the C_{60} molecules, which leads to the rigid cross-links.

Volume (3D) polymerization has been identified in Blank, Buga, et al. (1998) and Popov, Koga, et al. (2002). **Table 3** shows the sequence of structures obtained in C_{60} with increasing pressure treatment options, as it appears after the electron microscopic analysis. **Table 3** does not specify the processing parameters. This is due to some inconsistencies in the literature. The same processing parameters given in various articles do not always correspond to the same structure in the X-ray analysis as well. This, in turn, is associated with some experimental difficulties, nonuniform temperature and pressure distribution in the high-pressure chamber (Popov, Koga, et al., 2002).

The structure hardness as mentioned above increases in line with the index number in **Table 3** and reaches the highest values in columns 5 and 6. Often, these different structures appear in the same sample, and even coexist with each other. Each of them contains the parallel graphene planes, distorted by the formation of sp^3 bonds. In both cases, the sp^3 bonds location is regular.

3.20.6 Conclusion

A new class of superhard and ultrahard materials based on covalently bonded fullerenes and nanotubes was discussed.

The bulk modules for three-dimensionally polymerized fullerite and polymerized nanotubes were determined by piezospectroscopy under pressure against a diamond piezospectroscopy sensor. The unique mechanical properties of this new class of materials are due to both the properties of carbon nanoclusters themselves and the ability of curved sp^2 layers, forming the carbon nanoclusters to make sp^3 bonds between them.

Diamond plastically deforms at room temperature via indentation or scratching with an ultrahard fullerite indenter. Based on experimental data presented in this chapter, the shear strength (in the plane (111)) of diamond was determined, and it was found to be equal to the theoretical shear strength (55 GPa) of diamond.

The hardness of ultrahard fullerite, depending on the synthesis conditions, can range from 200 to 310 ± 40 Gpa. While the hardness of the diamond depends on its nitrogen content and for a nitrogen-free diamond, it is 140 and 160 GPa in the (100) plane $\langle 100 \rangle$ and $\langle 110 \rangle$ directions, respectively, and 175 GPa in the (111) plane. The hardness of polymerized nanotubes was found to be equivalent to that of diamond. The measured values were found to comply with assessments made within the concept of mechanical properties of superhard and ultrahard materials based on the carbon nanoclusters.

Wear-resistance studies further confirmed that ultrahard fullerite greatly exceeds the mechanical properties of diamond.

Crystalline and amorphous phases in C_{60} were also discussed. The thermobaric-threated structural transition sequence in C_{60} was defined. The formation of onions, ellipsoids, and other three-dimensional closed structures consisting of a set of shells was observed under pressures of 13–15 GPa and at temperatures between 1100 and 1800 K.

Cross-references

3.1 Introduction to Super Hard Materials
3.3 High-Pressure Phase Diagrams of the Systems Containing Carbon and BN
3.21 Nanostructured Superhard Carbon Phases Synthesized from Fullerene
3.25 High-Pressure Synthesis of Novel Superhard Materials

References

Adams, G. B., Page, J. B., et al. (1994). *Physical Review B, 50*, 17471.

Al-Jishi, R., & Dresselhaus, G. (1982). *Physical Review B, 26*, 4514.

Banhart, F. (1997). The transformation of graphitic onions to diamond under electron irradiation. *Journal of Applied Physics, 81*, 3440–3445.

Blank, V., Buga, S., et al. (1994a). Phase transitions and anomalous hardening of solid C60 in a shearing diamond high-pressure chamber. *Technical Physics Letters, 39*, 828–829.

Blank, V., Buga, S., et al. (1994b). Phase transitions in solid C60 under pressure up to 40 GPa. *Molecular Materials, 4*, 149–154.

Blank, V. D., Buga, S. G., et al. (1995a). Fullerene C60 under the influence of high pressure together with high shear stresses: how to scratch diamond. *New Journal of Chemistry, 19*, 253–262.

Blank, V. D., Buga, S. G., et al. (1995b). *Raman study of ultra- and superhard phases of C60*. High Pressure Science and Technology, World Scientific Publishing Co. pp. 713–715.

Blank, V. D., Buga, S. G., et al. (1995c). *Experimental study of the hardness and electric conductivity of superhard bulk samples created from solid C60 under pressure up to 13 GPa and temperature up to 1830 K*. High Pressure Science and Technology, World Scientific Publishing Co. pp. 707–709.

Blank, V. D., Buga, S. G., et al. (1996a). Manufacturing of superhard and ultrahard materials from C60 fullerite. Extremely low heat capacity of dense amorphous fullerites. In H. Kuzmany, J. Fink, M. Mehring, & S. Roth (Eds.), *Fullerenes and fullerene nanostructure* (pp. 613–617). World Scientific Publishing Co.

Blank, V. D., Buga, S. G., et al. (1996b). Phase transformations in solid C60 at high pressure-high temperature treatment and structure of 3D polymerized fullerites. *Physics Letters A, 220*, 149–157.

Blank, V. D., Buga, S. G., et al. (1996c). Synthesis of ultrahard and superhard materials from C60 fullerite. *Molecular Materials, 7*, 251–256.

Blank, V. D., Buga, S. G., et al. (1997). Physical properties of superhard and ultrahard fullerites created from solid C60 by high-pressure-temperature treatment. *Applied Physics A, 64*, 247–250.

Blank, V. D., Buga, S. G., et al. (1998a). High-pressure polymerized phases of C60. *Carbon, 36*, 319–343.

Blank, V. D., Buga, S. G., et al. (1998b). Structure and properties of 3D-polimerized C60: comparison with diamond and C70. In H. Kuzmany, J. Fink, M. Mehring, & S. Roth (Eds.), *Molecular nanostructures* (pp. 506–510). Scientific Publishing Company.

Blank, V. D., Buga, S. G., et al. (1998c). High pressure synthesis, structure and mechanical properties of C60 fullerite superhard and ultrahard phases. *Review of High Pressure Science and Technology, 7*, 972–974.

Blank, V. D., Buga, S. G., et al. (1998d). Structures and physical properties of superhard and ultrahard 3D polymerized fullerites created from solid C60 by high pressure high temperature treatment. *Carbon, 36*, 665–670.

Blank, V. D., Buga, S. G., et al. (1998e). Cluster structure and elastic properties of superhard and ultrahard fullerites. In H. Kuzmany, J. Fink, M. Mehring, & S. Roth (Eds.), *Electronic properties of novel materials – progress in molecular nanostructures* (pp. 499–503). New York: Woodbury.

Blank, V. D., Buga, S. G., et al. (2001). Superhard carbon material, a method for its production, and articles made there from. United States Patent No US 6,245,312.

Blank, V., Buga, S., et al. (2002). In E. Osawa (Ed.), *Properties and applications of superhard and ultrahard fullerites perspectives of fullerene nanotechnology* (pp. 223–233). Kluwer Academic Publishers.

Blank, V. D., Denisov, V. N., et al. (1998). Hard disordered phases produced at high-pressure-high-temperature treatment of C60. *Carbon, 36*, 1263–1267.

Blank, V., Kulnitskiy, B., et al. (1995). Structural studies of high pressure phases of C60. *Physics Letters A, 204*, 151.

Blank, V. D., Kulnitskiy, B. A., et al. (2005). *Fullerenes, Nanotubes, and Carbon Nanostructures, 13*, 167–177.

Blank, V., Popov, M., et al. (1993). Un fullerene extremement dur puisqu'il or raye le diamant. *CNRS – INFO, 275*(1), 9.

Blank, V., Popov, M., et al. (1994). Is C60 fullerite harder than diamond? *Physics Letters A, 188*, 281–286.

Blank, V., Popov, M., et al. (1997a). Nano-sclerometry measurements of superhard materials and diamond hardness using scanning force microscope with ultrahard fullerite C60 tip. *Journal of Material Research, 12*, 3109–3114.

Blank, V., Popov, M., et al. (1997b). Plasticity of diamond at room temperature and determination of its hardness using an atomic force microscope with an ultrahard C-60 fullerite tip. *Technical Physics Letters, 23*, 546–547.

Blank, V., Popov, M., et al. (1998). Ultrahard and superhard phases of fullerite C60: comparison with diamond on hardness and wear. *Diamond and Related Materials, 7*, 427–431.

Blank, V., Popov, M., et al. (1999a). Hardness measurements of diamond at room temperature by ultrahard fullerite indenter. In *Proceedings of applied diamond conference/frontier carbon technology*.

Blank, V., Popov, M., et al. (1999b). Mechanical properties of different types of diamond. *Diamond and Related Materials, 8*, 1531–1535.

Blank, V., Serebryanaya, N., et al. (1995). Ultrahard carbon phases produced from C60 by heating at high pressure: structural and Raman studies. *Physics Letters A, 205*, 208–216.

Blank, V., Tatyanin, Y., et al. (1997). New structure after thermobaric treatment of C60. *Physics Letters A, 225*, 121–126.

Blank, V. D., Zhigalina, O. M., et al. (1997). Distortion of an fcc-structure upon thermobaric treatment of C60. *Crystallography Reports, 42*(4), 588.

Born, M., & Huang, K. (1954). *Dynamical theory of crystal lattices.* Oxford Clarendon Press.

Bridgman, P. W. (1935). *Physical Review, 15*, 825.

Brookes, E. J., Comins, J. D., et al. (2000). A study of plastic deformation profiles of impressions in diamond. *Diamond and Related Materials, 9*, 1115–1119.

Chacham, H., & Kleinman, L. (2000). Instabilities in diamond under high shear stress. *Physical Review Letters, 85*, 4904–4907.

Chernozatonskii, L. A., Menon, M., et al. (2001). *JETP Letters, 74*, 467.

Chernozatonskii, L., Richter, E., et al. (2002). Crystals of covalently bonded carbon nanotubes: energetics and electronic structures. *Physical Review B*, 241404.

Chernozatonskii, L. A., Serebryanaya, N. R., et al. (2000). *Chemical Physics Letters, 316*, 199.

Chua, J. O., & Ruoff, A. L. (1975). Pressure dependence of the yield stress of potassium at low homologous temperature. *Journal of Applied Physics, 46*, 4659–4663.

Clerc, D. G., & Ledbetter, H. M. (1998). *Journal of Physics and Chemistry of Solids, 59*, 1071.

Cohen, M. L. (1985). *Physical Review B, 32*, 7988–7991.

Cynn, H., Klepeis, J. E., et al. (2002). *Physical Review Letters, 88*, 135701.

Danesh, P., Pantchev, B., et al. (2011). Effect of hydrogen on hardness of amorphous silicon. *Applied Physics A, 102*, 131–135.

Dieter, G. E. (1986). *Mechanical metallurgy.* New York: McGraw-Hill. p. 119.

Dresselhaus, M. S., Dresselhaus, G., et al. (1996). *Science of fullerenes and carbon nanotubes.* San Diego: Academic Press.

Duclos, S. J., Brister, K., et al. (1991). Effects of pressure and stress on C60 fullerite to 20 Gpa. *Nature, 351*, 380.

Eremets, M., Trojan, I., et al. (2005). The strength of diamond. *Applied Physics Letters, 87*, 141902.

Evans, A. G., & Charles, E. A. (1976). *Journal of the American Ceramic Society, 59*, 371–372.

Ferrari, A. C., & Robertson, J. (2000). *Physical Review B, 61*, 14095.

Field, J. E. (1992). *The properties of natural and synthetic diamond.* San Diego, CA: Academic Press.

Frenkel, J. (1926). *Zeitschrift für Physik, 37*, 572.

Gilman, J. J. (1968). *Journal of Applied Physics, 39*, 6086–6090.

Gilman, J. J. (1975a). Relationship between impact yield stress and indentation hardness. *Journal of Applied Physics, 46*(4), 1435–1436.

Gilman, J. J. (1975b). *Journal of Applied Physics, 46*, 5110–5113.

Gilman, J. J. (1993). Why silicon is hard. *Science, 261*, 1436–1439.

Gilman, J. J. (2002). Why diamond is very hard. *Philosophical Magazine A, 82*, 1811–1820.

Gogotsi, Y. G., Kailer, A., et al. (1997). Phase transformations in materials studied by micro-Raman spectroscopy of indentations. *Materials Research Innovations, 1*, 3–9.

Gogotsi, Y. G., Kailer, A., et al. (1998). Pressure-induced phase transformations in diamond. *Journal of Applied Physics, 84*, 1299–1304.

Gogotsi, Y. G., Kailer, A., et al. (1999). Transformation of diamond to graphite. *Nature, 401*, 663–664.

Goncharov, A. F., & Andreev, V. D. (1991). *JETP, 73*, 140.

Grigorovich, V. K. (1976). *Hardness and microhardness of metals.* Moscow: Nauka (in Russian).

Grimvall, G. (1999). *Thermophysical properties of materials.* Amsterdam: Elsevier.

Hall, E. O. (1951). *Proceedings of the Physical Society, London, Section B, 64*, 747.

Hanfland, M., Beister, H., et al. (1989). *Physical Review B, 39*, 12598.

Hanfland, M., Syassen, K., et al. (1985). *Physical Review B, 31*, 6896.

Harrison, W. A. (1970). *Solid state theory.* New York: McGraw-Hill Book Company.

Hirt, J., & Lote, I. (1972). *Theory of dislocations.* Moscow: Atomizdat (Russian Translation).

Iqbal, Z., Zhang, Y., et al. (2003). Evidence for a solid phase of dodecahedral C20. *European Physical Journal B, 31*, 509–515.

Irifune, T., Kurio, A., et al. (2003). Ultrahard polycrystalline diamond from graphite. *Nature, 421*, 599–600.

Iwasa, Y., Arima, T., et al. (1992). New phases of C60. Organic molecular soft ferromagnetism in a fullerene C60. *Science, 264*, 1570.

Jishi, R. A., Venkataraman, L., et al. (1995). *Physical Review B, 51*, 11176.

Johnson, K. L. (1985). *Contact mechanics.* Cambridge University Press.

Jorio, A., Saito, R., et al. (2001). Structural (n, m) determination of isolated single-wall carbon nanotubes by resonant Raman scattering. *Physics Review Letters, 86*, 1118.

Kailer, A., Gogotsi, Y. G., et al. (1977). Phase transformations of silicon caused by contact loading. *Journal of Applied Physics, 81*, 3057–3063.

Keita, B., Nadjo, L., et al. (1995). Chemical modifications of C60 under the influence of pressure and temperature: from cubic C60 to diamond. *New Journal of Chemistry, 19*, 769–772.

Koehler, J. S. (1970). *Physical Review B, 2*, 547.

Kroto, H. W. (1988). Space, stars, C60 and soot. *Science, 242*, 1139–1145.

Launois, P., Moret, R., et al. (1998). Pressure and charge induced polymerization of C60: a comparative study of lattice vibrations. In *Molecular nanostructures* (pp. 348–352). Singapore: World Scientific Publishing Co.

Levin, V. M., Blank, V. D., et al. (2000). Elastic modules of solid C60: measurement and relationship with nanostructure. *Journal of Physics and Chemistry of Solids, 61*, 1017–1024.

Liu, R., & Li, D. Y. (2001). *Wear, 251*, 956.

Lowther, J. E. (2000). *Physica Status Solidi B, 217*, 533.

Madelung, O. (1996). *Introduction to solid-state theory.* Springer.

Mao, H. K., Bell, P. M., et al. (1979). *Review of Scientific Instruments, 50*, 1002–1009.

Mencik, J., & Swain, M. V. (1995). *Journal of Materials Research, 10*, 1491.

Montigaud, H., Tanguy, B., et al. (2000). C3N4: dream or reality? Solvothermal synthesis as macroscopic samples of the C3N4 graphitic form. *Journal of Materials Science, 35*, 2547–2552.

Moret, R., Launois, P., et al. Orientational order and disorder in fullerene compounds. Europhysics Letters, 40, 55.

Nesladek, P., & Veprek, S. (2000). *Physica Status Solidi A, 177*, 53.

Novikov, N. V., & Dub, S. N. (1996). *Diamond and Related Materials, 5*, 1026.

Occelli, F., Farber, D. L., et al. (2004). *Physical Review Letters, 93*, 095502.

Ogata, S., Li, J., et al. (2004). Ideal shear strain of metals and ceramics. *Physical Review B, 70*, 104104.

O'Keeffe, M. (1991). *Nature, 352*, 674.

Park, S., Srivastava, D., et al. (2001). Endo-Fullerene and doped diamond nanocrystallite-based models of qubits for solid-state quantum computers. *Journal of Nanoscience and Nanotechnology, 1*, 1–7.

Peierls, R. E. Quantum theory of solids. Oxford: Clarendon Press.

Petch, N. J. (1953). *Journal of the Iron and Steel Institute, London, 174*, 25.

Pimenta, M. A., Jorio, A., et al. (2001). Diameter dependence of the Raman D-band in isolated single-wall carbon nanotubes. *Physical Review B, 64*, 041401.

Piskoti, C., Yarger, J., et al. (1998). *Nature, 393*, 771–774.

Popov, M. (2004). Pressure measurements from Raman spectra of stressed diamond anvils. *Journal of Applied Physics, 95*, 5509–5514.

Popov, M. (2010). Stress-induced phase transition in diamond. *High Pressure Research, 30*, 670–678.

Popov, M., & Koga, Y. (2002). Carbon nanocluster-based superhard materials. In S. R. P. Silva (Ed.), *Properties of amorphous carbon* (pp. 186–205). London: INSPEC.

Popov, M., Koga, Y., et al. (2002). Carbon nanocluster-based superhard materials. *New Diamond and Frontier Carbon Technology, 12*, 229–260.

Popov, M., Kyotani, M., et al. (2000). Synthesis of new superhard material from single wall nanotubes. In *Proceedings of 14-th diamond symposium, Tsukuba, Japan*.

Popov, M., Kyotani, M., et al. (2001a). Comparison of superhard phase of single wall carbon nanotube with fullerite and diamond. In *Proceedings of 15-th diamond symposium, Tokyo, Japan*.

Popov, M., Kyotani, M., et al. (2001b). High-pressure polymerization of single wall carbon nanotubes. In *Proceedings of the sixth applied diamond conference/second frontier carbon technology joint conference (ADC/FCT 2001)*. Alabama: Auburn.

Popov, M., Kyotani, M., et al. (2002a). Superhard phase of single wall carbon nanotube. *Physica B: Condensed Matter, 323*, 262–264.

Popov, M., Kyotani, M., et al. (2002b). Superhard phase of single wall carbon nanotube: comparison with fullerite C60 and diamond. In *Proceedings of 2nd symposium on frontier carbon technology, Tokyo, Japan*.

Popov, M., Kyotani, M., et al. (2002c). Superhard phase of single wall carbon nanotube: synthesis and comparison with fullerite C60 and diamond. In *Proceedings of the 9th international symposium on advanced materials (ISAM 2002), Tsukuba, Japan*.

Popov, M., Kyotani, M., et al. (2002d). Superhard phase composed of single wall carbon nanotubes. *Physical Review B, 65*, 033408.

Popov, M., Kyotani, M., et al. (2003a). Properties of superhard phase of single wall carbon nanotube in comparison with fullerite C60 and diamond. *High Pressure Research, 23*, 265–269.

Popov, M., Kyotani, M., et al. (2003b). Superhard phase of single wall carbon nanotube: comparison with fullerite C60 and diamond. *Diamond and Related Materials, 12*, 833–839.

Popov, M., Medvedev, V., et al. (2010). Fullerite of aluminum nanoclusters. *Journal of Applied Physics, 108*, 094317.

Porezag, D., & Frauenheim, T. (1999). Structural and vibrational properties of C60 oligomers. *Carbon, 37*, 463–470.

Porezag, D., Pederson, M. R., et al. (1995). *Physical Review B, 52*, 14963–14970.

Prokhorov, V. M., Blank, V. D., et al. (1999). *Synthetic Metals, 103*, 2439.

Rao, A. M., et al. (1993). *Science, 259*, 955.

Rao, A. M., Richter, E., et al. (1997). Diameter-selective Raman scattering from vibrational modes in carbon nanotubes. *Science, 275*, 187.

Reich, S., Jantoljak, H., et al. (2000). *Physical Review B, 61*, 13389.

Richter, A., Ries, R., et al. (2000). *Diamond and Related Materials, 9*, 170–184.

Rinzler, A. G., Liu, J., et al. (1998). Large-scale purification of single-wall carbon nanotubes: process, product, and characterization. *Applied Physics A, 67*, 29–37.

Roundy, D., & Cohen, M. L. (2001). Ideal strength of diamond, Si, and Ge. *Physical Review B, 64*, 212103.

Ruoff, R. S., & Ruoff, A. L. (1991a). *Applied Physics Letters, 59*, 1553–1555.

Ruoff, R. S., & Ruoff, A. L. (1991b). *Nature, 350*, 663.

Šandera, P., & Pokluda, J. (1993). Improvement of the Mackenzie theory on ideal shear strength. *Scripta Metallurgica et Materialia, 29*, 1445–1450.

Serebryanaya, N. R., Blank, V. D., et al. (1995). C60-polymorphous transformations at 300-1800 K up to 13 Gpa. In *High pressure science and technology*. World Scientific Publishing Co. pp. 719–721.

Serebryanaya, N. R., Blank, V. D., et al. (2001). *Solid State Communications, 118*, 183–187.

Sirdeshmukh, D. B., Sirdeshmukh, L., et al. (2006). *Micro- and macro-properties of Solids*. Springer.

Sumiya, H., Toba, N., et al. (1997). *Diamond and Related Materials, 6*, 1841.

Sumiyaa, H., & Irifune, T. (2004). Indentation hardness of nano-polycrystalline diamond prepared from graphite by direct conversion. *Diamond and Related Materials, 13*, 1771–1776.

Sundqvist, B., Edlund, U., et al. (1998). Structural analysis of phototransformed C60 by vibrational and mass spectroscopy studies. *Carbon, 36*, 657–660.

Sung, C. M., & Sung, M. (1996). *Materials Chemistry and Physics, 43*, 1.

Suzuki, K., Fujimori, H., et al. (1982). *Amorphous metals*. London: Butterworths.

Takemura, K. (2004). *Physical Review B, 70*, 012101.

Teter, D. M., & Hemley, R. J. (1996). *Science, 271*, 53.

Valiev, R. Z. (2004). Nanostructuring of metals by severe plastic deformation for advanced properties. *Nature Materials, 3*, 511.

Veprek, S. (1999). *Journal of Vacuum Science & Technology, A, 17*, 2401.

Vereschagin, L. F., & Slesarev, V. N. (1969(3)). *Doklady of the Academy of Sciences, 3*, 30–31.

Wang, Y., Tománek, D., et al. (1991). Stiffness of a solid composed of C60 clusters. *Physical Review B, 44*, 6562–6565.

Weinstein, B. A., & Zallen, R. (1984). *Pressure-Raman effects in covalent and molecular solids*. Berlin: Springer.

Wentorf, R. H., DeVries, R. C., et al. (1980). *Science, 208*, 873.

Westbrook, J. H., & Conrad, H. (1973). *The science of hardness testing and its research applications*. Metals Park, OH: American Society for Metals.

Wilks, E. M., & Wilks, J. (1982). *Wear, 81*, 329.

Wilks, E. M., & Wilks, J. (1987). *Wear, 118*, 161.

Wilks, J., & Wilks, E. (1991). *Properties and applications of diamond*. Oxford: Butterworth-Heinemann Ltd.

Williams, J. S., Haberl, B., et al. (2005). Nanoindentation of ion implanted and deposited amorphous silicon. *Materials Research Society Symposium Proceedings, Materials Research Society, 841*. R10.3.1/T6.3.1.

Xu, C. H., & Scuseria, G. E. (1995). What is the lowest-energy isomer of the C60 dimer? *Physical Review Letters, 74*, 274.

Yagi, T., et al. (1992). *Physical Review B, 46*, 6031.

3.21 Nanostructured Superhard Carbon Phases Synthesized from Fullerites under Pressure

Vadim Brazkin and Alexander Lyapin, Institute for High Pressure Physics, Russian Academy of Sciences, Troitsk, Moscow, Russia

3.21.1 Introduction

Superhard materials are of paramount importance in the modern industry, and this stimulates both scientific interest in such materials and regular attempts to synthesize new superhard substances with unusual properties. A fundamental problem, whose solution reflects the depth of our insight into the interrelation between the structure of a substance, interatomic forces, and its physical properties, exists in the physics of superhard materials. It is necessary to highlight the clear relations between mechanical properties of substances, their elastic moduli, atomic or electron density, and the real structure of different space scales, including defect states and material morphology. Carbon materials attract considerable interest from researchers because carbon–carbon bonds are among the shortest and strongest ones, and therefore, the majority of carbon phases should have an advantageous combination of high mechanical characteristics and low density. Carbon atoms can occupy the twofold, threefold, or fourfold (sp-, sp^2-, and sp^3-hybridized, respectively) sites in solids. Due to this diversity of chemical bonding in solid carbon, carbon allotropes are combined into a great family of materials with the covalent bonding geometry varying from zero dimensional (Van der Waals cluster solids) to three dimensional (3D). The reason for the occurrence of various types of chemical bonds between carbon atoms is related to the closeness of the bond energies per atom for various carbon states. In turn, this is due to the small size of the inner electron shell of the carbon atom and relatively close energies of σ and π bonding (Harrison, 1980).

Among the carbon phases, diamond and diamond-containing materials are attracting the special attention of researchers and technologists because of the unique intrinsic mechanical properties of such materials. Artificial diamond is ordinarily synthesized from graphite, which is stable under normal conditions. At the same time, from the standpoint of fundamental investigations and for technological applications, it is of enormous interest to study the possibility of synthesizing diamond and other hard carbon modifications from metastable carbon phases. In this respect, the production of a new, highly metastable, ordered phase of carbon, fullerite C_{60}, in macroscopic quantities (Krätschmer, Lamb, Fostiropolous, & Huffman, 1990) has led to new possibilities for synthesizing new hard carbon materials via nonequilibrium transformations of C_{60} under pressure (Brazhkin & Lyapin, 1996; Brazhkin, Lyapin, Popova, et al., 2002; Lyapin, 2002). Thermodynamic relations provide an actual opportunity to influence the kinetics of transformations from the metastable fullerite C_{60} to stable phases, diamond, and graphite, under high-pressure and high-temperature conditions.

The subject of the present review concerns the carbon phases prepared from fullerite C_{60} by pressure–temperature treatment. A large variety of all-carbon structures can be formed due to the covalent

http://dx.doi.org/10.1016/B978-0-08-096527-7.00058-1

interaction between C_{60} molecules and the subsequent high-temperature atomic rearrangement under pressure. Among the pressure-synthesized C_{60}-based phases, several ordered and disordered modifications have been clearly identified to date, including crystalline 1D and 2D C_{60} polymers (Agafonov, Davydov, Kashevarova, et al., 1997; Bennington, Kitamura, Cain, et al., 2000; Davydov, Kashevarova, Rakhmanina, et al., 1997, 1998, 2000; Iwasa, Arima, Fleming, et al., 1994; Marques, Hodeau, Núñez-Regueiro, & Perroux, 1996; Meletov, Kourouklis, Arvanitidis, Prassides, & Iwasa, 2003; Meletov, Davydov, Arvanitidis, et al., 2008; Núñez-Regueiro, Marques, Hodeau, Béthoux, & Perroux, 1995; Wood, Lewis, West, et al., 2000), very hard graphite-type (sp^2-based) disordered phases (Blank, Denisov, Ivlev, et al., 1998; Brazhkin, Solozhenko, Bugakov, et al., 2007; Kozlov, Hirabayashi, Nozaki, Tokumoto, & Ihara, 1995; Lasjaunias, Saint-Paul, Bilušić, et al., 2002; Lyapin, Brazhkin, Gromnitskaya, et al., 2000; Marques et al., 1996; Wood et al., 2000), 3D polymers with a varying degree of polymerization (Bennington et al., 2000; Blank, Buga, Serebryanaya, et al., 1995, 1996; Brazhkin, Lyapin, Antonov, et al., 1995; Brazhkin, Lyapin, & Popova, 1996; Brazhkin, Lyapin, Popova, et al., 1997; Brazhkin et al., 1998; Brazhkin & Lyapin, 2000; Horikawa, Suito, Kobayashi, & Onodera, 2001; Lyapin, Brazhkin, Lyapin, & Popova, 1998; Mezouar, Marques, Hodeau, et al., 2003; Talyzin & Dubrovinsky, 2003, 2004; Talyzin, Dubrovinsky, Oden, Le Bihan, & Jansson, 2002; Talyzin, Langenhorst, Dubrovinskaia, Dub, & Dubrovinsky, 2005; Wood, Lewis, Bennington, et al., 2002; Yamanaka, Kubo, Inamuru, et al., 2006), diamond-like (sp^3-based) amorphous phases (Brazhkin et al., 1997, 1998; Hirai, Kondo, Yoshizava, & Shiraishi, 1994; Hirai, Tabira, Kondo, Oikawa, & Ishizawa, 1995; Talyzin et al., 2005), and diamond–graphite nanocomposites (Brazhkin et al., 1997, 1998; Brazhkin, Lyapin, Voloshin, et al., 1999; Irifune, Kurio, Sukamoto, Inoue, & Sumiya, 2003; Sumiya, Yusa, Inoue, Ofuji, & Irifune, 2006). Here, we review our original data on the mechanical properties of various carbon phases, pressure synthesized from C_{60}, as well as the relevant results from the regular publications. The structural nature of the phases under discussion is considered in terms of the nonequilibrium transitional pressure–temperature diagram of C_{60}, where the types of transitions can be considered in terms of the covalent bonding geometry of involved parent and final phases. The data presented allow us to discuss the interplay between the bonding nature and the physical properties of covalent carbon compounds. The potential of pressure-synthesized C_{60}-based carbon materials is another issue of the current discussion. The main accent of this chapter is directed toward superhard materials prepared from C_{60}, whereas other topics concerning, for example, structural, electronic, and optical properties of polymeric C_{60} phases can be found in the existing reviews (Makarova, 2001; Sundqvist, 1999, 2001).

The chapter is structured as follows: in Section 3.21.2, we discuss about the problems of reliable measurements of hardness and elastic moduli. In Section 3.21.3, we consider the physical background of high elastic constants of superhard materials and the ways to get a "bridge" to "ideal" mechanical properties. In Section 3.21.4, we briefly present the experimental methods used in the original studies lying in the background of the current review. Section 3.21.5 is devoted to the general aspects of the transitional pressure–temperature phase diagram of C_{60}. In Section 3.21.6, we point out the areas in the transitional phase diagram of C_{60}, where one can obtain the hard carbon phases, and identify the role of external conditions in the formation of the hard carbon phases. In Section 3.21.7, we consider hard nanostructured carbon phases prepared at moderate pressures (0.1–1.5 GPa). The highest mechanical properties, observed for diamond-based nanocomposites among other phases produced from C_{60}, are considered in Section 3.21.8. The review of mechanical properties is presented in Section 3.21.9, where we also discuss their correlations with structure and density. In Section 3.21.10, we focus on the influence of nonhydrostatic stresses on the anisotropic elasticity and hardness. Finally, in the Conclusion (Section 3.21.11), we discuss the prospects for application of hard carbon materials prepared from C_{60} under pressure.

3.21.2 Problems of Hardness and Moduli Measurements

The hardness is defined as "the resistance of a material to the imprinting or scratching" or, in particular, as "the property of materials to resist the penetration of other bodies into them". There are about 10 various quantitative and semiquantitative definitions of the hardness and the corresponding scales. Vicker's method, according to which the hardness is determined from the equation $H_V = P/S$, where P is the load on the pyramid and S is the area of the lateral surface of corresponding imprint on the sample studied, is the most frequently used in physics for investigating the mechanical properties of superhard materials. In the classical variant of Vicker's method, the imprint area is measured after the indentation. However, it is well known that after removing the load, a partial elastic recovery of the imprint takes place. Moreover, in the limit of very low loads, the indentation regime can be completely elastic, and after the load removal, there will be virtually no imprint. The method of nanoindentation, in which the penetration depth (and, consequently, the imprint area) is measured in the process of loading the indenter as a function of the load value, has been developed recently and significantly extends the possibilities of experimenters. When the modern instruments for the nanoindentation with a continuous load increase are used, the loading curves contain information about both the elastic and plastic modes of indentation.

The initial segment of the loading curve virtually contains information about elastic properties of a substance. In the limit of low loads, at the indentation by an absolutely hard cone of pyramid, the solution of the Hertz elastic contact problem yields (Sneddon, 1965)

$$(P/S)_{\mathrm{elast}} = E \cdot \mathrm{ctg}\,\phi/2\left(1-\nu^2\right), \tag{1}$$

where E is Young's modulus, 2ϕ is the apex angle of the cone or pyramid, and ν is Poisson's ratio. In the regime of the elastic mode of indentation, the $(P/S)_{\mathrm{elast}}$ is at maximum on the whole loading curve. It is reasonable to introduce the concept of the limit of hardness for the ratio P/S. The real hardness, that is, measured in the particular indentation experiment, can depend on the temperature, rate and time of loading, intergranular structure and texture of the sample, presence of defects, etc. The role of these factors is controlled by their influence on the character of plastic deformation and processes of generation of defects determining the kinetics of plastic mass transfer. Temperature changes can result in replacing the brittle regime of indentation with the plastic one. For the majority of metals, such a transition takes place at temperatures considerably below room temperature. As a consequence, the hardness of the majority of metals under normal conditions is lower than the ideal hardness by a factor of several tens. For the majority of superhard materials, including diamond, the transition to the plastic regime of deformation occurs at temperatures substantially higher than room temperature. Comparing the hardness of various substances, one has to take into the account the temperature of measurements. For example, diamond, being the hardest material at normal conditions, is less hard than the binary compound SiC at $T \sim 1400$ K, for diamond $H_V \sim 20$ GPa, whereas for SiC $H_V \sim 25$ GPa. In the plastic regime, the similarity law $P \propto S \propto d^2$ (d is the imprint size) is not fulfilled rigorously. The hardness versus imprint size dependence can be described by simple empirical relations, for example, by the Mayer classical law $P = Ad^n$, where A and n are constants and n usually assumes the values in the interval from 1.5 to 2, or by simple algebraic formulas of the $P = a_1 d + a_2 d^2$ type (Gong, Wu, & Guang, 1999).

The value of the measured hardness can depend on the time characteristics of the experiment, because the indentation leads to rather complicated kinetics processes, including the generation of new defects, such as dislocations or twins and the plastic flow in conditions of strong gradients of pressures and stresses. Summarizing, it can be inferred that the hardness depends on a great number of factors and, therefore, is not a well-defined and unambiguous characteristic.

It should be noted that the experimental study of elastic moduli of superhard materials is also a rather difficult task. Moreover, theoretical estimations often yield more accurate data in this respect than do the experimental studies. For unambiguous measurements of the bulk and shear moduli, we need sufficiently large homogeneous samples, preferably as a large single crystals. Unfortunately, in most cases, the samples to be studied are small, inhomogeneous, textured, etc. During X-ray study of the compressibility (bulk modulus), the hydrostaticity of the pressure-transmitting medium is the most important and critical factor. In nonhydrostatic conditions, it is easy to overestimate the value of the bulk modulus by several times. For example, the 3D polymers of fullerite C_{60} have a bulk modulus of around 280 GPa (Mezouar et al., 2003), whereas wrong measurements, neglecting nonhydrostatic conditions of measurement, give the values 540 GPa (Serebryanaya, Blank, Ivdenko, & Chernozatonskii, 2001). For the ultrasonic and Brillouin scattering study of elastic moduli, the isotropy and homogeneity of the sample are the key properties for the correct determination of elastic characteristics. So, the neglecting of the texture for superhard amorphous carbon materials, prepared from fullerite C_{60}, leads to the overestimation of the bulk modulus by 3 times! (Lyapin, Mukhamadiarov, Brazhkin, et al., 2003). The whole set of experimental techniques, including high-pressure X-ray diffraction, ultrasonic measurements, Brillouin scattering technique, strain gauge method, etc., are needed to retrieve reliable data on the elastic modulus of superhard materials.

3.21.3 High Elastic Moduli and Bridge to Ideal Mechanical Characteristics

The existence of correlations between hardness and unambiguously determined physical characteristics is extremely important for the search for new superhard materials. The interrelation between the hardness and the molar volume of a substance or its density as well as the correlation of the hardness and elastic characteristics of a substance are of special interest. The tensor of the elastic moduli of a substance, unlike its hardness, depends only on the interatomic interactions. The elastic moduli of a polycrystalline material depend basically on the interatomic interactions, except for very specific cases of textured materials. The first-principle calculations of the elastic moduli of materials are at present quite a routine problem. It is obvious that materials with a high hardness should be searched for among substances with high elastic moduli (Brazhkin, Lyapin, & Hemley, 2002).

A good correlation is observed between the shear modulus and hardness. Hardness and Young's modulus are correlated somewhat poorer, whereas there is no monotonic interrelation between hardness and bulk modulus (**Figure 1**). By its very definition, hardness is related to the process of shear deformation under the indenter rather than isotropic compression. As was shown, the ideal hardness, being the upper elastic limit of the actual hardness, is unambiguously controlled by the Young's modulus value.

Summarizing, elastic moduli, primarily the bulk modulus, are controlled mainly by the atomic or, in a more general case, electron valence density, and the search for superhard materials should be conducted among substances with high values of the atomic and electron density and high bonding energies.

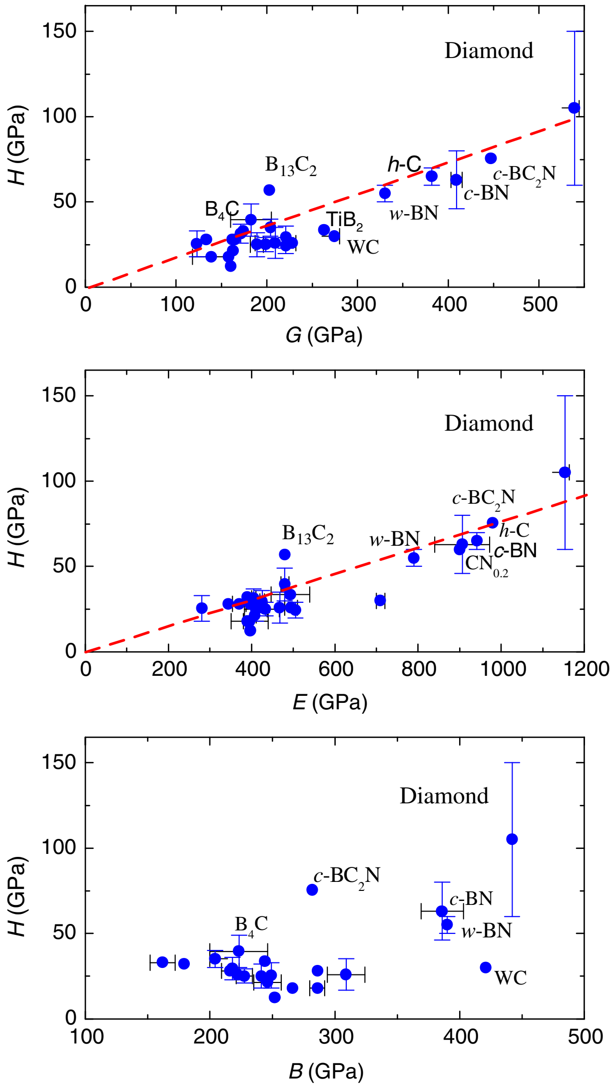

Figure 1 Hardness versus shear, Young's, and bulk moduli dependences for superhard materials according to the data collected by Brazhkin et al. (2002). Dashed lines illustrate the correlations between hardness and shear or Young's moduli.

It seems extremely important for creating new superhard materials to understand the role of purely geometric characteristics of the structure, such as the number of nearest neighbors and angles between the bonds. The idea that the covalent structure must become more rigid with the increasing number of nearest neighbors (the coordination number) can be quite clearly explained theoretically in the framework of the concept of rigidity percolation (Thorpe, 1983). At the critical coordination number $\langle z \rangle_c = 2.4$, the covalent network must become mechanically rigid. The model calculations for covalent networks in the general case or for amorphous sp^2–sp^3 carbon networks completely support this approach (Kelires, 2001). Therefore, from the standpoint of the search for superhard materials, only the structures with $\langle z \rangle \geq 3$ can be evidently of interest.

As was shown above, the natural limitations to elastic moduli consequently constrain ideal mechanical characteristics, including the ideal hardness. The elastic moduli and ideal hardness are completely controlled by the distribution of the electron density of valence electrons in metals and by geometry of atomic structure. However, a wide gap between the real and ideal hardnesses or strengths (for superhard materials, the ideal and real parameters differ by a factor of 3–10) stimulates the search for means, which would be capable of bringing the hardness and other mechanical characteristics closer to their ideal values. The control of the system morphology is the key way to the solution of this problem (**Figure 2**). We will not consider composite materials or superlattices that display distinguished mechanical properties and focus on nanomaterials.

The hardness and strength of the material are known to increase and approach their ideal values in two limiting cases: (1) for a defect-less single crystal containing virtually no dislocations (e.g., single-crystalline whiskers) and (2) for the amorphous or nanocrystalline state. In the latter case, the formation and motion of dislocations is difficult due to a defective structure of the material at the nanometer scale.

The nanostructures with a grain size of approximately 5–10 nm are optimal from the standpoint of the maximum hardness (Tai & Watanabe, 1998; Yip, 1998) (**Figure 2**). The existence of the optimal grain size is quite explicable. With a decrease in the grain size d and the corresponding increase in the fraction of intergranular boundaries, the value and density of barriers for the motion of dislocations increase. In this case, the known Hall–Petch law $H = H_0 + Ad^{-1/2}$, where d is the grain size, is observed for the hardness. However, for very small grains, the number of atoms at intergranular boundaries and inside grains becomes comparable. In this case, intergranular boundaries cease to be barriers for the motion of dislocations and the mechanism of the intergranular slip set to work. The size of the dislocation core becomes in this case comparable with the grain size, that is, the dislocation does not feel any inhomogeneities on its path. The mechanism of plastic deformation for the nanometer dimensions of crystals is still not fully elucidated, although a substantial progress in understanding the corresponding processes has been gained recently due to the work on computer simulation (Jacobsen & Schiøtz, 2002).

Nanopolycrystals actually possess unique mechanical properties. Thus, natural diamond polycrystals with ultrafine grains (carbonado) substantially exceed ordinary diamond single crystals in hardness and cracking resistance. Unfortunately, polycrystalline materials with fine grains are very difficult to obtain. Conventional methods of quenching from the melt yield a grain size of at least 100 nm. As a result, the standard approach to the obtaining of nanocrystals is the compaction (pressing) of nanoparticles. In this case, the resulting

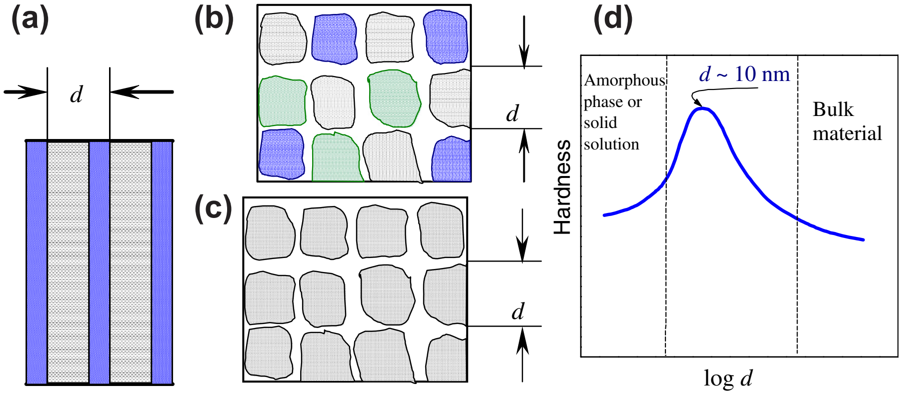

Figure 2 Nanostructured materials, including superlattices (a), multicomponent (b), and single-component (c) nanocrystalline composites, may demonstrate the maximum of hardness (d) for a definite size of crystallites or superlattice period.

porosity, chemical admixtures, and stresses at intergranular boundaries prevent the obtaining of the material with the optimal mechanical properties. Thus, the composites prepared by the compaction of diamond nanoparticles usually have the hardness 20–40 GPa. However, there exists an alternative method for obtaining nanocrystals through the crystallization of the amorphous state. In particular, as we will show below heating under pressure of amorphous carbon with the large fraction of sp^3 states obtained from fullerite produces the nanocomposite consisting of diamond and graphite grains with a size of 3–5 nm. Such a material, despite a substantial fraction of the graphite-like phase, has the hardness $H \sim 120$ GPa and fracture toughness $K_{1C} \sim 25$ MN/m$^{3/2}$, which is higher than the corresponding values for a diamond single crystal (Brazhkin et al., 1998). Very recently, diamond nanopolycrystals were obtained through the direct fullerite–diamond and graphite–diamond transition under pressures above 20 GPa (Irifune et al., 2003), as well as from nanotubes, also by heating under pressures exceeding 20 GPa (Yusa, 2002). Diamond polycrystals consisting of nanograins have extremely high values of hardness (>140 GPa at a load of 10 N).

3.21.4 Experimental Details

In a further discussion, we mainly deal with carbon materials obtained by the thermobaric treatment of a fullerite C_{60} followed by quenching to normal conditions. "Toroid" chambers of various sizes were used for creating a high pressure with a maximum pressure up to 17 GPa. For moderate pressure generation (<2 GPa), we used a large piston–cylinder apparatus and gasostatic high-pressure apparatus. The synthesis of fullerite-based samples was carried out from a powder containing not <99.9% of C_{60} with crystal grains of a size of approximately 100 mm. The structure of the samples was studied by X-ray diffraction (Cu K_α and Cr K_α). The structure of the samples was also examined by using a JEM 2010HR (JEOL) transmission electron microscope operating at 200 kV. The microstructure of the samples was characterized by bright-field and high-resolution transmission electron microscopy (HRTEM), as well as by selected area electron diffraction. The density of the samples ρ was measured by the Archimedes method. The electron energy-loss spectra of the B-K, and C-K edges were detected with a GIF 2000 (GATAN) parallel electron energy-loss spectrometer. The Raman scattering measurements were performed at 300 K using a Dilor XY system with a 514.5-nm Ar^+ ion laser as an excitation light.

The hardness of the samples was measured independently by means of three different techniques. The Vickers hardness H was found by using a PMT-3M instrument at 5-N loading. To obtain the correct data of the sizes of imprint, a thin layer of paint was applied on a polished surface of the sample. Hardness measurements of the sample have also been performed with a microhardness tester (Duramin-20, Struers) under 1- to 10-N load (H_1 notation). In situ measurements of the hardness (H^* notation) were carried out using Nano Indenter-II (MTS Systems Inc, Oak Ridge, TN, USA). It was also used for measuring Young's modulus (E^*). The Vickers hardness H_V and the fracture toughness (crack resistance) factor were calculated according to the procedure proposed in Evans and Wilshaw (1976). The elastic moduli (the bulk (B), shear (G), and Young's (E) moduli) were independently found through the ultrasonic measurements of the transverse and longitudinal velocities in a 5- to 10-MHz frequency range.

More experimental details can be found in the original papers (Brazhkin et al., 1995, 1996, 1997, 1998, 1999, 2007; Lyapin et al., 1998, 2000, 2003).

3.21.5 Transitional Phase Diagram of Fullerite C_{60}

A wide variety of ordered or disordered carbon phases synthesized from fullerite C_{60} by the application of high pressures and temperatures has been discussed in many papers, for example, in Brazhkin, Lyapin, et al. (2002), Lyapin (2002), Marques et al. (1996), Núñez-Regueiro et al. (1995), and Sundqvist (1999, 2001). Under high pressure, C_{60} molecules become close to each other and different kinds of polymerization between the molecules occurs (**Figure 3**). On the other hand, at high temperatures, the destruction of the molecules and transition to the atomic carbon phases takes place. Typical X-ray diffraction patterns for several key phases are shown in **Figure 4**. Whereas polymerized phases may be considered as molecular modifications of C_{60}, many of which can be depolymerized back to the starting fullerite (see, e.g., Dworkin, Szwarc, Davydov, et al. (1997) and Iwasa et al. (1994) for 2D and Brazhkin et al. (1996) for 3D polymers), disordered and nanocrystalline sp^2–sp^3 phases have an atomic-based structure, corresponding to the irreversible destruction of the C_{60} molecules.

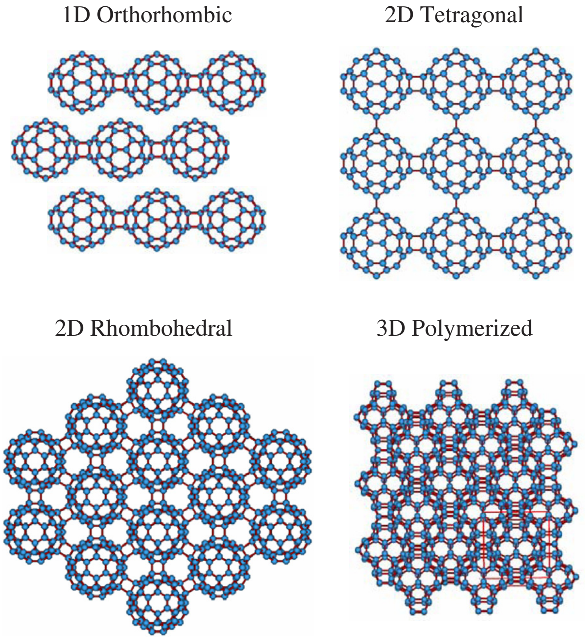

Figure 3 Illustration of 1D, 2D, and 3D polymerized phases of fullerite C_{60}.

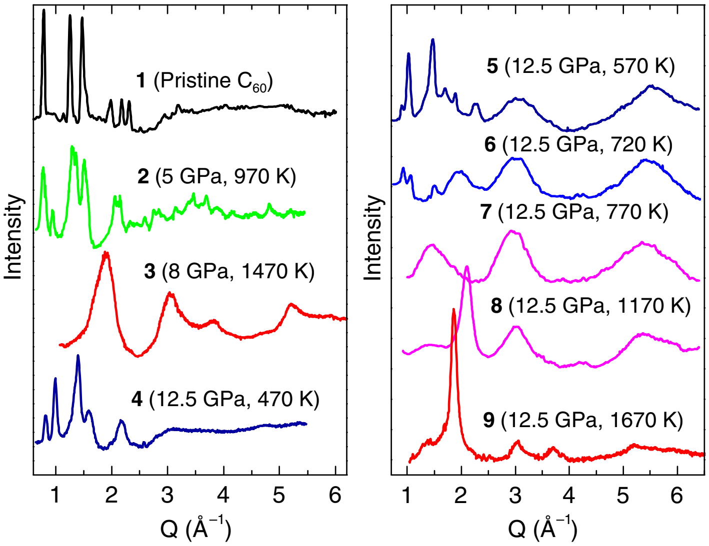

Figure 4 Typical X-ray diffraction patterns for carbon phases prepared from C_{60}, where synthesis pressure and temperature are shown in parentheses. The corresponding structures were identified as follows: 1—pristine C_{60}; 2—2D polymerized rhombohedral phase of C_{60}; 3—disordered atomic-based sp^2 phase; 4 and 5—3D polymerized fullerite C_{60} with different lattice parameters; 6—strongly disordered 3D polymerized phase; 7 and 8—disordered (amorphous) sp^2–sp^3 phases with different nanomorphology and sp^2/sp^3 ratio; 9—diamond-graphite nanocomposite.

A kinetic transitional phase diagram of structural transformations of C_{60} fullerite is presented in Figure 5. This diagram is constructed with regard to both original results and published data. The phase-transition curves in the monomeric C_{60} phase and the regions of the formation of 1D and 2D polyfullerenes are reproduced from Davydov et al. (2000) and Sundqvist (1999, 2001), respectively. The stability boundary of these phases (up to 8 GPa) is taken from Davydov et al. (2000) with taking into account the phase diagram from Marques et al. (1996) and the data from Davydov et al. (1997) and Lyapin et al. (2000). A concentration isoline for dimerization of C_{60} (i.e., the line of fixed fraction of $(C_{60})_2$ dimers in the fullerite) is first constructed in this diagram with regard to the results obtained by Davydov, Kashevarova, Rakhmanina, et al. (1999) and Kondrin, Lyapin, Brazhkin, and

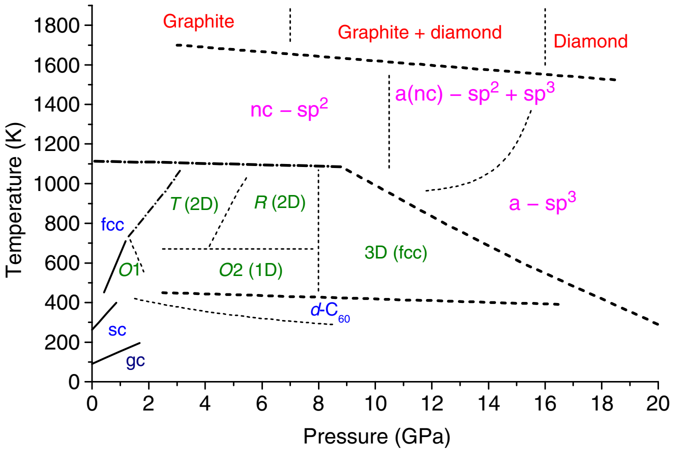

Figure 5 Nonequilibrium (kinetic) transitional pressure–temperature phase diagram of C_{60}. Solid lines correspond to the thermodynamic phase boundaries for monomeric C_{60} phases; dot-and-dashed lines correspond to the irreversible but sharp structural transformations; dashed lines correspond to the rather smooth transformations and separate regions of different classes of structures synthesized from C_{60}. The corresponding phases or classes of structures are designated as follows: fcc, sc, and gc correspond to the fcc, primitive cubic, and orientational glassy phases (all monomeric); *O*1, *O*2, *R*, and *T* are low-pressure and high-pressure 1D orthorhombic phases, and 2D rhombohedral and tetrahedral phases; *d*-C_{60} are phases with a predominant concentration of $(C_{60})_2$ dimers; nc – sp^2 are disordered (nanocrystalline) graphite-like phases; 3D (fcc) are 3D polymerized C_{60} phases; a – sp^3 and a(nc) – $sp^2 + sp^3$ are amorphous phases with possible nanocrystalline inclusions in the second case.

Popova (2002). The region $P > 10$ GPa is presented according to the results of our works (Brazhkin et al., 1996, 1997) and data from Horikawa, Suito, Kobayashi, & Onodera, 2001, Talyzin et al. (2002), and Wood et al. (2002). This version of the phase diagram has been presented for the first time in Brazhkin and Lyapin (2004).

The high-temperature region at pressures below 1.5–2 GPa has not been considered previously in detail. Recently, we found that this part of the transitional phase diagram has its own peculiarities. The detailed transitional *P*,*T*-phase diagram, including its low-pressure part, obtained through our experiments, is shown in **Figure 6**. At $P < 2$ GPa, the temperature stability of fullerite C_{60} to molecular destruction at heating is by 100–150 K higher than that at high pressures $P > 3$ GPa (**Figure 6**). Moreover, the structure of disordered carbon phases, obtained on heating the C_{60} fullerite at moderate pressures, differs considerably from that of nanographite modifications obtained at high pressures $P > 3$ GPa (see below). The possibility of the production of hard carbon materials from C_{60} fullerites at $P < 2$ GPa has not been looked into thus far, although it is known that the heating of C_{60} at ambient pressure leads to the formation of amorphous carbon at $T > 1200$ K. It should be noted that the breakup of the molecular structure and the formation of hard nanographite phases at $P > 2$ GPa takes place through intermediate polymerized C_{60}-based modifications, since at $P < 2$ GPa, the destruction of molecules on heating should occur directly in the initial molecular phase C_{60} (Brazhkin & Lyapin, 2004; Sundqvist, 1999). We will consider the transformation of fullerite to hard carbon phases in this moderate-pressure region in more detail in Section 3.21.7.

We emphasize that this diagram does not have conventional characteristics and, basically, cannot be unambiguous. The structure of the phases formed may depend not only on the kinetic conditions of the experiment (see, e.g., results of Davydov et al. (1997, 1999)), the path in the *P*–*T* plane, and the hydrostatic conditions but also on the starting orientational state of C_{60} molecules (Sundqvist, 1998). We distinguished between three classes of lines (**Figure 5**): phase boundaries for the monomeric C_{60} phase, which were determined thermodynamically for the molecular substance; lines of sharp structural transformations, such as the stability boundary of polymolecular phases; regions of gradual transformations, such as dimerization and 1D, 2D, or 3D polymerization, where the line has a fully conventional character and can be constructed in a physically definite way only from the percolation point of view.

The diagram of transformations presented here for the region of high pressures >10 GPa is notably different from that proposed previously by Blank et al. (1996), Blank, Buga, & Dubitsky, 1998, which was repeatedly reproduced in a number of reviews, for example, by Sundqvist (1999, 2001). The point of view presented in this work is confirmed by the synchrotron studies of Horikawa, Suito, Kobayashi, and Onodera (2001) and Wood et al. (2000, 2002).

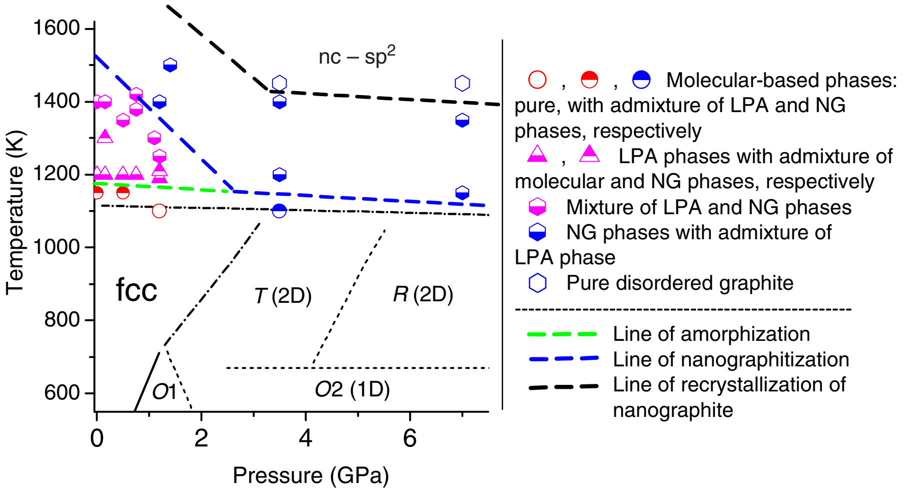

Figure 6 Development of the high-temperature and low/medium-pressure part of the phase diagram from **Figure 5** on the base of recent quenching experiments. Each point corresponds to *P–T* conditions of synthesis of a particular sample. The legend clarifies dominant and admixture phases in the samples, established by X-ray diffraction. LPA corresponds to “low-pressure amorphous” (i.e., with first maximum of structure factor at $Q \approx 1.3$ Å^{-1}, see Section 3.21.7) and NG to “nanographite” ($Q \approx 1.8$ Å^{-1}).

The pressure area in the presented diagram is restricted by 20 GPa and approximately corresponds to the stability pressure interval of C_{60} for compression at room temperature. Although there were intensive studies of C_{60} compressed to this and higher pressures at room temperature (Duclos, Brister, Haddon, Kortan, & Thiel, 1991; Hodeau, Tonnerre, Bouchet-Fabre, et al., 1994; Kosowsky, Hsu, Chen, et al., 1993; Moshary, Chen, Silvera, et al., 1992; Núñez-Regueiro, Abello, Lucazeau, & Hodeau, 1992; Núñez-Regueiro, Monceau, & Hodeau, 1992; Núñez-Regueiro, Monceau, Rassat, Bernier, & Zahab, 1991; Snoke, Raptis, & Syassen, 1992; Yoo & Nellis, 1991, 1992), the picture of transformations of C_{60} at compression >20 GPa is still not completely clear. The presented transitional diagram also does not reflect the data of shock-wave experiments (Hirai et al., 1994, 1995; Yoo, Nellis, Satler, & Musket, 1992), where an amorphous diamond has been obtained, since the corresponding experimental points are beyond the boundaries of this diagram. The points, corresponding to the recent results on preparation of superhard nanocrystalline diamond (Irifune et al., 2003; Sumiya et al., 2006), lie near the top right corner of our diagram.

3.21.6 Regions of Hard Carbon Phases

Since C_{60} molecules interact via only weak Van der Waals forces, pristine C_{60} is a very soft material with a hardness $H \approx 0.4$ GPa (Lyapin et al., 2000). Polymerization is a natural way for hardening this material, because the covalent bonds between molecules are much stronger than molecular forces. But 1D and 2D C_{60} polymers are still rather soft materials with a hardness $H \sim 1$–2 GPa (Blank, Denisov, et al., 1998; Lyapin et al., 2000).

Only the application of high pressure and/or high temperature provides the way to synthesize hard and superhard carbon materials. In this respect, one can select the three regions of hard phases at the transitional phase diagram (**Figure 5**): (1) the region of disordered sp^2-type atomic structures obtained at moderate pressures up to 8–10 GPa and high temperatures >1100 K, (2) the region of three-dimensionally polymerized C_{60} phases synthesized at moderate temperatures of 400–800 K and high pressures >8–10 GPa, and (3) the region of diamond-based amorphous and nanocomposite phases obtained at high pressures >10 GPa and temperatures >800 K. Below, we consider the particular properties of carbon phases synthesized in these three regions.

One of the most striking phenomena was first observed by Kozlov et al. (1995), when the hardness increased by more than one order of magnitude due to the destruction of the C_{60} molecular structure by heating to approximately 1000 K at a relatively low pressure near 3 GPa. The similar picture of transformation to disordered atomic-based graphite-type phases during heating is observed up to 8 GPa (Lyapin et al., 2000). The above-mentioned pressure and temperature parameters restrict approximately the boundaries of the first region of hard materials prepared from C_{60}. No density jump was observed within the acceptable range of experimental accuracy, whereas a substantial structural reconstruction from a molecular polymer to a disordered sp^2 network (**Figure 7**) occurred (Lyapin et al., 2000). The hardness of disordered phases seems to be independent of pressure, though the density somewhat increases in the pressure interval from 3.5 to 8 GPa. The variation of elastic moduli is not so drastic: the B and G moduli increase by a factor of 4–5 and 2–3 times, respectively, while the hardness of disordered structures is 100- to 200-fold greater than that of graphite (**Figure 7**). The reasons for superhard properties of disordered atomic-based graphite-type phases obtained from C_{60}, in spite of graphite being a soft material, will be discussed in the next sections. The moderate pressure–high temperature region of disordered sp^2 network formation (<2 GPa) has been studied only recently. The carbon phases prepared in this region has some specific features, and they will be considered separately in Section 3.21.7.

Among polymeric modifications of C_{60}, only 3D polymerized C_{60} phases correspond to hard carbon materials. The area of high pressure between 9 and 20 GPa and moderate temperatures in the range of 500–1000 K is the second pressure–temperature region, where one can synthesize the hard 3D polymers of C_{60}. The appearance of strong covalent bonds between C_{60} molecules in all three dimensions is the key property of 3D polymers resulting in their superhard mechanical characteristics.

3D polymerization is a gradual process occurring with the increase of temperature (**Figure 4**) (Bennington et al., 2000; Brazhkin et al., 1996, 1997, 1998; Brazhkin & Lyapin, 2000; Horikawa, Suito, Kobayashi, & Onodera, 2001; Lyapin et al., 1998; Wood et al., 2000). The structure of all crystalline polymerized phases prepared can be identified as face centered cubic (fcc) with the lattice parameter a decreasing with the increase in the synthesis temperature. The identification of polymerized phases as the fcc structures with various lattice parameters is rather typical for C_{60} even at low pressures (Iwasa et al., 1994; Lyapin et al., 2000; Matsumuro, Takada, Takahashi, Kondo, & Senoo, 1998). At the same time, there is evidence of existing 3D polymers with the molecular arrangement distorted with respect to the fcc structure (Blank, Kulnitskiy, & Tatyanin, 1995; Blank et al., 1996; Brazhkin et al., 1995; Mezouar et al., 2003; Talyzin & Dubrovinsky, 2003, 2004; Talyzin et al., 2005; Yamanaka et al., 2006). Moreover, the observation of the Debye–Scherrer ellipses from 3D C_{60} polymers by Marques, Mezouar, Hodeau, et al. (1999) demonstrates a systematic distortion of the cubic molecular short range

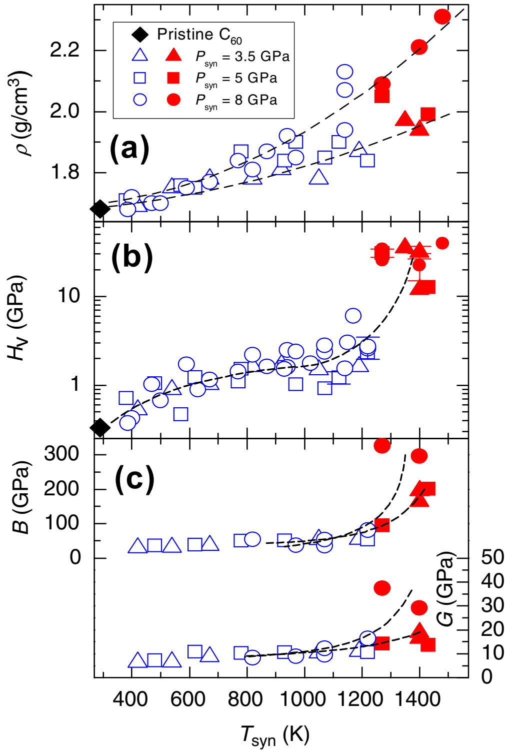

Figure 7 Dependences of (a) density, (b) Vickers hardness, and (c) ultrasonic elastic moduli for samples synthesized from C_{60} at pressures 3.5, 5, and 8 GPa. Open symbols correspond to 1D and 2D C_{60} polymerized phases, and solid (red) symbols correspond to disordered graphite-like phases. Dashed lines serve as guides for the eyes.

order structure as the memory signature of anisotropic pressure. Here, one should emphasize that all the experimental X-ray diffraction patterns of 3D polymers display, as a rule, at most five to six crystalline reflections, which is clearly insufficient for the precise identification of such complicated structures as C_{60} polymers.

Recently, a number of hypothetical 3D polymerized C_{60}-based ordered structures have been proposed (Berber, Osawa, & Tománek, 2004; Burgos, Halac, Weht, et al., 2000; Ivanovskaya & Ivanovskii, 2010; Okada, Saito, & Oshiyama, 1999; Perottoni & da Jornada, 2002; Talyzin, Dubrovinsky, & Jansson, 2001; Yamagami & Saito, 2009; Yang & Tse, 2007; Zipoli & Bernasconi, 2008). These structures are of interest for recognizing possible covalent configurations of the nearest neighbor molecules in 3D polymerized phases, but the available experimental data on 3D polymers cannot be described in terms of the strictly ordered crystalline molecular structure. The experimental 3D polymerized C_{60} phases seem to be orientationally disordered. The reasons for this are connected with the orientational randomization in pristine C_{60} and nonsynchronous character of the formation of covalent bonds between different nearest neighbor molecule pairs. Only the application of pressure to 1D and 2D C_{60} polymers can probably provide the experimental way for the synthesis of the ordered 3D polymers similar to those proposed theoretically, and there have been initial experimental attempts (Chi, Iwasa, Takano, et al., 2003; Meletov et al., 2003, 2008; Mezouar et al., 2003; Talyzin & Dubrovinsky, 2003, 2004; Talyzin et al., 2005; Yamanaka et al., 2006) in this respect.

In subsequent discussion, the 3D polymers will be considered as effective fcc molecular structures with the intention of correlating the molecular center positions. The two stages of 3D polymerization can be distinguished (Brazhkin et al., 1996, 1997) from experimental X-ray diffraction data: (1) a gradual formation of covalent bonds between molecules, probably, via the [2 + 2] cycloaddition mechanism (Goze, Rachdi, Hajji, et al., 1996) (for the lattice parameters of fcc structures $a \geq 12.3$ Å); (2) the appearance of additional covalent bonds ("overpolymerization") between molecules and simultaneous distortion of the initially spherical C_{60} units interconnected within the polymerized structure skeleton ($a < 12.3$ Å) and activation of the [3 + 3] cycloaddition mechanism of polymerization (Chi et al., 2003).

For describing the transition from the soft pristine C_{60} to strongly polymerized superhard 3D structures, it is adequate to use the elastic rigidity percolation theory (He & Thorpe, 1985; Thorpe, 1983), which should operate with the degree of covalent bonding between molecules, if we consider the contribution of van der Waals forces to be negligible. A 3D network of covalently bonded atoms becomes rigid, when the average coordination number exceeds the value of $Z_c = 2.4$ (He & Thorpe, 1985). The average coordination number for covalently bonded pairs of C_{60} molecules Z_p would be defined by their share n_p as $Z_p = n_p Z$, where $Z = 12$ is the coordination number of an fcc lattice. Considering the threshold covalent intermolecular coordination number for the appearance of hardness and elasticity in a system of partially covalently bonded C_{60} molecules to be equal to $Z_c = 2.4$, similarly to a covalent atomic network, we obtain the threshold concentration $n_c = 0.2$ and the corresponding lattice period $a_c \approx 13.8$ Å in the framework of the model proposed by Brazhkin et al. (1996, 1997) and Lyapin et al. (1998). **Figure 8** shows the dependence of the hardness for the 3D polymerized fcc phases of fullerite C_{60} versus the lattice parameter, which completely supports the picture following from the percolation theory. The hardness continuously increases with the average coordination number for molecules, similar to the increase of elastic constant in the model of rigidity percolation (He & Thorpe, 1985). Linear interpolation with the least squares fitting gives the threshold parameter close to the estimated value $a_c \approx 13.7$ Å.

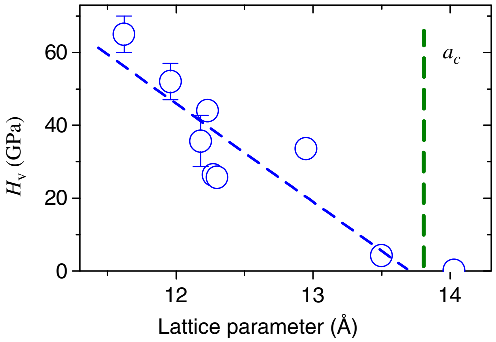

Figure 8 Vickers hardness of the 3D polymerized C_{60} phases as a function of the lattice parameter. Dashed lines serve as guides for the eyes. The vertical dashed line corresponds to the rigidity percolation threshold a_c. The hardness of the least-dense sample ($a = 14.4$ Å) is equal to 0.15 ± 0.05 GPa.

The heating of C_{60} to temperatures higher than the range of the 3D polymerization at pressures higher than approximately 12 GPa (particularly, to 800 K or to higher temperatures at 12.5 GPa (Brazhkin et al., 1997)) leads to the destruction of the molecular structure and to the formation of disordered atomic-based phases. The typical phases obtained during heating at 12.5 GPa are illustrated by the X-ray diffraction data in **Figure 4**. Nominally, we consider the third region of superhard materials (**Figure 5**). The temperature of disordering (amorphization) is pressure dependent (Núñez-Regueiro et al., 1991). The details of the structural analysis of diffraction patterns and Raman spectra for the disordered phases are described elsewhere (Brazhkin et al., 1997, 1998, 1999). One can select the following types of high-pressure disordered materials: (1) diamond-like (basically sp^3) amorphous phases; (2) sp^2–sp^3 nanocomposite amorphous phases consisting of both diamond-type and graphite-type clusters; (3) diamond-graphite nanocrystalline composites. From the width of diffraction peaks, one can estimate the sizes of structurally coherent clusters at approximately 10–20 Å for amorphous phases and at approximately 30–50 Å for nanocrystalline composites. There is some evidence of existing angular correlations in cluster orientations in the disordered phases (Blank, Tatyanin, & Kulnitskiy, 1997), similar to those observed for disordered graphite-type phases obtained at lower pressures (Blank, Kulnitskiy, et al., 1995; Tat'yanin, Lyapin, Mukhamadiarov, Brazhkin, & Vasiliev, 2005). With increasing pressure, the fraction of graphitic-type (sp^2) clusters vanishes and fullerite C_{60} undergoes temperature-induced transformation to amorphous (Hirai et al., 1994, 1995) and nanocrystalline (Irifune et al., 2003; Sumiya et al., 2006) diamond.

3.21.7 Hard Nanostructured Carbon Modifications Prepared at Moderate Pressures and High Temperatures

The large set of samples was produced in a piston–cylinder high-pressure device at synthesis pressures P_{syn} from 0.5 to 1.5 GPa and temperatures T_{syn} from 1100 to 1600 K. Besides several samples were obtained at $P_{syn} \approx 0.15$–0.2 GPa in a gas cell with the use of nitrogen gas pressure. The duration of the temperature treatment under pressure was approximately 5–10 min. The samples of carbon phases synthesized at pressures 0.15–1.5 GPa have quite a low density between 1.6 and 1.9 g/cm^3, while for the synthesis pressures 3–15 GPa the density is 2–2.8 g cm^{-3} (**Table 1**).

The transitional P,T-phase diagram, including its low-pressure part, obtained through our experiments, is shown in **Figure 6**. The selected typical structural data for the nanocarbon phases are presented in **Figure 9**. The structure of the samples obtained at moderate pressures is noticeably different from that of nanographite phases prepared at high pressures $P_{syn} > 3$ GPa. The main maximum of the structure factor of carbon phases obtained at low pressures corresponds to the wave vector value $Q \approx 1.3$ Å^{-1}, which is far from the main graphite peak (at approximately 1.87 Å^{-1}) and fairly close to the (220) line of molecular C_{60} (at approximately 1.25 Å^{-1}), determined by the distances between the centers of the C_{60} molecules, $d = 4\pi/Q_{(220)} \approx 10$ Å. At the treatment temperature exceeding 1300 K, an additional maximum, along with the first one, appears at $Q \approx 1.8$ Å^{-1}, which can be clearly associated with expanded graphite. The intensity of the maximum at $Q \approx 1.8$ Å^{-1} increases with the rise of the treatment temperature, while the peak intensity at $Q \approx 1.3$ Å^{-1} decreases. If the pressure of treatment is >3 GPa, the main peak of the structural factor corresponds to nanocrystalline graphite ($Q \approx 1.85$–1.9 Å^{-1}), and the halo at $Q \approx 1.3$ Å^{-1} is observed only in a narrow range of the synthesis temperatures from 1100 to 1250 K.

The HRTEM images from the samples (**Figure 10**) confirm the X-ray diffraction evidence that the structure of the nanocarbon modifications prepared at moderate pressures and temperatures $T_{syn} \sim 1300$ K incorporates interlinked curved molecular fragments, while at $T_{syn} \approx 1500$ K the material is mainly composed of graphite nanograins, although the atomic planes still show some curvature (**Figure 10(c)**). Only at higher pressures do the atomic planes become nearly parallel (**Figure 10(d)**).

The Raman spectra (**Figure 11**) are similar to those for disordered graphites and amorphous sp^2-based carbon modifications. Aside from the weak maxima near 450 and 800 cm^{-1}, all the spectra show two main maxima with the peak positions at 1330–1350 and 1580–1605 cm^{-1}. The given maxima are usually interpreted as corresponding to the D- and G-bands of disordered graphite (Kozlov et al., 1995; Wood et al., 2000). Note that the D-band, as a rule, is located at 1350–1360 cm^{-1}, and the G-band at 1580–1590 cm^{-1}, that is, the positions of the D- and G-bands in our experiments are slightly shifted. The lower the synthesis pressures, the higher are the frequencies of the corresponding peaks in spite of the lower density of the samples. All the features of the Raman spectra correspond to disordered carbon materials (Ferrari & Robertson, 2000).

Table 1 Synthesis conditions (P_{syn} and T_{syn}), density (ρ), elastic moduli (B, G, and E) from ultrasonic measurements, Young modulus from the nanoindentation curves (E^*), hardness (H) measured by different techniques, H/E ratio (where the hardness and Young modulus are averaged from different techniques), and elastic recovery (R) for different nanostructured carbon phases. Details of the notations are presented in Section 3.21.4. The last row shows absolute uncertainties

N	P_{syn} (GPa)	T_{syn} (K)	ρ (g cm^{-3})	B (GPa)	G (GPa)	E (GPa)	E* (GPa)	H (GPa)	H_1 (GPa)	H* (GPa)	H/E	R (%)
1	0.15	1300	1.6	15	12	28	28	4	3.7	3.5	0.13	78
2	0.5	1200	1.75	16	13	32		5	5.2		0.19	89
3	0.5	1350	1.75	26	18	44	45	6.5	7	7.5	0.16	83
4	0.75	1380	1.8	31	20	49		8.5	8		0.17	
5	0.75	1420	1.75	31	20	49		8.5	7.5		0.17	
6	1.1	1200	1.81	28	18	44.5		8.5	7		0.17	
7	1.1	1250	1.82	33	21	52	56	8.5	6.5	9	0.17	89
8	1.1	1300	1.82	35	22	55	57	8.5	7.5	10.2	0.18	88
9	1.2	1400	1.78	35	22	55	59	11.5	12.5	12.8	0.22	92
10	1.4	1500	1.87	42	17	46		6	5.5		0.14	
11	3.5	1200	1.95				59	8		9	0.13	77
12	3.5	1400	2.05				77	10.5		11	0.13	79
13	7.0	1150	2.2				115	18		16	0.14	82
14	7.0	1350	2.25				80	11		11.5	0.14	82
15	12.0	1100	2.5				98	13		12	0.13	80
16	15.0	800	2.8				410	55		46	0.12	93
17	15.0	1100	2.8				130			17	0.13	90
$\pm\Delta$	0.05–0.2	30–60	0.05	2	2	3	2	1.5	1	0.5	0.03	3

The results for the hardness and elastic moduli for several typical samples are presented in Table 1. The samples obtained at moderate pressures P_{syn} have sufficiently high hardness values $H \sim 5$–15 GPa and the record high H/E ratio values of approximately 0.18–0.22, as well as the record high values of the elastic recovery of approximately 85–92% (Figure 12). It should be mentioned that for the nanographite modifications prepared at high pressure (3–15 GPa), the H/E ratio is around 0.1 with a maximum value of approximately 0.14 (Table 1). The data of hardness and elastic moduli, obtained through various techniques, are in good agreement (Table 1). Let us note that the nanocarbon samples with hardness values $H > 8$ GPa can easily scratch a tungsten carbide hard alloy with hardness $H \approx 15$ GPa, the capability attributable to the high elastic recovery of the new phases. The values of the elastic moduli for the hard carbon phases produced at moderate pressures exceed those for graphite despite the lower density, although being below those for carbon modifications obtained at high pressures P_{syn} >3 GPa.

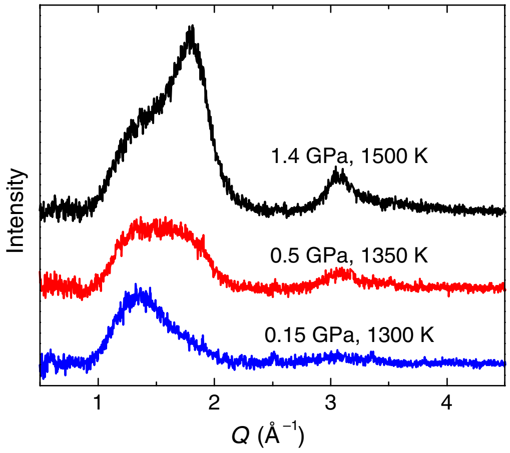

Figure 9 X-ray diffraction patterns from samples synthesized at low pressures. Pressure and temperature of synthesis mark the corresponding patterns.

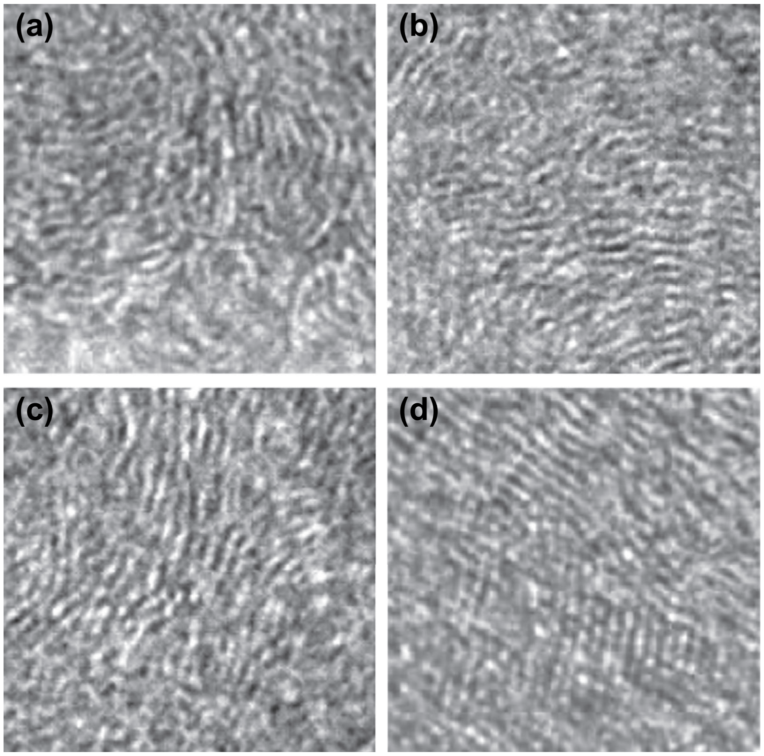

Figure 10 Typical HRTEM images for high-temperature amorphous and nanographite phase synthesized from C_{60}. The synthesis conditions are the following: (a) 0.15 GPa and 1300 K, (b) 0.5 GPa and 1350 K, (c) 1.4 GPa and 1500 K, and (d) 8 GPa and 1300 K. (a)–(c) Correspond to X-ray diffraction data in **Figure 9**. The size of images approximately corresponds to 10 nm.

Thus, the synthesis of nanocarbon modifications at moderate pressures in a narrow temperature region around 1400 K permits us to prepare a carbon material with a high hardness and elastic recovery.

High hardness and the record elastic recovery values of the samples under study are evidently related to the peculiarities of their structure on the nanometer scale. In this structure, being in some respect similar to the structure of schwarzite-1248 and amorphous schwarzite (Donadio, Colombo, & Benedek, 2004; Townsend,

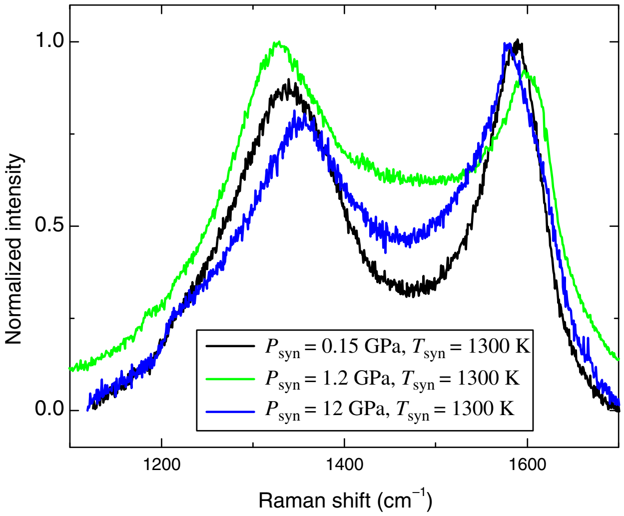

Figure 11 Typical Raman spectra for nanostructured carbon modifications synthesized from C_{60} at high temperatures and at low, moderate, and high pressure.

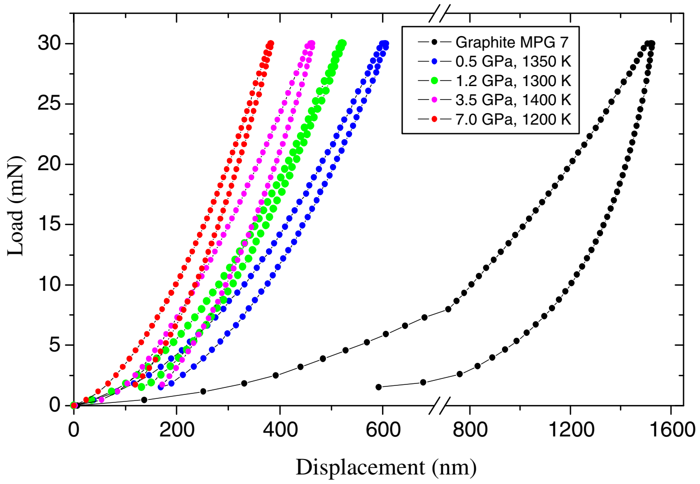

Figure 12 Nanoindentation curves for nanostructured carbon modifications synthesized from C_{60}, compared with that for ordinary high-quality dense graphite. The legend indicates the pressure and temperature of synthesis.

Lenosky, Muller, Nichols, & Elser, 1992), the interlinked curved parts of the C_{60} molecules and graphite nuclei that grow and absorb the curved parts on heating are combined. It is interesting that the predicted Young's modulus of the amorphous schwarzite of approximately 29 GPa (Donadio et al., 2004) is quite close to the value of the Young's modulus of the sample of 1–28 GPa. The randomness of the structure and the lack of "soft" directions ensure quite high values of the elastic moduli (by 1.5–2 times higher than those for graphite) in spite of the lower density. The difficulty of an intergrain sliding in the given structure, heterogeneous at the nanoscales, causes hardness to rise, approaching its "ideal" level. The high elastic recovery can be explained in the framework of a "squeezed chicken wire" model (Alexandrou, Scheibe, Kiely, et al., 1999). In a C_{60} molecule, the bonds between carbon atoms, as distinct from graphite, are disparate as there are both single and double ones. After the breakup of a molecular structure, a considerable portion of the double bands is obviously retained in nanocarbon phases, and it leads to a slight increase in the Raman G-band frequencies.

At $P_{syn} > 2$ GPa, the graphitization of a polymer C_{60} phase while heating is an easier process than the graphitization of a molecular C_{60} in the pressure range 0.15–1.5 GPa. This is due to the fact that the density of polymer C_{60} phases at $P_{syn} \sim 2$–10 GPa and $T_{syn} \sim 1000$ K is close to that for graphite, which facilitates the easy formation and growth of the nucleation centers. Part of carbon atoms ($\sim$10–20%) in polymer phases is in the sp^3 four-coordinated states; after the destruction of molecules, these atoms can serve as stress relaxation centers at the boundaries of the formed graphite nuclei. At moderate pressures of 0.15–1.5 GPa, a molecular C_{60} has a considerably lower density than that of graphite, and, after the destruction of molecules, it transforms into a disordered carbon state consisting of curved molecular fragments. Graphite nucleation begins only after significant overheating as a diffusion-driven nanorecrystallization. As a result, a wide pressure–temperature region appears, in which a new nanomaterial, representing a nanomixture of nanographite nuclei and curved molecular fragments, emerges. At the ratio of the nanographite atoms to molecular fragments being around 3:1 (synthesized at $T_{syn} \approx 1400$ K), one can achieve mechanical characteristics close to the "ideal" level.

Minimal pressures of the synthesis of hard nanocarbon phases $P_{syn} \approx 0.15$ GPa employed in this work are dictated by the necessity to compact a pristine C_{60} powder. If one has large C_{60} fullerite single crystals, it seems possible to produce hard carbon nanostructured phases by heating the samples at an ambient pressure. Moderate values of pressure of approximately 1 GPa required to obtain nanostructured carbon with a hardness of approximately 10–15 GPa and elastic recovery of approximately 90% enable one to synthesize samples of an optional shape of dozens of centimeters in size, which is promising for industrial applications of these new materials.

3.21.8 Amorphous Diamond-like Carbon and Diamond-based Nanocomposites

Strongly disordered diamond-based carbon materials, prepared from C_{60} at high pressures and high temperatures and corresponding to the third region discussed in Section 3.21.6, are of special interest since these materials reveal the highest record mechanical characteristics. It is well known that many mechanical properties of polycrystals improve as the grain size decreases (Barnett & Madan, 1998; Brazhkin et al., 2002; Yip, 1998). In this connection, it is of enormous interest to synthesize diamond-based nanocomposites. However, because of residual porosity, chemical impurities, and residual stresses at grain boundaries, the standard methods of compacting diamond nanopowders do not yield composites with high mechanical characteristics. An alternative method for obtaining a nanocrystalline state is by the crystallization of the corresponding amorphous phase. A distinctive feature of amorphous carbon modifications is that the average coordination number in them can actually vary from 2 to 4. It is natural to assume that amorphous phases with a large fraction of fourfold coordinated sp^3 states are preferred for obtaining diamond nanocomposites. To date, amorphous modifications of carbon with a large fraction of sp^3 states have been synthesized only in the form of thin films (Weiler, Sattel, Giessen, et al., 1996). The transformations of fullerite C_{60}, which were discussed above, open up new possibilities for obtaining 3D samples of amorphous and nanocrystalline diamond-like carbon.

The amorphous carbon obtained from C_{60} contains an appreciable fraction of atomic sp^3 states at pressures of 8–9 GPa, where a crossover is observed between temperature-induced 2D and 3D polymerizations (Brazhkin, Lyapin, et al., 2002; Hirai et al., 1995; Lyapin, 2002). However, the amorphous network becomes predominantly fourfold coordinated only at pressures 12–13 GPa (Brazhkin, Lyapin, et al., 2002; Lyapin, 2002). As a result, an appreciable yield of diamond from C_{60} without intermediate graphitization is kinetically reliable only at $P > 12$ GPa.

The amorphous samples obtained at lower temperatures of approximately 800–900 K at 12–13 GPa are uniform materials on a micron scale, while the high-temperature ~1000–1500 K samples have a complicated macroscopic morphology. The change in the morphology of the samples is due to the rearrangement of the structure on a nanoscale, while the sample remains amorphous on large scales. Crystallization of the amorphous nanocomposite starts near 1700 K at 12.5 GPa. At this temperature, diamond crystallites of an appreciable size are formed, since in addition to the (111) reflection peak there are weak (220) and (311) reflections, as are graphite clusters, since the peaks of the graphitic phase shift toward the exact positions of the (002) and (004) reflections of graphite. The crystallite sizes estimated from the widths of the X-ray peaks are approximately 50 Å for graphite and approximately 25 Å for diamond.

The data for the hardness and fracture toughness coefficient of amorphous and nanocomposite samples are presented in Figure 13 (which also show the points corresponding to 3D polymers). The large variance in the values obtained for the hardness makes it impossible to establish a systematic dependence on the load or type of phase. Nonetheless, the measurement accuracy is sufficient to conclude that an appreciable increase in hardness to values characteristic for diamond is observed for nanocomposite phases with a density in the range of 3.0–3.4 g/cm^3. The fracture toughness coefficient of such phases can be 1.5–2 times greater than the values for

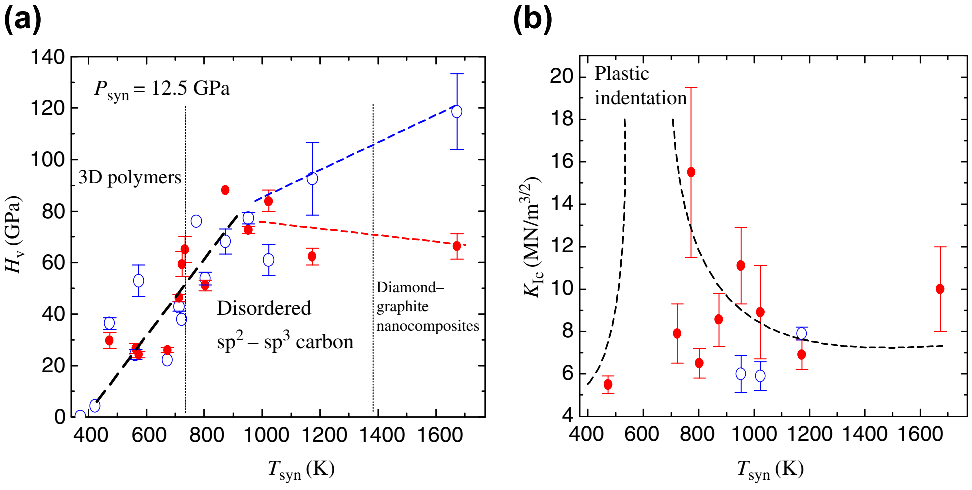

Figure 13 Vicker's hardness (a) and fracture toughness coefficient (b) versus synthesis temperature for C_{60}-based carbon phases obtained at pressures of 12.5–13.5 GPa. The measurements were carried out at the indenter loads 1.96 N (open symbols) and 5.42 N (solid symbols). The dashed lines serve as guides for the eyes. In the interval of 600–700 K, the fracture toughness is not measurable.

diamond 7–10 MN/m$^{3/2}$. Recently, we studied several amorphous sp^3-rich samples by the nanoindentation technique. The hardness value 40–50 GPa and huge elastic recovery (97%) have been found (**Figure 14**).

One can make several remarks on the mechanisms of formation of the superhard sp^3 amorphous and diamond-based nanocomposite phases. Although the formal thermodynamic equilibrium of fullerite C_{60} with diamond lies at negative pressures, kinetic factors determine the real structural evolution of C_{60} under pressure. Specifically, at pressures up to 8 GPa, the fullerite–diamond transition occurs through graphitization, just as for amorphous carbon, namely soot (Onodera, Irie, Higashi, Umemura, & Takenaka, 1991). However, graphitization of soot is observed at least up to 15 GPa (Onodera et al., 1991), whereas for C_{60}, the situation changes radically already at 12–13 GPa. An amorphous phase with a high fraction of sp^3 states (up to 80%) forms in this pressure range at rather low temperatures of approximately 800 K. The convex shape of the spherical molecules makes it possible for them to approach one another effectively under pressure and lends a high capacity for the formation of covalent bonds between molecules, with the appearance of sp^3 states. At the same time, the extremely high stability of C_{60} molecules prevents the formation of graphitic clusters. The formation of a disordered network of atoms from 3D polymers apparently occurs without the rupture of a large number of covalent bonds of the initial C_{60} molecules as structural units.

As the synthesis temperature increases, spatial separation of sp^2 and sp^3 atoms occurs (which is simply advantageous energetically), and first amorphous and then crystalline diamond-plus-graphite nanocomposites form. The yield of nanodiamonds accompanying the crystallization of such an amorphous state reaches 50–80%. The corresponding crystallization temperature ($\sim$1500–1700 K) is much lower than the temperature of the direct noncatalytic graphite-to-diamond transformation at these pressures.

It is interesting that the mechanical characteristics of the synthesized nanocomposites are extremely high, even though the materials contain a large fraction of graphitic clusters. Several reasons for such highest characteristics can be pointed out: (1) the optimal size of nanocrystallites ($\sim$50 Å) corresponding to the maximum hardness values; (2) the uniform character of the formation of composites from rather soft molecular phases without nanopores, impurities, and distinct nanocrystallite boundaries; (3) the formation of a rigid "skeleton" of diamond-like clusters; and (4) the binding effect of graphite-like clusters, whose elastic recovery perpendicular to the graphene planes is anomalously high, whereas the strength of the planes against longitudinal stresses is very high.

Here, we mainly discuss the disordered diamond (sp^3)-based phases obtained near 12–15 GPa, thus, containing a large fraction of sp^2 carbon (atomic sites or graphitic nanoclusters), but still being extremely hard materials with mechanical properties comparable to or exceeding those for diamond. On increasing the pressure and diminishing the fraction of graphitic-type (sp^2) clusters (atomic sites) to negligible or zero values, one can hope to obtain carbon materials, such as amorphous (Hirai et al., 1994, 1995) or nanocrystalline (Irifune et al., 2003; Sumiya et al., 2006) diamond, with higher mechanical characteristics.

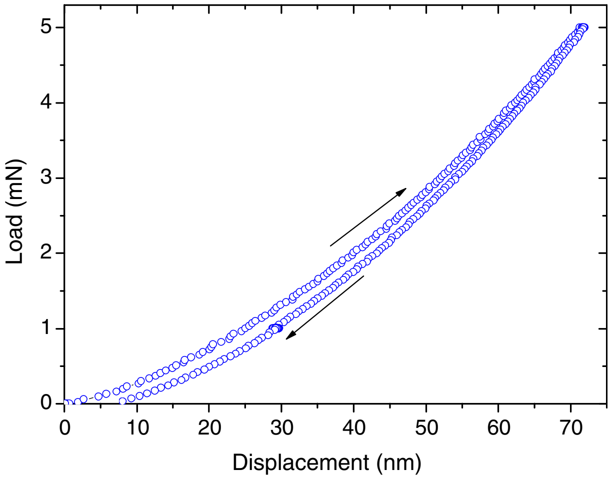

Figure 14 Nanoindentation curve for nanostructured carbon modification synthesized from C_{60} at 16 GPa and 900 K. Analysis of this curve gives the following characteristics of the sample: hardness is equal $H = 41.5$ GPa, Young's modulus $E = 395$ GPa, and elastic recovery $R = 93\%$.

3.21.9 Correlation between Density, Elasticity, and Hardness for New Carbon Phases

A vast variety of carbon phases, pressure synthesized from C_{60}, provide a unique possibility (e.g., comparing with other group IV elements) of experimental modeling of covalent structures with a variable bonding nature (in particular, the sp^2/sp^3 ratio), the effective dimension of covalent connectivity, the nanometer-scale atomic arrangement (cluster assembling), the degree of disorder, and so on. This offers a possibility of studying the correlation of various mechanical and physical properties of carbon phases with quite different structures. The correlations of this type are of general interest, because they give simple efficient criteria for predicting the mechanical properties of novel and hypothetical carbon materials.

The correlations between the electron density (the ordinary density for particular cases) and elastic characteristics, as well as between the elasticity (first of all, the shear elasticity) and hardness exist in the general case of solids, including superhard materials (Brazhkin, Lyapin, et al., 2002; Clerc & Ledbetter, 1998; Teter, 1998). In **Figure 15**, we consider the Vickers hardness versus density dependence, $H_V(\rho)$, for different carbon phases, prepared from fullerite C_{60}, in comparison with the linear interpolation for the similar data on amorphous carbon films (Weiler et al., 1996). Both sets of the data are correlated fairly well. There is a clear tendency for the increase of hardness with density. The hardness increase for 3D polymerized C_{60} phases directly indicates the increase in the number of sp^3 sites in accordance with the well-known dependence of density versus the share of sp^3 sites in amorphous carbon (Weiler et al., 1996). One should note that the materials discussed include both homogeneous (for the length scale of the medium-range order ~30 Å) and heterogeneous phases. The limited data (see, e.g. Blank, Serebryanaya, Dubitsky, et al. (1998), Brazhkin, Lyapin, Popova, et al. (1998), Patterson, Catledge, Vohra, Akella, and Weir (2000) on the hardness of materials synthesized from fullerites C_{70} or $C_{(2N)}$ (the mixture of various fullerene molecules, $50 < 2n < 180$)) are consistent with the data presented in **Figure 15** for C_{60}-based phases.

Not only the atomic-level structure and interactions but also the degree of homogeneity can vary in disordered and nanocrystalline forms of carbon and affect the mechanical properties. One can suggest that the dispersion of $H_V(\rho)$ points in **Figure 15** is related to the nanometer-scale morphology of samples. In particular, the disordered sp^2 phase and diamond-based nanocomposites correspond to the upper boundary of the $H_V(\rho)$ correlation area. Thus, the variation of the morphology, that is, the structure and texture on a length of 10–1000 nm, is another possibility for changing the properties of carbon materials.

One can suggest several reasons for the superhard property of disordered sp^2 phases, when their densities (**Figure 7**) are very close to that of graphite: (1) the nanometer-scale disorder of graphite-type covalent layers, providing the 3D arrangement of clusters with the 2D covalent geometry; (2) a possible presence of sp^3 carbon sites adopted from the preceding 2D polymerized phases; (3) a high elastic recovery of the graphite-type structures orientationally disordered at the medium-range order scale, similarly to fullerene-like (actually graphite) CN_x films (Sjöström, Stafström, Boman, & Sundgren, 1995). Considering the mechanical properties of the phase synthesized at low pressures, one should take into account a possible heterogeneity of samples, as

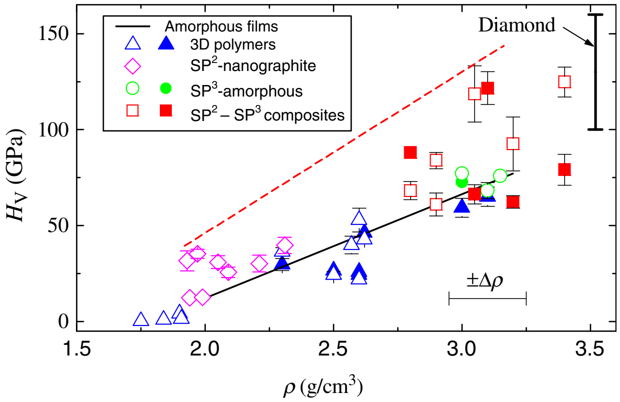

Figure 15 Hardness versus density for carbon phases synthesized from C_{60} (sp^3 amorphous phases are diamond-like). Open symbols correspond to an indenter load of approximately 2 N and solid symbols correspond to approximately 5 N. The data for diamond are taken for loads of 2–5 N. The solid line corresponds to the dependence for amorphous films from Weiler et al. (1996). The dashed line is the boundary of maximum possible hardness values for carbon phases obtained from C_{60}.

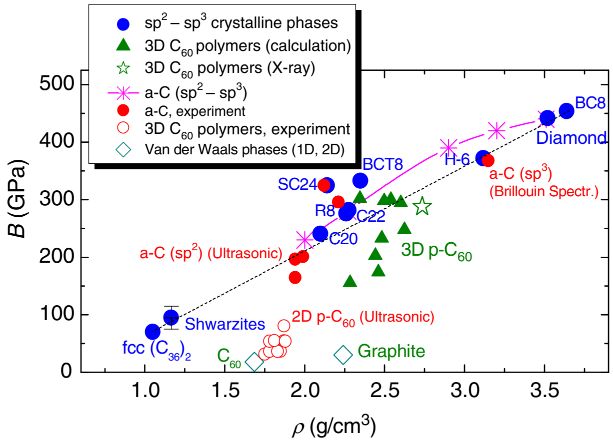

Figure 16 Bulk modulus versus density for allotropic carbon modifications and disordered phases (a-C) obtained from C_{60} (experimental methods are indicated in figure) and calculation data for various hypothetical amorphous and crystalline phases.

well as anisotropy related to the 2D covalent topology of low-pressure phases (Brazhkin, Glazov, Mukhamadiarov, et al., 2002; Lyapin, Mukhamadiarov, Brazhkin, et al., 2003; Mukhamadiarov, Lyapin, Popova, Brazhkin, & Glazov, 2003). From the point of view of the rigidity percolation theory (see the previous section), the disordered sp^2 phases can be a hard phase, since $Z = 3$ for them. But these phases should have a 3D atomic arrangement of covalent structure to be hard (covalently rigid) materials, opposite to soft graphite with an effectively 2D arranged covalent structure. The nanometer-scale cluster nature of the disordered sp^2 phases seems to cause the 3D arrangement of the atomic structure for $Z = 3$.

An even better correlation is observed between the bulk elastic modulus B and the density of carbon phases whose covalent structure is characterized by 3D ordering. In **Figure 16**, experimental data for the disordered sp^2–sp^3 phases synthesized from C_{60} (Brazhkin, Glazov, et al., 2002; Lyapin et al., 2000; Manghnani, Tkachev, Zinin, et al., 2001), for the 3D C_{60} polymers (Mezouar et al., 2003), and for the real allotropic carbon modifications are compared with numerous calculations for hypothetical phases, including amorphous structures (Kelires, 1994), 3D C_{60} polymers (Burgos et al., 2000; Perottoni & da Jornada, 2002; Zipoli & Bernasconi, 2008), sp^2 crystalline phases (Côté, Grossman, Cohen, & Louie, 1998; Jungnickel, Sitch, Frauenheim, et al., 1998; Liu, Cohen, Hass, & Tamor, 1991; Rosato, Celino, Benedek, & Gaito, 1999; Townsend et al., 1992), and the high-pressure BC8 phase (Mailhiot & McMahan, 1991). A good agreement basically between experimental and theoretical data is noteworthy. A more detailed discussion on this subject has been presented by Lyapin and Brazhkin (2002). One should note that only the phases with 1D or 2D covalent bonding (graphite and 1D or 2D C_{60} polymers), as well as the starting fullerite (a molecular van der Waals crystal with zero-dimensional covalent bonding), exhibit a much larger compressibility than the 3D bonded phases (**Figure 16**).

3.21.10 Nonhydrostatic Stresses and Anisotropy of Mechanical Properties of Hard Carbon Phases

Fullerite C_{60} is a highly metastable phase with respect to ordinary graphite and diamond. Moreover, covalent carbon–carbon bonds are rather strong, causing large energy barriers for the reconstruction of the carbon covalent structure. These circumstances result in specific features of the transitional pressure–temperature phase diagram of fullerite C_{60}. The first is the ambiguity of the carbon structure in a particular pressure–temperature point, since the structure of the obtained phase can strongly depend on the pressure–temperature path to the final point, as well as on the kinetic factors, such as the rate of pressure or temperature change. The ambiguity of the product phase during a different scenario of pressure–temperature treatment in the region of 1D and 2D polymerization (up to $P \approx 8$ GPa and $T \approx 1000$ K) is discussed in the original papers (e.g., Agafonov et al. (1997), Davydov et al. (1997, 1998, 2000)). One should also emphasize that the transformation of fullerite C_{60} during room-temperature pressurization can depend on particular experimental conditions (Duclos et al., 1991; Hodeau et al., 1994; Kosowsky et al., 1993; Moshary et al., 1992; Núñez-Regueiro, Abello, et al., 1992; Núñez-Regueiro, Monceau, et al., 1992; Núñez-Regueiro et al., 1991; Snoke et al., 1992; Yoo & Nellis, 1991, 1992). Previously, we also mentioned the importance of the starting orientational state of C_{60} molecules in the pristine phase (Sundqvist, 1998) and the possibility of different scenarios of 3D polymerization dependent on the mutual orientation of C_{60} molecules. Particularly, there is experimental evidence of a significant difference of pressure–temperature and temperature–pressure paths on the product structure of the 3D polymer and its stability (Talyzin & Dubrovinsky, 2003, 2004; Talyzin et al., 2005). The 3D polymerization processes of 2D polymers of C_{60}, preliminarily obtained during some pressure–temperature paths, also differ from that observed for pristine C_{60} (Chi et al., 2003; Meletov et al., 2003).

Another important feature of nonequilibrium transformations in fullerite C_{60} under pressure, which we consider here in detail, is a strong influence of nonhydrostatic pressure conditions and shear stresses on the anisotropy of product phases. This effect is known now for the 3D polymers of C_{60} (Manghnani et al., 2001; Marques et al., 1999), hard disordered graphite-type (sp^2) phases (Brazhkin, Glazov, et al., 2002; Lyapin et al., 2003; Mukhamadiarov et al., 2003), and 2D polymerized phases (Lyapin et al., 2003; Marques, Mezouar, Hodeau, & Núñez-Regueiro, 2002; Mukhamadiarov et al., 2003). The pressure anisotropy naturally occurs in quasihydrostatic conditions that occur, for example, in a toroid-type apparatus with a single loading axis (z-axes in a subsequent discussion).

In this respect, until now the bulk B and shear G moduli were calculated by using the isotropic medium approximation in the studies of the elastic properties of materials obtained from C_{60} (Levin, Blank, Prokhorov, Soifer, & Kobelev, 2000; Lyapin et al., 2000; Prokhorov, Blank, Buga, & Levin, 1999). Such calculations provided the values of Poisson's ratio that were anomalously high for covalent structures and the values of the bulk modulus that were nonphysically high (Levin et al., 2000; Prokhorov et al., 1999). However, the possible orientational anisotropy and inhomogeneity of materials were not taken into account in these calculations.

A detailed study of elastic properties was carried out for the hard disordered graphite-type (sp^2) phases (Brazhkin, Glazov, et al., 2002; Lyapin et al., 2003) and the rhombohedral 2D polymerized phases (Lyapin et al., 2003; Mukhamadiarov et al., 2003). The values obtained for the density and the microhardness, $\rho = 1.9–2.4$ g/cm^3 and $H_V = 21–32$ GPa, are in good agreement with the data reported for disordered phases in earlier publications. A fundamentally new result of (Brazhkin, Glazov, et al., 2002) is the strong anisotropy observed for the velocities of transverse and, especially, longitudinal ultrasonic waves propagating parallel and perpendicular to the Z axis (**Figures 17** and **18**), which corresponds to the loading axis during the sample synthesis. The anisotropy of the velocities reaches 20–30%. For microhardness, the values obtained with the indentation parallel to the z axis ($H_z = 27$ and 21 GPa for samples prepared at 1270 and 1450 K, respectively) and perpendicular to it ($H_x = 32$ and 27 GPa for the same samples) are also different, the microhardness

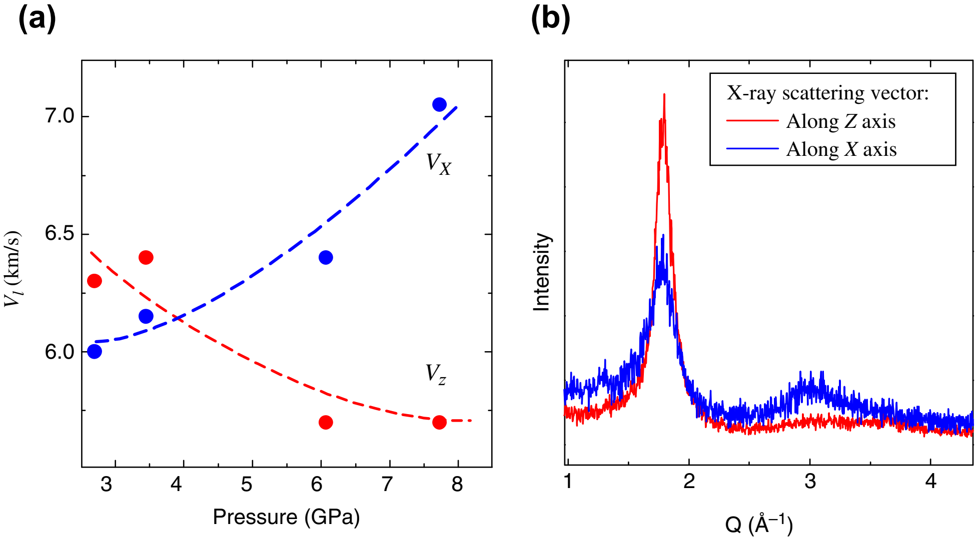

Figure 17 Anisotropy of the nanographite phases revealed by longitudinal ultrasonic velocities plotted as a function of the synthesis pressure (a) and by X-ray diffraction patterns (with the subtracted middle lines) recorded in the reflection mode for different geometries of the scattering vector (b). Z axis corresponds to the pressure chambers load direction (additional uniaxial pressure component).

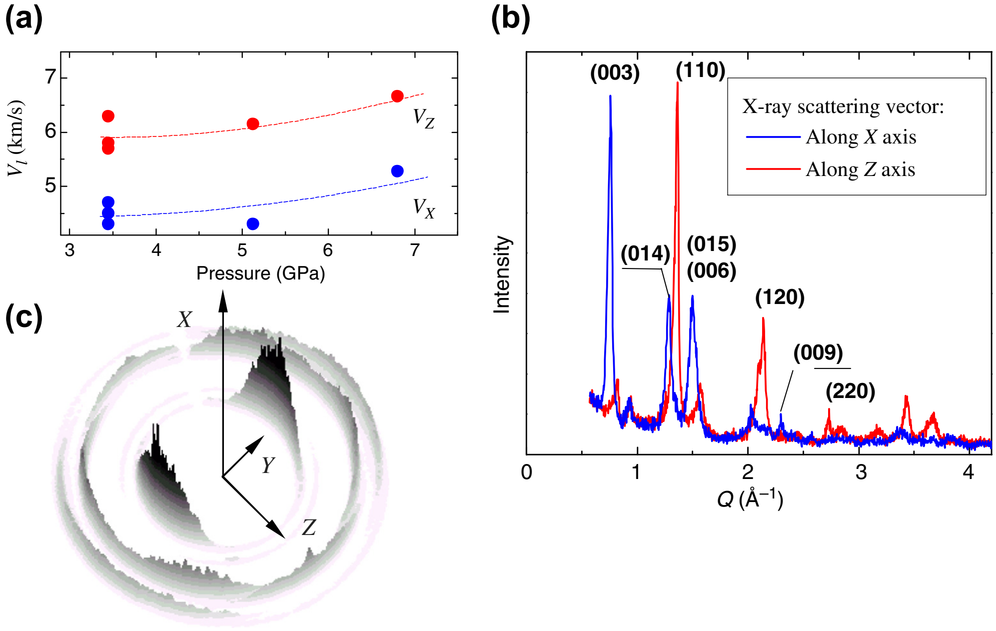

Figure 18 Anisotropy of the 2D polymerized rhombohedral C_{60} phases revealed by longitudinal ultrasonic velocities plotted as a function of the synthesis pressure (a), X-ray diffraction patterns (with the subtracted middle lines) recorded in reflection mode for different geometries of the scattering vector (b), and 3D plot of intensity from the 2D diffraction image obtained in the transmission mode with the X-ray beam along the X axis (c). The Z axis corresponds to the pressure chamber load direction (additional uniaxial pressure component).

anisotropy being within approximately 15–20%. An accurate calculation of elastic constants in the framework of model of elastic medium with a uniaxial anisotropy (Brazhkin & Lyapin, 2004; Mukhamadiarov et al., 2003) gives reliable values for bulk modulus (35–55 GPa) and Poisson's ratios for different directions (0.15–0.3).

The presence of anisotropy should be naturally attributed to the additional uniaxial pressure component that occurs in the quasihydrostatic conditions of the experiment. The X-ray diffraction data suggest that the sp^2 phases under consideration have a nanocluster structure in which the clusters can have the form of graphite-like crystallites with a parallel atomic packing or an amorphous conglomerate of the partially ordered nanometer regions. The velocities of ultrasonic waves propagating along the graphite planes are known to be higher than the propagation velocities in the perpendicular directions. It is natural to attribute the anisotropy of the elastic properties observed in the experiment to the anisotropy of the spatial orientation of the structure-forming clusters, namely, to the presence of the preferred orientation of graphite-like planes that is normal to the *z* axis, that is, the axes of additional uniaxial stress. The deviation from the spherically symmetric distribution of the orientation of graphite-like clusters leads to the formation of a sort of texture in the disordered samples. The correlations between the elastic and ultrasonic anisotropy for the both disordered graphite-type and rhombohedral 2D polymerized phases can be recognized in **Figures 17** and **18**. A more detailed analysis of these relations can be found in Brazhkin, Glazov, et al. (2002), Lyapin et al. (2003), and Mukhamadiarov et al. (2003). Transmission electron microscopy (Tat'yanin et al., 2005) and X-ray diffraction microtomography (Álvarez-Murga et al., 2011) highlight that nanocluster structure, existing of long-range correlations for the orientation of clusters, lamellar and tweed morphology and texture, and possible macroscopic anisotropy are intrinsic properties of the disordered graphite-type phases prepared from C_{60}, and all these properties can be recognized as a signature of stresses in the parent phase at different scales from the atomic level (atomic density modulation) to the macroscopic one (nonhydrostatic pressure environment).

Summarizing this section, one can conclude that any study of the physical properties of carbon materials obtained from C_{60} should take into account the prehistory of synthesized samples, such as the pressure–temperature paths, kinetic parameters of experiment, and nonhydrostatic component of pressure in pressure-transmitting medium.

3.21.11 Final Remarks

Finally, the following main trends can be recognized in the structural transformations of C_{60} under high pressure: (1) C_{60} fullerite under high pressure and temperature transforms to a more stable graphite or diamond through the intermediate polymolecular and disordered phases, (2) an increase in the temperature acting on C_{60} leads eventually to the irreversible destruction of the molecular structure, and (3) an increase in pressure on heating C_{60} leads to an increase in the density of the synthesized phases and in the mean coordination number of carbon atoms (in the interval from 3 to 4).

The data on the mechanical properties of pressure-synthesized phases provide the key information for potential ways of application of C_{60}-based materials. One can select three groups of novel C_{60}-based carbon materials with properties promising for future applications: (1) moderate pressure (0.1–8 GPa) disordered sp^2-based carbon phases; (2) superhard diamond-based nanocomposites (ceramics), synthesized at pressures $\geq$12 GPa and high temperatures; (3) 3D polymerized C_{60}-based materials (pressures $>$9 GPa and moderate temperatures).

The low-pressure disordered sp^2-based carbon phases have an interesting combination of high hardness up to 30 GPa and a high elastic recovery and low density (1.6–2.4 g/cm^3). There are two technological advantages in this material. The pressures necessary for the synthesis of these phases are available for operating large-volume high-pressure devices. Therefore, the synthesis of specimens with a large size and controllable shape is potentially accessible using the high-pressure techniques.

The superhard diamond-based high-pressure disordered phases can have mechanical properties including hardness and fracture toughness comparable to or even exceeding those of the best specimens of natural diamonds, due to the nanocomposite structure of these materials. The 3D-polymerized C_{60}-based materials have a unique combination of high hardness and high plasticity. All high-pressure C_{60}-based materials can be applied in future high-pressure techniques. In particular, we proposed in (Brazhkin et al., 1998) the use of the 3D polymerized phases as a material for gaskets employed in experiments with the generation of extremely high pressures.

Acknowledgments

The authors are grateful to S.M. Stishov, V.I. Bugakov, S. Dub, S.V. Popova, E.L. Gromnitskaya, V.A. Davydov, A.A. Pozdnyakov, S.G. Lyapin, O.V. Stal'gorova, V.V. Mukhamadiarov, Ye.V. Tatyanin, R.A. Sadykov, R.N. Voloshin, Yu.A. Klyuev, A.M. Naletov, and A.G. Glazov for helpful discussions and for experimental efforts in the present review.

References

Agafonov, V., Davydov, V. A., Kashevarova, L. S., et al. (1997). 'Low-pressure' orthorhombic phase formed from pressure-treated C_{60}. *Chemical Physics Letters, 267*, 193–198.

Alexandrou, I., Scheibe, H.-J., Kiely, C. J., et al. (1999). Carbon films with an sp^2 network structure. *Physical Review B, 60*, 10903.

Álvarez-Murga, M., Bleuet, P., Marques, L., et al. (2011). Microstructural mapping of C_{60} phase transformation into disordered graphite at high pressure, using X-ray diffraction microtomography. *Journal of Applied Crystallography, 44*, 163–171.

Barnett, S., & Madan, A. (January 1998). Superhard superlattices. *Physics World*, 45–48.

Bennington, S. M., Kitamura, N., Cain, M. G., et al. (2000). *In situ* diffraction measurement of the polymerization of C_{60} at high temperatures and pressures. *Journal of Physics: Condensed Matter, 12*, L451.

Berber, S., Osawa, E., & Tománek, D. (2004). Rigid crystalline phases of polymerized fullerenes. *Physical Review B, 70*, 085417.

Blank, V. D., Buga, S. G., & Dubitsky, G. A. (1998). High-pressure polymerized phases of C_{60}. *Carbon, 36*, 319–343.

Blank, V. D., Buga, S. G., Serebryanaya, N. R., et al. (1995). Ultrahard and superhard carbon phases produced from C_{60} by heating at high pressure: structural and Raman studies. *Physics Letters A, 205*, 208–216.

Blank, V. D., Buga, S. G., Serebryanaya, N. R., et al. (1996). Phase transformations in solid C_{60} at high-pressure–high-temperature treatment and the structure of 3D polymerized fullerites. *Physics Letters A, 220*, 149–157.

Blank, V. D., Denisov, V. N., Ivlev, A. N., et al. (1998). Hard disordered phases produced at high-pressure–high-temperature treatment of C_{60}. *Carbon, 36*, 1263–1267.

Blank, V. D., Kulnitskiy, B. A., & Tatyanin, Ye. V. (1995). Structural studies of high pressure phases of C_{60}. *Physics Letters A, 204*, 151–154.

Blank, V. D., Serebryanaya, N. R., Dubitsky, G. A., et al. (1998). Polymerization and phase diagram of solid C-70 after high-pressure–high-temperature treatment. *Physics Letters A, 248*, 415–422.

Blank, V. D., Tatyanin, Ye. V., & Kulnitskiy, B. A. (1997). New structure after thermobaric treatment of solid C_{60}. *Physics Letters A, 225*, 121–126.

Brazhkin, V. V., Glazov, A. G., Mukhamadiarov, V. V., et al. (2002). Elastic properties of carbon phases obtained from C_{60} under pressure: the first example of anisotropic disordered carbon solid. *Journal of Physics: Condensed Matter, 14*, 10911–10915.

Brazhkin, V. V., & Lyapin, A. G. (1996). Transformations of C_{60} fullerite under high pressure-high temperature conditions. *Physics-Uspekhi, 39*, 837–840.

Brazhkin, V. V., & Lyapin, A. G. (2000). Comment on “New metallic crystalline carbon: three dimensionally polymerized C_{60} fullerite”. *Physical Review Letters, 85*, 5671.

Brazhkin, V. V., & Lyapin, A. G. (2004). Hard carbon phases prepared from fullerite C_{60} under high pressure. *New Diamond and Frontier Carbon Technology, 14*, 259–278.

Brazhkin, V. V., Lyapin, A. G., Antonov, Yu. V., et al. (1995). Amorphization of fullerite (C_{60}) at high pressures. *JETP Letters, 62*, 350–355.

Brazhkin, V. V., Lyapin, A. G., & Hemley, R. J. (2002). Harder than diamond: dreams and reality. *Philosophical Magazine A, 82*, 231–253.

Brazhkin, V. V., Lyapin, A. G., & Popova, S. V. (1996). Mechanism of three-dimensional polymerization of fullerite C_{60} at high pressures. *JETP Letters, 64*, 802–807.

Brazhkin, V. V., Lyapin, A. G., Popova, S. V., et al. (1997). Metastable crystalline and amorphous carbon phases obtained from fullerite C_{60} by high pressure–high temperature treatment. *Physical Review B, 56*, 11465–11471.

Brazhkin, V. V., Lyapin, A. G., Popova, S. V., et al. (1998). Mechanical properties of the superhard polymeric and disordered phases prepared from C_{60}, C_{70}, and C_{2N} under high pressure. *Review of High Pressure Science and Technology, 7*, 989–991.

Brazhkin, V. V., Lyapin, A. G., Popova, S. V., et al. (2002). Interplay between the structure and properties of new metastable carbon phases obtained under high pressures from fullerite C_{60} and carbyne. *JETP Letters, 76*, 681–692.

Brazhkin, V. V., Lyapin, A. G., Popova, S. V., Klyuev, Yu. A., & Naletov, A. M. (1998). Mechanical properties of the 3D-polymerized, sp^2–sp^3 amorphous, and diamond-plus-graphite nanocomposite carbon phases prepared from C_{60} under high pressure. *Journal of Applied Physics, 84*, 219–226.

Brazhkin, V. V., Lyapin, A. G., Voloshin, R. N., et al. (1999). Mechanism of the formation of a diamond nanocomposite during transformations of C_{60} fullerite at high pressure. *JETP Letters, 69*, 869–875.

Brazhkin, V. V., Solozhenko, V. L., Bugakov, V. I., et al. (2007). Bulk nanostructured carbon phases prepared from C_{60}: approaching the “ideal” hardness. *Journal of Physics: Condensed Matter, 19*, 236209.

Burgos, E., Halac, E., Weht, R., et al. (2000). New superhard phases for three-dimensional C_{60}-based fullerites. *Physical Review Letters, 85*, 2328–2331.

Chi, D. H., Iwasa, Y., Takano, T., et al. (2003). Bond switching from two- to three-dimensional polymers of C_{60} at high pressure. *Physical Review B, 68*, 153402.

Clerc, D. G., & Ledbetter, H. M. (1998). Mechanical hardness: a semiempirical theory based on screened electrostatics and elastic shear. *Journal of Physics and Chemistry of Solids, 59*, 1071–1095.

Côté, M., Grossman, J. C., Cohen, M. L., & Louie, S. G. (1998). Theoretical study of a three-dimensional all-sp^2 structure. *Physical Review B, 58*, 664–668.

Davydov, V. A., Kashevarova, L. S., Rakhmanina, A. V., et al. (1997). Identification of the polymerized orthorhombic phase of C_{60} fullerene. *JETP Letters, 66*, 120–125.

Davydov, V. A., Kashevarova, L. S., Rakhmanina, A. V., et al. (1998). Tetragonal polymerized phase of C_{60}. *Physical Review B, 58*, 14786–14790.

Davydov, V. A., Kashevarova, L. S., Rakhmanina, A. V., et al. (1999). Particularities of C_{60} transformations at 1.5 GPa. *Journal of Physical Chemistry B, 103*, 1800–1804.

Davydov, V. A., Kashevarova, L. S., Rakhmanina, A. V., et al. (2000). Spectroscopic study of pressure-polymerized phases of C_{60}. *Physical Review B, 61*, 11936–11945.

Donadio, D., Colombo, L., & Benedek, G. (2004). Elastic moduli of nanostructured carbon films. *Physical Review B, 70*, 195419.

Duclos, S. J., Brister, K., Haddon, R. C., Kortan, A. R., & Thiel, F. A. (1991). Effects of pressure and stress on C_{60} fullerite to 20 GPa. *Nature, 351*, 380–382.

Dworkin, A., Szwarc, H., Davydov, V. A., et al. (1997). Thermal studies of C_{60} transformed by temperature and pressure treatments. *Carbon, 35*, 745–747.

Evans, A. R., & Wilshaw, T. R. (1976). Quasi-static solid particle damage in brittle solids. *Acta Metallurgica, 24*, 939–956.

Ferrari, A. C., & Robertson, J. (2000). Interpretation of Raman spectra of disordered and amorphous carbon. *Physical Review B, 61*, 14095–14107.

Gong, J., Wu, J., & Guang, Z. (1999). Examination of the indentation size effect in low-load Vickers hardness testing of ceramics. *Journal of the European Ceramic Society, 19*, 2625–2631.

Goze, C., Rachdi, F., Hajji, L., et al. (1996). High-resolution ^{13}C NMR studies of high-pressure-polymerized C_{60}: evidence for the $[2+2]$ cycloaddition structure in the rhombohedral two-dimensional C_{60} polymer. *Physical Review B, 54*, R3676–R3678.

Harrison, W. A. (1980). *Electronic structure and the properties of solids*. San Francisco: Freeman.

He, H., & Thorpe, M. F. (1985). Elastic properties of glasses. *Physical Review Letters, 54*, 2107–2110.

Hirai, H., Kondo, K., Yoshizava, N., & Shiraishi, M. (1994). Amorphous diamond from C_{60} fullerene. *Applied Physics Letters, 64*, 1797–1799.

Hirai, H., Tabira, Y., Kondo, K., Oikawa, T., & Ishizawa, N. (1995). Radial distribution function of a new form of amorphous diamond shock induced from C_{60} fullerene. *Physical Review B, 52*, 6162–6165.

Hodeau, J.-L., Tonnerre, J. M., Bouchet-Fabre, B., et al. (1994). High-pressure transformations of C_{60} to diamond and sp^3 phases at room temperature and to sp^2 phases at high temperature. *Physical Review B, 50*, 10311–10314.

Horikawa, T., Suito, K., Kobayashi, M., & Onodera, A. (2001). Time-resolved X-ray diffraction study of C_{60} at high pressure and temperature. *Physics Letters A, 287*, 143–151.

Irifune, T., Kurio, A., Sukamoto, Sh., Inoue, T., & Sumiya, H. (2003). Ultrahard polycrystalline diamond from graphite. *Nature, 421*, 599–600.

Ivanovskaya, V. V., & Ivanovskii, A. L. (2010). Simulation of novel superhard carbon materials based on fullerenes and nanotubes. *Journal of Superhard Materials, 32*, 67–87.

Iwasa, Y., Arima, T., Fleming, R. M., et al. (1994). New phases of C_{60} synthesized at high pressure. *Science, 264*, 1570–1572.

Jacobsen, K. W., & Schiøtz, J. (2002). Nanoscale plasticity. *Nature Materials, 1*, 15–16.

Jungnickel, G., Sitch, P. K., Frauenheim, Th., et al. (1998). Nitrogen doping in purely sp^2 bonded forms of carbon. *Physical Review B, 57*, R661–R665.

Kelires, P. C. (1994). Elastic properties of amorphous carbon networks. *Physical Review Letters, 73*, 2460–2463.

Kelires, P. C. (2001). Intrinsic stress and stiffness variations in amorphous carbon. *Diamond and Related Materials, 10*, 139–144.

Kondrin, M. N., Lyapin, A. G., Brazhkin, V. V., & Popova, S. V. (2002). The influence of dimerization on the orientational phase transition in the C_{60} fullerite. *Physics of the Solid State (St. Petersburg), 44*, 447–449.

Kosowsky, S. D., Hsu, C.-H., Chen, N. H., et al. (1993). X-ray study of pressure-collapsed fullerite. *Physical Review B, 48*, 8474–8475.

Kozlov, M. E., Hirabayashi, M., Nozaki, K., Tokumoto, M., & Ihara, H. (1995). Transformation of C_{60} fullerenes into a superhard form of carbon at moderate pressure. *Applied Physics Letters, 66*, 1199–1201.

Krätschmer, W., Lamb, L. D., Fostiropolous, K., & Huffman, D. R. (1990). Solid C_{60}: a new form of carbon. *Nature, 347*, 354–358.

Lasjaunias, J. C., Saint-Paul, M., Bilušić, A., et al. (2002). Acoustic and thermal transport properties of hard carbon formed from C_{60} fullerene. *Physical Review B, 66*, 014302.

Levin, V. M., Blank, V. D., Prokhorov, V. M., Soifer, Ja. M., & Kobelev, N. P. (2000). Elastic modules of solid C_{60}: measurement and relationship with nanostructure. *Journal of Physics and Chemistry of Solids, 61*, 1017–1024.

Liu, A. Y., Cohen, M. L., Hass, K. C., & Tamor, M. A. (1991). Structural properties of a three-dimensional all-sp^2 phase of carbon. *Physical Review B, 43*, 6742–6745.

Lyapin, A. G. (2002). Mechanical properties of polymerized, amorphous, and nanocrystalline carbon phases prepared from fullerite C_{60} under pressure. In E. Osawa (Ed.), *Perspectives of fullerene nanotechnology* (pp. 199–216). Dordrecht: Kluwer.

Lyapin, A. G., & Brazhkin, V. V. (2002). Correlations between the physical properties of the carbon phases obtained at a high pressure from C_{60} fullerite. *Physics of the Solid State (St. Petersburg), 44*, 405–409.

Lyapin, A. G., Brazhkin, V. V., Gromnitskaya, E. L., et al. (2000). Hardening of fullerite C_{60} during temperature-induced polymerization and amorphization under pressure. *Applied Physics Letters, 76*, 712–714.

Lyapin, A. G., Brazhkin, V. V., Lyapin, S. G., & Popova, S. V. (1998). Three-dimensional polymerization of fullerite C_{60} under high pressure. *Review of High Pressure Science and Technology, 7*, 811–813.

Lyapin, A. G., Mukhamadiarov, V. V., Brazhkin, V. V., et al. (2003). Structural and elastic anisotropy of carbon phases prepared from fullerite C_{60}. *Applied Physics Letters, 83*, 3903–3905.

Mailhiot, C., & McMahan, A. K. (1991). Atmospheric-pressure stability of energetic phases of carbon. *Physical Review B, 44*, 11578–11591.

Makarova, T. L. (2001). Electrical and optical properties of pristine and polymerized fullerenes. *Semiconductors (St. Petersburg), 35*, 243–278.

Manghnani, M. H., Tkachev, S., Zinin, P. V., et al. (2001). Elastic properties of superhard amorphous carbon pressure-synthesized from C_{60} by surface Brillouin scattering. *Physical Review B, 64*, 121403(R).

Marques, L., Hodeau, J.-L., Núñez-Regueiro, M., & Perroux, M. (1996). Pressure and temperature diagram of polymerized fullerite. *Physical Review B, 54*, R12633–R12636.

Marques, L., Mezouar, M., Hodeau, J.-L., et al. (1999). "Debye–Scherrer ellipses" from 3D fullerene polymers: an anisotropic pressure memory signature. *Science, 283*, 1720–1723.

Marques, L., Mezouar, M., Hodeau, J.-L., & Núñez-Regueiro, M. (2002). Imprinting of anisotropic stress during C_{60} high-pressure/high-temperature polymerization process. *Physical Review B, 65*, 100101(R).

Matsumuro, A., Takada, Y., Takahashi, Y., Kondo, I., & Senoo, M. (1998). Mechanical properties of C_{60} bulk materials synthesized at high pressure. *Review of High Pressure Science and Technology, 7*, 823–825.

Meletov, K. P., Davydov, V. A., Arvanitidis, J., et al. (2008). Photo- and pressure-induced transformations in the linear orthorhombic polymer of C_{60}. *Journal of Experimental and Theoretical Physics, 107*, 620–631.

Meletov, K. P., Kourouklis, G. A., Arvanitidis, J., Prassides, K., & Iwasa, Y. (2003). Pressure-induced transformation and phonon modes of the two-dimensional rhombohedral polymer of C_{60}: a Raman spectroscopic study. *Physical Review B, 68*, 094103.

Mezouar, M., Marques, L., Hodeau, J.-L., et al. (2003). Equation of state of an anisotropic three-dimensional C_{60} polymer: the most stable form of fullerene. *Physical Review B, 68*, 193414.

Moshary, F., Chen, N. H., Silvera, I. F., et al. (1992). Gap reduction and the collapse of solid C_{60} to a new phase of carbon under pressure. *Physical Review Letters, 69*, 466–469.

Mukhamadiarov, V. V., Lyapin, A. G., Popova, S. V., Brazhkin, V. V., & Glazov, A. G. (2003). Directional anisotropy in carbon phases prepared from fullerite C_{60} under high pressures. *High Pressure Research, 23*, 275–279.

Núñez-Regueiro, M., Abello, L., Lucazeau, G., & Hodeau, J.-L. (1992). Diamond from fullerenes: evidence from Raman measurements. *Physical Review B, 46*, 9903–9905.

Núñez-Regueiro, M., Marques, L., Hodeau, J.-L., Béthoux, O., & Perroux, M. (1995). Polymerized fullerite structures. *Physical Review Letters, 74*, 278–281.

Núñez-Regueiro, M., Monceau, P., & Hodeau, J.-L. (1992). Crushing C_{60} to diamond at room temperature. *Nature, 355*, 237–239.

Núñez-Regueiro, M., Monceau, P., Rassat, A., Bernier, P., & Zahab, A. (1991). Absence of a metallic phase at high pressures in C_{60}. *Nature, 354*, 289–291.

Okada, S., Saito, S., & Oshiyama, A. (1999). New metallic crystalline carbon: three dimensionally polymerized C_{60} fullerite. *Physical Review Letters, 83*, 1986–1989.

Onodera, A., Irie, Y., Higashi, K., Umemura, J., & Takenaka, T. (1991). Graphitization of amorphous carbon at high pressures to 15 GPa. *Journal of Applied Physics, 69*, 2611–2617.

Patterson, J. R., Catledge, S. A., Vohra, Y. K., Akella, J., & Weir, S. T. (2000). Electrical and mechanical properties of C_{70} fullerene and graphite under high pressures studied using designer diamond anvils. *Physical Review Letters, 85*, 5364–5367.

Perottoni, C. A., & da Jornada, J. A. H. (2002). First-principles calculation of the structure and elastic properties of a 3D-polymerized fullerite. *Physical Review B, 65*, 224208.

Prokhorov, V. M., Blank, V. D., Buga, S. G., & Levin, V. M. (1999). Scanning acoustic microscopy study of superhard C_{60}-based polymerized fullerites. *Synthetic Metals, 103*, 2439–2442.

Rosato, V., Celino, M., Benedek, G., & Gaito, S. (1999). Thermodynamic behavior of the carbon schwarzite fcc $(C_{36})_2$. *Physical Review B, 60*, 16928–16933.

Serebryanaya, N. R., Blank, V. D., Ivdenko, V. A., & Chernozatonskii, L. A. (2001). Pressure-induced superhard phase of C_{60}. *Solid State Communications, 118*, 183–187.

Sjöström, H., Stafström, S., Boman, M., & Sundgren, J.-E. (1995). Superhard and elastic carbon nitride thin films having fullerene like microstructure. *Physical Review Letters, 75*, 1336–1339.

Sneddon, I. N. (1965). The relation between load and penetration in the axisymmetric Boussinesq problem for a punch of arbitrary profile. *International Journal of Engineering Science, 3*, 47–57.

Snoke, D. W., Raptis, Y. S., & Syassen, K. (1992). Vibrational modes, optical excitations, and phase transition of solid C_{60} at high pressures. *Physical Review B, 45*, 14419–14422.

Sumiya, H., Yusa, H., Inoue, T., Ofuji, H., & Irifune, T. (2006). Conditions and mechanism of formation of nano-polycrystalline diamonds on direct transformation from graphite and non-graphitic carbon at high pressure and temperature. *High Pressure Research, 26*, 63–69.

Sundqvist, B. (1998). Comment on "Pressure and temperature diagram of polymerized fullerite". *Physical Review B, 57*, 3164–3165.

Sundqvist, B. (1999). Fullerenes under high pressures. *Advances in Physics, 48*, 1–134.

Sundqvist, B. (2001). Buckyballs under pressure. *Physica Status Solidi (B), 223*, 469–477.

Tai, W. P., & Watanabe, T. (1998). Preparation and mechanical properties of Al_2O_3 reinforced by submicrometer Co particles. *Journal of Materials Science, 33*, 5795–5801.

Talyzin, A. V., & Dubrovinsky, L. S. (2003). *In situ* Raman study of path-dependent C_{60} polymerization: isothermal compression up to 32 GPa at 800 K. *Physical Review B, 68*, 233207.

Talyzin, A. V., & Dubrovinsky, L. S. (2004). *In situ* Raman study of C_{60} polymerization during isothermal pressurizing at 800 K. *Journal of Physics: Condensed Matter, 16*, 757–772.

Talyzin, A. V., Dubrovinsky, L. S., & Jansson, U. (2001). *In situ* Raman study of C_{60} thin films at high pressures. *Physical Review B, 64*, 113408.

Talyzin, A. V., Dubrovinsky, L. S., Oden, M., Le Bihan, T., & Jansson, U. (2002). *In situ* x-ray diffraction study of C_{60} polymerization at high pressure and temperature. *Physical Review B, 66*, 165409.

Talyzin, A. V., Langenhorst, F., Dubrovinskaia, N., Dub, S., & Dubrovinsky, L. S. (2005). Structural characterization of the hard fullerite phase obtained at 13 GPa and 830 K. *Physical Review B, 71*, 115424.

Tat'yanin, E. V., Lyapin, A. G., Mukhamadiarov, V. V., Brazhkin, V. V., & Vasiliev, A. L. (2005). Mechanism of formation of the superhard disordered graphite-like phase from fullerite C_{60} under pressure. *Journal of Physics: Condensed Matter, 17*, 249–256.

Teter, D. M. (1998). Computational alchemy: the search for new superhard materials. *MRS Bulletin, 23*, 22–27.

Thorpe, M. F. (1983). Continuous deformations in random networks. *Journal of Non-Crystalline Solids, 57*, 355–370.

Townsend, S. J., Lenosky, T. J., Muller, D. A., Nichols, C. S., & Elser, V. (1992). Negatively curved graphitic sheet model of amorphous carbon. *Physical Review Letters, 69*, 921–924.

Weiler, M., Sattel, S., Giessen, T., et al. (1996). Preparation and properties of highly tetrahedral hydrogenated amorphous carbon. *Physical Review B, 53*, 1594–1608.

Wood, R. A., Lewis, M. H., Bennington, S. M., et al. (2002). *In situ* x-ray diffraction studies of three-dimensional C_{60} polymers. *Journal of Physics: Condensed Matter, 14*, 11615–11621.

Wood, R. A., Lewis, M. H., West, G., et al. (2000). Transmission electron microscopy, electron diffraction and hardness studies of high-pressure and high-temperature treated C_{60}. *Journal of Physics: Condensed Matter, 12*, 10411–10421.

Yamagami, Y., & Saito, S. (2009). Polymerized sp^2–sp^3 hybrid metallic phase of C_{60} as obtained via constant-pressure molecular dynamics. *Physical Review B, 79*, 045425.

Yamanaka, Sh., Kubo, A., Inamuru, K., et al. (2006). Electron conductive three-dimensional polymer of cuboidal C_{60}. *Physical Review Letters, 96*, 076602.

Yang, J., & Tse, J. S. (2007). First-principles investigation on the geometry and electronic structure of the three-dimensional cuboidal C_{60} polymer. *Journal of Chemical Physics, 127*, 134906.

Yip, S. (1998). The strongest size. *Nature, 391*, 532–533.

Yoo, C. S., & Nellis, W. J. (1991). Phase transformations in carbon fullerenes at high shock pressures. *Science, 254*, 1489–1491.

Yoo, C. S., & Nellis, W. J. (1992). Phase transition from C_{60} molecules to strongly interacting C_{60} agglomerates at hydrostatic high pressures. *Chemical Physics Letters, 198*, 379–382.

Yoo, C. S., Nellis, W. J., Satler, M. L., & Musket, R. G. (1992). Diamondlike metastable carbon phases from shock-compressed C_{60} films. *Applied Physics Letters, 61*, 273–275.

Yusa, H. (2002). Nanocrystalline diamond directly transformed from carbon nanotubes under high pressure. *Diamond and Related Materials, 11*, 87–91.

Zipoli, F., & Bernasconi, M. (2008). First principles study of three-dimensional polymers of C_{60}: structure, electronic properties, and Raman spectra. *Physical Review B, 77*, 115432.

3.22 Graphene Properties and Application

Shi Wun Tong and Kian Ping Loh, Department of Chemistry, National University of Singapore, Singapore

3.22.1 Introduction to Graphene

Since its first discovery (Novoselov, Geim, Morozov, et al., 2004; Novoselov, Geim, Morozov, et al., 2005; Zhang, Tan, Stormer, & Kim, 2005), many unique electronic (Novoselov et al., 2005; Zhang et al., 2005) and mechanical (Lee, Wei, Kysar, & Hone, 2008) properties have been discovered in graphene. Potential applications of this novel material have been proposed and demonstrated in various fields such as advanced electronics (transistor (Levendorf, Ruiz-Vargas, Garg, & Park, 2009), transparent electrode (Chang, Wang, Yang, et al., 2010; Kim, Mastro, & Hite, 2010), and sensor (Shao, Wang, Wu, et al., 2010)), energy storage (Li-ion storage for battery (Yoo, Kim, Hosono, et al., 2008) and hydrogen fuel cell (Elias, Nair, Mohiuddin, et al., 2009; Patchkovskii, Tse, Yurchenko, et al., 2005)), green energy (solar cell (Li, Zhu, Wang, et al., 2010; Roy-Mayhew, Bozym, Punckt, et al., 2010)), etc. For the most part, graphene's versatility as an electronic system, and the vast array of its potential technical applications, stems from its paradoxical combination of being a soft membrane and a very strong material with very high in-plane stiffness. The interplay between the elastic response of graphene and its electronic and optical properties are emerging as an active area of research.

Structurally, graphene inherits the honeycomb crystal lattice structure of graphite but is just one atom thick. The sp^2 bonded carbon atoms form a giant two-dimensional (2D) crystal, as shown in **Figure 1**, where the

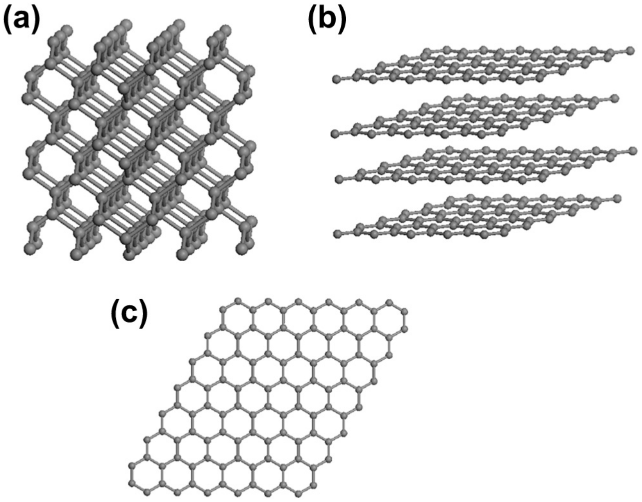

Figure 1 Structure of (a) diamond, (b) graphite and (c) graphene.

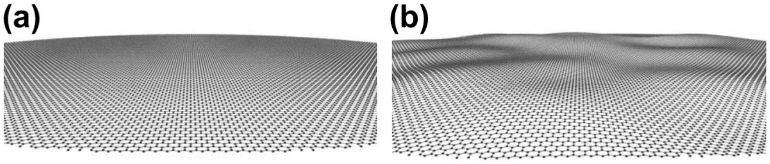

Figure 2 Structure of (a) flat and (b) rippled graphene. From Meyer et al. (2007), Figures 3(a) and 3(b).

structures of diamond and graphite are also shown for comparison. There are three extremely strong in-plane σ bonds which are responsible for the mechanical strength of the graphene sheet. Out-of-plane delocalized π orbitals between the carbon atoms are responsible for the electrical conduction in graphene. A suspended single layer of graphene is one of the stiffest known materials characterized by a high Young's modulus of ~1 TPa (Lee et al., 2008).

Perfect graphene exhibits peculiar electronic properties. Novoselov et al. first reported that electron transport in graphene is essentially governed by Dirac's equation. The charge carriers in graphene mimic relativistic particles with zero rest mass and have an effective speed of light of 10^6 m s^{-1} (Novoselov et al., 2005). With the combination of high intrinsic mobility (200,000 cm^2 V^{-1} s^{-1}) (Bolotin, Sikes, Jiang, et al., 2008; Morozov, Novoselov, Katsnelson, et al., 2008), good thermal conductivity (5000 Wm^{-1} K^{-1}) (Balandin, Ghosh, Bao, et al., 2008; Faugeras, Faugeras, Orlita, et al., 2010; Vadukumpully, Paul, Mahanta, & Valiyaveettil, 2011), high optical transmittance (97.7%) and good electrical conductivity, graphene is an interesting candidate for applications in ultrafast transistor and transparent conductive electrodes.

Graphene has been reported to exist in the rippled form when freely suspended as shown in **Figure 2**. Meyer et al. showed that suspended graphene sheets are not perfectly flat; they exhibit intrinsic microscopic roughening such that the surface normal varies by several degrees and out-of-plane deformations reach 1 nm (Meyer, Geim, Katsnelson, et al., 2007). The ripples on graphene are more or less randomly distributed, which could lead to unpredictable properties. Nevertheless, Bao et al. reported that the ripple structure can be controlled in suspended graphene sheets by using both spontaneously and thermally generated strains (Bao, Miao, Chen, et al., 2009).

While perfect graphene can be synthesized in a small area of several hundred microns without defects, achieving crystalline perfection over large area (>1 mm) remains challenging. One of the key reasons for this difficulty is the inevitable formation of polycrystal and grain boundaries in chemical vapor deposition (CVD) on metal substrate, since the metal substrate itself is a polycrystal and influences the growth of domains with different crystallographic orientations. Huang et al. reported that different grains in CVD graphene stitch together predominantly through pentagon–heptagon pairs, as shown in **Figure 3**. These grain boundaries severely weaken the mechanical strength of graphene membranes but do not as drastically alter their electrical properties (Huang, Ruiz-Vargas, van der Zande, et al., 2011).

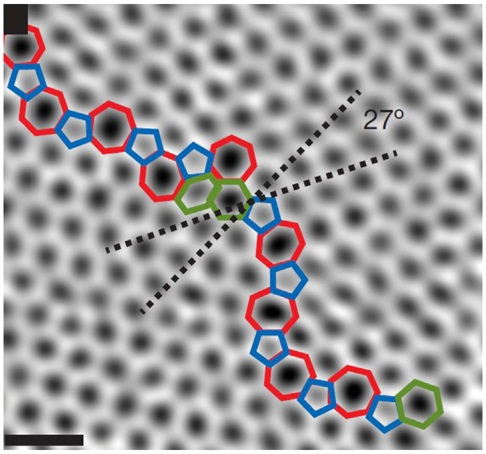

Figure 3 The image with the pentagons (blue), heptagons (red) and distorted hexagons (green) of the grain boundary outlined. From Huang et al. (2011), Figure 1(d).

The following section will discuss the latest findings concerning the mechanical, optical and electrical properties of graphene. Particular attention will be paid to the effect of strain on electronic properties, as well as the surface modification methods to achieve good performance in photovoltaic (PV) devices.

3.22.2 General Properties of Graphene

3.22.2.1 Hardness/Mechanical Strength

Hardness, or the mechanical strength, of materials is their ability to resist deformation under applied stress or force. The mechanical properties are usually determined by applying loading such as stress in the forms of stretching, shearing, bending and compressing on the materials. Information such as strength, stiffness, stability, stress–strain curve, Young's modulus, elasticity and spring constants are obtained. The Mohs scale—hardness measure of the minerals—has been categorized on a scale of 1–10 based on the scratch resistance of various minerals. On the Mohs scale, hard diamond and soft graphite have been classified as 10 and 1.5, respectively. Diamond has face-centered cubic structure with four covalent bonds bonded with the neighboring carbon atoms. The strong covalent bonds are responsible for a very high Young's modulus (1.06 TPa) of diamond (Huntington, 1958). In contrast, graphite consists of stacked layers of graphene sheets separated by 0.34 nm and held together by weak van der Waals forces. The weak interaction between the layers allows graphite to slide very easily and thus act as a soft material. However, along the basal plane of graphite (bond distance 0.142 nm), there are stronger in-plane bonds than those present in diamond (bond distance 0.154 nm) due to the shorter interatomic distance (Saada, 2000). Therefore, graphite has extremely high strength and stiffness along the basal plane. Low Young's modulus of 37 GPa and high in-plane modulus of 1.06 ± 0.02 TPa of graphite have been reported for stress applied perpendicular and parallel to the graphene planes, respectively (Blakslee, 1970).

Graphene has a similar reference plane as graphite. With a shorter bond distance (0.142 nm) than diamond (0.154 nm), graphene can be considered as a harder material than diamond in two dimensions. In fact, carbon atoms in diamond are interconnected by a series of sp^3-hybridized bonds. Among the sp-, sp^2- and sp^3-hybridized bonds, the sp^3 bonds of diamond are the weakest. Graphene is considered as a more rigid material than diamond, although only along a single plane. The uniqueness of diamond stems from the fact that it can have same strength in all directions. **Table 1** depicts the summary of the Young's modulus of diamond, graphite and graphene (Blakslee, 1970; Frank, Tanenbaum, van der Zande, & McEuen, 2007; Gomez-Navarro, Burghard, & Kern, 2008; Gupta, Dharamvir, & Jindal, 2005; Hernández, Goze, Bernier, & Rubio, 1998; Huntington, 1958; Konstantinova, Dantas, & Barone, 2006; Lier, Alsenoy, Doren, & Geerlings, 2000; Meo & Rossi, 2003; Saada, 2000).

Nanoindentation, which is carried out usually using atomic force microscope (AFM), is the most common technique for mechanical properties characterizations in nanosystems. A schematic drawing of nanoindentation using AFM is shown in **Figure 4** (Frank et al., 2007). Lee et al. first reported the elastic properties and intrinsic breaking strength of free-standing monolayer defect-free graphene membrane by nanoindentation in AFM. The intrinsic and breaking strengths are found to be 130 ± 10 GPa and 42 Nm^{-1}, respectively, while the Young's modulus is 1.0 TPa (Lee et al., 2008).

Increasingly, there are more reports concerning the use of the nanoindentation technique for studying the mechanical properties of graphene. Frank et al. reported the effective spring constants of graphene sheets which range from 1 to 5 Nm^{-1} (Frank et al., 2007). Schniepp et al. studied the bending characteristics of functionalized graphene sheets by AFM. They found that the sheets can be reversibly folded and unfolded multiple times and that the folding always occurs at the same location (Schniepp, Kudin, Li, et al., 2008). Li et al. reported the tearing, folding and deformation of graphene. They found that preferential directions of breaking and folding exist (Li, Liu, Chen, et al., 2006). Lee et al. reported the elastic properties and frictional characteristics of graphene of varying thickness (Lee, Wei, Li, et al., 2009). They determined that the local spring constant of the rippled graphene layer has larger value at concave region than at convex region (Lee, Yong, Kim, et al., 2010).

Raman spectroscopy is commonly used to monitor the change in mechanical properties of materials upon loadings. In the case of graphene, the Raman spectrum is characterized by two features called G peak and 2D peak which lie at around 1580 and 2700 cm^{-1}, respectively. These peaks are induced by the in-plane optical vibration and second-order zone boundary phonons, respectively. For example, Raman spectra of epitaxial graphene show a significant phonon "hardening" (blueshift of the G and 2D peaks), mainly due to the compressive strain induced by the silicon carbide substrate after growth (Frank et al., 2007).

Frank et al. also reported the effects of tensile and compressive load on monolayer graphene flake by probing its optical phonons (Frank, Tsoukleri, Parthenios, et al., 2010). Monolayer graphene is attached on the

Table 1 A summary about Young's Modulus of diamond, graphite and graphene

Material	*Young's modulus*	*Testing methods*	*Reference*
Diamond	1.063 TPa	–	Huntington (1958)
Graphite	37 GPa (Stress ⊥ basal plane)	Experimental: Ultrasonic, sonic resonance, and static test methods	Blakslee (1970)
Graphite	1.06 ± 0.02 TPa (Stress // basal plane)	Experimental: Ultrasonic, sonic resonance, and static test methods	Blakslee (1970)
Stack of graphene sheets (<5 layers)	0.5 TPa	Experimental: Nanoindentation by using AFM	Frank et al. (2007)
Monolayer graphene oxide	0.25 ± 0.15 TPa assuming the thickness is 1 nm	Experimental: Tip-induced deformation method	Gomez-Navarro et al. (2008)
Graphene	1.0 ± 0.1 TPa assuming the thickness is 0.335 nm. Intrinsic breaking strength is 130 ± 10 GPa	Experimental: Nanoindentation by using AFM	Lee et al. (2008)
Graphene	1.11 TPa	Theoretical simulation: Ab initio calculations	Lier et al. (2000)
Graphene	1.24 ± 0.01 TPa assuming the thickness is 0.34 nm	Theoretical simulation: Ab initio calculations	Konstantinova et al. (2006)
Graphene	1.206 TPa	Theoretical simulation: Semiempirical Nonorthogonal TB method	Hernández et al. (1998)
Graphene	1.272 TPa	Theoretical simulation: MD method with modified Brenner potential	Gupta et al. (2005)
Graphene	0.945 TPa	Theoretical simulation: Molecular mechanics theory	Meo and Rossi (2003)

AFM, Atomic force microscopy; TB, Tight binding; MD, Molecular dynamics.

cantilever beam that can be flexed up or down and subjecting the flake to compressive or tensile loads. As shown in Figure 5, the position of the G peak in graphene is measured as a function of the applied strain. Positive (negative) strain values denote data obtained under tension (compression). The G peak is split into two components, which have been termed as G^- and G^+ referring to polarization parallel and perpendicular to the strain, respectively (Huang, 2009; Mohiuddin, Lombardo, Nair, et al., 2009). Under both tension and compression, a larger Raman shift in G^- peak than in G^+ peak is observed because greater softening (redshift) or hardening (blueshift) is always experienced, while the E_{2g} phonon is parallel to applied strain. The relationship between Raman shift and strain (or stress) suggests that graphene can act as a mechanical sensor.

Tsoukleri et al. compared the mechanical properties of bare graphene and embedded graphene with poly(methyl methacrylate) (PMMA) (Tsoukleri, Parthenios, Papagelis, et al., 2009). The one-atom-thick monolayer graphene embedded in PMMA can provide reinforcement in compression to high values of strain; this finding is

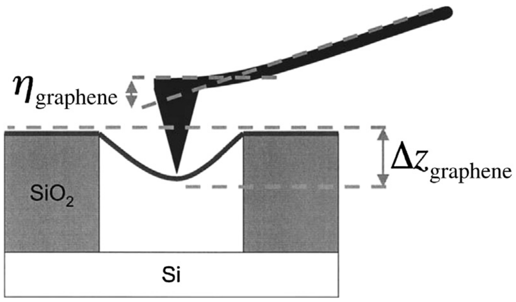

Figure 4 The schematic of an AFM tip that is deflected while pushing down on a suspended graphene sheet. From Frank et al. (2007), Figure 2.

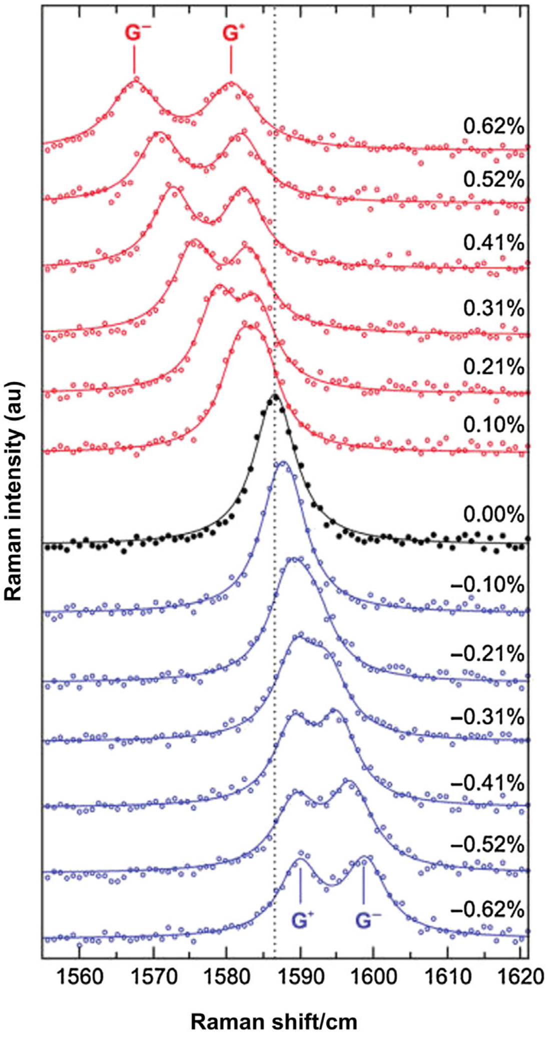

Figure 5 *G* band Raman spectra of graphene flake excited at 785 nm under uniaxial strain (positive values for tensile and negative for compressive strain). *G* peak splitting is observed under both tension and compression; softening (redshift) or hardening (blueshift) whereas the E_{2g^-} being parallel to strain is showing much greater rates of shifting in both cases. From Frank et al. (2010), Figure 2.

very significant for the development of nanocomposites for structural applications. It is interesting to note that even the bare flake that has only partial lateral support can still be loaded axially in compression albeit at a less efficient rate than the embedded graphene. The cantilever beam setup is shown in **Figure 6**. Pristine graphene has a Raman fingerprint at 2680 cm^{-1} (2D peak). **Figure 7** shows the shift of 2D peak position of the embedded graphene under tension and compression. Under tension and compression, 2D peak position (Pos(2D)) decreases and increases with strain, respectively. In compression, the sudden increase of Pos(2D) upon loading is attributed to two factors: (1) the efficient stress transfer due to the incorporation of the material into the substrate and (2) the graphene flake being already under compression at rest. Estimated critical buckling strain for a free graphene flake is −0.03% (Tsoukleri et al., 2009). This indicates that free graphene will buckle at rather small axial compressive strains. However, graphene can be prevented from full buckling by the lateral support offered by the surrounding material till the strains are >−0.7% under compression as shown in **Figure 7**. This finding suggests that the critical strain for buckling can be shifted to a much higher value by developing graphene nanocomposites.

The special mechanical properties of graphene can be useful in various applications, for example, in nanoelectromechanical systems (NEMS). The prototypical NEMS is a nanoscale resonator which vibrates in response to applied external force (Craighead, 2000). A schematic drawing of a suspended graphene resonator is shown in **Figure 8**. Materials such as silicon, silicon oxide, silicon nitride, silicon carbide, diamond and gallium

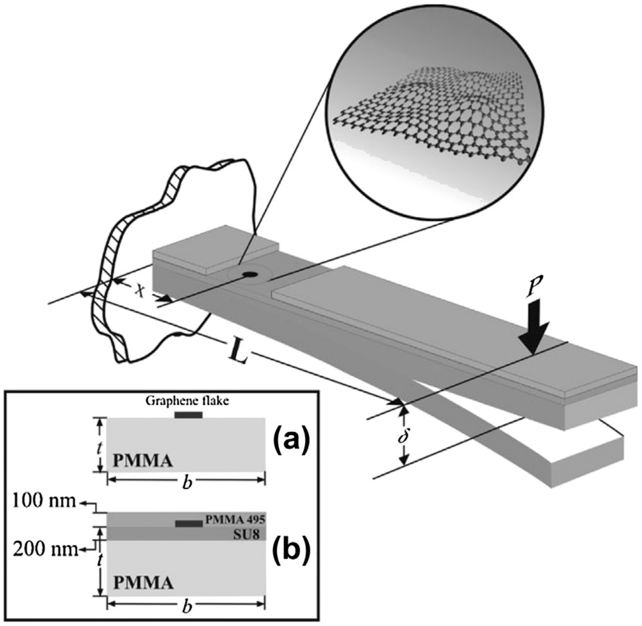

Figure 6 Cantilever beams for (a) bare and (b) embedded graphene flakes. From Tsoukleri et al. (2009), Figure 1.

arsenide have been studied with the prototypical resonator consisting of a nanoscale beam clamped on one or both ends (Ekinci & Roukes, 2005). Besides its stiffness and high mechanical strength, the large surface-to-mass ratio, high quality factor (high sensitivity to external perturbation) and high resonance frequencies (Poot & van der Zant, 2008) of graphene render it an ideal component for NEMS devices. Graphene membranes can also act as impermeable barriers between different environments, e.g. in vacuum or fluid cells, and can support pressure difference up to 1 atm. The high chemical sensitivity of graphene also offers the possibility of multidimensional sensing (Schedin, Geim, Morozov, et al., 2007).

Bunch et al. reported that a graphene-based nanoelectromechanical resonator can be used for ultralow mass detection and ultrasensitive force detection (Bunch, van der Zande, Verbridge, et al., 2007). van der Zande et al. reported the fabrication of single-layer graphene membrane resonators using CVD method. The CVD-grown resonators maintain the remarkable electronic and mechanical properties previously observed for exfoliated graphene (van der Zande, Barton, Alden, et al., 2010).

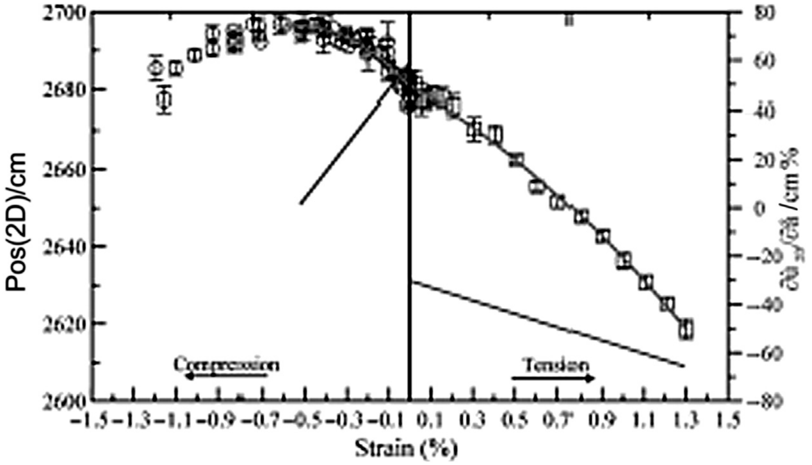

Figure 7 The 2D peak position as a function of tensile and compressive strain for embedded graphene. Linear decrease of the Raman slope for higher strains up to about −0.7% is indicative of the gradual collapse of the material under compression. From Tsoukleri et al. (2009), Figure 4.

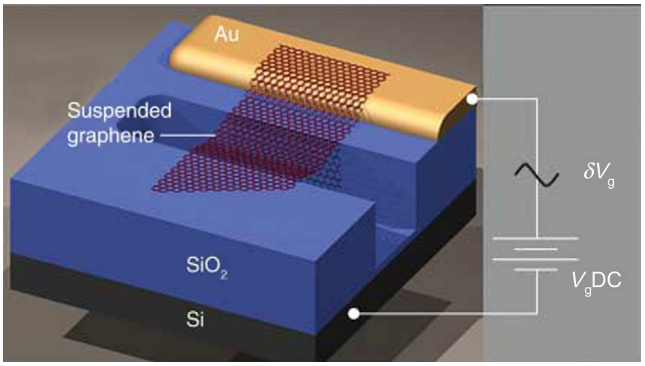

Figure 8 Schematic of a suspended graphene resonator. From Bunch et al. (2007), Figure 1(a).

Another application is to incorporate graphene sheets in composite materials. Various recent studies (Khan, May, O'Neill, & Coleman, 2010; Rafiee, Lu, Thomas, et al., 2010; Rafiee, Rafiee, Wang, et al., 2009; Stankovich, Dikin, Dommett, et al., 2006; Vadukumpully et al., 2011) have shown that graphene can be used as an additive to improve the mechanical properties of polymer-based composites in terms of Young's modulus, strength and toughness. The effect is usually compared with the use of carbon nanotube (CNT). Stankovich et al. first reported a general approach for the preparation of graphene–polymer composites via complete exfoliation of graphite and molecular-level dispersion of individual, chemically modified graphene sheets within polymer hosts. Such a bottom-up chemical approach provides a path to a broad new class of graphene-based materials (Stankovich et al., 2006).

Rafiee et al. reported enhanced mechanical properties of epoxy nanocomposites at low graphene content by comparing single-walled CNTs, multiwalled carbon nanotubes (MWNTs), and graphene nanoribbons (GNRs) as the additives. The results indicated that GNRs significantly outperform CNT additives in terms of Young's modulus, tensile strength and fracture toughness (Rafiee et al., 2010; Rafiee et al., 2009). The stress–strain relationships between graphene and MWNT composites are shown in **Figure 9** (Rafiee et al., 2010). Following are the factors responsible for enhanced effectiveness of GNR over MWNT include: (1) higher defect density of GNRs contributes to stronger interfacial interaction with the host epoxy; (2) GNRs have a larger surface area ($\sim$511 $m^2\,g^{-1}$) since both surfaces of each individual GNR can contact the epoxy, as opposed to only the outermost cylinder of the MWNT ($\sim$291 $m^2\,g^{-1}$); and (3) it is challenging for highly cross-linked polymers (e.g. epoxy) to wrap around tubular MWNTs and mechanically interlock with them. In contrast, the 2D geometry of GNRs can be adhered to epoxy more easily.

Khan et al. reported graphene–polyurethane composites. By varying the graphene weight percentage, they showed that it is possible to prepare composites with high modulus, stress at low strain and ultimate tensile strength as well as relatively high toughness and ductility (Khan et al., 2010). The improvement in composite strength is owing to binding chains between polyurethane soft segments and graphene sheets. Graphene sheets act as physical cross-links, binding chains together and disrupting chain motion. However, excessive amount of graphene addition results in aggregation. Disordered aggregates will act as stress raisers and weaken the composite.

Vadukumpully et al. reported a high mechanical strength of graphene nanoflakes/poly(vinylchloride) (PVC) composite thin film. A significant enhancement in the mechanical properties of pure PVC films was obtained with a 2 wt% loading of graphene, such as a 58% increase in Young's modulus and an almost 130% improvement of tensile strength (Vadukumpully et al., 2011). The enhancement comes from the strong interfacial adhesion between graphene flakes and PVC matrix. The presence of graphene flakes in the PVC matrix offers resistance to the segmental movement of the polymer chains upon application of the tensile stress which led to enhancement in modulus.

Another emerging area of application with wide-ranging importance is the use of graphene as transparent conductor, with a view toward replacing indium tin oxide (ITO) electrodes in optical devices including light-emitting devices and PVs (Arco, Zhang, Schlenker, et al., 2010; Wu, Agrawal, Becerril, et al., 2010). Graphene films can be widely used in flexible optoelectronics due to their mechanical flexibility and low cost, as opposed to the rising cost and brittleness of ITO. Arco et al. demonstrated that CVD graphene PV cell provides outstanding mechanical flexibility (Arco et al., 2010). Graphene anode withstood bending angle up to 138°

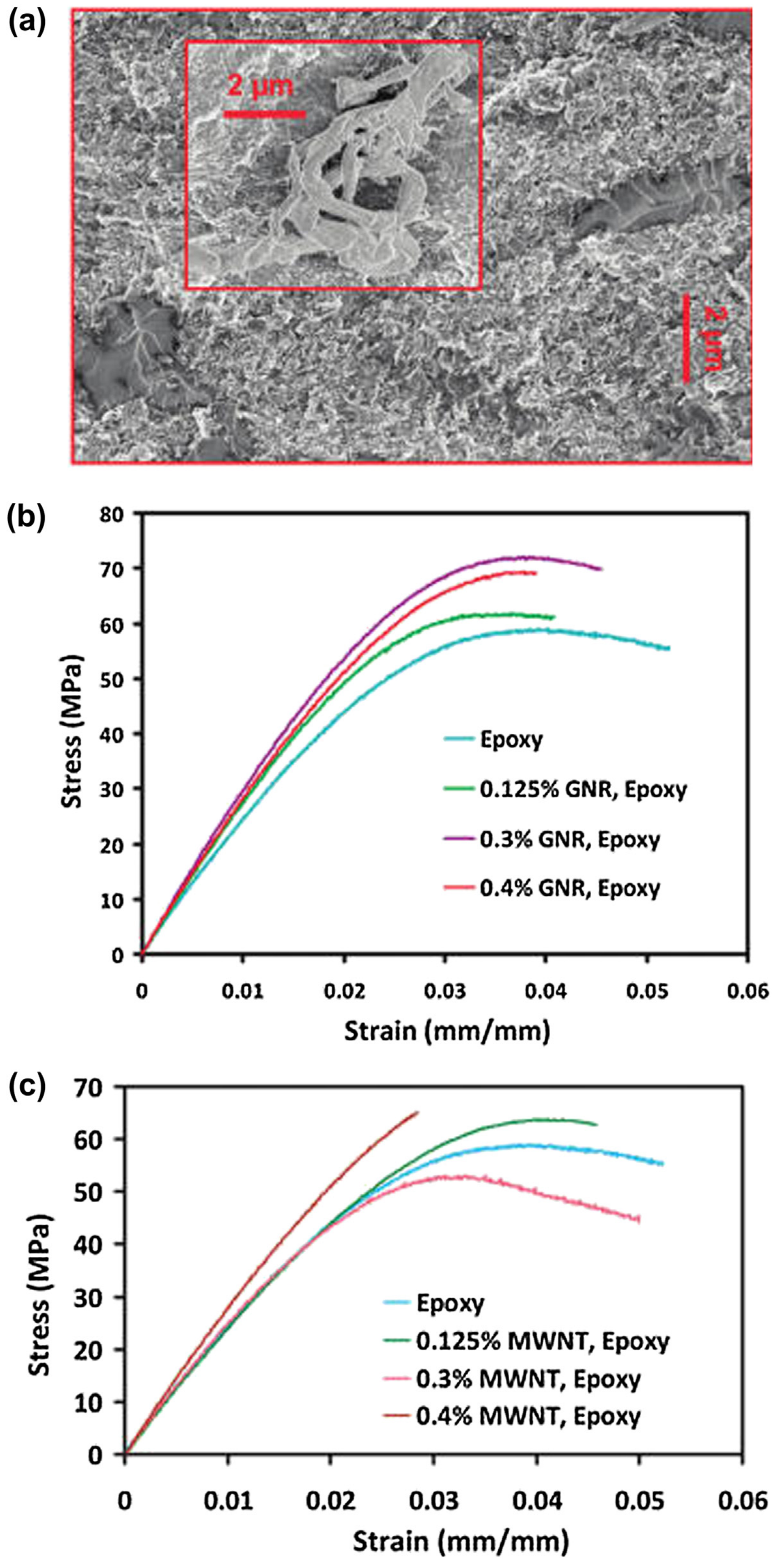

Figure 9 (a) Typical SEM image of free fractured surface of GNR epoxy composite with 0.3% weight of nanofillers. Inset shows a high-resolution image of an agglomerated nanoribbon cluster surrounded by the matrix-rich region. (b) Typical stress versus strain curve of the baseline epoxy and nanocomposite formulations with varying weight fractions of graphene nanoribbon additives. (c) Corresponding stress versus strain response for MWNT/epoxy composites. From Rafiee et al. (2010), Figure 2.

with minor deterioration in PV effect. In sharp contrast, the brittle nature of ITO cannot sustain bending angle higher than 60°; the fill factor (FF) rapidly decays to 0% due to the generation of microcracks which increase film resistance sharply. This finding indicates that graphene films can meet many important criteria in terms of conductivity, transparency and mechanical flexibility.

There are extensive theoretical investigations on the structural and mechanical properties of graphene (Choi, Jhi, & Son, 2010; Cocco, Cadelano, & Colombo, 2010; de Andres & Vergés, 2008; Faccio, Denis, Pardo, Goyenola, & Mombrú, 2009; Gao & Hao, 2009; Guinea, Katsnelson, & Geim, 2009; Hod & Scuseria, 2009; Kumar, Hembram, & Waghmare, 2010; Liu, Ming, & Li, 2007; Min & Aluru, 2011; Neek-Amal & Peeters, 2010; Pei, Zhang, & Shenoy, 2010; Scarpa, Adhikari, Gil, & Remillat, 2010; Wang, Mylvaganam, & Zhang, 2009; Zakharchenko, Katsnelson, & Fasolino, 2009; Zhao, Min, & Aluru, 2009; Zheng, Geng, Wang, Li, & Kim, 2010). Depending on the simulated system sizes, various methods such as continuum approach (Scarpa et al., 2010) and classical molecular dynamics (MD) (Gao & Hao, 2009; Min & Aluru, 2011; Neek-Amal & Peeters, 2010; Pei et al., 2010; Wang, Mylvaganam, et al., 2009; Zhao et al., 2009; Zheng et al., 2010) for large system, semi-empirical tight binding (TB) approach (Cocco et al., 2010) for middle system, and first principles density functional theory methods (Choi et al., 2010; de Andres & Vergés, 2008; Faccio et al., 2009; Hod & Scuseria, 2009; Kumar et al., 2010; Liu et al., 2007) and Monte Carlo method (Zakharchenko et al., 2009) for small system have been applied. MD is the most common method for studying the mechanical properties of materials because substantially large numbers of atoms are necessary to be included in the simulation for accurate description of the structural change of graphene under stress.

3.22.2.2 Strain Engineering in Graphene

Mechanical properties such as stretching (Choi et al., 2010; de Andres & Vergés, 2008; Faccio et al., 2009; Zhao et al., 2009), shearing (Cocco et al., 2010; Min & Aluru, 2011; Zakharchenko et al., 2009; Zheng et al., 2010), bending (Neek-Amal & Peeters, 2010; Scarpa et al., 2010), compressing (Gao & Hao, 2009; Kumar et al., 2010) and wrinkling (Wang, Mylvaganam, et al., 2009) are evaluated theoretically. In particular, strain engineering of graphene for band gap opening and zero-field quantum Hall effect (Guinea et al., 2009), band gap opening by shear strain (Cocco et al., 2010), stress-induced chemical activity on graphene (de Andres & Vergés, 2008), and band gap controlling by strain in bilayer graphene (Choi et al., 2010) are typical examples showing the use of strain engineering in graphene to tune electrical or optical properties.

Graphene has unique electronic properties which can be modified by stress/strain effectively. However, a bulk spectral gap cannot be induced in graphene by just stretching because of symmetry constraints which conserves the Diracness of the low-energy fermions in graphene. What is needed, as shown by Pereira and Neto, is the creation of local strain profile (Pereira & Neto, 2009), for example, by placing the graphene on two adjoining substrates with different thermal expansion coefficients. Pereira et al. showed that inside the locally strained regions, electron beam collimation, one-dimensional channels, surface states and confinement can be generated. As shown in **Figure 10**, different strain profiles can be generated on a patterned substrate (grooves, creases, steps, or wells) in which different regions interact differently with the graphene sheet. Electrical characteristics which are analogous to graphene ribbons and dots can be achieved by engineering the local strain, due to the fact that applied strain is capable of changing the in-plane hopping amplitude in an anisotropic way.

Pereira et al. extends the concept of strain engineering in graphene from electronic (Pereira & Neto, 2009; Guinea, Katsnelson, & Geim, 2010) properties to the optical properties of graphene (Pereira, Ribeiro, Peres, & Neto, 2010). The optical conductance of undoped graphene is independent of frequency over a wide range and

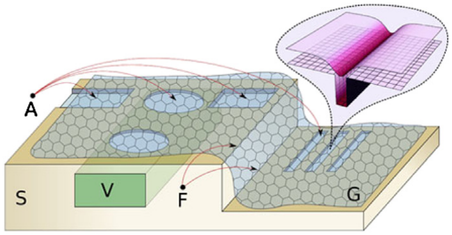

Figure 10 Artistic depiction of a substrate (S) patterned with folds (F), trenches, dots and wells (A), upon which rests a graphene sheet (G), electrostatic potential (V). From Pereira and Neto (2009), Figure 1(b).

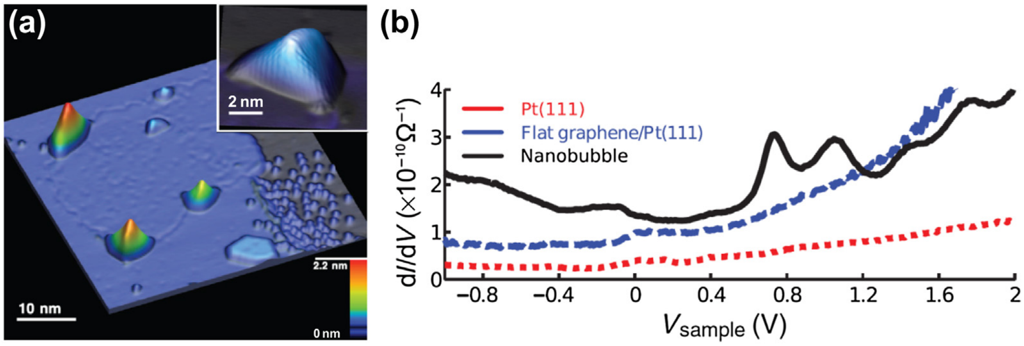

Figure 11 STM images and STS spectra taken at 7.5 K. (a) Graphene monolayer patch on Pt(111) with four nanobubbles at the graphene–Pt border and one in the patch interior. (Inset) High-resolution image of a graphene nanobubble showing distorted honeycomb lattice resulting from strain in the bubble. (b) STS spectra of bare Pt(111), flat graphene on Pt(111) (shifted upward by $3 \times 10^{-11}\ \Omega^{-1}$) and the center of a graphene bubble (shifted upward by $9 \times 10^{-11}\ \Omega^{-1}$). $V_{\text{mod}} = 20$ mV. From Levy et al. (2010), Figure 1.

is defined mainly by the fine structure constant. Even if the magnitude of the photoelastic effect in graphene at visible or infrared (IR) frequencies is limited by its small natural absorption of $\pi\alpha \sim 2\%$, it is nonetheless significant for an atomically thin membrane. The degree of anisotropy induced by strain is determined by how much the Dirac point is displaced from its position at K/K' in the Brillouin zone. The strain-induced anisotropy produces a clear photoresponse in the system, modulating its transmittance, reflectance and absorption, while simultaneously rotating the polarization of incoming light. One of the challenges in graphene research is to increase the Fermi energy to van Hove singularity (VHS); this will have the effect of dramatically increasing the electronic density of states (DOS) and allows many-body effects such as superconductivity to manifest. In this regard, the strain-induced tunability of the VHS can in principle facilitate this. The magnitude and direction of strain affects the optical response at frequencies resonant with the van Hove transitions and absorption peak splitting. Induced strain can elevate the Fermi level of graphene up to the VHS. In this case, changing the strain by 10% can produce a 50% change in the position of the VHS. These photoelastic effects in graphene can be explored for making atomically thin, broadband optical elements.

The demonstration of enormous pseudo–magnetic fields further opens the door for strain engineering study (Levy, Burke, Meaker, et al., 2010). Levy et al. reports the giant strain-induced pseudo–magnetic fields (B_s) in highly strained graphene nanobubbles grown on the Pt (111) surface. Scanning tunneling microscopic image of graphene nanobubbles shows its triangular shape (**Figure 11(a)**, inset), which matches the lattice symmetry of the graphene and the underlying Pt surface. The variation in the local DOS in graphene nanobubble is measured by scanning tunneling spectroscopy (STS) to record the differential conductance (dI/dV) curves (**Figure 11(b)**). STS spectrum of the center of the graphene bubble is shifted upward by $9 \times 10^{-11}\ \Omega^{-1}$ because of the enormous strain-induced B_s. Both the experimental and the simulated B_s profile across a nanobubble are compared and shown in **Figures 12(a) and (d)**. The simulated and experimental nanobubbles both exhibit a relatively uniform strain-induced pseudo–magnetic field of 200–400 T across the central region with increasing field at the edges.

3.22.2.3 Optical Transparency

The optical transmittance $T = (1 + 1/2\pi\alpha)^{-2}$ for normal incidence light (where $\alpha = 2\pi e^2/hc \approx 1/137$, e is the electronic charge, c is the light speed, and h is the Planck's constant). The opacity is $(1 - T) \approx \pi\alpha \approx 2.3\%$. The expression of T in terms of fundamental constants is stated to be a result of the electronic and structural properties of graphene (Peres, 2009). The high and constant transmittance of one- to eight-layer graphene films are observed in the visible wavelength as shown in **Figure 13**. The transmittance decreases linearly with the increasing number of graphene layers at 550 nm. The behavior provides a simple mean to investigate graphene morphology and to distinguish the number of graphene layers on the sample. The optical contrast of graphene on various substrates relies on the angle (Yu & Hilke, 2009) and wavelength (Blake, Hill, Neto, et al., 2007) of the incident light. So far, substrates which provide good optical contrast include SiO_2/Si (Blake et al., 2007; Ni, Wang, Kasim, et al., 2007; Roddaro, Pingue, Piazza, et al., 2007), Si_3N_4/Si (Jung, Pelton, Piner, et al., 2007), SiC

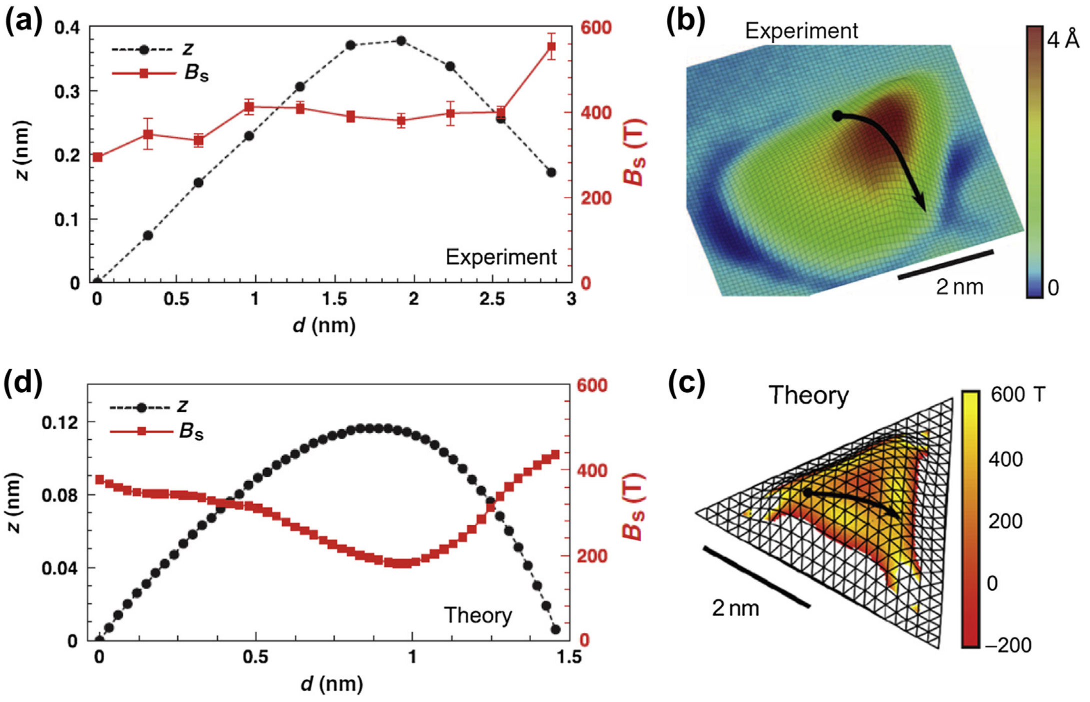

Figure 12 (a) Experimental topographic line scan and experimentally determined B_S profile over the tip trajectory shown by black line in (b). (b) STM topography of graphene nanobubble. (c) Topography of theoretically simulated graphene nanobubble with calculated B_S color map. (d) Simulated topographic line scan and B_S profiles extracted from line shown in (c). The simulated and experimental nanobubbles both exhibit a relatively uniform strain-induced pseudo–magnetic field of 200–400 T across the central region with increasing field at the edges. From Levy et al. (2010), Figure 3.

(Abergel, Russell, & Fal'ko, 2007), and Al_2O_3/Si (Gao, Ren, Li, & Cheng, 2008). **Figure 14** shows the apparent optical contrast of one- to three-layer graphene films on SiO_2/Si substrate under the optical microscope with white light illumination.

For low-energy incident photons (<0.5 eV), a deviation from this phenomenon is observed owing to the finite temperature and a doping-induced chemical potential shift of the Dirac point (Mak, Sfeir, Wu, et al., 2008). Numerous researches have studied the gate-dependent optical transitions in graphene by IR spectroscopy (Wang, Zhang, Tian, et al., 2008). Dramatic change in graphene transmission can be induced by gate voltage that can vary the charge density and shift the Fermi level.

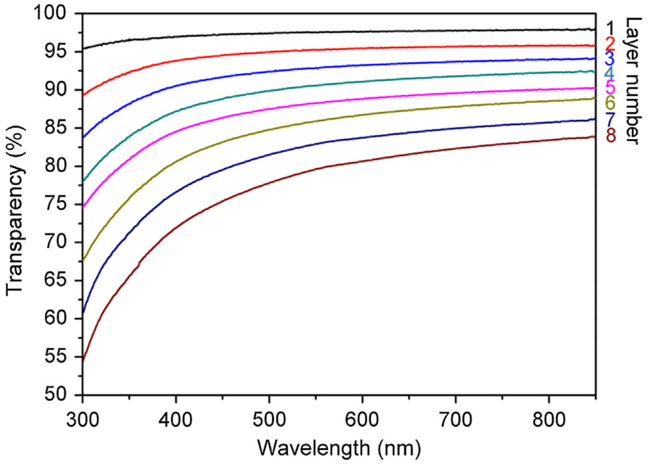

Figure 13 Optical transparency of multilayered graphene films (from one to eight layers) on a quartz substrate.

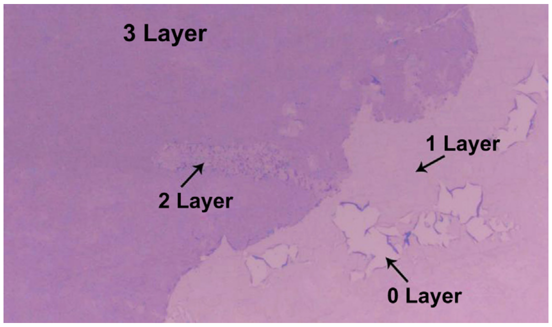

Figure 14 Typical optical microscope images of one- to three-layer graphene films on SiO_2/Si substrates.

3.22.2.4 Electrical Property

Charge carriers in graphene behave as massless relativistic particles and exhibit ballistic transport on the submicrometer scale at room temperature. An exceptionally high mobility 200,000 $cm^2\ V^{-1}\ s^{-1}$ of graphene has been demonstrated, attributed to carrier confinement and coherence (Bolotin et al., 2008). Both optical and electric property of graphene are not affected even after radical bending and stretching (Son, Kim, Shim, et al., 2010). At low temperatures and high magnetic fields, the exceptional mobility of graphene allows for the observation of the quantum hall effect for both electrons and holes.

Electrical conductivity and optical transparency of graphene are the two most important properties for its application in flexible electronics. **Table 2** summarizes the sheet resistance and the optical transmittance of graphene films synthesized by various methods. Graphene can be prepared on the substrates by various techniques, including Langmuir–Blodgett assembly (Cote, Kim, & Huang, 2009), spray coating (Blake, Brimicombe, Nair, et al., 2008; Li, Muller, & Gilje, 2008), vacuum filtration (Eda, Fanchini, & Chhowalla, 2008; De, King, Lotya, et al., 2010), spin coating (Yamaguchi, Eda, Mattevi, et al., 2010; Zhu, Cai, Piner, et al., 2009) and liquid–liquid assembly (Biswas & Drzal, 2009) of graphene platelets or graphene oxide followed by reduction process and thermal annealing. These solution-processable graphene coatings can be easily scaled up for fabricating large-sized transparent conductor. At present, the sheet resistance values (10^2–$10^7\ \Omega\ sq^{-1}$) of graphene oxide-derived films vary over a wide range due to the inhomogeneity of surface functionalities and defects introduced in the synthesis process.

Table 2 A summary of sheet resistance and optical transmittance of graphene films

Method in synthesizing graphene film	*Sheet resistance (Ω sq^{-1})*	*Transmittance at 550 nm (%)*	*Reference*
LB assembly of graphene oxide/reduction	1.9×10^7	95	Cote et al. (2009)
Spray coating of modified graphene oxide at pH 10	2.0×10^7	96	Li et al. (2008)
Vacuum filtration of graphene oxide/reduction	4.3×10^4	73	Eda et al. (2008)
Spin assisted self-assembly of reduce graphene oxide	1.1×10^4	87	Zhu et al. (2009)
Spin coating of reduced graphene oxide	5×10^3–1×10^6	80	Zhu et al. (2009)
Spin coating of reduced graphene oxide	1×10^3	70	Yamaguchi et al. (2010)
Vacuum filtration of graphene platelets	3×10^3	75	De et al. (2010)
Spray coating of graphene platelets	5×10^3	90	Blake et al. (2008)
Liquid–liquid assembly of graphene platelets	100	70	Biswas and Drzal (2009)
Transfer of CVD MLG from Ni	770–1×10^3	90	Reina et al. (2009)
Transfer of CVD MLG from Ni	280	80	Kim et al. (2009)
Transfer of CVD MLG from Ni	230	72	Lin, Penchev, et al. (2010)
LBL transfer of CVD graphene from Cu (four layers)	350	90	Li et al. (2009)
LBL transfer of CVD graphene from Cu (four layers) after HCl + HNO_3 doping	80	90	Wang et al. (in press)
RTR transfer of CVD graphene from Cu (four layers) after HNO_3 doping	30	90	Bae et al. (2010)

MLG, multilayered graphite; RTR, roll to roll.

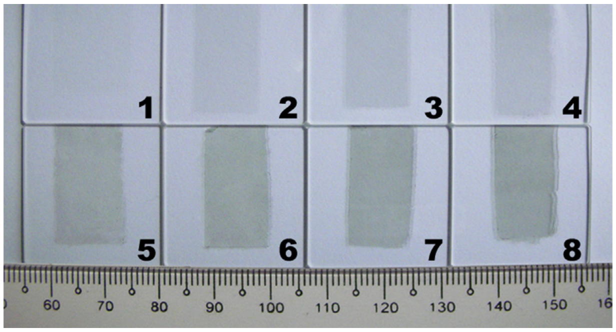

Figure 15 Optical image of one–eight layers of LBL transferred graphene films.

Comparably, graphene growth by CVD on Ni or Cu foil exhibits significantly higher electrical conductivity (Bae, Kim, Lee, et al., 2010; Kim, Zhao, Jang, et al., 2009; Li, Zhu, Cai, et al., 2009; Lin, Penchev, Wang, et al., 2010; Reina, Jia, Ho, et al., 2009; Wang, Tong, Xu, et al., in press) than graphene oxide-derived films. Cai et al. showed that the sheet resistance and transmittance of CVD-grown graphene followed the relationship predicted by the Beer–Lambert law. Graphene film with a sheet resistance of $200\,\Omega\,\mathrm{sq}^{-1}$ has a transmittance of 85% at a wavelength of 550 nm (Cai, Zhu, Li, et al., 2009). The sheet resistance of graphene is given by $R_s = (\sigma_{2D}N)^{-1}$ where σ_{2D} is the 2D sheet conductivity and N is the number of layers. The intrinsic sheet resistance of single-layer graphene is calculated to be $\sim 6\,\mathrm{k}\Omega$ and is inferior to that of ITO (10–$20\,\Omega\,\mathrm{sq}^{-1}$). In principle, increasing the thickness (increasing N) of graphene using layer-by-layer (LBL) stacking and doping the graphene (increasing σ_{2D} by increasing carrier concentration) can allow the extrinsic sheet resistance values to be reduced to as low as $20\,\Omega\,\mathrm{sq}^{-1}$, although it is not trivial to reach this limit at present.

An LBL transfer process in stacking several layers of CVD graphene was recently reported by Li et al. (2009). In this process, PMMA was applied as a support material for holding ultrathin graphene. The transfer sequence includes: (1) deposit a single layer of CVD-derived graphene on both sides of Cu foil; (2) coat PMMA on one side of the graphene film, followed by Cu etching; (3) transfer free-standing graphene/PMMA stack on a targeted substrate; and (4) dissolve PMMA in acetone. By repeating steps (1)–(4) four times, four layers of graphene films with a sheet resistance of $350\,\Omega\,\mathrm{sq}^{-1}$ at a transmittance of 90% can be obtained. As opposed to the method reported by Li et al. where PMMA needs to be spin-coated and removed N times for the transfer of N layers (Li et al., 2009), Wang et al. have developed a method that spin coats PMMA on the first layer graphene once (Wang et al., in press). The PMMA-coated graphene (first layer) is then directly transferred to the second layer graphene on copper foil. After etching the copper foil, the two-layer graphene film can be directly transferred onto third layer graphene on copper foil, forming a three-layer graphene film. The LBL four-layered graphene film has a sheet resistance of $180\,\Omega\,\mathrm{sq}^{-1}$ and a transmittance of 90%. Figure 15 shows the LBL-stacked graphene films from one to eight layers, transferred onto quartz. The individual layers were doped with hydrochloric acid during the transfer process, followed by nitric acid doping at the surface of the film after the removal of the top PMMA. The LBL, acid-doped, four-layer graphene films has a sheet resistance of $\sim 80\,\Omega\,\mathrm{sq}^{-1}$ and a transmittance of 90%.

Bae et al. have scaled up the transfer process to a 30-inch roll-to-roll process using thermal release tape (Bae et al., 2010). Graphene was mechanically supported by thermal release tape before etching Cu foil. By inserting a flexible substrate with the graphene/tape stack to the rolls and exposing to a mild heat treatment, a highly transparent (90%) graphene film with low sheet resistance of $30\,\Omega\,\mathrm{sq}^{-1}$ was achieved.

The CVD-grown graphene film exhibits good mechanical stretchability (Kim et al., 2009; Li et al., 2009). Graphene transferred on polydimethylsiloxane substrates can withstand a tensile strain of 6.5% with minor resistance increase and the original resistance can be restored after a tensile strain of 18.7% (Kim et al., 2009). Monolayer graphene transferred on polyethylene terephthalate substrates has shown a resistance that is independent of the tensile bending of up to 5% strain, even after 100 bending cycles (Li et al., 2009).

3.22.3 Surface Modification Effects on Graphene and its Application in PV Cells

Due to its atomic layer thickness and the absence of a bulk, graphene is defined by its surface. Therefore, the modification of its surface can change the properties of graphene dramatically (Cui, Kim, Jones, et al., 2010; Dongil, Bachiller-Baeza, Guerrero-Ruiz, et al., 2011; Economopoulos, Rotas, Miyata, et al., 2010; Xie, Qu, Zhou,

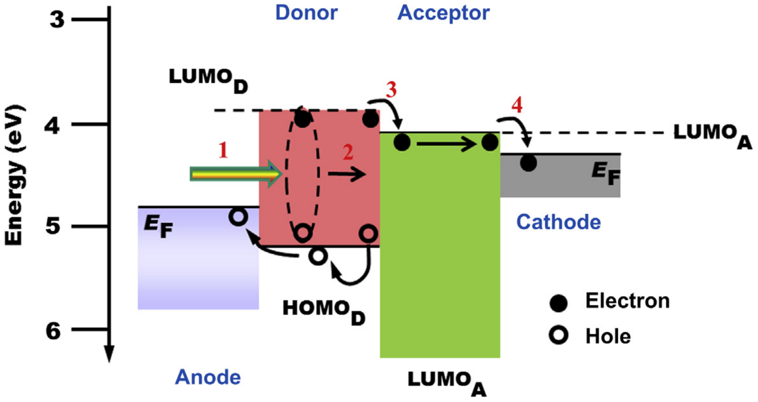

Figure 16 Energy diagram of an organic solar cell. Four steps to generate photocurrent include: (1) absorption of an incident photon to create an exciton, (2) diffusion of an exciton toward the donor–acceptor interface, (3) charge transfer of an exciton into an electron in the acceptor and hole in the donor, and (4) collection of electrons and holes at the cathode and anode, respectively. E_F and LUMO present the Fermi level of contacts and the lowest unoccupied molecular orbital of donor/acceptors.

et al., 2010). This section introduces recent methods of modifying graphene for achieving high-performance solar cell via synthesis, transfer method and doping.

Driven by the demand for cheap, clean and renewable energy source, the interest in utilizing organic PV cells is growing. In organic solar cells, the process that converts incident solar illumination to photocurrent can be divided into four stages, as indicated in Figure 16. To date, poly(3-hexylthiophene-2,5-diyl): (6,6)-phenyl C_{61} butyric acid methyl ester (P3HT:PCBM) and copper phthalocyanine/fullerene (CuPc/C_{60}) are the photoactive materials of choice in most polymer-based and small molecule-based solar cells, respectively, due to their high stability, high mobility, and widespread availability.

3.22.3.1 Conductivity Improvement

ITO is a leading transparent conductive anode in the organic-based devices for almost four decades. The sheet resistance of ITO with 80% transparency can be less than 100 $\Omega\,sq^{-1}$ on glass. However, the conductivity of ITO dramatically degrades after bending, which limits its application in flexible organic electronics. Deficiency of indium source also raises the production cost of ITO-based devices. The low cost, transparency, high electrical conductivity, chemical robustness and flexibility of graphene render it an attractive candidate to replace ITO. Table 3 summarizes the performance of the PV cells based on graphene electrodes.

Solution-based approaches to the fabrication of electrodes typically involve the use of reduced graphene oxide flakes (Hong, Kim, Kim, et al., 2010). Alternatively, a chemical bottom-up approach involves the cross-linking of giant polycyclic aromatic hydrocarbons to form graphene nanosheets (Wang, Zhi, Tsao, et al., 2008). However, poor interlayer junction contact resistance and the presence of structural defects limit the conductivity, which produces low power conversion efficiency (PCE) of 0.1–0.68%. To make an attempt to improve the conductivity, CNTs were selected to combine with graphene to form a hybrid layer (Tung, Chen, Allen, et al., 2009). This hybrid material can exhibit a quite high conductivity behavior (sheet resistance is 600 $\Omega\,sq^{-1}$). However, this approach sacrifices the high optical transparency of graphene because of the relatively low optical transmittance of CNTs. Overall, PCE of the device is still limited to 0.85%.

3.22.3.2 Work Function Engineering

Besides good conductivity and transparency of the electrodes, the performance of PV cells strongly relies on the carrier collection efficiency through the contact between electrodes and photoactive material. Thus the interfacial energy offset between graphene and the photoactive materials has to be matched in order to optimize charge transfer. The tunable work function of graphene electrode allows the work function of graphene anode (cathode) and highest occupied molecular orbital (HOMO) (lowest unoccupied molecular orbital) of organic material to be matched. Previous studies have established that the work function of graphene ranges between 4.3 and 4.6 eV (Wildoer, Venema, Rinzler, et al., 1998). The work function can be tuned through doping by $AuCl_3$ (Park, Rowehl, Kim, et al., 2010; Shi, Kim, Reina, et al., 2010), pyrenebutanoic acid succinimidyl ester (PBASE) (Wang, Chen,

Table 3 Main device parameters of organic solar cells with graphene electrode

Graphene type	*Device structure*[a] *Graphene is denoted as* ***G***	*Sheet resistance* (Ω *sq*$^{-1}$)	*Transparency at 550 nm* (%)	V_{oc} (*V*)	J_{sc} (*mA/cm*^{2})	*FF* (%)	*PCE* (%)	*Reference*
G-CNTs hybrid	PET/**G**-CNTs/PEDOT/P3HT:PCBM/Ca:Al	600	87	0.58	3.47	42	0.85	Tung et al. (2009)
CVD MLG	PET/**G**/PEDOT/CuPc/C60/BCP/Al	230	72	0.48	4.73	52	1.18	Arco et al. (2010)
CVD MLG	Glass/PBASE modified **G**/PEDOT/P3HT:PCBM/LiF/Al	210–1.4 k	72–91	0.55	6.1	51	1.71	Wang, Chen, et al. (2009)
CVD MLG	Glass/WPF-6-oxy-F modified **G**/P3HT:PCBM/PEDOT/Al	520–850	85–90	0.57	6.61	33	1.23	Oh et al. (2010)
CVD LBL G	Glass/$AuCl_3$ doped **G**/PEDOT/CuPc/C60/BCP/Ag	300	91.2	0.43	9.2	42	1.63	Park et al. (2010)
CVD LBL G	Quartz/HCL + HNO_3 doped **G**/MoO_3 + PEDOT/P3HT:PCBM/LiF/Al	80	90	0.59	8.5	51	2.5	Wang et al. (in press)

[a] *PEDOT, poly(3,4-ethylenedioythiophene):poly(styrenesulfonate); P3HT, poly(3-hexylthiophene-2,5-diyl); PCBM, (6,6)-phenyl* C_{61} *butyric acid methyl ester; CuPc, copper phthalocyanine;* C_{60}*, fullerene; BCP, bathocuproine; PET, polyethylene terephthalate; LiF, lithium fluoride; PBASE, pyrene buanoic acid succidymidyl ester; WPF-6-oxy-F, poly[9,9-*bis*((6′-(*N,N,N*-trimethylammonium)hexyl)-2,7-fluorene)-*alt*-(9,9-*bis*(2-(2-(2-methoxyethoxy) ethoxy) ethyl)-9-fluorene)] dibromide;* MoO_3*, Molybdenum oxide.*

All measurements were taken under incident light intensity of 100 mW/cm^2. AM 1.5G.

Zhong, et al., 2009), molybdenum oxide (MoO_3) (Wang et al., in press), tetrafluoro-tetracyanoquinodimethane (Chen, Chen, Qi, et al., 2007), gas molecules (Schedin et al., 2007), aromatic molecules (Das, Voggu, Rout, et al., 2008; Dong, Fu, Fang, et al., 2009) and electric field (Yu, Zhao, Ryu, et al., 2009).

Shi et al. showed that $AuCl_3$ doping not only increases graphene conductivity but also induces 0.5 eV of upward surface potential shift in graphene (Shi et al., 2010). This shift can increase open circuit voltage (V_{oc}). The PCE in the doped graphene/*n*-Si PV devices is 40 times larger than that of the undoped device. Noncovalent functionalization with PBASE was also found to increase CVD graphene work function by 0.5 eV. The hole collection barrier height in the PBASE-modified graphene anode was thus reduced by 0.5 eV and improves the PCE (Wang, Chen, et al., 2009). The advantage is that PBASE modification does not disrupt the conjugated structure of graphene surface. Such interactions only depend on π–π stacking between PBASE molecules and graphene plane (Xu, Bai, Lu, et al., 2008).

High-work-function transition metal such as MoO_3 (6.1–6.6 eV) (Lin, Yeh, Chen, et al., 2010; Yi, Jeon, Lee, et al., 2009) and V_2O_5 (Wang, Helander, Qiu, et al., 2010) also contributes to the large increment in work function of graphene (Chen, Santoso, Wang, et al., 2010; Sun, Wang, Shi, et al., 2010). Wang et al. reported that a thin layer of MoO_3 can increase the work function of LBL CVD graphene stacks by 1.1 eV. A high V_{oc} of 0.6 V results from the barrierless hole extraction between HOMO of P3HT (5.2 eV) (Kim, Kim, Lee, et al., 2006) and the work function of MoO_3-coated graphene (5.47 eV). The high-electron-affinity MoO_3 also causes a surface transfer doping effect on graphene, resulting in a p-type doping (Chen et al., 2010).

Work function-engineered graphene film was also demonstrated in the inverted PV cell by Jo et al. In this case, work function of CVD graphene film was decreased by poly[9,9-*bis*((6′-(*N*,*N*,*N*-trimethylammonium) hexyl)-2,7-fluorene)-*alt*-(9,9-*bis*(2-(2-(2-methoxyethoxy) ethoxy) ethyl)-9-fluorine)] dibromide (denoted as WPF-6-oxy-F). The work function of the modified graphene cathode drops from 4.58 to 4.25 eV because of ionic/polar groups of WPF-6-oxy-F that can form interfacial dipoles on graphene effectively (Oh, Na, Jo, et al., 2010).

3.22.3.3 Surface Hydrophilicity and Hydrophobicity

Surface wettability of graphene is the third essential factor to achieve high-performance PV cells. For optimal performance, graphene anode is coated with a thin layer of the conducting polymer poly(3, 4-ethylenedioythiophene):poly(styrenesulfonate) (PEDOT:PSS) that further reduces resistance, prevents

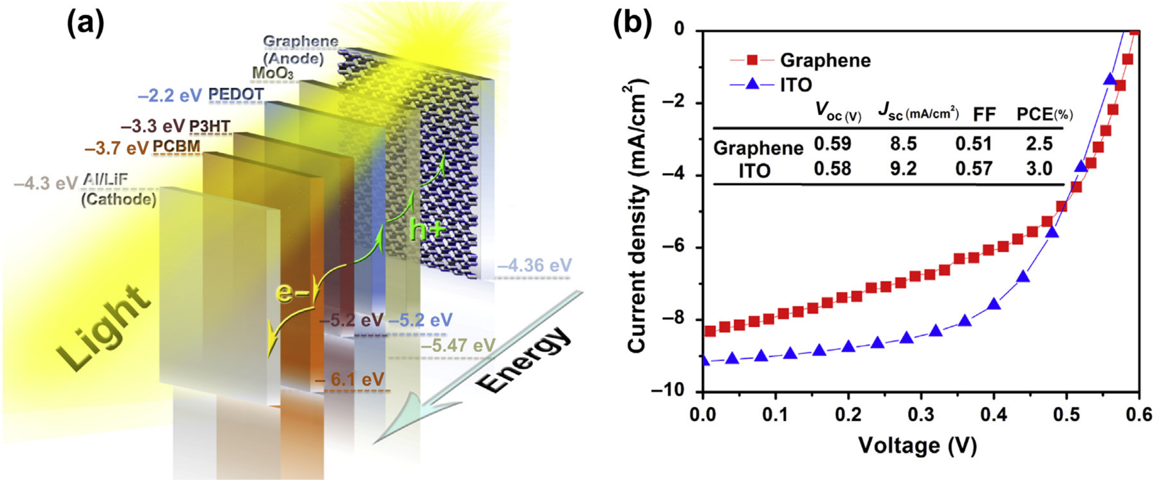

Figure 17 (a) Schematic diagram of PV device structure with graphene/MoO_3/PEDOT:PSS/P3HT:PCBM/LiF/Al. (b) *J*–*V* characteristics of devices with either graphene or ITO under light illumination.

electron leakage and helps to planarize the graphene films. However, PEDOT:PSS cannot be spread well on the as-grown graphene due to its low surface free energy (Wang, Zhang, Abidi, & Cabrales, 2009). UV/ozone treatment is an effective means of tuning the aromatic rings of graphene into hydrophilic ones by introducing OH and C=O groups. However, this surface treatment also disrupts the conductive network of graphene owing to covalent bonding with oxygen groups. Therefore P3HT:PCBM-based PV cell with UV/ozone-treated graphene anode can only attain a PCE of 0.74% (Wang, Chen, et al., 2009). As mentioned earlier, PBASE molecules have π–π interactions with graphene plane. These interactions improve the hydrophilic property of graphene and allow PEDOT:PSS to wet the surface effectively, which results in better planarization of the film surface and facilitation of hole injection. Utilization of PBASE-modified graphene anode can provide a PCE of 1.71% which is 55.2% of the standard ITO anode (Wang, Chen, et al., 2009). By increasing the hydrophilicity of graphene via a thin layer of MoO_3, same improvement in achieving the homogeneous PEDOT:PSS was reported (Wang et al., in press). Combined with the increased work function of MoO_3-coated graphene, a high PCE of 2.5% is attained in P3HT:PCBM PV cell that reaches ~83.3% PCE of control devices based on ITO as the anode (**Figure 17**).

3.22.4 Conclusions

The uniqueness of graphene is the convolution of its mechanical, optical and electronic properties, such that creating a handle to tune one of these properties can produce dramatic changes in another. This forms the underlying principle for the fabrication of strain-engineered devices where the optoelectronic properties can be tuned by creating strain. The soft membrane nature of graphene allows it to be integrated with microfabricated structures to create a new class of atomic-scale membrane-based devices. Graphene is also emerging as a transparent conductor which can replace ITO. In order to surpass the properties of ITO, surface modification of graphene is needed to tune its work function as well as wetting properties.

References

Abergel, D. S. L., Russell, A., & Fal'ko, V. I. (2007). Visibility of graphene flakes on a dielectric substrate. *Applied Physics Letters, 91*, 063125.
Arco, L. G. D., Zhang, Y., Schlenker, C. W., et al. (2010). Continuous, high flexible, and transparent graphene films by chemical vapor deposition for organic photovoltaics. *ACS Nano, 4*, 2865–2873.
Bae, S., Kim, H., Lee, Y., et al. (2010). Roll-to-roll production of 30-inch graphene films for transparent electrodes. *Nature Nanotechnology, 5*, 574–578.
Balandin, A. A., Ghosh, S., Bao, W. Z., et al. (2008). Superior thermal conductivity of single-layer graphene. *Nano Letters, 8*, 902–907.
Bao, W., Miao, F., Chen, Z., et al. (2009). Controlled ripple texturing of suspended graphene and ultrathin graphite membranes. *Nature Nanotechnology, 4*, 562–566.
Biswas, S., & Drzal, L. T. (2009). A novel approach to create a highly ordered monolayer film of graphene nanosheets at the liquid–liquid interface. *Nano Letters, 9*, 167–172.

Blake, P., Brimicombe, P. D., Nair, R. R., et al. (2008). Graphene-based liquid crystal device. *Nano Letters, 8*, 1704–1708.

Blake, P., Hill, E. W., Neto, A. H. C., et al. (2007). Making graphene visible. *Applied Physics Letters, 91*, 063124.

Blakslee, O. L. (1970). Elastic constants of compression-annealed pyrolytic graphite. *Journal of Applied Physics, 41*, 3373–3382.

Bolotin, K. I., Sikes, K. J., Jiang, Z., et al. (2008). Ultrahigh electron mobility in suspended graphene. *Solid State Communications, 146*, 351–355.

Bunch, J. S., van der Zande, A. M., Verbridge, S. S., et al. (2007). Electromechanical resonators from graphene sheets. *Science, 315*, 490–493.

Cai, W., Zhu, Y., Li, X., et al. (2009). Large area few-layer graphene/graphite films as transparent thin conducting electrodes. *Applied Physics Letters, 95*, 123115.

Chang, H. X., Wang, G. F., Yang, A., et al. (2010). A transparent, flexible, low-temperature, and solution-processable graphene composite electrode. *Advanced Functional Materials, 20*, 2893–2902.

Chen, W., Chen, S., Qi, D. C., et al. (2007). Surface transfer p-type doping of epitaxial graphene. *Journal of the American Chemical Society, 129*, 10418–10422.

Chen, Z., Santoso, I., Wang, R., et al. (2010). Surface transfer hole doping of epitaxial graphene using MoO_3 thin film. *Applied Physics Letters, 96*, 213104.

Choi, S. M., Jhi, S. H., & Son, Y. W. (2010). Controlling energy gap of bilayer graphene by strain. *Nano Letters, 10*, 3486–3489.

Cocco, G., Cadelano, E., & Colombo, L. (2010). Gap opening in graphene by shear strain. *Physical Review B, 81*, 241412(R).

Cote, L. J., Kim, F., & Huang, J. X. (2009). Langmuir–Blodgett assembly of graphite oxide single layers. *Journal of the American Chemical Society, 131*, 1043–1049.

Craighead, H. G. (2000). Nanoelectromechanical systems. *Science, 290*, 1532–1535.

Cui, Y., Kim, S. N., Jones, S. E., et al. (2010). Chemical functionalization of graphene enabled by phage displayed peptides. *Nano Letters, 10*, 4559–4565.

Das, B., Voggu, R., Rout, C. S., et al. (2008). Changes in the electronic structure and properties of graphene induced by molecular charge-transfer. *Chemical Communications, 41*, 5155–5157.

de Andres, P. L., & Vergés, J. A. (2008). First-principles calculation of the effect of stress on the chemical activity of graphene. *Applied Physics Letters, 93*, 171915.

De, S., King, P. J., Lotya, M., et al. (2010). Flexible, transparent, conducting films of randomly stacked graphene from surfactant-stabilized, oxide-free graphene dispersions. *Small, 6*, 458–464.

Dong, X. C., Fu, D. L., Fang, W. J., et al. (2009). Doping single-layer graphene with aromatic molecules. *Small, 5*, 1422–1426.

Dongil, A. B., Bachiller-Baeza, B., Guerrero-Ruiz, A., et al. (2011). Surface chemical modifications induced on high surface area graphite and carbon nanofibers using different oxidation and functionalization treatments. *Journal of Colloid and Interface Science, 355*, 179–189.

Economopoulos, S. P., Rotas, G., Miyata, Y., et al. (2010). Exfoliation and chemical modification using microwave irradiation affording highly functionalized graphene. *ACS Nano, 4*, 7499–7507.

Eda, G., Fanchini, G., & Chhowalla, M. (2008). Large-area ultrathin films of reduced graphene oxide as a transparent and flexible electronic material. *Nature Nanotechnology, 3*, 270–274.

Ekinci, K. L., & Roukes, M. L. (2005). Nanoelectromechanical systems. *Review of Scientific Instruments, 76*, 061101.

Elias, D. C., Nair, R. R., Mohiuddin, T. M. G., et al. (2009). Control of graphene's properties by reversible hydrogenation: evidence for graphene. *Science, 323*, 610–613.

Faccio, R., Denis, P. A., Pardo, H., Goyenola, C., & Mombrú, Á. W. (2009). Mechanical properties of graphene nanoribbons. *Journal of Physics: Condensed Matter, 21*, 285304.

Faugeras, C., Faugeras, B., Orlita, M., et al. (2010). Thermal conductivity of graphene in corbino membrane geometry. *ACS Nano, 4*, 1889–1892.

Frank, I. W., Tanenbaum, D. M., van der Zande, A. M., & McEuen, P. L. (2007). Mechanical properties of suspended graphene sheets. *Journal of Vacuum and Science Technology B, 25*, 2558–2561.

Frank, O., Tsoukleri, G., Parthenios, J., et al. (2010). Compression behavior of single-layer graphenes. *ACS Nano, 4*, 3131–3138.

Gao, Y., & Hao, P. (2009). Mechanical properties of monolayer graphene under tensile and compressive loading. *Physica E, 41*, 1561–1566.

Gao, L. B., Ren, W. C., Li, F., & Cheng, H. M. (2008). Total color difference for rapid and accurate identification of graphene. *ACS Nano, 2*, 1625–1633.

Gomez-Navarro, C., Burghard, M., & Kern, K. (2008). Elastic properties of chemically derived single graphene sheets. *Nano Letters, 8*, 2045–2049.

Guinea, F., Katsnelson, M. I., & Geim, A. K. (2009). Energy gaps and a zero-field quantum Hall effect in graphene by strain engineering. *Nature Physics, 6*, 30–33.

Guinea, F., Katsnelson, M. I., & Geim, A. K. (2010). Energy gaps and a zero-field quantum Hall effect in graphene by strain engineering. *Nature Physics, 6*, 30.

Gupta, S., Dharamvir, K., & Jindal, V. K. (2005). Elastic moduli of single-walled carbon nanotubes and their ropes. *Physical Review B, 72*, 165428.

Hernández, E., Goze, C., Bernier, P., & Rubio, A. (1998). Elastic properties of C and $B_xC_yN_z$ composite nanotubes. *Physical Review Letters, 80*, 4502–4505.

Hod, O., & Scuseria, G. E. (2009). Electromechanical properties of suspended graphene nanoribbons. *Nano Letters, 9*, 2619–2622.

Hong, S. K., Kim, J. E., Kim, S. O., et al. (2010). Flexible resistive switching memory devices based on graphene oxide. *IEEE Electron Device Letters, 31*, 1005–1007.

Huang, M. Y. (2009). Phonon softening and crystallographic orientation of strained graphene studied by Raman spectroscopy. *Proceeding of the National Academy of Sciences of the United States of America*, 7304–7308.

Huang, P. Y., Ruiz-Vargas, C. S., van der Zande, A. M., et al. (2011). Grains and grain boundaries in single-layer graphene atomic patchwork quilts. *Nature, 469*, 389–393.

Huntington, J. B. (1958). *Solid state physics*. New York: Academic Press Inc.

Jung, I., Pelton, M., Piner, R., et al. (2007). Simple approach for high-contrast optical imaging and characterization of graphene-based sheets. *Nano Letters, 7*, 3569–3575.

Khan, U., May, P., O'Neill, A., & Coleman, J. N. (2010). Development of stiff, strong, yet tough composites by the addition of solvent exfoliated graphene to polyurethane. *Carbon, 48*, 4035–4041.

Kim, J. Y., Kim, S. H., Lee, H. H., et al. (2006). New architecture for high-efficiency polymer photovoltaic cells using solution-based titanium oxide as an optical spacer. *Advanced Materials, 18*, 572.

Kim, B. J., Mastro, M. A., & Hite, J. (2010). Transparent conductive graphene electrode in GaN-based ultra-violet light emitting diodes. *Optics Express, 18*, 23030–23034.

Kim, K. S., Zhao, Y., Jang, H., et al. (2009). Large-scale pattern growth of graphene films for stretchable transparent electrodes. *Nature, 457*, 706–710.

Konstantinova, E., Dantas, S. O., & Barone, P. M. V. B. (2006). Electronic and elastic properties of two-dimensional carbon planes. *Physical Review B, 74*, 035417.

Kumar, S., Hembram, K. P. S. S., & Waghmare, U. V. (2010). Intrinsic buckling strength of graphene: first-principles density functional theory calculations. *Physical Review B, 82*, 115411.

Lee, C., Wei, X. D., Kysar, J. W., & Hone, J. (2008). Measurement of the elastic properties and intrinsic strength of monolayer graphene. *Science, 321*, 385–388.

Lee, C., Wei, X., Li, Q., et al. (2009). Elastic and frictional properties of graphene. *Physica Status Solidi B, 246*, 2562–2567.

Lee, H., Yong, H., Kim, K. B., et al. (2010). Mechanical properties of rippled structure in suspended stacks of graphene. *Journal of Applied Physics, 108*, 014302.

Levendorf, M. P., Ruiz-Vargas, C. S., Garg, S., & Park, J. (2009). Transfer-free batch fabrication of single layer graphene transistors. *Nano Letters, 9*, 4479–4483.

Levy, N., Burke, S. A., Meaker, K. L., et al. (2010). Strain-induced pseudo-magnetic fields greater than 300 Tesla in graphene nanobubbles. *Science, 329*, 544–547.

Lier, G. V., Alsenoy, C. V., Doren, V. V., & Geerlings, P. (2000). Ab initio study of the elastic properties of single-walled carbon nanotubes and graphene. *Chemical Physics Letters, 326*, 181–185.

Li, L. X., Liu, R. P., Chen, Z. W., et al. (2006). Tearing, folding and deformation of a carbon–carbon sp^2-bonded network. *Carbon, 44*, 1544–1547.

Li, D., Muller, M. B., & Gilje, S. (2008). Processable aqueous dispersions of graphene nanosheets. *Nature Nanotechnology, 3*, 101–105.

Li, X., Zhu, Y., Cai, W., et al. (2009). Transfer of large-area graphene films for high-performance transparent conductive electrodes. *Nano Letters, 9*, 4359–4363.

Li, X. M., Zhu, H. W., Wang, K. L., et al. (2010). Graphene-on-silicon Schottky junction solar cells. *Advanced Materials, 22*, 2743–2748.

Lin, J. A., Penchev, M., Wang, G. P., et al. (2010). Heterogeneous graphene nanostructures: ZnO nanostructures grown on large-area graphene layers. *Small, 6*, 2448–2452.

Lin, C. T., Yeh, C. H., Chen, M. H., et al. (2010). Influences of evaporation temperature on electronic structures and electrical properties of molybdenum oxide in organic light emitting devices. *Journal of Applied Physics, 107*, 053703.

Liu, F., Ming, P., & Li, J. (2007). Ab initio calculation of ideal strength and phonon instability of graphene under tension. *Physical Review B, 76*, 064120.

Mak, K. F., Sfeir, M. Y., Wu, Y., et al. (2008). Measurement of the optical conductivity of graphene. *Physical Review Letters, 101*, 195405.

Meo, M., & Rossi, M. (2003). Prediction of Young's modulus of single wall carbon nanotubes by molecular-mechanics based finite element modeling. *Composites Science and Technology, 66*, 1597–1605.

Meyer, J. C., Geim, A. K., Katsnelson, M. I., et al. (2007). The structure of suspended graphene sheets. *Nature, 446*, 60–63.

Min, K., & Aluru, N. R. (2011). Mechanical properties of graphene under shear deformation. *Applied Physics Letters, 98*, 013113.

Mohiuddin, T. M. G., Lombardo, A., Nair, R. R., et al. (2009). Uniaxial strain in graphene by Raman spectroscopy: *G* peak splitting, Gruneisen parameters, and sample orientation. *Physical Review B, 79*, 205433.

Morozov, S. V., Novoselov, K. S., Katsnelson, M. I., et al. (2008). Giant intrinsic carrier mobilities in graphene and its bilayer. *Physical Review Letters, 100*, 016602.

Neek-Amal, M., & Peeters, F. M. (2010). Graphene nanoribbons subjected to axial stress. *Physical Review B, 82*, 085432.

Ni, Z. H., Wang, H. M., Kasim, J., et al. (2007). Graphene thickness determination using reflection and contrast spectroscopy. *Nano Letters, 7*, 2758–2763.

Novoselov, K. S., Geim, A. K., Morozov, S. V., et al. (2004). Electric field effect in atomically thin carbon films. *Science, 306*, 666–669.

Novoselov, K. S., Geim, A. K., Morozov, S. V., et al. (2005). Two-dimensional gas of massless Dirac fermions in graphene. *Nature, 438*, 197–200.

Oh, S.-H., Na, S.-I., Jo, J., et al. (2010). Water-soluble polyfluorenes as an interfacial layer leading to cathode-independent high performance of organic solar cells. *Advanced Functional Materials, 20*, 1977–1983.

Park, H., Rowehl, J. A., Kim, K. K., et al. (2010). Doped graphene electrodes for organic solar cells. *Nanotechnology, 21*, 505204.

Patchkovskii, S., Tse, J. S., Yurchenko, S. N., et al. (2005). Graphene nanostructures as tunable storage media for molecular hydrogen. *Proceedings of the National Academy of Sciences of the United States of America, 102*, 10439–10444.

Pei, Q. X., Zhang, Y. W., & Shenoy, V. B. (2010). A molecular dynamics study of the mechanical properties of hydrogen functionalized graphene. *Carbon, 48*, 898–904.

Pereira, V. M., & Neto, A. H. C. (2009). Strain engineering of graphene's electronic structure. *Physical Review Letters, 103*, 046801.

Pereira, V. M., Ribeiro, R. M., Peres, N. M. R., & Neto, A. H. C. (2010). Optical properties of strained graphene. *Europhysics Letters, 92*, 67001.

Peres, N. M. R. (2009). Scattering in one-dimensional heterostructures described by the Dirac equation. *Journal of Physics-Condensed Matter, 21*, 095501.

Poot, M., & van der Zant, H. S. J. (2008). Nanomechanical properties of few-layer graphene membranes. *Applied Physics Letters, 92*, 063111.

Rafiee, M. A., Lu, W., Thomas, A. V., et al. (2010). Graphene nanoribbon composites. *ACS Nano, 4*, 7415–7420.

Rafiee, M. A., Rafiee, J., Wang, Z., et al. (2009). Enhanced mechanical properties of nanocomposites at low graphene content. *ACS Nano, 3*, 3884–3890.

Reina, A., Jia, X. T., Ho, J., et al. (2009). Large area, few-layer graphene films on arbitrary substrates by chemical vapor deposition. *Nano Letters, 9*, 30–35.

Roddaro, S., Pingue, P., Piazza, V., et al. (2007). The optical visibility of graphene: interference colors of ultrathin graphite on SiO_2. *Nano Letters, 7*, 2707–2710.

Roy-Mayhew, J. D., Bozym, D. J., Punckt, C., et al. (2010). Functionalized graphene as a catalytic counter electrode in dye-sensitized solar cells. *ACS Nano, 4*, 6203–6211.

Saada, D. (2000). Diamond and Graphite Properties.

Scarpa, F., Adhikari, S., Gil, A. J., & Remillat, C. (2010). The bending of single layer graphene sheets: the lattice versus continuum approach. *Nanotechnology, 21*, 125702.

Schedin, F., Geim, A. K., Morozov, S. V., et al. (2007). Detection of individual gas molecules adsorbed on graphene. *Nature Materials, 6*, 652–655.

Schniepp, H. C., Kudin, K. N., Li, J. L., et al. (2008). Bending properties of single functionalized graphene sheets probed by atomic force microscopy. *ACS Nano, 2*, 2577–2590.

Shao, Y., Wang, J., Wu, H., et al. (2010). Graphene based electrochemical sensors and biosensors: a review. *Electroanalysis, 22*, 1027–1036.

Shi, Y. M., Kim, K. K., Reina, A., et al. (2010). Work function engineering of graphene electrode via chemical doping. *ACS Nano, 4*, 2689–2694.

Son, D. I., Kim, T. W., Shim, J. H., et al. (2010). Flexible organic bistable devices based on graphene embedded in an insulating poly(methyl methacrylate) polymer layer. *Nano Letters, 10*, 2441–2447.

Stankovich, S., Dikin, D. A., Dommett, G. H. B., et al. (2006). Graphene-based composite materials. *Nature, 442*, 282–286.

Sun, T., Wang, Z. L., Shi, Z. J., et al. (2010). Multilayered graphene used as anode of organic light emitting devices. *Applied Physics Letters, 96*, 133301.

Tsoukleri, G., Parthenios, J., Papagelis, K., et al. (2009). Subjecting a graphene monolayer to tension and compression. *Small, 5*, 2397–2402.

Tung, V. C., Chen, L.-M., Allen, M. J., et al. (2009). Low-temperature solution processing of graphene–carbon nanotube hybrid materials for high-performance transparent conductors. *Nano Letter, 9*, 1949–1955.

Vadukumpully, S., Paul, J., Mahanta, N., & Valiyaveettil, S. (2011). Flexible conductive graphene/poly(vinyl chloride) composite thin films with high mechanical strength and thermal stability. *Carbon, 49*, 198–205.

van der Zande, A. M., Barton, R. A., Alden, J. S., et al. (2010). Large-scale arrays of single-layer graphene resonators. *Nano Letters, 10*, 4869–4873.

Wang, Y., Chen, X. H., Zhong, Y. L., et al. (2009). Large area, continuous, few-layered graphene as anodes in organic photovoltaic devices. *Applied Physics Letters, 95*, 063302.

Wang, C. Y., Mylvaganam, K., & Zhang, L. C. (2009). Wrinkling of monolayer graphene: a study by molecular dynamics and continuum plate theory. *Physical Review B, 80*, 155445.

Wang, S., Zhang, Y., Abidi, N., & Cabrales, L. (2009). Wettability and surface free energy of graphene films. *Langmuir, 25*, 11078–11081.

Wang, Z. B., Helander, M. G., Qiu, J., et al. (2010). Direct hole injection in to 4,4′-*N*,*N*′-dicarbazole-biphenyl: a simple pathway to achieve efficient organic light emitting diodes. *Journal of Applied Phyiscs, 108*, 024510.

Wang, Y., Tong, S. W., Xu, X. F., et al. (2011). Interface engineering of layer-by-layer stacked graphene anodes for high-performance organic solar cells. *Advanced Materials, 23*, 1514–1518.

Wang, F., Zhang, Y. B., Tian, C. S., et al. (2008). Gate-variable optical transitions in graphene. *Science, 320*, 206–209.

Wang, X., Zhi, L., Tsao, N., et al. (2008). Transparent carbon films as electrodes in organic solar cells. *Angewandte Chemie International Edition, 47*, 2990–2992.

Wildoer, J. W. G., Venema, L. C., Rinzler, A. G., et al. (1998). Electronic structure of atomically resolved carbon nanotubes. *Nature, 391*, 59–62.

Wu, J., Agrawal, M., Becerril, H. A., et al. (2010). Organic light-emitting diodes on solution-processed graphene transparent electrodes. *ACS Nano, 4*, 43–48.

Xie, X. J., Qu, L. T., Zhou, C., et al. (2010). An asymmetrically surface-modified graphene film electrochemical actuator. *ACS Nano, 4*, 6050–6054.

Xu, Y. X., Bai, H., Lu, G. W., et al. (2008). Flexible graphene films via the filtration of water-soluble noncovalent functionalized graphene sheets. *Journal of the American Chemical Society, 130*, 5856.

Yamaguchi, H., Eda, G., Mattevi, C., et al. (2010). Highly uniform 300 mm wafer-scale deposition of single and multilayered chemically derived graphene thin films. *ACS Nano, 4*, 524–528.

Yi, Y., Jeon, P. E., Lee, H., et al. (2009). Interface state assisted charge transport at the MoO_3/metal interface. *Journal of Chemical Physics, 130*, 094704.

Yoo, E. J., Kim, J., Hosono, E., et al. (2008). Large reversible Li storage of graphene nanosheet families for use in rechargeable lithium ion batteries. *Nano Letters, 8*, 2277–2282.

Yu, V., & Hilke, M. (2009). Large contrast enhancement of graphene monolayers by angle detection. *Applied Physics Letters, 95*, 151904.

Yu, Y. J., Zhao, Y., Ryu, S., et al. (2009). Tuning the graphene work function by electric field effect. *Nano Letters, 9*, 3430–3434.

Zakharchenko, K. V., Katsnelson, M. I., & Fasolino, A. (2009). Finite temperature lattice properties of graphene beyond the quasiharmonic approximation. *Physical Review Letters, 102*, 046808.

Zhang, Y., Tan, J. W., Stormer, H. L., & Kim, P. (2005). Experimental observation of the quantum Hall effect and Berry's phase in graphene. *Nature, 438*, 201–204.

Zhao, H., Min, K., & Aluru, N. R. (2009). Size and chirality dependent elastic properties of graphene nanoribbons under uniaxial tension. *Nano Letters, 9*, 3012–3015.

Zheng, Q., Geng, Y., Wang, S., Li, Z., & Kim, J. K. (2010). Effects of functional groups on the mechanical and wrinkling properties of graphene sheets. *Carbon, 48*, 4315–4322.

Zhu, Y., Cai, W., Piner, R. D., et al. (2009). Transparent self-assembled films of reduced graphene oxide platelets. *Applied Physics Letters, 95*, 103104.

SECTION VII

III-V BASED AND NOVEL MATERIALS

3.23 Synthesis and Properties of Single Crystalline cBN and Its Sintered Body

Takashi Taniguchi, Advanced Key Technology Division, National Institute for Materials Science, Tsukuba, Ibaraki, Japan

Boron nitride (BN) is positioned in the upper row of the Periodic Table as a III–V compound, and is used in a diverse range of applications. In practical applications such as heat insulation and heat-resistant materials, BN is normally a hexagonal crystal system which is known as hexagonal boron nitride (hBN) and has a lamellar structure similar to that of graphite. On the other hand, cubic boron nitride (cBN), which has a sphalerite crystal structure similar to diamond, can be obtained by converting hBN to a high-density phase under high pressure and high temperature, in the same way that diamond is a high-density phase of graphite. cBN is known as a superhard material which possesses hardness second only to that of diamond.

3.23.1 Single Crystal Cubic Boron Nitride

cBN has a crystal structure similar to that of diamond. This substance does not occur in nature, and was first synthesized by Robert H. Wentorf, Jr. of General Electric in the United States (Wentorf, 1957), who carried out pioneering research on the synthesis of diamonds by a high-pressure process. Although its hardness is approximately half that of diamond, its heat resistance and chemical stability are superior (DeVries, 1972; Wentorf, De Vries, & Bundy, 1980). In particular, one feature of cBN is its remarkably low reactivity with ferrous metal materials in comparison with diamond.

Diamonds are normally synthesized under high pressure by using graphite as the starting material and transition metals such as iron, nickel, cobalt, etc. as the solvent. Graphite is dissolved in these solvent of transition metals under pressure/temperature conditions at which diamond is thermodynamically stable, and precipitates as diamond. This process is currently used in industrial production of diamond particles with various particle sizes. It is also possible to obtain good-quality, large-scale single crystals by imposing a temperature gradient on the reaction field under high pressure and controlling the degree of saturation of the carbon in the solvent so as to control the crystallization of the diamond.

In the synthesis of cBN, the process is controlled based on its similarity with high-pressure synthesis of diamonds, as described above. However, many differences between the two have also been found. Synthesis of diamonds, which have been produced industrially as single crystals in sizes of several carats (10 mm and larger), is a mature process which was developed through a long history of research. In contrast to this, the sizes of the cBN single crystals which have been obtained to date are on the order of 3 mm. The issues in research on the synthesis of cBN are how to take good quality similar to the artificial diamond. Controlling the nucleation and growth process of cBN under high pressure and obtaining its good quality, large-scale single crystals have, therefore, been still the subject of the study for long time.

Learning from the high-pressure synthesis process of diamond single crystals, studies on single-crystal growth of cBN had been performed by the temperature-gradient process using a solvent under high-pressure, high-temperature conditions near 5 GPa and 1400–1500 °C (Mishima & Era, 2000). Unlike the synthesis of diamonds, in which a transition metal system solvent is used, alkali and/or alkali-earth BN such as Li_3BN_2 is used for the solvent of cBN synthesis (DeVries & Fleisher, 1972; Kagamida et al., 1989, Mishima et al., 1987). Since these alkali-base solvents are easily reacted with oxygen and humidity, their quality control is important in dry-nitrogen atmosphere. This may arise one of the difficulties for obtaining good-quality crystals as compared to diamond. When the quality of the solvent was degraded, the reproducibility of the crystals growth was affected.

http://dx.doi.org/10.1016/B978-0-08-096527-7.00060-X

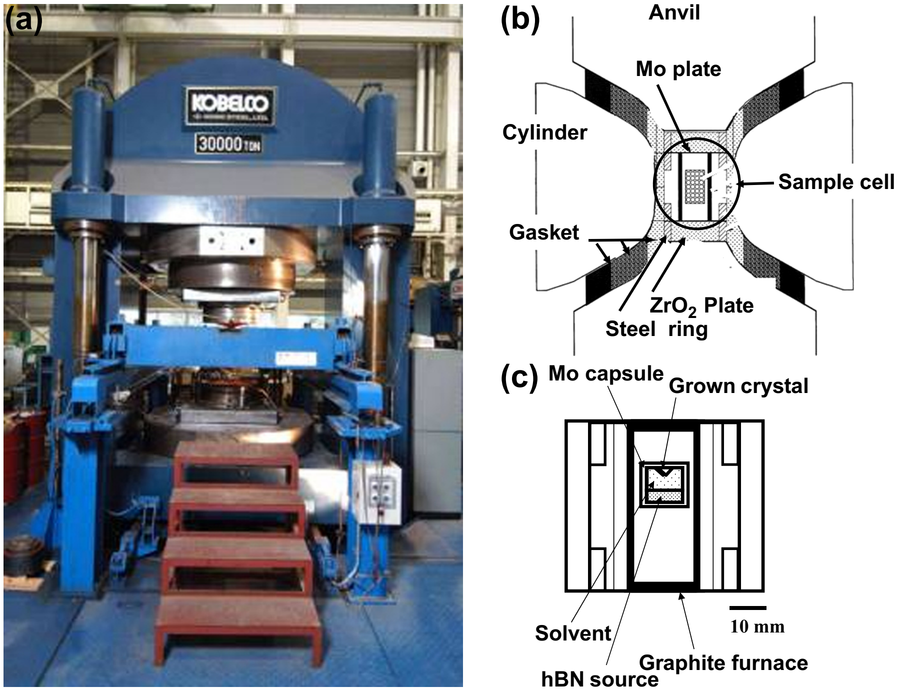

Figure 1 (a) Belt-type high-pressure apparatus, (b) sectioned view of Belt-type fixture, (c) sectioned view of sample assembly.

An example of the sample assembly in single-crystal growth under high pressure and a belt-type high-pressure apparatus is shown in Figure 1. As shown in Figure 1(b), pressure is generated by arranging a cylindrical sample cell inside a cylinder and applying pressure to this using a top-and-bottom opposed pair of anvils. In the high-pressure cell shown in Figure 1(c), hBN is used as the source materials, and a molybdenum (Mo) capsule containing the solvent and hBN in a layered form is arranged at a position slightly separated in the vertical direction from the center of the cylindrical graphite furnace. The source material diffuses from the high-temperature central part, and a single crystal is obtained by recrystallization of this source material on the low-temperature side of the solvent.

As compared to diamond crystals growth, one of the disadvantages for cBN is lack of good-quality seed crystals as a seed. With the analogy of diamond crystal growth in the temperature-gradient process, high-quality crystals is expected to be obtained on the seed crystals by suppressing spontaneous nucleations which affect the steady-growth circumstance on the seed surfaces. To overcome this disadvantage for the seed crystal, attempts were made to grow cBN crystals on diamond as a seed crystal under high pressure by exploiting the small lattice mismatch of 1.35% between diamond and cBN (Sei, Akaishi, Kanda, & Yamaoka, 1991; Taniguchi et al., 2000). Figure 2 shows the heteroepitaxially grown cBN crystals on diamond seed of (100) and (111) surfaces by using Li_3BN_2 as a solvent. On the (100) surface, the <110> growth striation appeared, crossing the cBN (100) surface of 90°. Growth of polar crystal of cBN on a (100) diamond lattice exhibits the typical antiphase domain (APD) as seen in the growth of GaAs on an Si substrate (Morizane, 1977). The formation of APD seems to be enhanced by etching of the diamond seed surface by the solvent at the initial growth stage. On the (111) surface, the variation of morphology of the grown cBN crystals was affected by a temperature gradient. With larger temperature gradient, (113) face was dominated on the (100) diamond seed crystal, while (100) growth was seen in relatively smaller temperature gradient. Since the size of grown cBN crystals can be controlled by diamond seed crystal, surface structural analysis of cBN crystal by using spectroscopy technique was carried out to realize cBN surface chemistry affected by hydrogen and/or oxygen terminations (Loh, Sakaguchi, Nishitani-Gamo, Tanigcuhi, & Ando, 1997; 1998a,b). By keeping the growth temperature lower, spontaneous nucleation of cBN crystals was suppressed so as to obtain finer crystals on the seed. The growth rate of this condition was, however, significantly smaller as that compared to diamond crystals growth under high pressure. The study of cBN heteroepitaxial growth on diamond seed revealed the fact that reasonable growth rate is required to obtain large cBN single crystals even with occurrence of spontaneous nucleation. Consequently, relatively larger cBN crystals were obtained by the spontaneous nucleation followed by steady growth for some duration period, such as 100 h.

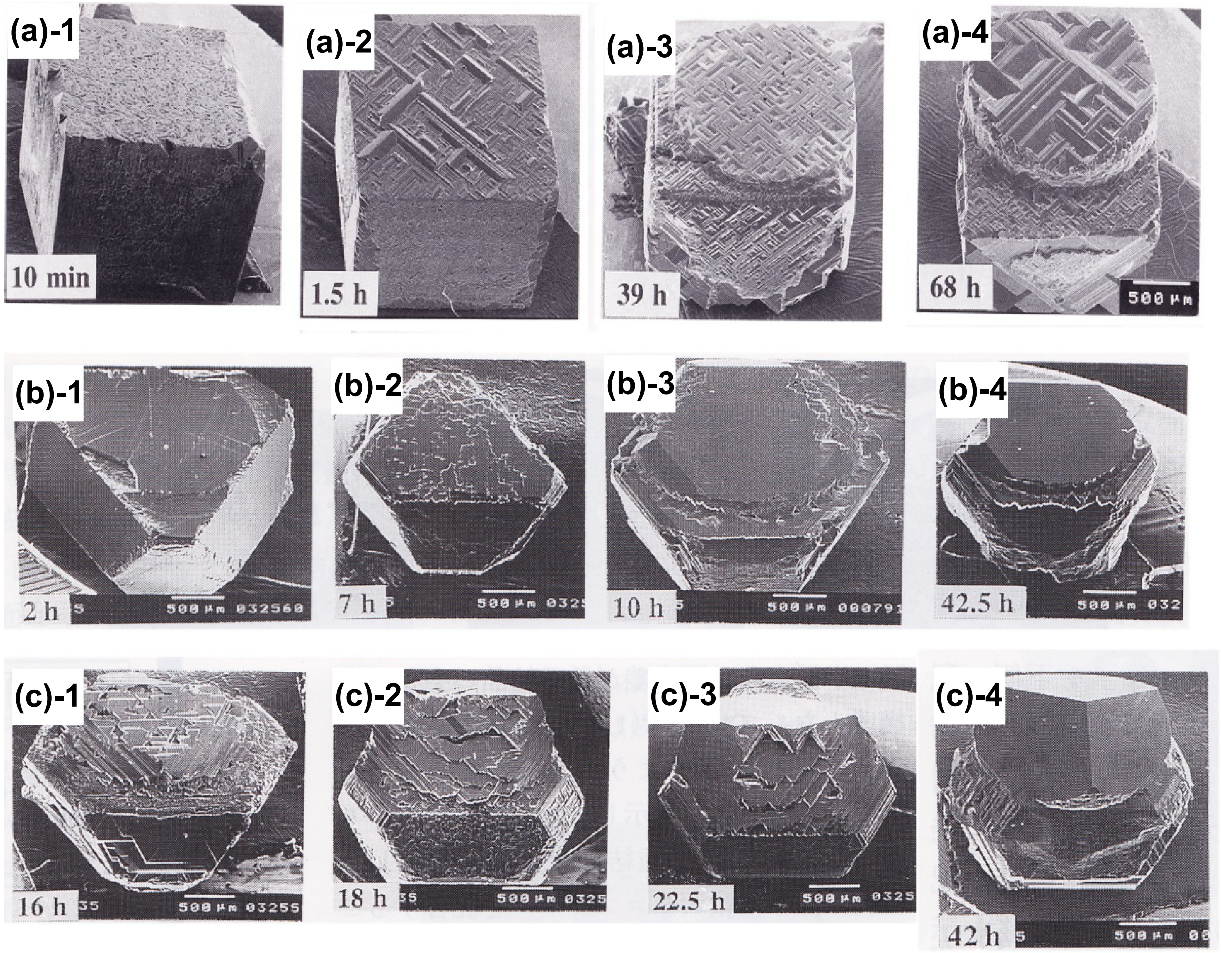

Figure 2 Morphology of cBN crystals grown on diamond-seed crystals under 1500 °C and 5.5 GPa. (a) Grown on (100) surface of diamond seed, (b) grown on (111) surface of diamond seed, (c) grown on (111) surface of diamond seed. Temperature gradient in (b) series is slightly higher than that of (c) series.

With the current cBN crystal growth technology by using temperature-gradient method with spontaneous nucleation, relatively good-quality crystals have been synthesized up to a size of approximately 2–3 mm in length on the longest side, as shown in the photograph in **Figure 3** (Taniguchi & Yamaoka, 2001). Together with its properties as a superhard material second only diamond, cBN is also expected to have a large bandgap on the order of 6.2 eV. Although its intrinsic color should be colorless, many of the cBN single crystals obtained by high-pressure synthesis display a so-called amber color, as can be seen in **Figure 3**. This is thought to be due to the effects of oxygen and carbon impurities in the single crystal. Although the yellow color of artificial diamonds is known to originate from nitrogen impurities, in the case of cBN, the main impurities are expected to be C and O, which are neighboring elements of B and N.

Regarding achievement of semiconductor properties in cBN crystals, the synthesis of crystals with both *p*- and *n*-type properties was first reported (Wentorf, 1962). Beryllium (Be) is known to be an acceptor for obtaining *p*-type cBN, and blue crystals can be obtained, in a manner similar to that when boron is added to diamond (Mishima et al., 1987; Taniguchi et al., 2003; Wentorf, 1962). As donors for the *n*-type property, among other elements, silicon and sulfur can be mentioned (Mishima et al., 1987; Taniguchi, Teraji, Koizumi, Watanabe, & Yamaoka, 2002; Wentorf, 1962). In crystals with the amber color resulting from oxygen and carbon impurities, as described above, an *n*-type semiconductor property has been observed by Hall effect measurement (Taniguchi et al., 2002).

Nitrogen impurities in diamond single crystals form TiN and/or AlN by addition of Ti and/or Al to the solvent, and as a result, the N concentration in the diamond can be reduced to <1 ppm (Sumiya & Sato, 1996).

Figure 3 Optical photograph of cBN single crystals obtained at high pressure.

In the past, a search for similar so-called impurity getters was carried out in order to realize high purity in cBN, but thus far, no effective additive has been discovered. On the other hand, when barium (Ba) was used as the solvent component, a virtually colorless, transparent cBN crystal was obtained (Taniguchi & Watanabe, 2007). This crystal has a high-electrical insulation property, and judgment of *p*- or *n*-type was not possible in Hall effect measurement. The pressure–temperature boundary for obtaining cBN crystals by using Ba–BN solvent was shown in **Figure 4**. **Figure 5** shows the optical microscope images of (a) an *n*-type crystal and (c) a *p*-type crystal, which were obtained by doping with S or Be, respectively, (b) amber-colored crystals, which were unintentionally doped with impurities and display an *n*-type property, and (d) virtually colorless crystals with a high-insulating property, which were obtained using a Ba–BN system solvent. The semiconductor properties of these *p*- and *n*-type crystals were previously characterized by Hall effect measurement and theoretical calculations, and their respective levels were clarified (Oba, Taknaka, Watanabe, Taniguchi, & Togo, 2010; Taniguchi et al., 2002; Taniguchi et al., 2003).

Figure 6 shows the absorption spectra of the crystals shown in **Figure 5** (Taniguchi, Watanabe, & Koizumi, 2004). With the S-doped and amber-colored crystals, remarkable absorption can be seen around a wavelength

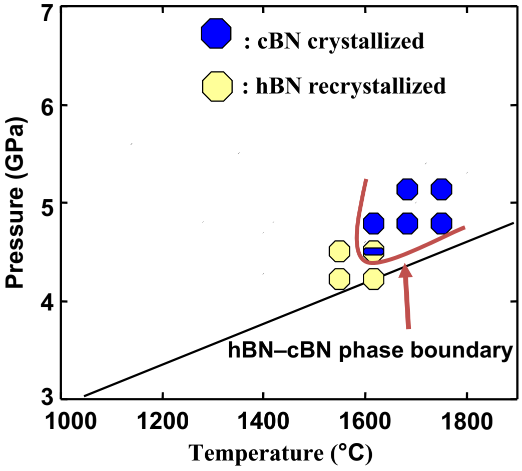

Figure 4 Synthesis region of cBN crystals by using Ba–BN solvent. Solid line: hBN–cBN phase boundary (Fukunaga, 2000).

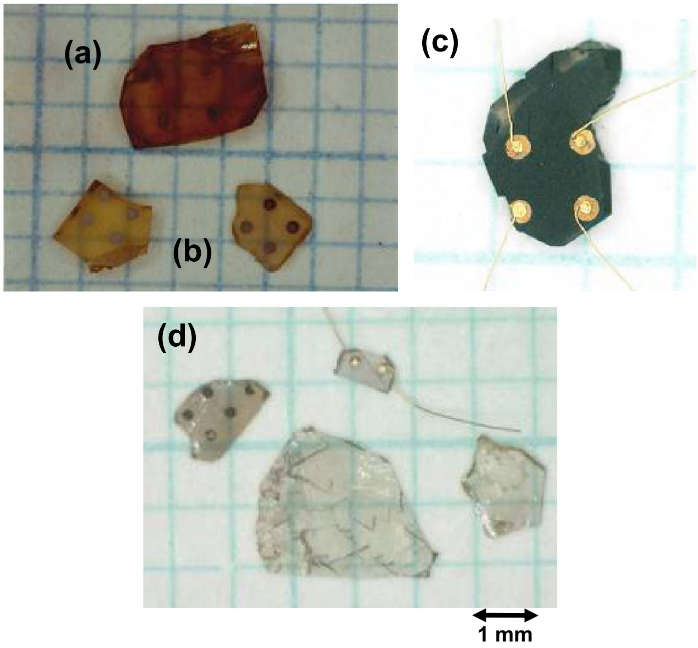

Figure 5 cBN single crystals. (a) *n*-type semiconducting crystals, (b) *p*-type semiconducting crystals, (c) virtually colorless crystals.

of 400 nm. Although this can be thought to be an effect of oxygen or carbon impurities, this absorption has still been observed in virtually colorless crystals, suggesting the space for the improvement in the purity for the virtually colorless crystals.

Figure 7 shows the results of Secondary Ion Mass Spectroscopy (SIMS) analysis of the hBN source material, an amber cBN crystal, and the virtually colorless cBN crystal obtained using the Ba–BN solvent (Taniguchi & Watanabe, 2007). The carbon and oxygen impurities in the source remained at similar levels (10^{19}/cm^3 and 10^{20}/cm^3 order for C and O, respectively) in the amber crystal while the amounts of these substances decreased by approximately two orders in the colorless crystal.

Figure 8 shows an example of crystals in which point defects were characterized by etching with molten NaOH. The etch-pit density of the aforementioned amber crystal was on the order of 10^7/cm^2, but in contrast, that of the colorless crystal was approximately 10^4/cm^2 (Taniguchi, Watanabe, et al., 2004).

By using the virtually colorless higher purity cBN crystal, single-crystal elastic moduli was determined by Brillouin scattering measurement at ambient condition and obtain values are $C_{11} = 798.4 \pm 1.1$ GPa, $C_{22} = 469.0 \pm 0.6$ GPa, and $C_{33} = 172.4 \pm 1.0$ GPa, from which the isotropic aggregate bulk modulus

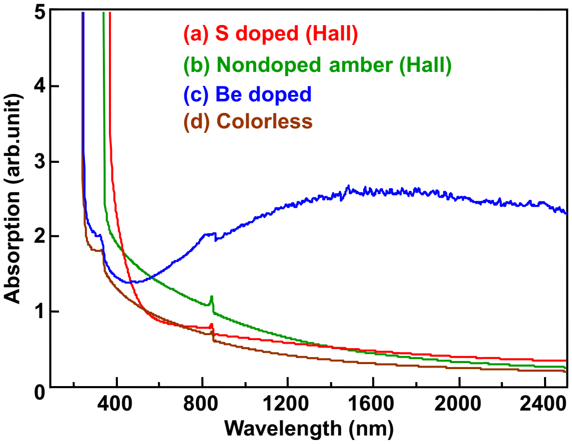

Figure 6 Optical absorption spectra of cBN crystals.

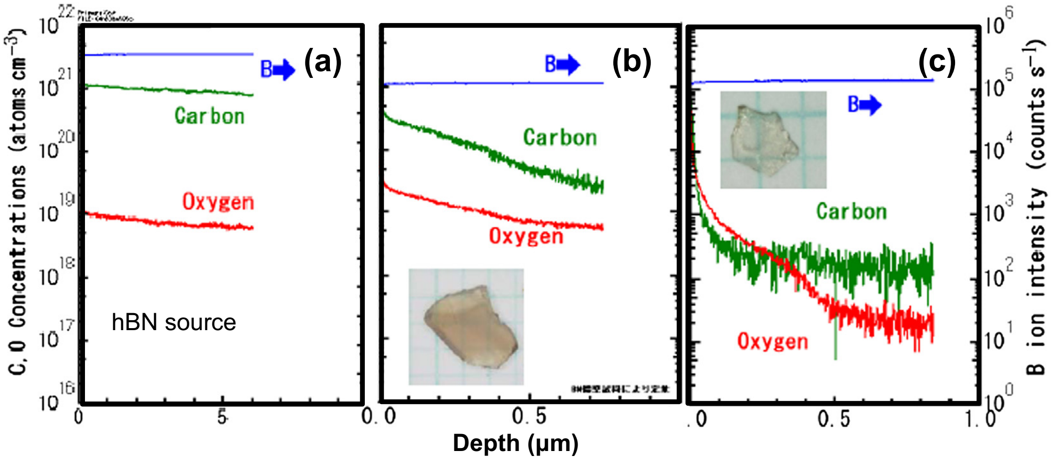

Figure 7 SIMS depth profiles. (a) Source of hBN crystal; (b) amber-colored cBN crystals; (c) virtually colorless cBN crystals. Standard samples for the determination of oxygen and carbon concentrations were prepared by using binder-less cBN-sintered bodies, in which oxygen and carbon implantation was conducted.

Ks = 381.1 ± 1.0 GPa and shear modulus $G = 398.78 \pm 0.6$ GPa were calculated (Zhang, Bass, Taniguchi, & Goncharov, 2011).

Furthermore, with the colorless crystal, the band-edge emission obtained by cathode luminescence was around a wavelength of 200 nm (Taniguchi, 2007; Watanabe, Taniguchi, & Kanda, 2004), as shown in **Figure 9**, suggesting the possibility that the reduction action of the Ba–BN solvent itself was successful. However, it should be noted that residual impurities still remained at the level of 10^{17}–10^{18}/cm^3, even in the virtually colorless higher purity crystals and observed free-exciton emissions was coexisted with the large broad spectrum originating from impurities and/or defects. Thus, in order to obtain higher quality high-purity crystals, in the future, it will be necessary to clarify the mechanism by which high purity is realized and to continuously seek and study excellent solvents.

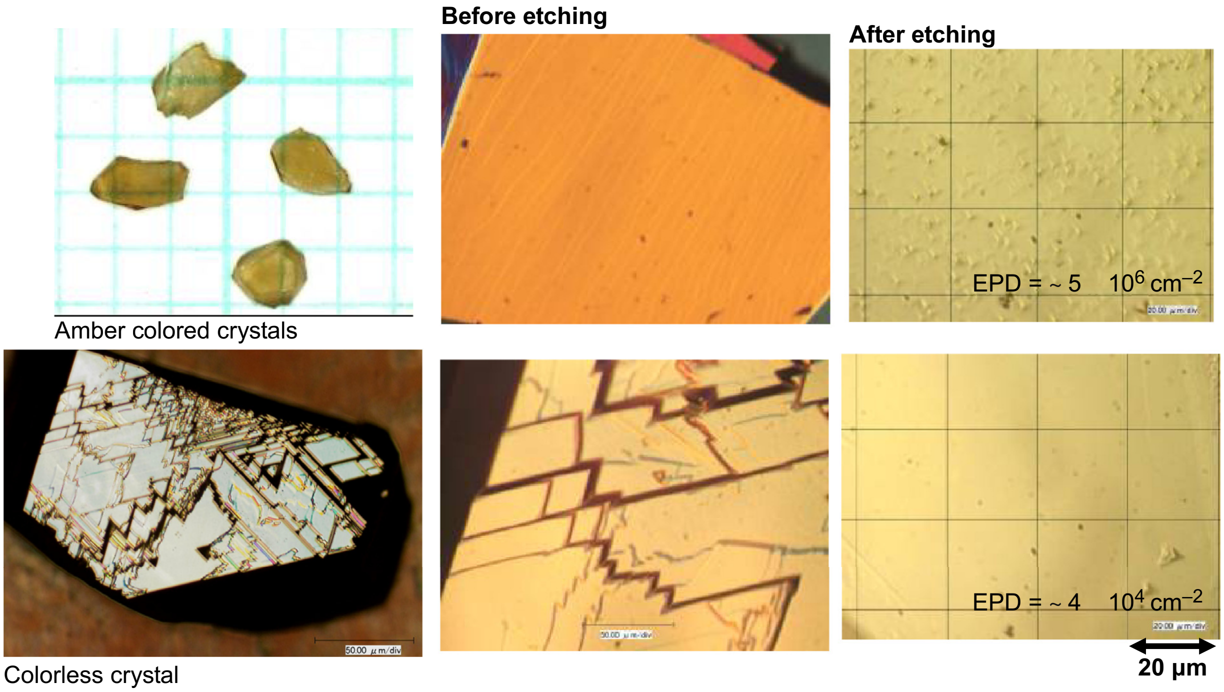

Figure 8 Optical photographs of etched cBN crystal surface by using molten NaOH.

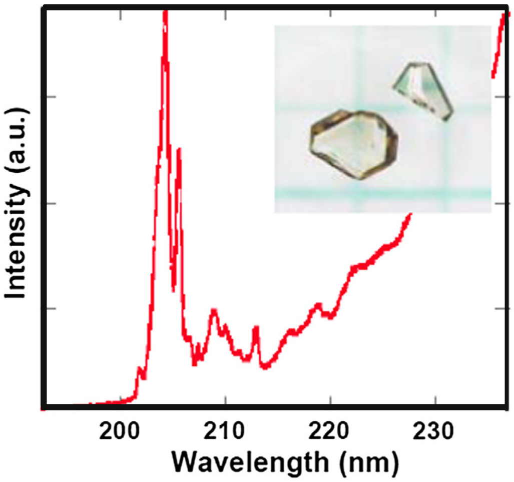

Figure 9 Cathode luminescence spectra of virtually colorless cBN single crystal.

3.23.1.1 Transition Metal System Solvents

A high-pressure synthesis process for cBN using an alkali metal system solvent was introduced in the previous section. As the dimensions which can be obtained with this process in its current state are on the order of 3 mm, it is considered important to search for the optimum solvent as a breakthrough for obtaining larger, higher quality cBN crystals. Based on this recognition, a search of diverse types of solvents was carried out previously. In this section, an example of a cBN synthesis process using a nickel (Ni)-base alloy solvent was introduced. Unlike alkali metals and other substances which display high reactivity with water and oxygen, Ni can be handled in atmospheric air, and impurity control and composition control are easy. Although this Ni alloy is one of the main work materials to which cBN is applied in the machining field, the reactivity of these two substances in the high-temperature region had not necessarily been clarified.

Figure 10 shows the sample composition when synthesis of cBN was attempted using Ni as the solvent (Taniguchi, Akaishi, Kanke, & Yamaoka, 2004). In the first attempt, in the standard sample composition shown in **Figure 1(b)**, an Ni disk was arranged in the Mo capsule in place of the alkali metal system solvent. The seed crystal was placed on the bottom side considering the difference in the specific gravities of the solvent and cBN. Unlike the lithium system, alkaline metal solvent in the previous section and similar solvents, when a metal solvent with a larger specific gravity than cBN is used, if the seed crystal is arranged on the top side, there is concern that the crystal on the source side may float up in the solvent, hindering stable crystal growth. **Figure 10(c)** shows the optical microscope images of the interface between the solvent and source material recovered after growth for approximately 40 h, and **Figure 10(b)** shows the schematic diagram of the observation position. Initially, the cBN crystal had been expected to grow on the low temperature side. However, in the experiment, the crystal grew toward the circumferential direction of the solvent (a photograph of crystals after acid treatment is shown in **Figure 10(d)**). Although temperature gradients occur in the high-pressure vessel not only in the vertical direction but also in the radial direction, the gradient in the radial direction is small. The growth which can be seen in **Figure 10(c)** is not due to this temperature gradient, but rather, was thought to be caused by some factor which enhances growth effect with Mo at the interface of the Ni–Mo capsule.

Therefore, an experiment in which hBN was converted to cBN was performed using Ni and an Ni–Mo alloy as the solvents, respectively (Kubota & Taniguchi, 2008; Kubota, Watanabe, & Taniguchi, 2007). Consequently as shown in **Figure 11**, the results revealed that the efficiency of conversion to cBN is remarkably improved by adding Mo to Ni.

Specifically, the growth at the Ni–Mo interface with the cBN seen in **Figure 10(c)** is considered to be due to the addition of Mo to Ni. Judging from an elemental analysis of the composition of the recovered metal solvent, as well as past reports on the solubility of the various elements in metals (Kowanda & Speidel, 2003), in metal system solvents such as Ni, the solubility of nitrogen is extremely low in comparison with that of boron, and this must be improved for this substance to demonstrate a function as a solvent for cBN. In contrast, it has been reported that addition of Mo to Ni increased the solubility of Ni in this alloy by approximately 40 times. The increase in cBN synthesis yield with the Ni–Mo system alloy discovered in this research can be understood as

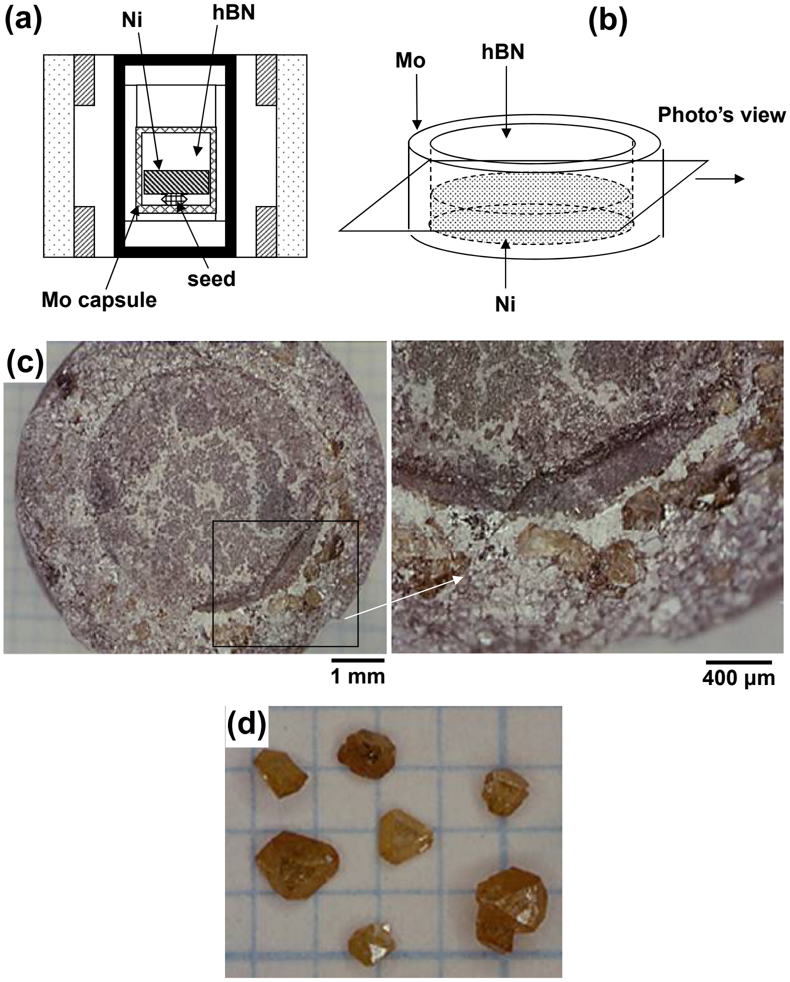

Figure 10 Schematic illustration of high-pressure cell assembly for crystal growth: (a) illustration of sample fixture; (b) optical photographs of recovered grown crystal correspond to the photo's view in (b); (c) optical photograph of recovered grown crystals.

the result of this improvement in Ni solubility. According to the same report, further improvement in Ni solubility can also be expected by addition of Cr (Kowanda & Speidel, 2003).

Figure 12 shows the formation region of cBN when using Ni, Ni–Cr–Mo, and Ni–Cr–Mo–Al alloys as solvents (Kubota & Taniguchi, 2008, 2009). With simple Ni, only extremely slight formation of cBN was observed under conditions of 5.5 GPa and 1500 °C or higher. This yield was improved by addition of Mo and/or Cr. It should also be noted that addition of a trace amount of Al to this system expanded the formation region to 4.2 GPa and around 1400 °C.

Figure 13 shows the relationship between the yield of cBN and the amount of Al addition to the Ni–Cr–Mo alloy under synthesis conditions of 4.5 GPa and 1400 °C. Synthesis of cBN using an Ni alloy with addition of Al has been reported (Saito, Ushio, & Nagano, 1970; Wentrof, 1975; DeVries & Fleisher, 1975; Fukunaga et al., 2004; Kubota, Kosuda, & Taniguchi, 2007; Fukunaga, Takeuchi, & Taniguchi, 2011; Eko, Fukunaga, & Ohtake, 2013). As shown in **Figure 13**, formation of cBN with an Ni–Mo–Cr system solvent was accelerated by adding approximately 0.3 wt% of Al.

The above results show that in the high-temperature region of 1400 °C and higher, a slight amount of BN dissolves in Ni, the solubility of BN can be increased by adding Cr and Mo to the solvent, and an effect which enhances the generation of cBN nuclei can be obtained by adding a trace amount of Al.

Figure 14 compares the growth rate of cBN crystals obtained by the temperature-gradient process under high pressure using Ni-base alloy and alkaline system solvents, with that of diamond. (As Ni-base alloys, the above-mentioned Ni–Cr–Mo–Al system and Hastelloy C276 were used as solvents.) As shown in the figure, growth rate of cBN is significantly small as compared to that of diamond. The crystal growth rate was the slowest with

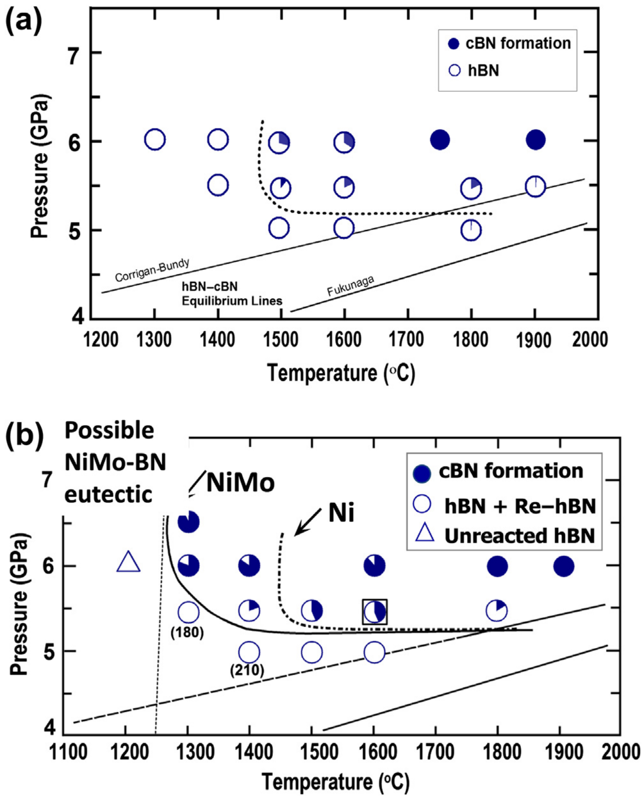

Figure 11 (a) Reaction boundary of cBN formation region by using Ni solvent; (b) cBN formation region by using Ni–Mo solvent.

the metal system solvents, which is attributed to the fact that the solubility of BN (and particularly N) in the solvents is still slight.

In other words, due to this poor reactivity (solubility), cBN is stable in the presence of ferrous metals in comparison with diamond.

On the other hand, the difference of the crystal growth rates in between the Ni-base metal system solvents and the above-mentioned alkaline metal system solvents are not so significant, as shown in Figure 14, while the easy handling as a solvent is an advantage in the metal system solvents. In the case of alkali metal system solvents, further improvement in the solvent quality by optimization of composition is also required, but all adjustments and handling of this type of solvent must be performed in a dry-nitrogen atmosphere as these solvents are remarkably affected by oxygen and moisture. In contrast, the metal system solvents offer a high degree of freedom in alloy composition control and handling, and changes and tracking of the alloy composition after recovery can be fed back to research on optimization of their composition.

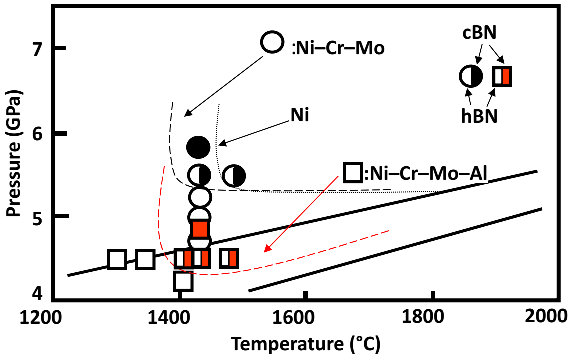

Figure 12 Reaction boundaries of cBN formation region by using Ni, Ni–Cr–Mo and Ni–Cr–Mo–Al solvent.

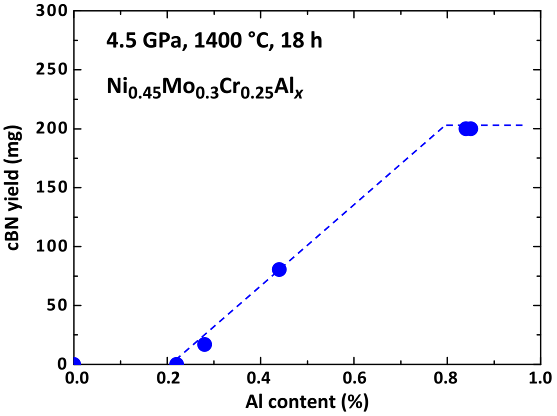

Figure 13 Effect of Al additive on cBN formation by using Ni–Mo–Cr solvent at 4.5 GPa and 1400 °C for 18 h.

The quality of the cBN crystals obtained using metal system solvents to date has not reached that of cBN crystals produced by the alkali metal system solvents discussed in the previous section. On the other hand, the accumulation of past research on metal system solvents is slight in comparison with research on the existing alkali metal system solvents. Further improvement of the composition of these metal alloy system solvents is recognized as one area of important subject, aiming at a breakthrough for large-scale, high-quality cBN single crystals. Optimization of the metal solvent system for improvement of the growth rate is key, and the issues for this research are securing effective nitrogen solubility and achieving high purity in the obtained crystals.

From the viewpoint of application as a superhard material, fabrication of machining tools using cBN single crystals and cutting tests of ferrous metals have been attempted several times in the past (Yazu, Degawa, & Tsuji, 1989; Grimm & Taniguchi, 2008). However, as the synthesis of good-quality, large-scale cBN single crystals themselves is a subject of research, it may be assumed that there is room for improvement in the properties of the respective single crystals used in these cutting tests. A further accumulation of research for obtaining a definitive solution to questions regarding the wear-resistance properties of cBN is necessary, including their potential as precision cutting tools and similar issues.

Industrially, cBN grains of diverse sizes are supplied as cutting abrasives, raw material for sintered compacts, etc. Since the ferrous transition metals which are effective in the synthesis of diamonds have less reactivity with BN as described above, cBN production was performed in industry by using alkali-base solvent under high pressure. This point, namely, the feature of less reactivity between cBN and the transition metals, is important for practical applications. In other words, cBN has established a complementary relationship with diamond as a superhard material having excellent properties as a cutting tool for ferrous metal materials.

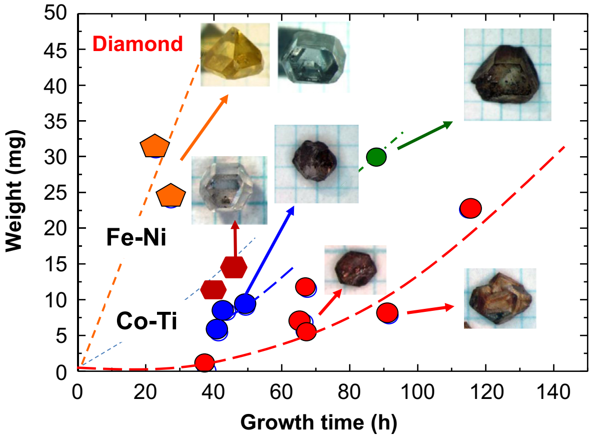

Figure 14 Typical growth rate of cBN single crystals by using metallic solvent and alkali-base solvents. Blue: Ni–Cr–Mo–Al solvent; red: Hastelloy C276 alloy solvent (Ni57%, Mo15–17%, Cr14.5–16.5%, Fe4–7%, W3–4.5%, Co2.5%, Mn1%, C0.02%, V0.35%, Si0.08%). Green: Ba–Li–BN solvent; Orange: diamond formation by using Co–Ti solvent.

Based on the knowledge of cBN crystal synthesis using metal system solvents introduced above, however, when cBN crystals are to be applied as cutting tools, if the work contains a high concentration of Mo, Cr, etc., it is necessary to consider the reaction under high temperature (under normal pressure, reverse conversion of cBN → hBN, etc.). It is known that cBN is not generally suitable for cutting of Al-base alloys. However, as this is related to the expansion of the cBN formation region by addition of Al, as discussed above, a detailed clarification of this can also be considered an important issue for research.

3.23.2 cBN Sintered Body

The main application of superhard materials is grinding and cutting of difficult-to-machine materials, which are difficult to process with hard materials such as tungsten carbide (WC) and silicon carbide (SiC). Recently, attempts have been made to change the grinding process using abrasive grains to a cutting process using superhard materials. As a result, demand for cutting tools using cBN-sintered compacts as a base has increased in recent years. The cBN tools which are mass-produced industrially are sintered compacts in which cBN grains are sintered together with sintering additives under high pressure. These can be broadly divided into sintered composites with a cBN content of 90% or more (sintering additive: cobalt, etc.), in which some type of bonding exists between the cBN particles, and those in which the cBN content is small, being on the order of 60%, and the remainder consists of aluminum nitride (AlN), titanium nitride (TiN), etc. Both are sintered under a pressure of approximately 4–5 GPa, but the two types are used in different applications, depending on the type of material being processed (heat-treated hard steel, untreated soft steel, etc.). These cBN compacts with variety of binders have already been actively developed and practically utilized in the industry. While the study for further improvement of these cBN compacts is important in industry, recent alternative attempts for achieving binder-less sintering were featured in this chapter.

Responding to demand for increased hardness in the steel materials being processed and increased machining efficiency, realizing higher performance in cBN-sintered tools has become an important research subject in recent years. The development of working tools with excellent cutting performance is also significant for reducing the environmental loads associated with cutting processes due to the disposal of large amounts of abrasive grains and lubricating oils as waste. Although the properties of cBN-sintered tools depend on the ratio of the constituent elements of cBN and sintering additives and their mode of bonding, if it is possible to synthesize a cBN-sintered compact which is completely free of sintering additives, the mechanical properties of that compact will be extremely interesting.

As mentioned previously, cBN, which is a high-density phase of hBN, is formed by a process of dissolution in a solvent and precipitation under high pressure and high temperature. The necessary pressure and temperature conditions in this process are approximately 4–5 GPa and 1300–1500 °C, respectively. On the other hand, under conditions in which a solvent is not present, the conversion reaction from hBN to cBN will progress in a solid phase, provided a higher pressure condition is applied. Strictly speaking, hBN undergoes a phase transition without diffusion to wurtzite-structured BN (wBN) as a result of compression, and is then converted to sphalerite-type BN (cBN) by solid-phase diffusion under high temperature. This phenomenon was reported by General Electric company (Corrigan & Bundy, 1975). Subsequently, Japanese researchers clarified the effects of appropriate control by pressure/temperature conditions and high-purification treatment of the hBN starting material, and reported the synthesis of a light-transparent high-purity cBN-sintered body (Akaishi, Satoh, Ishii, Taniguchi, & Yamaoka, 1993). This was a sintered body that contained absolutely no sintering additives. Development of production is being carried out by several companies, including some in Japan (Sumiya, Uesaka, & Satoh, 2000). Binder-less high-purity sintered body possess hardness approximately 30% superior to that of the conventional sintered composites and also display excellent cutting performance (Sumiya et al., 2000; Yamaoka, Akaishi, & Ueda, 1991).

Synthesis of the high-purity cBN-sintered compact was realized by solid-state reaction sintering accompanying phase conversion from a low-pressure phase to a high-pressure phase in the 7.7 GPa and 2000 °C region. The raw material used in this process was hBN after ordinary deoxidation treatment. In this research, it was reported that (1) at synthesis temperatures around 1800 °C, even though conversion to cBN continued to progress, strength was inadequate due to a residual low-pressure phase; (2) a light-transparent dense sintered compact was obtained at approximately 2300 °C and higher; and (3) the strength of the sintered compact decreased due to grain growth when the sintering temperature was excessive. In addition, (4) the grain size of the sintered compact obtained under the optimum sintering conditions was on the

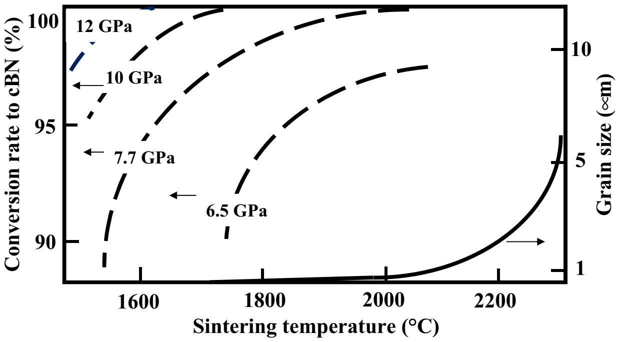

Figure 15 Relationship between sintering temperature and conversion rate of cBN as a function of applied pressure.

submicron order, and the resulting sintered compact showed excellent wear resistance as a cutting tool for ferrous metal materials.

Figure 15 shows the relationship of the conversion rate to cBN and the sintering temperature in high-pressure/high-temperature treatment of hBN, and the grain size of the cBN converted in this process, under various synthesis pressure conditions. When hBN is used as the raw material, 100% conversion to cBN was not achieved under any temperature conditions when the pressure was 7 GPa or less, and a cBN single-phase sintered body with a grain size of approximately 500 nm was obtained in the 8 GPa region. As typical conditions for further reducing of this grain size (to <100 nm) while retaining the cBN single-phase composition, it is necessary, for example, to reduce the sintering temperature to around 1700 °C and this can be performed in the 10 GPa-pressure region (Taniguchi et al., 2004).

Figure 16 shows the X-ray diffraction profile of a cBN-sintered body obtained in the 10 GPa-pressure region. A slight amount of the low-density phase was remained up to a temperature of around 1600 °C, but conversion to a single phase of cBN was achieved at 1700 °C.

Images of the sintered body taken using an optical microscope and a scanning electron microscope are shown in **Figure 17**. In addition to displaying slight transparency, a fine microstructure of approximately 100 nm or less can be observed in this body. According to a separate evaluation, Vickers hardness above 50 GPa was obtained with a 98 N indentation load. A specimen of this sintered body was cut out and processed to a cutting edge for use in a cutting test, and a cutting test was performed with ferrous metal materials and others.

Figure 18 shows the tool fabricated for use in a precision cutting test and an optical microscope photograph of the surface of the work piece after processing. In precision cutting of stainless steel (SUS420), a satisfactory cut surface was obtained, with maximum surface roughness of 116 nm and average surface roughness of approximately 20 nm (Fujisaki et al., 2009).

The indentation load dependency of the Vickers indentation of the high-purity cBN-sintered body and the measured hardness are shown in **Figure 19** (Taniguchi, Akaishi, & Yamaoka, 1996). Generally, the hardness of materials is evaluated by the size of the indentation produced by a diamond indenter. However, because indentation load dependency is remarkable in the case of superhard material, as illustrated in **Figure 19**, care is

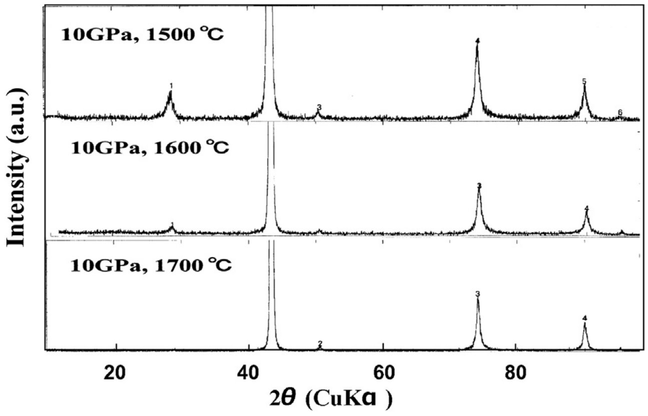

Figure 16 X-ray diffraction profiles of binder-less cBN-sintered bodies obtained at 10 GPa and 1500–1700 °C.

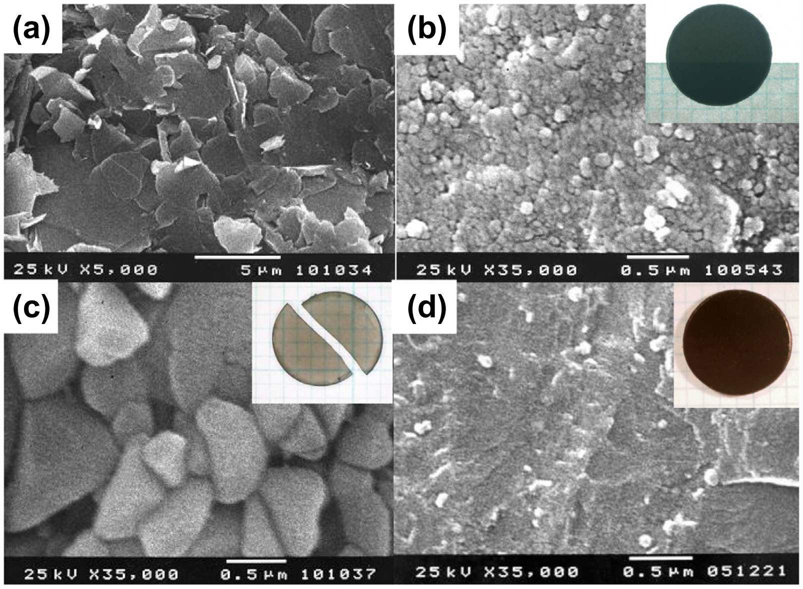

Figure 17 SEM photographs of samples: (a) starting hBN; (b) fracture surface of cBN-sintered body obtained at 10 GPa and 1700 °C; (c) 10 GPa and 2000 °C; (d) 12 GPa and 1600 °C.

necessary in evaluating this factor. It has been suggested that the morphology of propagating cracks caused by indentation with the diamond indenter changes depending on the load. Therefore, it is important to perform evaluations based on an adequate indentation load for superhard materials.

The above mentioned series of studies on reaction sintering of cBN from low density form of BN such as hBN and pBN have been carried out by using Belt type HP apparatus at 10GPa region. Similar trials for obtaining binderless cBN sintered bodies have recently been also carried out by using multi-anvil type HP apparatus. In those studies, it was claimed that the cBN sintered bodies with finer grain size with order of few tens nm exhibit extremely large Vicker's hardness value, though the applied indentation load were in the range of 5-10N. (Dubrovinskaia, et. al., 2007; Solozhenko, et. al., 2012; Tian, 2013). On the other hand, it was also reported that cBN sintered bodies obtained with almost similar condition exhibit ordinary level of Koop hardness value (Sumiya, 2014). The precise assessment for the hardness of ultra-fine-graind cBN sintered bodies without any binder seems remain the space for the study for the future work. Comparing the series of synthesis conditions for reaction sintereing of cBN, the threshold temperature fully converted to cBN depends upon the mode of pressure applied by belt-type and multi-anvil HP apparatus.

As outlined above, it is continuing to become possible to synthesize dense, high-purity sintered bodies with grain sizes reaching the ultrafine particle level, from the submicron to the nanometer order. The fact that these high-purity cBN-sintered bodies obtained by direct conversion possess excellent cutting properties in comparison with the conventional compound sintered bodies has also been clarified. However, because the

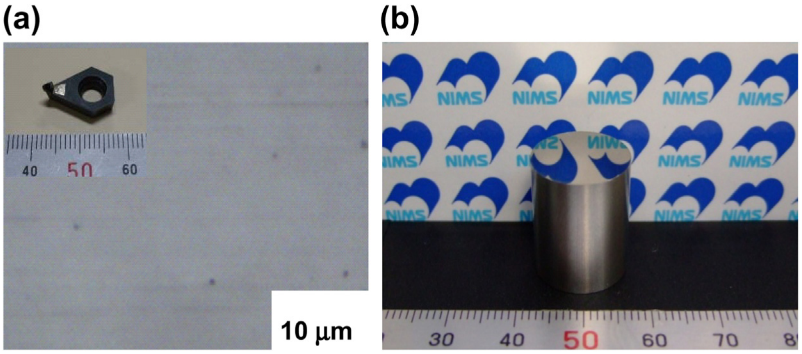

Figure 18 (a) Optical photographs of fabricated cBN cutting tool and polished surface after precision machining. (b) Whole view of work piece of SUS420J2 after precision machining.

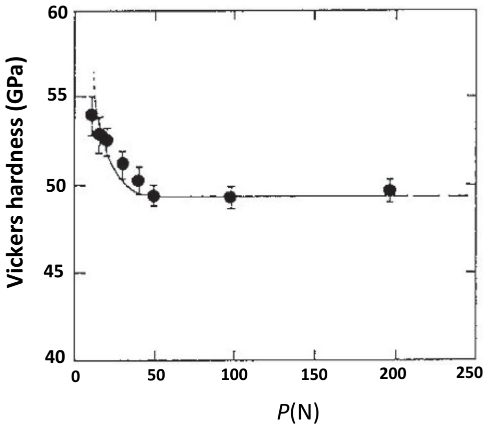

Figure 19 Vickers hardness as a function of indentation load of binder-less cBN-sintered body obtained at 7.7 GPa and 2300 °C.

high-pressure synthesis conditions for these sintered bodies are excessively severe for mass production of tool materials at the industrial scale, realizing binder-less sintered bodies with similar properties under lower pressure/temperature conditions is currently an important subject of research.

Even in direct sintering in a solid phase using cBN particles as the raw material in place of low-pressure-phase BN, additive-free light-transparent sintered bodies could be obtained in the 8 GPa and 2000 °C region, and these materials displayed mechanical properties comparable to those of the above-mentioned high-purity sintered bodies (Taniguchi et al., 1999). With this method, it is possible to control the grain size of the sintered body corresponding to the initial grain size of the raw material. Using this method, high-purity light-transparent cBN-sintered bodies with various grain sizes from approximately 0.5–10 μm were obtained, as shown in **Figure 20**. The relationship between the initial grain size and the hardness of the obtained sintered compacts is shown in **Figure 21**. According to this figure, an optimum sintering temperature exists, corresponding to the initial grain size, and sintering progresses in a lower temperature region (around 2200 °C) as the grain size decreases. On the other hand, in the high-temperature region, the strength of the sintered bodies decreases rapidly due to abnormal grain growth.

Table 1 summarizes the elastic and mechanical properties by measurement of elastic wave velocity with dynamic resonance method and by indentation microfracture method, respectively, in binder-less cBN-sintered bodies obtained by solid-state sintering of cBN particles with various sintering conditions (D'Evelyn & Taniguchi, 1999). Since the initial grain size and sintering temperature affected the resultant properties of sintered bodies, there are optimum conditions in each initial grain size. As shown in **Figure 22**, the superior properties were achieved near 2200 °C in the 2–4 μm grain size, as similar trend was shown in **Figure 21**. The

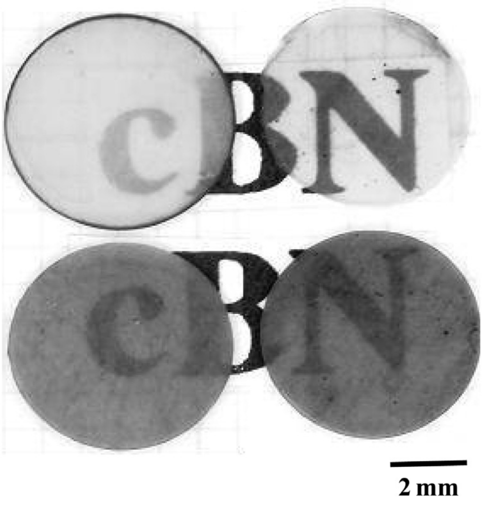

Figure 20 Optical photograph of binder-less cBN-sintered body by sintering cBN powders at 7.7 GPa and 2000 °C region.

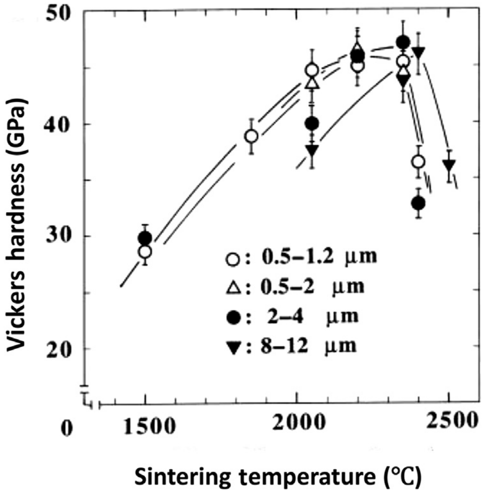

Figure 21 Vickers hardness versus sintering temperatures of binder-less cBN-sintered bodies obtained at 7.7 GPa by using cBN particles with different grain size as starting materials. Indentation load of hardness test: 39 N.

Table 1 Mechanical properties of cBN-sintered body

Grain size (μm)	T *(°C)*	E *(GPa)*	G *(GPa)*	γ	B *(GPa)*	H_V *(GPa)*	K_{IC} *MPa m*$^{1/2}$
2–4	2100	766	337	0.14	352	44	6.3
2–4	2200	894	402	0.11	382	47	6.8
2–4	2300	849	380	0.12	370	42	6.7
8–12	2100	665	297	0.12	290	38	6.2
8–12	2200	790	345	0.14	371	41	6.6
8–12	2350	853	380	0.12	376	44	6.7
BNZ8100[a] (60% cBN)		648	275	0.18	333	30	7.8
BNZ7000 (80% cBN)		709	309	0.15	335	34	7.7
BNZ6000 (90% cBN)		737	318	0.16	360	37	10.8

[a] *GE Borazon compact.*

E, Young modulus; *G*, shear modulus; γ, poisson's ratio; *B*, bulk modulus; H_V, Vicker's hardness.

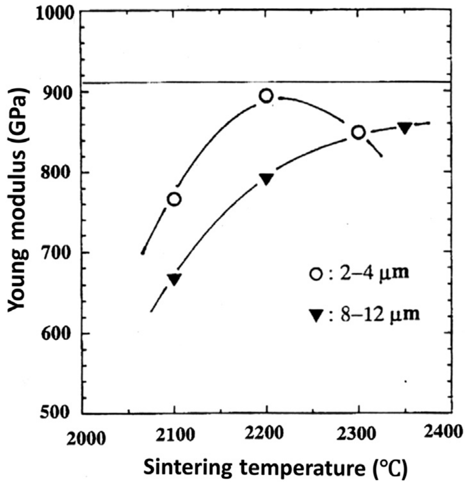

Figure 22 Young modulus versus sintering temperatures of binder-less cBN-sintered bodies obtained at 7.7 GPa by using cBN particles with 2–4 μm and 8–12 μm as starting materials.

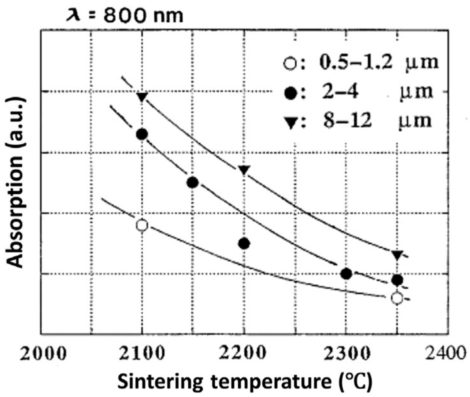

Figure 23 Absorption versus sintering temperatures of binder-less cBN-sintered bodies obtained at 7.7 GPa by using cBN particles with different grain size as starting materials.

fracture toughness K_{IC} of ceramic materials can be evaluated using the so-called *indentation microfracture method*, wherein the lengths of median/radial-type cracks associated with Vickers indentations are measured as a function of applied load (Evans & Charles, 1976). In the formulation which has been most widely applied to superhard materials, the fracture toughness is evaluated from

$$K_{IC} = A(E/H)^{1/2}P/C_0^{3/2} \tag{1}$$

where $A = 0.016 \pm 0.004$ (Antis, Chantikul, Lawn, & Marshall, 1981), H is the hardness, P is the applied load, and C_0 is the crack length. The average of the maximum Young's modulus values measured with cBN-sintered bodies synthesized from 2–4 and 8–12 mm cBN in **Table 1** is 874 GPa. Combining this value with the previously measured values of H and $P/C_0^{3/2}$, a value of $K_{IC} = 6.8$ MPa m$^{1/2}$ for optimally sintered binder-less cBN was obtained from Eqn (1).

The evaluated bulk modulus is consistent with the number characterized by elastic moduli of high-purity cBN single crystals as mentioned in the previous section (Zhang et al., 2011) and is next high value after diamond within the materials in practically used in the industry.

The transmittance of sintered bodies is frequently the focus of attention as an indicator of the degree of progress in sintering. A quantitative evaluation of transmittance in the visible light region was carried out for various types of light-transparent cBN-sintered bodies sintered at 2000 °C or higher. **Figure 23** shows the relationship between the sintering temperature of cBN particles with three different grain sizes and the transmittance (absorption) of the respective sintered bodies at the wavelength of 800 nm. From this figure, it is clear that transmittance increases monotonously as the sintering temperature increases, and at a given sintering temperature, the transmittance of the obtained samples is higher with bodies having a smaller initial grain size.

As can be seen in **Figure 23**, smaller initial grain size shows a correspondence with easier progress of sintering. On the other hand, even under conditions in which abnormal grain growth occurs on the higher temperature, the transmittance of the samples shows a monotonous increase. This indicates that it is difficult to judge deterioration of mechanical properties, such as the hardness and fracture toughness of sintered bodies, which are remarkably affected by abnormal grain growth, etc., simply from the transmittance of samples.

3.23.3 Summary and Future Perspective

Synthesis of high quality with large-scale cBN single crystals is still the subject of study, while the largest size amber-colored crystals was up to 3 mm range so far. The improvement of solvent system with reasonable growth rate and also capability of the impurity control is the key issue to be achieved in this subject.

Low-pressure synthesis of cBN crystals is also important subject in view to search for alternative hard material instead of rare metal of tungsten (W). If one can obtain cBN crystals at pressure lower than 2–3 GPa, huge benefit may be brought in the industry by replacing WC. In this perspective, search for the new solvent system capable to lower the synthesis pressure threshold for cBN nucleation is important. Since the number of efforts searching suitable solvent for cBN seems limited so far in the metallic compound solvent system as mentioned before, further trials are expected to achieve some breakthrough for the cBN crystals growth with high quality.

On the other hand, cBN thin-film growth technology is also important for the future application of cBN's attractive potential for the industry. Although study of cBN-film synthesis was not involved in this chapter, recent achievement of the issue seems promising for its realization near future (Matsumoto & Zhang, 2000; Kimoto & Taniguchi, unpublished).

For the practical application of cBN as superhard materials, continuous approach to obtain its high-grade sintered bodies is also important. Considering sintering nature of ceramic materials with finer particle systems, it is difficult to optimize sintering conditions in order to obtain dense sintered bodies while also suppressing grain growth. However, if the appropriate conditions can be arranged, there is a possibility that synthesis of high-purity cBN-sintered bodies with fine structures can be realized in a low-pressure, low-temperature region. The optimization of the sintering condition including preparation of finer cBN grains as a starting material is the key issue for the future practical realization of the binder-less cBN cutting tool in industry.

Figure 24 is the mapping images of oxygen impurities at the grain boundaries in high-resolution transmission electron microscope observation combined with Electron Energy Loss Spectroscopy (EELS) mapping technique (Kimoto & Taniguchi, 2000) of samples obtained by solid-phase sintering of cBN particles in the 5 GPa region and those obtained by reaction sintering in the 10 GPa region. Although the grain size of the two samples is substantially identical, the hardness of the latter is approximately 20% higher. As shown in **Figure 24**, clear image of existence of oxygen was seen near grain boundary in the sample with lower hardness. Differences in the properties of these two types of binder-less cBN-sintered bodies seem greatly affected by oxygen impurities near grain boundary. Microstructure and the effect of oxygen segregation near the grain boundaries of binderless cBN sintered bodies have also recently been studied (Chen et. al., 2013a, 2013b). When the initial grain size becomes smaller, the driving force for the sintering increases due to its larger surface area. On the other hand, the cleanliness of such large surface is of cBN individual finer grains used as a raw material for sintering should become serious issue to obtained adequate bonding in the grain boundaries. Normally cBN grains are cleaned up by acid treatment after high-pressure synthesis. In this process, the surfaces of the cBN grains are oxidized and this may affect the properties of the sintered body. The establishment of surface cleaning process of the finer cBN grain for eliminating oxide should be the important for the future study.

While nitrogen is known as major impurity in diamond, oxygen and carbon are the major ones in cBN crystals. As compared to diamond, however, the impurity control in cBN crystals has still not been adequately achieved. Although there are some studies on the surface structure of cBN crystals (Loh, Sakaguchi, Nishitani-Gamo,

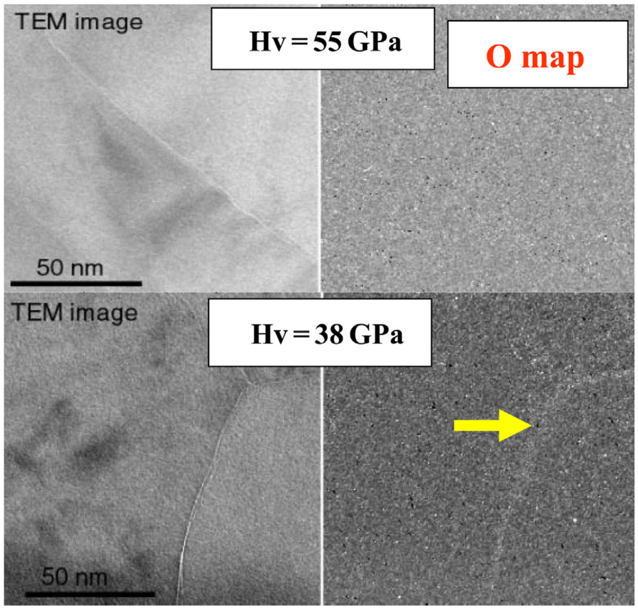

Figure 24 TEM and EELS mapping images of binder-less cBN-sintered bodies. Upper picture: sample obtained by using reaction sintering method at 7.7 GPa. Lower pictures: sample obtained by using solid-state sintering method for cBN fine grains at 5.5 GPa. Left picture: TEM image. Right picture: oxygen EELS mapping image at the same area of the left pictures.

Tanigcuhi, & Ando, 1997, 1998a), further understanding such as surface-state modification technique of cBN may provide better way not only to control its sintering behavior but also to realize the new functional properties of cBN as a wide bandgap material.

Cubic BN is so far practically utilized in superhard materials field in industry. However, cBN has other attractive potentials as a wideband gap material. Learning from the diamond technology, which has been well developed through numbers of pioneer's efforts, further continuous efforts on cBN's single crystal growth technology is primarily important for the fundamental understanding of its properties as well as for realization of new functions.

References

Akaishi, A., Satoh, T., Ishii, M., Taniguchi, T., & Yamaoka, S. (1993). Synthesis of translucent sintered cubic boron nitride. *Journal of Materials Science, 12*, 1883.

Antis, G. R., Chantikul, P., Lawn, B. R., & Marshall, D. B. (1981). A critical evaluation of indentation techniques for measuring fracture toughness: I, direct crack measurements. *Journal of American Ceramic Society, 64*, 533.

Chunlin Chen, Lv, S., Wang, Z., Saito, M., Shibata, N., Taniguchi, T., & Ikuhara, Y. (2013a). Oxygen segregation at coherent grain boundaries of cubic boron nitride. *Applied Physics Letters, 102*, 091607.

ChunLin Chen, Huang, R., Wang, Z., Shibata, N., Taniguchi, T., & Ikuhara, Y. (2013b). Microstructures and grain boundaries of cubic boron nitrides. *Diamond and Related Materials, 32*, 27–31.

Corrigan, F. R., & Bundy, F. P. (1975). Direct transitions among the allotropic forms of boron nitride at high pressure and temperatures. *Journal of Chemical Physics, 63*, 3812.

D'Evelyn, M. P., & Taniguchi, T. (1999). Elastic properties of translucent polycrystalline cubic boron nitride as characterized by the dynamic resonance method. *Diamond and Related Materials, 8*, 1522.

DeVries, R. C., & Fleisher, J. F. E. (1972). Phase equilibria pertinent to the growth of cubic boron nitride. *Journal of Crystal Growth, 13–14*, 88–92.

DeVries, R. C., & Fleisher, J. F. E. (1975). US Patent 3,918,931, Nov. 11.

DeVries, R. C. (1972). GE Technical Report, 72CRD178, General Electric Co., USA.

Dubrovinskaia, N., Solozhenko, V. L., Miyajima, N., Dmitriev, V., Kurakevych, O. O., & Dubrovinsky, L. (2007). Superhard nanocomposite of dense polymorphs of boron nitride: noncarbonmaterial has reached diamond hardness. *Applied Physics Letters, 90*, 101912.

Eko, A., Fukunaga, O., & Ohtake, N. (2013). Synthesis and grain size control of cubic BN using Co -Cr -Al base alloy solvents under high pressure. *Diamond and Related Materials, 40*, 1–6.

Evans, A. G., & Charles, E. A. (1976). Fracture toughness determinations by indentation. *Journal of American Ceramic Society, 59*, 371.

Fujisaki, K., et al. (2009). Development of ultra-fine-grain binderless cBN tool for precision cutting of ferrous materials. *Journal of Materials Processing Technology, 209*, 5646.

Fukunaga, O., Nakano, S., & Taniguchi, T. (2004). Nucleation and growth of cubic boron nitride using a Ca-B-N solvent. *Diamond and Related Materials, 13*, 1709–1713.

Fukunaga, O., Takeuchi, S., & Taniguchi, T. (2011). High-pressure synthesis of cubic BN using Fe-Mo-Al and Co-Mo-Al alloy solvents. *Diamond and Related Materials, 20*, 752–755.

Fukunaga, O. (2000). The equilibrium phase boundary between hexagonal and cubic boron nitride. *Diamond and Related Materials, 9*, 7–12.

Grimm, U., & Taniguchi, T., 2008.

Kagamida, M., Kanda, H., Akaishi, M., Nukui, A., Osawa, T., & Yamaoka, S. (1989). Crystal growth of cubic boron nitride using Li_3BN_2 solvent under high temperature and pressure. *Journal of Crystal Growth, 94*, 261–269.

Kimoto, K., & Taniguchi, T., unpublished work.

Kowanda, K., & Speidel, M. O. (2003). Solubility of nitrogen in liquid nickel and binary Ni-X_i alloys (X_i=Cr, Mo, W, Mn, Fe, Co) under elevated temperature. *Scripta Materiallia, 48*, 1073–1078.

Kubota, Y., Kosuda, K., & Taniguchi, T. (2007). Effect of Al on the formation of cubic boron nitride using Ni_3Al solvent under high pressure. *Japanese Journal of Applied Physics, 46*, 7388.

Kubota, Y., & Taniguchi, T. (2008). Synthesis of cubic boron nitride using Ni-Mo alloy as a solvent. *Japanese Journal of Applied Physics, 47*, 8375.

Kubota, Y., & Taniguchi, T. (2009). Synthesis of cubic boron nitride crystals using Ni-Cr and Ni-Cr-Al solvents under high pressure. *Japanese Journal of Applied Physics, 48*, 71004.

Kubota, Y., Watanabe, K., & Taniguchi, T. (2007). Synthesis of cubic and hexagonal boron nitrides by using Ni solvent under high pressure. *Japanese Journal of Applied Physics, 46*, 311.

Loh, K. P., Sakaguchi, I., Nishitani-Gamo, M., Tanigcuhi, T., & Ando, T. (1997). Surface structure of single crystal cubic boron nitride(111) studied by LEED, EELS and AES. *Physical Review B, 56*, 12791.

Loh, K. P., Sakaguchi, I., Nishitani-Gamo, M., Tanigcuhi, T., & Ando, T. (1998a). Hydrogen-induced surface structuring of cubic boron nitride (100) face studied by low-energy electron diffraction and electron spectroscopic techniques. *Physical Review B, 57*, 7266–7274.

Loh, K. P., Sakaguchi, I., Nishitani-Gamo, M., Tanigcuhi, T., & Ando, T. (1998b). Thermal stability of the negative electron affinity condition on cubic boron nitride. *Applied Physics Letters, 72*, 3023.

Matstumoto, S., & Zhang, W. (2000). High-rate deposition of high-quality, thick cubic boron nitride films by bias-assisted DC jet plasma chemical vapor deposition. *Japanese Journal of Applied Physics, 39*, L442–L444.

Mishima, O., & Era, K. (2000). In Y. Kumashiro (Ed.), *Electric refractory materials* (pp. 495). New York: Marcel Dekker, Inc.

Mishima, O., Tanaka, J., Yamaoka, S., & Fukunaga, O. (1987). High-temperature cubic boron nitride p-n junction diaode made at high pressure. *Science, 238*, 181–183.

Mishima, O., Yamaoka, S., & Fukunaga, O. (1987). Crystal growth of cubic boron nitride by temperature difference method at ∼55 kbar and ∼1800 °C. *Journal of Applied Physics, 61*, 2822.

Morizane, K. (1977). Antiphase domain structures in GaP and GaAs epitaxial layers grown on Si and Ge. *Journal of Crystal Growth, 38*, 249–254.

Oba, F., Taknaka, I., Watanabe, K., Taniguchi, T., & Togo, A. (2010). Doping of hexagonal boron nitride via intercalation: a theoretical prediction. *Physical Review B, 81*, 075125–075125-6.

Saito, H., Ushio, M., & Nagano, S. (1970). *Japanese Ceramic Society Yogyo Kyokai Shi, 78*, 18 (in Japanese).

Sei, H., Akaishi, M., Kanda, H., & Yamaoka., S. (1991). Epitaxial growth of cubic boron nitride single crystal on diamond seed under high pressure. In R. Messier (Ed.), *Mater. res. proceedings: Vol. 472. New diamond science and technology* (pp. 1057). Pittsburgh.

Solozhenko, V. L., Kurakevych, O. O., & Le Godec, Y. (2012). Creation of nanostructures by extreme conditions: high-pressure synthesis of ultrahard nanocrystalline cubic boron nitride. *Advanced Materials, 24*, 1540–1544.

Sumiya, H., & Sato, S. (1996). High-pressure synthesis of high-purity diamond crystal. *Diamond and Related Materials, 5*, 1359–1365.

Sumiya, H., Uesaka, S., & Satoh, S. (2000). Mechanical properties of high purity polycrystalline cBN synthesized by direct conversion sintering method. *Journal of Materials Science, 35*, 1181–1186.

Sumiya, H., Harano, K., & Ishida, Y. (2014). Mechanical properties of nano-polycrystalline cBN synthesized by direct conversion sintering under HPHT. *Diamond and Related Materials, 41*, 14–19.

Taniguchi, T. (2004). Growth of cubic boron nitride single crystals using a metal solvent under high pressure. *New Diamond and Frontier Carbon Technology, 14*, 289.

Taniguchi, T., Akaishi, M., & Yamaoka, S. (1996). Mechanical properties of polycrystalline cubic boron nitride as characterized by the Vickers indentation method. *Journal of American Ceramic Society, 79*, 547.

Taniguchi, T., Akaishi, M., & Yamaoka, S. (1999). Sintering of cubic boron nitride without additives at 7.7GPa and above 2000 °C. *Journal of Materials Research, 14*, 162.

Taniguchi, T., Akaishi, M., Kanke, Y., & Yamaoka, S. (2004). TiC-diamond composite disk-heater cell assembly to generate temperature of 2000 °C in a large-volume belt-type high-pressure apparatus at 10GPa. *Review of Scientific Instruments, 75*, 1959.

Taniguchi, T., Teraji, T., Koizumi, S., Watanabe, K., & Yamaoka, S. (2002). Appearance of n-type semiconducting properties of cBN single crystals grown under high pressure. *Japanese Journal of Applied Physics, 41*, L109.

Taniguchi, T., Watanabe, K., & Koizumi, S. (2004). Defect characterization of cBN single crystals grown under HP/HT. *Physica Status Solidii (A), 201*, 2573.

Taniguchi, T., Watanabe, K., Koizumi, S., Sekiguchi, T., Sakaguchi, I., & Yamaoka, S. (2003). High pressure synthesis of UV-light emitting cubic boron nitride single crystals. *Diamond and Related Materials, 12*, 1098–1102.

Taniguchi, T., & Yamaoka, S. (2000). Heteroepitaxial growth of cBN single crystals on the (100) surface of diamond seed crystals under high pressure. *New Diamond and Frontier Carbon Technology, 10*, 291.

Taniguchi, T., & Yamaoka, S. (2001). Spontaneous nucleation of cubic boron nitride single crystal by temperature gradient method under high pressure. *Journal of Crystal Growth, 222*, 549–557.

Tian, Y., Xu, B., Yu, D., Ma, Y., Wang, Y., Jiang, Y., Hu, W., Tang, C., Gao, Y., Luo, K., Zhao, Z., Wang, L., Wen, B., He, J., & Liu, Z. (2013). Ultrahard nanotwinned cubic boron nitride. *Nature, 493*, 385–388.

Watanabe, K., Taniguchi, T., & Kanda, K. (2004). Ultraviolet luminescence spectra of boron nitride single crystal grown under high pressure and high temperature. *Physica Status Solidii (A), 201*, 2561–2565.

Wentorf, R. H., Jr. (1957). Cubic form of boron nitride. *Journal of Chemical Physics, 26*, 956.

Wentorf, R. H., Jr. (1962). Preparation of semiconducting cubic boron nitride. *Journal of Chemical Physics, 36*, 1990–1991.

Wentorf, R. H., Jr. (1975). US Patent 3,918,219 Nov. 11.

Wentorf, R. H., Jr., De Vries, C. D., & Bundy, F. P. (1980). Sintered superhard materials. *Science, 208*, 873–880.

Yamaoka, S., Akaishi, M., & Ueda, F. (1991). *New Diamond, 22*, 28 (in Japanese).

Yazu, S., Degawa, J., & Tsuji, K. (1989). *New Diamond, 15*, 20 (in Japanese).

Zhang, J. S., Bass, J. D., Taniguchi, T., & Goncharov, A. F. (2011). Elasticity of cubic boron nitride under ambient conditions. *Journal of Applied Physics, 109*, 063521-1–063521-5.

3.24 Cubic Boron Nitride Films: Properties and Applications

Wenjun Zhang, Y.M. Chong, Bin He, I. Bello, and Shuit-Tong Lee, Center of Super-Diamond and Advanced Films (COSDAF), and Department of Physics and Materials Sciences, City University of Hong Kong, Tat Chee Avenue, Hong Kong SAR, P.R. China

3.24.1 Introduction

Cubic boron nitride (cBN) is an isostructural material of diamond; the strong covalent B–N bonding results in very close atomic packing of cBN phase and its physical and chemical properties are comparable or even superior to those of diamond, as illustrated in **Table 1**. cBN has the second highest atomic density (1.68×10^{23} cm^{-3}), the second highest hardness (70 GPa), and the second highest thermal conductivity (13 W/cm K) next to diamond. However, cBN has higher thermal and chemical stability, and higher oxidation and graphitization resistance as compared with diamond (Mirkarimi, Mecarty, Medlin, et al., 1997; Zhang, Bello, Lifshitz, & Lee, 2003; Zhang, Chong, Bello, & Lee, 2007). cBN resists oxidation in ambient environment up to 1200 °C which is twice higher than that of diamond (Komatsu, Kakudate, & Fujiwara, 1996). The sp^3 to sp^2 BN phase transformation temperature is 1550 °C, whereas diamond transforms to graphite at 1400 °C (Demazeau, 1995; Will, Nover, & von der Gönna, 2000). Unlike diamond, cBN is chemically inert when it contacts with molten ferrous materials (De Vries, 1972). In addition, cBN has the widest bandgap (6.2 ± 0.2 eV) among all group IV and III–V semiconductor materials and can be doped for both p- and n-type conductivity (Mirkarimi, Mecarty, et al., 1997; Zhang, Bello, et al., 2003; Zhang et al., 2007). The excellent properties of cBN make it a very promising candidate for hard coatings, tooling, and electronic and optoelectronic device applications such as deep-ultraviolet (DUV) detectors, light-emitting diodes, and high-power, high-speed transistors for operation at high temperatures in harsh environments. In addition, cBN is transparent to a broad range of electromagnetic radiation from ultraviolet to infrared region. Therefore, cBN is also an excellent material for UV–Vis–IR transparent optical devices such as lens and windows.

The study on the synthesis and characterization of cBN and diamond started almost at the same time in the early 1960s. The first synthesis of cBN was performed by conversion of hexagonal BN (hBN) using a high-pressure high-temperature (HPHT) method (Wentorf, 1957). Since then the HPHT synthesis of cBN has improved considerably and HPHT cBN has been commercialized. To date, commercially available cBN powder with sizes ranging from submicron to millimeters has been synthesized in large quantities by HPHT methods under dynamic and static pressures and high temperatures and with aid of catalysts (Vel, Demazeau, & Etourneau, 1991). Despite considerable effort, the synthesis of larger crystals failed, and therefore industrial products including cutting inserts and other tools are made by cementing of cBN powders employing molding and metal binders. The severe nature of the HPHT methods and the limited size of cBN grains produced prohibit their extensive applications in the electronic devices and motivate the thin-film synthesis of cBN. Thus far, cBN films have been prepared by a variety of ion-bombardment physical vapor deposition (PVD) and plasma-enhanced chemical vapor deposition (PECVD) methods (Mirkarimi, Mecarty, et al., 1997; Zhang, Bello,

http://dx.doi.org/10.1016/B978-0-08-096527-7.00061-1

Table 1 A comparison of properties between diamond and cBN

Properties	*Diamond*	*cBN*
Structure	CubFd3m	CubF43m
Unit cell (Å)	3.567	3.615
Atomic density (cm^{-3})	1.77×10^{23}	1.68×10^{23}
Interatomic distance (Å)	1.54	1.57
Density (g/cm)	3.51	3.48
Hardness (GPa)	100	60–75
Elastic modulus (GPa)	1140	850
Thermal conductivity(W/cm K)	20	13
Oxidation stability (°C)	600	1200
Graphitization (°C)	1400	>1550
Refractive index	2.4	2.1
Bandgap (eV)	5.51	6.2–6.6
Breakdown voltage (V/cm)	10^7	8×10^6
Dielectric constant at 300 K	5.7	5.8 (7.1)

et al., 2003; Zhang et al., 2007). Dependence of phase purity, crystallinity, residual stress, and adhesion of cBN films on deposition conditions has been studied extensively. However, due to the energetic ion bombardment required for the formation of cBN phase, the PVD cBN films show inherent drawbacks of large residual stress, delamination, limited film thickness (<200 nm), and nanocrystalline nature.

Recent progress in the fluorine-assisted CVD growth and interface engineering has made the deposition of cBN at reduced ion energies (<10 eV) (Zhang, Bello, et al., 2003; Zhang et al., 2007) possible. cBN films with thickness over 20 μm and decreased residual stress were achieved. These films showed improved crystallinity, good adhesion to the substrates, and long-term stability, which opened the door for the practical applications of cBN films. In this chapter, we start with the thermodynamics of BN phases, then we briefly review the progress in deposition techniques and property study of cBN films, in particular those emerged with the fluorine-assisted CVD approaches. Finally, several potential applications of cBN films in tooling, hydrophobic hard coatings, electronic devices, solar-blind DUV detectors, and chemical and biological sensing are also discussed.

3.24.2 Thermodynamics of BN Phases

Wentorf et al. proposed the first-phase diagram of BN at pressure higher than 4 GPa several years later after their success in converting hBN to cBN under the HPHT condition (Bundy & Wentrof, 1963). According to the phase diagram, cBN was predicted to be a thermodynamically stable phase at standard temperature and pressure (STP) based on extrapolation of the curve. Corrigan and Bundy, who suggested a cBN/hBN equilibrium line similar to the graphite/diamond line in the carbon system, as shown in **Figure 1**, proposed a revision of the phase diagram.

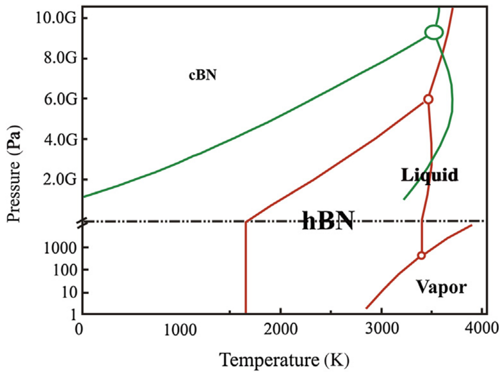

Figure 1 The phase diagrams of BN phases proposed by Bundy and Corrigan in 1975 (green lines) (Corrigan & Bundy, 1975), and the refined version by Solozhenko, Turkevich, and Holzapfel (1999) (red lines).

This phase diagram was well adopted till the calorimetric results of burning cBN and related theoretical calculations were reported by Solozhenko et al. in late 1980s (Leonidov, Timofeev, Solozhenko, & Rodinov, 1987; Solozhenko & Leonidov, 1988). The enthalpy for the formation of hBN and cBN were reported to be −253.9 and −266.1 kJ/mol under STP, respectively; a transformation temperature between hBN and cBN at 1200 °C was observed, below which cBN is stable. Additionally, the equilibrium of hBN–cBN transition under the HPHT conditions with the assistance of different flux solvents, including MgB_2, LiN, AlN, and Mg_3N_2, was investigated (Solozhenko, 1988; Solozhenko, 1992; Solozhenko, 1994; Solozhenko, Slutsky, & Ignatiev, 1992). cBN crystallites were found to spontaneously crystallize at pressures down to 2 GPa in the temperature range of 1200–1600 K. The efficiency of hBN to cBN transformation exceeded 95% at pressures above 2.5 GPa, which indicated that cBN crystals could be formed below the cBN equilibrium in the Corrigan–Bundy (C–B) line. Therefore, the BN phase diagram was further refined, as shown by the red curves in **Figure 1**. According to that, the hBN–cBN equilibrium line intersects the zero pressure at 1600 K, and it shifts to lower temperature with the increase of surface defects and the reduction of crystallite size of hBN (Sachdev, Haubner, Nöth, & Lux, 1997). In addition to the experimental observations, the BN phase diagram has been theoretically investigated. Albe (1997) calculated the cBN–hBN equilibrium line based on density functional theory within the local density approximation (LDA), and the results were comparable to those proposed by Solozhenko et al. A similar BN phase diagram was also suggested by Yu et al. based on the Vienna ab initio simulation package, indicating that cBN is stable at STP (Yu, Lau, Chan, Liu, & Zheng, 2003).

According to the phase diagram, cBN is a thermodynamically stable phase under the STP condition. However, growth of cBN films has been shown to be extremely difficult as compared to the deposition of diamond, which is a metastable phase. A qualitative elucidation for this contradictory observation can be drawn based on Ostwald and Ostwald–Volmer rules (Bohr, Haubner, & Lux, 1995). The Ostwald rule suggests that a system will not reach the stable ground state directly if there are several intermediate energy states. Instead it will pass through all intermediate metastable states stepwise. In contrast, the Ostwald–Volmer rule states that the lower density phase would nucleate first. If there is contradiction between two conditions, Ostwald–Volmer rule has the priority over the Ostwald rule. Based on these two rules, in the case of BN system, the preferential formation of hBN phase in the deposition of BN films at low pressure is understandable because hBN is the metastable phase having a lower atomic density.

In the study of nucleation thermodynamics of cBN in both high- and low-temperature synthesis, the size effect of the surface tension of cBN nanocrystals was investigated by incorporation of the Laplace–Young relation in calculating the Gibbs free energy (Wang, Liu, Yang, 2004; Wang & Yang, 2005; Wang, Yang, Liu, Yang, 2004). It was suggested that the formation of nanoscaled nuclei would induce additional pressure to the system due to the ultrahigh surface-to-volume ratio, which should be taken into account in the calculation. The nucleation of cBN via HPHT supercritical fluid system was limited in nanometers with gas-like properties. In this case, the phase diagram no longer followed that proposed by Solozhenko but matched well with the C–B line. By considering the thermodynamic of nucleation, the calculated threshold pressure decreased with the decrease of the size of critical cBN nuclei. A threshold pressure of 2.3–3 GPa was obtained for the nucleus radius of 2.8 nm, which is in excellent agreement with the experimental data (Solozhenko et al., 1992). On the other hand, for the nucleation of cBN films by CVD or PVD, the additional pressure was also induced and accumulated by the energetic ion bombardment; nucleation of cBN occurred above the C–B line. According to the calculation, the aBN/tBN interlayers were formed to minimize the interfacial energy difference between cBN and substrate, which could be minimized or eliminated by proper selection of substrate with the surface energy closed to cBN. The above works suggest that the phase diagram predicted by Corrigan and Bundy is still valid if the additional pressure for the cBN nucleation at nanoscale is considered.

3.24.3 Low-Pressure Depositions of BN Films and Mechanism

3.24.3.1 Physical Vapor Deposition of cBN Films

Studies on the synthesis of cBN films started around 1980 after the observation of ion-bombarded BN in electron diffraction (ED) patterns by Sokolowski (1979). Inagawa, Watanabe, Ohsone, Saitoh, and Itoh (1987) reported the formation of cBN by applying a negative biased potential to the substrate in an activated reactive environment composed of argon, nitrogen, and evaporated boron. The negative substrate bias was found to play an important role in the growth of cBN through energetic ion bombardment. Following that a variety of PVD methods have been developed for the synthesis of cBN films.

Among the deposition methods, magnetron sputtering is the most widely used due to its capability of being scaled up industrially (Mirkarimi, Mecarty, et al., 1997; Zhang, Bello, et al., 2003; Zhang et al., 2007). Various targets including boron carbide (B_4C), hBN, and boron have been utilized. For example, Lüthje, Bewilogua, Daaud, Johansson, and Hultman (1995) deposited cubic phase rich BN thin films by a radio-frequency magnetron sputtering (RFMS) with a B_4C target. Recently, Ulrich et al. demonstrated the addition of a tiny amount of oxygen could relieve the residual stress cBN films using an hBN target in RFMS. A complex layer system consisting of a two-step adhesion-promoting base layer, a compositional-graded nucleation layer obtained by a stepwise decrease of the oxygen content in the $Ar/N_2/O_2$ atmosphere, and a low-stressed cBN:O top layer with controlled oxygen addition was developed to grow thicker films (~ 2 μm) with improved adhesion (Ziebert, Ye, Sell, & Ulrich, 2006). For the boron target which is sufficiently conductive >800 °C, the effect of direct current (DC) and RF sputtering sources on the deposition rate and phase composition of cBN films was studied (Hahn, Friedrich, Pintaske, et al., 1996). It was shown that the ion flux of DC sputtering on the substrate was one-third of that of the RF sputtering at pressure of 0.2 Pa. As a result, a higher substrate bias was required in DC sputtering to synthesize high percentage of cBN ($\sim$80%) as compared to the RF sputtering.

Ion-assisted pulsed laser deposition (IAPLD) is another technique widely used for the preparation of cBN films. For example, Mineta, Kohata, Yasunaga, and Kikuta (1990) prepared cBN/hBN mixed phase films by combining ablating hBN target using a CO_2 laser with assistance of ion flux from a Kaufman source. By ablating pyrolytic hBN target, Friedmann, Mirkarimi, Medlin, et al. grew 85% pure cBN films with a KrF (248 nm) laser together with aids of $\sim$1000 eV argon–nitrogen ion irradiation. Although IAPLD leads to the synthesis of cBN films with high cubic content, the limited deposition area of PLD restricts its potential for industrial applications.

Moreover, ion beam-assisted deposition (IBAD) was also employed for the growth of cBN films. In particular, IBAD offers advantages of precise control of ion fluxes and ion energies that are beneficial to investigate the formation mechanism of cBN. Kester and Messier (1992) studied the formation mechanism of cBN using IBAD, and proposed that at a given temperature (300–400 °C), the momentum transfer into the growing film per deposited atom is the most critical parameter governing the hBN to cBN conversion. Hofsäss, Ronning, Griesmeier, et al. (1995) synthesized cBN films using mass selected ion beam deposition (MSIBD) with controlled B^+ and N^+ kinetic energy. By exclusive deposition of singly charged ions, nanocrystalline cBN (N-cBN) films with 80% phase purity were prepared at ion energies of 500 eV and substrate temperatures of 350 °C without the need of Ar^+ irradiation. Although IBAD and MSIBD methods can precisely control the ion dosage and ion energy, the high equipment cost, low deposition rate, and the limited effective deposition area hampered the industrialization of the techniques.

Hofsäss, Eyhusen, and Ronning (2004) have reviewed the growth conditions of cBN films by various PVD methods, and drawn a window in deposition parameters for cBN formation, as shown in **Figure 2**. It was revealed that an ion bombardment with energy ranging from 60 to 1000 eV is essential for cBN growth by usual PVD methods. The minimum limit of 60 eV here is the threshold for cBN nucleation, which is higher than that required for growth (40 eV). Above 1000 eV, ion bombardment induces strong resputtering and no film can be deposited. Among PVD methods, MSIBD is an exception, which has no resputtering limit and a maximum ion bombardment energy up to 27 keV for cBN growth.

Kester and Messier (1992) suggested that the formation of cBN was associated with the momentum transferred into the films by the bombarding ions per deposited atom, and a sharp P/a (the ratio of the ion flux to the atom flux) threshold of $\sim 200\ (\mathrm{eV\ amu})^{1/2}$ for the cBN formation was reported. Mirkarimi et al. suggested that the threshold for cBN formation scaled best with the total momentum of the bombarding ions. Experimentally, a continuous aBN/tBN top surface layer was normally observed on PVD cBN films, as illustrated in **Figure 3**(Meng, Zhang, Chan, et al, 2006). Based on the observation of surface non-cBN layer and the critical deposition parameters, the formation of cBN involving the physical phase transformation from sp^2- to sp^3-hybridized BN in the subsurface region was realized, and various growth models including stress-induced formation (McKenzie, Mcfall, Sainty, Davis, & Collins, 1993; Mirkarimi, McCarty, Medlin, et al., 1994), selective sputtering (Reinke, Kuhr, & Kulisch, 1994; Reinke, Kuhr, Kulisch, & Kassing, 1995), subplantation (Lifshitz, Kasi, & Rabalais, 1989; Robertson, 1996), and thermal spike (Hofsäss, Feldermann, Merk, Sebastian, & Ronning, 1998; Seitz & Koehler, 1957, p. 30) have been proposed. The above models and their combinations could more or less explain the dependence of cBN formation on deposition parameters. Mirkarimi, Mecarty, et al. (1997) reviewed a brief introduction to the growth models.

Bombardment of energetic species (tens to hundreds of eV) plays an indispensable role for the formation of the cBN phase. The ion bombardment is, however, inevitably accompanied with a significant build-up of

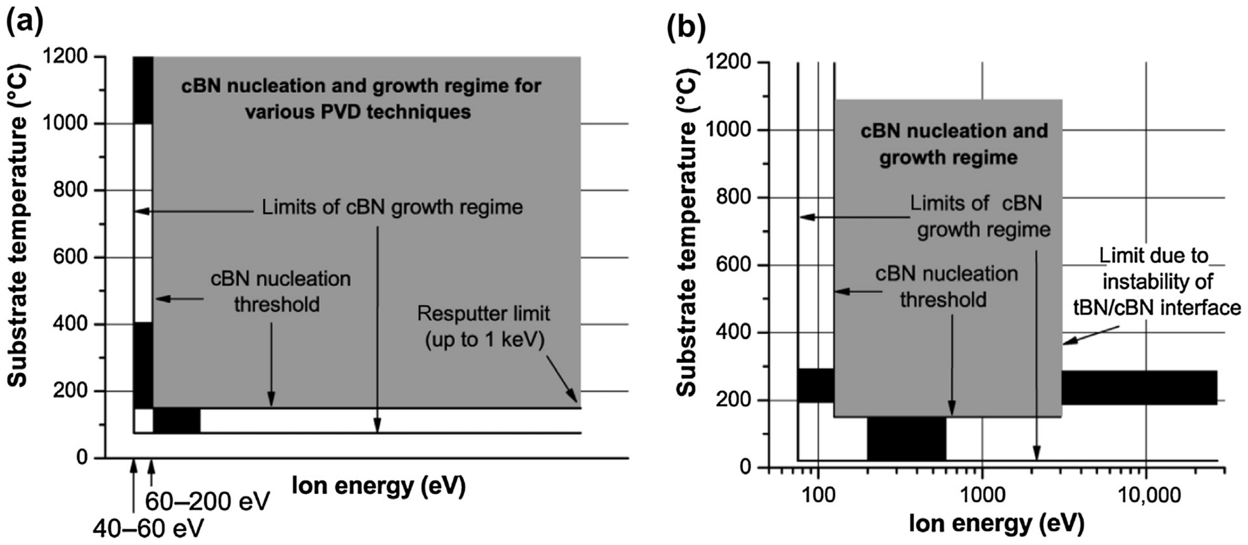

Figure 2 (a) Schematic temperature and energy parameter regime for cBN nucleation and growth for various PVD techniques, with the exception of MSIBD (after Kulisch & Ulrich, 2003). Within the grey area, growth as well as nucleation of cBN on tBN takes place. The black areas indicate the experimentally investigated regions for cBN growth below the nucleation threshold. The upper energy limit of the growth region is determined by resputtering. The nucleation threshold energies vary between approximately 60 and 200 eV depending on the growth method. The growth threshold energies are 20–40 eV lower and vary between approximately 40 and 160 eV depending on the growth method. (b) Temperature and energy parameter regime of cBN nucleation and growth using the MSIBD technique (after Eyhusen, Hofsäss, & Ronning, 2004; Eyhusen, Gerhards, Hofsäss, et al., 2003; Hofsäss, Feldermann, Sebastian, & Ronning, 1997; Hofsäss, Feldermann, Eyhusen, & Ronning, 2002). Within the grey area, growth of cBN as well as nucleation of cBN on tBN is experimentally verified. The black areas indicate the experimentally investigated regions for cBN growth below the nucleation thresholds. The upper energy limit for cBN growth is at least 27 keV. Reprinted with permission from Eyhusen et al. (2004).

compressive stress (5–20 GPa) and creation of crystal defects that lead to the nanocrystalline nature of the films. As a result of the high internal stress, cBN films usually delaminate above a thickness larger than 200 nm. In addition, cBN films generally do not grow directly on most of the substrates but through sequential evolution of amorphous (aBN) and turbostratic (tBN) layers of BN, as discussed below. These incubation layers are weak, reactive, and humid sensitive, which result in poor adhesion of cBN films and further restrict the growth of thick cBN films. A large number of grain boundaries in the cBN films, the presence of foreign phases, high internal stress, poor adhesion, and limited thickness pose a serious obstacle to the further advances in cBN techniques.

To overcome the illustrated problems, several approaches have been undertaken including (1) deposition at reduced ion energy (Amagi, Takahashi, & Yoshida, 1997; Litvinov & Clarke, 1997; Litvinov & Clarke, 1999; Mckenzie, McFall, Smith, et al., 1995; Mirkarimi, Medlin, McCarty, et al., 1997); (2) deposition at elevated substrate temperatures (Litvinov & Clarke, 1999; Mirkarimi, Medlin, et al., 1997); (3) postgrowth thermal treatment (Donner, Dosch, Ulrich, Ehrhardt, & Abernathy, 1998; Fitz, Kolitsch, & Fukarek, 2001; Kim, Kim, Kim, & Lee, 1996; Ulrich, Schwan, Donner, & Ehrhardt, 1996); (4) irradiation with ions of medium energy (Boyen, Widmayer, Schwertberger, Deyneka, & Ziemann, 2000; Fitz, Kolitsch, Möller, & Fukarek, 2002; Ullmann, Baglin, & Kellock, 1998; Widmayer, Ziemann, Ulrich, & Ehrhardt, 1997); and (5) introducing halogen chemistry (Berns & Cappelli, 1996; Berns & Cappelli, 1997; Matsumoto, Nishida, Akashi, & Sugai, 1996). On silicon substrates, cBN films up to 2 μm have been obtained by a single method or a combination of the above methods; nevertheless, films thus deposited are still nanocrystalline with poor adhesion and high defect density. For the practical applications, it is still a challenging task to grow cBN films with reasonable thickness, improved crystallinity, and enhanced adhesion by PVD methods.

3.24.3.2 Chemical Vapor Deposition of cBN Films

In the case of CVD, conventional (thermally driven) processes failed and only PECVD has been employed successfully for growing cBN films. Thus far, various PECVD deposition methods have been employed for the synthesis of cBN films, e.g. DC jet plasma CVD (Saitoh, Morino, & Ichinose, 1993), RF plasma CVD

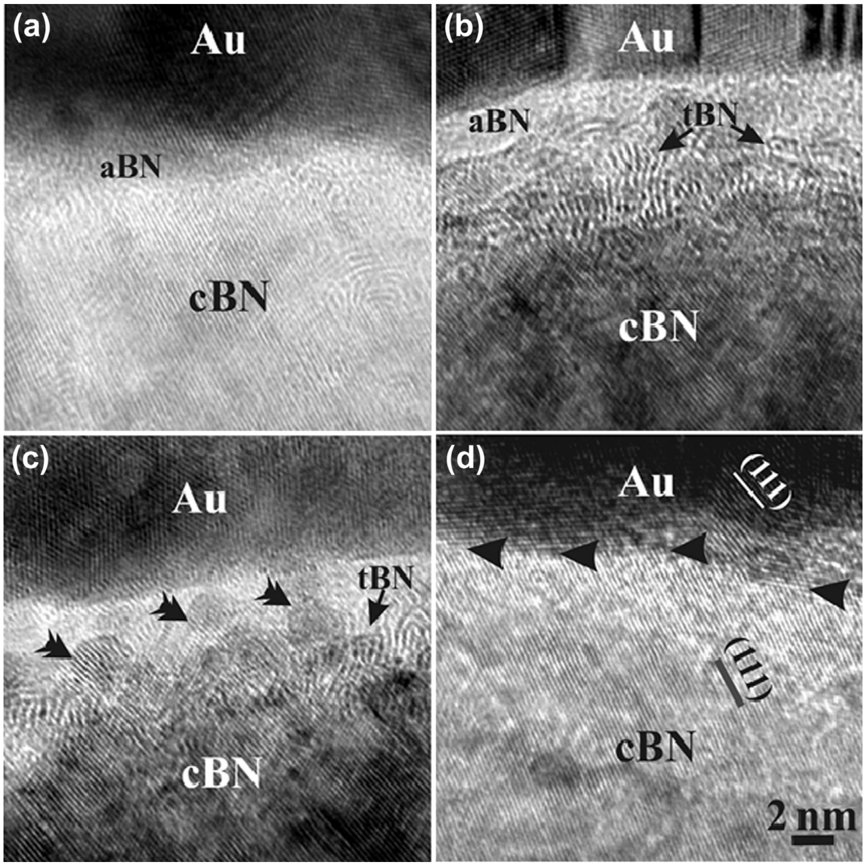

Figure 3 HRTEM images of the surfaces of the cBN films deposited by (a–c) magnetron sputtering, and (d) ECR MPCVD in a gas mixture of $He/Ar/N_2/BF_3/H_2$. A gold film precoated on the surface of BN films served to protect the BN surface against ion damages during sample preparation, and to separate and distinguish the film surface structure from the TEM glue. Reprinted with permission from Meng et al. (2006).

(Dworschak, Jung, & Ehrhardt, 1994; Karim, Cameron, Murhy, & Hashmi, 1991), inductively coupled PECVD (Freudenstein, Reinke, & Kulisch, 1997; Ichiki & Yoshida, 1994; Kuhr, Reinke, & Kulisch, 1995b), and electron cyclotron resonance microwave plasma CVD (ECR MPCVD) (Okamoto, Yokoyama, & Osaka, 1990; Weber, Bringmann, Nikulski, & Klages, 1993). Different gases, including N_2, NH_3, B_2H_6, BH_3NH_3, H_2, and trimethyl borazol, were used as reactants, and substrate temperature ranged from hundreds to over a thousand degrees.

It has been demonstrated that in the preparation of diamond films by CVD, atomic hydrogen plays an essential role, i.e. removing sp^2 carbon preferentially and stabilizing sp^3 carbon. Owing to the similarity in structure and properties between BN and diamond, it is logical to expect that cBN could be realized based on hydrogen chemistry. Indeed, high-resolution Auger electron spectroscopic observations of the tBN and aBN surfaces revealed that Auger features specific for sp^2 BN became much weaker or even disappeared after hydrogen plasma treatment (Konyashin, Khvostov, Babaev, et al., 1999). However, it was also observed that there was no significant difference in etching rates between cBN and hBN in hydrogen plasma (Bartl, Bohr, Haubner, & Lux, 1996; Kim & Kim, 2000), and the incorporation of hydrogen into the CVD process of cBN films was found to cause a delay in the nucleation of cBN phase (Konyashin et al., 1999; Kim & Kim, 2000; Dworschak, Jung, & Ehrhardt, 1995). Moreover, addition of a small amount of H_2 ($<2\%$ in the total gas flow rate) into the gas phase resulted in a decrease of cBN content in the films deposited by PVD, and hydrogen was found incorporated within the sp^2 regions (Freudenstein et al., 1997; Dworschak et al., 1995; Kuhr, Freudenstein, Reinke, et al., 1996). Therefore, ion bombardment of the substrate is still required for the formation of the cubic phase. For example, by using inductively coupled plasma CVD (ICPCVD), Chattopadhyay, Matsumoto, Zhang, et al. (1999) reported formation of cBN films using diborane and nitrogen as precursors with a substrate bias of -170 V and Yang and Yoshida (2005) synthesized cBN films in $Ar–N_2–He–B_2H_6$ gas mixture at a substrate bias of −150 V. cBN synthesis by these CVD methods can be considered still involving physical effects (as in PVD methods) instead of chemical effects of the plasma reactive species, and cBN films deposited by such CVD methods show similar features as summarized for PVD films. In such a case it is difficult to differentiate between the PVD and PECVD methods.

In contrast to the hydrogen-based plasmas, BN films with a cubic phase content of higher than 90% were deposited by employing a low-pressure plasma jet in an Ar–N_2–BCl_3 system (Berns & Cappelli, 1996; Berns & Cappelli, 1997). Using BCl_3 as the boron source, the substrate bias voltage necessary for cBN deposition was reduced to −75 V, and correspondingly, the mean ion energies involved in ion bombardment was reduced to about 20 eV. cBN films of 0.5 μm thick were grown; however, the films were nanocrystalline with a compressive stress of ~7.5 GPa, leading to stress-relief cracking and film delamination.

Recently, Matsumoto and Zhang (2000) and Zhang and Matsumoto (2000b) reported the deposition of 20 μm-thick cBN by DC plasma jet method employing BF_3 as the boron source in gas mixture of Ar–N_2–H_2. The threshold substrate bias voltage for growing cBN was reduced to about −80 V. Considering the higher deposition pressure, the ion energies was ~10 eV. The low threshold ion energy enables the synthesis of thick cBN films with reduced stress, and significantly improved crystallinity, adhesion, and coating stability. **Figure 4(a) and (b)** shows the cross-sectional SEM morphologies of cBN films deposited for 10 and 60 min, respectively. A 10 μm-thick cBN film was achieved after growth for 60 min.

Figure 4(c) shows the Raman spectra of two cBN films deposited by fluorine-assisted CVD for 10 and 60 min, respectively (Zhang & Matsumoto, 2001a). The Raman spectra of HPHT cBN crystals of size 4–8 μm and 0.4 mm are also given for reference. It is known that Raman signals are very much dependent on the grain size and defect density. In fact, no reliable Raman spectra were reported for the PVD cBN films. Therefore, the appearance of cBN Raman signals could serve as an indication for high-quality films deposited by the fluorine-assisted CVD method. The peak position and full width at half maximum of each spectrum are summarized in **Table 2**. It can be seen that both transverse optical (TO) and longitudinal (LO) cBN modes appear strongly in the spectra. For HPHT crystals, the peak position is downshifted and the peaks become asymmetrically broad as the crystal size decreases. Similarly, a decrease of Raman line width was also observed as the growth time increased, indicating the improvement of crystallinity of cBN films with the deposition time. Based on the modified spatial correlation model (Herchen & Cappelli, 1993; Parayanthal & Pollak, 1984; Yoshikawa, Mori, Maegawa, et al., 1993) and stress-induced peak shift (Sanjurjo, López-Cruz, Vogl, & Cardona, 1983), the Raman spectra HPHT crystallites and films could be well fitted, and it was revealed that the residual stress in cBN films

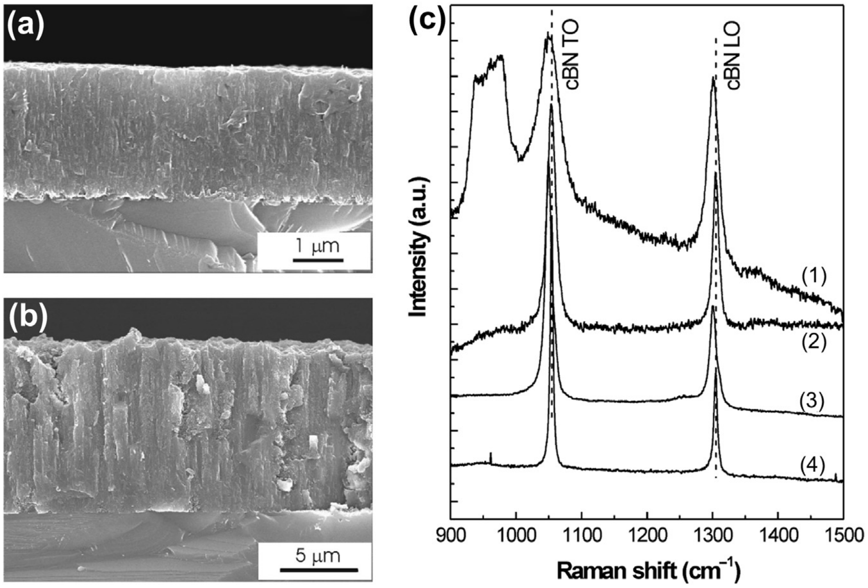

Figure 4 SEM cross-sectional morphologies of the cBN films deposited on silicon substrates by DC jet plasma CVD for (a) 10 and 60 min (b). (c) Raman spectra of a cBN film deposited (1) for 10 min (3 μm thick), and (2) for 60 min (12 μm thick) by DC jet plasma CVD, (3) 4–8 μm and (4) 0.4 mm commercially available HPHT cBN crystallites. Reprinted with permission from Zhang and Matsumoto (2001a).

Table 2 Peak position and FWHM of TO and LO Raman modes of the spectra shown in **Figure 4**

Sample	*Mode*	*Peak position (cm^{-1})*	*FWHM (cm^{-1})*
CVD 10 min	TO	1048.4	28.8
	LO	1301.8	19.7
CVD 60 min	TO	1053.6	14.8
	LO	1304.8	10.4
HPHT 4–8 μm	TO	1049.6	12.5
	LO	1301.3	11.1
HPHT 0.4 mm	TO	1054.8	5.1
	LO	1304.8	7.2

decreased from −1.5 to −1 GPa in the film as the deposition time was prolonged from 10 to 60 min (Zhang & Matsumoto, 2001a). The result agrees well by analyzing the corresponding X-ray diffraction pattern of the film (Zhang & Matsumoto, 2001a, 2001b). Significantly, faceted cBN films were obtained for the first time by using a two-step approach (i.e. reducing substrate bias voltage and increasing substrate temperature when switched from the nucleation to the growth process), as illustrated in **Figure 5** (Zhang, Jiang, et al., 2001; Zhang, Matsumoto, Li, Bello, & Lee, 2002). These cBN films were textured with their [001] orientation perpendicular to the film surface as revealed by pole-figure X-ray diffraction. The scattering width (polar misorientation) of grain orientation was 16.3° (Jiang, Helming, Zhang, & Matsumoto, 2002).

By using ECR MPCVD, Zhang, Chan, Chan, et al. (2003) synthesized several micrometers-thick cBN films with high crystallinity and phase purity in a He–Ar–N_2–BF_3–H_2 gas mixture with substrate bias of −40 V. As compared with DC plasma jet CVD, ECR MPCVD has a low growth rate (0.2–0.5 μm/h versus ~10 μm/h). However, it has the advantages of being able to grow cBN films over a larger area and be free from the contamination from electrode materials. It is noteworthy that hydrogen is still needed in the depositions of cBN films by carrying out fluorine-assisted CVD growth. However, hydrogen plays a completely different role

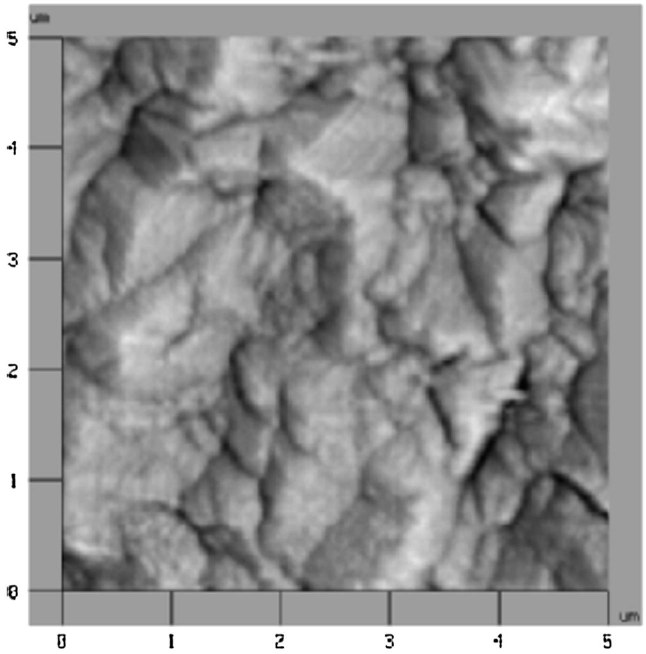

Figure 5 Atomic Force Microscope (AFM) surface morphology of cBN film deposited by a two-step process and by performing the fluorine chemistry in DC jet plasma CVD. Clear crystal facets can be distinguished in the film surface. The observation of crystal facets also demonstrates an improvement of the crystallinity of the film as the grain boundaries of the nanostructure in the surface decrease. Reprinted with permission from Zhang, Jiang, and Matsumoto (2001).

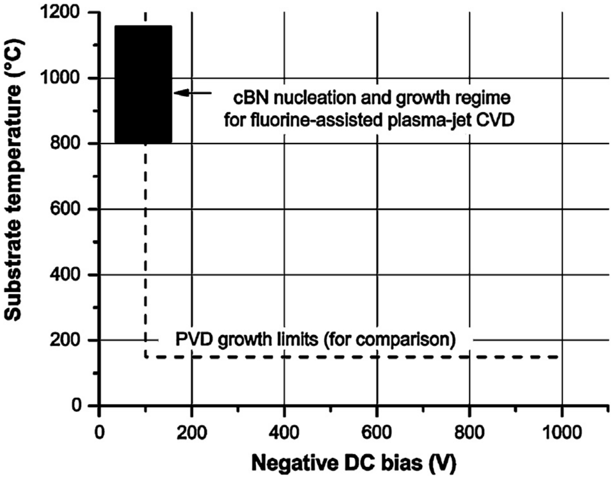

Figure 6 Temperature and substrate bias parameter regime for cBN growth by plasma-jet CVD using an Ar–N_2–BF_3–H_2 gas mixture (after Chan, Zhang, Matsumoto, Bello, & Lee, 2003; Jiang, Philip, Zhang, Hessm, & Matsumoto, 2003; Matsumoto & Zhang, 2000; Matsumoto & Zhang, 2001a, 2001b, 2001c; Yu & Matsumoto, 2003; Zhang & Matsumoto, 2000b, 2000c; Zhang & Matsumoto, 2001a; Zhang, Jiang, et al., 2001; Zhang, Kanda, Matsumoto, 2002; Zhang, Matsumoto, et al., 2002; Zhang, Matsumoto, Kurashima, & Bando, 2001; Zhang, Tansho, Matsumoto, & Mori, 2001). The black area marks the narrow experimentally verified cBN nucleation and growth window. The dashed line indicates the threshold values for PVD techniques for comparison (assuming for simplicity ion energy = *ex* bias voltage). Reprinted with permission from Hofsäss et al. (2004).

from that in the CVD growth of diamond films. Here the addition of H_2 leads to the formation of BN composite which can be described by the following reaction (Kalss, Haubner, & Lux, 1998): $2BF_3 + N_2 + 3H_2 \rightarrow 2BN + 6HF$. The fluorine ions act as the etching agent to remove sp^2 BN and the hydrogen balanced the etching ability of fluorine by forming a stable product of HF. By controlling the ratio between BF_3/H_2, BN thin films with different sp^3/sp^2 ratio can be achieved (Zhang & Matsumoto, 2000c). It has also been shown that a high plasma density would benefit the growth of cBN films at a reduced substrate bias. Therefore, deposition of cBN films in fluorine-assisted MPCVD process required a high bias voltage of about −400 V as compared with DC jet and ECR MPCVD.

The nucleation and growth regime of cBN films by fluorine-assisted CVD exceeding the cBN PVD growth limit (**Figure 6**) suggests a new growth mechanism of cBN films. Moreover, as depicted in the cross-sectional high-resolution transmission electron microscopy (HRTEM) image in **Figure 3(d)** (Meng et al., 2006), the cBN films deposited by ECR MPCVD in a gas mixture of He(Ar)/N_2/BF_3/H_2 show a clear interface between the cBN surface and the gold layer without an sp^2 BN amorphous cover layer. Based on experimental observations and thermodynamic/quantum mechanical calculations (Barreto, Vilela, & Gargano, 2005; Larsson & Carlsson, 1999; Märlid, Larsson, & Carlsson, 1999), the growth of cBN film via a surface chemical approach was suggested in the fluorine-assisted CVD processes (Zhang, Chan, Meng, et al., 2005). In this case, excited reactive gas species including H, F, BF_x, and NH_x are generated. Among them, BF_x and NH_x are the precursors leading to cBN growth; F atoms are responsible for selective etching of hBN (Zhang & Matsumoto, 2000c). The hydrogen flow rate controls the solid BN production rate from the gas phase, and the ratio of hydrogen to fluorine controls the equilibrium between film formation and etching. During the growth, the cBN crystal surface is activated by surface abstraction due to impingement of plasma species providing free unsaturated sites for further growth. B is added to N activated sites by incorporation of BF_x species, while N is added to B activated sites by incorporation of NH_x species. The N–H bonds of N–H terminated surface sites were found energetically effective in abstraction and adsorption of incoming B-containing species (Larsson & Carlsson, 1999; Märlid et al., 1999). The H atoms terminating an N surface atom will be abstracted by plasma fluorine atoms forming HF and leaving room for BF_x adsorption. However, the chemical bond strength of B–F is large, making it resistant to abstraction and adsorption of NH_x. The breaking of B–F bonds and formation of a dangling bond needed for NH_x adsorption and further cBN growth is most likely facilitated by the low kinetic energy ion bombardment (<20 eV) which is still needed for cBN growth from fluorine chemistry. It must be clarified that the role of ion bombardment here is completely different from that as a driving force for the subsurface physical transformation from sp^2 to sp^3-configurated BN phase in PVD processes of cBN films.

Substrate temperature was a predominant parameter which affects the nucleation and growth of cBN films grown by PVD and CVD methods, and consequently their phase composition and structure. A very large span of deposition temperatures was particularly observed at cBN growth using PVD techniques. This contrasts the narrow growth window of kinetic energies or bias voltages. At cBN growth and constant kinetic energy of particles, a threshold value of substrate temperature was nevertheless observed. For example, Mirkarimi, Medlin, and McCarty (1995) resolved the deposition into nucleation and growth steps and found that the threshold temperature for cBN nucleation was ∼130 °C, and cBN did not emerged below 100 °C using IAPLD. Kester, Ailey, Lichtenwalner, and Davis (1994) reported increasing the substrate temperature in nucleation stage led to thicker aBN/tBN incubation layers at their experimental conditions. MSIBD at room temperature after nucleation at 200 °C yielded BN films with 89% cubic phase (McCarty & Barbour, 1999). IBAD of BN in the range of 200–700 °C showed optimal cBN deposition temperature to be 400 °C, whereas cBN was not detected above 700 °C (Kester et al., 1994). Friedmann et al. denoted the optimum temperature range for growing cBN between 150 and 500 °C at using their IAPLD technique. Reducing the cBN content at temperature above 500 °C was assigned to the thicker aBN/tBN interfacial layers.

Both PVD and PECVD techniques also enable the growth of cBN in a wide range of temperatures that, however, shift toward higher temperature values. For instance, Kuhr, Reinke, & Kulisch (1995a) prepared BN at 500 °C by ICPCVD. The BN films contained 75% cBN. cBN films were deposited at temperature ranging from 840 to 1080 °C by fluorine-assisted DC jet plasma CVD and the highest cBN content was obtained at 960 °C (Zhang & Matsumoto, 2000a). It has been observed that high temperatures resulted in low stress and thick cBN films (Zhang & Matsumoto, 2000b; Zhang & Matsumoto, 2001b). The high temperature (>900 °C) is undeniably the vital parameter for growing cBN films in epitaxial relationships with diamond substrates employing both PECVD (Zhang, Bello, Lifshitz, et al., 2004a) and PVD (Zhang, Boyen, Deyneka, et al., 2003) methods. A systematic study on the effects of substrate temperature (within a range of 200–1100 °C) in the deposition of cBN films on polycrystalline diamond (polyD) surfaces by fluorine-assisted ECR MPCVD and RFMS deposition also revealed that the cBN growth can thus be conducted at lower temperatures by PVD than in the case of the presented PECVD. However, cBN films with high crystalline quality and better adherence to the substrate were deposited only at the highest temperature (900–1000 °C). cBN films quality deteriorated at temperatures lower than 700 and 800 °C for the RFMS and ECR MPCVD method, respectively (Chong, Leung, Ma, et al., 2006).

3.24.4 Phase Composition and Structures of cBN Films

cBN films deposited via subsurface physical phase transformation and surface chemical approach as discussed above show distinct characteristics, which are demonstrated to be associated with the growth parameters such as ion bombardment energy and growth temperature and as well the substrate materials. **Figure 7(a)** shows a low-magnification cross-sectional TEM image of the cBN film deposited on silicon substrate by fluorine-assisted DC jet plasma CVD (Zhang, Matsumoto, et al., 2001). An interface was observed between the cBN film and the silicon substrate. Close observation by HRTEM revealed a sequential layered structure of Si, aBN, tBN, and cBN. tBN has its basal planes perpendicular to the substrate, and cBN nucleates on the edge of tBN planes with 3:2 lattice matching between cBN (111) and tBN (0002). Upon the tBN layer, the columnar growth of cBN is clearly observed. The columns nucleate on the top of the tBN layer and elongate across the film thickness toward the film surface. Meanwhile, the columns also extend in lateral size from bottom to top. The ED pattern shown in the inset in **Figure 7(a)** verifies the single crystal nature of the columns. The electron energy loss spectroscopy (EELS) spectra in **Figure 7(b)** further verified the layered structure of cBN films grown on silicon substrates.

Similarly a non-cBN interface was also observed for the cBN deposition on silicon substrates by PVD. **Figure 8** shows the cross-sectional structure of cBN film deposited by magnetron sputtering on silicon substrates via a B_4C interlayer (Yamamoto, Keunecke, Bewilogua, Czigany, & Hultman, 2001). The film is about 200 nm thick, and the points for the analysis of selective area electron diffraction are indicated in the dark field image. From point A, a diffused pattern with very weak spot from textured hBN (0002) was observed which indicated this area was amorphous in nature with tiny amount of hBN. Polycrystalline hBN (0002) plane, cBN (111), and cBN (220) were found at point B (gradient layer) that could be due to the mixed phase of BN in this region or the interference from the top cBN layer. The diffraction pattern of point C showed single phased and polycrystalline cBN. It should be noted that, like the cBN films deposited by fluorine-assisted CVD (**Figure 8**), this sample also present aBN/tBN/cBN layered structure and columnar growth behavior. However, in contrast to the single crystal nature of the columns in CVD cBN films, the columns here are composed on nanometer-sized

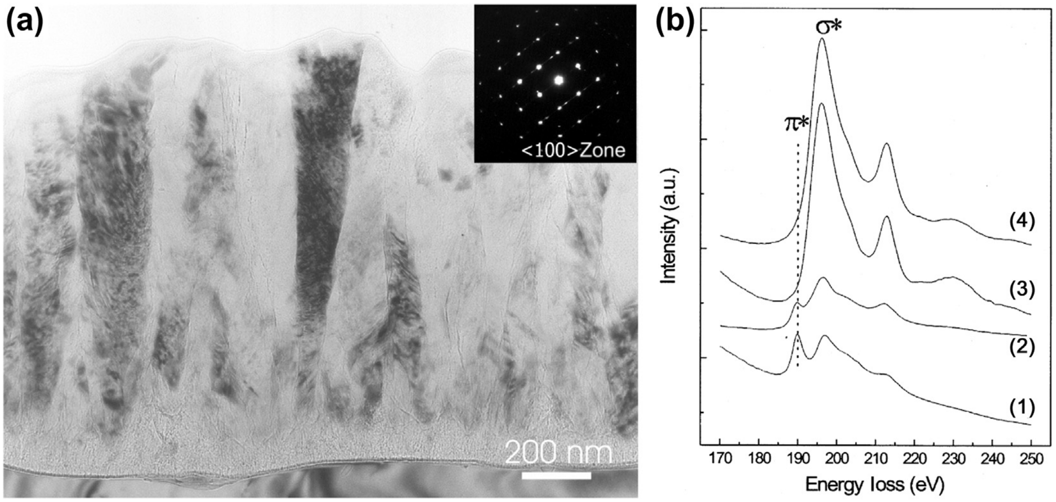

Figure 7 (a) Low-magnification cross-sectional TEM image of cBN film deposited on silicon substrate by using DC jet plasma CVD. An interface of amorphous/tetrahedral BN was observed between the cBN film and silicon substrate. The average thickness of the interface was about 100 nm. Upon the tBN layer, a columnar growth of cBN was clearly shown. The inset is the electron diffraction pattern obtained from one column. (b) EELS spectra near the B K-edge measured in image mode from the interface to the surface of the film. At the interface layer (spectrum 1), intensive π^* and σ^* peaks were observed, and the strong π^* peak indicated the sp^2-bonding of the BN in the interface. At the nucleation site of the columns (spectrum 2), the intensity of the π^* peak decreased, representing a decrease in the sp^2-bonded content in this region. In the spectra obtained from the middle and top of the cBN column (spectra 3 and 4), the π^* peak completely disappeared and only strong σ^* peaks were observed; therefore, pure cubic phase was identified in the columns. Reprinted with permission from Zhang, Matsumoto, et al. (2001).

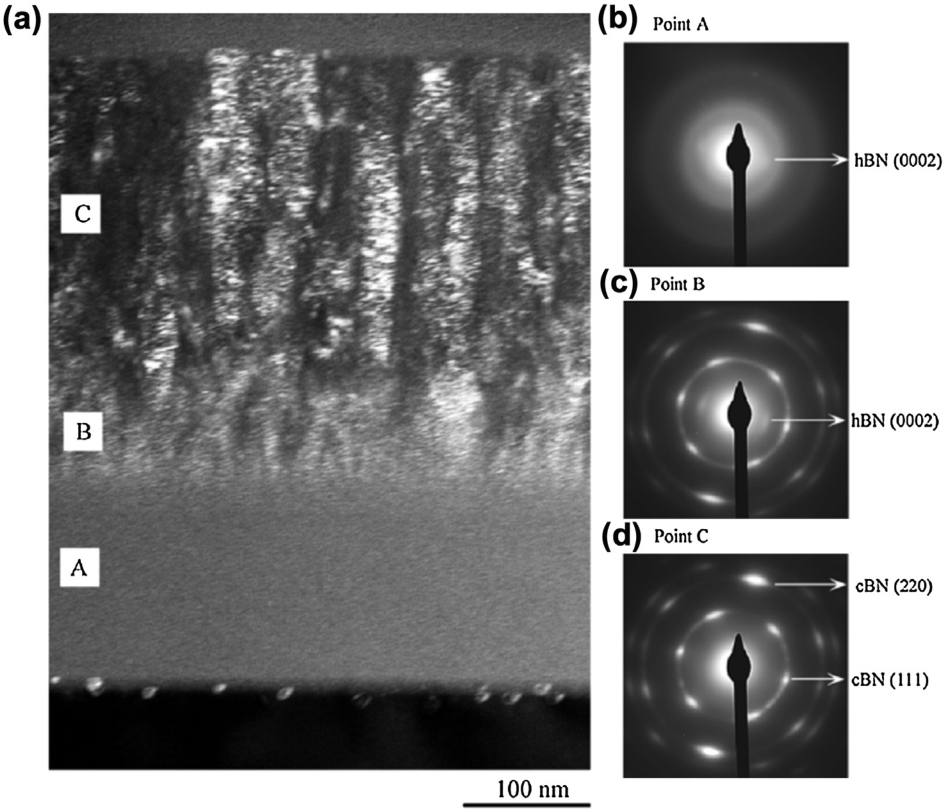

Figure 8 (a) Dark field image of the B–C–N gradient layer with a thin cBN layer which was taken from the cBN (111) reflection. Indexes A, B, and C show the points of the SAED patterns: SAED patterns of (b) point A, (c) point B, and (d) point C. Reprinted with permission from Yamamoto et al. (2001).

polycrystalline crystallites, which is believed to be due to the enhanced secondary nucleation induced by strong ion bombardment in magnetron sputtering.

The layered structure and the preferable orientation of tBN basal planes in cBN films grown by PVD and CVD methods were also demonstrated with an X-ray absorption study (Zhou, Sham, Chan, et al., 2006a, 2006b; Zhou, Sham, Zhang, et al., 2006, 2007). The formation of aBN/tBN interfacial layer is induced by ion bombardment, and its thickness depends on the deposition conditions, particularly the particle kinetic energy and substrate temperature (Zhou et al., 2006b; Zhou et al., 2006, 2007). The presence of the soft aBN/tBN interlayer makes the epitaxial growth of cBN on silicon substrates not possible. The similarity in B–N bonding configurations and matching the $(111)_{\mathrm{cBN}}$ and $(0002)_{\mathrm{tBN}}$ interplanar spacings with approximately 3:2 lattice registry enable a parallel interplanar alignment of $(111)_{\mathrm{cBN}}//(0002)_{\mathrm{tBN}}$. Very similar interfacial structures are detected at the nucleation of diamond on graphite (Mirkarimi, Mecarty, et al., 1997). In addition, the nucleation of cBN via the formation of rBN phase was also observed (Takamura, Tsuda, Ichinose, & Yoshida, 1999). Strong correlations between rBN{003} and cBN{111}, and between rBN{101} and cBN{111}, similar to those predicted for pressure-induced direct diffusionless conversion of rBN to cBN, were demonstrated. Recently, by optimizing the pretreatment and other deposition parameters, direct contact of cBN nanoparticles (111) on Si (111) was also observed in local area, although tBN was still predominant in the interface (Yang, Iwamoto, & Yoshida, 2007).

Since the aBN/tBN interlayers are soft and humidity-sensitive, numerous investigations have been carried out to eliminate or suppress their formation. The utilization of highly oriented wurtzite aluminum nitride (w-AlN) enabled cBN deposition in direct contact with AlN substrate with no detectable aBN interlayer by using a MSIBD. It was also observed that N-cBN and wurtzite BN (w-BN) nanocrystallites could nucleate directly on AlN or via a tBN transition layer (Feldermann, Ronning, Hofsäss, Huang, & Seibt, 2001). This implies that an interfacial layer like AlN with a well-defined orientation may substitute the in-plane misoriented tBN layer as a preferential nucleation site, which could lead to the epitaxial growth of cBN films. In contrast to AlN, deposition of cBN films on β-SiC substrates using ion-assisted (800 eV) pulsed laser ablation revealed that cBN could be deposited via a very thin amorphous layer of <1 nm, and in some regions, a few cBN crystals even extended to within 1 nm of the SiC interface (Mirkarimi et al., 1995). Moreover, by introducing transition layers of boron carbide/B–C–N gradient layer (Keunecke, Yamamoto, & Bewilogua, 2001; Yamamoto, Keunecke, & Bewilogua, 2000) and tetrahedral carbon (ta-C) (Leung, Chan, Chong, et al., 2005), cBN films with larger thickness and improved adhesion were grown on WC and Si substrates, respectively.

Considering the crystal structure, lattice matching and the surface energy (6 J/m for {111} planes) (Field, 1979), diamond is naturally the most suitable substrate for heteroepitaxial cBN growth. cBN heteroepitaxy on single-crystal and CVD diamond has been achieved by using HPHT method (Lux, Kalss, Haubner, & Taniguchi, 1999; Sei, Akaishi, Kanda, Osawa, & Yamaoka, 1991). However, the early works using IBAD revealed a typical aBN/tBN/cBN layered structure on diamond, which was considered to be due to the product of amorphization and consequential bilateral stresses induced by the relatively high kinetic energy of ions (500–1000 eV) (Kester et al., 1994; Pascallon, Stambouli, Ilias, et al., 1999). Since these energies far exceed the atomic displacement energy, diamond in the top surface regions tends to be amorphized. Moreover, deposition on CVD polycrystalline (faceted and rough) diamond films resulted in a higher fraction of non-cBN, due to the geometrical effects associated with energetic bombardment of a rough surface. Planarization and special polishing of diamond was essential to improve the cBN content of the film with respect to that deposited on silicon. When the ion beam energy is reduced to 280 eV, local epitaxial nucleation of cBN on diamond can be obtained though considerable ion impact results in secondary nucleation and nanocrystalline nature of the deposited cBN films (Zhang, Boyen, et al., 2003). The small size of crystallites and extensive defects induced do not yield cBN Raman peaks.

By employing the fluorine-assisted ECR MPCVD, cBN films were deposited on poly- and nanocrystalline diamond substrates with further reduced ion energy, i.e. a critical bias voltage of -10 V was identified for maintaining the cBN growth (effective substrate bias $= -12$ V including the plasma potential of 2 V), as shown in **Figure 9(a)** (Bello, Chong, Leung, et al., 2005). Controlled experiments on the silicon substrates revealed that no cubic phase was formed for the substrate biases lower than -40 V. Interfacial observation by HRTEM verifies that cBN grows directly and epitaxially on diamond layer with their (111) planes parallel to each other, as shown in **Figure 10** (Zhang, Bello, Lifshitz, et al., 2004b; Zhang et al., 2004a). No aBN and tBN phases were observed at the interface. It is interesting to note that stress is built up in the interfacial region, as indicated by the contrast irregularity in **Figure 10(a)** (Zhang et al., 2004a). The accumulated stress in this epitaxial region is probably induced by the local lattice strain mainly originated from the 1.36% lattice mismatch between cBN

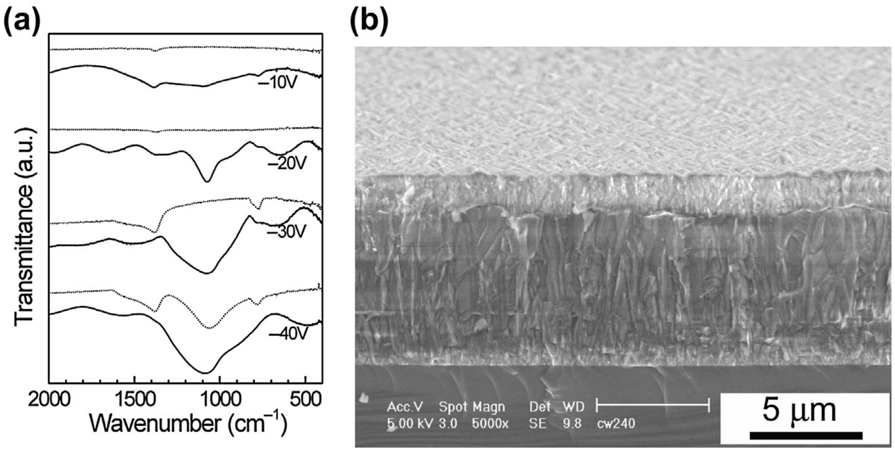

Figure 9 (a) FTIR spectra of cBN films deposited by ECR MPCVD at different substrate bias voltage. The solid lines correspond to the films deposited on polyD substrates, and the dotted lines designate the films grown on Si substrates. Reprinted with permission from Bello et al. (2005). (b) SEM cross-sectional image showing a 2-μm-thick cBN grown on poly-D coated silicon substrate at a low substrate bias of −20 V (Zhang et al., 2004b).

(F43m lattice structure; lattice constant $a_{\mathrm{cBN}} = 3.62$ Å) and diamond (Fd3m lattice structure; $a_{\mathrm{D}} = 3.57$ Å). The stress induced by lattice mismatch can hardly be reduced when epitaxial growth is strictly preserved. In addition to the epitaxial relationship, small-angle grain boundaries and twining crystals between cBN and the underlying diamond were also observed. Because epitaxial diamond films have been successfully deposited on various substrates, epitaxial growth of cBN films on these substrates can also be achieved via a diamond interface layer (Zhang et al., 2004a; Zhang, Meng, Chan, et al., 2005).

Based on the direct and epitaxial growth of cBN on diamond, N-cBN/nanodiamond (ND) multilayer structure, i.e. alternating deposition of N-cBN/ND/N-cBN… with equivalent layer thickness of ∼100 nm were synthesized on the basal ND film-coated silicon substrates. The N-cBN and ND films were prepared by swapping RFMS and microwave plasma CVD, respectively, as shown in **Figure 11(a)** (Li, Leung, Ma, et al., 2007). The multilayers show enhanced mechanical properties surpassing those of monolithic films from which the multilayers were composed. The stress in multilayer reduced significantly with respect to the monolithic N-cBN of the equivalent thickness, while the hardness increased to 82 GPa which was greater than that of monolithic N-cBN and ND by 9 and 14 GPa, respectively (**Figure 11(b)**). The multilayers showed a smooth

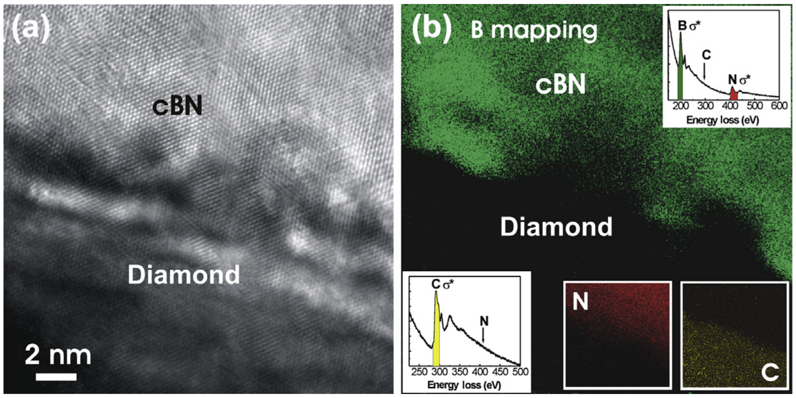

Figure 10 (a) Cross-sectional HRTEM image of the diamond/cBN interface. The cBN grows directly on diamond with no aBN or tBN layer. The diamond/cBN interface is seamless and the actual interface cannot be determined by observation. The epitaxy is obvious with the trivial relation of $(111)_{\mathrm{Diamond}}//(111)_{\mathrm{cBN}}$. (b) B (main image), N (inset, lower part, middle), and C (inset, lower part, right) elemental mapping indicating an interface between cubic BN and diamond. Also shown are EELS measurements (cBN region—inset, upper part; diamond region—inset, lower part, left) of spots at the interface region indicating pure cBN on top of pure diamond. The energy windows used for elemental mapping are indicated in the EELS spectra. Reprinted with permission from Zhang et al. (2004a).

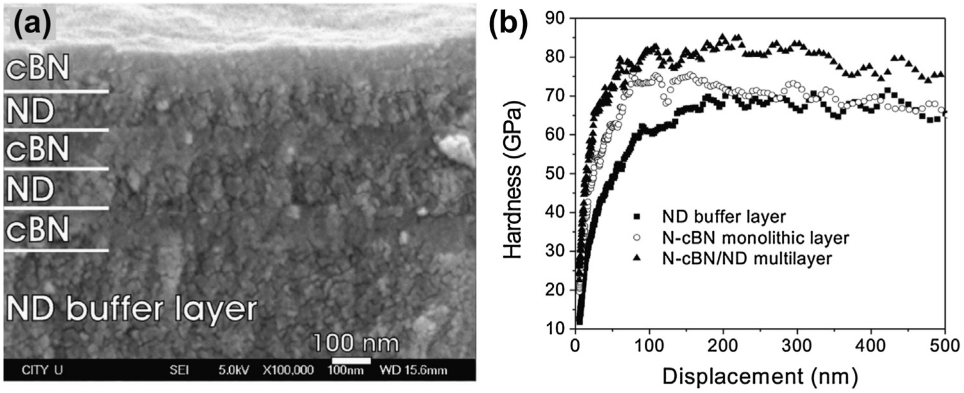

Figure 11 (a) Cross-sectional SEM micrograph showing the N-cBN/ND multilayer grown on a thick ND buffer layer. (b) Hardness versus displacement curves measured by nanoindentation on ND buffer layer, N-cBN monolithic layer, and N-cBN/ND multilayer in the plain-view direction. Reprinted with permission from Li et al. (2007).

surface with the root mean square (RMS) roughness remaining at the level of the basal ND layer, i.e. ~10 nm. Moreover, the top N-cBN layer in the multilayer structure preserved practically the same chemical stability and chemical corrosion resistance as the monolithic N-cBN.

3.24.5 Properties and Applications of cBN Films

3.24.5.1 Mechanical and Tribological Properties

The hardness of HPHT cBN crystals has been evaluated by carrying out different analytical techniques. For ensuring the accuracy of the measurement, translucent polycrystalline cBN crystals synthesized by HPHT were mechanical polished by 0.5 μm diamond paste to produce an optically flat surface, and the routine Vickers indentation measurement revealed a hardness of 54–50 GPa for loads ranging from 9.8 to 294 N. The fracture toughness of cBN ($K_{1C} = 5.0 \pm 0.5$ MPa m$^{1/2}$) was estimated for the first time based on the length of the indent cracks (Taniguchi, Akaishi, & Yamaoka, 1996). Sumiya et al. reported the temperature dependence of the hardness and transverse rupture strength (TRS) of polycrystalline cBN (Sumiya, Uesaka, & Satoh, 2000). The hardness measurement was carried out in vacuum at 1×10^{-3} Torr and the TRS was examined in a nitrogen atmosphere. The temperature was varied in a wide range from 20 to 1200 °C. Likewise, the samples were mechanically polished prior to measurement. It was found that the cBN crystallites smaller than 500 nm in size exhibited hardness of 6000 Hv at room temperature (R.T.) and it reduced to 2000 Hv at 1000 °C. For the cBN grains of 2–5 μm in size, the hardness of 5500 Hv at R.T. and 1000 Hv at 1000 °C were obtained. In contrast, the cBN fine grains (~500 nm) showed TRS of 135 kg/mm at R.T. and 160 kg/mm at 1000 °C, and the larger cBN grains (2–5 μm) revealed the TRS maximum of 60 kg/mm at R.T. and 30 kg/mm at 1000 °C, suggesting contradictory performance of TRS for cBN grains of different sizes. From the fracture surfaces, it was showed that the fracture of the fine-grained cBN was intragranular based, whereas the intergranular facture was dominated in larger (coarse-grained) cBN. The observations suggest that cBN fine grains are more preferable for the manufacture of cutting tools.

In the case of cBN films deposited by PVD, Vickers and Knoop indentation were adopted previously to measure the microhardness of cBN films (Murakawa & Watanabe, 1990; Nishiyama, Kuratani, Ebe, & Ogata, 1993; Wada & Yamashita, 1992). The loads in the range of tens to hundreds milliNetwons were used for measurements. Correspondingly, the indent depth was comparable to or even larger than the film thickness; hence the substrate effects could lead to great errors in measurements. In addition, the static microindentation technique applied in the Vickers and Knoop hardness measurements only involved the assessment of residual imprint, which also led to the difficulties in obtaining a reliable hardness of cBN films of high elasticity.

Nanoindentation technique, which is capable of controlling the loadings as small as tens of microNewtons, was also performed to measure the hardness and elastic modulus of cBN films deposited by PVD (Dworschak et al., 1994; McKenzie, 1993; Mirkarimi, Medlin, et al., 1997; Yamada, Tsuda, & Yoshida, 1998). Even by using such small loadings, the indent depth was still comparable to the film thickness for most PVD films thinner than

200 nm. Mirkarimi, Medlin, et al. (1997) deposited 700-nm-thick cBN films by a two-step process of PVD (reducing the substrate bias after cBN nucleated and performing growth at a high substrate temperature), and employed nanoindentation measurements using indent depths of 100 nm. A hardness of about 60–70 GPa was obtained. In the same work, it was demonstrated that the substrate effects could become substantial for indent depth beyond 12% of film thickness. However, B_4C target was used as the boron source in their experiments, and the carbon incorporation could reach as high as 5% in the deposited films. Therefore, the hardness should be considered arising from a B–N–C composite. Keunecke et al. (2001) deposited about 1-μm-thick cBN by RF (13.56 MHz) diode sputtering on cemented carbide inserts with multibuffer layers. The cemented carbide was firstly coated with either TiN or TiAlN and subsequently with $B_4C + B–C–N$ gradient layer prior to the deposition of top cBN layer. Boron carbide was used as target materials for growing cBN and the substrate temperature maintained at about 600 °C. The substrate bias was reduced after cBN nucleation. It was revealed that the cBN coating had a nanohardness ranged between 53 and 60 GPa and the elastic modulus ranged between 500 and 550 GPa.

The mechanical properties of 5-μm-thick, high-quality cBN films synthesized by DC jet plasma CVD employing fluorine chemistry were studied (Chan, Zhang, Matsumoto, Bello, & Lee, 2003). The effects of grain boundaries, crystal size, and crystallinity on the mechanical properties of the films were systematically investigated by nanoindentation measurements performed in both cross-sectional and plane views in conjunction with the scanning electron microscopy (SEM), TEM, and micro-Raman scattering characterization. The films were smoothed with fine diamond powders to rule out the error caused by the high surface roughness of the as-deposited samples. The hardness and elastic modulus of the polished cBN surface measured at varying displacements were depicted in **Figure 12** (Chan et al., 2003). The results were quite repeatable at different sampling regions. For hardness measurements, a plateau of hardness values over a wide range of displacements ranging from 100 to 300 nm was observed. Beyond this region, the hardness decreased. This observation agrees well with the observation that substrate effects begin to play a role when the displacement is larger than 300 nm. From this plateau, a hardness of about 70 GPa was acquired, and the corresponding elastic modulus of the cBN film distributed from 680 to 800 GPa, comparable to those of HPHT cBN crystals. The achievement of the high hardness of CVD cBN films is believed to be resulted from the high crystallinity and large crystal size (Zhang, Matsumoto, et al., 2002). In addition, because the cBN films measured in the work have a residual stress (~1 GPa) (Zhang & Matsumoto, 2001a), the influence of the high compressive stress normally observed in the films deposited by PVD methods on the hardness measurements (Veprek & Argon, 2001) was effectively diminished, which can also improve the accuracy of measurements. cBN films of 2.8 μm thickness were deposited on diamond-coated WC:Co cutting inserts by using ECR MPCVD with assistance of fluorine chemistry, as shown in **Figure 13**. An enhanced mechanical stability of cBN films was achieved due to the structural compatibility of interfacing diamond and cBN layers. The hardness of the cBN was measured by nanoindentation to be about 70 GPa, respectively. The combined super hardness and chemical inertness of cBN/diamond bilayers on WC inserts suggest potential use of cBN/diamond coatings in industrial practice (Chong, Zhang, Yang, et al., 2009).

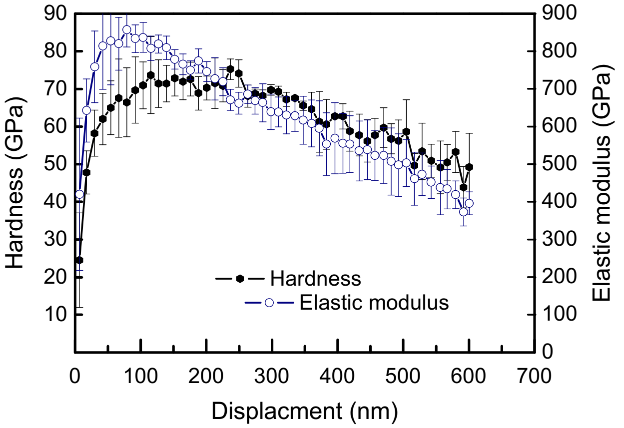

Figure 12 Hardness and elastic modulus of a polished cBN film obtained from a plain-view nanoindentation using continuous stiffness measurement technique. Reprinted with permission from Chan et al. (2003).

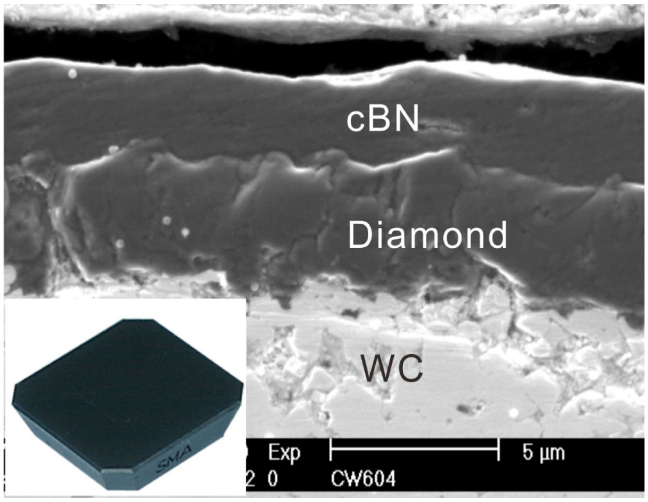

Figure 13 The cross-sectional SEM micrograph of the polished BN film deposited on diamond-coated WC inserts. Reprinted with permission from Chong et al. (2009). Insert shows the optical microscopic image of the cBN-coated WC:Co insert.

The tribological behaviors of BN films with different cubic and hexagonal phase compositions deposited by magnetron sputtering and ECR MPCVD were investigated systematically using a ball-on-disc tribometer with silicon nitride as the counterpart. The influence of phase compositions and surface roughness of BN coatings on their tribological characteristics was studied. The frictional behaviors of the BN samples are illustrated in Figure 14 and summarized as follows (Chong, Ye, Yang, et al., 2010). (1) The coefficient of friction (COF) of the cBN films prepared by RFMS was ∼0.85 for the first 1000 cycles, then it reduced to 0.42 and maintained constant thereafter to 10,000 cycles. (2) cBN films prepared by ECR MPCVD showed a similar trend with an initial COF of ∼0.65 up to 1000 cycles, and then reduced to 0.42–0.45 till 8000 cycles. Thereafter, the COF gradually increased to 0.55 at the end of test (10,000 laps). (3) The COF of sintered cBN increased abruptly from 0.25 to 0.42 in the first 100 cycles and then it maintained this value till the end of the test. (4) The COF of the BN composite film prepared by RFMS fluctuated from 0.4 to 0.55 during the test up to 6800 rotation cycles, and stabilized around 0.45 afterward. (5) The friction behavior of pure hBN films was greatly different from that of cBN and cBN/hBN composite films. The COF of hBN films was 0.45 for the first 300 cycles, then dropped to

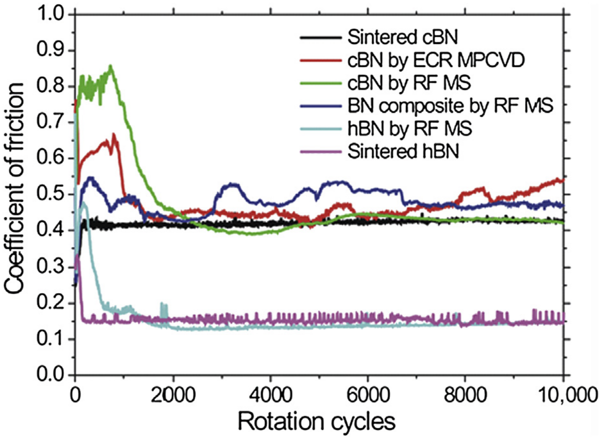

Figure 14 COF of BN films as a function of rotation cycles. The measurements were performed on a sintered cBN insert, a cBN film by ECR MPCVD, a cBN film by RF MS, a cBN/hBN composite film by RF MS, an hBN film by RF MS, and a sintered hBN compact. Si_3N_4 balls were used as counterparts. The temperature and relative humidity were kept between 21 and 25 °C and 38–55%, respectively. The sliding speed of 12.5 cm/s was typically preset at a load of 5 N. The balls slid on a circular track with a radius of 2 mm, and the sliding cycles of 10,000 laps correspond to a sliding distance of 125 m. The maximum Hertzian contact pressure is 1.15 GPa for the cBN films indented by Si_3N_4 balls. Reprinted with permission from Watanabe et al. (2004).

0.14 and remained constant throughout the whole test. In the experiment, hBN films were deposited on silicon substrates via ND interlayer. Therefore, the soft hBN layer was removed rapidly in the early stage of test and the low COF of 0.14 is the result of the contact between the inherently smooth ND and the Si_3N_4 ball. Comparative studies were performed on bulky hBN compact, and a COF around 0.15 was observed after first 20 sliding cycles. The low friction of sintered hBN is the characteristic nature of its hexagonal lamellar structure. In this work, the total sliding length and sliding speed were much larger than the maximum values utilized previously, i.e. 125 m versus 3 m, and 12.5 cm/s versus 1 cm/s, respectively (Watanabe, Miyake, Jin, & Murakawa, 2004). Under the given conditions, all cBN surfaces showed a steady COF value at about 0.45 after 1000 test cycles, insensitive to the preparation method and initial surface roughness. Nevertheless, in the initial COF tests up to 1000 cycles (corresponding to a sliding distance of 12.5 m), the COFs measured were not stable, which was considered to be strongly affected by the initial contact and surface contamination. Therefore, more reliable COFs could be revealed from long run tests.

The COFs of BN films reported previously distributed over a wide range. Nevertheless, it should be noted that the comparison of the COFs of cBN films is meaningless since the surfaces of each pair of interacting materials are unique and testing conditions are different from each other. For example, COF of about 0.1 was reported for amorphous BN films by scratching tests with a diamond pin (sliding length, 10 mm; speed, 12 mm/min) (Miyoshi, Buckley, Pouch, Alterovitz, & Sliney, 1987). The COF of BN against diamond by using nanoscratch tests was shown to reduce from 0.25 to 0.15 when the normal load was increased from 2 to 20 mN (Charitidis, Panayiotatos, & Logothetidis, 2003). Watanabe, Miyake, and Murakawa (1991) studied tribological properties of cBN and hBN films deposited by magnetically enhanced plasma ion plating using a reciprocal friction testing instrument. The measurements were performed with a stainless steel (quenched SUS 440C) ball indenter of 3 mm in diameter under a normal load of 5 N. The tests were performed at room temperature and ambient condition with a relative humidity of 50–60%. The tested distance was 10 mm per stroke at a speed of 1.66 mm s^{-1}, and the total test distance was 1 m. They observed that the COF of cBN film was initially 0.19 and then attained the value of 0.33 at the end of the test. The cBN film was stable and showed no wear mark. Under the same test conditions, the COF of hBN film was estimated to be 0.4–0.6 up to 25 test cycles, and thereafter increased rapidly to above 0.8 after 40 cycles. Peeling of hBN films was observed after 50 cycles. The COF of cBN films obtained by sliding a cBN-coated sintered WC–Co ball was 0.6. After 100 reciprocating cycles, the cBN film was damaged (Watanabe et al., 2004). When a diamond stylus tip (radius = 1 mm) and diamond-like carbon coated WC ball (radius = 3 mm) were employed as the counterpart materials, COF of cBN smaller than 0.1 was reported (Watanabe, Miyake, & Murakawa, 1995).

The wear rate of materials is defined as the volume loss per unit loading per unit sliding distance. The wear volume of ball materials is usually estimated from the diameter of the worn cap of the static counterpart while the wear volume of coating is estimated by measuring the cross-sectional area of the wear track. In this work, the wear test up to 10,000 cycles just led to slight thinning/polishing of the cBN surfaces due to much higher hardness of cBN over Si_3N_4 (70 versus 18 GPa). The surface of cBN showed very high wear resistance against Si_3N_4 balls. Hence, to evaluate the wear rate of cBN films induced by sliding Si_3N_4 balls, wear measurements were conducted on the cBN film prepared by ECR MPCVD with prolonged sliding cycles (distances) of 1,000,000 (12.56 km). The wear rate of the cBN was estimated from the cross-sectional area of the wear track using a surface profilometer. The wear area was determined as the average value from three different scans. **Figure 15** depicts a representative cross-sectional profile of the wear track created after rotation of 1,000,000 cycles. The average wear area is 510 μm^2 while the maximum wear depth is 930 nm. As a result, the wear rate of

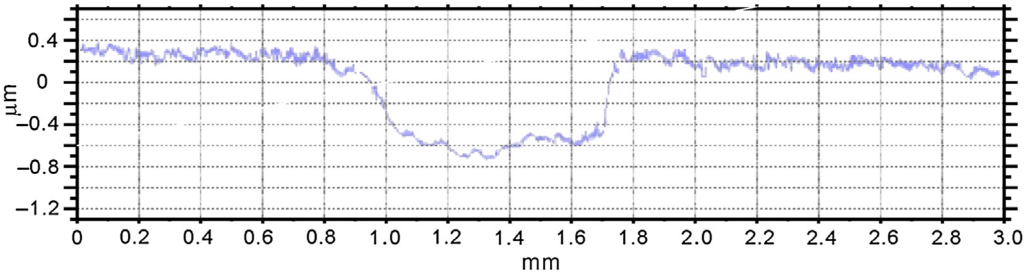

Figure 15 The cross-sectional wear profile of the cBN film prepared by ECR MPCVD after sliding with a Si_3N_4 ball for 1,000,000 cycles (corresponding to a sliding distance of 12.5 km). Reprinted with permission from Chong et al. (2010).

cBN films was calculated to be about 1.0×10^{-7} $mm^3/N \cdot m$. The cBN films exhibit excellent wear resistance when rubbed with tough and hard Si_3N_4 balls. As a reference, a wear rate of 4×10^{-10} $mm^3/N \cdot m$ for cBN coatings was reported by tests utilizing a ball crater (Keunecke et al., 2001). However, the counter material and experimental details were not provided in the work. It is therefore pointless to compare the two works.

3.24.5.2 Electrical and Electronic Properties of cBN

Soon after being invented by using HPHT method in 1957 (Wentorf, 1957), the electrical properties of cBN crystals were investigated. The as-synthesized cBN was a highly insulating material with the resistivities about 10^{16} Ω cm (Karim, Cameron, & Hashmi, 1993). Nevertheless, in contrast to diamond, both p- and n-type conductivities of cBN can be achieved by using different dopants (De Vries, 1972; Mishima, Tanaka, Yamaoka, & Fukunaga, 1987; Wentrof, 1962), as summarized in **Table 3**. It was illustrated that the addition of 0.01–1.0 wt% Be led to the formation of blue cBN crystals with p-type resistivity in the range 10^2–10^3 Ω cm at 25 °C, an activation energy of 0.19–0.23 eV was obtained. Sulfur doping resulted in pale yellow crystallites with n-type resistivity of $10^3 \sim 10^4$ Ω cm at 25 °C, and the corresponding activation energy was about 0.05 eV. In addition, due the grain boundaries, semiconducting polycrystalline cBN compacts made of sintered Be-doped cBN powder showed higher resistivity than Be-doped single crystals, although the activation energy (0.3 eV) obtained was comparable to that of single crystals (Taniguchi, Tanaka, Mishima, Ohsawa, & Yamaoka, 1993). Zn and Mg doping were also tried in the HPHT synthesis processes but no effective doping was observed.

Mishima et al. achieved the first cBN p–n junction by growing the Be-doped cBN seeds in the Si containing solvent at 1700 °C and 5.5 GPa by employing the temperature-difference solvent method (Mishima et al., 1987; Mishima, Yamaoka, Fukunaga, 1987). The voltage–current characteristics illustrated a clear reproducible rectifying effect from room temperature to 530 °C measured by four point probes. More significantly, a broad emission from UV (215 nm) to visible was first observed on the p–n junctions, which demonstrated the possibility of cBN in electronic devices (Mishima, Era, Tanaka, & Yamaoka, 1988). The capacity in n- and p-type doping of cBN and also the extreme thermal and chemical stability of cBN make it an outstanding candidate for high-power and high-temperature electronic devices operating in harsh environments.

The research on the electrical and electronic properties of cBN thin films is far more behind that of HPHT cBN, mainly due to the difficulties in preparing high-quality cBN films. It was shown that the intrinsic cBN films prepared by IBAD had a high resistivity of about 10^{10} Ω cm (Ronning, Dreher, Feldermann, et al., 1997). In the deposition of BN films using neutralized nitrogen beam and electron beam evaporation of boron, different amounts of Mg were introduced by a standard effusion cell (Lu et al., 1996). A minimum resistivity of about

Table 3 Electrical and electronic properties of cBN doped with different impurities

	Dopant	*Carrier density (cm^{-3})*	*Activation energy (meV)*	*Mobilities (cm^2 V/s)*	*Resistivity (Ω cm)*	*Ref*	*Remarks*
p-type	Be	5×10^{17}	220	2		Taniguchi, Koizumi, Watanabe, et al. (2003)	Single crystal
			260			Taniguchi et al. (1993)	Polycrystalline
			230		1–10^2	Mishima et al. (1988)	Single crystal
		5×10^{16}	240			Tomokage, Nomura, Taniguchi, and Ando (2000)	Single crystal
	Zn		100		10^2	Nose, Oba, and Yoshida (2006)	PVD cBN film
	Mg	5×10^{18}	300	27	5×10^{-2}	Lu, Bousetta, Bensaoula, Waters, and Schultz (1996)	PVD mixed BN
	None	5×10^{18}	60	500		Litvinov, Taylor, and Clarke (1998)	PVD cBN film
		5×10^{16}		177	8×10^{-2}	Lu et al. (1996)	PVD mixed BN
n-type	S	10^{12}–10^{14}	320–470	1	2×10^4	Taniguchi, Teraji, Koizumi, Watanabe, and Yamaoka (2002)	Single crystal
			50			Wentrof (1962)	Single crystal
	Si		240		10–10^3	Mishima et al. (1988)	Single crystal
		1.5×10^{17}		825	10^{-1}	Wang, Yang, Zhang, et al. (2003)	Single crystal
	None	10^{12}	470	20	5×10^5	Sokolowski (1979)	Single crystal

$10^{-2}\,\Omega$ cm was achieved. Yet the phase purity of the corresponding film is very low (~21% cubic phase), therefore the variation of conductivity is from mixed BN phases (possibly mainly sp^2 BN phase) instead of cBN itself. Ronning, Feldermann, and Hofsäss (2000) reported the incorporation of silicon into BN films during IBAD process. A gradual change from cBN to hBN was observed with increasing silicon concentration. The ultraviolet photoelectron spectroscopy revealed that the Fermi level of BN did not change upon Si doping, and n-type conductivity was thus excluded. The failure in Si doping in cBN thin films grown by PVD methods may be associated with the nanocrystalline nature of such cBN films which contain a large amount of grain boundaries and may prevent effective doping of Si into cBN grains.

Nose et al., (2006), Nose and Yoshida (2007), and Kojima, Nose, Kambara, and Yoshida (2009) studied in situ of BN films by inserting Zn and Mg targets into the plasma and applying a negative bias to them. It was revealed that the room-temperature conductivity of Zn-doped BN films deposited in pure Ar plasma increased from 10^{-8} to $10^{-2}\ \Omega^{-1}\ \mathrm{cm}^{-1}$ with increasing Zn concentration from 400 to 20,000 ppm. Similarly, Mg-doped films deposited in pure argon showed an increase of electric conductivity by 10^4 as compared to undoped films. The Hall measurements demonstrated that the films containing 2.1 at% Mg presented p-type conduction with carrier concentration and mobility of $4 \times 10^{14}\ \mathrm{cm}^{-3}$ and $6\ \mathrm{cm}^2\ \mathrm{V}^{-1}\ \mathrm{s}^{-1}$, respectively, at 380 K. However, for most of the samples, no reliable Hall data were obtained. Moreover, in both Zn- and Mg-doped BN films, the conductivity increment was accompanied by a linear increase in the $B/(B+N)$ ratio. No modification of the conductivity was observed for the films grown in Ar/N_2 mixtures, therefore, the conductivity variation by Zn/Mg doping in Ar plasma was considered to be due to the substitution for nitrogen atoms in BN by Zn and Mg. The extremely high Zn/Mg content in the films, obvious deviation from BN stoichiometry, and the absence of reliable Hall data of doped BN films require further study on the in situ doping effect of Zn and Mg in cBN films.

The cBN films with various Si concentrations varying from 0 to 15.7 at% were prepared by in situ cosputtering of Si during the growth of cBN films by IBAD (Ying, Zhang, Fan, Tan, & Yin, 2010). The cubic phase content remained stable with the incorporation of Si up to a concentration of 3.3 at%. It was noticed that the Si atoms replaced only B atoms and combined with N atoms to form Si–N bonds, and no evidence of the existence of Si–B bonds was observed. The resistance of the Si-doped cBN films decreased with increasing Si concentration, and the resistivity of the cBN film with 3.3 at% Si was two orders of magnitude lowered as compared to undoped films. According to the experiments, Si was suggested to be an n-type dopant for cBN; however, more experimental data such as Hall measurements are needed to verify the role of Si in varying the resistivity of cBN films.

Ion implantation is another method used to dope cBN films. As a routine approach for doping semiconductors, ion implantation allows the introduction of a precisely controlled amount of impurity into the crystal independent of the solubility of the impurity. The unique capability provides an effective means to introduce almost any dopant into selected regions of a substrate. Be implantation was carried out to achieve p-type conductivity of polycrystalline cBN films grown by fluorine-assisted ECR MPCVD (He, Zhang, Zou, et al., 2008). The cBN films had a very high cubic phase purity. The ion dose and postimplantation annealing was demonstrated to affect strongly the electrical properties of cBN films. For the cBN film implanted with a total dose of $2.5 \times 10^{15}\ \mathrm{cm}^{-2}$ and annealed at 1420 K, while no deterioration in cubic phase purity was evidenced, a drastic reduction in resistivity by seven orders of magnitude was observed, as shown in **Figure 16**. The Hall measurements revealed a corresponding hole concentration of $6.1 \times 10^{18}\ \mathrm{cm}^{-3}$ and mobility $3\ \mathrm{cm}^2\ \mathrm{V/s}$. The activation energy was measured to be 0.20 ± 0.02 eV. The hall mobility and activation energy of Be-implanted cBN films are comparable to those of Be-doped cBN single crystals synthesized by HPHT method. By Be implantation in BN films deposited on n-type silicon substrates by sputtering, a cBN/Si p–n heterojunction was also fabricated (He, Chen, Li, Deng, & Zhang, 2008). However, the BN films had a mixed phase composition of sp^2- and sp^3-hybridized BN.

Yin, Boyen, Ziemann, et al. (2008), and Yin, Pongrac, and Ziemann (2008) reported the Si implantation in cBN films. It was shown that pure cubic phase was conserved after Si implantation up to a concentration of $2 \times 10^{20}\ \mathrm{cm}^{-3}$ and after annealing at 900 °C. The temperature-dependent sheet resistance was lowered by seven orders of magnitude as compared to undoped films, as shown in **Figure 17**. By temperature-dependent Hall effect measurements, n-type conduction was confirmed for the heavily Si-implanted cBN films. Due to the high Si doping levels, a semiconductor-to-metal transition was observed, which was accompanied with extremely small activation energies of about 0.05 eV and an almost temperature-independent negative carrier concentration up to 470 K. At higher temperatures, an additional activated process was revealed, which resulted in a further increase in carrier concentration with an activation energy of 0.4 eV.

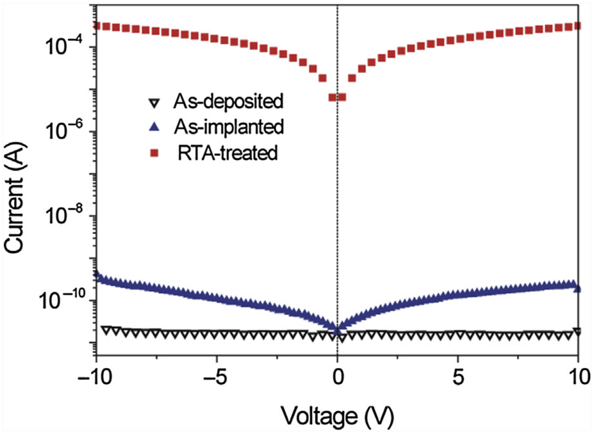

Figure 16 Surface *I–V* characteristic of as-deposited, as-implanted, and RTA-treated cBN films. Quite good linear *I–V* dependence was revealed for the sample after RTA treatment, indicating the formation of Ohmic contacts between silver electrodes and the sample. Reprinted with permission from He, Zhang, et al. (2008).

Theoretically, Gubanov, Lu, Klein, and Fong (1996), Gubanov, Hemstreet, Fong, and Klein (1996), and Gubanov, Pentaleri, Fong, and Klein (1997) studied the electronic structures of Be-, Mg-, and Si-doped cBN and the effects of B and N vacancies in the electronic properties of cBN by tight-binding linearized muffin-tin-orbitals technique (TB-LMTO) within the LDA. It was calculated that Be and Mg atoms could substitute B in cBN lattice with a low formation energy and induce a shallow acceptor level close to the valence band minimum. The probability for Be and Mg impurities to substitute N atoms in the cBN lattice was revealed to be very small. However, Be-induced hole states were strongly delocalized, while Mg-induced impurity states were more localized. Therefore, Be was suggested to be a more effective dopant for p-type conductivity of cBN films. Concerning about Si, the substitution of N sublattices was observed but an energy of 1.1–1.4 eV was required to activate these states, thus the p-type conductivity was excluded. Silicon doping in B sublattices was found to be delocalized and overlap with the conduction band edge, thus resulting in n-type conductivity.

Furthermore, in the absence of dopants, boron and nitrogen vacancies (composition deviated from ideal stoichiometry) were also calculated to induce p- and n-type conductivity, respectively. The theoretical simulation agrees very well with the experimental results obtained thus far.

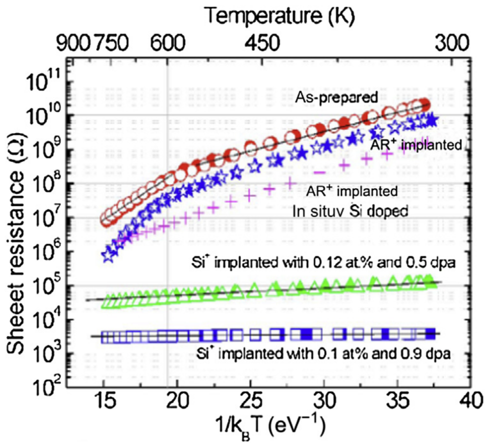

Figure 17 Temperature dependence of the sheet resistance of three cBN films, which were implanted with Si^+ at high energies (squares) and low energies (triangles) and with Ar^+ at high energies (stars) applying cold implantation and rapid annealing (CIRA) routines. The results for an in situ Si-doped cBN sample, which was subsequently Ar^+ implanted, applying CIRA routines are also added (crosses). The filled symbols were measured during heating and the open symbols during subsequent cooling. Reprinted with permission from Yin, Pongrac, et al. (2008).

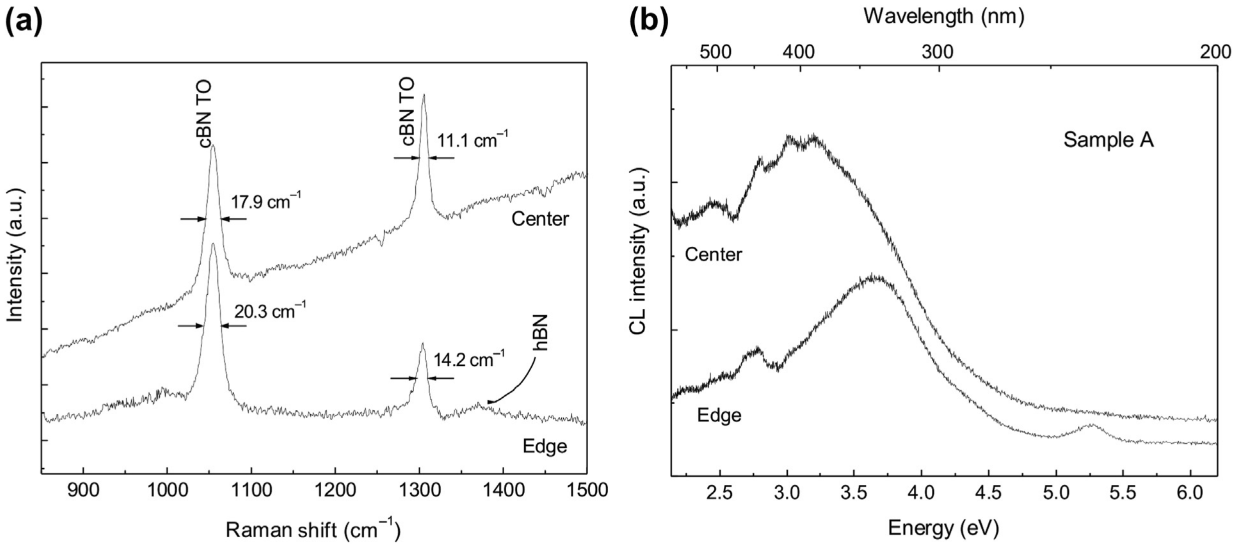

Figure 18 (a) Raman and (b) CL spectra measured in the center and the edge region of a cBN film deposited by DC jet plasma CVD. Reprinted with permission from Zhang, Kanda, et al. (2002).

3.24.5.3 Optical and Photoconductive Properties

cBN has the widest bandgap between all VI and III–V semiconductor materials. Miyata et al., (1989) estimated the optical absorption of cBN crystallites was 6.1 ± 0.2 eV from the transmission and reflection spectra. The bandgap of BN was shifted from 4.3 to >6.0 eV when the cBN content increased from 0 to 88%.

The cathodoluminescence (CL) characteristics of cBN thin films deposited by DC jet plasma CVD using a gas mixture of Ar–N_2–BF_3–H_2 were investigated (Yu, Ong, Wong, Lau, & Matsumoto, 2006; Zhang, Kanda, et al., 2002), which was demonstrated to depend strongly the phase composition and crystallinity of the films. In addition, the crystallinity of the films was investigated by Raman spectroscopy. **Figure 18(a)** shows the Raman spectra measured in the center and edge region of a cBN film. The cubic phase content >90% as evidenced by FTIR was obtained in the region. In both spectra, two intensive peaks located at about 1054 (TO) and 1303 cm^{-1} (LO) were observed; and a broad peak at about 1360 cm^{-1} for hBN phase appeared in the spectrum obtained in the edge. Based on the peak broadening, the cBN film has higher crystallinity (larger crystal size or less defect states) at the center region.

Figure 18(b) shows the CL spectra measured in the center and the edge of the sample. For the center region, a broad emission band centered at about 3.12 eV dominated the spectrum. In addition, four emission peaks centered at about 2.48, 2.81, 3.01, and 3.20 eV were observed. According to the CL study on the HPHT cBN crystals, the emission band at about 2.48 eV was assigned to the namely A and B bands which are caused by multivacancy complexes of boron and nitrogen vacancies in cBN single crystals (Shipilo, Shishonok, Zaitsev, Melnikov, & Olekhnovich, 1988). The main broad peak at about 3.12 eV closes to the band UCL (or US-1) luminescence centers reported previously (Mishima & Era, 2000). The origin of this emission band has not been identified so far, but it was commonly observed in undoped cBN crystals synthesized by various methods. This band normally shows a vibration structure with notable anharmonicity, which is considered to correspond to the energies of characteristic cBN optical phonons (Mishima & Era, 2000). However, if the peaks at 2.81, 3.01, and 3.20 eV are considered to be due to such a vibration structure, the participating vibration energy is about 200 meV, which is higher than the energies of characteristic cBN optical phonons: 131 meV for TO and 162 meV for LO mode. Therefore, these three peaks were considered to generate from other unidentified origins. For the edge region of the sample, the main emission band shifted to 3.68 eV. The peak at 2.81 eV still existed while the intensity of the peaks at 3.01 and 3.12 eV decreased and the peak at 2.48 eV disappeared. A new peak centered at 5.28 eV was observed in the spectrum, which is believed the near-band-gap UV emission as observed in pure hBN films deposition on silicon substrates (Taylor, Brown, Subramaniam, et al., 1994).

The wide bandgap of cBN makes it a very promising candidate for fabricating DUV (solar-blind) photodetector. For this purpose, 1-μm-thick cBN films were grown by ECRMP CVD on 4-μm-thick diamond interlayers

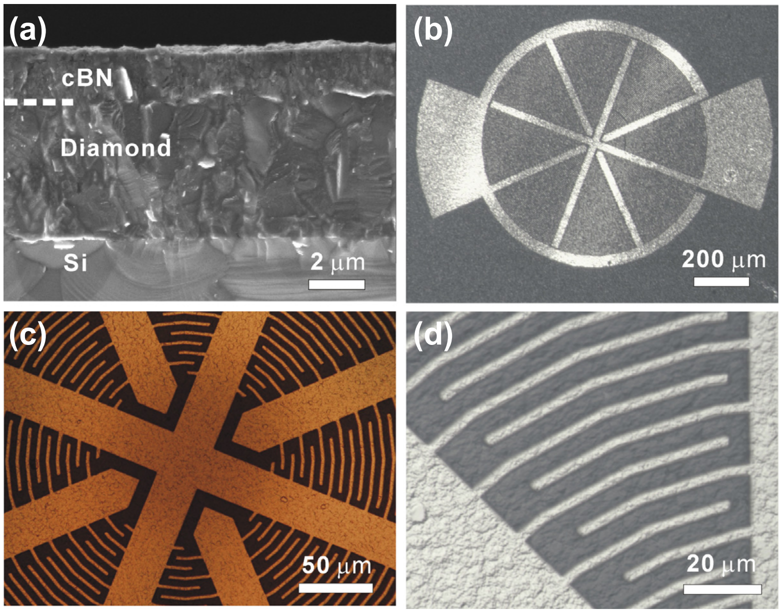

Figure 19 (a) SEM cross-sectional morphology of the cBN/diamond composite film. (b) Optical microscopy image of a cBN photodetector of 1 mm in diameter and (c) enlarged view of the circular interdigitated electrodes at center region. (d) Enlarged SEM view showing the width and spacing of electrodes. Reprinted with permission from Soltani et al. (2008).

on silicon substrate, as shown in **Figure 19(a)** (Soltani, Barkad, Mattalah, et al., 2008). The cBN film has high phase purity and crystallinity as evaluated by FTIR and micro-Raman spectroscopy. The MSM photodetectors were fabricated by depositing patterned Mo/Au (40/300 nm) electrodes on cBN surface using electron beam deposition. To achieve high homogeneity of the electric field between pads, the electrodes were patterned to a circular interdigitated configuration (**Figure 19(b) and (c)**) via photolithographic technique. The diameter of the devices varied from 1 to 3 mm. The finger width is 2 μm, and the interspacing between contact pads is 5 μm, as shown in **Figure 19(d)**. The electrode fill factor (metallic/cBN area ratio) is $<33\%$.

The absolute spectral responsivity curves and more precisely the external quantum efficiency of the MSM photodetectors based on diamond, cBN, and AlN films are shown in **Figure 20** (BenMoussa, Soltani, Schuehle, et al., 2009). The maximum photoresponse of the cBN MSM photodiode was observed at 180 nm with 21 mA/W at +30 V bias. The cut-off wavelength of the device is around 193 nm (6.42 eV), which is the shortest value achieved for semiconductor detectors so far and agrees well with the bandgap of the bulk cBN. The rejection ratio between 180 and 250 nm (noise limited) is around four orders of magnitude (1.05×10^4). The high rejection ratio has important implication for using the cBN MSM detectors in direct detection of DUV light without any filters required to block visible to middle UV wavelength (300–200 nm) of light, thus the detector in fact is solar-blind. The cBN photodetectors are stable over a wide temporal range for the bias voltage less than −40 V, and they show a very small room temperature dark current. However, increase in bias voltage above −40 V lead to a larger dark current (leakage current) and the device becomes unstable under DUV illumination. Under such circumstances, both the photoconductive gain and the device sensitivity increase, but on the other hand, the induced persistent photoconductive effect slows down the device performance.

3.24.5.4 Surface Nanostructuring and Superhydrophobic Properties of cBN Films

The properties of materials can be modified and enhanced by surface nanostructuring. Thus, the potential applications of cBN depend not only on its intrinsic properties but also on the surface morphologies and micro- and nanostructures of cBN. The surfaces of diamond (Hsu, Lo, Chen, et al., 2004; Wang, Wang, Li, et al., 2006; Yang, Uetsuka, Osawa, & Nebel, 2008; Yoshida, Urushido, Miyake, & Hiramatsu, 2001; Zhang, Meng, Chan, et al., 2003; Zhang, Wu, Wong, et al., 2003; Zou, Yang, Zhang, et al., 2008) and other materials such as Si, III-V (AlN, GaN, and GaAs), semiconductors, and sapphire (Calarco, Marso, Richter, et al., 2005; Davidson, Schricker, Wiacek, & Korgel, 2004; Dick, Deppert, Karlsson, et al., 2005; He et al., 2006; Kim, Lee, Cho, et al.,

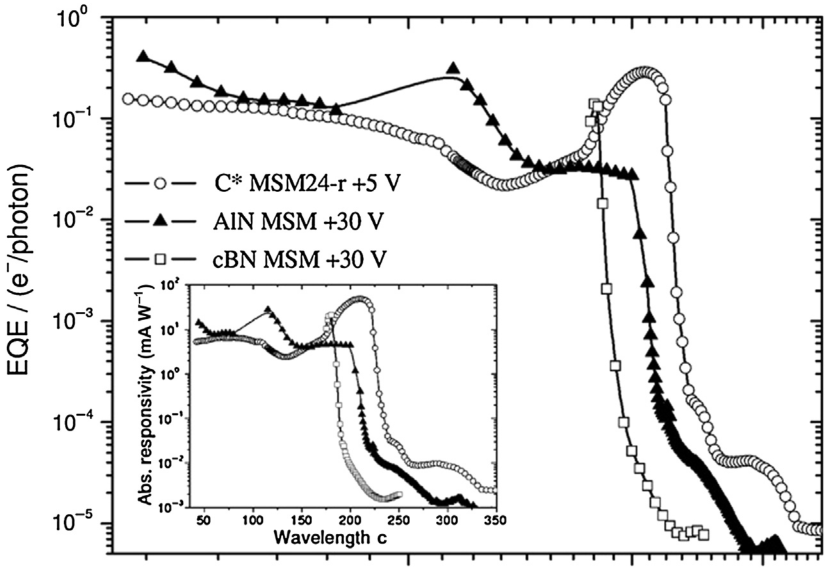

Figure 20 External quantum efficiencies (EQE) of the diamond MSM24-r photodetector at 5 V bias, of the c-BN MSM photodiode at +30 V bias (in the range between 175 and 250 nm), and of the AlN MSM photodiode at +30 V bias, in the wavelength range between 40 and 360 nm. The inset shows the corresponding absolute spectral responsivity in the same wavelength range. Reprinted with permission from BenMoussa et al. (2009).

2006; Liu, Hu, Wu, et al., 2005; Paiano, Prete, Loverqine, & Mancini, 2006; Persson, Larsson, Stenstrom, et al., 2004; Shi, Chen, Chattopadhyay, et al., 2005) have been successfully nanostructured, and the formed nanostructures, including nanopillars, nanocones, and nanowires, have shown promising applications in diverse fields including photonics, electronics, catalysis biochemistry, and sensing devices. However, due to the synthetic difficulty, poor quality, and extreme chemical inertness of cBN films, to construct cBN nanostructures and study their corresponding properties is more challenge work.

By employing bias-assisted reactive ion etching (RIE), cBN nanopillar and nanocone arrays were constructed. To nanostructure the cBN surface, the cBN films deposited on diamond-coated silicon substrates by ECR MPCVD were coated with a 5 nm thin gold film using magnetron sputtering. Heating the gold-coated cBND films to 800 °C in H_2 plasma for 6 min without applying negative bias caused aggregation of the gold layer to nanodots. The formation of the Au dot matrix is mainly due to the thermal effect, and the dot size and density depend also on the substrate surface roughness. Under the continual ion bombardment during RIE, the gold nanodots served as local nano-sized etching masks preventing the etching of the cBN structure beneath the gold nanodots.

Under bias-assisted RIE, cBN is removed due to the combined actions of physical etching by energetic ion impact along the electric field direction and chemical etching by reactive hydrogen atoms/ions, whereas hydrogen ion sputtering only affects the removal of gold dots. The reactions involved in the chemical etching of cBN are suggested to be as follows:

$$\mathrm{N_{(surface)}} + \mathrm{xH(g)} \rightarrow \mathrm{NH_x(g)}$$

$$\mathrm{B_{(surface)}} + \mathrm{xH(g)} \rightarrow \mathrm{BH_x(g)}$$

The chemical inertness of the gold against the hydrogen activated species leads to the preferential etching of cBN over the gold dots template. The ratio of etching yield of cBN to that of gold mask will then determine the final structure of the cBN surface. In the case of a lower bias voltage, the gold dots are gradually reduced in size, leading to the shrinking of the masked cBN area and exposure of fresh cBN surfaces around the gold dots with continual RIE. The freshly bare cBN surfaces around the gold dots are subjected to ion etching condition. Gradual reduction of gold dots and continuing exposure of new surfaces surrounding the gold dots then lead to the development of pyramidal cones and the eventual formation of cBN cone arrays (**Figure 21**) (Zhou, Yang, Liu, et al., 2010).

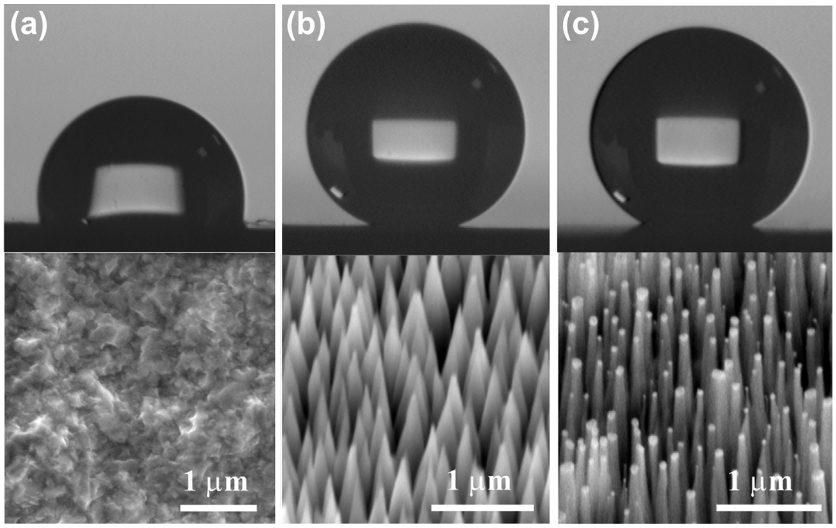

Figure 21 (upper images) The corresponding optical microscopic images of water droplets contacted on cBN films with (lower images) (a) flat, (b) nanocone, (c) nanopillar array surfaces. The cBN films were chemically modified with perfluorosilane. Reprinted with permission from Zhou et al. (2010).

The increase in bias voltage leads to higher ion kinetic energies in the plasma, and a higher etching rate of BN phase, in particular higher chemical etching by energetic plasma radicals, than that of gold dots mask. The higher ion kinetic energy induces a higher etching rate of cBN over that of the masking gold dots, thus leading to the formation of cBN columnar nanopillars instead of nanocones (**Figure 21**). Based on the experimental observations, it was shown that the ratio of etching yield of cBN to that of mask material is an important factor in determining the final cBN nanostructures. In fact, Ti and Al etching masks were also used in the experiments. However, the resulting cBN nanostructures were not as good as that obtained with gold etching mask, i.e. it was difficult to achieve a uniform cBN nanostructure array, and only irregular hillocks or trenches were obtained under the same RIE conditions.

cBN is inherently a hydrophilic material due to its large surface energies (Zhang, Ma, Xu, & Xin, 2003; Ooi & Adams., 2005). The wettability of the cBN films before and after surface nanostructuring and chemical modification with perfluorosilane was evaluated by measuring the water contact angles at room temperature. The as-deposited cBN surfaces are also hydrophilic with a water contact angle about 74°; and it increased to 99° after surface modification with perfluorosilane, as shown in **Figure 21**. Significantly, cBN surfaces showed contact angles of 135° for nanopillar and 153° for nanocone arrays after surface nanostructuring and modification (**Figure 21**). Moreover, a sliding angle smaller than 10° was observed on cBN nanocone arrays after surface modification. Considering both the static and dynamic angles, it can be concluded that the cBN nanocone arrays satisfy the criteria for superhydrophobic surfaces. The nanostructured cBN surfaces are composed of microscaled voids and nanostructure tips. When a water droplet sits on the nanoarrayed surface, vapor pockets trapped in the microvoids reduce greatly the solid–liquid contact area and thus the apparent contact angle increases, which is in accordance with the Cassie mode (Cassie & Baxter, 1944; Wenzel, 1949). The hydrophobic properties of the cBN surfaces are on a large extent dominated by the air packets trapped in the nanostructures, and the cBN nanocone array structures with sharp tips are more efficient in reducing the fraction of solid–liquid contact area and achieving the superhydrophobicity. Combined with their inherent outstanding properties, e.g. super hardness and chemical inertness, the achievement of superhydrophobicity on cBN surfaces may further extend their applications such as self-cleaning protective coatings and antiadherent scalpels.

3.24.5.5 Functionalization of cBN Surfaces for Chem- and Biosensing

Fluorescent film sensors have facilitated the sensing process because they can be used conveniently to achieve real-time and real-space monitoring (Basabe-Desmonts, Zimmerman, Reinhoudt, & Calama, 2005, p. 169; Gu, di Su, & Loh, 2005; Kim, Kim, Kim, & Kim, 2008; Motesharei & Myles, 1998). For this purpose specific molecules with controlled structural order and composition are covalently attached/modified on solid surface, and self-assembled monolayers (SAMs) offer advantages such as a unidirectional responding surface, ease and reproducibility of synthesis, and fast response times. For example, SAMs of organosilanes by covalently grafting of fluorophores on various surfaces have been used recently in detection of ions, anions, neutral molecules, and biomolecules (Basabe-Desmonts, Beld, Zimmerman, et al., 2004; Baur, Steinhoff, Hernando, et al., 2005; Crego-Calama & Reinhoudt, 2001; Gao, Fang, Wen, Li, & Hu, 2004; van der Veen, Flink, Deij, et al., 2000; Zimmerman, Basabe-Desmonts, van der Baan, Reinhoudt, & Crego-Calama, 2005). SiO_2 substrates were usually used as bases in fluorescent chemosensors, and the extremely wide bandgap ($\sim$8.9 eV) of SiO_2 substrates prohibits the electron transfer between the substrate and fluorescent probes and thus the substrate-induced fluorescence quenching. However, the operation of SiO_2-based devices in aqueous solutions suffers form various difficulties, especially chemical instability. Therefore various materials such as diamond (Clare, Clare, Nichols, Abbott, & Hamers, 2005; Knickerbocker, Strother, Schwartz, et al., 2003; Lasseter, Clare, Abbott, & Hamers, 2004; Weng, Xue, Wang, et al.; Yang, Auciello, Butler, et al., 2002; Yang, Baker, Butler, et al., 2005), AlN (Baur et al., 2005), GaN, AlGaN (Steinhoff, Purrucker, Tanaka, Stutzmann, & Eickhoff, 2003), and Al_2O_3 (Fujiwara & Amao, 2004) have been used as substrates to improve the chemical stability of fluorescent film sensors. As discussed above, cBN is a wide bandgap material with excellent chemical inertness even superior to that of diamond. The unique combination of outstanding physical and chemical properties makes cBN a highly promising material for fabrication of sensors with further improved stability and reproducibility for use in harsh environments.

Functionalization of hydrogen-terminated cBN surfaces with amino groups via a photochemical reaction with allylamine was achieved, as shown in **Figure 22** (Zhou, Zhi, Wang, et al., 2008). The X-ray photoelectron spectroscopy (XPS) analysis verified that the hydrogen-terminated cBN surface had indeed been partly converted to amine-terminated surfaces, and the allylamine molecules were covalently bonded to the B and/or N atoms on cBN surface. Gold nanoparticles were shown to be able to be immobilized onto the aminated cBN surface via electrostatic interaction with a high density (4×10^{10} versus 3×10^{7}/cm for the hydrogen-terminated surface) and a homogenous distribution.

The amine-terminated cBN films were modified with amine-modified DNA probes to elucidate their applications as DNA biosensors. **Figure 23** presents the fluorescence images obtained after hybridization with carboxyfluorescein (FAM)-labeled DNA targets. Clear fluorescence with high density and high brightness was only observed on the amine-terminated cBN surface, demonstrating that DNA probes have been bound to the surface. However, only a few bright spots were observed on the AuNPs-modified cBN surface, which was suggested to be due to fluorescence quenching by AuNPs (Basabe-Desmonts et al., 2004; Ishikawa, Yogi, Ye, & Yasuda, 1998). On the hydrogen-terminated cBN surface (**Figure 23**c), similarly only a few bright spots were observed, which indicates that amino groups introduced on the surface are indeed a useful addition to biomolecules immobilization.

Apart from DNA sensors, cBN thin films have been demonstrated as mercury ion sensors. cBN surfaces were modified with an SAM of 3-aminopropyltriethoxy silane (ATPES) for the further immobilization of dansyl chloride ($C_{12}H_{12}ClNO_2S$) (Liu, Zhao, Zhang, et al., 2009). The modification schematic is illustrated in

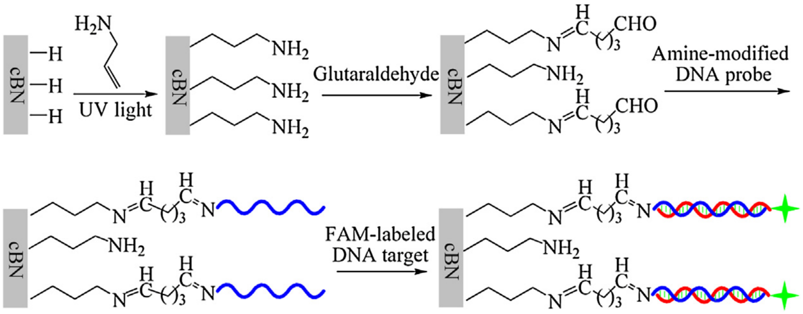

Figure 22 Illustration of photochemical modification of cBN film, subsequent attachment of amine-modified DNA probes and hybridization with FAM-labeled DNA targets. The DNA probes were immobilized on the surface by treating the amine-terminated cBN surface in a 2.5% glutaraldehyde solution for 1 h and reacting with 10 μl of 20 μM amine-modified DNA, which was covered with a slip. Hybridization was accomplished by incubating the above samples at 38 °C in a humidity chamber for 2 h and followed by an exposure to 10 μl of 1 μM FAM-labeled target DNA, covered with a slip, and hybridization at 38 °C in a humidity chamber for 2 h. Reprinted with permission from Zhou et al. (2008).

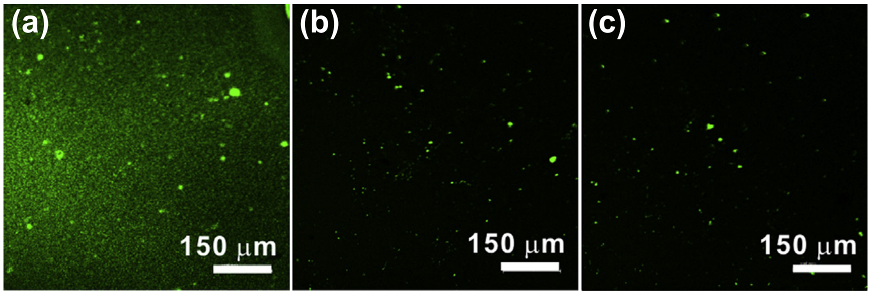

Figure 23 Fluorescence images of (a) amine-terminated, (b) AuNPs-modified, and (c) hydrogen-terminated cBN surfaces after immobilization of amine-modified DNA probe and hybridization of FAM-labeled DNA target (dimension approximately 200 × 200 μm). Reprinted with permission from Zhou et al. (2008).

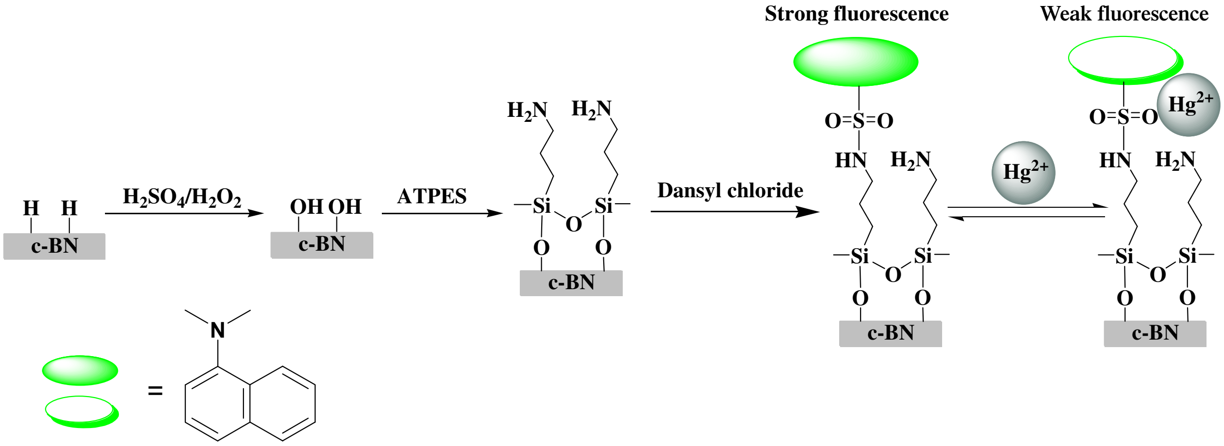

Figure 24 Illustration of the process to immobilize dansyl chloride on cBN surfaces. The hydrogen-terminated cBN films were immersed in H_2SO_4:H_2O_2 (3:1) solution for 30 min, rinsed with deionized water and dried under nitrogen. After hydroxylation the cBN films were agitated on a platform shaker at 100 rpm for 5 h in a solution of 5% ATPES in toluene. Then the samples were sonicated in toluene and isopropanol to remove excess silane and avoid polymerization. To immobilize dansyl chloride on the cBN surfaces, the samples were submerged in 10 ml of 1 mM acetonitrile solution of dansyl chloride under N_2. After 8 h, the films were removed from the solution and rinsed sequentially with acetonitrile, ethanol, and dichloromethane to remove physisorbed materials, and then dried in an air stream. Reprinted with permission from Liu et al. (2009).

Figure 24. The attachment of ATPES to hydroxylated cBN surfaces was verified by XPS analysis. We modify cBN surfaces with an SAM of ATPES, which is used to immobilize dansyl chloride. The dansyl chloride-modified cBN film sensors are shown to have excellent selectivity and sensitivity to Hg^{2+} cations, and recyclability by immersion in HCl solutions.

Fluorescence spectra of dansyl chloride-functionalized cBN film sensors upon addition of diverse cations in ethanol solutions are displayed in Figure 25(a). To study the selectivity of the sensors, all measurements were conducted in 10^{-3} M ethanol solutions of perchlorate salts of Hg^{2+}, Zn^{2+}, Ca^{2+}, Pb^{2+}, C^{u2+}, and Fe^{2+}. It is obvious that the fluorescence intensity of cBN film sensors was quenched upon addition of all analytes. However, the decrease of fluorescence intensity upon addition of Hg^{2+} ($I_o/I \sim 3.5$ times) is much greater than that induced by other cations ($I_o/I < 1.5$ times), which shows the great selectivity of the sensor to Hg^{2+}. It has been demonstrated that open-shell transition and posttransition cations would quench the fluorescence of fluorophores due to electron or energy transfer between metal cations and fluorophores (Resendiz, Noveron, Disteldorf, Fischer, & Stang, 2004). The selectivity of dansyl chloride-functionalized cBN film sensors is considered to be due to the stronger affinity of sulfur in dansyl chloride to Hg^{2+} over other metals. Furthermore, the dependence of fluorescence intensity on Hg^{2+} concentration was also studied. It was revealed that the emission intensity decreased with increasing the concentration of Hg^{2+} in ethanol solutions, as shown in Figure 25(b). The detection limits of Hg^{2+} was approximately 1×10^{-4} M, which is comparable to the detection limit for metal ions by other fluorescent film sensors (Basabe-Desmonts et al., 2004; Zimmerman

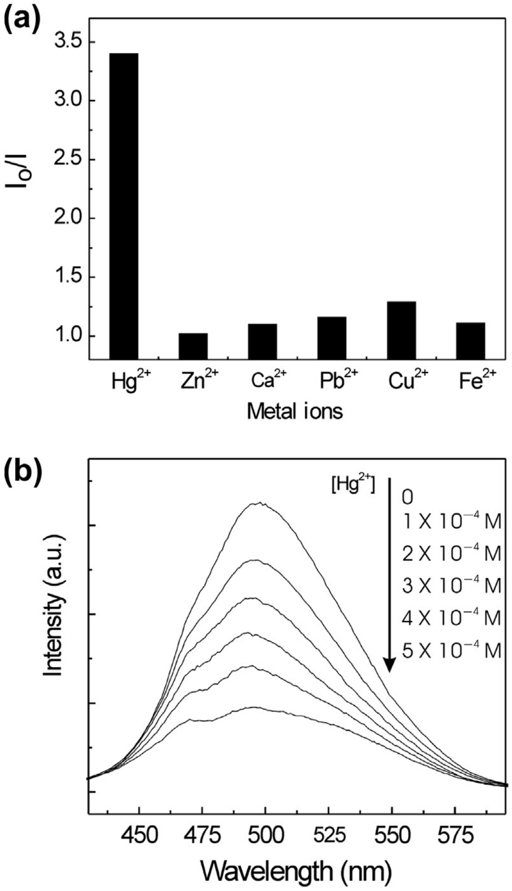

Figure 25 (a) The fluorescence intensity quenching ratio (I_o/I) of dansyl chloride-functionalized cBN film sensors upon the addition of different metal cations in ethanol solutions at a constant concentration of 10^{-3} M. (b) The dependence of the fluorescence intensity on the Hg^{2+} concentration. The emission spectra were recorded with excitation at 350 nm. The monochromator consists of a large aperture stigmatic concave diffraction grating of 900 lines per mm. Reprinted with permission from Liu et al. (2009).

et al., 2005). Significantly, the dansyl chloride-functionalized cBN film sensors was demonstrated to be used repeatedly via regeneration after each sensing test to Hg^{2+} ions. The cBN-based film sensors have the potentials to be integrated into sensing devices/chips, making them very promising for the simple, on line, reusable chemi- and biosensing with reasonable sensitivity.

References

Albe, K. (1997). Theoretical study of boron nitride modifications at hydrostatic pressures. *Physical Review B, 55*, 6203–6210.

Amagi, S., Takahashi, D., & Yoshida, T. (1997). Threshold sheath potential for the nucleation and growth of cubic boron nitride by inductively coupled plasma enhanced chemical-vapor deposition. *Applied Physics Letters, 70*, 946–948.

Barreto, P. R. P., Vilela, A. F. A., & Gargano, R. (2005). Thermochemistry of molecules in the B/F/H/N system. *International Journal of Quantum Chemistry, 103*, 659–684.

Bartl, A., Bohr, S., Haubner, R., & Lux, B. (1996). A comparison of low-pressure CVD synthesis of diamond and c-BN. *International Journal of Refractory Metals and Hard Materials, 14*, 145–157.

Basabe-Desmonts, L., Beld, J., Zimmerman, R. S., Hernando, J., Mela, P., García Parajó, M. F., et al. (2004). A simple approach to sensor discovery and fabrication on self-assembled monolayers on glass. *Journal of American Chemical Society, 126*, 7293--7299.

Basabe-Desmonts, L., Zimmerman, R. S., Reinhoudt, D. N., & Calama, C. M. (2005). Frontiers in chemical sensors: novel principles and techniques. In *Springer series on chemical sensors and biosensors, Vol. 3*, (pp. 169). Berlin: Springer.

Baur, B., Steinhoff, G., Hernando, J., Purrucker, O., Tanaka, M., Nickel, B., et al. (2005). Chemical functionalization of GaN and AlN surfaces. *Applied Physics Letters, 87*, 263901.

Bello, I., Chong, Y. M., Leung, K. M., Chan, C. Y., Ma, K. L., Zhang, W. J., et al. (2005). Cubic boron nitride films for industrial applications. *Diamond and Related Materials, 14*, 1784–1790.

BenMoussa, A., Soltani, A., Schuehle, U., Haenen, K., Chong, Y. M., Zhang, W. J., et al. (2009). Recent developments of wide-bandgap semiconductor based UV sensors. *Diamond and Related Materials, 18*, 860–864.

Berns, D. H., & Cappelli, M. A. (1996). Cubic boron nitride synthesis in low-density supersonic plasma flows. *Applied Physics Letters, 68*, 2711–2713.

Berns, D. H., & Cappelli, M. A. (1997). Low energy ion impact-enhanced growth of cubic boron nitride in a supersonic nitrogen/argon plasma flow. *Journal of Materials Research, 12*, 2014–2026.

Bohr, S., Haubner, R., & Lux, B. (1995). Comparative aspects of c-BN and diamond CVD. *Diamond and Related Materials, 4*, 714–719.

Boyen, H.–G., Widmayer, P., Schwertberger, D., Deyneka, N., & Ziemann, P. (2000). Sequential ion-induced stress relaxation and growth: a way to prepare stress-relieved thick films of cubic boron nitride. *Applied Physics Letters, 76*, 709–711.

Bundy, F. P., & Wentrof, R. H. (1963). Direct transformation of hexagonal boron nitride to denser forms. *Journal of Chemical Physics, 38*, 1144–1149.

Calarco, R., Marso, M., Richter, T., Aykanat, A. I., Meijers, R., Hart, A.v.d., et al. (2005). Size-dependent photoconductivity in MBE-grown GaN-nanowires. *Nano Letters, 5*, 981–984.

Cassie, A. B. D., & Baxter, S. (1944). Wettability of porous surfaces. *Transactions of the Faraday Society, 40*, 546–551.

Chan, C. Y., Zhang, W. J., Matsumoto, S., Bello, I., & Lee, S. T. (2003). A nanoindentation study of thick cBN films prepared by chemical vapor deposition. *Journal of Crystal Growth, 247*, 438–444.

Charitidis, C., Panayiotatos, Y., & Logothetidis, S. (2003). A quantitative study of the nano-scratch behavior of boron and carbon nitride films. *Diamond and Related Materials, 12*, 1088–1092.

Chattopadhyay, K. K., Matsumoto, S., Zhang, Y. F., Sakaguchi, I., Nishitani-Gamo, M., & Ando, T. (1999). Cubic boron nitride thin film synthesis on silica substrates by low-pressure inductively-coupled r.f. Plasma chemical vapor deposition. *Thin Solid Films, 354*, 24–28.

Chong, Y. M., Leung, K. M., Ma, K. L., Zhang, W. J., Bello, I., & Lee, S. T. (2006). Growing cubic boron nitride films at different temperatures. *Diamond and Related Materials, 15*, 1155–1160.

Chong, Y. M., Ye, Q., Yang, Y., Zhang, W. J., Bello, I., & Lee, S. T. (2010). Tribological study of boron nitride films. *Diamond and Related Materials, 19*, 654–660.

Chong, Y. M., Zhang, W. J., Yang, Y., Ye, Q., Bello, I., & Lee, S. T. (2009). Deposition of cubic boron nitride films on diamond-coated WC:Co inserts. *Diamond and Related Materials, 18*, 1387–1392.

Clare, T. L., Clare, B. H., Nichols, B. M., Abbott, N. L., & Hamers, R. J. (2005). Functional monolayers for improved resistance to protein adsorption: oligo(ethylene glycol)-modified silicon and diamond surfaces. *Langmuir, 21*, 6344–6355.

Corrigan, F. R., & Bundy, F. P. (1975). Direct transitions among the allotropic forms of boron nitride at high pressures and temperatures. *Journal of Chemical Physics, 63*, 3812–3820.

Crego-Calama, M., & Reinhoudt, D. N. (2001). New materials for metal ion sensing by self-assembled monolayers on glass. *Advanced Materials, 13*, 1171–1174.

Davidson, F. M., Schricker, A. D., Wiacek, R. J., & Korgel, B. A. (2004). Supercritical fluid-liquid-solid synthesis of gallium arsenide nanowires seeded by alkanethiol-stabilized gold nanocrystals. *Advanced Materials, 16*, 646–649.

De Vries, R. C. (Ed.), (1972). *Cubic boron nitride: handbook of properties. In rep 72*, (pp. 178). Schenectady: General Electric Corporate Research and Development.

Demazeau, G. (1995). High pressure diamond and cubic boron nitride synthesis. *Diamond and Related Materials, 4*, 284–287.

Dick, K. A., Deppert, K., Karlsson, L. S., Wallenberg, L. R., Samuelson, L., & Seifert, W. (2005). A new understanding of Au-assisted growth of III-V semiconductor nanowires. *Advanced Functional Materials, 15*, 1603–1610.

Donner, W., Dosch, H., Ulrich, S., Ehrhardt, H., & Abernathy, D. (1998). Strain relaxation of boron nitride thin films on silicon. *Applied Physics Letters, 73*, 777–779.

Dworschak, W., Jung, K., & Ehrhardt, H. (1994). Growth of cubic boron nitride coatings in a magnetic field enhanced r.f. glow discharge. *Diamond and Related Materials, 3*, 337–340.

Dworschak, W., Jung, K., & Ehrhardt, H. (1995). Growth mechanism of cubic boron nitride in a r.f. glow discharge. *Thin Solid Films, 254*, 65–74.

Eyhusen, S., Gerhards, I., Hofsäss, H., Ronning, C., Blomenhofer, M., Zweck, J., et al. (2003). Ion energy thresholds and stability of cubic boron nitride. *Diamond and Related Materials, 12*, 1877–1882.

Eyhusen, S., Hofsäss, H., & Ronning, C. (2004). The role of ion energy on the growth mechanism of cubic boron nitride films. *Thin Solid Films, 447*, 125–130.

Feldermann, H., Ronning, C., Hofsäss, H., Huang, Y. L., & Seibt, M. (2001). Cubic boron nitride thin film heteroepitaxy. *Journal of Applied Physics, 90*, 3248–3254.

Field, J. E. (Ed.), (1979). *The properties of diamond*. London: Academic.

Fitz, C., Kolitsch, A., & Fukarek, W. (2001). Stress relaxation during annealing of boron nitride films. *Thin Solid Films, 389*, 173–179.

Fitz, C., Kolitsch, A., Möller, W., & Fukarek, W. (2002). Growth of low-stress cubic boron nitride films by simultaneous medium-energy ion implantation. *Applied Physics Letters, 80*, 55–57.

Freudenstein, R., Reinke, S., & Kulisch, W. (1997). The influence of hydrogen on nucleation and growth of cubic boron nitride films. *Surface and Coatings Technology, 97*, 270–274.

Friedmann, T. A., Mirkarimi, P. B., Medlin, D. L., Mirkarimi, P. B., Medlin, D. L., McCarty, K. F., et al. Ion-assisted pulsed laser deposition of cubic boron nitride films. Journal of Applied Physics, 76, 3088–3101.

Fujiwara, Y., & Amao, Y. (2004). Novel optical oxygen sensing material: 1-pyrenedecanoic acid and perfluorodecanoic acid chemisorbed onto anodic oxidized aluminium plate. *Sensors and Actuators, B, 99*, 130–133.

Gao, L. N., Fang, Y., Wen, X. P., Li, Y. G., & Hu, D. D. (2004). Monomolecular layers of pyrene as a sensor to dicarboxylic acids. *Journal of Physical Chemistry B, 108*, 1207–1213.

Gu, H., di Su, X., & Loh, K. P. (2005). Electrochemical impedance sensing of DNA hybridization on conducting polymer film-modified diamond. *Journal of Physical Chemistry B, 109*, 13611–13618.

Gubanov, V. A., Hemstreet, L. A., Fong, C. Y., & Klein, B. M. (1996). Lattice relaxation and pressure dependence of carbon and silicon impurity states in cubic boron nitride. *Applied Physics Letters, 69*, 227–229.

Gubanov, V. A., Lu, Z. W., Klein, B. M., & Fong, C. Y. (1996). Electronic structure of defects and impurities in III-V nitrides: vacancies in cubic boron nitride. *Physical Review B, 53*, 4377–4385.

Gubanov, V. A., Pentaleri, E. A., Fong, C. Y., & Klein, B. M. (1997). Electronic structure of defects and impurities in III-V nitrides. 2. Be, Mg, and Si in cubic boron nitride. *Physical Review B, 56*, 13077–13086.

Hahn, J., Friedrich, M., Pintaske, R., Schaller, M., Kahl, N., Zahn, D. R. T., et al. (1996). Cubic boron nitride films by d.c. and r.f. magnetron sputtering: layer characterization and process diagnostics. *Diamond and Related Materials, 5*, 1103–1112.

He, B., Chen, G. H., Li, Z. Z., Deng, J. X., & Zhang, W. J. (2008). P-BN/n-Si heterojunction prepared by beryllium ion implantation. *Chinese Physics Letters, 25*, 219–222.

He, B., Zhang, W. J., Zou, Y. S., Chong, Y. M., Ye, Q., Ji, A. L., et al. (2008). Electrical properties of Be-implanted polycrystalline cubic boron nitride films. *Applied Physics Letters, 92*, 102108.

He, J. H., Yang, R. S., Chueh, Y. L., Chou, L. J., Chen, L. J., & Wang, Z. L. (2006). Aligned AlN nanorods with multi-tipped surfaces – growth, field-emission, and cathodoluminescence properties. *Advanced Materials, 18*, 650–654.

Herchen, H., & Cappelli, M. A. (1993). Temperature dependence of the cubic boron nitride Raman lines. *Physical Review B, 47*, 14193–14199.

Hofsäss, H., Eyhusen, S., & Ronning, C. (2004). On the mechanisms of cubic boron nitride film growth. *Diamond and Related Materials, 13*, 1103–1110.

Hofsäss, H., Feldermann, H., Eyhusen, S., & Ronning, C. (2002). Fundamental role of ion bombardment for the synthesis of cubic boron nitride films. *Physical Review B, 65*, 115410.

Hofsäss, H., Feldermann, H., Merk, R., Sebastian, M., & Ronning, C. (1998). Cylindrical spike model for the formation of diamond like thin films by ion deposition. *Applied Physics A, 66*, 153–181.

Hofsäss, H., Feldermann, H., Sebastian, M., & Ronning, C. (1997). Thresholds for the phase formation of cubic boron nitride thin films. *Physical Review B, 55*, 13230–13233.

Hofsäss, H., Ronning, C., Griesmeier, U., Gross, M., Reinke, S., & Kuhr, M. (1995). Cubic boron nitride films grown by low energy B^+ and N^+ ion beam deposition. *Applied Physics Letters, 67*, 45–48.

Hsu, C. H., Lo, H. C., Chen, C. F., Chien, T. W., Hwang, J. S., Das, D., et al. (2004). Generally applicable self-masked dry etching technique for nanotip array fabrication. *Nano Letters, 4*, 471–475.

Ichiki, T., & Yoshida, T. (1994). Preparation of cubic boron-nitride films by low-pressure inductively-coupled plasma-enhanced chemical-vapor-deposition. *Applied Physics Letters, 64*, 851–853.

Inagawa, K., Watanabe, K., Ohsone, H., Saitoh, K., & Itoh, A. (1987). Preparation of cubic boron-nitride film by activated reactive evaporation with a gas activation nozzle. *Journal of Vacuum Science & Technology, A, 5*, 2696–2700.

Ishikawa, M., Yogi, O., Ye, J. Y., & Yasuda, T. (1998). Grouping of independent single molecules on silicon surfaces. *Analytical Chemistry, 70*, 5198–5208.

Jiang, X., Helming, K., Zhang, W. J., & Matsumoto, S. (2002). Growth characteristics and texture of cubic boron nitride films produced by CVD. *Chemical Vapor Deposition, 8*, 262–265.

Jiang, X., Philip, J., Zhang, W. J., Hessm, P., & Matsumoto, S. (2003). Hardness and Young's modulus of high-quality cubic boron nitride films grown by chemical vapor deposition. *Journal of Applied Physics, 93*, 1515–1519.

Kalss, W., Haubner, R., & Lux, B. (1998). Preparation of BN films in the B-N-F system. *Diamond and Related Materials, 7*, 369–375.

Karim, M. Z., Cameron, D. C., & Hashmi, M. S. J. (1993). Characterization of mixed-phase BN thin films deposited by plasma CVD. *Surface and Coatings Technology, 60*, 502–505.

Karim, M. Z., Cameron, D. C., Murhy, M. J., & Hashmi, M. S. J. (1991). Plasma deposition of cubic boron nitride films from non-toxic material at low temperatures. *Surface and Coatings Technology, 49*, 416–421.

Kester, D. J., Ailey, K. S., Lichtenwalner, D. J., & Davis, R. F. (1994). Growth and characterization of cubic boron nitride thin films. *Journal of Vacuum Science & Technology, A, 12*, 3074–3081.

Kester, D. J., & Messier, R. (1992). Phase-control of cubic boron-nitride thin-films. *Journal of Applied Physics, 72*, 504–513.

Keunecke, M., Yamamoto, K., & Bewilogua, K. (2001). Mechanical and tribological properties of cBN films on silicon and tungsten carbide substrates. *Thin Solid Films, 398*, 142–149.

Kim, I. H., Kim, K. S., Kim, S. H., & Lee, S. R. (1996). Synthesis of cubic boron nitride films using a helicon wave plasma and reduction of compressive stress. *Thin Solid Films, 290–291*, 120–125.

Kim, K. B., & Kim, S. H. (2000). Adhesion improvement of cubic BN:C film synthesized by a helicon wave plasma chemical vapor deposition process. *Journal of Vacuum Science & Technology, A- Vacuum, Surfaces and Films, 18*, 900–906.

Kim, T. H., Lee, S. Y., Cho, N. K., Seong, H. K., Choi, H. J., & Jung, S. W. (2006). Dielectrophoretic alignment of gallium nitride nanowires (GaN NWs) for use in device applications. *Nanotechnology, 17*, 3394–3399.

Kim, Y. R., Kim, H. J., Kim, J. S., & Kim, H. (2008). Rhodamine-based "turn-on" fluorescent chemodosimeter for Cu(II) on ultrathin platinum films as molecular switches. *Advanced Materials, 20*, 4428–4432.

Knickerbocker, T., Strother, T., Schwartz, M. P., Russell, J. N., Jr., Butler, J., Smith, L. M., et al. (2003). DNA-modified diamond surfaces. *Langmuir, 19*, 1938–1942.

Kojima, K., Nose, K., Kambara, M., & Yoshida, T. (2009). Effects of magnesium doping on growth and electric conductivity of nanocrystalline cubic boron nitride thin films. *Journal of Physics D: Applied Physics, 42*, 055304.

Komatsu, T., Kakudate, Y., & Fujiwara, S. (1996). Heat resistance of a shock-synthesized B–C–N heterodiamond. *Journal of the Chemical Society, Faraday Transaction, 92*, 5067–5071.

Konyashin, I., Khvostov, V., Babaev, V., Guseva, M., Bill, J., & Aldinger, F. (1999). The influence of excited hydrogen species on the surface state of sp^2-hybridized boron nitride. *Diamond and Related Materials, 8*, 2053–2058.

Kuhr, M., Freudenstein, R., Reinke, S., Kulisch, W., Dollinger, G., & Bergmaier, A. (1996). Hydrogen incorporation during nucleation and growth of c-BN films. *Diamond and Related Materials, 5*, 984–989.

Kuhr, M., Reinke, S., & Kulisch, W. (1995a). Deposition of cubic boron nitride with an inductively coupled plasma. *Surface and Coatings Technology, 74–75*, 806–812.

Kuhr, M., Reinke, S., & Kulisch, W. (1995b). Nucleation of cubic boron nitride (c-BN) with ion-induced plasma-enhanced CVD. *Diamond and Related Materials, 4*, 375–380.

Kulisch, W., & Ulrich, S. (2003). Parameter spaces for the nucleation and the subsequent growth of cubic boron nitride films. *Thin Solid Films, 423*, 183–195.

Larsson, K., & Carlsson, J. O. (1999). Surface processes in cubic boron nitride growth: a theoretical study. *Journal of Physical Chemistry B, 103*, 6533–6538.

Lasseter, T. L., Clare, B. H., Abbott, N. L., & Hamers, R. J. (2004). Covalently modified silicon and diamond surfaces: resistance to nonspecific protein adsorption and optimization for biosensing. *Journal of American Chemical Society, 126*, 10220–10221.

Leonidov, V. Ya., Timofeev, I. V., Solozhenko, V. L., & Rodinov, I. V. (1987). Enthalpies of the formation of cubic boron-nitride. *Russian Journal of Physical Chemistry, 61*, 1503–1504.

Leung, K. M., Chan, C. Y., Chong, Y. M., Yao, Y., Ma, K. L., Bello, I., et al. (2005). Studying the growth of cubic boron nitride on amorphous tetrahedral carbon interlayers. *Journal of Physical Chemistry B, 109*, 16272–16277.

Li, H. Q., Leung, K. M., Ma, K. L., Ye, Q., Chong, Y. M., Zou, Y. S., et al. (2007). Nanocubic boron nitride nanodiamond multilayer structures. *Applied Physics Letters, 91*, 201918.

Lifshitz, Y., Kasi, S. R., & Rabalais, J. W. (1989). Subplantation model for film growth from hyperthermal species: application to diamond. *Physical Review Letters, 62*, 1290–1293.

Litvinov, D., & Clarke, R. (1997). Reduced bias growth of pure-phase cubic boron nitride. *Applied Physics Letters, 71*, 1969–1971.

Litvinov, D., & Clarke, R. (1999). In situ texture monitoring for growth of oriented cubic boron nitride films. *Applied Physics Letters, 74*, 955–957.

Litvinov, D., Taylor, C. A., & Clarke, R. (1998). Semiconducting cubic boron nitride. *Diamond and Related Materials, 7*, 360–364.

Liu, C., Hu, Z., Wu, Q., Wang, X. Z., Chen, Y., Sang, H., et al. (2005). Vapor-solid growth and characterization of aluminum nitride nanocones. *Journal of American Chemical Society, 127*, 1318–1322.

Liu, W. M., Zhao, W. W., Zhang, H. Y., Wang, P. F., Chong, Y. M., Ye, Q., et al. (2009). A cubic boron nitride film-based fluorescent sensor for detecting Hg^{2+}. *Applied Physics Letters, 94*, 183105.

Lu, M., Bousetta, A., Bensaoula, A., Waters, K., & Schultz, J. A. (1996). Electrical properties of boron nitride thin films grown by neutralized nitrogen ion assisted vapor deposition. *Applied Physics Letters, 68*, 622–624.

Lüthje, H., Bewilogua, K., Daaud, S., Johansson, M., & Hultman, L. (1995). Preparation of cubic boron-nitride films by use of electrically conductive boron-carbide targets. *Thin Solid Films, 257*, 40–45.

Lux, B., Kalss, W., Haubner, R., & Taniguchi, T. (1999). Nucleation of c-BN on various substrate materials under high-pressure-high-temperature conditions. *Diamond and Related Materials, 8*, 415–422.

Märlid, B., Larsson, K., & Carlsson, J. O. (1999). Theoretical investigation of hydrogen- and halogen-terminated c-BN (111) clusters. *Physical Review B, 60*, 16065–16072.

Matsumoto, S., Nishida, N., Akashi, K., & Sugai, K. (1996). Preparation of BN films by rf thermal plasma chemical vapour deposition. *Journal of Materials Science, 31*, 713–720.

Matsumoto, S., & Zhang, W. J. (2000). High-rate deposition of high-quality, thick cubic boron nitride films by bias-assisted DC jet plasma chemical vapor deposition. *Japanese Journal of Applied Physics, 39*, L442–L444.

Matsumoto, S., & Zhang, W. J. (2001a). CBN synthesis by bias assisted plasma jet CVD in an Ar-N-2-BF3-H-2 gas system. *New Diamond Frontier Carbon Technology, 11*, 1–10.

Matsumoto, S., & Zhang, W. J. (2001b). Synthesis of boron nitride films by microwave plasma chemical vapor deposition in fluorine-containing gases. *Japanese Journal of Applied Physics, 40*, L570–L572.

Matsumoto, S., & Zhang, W. J. (2001c). The introducing of fluorine into the deposition of BN: a successful method to obtain high-quality, thick cBN films with low residual stress. *Diamond and Related Materials, 10*, 1868–1874.

McCarty, F., & Barbour, J. C. (1999). Room temperature growth of cubic boron nitride. *Applied Physics Letters, 74*, 1552–1554.

McKenzie, D. R. (1993). Generation and applications of compressive stress induced by low energy ion beam bombardment. *Journal of Vacuum Science & Technology, B, 11*, 1928–1935.

McKenzie, D. R., Mcfall, W. D., Sainty, W. G., Davis, C. A., & Collins, R. E. (1993). Compressive stress induced formation of cubic boron nitride. *Diamond and Related Materials, 2*, 970–976.

Mckenzie, D. R., McFall, W. D., Smith, H., Higgins, B., Boswell, R. W., Durandet, A., et al. (1995). High pressure phases produced by low energy ion implantation with reference to cubic boron nitride. *Nuclear Instruments & Methods in Physical Research B, 106*, 90–95.

Meng, X. M., Zhang, W. J., Chan, C. Y., Lee, C. S., Bello, I., & Lee, S. T. (2006). Surface microstructure analysis of cubic boron nitride films by transmission electron microscopy. *Applied Physics Letters, 88*, 031904.

Mineta, S., Kohata, M., Yasunaga, N., & Kikuta, Y. (1990). Preparation of cubic boron nitride film by CO_2 laser physical vapour deposition with simultaneous nitrogen ion supply. *Thin Solid Films, 189*, 125–138.

Mirkarimi, P. B., Mecarty, K. F., & Medlin, D. L. (1997). Review of advances in cubic boron nitride film synthesis. *Materials Science and Engineering, R, 21*, 47–100.

Mirkarimi, P. B., McCarty, K. F., Medlin, D. L., Wolfer, W. G., Friedmann, T. A., Klaus, E. J., et al. (1994). On the role of ions in the formation of cubic boron nitride films by ion-assisted deposition. *Journal of Materials Research, 9*, 2925–2938.

Mirkarimi, P. B., Medlin, D. L., & McCarty, K. F. (1995). Growth of cubic BN films on β-SiC by ion-assisted pulsed-laser deposition. *Applied Physics Letters, 66*, 2813–2815.

Mirkarimi, P. B., Medlin, D. L., McCarty, K. F., Dibble, D. C., Clift, W. M., Knapp, J. A., et al. (1997). The synthesis, characterization, and mechanical properties of thick, ultrahard cubic boron nitride films deposited by ion-assisted sputtering. *Journal of Applied Physics, 82*, 1617–1625.

Mishima, O., & Era, K. (2000). In Y. Kumashilo (Ed.), *Electronic refractory materials* (pp. 495). New York: Marcel Dekker.

Mishima, O., Era, K., Tanaka, J., & Yamaoka, S. (1988). Ultraviolet light-emitting diode of a cubic boron nitride pn junction made at high pressure. *Applied Physics Letters, 53*, 962–964.

Mishima, O., Tanaka, J., Yamaoka, S., & Fukunaga, O. (1987). High-temperature cubic boron nitride p-n junction diode made at high pressure. *Science, 238*, 181–183.

Mishima, O., Yamaoka, S., & Fukunaga, O. (1987). Crystal growth of cubic boron nitride by temperature difference method at 55 kbar and 1800 °C. *Journal of Applied Physics, 61*, 2822–2825.

Miyata, N., Moriki, K., Mishima, O., Fujisawa, M., & Hattori, T. (1989). Optical constants of cubic boron nitride. *Physical Review B, 40*, 12028–12029.

Miyoshi, K., Buckley, D. H., Pouch, J. J., Alterovitz, S. A., & Sliney, H. E. (1987). Mechanical strength and tribological behavior of ion-beam-deposited boron-nitride films on non-metallic substrates. *Surface and Coatings Technology, 33*, 221–233.

Motesharei, K., & Myles, D. C. (1998). Molecular recognition on functionalized self-assembled monolayers of alkanethiols on gold. *Journal of American Chemical Society, 120*, 7328–7336.

Murakawa, M., & Watanabe, S. (1990). The synthesis of cubic BN films using a hot cathode plasma discharge in a parallel magnetic-field. *Surface and Coatings Technology, 43/44*, 128–136.

Nishiyama, S., Kuratani, N., Ebe, A., & Ogata, K. (1993). The synthesis and properties of BN films prepared by ion irradiation and vapor-deposition. *Nuclear Instruments and Methods, B, 80–81*, 1485–1488.

Nose, K., Oba, H., & Yoshida, T. (2006). Electric conductivity of boron nitride thin films enhanced by in situ doping of zinc. *Applied Physics Letters, 89*, 112124.

Nose, K., & Yoshida, T. (2007). Semiconducting properties of zinc-doped cubic boron nitride thin films. *Journal of Applied Physics, 102*, 063711.

Okamoto, M., Yokoyama, H., & Osaka, Y. (1990). Formation of cubic boron nitride film on Si with boron buffer layers. *Japanese Journal of Applied Physics, 29*(Part 1), 930–933.

Ooi, N., & Adams, J. B. (2005). Ab initio studies of the cubic boron nitride (110) surface. *Surface Science, 574*, 269–286.

Paiano, P., Prete, P., Loverqine, N., & Mancini, A. M. (2006). Size and shape control of GaAs nanowires grown by metalorganic vapor phase epitaxy using tertiarybutylarsine. *Journal of Applied Physics, 100*, 094305.

Parayanthal, P., & Pollak, F. H. (1984). Raman scattering in alloy semiconductors: "spatial correlation" model. *Physical Review Letters, 52*, 1822–1825.

Pascallon, J., Stambouli, V., Ilias, S., Bouchier, D., Nouet, G., Silva, F., et al. (1999). Microstructure of c-BN thin films deposited on diamond films. *Diamond and Related Materials, 8*, 325–330.

Persson, A. I., Larsson, M. W., Stenstrom, S., Ohlsson, B. J., Samuelson, L., & Wallenberg, L. R. (2004). Solid-phase diffusion mechanism for GaAs nanowire growth. *Nature Materials, 3*, 677–681.

Reinke, S., Kuhr, M., & Kulisch, W. (1994). Mechanisms in ion induced c-BN growth. *Diamond and Related Materials, 3*, 341–345.

Reinke, S., Kuhr, M., Kulisch, W., & Kassing, R. (1995). Recent results in cubic boron nitride deposition in light of the sputter model. *Diamond and Related Materials, 4*, 272–283.

Resendiz, M. J. E., Noveron, J. C., Disteldorf, N. H., Fischer, S., & Stang, P. J. (2004). A self-assembled supramolecular optical sensor for Ni(II), Cd(II), and Cr(III). *Organic Letters, 6*, 651–653.

Robertson, J. (1996). Deposition mechanism of cubic boron nitride. *Diamond and Related Materials, 5*, 519–524.

Ronning, C., Dreher, E., Feldermann, Gross, M., Sebastian, M., & Hofsäss, H. (1997). Electrical properties and thermal stability of ion beam deposited BN thin films. *Diamond and Related Materials, 6*, 1129–1134.

Ronning, C., Feldermann, H., & Hofsäss, H. (2000). Growth, doping and applications of cubic boron nitride thin films. *Diamond and Related Materials, 9*, 1767–1773.

Sachdev, H., Haubner, R., Nöth, H., & Lux, B. (1997). Investigation of the c-BN/h-BN phase transformation at normal pressure. *Diamond and Related Materials, 6*, 286–292.

Saitoh, H., Morino, H., & Ichinose, Y. (1993). Deposition rate of boron nitride films using plasma jet technique. *Japanese Journal of Applied Physics, 32* (Part 2), L1684–L1687.

Sanjurjo, J. A., López-Cruz, E., Vogl, P., & Cardona, M. (1983). Dependence on volume of the phonon frequencies and their effective charges of several III-V semiconductors. *Physical Review B, 28*, 4579–4584.

Sei, H., Akaishi, M., Kanda, H., Osawa, T., & Yamaoka, S. (1991). In R. Messier (Ed.), *Proc. new diamond science and technology* (pp. 1057). Pittsburgh: Materials Research Society.

Seitz, F., & Koehler, J. S. (1957). In *Progress in solid state physics, Vol. 2*, (pp. 30). New York: Academic Press.

Shi, S. C., Chen, C. F., Chattopadhyay, S., Lan, Z. H., Chen, K. H., & Chen, L. C. (2005). Growth of single-crystalline wurtzite aluminum nitride nanotips with a self-selective apex angle. *Advanced Functional Materials, 15*, 781–786.

Shipilo, V. B., Shishonok, E. M., Zaitsev, A. M., Melnikov, A. A., & Olekhnovich, A. I. (1988). Influence of high-pressure on cathodoluminescence of cubic boron-nitride. *Physica Status Solidi A, 108*, 431–436.

Sokolowski, M. (1979). Deposition of wurtzite type boron-nitride layers by reactive pulse plasma crystallization. *Journal of Crystal Growth, 46*, 136–138.

Solozhenko, V. L. (1988). On the phase-diagram of boron-nitride. *Doklady Physical Chemistry, 301*, 592–594.

Solozhenko, V. L. (1992). A new boron nitride phase diagram and chemical interaction in the b-n system at high pressures. *High Pressure Research, 9*, 140–143.

Solozhenko, V. L. (1994). Phase diagram of BN. In H. J. Edgar (Ed.), *Properties of group III nitrides* (pp. 43–64). London: INSPEC, the Institution of Electrical Engineers.

Solozhenko, V. L., & Leonidov, V. Ya (1988). Thermodynamics of the conversion of graphitic modification of boron-nitride to cubic. *Russian Journal of Physical Chemistry, 62*, 1646–1647.

Solozhenko, V. L., Slutsky, A. B., & Ignatiev, Yu. A. (1992). *Journal of Superhard Materials, 14*, 61.

Solozhenko, V. L., Turkevich, V. Z., & Holzapfel, W. B. (1999). Refined phase diagram of boron nitride. *Journal of Physical Chemistry B, 103*, 2903–2905.

Soltani, A., Barkad, H. A., Mattalah, M., Benbakhti, B., De Jaeger, J. C., Chong, Y. M., et al. (2008). 193 nm deep-ultraviolet solar-blind cubic boron nitride based photodetectors. *Applied Physics Letters, 92*, 053501.

Steinhoff, G., Purrucker, O., Tanaka, M., Stutzmann, M., & Eickhoff, M. (2003). AlxGa1-xN – a new material system for biosensors. *Advanced Functional Materials, 13*, 841–846.

Sumiya, H., Uesaka, S., & Satoh, S. (2000). Mechanical properties of high purity polycrystalline cBN synthesized by direct conversion sintering method. *Journal of Materials Science, 35*, 1181–1186.

Takamura, Y. Y., Tsuda, O., Ichinose, H., & Yoshida, T. (1999). Atomic-scale structure at the nucleation site of cubic boron nitride deposited from the vapor phase. *Physical Review B, 59*, 10351–10355.

Taniguchi, T., Akaishi, M., & Yamaoka, S. (1996). Mechanical properties of polycrystalline translucent cubic boron nitride as characterized by the Vickers indentation method. *Journal of the American Ceramic Society, 79*, 547–549.

Taniguchi, T., Koizumi, S., Watanabe, K., Sakaguchi, I., Sekiguchi, T., & Yamaoka, S. (2003). High pressure synthesis of UV-light emitting cubic boron nitride single crystals. *Diamond and Related Materials, 12*, 1098–1102.

Taniguchi, T., Tanaka, J., Mishima, O., Ohsawa, T., & Yamaoka, S. (1993). High pressure synthesis of semiconducting Be-doped polycrystalline cubic boron nitride and its electrical properties. *Applied Physics Letters, 62*, 576–578.

Taniguchi, T., Teraji, T., Koizumi, S., Watanabe, K., & Yamaoka, S. (2002). Appearance of n-type semiconducting properties of cBN single crystals grown at high pressure. *Japanese Journal of Applied Physics, 41*(Part 2), L109–L111.

Taylor, C. A., Brown, S. W., Subramaniam, V., Kidner, S., Rand, S. C., & Clarke, R. (1994). Observation of near-band-gap luminescence from boron nitride films. *Applied Physics Letters, 65*, 1251–1253.

Tomokage, H., Nomura, N., Taniguchi, T., & Ando, T. (2000). Electron-beam-induced currents on beryllium-doped cubic boron nitride single crystal. *Diamond and Related Materials, 9*, 605–608.

Ullmann, J., Baglin, J. E. E., & Kellock, A. J. (1998). Effects of MeV ion irradiation of thin cubic boron nitride films. *Journal of Applied Physics, 83*, 2980–2987.

Ulrich, S., Schwan, J., Donner, W., & Ehrhardt, H. (1996). Knock-on subplantation-induced formation of nanocrystalline c-BN with r.f. magnetron sputtering and r.f. argon ion plating. *Diamond and Related Materials, 5*, 548–551.

van der Veen, N. J., Flink, S., Deij, M. A., Egberink, R. J. M., van Veggel, F. C. J. M., & Reinhoudt, D. N. (2000). Monolayer of a Na^+-selective fluoroionophore on glass: connecting the fields of monolayers and optical detection of metal ions. *Journal of American Chemical Society, 122*, 6112–6113.

Vel, L., Demazeau, G., & Etourneau, J. (1991). Cubic boron nitride: synthesis, physicochemical properties and applications. *Materials Science and Engineering B, 10*, 149–164.

Veprek, S., & Argon, A. S. (2001). Mechanical properties of superhard nanocomposites. *Surface and Coatings Technology, 146–147*, 175–182.

Wada, T., & Yamashita, N. (1992). Formation of cBN films by ion-beam assisted deposition. *Journal of Vacuum Science & Technology, A, 10*, 515–520.

Wang, C. X., Liu, Q. X., & Yang, G. W. (2004). A nanothermodynamic analysis of cubic boron nitride nucleation upon chemical vapor deposition. *Chemical Vapor Deposition, 10*, 280–283.

Wang, Q., Wang, Z. L., Li, J. J., Huang, Y., Li, Y. L., Gu, C. Z., et al. (2006). Field electron emission from individual diamond cone formed by plasma etching. *Applied Physics Letters, 89*, 063105.

Wang, C. X., & Yang, G. W. (2005). Thermodynamics of metastable phase nucleation at the nanoscale. *Materials Science and Engineering, R, 49*, 157–202.

Wang, C. X., Yang, G. W., Zhang, T. C., Liu, H. W., Han, Y. H., Luo, J. F., et al. (2003). High-quality heterojunction between p-type diamond single-crystal film and n-type cubic boron nitride bulk single crystal. *Applied Physics Letters, 83*, 4854–4856.

Wang, C. X., Yang, Y. H., Liu, Q. X., & Yang, G. W. (2004). Nucleation thermodynamics of cubic boron nitride upon high-pressure and high-temperature supercritical fluid system in nanoscale. *Journal of Physical Chemistry B, 108*, 728–731.

Watanabe, S., Miyake, S., Jin, M., & Murakawa, M. (2004). Frictional behavior of cubic BN films sliding against DLC. *Tribology International, 37*, 923–927.

Watanabe, S., Miyake, S., & Murakawa, M. (1991). Tribological properties of cubic, amorphous and hexagonal boron-nitride films. *Surface and Coatings Technology, 49*, 406–410.

Watanabe, S., Miyake, S., & Murakawa, M. (1995). Tribological behavior of cubic boron nitride film sliding against diamond. *Journal of Tribology, 117*, 629–633.

Weber, A., Bringmann, U., Nikulski, R., & Klages, C.-P. (1993). Electron cyclotron resonance plasma deposition of cubic boron nitride using n-trimethylborazine. *Surface and Coatings Technology, 60*, 493–497.

Weng, J., Xue, J., Wang, J., Ye, J.S., Cui, H.F., Sheu, F.S., et al. (2005). Gold-cluster sensors formed electrochemically at boron-doped-diamond electrodes: detection of dopamine in the presence of ascorbic acid and thiols. *Advanced Functional Materials*, 15, 639–647.

Wentorf, R. H., Jr (1957). Cubic form of boron nitride. *Journal of Chemical Physics, 26*, 956.

Wentrof, R. H., Jr (1962). Preparation of semiconducting cubic boron nitride. *Journal of Chemical Physics, 36*, 1990–1991.

Wenzel, R. N. (1949). Surface roughness and contact angle. *Journal of Physical and Colloid Chemistry, 53*, 1466–1467.

Widmayer, P., Ziemann, P., Ulrich, S., & Ehrhardt, H. (1997). Phase stability and stress relaxation effects of cubic boron nitride thin films under 350 keV ion irradiation. *Diamond and Related Materials, 6*, 621–625.

Will, G., Nover, G., & von der Gönna, J. (2000). New experimental results on the phase diagram of boron nitride. *Journal of Solid State Chemistry, 154*, 280–285.

Yamada, Y., Tsuda, O., & Yoshida, T. (1998). Microstructure and nanomechanical properties of cubic boron nitride films prepared by bias sputter deposition. *Thin Solid Films, 316*, 35–39.

Yamamoto, K., Keunecke, M., & Bewilogua, K. (2000). Adhesion improvement of cBN film by b-c-n gradient layer system. *New Diamond and Frontier Carbon Technology, 10*, 225–230.

Yamamoto, K., Keunecke, M., Bewilogua, K., Czigany, Z., & Hultman, L. (2001). Structural features of thick c-boron nitride coatings deposited via a graded b-c-n interlayer. *Surface and Coatings Technology, 142*, 881–888.

Yang, N. J., Uetsuka, H., Osawa, E., & Nebel, C. E. (2008). Vertically aligned diamond nanowires for DNA sensing. *Angewandte Chemie International Edition, 47*, 5183–5185.

Yang, H. S., Iwamoto, C., & Yoshida, T. (2007). Direct nucleation of cubic boron nitride on silicon substrate. *Diamond and Related Materials, 16*(64), 2–644.

Yang, H. S., & Yoshida, T. (2005). Mechanical properties of boron nitride films prepared by plasma-enhanced chemical vapor deposition. *Surface and Coatings Technology, 200*, 984–987.

Yang, W., Baker, S. E., Butler, J. E., Lee, C. S., Russell, J. N., Jr., Shang, L., et al. (2005). Electrically addressable biomolecular functionalization of conductive nanocrystalline diamond thin films. *Chemistry of Materials, 17*, 938–940.

Yang, W. S., Auciello, O., Butler, J. E., Cai, W., Carlisle, J. A., Gerbi, J. E., et al. (2002). DNA-modified nanocrystalline diamond thin-films as stable, biologically active substrates. *Nature Materials, 1*, 253–257.

Yin, H., Boyen, H.-G., Ziemann, P., Dohuard, B., Houssiau, L., Renaux, F., et al. (2008). Purity of epitaxial cubic boron nitride films on (001) diamond – a prerequisite for their doping. *Diamond and Related Materials, 17*, 276–282.

Yin, H., Pongrac, I., & Ziemann, P. (2008). Electronic transport in heavily Si doped cubic boron nitride films epitaxially grown on diamond (001). *Journal of Applied Physics, 104*, 023703.

Ying, J., Zhang, X. W., Fan, Y. M., Tan, H. R., & Yin, Z. G. (2010). Effects of silicon incorporation on composition, structure and electric conductivity of cubic boron nitride thin films. *Diamond and Related Materials, 19*, 1371–1376.

Yoshida, H., Urushido, T., Miyake, H., & Hiramatsu, K. (2001). Formation of GaN self-organized nanotips by reactive ion etching. *Japanese Journal of Applied Physics, 40*, L1301–L1304.

Yoshikawa, M., Mori, Y., Maegawa, M., Katagiri, G., Ishida, H., & Ishitani, A. (1993). Raman scattering from diamond particles. *Applied Physics Letters, 62*, 3114–3116.

Yu, J., & Matsumoto, S. (2003). Controlled growth of large cubic boron nitride crystals by chemical vapor deposition. *Diamond and Related Materials, 12*, 1539–1543.

Yu, J., Ong, H. C., Wong, K. Y., Lau, W. M., & Matsumoto, S. (2006). Morphology dependence of cathodoluminescence from cubic boron nitride films deposited by chemical vapor deposition. *Journal of Applied Physics, 99*, 124915.

Yu, W. J., Lau, W. M., Chan, S. P., Liu, Z. F., & Zheng, Q. Q. (2003). Ab initio study of phase transformations in boron nitride. *Physical Review B, 67*, 014108.

Zhang, J. M., Ma, F., Xu, K. W., & Xin, X. T. (2003). Anisotropy analysis of the surface energy of diamond cubic crystals. *Surface and Interface Analysis, 35*, 805–809.

Zhang, W. J., Bello, I., Lifshitz, Y., & Lee, S. T. (2003). Recent advances in cubic boron nitride deposition. *MRS Bulletin, 28*, 184–188.

Zhang, W. J., Bello, I., Lifshitz, Y., Chan, K. M., Meng, X. M., Wu, Y., et al. (2004a). Epitaxy on diamond by chemical vapor deposition: a route to high-quality cubic boron nitride for electronic applications. *Advanced Materials, 16*, 1405–1408.

Zhang, W. J., Bello, I., Lifshitz, Y., Chan, K. M., Wu, Y., Chan, C. Y., et al. (2004b). Thick and adherent cubic boron nitride films grown on diamond interlayers by fluorine-assisted chemical vapor deposition. *Applied Physics Letters, 85*, 1344–1346.

Zhang, W. J., Chan, C. Y., Chan, K. M., Bello, I., Lifshitz, Y., & Lee, S. T. (2003). The deposition of high-quality cubic boron nitride films by ECR-enhanced microwave plasma CVD. *Applied Physics A, 76*, 953–955.

Zhang, W. J., Chan, C. Y., Meng, X. M., Fung, M. K., Bello, I., Lifshitz, Y., et al. (2005). The mechanism of chemical vapor deposition of cubic boron nitride films from fluorine-containing species. *Angewandte Chemie International Edition, 44*, 4749–4753.

Zhang, W. J., Chong, Y. M., Bello, I., & Lee, S. T. (2007). Nucleation, growth and characterization of cubic boron nitride (cBN) films. *Journal of Physics D, 40*, 6159–6174.

Zhang, W. J., Jiang, X., & Matsumoto, S. (2001). High-quality, faceted cubic boron nitride films grown by chemical vapor deposition. *Applied Physics Letters, 79*, 4530–4532.

Zhang, W. J., Kanda, H., & Matsumoto, S. (2002). Cathodoluminescence of cubic boron nitride films deposited by chemical vapor deposition. *Applied Physics Letters, 81*, 3356–3358.

Zhang, W. J., & Matsumoto, S. (2000a). Influence of experiment parameters on the growth of cBN films by bias-assisted direct current jet plasma chemical vapor deposition. *Journal of Materials Research, 15*, 2677–2683.

Zhang, W. J., & Matsumoto, S. (2000b). The effects of DC bias voltage on the crystal size and crystal quality of cBN films. *Applied Physics A, 71*, 469–472.

Zhang, W. J., & Matsumoto, S. (2000c). The roles of hydrogen and fluorine in the deposition of cubic boron nitride films in Ar-N_2-BF_3-H_2 system. *Chemical Physics Letters, 330*, 243–248.

Zhang, W. J., & Matsumoto, S. (2001a). Investigations of crystallinity and residual stress of cubic boron nitride films by Raman spectroscopy. *Physical Review B, 63*, 073201.

Zhang, W. J., & Matsumoto, S. (2001b). Raman scattering of cubic boron nitride films deposited from the low-pressure gas phase. *Journal of Materials Research, 16*, 3430–3442.

Zhang, W. J., Matsumoto, S., Kurashima, K., & Bando, Y. (2001). Structure analysis of cBN films prepared by DC jet plasma CVD from an Ar-N_2-BF_3-H_2 gas system. *Diamond and Related Materials, 10*, 1881–1885.

Zhang, W. J., Matsumoto, S., Li, Q., Bello, I., & Lee, S. T. (2002). Growth behavior of cubic boron nitride films in a two-step process changing bias voltage, gas composition, and substrate temperature. *Advanced Functional Materials, 12*, 250–254.

Zhang, W. J., Meng, X. M., Chan, C. Y., Wu, Y., Bello, I., & Lee, S. T. (2003). Oriented single-crystal diamond cones and their arrays. *Applied Physics Letters, 82*, 2622–2624.

Zhang, W. J., Meng, X. M., Chan, C. Y., et al. (2005). Interfacial study of cubic boron nitride films deposited on diamond. *Journal of Physical Chemistry B, 109*, 16005.

Zhang, W. J., Tansho, M., Matsumoto, S., & Mori, T. (2001). B-11 and B-10 magic-angle spinning nuclear magnetic resonance studies of cubic boron nitride films prepared by plasma chemical vapor deposition. *Journal of Applied Physics, 89*, 1734–1737.

Zhang, W. J., Wu, Y., Wong, W. K., Meng, X. M., Chan, C. Y., Bello, I., et al. (2003). Structuring nanodiamond cone arrays for improved field emission. *Applied Physics Letters, 83*, 3365–3367.

Zhang, X. W., Boyen, H.–G., Deyneka, N., et al. (2003). Epitaxy of cubic boron nitride on (001)-oriented diamond. *Nature Materials, 2*, 312–315.

Zhou, X. T., Sham, T. K., Chan, C. Y., Zhang, W. J., Bello, I., Lee, S. T., et al. (2006a). Preferable orientation of turbostratic BN basal planes from an X-ray absorption study. *Journal of Materials Research, 21*, 147–152.

Zhou, X. T., Sham, T. K., Chan, C. Y., Zhang, W. J., Bello, I., Lee, S. T., et al. (2006b). Effect of substrate surface on the structure and electronic properties of cubic boron nitride films. *Journal of Applied Physics, 100*, 014909.

Zhou, X. T., Sham, T. K., Zhang, W. J., Chan, C. Y., Bello, I., Lee, S. T., et al. (2006). Cubic phase content and structure of BN films from an X-ray absorption study. *Analytical Chemistry, 78*, 6314–6319.

Zhou, X. T., Sham, T. K., Zhang, W. J., Chan, C. Y., Bello, I., Lee, S. T., et al. (2007). X-ray absorption studies on cubic boron nitride thin films. *Journal of Applied Physics, 101*, 013710.

Zhou, Y. B., Yang, Y., Liu, W. M., Ye, Q., He, B., Zou, Y. S., et al. (2010). Preparation of superhydrophobic nanodiamond and cubic boron nitride films. *Applied Physics Letters, 97*, 133110.

Zhou, Y. L., Zhi, J. F., Wang, P. F., Chong, Y. M., Zou, Y. S., Zhang, W. J., et al. (2008). Surface functionalization of cubic boron nitride films for biological sensing applications. *Applied Physics Letters, 92*, 163105.

Ziebert, C., Ye, J., Sell, K., & Ulrich, S. (2006). High-resolution depth profiling of mechanical properties of thick cubic boron nitride coatings. *Surface and Coatings Technology, 200*, 6454–6458.

Zimmerman, R., Basabe-Desmonts, L., van der Baan, F., Reinhoudt, D. N., & Crego-Calama, M. (2005). A combinatorial approach to surface-confined cation sensors in water. *Journal of Materials Chemistry, 15*, 2772–2777.

Zou, Y. S., Yang, Y., Zhang, W. J., Chong, Y. M., He, B., Bello, I., et al. (2008). Fabrication of diamond nanopillars and their arrays. *Applied Physics Letters, 92*, 053105.

3.25 High-Pressure Synthesis of Novel Superhard Phases

Vladimir L. Solozhenko, LSPM–CNRS, Université Paris 13, Villetaneuse, France

3.25.1 Introduction

Superhard materials (usually compounds of light elements such as boron, carbon, nitrogen and oxygen) can be defined as having microhardness exceeding 40 GPa. In addition to high hardness, they usually possess other unique properties such as compressional strength, shear resistance, large bulk moduli, high melting temperatures and chemical inertness. This combination of properties makes these materials highly desirable for a number of industrial applications.

Recent achievements in search for novel superhard materials indicate that synthesis of phases with hardness exceeding that of diamond (Knoop hardness 116–130 GPa for single-crystal and 120–145 GPa for nanocrystalline diamond; Sumiya & Irifune, 2004; Sumiya, Toda, & Satoh, 1997; respectively) is unlikely. Rather than harder, one should consider the possibility to synthesize materials that are more useful i.e. thermally and chemically more stable than diamond, and harder than cubic boron nitride (cBN) (DeVries, 1972; Edgar, 1994) and boron suboxide (B_6O) (Kurakevych & Solozhenko, 2011).

In this chapter recent results on high pressure–high temperature synthesis of novel superhard phases in the B–C–N–O system (**Figure 1**) are reviewed.

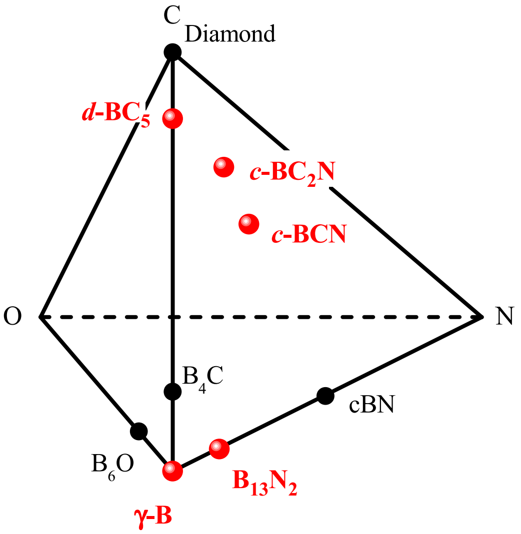

Figure 1 Superhard phases of the B–C–N–O quaternary system. Novel phases are shown in red.

3.25.2 Synthesis of New Boron Allotrope, Orthorhombic γ-B28

Among 16 allotropes of boron mentioned in the literature, only three phases seem to correspond to the pure element, namely, α-B_{12} rhombohedral low-temperature, β-B_{106} rhombohedral high-temperature low-pressure, and t-B_{192} tetragonal high-temperature high-pressure phases (Oganov & Solozhenko, 2009; Oganov, Solozhenko, Gatti, Kurakevych, & Le Godec, 2011). Recently, a new high-pressure phase of boron, orthorhombic γ-B28, has been synthesized from crystalline β-B_{106} in a multianvil press at pressures from 12 to 20 GPa and temperatures from 1800 to 2000 K. The structure of this phase has been established by powder X-ray diffraction and ab initio calculations (Oganov et al., 2009a). Later, Zarechnaya et al. (2009, 2010) grew micron-sized single-crystals of γ-B28 from boron solutions in metal melts at 12 GPa and confirmed the crystal structure of this phase.

At ambient conditions γ-B28 has an orthorhombic structure (space group *Pnnm*) with unit cell parameters $a = 5.054(2)$ Å, $b = 5.612(3)$ Å and $c = 6.966(5)$ Å (Oganov et al., 2009a). The structure can be represented as a NaCl-type arrangement of two types of boron clusters, B_{12} icosahedra and B_2 pairs (**Figure 2**). Although the chemical bonding in γ-B28 is predominantly covalent, there is a significantly high charge transfer (of about 0.5) from B_2 to B_{12} clusters (Oganov et al., 2009a, 2009b) that is very unusual for elemental crystals. Recently, the nature of chemical bonding in γ-boron has been explicitly discussed by Macchi (2011).

A 300-K equation of state of polycrystalline γ-B28 has been measured by Le Godec, Kurakevych, Munsch, Garbarino, and Solozhenko (2009) in the neon pressure medium up to 65 GPa using a diamond anvil cell (DAC) and powder X-ray diffraction with synchrotron radiation. A fit of the experimental p–V data to the Vinet equation of state yields the value of the bulk modulus, B_0, of 237 GPa with the pressure derivative $B_0{}' = 2.7$. These values agree well with theoretical calculations at the Density Functional Theory - Generalized Gradient Approximation (DFT-GGA) level ($B_0 = 241$ GPa and $B_0{}' = 2.34$; Isaev et al., 2011) and single-crystal X-ray diffraction experiments up to 40 GPa ($B_0 = 237$ GPa and $B_0{}' = 2.5$; Isaev et al., 2011). Thus, γ-B28 is the densest and least compressible form of elemental boron (Le Godec, 2011).

Bulk polycrystalline samples of γ-B28 have Vickers hardness of 50 GPa (Solozhenko, Kurakevych, & Oganov, 2008) (**Figure 3**), which is higher than the hardness of other boron allotropes and agrees well with the 48.8 GPa value calculated by Mukhanov, Kurakevych, and Solozhenko (2009, 2010) within the thermodynamic model of hardness. The Vickers hardness value of 58 GPa reported by Zarechnaya et al. (2009) seems to be an overestimation.

The discovery of γ-B28 provided the missing piece of a puzzle of the phase diagram of boron (Oganov et al., 2009a) (**Figure 4**). The thermodynamic stability region of this phase is larger than those of all known boron polymorphs combined, however, the upper pressure limit of γ-B28 stability remains to be investigated. The existence of a α-Ga-type metallic phase above 74 GPa (Segall & Arias, 2003) was theoretically confirmed by Oganov et al. (2009a), except that the pressure of this phase transition was shifted to a higher value, 89 GPa, by the presence of γ-B28.

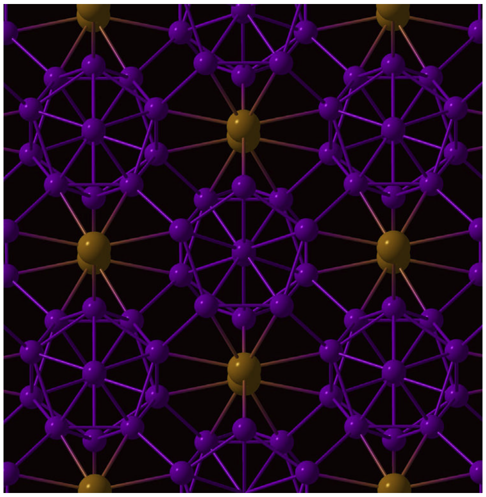

Figure 2 Crystal structure of γ-B_{28} (Oganov et al., 2009a). Two oppositely charged sublattices are marked by different colors (cationic, orange; anionic, violet).

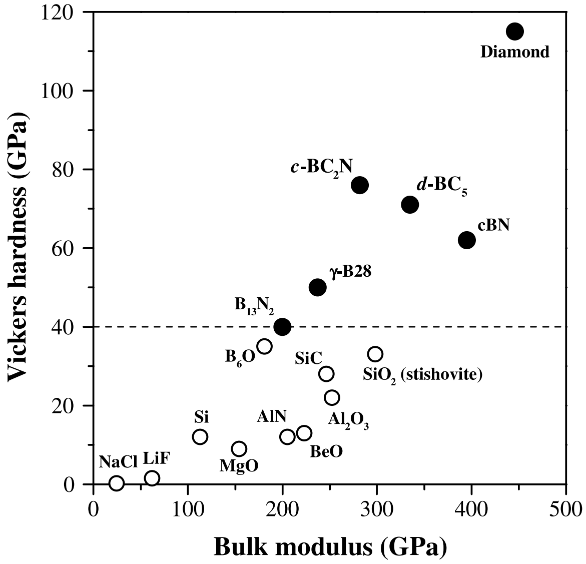

Figure 3 Vickers hardness versus bulk modulus for superhard phases of the B–C–N–O quaternary system (black symbols) and some other materials.

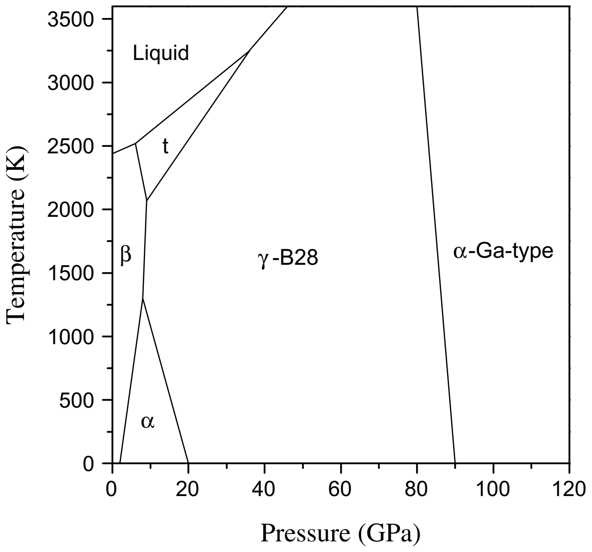

Figure 4 p–T phase diagram of boron (Oganov et al., 2009a). α, β and t are α-B_{12}, β-B_{106} and t-B_{192} boron allotropes, respectively.

Thus, a new high-pressure phase of boron, γ-B28 with the highest hardness (Solozhenko, Kurakevych, & Oganov, 2008) and bulk modulus (Le Godec et al., 2009) among the known boron crystalline allotropes was predicted to be stable in a wide p–T range (Oganov et al., 2009a).

3.25.3 New Superhard Binary B–C and B–N Phases

3.25.3.1 Synthesis of Diamond-like BC_5

Using a laser-heated DAC a new superhard phase, diamond-like BC_5 (d-BC_5), has been recently synthesized by Solozhenko, Kurakevych, Andrault, Le Godec, and Mezouar (2009) by direct phase transformation of graphite-like B–C solid solutions at pressures above 25 GPa and temperatures of about 2200 K. Structure of the phase has been studied by angle-dispersive X-ray diffraction with synchrotron radiation, high-resolution transmission electron microscopy and electron energy loss spectroscopy (EELS). The structure of diamond-like BC_5 is closely

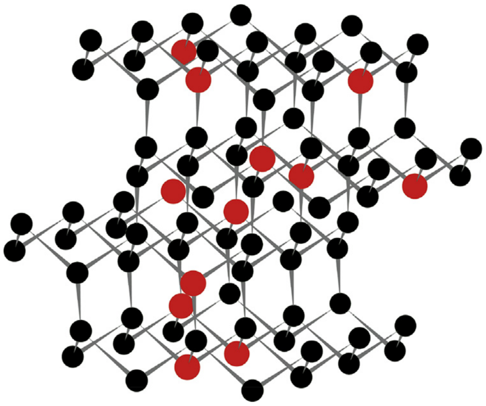

Figure 5 Crystal structure of diamond-like BC_5. The red and black balls represent the boron and carbon atoms, respectively. The boron atoms are randomly distributed allover the diamond-like lattice.

related to diamond (**Figure 5**). The lattice parameter at ambient conditions $a = 3.635(8)$ Å, is larger than that of diamond (3.5667 Å, JCPDS No. 6-0675), but is in reasonable agreement with the 3.646 Å value expected from ideal mixing (Vegard's law) between diamond and "diamond-like boron" ($a = 4.04$ Å corresponding to the B–B bond length of 1.75 Å; Emsley, 1991) as well as with theoretical predictions by Lowther (2005) (**Figure 6**). This is consistent with the fact that B–C bonds are longer than C–C and B–N bonds due to the weakened bonding caused by the electron-deficient character of the boron atoms (Emsley, 1991). The Electron Energy Loss Spectroscopy (EELS) elemental mapping shows a homogeneous distribution of boron and carbon atoms allover the crystal lattice, while the valence state mapping reveals homogeneity of the atomic hybridization (sp^3 for both B and C atoms); thus proving the existence of *d*-BC_5 as an individual phase.

The relatively narrow (~200 K) temperature range of the *d*-BC_5 formation clearly indicates the metastable character of this phase, e.g. its slight overheating leads to the phase segregation into more thermodynamically stable boron-doped diamond (~2 at% B according to the lattice parameter) and boron carbide B_4C. However, at ambient pressure *d*-BC_5 has been found to be more thermally stable than polycrystalline diamond.

The 300-K equation of state of diamond-like BC_5 has been measured up to 40 GPa in three independent runs (Solozhenko, Kurakevych, Andrault, et al., 2009). The fitted parameters are $B_0 = 335$ GPa and $B_0' = 4.5$, with the zero-pressure cell volume $V_0 = 48.02$ Å^3. Among superhard phases, the bulk modulus of diamond-like BC_5 is exceeded only by the bulk moduli of diamond (446 GPa; Gillet, Fiquet, Daniel, & Reynard, 1999) and cBN (395 GPa; Datchi, Dewaele, Le Godec, & Loubeyre, 2007).

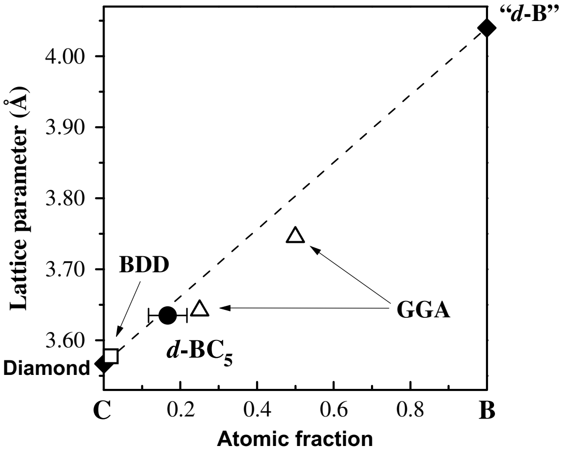

Figure 6 Lattice parameters of boron substituted diamonds versus boron content. The dashed line represents Vegard's law, while solid circle with error bar shows the value for diamond-like BC_5 (Solozhenko, Kurakevych, Andrault, et al., 2009) in comparison with boron-doped diamond with 1.8 at% B (open square, Solozhenko, Dubrovinskaia, & Dubrovinsky, 2004) and theoretical data (triangles, Lowther, 2005).

Well-sintered millimeter-sized bulks of nanocrystalline diamond-like BC_5, have been synthesized using multianvil press and comprehensively studied by various characterization techniques (Solozhenko, Kurakevych, Andrault, et al., 2009). The material is semiconductive ($\sim 0.6\ \Omega\cdot\mathrm{m}$ at room temperature) and occurs as nanocrystalline aggregates with clearly visible but very small grains with an average size of 10–15 nm. The calculated Vickers hardness of diamond-like BC_5 under loads from 1 to 20 N decreases with the load and reaches the asymptotic value at 2–3 N. As recommended for hard and brittle materials (Brazhkin et al., 2004), the sample hardness was estimated in the asymptotic-hardness region as $H_V = 71$ GPa (**Figure 3**). This value is in excellent agreement with the values predicted in the framework of the thermodynamic model of hardness, i.e. 70.6 GPa (Mukhanov, Kurakevych, & Solozhenko, 2008a, 2008b; Mukhanov et al., 2009) and on the basis of microscopic hardness model, i.e. 70 GPa (Li et al., 2010). Under the 10-N and 20-N loads cracks have been observed that allowed the calculation of a reliable load-independent value of fracture toughness, $K_{Ic} = 9.5\ \mathrm{MPa\ m}^{1/2}$. Nanoindentation measurements (Richter, Daghlian, Ries, & Solozhenko, 2006) have shown extremely high value of d-BC_5 nanohardness, i.e. 73 GPa.

At ambient pressure in nonoxidizing environment bulk diamond-like BC_5 remains stable up to 1890 K, and, hence, is characterized by 500-K higher thermal stability than nanocrystalline diamond with the same grain size. This can be attributed to the increase of decomposition activation barrier due to the presence of boron in the diamond lattice. At higher temperatures, d-BC_5 decomposes into disordered graphite and amorphous boron and/or boron carbides (Solozhenko, Kurakevych, Andrault, et al., 2009).

Thus, diamond-like BC_5 exhibits extreme hardness and unusually high for superhard materials fracture toughness, which in combination with high thermal stability makes it an exceptional superabrasive overcoming diamond (Solozhenko, Kurakevych, Andrault, Le Godec, & Mezouar, 2009).

3.25.3.2 Synthesis of Boron Subnitride $B_{13}N_2$

Boron-rich phases of the B–C–N–O system with an α-rhombohedral-boron-like structure (boron carbide B_4C, boron suboxide B_6O, etc.) combine high hardness and wear resistance, chemical inertness, high melting point as well as high cross-section for neutron absorption. Solid-state synthesis of boron subnitride, B_6N, as a result of chemical interaction between boron and boron nitride at 7.5 GPa and ~2000 K has been reported by Hubert, Garvie, Buseck, Petuskey, and McMillan (1997). However, a critical analysis of the results has shown that the evidence for the formation of boron subnitride with B_6O-like structure is inconclusive. Recently, Solozhenko, Le Godec, and Kurakevych (2006) have studied in situ the interaction between boron and BN at the same p–T conditions using X-ray diffraction with synchrotron radiation. At 7.4 GPa and temperatures up to 2000 K the formation of a new phase was not observed. At the same time, high pressure–high temperature treatment has resulted in strong and unpredictable preferred orientation of boron crystallites. This leads to the rise of some weak boron reflections that might be erroneously attributed to the appearance of a new phase. From these observations it can be concluded that the evidence for the solid-state synthesis of boron subnitride B_6N with B_6O-like structure previously reported by Hubert et al. (1997) is inconclusive.

Using X-ray diffraction with synchrotron radiation in a MAX80 multianvil high-pressure apparatus Solozhenko and Kurakevych (2008, 2009) have studied in situ chemical interaction and phase relations in the B–BN system at pressures up to 5.3 GPa and temperatures up to 2800 K. A new rhombohedral boron subnitride $B_{13}N_2$ has been synthesized by crystallization from the B–BN melt at 5 GPa. This new phase has been studied by powder X-ray diffraction (conventional and with synchrotron radiation), Raman spectroscopy, high-resolution transmission electron microscopy and EELS. The structure of $B_{13}N_2$ belongs to the R-3m space group ($a = 5.4585(8)$ Å, $c = 12.253(2)$ Å) and represents a new structural type produced by the distorted B_{12} icosahedra linked together by N–B–N chains and inter-icosahedral B–B bonds (**Figure 7**) (Kurakevych & Solozhenko, 2007). The Raman data (Solozhenko & Kurakevych, 2008, 2009) are consistent with the fact that the subnitride belongs to a group of boron-rich compounds with structures related to α-rhombohedral boron. The boron subnitride is an individual compound and not a solid solution, in contrast to boron carbide. The reliable composition of the phase obtained by the refinement of the starting B_4C-like unit cell makes $B_{13}N_2$ (Kurakevych & Solozhenko, 2007). The site occupancies of atoms of each type are close to unit, so the synthesized $B_{13}N_2$ phase is stoichiometric. Additionally, the formation of two other boron-rich B–N phases denoted as "B_6N" and "$B_{50}N_2$" has been observed (Solozhenko & Kurakevych, 2008, 2009). Their structures seem to be much more complicated and have not been resolved to present time.

Solozhenko, Kurakevych, Turkevich, and Turkevich (2009, 2010) have found that $B_{13}N_2$ is the only thermodynamically stable boron subnitride, while "$B_{50}N_2$" and "B_6N" are metastable. At 5 GPa, $B_{13}N_2$ melts

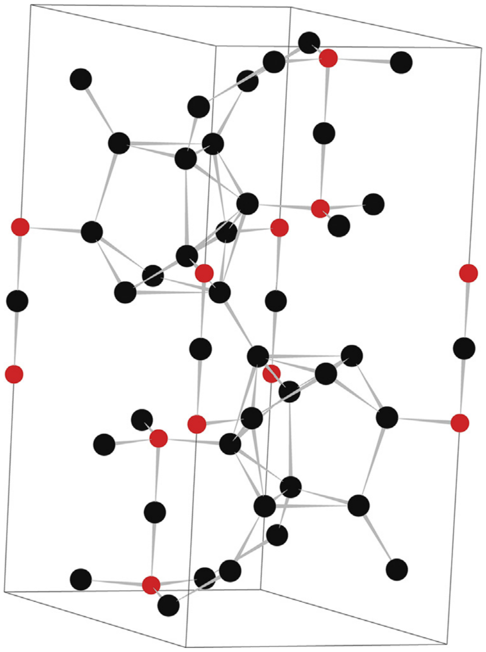

Figure 7 Crystal structure of rhombohedral $B_{13}N_2$ (Kurakevych & Solozhenko, 2007). The black and red balls represent the boron and nitrogen atoms, respectively.

incongruently at 2600 K and forms an eutectic equilibrium with boron. The equilibrium phase diagram of the B–BN system at 5 GPa (**Figure 8**) is characterized by the following nonvariant equilibria: $L + BN = B_{13}N_2$ of peritectic type at 2600 K; $L = \beta\text{-}B + B_{13}N_2$ of eutectic type at 2300 K; and $L = \beta\text{-}B + BN$ metastable eutectic at 2120 K that assures the appearance of the liquid phase, from which $B_{13}N_2$ crystallizes (Solozhenko et al., 2010).

The 300-K equation of state of $B_{13}N_2$ has been measured by Kurakevych and Solozhenko (2009) up to 30 GPa in DAC in neon pressure medium using angle-dispersive powder X-ray diffraction with synchrotron radiation. The value of bulk modulus, $B_0 = 200$ GPa, has been estimated by plotting the normalized pressure versus the Eulerian strain (the B_0' value was fixed to 4).

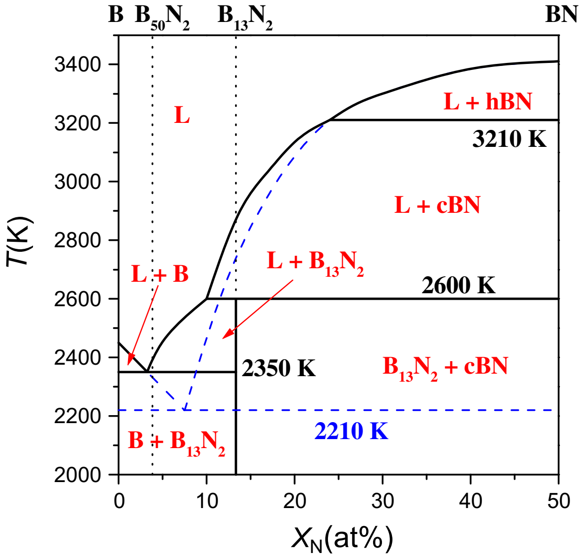

Figure 8 Phase diagram of the B–BN system at 5 GPa (Solozhenko et al., 2010). Solid lines show the equilibrium phase diagram; while dashed lines, metastable diagram.

According to the predictions made by Mukhanov et al. (2008b, 2009, 2010) in the framework of the thermodynamic model of hardness, the $B_{13}N_2$ subnitride is expected to exhibit microhardness of 40 GPa (**Figure 3**) comparable to those of commercial polycrystalline cBN.

3.25.4 Novel Superhard Diamond-like Ternary B–C–N Phases

3.25.4.1 Synthesis of Superhard Cubic BC_2N

Phase transitions of graphite-like BN–C solid solutions synthesized by the chemical route (Hubáček & Sato, 1995) have been studied by Solozhenko, Andrault, Fiquet, Mezouar, and Rubie (2001) up to 30 GPa and 3000 K using a laser-heated DAC and angle-dispersive X-ray diffraction with synchrotron radiation. A novel superhard phase, cubic BC_2N (c-BC_2N), was synthesized at pressures above 18 GPa and temperatures higher than 2200 K by direct solid-state phase transition of graphite-like $(BN)_{0.48}C_{0.52}$. At lower pressures, graphite-like BN–C solid solutions undergo segregation into cBN and diamond (or disordered graphite), and no formation of dense ternary B–C–N phase(s) is observed.

The diffraction patterns of c-BC_2N exhibit only *111*, *220*, and *311* Bragg reflections of the cubic lattice, which correspond to the Fd-$3m$ space group. The absence of the *200* reflection indicates that the atomic scattering factors of two *fcc* sublattices of the zinc-blende lattice are equal, which is possible only if B, C and N atoms are uniformly distributed over both sublattices. The lattice parameter of c-BC_2N at ambient conditions is $a = 3.642(2)$ Å (Solozhenko, 2002; Solozhenko, Andrault, et al., 2001), which was larger than those of both diamond (3.5667 Å, JCPDS No. 6-0675) and cBN (3.6158 Å, JCPDS No. 35-1365) (**Figure 9**). The large positive deviation of the lattice parameter of cubic BC_2N from the value expected from ideal mixing between diamond and cBN testifies that the synthesized phase is distinct from the so-called "diamond–cBN alloys" reported earlier by Knittle, Kaner, Jeanloz, and Cohen (1995).

To synthesize macroscopic (about 2 mm^3) samples of cubic BC_2N, Solozhenko, Andrault, et al. (2001) used a 6-8 type large-volume multianvil apparatus with a 5000-ton press at Bayerisches Geoinstitut. The diffraction patterns of the quenched samples showed the presence of a cubic phase with the lattice parameter of 3.640(4) Å that is very close to that of the DAC-synthesized c-BC_2N. From the full X-ray emission spectra of boron, carbon and nitrogen, the stoichiometry of the sample was determined to be $B_{0.4\pm0.1}C_{1.1\pm0.1}N_{0.5\pm0.1}$. Taking into account large errors when analyzing light elements, the phase stoichiometry can be assumed to be BC_2N.

According to analytical transmission electron microscopy, the grain size of cubic BC_2N ranged from 10 to 30 nm (Langenhorst & Solozhenko, 2002; Solozhenko, 2002). The largest grains were of a regular cubic or tetrahedral form, while fine grains were of a round form. Selected area electron diffraction patterns exhibit rings corresponding to the *111*, *220* and *311* reflections of the cubic phase. The absence of superstructure lines points to the statistically uniform distribution of B, C, and N atoms in the crystal lattice. Boron, carbon and

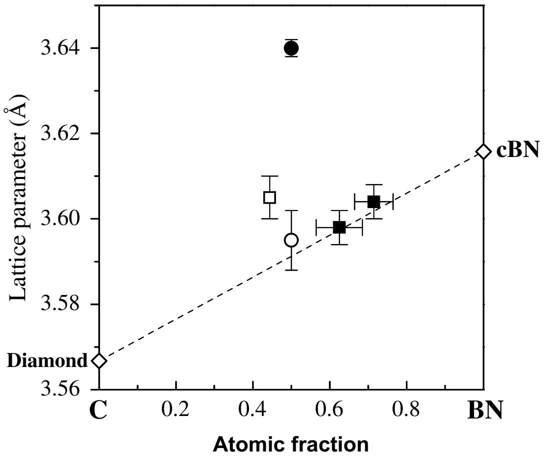

Figure 9 Lattice parameters of cubic BC_2N (Solozhenko, Andrault, et al., 2001) (solid circle), zinc-blende BC_2N (Zhao et al., 2002) (open circle), $BC_{2.5}N$ heterodiamond (Komatsu et al., 1999) (open square) and diamond-like BN–C solid solutions (Solozhenko, 2002) (solid squares). The dashed line represents ideal mixing between diamond and cubic boron nitride.

nitrogen *K*-edge EELS spectra of cubic BC_2N have been studied by Langenhorst and Solozhenko (2002). The presence of characteristic δ^* peaks in the electron energy-loss near-edge structure spectra reveals an sp^3 type atomic bonding and gives clear evidence for the formation of diamond-like B–C–N ternary phase. The granular structure of bulk *c*-BC_2N has been investigated by atomic force microscopy. The average size of grains observed in the AFM images was measured to be about 200 nm. The grains have the fine structure that can be attributed to small crystallites of 20–30 nm, which are combined into larger aggregates (Zinin, Solozhenko, Malkin, & Ming, 2005).

A broad Raman band corresponding to sp^3-coordinated atoms (diamond-like structure) can be seen in spectra of cubic BC_2N excited with UV ($\lambda = 228.9$ nm) and visible ($\lambda = 488$ nm) lasers (Hubble et al., 2004). Position of the Raman band measured with UV laser excitation was found to be 1324.8(6) cm^{-1} and was consistent with the position of the peak provided by visible laser, 1326.3(19) cm^{-1}. Combining all measurements together gives a mean Raman shift of 1325.7(16) cm^{-1}. This position of the Raman band is located between the Raman peaks of diamond and cBN, and that can be attributed to LO mode of *c*-BC_2N phase. The large width (FWHM is about 25 cm^{-1}) of the observed Raman band most likely reflects random substitution of carbon atoms by boron and nitrogen in the diamond lattice.

The 300-K equation of state of cubic BC_2N was measured by Solozhenko, Andrault, et al. (2001) up to 30 GPa using DAC and angle-dispersive X-ray diffraction with synchrotron radiation. The experimental p–V data were fitted to the Birch equation of state. The parameters obtained were $B_0 = 282$ GPa and $B_0' = 4.3$, with the zero-pressure cell volume $V_0 = 48.49$ Å^3. The bulk modulus of cubic BC_2N is smaller than the 420 GPa value expected from ideal mixing between diamond and cBN, and is in agreement with the 259 GPa value obtained by Brillouin scattering (Tkachev, Solozhenko, Zinin, Manghnani, & Ming, 2003).

Micro- and nanoindentation were used by Solozhenko, Andrault, et al. (2001), Solozhenko, Dub, and Novikov (2001) to examine the mechanical properties of *c*-BC_2N. The nanohardness and Young modulus were calculated from the load-displacement curves according to the Oliver–Pharr method. The values of nanohardness ($H_N = 75$ GPa) and elastic moduli (E, G) of *c*-BC_2N as well as Vickers ($H_V = 76$ GPa) and Knoop ($H_K = 55$ GPa) microhardness are intermediate between those of diamond and cBN that makes cubic BC_2N the second hardest known material (**Figures 3** and **10**). The elastic recovery of *c*-BC_2N has been found to be 68% which is higher than the corresponding value for cBN (60%), and is approaching that of diamond.

Using the platelet scattering geometry Brillouin scattering measurements on cubic BC_2N have been successfully performed by Tkachev et al. (2003). The azimuth dependencies of longitudinal (V_L) and shear (V_S) velocities do not show any velocity anisotropy and therefore provide evidence that the nanocrystalline cubic BC_2N is elastically isotropic. From the $V_L = 13.09$ km/s and $V_S = 8.41$ km/s values, the bulk and shear moduli

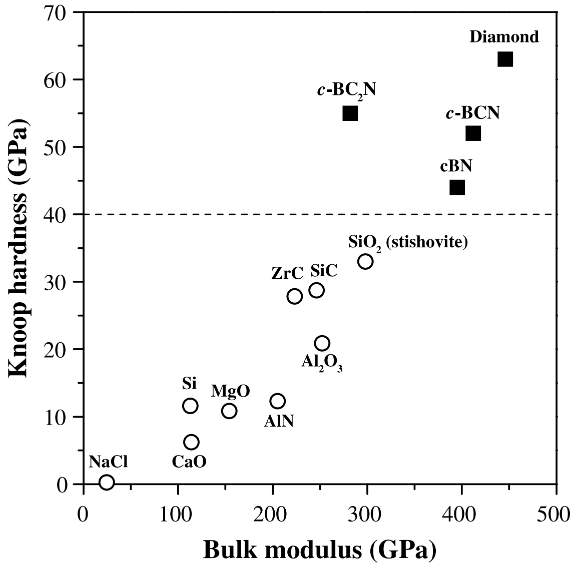

Figure 10 Knoop hardness versus bulk modulus for superhard phases of the B–C–N–O quaternary system (black symbols) and some other materials.

of cubic BC_2N have been calculated as 259 and 238 GPa, respectively. The shear modulus of 447 GPa evaluated earlier by Solozhenko, Dub, et al. (2001) from the load-displacement curves is most likely an overestimate due to distinct deformation of the diamond indenter during nanohardness measurements.

Thus, cubic BC_2N phase has an unusual combination of mechanical properties: its elastic moduli measured by Brillouin scattering and X-ray diffraction are lower than those of cBN, whereas its hardness measured independently by micro- and nanoindentation techniques is higher than that of single-crystal cBN and only slightly lower than that of diamond.

The thermal stability of cubic BC_2N in a high-purity argon atmosphere at ambient pressure has been studied by Solozhenko and Andrault (unpublished results) using energy-dispersive X-ray diffraction with synchrotron radiation. It was found that *c*-BC_2N remains stable up to 1800 K, and, hence, is characterized by a higher thermal stability than polycrystalline diamond with the same grain size. Studies of the thermal stability of *c*-BC_2N in the 25–32 GPa pressure range using laser-heated DAC and X-ray diffraction with synchrotron radiation have shown that at temperatures above 2900 K this phase decomposes into diamond and cBN (Solozhenko, 2002).

Successful synthesis of nanostructured bulk zinc-blende BC_2N material from ball-milled mixture of graphite and hexagonal boron nitride, at 20 GPa and 2200–2250 K, has been reported by Zhao et al. (2002). The final products were well-sintered translucent chunks with nominal Vickers hardness of 62 GPa. According to high-resolution transmission electron microscopy, the synthesized BC_2N samples were nanocrystalline with a grain size of about 5 nm, whereas grain boundaries between nanocrystallites appeared to be amorphous. The diffraction pattern of the crystalline BC_2N is consistent with a face-centered cubic zinc-blende structure with lattice parameter $a = 3.595$ Å which is in a good agreement with Vegard's law and differs significantly from the lattice parameter of cubic BC_2N synthesized by Solozhenko, Andrault, et al. (2001) (**Figure 9**).

First-principle calculations have been performed by Kim, Pang, Utsumi, Solozhenko, and Zhao (2007) to identify different phases of cubic BC_2N synthesized experimentally. With a proper choice of the supercell, cutoff energy and sampling *k* points, the cubic phases were found to be theoretically stable. The bulk modulus from elastic stiffness constants for each of the phases (high-density phase with C–B–N layered superstructure, high-density phase without any C–B–N layers, and low-density phase; all the phases are defect-free and do not possess any B–B or N–N bond) is in excellent agreement with available experimental data. The low-density phase synthesized by Solozhenko, Andrault, et al. (2001) is characterized by the absence of C–C bonds, whereas the high-density phase synthesized by Zhao et al. (2002) is characterized by the existence of C–C bonds. From the calculated equation of state and available experimental data, it has been found that the unique feature of each of the cubic BC_2N phases is a direct result of the corresponding local electronic structure and chemical bonding in the system.

Elastic moduli and strength of nanocrystalline zinc-blende BC_2N under nonhydrostatic compression up to 100 GPa have been recently studied by Dong, He, Duffy, and Zhao (2009) using DAC and X-ray diffraction with synchrotron radiation. It was found that the material could support a maximum differential stress of 38 GPa when it started to yield at about 66 GPa under uniaxial compression.

3.25.4.2 Shock-Compression Synthesis of Diamond-like BN–C Solid Solutions

Komatsu, Samedima, Awano, Kakadate, and Fujiwara (1999) reported synthesis of B–C–N heterodiamond of the $BC_{2.5}N$ stoichiometry from graphitic B–C–N precursors in a copper matrix at 50 GPa and 3500 K using the cylindrical shock-compression apparatus and AN-TNT explosives. The X-ray diffraction patterns indicate a cubic system with a lattice parameter of 3.605 Å which is close to that of cBN (3.6158 Å, JCPDS No. 35-1365) (**Figure 9**). The recovered powders were nanocrystalline with grain size of 5–20 nm and oxidation resistance close to that of diamond. The authors were unable to measure the hardness of the material, but from the estimated bulk modulus (401 GPa) they claimed its superhardness and even suggested that B–C–N heterodiamond is the hardest material next to diamond.

Shock-compression synthesis of diamond-like B–C–N phases has been performed by Kurdyumov et al. (2000) and Solozhenko (2002) using cylindrical recovery containers with a ring gap that allowed concentration of explosion energy in a given direction and multiple reflection of shock waves at the walls of the container. The incident shock pressures on the samples was controlled by choosing an explosive, RDX–TNT (Kurdyumov et al., 2000) or RDX–ANFO or different compositions of RDX–Nobelit 100 (Solozhenko, 2002). The use of the special additive that is characterized by a high shock temperature and a high compressibility, allowed a sample heating up to 3500 K, and its abrupt ($\sim 10^8$ K s^{-1}) cooling at decompression.

Solozhenko (2002) found that shock compression of graphite-like $(BN)_xC_{1-x}$ ($0.48 \leq x \leq 0.61$) solid solutions resulted in the formation of diamond-like phases, and that the content of the recovered samples drastically increased with pressure and attains 80 wt% at 30 GPa. According to electron microprobe analysis, diamond-like phases of $BC_{1.2\pm0.2}N$ and $BC_{0.9\pm0.2}N$ stoichiometries were synthesized, provided that graphite-like $(BN)_{0.48}C_{0.52}$ and $(BN)_{0.61}C_{0.39}$, respectively were used as starting materials. Taking into account considerable errors in determination of light elements, the stoichiometry of both phases might be assumed to be BCN.

X-ray diffraction patterns of diamond-like BCN exhibit *111*, *220* and *311* reflections of the cubic lattice while the *200* reflection was missing. The latter indicates that B, C and N atoms are statistically uniformly distributed over crystal lattice due to extremely high temperatures achieved in the experiments. From the profile analysis of *220* and *311* lines of both cubic BCN phases it follows that the experimentally observed diffraction patterns are attributable to the diamond-like BN–C uniform solid solutions, and not to a mechanical mixture of diamond and cBN (Kurdyumov et al., 2000).

The lattice parameters of c-$BC_{1.2\pm0.2}N$ and c-$BC_{0.9\pm0.2}N$ have been found to be 3.598 and 3.604 Å, respectively (Solozhenko, 2002), and are in a good agreement with corresponding values that should be expected from ideal mixing between diamond and cBN (**Figure 9**).

According to analytical transmission electron microscopy studies (Langenhorst & Solozhenko, 2002; Solozhenko, 2002), a mean grain size of both c-BCN phases is about 5 nm. The coarsest grains are of a tetrahedron habit, while fine grains are of a round shape. Selected area electron diffraction patterns are fully consistent with diamond-like BN–C solid solutions. A superstructure was not observed, indicating that B, C and N atoms are randomly distributed in the crystal lattice. The stoichiometry of c-BCN phases was estimated from the BK, CK, and NK EELS spectra, and found to be BCN in both cases.

The 300-K equation of state of c-$BC_{0.9\pm0.2}N$ was measured by Solozhenko (2002) up to 45 GPa using DAC and energy-dispersive X-ray diffraction. The experimental p–V data were fitted to the Birch–Murnaghan equation of state. The parameters of the fit were $B_0 = 412$ GPa and $B_0' = 4.3$. The bulk modulus of c-BCN is higher than that of cBN (395 GPa, Datchi et al. 2007), and is close to the 420 GPa value that is expected from ideal mixing between diamond and cBN. Thus, the synthesized diamond-like BN-C solid solution has one of the largest bulk moduli known for superhard phases, being second only to diamond (446 GPa; Gillet et al., 1999).

Knoop hardness of bulk c-BCN sample sintered from shock-synthesized c-$BC_{0.9\pm0.2}N$ powder at high pressures and temperatures makes 52 GPa (Solozhenko, 2002) which is only slightly lower than that of cubic BC_2N (Solozhenko, Andrault, et al., 2001; Solozhenko, Dub, et al., 2001) (**Figure 10**).

Thus, shock compression of graphite-like BN–C solid solutions to 30 GPa and 3500 K results in formation of the ideal cubic BN–C solid solution with the stoichiometry close to BCN and statistically uniform atom distribution. This new cubic BCN phase is characterized by the very high values of bulk modulus and Knoop hardness.

3.25.5 Conclusions

The possibility to synthesize novel superhard phases—both thermodynamically stable (orthorhombic γ-B28 and rhombohedral $B_{13}N_2$) and metastable ones (diamond-like BC_5 and cubic ternary B–C–N phases) using modern high-pressure tools (DAC, multianvil press and shock compression) has been discussed. Complete recovery of the synthesized products to ambient conditions will eventually lead to the development of new technological materials.

References

Brazhkin, V., Dubrovinskaia, N., Nicol, M., Novikov, N., Riedel, R., Solozhenko, V., et al. (2004). What does “harder than diamond” mean? *Nature Materials, 3*, 576–577.

Datchi, F., Dewaele, A., Le Godec, Y., & Loubeyre, P. (2007). Equation of state of cubic boron nitride at high pressures and temperatures. *Physical Review B, 75*, 214104.

DeVries, R. C. (1972). *Cubic boron nitride: Handbook of properties*. General Electric Technical Information Series No. 72CRD178. Schenectady: GE Co R&D.

Dong, H., He, D., Duffy, T. S., & Zhao, Y. (2009). Elastic moduli and strength of nanocrystalline cubic BC_2N from x-ray diffraction under nonhydrostatic compression. *Physical Review B, 79*, 014105.

Edgar, J. H. (1994). Crystal structure, mechanical properties and thermal properties of BN. In J. H. Edgar (Ed.), *Properties of group III nitrides* (pp. 7–21). London: INSPEC.

Emsley, J. (1991). *The elements*. Oxford: Clarendon Press.

Gillet, Ph., Fiquet, G., Daniel, I., & Reynard, B. (1999). Equations of state of ^{12}C and ^{13}C diamond. *Physical Review B, 60*, 14660–14664.

Hubáček, M., & Sato, T. (1995). Preparation and properties of a compound in the B–C–N system. *Journal of Solid State Chemistry, 114*, 258–264.

Hubble, H. W., Kudryashov, I., Solozhenko, V. L., Zinin, P. V., Sharma, S. K., & Ming, L. C. (2004). Raman studies of cubic BC_2N, a new superhard phase. *Journal of Raman Spectroscopy, 35*, 822–825.

Hubert, H., Garvie, L. A. J., Buseck, P. R., Petuskey, W. T., & McMillan, P. F. (1997). High-pressure, high-temperature syntheses in the B–C–N–O system. *Journal of Solid State Chemistry, 133*, 356–364.

Isaev, E. I., Simak, S. I., Mikhaylushkin, A. S., Vekilov, Y. K., Zarechnaya, E. Y., Dubrovinsky, L., et al. (2011). Impact of lattice vibrations on equation of state of the hardest boron phase. *Physical Review B, 83*, 132106.

Kim, E., Pang, T., Utsumi, W., Solozhenko, V. L., & Zhao, Y. (2007). Cubic phases of BC_2N: a first-principles study. *Physical Review B, 75*, 184115.

Knittle, E., Kaner, R. B., Jeanloz, R., & Cohen, M. L. (1995). High-pressure synthesis, characterization, and equation of state of cubic C–BN solid solutions. *Physical Review B, 51*, 12149–12156.

Komatsu, T., Samedima, M., Awano, T., Kakadate, Y., & Fujiwara, S. (1999). Creation of superhard B–C–N heterodiamond using shock wave compression technology. *Journal of Materials Processing Technology, 85*, 69–73.

Kurakevych, O. O., & Solozhenko, V. L. (2007). Rhombohedral boron subnitride, $B_{13}N_2$, by X-ray powder diffraction. *Acta Crystallographica, Section C, 63*, i80–i82.

Kurakevych, O. O., & Solozhenko, V. L. (2009). 300-K equation of state of rhombohedral boron subnitride, $B_{13}N_2$. *Solid State Communications, 149*, 2169–2171.

Kurakevych, O. O., & Solozhenko, V. L. (2011). High-pressure route to superhard boron-rich solids. *High Pressure Research, 31*, 48–52.

Kurakevych, O. O., & Solozhenko, V. L. (2011). Experimental study and critical review of structural, thermodynamic and mechanical properties of superhard refractory boron suboxide, B_6O. *Journal of Superhard Materials, 33*, 421–428.

Kurdyumov, A. V., Solozhenko, V. L., Hubaček, M., Borimchuk, N. I., Zelyavskii, W. B., Ostrovskaya, N. F., et al. (2000). Shock synthesis of ternary diamond-like phases in the B–C–N system. *Powder Metallurgy and Metal Ceramics, 39*, 467–473.

Langenhorst, F., & Solozhenko, V. L. (2002). ATEM-EELS study of new diamond-like phases of the B–C–N system. *Physical Chemistry Chemical Physics, 4*, 5183–5188.

Le Godec, Y. (2011). Comparative review of theoretical and experimental equations of state of orthorhombic boron γ-B_{28}. *Journal of Superhard Materials, 33*, 388–393.

Le Godec, Y., Kurakevych, O. O., Munsch, P., Garbarino, G., & Solozhenko, V. L. (2009). Equation of state of orthorhombic boron, γ-B_{28}. *Solid State Communications, 149*, 1356–1358.

Li, Q., Wang, H., Tian, Y., Xia, Y., Cui, T., He, J., et al. (2010). Superhard and superconducting structures of BC_5. *Journal of Applied Physics, 108*, 023507.

Lowther, J. E. (2005). Potential super-hard phases and the stability of diamond-like boron-carbon structures. *Journal of Physics: Condensed Matter, 17*, 3221–3229.

Macchi, P. (2011). On the nature of chemical bonding in γ-boron. *Journal of Superhard Materials, 33*, 380–387.

Mukhanov, V. A., Kurakevych, O. O., & Solozhenko, V. L. (2008a). Thermodynamic aspects of materials' hardness: prediction of novel superhard high-pressure phases. *High Pressure Research, 28*, 531–537.

Mukhanov, V. A., Kurakevych, O. O., & Solozhenko, V. L. (2008b). The interrelation between hardness and compressibility of substances and their structure and thermodynamic properties. *Journal of Superhard Materials, 30*, 368–378.

Mukhanov, V. A., Kurakevych, O. O., & Solozhenko, V. L. (2009). Hardness of materials at high temperature and high pressure. *Philosophical Magazine, 89*, 2117–2127.

Mukhanov, V. A., Kurakevych, O. O., & Solozhenko, V. L. (2010). Thermodynamic model of hardness: particular case of boron-rich solids. *Journal of Superhard Materials, 32*, 167–176.

Oganov, A. R., Chen, J., Gatti, C., Ma, Y., Ma, Y., Glass, C. W., et al. (2009a). Ionic high-pressure form of elemental boron. *Nature, 457*, 863–867.

Oganov, A. R., Chen, J., Gatti, C., Ma, Y., Ma, Y., Glass, C. W., et al. (2009b). Addendum: ionic high-pressure form of elemental boron. *Nature, 460*, 292.

Oganov, A. R., & Solozhenko, V. L. (2009). Boron: a hunt for superhard polymorphs. *Journal of Superhard Materials, 31*, 285–291.

Oganov, A. R., Solozhenko, V. L., Gatti, C., Kurakevych, O. O., & Le Godec, Y. (2011). The high-pressure phase of boron, γ-B_{28}: Disputes and conclusions of 5 years after discovery. *Journal of Superhard Materials, 33*, 363–379.

Richter, A., Daghlian, C. P., Ries, R., & Solozhenko, V. L. (2006). Investigation of novel superhard materials by multi-cycling nanoindentation. *Diamond and Related Materials, 15*, 2019–2023.

Segall, D. E., & Arias, T. A. (2003). Ab initio approach for high-pressure systems with application to high-pressure phases of boron: perturbative momentum-space potentials. *Physical Review B, 67*, 064105.

Solozhenko, V. L. (2002). Synthesis of novel superhard phases in the B–C–N system. *High Pressure Research, 22*, 519–524.

Solozhenko, V. L., & Andrault, D. (unpublished results).

Solozhenko, V. L., Andrault, D., Fiquet, G., Mezouar, M., & Rubie, D. C. (2001). Synthesis of superhard cubic BC_2N. *Applied Physics Letter, 78*, 1385–1387.

Solozhenko, V. L., Dub, S. N., & Novikov, N. V. (2001). Mechanical properties of cubic BC_2N, a new superhard phase. *Diamond and Related Materials, 10*, 2228–2231.

Solozhenko, V. L., Dubrovinskaia, N. A., & Dubrovinsky, L. S. (2004). Synthesis of bulk superhard semiconducting B–C material. *Applied Physics Letter, 85*, 1508–1510.

Solozhenko, V. L., & Kurakevych, O. O. (2008). New boron subnitride $B_{13}N_2$: HP-HT synthesis, structure and equation of state. *Journal of Physics: Conference Series, 121*, 062001.

Solozhenko, V. L., & Kurakevych, O. O. (2009). Chemical interaction in the B–BN system at high pressures and temperatures. Synthesis of novel boron subnitrides. *Journal of Solid State Chemistry, 182*, 1359–1364.

Solozhenko, V. L., Kurakevych, O. O., Andrault, D., Le Godec, Y., & Mezouar, M. (2009). Ultimate metastable solubility of boron in diamond: synthesis of superhard diamondlike BC_5. *Physical Review Letter, 102*, 015506.

Solozhenko, V. L., Kurakevych, O. O., Andrault, D., Mezouar, M., & Le Godec, Y. (2007). Patent FR 2914918 Carbure de bore et son procédé de fabrication.

Solozhenko, V. L., Kurakevych, O. O., & Oganov, A. R. (2008). On the hardness of a new boron phase, orthorhombic γ-B_{28}. *Journal of Superhard Materials, 30*, 428–429.

Solozhenko, V. L., Kurakevych, O. O., Turkevich, V. Z., & Turkevich, D. V. (2009). On the problem of the phase relations in the B–BN system at high pressures and temperatures. *Journal of Superhard Materials, 31*, 1–6.

Solozhenko, V. L., Kurakevych, O. O., Turkevich, V. Z., & Turkevich, D. V. (2010). Phase diagram of the B–BN system at 5 GPa. *Journal of Physical Chemistry B, 114*, 5819–5822.

Solozhenko, V. L., Le Godec, Y., & Kurakevych, O. O. (2006). Solid-state synthesis of boron subnitride, B_6N: myth or reality? *Comptes Rendus Chimie, 9*, 1472–1475.

Sumiya, H., & Irifune, T. (2004). Indentation hardness of nano-polycrystalline diamond prepared from graphite by direct conversion. *Diamond and Related Materials, 13*, 1771–1776.

Sumiya, H., Toda, N., & Satoh, S. (1997). Mechanical properties of synthetic type IIa diamond crystal. *Diamond and Related Materials, 6*, 1841–1846.

Tkachev, S. N., Solozhenko, V. L., Zinin, P. V., Manghnani, M. H., & Ming, L. C. (2003). Elastic moduli of the superhard cubic BC_2N phase by Brillouin scattering. *Physical Review B, 68*, 052104.

Zarechnaya, E. Y., Dubrovinskaia, N., Dubrovinsky, L., Filinchuk, Y., Chernyshov, D., & Dmitriev, V. (2010). Growth of single crystals of B_{28} at high pressures and high temperatures. *Journal of Crystal Growth, 312*, 3388–3394.

Zarechnaya, E. Y., Dubrovinsky, L., Dubrovinskaia, N., Filinchuk, Y., Chernyshov, D., Dmitriev, V., et al. (2009). Superhard semiconducting optically transparent high pressure phase of boron. *Physical Review Letter, 102*, 185501.

Zhao, Y., He, D. W., Daemen, L. L., Shen, T. D., Schwarz, R. B., Zhu, Y., et al. (2002). Superhard B–C–N materials synthesized in nanostructured bulks. *Journal of Materials Research, 17*, 3139–3145.

Zinin, P. V., Solozhenko, V. L., Malkin, A. J., & Ming, L. C. (2005). Atomic force microscopy studies of cubic BC_2N, a new superhard phase. *Journal of Materials Science, 40*, 3009–3011.

INDEX

Note: Page numbers followed by "f" denote figures; "t" tables.